VI International Conference on Particle-Based Methods. Fundamentals and Applications

PARTICLES 2019

28-30 October, 2019
Barcelona, Spain

E. Oñate, P. Wriggers, T. Zohdi, M. Bischoff and D.R.J. Owen (Eds.)

VI International Conference on PARTICLE-BASED METHODS. Fundamentals and Applications

PARTICLES 2019

28 – 30 October 2019
Barcelona, Spain

A publication of:

TABLE OF CONTENTS

PREFACE

This volume contains the full papers presented at the VI International Conference on Particle-based Methods (PARTICLES 2015), held in Barcelona on 28 - 30 Ocober, 2019. The fifth previous conferences of the series were held in Barcelona, Spain, in the years 2009 and 2011, and in Stuttgart, Germany, in September 2013, in Barcelona on 2015, and in Hannover 2017.

Particles 2019 addresses fundamentals and applications of particle-based computational methods, including both *discrete* modeling concepts and *discretization* methods. A total of 246 lectures, including 7 plenary lectures and 12 invited sessions cover discrete element methods, smoothed particle hydrodynamics, material point methods, moving particle simulations and meshless methods as well as aspects of parallel computing for solid und fluid mechanics, multi-scale and multi-phase problems, damage, fracture and fragmentation, granular materials, soft matter, geo- and bio-mechanics, micro-macro transitions, coupling of discrete and continuous models and discretizations, fluid-structure interaction and industrial applications.

The conference is held under the auspices of the European Community on Computational Methods in Applied Sciences (ECCOMAS) and the International Association for Computational Mechanics (IACM). The organizers would like to thank all the participants and the supporting organizations for their help in making PARTICLES 2019 possible.

PARTICLES 2019 Organizers

Eugenio Oñate (Chair)
CIMNE / Universitat Politècnica de Catalunya (UPC)
Barcelona, Spain

| **M. Bischoff** | **D.R.J. Owen** |
| *Universität Stuttgart, Germany* | *Swansea University, United Kingdom* |

| **P. Wriggers** | **T. Zohdi** |
| *Leibniz Universität Hannover, Germany* | *University of California, Berkeley, USA* |

ACKNOWLEDGEMENTS

The conference organizers acknowledge the support towards the organization of PARTICLES 2017 to the following organizations:

International Center for Numerical Methods in Engineering (CIMNE)

Universitat Politècnica de Catalunya (UPC)

Leibniz Universität Hannover

European Community on Computational Methods in Applied Sciences (ECCOMAS)

International Association for Computational Mechanics (IACM)

Computational Particle Mechanics, a Springer Journal

We thank the **Plenary Speakers**, the **Invited Sessions Organizers** and the **Authors** for their help in the setting up of a high standard Scientific Programme.

SUMARY

INVITED SESSIONS

CONTRIBUTED SESSIONS

CONTENTS

INVITED SESSIONS

IS - Engineering Applications with Smoothed Particle Hydrodynamics

IS - Fracture and Fragmentation with DEM

IS - Granular Plasticity

IS - Micro-Macro: From Particles to Continuum

IS - New advances on SPH method: Algorithms and Applications

IS - Parallel Algorithms for Particle Systems

IS - Particle-Based Methods for the Simulation of Natural Hazards

IS - Vortex Particle Method in Fluid Dynamics

CONTRIBUTED SESSIONS

CS - Bio Medical Engineering

CS - Discrete / Distinct Element Method (DEM) I

CS - Geomechanics

CS - High Performance Computing

CS - Industrial Applications

CS - Lattice-Boltzmann Method (LBM)

CS - Material Point Method (MPM)

CS - Meshless methods

CS - Mining engineering

CS - Moving Particle Simulation (MPS) Methods

CS - Multiphase Flows

CS - Smoothed Particles Hydrodynamics (SPH)

CS - Structural Damage

LECTURES

HEADWAY IN LARGE-EDDY-SIMULATION WITHIN THE SPH MODELS

M. Antuono[1], A. Di Mascio[2], S. Marrone[1], D.D. Meringolo[1] and A. Colagrossi[1,3]

[1] Consiglio Nazionale delle Ricerche - Istituto di iNgegneria del Mare (CNR - INM)
Via di Vallerano 139, 00128, Rome, Italy,
e-mail: matteo.antuono@cnr.it, salvatore.marrone@cnr.it, andrea.colagrossi@cnr.it

[2] Dipartimento di Ingegneria Industriale e dell'Informazione e di Economia (DIIIE)
University of l'Aquila, Via Giovanni Gronchi 18, 67100, l'Aquila, Italy

[3] Ecole Centrale Nantes, LHEEA research dept. (ECN and CNRS), Nantes, France

Key words: Smoothed Particle Hydrodynamics, Large Eddy Simulation, Turbulence, Particle Methods

Abstract. In the present paper we show some preliminary results of a novel LES-SPH scheme that extends and generalizes the approach described in [2]. Differently from that work, the proposed scheme is based on the definition of a Quasi-Lagrangian Large-Eddy-Simulation model where a small velocity deviation is added to the actual fluid velocity. When the LES equations are rearranged in the SPH framework, the velocity deviation is modelled through the Particle Shifting Technique (PST), similarly to the δplus-SPH scheme derived in [3]. The use of the PST allows for regular particle distributions, reducing the numerical errors in the evaluation of the spatial differential operators. As a preliminary study of the proposed model, we consider the evolution of freely decaying turbulence in 2D. In particular we show that the present scheme predicts the correct tendencies for the direct and inverse energy cascades.

1 INTRODUCTION

In the last years an increasing number of papers have been dedicated to the extension of the Smoothed Particle Hydrodynamics (SPH) to model problems characterized by turbulent flows [13, 17, 18, 16]. Among the different approaches, the Large-Eddy-Simulation appears as the most suited method to be included in the SPH framework, being based on a filtering of the Navier-Stokes equations that resembles that adopted for the derivation of the smoothed differential operators of the SPH. The present work follows the above-mentioned line of research and extends and generalizes the approach described in [2] where a Lagrangian LES-SPH scheme was proposed. Specifically, the proposed scheme is based on the definition of a Quasi-Lagrangian Large-Eddy-Simulation

model where a small velocity deviation is added to the actual fluid velocity. This approach allows us to cast the LES in the framework of the most advanced SPH schemes which rely on a quasi-Lagrangian motion of the fluid particles [19, 20]. In particular, when the LES equations are rearranged in the SPH formalism, the velocity deviation is modelled through the Particle Shifting Technique (PST), similarly to the δplus-SPH scheme derived in [3]. The latter technique proved to be a crucial numerical tool to obtain regular particle distributions, reducing the numerical errors in the evaluation of the spatial differential operators.

The presence of the velocity deviation with respect to the actual fluid velocity leads to the appearance of additional terms in the continuity and momentum equations of the proposed LES-SPH scheme that need proper turbulence closures. Specifically, the term in the momentum equation is represented through a classical LES closure while that in the continuity equation is modelled through the diffusive term of the δ-SPH scheme (see, for example, [1]).

The paper is organized as follows: section §2 briefly introduces the theoretical model and corresponding the numerical scheme and section §3 shows the preliminary results obtained for the evolution of freely decaying turbulence in 2D.

2 QUASI-LAGRANGIAN δLES-SPH

Let us consider the Navier-Stokes equations for a barotropic weakly-compressible Newtonian fluid:

$$\begin{cases} \rho_t \,+\, \nabla \cdot (\rho\, \boldsymbol{u}) \,=\, 0\,, \\[2mm] \boldsymbol{u}_t \,+\, (\boldsymbol{u} \cdot \nabla)\, \boldsymbol{u} \,=\, -\,\frac{\nabla p}{\rho} \,+\, \nu \Delta \boldsymbol{u} \,+\, (\lambda' + \nu)\, \nabla \left(\nabla \cdot \boldsymbol{u}\right), \end{cases} \tag{1}$$

where $\boldsymbol{u}$ is the flow velocity, p and ρ denote the pressure and density fields respectively and are related through a state equation, namely $p = F(\rho)$. The hypothesis that the fluid is weakly-compressible corresponds to assume:

$$\frac{dp}{d\rho} \,=\, c^2 \,\gg\, \max\left(\|\boldsymbol{u}\|^2, \frac{\delta p}{\rho}\right), \tag{2}$$

where δp indicates the variation of the pressure field and $c = c(\rho)$ is the sound speed (see e.g. [5, 4]). The viscosity coefficients ν, λ' indicate the ratios between the Lamé constants μ, λ and the density ρ. Since the fluid is weakly-compressible, ν and λ' are assumed constant. Now, let us define a generic filter in $\mathbb{R}^3 \times \mathbb{R}$ as follows:

$$\phi = \phi\left(\tilde{\boldsymbol{x}}_p(t) - \boldsymbol{y}, t - \tau\right). \tag{3}$$

The above filter is supposed to have a compact support, to depend only on $\|\tilde{\boldsymbol{x}}_p(t) - \boldsymbol{y}\|$ and $|t - \tau|$, and to be an even function with respect to both arguments. Here $\tilde{\boldsymbol{x}}_p(t)$ indicates the position of a *quasi-lagrangian* point that moves in the fluid domain according to the

following equation:

$$\frac{d\tilde{\boldsymbol{x}}_p}{dt} = \tilde{\boldsymbol{u}}(\,\tilde{\boldsymbol{x}}_p(t),t\,) + \delta\tilde{\boldsymbol{u}}(\,\tilde{\boldsymbol{x}}_p(t),t\,)\,, \tag{4}$$

where $\delta\tilde{\boldsymbol{u}}$ is a (small) arbitrary velocity deviation (to be specified later) while $\tilde{\boldsymbol{u}}$ is given by the following definition:

$$\tilde{\boldsymbol{u}}(\,\tilde{\boldsymbol{x}}_p(t),t\,) = \int_{\mathbb{R}^3}\int_{-\infty}^{+\infty}\phi\,(\,\tilde{\boldsymbol{x}}_p(t)-\boldsymbol{y},t-\tau\,)\,\boldsymbol{u}(\boldsymbol{y},\tau)\,d\tau\,dV_y\,. \tag{5}$$

Hereinafter, we refer to $\tilde{\boldsymbol{x}}_p$ and $\tilde{\boldsymbol{u}}$ as the filtered position and velocity, respectively. Accordingly, the main idea is to rewrite the system (2) in terms of the filtered quantities and obtain a quasi-Lagrangian LES scheme. With respect to this point, we observe that, since the state equation is generally nonlinear, $\widetilde{F(\rho)}$ is different from $F(\tilde{\rho})$ and, consequently, the filtering procedure cannot be applied to both pressure and density. To avoid inconsistency, when we refer to *filtered* pressure we mean $\tilde{p} = F(\tilde{\rho})$. Under this hypothesis, we apply the filter in (3) to the Navier-Stokes equations for weakly-compressible flows and, integrating over $\mathbb{R}^3 \times \mathbb{R}$, we obtain:

$$
\begin{cases}
\dfrac{d\tilde{\rho}}{dt} = -\tilde{\rho}\,\nabla\cdot(\,\tilde{\boldsymbol{u}}+\delta\tilde{\boldsymbol{u}}\,) + \nabla\cdot(\,\tilde{\rho}\tilde{\boldsymbol{u}}-\widetilde{\rho\boldsymbol{u}}\,) + \nabla\cdot(\,\tilde{\rho}\,\delta\tilde{\boldsymbol{u}}\,)\,, \\[2mm]
\dfrac{d\tilde{\boldsymbol{u}}}{dt} = -\dfrac{\nabla\tilde{p}}{\tilde{\rho}} + \nu\Delta\tilde{\boldsymbol{u}} + (\lambda'+\nu)\,\nabla\,(\nabla\cdot\tilde{\boldsymbol{u}}) - \nabla\left[\widetilde{G(\rho)}-G(\tilde{\rho})\right] + \nabla\cdot\mathbb{T}_\ell \\[2mm]
\quad + \widetilde{\boldsymbol{u}\,\nabla\cdot\boldsymbol{u}} + \nabla\cdot(\,\tilde{\boldsymbol{u}}\otimes\delta\tilde{\boldsymbol{u}}\,) - \tilde{\boldsymbol{u}}\,(\nabla\cdot\delta\tilde{\boldsymbol{u}})\,, \\[2mm]
\dfrac{d\tilde{\boldsymbol{x}}_p}{dt} = \tilde{\boldsymbol{u}}+\delta\tilde{\boldsymbol{u}}\,, \qquad \tilde{p}=F(\tilde{\rho})\,, \qquad G(\rho)=\int^{\rho}\dfrac{1}{s}\dfrac{dF}{ds}\,ds\,,
\end{cases} \tag{6}
$$

where the total time derivatives d/dt is done with respect to the velocity $\tilde{\boldsymbol{u}}+\delta\tilde{\boldsymbol{u}}$ and $\mathbb{T}_\ell = \tilde{\boldsymbol{u}}\otimes\tilde{\boldsymbol{u}} - \widetilde{\boldsymbol{u}\otimes\boldsymbol{u}}$. Note that the latter tensor is equivalent to the sub-grid stress tensor. Following the derivation shown in [2], we now rearrange the system (6) in the framework of the Smoothed Particle Hydrodynamics (SPH) scheme. To this purpose, we split the filter ϕ into

$$\phi\,(\,\tilde{\boldsymbol{x}}_p(t)-\boldsymbol{y},t-\tau\,) = W(\,\tilde{\boldsymbol{x}}_p(t)-\boldsymbol{y}\,)\,\theta(\,t-\tau\,)\,, \tag{7}$$

where W indicates the SPH kernel and denote the spatial and time filtering as below:

$$\langle f\rangle(\,\tilde{\boldsymbol{x}}_p(t),t\,) = \int_{\mathbb{R}^3} W(\,\tilde{\boldsymbol{x}}_p(t)-\boldsymbol{y}\,)\,f(\boldsymbol{y},t)\,dV_y \qquad \overline{f}\,(\boldsymbol{y},t) = \int_{\mathbb{R}}\theta(\,t-\tau\,)\,f(\boldsymbol{y},\tau)\,d\tau\,.$$

Using the above definitions it is easy to prove that $\tilde{f} = \langle\overline{f}\rangle$ and that, generally, the time and space filters do not commute, i.e. $\langle\overline{f}\rangle \neq \overline{\langle f\rangle}$ (see, for example, [2]). Since the

time filter is the inner one, the overall LES-SPH scheme may be regarded as a spatial Lagrangian filter applied to a set of time-averaged variables. In this sense, the time filter may be thought as an implicit filter whose presence is accounted for through the modeling of the additional terms.

Now, suppose that we want to model a high Reynolds number flow, for which LES filtering is required. Then, we need the filtered variables $\tilde{\boldsymbol{u}}, \tilde{p}, \tilde{\rho}$ for each fluid particle at positions $\tilde{\boldsymbol{x}}_p$; at the same time, we want to approximate the operators in equation (6) in the SPH fashion. For example, using the above definitions, we can rearrange the gradient of $\tilde{f}$ as follows:

$$\nabla \tilde{f} = \langle \nabla \cdot \overline{f} \rangle = \langle \nabla (\overline{f} + \tilde{f} - \tilde{f}) \rangle = \langle \nabla \tilde{f} \rangle + \langle \nabla (\overline{f} - \tilde{f}) \rangle \,, \tag{8}$$

where the first term in the right-hand side is the SPH operator while the latter term accounts for small scale "fluctuations" in space, hereinafter denoted through $f' = \overline{f} - \tilde{f}$. For confined flows, the non-commutability of filtering and differentiation must be taken into account for a rigorous extension of the filtering close to the boundaries (i.e. in those points whose distance from the boundaries is smaller than the kernel radius). The above procedure can be applied to all the remaining operators. By doing so, in SPH formalism the system (6) reads:

$$\begin{cases} \dfrac{d\tilde{\rho}}{dt} = -\tilde{\rho}\,\langle \nabla \cdot (\tilde{\boldsymbol{u}} + \delta\tilde{\boldsymbol{u}}) \rangle + \langle \nabla \cdot (\tilde{\rho}\,\delta\tilde{\boldsymbol{u}}) \rangle + \mathcal{C}_1 + \mathcal{C}_2 + \mathcal{C}_3 \,, \\[2mm] \dfrac{d\tilde{\boldsymbol{u}}}{dt} = -\dfrac{\langle \nabla \tilde{p} \rangle}{\tilde{\rho}} + \nu \langle \Delta \tilde{\boldsymbol{u}} \rangle + (\lambda' + \nu)\,\langle \nabla (\nabla \cdot \tilde{\boldsymbol{u}}) \rangle \\[2mm] \qquad + \langle \nabla \cdot (\tilde{\boldsymbol{u}} \otimes \delta\tilde{\boldsymbol{u}}) \rangle - \tilde{\boldsymbol{u}}\,\langle \nabla \cdot \delta\tilde{\boldsymbol{u}} \rangle + \mathcal{M}_1 + \mathcal{M}_2 + \mathcal{M}_3 \,, \\[2mm] \dfrac{d\tilde{\boldsymbol{x}}_p}{dt} = \tilde{\boldsymbol{u}} + \delta\tilde{\boldsymbol{u}} \,, \qquad \tilde{p} = F(\tilde{\rho}) \,, \end{cases} \tag{9}$$

where:

$$\mathcal{C}_1 = -\tilde{\rho}\,\langle \nabla \cdot \boldsymbol{u}' \rangle \,, \qquad \mathcal{C}_2 = \nabla \cdot (\tilde{\rho}\tilde{\boldsymbol{u}} - \widetilde{\rho \boldsymbol{u}}) \,, \tag{10}$$

$$\mathcal{C}_3 = -\tilde{\rho}\,\nabla \cdot (\delta\tilde{\boldsymbol{u}} - \langle \delta\tilde{\boldsymbol{u}} \rangle) + \nabla \cdot (\tilde{\rho}\,\delta\tilde{\boldsymbol{u}} - \langle \tilde{\rho}\,\delta\tilde{\boldsymbol{u}} \rangle) \,, \tag{11}$$

$$\mathcal{M}_1 = -\dfrac{\langle \nabla p' \rangle}{\tilde{\rho}} + \nu \langle \Delta \boldsymbol{u}' \rangle + (\lambda' + \nu)\,\langle \nabla (\nabla \cdot \boldsymbol{u}') \rangle \,, \tag{12}$$

$$\mathcal{M}_2 = -\nabla \left[\widetilde{G(\rho)} - G(\tilde{\rho}) \right] + \widetilde{\boldsymbol{u}\,\nabla \cdot \boldsymbol{u}} + \nabla \cdot \mathbb{T}_\ell \tag{13}$$

$$\mathcal{M}_3 = \nabla \cdot (\tilde{\boldsymbol{u}} \otimes \delta\tilde{\boldsymbol{u}} - \langle \tilde{\boldsymbol{u}} \otimes \delta\tilde{\boldsymbol{u}} \rangle) - \tilde{\boldsymbol{u}}\,\nabla \cdot (\delta\tilde{\boldsymbol{u}} - \langle \delta\tilde{\boldsymbol{u}} \rangle) \,. \tag{14}$$

Here $\mathcal{C}_1$ and $\mathcal{M}_1$ come from the SPH approximation procedure and require a SPH closure, whereas $\mathcal{C}_2$ and $\mathcal{M}_2$ include all terms from the Lagrangian LES and require a LES closure.

Finally, $\mathcal{C}_3$ and $\mathcal{M}_3$ come from the use of the generic deviation velocity $\delta\tilde{\boldsymbol{u}}$. Using a Taylor expansion and the hypothesis that the fluid is weakly-compressible, it is possible to show that both $\mathcal{C}_3$ and $\mathcal{M}_3$ are negligible while $\mathcal{C}_1$ and $\mathcal{M}_1$ play a minor role with respect to the terms $\mathcal{C}_2$ and $\mathcal{M}_2$. As a consequence, only $\mathcal{C}_2$ and $\mathcal{M}_2$ are retained and modelled following a LES closure approach. In particular, $\mathcal{M}_2$ is modelled as done in [2]:

$$\mathcal{M}_2 \simeq \nabla \cdot \left[-\frac{q^2}{3}\mathbb{1} - \frac{2}{3}\nu_T \operatorname{Tr}(\widetilde{\mathbb{D}})\,\mathbb{1} + 2\,\nu_T\,\widetilde{\mathbb{D}} \right], \qquad (15)$$

where q^2 represents the turbulent kinetic energy, ν_T is the turbulent kinetic viscosity and $\widetilde{\mathbb{D}}$ is the strain-rate tensor, that is $\widetilde{\mathbb{D}} = (\nabla\tilde{\boldsymbol{u}} + \nabla\tilde{\boldsymbol{u}}^T)/2$. Similarly to [12], we assume:

$$q^2 = 2\,C_Y\,\ell^2\,\|\,\widetilde{\mathbb{D}}\,\|^2, \qquad \nu_T = (C_S\,\ell)^2\,\|\,\widetilde{\mathbb{D}}\,\|, \qquad (16)$$

where $\|\widetilde{\mathbb{D}}\|$ is a rescaled Frobenius norm, namely $\|\,\widetilde{\mathbb{D}}\,\| = \sqrt{2\,\widetilde{\mathbb{D}}:\widetilde{\mathbb{D}}}$ and ℓ is the radius of the SPH spatial kernel. The dimensionless parameters C_Y and C_S are respectively called the Yoshizawa and Smagorinsky constants.

For what concerns $\mathcal{C}_2$, the closure proposed in [2] corresponds to $\mathcal{C}_2 = \nabla\cdot(\nu_\delta\,\nabla\tilde{\rho})$ where ν_δ is assumed to be a function of $\widetilde{\mathbb{D}}$. In agreement with the usual approaches adopted in the LES framework, this is equivalent to model $\mathcal{C}_2$ as a diffusive term. In the present work we adopt a finer closure and write:

$$\mathcal{C}_2 = \ell^2\,\nabla\cdot(\nu_\delta\,\nabla\,\Delta\tilde{\rho}). \qquad (17)$$

In the SPH framework a simple way to model $\mathcal{C}_2$ is obtained by using the diffusive term proposed in [10], since this contains fourth-order spatial derivatives of the density field.

2.1 Numerical Scheme

To write the system (6) in the discrete formalism, we rely on the work of Sun et al. [3] where the additional $\delta\tilde{\boldsymbol{u}}$-terms are included in the SPH framework in a consistent way. In particular we obtain:

$$
\begin{cases}
\dfrac{d\tilde{\rho}_i}{dt} = -\tilde{\rho}_i \sum_j \left[(\tilde{\boldsymbol{u}}_j + \delta\tilde{\boldsymbol{u}}_j) - (\tilde{\boldsymbol{u}}_i + \delta\tilde{\boldsymbol{u}}_i)\right] \cdot \nabla_i W_{ij}\,V_j + \\[2mm]
\qquad \sum_j (\tilde{\rho}_j\delta\tilde{\boldsymbol{u}}_j + \tilde{\rho}_i\delta\tilde{\boldsymbol{u}}_i)\cdot\nabla_i W_{ij}\,V_j + \sum_j \delta_{ij}\,\boldsymbol{\psi}_{ji}\cdot\nabla_i W_{ij}\,V_j \\[3mm]
\dfrac{d\tilde{\boldsymbol{u}}_i}{dt} = -\dfrac{1}{\tilde{\rho}_i}\sum_j(\tilde{p}_j + \tilde{p}_i)\nabla_i W_{ij}\,V_j + \dfrac{\rho_0}{\tilde{\rho}_i}\,K\sum_j \alpha_{ij}\,\pi_{ij}\nabla_i W_{ij}\,V_j + \\[2mm]
\qquad \dfrac{\rho_0}{\tilde{\rho}_i}\sum_j(\tilde{\boldsymbol{u}}_j\otimes\delta\tilde{\boldsymbol{u}}_j + \tilde{\boldsymbol{u}}_i\otimes\delta\tilde{\boldsymbol{u}}_i)\cdot\nabla_i W_{ij}\,V_j \\[3mm]
\dfrac{d\tilde{\boldsymbol{x}}_i}{dt} = \tilde{\boldsymbol{u}}_i + \delta\tilde{\boldsymbol{u}}_i, \qquad \tilde{p}_i = F(\tilde{\rho}_i), \qquad V_i = \dfrac{m_i}{\tilde{\rho}_i},
\end{cases} \qquad (18)
$$

where m_i is the i-th particle mass (assumed to be constant) and V_i is its volume while $W_{ij} = W(\tilde{\boldsymbol{x}}_i - \tilde{\boldsymbol{x}}_j)$. The coefficient of the viscous term is $K = 2(n+2)$ where n is the number of spatial dimensions while its arguments are:

$$\pi_{ij} = \frac{(\tilde{\boldsymbol{u}}_j - \tilde{\boldsymbol{u}}_i) \cdot (\tilde{\boldsymbol{x}}_j - \tilde{\boldsymbol{x}}_i)}{\|\tilde{\boldsymbol{x}}_j - \tilde{\boldsymbol{x}}_i\|^2} \qquad \alpha_{ij} = \frac{\mu}{\rho_0} + 2 \frac{\nu_i^T \nu_j^T}{\nu_i^T + \nu_j^T},$$

where $\nu_i^T = (C_s \ell)^2 \|\widetilde{\mathbb{D}}_i\|$ and C_s is the Smagorinsky constant (set equal to 0.12). The first contribution in the expression of α_{ij} represents the actual fluid viscosity while the latter one is the LES closure for turbulence. Note that all contributions related to the fluid compressibility have been neglected, since they are negligible in comparison to the leading order stress tensor. The symbol ψ_{ij} is the argument of the diffusive term of [10], namely:

$$\boldsymbol{\psi}_{ij} = \left[(\rho_j - \rho_i) - \frac{1}{2} \left(\langle \nabla \rho \rangle_i^L + \langle \nabla \rho \rangle_j^L \right) \cdot (\tilde{\boldsymbol{x}}_j - \tilde{\boldsymbol{x}}_i) \right] \frac{(\tilde{\boldsymbol{x}}_j - \tilde{\boldsymbol{x}}_i)}{\|\tilde{\boldsymbol{x}}_j - \tilde{\boldsymbol{x}}_i\|^2}. \tag{19}$$

Here the superscript L indicates that the gradient is evaluated through the renormalized gradient formula [9] as follows:

$$\begin{cases} \langle \nabla \rho \rangle_i^L = \sum_j (\rho_j - \rho_i) \boldsymbol{L}_i \nabla_i W_{ij} V_j, \\[2ex] \boldsymbol{L}_i = \left[\sum_j (\tilde{\boldsymbol{x}}_j - \tilde{\boldsymbol{x}}_i) \otimes \nabla_i W_{ij} V_j \right]^{-1} \end{cases} \tag{20}$$

As done in [2] and in [11], the diffusive term is not multiplied by an external parameter but the latter is included directly inside the summation and modelled as a viscous-like coefficient following a standard LES approach. In particular we choose:

$$\delta_{ij} = 2 \frac{\nu_i^\delta \nu_j^\delta}{\nu_i^\delta + \nu_j^\delta}, \qquad \text{where} \quad \nu_i^\delta = (C_\delta \ell)^2 \|\widetilde{\mathbb{D}}_i\|. \tag{21}$$

in which C_δ is a dimensionless constant set equal to 1.5 . The value of this constant has been calibrated in [2] by simulating free decay turbulence in periodic domains in both 2D and 3D frameworks.

As often done for weakly-compressible fluids, the state equation is linearized around the reference density ρ_0, leading to $\tilde{p}_i = c_0^2 (\tilde{\rho}_i - \rho_0)$ where $c_0 = c(\rho_0)$ is a numerical sound speed that satisfies the following requirement:

$$M_a = \frac{U_{ref}}{c_0} \leq 0.1 \qquad \text{with} \quad U_{ref} = \max \left(U_{max}, \sqrt{\frac{\delta \tilde{p}_{max}}{\rho_0}} \right). \tag{22}$$

Here U_{max} and $\delta \tilde{p}_{max}$ indicate the maximum fluid velocity and the maximum pressure variation expected during the simulation. The above inequality allows the density variations to be below 1% (see [5]).

Finally, following [3], the velocity deviation is defined as:

$$\delta \tilde{\boldsymbol{u}}_i = \min\left(\|\delta\hat{\boldsymbol{u}}_i\|,\frac{U_{\max}}{2}\right)\frac{\delta\hat{\boldsymbol{u}}_i}{\|\delta\hat{\boldsymbol{u}}_i\|} \tag{23}$$

where:

$$\delta\hat{\boldsymbol{u}}_i = -M_a\,\ell\,c_0\sum_j\left[1 + R\left(\frac{W_{ij}}{W(\Delta x)}\right)^n\right]\nabla_i W_{ij}V_j\,. \tag{24}$$

and Δx is the initial mean particle distance. Here the constants R and n are set equal to 0.2 and 4 respectively. The expression in (23) has to be further corrected for particles close to the domain boundaries to avoid a non-physical particle motion. For further details we address the interested reader to [3].

3 APPLICATIONS

In the next section we consider the evolution of freely decaying turbulence in a two-dimensional bi-periodic squared domain. The Taylor-Green vortex solution (see [14]) is used to initialize the computations. In particular a path of 8×8 vortex cells is considered. The Reynolds number is defined as $Re = UL/\nu$ where L is the side of the squared domain (that is, $L = 8\,\ell$ where ℓ is the length of a vortex cell), U is the reference initial velocity and ν is the kinematic viscosity. The SPH particles are placed by using the Particle Packing Algorithm described in [15].

3.1 Freely decaying turbulence in 2D

Figure 1 shows the comparison between the energy spectra at $Re = 10,000$ obtained by using three different SPH models for turbulence, namely the LES model of [13], the δ-LES SPH scheme defined in [2] and the present scheme. The spectra have been computed by using a Moving Least Square interpolation with a Gaussian kernel with the same radius of that adopted in the SPH simulations. Four different spatial resolutions have been considered, that is $L/\Delta x = 150, 300, 600, 1200$ where Δx is the initial mean particle distance. In the figure the direct and inverse cascade trends have been plotted by green and orange dashed lines respectively and the wave number associated with the kernel radius has been indicated by the symbol k_R. Generally, all the SPH models correctly predict these trends but show a non-physical increase of the energy spectrum at wave numbers comparable with k_R as the resolution increases. This behaviour is common to all the SPH schemes considered here and seems to be an intrinsic characteristic of the SPH models themselves. In any case, the proposed model, thanks to the action of the Particle Shifting Technique, predicts a reduction of the energy at large wave numbers in comparison to the LES model of [13] and the δ-LES SPH scheme of [2]. This overall trend is confirmed in figure 2 where the same results are displayed for $Re = 1,000,000$.

To understand if the LES closures described in the equations (15) and (17) work properly, it is useful to analyse the evolution of the heat generated by $\mathcal{M}_2$ and $\mathcal{C}_2$ in comparison with the heat produced by the viscous fluid term $\nu\langle\Delta\tilde{\boldsymbol{u}}\rangle$. Hereinafter we
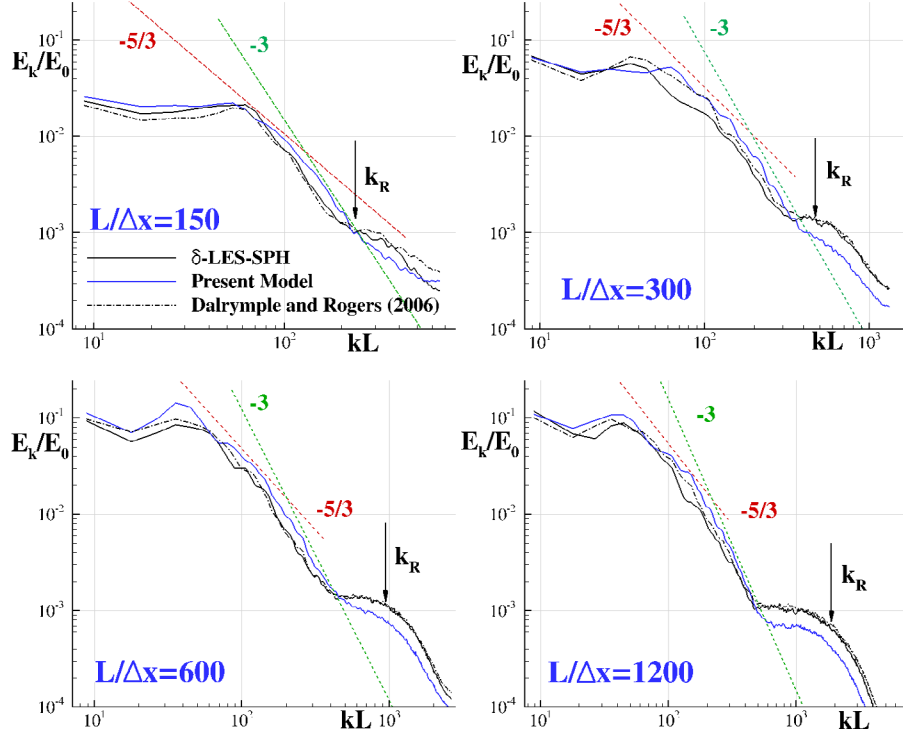
Figure 1: Freely decaying turbulence at $Re = 10,000$ for different spatial resolutions. The symbol k_R indicates the wave number associated to the kernel radius while Δx is the initial mean particle distance.
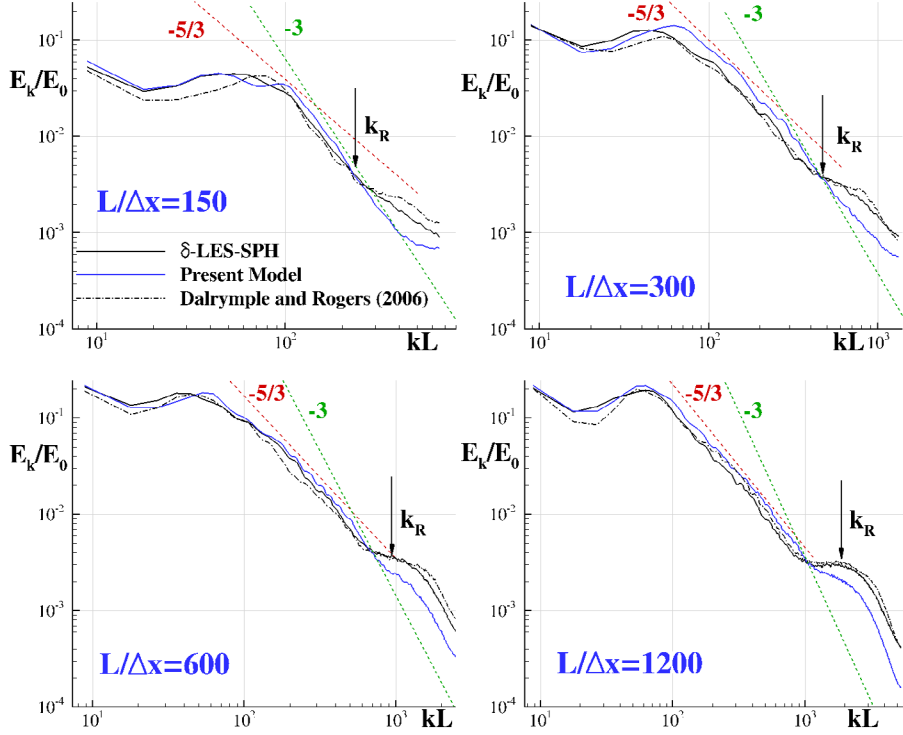
Figure 2: Freely decaying turbulence at $Re = 1,000,000$ for different spatial resolutions. The symbol k_R indicates the wave number associated to the kernel radius while Δx is the initial mean particle distance.
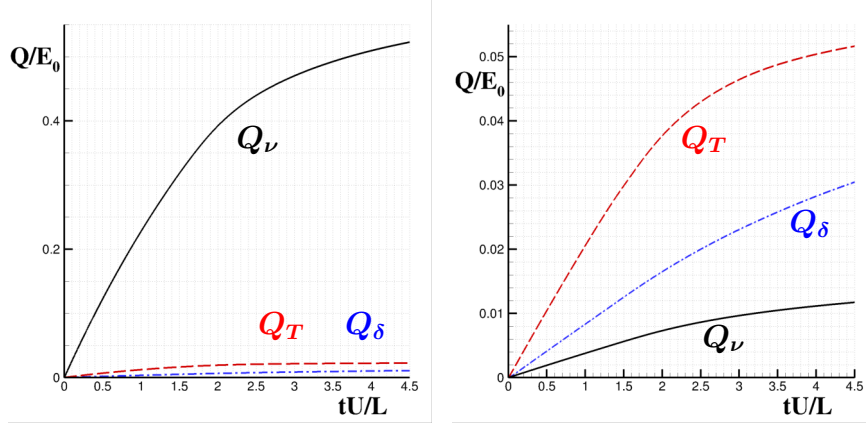
Figure 3: Freely decaying turbulence: the heat generated in the present model by the fluid viscous term (namely, Q_ν), by the LES model in the momentum equation (that is Q_T) and by the LES model in the continuity equation (i.e. Q_δ) for $Re = 10,000$ (left panel) and $Re = 1,000,000$ (right panel) for $L/\Delta x = 1,200$.

indicate these contributions through Q_T, Q_δ and Q_ν respectively. Figure (3) shows these terms for the finest spatial resolutions, namely $L/\Delta x = 1,200$, and for $Re = 10,000$ (left panel) and $Re = 1,000,000$ (right panel). In the former case, the simulation is very close to a DNS simulation and, consistently, the heat produced by the terms related to the LES closures (namely Q_T and Q_δ) is small in comparison to the dissipation caused by the actual viscosity of the fluid (i.e. Q_ν). On the contrary, for $Re = 1,000,000$, the spatial resolution is too coarse for a DNS simulation and, consequently, the LES terms give the main contribution to the heat production and make Q_T and Q_δ predominant over Q_ν.

Finally, in figure (4) we compare some snapshots of the pressure field for the three models under investigation, namely the LES model of [13] (top panels), the δ-LES SPH scheme defined in [2] (middle panels) and the present scheme (bottom panels) for the finest spatial resolution (that is $L/\Delta x = 1,200$). The left column displays the outputs obtained for $Re = 10,000$ while the right column contains the results for $Re = 1,000,000$. In both the cases, the pressure field predicted by the model described in [13] is much more noisy than those obtained though the LES model of [2] and by the present one. In particular, the latter are comparable even though the present model tends to preserve the larger eddies more efficiently, consistently with the energy spectra of figures (1) and (2).

4   CONCLUSIONS

In the present work we propose an extension of the LES model described in [2] using a quasi-Lagrangian LES formulation. This model is based on the assumption that the fluid particles move following a velocity that is made by the actual fluid velocity plus a small deviation. The latter is modelled through the Particle Shifting Technique, as described in [3].

The proposed model is preliminary tested by simulating the problem of freely decaying turbulence and comparing the results with the LES models described in [13] and [2]. The
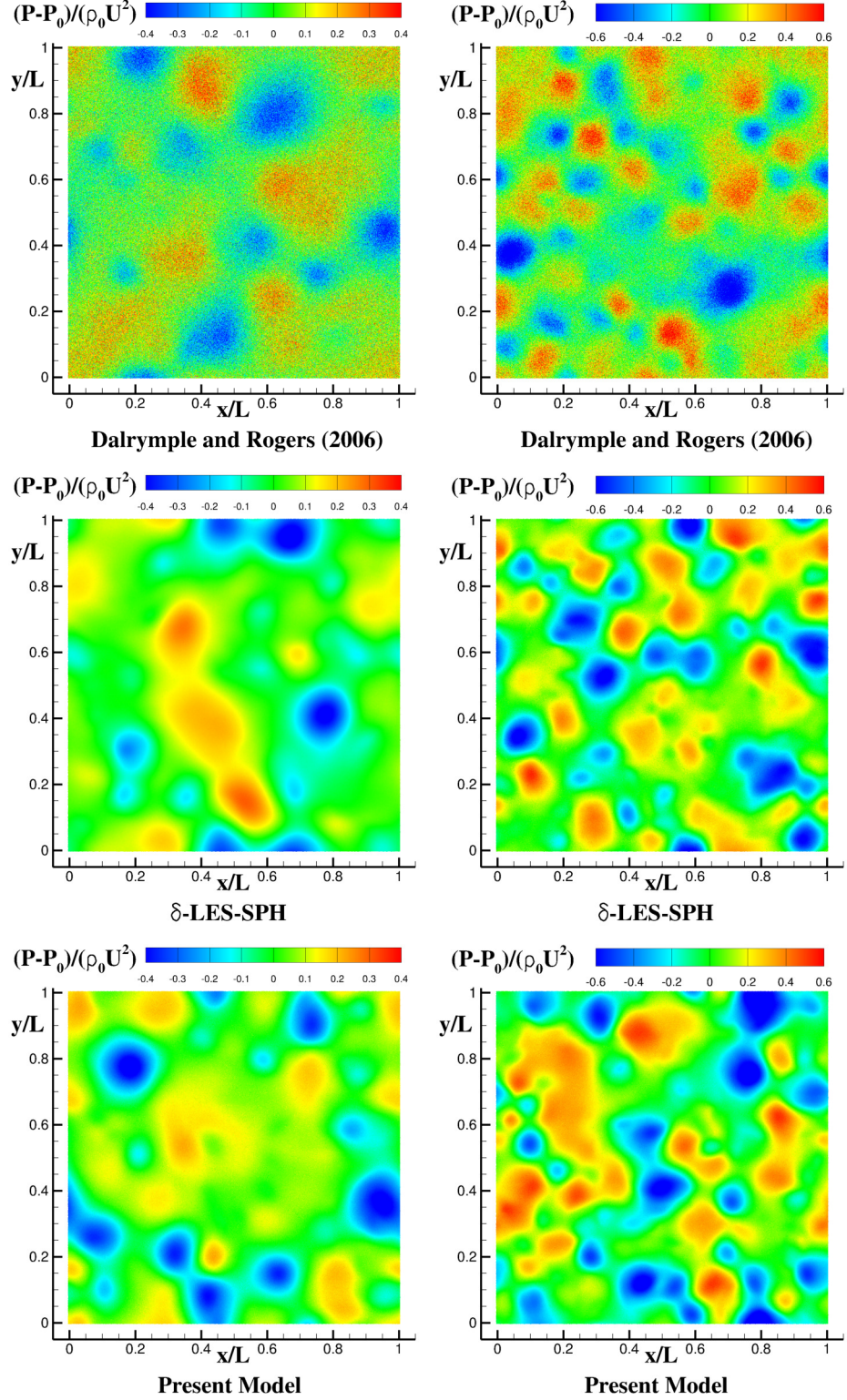
Figure 4: Freely decaying turbulence: pressure field predicted by the different SPH models at $Re = 10,000$ (left column) and $Re = 1,000,000$ (right column) for $L/\Delta x = 1,200$.

results show that the present model reduces the amount of energy at large wave numbers in comparison with the above models. Further, similarly to the scheme of [2], it predicts a pressure field that is free from high-frequency spurious noise.

Acknowledgements

REFERENCES

[1] Antuono M., Colagrossi A., and Marrone S., Numerical diffusive terms in weakly-compressible SPH schemes, *Computer Physics Communications*, (2012) **183**(12):2570–2580.

[2] Di Mascio A., Antuono M., Colagrossi A., and Marrone S., Smoothed particle hydrodynamics method from a large eddy simulation perspective. *Physics of Fluids*, (2017) **29**(035102).

[3] Sun P. N., Colagrossi A., Marrone S., Antuono M., and Zhang A. M., A consistent approach to particle shifting in the δ-Plus-SPH model. *Computer Methods in Applied Mechanics and Engineering*, (2019) **348**:912–934.

[4] Marrone S., Colagrossi A., Di Mascio A., and Le Touzé D., Prediction of energy losses in water impacts using incompressible and weakly compressible models, *Journal of Fluids and Structures*, (2015) **54**:802–822.

[5] Monaghan J., Simulating Free Surface Flows with SPH, *J. Comp. Phys.*, (1994) **110**(2):39–406

[6] Colagrossi A., Antuono M., and Le Touzé D., Theoretical considerations on the free-surface role in the Smoothed-particle-hydrodynamics model, *Physical Review E*, (2009) **79**(5):056701.

[7] Colagrossi A., Antuono M., Souto-Iglesias A., and Le Touzé D., Theoretical analysis and numerical verification of the consistency of viscous smoothed-particle-hydrodynamics formulations in simulating free-surface flows, *Physical Review E*, (2011) **84**:026705.

[8] Moin P., Squires K., Cabot W., and Lee S., A dynamic subgrid-scale model for compressible turbulence and scalar transport, *Physics of Fluids A*, (1991) **3**(11):2746–2757.

[9] Antuono M., Colagrossi A., Marrone S., Molteni D., Free-surface flows solved by means of SPH schemes with numerical diffusive terms, *Comp. Phys. Comm.*, (2010) **181**:532–549.

[10] Antuono M., Colagrossi A., Marrone S., Numerical diffusive terms in weakly-compressible SPH schemes, *Comp. Phys. Comm.*, (2012) **183**:2570–2580.

[11] Meringolo D.D., Marrone, S. Colagrossi A., Liu Y., A dynamic δ-SPH model: How to get rid of diffusive parameter tuning, *Computers & Fluids* (2019) **179**:334–355.

[12] Yoshizawa A., Statistical theory for compressible turbulent shear flows, with the application to subgrid modeling, *Physics of Fluids*, (1986) **29**:2152.

[13] Dalrymple R. and Rogers B., Numerical modeling of water waves with the SPH method, *Coastal Eng.*,(2006) **53**(2-3): 141–147.

[14] Taylor, G. I. and Green, A. E., Mechanism of the Production of Small Eddies from Large Ones, *Proc. R. Soc. Lond. A*, (1937) **158**: 499–521.

[15] Colagrossi A., Bouscasse B., Antuono M., and Marrone S., Particle packing algorithm for SPH schemes, *Comput. Phys. Commun.* (2012) **183**: 1641–1653.

[16] Mayrhofer A., Laurence D., Rogers B., and Violeau D., DNS and LES of 3-D wall-bounded turbulence using smoothed particle hydrodynamics, *Comput. Fluids* (2015) **115**: 86–97.

[17] Shao S., Ji C., SPH computation of plunging waves using a 2-D sub-particle scale (SPS) turbulence model. *International Journal for numerical methods in fluids*, (2006) **51**(8): 913–936.

[18] Price D.J., Resolving high Reynolds numbers in smoothed particle hydrodynamics simulations of subsonic turbulence. *Monthly Notices of the Royal Astronomical Society: Letters*, (2012) **420**(1): L33–L37.

[19] Xu, R., Stansby P., Laurence D., Accuracy and stability in incompressible SPH (ISPH) based on the projection method and a new approach. *Journal of computational Physics*, (2009) **228**(18): 6703–6725.

[20] Nestor R.M., Basa M., Lastiwka M., Quinlan N.J., Extension of the finite volume particle method to viscous flow. *Journal of Computational Physics*, (2009) **228**(5): 1733–1749.

LIMIT MECHANISMS FOR ICE LOADS: FEM-DEM AND SIMPLIFIED LOAD MODELS

JANNE RANTA, ARTTU POLOJÄRVI AND JUKKA TUHKURI

Aalto University
Department of Mechanical Engineering
P.O. Box 14300, FI-00076 AALTO, Finland
e-mail: arttu.polojarvi@aalto.fi

Key words: FEM-DEM, Force Chain Buckling, Local Crushing, Ice Mechanics

Abstract. This work summarizes our recent findings on mechanisms and limits for the ice loads on wide inclined Arctic marine structures, like drilling platforms or harbour structures. The fresults presented are based on hundreds of two-dimensional combined finite-discrete element method (FEM-DEM) simulations on ice-structure interaction process. In such processes, a floating sea ice cover, driven by winds and currents, fails against a structure and fragments into a myriad of ice blocks which interact with each other and the structure. The ice load is the end result of this interaction process. Using the simulation data, we have studied the loading process, analysed the statistic of ice loads, and recently introduced a buckling model [1] and extended it to a simple probabilistic limit load model and algorithm [2], which predict the peak ice load values with good accuracy. These models capture and quantify the effect of two factors that limit the values of peak ice loads in FEM-DEM simulations: The buckling of force chains and local ice crushing in ice-to-ice contacts. The work here describes the models and demonstrates their applicability in the analysis of ice-structure interaction.

1 INTRODUCTION

Development of safe Arctic operations, such as marine transportation, offshore wind energy and offshore drilling, requires reliable prediction of maximum sea ice loads. The ice loads arise from a complex and stochastic ice-structure interaction process. This paper uses 2D combined finite-discrete element method (2D FEM-DEM) simulations to study the mechanisms that limit peak ice loads on wide, inclined, structures. Particle based methods, such as DEM and FEM-DEM, allow detailed studies on complex ice loading scenarios and they are often used in ice engineering [3]. Figure 1 illustrates our simulations, which have a floating and continuous ice sheet pushed against an inclined rigid structure. The initially intact ice sheet fails into a rubble pile of ice blocks, which interact with each other and the structure.

An important feature of discrete element simulations is that they can describe force chains [4]. In the case of ice-structure interaction, the force chains are chainlike groups of
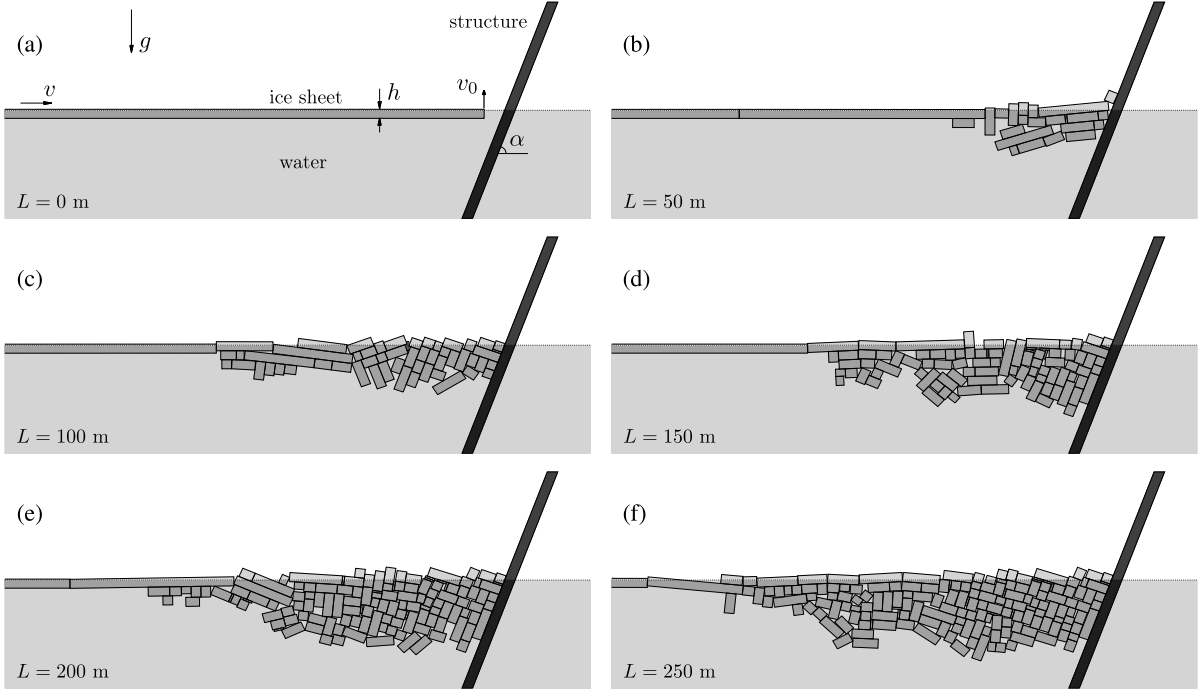
Figure 1: Snapshots of a 2D FEM-DEM-simulated ice-structure interaction process described by the length L of the ice pushed against an inclined structure. The ice sheet moves with velocity v and breaks into ice blocks in the vicinity of the structure. Broken ice forms an ice rubble pile in front of the structure. The first figure shows the initial vertical velocity perturbation v_0. Ice sheet thickness h was 1.25 m here. Figure is from [9]

ice blocks, or ice floes, that transmit the loads from the intact ice sheet to the structure. Figure 2 shows a maximum peak ice load event, in which the ice load is transmitted to the structure through a force chain. Paavilainen and Tuhkuri [5] observed that force chains exists within the ice rubble mass during peak ice load events.

This paper describes how to quantify the effects of force chain buckling and local ice crushing on maximum ice loads using fairly simple mechanical models. We first describe our simulations and a simple buckling model that captures the effect of force chain buckling. We demonstrate that the model predicts the peak ice loads in our simulations and yields plausible ice floe size predictions. Then we briefly discuss how the model can be extended to account for the local crushing of ice in contacts. The paper summarizes the work presented in detail in Ranta et al. [1] and Ranta and Polojärvi [2].

2 SIMULATIONS

The model is based on 2D FEM-DEM simulations, performed with an in-house code of Aalto University ice mechanics group. The code is based on the models described in Hopkins [6] and Paavilainen et al. [7] and its results were validated by Paavilainen et al. [7] and Paavilainen and Tuhkuri [8]. Figures 1a-f describe our simulations, in which an ice sheet of thickness h pushed against an inclined rigid structure with a constant horizontal
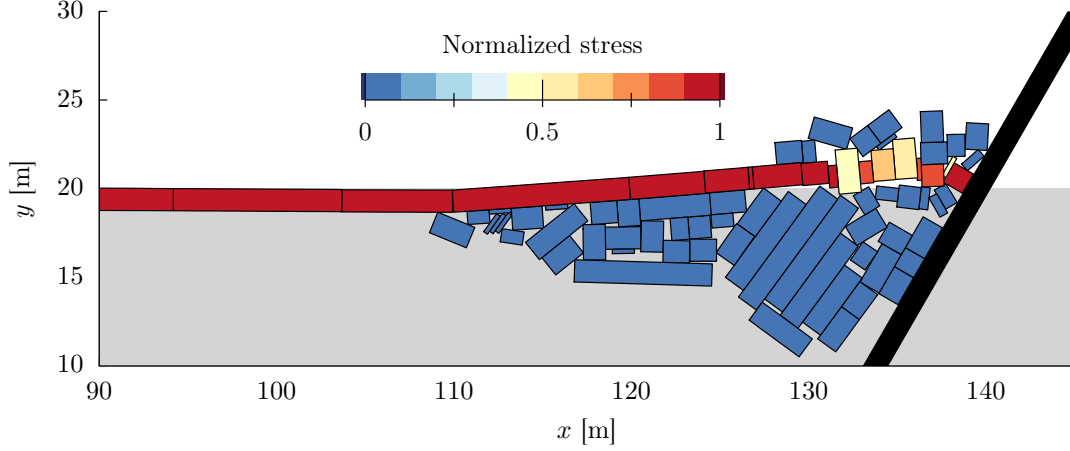
Figure 2: Snapshot from a simulation showing a force chain — a sequence of ice blocks in contact due to high compressive stress — transmitting the load from the intact ice sheet, moving towards the structure from the left. Colors indicate the normalized particle stress [4]. Figure is from [2].

velocity $v = 0.05$ m/s. Approximately 100 m from the structure, a viscous damping boundary condition is used to mimic a semi-infinite ice sheet. The sheet itself consists of rectangular discrete elements connected by viscous-elastic Timoshenko beams, which fail at locations where the beams meet a pre-defined failure criterion [10]. The beams went through a cohesive softening process upon failure [11], with the energy dissipated due to this process matching that of the fracture energy of ice [12]. Table 1 gives the main parameters of the simulations.

Contact forces were solved using an elastic-viscous-plastic normal contact force model, together with an incremental tangential contact force model with Coulomb friction [6, 7]. The model describes local crushing at ice-block-to-ice-block and ice-structure contacts. The amount of local crushing was governed by the plastic limit parameter, σ_p, which relates the maximum contact load to the contact geometry. Plastic limit parameter σ_p accounts for the local crushing between the contacting ice blocks. No new ice features were created, nor did the block geometries change during the local crushing. Water was accounted for by applying a buoyant force and simplified drag model.

The load model development was based on 350 simulations with Table 1 giving the parameters of the simulations and Table 2 summarizing the seven simulations sets, S1…S7. Each set contained 50 simulations where all parameters were constant, but the initial conditions slightly differed: An initial vertical velocity of the order of 10^{-12} m/s was applied at the free edge of the ice sheet at the start of the simulation (see [13] for details). Simulations within each set, differing by their initial conditions only, produced different ice loading processes (Figure 3) and different maximum peak ice load F^p values. As shown in Table 2, the simulation sets S1…S6 differed from each other by the values of h and σ_p. Simulation set S7 had thick ice, $h = 1.25$ m, and a high value of 8 MPa for σ_p.
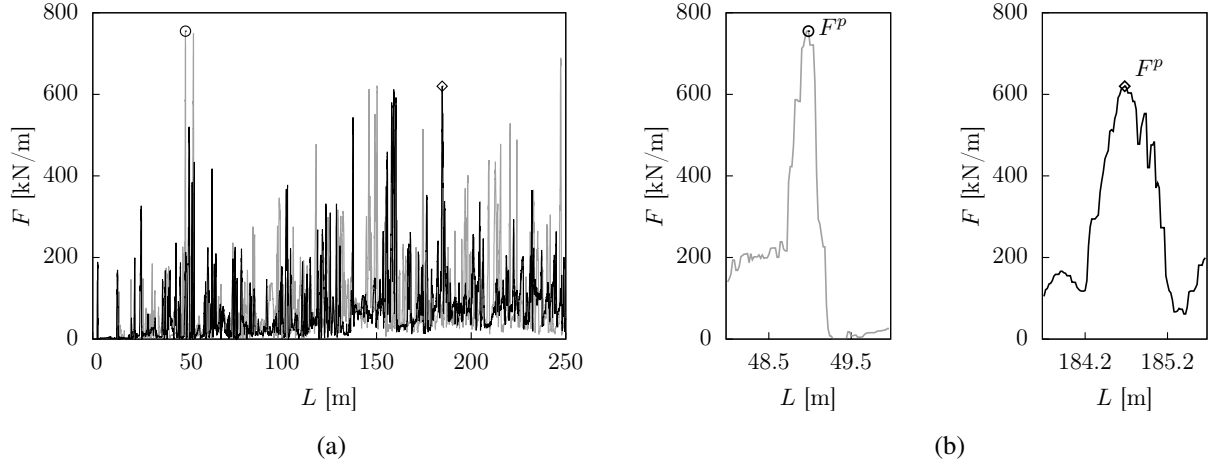
Figure 3: Two ice load F-records from two simulations with same parameterization but different initial conditions: (a) F plotted against length of pushed ice, L, and (b) close-ups of the maximum peak ice load, F^p, events. The value of F^p differs between the simulations. Here the ice thickness $h = 1.25$ m and the plastic limit $\sigma_p = 1$ MPa. Figure is from [2].

BUCKLING MODEL

In Ranta et al. [1] we showed that a simple buckling model can be used to describe how force chain buckling limits the ice load values on a wide, inclined, structure. The model, shown in Figure 4, consists of a rigid system of ice floes, having a total length of L_f, lying on an equilibrium on an elastic foundation. The modulus k of the elastic foundation,

Table 1: Main simulation parameters. The parameter values were mostly chosen following [14].

	Description and symbol		Unit	S1…S7
General	Gravitational acceleration	g	m/s^2	9.81
	Ice sheet velocity	v	m/s	0.05
	Drag coefficient	c_d		2.0
Ice	Thickness	h	m	0.5, 0.875, 1.25
	Effective modulus	E	GPa	4
	Poisson's ratio	ν		0.3
	Density	ρ_i	kg/m^3	900
	Tensile strength	σ_f	MPa	0.6
	Shear strength	τ_f	MPa	0.6
Contact	Plastic limit	σ_p	MPa	1.0, 2.0, 8.0
	Ice-ice friction coefficient	μ_{ii}		0.1
	Ice-structure friction coefficient	μ_{iw}		0.1
Water	Density	ρ_w	kg/m^3	1010
Structure	Slope angle	α	deg	70
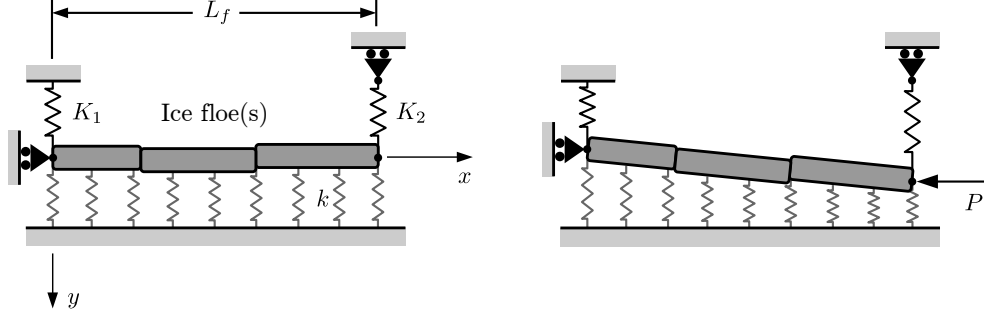
Figure 4: The buckling model we used in its initial (left) and buckled (right) states. The model consisted of a rigid ice floe of length L_f resting on an elastic foundation with modulus k presenting water. Springs K_1 and K_2 modeled the boundary conditions for the buckling modes of Table 3. Compressive force P is due to the other floes or the structure. Figure is from [2].

chosen after the specific weight of water, was $\rho_w g$, where ρ_w is the mass density of the water and g the gravitational acceleration.

The buckling model can describe different buckling modes depending on the values of the spring constants K_1 and K_2 of the springs at the ends of the floe. Table 3 shows the different modes together with the corresponding K_1 and K_2 values. Out of the four modes of the table, modes 1 and 2 assume that the elastic bending of the intact ice sheet does not have a role in a peak load event. Modes 3 and 4, on the other hand, assume that the elastic ice sheet behind the buckling floe generates a lateral support for the left end of it. The buckling load P for the model is [1]

$$P = \frac{k^2 L_f^3 + 4k(K_1 + K_2)L_f^2 + 12K_1 K_2 L_f}{12(kL_f + K_1 + K_2)}. \tag{1}$$

The characteristic length $L_c = \sqrt[4]{4EI/k}$ of a beam on elastic foundation [15] is introduced into Equation 1 by substitution of $L_f = \chi L_c$, where χ is a dimensionless buckling

Table 2: Simulation sets S1...S7 of this study. The able also shows the number N and the indices (ID) of the simulations in each set. More detailed list of simulation parameters is given in Table 1.

Set	IDs	N	h [m]	σ_p [MPa]
S1	1-50	50	0.5	1
S2	51-100	50	0.5	2
S3	101-150	50	0.875	1
S4	151-200	50	0.875	2
S5	201-250	50	1.25	1
S6	251-300	50	1.25	2
S7	301-350	50	1.25	8

length factor. L_c and χ allow expressing P for all buckling modes of Table 3 in form

$$P = a(\chi)\sqrt{kEI}, \qquad (2)$$

where a is a buckling-mode-dependent dimensionless multiplier given in Table 3. This equation can be used to study the relation between buckling and peak loads as follows. The F^p values from all simulations (Figure 3), together with the simulation parameters (k, E and I), are collected and substituted to the previous equation, which is then solved for $a(\chi) = F^p/\sqrt{kEI}$. If the simple buckling model describes well how force chain buckling limits the values of F^p, the a values for all simulations should be approximately equal; the F^p values should become normalized by factor $\sqrt{kEI}$.

3 RESULTS AND DISCUSSION

Figure 5a shows the maximum peak ice load F^p values (Figure 3a and b) from our FEM-DEM simulations. Additionally, it shows the mean F^p values with their standard deviations for the simulations of each set, S1...S7 (Table 2). While the F^p values from the simulations in a given set show scatter, the mean F^p values of the sets S1...S7 differed considerably, by up to about 500 %, mainly due to a difference in ice thickness h between the sets.

The simulations of set S7 with high σ_p yielded larger values than sets S5 and S6 with the same ice thickness $h = 1.25$ m. The values of a, solved by normalizing the F^p data of Figure 5a by factor $\sqrt{kEI}$, are shown in Figure 5b. These indicate that the peak load events were related to buckling: All mean values of a are in the same range and there is no dependency between a and h. Nonetheless, the data shows scatter not explained by the buckling model as, for example, the mean a value is clearly larger for set S7 having high σ_p.

As a appears somewhat constant, we can solve χ to estimate the lengths $L_f = \chi L_c$

Table 3: Four buckling modes considered in our study with the corresponding spring constants K_1 and K_2 (Figure 4). The buckling load $P = a(\chi)\sqrt{kEI}$, where a is a mode-dependent multiplier. Factor χ gives the buckling length as described in the text. Table is from [1]

mode		K_1	K_2	a
1		0	0	$\dfrac{\chi^2}{6}$
2		∞	0	$\dfrac{2\chi^2}{3}$
3		$\dfrac{1}{2}kL_c - \dfrac{3}{4}\dfrac{P}{L_c}$	∞	$\dfrac{12\chi + 8\chi^2}{9\chi + 12}$
4		$kL_c - \dfrac{P}{2L_c}$	∞	$\dfrac{12\chi + 4\chi^2}{3\chi + 6}$
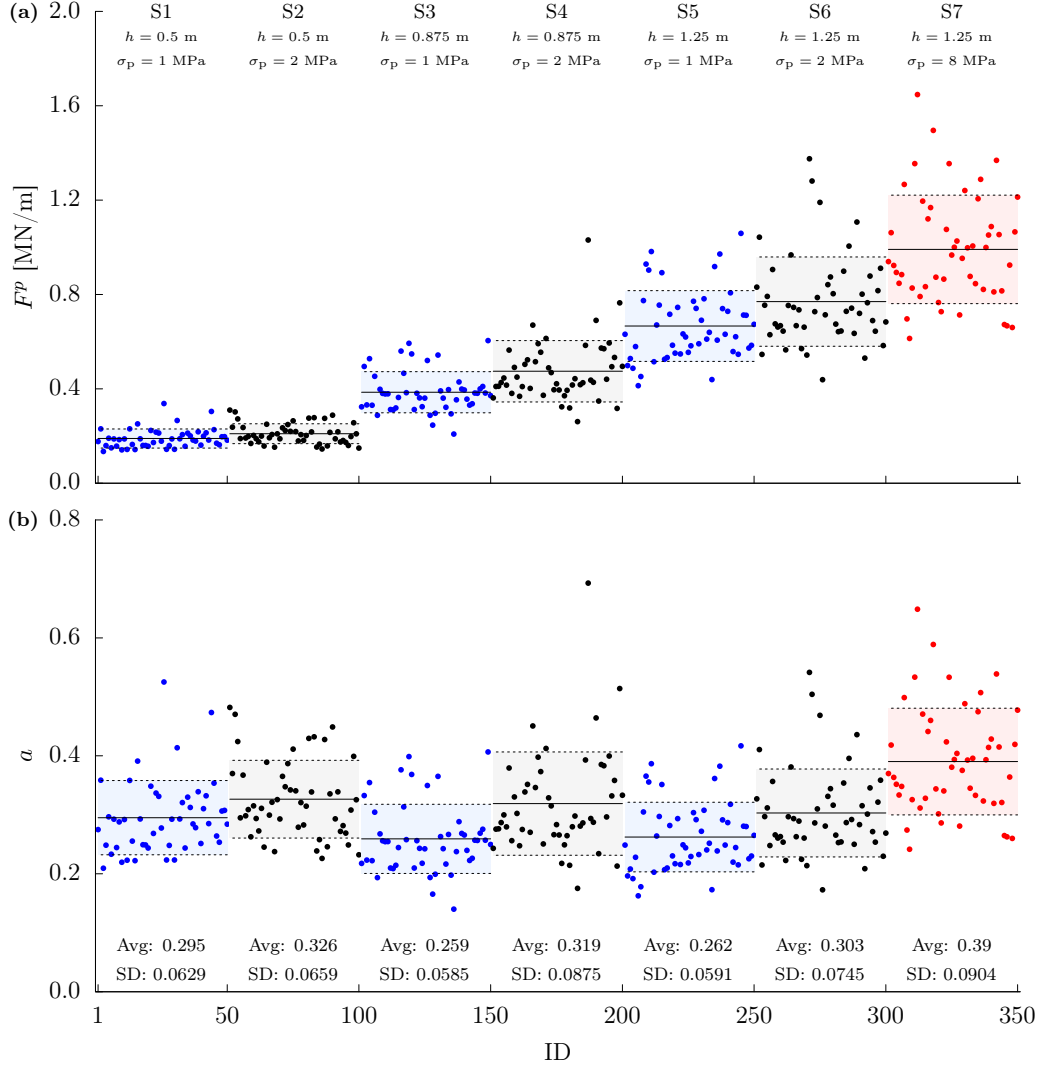
Figure 5: The values of (a) maximum peak ice load F^p values from all simulations (sets S1 … S7, Table 2) and (b) dimensionless a factors derived using F^p data. In addition to the data points, the graphs show the mean values (Avg, solid lines) and standard deviations (SD, dashed lines) for the data.

of buckling floes. Figure 6 illustrates how the ice floes, having been compressed between the ice sheet and the structure, have gone through a buckling-like failure between the two time instances. The data points of Figure 7 are the χ values from all simulations in sets S1...S6 for modes 2-4 of Table 3. (For each a value, we get four values for χ, one for each mode, as described by Table 3.) The mean χ value for mode 1 was 1.32 ± 0.2, but χ factors for mode 1 are not shown in the figure, as this mode is physically unfeasible. It is justified to assume $L_f < L_c$, as the floes breaking off of the intact ice sheet in bending (occurring prior the peak load event) would have the length of about L_c at maximum.

The two horizontal lines of Figure 7a correspond to the χ values, which we calculated for the reported minimum and maximum values for average breaking lengths of an ice
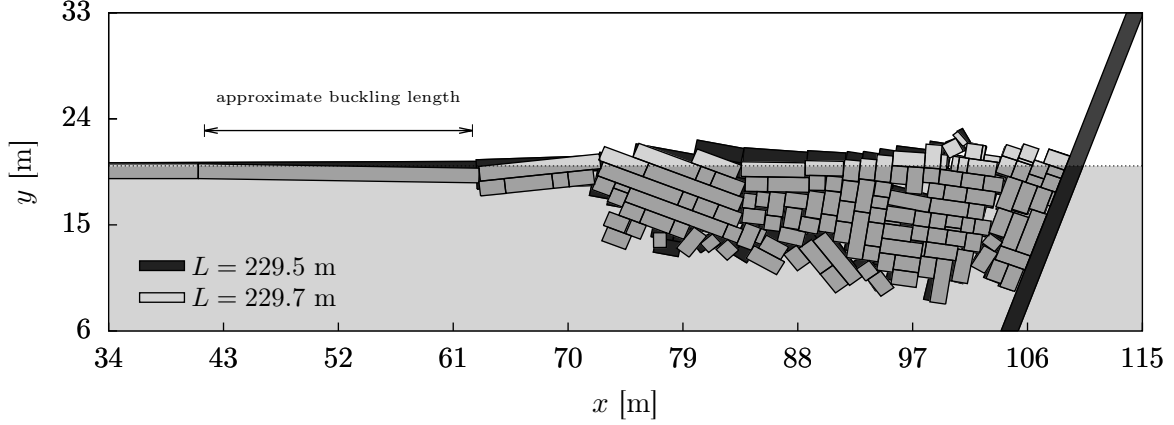
Figure 6: An example of a peak ice load event, which this simulation reached at $L = 229.5$ m. The figure also shows the model at $L = 229.7$ m (four seconds later). Buckling occurred at $x \approx 61$ m. The line in the figure illustrates the approximate buckling length. Here h and the plastic limit σ_p were 1.25 m and 2 MPa, respectively. Figure is from [1].
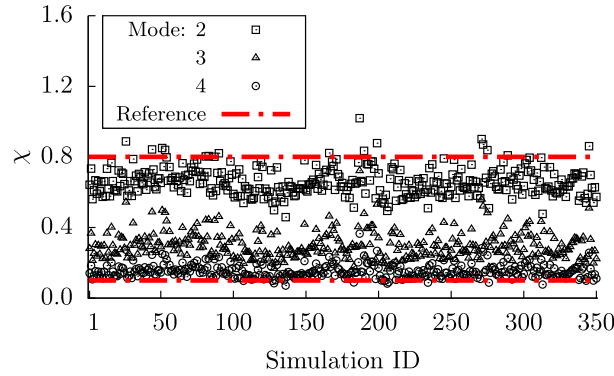
Figure 7: The dimensionless χ factor values for buckling modes 2 and 4 of Table 3 using the a values of Figure 5b. The two horizontal dash-dot lines correspond to full-scale observations on maximum and minimum breaking lengths [18]. Figure is from [1].

sheet in a full-scale ice-structure interaction process [16, 17, 18] . The figure shows that almost all of the χ values resulting from the simulated ice-structure interaction processes fall between these limits. This gives confidence on both, our simulation results and on our simplified buckling load model.

The above-described buckling model does not account for the effect of compressive strength of ice, σ_p, on the results, which would allow the buckling model to yield peak load values exceeding the compressive capacity of the ice. The lack of the effect of σ_p leads to the mean of a showing a systematic change with a change in σ_p (Figure 5b): Increase in σ_p leads to increase in a when h is kept constant. The so-called probabilistic limit load model, described in detail in Ranta and Polojärvi [2], extends the buckling model by (1) supplementing the buckling model with a local crushing model and (2) by accounting for the stochasticity in the contact geometries of the blocks belonging to the force chains.

An elementary unit of the model is one contact interface between a pair of ice blocks
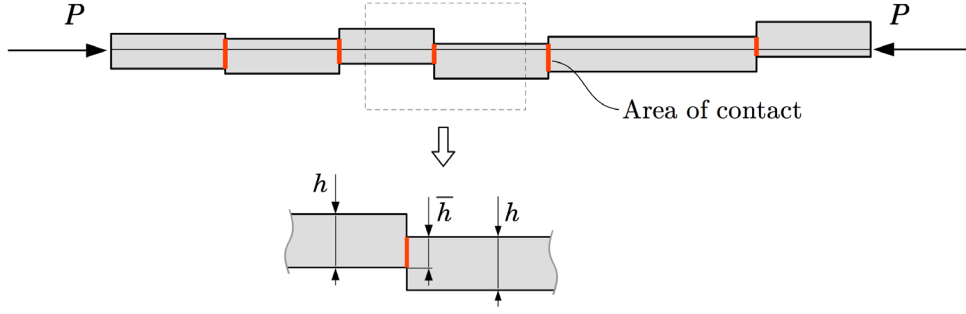
Figure 8: Force chain transmitting a load P and one contact interface between a pair of ice blocks, an elementary unit of the probabilistic limit load model. Blocks are of thickness h and the contact has a length of $\bar{h}$. Figure is from [2].

belonging to a force chain (Figure 8). The blocks are in a partial face-to-face contact due to a compressive load P. Local crushing is assumed to occur in a contact interface when $P \geq \bar{h}\sigma_p$, where $\bar{h}$ is the length of the contact interface and σ_p is the limit for compressive stress. In Ranta and Polojärvi [2] we show that this model for crushing, even with a simple triangular distribution for the contact lengths $\bar{h}$, leads to the model being able to capture the combined effect of h and σ_p on peak ice loads.

4   CONCLUSIONS

This paper summarized our work on limiting mechanisms on ice loads on inclined structure [1, 2]. The peak ice load data from ice-inclined structure processes was normalized with good accuracy by multiplying the load values with $1/\sqrt{h^3}$. This suggests that the peak ice loads in ice-inclined structure interaction process are governed by buckling. The buckling model quantifies the force chain buckling-related peak ice load values in an ice-inclined structure interaction process with fair accuracy.

The extension of the model to cover the effect of local ice crushing was also shortly discussed. The extended model accounts for a mixed-mode ice failure process where the root cause of ice failure can be due to either ice buckling or local crushing. Here we only briefly described the use of the extended model, but more details can be found from [2], where the model is even further extended into an algorithm, capable of producing large amounts of virtual ice load data that compares fairly well with full-scale observations. We believe the simple load limit load models have potential of yielding insight for the analysis of complex ice-structure interaction processes.

REFERENCES

[1] Ranta, J., Polojärvi, A., Tuhkuri, J. Limit mechanisms for ice loads on inclined structures: Buckling. *Cold Regions Science and Technology* (2018) 147:34-44.

[2] Ranta, J., Polojärvi, A. Limit mechanisms for ice loads on inclined structures: Local crushing. *Marine Structures* (2019) 67, 102633.

[3] Tuhkuri, J., Polojärvi, A. A review of discrete element simulation of ice-structure interaction. *Philosophical Transactions of the Royal Society A: Mathematical, Physical and Engineering Sciences* (2018) 376 (2129), art. no. 20170335.

[4] Peters, J., Muthuswamy, M., Wibowo, J., Tordesillas, A. Characterization of force chains in granular material. *Physical Review E - Statistical, Nonlinear, and Soft Matter Physics* (2005) 72(4)

[5] Paavilainen, J., Tuhkuri, J. Pressure distributions and force chains during simulated ice rubbling against sloped structures. *Cold Regions Science and Technology* (2013) 85:157-174.

[6] Hopkins, M. Numerical simulation of systems of multitudinous polygonal blocks. *Tech. Rep. 92–22; Cold Regions Research and Engineering Laboratory, CRREL* (1992)

[7] Paavilainen, J., Tuhkuri, J., Polojärvi, A. 2D combined finite-discrete element method to model multi-fracture of beam structures. *Engineering Computations* (2009) 26(6):578-598.

[8] Paavilainen, J., Tuhkuri, J. Parameter effects on simulated ice rubbling forces on a wide sloping structure. *Cold Regions Science and Technology* (2012) 81:1-10.

[9] Ranta, J., Polojärvi, A., Tuhkuri, J. The statistical analysis of peak ice loads in a simulated ice-structure interaction process. *Cold Regions Science and Technology* (2017) 133;46–55.

[10] Schreyer, H., Sulsky, D., Munday, L., Coon, M., Kwok, R. Elastic–decohesive constitutive model for sea ice. *Journal of Geophysical Research: Oceans* (2006) 111(11).

[11] Hillerborg, A., Modéer, M., Petersson, P.E. Analysis of crack formation and crack growth in concrete by means of fracture mechanics and finite elements. *Cement and Concrete Research* (1976) 6:773–782.

[12] Dempsey, J., Adamson, R., Mulmule, S. Scale effects on the in-situ tensile strength and fracture of ice. Part II: first-year sea ice at resolute, N.W.T. *International Journal of Fracture* (1999);95:347–366.

[13] Ranta, J., Polojärvi, A., and Tuhkuri, J. Ice loads on inclined marine structures - virtual experiments on ice failure process evolution. *Marine Structures* (2018) 57:72-86.

[14] Timco, G., Weeks, W. A review of the engineering properties of sea ice. *Cold Regions Science and Technology* (2010) 60(2):107129.

[15] Hetényi, M. *Beams on elastic foundation: Theory with applications in the fields of civil and mechanical engineering.* Ann Arbor: The University of Michigan Press (1979).

[16] Lau, M., Molgaard, J., Williams, F., and Swamidas, A. An analysis of ice breaking pattern and ice piece size around sloping structures. *In Proceedings of OMAE99, 18th International Conference on Offshore Mechanics and Arctic Engineering* (1999) 199-207.

[17] Frederking, R. Dynamic ice force on an inclined structure. *In Physics and Mechanics of Ice. IUTAM Symposium* (1980) 104116.

[18] Li, F., Yue, Q., Shkhinek, K., and Kärnä , T. A qualitative analysis is of breaking length of sheet ice against conical structures. *In Proceedings of the 17th International Conference on Port and Ocean Engineering under Arctic Conditions (POAC03)* (2003) 293-304.

ROLE OF SLIDING CONTACTS IN SHEAR BANDING AFFECTING GRANULAR MATERIALS

J. LIU[1], F. NICOT[2], A. WAUTIER[3] AND W. ZHOU[1]

[1] State Key Laboratory of Water Resources and Hydropower Engineering Science
Wuhan University
299 Bayi Road, 430072 Wuhan, China
e-mail: liujy@whu.edu.cn (Jiaying Liu) ; zw_mxx@whu.edu.cn (Wei Zhou)

[2] ETNA, IRSTEA
Université Grenoble Alpes
Domaine Universitaire, 38402 Saint Martin d'Hères, France
e-mail: francois.nicot@irstea.fr

[3] Aix-Marseille University, IRSTEA, UR RECOVER
3275 Rte Cézanne, CS 40061, 13182 Aix-en-Provence Cedex 5, France
e-mail: antoine.wautier@irstea.fr

Key words: granular materials, DEM, contact sliding, meso-structures, shear banding

Abstract. Shear banding is a widely concerned issue caused by shearing in the field of granular geomechanics. At the macroscopic scale, the constitutive models meet difficulties to describe how and why the shear band forms within the discrete granular assembly. The contact network inside the overall granular assembly helps us to understand the origin of some macroscopic features. Between contacting particles, sliding can occur, which is associated with the plastic dissipation. This local contact sliding may induce the rearrangement of local structures, and then contribute to the macroscopic failure characterized by larger patterns, such as shear banding. In this paper, we conduct DEM simulations using a dense specimen, and during the loading process an evident shear band appears. Then the contact sliding ratio, sliding index, and the relationship between the contact sliding and the mesostructural changes are investigated. Main conclusions are: sliding contacts firstly distribute randomly within the granular assembly, and will concentrate within the shear band after the stress peak; the sliding ratio and the sliding index show different evolution trend and distribution properties; sliding contacts are not within the strong contact network when the threshold to distinguish the strong and weak network is proper, but will be strongly influenced by the force chain buckling; considering the relation between the sliding and the meso loop exchanges, the topological dilations are related to the higher probability of contact sliding and plastic dissipation.

1 INTRODUCTION

Granular materials are quite common and simple in nature and they have been widely utilized as construction materials in the field of civil engineering. Then the mechanical

behaviours of granular materials have attracted much attention among engineers and researchers. For decades, the shear banding problem in frictional granular materials has been concerned, which contains a number of challenges in mathematical description and constitutive modelling [1,2]. Many publications incorporate micromechanical features, such as contact fabric, particle rolling and contact sliding, to reveal the original mechanism of shear banding [3-6].

Microscopic features could be related to some macroscopic evolutions in granular materials. For example, the stress-force-fabric (SFF) relationship has built the direct links between micro contact forces and macro stress quantity [7-11]. Considering the contacts and particles at the microscale, the sliding between particles may occur when the Mohr-Coulomb criterion is fulfilled. The microscopic failure, or microscopic shear behaviours, should contribute to the macroscopic shear failures such as shear banding.

The discrete numerical simulation has been widely applied in simulating the multiscale behaviours of granular media, owing to its simplicity of obtaining the microscopic information and the reasonable accordance of macroscopic responses to laboratory tests. Classical Discrete Element Method (DEM) has been adopted in investigating the strain localization for granular materials [12-14]. Besides, the modified or combined methods for DEM are capable to investigate the influences of the irregular shape and particle breakage on the shear banding [15,16]. For DEM simulations, the contact sliding is the unique mechanism in plastic energy dissipation. How the sliding contacts distribute and evolve should affect the mesostructural rearrangements in granular assemblies. Since the strong contact network (usually selected using the average normal contact ratio [17,18]) and the mesostructural topology (in 2D, loop structures are important [19-21]) are important characterizations in granular materials, the relationship between the contact sliding and them should also been further considered.

In this paper, we focus on the micro- and mesoscopic evolutions in granular materials during the shear band forming. Investigations are based on the quasi-2D biaxial DEM simulations (with a single layer of 3D particles), under the same loading conditions as our previous work [22]. The evolution and distribution of the contact sliding ratio and the sliding index are considered, and the sliding behaviours within the strong contact network as well as the topological changes are explored to identify the specific roles of sliding in shear banding.

2 DEM SIMULATION AND SHEAR BANDING

2.1 Parameters and models of DEM

We use the Discrete Element Method (DEM) proposed by Cundall and Strack [23] for the numerical simulations, based on the open-source software YADE [24]. The simple linear contact model is adopted, in which the normal and tangential contact forces (F_n and F_t) are computed as follows:

$$\begin{cases} F_n = k_n \delta_n, \\ dF_t = k_t d\delta_t, \quad F_t \leq F_n tan\phi \end{cases} \tag{1}$$

where k_n, k_t are the normal and tangential stiffness respectively, δ_n, δ_t are the corresponding relative displacements in normal and tangential direction, and ϕ is the friction angle which is a threshold limiting the relative sliding between particles. Relative sliding behaviour between spheres in a contact will take place when the tangential contact force reaches the maximum

value, as described by Eq. (1).

The quasi-2D biaxial test using DEM is carried out to model the mechanical behaviours and the shear band formation. The numerical simulation is conducted by using a model containing a single layer of 20,000 spheres within a rectangle domain, as shown in Fig. 1. The particle sizes obey a uniform distribution with average radii $D_{50} = 0.008m$ and $d_{max}/d_{min} = 2$. To create the sample, particles are randomly generated within the domain and their sizes are growing to reach the final isotropic state under a confining pressure of 100 kPa. The gravity is not considered, and the boundaries are set as rigid frictionless walls. The key parameters for the contact model: k_n/D_s is set to 300 MPa, where $D_s = R_1 R_2/(R_1 + R_2)$; k_t/k_n is set to 0.5; the friction angle ϕ is 35°.

After confining, the numerical specimen reaches a relative dense state (initial porosity is 0.161). Then we apply the biaxial loading is applied, as shown in Fig. 1: the compression is imposed in the vertical direction (σ_{22} and ε_{22}) with a strain rate of the upper and lower walls equals to 0.01 /s. In the lateral direction (σ_{11} and ε_{11}), the pressure is maintained constant to 100 kPa. The stress and strain characterization are then described as follows: deviatoric stress $q = \sigma_{22} - \sigma_{11}$ and volumetric strain $\varepsilon_v = \varepsilon_{11} + \varepsilon_{22}$.
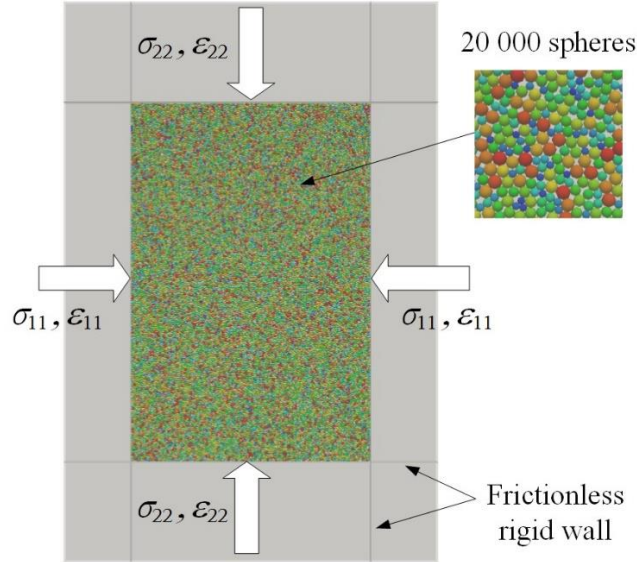
Figure 1: DEM model for biaxial tests

2.2 Macroscopic responses

Figure 2 gives the macroscopic evolutions of the deviatoric stress q and the volumetric strain ε_v. Similar to other publications [4,12,13], the deviatoric stress q experiences the hardening and the softening phases, while ε_v manifests a clear tendency of dilation. We select States from A to G, to track the evolution of the strain localization pattern and the macroscopic stress and strain features. The corresponding incremental deviatoric strain fields of the 7 states are shown in Fig. 3, demonstrating the evolution of local strain distribution pattern from homogeneity to heterogeneity in space. The Moran's Index can quantitatively capture the heterogeneity evolution, which was detailed explained in our previous work [22].
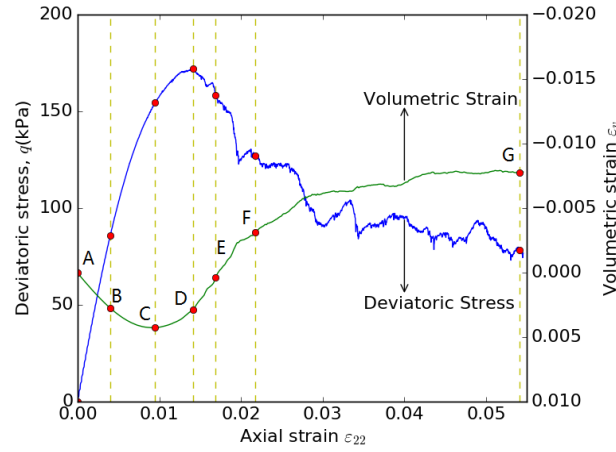
Figure 2: Strain softening process of dense specimen under biaxial test
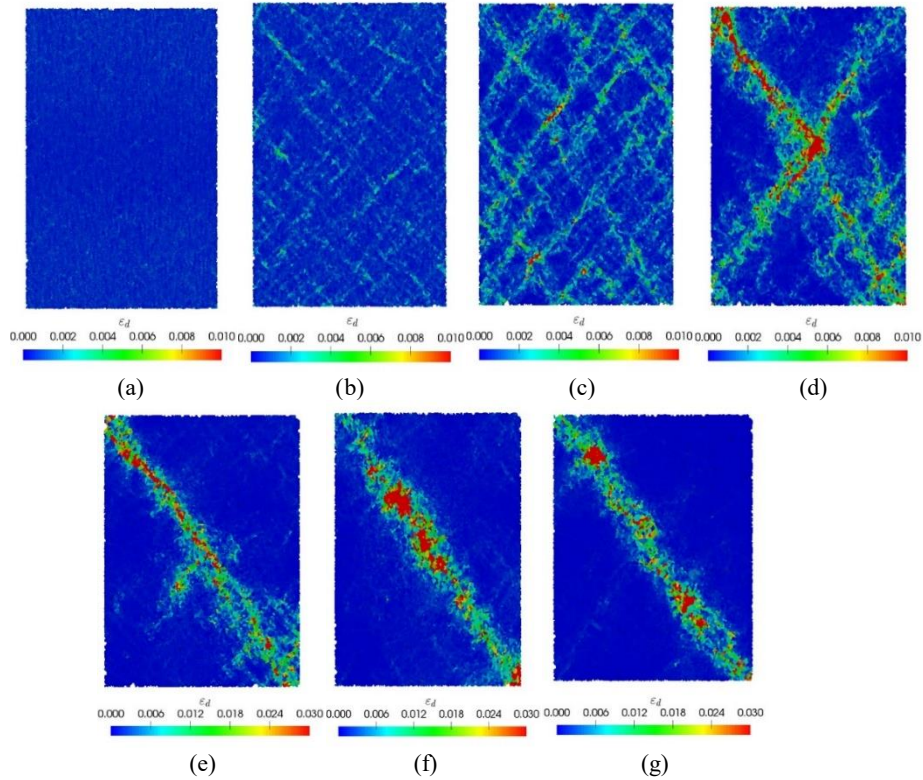
Figure 3: Spatial distributions of the incremental deviatoric strain for different loading states. (a) State A: ε_{22} = 0.0; (b) State B: ε_{22} = 0.0040; (c) State C: ε_{22} = 0.0095; (d) State D: ε_{22} = 0.0141; (e) State E: ε_{22} = 0.0169; (f) State F: ε_{22} = 0.0217; (g) State G: ε_{22} = 0.0541.

3 SLIDING CONTACTS AND RELATIVE MESO-STRUCTURES

3.1 Distribution of sliding contacts

Based on the framework of DEM, relative sliding behavior between connected spheres will take place when the tangential contact force reaches the maximum value, which is limited by

both the normal force and the friction angle, as described by Eq. (1). The sliding at one contact means the failure or dissipative mechanism at the microscopic scale. The ratio of sliding contacts, defined as $S_r = N_s/N_c$, can describe the proportion of microscopic failure for the granular assembly, in which N_s denotes the number of sliding contacts and N_c is the number of the total. The evolution of the ratio of sliding contacts is shown in Fig. 4, and S_r is divided into two parts (inside and outside the shear band, in these conditions N_s and N_c are considered for the corresponding domains) after the State E. At the beginning, the proportion of the sliding contacts rises gradually until the State C, which denotes that rearrangements of the bulk attains the maximum. After the peak value of the sliding ratio, the probability of sliding reduces gradually. When the single shear band ultimately appears, the sliding ratio stabilize, at the level about 0.007. During this period, the magnitudes of sliding ratios inside the shear band and outside the shear band manifest differently. The sliding contacts are mostly centralized within the shear band area, while only a small proportion of sliding contacts appear outside this area, which can be intuitively seen in Fig. 5 for States D and F.
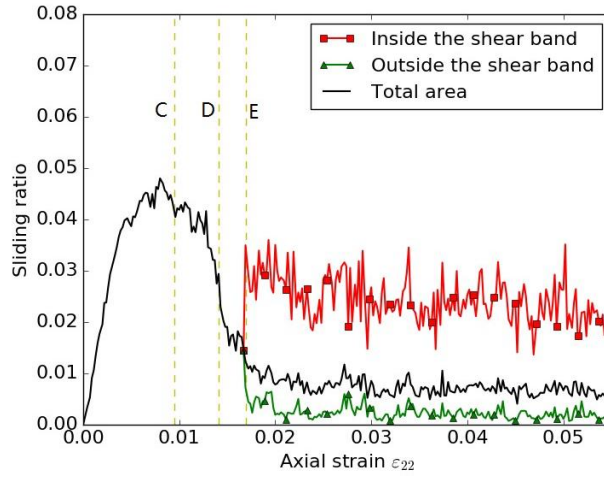
Figure 4: Evolution of the sliding ratio versus axial strain

(a)   (b)
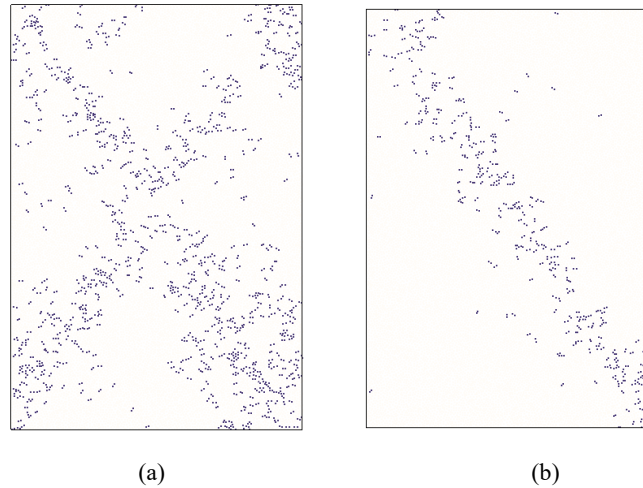
Figure 5: Distribution of sliding contacts: (a) State D and (b) State F

To better describe the degree of frictional mobilization for all the contacts, not only the sliding ones, a sliding index Ip is defined as:

$$I_{\mathrm{p}} = \frac{F_t}{F_n \tan \phi} \tag{2}$$

When I_p is near to 1.0, the contact is prone to slide; on the contrary, when I_p is near to 0, the contact is regarded as quite stable. Figure 6 shows the evolution of the average sliding index during the biaxial loading process, with the separate curves for areas inside and outside the shear band after State E. Similar to the evolution of the sliding ratio in Fig. 5, the average I_p experiences an increase at the beginning, and then decreases to a steady value during the development of the final shear band. The peak value of the sliding index appears at State D, which is associated with the stress peak. The S_r peak comes earlier than the I_p peak. Indeed, it can be assumed that sliding contacts belong to discrete local failures, without propagating to the total area; however, the average I_p is considered for all the contacts within the assembly. Therefore, the overall responses of I_p can reflect the evolving tendency of the stress. After the peak, I_p declines a little with small discrepancies of the two domains when shear band forms.

Besides, the distribution of I_p is quite different from the distribution of S_r in space, as shown in Fig. 7(a). At State F, there exists a clear single shear band, however, the sliding ratio distribution in space does not show any strain localization patterns. Then, we choose another parameter, the incremental sliding index dI_p between steps. It can be calculated using the difference of the sliding index between the current step i and the previous step $i-1$, i.e. d$I_p = I_p^i - I_p^{i-1}$. According to the definition, dI_p should fall in the range [-1, 1]. Positive values denote that the contact is nearer to the sliding, while negative values means that the contact is less possible to slide compared to the previous step. It can be seen that in Fig. 7(b), both large and small values of dI_p concentrate within the shear band area. That is to say, inside the shear band, large changes in contact state are involved, which can induce the quick and temporal rearrangements.
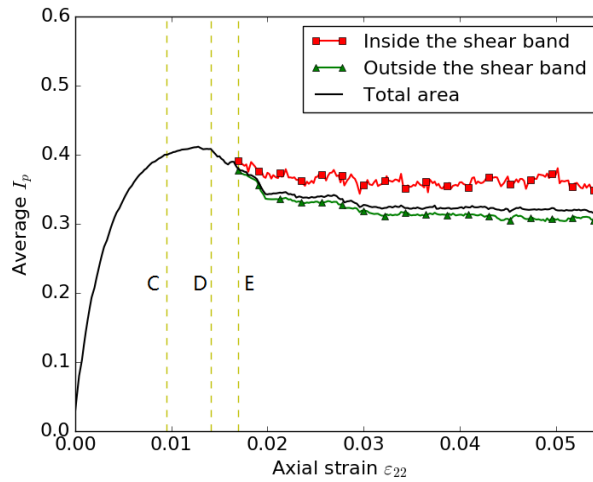
Figure 6: Evolution of average sliding index I_p
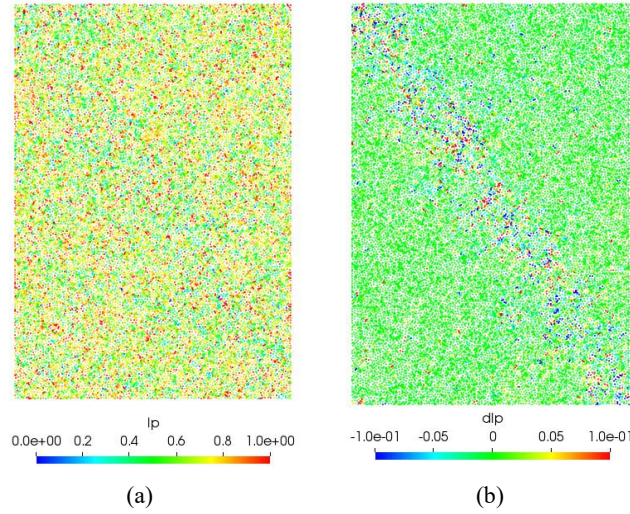
Figure 7: Distributions of sliding index I_p (a) and incremental sliding index dI_p (b) within the granular sample at State F

3.2 Sliding contacts and strong contact network

The contact network within the granular assembly can be divided into the strong and weak phase using the contact force threshold [17,18]. In most cases, the average contact force is used as the threshold, and the strong contact subnetwork is regarded as the important force transmission path. By introducing assumptions such as the linear path and the particle number, force chain structures can be selected from the strong contact network [21,25].

In this paper, we consider the accurate and comprehensive effects of strong contact network, and the sets of contacts with forces larger than several given values are considered. The cutoff ζ, denoting the ratio to the average normal contact force, is used to identify the set S_ζ. Then S_ζ contains the contacts which undertake forces larger than ζf_0, where f_0 denotes the average contact force within the granular assembly.

Within the different strong contact networks distinguished by ζ, the sliding ratio diverges. Figure 8 show the evolution of sliding ratio S_r versus ζ for the 7 selected states. Almost all the curves in Fig. 8 reflect the fact that sliding contacts do not exist in the strong contact network when $\zeta > 1.5$. That is to say, the contact sliding as the microscopic failure, is excluded from the really strong contacts. As for the range $\zeta < 1.0$, the sliding ratio of State C owns the highest magnitude, which is corresponding to Fig. 4. Considering the unique features of sliding ratio of strong contact network of all states, possibly the better threshold for the strong and weak phase of the contact network should fall in $[1.0f_0, 1.5f_0]$.

Liu et al. [22] have defined the average sliding ratio S_{rp} around the particles, and based on this concept, they found that contact sliding is not directly relating to the force chain buckling, but will be influenced around the force chain buckling area. Since force chains are selected within the strong contact network when $\zeta = 1.0$, it can be assumed that the contact sliding has no intersection with the strong contact network, but the failure within the strong contact network may induce the sliding occurring and accumulating.
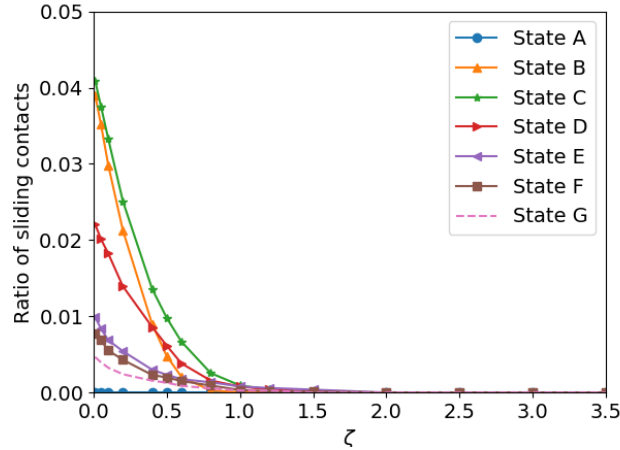
Figure 8: Sliding ratio within the strong contact network distinguished by ζ

3.3 Sliding contacts and loop transformation

The overall contact network of the granular assembly can be tessellated into meso loops, which are quite convenient to analyze the local deformation features in 2D granular materials [26,27]. From step to step, loops may keep constant or transform to other structures. The transformations or exchanges between local structures are temporal and complex, which will lead to the systematic change of the overall structure.

Loops within the granular assembly can be categorized by the number of particles of the circle. L6, denoting the cell connected by 6 spheres in 2D simulations, has been deeply investigated in many publications [12,19,21] for its capability of deformation. In this paper we take L6 as an example to explore the topological exchanges, and possible changes for L6 can be shown in Fig. 10. The change in next step, we call it "Future", and we name 3 types of changes:

- Future_6C, for unchanged L6
- Future_6S, for L6 which will decompose to smaller ones
- Future_6L, for L6 which will change to a larger loop

The transformations and exchanges of loops are corresponding to the contact loss and gain within the contact network. Whether these changing contacts are sliding will indicate the plastic energy dissipation. Figure 9 give the average sliding ratio information for L6 with different futures respectively. Loops associated with changes, i.e. Future_6L and Future_6S, obtain higher sliding ratios than the constant ones during the biaxial loading. Furthermore, dilative loops (Future_6L) are more likely to involve a higher probability of sliding contacts and dissipating behaviors than the contractive ones (Future_6S) do.

53
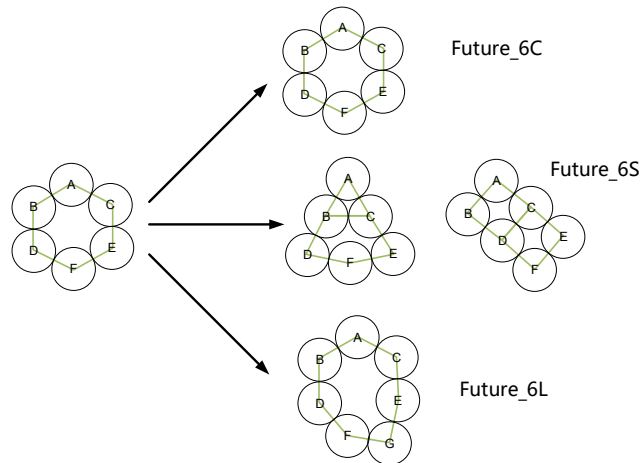
Figure 9: Possible changes for L6 loops between steps

Considering the average sliding ratios of L6 with different futures inside and outside the shear band, the dissipative behaviors could diverse, especially for the dilative changes. We can see that in Figure 11, loop exchanges within the shear band are associated with larger sliding ratios, especially for the dilative changes which reach the magnitude nearly 0.1. Even though there exist a few enlargements outside the shear band, the involving dissipation is not very obvious in comparison with the constant cells and the shrinkage ones inside the shear band.

Dilative loops at the mesoscopic scale should be related to the macroscopic dilatancy, which has been regarded as an irreversible plastic characteristic in soil mechanics [28][29]. The sliding ratio evolutions within the meso structures has revealed that the correlation between plastic energy dissipation and the dilatancy at the mesoscale. The contact sliding may not lead to the contact loss or gain, also the contact loss and gain may not involve plastic sliding behaviors. However, the sliding behaviors are easier to break the contacts and form larger local structures which lead to the dilatancy. The process should be irreversible, and once these kinds of behaviors accumulate and reach a high percentage, the plastic phase of the bulk appears. Shear banding is one kind of shear failures that local rearrangements concentrate within the localized area, and the dilative exchanges of loops should mainly occur within the banding zones.
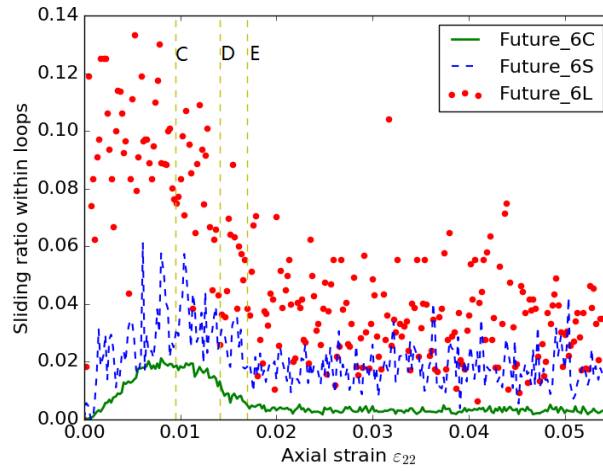
Figure 11: Sliding ratios within L6 for different futures
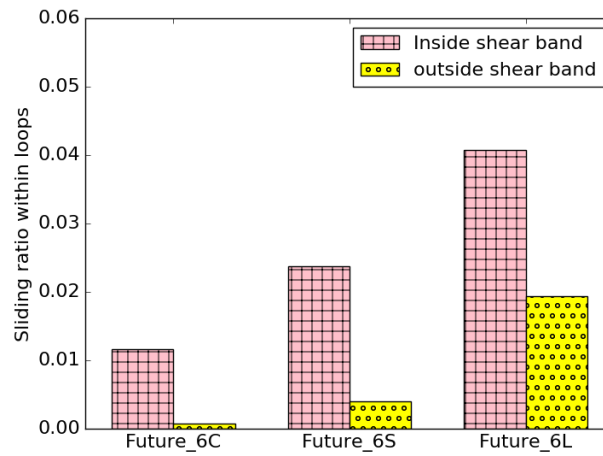
Figure 12: Sliding ratios of L6 with different futures in different domains

4   CONCLUSIONS

By conducting numerical DEM biaxial tests for a dense granular assembly, this paper investigates the contact sliding evolution and distribution within the specimen during shear banding, and identifies the relationships between the mesostructural changes and the contact sliding. Main conclusions are as follows:

- According to the spatial distribution of incremental shear strains of the dense granular assembly, it can be concluded that the heterogeneity develops gradually along the biaxial loading, until the final shear band forms. Inside the shear band, the sliding contacts, high values of incremental sliding index magnitude and loop exchanges are concentrated.
- Both the sliding ratio and sliding index demonstrate a peak in the evolution curves,

which is earlier or close to the macro stress peak. Furthermore the peak of sliding index could reflect the macro stress peak. By using different threshold to distinguish the strong and weak contact network, it is concluded that sliding contacts are located outside strong contact network and the threshold for the strong contact network may be 1 to 1.5 times average contact force.

- During the biaxial loading process, the loop type L6 could be constant, dilative or contractive in topology. The higher contact sliding ratio is associated with the dilative exchanges, which indicates that the plastic dissipation is quite essential to the dilatancy at the meso-scale.

- Thanks to this characterization of the microstructure features inside shear band domain, the present study paves the way for a deeper understanding of the micromechanical mechanisms responsible for the existence of shear bands in dense granular materials. The understanding of the link between contact sliding, mesostructure deformations and macroscopic shear banding and softening are now within reach.

REFERENCES

[1] Vardoulakis, I. and Graf, B. Calibration of constitutive models for granular materials using data from biaxial experiments. *Géotechnique* (1985) **35(3)** : 299-317.

[2] Borja, R. I. and Atilla A. Computational modeling of deformation bands in granular media. I. Geological and mathematical framework. *Comput. Method. Appl. Mech. Eng.* (2004) **193.27-29**: 2667-2698.

[3] Tordesillas, A. Force chain buckling, unjamming transitions and shear banding in dense granular assemblies. *Philos. Mag* (2007) **87.32**: 4987-5016.

[4] Zhou, B., Huang, R., Wang, H. and Wang, J. DEM investigation of particle anti-rotation effects on the micromechanical response of granular materials. *Granul. Matter* (2013)**15.3**: 315-326.

[5] Oda, M. and Kazuyoshi I. Study on couple stress and shear band development in granular media based on numerical simulation analyses. *Int. J. Eng. Sci* (2000)**38.15**: 1713-1740.

[6] Zhao, J. and Guo N. The interplay between anisotropy and strain localisation in granular soils: a multiscale insight. *Géotechnique* (2015)**65.8**: 642-656.

[7] Li, X. and Yu, H-S. On the stress–force–fabric relationship for granular materials. *Int. J. Solids. Struct* (2013)**50.9**: 1285-1302.

[8] Guo, N. and Zhao J. The signature of shear-induced anisotropy in granular media. *Comput. Geotech* (2013)**47**: 1-15.

[9] Bathurst, R.J. and Rothenburg, L. Observations on stress-force-fabric relationships in idealized granular materials. *Mech. Mater* (1990)**9.1**: 65-80.

[10] Kruyt, N. P. Micromechanical study of fabric evolution in quasi-static deformation of granular materials. *Mech. Mater* (2012)**44**: 120-129.

[11] Ouadfel, H. and Rothenburg, L. Stress–force–fabric'relationship for assemblies of ellipsoids. *Mech. Mater* (2001)**33.4**: 201-221.

[12] Zhu, H., Nguyen, H. N., Nicot, F. and Darve, F. On a common critical state in localized and diffuse failure modes. *J. Mech. Phys. Solids* **(2016)**95: 112-131.

[13] Gu, X., Huang M. and Qian J. Discrete element modeling of shear band in granular materials. *Theor. Appl. Fract. Mech* (2014) **72**: 37-49.

[14] Jiang, M. and Zhang W. DEM analyses of shear band in granular materials. *Eng. Computations* (2015)**32.4**: 985-1005.

[15] Zhou, W., Yang, L., Ma, G., Xu, K., Lai, Z. and Chang, X. DEM modeling of shear bands in crushable and irregularly shaped granular materials. *Granul. Matter* (2017)**19.2**: 25.

[16] Ma, G., Regueiro, R. A., Zhou, W., Wang, Q. and Liu, J. Role of particle crushing on particle kinematics and shear banding in granular materials. *Acta. Geotech* (2018)**13.3**: 601-618.

[17] Radjai, F., Stéphane R. and Moreau J. J. Contact forces in a granular packing. *Chaos: An*

Interdisciplinary Journal of Nonlinear Science (1999)**9.3**: 544-550.

[18]   Voivret, C., Radjai, F., Delenne, J. Y. and El Youssoufi, M. S. Multiscale force networks in highly polydisperse granular media. *Phys. Rev. Lett* (2009)**102.17**: 178001.

[19]   Zhu, H., François N. and Darve F. Meso-structure organization in two-dimensional granular materials along biaxial loading path. *Int. J. Solids. Struct* (2016) **96**: 25-37.

[20]   Tordesillas, A., Zhang J. and Behringer R. Buckling force chains in dense granular assemblies: physical and numerical experiments. *Geomechanics and Geoengineering: An International Journal* (2009)**4.1**: 3-16.

[21]   Tordesillas, A, Walker D. M. and Lin, Q. Force cycles and force chains. *Phys. Rev. E* (2010)**81.1**: 011302.

[22]   Liu, J., Nicot F. and Zhou W. Sustainability of internal structures during shear band forming in 2D granular materials. *Powder. Technol* (2018)**338**: 458-470.

[23]   Cundall, P. A. and Strack, O. D. A discrete numerical model for granular assemblies. *Géotechnique* (1979) **29.1**: 47-65.

[24]   Šmilauer, Václav, et al. "Using and programming." *The Yade Project, doi* 10 (2015).

[25]   Peters, J. F., Muthuswamy, M., Wibowo, J. and Tordesillas, A. Characterization of force chains in granular material. *Phys. Rev. E* (2005)**72.4**: 041307.

[26]   Kruyt, N. P. and Rothenburg, L. On micromechanical characteristics of the critical state of two-dimensional granular materials. *Acta. Mech* (2014) 225(8): 2301-2318.

[27]   Kruyt, N.P. and Rothenburg, L. A micromechanical study of dilatancy of granular materials. *J. Mech. Phys. Solids* (2016)**95**: 411-427.

[28]   Collins, I. F. and Muhunthan, B. On the relationship between stress–dilatancy, anisotropy, and plastic dissipation for granular materials. *Geotechnique* (2003)**53.7**: 611-618.

[29]   Li, X. S. and Dafalias, Y. F. Dilatancy for cohesionless soils. *Geotechnique* (2000) **50.4**: 449-460.

STRESS DISTRIBUTION IN TRIMODAL SAMPLES

DEYUN LIU[1], CATHERINE O'SULLIVAN[2] AND ANTONIO CARRARO[3]

[1]Department of Civil and Environmental Engineering, Imperial College London
London SW7 2AZ
d.liu18@imperial.ac.uk

[2] Department of Civil and Environmental Engineering, Imperial College London
London SW7 2AZ
cath.osullivan@imperial.ac.uk

[3] Department of Civil and Environmental Engineering, Imperial College London
London SW7 2AZ
antonio.carraro@imperial.ac.uk

Key words: Granular Materials, DEM, Contact Problems, Trimodal Materials, Stress distribution

Abstract. The distribution of stress between coarser and finer particles in gap-graded soils is considered a key factor contributing to the risk of internal instability or suffusion, amongst other soil properties. In reality soils can have more complex size distributions than being purely bimodal. In this study, the discrete element method was used to investigate the stress distribution of trimodal gap-graded materials with different grading curves. The quantification of stresses and contacts forces at particle scale data indicates that the stress distribution in trimodal materials are influenced by the percentage of fines, the proportion of the medium fraction, and the initial density. Specifically, when the stress transfer within trimodal material was partitioned into six contacts classes, the results indicate that the stress carried out by each contact type is strongly associated with their percentage fractions and the size ratio between the different particle types.

1 INTRODUCTION

The particle size distribution (PSD), i.e. the cumulative distribution by particle mass (volume) of particle sizes (diameters), is one of the most basic ways to characterize a soil in both geotechnical research and practice. Soils are described as uniformly graded, broadly graded or gap-graded depending on the shape of the particle size distribution. While the PSD shape is understood to influence the engineering behaviour of soil, the fundamental mechanics of the influence of PSD shape on behaviour are poorly understood.

Restricting consideration to non-plastic, cohesionless soils, it is clear that there have been a large number of experimental studies looking at gap-graded soils. In most cases a finer grained sand was mixed with a coarser grained sand or fines were added to a host sand so that the resulting mixtures in both cases were almost bimodal. The proportion of the overall mass taken up by the finer grains (typically representing silts and clays) is then termed the fines content

(FC). Zuo and Baudet (2015) give a review of the relevant literature, focusing on the idea of a transitional FC, where the material behaviour transitions from being dominated by the coarse grains to become dominated by the finer grains. Developing on ideas put forward by Skempton and Brogan (1994), Shire et al. (2014) carried out a series of DEM simulations on gap-graded samples of spheres. They calculated the average stress in the finer grains normalized by the overall applied stress, this approximates to the proportion of stress transmitted by the finer grains. Shire's data showed that the extent to which the fines participate in stress transmission depends on the fines content and on the ratio between the coarse and finer grain sizes. The data do not support the concept of a single transitional FC, rather a more gradual transition between coarse- and fines-dominated behaviour.

Natural geological deposits of purely bimodal material are rare and so a comprehensive and relevant understanding of stress distribution in materials needs to consider more complex particle size distributions. More robust analyses of the effect of PSD shape on the mechanical behaviour of soil mixtures may therefore require varying PSDs in a more systematic way, from uniformly graded to well graded PSDs. In a first step to develop this broader perspective, this study considers trimodal materials, with fine, coarse and medium-sized grains. Rather than considering the stresses in the particles, the sample is partitioned into six classes: stress transmitted via (i) coarse-coarse particle contacts, (ii) coarse-medium contacts, (iii) medium-medium contacts, (iv) medium-fine contacts, (v) coarse-fine contacts and (vi) fine-fine contacts. DEM samples are compressed from an initial non-contacting cloud of grains to an isotropic stress of 500 kPa. Initially a purely bimodal material containing 25% fines is considered and the proportion of the medium-sized grains is then systematically increased.

2 PARTICLE SIZE DISTRIBUTION CONSIDERED

A total of 9 trimodal specimens were created; their grading curves are shown in Fig. 1. The minimum and maximum particle diameters used in each simulation specimen were 0.076 mm and 0.425 mm, respectively. Three size ratios (i.e. the size ratio between coarse and fines-sized grains, SR_{cf}; the size ratio between Coarse and medium-sized grains, SR_{cm}; the size ratio between medium and fines-sized grains, SR_{mf}) and three particles fraction (i.e. fines fraction; medium fraction; coarse fraction) are considered in this study. As shown in Fig.1, for all 9 grading curves, the size ratio SR_{cf} is constant, which is 5.6 in this study. For clarity, each of those specimens is named as A Tri B%_C%, where A represents a size ratio SR_{mf}, B% is a number representing a fines fraction percent by mass/volume, and C% represents a medium fraction. For instance, '1.54 Tri 25.0%_50.0%' indicates a trimodal specimen with the fines fraction of 25% and the medium fraction of 50%, and the size ratio SR_{mf} of this specimen is 1.54.
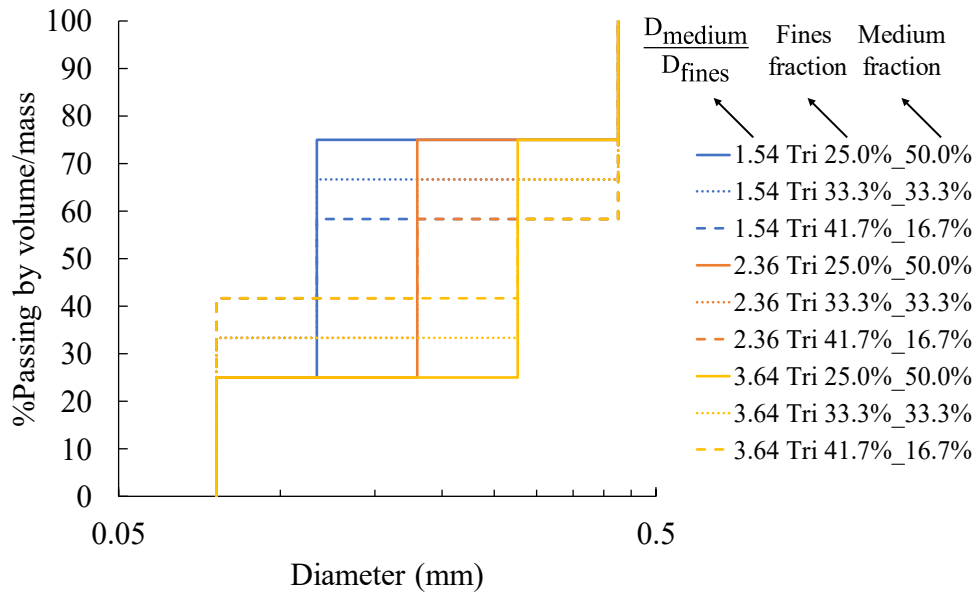
Figure 1: Particle size distribution of simulation specimens

3 DEM SIMULATIONS AND SETUP

All DEM simulations were conducted on cubic samples by means of a modified version of the open-source DEM code Granular LAMMPS (Plimpton, 1995). Periodic boundary conditions were employed to generate all specimens due to its efficiency in reducing boundary effects (e.g. Shire et al., 2014). A simplified Hertz-Mindlin contact model was used, the basic input simulation parameters were shear modulus (G = 29.17 GPa), particle density (2670 kg/m³), Poisson's ratio (ν = 0.2). These input parameters were used in previous DEM works (e.g. Huang et al., 2014) and were similar to experimentally derived values (e.g. Barreto, 2008). All DEM specimens were initially created in random positions by means of an in-house placement code (Fig. 2), followed by periodic isotropic compression through the method proposed by Cundall (1988). A stress-controlled algorithm was used to achieve the target isotropic mean effective stress of 500 kPa. To investigate the density effect, three inter-particle friction coefficient μ were used for isotropic compression: (1) μ = 0.001, referring to a dense condition; (2) μ = 0.1, referring to a moderate condition; (3) μ = 0.3. referring to a loose condition.

All simulations were carried out by means of the high-performance computing (HPC) service CX1 at Imperial College London. Although particle shape is known to be a significant factor in influencing soil behaviour, the high computational cost of simulations necessitated the selection of spherical particles. All simulations were terminated when the mean effective stress reached the desired values of 500 kPa, with coordination number, void ratio remaining constant.
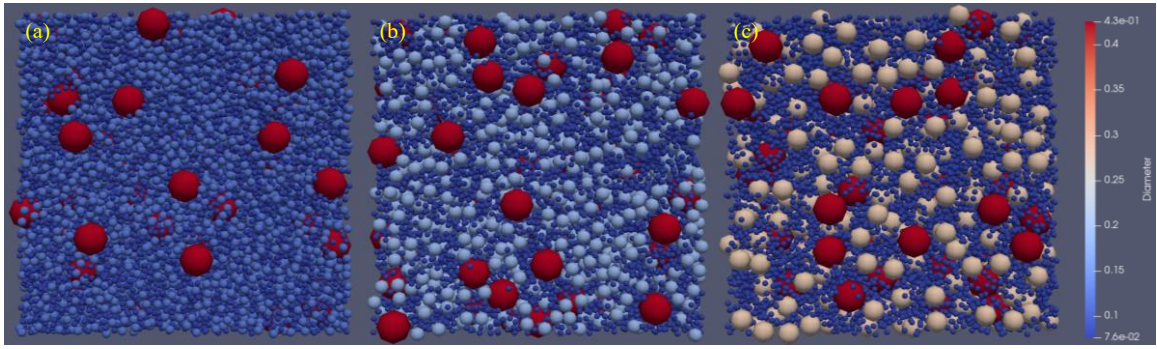
Figure 2: Typical generated simulation specimens: (a) 1.54 Tri 25.0%_50.0%; (b) 2.36 Tri 25.0%_50%; (c)3.64 Tri 25.0%_50%

4   RESULTS AND DISCUSSION

4.1 Detailed data for 3.64 Tri 25.0%_50.0%

A simulation test of 3.64 Tri 25.0%_50.0% (particle size distribution illustrated on Fig. 3a) with $\mu = 0.1$ (i.e. a moderately dense condition) is considered in detail to better understand the stress transfer within trimodal materials. Fig. 3b shows the cumulative distribution of particle connectivity by number for simulation, where the connectivity is the number of contacts involving an individual particle. The distributions for the coarse, medium and fines-sized grains are presented separately. As shown in Fig. 3b, the connectivity values for both the coarse and medium-sized grains are always greater than 0, which suggests that all of the particles in these size fractions are active in stress transmission when subjected to isotropic compression. However, for approximately 50% of the fines-size grains, the connectivity number is 0, which suggests those particles sit loosely in the void space and do not transfer stress. Fig. 3c shows the cumulative distribution of particle mean stresses by number for the simulation. Fig. 3c confirms that the coarse and medium-sized grains transmit stress, while approximately 50% of the fines-sized grains are not active in transferring stress.

Fig. 3d presents the cumulative distribution of contact forces by number for this simulation. As illustrated in Fig 4a, for trimodal materials, a total of six contacts classes support the whole structure: (i) coarse-coarse contacts (C-C contacts), (ii) coarse-medium contacts (C-M contacts), (iii) medium-medium contacts (M-M contacts), (iv) medium-fines contacts (M-F contacts), (v) coarse-fine contacts (C-F contacts) and (vi) fines-fines contacts (F-F contacts). As shown in Fig. 3d, for approximately 99% of the F-F contacts, M-F contacts and C-F contacts, the contact forces are lower than 0.04 N, on the contrary, the contact force values of C-C contacts, C-M contacts and M-M contacts have a much broader distribution. Those results show that those contact forces that do exist involving the fine-sized grains are very small compared to other grains, i.e. even where the fine grains have contacts, their contribution to the overall stress transmission is very small.
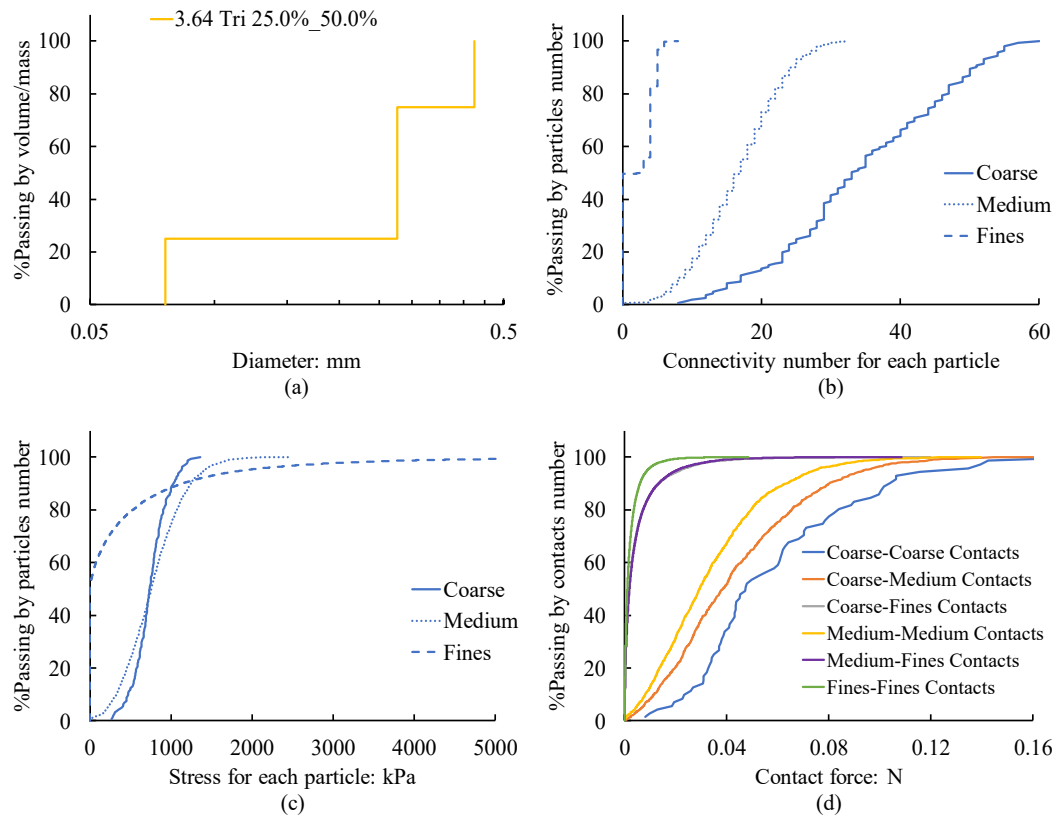
Figure 3: Detailed data for 3.64 Tri 25%_50% test: (a) particle size distribution; (b) connectivity number distribution; (c) stress level distribution; (d) contact force distribution
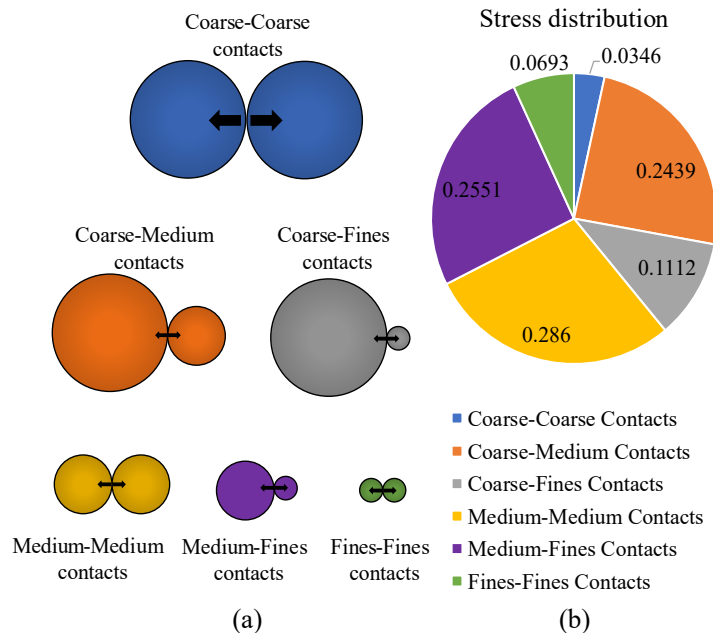
Figure 4: Analysis of contacts for 3.64 Tri 25%_50% test: (a) six contacts types; (b) stress distribution determined by contact forces

62

4.2 Analysis of contacts and stress distribution

In DEM, the contacts force data can be used to calculate the stresses within the material. As illustrated in O'Sullivan (2011) (for example) the 3D stress tensor is calculated by equation (1):

$$\sigma_{ij} = \frac{1}{V} \sum_{C=1}^{N_{c,V}} f_i^c l_j^c \tag{1}$$

Where $N_{c,V}$ is the total number of contacs in the volume V, $f_i^c = (f_x^c \; f_y^c \; f_z^c)$ is the force vector for contact c and $l_j^c = (l_x^c \; l_y^c \; l_z^c)$ is the branch vector for contact c. The contribution of each set of contacts to the overall stress tensor can be determined by restricting the summation to contacts within that set (i.e. for the C-C contacts the summation considers only C-C contact forces). Fig. 4b illustrates the proportion of the mean stress ($\frac{1}{3}\sigma_{ii}$) carried by each set of contacts for the simulation test above (i.e. 3.64 Tri 25.0%_50.0%, μ = 0.1). The medium fraction accounts for largest proportion of the specimen by mass and so it can be seen that C-M contacts, M-M contacts and M-F contacts contribute to the most proportion of the stress transmission of the structure. Specifically, the M-M contacts transmit the largest proportion (i.e. 0.286) of the stresses, which is 0.286 × 500 kPa = 143 kPa.

On the contrary, the stresses carried out by C-C contacts are relatively small compared to those of other contacts, which may be attributed to that both medium and fines-sized grains separate the coarse-sized grains during isotropic compression. Furthermore, F-F contacts account for a small proportion (i.e. 0.0693) of the stress transmission of the structure, which agrees with results identified in Fig. 3b and Fig. 3c.

4.3 Density effect

Shire et al. (2014) carried out a series of DEM simulations on bimodal gap-graded soils and highlighted the significant influence of initial density on the stress transmission, therefore, it is worthwhile to investigate the density effect for trimodal materials. As shown in Fig. 5, the initial density strongly affects stress transmission in the trimodal material considered, for instance, Fig. 5a shows that the connectivity number of approximately 14% particles is 0 when the specimen is in the dense condition. On the contrary, in the loose condition, approximately 83% particles do not connect with other particles, which suggests those particles are not active in support the structure. The similar tendency is also identified in Fig. 5b and Fig. 5c. Prior analyses of bi-modal materials suggest that the susceptibility of the stress distribution to changes in density will depend on the proportion of each particle type and the ratios of particle sizes.

Fig. 5d illustrates the variation in the stress distribution by contact type with density. AS the density increases from the loose state, it can be seen that the stresses carried out by M-F and F-F contacts significantly increase, while the stresses transferred by C-C and C-M contacts decrease at the same time. Those results highlight the significant influence of initial density on the stress distribution for within the trimodal material considered here.
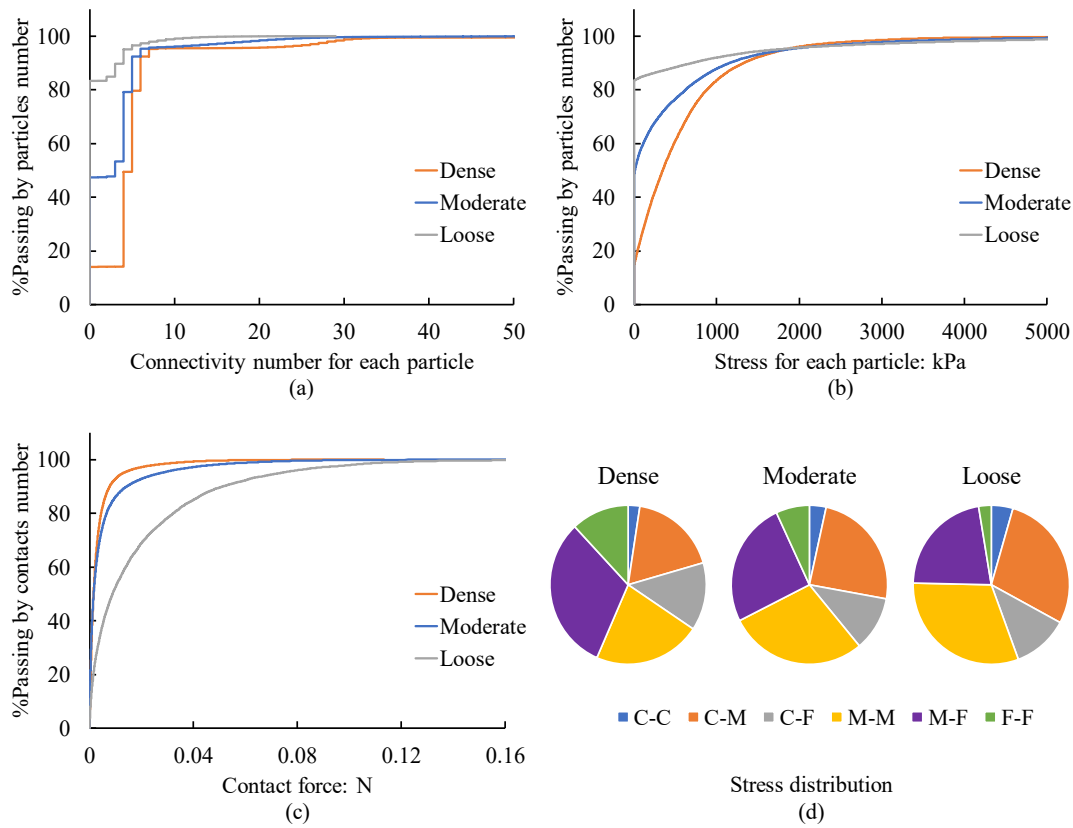
Figure 5: 3.64 Tri 25%_50% tests with three density conditions: (a) connectivity number distribution; (b) stress level distribution; (c) contact force distribution; (d) stress distribution determined by contact forces

4.4 Fines and medium content effects

Various combinations of fine and medium fractions considered to better understand how the proportion of the different fractions influences the overall stress transmission. Typical simulation tests with $\mu = 0.3$ were selected as illustrated in Fig. 6a, the size ratio SR_{mf} of three specimens is fixed of 3.64 with the fines and medium fractions changing in a wide range. Fig. 6b shows the stress distributions for three specimens, the results indicate that the stresses carried out by C-F and F-F contacts significantly increases with an increase in the fines fraction, while the amount of the overall stresses carried out by the C-M and M-M contacts declines as the proportion of the medium fraction decreases. Furthermore, the stresses transferred by M-F contacts vary significantly.
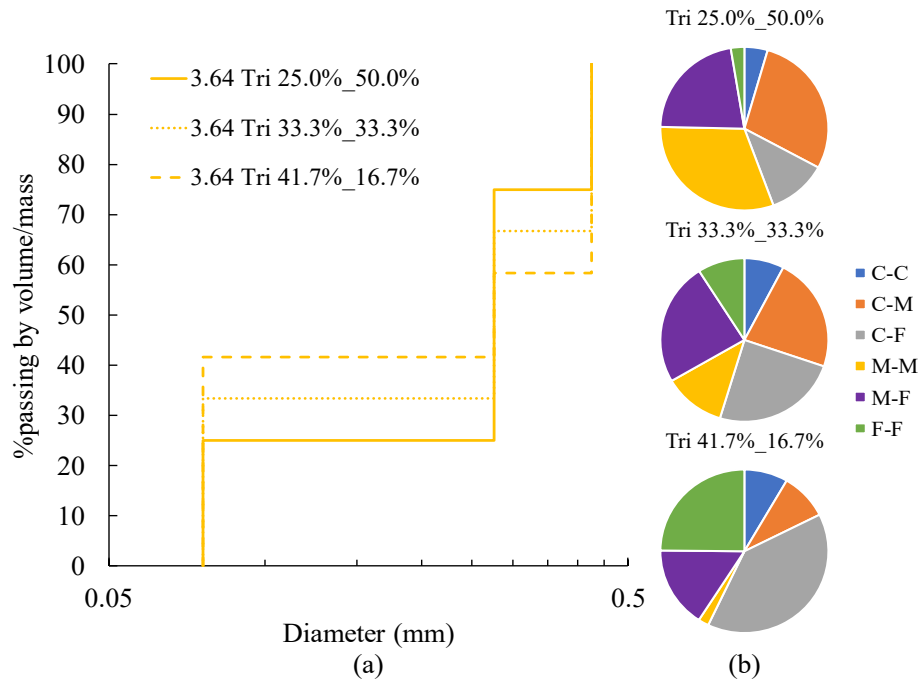
Figure 6: Fines and medium content effects: (a) particle size distributions; (b) stress distribution

4.5 Size ratio effect

The size ratio effect was studied by keeping the fine and medium fractions fixed, as illustrated in Fig. 7a. Restricting consideration to a loose condition, Fig. 7b considers the stress distributions three specimens with size ratios SR_{mf} changing from 1.54 to 3.64. The results show that the stress transmission is strongly associated with the size ratio SR_{mf}. For instance, the stresses carried out by M-F contacts significantly decrease with the rise of the size ratio SR_{mf}, which suggests that the interaction between medium and fines-sized grains decreases with the size ratio SR_{mf} increase.

On the contrary, the stresses transferred by C-M contacts increase with increasing size ratio SR_{cm}. Furthermore, it can be seen that the stresses transmitted by the C-F contacts fluctuated in a narrow range for those three tests, which may be attributed to the constant size ratio SR_{cf} for these specimens.
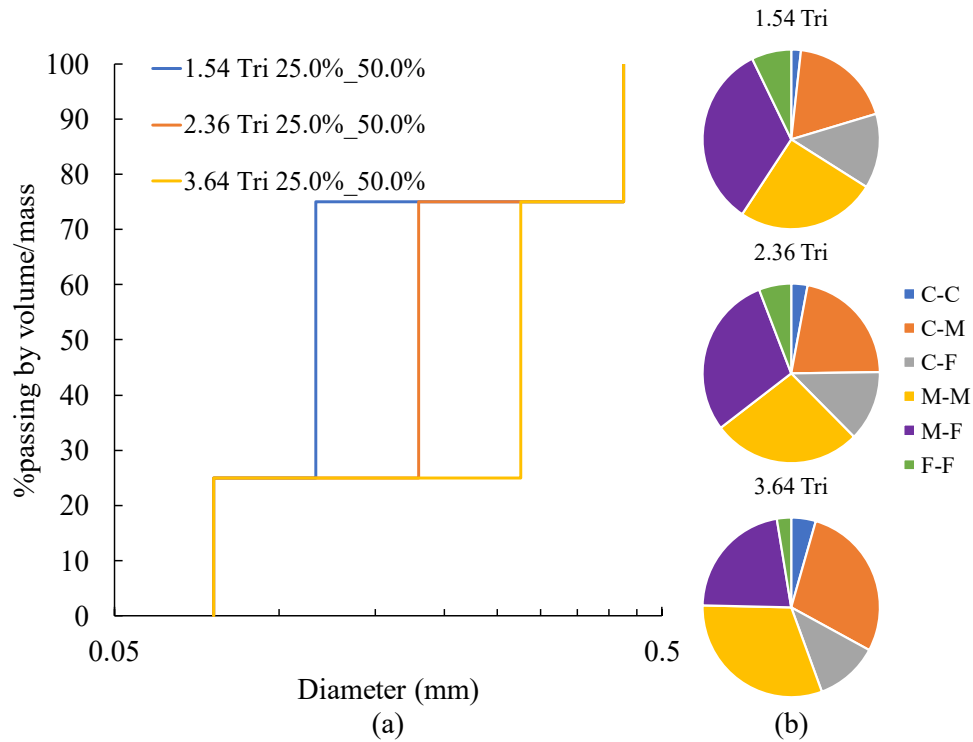
Figure 7: Size ratio effect: (a) particle size distributions; (b) stress distribution

5 CONCLUSIONS

This paper presents a total of 27 DEM simulation at three initial densities to study the stress distribution on trimodal materials of isotropic compression. The results highlighted the significance influence of initial density on the stress distribution of trimodal materials. In addition, the results show that the stress distributions in trimodal materials are strongly associated with fines fraction, medium fraction and the size ratios among those grains.

REFERENCES

[1] Zuo, L., and Baudet, B. A. Determination of the transitional fines content of sand-non plastic fines mixtures. *Soils and Foundations* (2015) **55(1)**: 213-219.

[2] Skempton, A. W., and Brogan, J. M. Experiments on piping in sandy gravels. *Géotechnique* (1994) **44(3)**: 449-460.

[3] Shire, T., O'Sullivan, C., Hanley, K. J., and Fannin, R. J. Fabric and effective stress distribution in internally unstable soils. *Journal of Geotechnical and Geoenvironmental Engineering* (2014) **140(12)**: 04014072.

[4] Plimpton, S. Fast parallel algorithms for short-range molecular dynamics. *Journal of computational physics* (1995) **117(1)**: 1-19.

[5] Huang, X., Hanley, K. J., O'Sullivan, C., and Kwok, C. Y. Exploring the influence of interparticle friction on critical state behaviour using DEM. *International Journal for*

Numerical and Analytical Methods in Geomechanics (2014) **38(12)**: 1276-1297.

[6] Barreto, D. Numerical and experimental investigation into the behaviour of granular materials under generalised stress states. *Ph.D. thesis, Imperial College London, London* (2008)

[7] Cundall, P. A. Computer simulations of dense sphere assemblies. In *Studies in Applied Mechanics* (1988) **20**: 113-123. Elsevier.

[8] O'Sullivan, C. Particulate discrete element modelling: a geomechanics perspective (2011) CRC Press.

SIMULATION OF ESPRESSO COFFEE EXTRACTION USING SMOOTHED PARTICLE HYDRODYNAMICS

M. ELLERO[1] AND L. NAVARINI [2]

[1] Basque Center for Applied Mathematics
Alameda de Mazarredo 14, 48400 Bilbao, Spain
Email: mellero@bcamath.org

[2] Illycaffe' S.p.A
Via Flavia 110, Trieste 34147, Italy
Email: luciano.navarini@illy.com

Key words: Porous media, particle migration, coffee extraction, concentration kinetics

Abstract.   A mesoscopic model for the simulation of espresso extraction based on the Smoothed Particle Hydrodynamics method is presented. The model incorporates some essential features such as bimodal granulometry (fines-coarses) of the coffee bed, double (liquid/intra-granular) molecular diffusion and solid-liquid release mechanism. The porous structures ('coarses') are modelled as stationary solid regions whereas the migration of cellular fragments ('fines') is described by single-particles advected by the flow. The boundary filter is modelled as a buffer region where fines are immobilized while entering it, therefore providing a transient flow impedance. The model captures well the transient permeability of the coffee bed under direct-inverse discharge observed in experiments, showing the importance of fines migration on the hydrodynamics of the extraction. The concentration kinetics for different molecular compounds are also studied. The present work lays down the basis for the virtual analysis of coffee flavors by monitoring the hydrodynamic and microstructural effects on the balance of extracted key-odorant or taste-actives compounds in the beverage.

1   INTRODUCTION

Coffee is one of the most widely consumed beverages in the world. Several brewing methods can be used to prepare the beverage depending on consumer's taste as well as cultural and geographical habits. In many countries, drip brew, or filter coffee, is the traditionally consumed beverage. This method for brewing coffee involves pouring water over roasted and ground coffee contained on a filter. Water seeps through the coffee, absorbing its extractable fraction solely under gravity, and then passes through the bottom of the filter. The used coffee grounds are retained in the filter with the liquid falling (dripping) into a collecting vessel such as a carafe or pot. In addition to this popular coffee beverage, espresso coffee is gaining a big world-wide success not only as a phenomenon of

fashion. This is also due to the greater sensory satisfaction it gives to the consumer when compared with coffees prepared with other brewing methods [1]. Traditional espresso brewing requires specialized equipments that have to heat water to a temperature between 92C and 94C and pressurize it to 9 ± 2 bar. The process is applied (percolation time) until the beverage volume in the cup meets consumer's personal preference or the regional traditions. For example, in Italy, the volume ranges from 20 mL or less (ristretto) to 50 mL or more (lungo), with a typical volume of 20 to 30 mL for regular espresso shot [2]. The application of pressure, makes espresso brewing more complex than drip brewing from a physico-chemical process point of view [3]. In particular, during the passage of hot water through the layer of roasted and ground coffee (coffee bed), the following chemical and physical phenomena can be described [4]: (A) *Initial imbibition* of the porous coffee matrix with consequent irreversible progressive swelling of the coffee particles, this causes a progressive decrease in the porosity of the matrix and therefore an increase in hydraulic resistance. During this process, reversible migration of small coffee particles in the direction of water flow also occurs. (B) *Solubilization* of the hydrophilic substances contained in the coffee bed resulting in a progressive increase of density and viscosity of the percolating fluid flow and the concomitant partial erosion of the coffee particles. (C) *Stripping* of coffee lipids thanks to the pressurized hot water and progressive emulsification of lipophilic substances due to the action of surfactants naturally occurring in roasted coffee, with a further progressive increase in viscosity of the percolating fluid.
From a coffee cup quality point of view, in addition to model the physics of the espresso extraction, it is necessary to take into the account the modelling of the mass transfer during the process and preferably, the taste-wise chemical compounds mass transfer in order to follow the extraction of solubles (and if possible also of not-solubles) from roasted coffee.

The goal of this work is to provide a novel simulation framework based on the Smoothed Particle Hydrodynamic (SPH) method to describe coffee espresso extraction taking into account the complex mesoscopic structure of the coffee bed. SPH is a popular Lagrangian method to resolve the flow of simple and complex liquids by relying on an kernel-based discretization of prescribed set of partial differential equations (e.g. Navier-Stokes equations for the momentum, advection-diffusion equation for suspended solute etc.) describing the flow locally. This generally leads to a discrete set of ordinary differential equations for fluid particles interacting pair-wisely [5]. Due to its Lagrangian meshless character the technique is able to tackle complex geometries, such as those arising in a deformable porous media, as well as to model Lagrangian particulate transport [6], memory effects in complex fluids [7] and multiphase flow [8] in a natural way . The technique has been also generalized to incorporate Brownian fluctuations (when needed) on hydrodynamic variables by using the so-called GENERIC framework (an acronym for General Equation for Non-equilibrium Reversible-Irreversible Coupling) [9]. This has allowed it to be extended to the regime of fluctuating hydrodynamics both for simple [10] and complex non-Newtonian fluids [11].
In this work we present a new SPH model of coffee filtration able to describe the entire complex mesoscopic structure of the coffee bed and its potential influence on the flow of the

liquid through the filter as well as the transport/release of solute. Complex granulometry of the coffee bed is described on different scales, from the fixed porous medium represented by the large solid grains, to the small free cellular fragments - i.e. the 'fines' - down to the molecular solute (e.g. caffeine) modelled via a concentration field. Moreover, for the dynamics of the molecular solute within liquid phase is taken into account together with a mass transfer model due to stripping from the solid-liquid interface. The mesoscopic model naturally leads to the transient flow permeability effects observed in experiments [12] - as well as its effect on the concentration dynamics - which have been traditionally interpreted in terms of microstructural changes such as pore's swelling or fines particles migration [13]. An extended model fully coupled with intra-granular transport of solute has been recently presented in [14].

2 MESOSCOPIC PARTICLE MODEL

In this section the mesoscopic model of coffee filtration is presented. The solid phases will be modelled based on the different characteristic dimensions of the specific components. In particular, in the problem of coffee filtration three main characteristic dimensions are associated to distinct dispersed phases: (i) solid grains ($\approx$450 μm) representing the fixed porous structure; (ii) the so-called 'fines' ($\approx$30 μm) representing the flowing cellular fragments and (iii) the molecular components, e.g. volatile or non volatile compounds such as caffeine etc. ($\approx$ 1-10 nm). Water flowing through the porous structure and coupled with material transport will be modelled based on standard Newtonian hydrodynamics. A sketch of the model is given in Fig. (1).
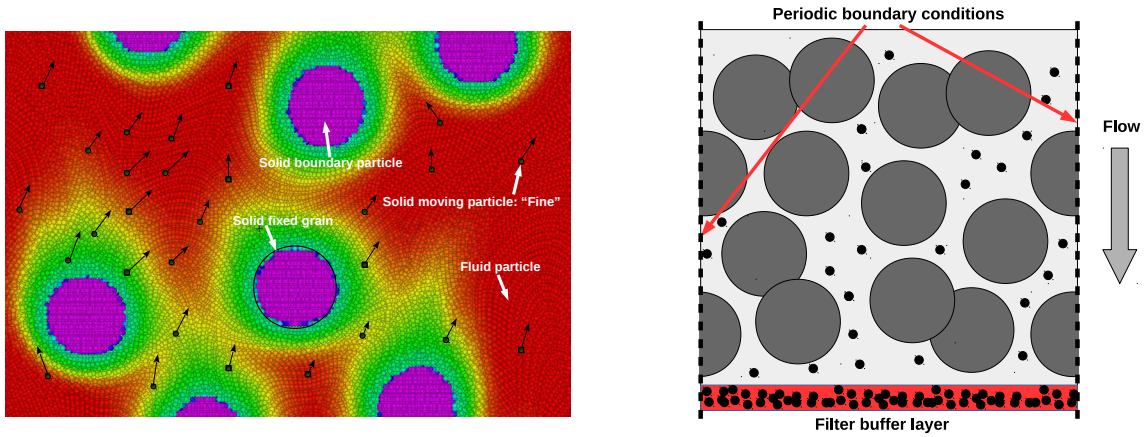
Figure 1: Left: sketch of the SPH model. Solid dispersed phases is described at different levels. (a) Large solid grains representing the fixed porous structures are denoted as violet regions. (b) Small solid fragments, i.e. the "fines", are modelled as independent solid moving particles. (c) The smallest dispersed molecular components - the chemical species - are treated on a continuum level via a concentration field (color map). Right: sketch of the filter model. Fines are advected by the flow. Filter is modelled as a buffer region (red area in the figure) of specified thickness. When fines enter this region they are 'immobilized' and provide transient mechanical impedance depending on the instantaneous concentration of trapped fines.

2.1 Suspending fluid phase model: Smoothed Particle Hydrodynamics

The fluid phase dynamics is governed by the isothermal Navier-Stokes equations. The model adopted in this work is the Smoothed Particle Hydrodynamics (SPH) which is a Lagrangian meshless method for the numerical solution of partial differential equations [5]. In SPH a set of fluid particles $i = 1, .., N$ are distributed homogeneously over the domain and move according to conservative and dissipative interparticle forces $\mathbf{F}_{ij}^{C,D}$ estimated from their local neighborhood. In the isothermal case, the following set of ordinary differential equations for the particle positions, velocities are solved numerically and represent a Lagrangian discretization of the Navier-Stokes equations [5]

$$\dot{\mathbf{r}}_i = \mathbf{v}_i, \qquad m\dot{\mathbf{v}}_i = -\sum_j \overbrace{\left(\frac{p_i}{d_i^2} + \frac{p_j}{d_j^2}\right) W_{ij}' \mathbf{e}_{ij}}^{\mathbf{F}_{ij}^C} + 4\sum_j \overbrace{\bar{\eta}_{ij}\frac{W_{ij}'}{d_i d_j r_{ij}}\mathbf{v}_{ij}}^{\mathbf{F}_{ij}^D} + \mathbf{g}_i, \qquad (1)$$

$$\underbrace{\phantom{-\sum_j \left(\frac{p_i}{d_i^2} + \frac{p_j}{d_j^2}\right) W_{ij}' \mathbf{e}_{ij}}}_{(\nabla p/\rho)_i} \qquad \underbrace{\phantom{4\sum_j \bar{\eta}_{ij}\frac{W_{ij}'}{d_i d_j r_{ij}}\mathbf{v}_{ij}}}_{\eta(\nabla^2\mathbf{v}/\rho)_i}$$

where the time derivative is Lagrangian and $W_{ij} = W(r = r_{ij})$ is a kernel function and $W_{ij}' = \partial W(r)/\partial r|_{r=r_{ij}}$ its spatial derivative. $r_{ij} = \|\mathbf{r}_{ij}\| = \|\mathbf{r}_i - \mathbf{r}_j\|$, $\mathbf{e}_{ij} = \mathbf{r}_{ij}/r_{ij}$ is the unit vector joining particles i and j, whereas $\mathbf{v}_{ij} = \mathbf{v}_i - \mathbf{v}_j$ their corresponding velocity difference. $\bar{\eta}_{ij} = (\eta_i + \eta_j)/2$ is the averaged dynamic viscosity of the fluid and η_i is the local value of viscosity associated to particle i. p_i represents the pressure associated to particle i, calculated via a suitable equation of state (EOS). Here we choose an ideal EOS $p_i = c_s^2(\rho_i - \rho_0)$ where $\rho_i = md_i$ is the mass density associated to the particle i (m is the constant particle mass) and c_s is the sound speed in the liquid. $d_i = \sum_j W_{ij}$ is the corresponding number density and $\mathbf{g}_i$ represents any external body force. Finally, in the previous expression for the EOS the speed of sounds c_s must be chosen sufficiently larger than any other velocity present in the problem in order to avoid artificial compressibility effects [5]. The SPH model can be generalized to fluctuating hydrodynamics by casting it into the so-called GENERIC formulation [9] which allows to incorporate additional stochastic terms in Eq.(1) satisfying Fluctuation-Dissipation Theorem [10].

2.2 Porous solid phase model

Solid regions of arbitrary shapes can be created by immobilizing a certain number of solid SPH particles located within a prescribed fixed porous structure (i.e. the solid coffee grains) in a similar way to what done in [15] (see Fig.1 left). No-slip velocity condition is enforced on the liquid-solid interface where boundary particle velocities are set to zero. Solid SPH particles (violet in the figure) interact with fluid SPH particles by means of the same forces presented in Eq.(1), but differently to fluid particles, they are not allowed to move.

2.3 Dispersed molecular phase continuum model

Due to the large scale separation existing between molecular compounds (e.g. caffeine: $\approx$ 1nm) and the solid grains forming the porous structure ($\approx 450\mu$m), the dispersed

molecular phase can be treated as a continuum and modelled through a concentration field. In this case, each SPH fluid particle is equipped with an additional microstructural variable, i.e. a scalar concentration field c_i, whose dynamics is governed by an inhomogeneous advection-diffusion equation. We consider here the most general case where the diffusion coefficient $D(\mathbf{r})$ can be space-dependent. The corresponding Lagrangian SPH discretization reads

$$\dot{c}_i = 4 \underbrace{\sum_j \bar{D}_{i,j} \frac{W'_{ij}}{d_i d_j} \frac{c_{ij}}{r_{ij}}}_{D(\nabla^2 c)_i} \tag{2}$$

where the time derivative is Lagrangian and $c_{ij} = c_i - c_j$ and $\bar{D}_{i,j} = (D_i + D_j)/2$ is the average interparticle diffusion coefficient and D_i is the local diffusion coefficient associated to particle i. Note that advection is implicitly taken into account through the Lagrangian motion of the particles. Note also that the term within the summation in Eq.(2) is anti-symmetric by swapping i, j indices and therefore the mass of solute is automatically conserved. Fig. (1) shows a color map describing a frame of the concentration field of a given molecular compound released from the solid grains (violet: maximum - red: zero). Note that different $\bar{D}_{i,j}$ values can be associated to different SPH particles-pairs: this is important, for example, to model the diffusive molecular processes, separately, in the liquid phase and within the solid grain. In practice, several volatile or non-volatile taste-active compounds with different diffusional properties are associated to the final sensorial experience (fruity, malty, honey-like, buttery, roasty etc.). In the process of coffee filtration it is therefore important to assess the instantaneous time-dependent concentration of different compounds (i.e. characterized by different $D_{b,s}$) in the cup, in order to optimize the product and/or target specific flavors [16].

2.4 Discrete "fines" model

"Fines" are modelled as single solid SPH particles advected by the flow. We adopt here the so-called *minimal single-particle model* proposed in the context of Dissipative Particle Dynamics [17]. We select randomly a number of SPH particles in the fluid domain and, according to the target fines concentration, we regard them as a solid flowing particles (black spheres in Fig. (1)). It should be noted that in the bulk flow the fines are just passive tracers and do not have any influence on the flow. However, if their positions are constrained they are characterized by a well-defined hydrodynamic radius (approximately equal to the kernel cutoff radius r_c) and therefore they provide a mechanism of mechanical impedance for the bulk flow itself. This feature is important in the model of the physical filter.

2.5 Filter model

The filter at the bottom (or upper) boundary of the coffee bed is modelled as an additional buffer region of finite thickness (red area in Fig. 1: right). The fines move with the flow under the action of an external pressure force and eventually percolate the porous structure; when they finally enter the bottom buffer region, their identity change

and they are regarded as fixed solid boundary particles with zero velocity - of the same type of those used to model the solid region inside a grain (see Fig. 1 left). As a consequence, they present an obstacle to the flow of the down-streaming fluid particles which exit the domain. Depending on the initial concentration of fines dispersed in the liquid domain (denoted as θ) the total number of fines trapped in the filter can significantly change together with the values of filter resistance leading to a simple model of transient coffee bed permeability [12].

3 NUMERICAL RESULTS

3.1 Numerical parameters

In order to model numerically the physical system discussed above, we chose the following setup. (A) **Coarse coffee grains** ('coarses': 500μm) : they are modelled as fixed spherical solid regions of size $d_{grain} = 2.0$ using 16 SPH particles per diameter (see Fig. 1). The 'coarses' solid volume fraction is $\phi = 0.48$. (B) **Fine particles** ('fines': 30μm): they are modelled as mobile single SPH particles (passive tracers). Being the SPH resolution of the grain 16, we have a computational ratio $d_{grain}/d_{fine} \approx 16$ ($d_{fine} \approx$ hydrodynamic radius SPH particle) which is consistent with the physical ration in real coffee bed. The 'fines' solid volume fraction will range in $\theta = 0.001 - 0.01$. (C) **Molecular compounds** (e.g. caffeine, hyperfines etc.: $\ll 1\mu$m). Their small size compared to the other characteristic lengths (H, d_{grain}, d_{fine}) justifies a continuum approach based on the solution of an advection-diffusion equation for the corresponding concentration field (Eq.(2)). Different species can in principle have different size and therefore different bulk diffusion coefficients D_b as well as release rates D_r. (D) **Coffee bed** (2cm thickness):to model a realistic coffee bed of, say, 2cm thickness[18] we consider a height of the simulation domain $L_y = 80$ (y is the direction of filtration), leading to a numerical ratio $L_y/d_{grain} = 40$. In the transversal direction (x) it is assumed that the coffee bed is homogeneous and periodic boundary conditions can be imposed. This allows to minimize the size of the simulation domain and computing time. Finite size effects can be eliminated by taking $L_x = 10 = 5d_{fine}$. In conclusion, we consider a two-dimensional domain $L_x \times L_y = 10 \times 80$, discretized with $N = 80 \times 640 = 51,200$ SPH particles.
Fluid density is chosen to be $\rho = 1$, whereas viscosity $\mu = 3$. The average flow velocity (which controls the effective Reynolds number) is tuned by applying an effective body acceleration mimicking a pressure drop, i.e. $F = \Delta p/(L_y\rho)$. For example, a value of $F = 2000$ leads to peak average velocity $V_{max} \approx 15$ and peak Reynolds number (in absence of fines: just fixed solid grains) $\text{Re}_{max} = d_{grain}V_{max}\rho/\eta \approx 10$, matching experimental conditions. The speed of sound is chosen sufficiently large than V_{max} to reduce density fluctuations, i.e. $c_s = 500 \gg V_{max}$. Finally, the bulk diffusion coefficient for a specific compound will range in $D_b = 0.005 - 0.1$ to give a bulk Peclet number $\text{Pe} = 600 - 6000$ corresponding to transient peak flow velocity. Values for the corresponding rate of of release coefficients will be typically a factor 10 smaller than the the bulk free diffusion, i.e. $D_r = 0.001 - 0.1$, but different conditions will be explored.

3.2 Inverse filtration process: transient permeability

In order to understand the different transport processes involved in the percolation of water through the coffee bed system, a transient direct/inverse filtration is considered and results are discussed in relation to experimental data [18]. In this section we focus on the hydrodynamic response of the system. In particular, Fig.2 shows the dynamics
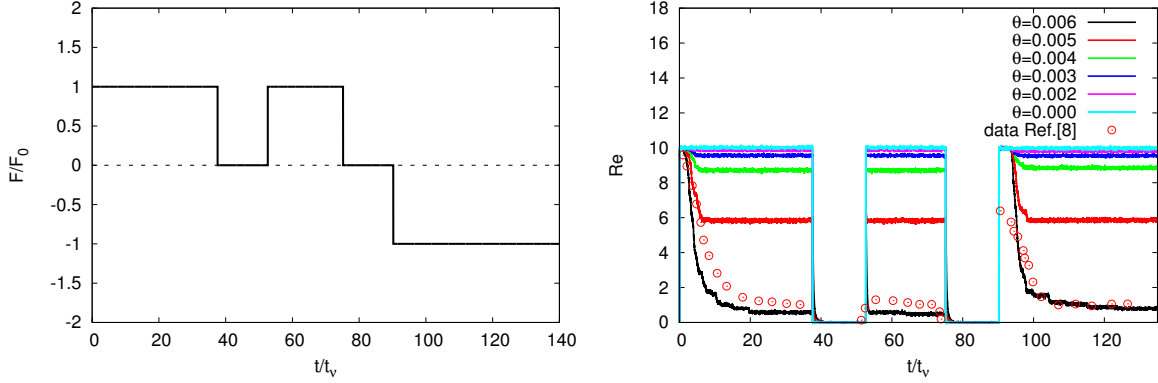
Figure 2: Inverse discharge. Left: time-dependent dimensionless applied forcing. Right: time-dependent Reynolds number (absolute value) for different fines concentration θ. Slow permeability decay is evident as result of increase fine concentration.

of the full direct/inverse discharge. Left: the time-dependent dimensionless forcing (i.e. pressure drop). Right: time-dependent Reynolds number based on spatially-averaged flow velocity (absolute value) for different fines-concentration θ. Experimental data for the transient direct/inverse discharge flow reported in [13] have been also showed as reference. Note that in the experimental data the initial transient flow increase have been removed since (in experiment) it is due to an applied pressure raising over a finite time, i.e. not 'instantaneously' applied as in the simulations. Time has been made dimensionless with the viscous liquid time $\tau_\nu = d_{grain}^2/\nu = 2^2/3 = 1.33$. In order to compare with experiments, corresponding real viscous time in SI units should be $\tau_\nu = d_{grain}^2/\nu = (400 \times 10^{-6})^2/10^{-6} = 0.16$s.

Initially a *direct discharge* process with constant pressure forcing is applied up to dimensionless times approximately equal to $t^* = t/\tau_\nu = 38$. This is followed by a resting state (zero applied force for t^*=38-55) after which the same constant forcing is applied again. Finally, an additional resting condition (t^*=75-90) is followed by a constant pressure force applied in the opposite direction (*inverse discharge*).

We consider first the flow response of the pure porous structure, i.e. for fine concentration $\theta = 0$ (light blue line in Fig.2). After application of pressure drop, flow rate increases quickly and reaches a steady state value (Re $\approx$ 10). The small transient at $\theta = 0$ (not visible in the figure) occurs on typical viscous time scales of order τ_ν. After removal of the forcing, flow rates decay quickly to zero (relaxation time scales $\approx \tau_\nu$) and then again reach the same value upon re-activation of the forcing in the same direction. After forcing reversal, again the flow responds very quickly reaching the same value of the Reynolds

number (absolute value is shown in the figure). Under these conditions ($\theta = 0$), coffee bed permeability is constant and the results are in agreement with previous simulations. The case where fines are present ($\theta \neq 0$) is, however, qualitatively different. We have studied different fine concentrations ranging from 0.002 to 0.006 as shown in Fig.2 (right). Initially (direct discharge at $t^* < 3$) the flow reaches the same peak Reynolds number during the very short viscous time scales. This again corresponds to the fast viscous relaxation consistent with a fixed porous structure. In this case, however, it does not represent a steady state but a transient peak. In fact, the meta-stable state at Re=10 is followed by a transient decay characterized by a significant longer relaxation time compared to τ_ν. This slow decay ($3 < t^* < 10$) is due to the fines be displaced and their transient accumulation in the filter. In fact, fines need some finite time to migrate from their initial positions (randomly dispersed in the liquid phase) to the filter at the boundary of the domain. As the number of trapped particles increases, so does the overall flow resistance leading to the observed transient permeability.

Flow rate eventually reaches a steady-state value which depends on the initial concentration of fines present in the liquid phase. Small values of $\theta = 0.001$ (violet line) do not alter significant the filtration hydrodynamics respect to simple fixed porous case. However, $\theta = 0.006$ (black line) leads to a significant reduction of flow permeability (nearly one order in the averaged steady Reynolds number) in substantial agreement with experimental data of espresso extraction reported in Ref.[18].

If the forcing term is temporarily switched off and then re-activated, the flow rate reaches instantaneously the same steady state. This means that the water flows through the same geometrical configuration corresponding to the fixed porous structure with an additional mechanical impedance offered by the unchanged amount of fines trapped in the filter. Finally, if we invert the flow we observe again the same relaxation process characterized by the long relaxation time as at the beginning of the simulation. The reversed flow forces the fines to move in the opposite direction and be released by the filter, i.e. again through the coffee bed. A typical dimensionless time $\tau_m^* \approx H/(V_{max}\tau_\nu) = 7.1$ is required for all fines to migrate towards the bottom filter, after which the permeability reaches again a steady state. This is in remarkable good agreement with the transient decay observed in Fig.2 (right) and in experiment of inverse coffee discharge. These results show that fines migration is the main mesoscopic transport process responsible for the reversible transient permeability observed in experiments [13, 12, 18].

3.3   Concentration dynamics

After validation of the hydrodynamic response and transient permeability made in the previous section, we study here the release and dynamics of a passive scalar field (the molecular compound concentration, e.g. caffeine) during the filtration process. In particular, we are interested in the resulting *cumulative output concentration* in the cup for different choice of physical parameters, namely the concentration of fines θ, the bulk diffusion coefficients D_b of the molecular compound and release rates D_r. In this work intra-granular diffusion coefficients D_s is set to zero.
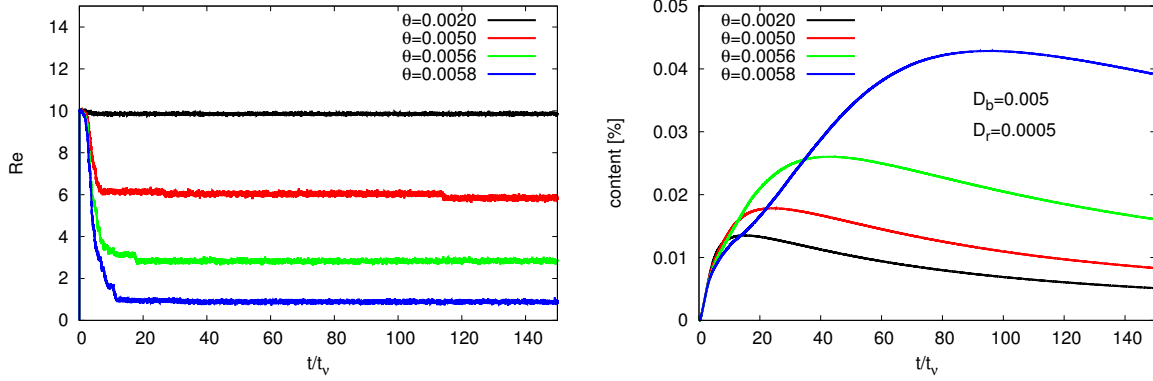
Figure 3: Direct discharge. Left: time-dependent Reynolds number (absolute value) for different fines concentration θ. Right: cumulative output concentration.

The cumulative output concentration is defined as compound-to-total mass ratio, i.e. $M_{compound}(t)/M_{tot}(t)$, where both quantities refer to the instantaneous values collected at the output and depend on time. We consider here the case of direct discharge (Fig.3: left). According to the time scale shown Fig.3, the temporal window explored is in the range of [0-25]s when dimensionalized by $\tau_\nu = 0.16s$, which corresponds to the typical time for an espresso preparation.

3.3.1 Effect of fine concentration θ

We first select two typical values of diffusion coefficients consistent with the discussion given in Sec.III.A, that is $D_b = 0.005$ (corresponding to peak/steady Peclet numbers Pe$_{bulk}$ =6000/600) and $D_r = 0.0005 = 0.1D_b$, and check the effect of the fines concentration θ on the the cumulative molecular concentration. In this work intra-granular diffusion coefficients $D_s = 0$ so release mechanism is limited to the molecular compounds located inside a grain near the solid/liquid interface. Effect of different intra-granular diffusion coefficients D_s have been discussed in [14].

From Fig.3 (left) it can be seen how for small values of the fines concentration (e.g. $\theta = 0.002$) no transient permeability is observed. The resulting dynamics of the output compound concentration (Fig.3: right) exhibits a peak value ($\approx 1.4\%$) at short times ($t^* \approx 15$) after which the output compound concentration in the cup decreases softly. This peak value is shifted towards larger times and increases in magnitude for increasing θ. For example, for $\theta = 0.0058$, peak concentration ($\approx 4\%$) is reached at dimensionless time $t^* \approx 95$. Therefore, the present results shows that incorporation of a finite amount of fines, by inducing a transient permeability of the coffee bed, leads to smaller steady flow rates during filtration (Re ≈ 1). This, in turn, increases the residence time of the flow in contact with the solid surface of grains, therefore maximizing the molecular release process. In the case of fast flow (Re ≈ 10 for $\theta = 0.002$), water is washed quickly through the coffee bed preventing a proper release of substances into the fluid.
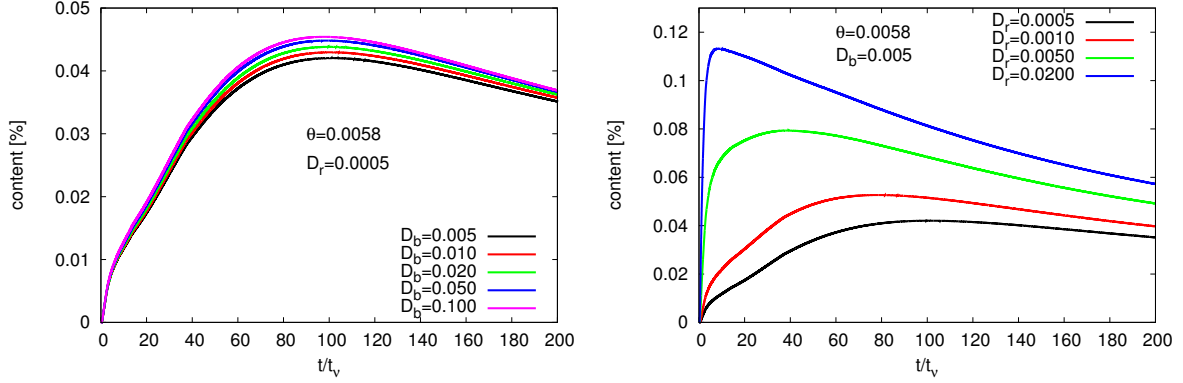
Figure 4: Direct discharge. Left: cumulative output caffeine concentration for fixed solid grain's release rate $D_r = 0.0005$ and $\theta = 0.0058$. Right: cumulative output caffeine concentration for fixed bulk diffusion $D_r = 0.0005$ and $\theta = 0.0058$.

3.3.2 Effect of bulk diffusion coefficient D_b and release rate D_r

In a second stage, we focus on the system with fines concentration $\theta = 0.0058$ (blue line in Fig.3) which reproduces reasonably well the transient flow rate reported in experiments with coffee filtration [13], i.e. a peak/minimal Reynolds numbers $Re \approx 10 - 1$.
In Fig.4 we look at the effect of several parameters on the resulting output cumulative molecular concentration. In particular, in Fig.4 (left) the cumulative output concentration is shown for fixed solid grain's release rate $D_r = 0.0005$ and different bulk diffusion coefficients $D_b \in [0.005 : 0.1]$, spanning nearly two orders of magnitude in the bulk molecular Peclet number. It can be seen that D_b has only a minor effect on the final output concentration. There is a small consistent increase (less than 5%) in the peak for increasing D_b which can be attributed to difference in the release of molecular compounds in areas of stagnating flow. For molecular species released in these areas, the only possible mechanism of escape is by molecular diffusion, i.e. by slowly diffusing into region of large flow where the material is efficiently advected.

More interesting is the effect of the solid/liquid molecular release rate D_r on the cumulative output concentration (Fig.4: right). Here we consider a molecular compound with fixed bulk diffusion $D_b = 0.005$ at fine concentration $\theta = 0.0058$ and look at different release rates coefficients $D_r \in [0.0005 : 0.02]$. It is clear that D_r is the most relevant parameter controlling the final concentration of substance in the cup. For small values of the release coefficient (e.g $D_r = 0.0005$: black line) only a small peak (4%) is reached at relatively long times after which the cumulative concentration decay very slowly. On the other hand, large values of D_r (e.g $D_r = 0.02$: blue line) lead to a peak in the order of 12%. Moreover, all the material is released very efficiently in the very early stage of filtration ($t^* < 30$) with significant decay occurring later on. Maximization of molecular concentration in the cup can be therefore reached on extremely fast filtration processes by tuning the release mechanism. This is independent on the molecular property of the substance in the fluid (i.e. the diffusion coefficient D_b in water). However, it depends

strongly on D_r and can also depend on the intra-granular diffusion coefficient D_s of the molecular compound which indirectly affects D_r.

It is interesting to note that different compounds (i.e. different release coefficients) are clearly characterized by distinct kinetics which suggests that, depending on molecular specificity, the balance between different compounds is altered if extraction is stopped at different times. Because different compounds are tightly connected to specific flavors, and being taste perception a highly non-linear process [19], only minor changes in this delicate balance can lead to very different sensorial experience. For example caffeine and trigonelline are typically associated to degree of bitterness, whereas chlorogenic acids to acidic taste. These results indicate clearly that different preparation time for espresso can potentially lead to significant changes in taste perception and therefore the current framework can pave the way for a better flavor-engineering of espresso [14].

4 CONCLUSIONS

We have presented a SPH model for the simulation of espresso extraction which incorporates some essential physical features, i.e. (i) bimodal granulometry; (ii) double porosity model of molecular concentrations dynamics (enabling liquid-bulk and intra-granular solid diffusion); (iii) stripping mechanism of solid/liquid molecular release; and (iv) a model of mechanical filter. The correct transient permeability of the coffee bed has been reproduced under direct-inverse discharge conditions, showing the importance of fines migration on the hydrodynamic properties of the percolation and extraction process. Concentration dynamics for different molecular compounds have been studied. It was shown that the presence of the fines, leading to larger flow resistance leads to a dramatic increase of the residence time of water near the grain surface, therefore maximizing the release process. The long-term goal of this work is to use the current framework to control coffee flavors by monitoring the balance of specific taste-actives compound in the beverage.

REFERENCES

[1] Parenti, A., Guerrini, L., Masella, P., Spinelli, S., Calamai, L., Spugnoli, P., "Comparison of espresso coffee brewing techniques". *J. Food Eng.* **121**, 112-117 (2014).

[2] M. Ferrari, L. Navarini, L. Liggieri, F. Ravera, and F. Liverani, "Interfacial properties of coffee-based beverages", *Food hydrocolloids.* **21**, 1374-1378 (2007).

[3] E. Illy, The complexity of coffee, *Sci. Am.* **286**, 92-98 (2002).

[4] Voilley, A., Simatos, D., "Modeling the solubilization process during coffee brewing" *J. Food Process. Eng.* **3**, 185-198 (1979).

[5] Ellero, M., Adams, N.A., "SPH simulations of flow around a periodic array of cylinders confined in a channel". *Int. J. Numer. Methods Eng.* **86**, 1027-1040 (2011).

[6] Vázquez-Quesada, A., Ellero, M. "Rheology and microstructure of non-colloidal suspensions under shear studied with smoothed particle hydrodynamics". *J. Non-Newtonian Fluid Mech.* **233**, 37-47 (2016).

[7] Ellero, M., Tanner, R.,"SPH simulations of transient viscoelastic flows at low Reynolds number". *J. Non-Newtonian Fluid Mech.* **132**, 61-72 (2005).

[8] Hu, X., Adams, N., "A multi-phase sph method for macroscopic and mesoscopic flows". *J. Comput. Phys.* **213**, 844-861 (2006).

[9] Grmela, M., Öttinger, H.C., "Dynamics and thermodynamics of complex fluids: development of a general formalism". *Phys. Rev. E* **56**, 6620-6632 (1997).

[10] Vázquez-Quesada, A., Ellero, M., Español, P.,"Consistent scaling of thermal fluctuations in smoothed dissipative particle dynamics". *J. Chem. Phys.* **130**, 034901 (2009).

[11] Vázquez-Quesada, A., Ellero, M., Español, P., "Smoothed particle hydrodynamic model for viscoelastic fluids with thermal fluctuations". *Phys. Rev. E* **79**, 056707 (2009).

[12] Navarini, L., Nobile, E., Pinto, F., Scheri, A., Suggi-Liverani, F., "Experimental investigation of steam pressure coffee extraction in a stove-top coffee maker". *Appl. Therm. Eng.* **29**, 998-1004 (2009).

[13] Petracco, M., Suggi Liverani, F., "Espresso coffee brewing dynamics: development of mathematical and computational model". In: *Proceedings. 15th International Scientific Colloquium on Coffee.* ASIC (1993),

[14] Ellero, M., Navarini,"Mesoscopic modelling and simulation of espresso coffee extraction". *J. Food Eng.* **263** 181-194 (2019).

[15] Bian, X., Litvinov, S., Qian, R., Ellero, M., Adams, N.A., "Multiscale modeling of particle in suspension with smoothed dissipative particle dynamics". *Phys. Fluids* **24**, 012002 (2012).

[16] Severini, C., Ricci, I., Marone, M., Derossi, A., De Pilli, T., "Changes in the aromatic profile of espresso coffee as a function of the grinding grade and extraction time: a study by the electronic nose system. J. Agric". *Food Chem.* **63**, 2321-2327 (2015).

[17] Pan, W., Pivkin, I.V., Karniadakis, G.E., "Single-particle hydrodynamics in DPD: a new formulation". *EPL (Europhysics Letters)* **84**, 10012 (2008).

[18] Bandini, S., Casati, R., Illy, E., Simone, C., Suggi Liverani, F., Tisato, F. "A reaction-diffusion computational model to simulate coffee percolation". In: *Proceedings. 17th International Scientific Colloquium on Coffee.* ASIC (1997).

[19] Mestdagh, F., Glabasnia, A., Giuliano, P., "Chapter 15 - the brewextracting for excellence". In: Folmer, B. (Ed.), *The Craft and Science of Coffee.* Academic Press, pp. 355380 (2017).

MULTI-LEVEL LOAD BALANCING FOR PARALLEL PARTICLE SIMULATIONS

Godehard Sutmann[1,2]

[1] Jülich Supercomputing Centre (JSC), Institute for Advanced Simulation (IAS),
Forschungszentrum Jülich (JSC), D-52425 Jülich, Germany
e-mail: g.sutmann@fz-juelich.de   http://www.fz-juelich.de/ias/jsc/staff/g_sutmann

[2] ICAMS, Ruhr-University Bochum, D-44801 Bochum, Germany

Key words: Parallel Computing, Particle Methods, Load Balancing, Multi-Level Methods, Multigrid

Abstract. Ideas from multi-level relaxation methods are combined with load balancing techniques to achieve a convergence acceleration for a homogeneous work load distribution over a given set of processors when the underlying work function is inhomogeneously distributed in space. The algorithm is based on an orthogonal recursive bisection approach which is evaluated via a hierarchically refined coarse integration. The method only requires a minimal information transfer across processors during the tree traversal steps. It is described of how to partition the system of processors to geometrical space, when global information is needed for the spatial tesselation.

1 INTRODUCTION

Load imbalance is a common problem for parallel applications, which often arises when work load distributions are inhomogeneously distributed in the global system setup, or may occur when local inhomogeneities in the work density show up when increasing the number of processors. In fact, for many parallel applications which rely on domain decomposition as a parallel strategy, the processors define a spatial discretisation. Increasing the processor count, the spatial resolution is increased, which resolves density differences (which are often related to differences in work distribution) on a finer scale which consequently lead to runtime differences on the individual processors. Since differences in work load do lead to reduced parallel efficiency, various methods for an improved load balance between the processors have been proposed [1, 2, 3, 4]. In the present article, problems related to particle distributions or mesh vertices are considered. Since vertices might be considered as a kind of abstract particle in the sense that they have properties and relations to their neighbourhood we will use in the present article the notion of *particle*, which might be understood in a more general context.

The problem of load balancing has to consider redistribution of work between processors in such a way that all processors are actively working for a period of time and reaching

either the end of the program or a synchronization point at almost the same time, so that overhead- and waiting-times are minimized. This either includes active redistribution of work by sending tasks over the network, which reside on the other processors, or by, e.g., work stealing procedures, which includes forth and back communication between processors for both task distribution and gathering of results. In the present article we focus on redistribution of work load such that degrees of freedom (e.g. particles, vertices, etc.) are communicated between processors as a result of redefining the geometry of the domains. The basic principle is therefore a modification of the shape and size of domains such that local work $W_i^{(n+1)}$ is increased, if $W_i^{(n)} < \langle W \rangle_P$, where $W_i^{(n)}$ is the total work on processor $i \in [0, P-1]$, P the number of processors and $\langle W \rangle_P$ the average work of a processor. In analogy, $W_j^{(n+1)}$ is reduced, if $W_j^{(n)} > \langle W \rangle_P$. The goal is that shapes and sizes of domains are adjusted in such a way that $W_i^{(n)} = \langle W \rangle_P \pm \delta W_i$, where δW_i is a tolerable difference on each processor from the optimal load, for which holds $\sum_{i=0}^{P-1} \delta W_i = 0$.

In that sense, the problem of balancing the load between the processors has different levels of complexity: (i) how to properly define the load; (ii) which is the proper shape and size of a domain; (iii) how to control or minimise additional costs, e.g. increased number of communication partners; (iv) how to minimise the procedure of work redistribution, domain size and shape, e.g., with minimal communication costs between the global processor grid. In the present article we will mainly focus on issue (iv), which is related to the computational costs introduced by the chosen load balancing procedure and which should, of course, be much smaller than the computational overhead which is related to the work imbalance, i.e. the overhead which exists without any application of load balancing. Concerning issue (i) we will assume a properly chosen function, which characterises the work and which is properly measurable. In practice, this could be, e.g., the number of particles on each processor, the number of interactions, the total time of interactions or the wall clock time of one full time step. For convenience we choose for discrete systems the number of particles, N_i, on each processor. Concerning issue (ii) there were a number of different approaches discussed in the literature, including (a) orthogonal shapes in the case of orthogonal recursive bisection method [5] or tensor product method [6]; (b) irregular cells in the case of, e.g., Voronoi tesselation [7] or graph partitioning [8]; (c) distorted meshes with conserved topology [9, 10]. These methods differ mainly in how the work is redistributed and which constraints for the individual domains are considered. For most proposed methods the computational costs on the domain are considered, but communication between neighbour domains is neglected or, at least, not minimised. The latter issue usually leads to a coupled problem, which on the one hand increases complexity of the minimisation procedure and, on the other hand, leads sometimes to a non-smooth objective function since communication partners, and therefore also the communication overhead, may change discontinuously when increasing or reducing communication partners during minimisation. This communication overhead is related to the work on each domain *after* the load balancing step is finished. But the load balancing itself needs information which invokes communication between processors and in the worst case the required information has to be communicated between *all* processors,

which especially leads to a big overhead for a large number of processors (i.e. those cases where load balancing is often crucial for a good parallel efficiency). This overhead might get crucial, especially when the load balancing has to be performed frequently in the simulation. This is a common problem for dynamic systems with high density contrasts or regions, which temporally does not contain any load. In such cases, the domain sizes and shapes might be reconstructed frequently, e.g. as it is for graph partitioning methods, or might be smoothly adjusted to a new (smoothly varying in time) work load change, which allows for iterative schemes, following the work load in time. This, however, has an important requirement, namely that the change in work load has a slower relaxation time than the load balancing scheme. Otherwise the load balancing method would lag behind the work load, not reaching an equal distribution of load.

The current work does not focus on a new formulation of an objective function for minimising computational work and communication overhead, but on an approach which minimises the communication volume during the load balancing step for the case when global information exchange is necessary within the processor mesh. Necessary global communication in load balancing steps is performed on a hierarchical tree with minimal information exchange. We will focus on the class of *Orthogonal Recursive Bisection* (ORB), which is by itself a hierarchical scheme.

Since the work load on a domain is determined by the local degrees of freedom on each domain, also information about the distribution of work on the domain is necessary, if it cannot be mapped to a simple mask, which could be communicated over the network. Therefore, we consider here an approach, which adapts elements from multigrid method [11], which uses the property that inhomogeneities on small scales are smoothed on a coarser scale. Since the number of degrees of freedom might get large (e.g. $N > 10^9$) on high processor counts (e.g. $P > 10^5$), the present approach is formulated in terms of reduced properties, i.e. only local work densities and domain coordinates are required to balance the load quite efficiently, even for very inhomogeneous work distributions, i.e., computational degrees of freedom, e.g. particles, are only exchanged / redistributed on the highest tree level and not explicitly communicated along the tree.

The article is organised as follows: In Sec. 2 the method is introduced from a formal point of view. In Sec. 3 results are shown for various test cases, which include exact function descriptions (in order to consider convergence properties) and sample systems, consisting of discrete particle distributions.

2 METHOD

2.1 Multi-Level Description of Workload

The goal of the formal characterization of work load is to describe it as hierarchical subdivision, where domains on level $l+1$ in the hierarchical description are constructed by a bisection of domains of a given level l. In this sense, the coarsest level, $l = 0$, consists of the whole system, whereas the finest level $l = L$ consists of 2^L sub-domains. The original computational domains, which are administered by 2^L processes are the target regions for balancing the work load, such that each process has to fulfil the same amount

of computational work. Therefore, the target work load for each process can be written as the average work on a given level, i.e.

$$\langle W \rangle_l = 2^{-l} W \tag{1}$$

For the highest level L the target distribution of work is

$$\langle W \rangle_L \;=\; 2^{-L} W \tag{2}$$

$$=\; \frac{1}{P} \sum_{m=0}^{2^L - 1} W_{L,m}^{(n)} \tag{3}$$

$$=\; \frac{1}{P} W \tag{4}$$

where $W_{L,m}^{(n)}$ is the work on level L on preocess m during multi-level iteration n. Since this represents the total sum over all partial work distributions, this relation holds for each iteration n. Splitting a domain into two sub-domains can therefore be described as

$$W_{l+1,2k}^{(n)} = \langle W \rangle_l + \delta W_{l+1,2k}^{(n)} \tag{5}$$

$$W_{l+1,2k+1}^{(n)} = \langle W \rangle_l + \delta W_{l+1,2k+1}^{(n)} \tag{6}$$

where

$$\delta W_{l+1,2k}^{(n)} \;=\; \int_0^{x_{1/2}} dx\, \rho(x \,|\, x \in \Omega_{l+1,2k}^{(n)}) - \int_0^{\delta x_{l+1,2k}^{(n)}} dx\, \hat{\rho}_{l+1,2k}^{(n)}(x) \tag{7}$$

$$=\; \frac{1}{2} \left[W_{l+1,2k}^{(n)} + W_{l+1,2k+1}^{(n)} \right] - \sum_{\{\ell\}} V_{l+1,\ell}^{(n)}(\{\ell\})\, \hat{\rho}_{l+1,\ell}^{(n)}(\{\ell\}) \tag{8}$$

with the set

$$\{\ell\}_{l+1,2k}^{(n)} = \{\ell \,|\, \Omega_{L,\ell}^{(n)} \cap \Omega_{l+1,2k}^{(n)} \notin \{\emptyset\}\} \tag{9}$$

meaning that all volume and density contributions from the highest level L are sampled onto the geometric region $2k$ with finite intersection. $\delta x_{l+1,2k}^{(n)}$ is an approximation for the location of the division point (in 2d division line, in 3d division plane) which subdivides a domain on level l into two sub-domains on level $l+1$ with approximately equal work load. In this stage, $\delta x_{l+1,2k}^{(n)}$, can only be computed approximately, since it is based on an average underlying work density, which does not contain any information about inhomogeneities in work distribution on a given process, i.e., the density $\hat{\rho}_{l+1,2k}^{(n)}(x)$ is constructed as a coarse grain approximation on the highest level L, which is iteratively refined during the multi-level procedure. Within multi-level cycle n, a density map of the system on level l is constructed by concatenating the average densities within the domain geometries, $\Omega_{l,k}^{(n)}$. On the lowest level $l = 0$ this can be expressed as the complete map

$$\hat{\rho}_{0,0}^{(n)}(x) = \bigcup_{i=0}^{2^L - 1} \left\langle \frac{W_{L,i}^{(n)}}{V_{L,i}^{(n)}} \right\rangle_{\Omega_{L,i}^{(n)}} \tag{10}$$

This results in a step or plateau function, where constant values are assigned to the density within the domain boarders of each domain on level $l = L$.

This approach offers a low communication approach to the implementation, since only the domain geometries and the local work has to be transferred along the tree traversal. The communication part is described in more detail in the next sections.

2.2 Tree Down-Traversal: Merging domains between two levels

The amount of communicated data down the tree is reduced to $\#_{l,i}^{(n)} = (2 \times d + 1) \times 8 \times |\{\ell\}_{l,2k}^{(n)}|$ bytes, where d is the dimension of the parallel sub-decomposition and which essentially contains the lower-left- and upper-right-corner of the domain (given that it is an orthogonal decomposition) and the work function value. To describe the basic procedure, we consider for the initial geometry a non-staggered, orthogonal decomposition of domains in 3-dimensional space on level L, which means that each domain has 6 neighbours, separated by domain interfaces. Here, we consider tilings in each cartesian direction which contain domains of multiples of 2, i.e. $\Omega = \mathcal{D}_x \otimes \mathcal{D}_y \otimes \mathcal{D}_z$, where $|\mathcal{D}_\alpha| = 2^{l_\alpha}$ (note that other tilings of arbitrary number of domains, including prime numbers, are possible and will be discussed elsewhere [12]). The procedure of merging is then straightforward. We describe each level l as combination of levels in cartesian directions, i.e.

$$l = l_x + l_y + l_z \tag{11}$$

If we consider a given level l, the merging of two adjacent sub-domains is performed in one of the cartesian directions α, which reduces the next level by one through

$$l - 1 = (l_\alpha - 1) + l_\beta + l_\gamma \tag{12}$$

where α, β, γ is any permutation of x, y, z. If we denote 2 adjacent index pairs in the multi-level decomposition as $([i_l]_\alpha, [i_l + 1]_\alpha)$, which are subject to be merged in direction α, then we can write

$$i_x \in [0, 2^{l_x-1} - 1] \quad i_y \in [0, 2^{l_y} - 1] \quad i_z \in [0, 2^{l_z} - 1]$$
$$[i_l]_x = 2^{L_x-l_x} 2i_x + 2^{L_x+L_y-l_y} i_y + 2^{L_x+L_y+L_z-l_z} i_z \tag{13}$$
$$[i_l + 1]_x = 2^{L_x-l_x} (2i_x + 1) + 2^{L_x+L_y-l_y} i_{l_y} + 2^{L_x+L_y+L_z-l_z} i_z \tag{14}$$

$$i_x \in [0, 2^{l_x} - 1] \quad i_y \in [0, 2^{l_y-1} - 1] \quad i_z \in [0, 2^{l_z} - 1]$$
$$[i_l]_y = 2^{L_x-l_x} i_x + 2^{L_x+L_y-l_y} 2i_y + 2^{L_x+L_y+L_z-l_z} i_z \tag{15}$$
$$[i_l + 1]_y = 2^{L_x-l_x} + 2^{L_x+L_y-l_y} (2i_{l_y} + 1) + 2^{L_x+L_y+L_z-l_z} i_z \tag{16}$$

$$i_x \in [0, 2^{l_x} - 1] \quad i_y \in [0, 2^{l_y} - 1] \quad i_z \in [0, 2^{l_z-1} - 1]$$
$$[i_l]_z = 2^{L_x-l_x} i_x + 2^{L_x+L_y-l_y} i_y + 2^{L_x+L_y+L_z-l_z} 2i_z \tag{17}$$
$$[i_l + 1]_z = 2^{L_x-l_x} + 2^{L_x+L_y-l_y} i_{l_y} + 2^{L_x+L_y+L_z-l_z} (2i_z + 1) \tag{18}$$

The enumeration of the next lower level is then accordingly $[i_{l-1}]_\alpha = [i_l]_\alpha$. Moving down the tree and merging domains in direction α, the separating surface between domains is removed and it is $\Omega_{l-1,i} = \Omega_{l,i_1} \cup \Omega_{l,i_2}$, with $i = [i_{l-1}]_\alpha$, $i_1 = [i_l]_\alpha$, $i_2 = [i_l + 1]_\alpha$.
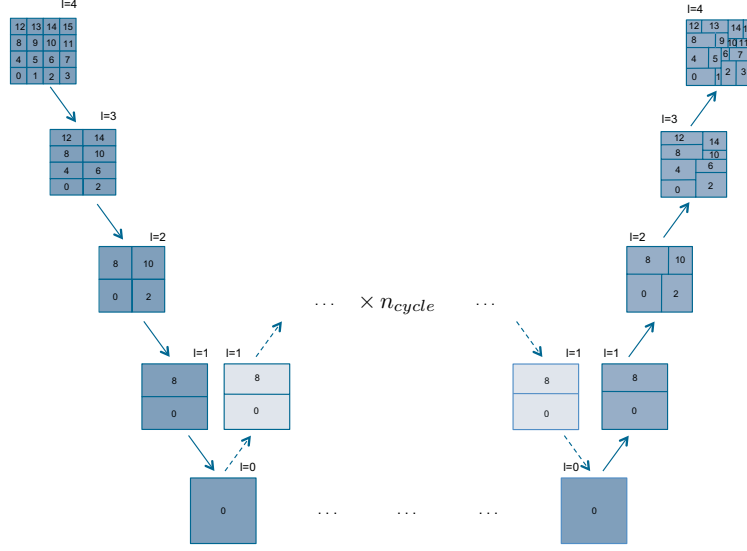
Figure 1: Schematics of the parallel implementation of the multi-level load balancing scheme. On lower levels, only processors with even indices are active.

Merging implies that the domain with index $[i_l]_\alpha$ is the *master domain*, which combines information of two sub-domains and takes part in the merging process on the next lower level. To have all information available, a communication from $[i_l + 1]_\alpha$ to $[i_l]_\alpha$ has to be performed which contains the lower left, upper right coordinates of the domain and its total work. On this stage, also the coarse density field of domains on level L, which overlaps with domain $[i_l + 1]_\alpha$ is communicated to ensure that on each level in the up-traversal later on the computation of the separating surface can be accomplished.

2.3 Tree Up-Traversal: Splitting domains on a level

The density field of work which has to be integrated to find the proper coordinate for domain splitting on level l, is fixed on the highest level L in the tree, i.e., it contains the average work within the geometry of individual domains in a given iteration step k. For simplicity we first consider a 1-dimensional case. This means that at lower levels, several sub-volumes from the highest level contribute to the work density field, which means that several integrals have to be evaluated to find the location of $x_{1/2} = \{x : P(x) = 1/2\}$, where $P(x)$ is the cumulative distribution function of work on a domain. From Fig. 1 it is understood that $x_{1/2}$ can be found by the geometric consideration

$$x_{1/2} = x_{k-1} + \frac{\frac{1}{2} - P(x_{k-1})}{W_k} (x_k - x_{k-1}) \tag{19}$$

$$= x_{k-1} + \frac{1}{2} \frac{1 - 2P(x_{k-1})}{P(x_k) - P(x_k - 1)} (x_k - x_{k-1}) \tag{20}$$

Here k is the domain, for which holds

$$k = \left\{ k : P(x_{k-1}) < \frac{1}{2} \land P(x_k) > \frac{1}{2} \right\} \tag{21}$$

In a multi-dimensional setting this is a bit more involved. The splitting of a domain is performed in a given direction $\mathbf{n}_\alpha$ by an intersection plane, which is orthogonal to the splitting direction. The splitting plane is then introduced at the relative position $r_\alpha(1/2)$, for which the integral holds

$$\int_{r_{\alpha,0}}^{r_\alpha(1/2)} dr_\alpha \int_{r_{\beta,0}}^{r_{\beta,L}} dr_\beta \int_{r_{\gamma,0}}^{r_{\gamma,L}} dr_\gamma \, \rho(\mathbf{r}) = \frac{1}{2} \, W \tag{22}$$

In a discrete set of domains, where the density might change abruptly, depending on the work distribution over the processors, one can write for the total work on the domain

$$W = \sum_{i_\alpha=0}^{p_\alpha-1} \int_{r_{\alpha,I[i_\alpha]}}^{r_{\alpha,I[i_\alpha+1]}} dr_\alpha \sum_{i_\beta=0}^{p_\beta-1} \int_{r_{\beta,i_\beta}}^{r_{\beta,i_\beta+1}} dr_\beta \int_{r_{\gamma,0}}^{r_{\gamma,L}} dr_\gamma \sum_{i_\gamma=0}^{p_\gamma-1} \int_{r_{\gamma,i_\gamma}}^{r_{\gamma,i_\gamma+1}} dr_\gamma \, \rho_{i_\alpha,i_\beta,i_\gamma} \tag{23}$$

In this formulation, $I[i]$ is an ordered set as such that the domains of the highest level, intersecting with the domain on the coarse level l, are sorted according to their lower boarder in direction $\mathbf{n}_\alpha$. Since the densities are approximated as constant over the domains at the highest level, the integrals can be computed exactly. Selecting for the splitting e.g. the z-direction can be formulated as a sum of sub-domains, $W_l^<$, located completely below $z_{1/2}$ and those, $\delta W_l^{1/2}$, which are cut by the xy-plane cutting the z-axis at $z_{1/2}$

$$W_l^{1/2} = W_l^< + \delta W_l^{1/2} \tag{24}$$

where

$$W_l^< = \sum_{p \in \mathcal{P}_z} (x_{p,1} - x_{p,0}) (y_{p,1} - y_{p,0}) (z_{p,1} - z_{p,0}) \rho_p \tag{25}$$

and

$$\delta W_l^{1/2} = \sum_{p \in \mathcal{P}_{1/2}} (x_{p,1} - x_{p,0}) (y_{p,1} - y_{p,0}) (z_{1/2} - z_{p,0}) \rho_p \tag{26}$$

which leads to the following expression for $z_{1/2}$

$$z_{1/2} = \frac{W_l^{1/2} - W_l^< + \sum_{p \in \mathcal{P}_{1/2}} (x_{p,1} - x_{p,0}) (y_{p,1} - y_{p,0}) z_{p,0} \, \rho_p}{\sum_{p \in \mathcal{P}_{1/2}} (x_{p,1} - x_{p,0}) (y_{p,1} - y_{p,0}) \, \rho_p} \tag{27}$$

Here, the sets $\mathcal{P}_z$ and $\mathcal{P}_{1/2}$ contains all subdomains p on the highest level L for which

$$\mathcal{P}_z = \left\{ \{p\} \,|\, \Omega_{L,p} \cup \Omega_l \notin \{\emptyset\} \land z_{p,1} > z_{1/2} \land z_{p,1} \le z_{1/2} \right\} \tag{28}$$

$$\mathcal{P}_{1/2} = \left\{ \{p\} \,|\, \Omega_{L,p} \cup \Omega_l \notin \{\emptyset\} \land z_{p,0} < z_{1/2} \land z_{p,1} > z_{1/2} \right\} \tag{29}$$
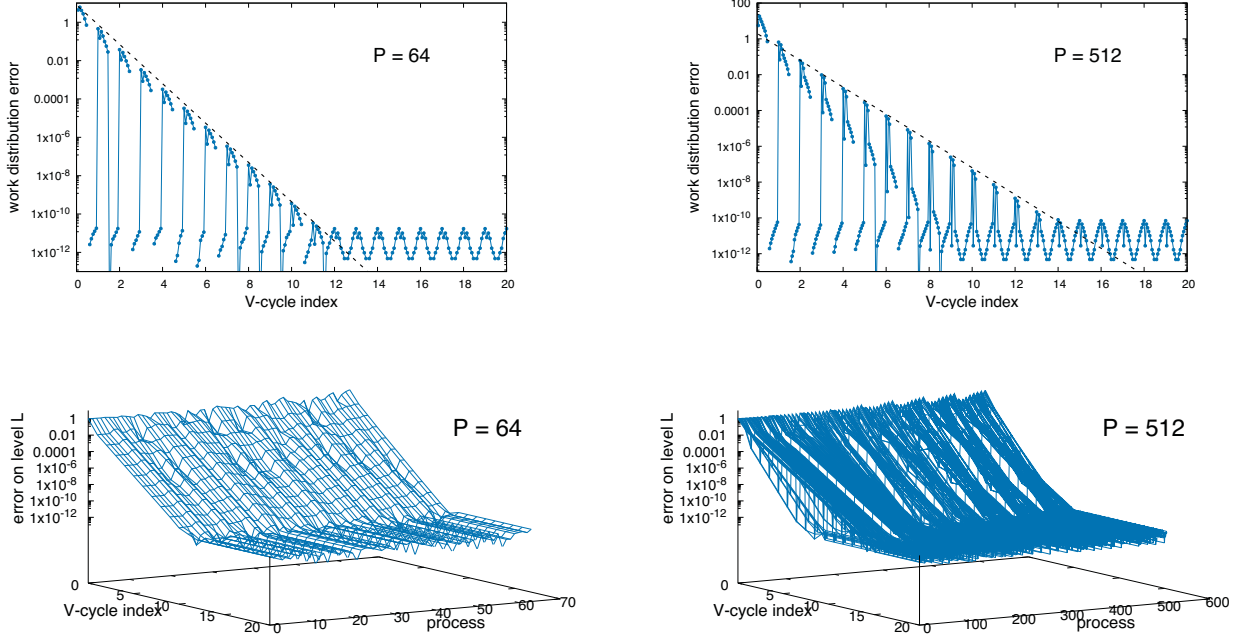
Figure 2: Results for Model 1, the trilinear model with an error threshold $\epsilon_{1/2} = 10^{-12}$ for the detection of the intersection plane during the up-traversal step of the tree walk. Compared are results for $P = 64$ and $P = 512$ domains, which are partitioned applying a multi-level V-cycle. The longer relaxation time for larger number of domains is in part due to a more inhomogeneous convergence behaviour of some domains.

Therefore, in order to split the domain Ω_l, requires a map of the underlying Ω_L distribution. Once this map is known on the coarse domain Ω_l, the cutting plane for the generation of two sub-domains on level Ω_{l+1} can be done exactly according to the underlying density distribution.

It is noted that between multi-level iteration cycles the exact work distribution does not change, since the sources of work, i.e. particles or mesh points are not moved or re-weighted. However, after each multi-level cycle, the domain geometries on level L are adjusted and accordingly the work in each domain is changed, i.e., also the work density for each domain is modified in general. As a consequence, the underlying domain map and also the density tesselation is changed, leading to an iteratively converging partitioning of the domains on level L.

2.4 Generation of the underlying density map

In each multi-level iteration step, the density map has to be known by all levels $l \in \{0, L\}$. The multi-level cycle starts from the finest level L, corresponding to the computational domain of each processor. On that level, the work per domain is explicitly known and transferred as a characteristic quantity to the load balancing method. Going down the tree to the coarsest level $l = 0$, means to merge two adjacent domains and com-
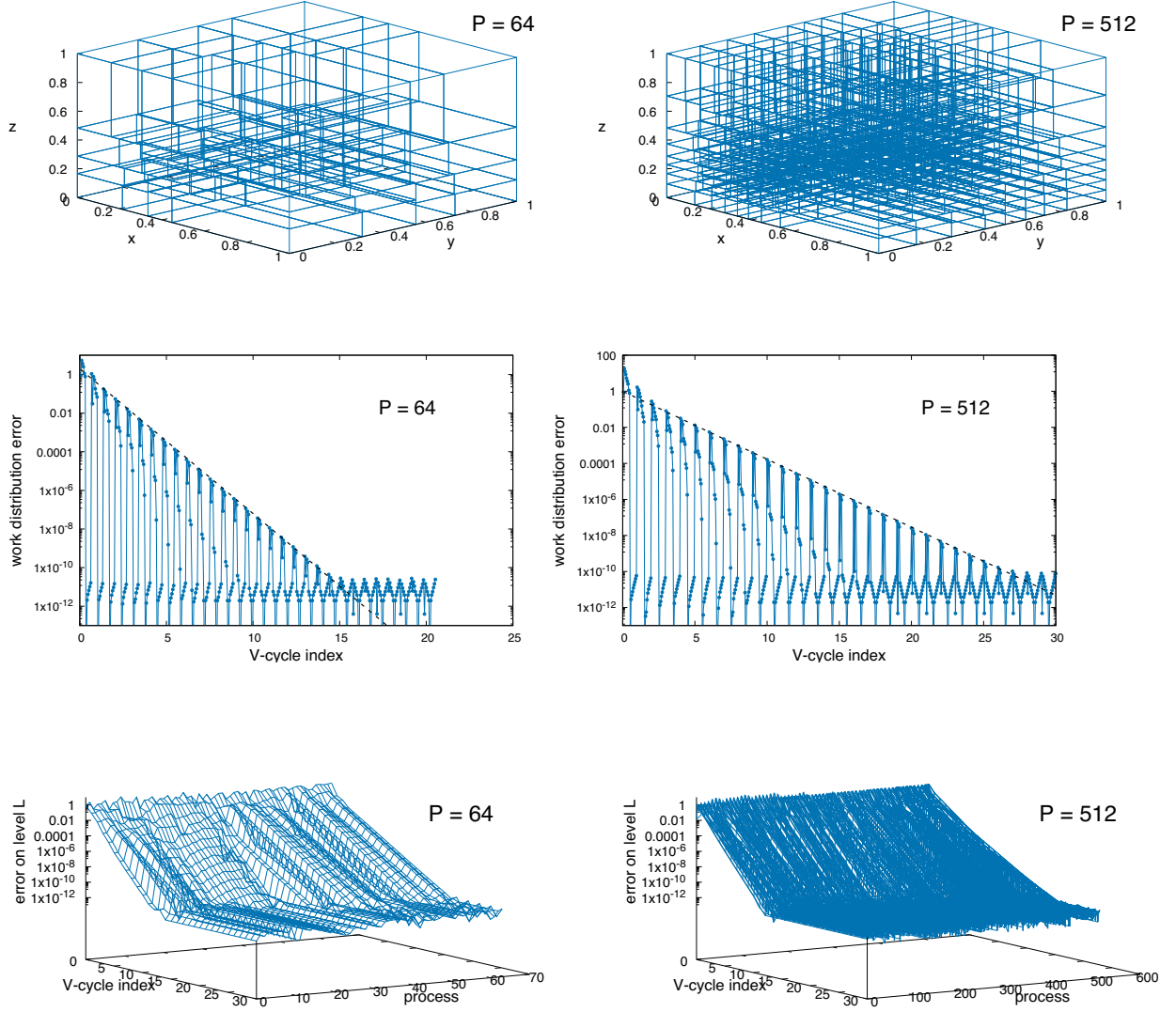
Figure 3: Results for Model 2, the Gaussian superposition model with an error threshold $\epsilon_{1/2} = 10^{-12}$ for the detection of the intersection plane during the up-traversal step of the tree walk. As in Fig. 2, results are compared for $P = 64$ and $P = 512$ domains, which are partitioned applying a multi-level V-cycle. For this case, there is also some inhomogeneous convergence behaviour observed for some domains. As an example for the result of the partitioning, the domain structure on the highest level, L, is shown (top).

bine their individual work, i.e. $W_{p,l} = W_{2p,l+1} + W_{2p+1,l+1}$. Since on the lower level, we do not want to introduce coarser density descriptions, we keep the context of the density distribution, i.e. $L-1$, there will be two distinct regions in the boarder of Ω_L domains, which have different densities. To distribute the density distribution over the tree, the processor containing the region $\Omega_{2p+1,l+1}$ communicates its density to processor $2p$, which will contain $\Omega_{p,l}$ on the next coarser level. This can be continued along the walk down the tree, so that on the lowest level the remaining processor p knows about the complete density map of the system. Having this information available, it is possible to use the formalism described above to construct a numerically exact subdivision with domains of equal work load.

3 RESULTS

Model 1: Trilinear function: The density field is defined as

$$\rho_w(x, y, z) = x\, y\, z \tag{30}$$

resulting in the total work on level L on domain k, $\Omega_{L,k}$

$$W_{\Omega_{L,k}} = \frac{1}{8} \left(x_{1,k}^2 - x_{0,k}^2 \right) \left(y_{1,k}^2 - y_{0,k}^2 \right) \left(z_{1,k}^2 - z_{0,k}^2 \right) \tag{31}$$

Model 2: Gaussian superposition: The density field is defined as

$$\rho_w(x, y, z) = \frac{1}{n_g} \sum_{j=1}^{n_g} \prod_{\alpha=x,y,z} \frac{1}{\sqrt{2\pi}\sigma_{\alpha,j}}\, e^{-(\alpha-\mu_{\alpha,j})^2/2\sigma_{\alpha,j}^2} \tag{32}$$

resulting in the total work on level L on domain k, $\Omega_{L,k}$

$$W_{\Omega_{L,k}} = \frac{1}{n_g} \sum_{j=1}^{n_g} \prod_{\alpha=x,y,z} \operatorname{erf}\left(-\frac{\alpha_{0,k}-\mu_{\alpha,j}}{\sqrt{2}\sigma_{\alpha,j}}\right) - \operatorname{erf}\left(-\frac{\alpha_{1,k}-\mu_{\alpha,j}}{\sqrt{2}\sigma_{\alpha,j}}\right) \tag{33}$$

Model 3: Gaussian particle distribution: The probability for finding a particle in the volume $dx\, dy\, dz$ is given by

$$p(x, y, z)dxdydz = p_g(x)p_g(y)p_g(z)dxdydz \tag{34}$$

with

$$p_g(\alpha) = \frac{e^{(\alpha-\mu_\alpha)^2/2\sigma_\alpha^2}}{\int_{L_\alpha} d\alpha\, e^{(\alpha-\mu_\alpha)^2/2\sigma_\alpha^2}} \tag{35}$$

The work function is the result of the underlying discrete distribution of N particles, so that the total work on the highest level L, i.e., on each process is given by

$$W_{\Omega_{L,k}} = \frac{1}{N} \sum_{i=1}^{N} \mathbb{1}(\{i \,|\, \alpha_{0,k} < \alpha_i < \alpha_{1,k}, \alpha = x, y, z\}) \tag{36}$$
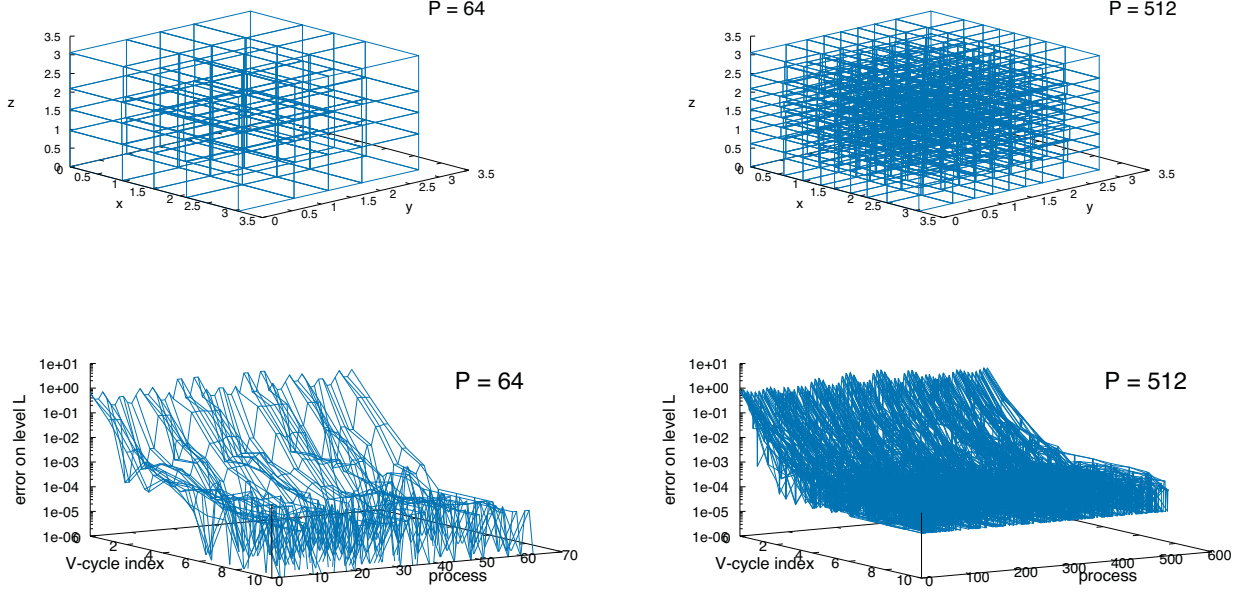
Figure 4: Results for Model 3, the Gaussian density for particle distribution function with an error threshold $\epsilon_{1/2} = 10^{-12}$ for the detection of the intersection plane during the up-traversal step of the tree walk. Compared are results for $P = 64$ and $P = 512$ domains, which are partitioned applying a multi-level V-cycle. Obviously, due to discreteness of particles, the error of work distribution does not decrease to the prescribed error threshold.

where $\mathbb{1}(\{i\,|\,.\})$ is the indicator function, which is 1 if the criteria for α_i are met and 0 otherwise. Therefore, we consider the number of particles on each process as a measure for the work. In other scenarios, the number of interactions between particles or the wall clock time of a time step could be chosen as work function on a process.

Each load balancing experiment starts on a regular cartesian mesh. The errors are computed as local errors of process i

$$\epsilon_i = \left| 1 - \frac{W_i}{\langle W \rangle} \right| \tag{37}$$

and global errors as

$$\epsilon = \sqrt{\frac{1}{P} \sum_{i=0}^{P-1} \epsilon_i^2} \tag{38}$$

All three models have been tested for $P = 64$ and $P = 512$ processes. Model 1 shows a quite smooth relaxation behaviour to the prescribed error threshold for $P = 4^3 = 64$ processes. For the case of $P = 8^3 = 512$ processes, Fig. 2(right) shows that there are different modes present with different relaxation times. It is not yet clear whether this is an inherent system property, or whether a numerical condition is responsible for this

behaviour which might be lifted by a correction technique. Qualitatively, the same behaviour is observed for Model 2, where for both numbers of processes this inhomogeneous relaxation can be observed. Nevertheless, although there might be a delay in relaxation (which might be possible to minimise) the system is converging to a stable final configuration of domain distribution, which is shown in Fig. 3(top). A stronger effect of this behaviour is observed for the discrete particle system. It is understood that the exact work distribution can ideally only be found if the number of particles is a multiple of the number of processes. If this is not the case there is an inherent discretisation error, which brings the error of work distribution $\delta\epsilon = \mathcal{O}(P/N)$, which is likely to reach the percentage range. For the cases studied, the observed local errors in the relaxed state are in the range of $\epsilon_i < 10^{-3}$ for $P = 64$ and for $P = 512$ they are found to be in the range of $\epsilon_i < 5 \times 10^{-3}$, which is still below the percentage threshold.

4 CONCLUSIONS

We have developed a mathematical description of a multi-level orthogonal recursive bisection method for the balanced work distribution on parallel processes in particle systems. The method uses a minimal basis for information exchange between processors, i.e. communicating information about local domain geometries and a scalar work descriptor of the underlying finest domain splitting, i.e. the average work on each processor on the highest level L in the tree. This density field is iteratively refined by correcting the domain geometries on each intermediate level l during the up-traversal step, resulting in an improved work density description on the highest level, which in turn is applied to the domain-splitting step in the next up-traversal step. This procedure resembles the classical geometric multigrid scheme and is implemented in analogy as a sequence of V-cycles [11]. For three test cases it has been shown that a domain partitioning can be efficiently computed, which could reduce the work imbalance error in a few steps by several orders of magnitude. For continuous test cases it could be shown that the global error can even be reduced to $\epsilon < 10^{-10}$. For discrete systems, smoothness of the problem is lacking and the error is saturating at a level of $\epsilon < 10^{-3}$, which is certainly satisfying for any realistic simulation scenario, since dynamics of the underlying particle system is likely to increase load imbalance quickly into the low percentage range. Analysing the relaxation behaviour of each domain, it could be observed that the final accuracy of work imbalance is nearly the same for all processes, but that the relaxation is non-homogeneous, i.e. relaxation time is not unique for all processes. This might be related to the inhomogeneous work density distribution, or the convergence of the coarse density field to the *true* density map. To investigate the origin, will be a matter of investigation. Also it could be observed that the final error of the work distribution shows a slight oscillatory behaviour for the case of the discrete particle system. This is a signature of oscillations of the domain boarder geometries, i.e. no fix-point has been found for the domain geometry. Whether the system is trapped in a local minimum, or an incommensurability of equal work distribution has been occurred due to the discrete nature and, consequently, possible discretisation error, will be investigated in a future work. Furthermore, a more detailed analysis of the convergence behaviour will be conducted and possible criteria for not finding the absolute

minimum of the work distribution error will be discussed. It is a matter of the underlying system dynamics which contains the information of how often the load balancing procedure has to be called by the program. Experimental studies will be conducted in future to understand the interplay between system dynamics, gain in load balancing and penalty costs of calling the load balancing routine.

REFERENCES

[1] G. Karypis and V. Kumar. Multilevel algorithms for multi-constraint graph partitioning. In *Proceedings of the 1998 ACM/IEEE Conference on Supercomputing (SC ?98)*, pages 1–13, Washington, DC, USA, 1998. IEEE Computer Society.

[2] G. Karagiorgos and N.M. Missirlis. Accelerated diffusion algorithms for dynamic load balancing. *J. Inform. Proc. Lett.*, 84:61–67, 2002.

[3] E.G. Boman, U.V. Catalyurek, C. Chevalier, and K.D. Devine. The Zoltan and Isorropia Parallel Toolkits for Combinatorial Scientific Computing: Partitioning, Ordering, and Coloring. *Sci. Program.*, 20:129–150, 2012.

[4] F. Schornbaum and U. Rüde. Extreme-Scale Block-Structured Adaptive Mesh Refinement. *SIAM J. Sci. Comput.*, 40:C358–C387, 2018.

[5] H.D. Simon and S.H. Teng. How good is recursive bisection? *SIAM J. Sci. Comp.*, 18:1436–1445, 1997.

[6] J.E. Boillat, F. Brugè, and P.G. Kropf. A dynamic load balancing algorithm for molecular dynamics simulation on multi-processor systems. 96:1–14, 1991.

[7] J.-L. Fattebert, D.F. Richards, and J.N. Glosli. Dynamic load balancing algorithm for molecular dynamics based on Voronoi cells domain decompositions. *Comp. Phys. Comm.*, 183:2608–2615, 2012.

[8] Karen D. Devine, Erik G. Boman, Robert T. Heaphy, Rob H. Bisseling, and Umit V. Catalyurek. Parallel hypergraph partitioning for scientific computing. IEEE, 2006.

[9] A. Nakano and T. Campbell. An adaptive curvilinear-coordinate approach to dynamic load balancing of parallel multiresolution molecular dynamics. *Parallel Comp.*, 23:1461–1478, 1997.

[10] C. Begau and G. Sutmann. Adaptive Dynamic Load-Balancing Method for Particle Simulations. *Comp. Phys. Comm.*, 190:51–61, 2015.

[11] U. Trottenberg, C. W. Oosterlee, and A. Schüller. *Multigrid.* Academic Press, San Diego, 2001.

[12] G. Sutmann. Load Balancing with Generalized Multi-Level Orthogonal Recursive Bisection, 2019. (in preperation).

EVALUATION OF DYNAMIC EXPLICIT MPM FORMULATIONS FOR UNSATURATED SOILS

F. CECCATO[1], V. GIRARDI[1], A. YERRO[2] AND P. SIMONINI[1]

[1] Department of Civil Environmental and Architectural Engineering (DICEA)
University of Padua
Via Ognissanti 39, 35219, Padua, Italy
e-mail: francesca.ceccato@dicea.unipd.it
[2] Department of Civil and Environmental Engineering
Virginia Polytechnic Institute and State University
Blacksburg, VA, United States

Key words: MPM, Unsaturated soil, infiltration

Abstract. Many applications in geohazards prevention involve large deformations of unsaturated soils, e.g. rainfall induced landslides, embankment collapses due to wetting etc. These phenomena can be investigated with multiphase implementations of the Material Point Method (MPM) able to account for the behaviour of unsaturated soils. This paper compares two formulations: (i) a fully coupled three-phase formulation (3P) in which the governing equations are derived from the momentum balance and the mass balance equations of solid, liquid and gas phase assuming non-zero gas pressure, the primary unknowns are the absolute accelerations of the phases (a_S–a_L–a_G formulation); (ii) a simplified approach that neglects the momentum balance equation of the gas (2P_s). Potentialities and limitations of these approaches are highlighted considering a 1D infiltration problem. Despite the introduced simplifications, the simplified formulation gives reasonably good results in many engineering cases.

1 INTRODUCTION

Many natural hazards involve large deformations of unsaturated soils, e.g. rainfall induced landslides, embankment collapses due to wetting etc. These phenomena can be investigated with multiphase implementations of the Material Point Method (MPM) able to account for the behavior of unsaturated soils.

Recently, Yerro et al. [1] proposed a single-point three-phase (SP-3P) MPM formulation in which the governing equations are derived from the momentum balance and the mass balance equations of solid, liquid and gas phase assuming non-zero gas pressure. This approach takes into account the relative accelerations and relative velocities of the pore fluids and the primary unknowns are the absolute accelerations of the phases (a_S–a_L–a_G formulation). The formulation is lagrangian for the solid phase; the material points (MPs) move with the kinematic of the solid skeleton, but carry the information of all phases (single-point approach).

In contrast, Bandara et al. [2] and Wang et al. [3] used a simplified approach, which neglects the momentum and the mass balance equations of the gas, thus reducing the computational cost. The formulation proposed in Wang et al. is an extension of the two-phase formulation developed in [4] for saturated soils. The governing equations are derived from the dynamic

equilibrium of the liquid phase and the mixture and the primary unknowns are the absolute accelerations of the soild and the liquid (aS–aL formulation). In Section 2.2 this formulation is introduced showing that can be derived as a simplified version of the one presented in Yerro et al. [1]. In Bandara et al. the relative acceleration of the liquid with respect to the solid skeleton is neglected and the primary unknowns are the absolute acceleration of the solid skeleton and the relative velocity of the fluid.

The simplifying assumptions introduced in [2,3] are reasonable in many engineering cases, but sometimes deviations from the full three-phase formulation can be relevant. This paper highlights the differences between these approaches, considering a 1D infiltration example simulated with an internal version of the software Anura3D (www.anura3D.eu) (Section 3).

2 MPM FORMULATIONS FOR UNSATURATED SOILS

The unsaturated porous media are assumed to be a combination of three different phases (ph): solid (S), liquid (L) and gas (G). The solid phase is made by solid grains that constitutes the solid skeleton of the media; meanwhile the liquid and the gas phases fill the voids. The fluids are a mixture of two components (c): water (w) and dry air (a) (Fig. 1). The mass fraction of a component in a phase are defined as:

$$\omega_{ph}^c = \frac{m_{ph}^c}{m_{ph}}$$

(1)

The total mass of a component is:

$$m^c = \sum_{ph} m_{ph}^c$$

(2)

The volumetric concentration ratio of solid, liquid, and gas are defined respectively as n_S, n_L, and n_G, moreover $n_S + n_L + n_G = 1$, $n = 1 - n_S = n_L + n_G$=porosity. Note that in unsaturated soils, the concentration ratio of porous fluids (n_L and n_G) is controlled by the degree of saturation $S_{ph} = V_{ph}/V_{void}$ ($S_L = 1 - S_G$) as $n_L = nS_L$ and $n_G = nS_G$.
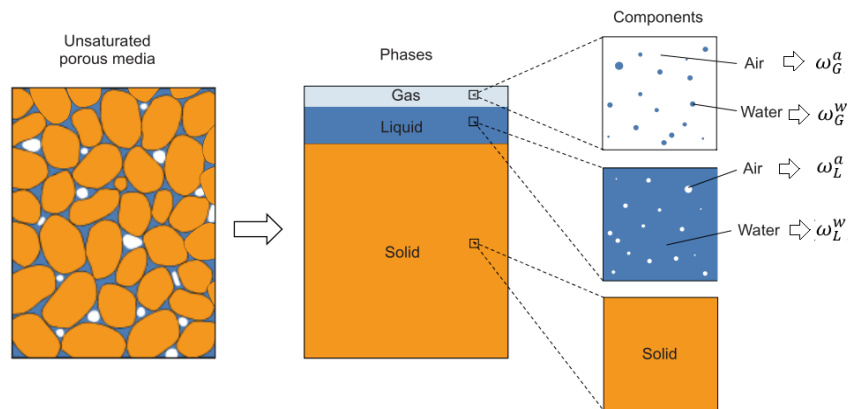
Figure 1 Definition of phases and components in an unsaturated medium (after [1])

2.1 Three-phase (3P)

The 3P-SP formulation [1] considers one set of MPs that represent a partially saturated porous media. Each MP carries information of the three phases interacting in the continuum (i.e., solid skeleton "S", liquid "L, and gas "G"), and while it provides a Lagrangian description of the solid (MPs move according to the solid), the fluid phases filling the voids are represented by means of a Eulerian approach.

Three main governing equations are posed at the nodes of the computational grid: the dynamic linear momentum balances of the gas phase (Eq. 3), liquid phase (Eq. 4), and mixture (Eq. 5), being the accelerations of each phase ($\boldsymbol{a}_G$, $\boldsymbol{a}_L$, and $\boldsymbol{a}_S$) the primary unknowns of the system.

$$\rho_G \boldsymbol{a}_G = \nabla p_G - \boldsymbol{f}_G^d + \rho_G \boldsymbol{b} \tag{3}$$

$$\rho_L \boldsymbol{a}_L = \nabla p_L - \boldsymbol{f}_L^d + \rho_L \boldsymbol{b} \tag{4}$$

$$n_S \rho_S \boldsymbol{a}_S + n_L \rho_L \boldsymbol{a}_L + n_G \rho_G \boldsymbol{a}_G = \nabla \cdot \boldsymbol{\sigma} + \rho_m \boldsymbol{b} \tag{5}$$

where the density of the mixture is $\rho_m = n_S \rho_S + n_L \rho_L + n_G \rho_G$, the liquid and gas pressures are p_L and p_G respectively, and $\boldsymbol{\sigma}$ is the total stress tensor. One assumption is that the liquid and gas seepages are assumed laminar in slow velocity regime; hence, drag forces ($\boldsymbol{f}_G^d$ and $\boldsymbol{f}_L^d$) fulfill Darcy's law.

As usual in MPM, Eq. 3, 4, and 5 are discretized in space by means of the Galerkin method and solved in time with a semi-explicit time discretization scheme.

The model enables mass exchange between fluid phases, in order to account for dissolved air in the liquid and water vapour in the gas, and the mass balance equations are formulated for each component (i.e. solid, water "w", air "a"):

$$\sum_{ph} \left[\frac{\partial}{\partial t} \left(\frac{m_{ph}^c}{V} \right) + \nabla \cdot \boldsymbol{j}_{ph}^c \right] = 0 \tag{6}$$

Where V is the volume of the mixture and $\boldsymbol{j}_{ph}^c$ is the flux of the component in the phase. Yerro et. al [1] show that the mass balance equations of the solid, water, and air, can be manipulated, leading to the following expressions:

$$\frac{Dn}{Dt} = n \nabla \cdot \boldsymbol{v}_S \tag{7}$$

$$
\begin{aligned}
n \frac{\partial(\omega_L^w \rho_L S_L + \omega_G^w \rho_G S_G)}{\partial p_L} \dot{p}_L &+ n \frac{\partial(\omega_L^w \rho_L S_L + \omega_G^w \rho_G S_G)}{\partial p_G} \dot{p}_G \\
&= -\boldsymbol{\nabla} \cdot [\omega_G^w n \rho_G S_G (\boldsymbol{v_G} - \boldsymbol{v_S})] - \boldsymbol{\nabla} \cdot [\omega_L^w n \rho_L S_L (\boldsymbol{v_L} - \boldsymbol{v_S})] \\
&\quad - (\omega_G^w \rho_G S_G + \omega_L^w \rho_L S_L) \boldsymbol{\nabla} \cdot \boldsymbol{v_S} - \boldsymbol{\nabla} \cdot \boldsymbol{i}_G^w
\end{aligned} \tag{8}
$$

$$
\begin{aligned}
\frac{\partial(\omega_L^a \rho_L S_L + \omega_G^a \rho_G S_G)}{\partial p_L} \dot{p}_L &+ n \frac{\partial(\omega_L^a \rho_L S_L + \omega_G^a \rho_G S_G)}{\partial p_G} \dot{p}_G \\
&= -\boldsymbol{\nabla} \cdot [\omega_G^a n \rho_G S_G (\boldsymbol{v_G} - \boldsymbol{v_S})] - \boldsymbol{\nabla} \cdot [\omega_L^a n \rho_L S_L (\boldsymbol{v_L} - \boldsymbol{v_S})] \\
&\quad - (\omega_G^a \rho_G S_G + \omega_L^a \rho_L S_L) \boldsymbol{\nabla} \cdot \boldsymbol{v_S} - \boldsymbol{\nabla} \cdot \boldsymbol{i}_L^a
\end{aligned} \tag{9}
$$

Where i_{ph}^c is the diffusive flux, modelled by the Fick's law. Note that the previous expressions can be simplified when the liquid and gas phases are considered as simply water ($\omega_L^a = 0$; $i_G^w = \mathbf{0}$) and dry air ($\omega_G^w = 0$; $i_L^a = \mathbf{0}$); the examples in Section 3 are solved under these hypothesis..

The mass balance equations (Eq. 7, 8, 9) are posed at the MPs and solved in terms of changes in porosity, liquid pressure and gas pressure. In this formulation, the solid mass remains constant thorough the calculation, and the mass balance of the solid phase is automatically fulfilled. However, the conservation of the fluid masses is totally controlled by the accuracy in which the mass balance equations are solved.

The constitutive stresses controlling the unsaturated soil behavior, net stress ($\overline{\boldsymbol{\sigma}} = \boldsymbol{\sigma} - p_G \boldsymbol{I}$) and suction ($s = p_G - p_L$), are updated at the MPs by considering a constitutive equation. Finally, the degree of saturation and the hydraulic permeability are updated taking into account the corresponding hydraulic constitutive equations, i.e., the soil-water retention curve, and the Hillel expression, respectively as introduced in Section 2.3.

2.2 Two-phase with suction (2P_s)

The governing equations of the two-phase formulation with suction effect (2P_s) are derived in this section highlighting the additional hypothesis introduced with respect to the 3P formulation explained in Section 2.1.

Assuming that:
1) no air is dissolved in liquid ($\omega_L^a = 0$, $\omega_G^a = 1$) and no water vapour is present in the gas phase ($\omega_G^w = 0$, $\omega_L^w = 1$),
2) no diffusion fluxes of air in the liquid phase ($i_L^a \approx 0$) and water in the gas ($i_G^w \approx 0$)
3) gas density is negligible compared to the other phases ($\rho_G \approx 0$),
4) the gas pressure is constant and equal to 0,
5) the gradient of the product $n\rho_L S_L$ is negligible, i.e. $\nabla(n\rho_L S_L) \approx \mathbf{0}$

the momentum balance equation and the mass balance equation of the gas can be neglected, while the momentum balance of the mixture reduces to Eq. 10.

$$n_S \rho_S \boldsymbol{a}_S + n_L \rho_L \boldsymbol{a}_L = \nabla \cdot \boldsymbol{\sigma} + \rho_m \boldsymbol{b} \tag{10}$$

where the mixture density is $\rho_m = n_S \rho_S + n_L \rho_L$.

The mass balance equation of the liquid is rewritten as:

$$n \frac{D(\rho_L S_L)}{D p_L} \dot{p}_L = -(1-n)(\rho_L S_L)\nabla \cdot \boldsymbol{v_S} - n(\rho_L S_L)\nabla \cdot \boldsymbol{v_L} \tag{11}$$

The left hand side of Eq. 11 can be reformulated by
1) introducing the constitutive equation for the water: $\dot{\rho}_L = -\rho_L/K_L \dot{p}_L$, K_L=liquid bulk modulus
2) considering that S_L is a function of p_L which leads to Eq. 12.

$$\left[-\frac{S_L n}{K_L} + n\frac{\partial S_L}{\partial p_L}\right]\dot{p}_L = n S_L \nabla \cdot \boldsymbol{v_L} + (1-n)S_L \nabla \cdot \boldsymbol{v_S} \tag{12}$$

The derivative of the degree of saturation with respect to suction is given by the soil-water retention curve (Section 2.3).

Note that, due to the introduced simplifications, the difference between the 3P and the 2P_s formulation increases when
1) gas density increases
2) suction increases
3) gas pressure is not zero (i.e. atmospheric pressure)
4) degree of saturation decreases
5) derivative of the degree of saturation increases
The effect of these simplifications will be more clear with the infiltration examples reported in Section 3.

2.3 Hydraulic constitutive equations

The well know Van Genuchten soil-water retention curve (SWRC) [5] can be used with assumed constant parameters λ and p_0.

$$S_L = S_{min} + \left[1 + \left(\frac{s}{p_0}\right)^{\frac{1}{1-\lambda}}\right]^{-\lambda} (S_{max} - S_{min}) \tag{13}$$

Alternatively, an approximated linear law (Eq.14) can be used to compute S_L.

$$S_L = 1 - a_v \cdot s \tag{14}$$

Furthermore, since the hydraulic conductivity parameter is susceptible of variable water content in soil unsaturated zones, the seepage process should be modelled with permeability laws function of S_L. An example of this kind of law is the Hillel expression [6] as function of the saturated hydraulic conductivity and an exponent r, which assumes values between 2 and 4.

$$k_L = k_{sat} \cdot S_L{}^r \tag{15}$$

3   NUMERICAL EXAMPLES

In order to compare the formulations presented in the previous section a one-dimensional infiltration problem, similar to the one presented in [7], is considered here. A 1m column has an initial suction of $s_0 = 500$kPa; for $t > 0$, zero suction is applied at the head of the column and the suction begins to decrease with time.

The equation that represents the movement of water in unsaturated soils is the Richards equation. However, because of the nonlinearities of soil hydraulic parameters (for instance, permeability depends on degree of saturation, and degree of saturation depends on fluid pressures), it is very difficult to obtain an analytical solution to describe the unsaturated flow. In order to derive an analytical solution the following assumptions are introduced [8]:
• vertical liquid flow,
• deformability of the solid skeleton and the solid grains are neglected,
• neither water vapour nor dissolved air are considered in the gas and liquid phases respectively,
• validity of the Darcy's law and constant permeability,
• barotropic behaviour of the liquid,
• linearized water retention curve, i.e. Eq. 14

The mathematical expression that describes the one-dimensional vertical water flow within an unsaturated soil can be derived from the mass balance equation of the liquid (Eq. 11).

Under the aforementioned assumptions it reduces to Eq. 16

$$\left[\frac{nS_L}{K_L} + na_v\right]\frac{\partial p_L}{\partial t} = \frac{k}{\rho_L g}\frac{\partial^2 p_L}{\partial y^2} \tag{16}$$

Which can be written as

$$\frac{\partial p_L}{\partial t} = C_i \frac{\partial^2 p_L}{\partial y^2} \tag{17}$$

This expression is the diffusion equation, where y is the infiltration direction and C_i corresponds to

$$C_i = \frac{k}{n\rho_L g\left(\frac{S_L}{K_L} + a_s\right)} \tag{18}$$

Assuming that the variation of C_i is small in the considered process, a dimensionless time T can be defined as function of C_i and the column height h as

$$T = \frac{C_i t}{h^2} \tag{19}$$

The analytical solution that comes out applying the boundary conditions previously described, is the following:

$$\frac{s}{s_0} = \frac{4}{\pi}\sum_{j=1}^{\infty}\frac{(-1)^{j-1}}{2j-1}\cos\left[(2j-1)\frac{\pi}{2}\frac{y}{h}\right]e^{-(2j-1)^2\frac{\pi^2}{4}\frac{C_i t}{h^2}} \tag{20}$$

being s suction ($s = p_G - p_L$), s_0 initial suction, h the infiltration length, and t time.

Note that the previous equation is equivalent to the one-dimensional consolidation problem in saturated media, the well-known Terzaghi's solution.

Figure 2 compares the numerical results with the analytical solution for different values of a_v assuming s_0=500kPa. Material parameters are summarized in Table 1. In this conditions the degree of saturation varies between 0.5 and 1 for the case a_v=1.0e-3 kPa^{-1} and between 0.995 and 1 for the case a_v=1.0e-5 kPa^{-1}. When S_L is close to 1 and the derivative $\partial S_L/\partial s$ is small, the additional terms comparing in the 3P formulation are small, thus the two formulations give the same results. When reducing the initial suction to 5kPa in case a_v=1e-3kPa^{-1}, a good agreement between the two formulations is recovered as the suction varies only between 0.995 and 1.

Table 1. Material Parameters of the infiltration problem (* parameters not used in 2P_s)

Solid density	2700 kg/m³	Gas bulk modulus*	10 kPa
Liquid density	1000 kg/m³	Intrinsic permeability liquid	5·10⁻¹¹m²/s
Gas density*	10 kg/m³	Intrinsic permeability gas*	5·10⁻¹¹m²/s
Porosity	0.3	Liquid viscosity	10⁻⁶ kPa s
Liquid bulk modulus	80000 kPa	Gas viscosity*	2·10⁻⁸ kPa s
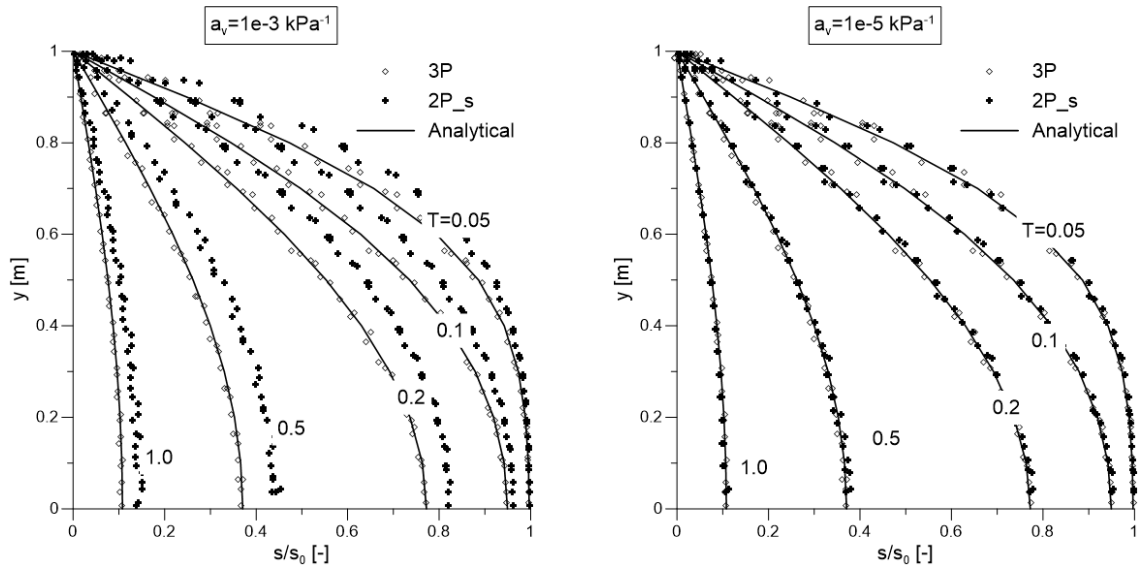
Figure 2: Numerical results of normalized suction evolution along depth; comparison between 2P_s and 3P for a_v=1e-3kPa^{-1} and a_v=1e-5kPa^{-1} in case s_0=500kPa
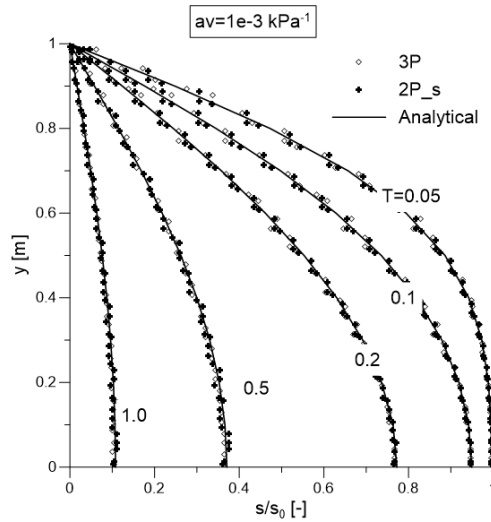
Figure 3: Numerical results of suction evolution along depth y, comparison between 2P_s and 3P for a_v=1e-3kPa^{-1} in case s_0=5kPa

The simulations are now repeated using the Van Genuchten water retention curve and the Hillel law. Two sets of parameters have been used (Tab. 2, Fig. 4), which are close to typical values for clay (soil A) and sand (soil B).

Assuming an initial suction corresponding to an initial degree of saturation of 0.85 the 3P and the 2P_s gives very similar results (Fig. 5). The normalized time T in Figure 5 is computed for a value of $C_{i,ref}$ calculated with the values of k, S_L, and $a_v = \partial S_L/\partial p_L$ at the beginning of the simulation.

These conditions are probably the most frequent in many geohazard problems such as dam and levee stability or shallow landslides.

When running these simulations in a common laptop computer, the 2P_s is 6 times faster than the 3P, thus the use of the 2P_s can be more convenient for problems when S_L is relatively close to 1 and varies in a narrow range.

Table 2: Parameters of Van Genuchten SWRC

	Soil A	Soil B
S_{min}	0.2	0.125
S_{max}	1	1
p_0	5	3
λ	0.17	0.7
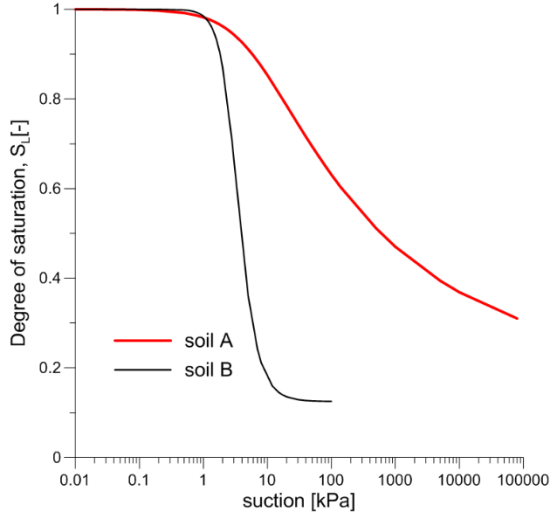
Figure 4: SWRC for parameters in Table 2
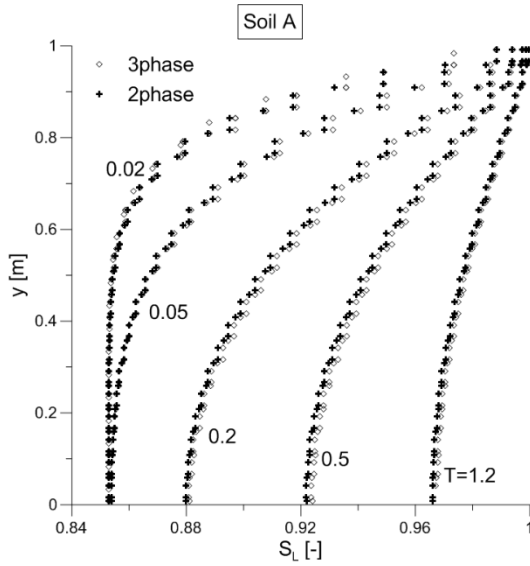
(a) Soil A, s_0=10kPa
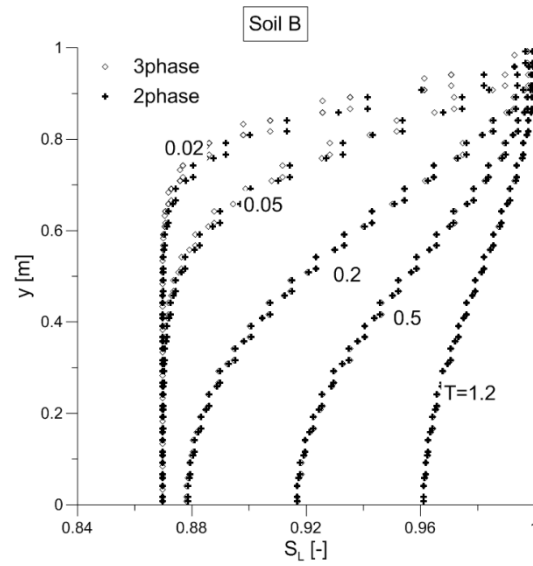
(b) Soil B, s_0=2kPa

Figure 5: Comparison between MPM results using different hydraulic conductivity curves: evolution of the degree of saturation with depth for soil A (a) and B (b).

Increasing the suction to values corresponding to an effective degree of saturation $S_e = \frac{S_L - S_{min}}{S_{max} - S_{min}} = 0.13$ the results obtained by the two formulations are slightly different, especially for the lower values of S_L.

(a) Soil A, s_0=80000kPa

(b) Soil B, s_0=7kPa
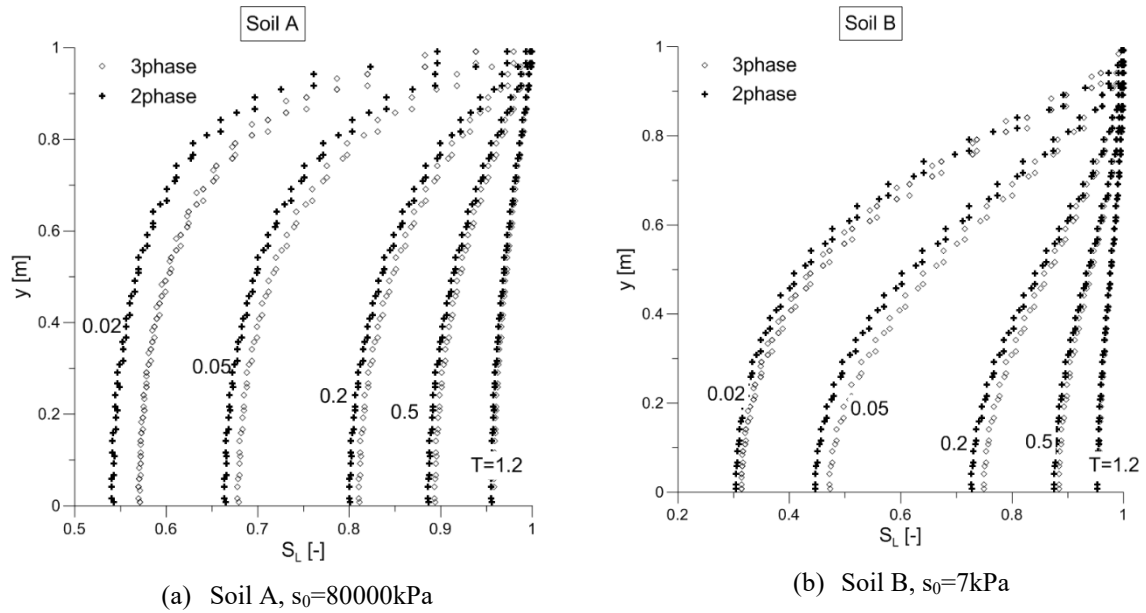
Figure 6 Comparison between MPM results using different hydraulic conductivity curves: evolution of the degree of saturation with depth for soil A (a) and B (b).

4   CONCLUSIONS

This paper briefly illustrates two mathematical formulations for unsaturated soils recently implemented in the MPM code Anura3D, namely the full three-phase formulation and the simplified two-phase formulation with suction effect. The results obtained with 3P and 2P_s are compared for different material parameters in a one-dimensional infiltration case showing that the differences increases when
1) suction increases
2) degree of saturation decreases
3) derivative of the degree of saturation increases, i.e. the SWRC is relatively steep like in Soil B of Fig. 4

In many real cases under analysis for geohazard assessment the differences between 3P and 2P_s are negligible, thus the simplified formulation can be used to reduce significantly the computational cost.

5   REFERENCES

[1]   Yerro A, Alonso EE, Pinyol NM. The material point method for unsaturated soils. *Geotechnique*, **65**, 201–17 , 2015.

[2]   Bandara SS, Ferrari A, Laloui L. Modelling landslides in unsaturated slopes subjected to rainfall infiltration using material point method. *Int. J. Numer. Anal. Methods Geomech. (published online)*, , 2016.

[3]   Wang B, Vardon PJ, Hicks MA. Rainfall-induced slope collapse with coupled material point method. *Eng. Geol.*, **239**, 1–12 , 2018.

[4]   Jassim I, Stolle D, Vermeer P. Two-phase dynamic analysis by material point method. *Int. J. Numer. Anal. Methods Geomech. Anal. methods Geomech.*, **37**, 2502–22 , 2013.

[5]   Van Genuchten M. A closed-form equation for predicting the hydraulic conductivity of unsaturated soils. *Soil Sci. Soc. Am. J.*, **44**, 892–8 , 1980.

[6]   Hillel D. *Soil and water – physical principles and processes*. Academic press, London (UK), (1971).

[7]   Yerro A, Alonso E, Pinyol N. Modelling large deformation problems in unsaturated soils, E-UNSAT 2016, 2016, pp.1–6.

[8]   Alonso EE, Lloret A. Evolution in time of the reliability of slopes in partially saturated soils, International conference on applications of statistics and probability in soil and structural engineering, 1983, pp.1363–76.

VERIFICATION AND VALIDATION IN HIGHLY VISCOUS FLUID SIMULATION USING A FULLY IMPLICIT SPH METHOD

Daniel S. Morikawa[1], Mitsuteru Asai[1] and Masaharu Isshiki[2]

[1] Departament of Civil Engineering
Kyushu University
744 Motooka Nishi-ku, 819-0395 Fukuoka, Japan
e-mail: daniel@civil.doc.kyushu-u.ac.jp, web page:
https://kyushu-u.wixsite.com/structural-analysis

[2] Graduate School of Science and Engineering
Ehime University
3 Bunkyo-cho, 790-8577 Fukuoka, Japan

Key words: SPH, Implicit time integration, Non-Newtonian fluids, Ghost particles

Abstract. Catastrophes involving mass movements has always been a great threat to civilizations. We propse to simplify the behavior of the mass movement material as a highly viscous fluid, possibly non-Newtonian. In this context, this study describes the application of two improvements in highly viscous fluid simulations using the smoothed particle hydrodynamics (SPH) method: an implicit time integration scheme to overcome the problem of impractically small time-step restriction, and the introduction of air ghost particles to fix problems regarding the free-surface treatment. The application of a fully implicit time integration method implies an adaptation of the wall boundary condition, which is also covered in this study. Furthermore, the proposed wall boundary condition allows for different slip conditions, which is usually difficult to adopt in SPH. To solve a persistent problem on the SPH method of unstable pressure distributions, we adopted the incompressible SPH [1] as a basis for the implementation of these improvements, which guarantees stable and accurate pressure distribution. We conducted non-Newtonian pipe flow simulations to verify the method and a variety of dam break and wave generated by underwater landslide simulations for validation. Finally, we demonstrate the potential of this method with the highly viscous vertical jet flow over a horizontal plate test, which features a complex viscous coiling behavior.

1 INTRODUCTION

Landslide, debris flow, avalanche and dam collapse are examples of mass movement events. They are among the most harmful and widespread forms of disasters either natural or manmade. For instance, the 2019 tsunami in Indonesia, aka 2018 Sunda Strait tsunami, was caused by an underwater landslide triggered by Anak Krakatau volcano eruption. It

caused more than 400 deaths and 14 thousand injured people. Another example is the Brumadinho dam disaster in Brazil, 2019. The iron ore tailings dam collapse led to a mudflow that inundated a large area of the city of Brumadinho. More than 200 people lost their lives. Given the recent concern in this topic, it is essential for present and future public administrators to prepare preventive measures for mass movement events, which requires extensive studies on the phenomenon.

We propose to use the SPH method to simulate the bahavior of mass movements approximating its rheology into a non-Newtonian fluid, which can reach high viscosities. Here, we show a verification and validation (V & V) procedure of the method for different settings, which resulted in good agreement with theoretical solutions and past physical experiments.

2 SPH METHOD FORMULATION

The SPH method is one of the several Lagrangian mesh-free particle methods which was first proposed simultaneously by Lucy [2] and Gingold and Monaghan [3] in 1977 and it is widely applied to fluid dynamics problems. In this section, we present the basic aspects of this method.

2.1 Governing equations

The ISPH is designed to solve numerically the two main equations of hydrodynamic problems of incompressible flows, the continuity equation and the NavierStokes equation, respectively,

$$\nabla \cdot \mathbf{v} = 0, \tag{1}$$

$$\frac{D\mathbf{v}}{Dt} = -\frac{\nabla P}{\rho} + \nabla^2(\nu \mathbf{v}) + \mathbf{g}, \tag{2}$$

where $\mathbf{v}$ is the velocity vector, D/Dt the time derivative, P the pressure field, ρ the density of the fluid, ν the kinematic viscosity, $\mathbf{g}$ the external forces vector, and t the time.

2.2 SPH approximations

The SPH method is a space integration method that smoothly approximates the value of functions and its derivatives by integrating the contribution of the neighbor particles varying its influence according to a weight function W, which is chosen from a wide range of possibilities. In this study, we speted for the quintic spline function [4]. Then, one can approximate the value of a generic function ϕ for a given particle and its derivatives as

$$\langle \phi_i \rangle = \sum_{j=1}^{N} \frac{m_j}{\rho_j} \phi_j W(\mathbf{r}_{ij}, h), \tag{3}$$

$$\langle \nabla \phi_i \rangle = \frac{1}{\rho_i} \sum_{j=1}^{N} m_j (\phi_j - \phi_i) \nabla W(\mathbf{r}_{ij}, h), \tag{4}$$

$$\langle \nabla \phi_i \rangle = \rho_i \sum_{j=1}^{N} m_j \left(\frac{\phi_j}{\rho_j^2} + \frac{\phi_i}{\rho_i^2} \right) \nabla W(\mathbf{r}_{ij}, h), \tag{5}$$

$$\langle \nabla^2 \phi_i \rangle = \frac{2}{\rho_i} \sum_{j=1}^{N} m_j \frac{\mathbf{r}_{ij} \cdot \nabla W(\mathbf{r}_{ij}, h)}{\mathbf{r}_{ij}^2} (\phi_i - \phi_j), \tag{6}$$

where the subscripted indices i and j labels the target and neighboring particles, respectively, m is the mass, $\mathbf{r}_{ij} = \mathbf{x}_i - \mathbf{x}_j$ the relative position vector between particles i and j, and symbol $\langle \ \rangle$ signifies the application of the SPH approximation. Note that there are two formulations to approximate the first spatial derivative of a function as expressed by Eqs. 4 and 5.

3 FULLY IMPLICIT TIME INTEGRATION SCHEME

The original time integration scheme for the ISPH method [1] is based on a projection method which updates the velocity in a semi-implicit manner divided into two steps: predictor and corrector steps. In a similar way, we propose a fully-implicit time integration scheme using the same predictor and corrector steps [5]. The objective is to avoid the Courant-Friedrichs-Lewy condition [6] on the maximum allowed time increment, which could lead to infeasibly small values for highly viscous fluid simulations.

3.1 Time integration based on the projection method

First, the contribution of the viscous term and the external forces of Eq.2 results in a predicted velocity field calculated implicitly as

$$\mathbf{v}^* = \mathbf{v}^n + \Delta t (\nabla^2 (\nu \mathbf{v}^*) + \mathbf{g}). \tag{7}$$

Then, the pressure is calculated from a pressure Poisson equation

$$\nabla^2 P^{n+1} = \frac{\rho_0}{\Delta t} \nabla \cdot \mathbf{v}^* + \alpha \frac{\rho_0 - \rho^n}{\Delta t^2}. \tag{8}$$

Finally, adding the contribution of the pressure field, we calculate implicitly the updated velocity field as

$$\mathbf{v}^{n+1} = \mathbf{v}^* + \Delta t \left(-\frac{\nabla P^{n+1}}{\rho_0} \right). \tag{9}$$

In the above equations, Δt is the time increment, ρ_0 the reference density of the fluid, ρ_n a SPH approximation of the density based on Eq.3, α a relaxation coefficient, n and $n+1$ indices referring to the current and next iterations, and the superscript $*$ indicates the predictor step. Eqs. 7 and 9 are referred to as the predictor and corrector steps, respectively.

3.2 Rheological model

In this study, we use three different rheological models: Newtonian, Bingham plastic and Bingham pseudoplastic fluids.

In Newtonian fluids, the viscosity parameter has a fixed value, so $\nu = \nu_0$. In contrast, Bingham plastic and Bingham pseudoplastic rheologies are evaluated using the cross model and the Herschel-Bulkley model, respectively,

$$\tilde{\nu} = \nu_0 + \frac{\tau_y}{\dot{\gamma}\rho_0}, \tag{10}$$

$$\tilde{\nu} = \frac{K\dot{\gamma}^{n_0-1}}{\rho_0} + \frac{\tau_y}{\dot{\gamma}\rho_0}, \tag{11}$$

where $\tilde{\nu}$ represents the approximated viscosity, ν_0 the initial viscosity, K the consistency index, n_0 the flow behavior index, τ_y the yield stress, and $\dot{\gamma}$ the equivalent strain rate approximated as [7]

$$\dot{\gamma}_i^2 = \frac{1}{2}\sum_{j=1}^{N} m_j \frac{\rho_i + \rho_j}{\rho_i\rho_j} \frac{\mathbf{r}_{ij} \cdot \nabla W(\mathbf{r}_{ij}, h)}{\mathbf{r}_{ij}^2} |\mathbf{v}_i - \mathbf{v}_j|^2. \tag{12}$$

To avoid numerical problems of dividing by zero, the final viscosity is evaluated as

$$\nu = \begin{cases} \nu_{MAX} & \text{if } \tilde{\nu} > \nu_{MAX} \\ \tilde{\nu} & \text{otherwise.} \end{cases} \tag{13}$$

3.3 Discretization of the governing equations

Using the SPH approximations of Eqs. 4, 5 and 6, we discretize Eqs. 7, 8 and 9 as

$$\mathbf{v}_i^* = \mathbf{v}_i^n + \Delta t\Big(\sum_{j=1}^{N} B_{ij}(\mathbf{v}_i^* - \mathbf{v}_j^*) + \mathbf{g}\Big), \tag{14}$$

$$\sum_{j=1}^{N} A_{ij}(P_i^{n+1} - P_j^{n+1}) = b_i, \tag{15}$$

$$\mathbf{v}_i^{n+1} = \mathbf{v}_i^* + \Delta t\Big(-\sum_{j=1}^{N} m_j\Big(\frac{P_j^{n+1}}{\rho_j^2} + \frac{P_i^{n+1}}{\rho_i^2}\Big)\nabla W(\mathbf{r}_{ij}, h)\Big). \tag{16}$$

where

$$B_{ij} = m_j \frac{\rho_i\nu_i + \rho_j\nu_j}{\rho_i\rho_j} \frac{\mathbf{r}_{ij} \cdot \nabla W(\mathbf{r}_{ij}, h)}{\mathbf{r}_{ij}^2}, \tag{17}$$

$$A_{ij} = \frac{2}{\rho_i} m_j \frac{\mathbf{r}_{ij} \cdot \nabla W(\mathbf{r}_{ij}, h)}{\mathbf{r}_{ij}^2}, \tag{18}$$

$$b_i = \frac{1}{\Delta t}\sum_{j=1}^{N} m_j(\mathbf{v}_i - \mathbf{v}_j)\nabla W(\mathbf{r}_{ij}, h) + \alpha\frac{\rho_0 - \rho_i^n}{\Delta t^2}. \tag{19}$$

Notice that Eq.17 uses a slightly different SPH discretization compared to Eq.6 to result in a symmetric linear equation. In addition, it was necessary to simplify the viscosity term on Eq.17 as the viscosity of the previous time step n, since the strain rate (Eq.12) is non-linear by nature.
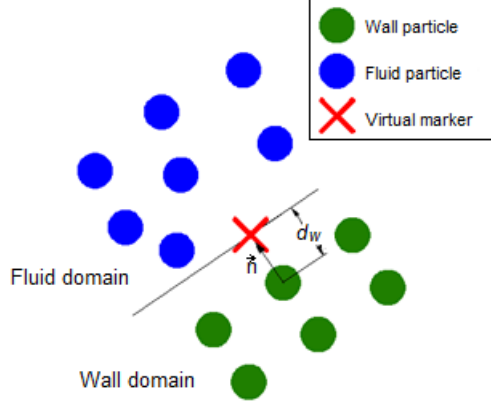
Figure 1: Wall boundary particles input information and virtual marker

4 BOUNDARY TREATMENT

For the correct application of the abovementioned equations, we need to define the boundary conditions accordingly. We propose the usage of ghost particles for both solid wall and free-surface boundaries.

4.1 Solid wall boundary

Following a similar procedure as [8], we selected a fixed wall ghost particle (FWGP) approach for the treatment of the solid wall boundary. First, fixed wall particles are placed in the wall domain, in which, for every wall particle, it is necessary to provide the normal direction $\mathbf{n}$ and the distance to the wall surface d_w as input information. Then, a virtual marker is placed on the boundary surface, as Fig.1 shows schematically.

To evaluate different slip conditions, we define the γ_{slip} parameter, which correspond to the percentage of slip on the projection of the velocity over the wall surface; that is, $\gamma_{slip} = 0$ means no-slip condition, $\gamma_{slip} = 0$, free-slip condition, and $1 > \gamma_{slip} > 0$, general slip condition.

Decomposing the velocity of a fluid particle(subscript f) near a wall particle (subscript w) into normal (subscript n) and orthogonal directions (subscript t) leads to

$$\mathbf{v}_{f,n} = (\mathbf{n}_w \cdot \mathbf{v}_f)\mathbf{n}_w, \tag{20}$$

$$\mathbf{v}_{f,t} = \mathbf{v}_f - \mathbf{v}_{f,n}. \tag{21}$$

where $\mathbf{n}_w$ represents the normal direction of a wall neighbouring particle.

Then, we derived the geometrical relationship

$$\mathbf{v}_{w,t} = C\mathbf{v}_{f,t}, \tag{22}$$

where

$$C = \gamma_{slip} - \frac{(1 - \gamma_{slip})d_w}{|\mathbf{x}_f - \mathbf{x}_w|cos\theta - d_w}, \tag{23}$$

$$cos\theta = \frac{\mathbf{n}_w \cdot (\mathbf{x}_f - \mathbf{x}_w)}{|\mathbf{x}_f - \mathbf{x}_w|}. \tag{24}$$

Let's define the no-penetration condition as

$$\mathbf{v}_{w,n} = -\mathbf{v}_{f,n}. \tag{25}$$

Then, using Eqs. 22 and 25 leads to

$$\mathbf{v}_w = C\mathbf{v}_f - (1+C)(\mathbf{n}_w \cdot \mathbf{v}_f)\mathbf{n}_w, \tag{26}$$

which can be interpreted as a relationship between the velocity of a target fluid particle and its wall neighbouring particle; therefore, can be applied on Eq.7.

Next, we define the pressure in the wall ghost particles based on a Neumann boundary condition stating that the acceleration $\mathbf{a}$ of the water particles close to the boundary surface in the normal direction of the wall should be zero; in other words,

$$\mathbf{a} \cdot \mathbf{n} = 0. \tag{27}$$

We then project the NavierStokes equation, Eq.2, along the normal to derive

$$\mathbf{a} \cdot \mathbf{n} = [-\frac{\nabla P}{\rho} + \nabla^2(\nu\mathbf{v}) + \mathbf{g}] \cdot \mathbf{n}, \tag{28}$$

$$\frac{\partial P}{\partial \mathbf{n}} = \rho(\nabla^2(\nu\mathbf{v}) + \mathbf{g}) \cdot \mathbf{n}, \tag{29}$$

$$P_w = P_{w,VM} - d_w\rho(\nabla^2(\nu\mathbf{v}) + \mathbf{g}) \cdot \mathbf{n}, \tag{30}$$

where the index VM represents the virtual marker of a wall particle.

Similarly to the velocity boundary condition, Eq. 30 can be applied to Eq.15 in the case of a target fluid i particle and its neighbouring wall particle j, since it is a general relationship between fluid and wall particles. However, to simplify this calculation, similarly to [8], we propose to approximate the pressure of a virtual marker J linked to the neighbouring wall particle j as

$$P_J^{n+1} = (1-\beta)P_i^{n+1}. \tag{31}$$
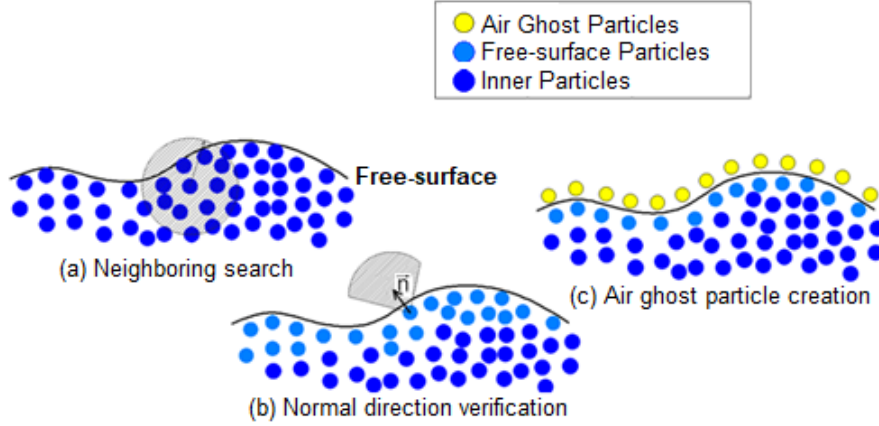
Figure 2: Process of creating AGPs

4.2 Free-surface boundary

In the original SPH method, there is no transition between inner fluid particles and void spaces outside the fluid domain, which causes some instability on the free-surface particles. Here, we propose the implementation of AGPs to create a fictitious mass around the free-surface to overcome this problem.

The algorithm described here is inspired by the space potential particle implementation [9] as follows. First, during the neighbouring search procedure, we attach the free-surface particle label for those with less than 160 neighboring particles in 3D simulations. Then, with an algorithm proposed by Marrone et al. [10], we reaffirm the free-surface particle label for those that have no particles in the conical plus a hemispherical region in the normal direction of each particle. Lastly, we create an AGP in the normal direction of each free-surface particle. Fig. 2 schematically illustrates this process.

If necessary, one may repeat processes (b) and (c) in Fig. 2 as often as needed to fill entirely the domain of influence of all free-surface particles. For the quintic spline weight function used in this study, three layers of AGPs are necessary to achieve the highest accuracy.

Null divergence of the velocity field on the free-surface particles boundary condition must be satisfied, which leads to a simplification in which the velocities of neighbouring AGPs are equal to the velocity of the fluid target particle. In addition, the zero pressure Dirichlet boundary condition must be satisfied on the AGPs.

5 NUMERICAL EXAMPLES

Here, we demonstrate the efficiency of the proposed SPH method with several numerical examples. The objective is to show a full process of verification and validation (V & V). First, the implicit time integration scheme is verified through several pipe flow simulations. Then, we validate it with dam break numerical tests, channel flow and underwater landslide. To finalize, we demonstrate the robustness of this method with the viscous coiling behavior.
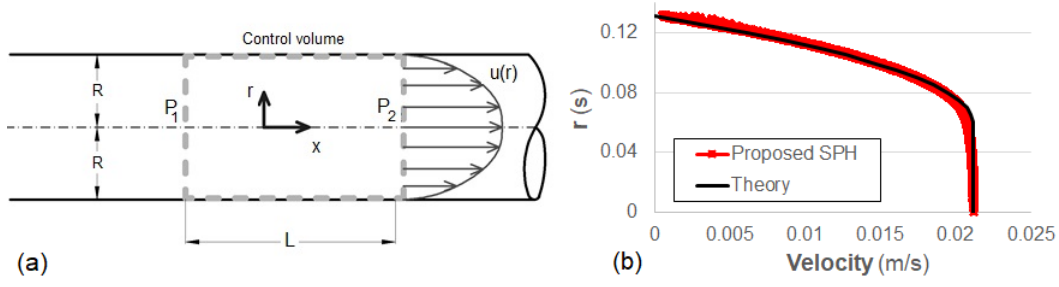
Figure 3: (a) Geometrical parameters of the pipe flow ; (b) Comparison between numerical and theoretical results of the non-Newtonian pipe flow simulation

5.1 Non-Newtonian pipe flow

We conducted the non-Newtonian pipe flow problem for the Bingham fluid, to verify our implicit time integration technique of the viscous term and the wall boundary treatment. Fig.3(a) illustrates the geometrical parameters of this problem. We utilized the following parameters during the simulation: R = 0.1325m, P1 = 2000Pa and P2 = 1000Pa (P = 1000Pa), L = 0.6m, 0 = 0.1m2/s, and d = 0.005m. Fig.3(b) is a graph comparing the numerical results with the theoretical solution. The theoretical value of the pipe flow velocity for Bingham plastic fluid is defined as [11]

$$
u(r) = \begin{cases} \frac{\Delta P R^2}{4\rho\nu_0 L}\left[\left(1 - \frac{2L\tau_y}{\Delta R}\right)^2\left(\frac{r}{R} - \frac{2L\tau_y}{\Delta R}\right)^2\right] & \text{if } r > r_0 \\ \frac{\Delta P R^2}{4\rho\nu_0 L}\left[\left(1 - \frac{r_0}{R}\right)^2\right] & \text{if } r \leq r_0, \end{cases}
\tag{32}
$$

where

$$
r_0 = \frac{2L\tau_y}{\Delta P}.
\tag{33}
$$

As expected, the numerical results are very consistent with the theoretical values.

5.2 Non-Newtonian Dam break

In this section, we conducted a series of dam break validation tests. First, we selected the well-known experimental study from Martin and Moyce [12] to verify the proposed SPH method applied on simple low viscosity case. To maintain the same notation as utilized in [12], lets define the non-dimensional quantities

$$
T = t\left(\frac{g}{a}\right)^{1/2},
\tag{34}
$$

$$
Z = \frac{z}{a},
\tag{35}
$$

where t is the time after the dam collapse, g is the gravity acceleration, a is the base length of the fluid, and z is the distance of the surge front from the initial wall. The chosen parameters in this validation test are $Height = a = 0.056m$, width $= 0.056m$, $d = 0.002m$, $\rho_0 = 1000kg/m^3$, $\nu_0 = 1.4 \cdot 10^{-7}m^2/s$, and $\Delta t = 1 \cdot 10^{-4}s$.
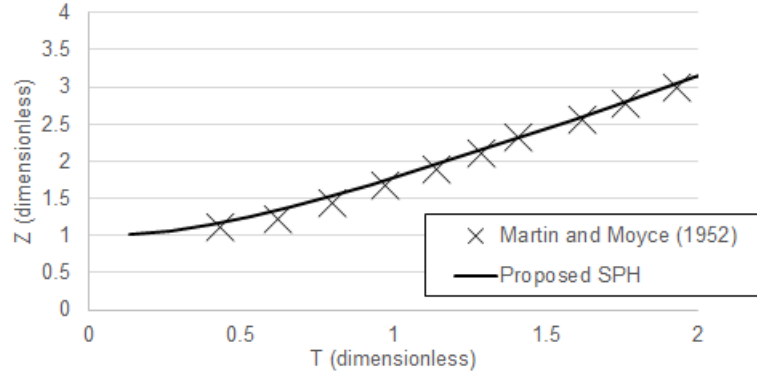
Figure 4: Comparison between numerical and experimental results of the Newtonian dam break simulation
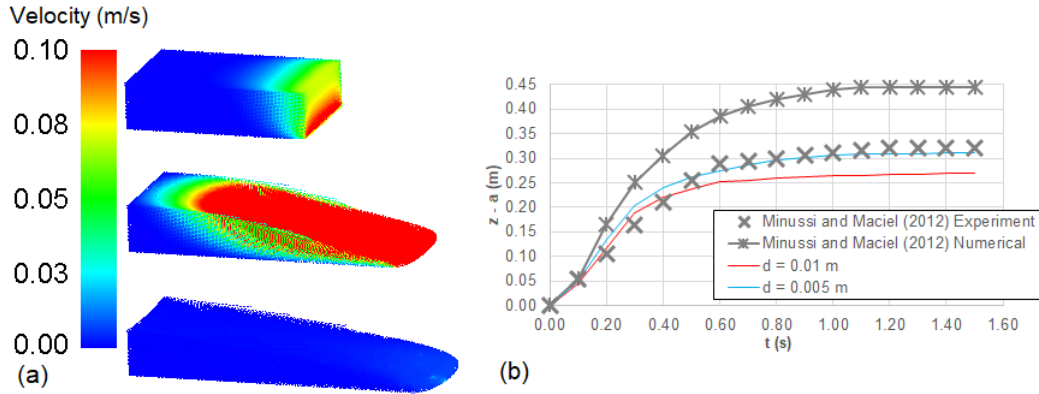
Figure 5: Non-Newtonian dam break: (a) Particle positioning after 0s, 1s and 1.5s of simulation; (b) Comparison of the non-Newtonian dam break results with [13]

Fig. 5.2 shows the simulation results graphically for the proposed SPH method. As expected, the results are very accurate.

Next, we analyze the dam break of a Bingham pseudoplastic fluid comparing with experimental results from Minussi and Maciel [13]. The following parameters were used in this verification test: height $= 0.13m$, $a = 0.5m$, width $= 0.32m$, $\rho_0 = 1000 kg/m^3$, $\tau_y = 49.179 Pa$, $k = 7.837 Pa \, s^{n_0}$, $n_0 = 0.442$, $\nu_{MAX} = 100 m^2/s$, and $\Delta t = 1 \cdot 10^{-4} s$.

Fig.5(a) shows the particle distribution of the non-Newtonian daybreak verification test after 0s, 1s and 1.5s of simulation, and Fig.5(b) shows the comparison between the results with different particle resolutions ($d = 0.01m$ and $d = 0.005m$). The results become more accurate as the particle resolution is finer, which shows the convergence of the proposed method. Also, as showed in Fig.5(b), our proposed method resulted in a better accuracy than the reference numerical solution presented in [13].
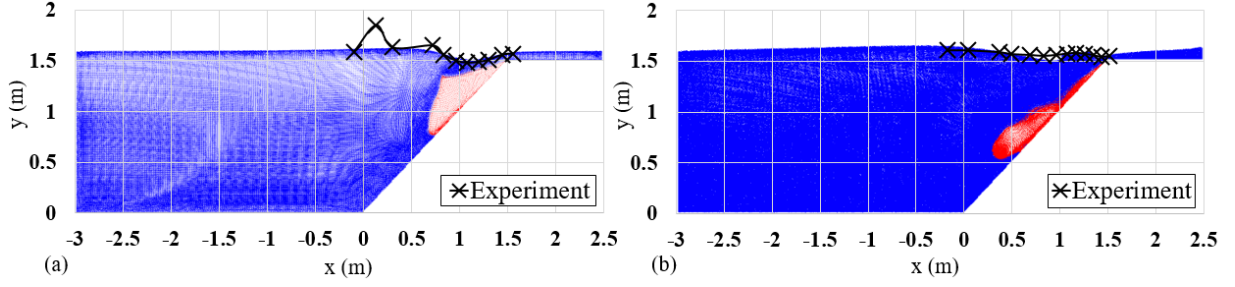
Figure 6: Underwater landslide comparison between the numerical solution and experiments from [16] at (a) 0.4s and (b) 0.8s

5.3   Underwater landslide

The next example is a validation test involving a multi-phase problem. [16] in collaboration with CEMAGREF institute (Centre National du Machinisme Agricole du Gnie Rural des Eaux et des Forts, France) conducted an experiment to evaluate the waves generated by underwater mass movements in a small scale experiment. The experiments consists of a portion of sand sliding over a frictionless plane inclined at 45 degrees. Initially, the channel with geometry specified in Fig.6 is filled with water at 1.6m depth and a sand mass of triangular cross section of 0.65m x 0.65m is positioned at the top of the inclined plane.

The numerical parameters are listed in table 1. As demonstrated in Fig.6, the numerical results are consistent with the experimental results, with the exception of one instance at 0.4s, which shows one data point that seems to not agree with the present numerical solution. We hypothesize that this one divergent data point might have been generated by the abrupt opening of the gate that was holding the sand mass at the initial position. In addition, this example shows the capability of our proposed method to simulate the no-slip condition at the inclined plane ($\gamma_{slip} = 0$).

Table 1: Parameters of the underwater landslide numerical test

d (m)	Δt (s)	$\rho_{0,water}$ (kg/m^3)	ν_{water} (m^2/s)	$\rho_{0,sand}$ (kg/m^3)	$\nu_{0,sand}$ (m^2/s)	$\tau_{y,sand}$ (Pa)
0.01	$1 \cdot 10^{-5}$	1000	$1.4 \cdot 10^{-7}$	1950	$5 \cdot 10^{-5}$	250

5.4   Viscous coiling

The viscous coiling behavior is a widely used benchmark test for highly viscous fluid simulation, since it is not possible to generate it without special treatment citeVileauRodgers. It is expected that viscous coiling behavior occurs on a vertical jet flow over a horizontal plate experiment, with a high enough viscosity and H/D (height over diameter) proportion [15].
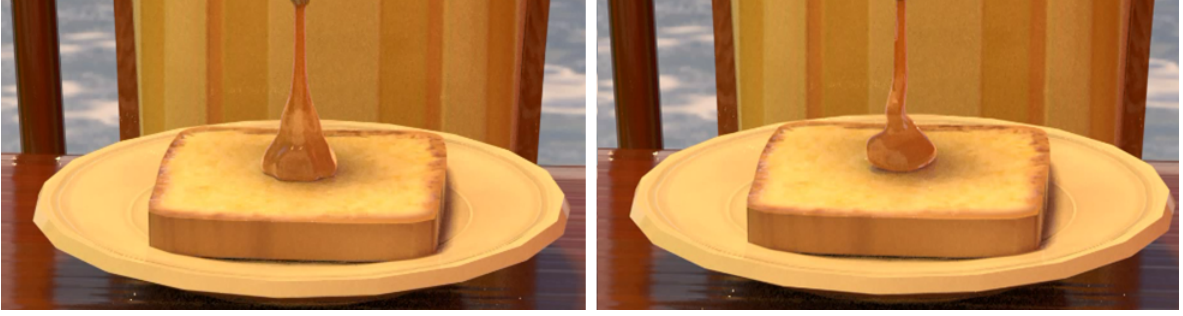
Figure 7: Vertical jet flow example without (left) and with (right) AGPs

The objective is to represent the behavior of honey falling over a bread. First, Fig.7 (left) reveals a rendered visualization of the vertical jet flow without the application of AGPs. Since the free-surface condition is not well verified, coiling could not occur, and the result is a radial motion. As oppose to that, Fig.7 (right) shows the same simulation solved with the introduction of AGPs. In this example, coiling occurs as a result of the improved free-surface treatment, and the movement appears to be very natural.

6   CONCLUSIONS

We proposed several improvements for highly viscous fluid and non-Newtonian fluid simulations using the SPH method. The main improvements are related to an implicit time integration scheme with a special boundary treatment of both the free-surface and the wall boundary using ghost particles. In addition, our proposed wall boundary approach (FWGP) may be applied to different slip conditions.

In the numerical tests, we validated our method using pipe flow numerical tests with non-Newtonian Bingham plastic rheology model. Next, we validated it with several dam break and underwater landslide simulations, which exhibited highly accurate results compared to previous experiments. Furthermore, we demonstrated the robustness of our improvements with a coiling behavior test of a highly viscous fluid. Although the free-surface treatment without AGPs in this last example could not reproduce the coiling behavior, our proposed model with FWGPs and AGPs naturally reproduces the coiling behavior.

As for future work, we plan to test the accuracy of this method in simulating large scale disasters such as landslides and debris flow. For this, we need to increase the computational speed and memory capacity of the program using high-performance computing (HPC) with expanding slice grid domain decomposition. In addition, we plan to couple this method with an SPH formulation for solid Mechanics to forecast the occurrence of landslides for different situations.

REFERENCES

[1] Asai, M., Aly, A.M., Sonoda, Y. and Sakai Y. A stabilized incompressible SPH method by relaxing the density invariance condition. *Int. J. Appl. Math.* (2012)

2012:139583. https://doi.org/10.1155/2012/139583.

[2] Lucy, L.B. A Numerical Approach to the Testing of the Fusion Process. *Astron. J.* (1977) **88**:1013-1024.

[3] Gingold R.A., Monaghan J.J. Smoothed Particle Hydrodynamics: Theory and Application to Non-Spherical Stars. *Astron. Soc.* (1977) **181**:375-389. https://doi.org/10.1155/2012/139583.

[4] Schechter H., Bridson R. Ghost SPH for Animating Water. *Proceedings of SIG-GRAPH 2012 Conference 31* (2012) **4**, Article No. 61.

[5] Morikawa, D.S., Asai, M., Nur'Ain, I., Imoto, Y., Isshiki, M. Improvements in highly viscous fluid simulation using a fully implicit SPH method. *Comp. Part. Mech.* (2019) https://doi.org/10.1007/s40571-019-00231-6.

[6] Violeau D., Leroy A. On the maximum time step in weakly compressible SPH. *J. Comput. Phys.* (2014) **256**:388-415. <hal-00946833>.

[7] Violeau D., Issa R. Numerical modelling of complex turbulent free-surface flows with the SPH method: an overview. *Int. J. Numer. Meth. Fl.* (2007) **53**:277-304. <10.1002/d.1292><hal-01097824>.

[8] Idris, N.A., Sonoda, Y. A Multi-Scale Tsunami Simulations Based on 2D Finite Difference Method and 3D Particle Method with a Virtual Wave Maker. *Kyushu University Doctoral Dissertation* (2017).

[9] Tsuruta N., Khayyer A., Gotoh H. Space Potential Particles to Enhance the Stability of Projection-based Particle Methods. *Int. J. Numer. Meth. Fl.* (2015) DOI: 10.1080/10618562.2015.1006130.

[10] Marrone S., Colagrossi A., Le Touz D., Graziani G. Fast Free-surface Detection and Level-set Function Definition in SPH Solvers. *J. Comput. Phys.* (2010) **229**:3652-3663.

[11] Mattiusi E.M. Escoament Laminar de Fluid Newtonianos Generalizados em Tubos de Seo Transversal Elptica. *Doctoral Dissertation of the Federal Technological University of Paran* (2007).

[12] Martin J., Moyce W. An experimental study of the col-lapse of liquid columns on a rigid horizontal plane. *Philos. Trans. R. Soc. Lond.* (1952) **244**:312-324.

[13] Minussi R.B., Maciel G.F. Numerical experimental com-parison of dam break flows with non-Newtonian fluids. *J. of the Braz. Soc. of Mech. Sci. Eng.* (2012) **XXXIV**:2/167.

[14] Violeau D., Rogers B.D. Smoothed Particle Hydrodynamics (SPH) for Free Surface Flows: Past, Present and Future. *J. Hydraul. Res.* (2016) **54**:1-26.

[15] Tom M.F. et. al. A Numerical Method for Solving Three-dimensional Generalized Newtonian Free Surface Flows. *J. Nonnewton. Fluid Mech.* (2004) **123**:85-103.

[16] Rzadkiewicz, S.A., Mariotti, C. and Heinrich, P. Modelling of submarine landslides and generated water waves. *Phys. Chem. Earth* (2004) **123**:-2, pp.7-12 (1996).

ACCURATE SOLUTION OF THE BOUNDARY INTEGRAL EQUATION IN 2D LAGRANGIAN VORTEX METHOD FOR FLOW SIMULATION AROUND CURVILINEAR AIRFOILS

IRINA A. SOLDATOVA[1], ILIA K. MARCHEVSKY[1,2] AND KSENIIA S. KUZMINA[1,2]

[1] Bauman Moscow State Technical University
105005, 2-nd Baumanskaya st., 5, Moscow, Russia

[2] Ivannikov Institute for System Programming of the Russian Academy of Sciences
109004, Alexander Solzhenitsyn st., 25, Moscow, Russia

i-soldatova@bk.ru, iliamarchevsky@mail.ru, kuz-ksen-serg@yandex.ru

Key words: Vortex Method, Boundary Integral Equation, Curvilinear Panels, Galerkin Approach, High-Order Scheme, Correction Procedure, Analytical Solution

Abstract. The problem of numerical solution of the boundary integral equation is considered for 2D case. Viscous vortex domains (VVD) method is used for flow simulation, so vorticity is generated on the whole surface line of the airfoil, and there are a lot of vortex elements close to the airfoil. The aim of the research is to provide high accuracy of numerical solution of the integral equation; at the same time the computational complexity of the numerical algorithm should be at rather low level. The third-order accuracy numerical scheme, based on piecewise-quadratic solution representation on the curvilinear panels is presented, approximate analytic expressions are obtained for the matrix coefficients.

These schemes work perfect in the case of potential flow simulation, when vorticity is absent and also when vortex elements are placed rather far from the airfoil surface line. A trivial way to the accuracy improvement for the closely located vortices, which consists in extremely fine surface line discretization, leads to unacceptably high numerical complexity of the algorithm. This problem is solved by developing semi-analytical correction procedure which makes it possible to achieve high accuracy at extremely coarse surface line discretization. For example, in the model problem of flow simulation around elliptical airfoil with 2:1 semiaxes ratio only 20 panels are required to achieve the error level less than 1 % for arbitrary position of the vortex element in the flow.

1 Introduction

Despite the fact that vortex methods are being developed for more than 50 years, there are a lot of problems to be solved. The most part of the researchers pay their attention to the problems, connected with vorticity evolution simulation in the flow, whereas vorticity generation on the streamlined surface is much less investigated area.

Even for 2D flows, which are much easier in comparison to three-dimensinal case due to orthogonality of vorticity and velocity vectors, the existing numerical schemes for flow simulation around airfoils sometimes are based on some semi-empirical hypotheses and not fully proven; their accuracy can be rather poor, that requires very detailed discretization of the airfoil surface line. However, even detailed and uniform discretization sometimes doesn't permit to achieve high accuracy. The source of such problems is connected with the properties of the mathematical model — the boundary integral equation (BIE). In well-known modifications of 2D vortex methods the singular BIE is usually considered with Hilbert-type kernel; the corresponding integrals are understood in Cauchy sense, and the numerical procedure of its calculation is non-trivial [1, 2]. Moreover, it is not easy to provide its correct calculation for non-uniform airfoil surface line discretization.

As it is mentioned in [2], it is impossible to develop higher-order numerical scheme without explicit taking into account the curvature of the airfoil surface line. In the present paper the other approach is developed which makes it possible to consider Fredholm-type BIE of the 2-nd kind with bounded (or absolutely integrated) kernel [3, 4, 5]. This allows arbitrary airfoil surface line discretization into panels, taking into account the curvilinearity of the airfoil, developing higher-order numerical schemes according to well-known Galerkin approach. Such schemes work perfect in the case of potential flow simulation, when vorticity in the flow domain is absent or it presents, but located rather far from the airfoil.

A successive attempt was made to derive approximate analytical expressions also for the integrals, arising in the right-hand side coefficients for closely placed vortex elements, at least for piecewise-constant and piecewise-linear numerical schemes [6, 7, 8], but such representation of the numerical solution doesn't permit one to approximate the exact solution with high accuracy in principally if there are vortex elements in the flow domain, placed at the distance smaller than the panel's length to the airfoil surface line. A trivial way to the accuracy improvement which consists in extremely fine surface line discretization, leads to unacceptably high numerical complexity of the numerical algorithm, especially for flow simulation around a system of movable airfoils. In order to solve this problem, semi-analytical approach can be used which makes it possible to achieve high accuracy even for extremely coarse surface line discretization. It consists in explicit addition of the terms, which correspond to the exact solution taking into account the influence of the vortex elements placed close to the panel, which, in turn, is approximately considered as the arc of an osculating circle.

2 The governing equations

Two-dimensional flow of the viscous incompressible media is described by the Navier — Stokes equations

$$\nabla \cdot \boldsymbol{V} = 0, \qquad \frac{\partial \boldsymbol{V}}{\partial t} + (\boldsymbol{V} \cdot \nabla)\boldsymbol{V} = \nu \Delta \boldsymbol{V} - \frac{\nabla p}{\rho}, \tag{1}$$

where $\boldsymbol{V}$ is the flow velocity field; p is the pressure field; $\rho = \mathrm{const}$ and ν are the density and kinematic viscosity coefficient, respectively.

For simplicity we consider the flow around immovable airfoil, however all the results can be applied to more general case of arbitrary movable and deformable airfoil or system of airfoils. The boundary condition on the airfoil surface line K is the no-slip condition:

$$\boldsymbol{V}(\boldsymbol{r}, t) = \boldsymbol{0}, \quad \boldsymbol{r} \in K.$$

The unbounded flow domain is considered, and the perturbation decay conditions are satisfied on infinity:

$$\boldsymbol{V}(\boldsymbol{r}) \to \boldsymbol{V}_\infty, \quad p(\boldsymbol{r}) \to p_\infty, \quad |\boldsymbol{r}| \to \infty,$$

where $\boldsymbol{V}_\infty$ and p_∞ are the velocity and pressure in the incident flow.

The most efficient modification of 2D vortex methods is the Viscous Vortex Domains method (VVD), developed by prof. G.Ya. Dynnikova and described in [10, 11]. The vorticity is a primary computational variable, and the velocity field can be reconstructed in the flow domain by using the Biot — Savart law, which can be considered as a particular case of the Generalized Helmholtz Decomposition (GHD) [3]:

$$\boldsymbol{V}(\boldsymbol{r}) = \boldsymbol{V}_\infty + \frac{1}{2\pi} \oint_K \frac{\boldsymbol{\gamma}(\boldsymbol{\xi}) \times (\boldsymbol{r} - \boldsymbol{\xi})}{|\boldsymbol{r} - \boldsymbol{\xi}|^2} dl_\xi + \frac{1}{2\pi} \int_S \frac{\boldsymbol{\Omega}(\boldsymbol{\xi}) \times (\boldsymbol{r} - \boldsymbol{\xi})}{|\boldsymbol{r} - \boldsymbol{\xi}|^2} dS_\xi, \tag{2}$$

where $\boldsymbol{\Omega} = \Omega \boldsymbol{k}$ is known vorticity distribution in the flow domain S; $\boldsymbol{\gamma}(\boldsymbol{\xi}) = \gamma(\boldsymbol{\xi})\boldsymbol{k}$ is unknown intensity of the vortex sheet on the airfoil surface line K; $\boldsymbol{k}$ is unit vector orthogonal to the flow plane.

The GHD, being considered at the airfoil surface line and taking into account the no-slip boundary condition, makes it possible to write down the BIE with respect to unknown vortex sheet intensity $\boldsymbol{\gamma}(\boldsymbol{\xi})$, $\boldsymbol{\xi} \in K$. It is proven in [3], that in order to solve it, two approaches can be used:

- the equation can be projected onto outer normal direction, that leads to "traditional" numerical schemes of vortex methods with singular BIE of the 1-st kind; the disadvantages of such approach have been mentioned above;

- the equation can be projected onto tangent direction, that allows obtaining the 2-nd kind integral equation:

$$\oint_K \frac{(\boldsymbol{r} - \boldsymbol{\xi}) \cdot \boldsymbol{n}(\boldsymbol{r})}{2\pi|\boldsymbol{r} - \boldsymbol{\xi}|^2} \gamma(\boldsymbol{\xi}) dl_\xi - \frac{\gamma(\boldsymbol{r})}{2} = \underbrace{-\int_S \frac{(\boldsymbol{r} - \boldsymbol{\xi}) \cdot \boldsymbol{n}(\boldsymbol{r})}{2\pi|\boldsymbol{r} - \boldsymbol{\xi}|^2} \Omega(\boldsymbol{\xi}) dS_\xi - \boldsymbol{V}_\infty(\boldsymbol{r}) \cdot \boldsymbol{\tau}(\boldsymbol{r})}_{f(\boldsymbol{r})}, \quad \boldsymbol{r} \in K.$$

$$\tag{3}$$

Here $\boldsymbol{n}(\boldsymbol{r})$ and $\boldsymbol{\tau}(\boldsymbol{r})$ are unit outer normal vector and tangent vector, respectively.

The unique solution of the equation (3) can be selected with help of the additional condition [1]

$$\oint_K \gamma(\boldsymbol{r}) dl_r = \Gamma, \tag{4}$$

where Γ is given value of the velocity circulation along the airfoil.

3   Galerkin approach to the boundary integral equation numerical solution

Due to the boundedness (or integrability in the traditional sense) of the kernel of the BIE (3), the most efficient way to its numerical solution is the use of Galerkin method [4, 5, 12]. Let us briefly describe its main ideas.

1. We consider, that the airfoil surface line is parameterized with the arc length, then the equation (3) takes the form

$$\int_0^L Q(s,\,\sigma)\gamma(\sigma)d\sigma - \frac{\gamma(s)}{2} = f(s), \quad s \in [0,\,L], \tag{5}$$

   where L is total length of the surface line.

2. The surface line is split into N parts, traditionally called "panels", which endings correspond to arc length parameter values s_i, $i = 0,\,\ldots,\,N$, where $s_0 = 0$, $s_N = L$; the i-th panel corresponds to s in range $[s_{i-1},\,s_i]$.

3. The basis functions family $\{\phi_i^q(s)\}$, $i = 1,\,\ldots,\,N$, $q = 0,\,\ldots,\,m$ is introduced; we assume that the functions $\phi_i^q(s)$ can have non-zero values only at the i-th panel. The projection functions family $\{\psi_i^p(s)\}$ we choose coincide with the basis one.

4. The approximate solution has the following form:

$$\gamma(s) = \sum_{i=1}^N \sum_{q=0}^m \gamma_i^q \phi_i^q(s), \tag{6}$$

   where the coefficients γ_i^q are unknown and can be found from the orthogonality condition of the equation (3) residual to the projection functions:

$$\sum_{j=1}^N \sum_{q=0}^m \gamma_j^q \int_{s_{i-1}}^{s_i} \psi_i^p(s)ds \int_{s_{j-1}}^{s_j} Q(s,\,\sigma)\phi_j^q(\sigma)d\sigma - \frac{1}{2}\sum_{q=0}^m \gamma_i^q \int_{s_{i-1}}^{s_i} \psi_i^p(s)\phi_i^q(s)ds =$$
$$= \int_{s_{i-1}}^{s_i} \psi_i^p(s)f(s)ds, \quad i = 1,\,\ldots,\,N, \quad p = 0,\,\ldots,\,m. \tag{7}$$

The additional condition (4) now has the following form:

$$\sum_{i=1}^N \sum_{p=0}^m \gamma_i^p \int_{s_{i-1}}^{s_i} \phi_i^p(s)ds = \Gamma. \tag{8}$$

Thus, the initial BIE (3) and the unique solution condition (4) are discretized and represented as linear system (7)-(8). The main difficulty is the calculation of its coefficients.

This problem is considered in [4, 5, 7, 8] for rectilinear panels, where piecewise-constant and piecewise-linear basis functions have been used. The first and second order of accuracy

numerical schemes are developed. However they are suitable only for close to uniform airfoil discretization, and it is impossible to raise the accuracy by introducing quadratic basis functions. In order to do it, we should take into account explicitly the curvature of the airfoil. It can't be done exactly; in [6, 8] the original technique is developed for calculation of the matrix coefficients for curvilinear panels, but only for piecewise-constant and piecewise-linear basis functions. Those approximate formulae are obtained as Taylor expansions with respect to the panel length L_i, and the only terms, proportional to L_i^3 are taken into account.

Now we consider 3 families of the basis functions:

- piecewise-constant and piecewise-linear, as in [5, 8]

$$
\phi_i^0(s) = \begin{cases} 1, & s \in [s_{i-1}, s_i], \\ 0, & s \notin [s_{i-1}, s_i]; \end{cases} \qquad
\phi_i^1(s) = \begin{cases} \dfrac{s(\boldsymbol{r}) - s(\boldsymbol{c}_i)}{L_i}, & s \in [s_{i-1}, s_i], \\ 0, & s \notin [s_{i-1}, s_i]; \end{cases}
$$

- piecewise-quadratic

$$
\phi_i^2(s) = \begin{cases} 4\left(\dfrac{s(\boldsymbol{r}) - s(\boldsymbol{c}_i)}{L_i}\right)^2 - \dfrac{1}{3}, & s \in [s_{i-1}, s_i], \\ 0, & s \notin [s_{i-1}, s_i]. \end{cases}
$$

Here L_i is the length of the i-th panel, $\boldsymbol{c}_i$ is its center. Note, that the introduced in such a way basis functions are orthogonal.

The linear system (7)-(8) now has the following matrix form

$$
\begin{pmatrix} A^{00} + D^{00} & A^{01} & A^{02} & I \\ A^{10} & A^{11} + D^{11} & A^{12} & O \\ A^{20} & A^{21} & A^{22} + D^{22} & O \\ L^0 & O & O & 0 \end{pmatrix}
\begin{pmatrix} \gamma^0 \\ \gamma^1 \\ \gamma^2 \\ R \end{pmatrix} =
\begin{pmatrix} b^0 \\ b^1 \\ b^2 \\ \Gamma \end{pmatrix},
$$

where A^{pq} are matrix blocks of $N \times N$ size; D^{pp} are diagonal matrices; b^p is the right-hand side vector parts; $\gamma^p = (\gamma_1^p, \dots, \gamma_N^p)^T$ is vector of unknown coefficients, $p = 0, 1, 2$; I and O are the vectors/raws consist of units and zeros, respectively, L^0 is a raw consists of curvilinear panel lengthes; R is regularization variable [1].

The matrix and right-hand side coefficients are calculated as the following integrals:

$$
A_{ij}^{pq} = \int_{K_i} \phi_i^p(s)\,ds \left(\int_{K_j} Q(s, \sigma)\phi_j^q(\sigma)\,d\sigma \right), \quad
D_{ii}^{pp} = -\frac{1}{2}\int_{K_i} \phi_i^p(s)\phi_i^p(s)\,ds,
$$

$$
b_i^p = \int_{K_i} \phi_i^p(s)f(s)\,ds, \quad i, j = 1, \dots, N, \quad p, q = 0, 1, 2. \tag{9}
$$

The diagonal coefficients D_{ii}^{pp} can be calculated exactly:

$$
D_{ii}^{00} = -\frac{L_i}{2}, \quad D_{ii}^{11} = -\frac{L_i}{24}, \quad D_{ii}^{11} = -\frac{2L_i}{45}.
$$

For the A_{ij}^{pq} coefficients approximate calculation Taylor expansions technique similar to [6] is used, but now term of order L_i^4 also should be taken into account.

We denote the "signed curvature" as $\varkappa(s) = (\boldsymbol{r}'(s) \times \boldsymbol{r}''(s)) \cdot \boldsymbol{k}$, where $\varkappa > 0$ for the convex parts of the airfoil surface line; the formulae, similar to Serret — Frenet ones can be easily obtained for the derivatives of the vectors $\boldsymbol{n}(s)$ and $\boldsymbol{\tau}(s)$.

For the diagonal components of the matrices A_{ii}^{pq}, $p, q = 0, 1, 2$ we obtain

$$A_{ii}^{00} \approx \frac{36 L_i^2 \varkappa_i + L_i^4 \varkappa_i''}{144\pi}, \quad A_{ii}^{01} \approx \frac{\varkappa_i' L_i^3}{144\pi}, \quad A_{ii}^{02} \approx \frac{\varkappa_i'' L_i^4}{2160\pi},$$

$$A_{ii}^{10} \approx \frac{\varkappa_i' L_i^3}{72\pi}, \quad A_{ii}^{11} \approx \frac{\varkappa_i'' L_i^4}{3456\pi}, \quad A_{ii}^{12} \approx 0, \quad A_{ii}^{20} \approx \frac{\varkappa_i'' L_i^4}{720\pi}, \quad A_{ii}^{21} \approx 0, \quad A_{ii}^{22} \approx 0.$$

Here $\varkappa_i$ is the signed curvature at the center of the i-th panel, the prime mark denotes the derivative with respect to the arc length.

For non-diagonal coefficients, which calculation requires integration over different panels ($i \neq j$), we introduce auxiliary vector $\boldsymbol{d}_{ij} = \boldsymbol{c}_i - \boldsymbol{c}_j$, which connects centers of the corresponding panels, unit tangent vector $\boldsymbol{\tau}_i$ at the center of the i-th panel, and the angles α and β between the vectors $\boldsymbol{\tau}_i$, $\boldsymbol{\tau}_j$ and $\boldsymbol{d}_{ij}$, respectively (Fig. 1).
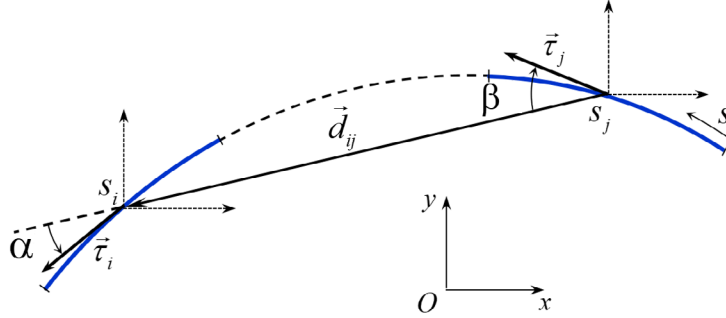
Figure 1: Two curvilinear panels, vector $\boldsymbol{d}_{ij}$ and the angles α and β

The resulting formulae have the following form:

$$A_{ij}^{00} \approx \frac{L_i L_j}{48\pi d^3} \Big[2\big(L_j^2 \sin(\alpha + 2\beta) + 12 d^2 \sin\alpha + L_i^2 \sin 3\alpha\big) +$$

$$+ d\big(L_j^2 \varkappa_j \cos(\alpha + \beta) + L_i^2\big(d\varkappa_i' \cos\alpha - \varkappa_i(3\cos 2\alpha + d\varkappa_i \sin\alpha)\big)\big)\Big],$$

$$A_{ij}^{01} \approx \frac{L_i L_j^2 \sin(\alpha + \beta)}{24\pi d^2}, \quad A_{ij}^{02} \approx \frac{L_i L_j^3 \big(d\varkappa_j \cos(\alpha + \beta) + 2\sin(\alpha + 2\beta)\big)}{180\pi d^3},$$

$$A_{ij}^{10} \approx \frac{L_i^2 L_j \cos\alpha \big(d\varkappa_i - 2\sin\alpha\big)}{24\pi d^2}, \quad A_{ij}^{11} \approx \frac{L_i^2 L_j^2 \big(d\varkappa_i \cos(\alpha + \beta) - 2\sin(2\alpha + \beta)\big)}{288\pi d^3},$$

$$A_{ij}^{20} \approx \frac{L_i^3 L_j}{180\pi d^3} \Big[2\sin 3\alpha - d\big(\varkappa_i(3\cos 2\alpha + d\varkappa_i \sin\alpha) - d\varkappa_i' \cos\alpha\big)\Big],$$

$$A_{ij}^{12} \approx 0, \quad A_{ij}^{21} \approx 0, \quad A_{ij}^{22} \approx 0.$$

Here $\varkappa_i$ is the curvature at the center of the i-th panel, the prime mark denotes the derivative with respect to the arc length; d is the length of the vector $\boldsymbol{d}_{ij}$.

In case of smooth airfoil the following approximate formulae can be used for the matrix coefficients which calculation requires integration over the neighboring panels ($|i-j| = 1$):

$$A_{ij}^{00} \approx \frac{L_i L_j}{288\pi}\Big[72\varkappa_{ij} \pm 12\big(L_j - 2L_i\big)\varkappa'_{ij} + \big(6L_i^2 - 3L_i L_j + 2L_j^2\big)\varkappa''_{ij}\Big],$$

$$A_{ij}^{01} \approx \frac{L_i L_j^2\big(4\varkappa'_{ij} \pm \big(L_j - L_i\big)\varkappa''_{ij}\big)}{576\pi}, \qquad A_{ij}^{10} \approx \frac{L_i^2 L_j\big(8\varkappa'_{ij} \pm \big(L_j - 3L_i\big)\varkappa''_{ij}\big)}{576\pi},$$

$$A_{ij}^{02} \approx \frac{L_i L_j^3 \varkappa''_{ij}}{2160\pi}, \qquad A_{ij}^{11} \approx \frac{L_i^2 L_j^2 \varkappa''_{ij}}{3456\pi}, \qquad A_{ij}^{20} \approx \frac{L_i^3 L_j \varkappa''_{ij}}{720\pi}, \qquad A_{ij}^{12} \approx A_{ij}^{21} \approx A_{ij}^{22} \approx 0.$$

Here $\varkappa_{ij}$ denotes the signed curvature of the airfoil at the common point of the neighboring panels; the prime, as earlier, means the derivative with respect to the arc length; sign "+" is used for $j = i + 1$, and "−" for $j = i - 1$.

Note, that in case of the airfoil with sharp edges [9], the formulae for rectilinear panels derived in [7, 8] are more suitable for the matrix coefficients corresponding to the panels which are adjacent to the angle points. Those formulae don't permit to take into account the curvilinearity of the panels, however, they are exact for rectilinear panels.

Let us consider firstly the potential flow when there is no vorticity in the flow domain and the right-hand side of the equation (5) has form $f(s) = -\boldsymbol{V}_\infty \cdot \boldsymbol{\tau}(s)$. In this case the right-hand side components of (3) can be calculated as following:

$$b_i^0 \approx -(\boldsymbol{V}_\infty \cdot \boldsymbol{\tau}_i)L_i + \frac{1}{24}\left((\boldsymbol{V}_\infty \cdot \boldsymbol{n}_i)\varkappa'_i + (\boldsymbol{V}_\infty \cdot \boldsymbol{\tau}_i)\varkappa_i^2\right)L_i^3,$$

$$b_i^1 \approx \frac{1}{12}(\boldsymbol{V}_\infty \cdot \boldsymbol{n}_i)\varkappa_i L_i^2, \qquad b_i^2 \approx \frac{1}{90}\left((\boldsymbol{V}_\infty \cdot \boldsymbol{n}_i)\varkappa'_i + (\boldsymbol{V}_\infty \cdot \boldsymbol{\tau}_i)\varkappa_i^2\right)L_i^3.$$

The described approach provides the 1st, 2nd and 3rd order of accuracy for the piecewise-constant, linear and quadratic solution representation, respectively. In the Table 1 the number of panels is shown, which is required to achieve the accuracy 10^{-3} (for unit incident flow velocity, angle of incidence $\pi/6$).

Table 1: Number of panels required to achieve the accuracy 10^{-3} for elliptical airfoils

	rectilinear panels		curvilinear panels	
	uniform discretization			
semiaxes ratio	piecewise-constant	piecewise-linear	piecewise-linear	piecewise-quadratic
2:1	9 600	244	136	52
5:1	13 400	760	360	196
10:1	24 000	2 000	900	640
	non-uniform discretization			
2:1	7 800	132	104	36
5:1	8 700	152	144	60
10:1	9 000	186	184	80

Note, that it seems to be reasonable to use non-uniform discretization of the airfoil (length of the panels are inversely proportional to the square root of the curvature) since it permits to reduce number of panels significantly; usage of the piecewise-quadratic solution representation for curvilinear panels makes it possible to reduce additionally number of panels by 2.5–3 times.

4 Vortex elements influence accounting by numerical solution correction

In practice there are a lot of vortex elements in the flow, which simulate vorticity distribution. However, due to the linearity of the governing integral equation (5), the influences of separate vortices can be taken into account independently, so here we consider a model problem, when there is only one vortex element. In this case the only difference in numerical scheme is the form of the right-hand side term $f(s)$, for which the corresponding coefficients b_i^p of the linear system can be calculated either numerically (e.g., by using Gaussian quadrature formulae), of approximately analytically [6]. In the Fig. 2, the results are shown for the cases, when the vortex element is placed at the distance, which corresponds to 10 %, 25 %, 50 % and 100 % of the panel length (uniform discretization of the elliptical airfoil with 2:1 semiaxes ratio, split into 20 panels is considered).
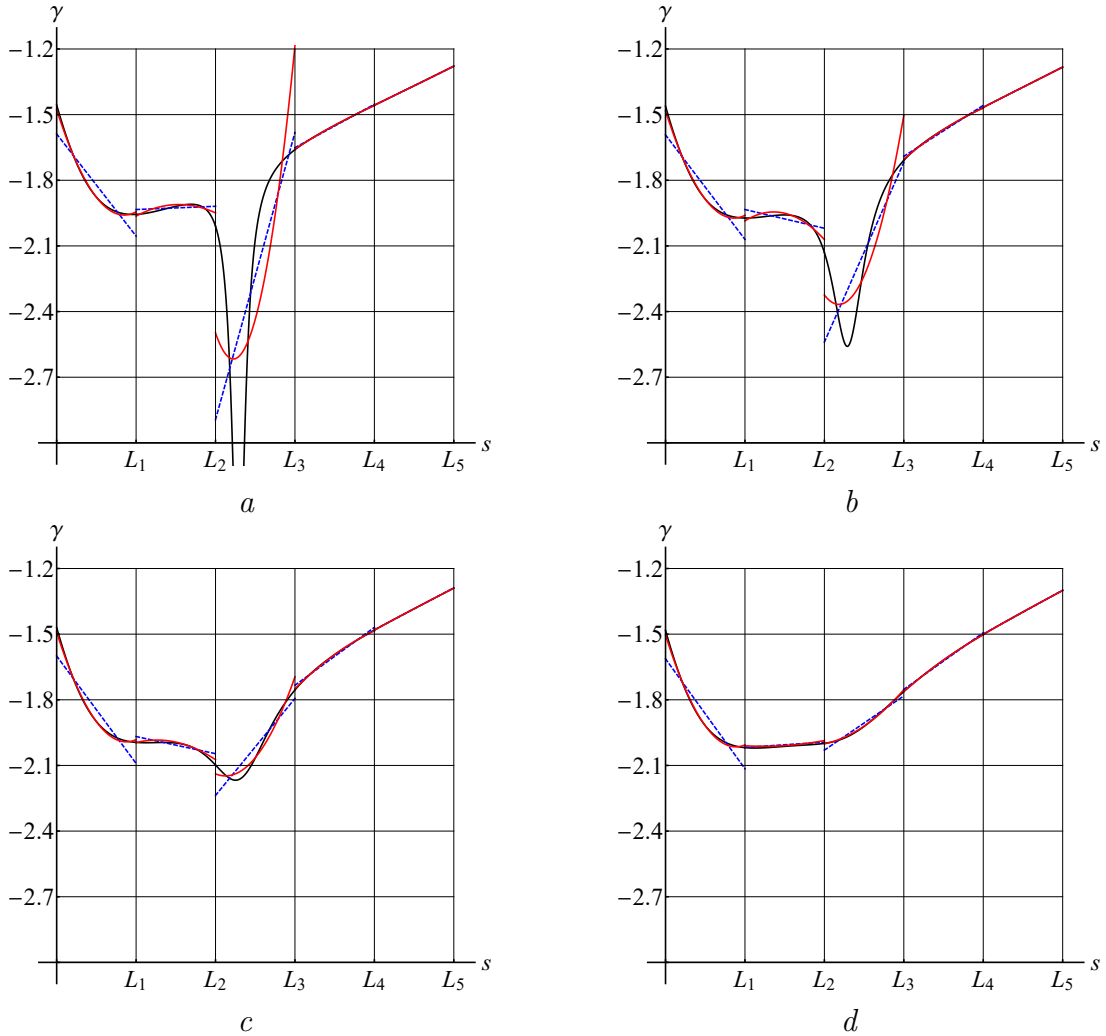
Figure 2: Exact solution (black solid line), piecewise-linear (blue dashed) and piecewise-quadratic (red solid) solutions for the vortex sheet intensity in presence of the vortex at the distance of 10 %, 25 %, 50 % and 100 % of panel size (a, b, c, d, respectively)

It is seen, that it is possible to obtain more or less correct numerical solution only for vortex elements, placed rather far from the airfoil surface line, i.e., at the distance which is not smaller than 50 % of the panel size. In practice, however, the typical distance from the vortex elements, which simulate the boundary layer, to the airfoil surface line has order of $10^{-6} \ldots 10^{-5}$ (with respect to the chord). It means, that the required number of panels should have order of 10^5; for smaller number of panels it is impossible to reconstruct it correctly.

However, this issue can be overcome by implementing the correction procedure.

Note that for the vortex placed at the arbitrary point of the flow domain, the exact solution for the vortex sheet intensity is known for circular airfoil. It has the following form [4]

$$\tilde{\gamma}(s) = \Gamma_g \left(\frac{\boldsymbol{r}(s) - \boldsymbol{r}_g}{2\pi |\boldsymbol{r}(s) - \boldsymbol{r}_g|^2} - \frac{\boldsymbol{r}(s) - \boldsymbol{r}^m}{2\pi |\boldsymbol{r}(s) - \boldsymbol{r}^m|^2} + \frac{\boldsymbol{r}(s) - \boldsymbol{r}^c}{2\pi |\boldsymbol{r}(s) - \boldsymbol{r}^c|^2} \right) \cdot \boldsymbol{n}(s), \qquad (10)$$

where $\boldsymbol{r}(s)$ is the point on the circle of radius R, $\boldsymbol{n}(s)$ in outer unit normal vector for the circle, $\boldsymbol{r}_g$ is position of the vortex, $\boldsymbol{r}^c$ is center of the circle, r^m is the position of the mirrored vortex,

$$\boldsymbol{r}_m = \boldsymbol{r}_c + \frac{R^2}{|\boldsymbol{r}_g - \boldsymbol{r}^c|^2}.$$

Now for the vortex, placed in neighborhood of the k-th panel we suppose that this panel can be approximately replaced with the osculating circle of radius $R_k = \varkappa_k^{-1}$, then we are able to take into account the influence of this vortex semi-analytically by explicit introducing to the numerical solution the term, similar to (10):

$$\gamma(s) = \sum_{i=1}^{N} \sum_{q=0}^{m} \gamma_i^q \varphi_i^q(s) + \sum_{k=k_b}^{k_f} \tilde{\gamma}_k(s) \varphi_k^0(s). \qquad (11)$$

Here

$$\tilde{\gamma}_k(s) = \Gamma_g \left(\frac{\boldsymbol{r}(s) - \boldsymbol{r}_g}{2\pi |\boldsymbol{r}(s) - \boldsymbol{r}_g|^2} - \frac{\boldsymbol{r}(s) - \boldsymbol{r}_k^m}{2\pi |\boldsymbol{r}(s) - \boldsymbol{r}_k^m|^2} + \frac{\boldsymbol{r}(s) - \boldsymbol{r}_k^c}{2\pi |\boldsymbol{r}(s) - \boldsymbol{r}_k^c|^2} \right) \cdot \boldsymbol{n}_k(s)$$

is additional term, which determines the influence of the system of mirrored vortices with respect to the k-th panel, $\boldsymbol{r}_k^m$ is the position of the vortex, mirrored with respect to the k-th panel, $\boldsymbol{r}_k^c$ is the center of the osculating circle, $\boldsymbol{n}_k(s)$ unit outer normal vector for the osculating circle; $k_b \ldots k_f$ is the range of panel numbers, for which the correction procedure is implemented. It can be easily shown, that the expression for $\tilde{\gamma}_k(s)$ can be simplified:

$$\tilde{\gamma}_k(s) = \Gamma_g \frac{\left(\boldsymbol{r}(s) - \boldsymbol{r}_g\right) \cdot \boldsymbol{n}_k(s)}{\pi |\boldsymbol{r}(s) - \boldsymbol{r}_g|^2}.$$

For such solution representation, the above described Galerkin approach remains applicable, but instead of the system (7) now we obtain the following linear system

$$\sum_{j=1}^{N}\sum_{q=0}^{m}\gamma_j^q \int_{s_{i-1}}^{s_i}\psi_i^p(s)ds \int_{s_{j-1}}^{s_j}Q(s,\sigma)\phi_j^q(\sigma)d\sigma - \frac{1}{2}\sum_{q=0}^{m}\gamma_i^q\int_{s_{i-1}}^{s_i}\psi_i^p(s)\phi_i^q(s)ds =$$

$$= -\sum_{\substack{k=k_b,\\k\neq i}}^{k_f}\int_{s_{i-1}}^{s_i}\psi_i^p(s)ds\int_{s_{k-1}}^{s_k}Q(s,\sigma)\tilde\gamma_k(\sigma)d\sigma + \sum_{\substack{k=k_b,\\k\neq i}}^{k_f}\int_{s_{i-1}}^{s_i}\psi_i^p(s)f_g(s)ds +$$

$$+ \int_{s_{i-1}}^{s_i}\psi_i^p(s)f_v(s)ds, \quad i=1,\ldots,N, \quad p=0,\ldots,m, \quad (12)$$

where it is denoted

$$f_v(s) = \boldsymbol{V}_\infty\cdot\boldsymbol{\tau}(s), \quad f_g(s) = \frac{\Gamma_g\big(\boldsymbol{r}(s)-\boldsymbol{r}_g\big)\cdot\boldsymbol{n}(s)}{2\pi\big|\boldsymbol{r}(s)-\boldsymbol{r}_g\big|^2}.$$

The system (12) can be written down in the matrix form:

$$\begin{pmatrix} A^{00}+D^{00} & A^{01} & A^{02} & I \\ A^{10} & A^{11}+D^{11} & A^{12} & O \\ A^{20} & A^{21} & A^{22}+D^{22} & O \\ L^0 & O & O & 0 \end{pmatrix}\begin{pmatrix}\gamma^0\\\gamma^1\\\gamma^2\\R\end{pmatrix} = \begin{pmatrix}b_v^0+b_g^0+b_\gamma^0\\b_v^1+b_g^1+b_\gamma^1\\b_v^2+b_g^2+b_\gamma^2\\\Gamma_w\end{pmatrix},$$

where the left-hand side remains the same as earlier (without correction), the coefficients b_v^p are connected with the incident flow influence, b_g^p — with influence of the vortices in the flow domain, which is taken account straightforwardly without correction; b_γ^p — additional terms, arising due to the correction procedure:

$$b_{v,i}^p = \int_{s_{i-1}}^{s_i}\psi_i^p(s)f_v(s)ds, \quad b_{g,i}^p = \sum_{\substack{k=k_b,\\k\neq i}}^{k_f}\int_{s_{i-1}}^{s_i}\psi_i^p(s)f_g(s)ds,$$

$$b_{\gamma,i}^p = -\sum_{\substack{k=k_b,\\k\neq i}}^{k_f}\int_{s_{i-1}}^{s_i}\psi_i^p(s)ds\int_{s_{k-1}}^{s_k}Q(s,\sigma)\tilde\gamma_k(\sigma)d\sigma, \quad i,j=1,\ldots,N, \quad p,q=0,1,2.$$

For the last component of the right-hand side vector the following expression is obtained:

$$\Gamma_w = \Gamma - \sum_{k=k_b}^{k_f}\int_{s_{k-1}}^{s_k}\tilde\gamma_k ds.$$

For computation of all the integrals, arising in the right-hand side, Gaussian quadratures can be used, as well as approximate analytical expressions.

In the Fig. 3 the results of computations for the model problem, considered in the previous section, but with implemented correction procedure, are shown. The correction is performed not only for the panel, closest to the vortex, but also for the neighboring panels on both sides. Note, that the correction procedure preserves the accuracy order of the initial scheme. Moreover, it provides the more accurate results, the closer vortex element is located to the airfoil. It seems reasonable to use correction technique for the vortices placed at the distance of not more, than 75 % of the panel length.
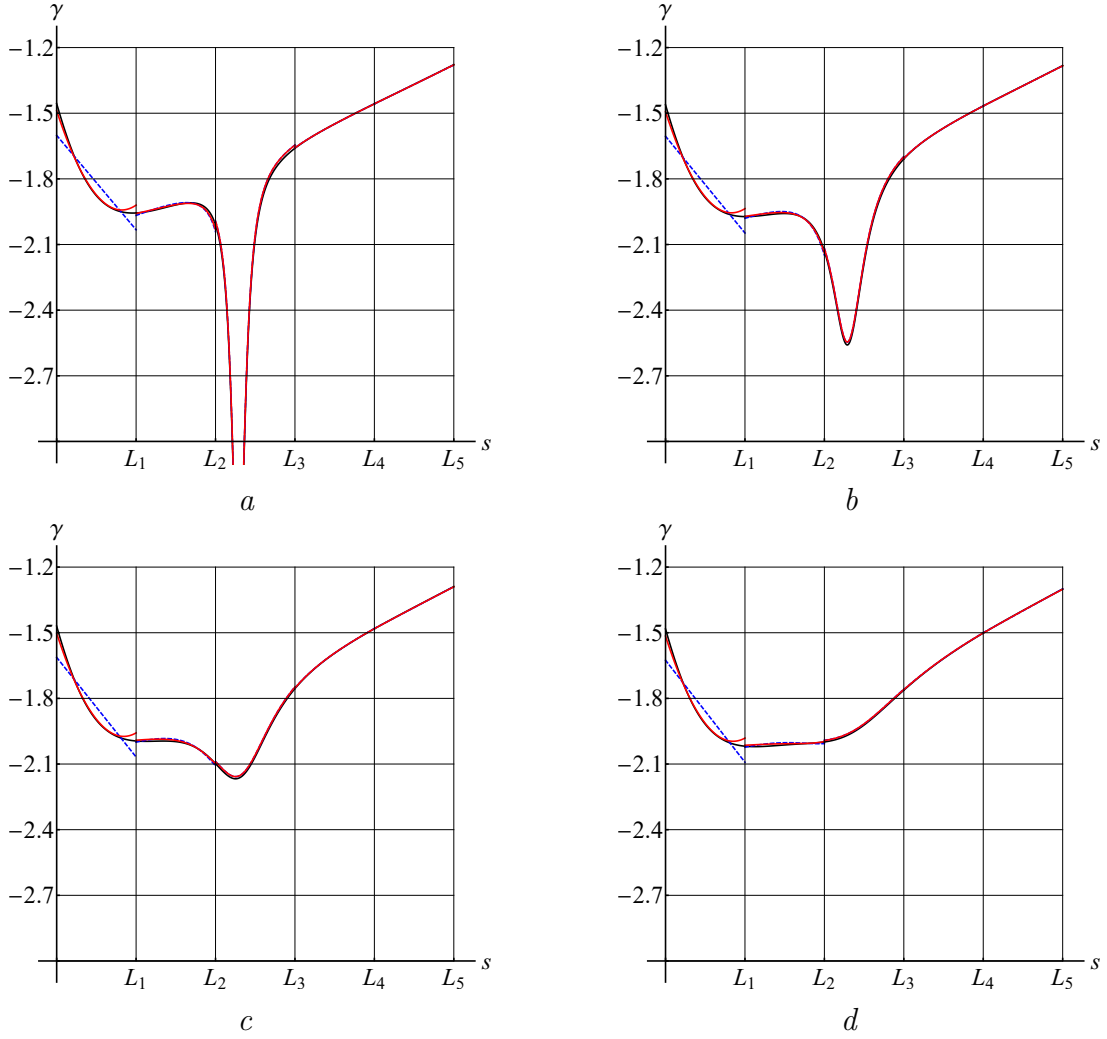
Figure 3: Exact solution (black solid line), piecewise-linear (blue dashed) and piecewise-quadratic (red solid) solutions for the vortex sheet intensity in presence of the vortex at the distance of 10 %, 25 %, 50 % and 100 % of panel size (*a*, *b*, *c*, *d*, respectively) after implementation of the correction procedure

5   CONCLUSIONS

In the present paper the numerical scheme of the third order of accuracy is developed by using the Galerkin approach, which takes into account the curvature of the surface line of the airfoil and piecewise-quadratic solution representation. This scheme makes it possible to deal with non-uniform discretization, moreover, considering panel lengths inverse proportional to the square root of the curvature permits to reduce number of panels significantly.

In order to take into account the influence of the vortex wake, simulated with separate vortices, the correction procedure is developed, which permits to consider arbitrary panel length with correct representation of the influence of closely placed vortices. Numerical experiments prove the properties of the developed scheme and the correction procedure.

Acknowledgement

REFERENCES

[1] Lifanov, I.K. *Singular Integral Equations and Discrete Vortices.* VSP, (1996).

[2] Cottet, G.-H. and Koumoutsakos, P.D. *Vortex methods: Theory and practice.* CUP, (2000).

[3] Kempka, S.N., Glass, M.W., Peery, J.S., Strickland, J.H. and Ingber, M.S. Accuracy considerations for implementing velocity boundary conditions in vorticity formulations. *SANDIA report.* (1996) **SAND96-0583, UC-700**.

[4] Kuzmina, K.S., Marchevskii, I.K. and Moreva, V.S. Vortex Sheet Intensity Computation in Incompressible Flow Simulation Around an Airfoil by Using Vortex Methods. *Mathematical Models and Computer Simulations.* (2018) **10(3)**:276–287.

[5] Kuzmina, K.S., Marchevskii, I.K., Moreva, V.S. and Ryatina, E.P. Numerical scheme of the second order of accuracy for vortex methods for incompressible flow simulation around airfoils. *Russian Aeronautics.* (2017) **60(3)**:398–405.

[6] Marchevsky, I., Kuzmina, K. and Soldatova, I. Improved algorithm of boundary integral equation approximation in 2D vortex method for flow simulation around curvilinear airfoil. *AIP Conference Proceedings.* (2018) **2027**:040048.

[7] Kuzmina, K.S., Marchevsky, I.K. and Ryatina, E.P. Exact analytical formulae for linearly distributed vortex and source sheets influence computation in 2D vortex methods. *Journal of Physics: Conference Series.* (2017) **918(1)**:012013.

[8] Kuzmina, K.S. and Marchevskii, I.K. On the calculation of the vortex sheet and point vortices influence at approximate solution of the boundary integral equation in two-dimensional vortex methods of computational hydrodynamics. *Fluid Dynamics.* (2019) **54(7)**. In press.

[9] Kuzmina, K.S., Marchevsky, I.K. and Moreva, V.S. On vortex sheet intensity computation for airfoils with angle point in vortex methods. *International Journal of Mechanical Engineering and Technology*, (2018) *9(2)*:799-809.

[10] Dynnikova, G.Ya. The Lagrangian approach to solving the time-dependent Navier-Stokes equations. *Doklady Physics.* (2004) **49(11)**:648–652.

[11] Andronov, P.R., Grigorenko, D.A., Guvernyuk, S.V. and Dynnikova, G.Ya. Numerical simulation of plate autorotation in a viscous fluid flow. *Fluid Dynamics.* (2007) **42(5)**:719–731.

[12] Ingber, M.S., Morrow, C.W. and Kempka, S.N. A Galerkin implementation of the generalized Helmholtz decomposition for use in vorticity formulations. *WIT Transactions on Modelling and Simulation.* (1999) **25**:397–410.

COMPARISON OF THE FINITE VOLUME METHOD WITH LAGRANGIAN VORTEX METHOD FOR 2D FLOW SIMULATION AROUND AIRFOILS AT INTERMEDIATE REYNOLDS NUMBER

KSENIIA S. KUZMINA[1,2], ILIA K. MARCHEVSKY[1,2] AND EVGENIYA P. RYATINA[1,2]

[1] Bauman Moscow State Technical University
105005, 2-nd Baumanskaya st., 5, Moscow, Russia

[2] Ivannikov Institute for System Programming of the Russian Academy of Sciences
109004, Alexander Solzhenitsyn st., 25, Moscow, Russia

e-mail: kuz-ksen-serg@yandex.ru

Key words: viscous vortex domain method, 2D flow, incompressible flow, open-source code, OpenFOAM, VM2D, backward-facing step

Abstract. The paper is dedicated to the numerical simulation of two-dimensional viscous incompressible flow. The Viscous Vortex Domains method is considered, which is one of the modifications of Lagrangian vortex methods. This method is implemented in the open-source VM2D code, which developes by the authors. Model problems of external and internal flow simulation are considered for VM2D testing. For the problem of the flow simulation around two closely spaced circular cylinders, VM2D is compared to OpenFOAM in terms of computational efficiency. As the internal flow problem the flow in a channel with a backward-facing step is considered. For both problems, the results obtained in VM2D are in good agreement with the results of other researchers.

1 INTRODUCTION

Today in computational hydrodynamics, different mesh methods are widely used, such as the finite difference method, the finite volume method and, rarely, the finite element method. There are a large number of their modifications; many of them are implemented in widely used software packages, both commercial and free: `Fluent`, `OpenFOAM`, `STAR-CCM`, `Flow Vision` and others. As a result, researchers and engineers have efficient tools for numerical simulation both in fundamental and industrial applications.

However, in recent decades meshless CFD methods are also gaining popularity. This class includes vortex methods, where vorticity is the primary calculated variable. The range of application of vortex methods is limited by incompressible flows; however, for such problems they can significantly exceed the efficiency of mesh methods. They are especially efficient for external flows simulation, since in this case the flow region with non-zero

vorticity is relatively small in comparison to the computational domain usually considered in mesh methods. The advantages of meshless methods are even more pronounced when simulating flows around movable/deformable bodies, due to no need of mesh deformation or reconstruction.

There are many modifications of vortex methods. The key difference between them is the approach to the viscous forces modeling. From this point of view, stochastic and deterministic algorithms can be distinguished. The stochastic approach, for example, the random walk method (called also Random Vortex Method) [1] was one of the first methods of taking viscosity effects into account. According to it, the diffusion of vorticity is simulated by a stochastic process. There are two deterministic approaches: the methods of circulations redistribution and the diffusive velocity methods. Among the circulations redistribution method, the Particle Strength Exchange method [2] and Vorticity Redistribution Method [3] can be pointed out. PSE is a quite popular method, and there are various two- and three-dimensional implementations [4, 5, 6, 7, 8].

In the present paper, only two dimensional flows are considered, and deterministic approach is used, called the Viscous Vortex Domains method (VVD) [9, 10], which is pure Lagrangian and belongs to a class of diffusive velocity methods. According to this approach, the vortex particles retain their circulations and move according to the velocity field, which is a superposition of the convective and diffusive velocities.

Despite the fact that there are number of scientific groups involved in vortex methods development, today there is a very limited number of available codes implementing vortex methods. Mostly, such implementations are in-house codes, which are used by a narrow circle of specialists. It is easy to found the `vvflow` code [11], implemented by scientists led by prof. G.Ya. Dynnikova in Moscow State University. The `vvflow` can be downloaded for free as executable (binary) application; the source code is not available, so it is impossible to study it and introduce any modifications.

This paper discusses the authors implementation of the VVD method — the `VM2D` code, which is open source and available on the `GitHub` platform [12]. The `VM2D` code is cross-platform and it has a modular structure. Parallel algorithms in `VM2D` are implemented using OpenMP, MPI and Nvidia CUDA technologies, that allows performing computations on multiprocessor systems with classical (CPU) architecture and using GPU accelerators. In `VM2D` it is possible to simulate incompressible flows around airfoil or system of airfoils, including transient regimes, to calculate hydrodynamic loads acting the airfoils, to solve fluid-structure interaction (FSI) problems when the airfoils move under the hydrodynamic loads. It is also possible to simulate internal flows.

The aim of this paper is to verify the `VM2D` code on number of model problems with intermediate Reynolds numbers ($\text{Re} \sim 10^2 \dots 10^3$) and to compare its efficiency with the `OpenFOAM` code, which implements the finite volume method. The structure of the paper is as follows. The second section briefly describes the main ideas of the VVD method and some specific aspects of its numerical implementation in the `VM2D` code. In the third section, a test problem of the flow simulation around two closely spaced circular airfoils of different diameters is considered. In [13] the results are given for hydrodynamic loads and the Strouhal number, obtained experimentally and numerically using the finite element

method. In the last section, the verification of the `VM2D` code for the simulation of internal flows is performed. For this purpose, the problem of flow simulation in a channel with a backward-facing step [14] is considered.

2 VISCOUS VORTEX DOMAINS METHOD AND VM2D CODE

In the VVD method, as in other vortex methods, the vorticity $\vec{\Omega}(\vec{r}, t) = \mathrm{curl}\vec{V}(\vec{r}, t)$ is the primary calculated variable. Its distribution in the flow domain is represented by a set of vortex elements, each of them is characterized by its circulation Γ_i and position $\vec{r}_i$. New vorticity, i.e., new vortex elements is generated only on the airfoil surface line (or on the outer boundaries in the case of internal flows). Further in the description of the algorithm only external flows and immovable airfoils are discussed, but all ideas and numerical schemes can be easily transferred to more general cases without significant modifications.

A time-step of the VVD algorithm implemented in the `VM2D` code can be divided into 4 blocks:

- vorticity generation on the airfoil surface line,

- vorticity transfer from the airfoil surface line to the flow area,

- vortex wake evolution simulation,

- pressure reconstruction and hydrodynamic loads calculation (if necessary).

1. *Vorticity generation.* The vorticity which is generated during a time-step period is simulated by a thin vortex sheet at the airfoil surface line K. Its intensity $\gamma(\vec{r})$ can be found from the no-slip boundary condition, which can be written down in the form of a boundary integral equation [16]

$$\oint_K \frac{\vec{k} \times (\vec{r} - \vec{\xi})}{2\pi|\vec{r} - \vec{\xi}|^2} \gamma(\vec{\xi}) dl_\xi - \frac{\gamma(\vec{r})}{2}\vec{\tau}(\vec{r}) = \vec{f}(\vec{r}), \quad \vec{r} \in K, \tag{1}$$

where $\vec{k}$ is unit vector orthogonal to the flow plane, $\vec{\tau}(\vec{r})$ is tangent unit vector, $\vec{f}(\vec{r})$ is a known function depending on the incident flow velocity, the airfoil surface line velocity and vorticity distribution in the flow. There are two possible ways to satisfy vector integral equation (1): by projecting it onto the normal or tangential direction on the airfoil surface line.

In the original VVD method, the projection onto the normal direction is used [9]; however it is possible to achieve higher accuracy by projecting (1) onto tangent direction [17, 18]. In the `VM2D` code "tangent" approach is implemented and the following boundary integral equation is solved:

$$\oint_K \frac{(\vec{r} - \vec{\xi}) \cdot \vec{n}(\vec{\xi})}{2\pi|\vec{r} - \vec{\xi}|^2} \gamma(\vec{\xi}) dl_\xi - \frac{\gamma(\vec{r})}{2} = \vec{f}(\vec{r}) \cdot \tau(\vec{r}), \quad \vec{r} \in K.$$

There are several numerical schemes for the numerical solution of this equation based on the Galerkin method and various approaches to airfoil surface line discretization [17, 18, 19]. In this paper, one of the simplest schemes is used, based on discretization of the airfoil surface line by a polygon and a piecewise-constant representation of the solution [17].

2. To *transfer the vorticity from the airfoil surface line to the flow domain* the distributed vorticity, which forms the vortex sheet at the airfoil surface line, is transformed into separate vortex elements (VE). They become part of the vortex wake.

3. *Vortex wake evolution simulation.* According to the VVD method, vortex elements in the flow with circulations Γ_i and positions $\vec{r}_i$, $i = 1, \ldots, N$, move along the velocity field $(\vec{V} + \vec{W})$:

$$\frac{d\vec{r}_i}{dt} = \vec{V}(\vec{r}_i) + \vec{W}(\vec{r}_i), \quad i = 1, \ldots, N,$$

where $\vec{V}$ is convective velocity and $\vec{W}$ is so called diffusive velocity. Convective velocity can be calculated from the vorticity distribution using the Biot — Savart law

$$\vec{V}(\vec{r}) = \vec{V}_\infty + \int_S \frac{\vec{\Omega}(\vec{r}) \times (\vec{r} - \vec{\xi})}{2\pi|\vec{r} - \vec{\xi}|^2} dS_\xi + \oint_K \frac{\vec{k} \times (\vec{r} - \vec{\xi})}{2\pi|\vec{r} - \vec{\xi}|^2} \gamma(\vec{\xi}) dl_\xi =$$

$$= \vec{V}_\infty + \sum_{i=1}^N \frac{\vec{k} \times (\vec{r} - \vec{r}_i)}{2\pi|\vec{r} - \vec{r}_i|^2} \Gamma_i dS_\xi + \oint_K \frac{\vec{k} \times (\vec{r} - \vec{\xi})}{2\pi|\vec{r} - \vec{\xi}|^2} \gamma(\vec{\xi}) dl_\xi, \quad \vec{r} \in S,$$

where $\vec{V}_\infty$ is incident flow velocity. Note, that direct calculation of the vortex elements velocities through the Biot — Savart law is time-consuming procedure for large number of vortices, so in practice fast approximate methods are used, which have logarithmic ($\sim N \log N$) complexity against quadratic one ($\sim N^2$).

The diffusive velocity [20]

$$\vec{W}(\vec{r}) = -\nu \frac{\nabla \vec{\Omega}(\vec{r})}{\Omega(\vec{r})}$$

is proportional to the flow viscosity ν and depends both on the vorticity distribution in the flow domain in a neighborhood to the point r and on the shape of the flow region boundary (if there is such in a neighborhood to r).

4. *Hydrodynamic loads calculation.* In order to reconstruct the pressure distribution in the flow domain, an analogue of the Cauchy — Lagrange integral can be used [21]. However, in practice, as a rule it is necessary to determine hydrodynamic loads (forces and torque) acting the airfoil in the flow. It is possible to use for this purpose the integral formulae derived by prof. G.Ya. Dynnikova and adapted to several types of problems being solved by means of vortex methods [10, 15, 22]:

- flow around an immovable airfoil;

- flow around a rigid airfoil in translational motion;

- flow around a rigid airfoil in rotational motion;

- flow around a rigid airfoil in arbitrary motion.

These integral formulae have been obtained by analytical integration of the pressure distribution over the airfoil surface line. There is also approximate formula for viscous stresses computation.

The `VM2D` source code is written in C++ and has a modular structure. It is a cross-platform code and can be compiled under Windows, Linux and MacOS by using MSVC, GCC, Intel C++ Compiler, Clang compilers (as well as other ones supporting the C++11 standard). The `Eigen` external library is used in `VM2D` for the numerical solution of linear equations systems. The OpenMP, MPI and Nvidia CUDA technologies are used for computation acceleration on multi-core and multiprocessor cluster systems, including hybrid architectures with graphic accelerators [23].

A detailed description of the code structure and instructions for compiling and running can be found in [12, 24]. There is also doxygen-documentation for the VM2D [12], to date only in Russian.

3 FLOW SIMULATION AROUND TWO CLOSELY SPACED CIRCULAR AIRFOILS

A series of model problems of the external flow simulation around two circular airfoils with different mutual positions is considered (fig. 1). The angle α varies from $0°$ to $180°$, as in [23], where numerical and experimental results for such problems are presented. The simulations were carried out for the regime with intermediate Reynolds number, namely $\mathrm{Re} = 10^3$. The Reynolds number is calculated with respect to the diameter of a large cylinder: $\mathrm{Re} = \frac{\rho D V_\infty}{\nu}$.
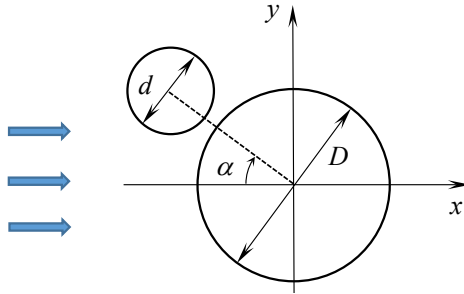
Figure 1: Mutual position of two circular cylinders with different diameters

For simulation in `OpenFOAM`, meshes with different number of cells were used: $50\,000$ cells, $150\,000$ cells, $450\,000$ cells. Computations in `VM2D` were performed with different discretization: the large circle was discretized into 250, 500 and 1000 elements (panels), which corresponds to approximately $15\,000$, $29\,000$ and $100\,000$ vortex elements in the vortex wake in steady-state mode, respectively.

The results obtained with different discretization show that for both codes the most coarse discretization is sufficient to obtain results that are in acceptable agreement with the results of 2D simulation in [13].

The following characteristics were investigated: the average values and the root mean square (RMS) amplitudes for the drag coefficient C_D and the lift coefficient C_L and the dimensionless vortex shedding frequency St. The drag and lift coefficients for the large cylinder are calculated as $C_{D1} = \frac{2F_{D1}}{\rho D V_\infty^2}$ and $C_{L1} = \frac{2F_{L1}}{\rho D V_\infty^2}$, respectively, and those on the small cylinder by $C_{D2} = \frac{2F_{D2}}{\rho d V_\infty^2}$ and $C_{L2} = \frac{2F_{L2}}{\rho d V_\infty^2}$, respectively, where F_D and F_L are the drag and lift forces acting the cylinder in the x- and y-direction, respectively, the subscripts 1 and 2 represent the large and small cylinders, respectively.

In the figures 2–3, average values of drag and lift coefficients are shown for different values of α (for the most coarse mesh/discretization) in comparison to the data given in [13].
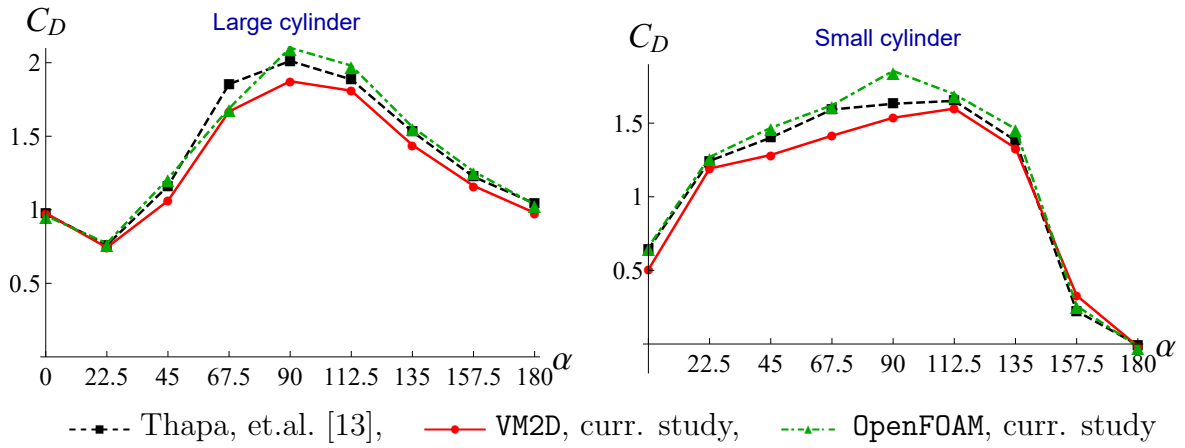
Figure 2: Average values of drag coefficients for large and small cylinders
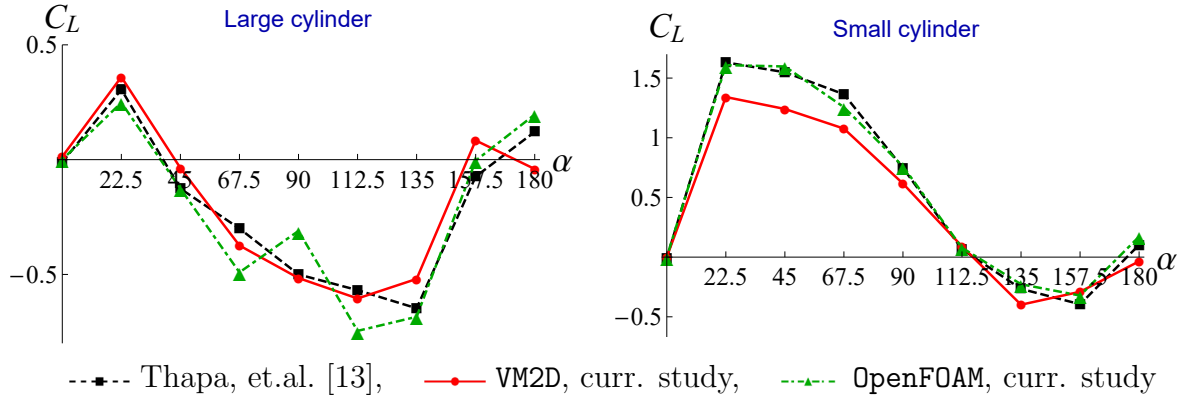
Figure 3: Average values of lift coefficients for large and small cylinders:

It is seen that the results obtained in OpenFOAM and VM2D are in acceptable agreement with the data given in [13]. The highest difference between VM2D and [13] results is observed for RMS of C_L for the small cylinder, while the graph for OpenFOAM is nearly

the same as the results [13]. However, for a large cylinder, the results for RMS of C_L obtained in `VM2D` and [13] correlate well enough, while `OpenFOAM` gives a notable error and incorrect tendency of dependence on the angle.

The vortex shedding frequency is determined by applying the Fast Fourier Transform to the lift coefficients of the large cylinder and choosing the dominant frequency from the spectra. The dependency of the Strouhal number, calculated as $St = fD/V_\infty$, where f is the dominant frequency of the oscillation of the lift coefficients, is shown in the figure 4.

--■-- Thapa, et.al. [13],   ——●—— VM2D, curr. study,   --▲-- OpenFOAM, curr. study
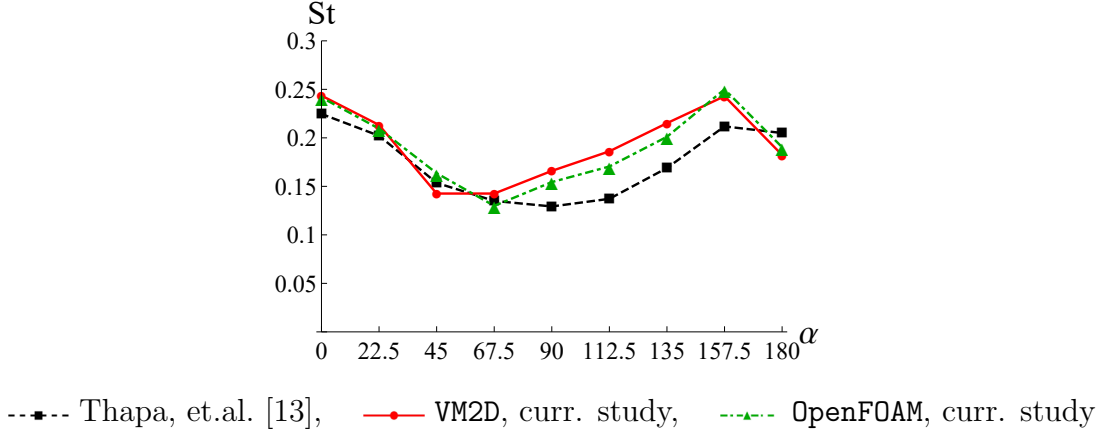
Figure 4: The dimensionless vortex shedding frequency

It is seen that the results obtained in `VM2D` and `OpenFOAM` agree with each other quite well, but slightly differ from the results [13].

The `VM2D` allows performing computations using GPU accelerators. Such technology is highly efficient due to the fact that vortex methods are particle methods. For the discussed model problem, the computations were carried out using two GPU accelerators: Nvidia GeForce GTX970 (with rather small peak performance, approx. 100 Gflops) and Nvidia Tesla V100 (flagship GPU accelerator for today, approx. 7 Tflops in peak). Simulations in `OpenFOAM` were performed using 12 CPU Intel Xeon X5670 (2.93 GHz).

The table 1 shows times of computations for simulations in `OpenFOAM` and `VM2D` using various discretization. Each simulation was performed for time period $T = 0 \ldots 150$. In `VM2D`, the time step was set manually, and in `OpenFOAM` it was selected automatically. For `VM2D`, number N of elements discretizing the airfoil surface line, the approximate number N_{wake} of vortex elements in the wake, and the number of time steps are specified. For `OpenFOAM`, the number N of mesh cells is specified.

It can be seen that simulations in `VM2D` using 1 GPU accelerator GeForce GTX970 with rather low performance require less computational time than simulations in `OpenFOAM` using 12 CPUs. When using a video card Tesla V100, simulations in `VM2D` require 5–10 times less computational time than simulations in `OpenFOAM`.

Table 1: The computation times for simulations in `VM2D` and `OpenFOAM`

VM2D					OpenFOAM		
N	N_{wake}	steps	Time GTX970	Time V100	N	steps	Time
250	13 500	18750	50 min	11 min	45 000	60 000	58 min
500	29 000	37500	300 min	41 min	125 000	120 000	340 min

4 FLOW SIMULATION IN A CHANNEL WITH A BACKWARD-FACING STEP

In this section, `VM2D` will be tested for the case of internal flow simulation. To this purpose, the flow inside the channel with a backward-facing step is considered. In [14], the results of experiments and numerical simulations are shown for this problem. The form of the channel is shown in the figure 5.
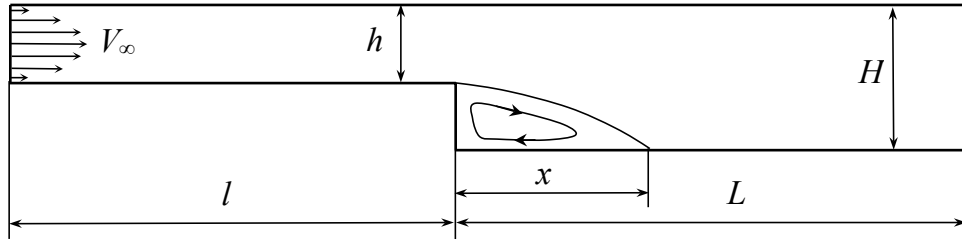
Figure 5: Scheme of the channel with backward-facing step

The channel with a backward-facing step has the following parameters: the height of the input part of the channel $h = 1$, the height of the output part $H = 1.94$. The figure 5 schematically shows the point of flow reattachment, the distance from step to this point is noted by x. An example of the flow for the Re = 100 is shown in the figure 6. The Reynolds number is calculated as

$$\mathrm{Re} = \frac{VD}{\nu},$$

where V is two-thirds of the measured maximum inlet velocity, D is the hydraulic diameter of the inlet (small) channel and is equivalent to twice its height, $D = 2h$, and ν is the kinematic viscosity.

We will compare the positions of the flow reattachment point obtained from the simulations in `VM2D` and from experiment in [14] for different Reynolds (50 . . . 400) numbers. In order to eliminate the influence of the front and back boundaries of the region, simulations were performed for channels with different lengths of the input and output parts l and L, respectively: $l = 7$, $L = 13$; $l = 10$, $L = 19$; and $l = 15$, $L = 28$. The simulations show that in all cases the results for the position of the point of flow reattachment are approximately the same.
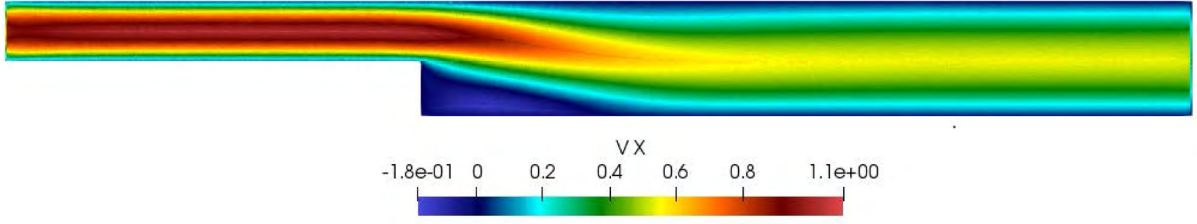
Figure 6: x-component of the flow velocity in the channel with backward-facing step

The figure 7 shows the dependency of the value $s = \frac{x}{H-h}$ on the Reynolds number. It can be seen that the results are in a very good agreement in the interval $\mathrm{Re} = 50 \ldots 300$. There is a significant difference between the results when $\mathrm{Re} > 300$, due to the fact that, as also noted by the authors of [14], the flow becomes three-dimensional and two-dimensional simulation is incorrect.
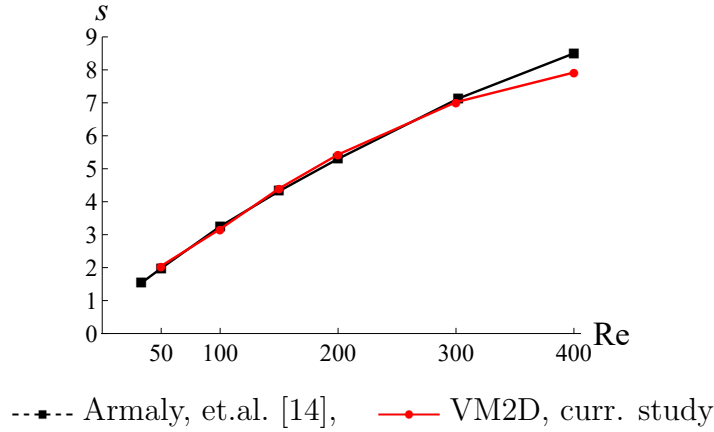
Figure 7: Positions of the flow reattachment point s for different Reynolds numbers

5   CONCLUSIONS

In this paper, using the model problems, the author's software package `VM2D` is verified for two-dimensional incompressible flows simulation. In `VM2D`, the Viscous Vortex Domains method is implemented, which is pure Lagrangian vortex method. For the problem of flow simulation around two circular closely spaced airfoils, the computational efficiency of `VM2D` was compared with the `OpenFOAM` code, where the Finite Volume Method is implemented. It is shown that for such problem, simulations in `VM2D` using one `GPU` accelerator take the same or even less time than simulations in `OpenFOAM` using dozens of CPU cores.

`VM2D` was also verified for internal flows. The flow in a channel with a backward-facing step was considered. The comparison of the numerical and experimental data for the flow reattachment point behind the step show a very good agreement between the results.

REFERENCES

[1] Chorin, A.J. Numerical study of slightly viscous flow. *J. Fluid Mech.* (1973) **57(4)**:785–796.

[2] Raviart, P-A. *Méthodes particulaires.* Lecutre Notes, Ecole d'été d'analyse numérique, Centre d'étude du Bréau-sans-nappe, France, (1987).

[3] Shankar, S. and VanDommelen, L. A new diffusion procedure for vortex methods. *J.Comput.Phys.* (1996) **127(1)**:88–109.

[4] Cottet, G.-H., Michaux, B., Ossia, S. and VanderLinden, G. A comaprison of spectral and vortex methods in three-dimensional incompressible flows. *J. Comput. Phys.* (2002) **175**:702–712.

[5] Najm, H.N. A Hybrid Vortex Method with Deterministic Diffusion. In: *Vortex Flows and Related Numerical Methods.* Eds: Beale, J.T., Cottet, GH., Huberson, S. NATO ASI Series (Series C: Mathematical and Physical Sciences), Springer, Dordrecht. (1993) **395**:207–222.

[6] Ploumhans, P., Winckelmans, G.S. and Salmon, J.K. Vortex particles and tree codes: I. Flows with arbitrary crossing between solid boundaries and particle redistribution lattice; II. Vortex ring encountering a plane at an angle, *ESAIM Proc.* (1999) **7**:335–348.

[7] Eldredge, J.D., Leonard, A. and Colonius, T. A general deterministic treatment of derivatives in particle methods. *J. Comput. Phys.* (2002) **180**:686–709.

[8] Kotsur, O.S. and Shcheglov, G.A. Implementation of the particle strength exchange method for fragmentons to account for viscosity in vortex element method. *Herald of the Bauman Moscow State Technical University, Series Natural Sciences.* (2018) **3**:48–67.

[9] Dynnikova, G.Ya. The lagrangian approach to solving the time-dependent navier-stokes equations. *Doklady Physics.* (2004) **49(11)**:648–652.

[10] Andronov, P.R., Grigorenko, D.A., Guvernyuk, S.V. and Dynnikova, G.Ya. Numerical simulation of plate autorotation in a viscous fluid flow. *Fluid Dynamics.* (2007) **42(5)**:719–731.

[11] *Vvflow CFD Suite (stable).* URL:https://packagecloud.io/vvflow/stable.

[12] *VM2D: Vortex method for 2D flow simulation.* URL: https://github.com/vortexmethods/VM2D.

[13] Thapa, J., Zhao, M., Cheng, L. and Zhou, T. Three-dimensional flow around two circular cylinders of different diameters in a close proximity. *Physics of Fluids.* (2015) **27**:085106.

[14] Armaly, B.F., Durst, F., Pereira, J.C.F. and Schonung, B. Experimental and theoretical investigation of backward-facing step flow. *J. Fluid Mech.* (1983) **127**:473–496.

[15] Guvernyuk, S.V. and Dynnikova, G.Ya. Modeling the flow past an oscillating airfoil by the method of viscous vortex domains. *Fluid Dynamics.* (2007) **42(1)**:1–11.

[16] Kempka, S.N., Glass, M.W., Peery, J.S., Strickland, J.H. and Ingber, M.S. Accuracy considerations for implementing velocity boundaryconditions in vorticity formulations. *SANDIA report.* (1996) **SAND96-0583, UC-700**.

[17] Kuzmina, K.S., Marchevskii, I.K. and Moreva, V.S. Vortex Sheet Intensity Computation in Incompressible Flow Simulation Around an Airfoil by Using Vortex Methods. *Mathematical Models and Computer Simulations.* (2018) **10(3)**:276–287.

[18] Kuzmina, K.S., Marchevskii, I.K., Moreva, V.S. and Ryatina, E.P. Numerical scheme of the second order of accuracy for vortex methods for incompressible flow simulation around airfoils. *Russian Aeronautics.* (2017) **60(3)**:398–405.

[19] Marchevsky, I., Kuzmina, K. and Soldatova, I. Improved algorithm of boundary integral equation approximation in 2D vortex method for flow simulation around curvilinear airfoil. *Mathematics and Mathematical Modeling.* (2018) **6**:22–51.

[20] Dynnikova, G.Ya. Vortex motion in two-dimensional viscous fluid flows. *Fluid Dynamics.* (2003) **38(5)**:670–678.

[21] Dynnikova, G.Y. An analog of the Bernoulli and Cauchy-Lagrange integrals for a time-dependent vortex flow of an ideal incompressible fluid. *Fluid Dynamics.* (2000) **35(1)**:24–32.

[22] Dynnikova, G.Y. and Andronov, P.R. Expressions of force and moment exerted on a body in a viscous flow via the flux of vorticity generated on its surface. *European Journal of Mechanics, B/Fluids.* (2018) **72**:293–300.

[23] Kuzmina, K.S., Marchevsky, I.K. and Ryatina, E.P. On CPU and GPU parallelization of VM2D code for 2D flows simulation using vortex method. *6th European Conference on Computational Mechanics (ECCM 6) 7th European Conference on Computational Fluid Dynamics (ECFD 7)*, 11–15 June 2018, Glasgow, UK. 2390–2401.

[24] Kuzmina, K.S., Marchevsky, I.K. and Ryatina, E.P. Open source code for 2D incompressible flow simulation by using meshless lagrangian vortex methods. *Proceedings of Ivannikov ISPRAS Open Conference.* (2017) 97–103.

LAGRANGIAN VORTEX LOOPS METHOD FOR HYDRODYNAMIC LOADS COMPUTATION IN 3D INCOMPRESSIBLE FLOWS

SERGEY A. DERGACHEV[1], ILIA K. MARCHEVSKY[1,2] AND GEORGY A. SHCHEGLOV[1,2]

[1] Bauman Moscow State Technical University
2-nd Baumanskaya st., 5, 105005 Moscow, Russia

[2] Ivannikov Institute for Sysyem Programming of the Russian Academy of Sciences
Alexander Solzhenitsyn st., 25, 109004 Moscow, Russia

iliamarchevsky@mail.ru,   shcheglov_ga@bmstu.ru

Key words: Vortex Method, 3D Flow, No-slip Boundary Condition, Boundary Integral Equation, Double Layer Potential, Vortex Loop

Abstract. A new approach is developed for incompressible 3D flow simulation around bodies by Lagrangian vortex method. Closed vortex loops are considered as vortex elements, which are generated on all the body surface and provide the satisfaction of the no-slip boundary condition. The procedure of double layer potential density reconstruction is considered, which consists of two steps. Firstly, the integral equation with respect to vortex sheet intensity is solved, which expresses the equality between the tangential components of flow velocity limit value and the body surface velocity. It is solved by using Galerkin approach. Secondly, the least-squares procedure is implemented, which permits to find nodal values of the double layer potential density. It is shown that the developed algorithm makes it possible to improve significantly the quality of solution for the bodies with very complicated geometry and low-quality surface meshes. The combination of this approach with vortex wake modelling with vortex loops, permits to simulate unsteady flows with higher resolution with acceptable numerical complexity. It can be useful for CFD applications and visual effects reproducing in computer graphics.

1 INTRODUCTION

Vortex methods are well-known tool for unsteady incompressible flows simulation and coupled FSI-problems solution in engineering applications [1, 2]. These methods are also useful in computer graphics in visual effects simulation [3]. One of the key problems in vortex methods is connected to boundary condition satisfaction with high accuracy.

There are number of known models of vortex elements for flow simulation around 3D bodies: closed vortex framework, vortex filament, vorton, vortex dipole, vortex fragmenton, etc. Each of them has some advantages and restrictions. In "classical" vortex

element methods, for example, in the discrete vortex method [4], vorticity is concentrated in vortex framework segments and it is absent outside them in the flow. However, this method requires number of empirical models to determine the location of the vortex sheet separation lines. In case of vortex methods with vortex particles (vortons, vortex blobs, etc.) flow separation zones are formed "naturally" due to vorticity flux approach – vortex elements are generated on the whole body surface and these elements self-organization in the flow [5, 6]. The main part of the vorticity is concentrated in neighbourhood of the vortex elements themselves, however, there is distributed non-zero "additional" vorticity in the flow domain, according to the Helmholtz theorems. Its intensity vanishes far from vortex elements. This additional vorticity may cause significant errors, both at computing aerodynamic loads acting the body, and the boundary condition satisfaction, because the "virtual" velocity field inside the body is not vorticity-free.

Some interesting approach has been proposed in [3] for 3D smoke dynamics simulation, which implies vorticity flux simulation through vortex loops generation of equal circulation on the body surface on the basis of the double layer potential density, which, in turn, provides the boundary condition satisfaction.

The aim of this paper is new numerical approach development in order to improve the existing numerical schemes of vortex methods.

2 INTEGRAL EQUATIONS ARISING IN VORTEX METHODS

The problem of 3D incompressible flow simulation around an immovable body is considered. The governing equations are the Navier – Stokes equations with no-slip boundary conditions on the body surface K and perturbation decay conditions.

It is well-known from physical point of view, that in order to take into account the presence of the body in the flow, it is possible to replace it with the vortex sheet of unknown intensity $.\boldsymbol{\gamma}(\boldsymbol{r})$, placed on the body surface, $.\boldsymbol{r} \in K$, which generates the velocity field $\boldsymbol{V}_\gamma(\boldsymbol{r})$. Then the summary velocity field is the superposition of the incident flow velocity $\boldsymbol{V}_\infty$, velocity field, generated by vorticity inside the flow domain $\boldsymbol{V}_\Omega(\boldsymbol{r})$, and the introduced field $\boldsymbol{V}_\gamma(\boldsymbol{r})$:

$$\boldsymbol{V}(\boldsymbol{r}) = \boldsymbol{V}_\infty + \boldsymbol{V}_\Omega(\boldsymbol{r}) + \boldsymbol{V}_\gamma(\boldsymbol{r}).$$

From mathematical point of view, the velocity $\boldsymbol{V}_\gamma$ potential can be expressed through unknown double layer potential density $g(\boldsymbol{r})$ [4]:

$$\Phi(\boldsymbol{r}) = \frac{1}{4\pi} \oint_K g(\boldsymbol{\xi}) \frac{\partial}{\partial \boldsymbol{n}(\boldsymbol{\xi})} \frac{1}{|\boldsymbol{r} - \boldsymbol{\xi}|} dS_\xi.$$

Note, that the velocity field, which corresponds to this potential

$$\boldsymbol{V}_\gamma(\boldsymbol{r}) = \nabla\Phi(\boldsymbol{r}) = \frac{1}{4\pi} \oint_K g(\boldsymbol{\xi}) \frac{\partial}{\partial \boldsymbol{n}(\boldsymbol{r})} \frac{\partial}{\partial \boldsymbol{n}(\boldsymbol{\xi})} \frac{1}{|\boldsymbol{r} - \boldsymbol{\xi}|} dS_\xi, \tag{1}$$

also can be written down in the following form [4]:

$$\boldsymbol{V}_\gamma(\boldsymbol{r}) = \nabla\Phi(\boldsymbol{r}) = \frac{1}{4\pi} \oint_K \frac{\boldsymbol{\gamma}(\boldsymbol{\xi}) \times (\boldsymbol{r} - \boldsymbol{\xi})}{|\boldsymbol{r} - \boldsymbol{\xi}|^3} dS_\xi, \tag{2}$$

where vector $\gamma(\boldsymbol{r}) = -\operatorname{Grad} g(\boldsymbol{r}) \times \boldsymbol{n}(\boldsymbol{r})$; Grad is surface gradient operator. One can notice, that the expression (2) coincides with the Biot – Savart law for incompressible flows. So the potential $g(\boldsymbol{r})$ is closely connected with vortex sheet intensity $\gamma(\boldsymbol{r})$. The velocity $\boldsymbol{V}(\boldsymbol{r})$ is discontinuous at the body surface; its limit value is

$$\boldsymbol{V}_-(\boldsymbol{r}) = \boldsymbol{V}(\boldsymbol{r}) - \frac{\operatorname{Grad} g(\boldsymbol{r})}{2} = \boldsymbol{V}(\boldsymbol{r}) - \frac{\gamma(\boldsymbol{r}) \times \boldsymbol{n}(\boldsymbol{r})}{2}, \quad \boldsymbol{r} \in K.$$

Taking into account the no-slip boundary condition in the form $\boldsymbol{V}_- = \boldsymbol{0}$ at the body surface, we obtain form (1) and (2) two forms of the integral equation:

$$\frac{1}{4\pi} \oint_K g(\boldsymbol{\xi}) \frac{\partial}{\partial \boldsymbol{n}(\boldsymbol{r})} \frac{\partial}{\partial \boldsymbol{n}(\boldsymbol{\xi})} \frac{1}{|\boldsymbol{r} - \boldsymbol{\xi}|} dS_\xi - \frac{\operatorname{Grad} g(\boldsymbol{r})}{2} = -(\boldsymbol{V}_\infty + \boldsymbol{V}_\Omega(\boldsymbol{r})), \quad \boldsymbol{r} \in K, \quad (3)$$

or

$$\frac{1}{4\pi} \oint_K \frac{\gamma(\boldsymbol{\xi}) \times (\boldsymbol{r} - \boldsymbol{\xi})}{|\boldsymbol{r} - \boldsymbol{\xi}|^3} dS_\xi - \frac{\gamma(\boldsymbol{r}) \times \boldsymbol{n}(\boldsymbol{r})}{2} = -(\boldsymbol{V}_\infty + \boldsymbol{V}_\Omega(\boldsymbol{r})), \quad \boldsymbol{r} \in K. \quad (4)$$

It is proven in [7], that in order to satisfy these equations, it is enough to satisfy them, being projected either on surface normal unit vector or on tangential plane.

3 DOUBLE LAYER POTENTIAL DENSITY DIRECT RECONSTRUCTION

The most common approach to solve of the problem is the equation (3) projection on normal unit vector, that leads to the hypersingular integral equation with respect to the double layer potential [8]. Its solution is normally found as piecewise-constant double layer density on surface mesh, which consists of polygonal panels. The efficient numerical formulae for the Hadamard principal values calculation of hypersingular integrals are suggested by I. K. Lifanov [4].

Note, that the i-th polygonal panel with double layer potential density $g_i = \text{const}$ put exactly the same contribution $\boldsymbol{V}_\gamma^{(i)}$ to the velocity field as closed vortex filament, placed on the panel circumfery, with circulation $\Gamma_i = g_i$. So the vorticity on the body surface automatically becomes represented as closed vortex lines, that corresponds to the Helmholtz fundamental theorems [9].

Numerical experiments show that such approach works satisfactory for flows simulation around smooth bodies of rather simple shape, when the surface mesh is close to uniform. However, even in this case the directions of vortex line on the body surface is determined by the mesh, and can differ significantly from true vorticity surface distribution. This can lead to significant error in velocity field reconstruction in neighborhood of the body surface, especially in the case of unsteady flow simulation around the body with vorticity generation on the surface (vorticity flux model) [1].

The mentioned problems can be overcomed by closed vortex filaments (vortex loops) reconstruction. Positions and circulations of vortex loops can be found according to the following algorithm [3, 10]:

1. the double layer potential density values are calculated at the surface triangular mesh vertices; if the surface mesh consists of polygonal cells, they should be split into triangular sub-panels, maybe by introducing additional nodes;

2. the double layer potential surface distribution is reconstructed by FEM-type interpolation using 1-st order shape functions;

3. vortex loops are generated along the level lines of this potential; vortex loops circulations are determined by the difference between potential density values at the neighboring level lines.

Such approach works perfect, for example, in computer graphics applications [3], where it is enough to provide only qualitative results and high accuracy is not required. Its usage for flow simulation and hydrodynamic forces calculation is restricted, again, with rather simple body geometries and uniform meshes [10].

4   VORTEX SHEET INTENSITY RECONSTRUCTION

The other way to the boundary condition satisfaction is developed in [7, 11] and it supposes the equation (4) projection on the tangential plane. It leads to the 2-nd kind equation

$$\frac{\boldsymbol{n}(\boldsymbol{r})}{4\pi} \times \left(\int_K \frac{\boldsymbol{\gamma}(\boldsymbol{\xi}, t) \times (\boldsymbol{r} - \boldsymbol{\xi})}{|\boldsymbol{r} - \boldsymbol{\xi}|^3} \times \boldsymbol{n}(\boldsymbol{r}) dS_\xi \right) - \frac{\boldsymbol{\gamma}(\boldsymbol{r}, t) \times \boldsymbol{n}(\boldsymbol{r})}{2} = \boldsymbol{f}(\boldsymbol{r}, t), \quad \boldsymbol{r} \in K, \quad (5)$$

where the right-hand side $\boldsymbol{f}(\boldsymbol{r}, t)$ is known vector function, which depends on the vortex wake influence and the incident flow velocity:

$$\boldsymbol{f}(\boldsymbol{r}, t) = -\boldsymbol{n}(\boldsymbol{r}) \times \left((\boldsymbol{V}_\infty + \boldsymbol{V}_\Omega(\boldsymbol{r})) \times \boldsymbol{n}(\boldsymbol{r}) \right).$$

Note, that the kernel of the equation (5) is unbounded when $|\boldsymbol{r} - \boldsymbol{\xi}| \to 0$, so in order to solve it numerically with rather high accuracy the following assumptions are introduced:

1. The body surface is discretized into N triangular panels K_i with areas A_i and unit normal vectors n_i, $i = 1, ..., N$.

2. The unknown vortex sheet intensity on the i-th panel is assumed to be constant vector $\boldsymbol{\gamma}_i$, $i = 1, ..., N$, which lies in the plane of the i-th panel, i. e., $\boldsymbol{\gamma}_i \cdot \boldsymbol{n}_i = 0$.

3. The integral equation (5) is satisfied on average over the panel, or, the same, in Galerkin sense: its residual is orthogonal to the basis function which is equal to the 1 on the j-th panel and equal to 0 on all other panels.

According to these assumptions the discrete analogue of (5) can be derived:

$$\frac{1}{4\pi A_i} \sum_{j=1}^{N} \int_{K_i} \left(\int_{K_j} \boldsymbol{n}_i \times \left(\frac{\boldsymbol{\gamma}_j \times (\boldsymbol{r} - \boldsymbol{\xi})}{|\boldsymbol{r} - \boldsymbol{\xi}|^3} \times \boldsymbol{n}_i \right) dS_\xi \right) dS_r - \frac{\boldsymbol{\gamma}_i \times \boldsymbol{n}_i}{2} = \frac{1}{A_i} \int_{K_i} \boldsymbol{f}(\boldsymbol{r}, t) dS_r,$$

$$i = 1, \ldots, N. \quad (6)$$

To write down (6) in the form of a linear algebraic system we choose local orthonormal basis on every cell ($\boldsymbol{\tau}_i^{(1)}$, $\boldsymbol{\tau}_i^{(2)}$, $\boldsymbol{n}_i$), where tangent vectors $\boldsymbol{\tau}_i^{(1)}$, $\boldsymbol{\tau}_i^{(2)}$ can be chosen arbitrary (in the plane of the cell, orthogonal one to the other) and $\boldsymbol{\tau}_i^{(1)} \times \boldsymbol{\tau}_i^{(2)} = \boldsymbol{n}_i$, so

$$\boldsymbol{\gamma}_i = \gamma_i^{(1)} \boldsymbol{\tau}_i^{(1)} + \gamma_i^{(2)} \boldsymbol{\tau}_i^{(2)},$$

and we can project (6) for every i-th panel on directions $\boldsymbol{\tau}_i^{(1)}$ and $\boldsymbol{\tau}_i^{(2)}$ [12, 13].

Note, that the obtained algebraic system has infinite set of solutions; in order to select the unique solution the additional condition for the total vorticity (the integral from the vorticity over the body surface) should be satisfied:

$$\int_K \boldsymbol{\gamma}(\boldsymbol{r}, t) dS_r = \boldsymbol{0},$$

which also should be written down in the discretized form.

The resulting algebraic system is overdetermined, it should be regularized similarly to [4] by introducing the regularization vector $\boldsymbol{R} = (R_1, R_2, R_3)^T$:

$$\frac{1}{4\pi A_i} \boldsymbol{\tau}_i^{(1)} \cdot \left(\sum_{j=1}^N \gamma_j^{(1)} \boldsymbol{\nu}_{ij}^{(1)} + \sum_{j=1}^N \gamma_j^{(2)} \boldsymbol{\nu}_{ij}^{(2)} \right) - \frac{\gamma_i^{(2)}}{2} + \boldsymbol{R} \cdot \boldsymbol{\tau}_i^{(2)} = \frac{b_i^{(1)}}{A_i},$$

$$\frac{1}{4\pi A_i} \boldsymbol{\tau}_i^{(2)} \cdot \left(\sum_{j=1}^N \gamma_j^{(1)} \boldsymbol{\nu}_{ij}^{(1)} + \sum_{j=1}^N \gamma_j^{(2)} \boldsymbol{\nu}_{ij}^{(2)} \right) + \frac{\gamma_i^{(1)}}{2} + \boldsymbol{R} \cdot \boldsymbol{\tau}_i^{(1)} = \frac{b_i^{(2)}}{A_i}, \qquad (7)$$

$$\sum_{j=1}^N A_j \left(\gamma_j^{(1)} \boldsymbol{\tau}_j^{(1)} + \gamma_j^{(2)} \boldsymbol{\tau}_j^{(2)} \right) = 0, \qquad i = 1, \ldots, N.$$

The semi-analytical numerical algorithm is developed [12, 13] for the integrals calculation in the coefficients

$$\boldsymbol{\nu}_{ij}^{(k)} = \int_{K_i} \left(\int_{K_j} \frac{\boldsymbol{\tau}_j^{(k)} \times (\boldsymbol{r} - \boldsymbol{\xi})}{|\boldsymbol{r} - \boldsymbol{\xi}|^3} dS_\xi \right) dS_r, \quad b_i^{(k)} = \int_{K_i} \boldsymbol{\tau}_i^{(k)} \cdot \boldsymbol{f}(\boldsymbol{r}, t) dS_r.$$

Numerical experiments show that the developed algorithm permits to reconstruct surface vorticity distribution with rather high accuracy, even on coarse meshes and, that more important for practice, on non-uniform meshes with refinements. Velocity field, generated by such vorticity, is rather smooth near to the body surface.

In order to use this approach in the above described in section 3 algorithm of the vortex loops generation, it is necessary to reconstruct the double layer potential at the vertices of the surface mesh. The solution of linear system (7) gives us piecewise-constant vortex sheet intensity distribution over the panels. From the other side, vortex sheet intensity is surface gradient of the double layer potential density. It means, that the most convenient way to double layer potential density recovery is its approximation by a function, which is piecewise-linear at the panels. To do it, we consider the nodal values of the potential g_j, $j = 1, \ldots, M$ to be unknown; M is number if vertices of the surface mesh. Then

the potential density can be recovered by FEM-type interpolation using 1-st order shape functions. Let us note positions of al the vertices of the surface mesh as $\boldsymbol{\rho}_j$, $j = 1, \ldots, M$, the vertices of the i-th triangular panel have indices p_i^k, $k = 1, 2, 3$. The shape functions, defined over the i-th panel, coincides with barycentric coordinates on the triangle:

$$\phi_i^{(k)}(\boldsymbol{\rho}) = \frac{|(\boldsymbol{\rho}_{p_i^l} - \boldsymbol{\rho}) \times (\boldsymbol{\rho}_{p_i^m} - \boldsymbol{\rho})|}{|(\boldsymbol{\rho}_{p_i^l} - \boldsymbol{\rho}_{p_i^k}) \times (\boldsymbol{\rho}_{p_i^m} - \boldsymbol{\rho}_{p_i^k})|}, \quad \boldsymbol{\rho} \in K_i,$$

where $(k, l, m) = (1, 2, 3)$, or $(2, 3, 1)$ or $(3, 1, 2)$, then the double layer density over the i-th panel is linear function with respect to $\boldsymbol{\rho}$ and has the form

$$g(\boldsymbol{\rho}) = \sum_{k=1}^{3} g_{p_i^k} \phi_i^{(k)}(\boldsymbol{\rho}), \quad \boldsymbol{\rho} \in K_i.$$

The gradient of the approximate double layer on the every i-th panel, multiplied by normal unit vector $\boldsymbol{n}_i$ gives the constant vector, which physical sense is approximate value of vortex sheet intensity at the corresponding panel:

$$\boldsymbol{\gamma}_i^* = -\sum_{k=1}^{3} g_{p_i^k} (\mathrm{Grad}\, \phi_i^{(k)} \times \boldsymbol{n}_i), \quad \boldsymbol{\rho} \in K_i,$$

where the surface gradients of the shape functions $\mathrm{Grad}\, \phi_i^{(k)}$ are constant vectors.

The unknown values g_j can be found from the least-squares procedure:

$$\Psi = \sum_{i=1}^{N} |\boldsymbol{\gamma}_i - \boldsymbol{\gamma}_i^*|^2 \to \min.$$

Taking partial derivatives of Ψ with respect to g_j, $j = 1, \ldots, M$, and making them equal to zero, we obtain linear system of $M \times M$ size with symmetric matrix.

This system is singular (in practice, due to the truncation errors, it is ill-conditioned), that follows from the fact, that the value of potential density can be chosen arbitrary at some arbitrary specified point. We assume $g_M = 0$, that means that the last row and last column in least-squares matrix should be nullified, the diagonal coefficient can be chosen arbitrary (non-zero); the last coefficient in the right-hand side also should be nullified. The resulting regularized matrix is symmetric and positively defined.

5   VORTEX WAKE SIMULATION

The developed modification of vortex method is based on the closed vortex loops usage for numerical simulation of the vortex wake and its evolution. The vortex wake is considered to consist of K closed vortex loops of the same circulation Γ.

The loop with index k, $k = 1, ..., K$ is simulated by the polygonal vortex line (vortex filament) with N_k vertices. These vertices are considered as the Lagrangian markers $\boldsymbol{r}_{k,i}$, $i = 1, ..., N_k$, moving in the flow along the streamlines; their motion is described by ODE:

$$\frac{d\boldsymbol{r}_{k,i}}{dt} = \boldsymbol{V}(\boldsymbol{r}_{k,i}, t), \boldsymbol{r}_{k,i}(0) = \boldsymbol{r}_{k,i}^0, i = 1, ..., N_k, k = 1, ..., K. \tag{8}$$

We assume the loop legs between two neighboring vertices to be rectilinear line segments, which are described by vectors

$$\Delta \boldsymbol{r}_{k,i} = \boldsymbol{r}_{k,i+1} - \boldsymbol{r}_{k,i}, i = 1, ..., N_k, k = 1, ..., K.$$

They induce the velocities $\Gamma \boldsymbol{v}_{k,i}(\boldsymbol{r})$, which can be calculated analytically as vortex fragmentons influences, regularized by introducing of small smoothing radius ε and finally give contribution to the velocity field $\boldsymbol{V}_\Omega$, generated by vortex wake:

$$\boldsymbol{V}_\Omega(\boldsymbol{r}, t) = \Gamma \sum_{l=1}^{K} \sum_{m=1}^{N_k} \boldsymbol{v}_{l,m}(\boldsymbol{r}, t).$$

Numerical integration of system (8) is carried out by using explicit Euler method with constant step Δt. Initial conditions for markers positions in (8) are parameters of the loops at the time of their generation on the body surface.

Firstly, maximal and minimal values of the double layer intensity for all the panels vertices on the body surface $g_{\max} = \max\limits_{j=1,...,M} g_j$ and $g_{\min} = \min\limits_{j=1,...,M} g_j$ should be found. The panels are assumed to be triangular, as it was mentioned above, so it is easy to construct level lines of the potential density, which correspond to potential values, which differ from one to another on value Γ. These level lines determine the initial shape of the vortex loops. For the given value of the potential density there can be one or more closed level lines, which correspond to separate vortex loops. The number of level lines values is determined as the integer part of expression

$$N_q = [(M - m)/\Gamma] - 1. \tag{9}$$

Then the generated vortex loops become part of vortex wake. The vortex loops, generated on the surface, should be shifted from the surface in normal direction on small constant distance Δ. It should be noted, that the contribution of the vortex loop to the velocity field $\boldsymbol{V}_\Omega(\boldsymbol{r}, t)$ is not considered at the time step immediately after its generation, and for velocity field influence of the corresponding panels on the body surface (which give contribution to $\boldsymbol{V}_\gamma(\boldsymbol{r}, t)$) is taken into account.

When vortex elements move in the flow, some marker positions can intersect the body surface, mainly due to numerical errors in velocity field reconstruction and vorticity motion equations integration. In such cases, the loop legs, which intersect the body surface, is replaced with some other loop legs, which lay on the body surface and provide the shortest way. The Dijkstra's algorithm is used for such procedure [14].

At every time step several procedures for smoothing of loops geometry, loop segments length alignment and loops reconnection are used [15]. It is necessary to control the angle values between the neighboring line segments in vortex loops:

$$\psi_{k,i} = \arccos\left(\frac{\Delta \boldsymbol{r}_{k,i} \cdot \Delta \boldsymbol{r}_{k,i-1}}{|\Delta \boldsymbol{r}_{k,i}| \cdot |\Delta \boldsymbol{r}_{k,i-1}|}\right).$$

If for some vortex loop vertex $\psi_{k,i} < \varphi$, where φ is a given constant, then vertex position should be corrected.

After angle correction, when the vortex loops are smooth enough, it is necessary to "rediscretize" them in order to provide nearly the same length h for all the segments. In this procedure cubic spline interpolation is used in order to reconstruct smooth shape of the vortex filaments.

Vortex loops reconnection is carried out according to the following algorithm. For each marker $\boldsymbol{r}_{k,i}$ the nearest marker $\boldsymbol{r}_{l,j}$ is searched ($j = 1, ..., N_l$, $l = 1, ..., K$), for which the conditions are satisfied:

$$|\boldsymbol{r}_{l\,j} - \boldsymbol{r}_{k\,i}| < \mu, \quad \arccos\left(\frac{\boldsymbol{D}_{k,i} \cdot \boldsymbol{D}_{l,j}}{|\boldsymbol{D}_{k,i}| \cdot |\boldsymbol{D}_{l,j}|}\right) > \varphi, \tag{10}$$

where $\mu > 0$ is some given value, $\boldsymbol{D}_{l,j} = \boldsymbol{r}_{l,j+1} - \boldsymbol{r}_{l,j-1}$, $\boldsymbol{D}_{k,i} = \boldsymbol{r}_{k,i+1} - \boldsymbol{r}_{k,i-1}$.

From all the marker pairs, for which conditions (10) are satisfied, that pair is selected, for which $|\boldsymbol{r}_{l,j} - \boldsymbol{r}_{k,i}|$ has minimal value, and the reconnected is performed for the copesponding legs. In this procedure either two vortex loops are formed from one, or, vice verca, two loops are merged into one. Then for the newly formed vortex loop (or loops) the reconnection algorithm is repeated.

6   NUMERICAL RESULTS

Let us consider firstly the results of double layer potential density reconstruction according to the "direct" method (see Section 3) and to the "indirect" one (through vortex sheet intensity recovery intermediate step, see Section 4).

The results are shown in the Fig. 1 for the sphere discretized into 714 triangular panels of nearly the same size. The incident flow is directed vertically (upward). It is seen that the indirect approach leads to more accurate results: level lines are more smooth and very close to be horizontal, that corresponds to the considered problem.
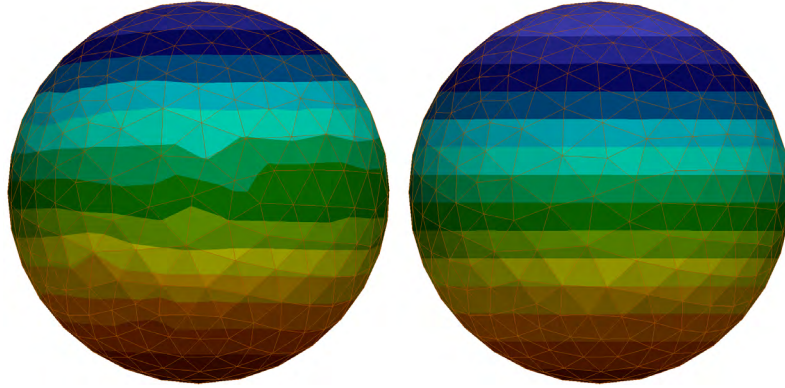
Figure 1: Level lines of the double layer potential density, obtained "directly" (left picture) and "indirectly" (right picture) on the uniform mesh

The "indirect" algorithm permits to obtain rather good results also on coarse and non-uniform meshes. In Fig. 2 the same sphere is split into 342 panels when the ratio of the largest panel area to the smallest one is close to 32. The quality of the level lines shape remains high for "indirect" method, in opposite to the "direct" one.
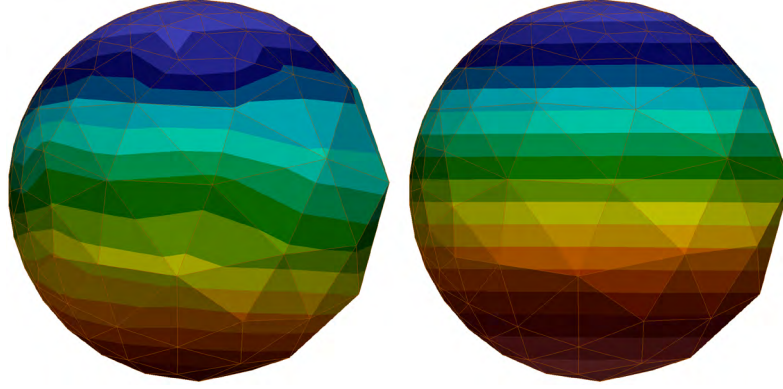
Figure 2: Level lines of the double layer potential density, obtained "directly" (left picture) and "indirectly" (right picture) on the coarse non-uniform mesh

The difference between two approaches is kept for the bodies of more complicated geometry. The example of the flow around doubly connected body: the model of sport weight is shown in Fig. 3; the incident flow is directed diagonally from low right to up left corner. The triangular mesh with local refinement was constructed in the Salome open-source software and consists of 636 panels.
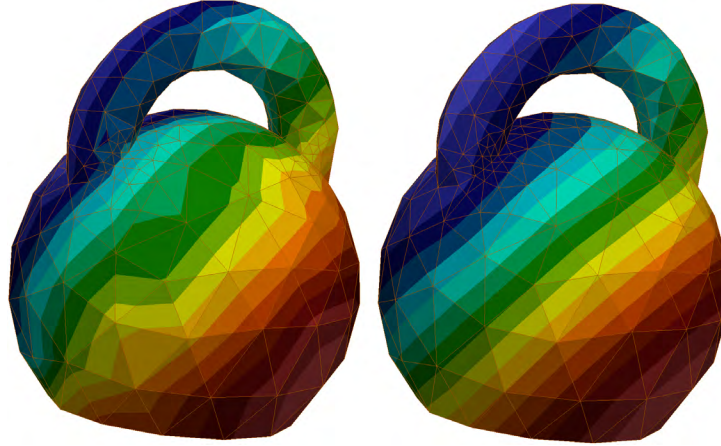
Figure 3: Level lines of the double layer potential density, obtained "directly" (left picture) and "indirectly" (right picture) for the body of complicated shape

For essentially non-uniform meshes, for example, obtained from the stl-file, which consist of large number of "bad" cells (elongated triangles with small angles) generated in some CAD software, the "direct" approach doesn't permit to obtain solution at all. At the same time the "indirect" approach makes it possible to reconstruct the solution with rather good quality (Fig. 4).

The example of unsteady flow simulation around the body of complicated shape (sport weight model) is shown in Fig. 5 for four different time steps. Number of loops during the simulation becomes rather small, however number of markers $P = \sum_{k=1}^{K} N_k$ grows, because the vortex loops length growth and their shape becomes complicate.
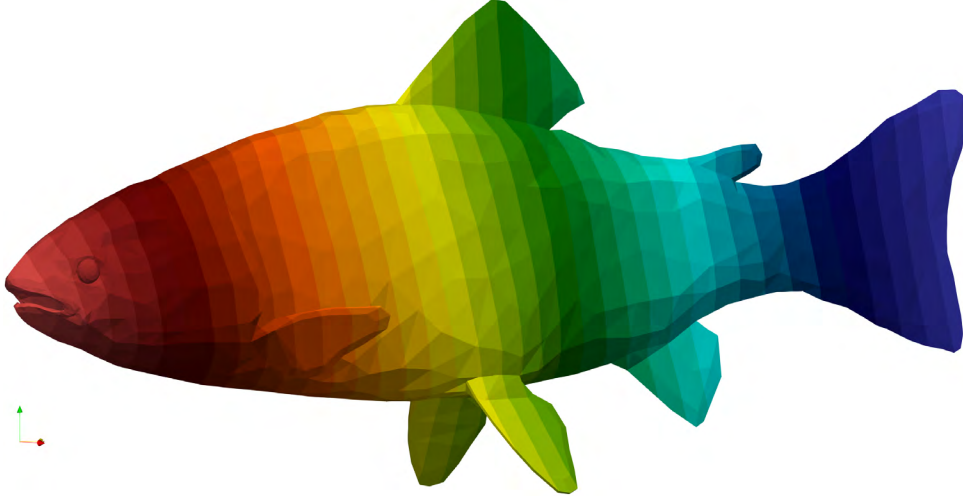
Figure 4: Level lines of the double layer potential density for the fish stl-model, obtained by using "indirect" method
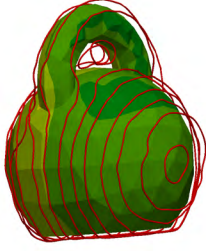
Time step no. 2.
Number of vortex loops $K = 17$
Number of markers $P = 2\ 077$
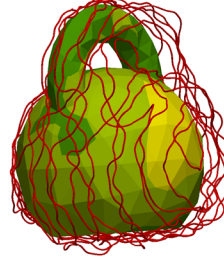
Time step no. 10.
Number of vortex loops $K = 8$
Number of markers $P = 13\ 386$
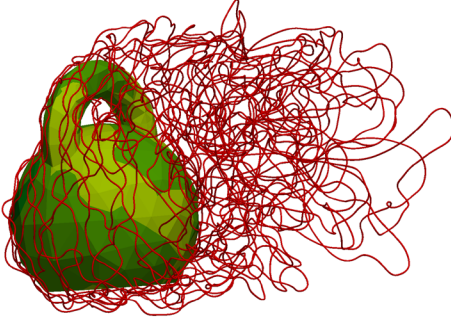
Time step no. 100.
Number of vortex loops $K = 7$
Number of markers $P = 9\ 713$
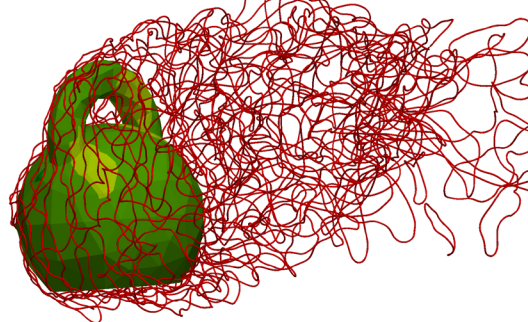
Time step no. 150.
Number of vortex loops $K = 14$
Number of markers $P = 12\ 573$

Figure 5: Vortex wake behind the sport weight model. Incident flow is directed from left to right. Vortex loops are shown as red lines

The application of the developed technique for the flow simulation around the wind model of the finite span (with elongation 5), is shown in Fig. 6. High quality of the boundary condition satisfaction on the body surface, provides good self-organization of the vortex wake. Clear structure of the Prandtl's horseshoe vortex is seen. Note, that this result is obtained without any additional hypotheses about flow separation line position or any equal suggestions.
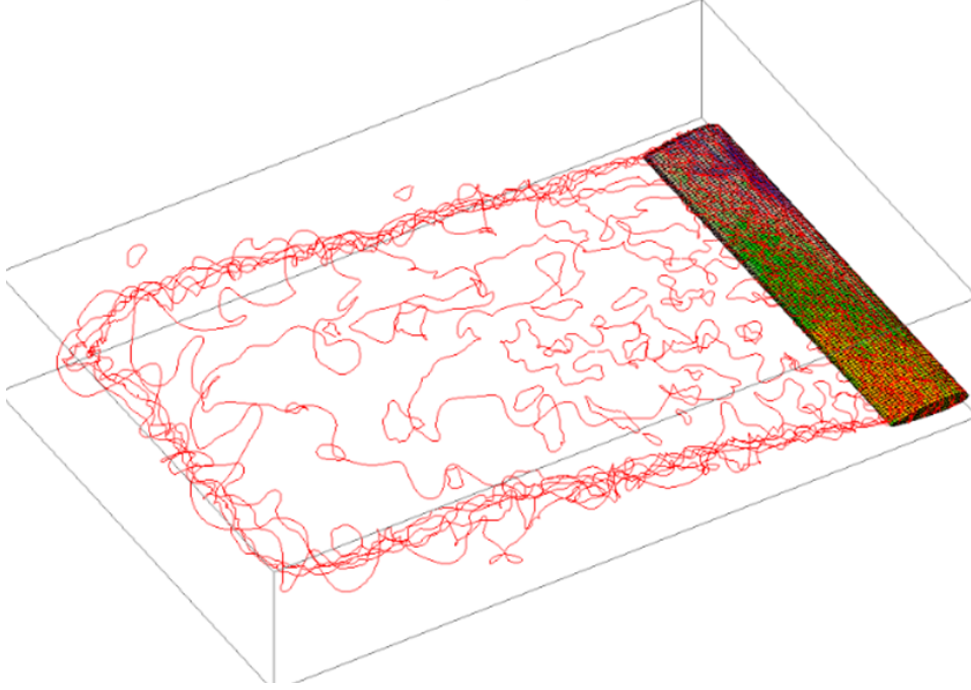
Figure 6: Vortex wake structure behind the wing model. Incident flow is directed from right to left. Time step no. 360, number of vortex loops $K = 109$, number of markers $P \approx 20\,000$.

7   CONCLUSION

The developed algorithm permits to improve significantly the quality of the double layer potential density reconstruction for the bodies with very complicated geometry and low-quality surface meshes. Its numerical complexity is higher than for the "direct" one due to solution of twice-larger linear system to recover vortex sheet intensity and the least-square problem. The combination of this approach with vortex wake modelling with vortex loops, makes it possible to simulte unsteady flows with higher resolution with acceptable numerical complexity. The developed approach can be useful for CFD applications and visual effects reproducing in computer graphics.

REFERENCES

[1] Cottet, G.-H. and Koumoutsakos, P. *Vortex Methods: Theory and Practice.* CUP, (2000).

[2] Lewis, R.I. *Vortex Element Methods for Fluid Dynamic Analysis of Engineering Systems.* CUP, (2005).

[3] Weissmann, S. and Pinkall, U. Filament-based smoke with vortex shedding and variational reconnection. *ACM Trans. Graph* (2010), **29(4)**:115.

[4] Lifanov, I.K., Poltavskii, L.N. and Vainikko, G.M. *Hypersingular Integral Equations and Their Applications.* CRC Press, (2003).

[5] Kamemoto, K. On Contribution of Advanced Vortex Element Methods Toward Virtual Reality of Unsteady Vortical Flows in the New Generation of CFD. *J. of the Brazilian Society of Mechanical Sciences and Engineering* (2004), **26(4)**:368–378.

[6] Alkemade, A.J.Q. *On Vortex Atoms and Vortons.* Ph.D. Thesis, Delft (1994).

[7] Kempka, S.N. et al, Accuracy considerations for implementing velocity boundary conditions in vorticity formulations. SANDIA Rep SAND96-0583 UC-700, 1996.

[8] Timofeev, V.N. Mathematical simulation of the subsonic flow around the lengthening bodies with the flow separation in the region of ground shear with the use of an equivalent body. *Journal of Physics: Conference. Series.* (2018) **1141**:012095.

[9] Saffman, P.G. *Vortex Dynamics.* CUP (1992).

[10] Shcheglov, G.A. and Dergachev, S.A. Hydrodynamic Loads Simulation for 3D Bluff Bodies by Using the Vortex Loops Based Modification of the Vortex Particle Method. *5th International Conference on Particle-Based Methods — Fundamentals and Applications* (2017), 725–731.

[11] Kuzmina, K.S., Marchevskii, I.K. and Moreva, V.S. Vortex Sheet Intensity Computation in Incompressible Flow Simulation Around an Airfoil by Using Vortex Methods. *Mathematical Models and Computer Simulations.* (2018). **10(3)**:276–287.

[12] Marchevsky, I.K. and Shcheglov, G.A. Efficient Semi-Analytical Integration of Vortex Sheet Influence in 3D Vortex Method. *5th International Conference on Particle-Based Methods — Fundamentals and Applications* (2017), 703–714.

[13] Marchevsky, I.K. and Shcheglov, G.A. Semi-analytical influence computation for vortex sheet with piecewise constant intensity distribution in 3D vortex methods. *6th Eur. Conf. on Comput. Mech. (ECCM 6), 7th Eur. Conf. on Comput. Fluid. Dyn. (ECFD 7)* (2018), 2410–2421.

[14] Dijkstra, E.W. A note on two problems in connexion with graphs. *Numerische Mathematik* (1959), **1**:269–271.

[15] Shcheglov, G.A. and Dergachev, S.A. Vortex Loops Based Method for Subsonic Aerodynamic Loads Calculation. *MATEC Web of Conferences* (2018) **221**:05004.

Locomotion of the fish-like foil under own effort

Yaroslav A. Dynnikov*, Galina Ya. Dynnikova*, Tatyana V. Malakhova[*]

[*] Lomonosov Moscow State University
Institue of Mechanics,
Michurinsky pr. 1, 119192, Moscow, Russia
e-mail: Yaroslav.dynnikov@gmail.com, dyn@imec.msu.ru, tatyana.malakhova@gmail.com

ABSTRACT

Self-locomotion of the fish-like foil is simulated by the mesh-free method of viscous vortex domains (VVD). The foil consists of three rigid sections connected by the spring hinges. The forcing periodic moment is applied between first and second sections imitating the muscular effort of the fish. The hinge between the second and third sections is elastic and passive. The task is solved as coupled flow-structure interaction.

Keywords: Flow-structure interaction, vortex method, VVD, flapping foil, elastic connections, Navier-Stokes equations

1. INTRODUCTION

To understand the bionic wings flow mechanism will be helpful to design high performance underwater vehicles and new conception aircrafts. Investigations of flapping wing thrust performance were carried out in a number of experimental and theoretical works (see, for example, [1-12]),

In most of theoretical works on this topic, the law of body motion in a constant incoming flow is set. The forces resulting from the movement are investigated. However, this formulation of the problem differs from the real situation, where the speed in a quasi-stationary motion is the result of applied efforts, the average horizontal hydrodynamic force is zero, and the vertical component balances the force of gravity if the density of the body exceeds the density of the medium. In addition, the speed of the body is not constant. To study such movement it is necessary to solve the flow-structure problem coupled motion. An effective method for solving such problems in a two-dimensional formulation based on the mesh-free method of viscous vortex domains (VVD) [13] was developed in [14, 15]. The method allows calculating the coupled motion of fluid and body systems with elastic connections.

2. METHODOLOGY

The model of a fish is represented by a foil consisting of three sections, which are connected by hinges (see fig. 1). The moment of force is applied between the first and second sections by harmonic law, resulting in the bending of the fish body. This simulates the muscular effort of a fish. The second hinge is elastic and passive. Its torque obeys the Hooke's law. The angles between the sections are determined by the dynamics equations. At the initial moment the fish begins bending in resting medium. This leads to the forward movement.

2.1 General governing equations

Fluid flow is described by the Navier–Stokes equations which are written for the vorticity ω in the form

$$\frac{\partial \omega}{\partial t} = \nabla(\mathbf{u}\omega), \quad \mathbf{u} = \mathbf{V} + \mathbf{V}_d, \quad \mathbf{V}_d = -\nu\frac{\nabla\omega}{\omega},$$
$$\boldsymbol{\omega} = \omega\mathbf{e}_z = \nabla \times \mathbf{V}, \tag{1}$$

where $\mathbf{V}$ is fluid velocity, $\mathbf{V}_d$ is so called diffusion velocity [16], ν is kinematic viscosity. The no-

slip condition is imposed on the foil surfaces.

The fish-like foil is composed of three sections connected by elastic hinges. The contour of each section consists of circular arcs and straight line segments tangent to the arcs (see fig.1).
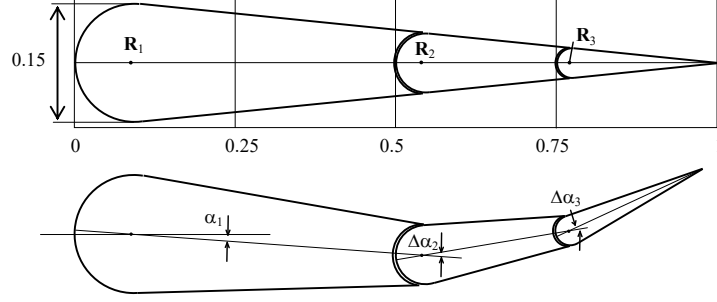
Fig.1 The fish-like model

The position of each section is described by the coordinates of the point $\mathbf{R}_i$, ($i = 1,2,3$) called the section axis and by the rotation angle α_i relative to the horizontal. The point $\mathbf{R}_i$, ($i = 2,3$) is connected with $\mathbf{R}_{i-1}$ and α_{i-1} as following

$$\mathbf{R}_i = \mathbf{R}_{i-1} + a_{i-1}\begin{pmatrix} \cos\alpha_{i-1} \\ \sin\alpha_{i-1} \end{pmatrix}, \quad a_{i-1} = |\mathbf{R}_i - \mathbf{R}_{i-1}| = const \tag{2}$$

The movement of the ith section is composed of the axis velocity $\mathbf{u}_i = \dot{\mathbf{R}}_i$ and the angular velocity $\Omega_i = \dot{\alpha}_i$. An arbitrary point $\mathbf{r}$ of the ith section moves at the velocity

$$\dot{\mathbf{r}} = \mathbf{U}_i + \mathbf{\Omega}_i \times (\mathbf{r} - \mathbf{R}_i) \tag{3}$$

Each section is acted upon by hydrodynamic forces $\mathbf{F}_H$ and moments $\mathbf{M}_H$, as well as forces and moments $\mathbf{F}_h$ and $\mathbf{M}_h$ in the hinges. We suppose that the friction in the hinges is missing, and the moment of elastic coupling is directly proportional to the deviation angle from the equilibrium position $\mathbf{M}_{h,i} = -k_i \Delta\alpha_i$, where ki is spring constant. In addition, a moment of force $\mathbf{M}_f$ is applied in the second hinge simulating the muscular efforts of the fish. The dynamic equations of the sections are:

$$
\begin{aligned}
&m_1 \dot{\mathbf{U}}_{m,1} = \mathbf{F}_{H,1} - \mathbf{F}_{h,2}\,,; \\
&m_2 \dot{\mathbf{U}}_{m,2} = \mathbf{F}_{H,2} + \mathbf{F}_{h,2} - \mathbf{F}_{h,3}; \\
&m_3 \dot{\mathbf{U}}_{m,3} = \mathbf{F}_{H,3} + \mathbf{F}_{h,3}; \\
&I_1 \dot{\mathbf{\Omega}}_1 = \mathbf{M}_{H,1} - \mathbf{M}_f - \mathbf{M}_{h,2} - (\mathbf{R}_2 - \mathbf{R}_1) \times \mathbf{F}_{h,2} - m_1 \dot{\mathbf{U}}_1 \times (\mathbf{r}_{m,1} - \mathbf{R}_1); \\
&I_2 \dot{\mathbf{\Omega}}_2 = \mathbf{M}_{H,2} + \mathbf{M}_f + \mathbf{M}_{h,2} - \mathbf{M}_{h,3} - (\mathbf{R}_3 - \mathbf{R}_2) \times \mathbf{F}_{h,3} - m_2 \dot{\mathbf{U}}_2 \times (\mathbf{r}_{m,2} - \mathbf{R}_2); \\
&I_3 \dot{\mathbf{\Omega}}_3 = \mathbf{M}_{H,3} + \mathbf{M}_{h,3} - m_3 \dot{\mathbf{U}}_3 \times (\mathbf{r}_{m,3} - \mathbf{R}_3).
\end{aligned}
\tag{4}
$$

Here I_i, $\mathbf{r}_{m,i}$, $\mathbf{U}_{m,i}$ are moment of inertia, coordinates and velocity of the center of mass of i-th section respectively. The hydrodynamic forces and moments of forces consist of pressure and friction components $\mathbf{F}_p$, $\mathbf{M}_p$ and $\mathbf{F}_w$, $\mathbf{M}_w$. The pressure forces acting on the contour between points A and B can be written as the following

151

$$\mathbf{F}_p = \int\limits_A^B p\mathbf{n}\,\mathrm{d}l = \mathbf{e}_z \times \int\limits_A^B p\frac{\mathrm{d}\mathbf{r}}{\mathrm{d}l}\,\mathrm{d}l = \mathbf{e}_z \times \left(p_B\mathbf{r}_B - p_A\mathbf{r}_A\right) - \mathbf{e}_z \times \int\limits_A^B \frac{\mathrm{d}p}{\mathrm{d}l}\mathbf{r}\,\mathrm{d}l$$

$$\mathbf{M}_p = \int\limits_A^B p\left(\mathbf{r} - \mathbf{R}_i\right) \times \mathbf{n}\,\mathrm{d}l = \mathbf{e}_z\int\limits_A^B p\left(\mathbf{r} - \mathbf{R}_i\right)\frac{\mathrm{d}\mathbf{r}}{\mathrm{d}l}\,\mathrm{d}l = \tag{5}$$

$$= \frac{\mathbf{e}_z}{2}\left(p_B\left(\mathbf{r}_B - \mathbf{R}_i\right)^2 - p_A\left(\mathbf{r}_A - \mathbf{R}_i\right)^2\right) - \frac{\mathbf{e}_z}{2}\int\limits_A^B \frac{\mathrm{d}p}{\mathrm{d}l}\left(\mathbf{r} - \mathbf{R}_i\right)^2\,\mathrm{d}l$$

The pressure difference $p_B - p_A$ is

$$p_B - p_A = \int\limits_A^B \frac{\partial p}{\partial l}\,\mathrm{d}l \tag{6}$$

Equations (5) – (6) make it possible to express forces and moments acting on the sections as integral of the function $\partial p / \partial l$ over its contour. The partial derivative along the contour $\partial p / \partial l$ is expressed from the Navier-Stokes equation

$$\frac{\partial p}{\partial l} = \mathbf{e}_l \nabla p = -\rho\left(\mathbf{e}_l \cdot \dot{\mathbf{V}}_c - \left(\mathbf{n} \cdot \mathbf{V}_d\right)\omega\right), \tag{7}$$

where $\dot{\mathbf{V}}_c$ is the fluid acceleration at the body surface. Due to the no-slip condition it is equal to the acceleration of the surface. The term $\left(\mathbf{n} \cdot \mathbf{V}_d\right)\omega$ is the vortex flux density from the surface.

For calculating the friction stress the following formula was used [17]

$$\mathbf{F}_w = -\nu\rho_f \int\limits_{C_i} \mathbf{n} \times \boldsymbol{\omega}\,\mathrm{d}l,$$

$$\mathbf{M}_w = -\nu\rho_f\left(4\Omega_i S_i + \int\limits_{C_i}\left(\mathbf{r} - \mathbf{R}_i\right) \times \left(\mathbf{n} \times \boldsymbol{\omega}\right)\mathrm{d}l\right)$$

2.2 Numerical method

The equation of the vorticity evolution (1) is solved here by the fully Lagrangian method of Viscous Vortex Domains (VVD) [13] which is the improved kind of the Diffusion Velocity method [16]. As well as in [16], the vortex region of the flow is presented by the set of vortex "particles" (domains). The domains move at the velocity $\mathbf{u} = \mathbf{V} + \mathbf{V}_d$. The circulation of each domain are not varied. The main advantage of the VVD method is its more accurate way of calculating the diffusion velocity near the surfaces. New vortex domains are generated near the nodes of the body contour at each time step. The values of the new domains circulation γ_i^{new} must provide the boundary conditions. These conditions are written as the linear equations relative to these values. It was shown in [17] that the value $\left(\mathbf{n} \cdot \mathbf{V}_d\right)\omega$ is the vortex flux density from the surface. For k-th segment of the surface contour it can be approximated as the following

$$\left(\mathbf{n} \cdot \mathbf{V}_d\right)\omega = \frac{\gamma_k^{new}}{\Delta l_k \Delta t},$$

This equality leads to the expressions of the hydrodynamic forces and moments of force (5) via unknown values γ_k^{new}. As a result equations (4) together with boundary conditions equations and equalities (2) form a closed system of linear equations for all unknown quantities γ_k^{new}, $\mathbf{u}_i$ Ω_i [18]. Solution of this system satisfies the boundary conditions and the dynamic equations of the body simultaneously.

3. NUMERICAL RESULTS

The moment of force imitating the muscular efforts of the fish was set as $\mathbf{M}_f = \mathbf{M}_{f0} \sin(2\pi ft)$. The task was solved in the dimensionless variables. All linear dimensions are related to the length of the foil L, time is $t = \bar{t}/f$, velocity is $V = \bar{V}Lf$ moments of force per unit span $M = \bar{M}\rho_f L^4 f^2$, where ρ_f is fluid density, $Re = L^2 f/\nu$, $k = \bar{k}\rho_f L^4 f^2$, the body density $\rho = \bar{\rho}\rho_f$.

A vortex pattern obtained at $\bar{\mathbf{M}}_{f0} = 5.5$, $Re = 1000$, $\bar{k}_2 = 13.4$, $\bar{k}_3 = 3.33$ is depicted in fig.2. Blue and red points depict clock-wise and counter clock-wise vortex domains. As can be seen from the figure, the vortex street is not reversive, since the motion is close to quasi-stationary. Average dimensionless velocity $\bar{U} = 0.96$.

.
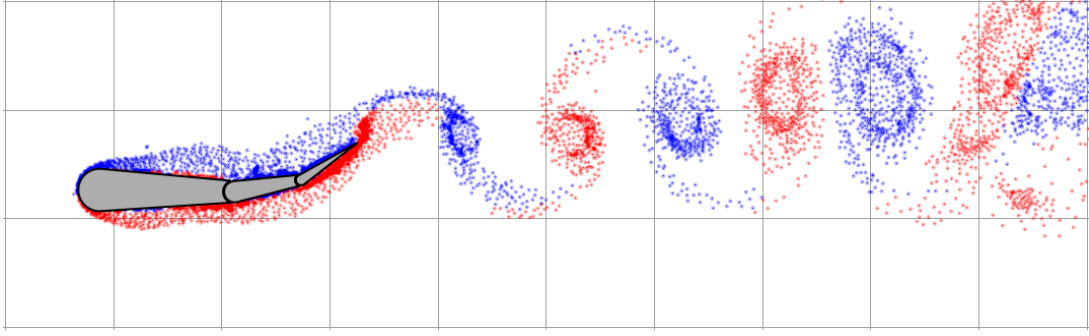
Figure 2 The vortex pattern around the self-moved fish-like foil

Dependency of the quasi-stationary velocity on the spring constant between the second and third sections $\bar{k}_3$ at different dimensionless amplitude of the forcing moment is presented in fig.4 at Re = 1078, and $\bar{k}_2 = 0.06$. One can see that the dependencies are not monotonical, that is, in each case there is an optimal value of $\bar{k}_3$.
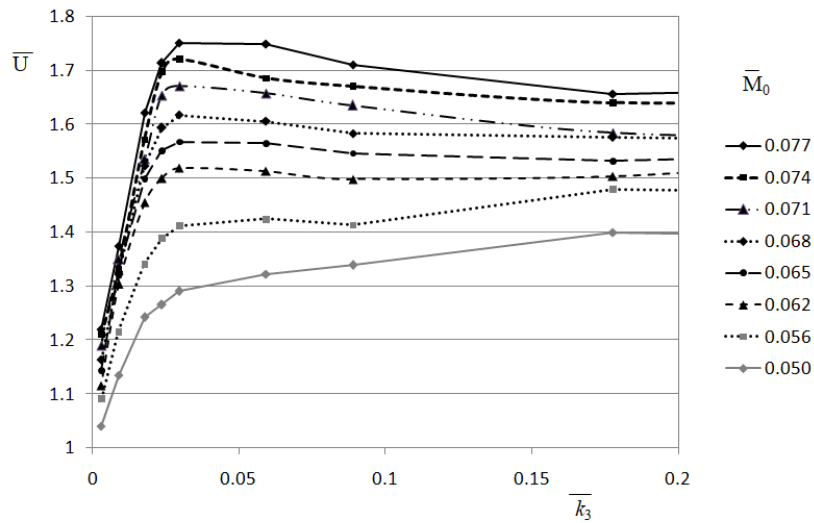
Figure 3. Dependency of the quasi-stationary velocity on the spring constant between the second and third sections at different amplitude of the forcing moment. Re = 1078, $\bar{k}_2 = 0.06$

Dependence of the quasi-stationary velocity on the dimensionless amplitude of the forcing moment at different spring constant between the second and third sections $\overline{k}_3$ is presented in fig.4 at Re = 1078, and $\overline{k}_2 = 0.06$.
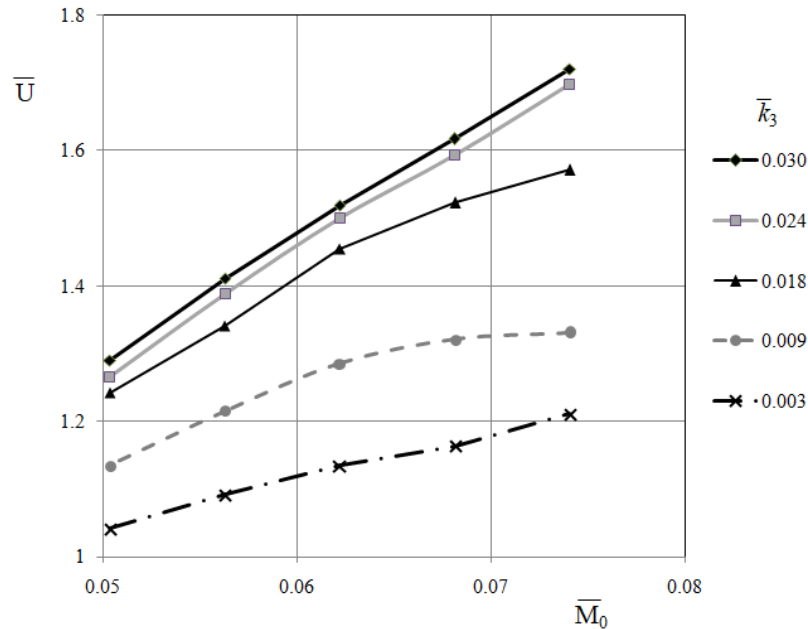
Figure 4. Dependence of the quasi-stationary velocity on the amplitude of the forcing moment at different spring constant between the second and third sections. Re = 1078, $\overline{k}_2 = 0.06$

4. CONCLUSIONS

The methodology of modeling body self-locomotion is presented. A method is applied for modeling the calculations performed by the developed method have shown its effectiveness. The dependency of the obtained quasi-stationary velocity on the recovery coefficient is investigated. It is shown that very low spring constant of the hinge is not optimal as well as very high one.

ACKNOWLEGMENT

REFERENCES

[1] P. Domenici, R. W. Blake. *The kinematics and performance of the escape response in the angelfish (Pterophyllum eimekei).* Journal of Experimental Biology. 156, 187-205 (1991)
[2] Fritz-Olaf Lehmann, Simon Pick. *The aerodynamic benefit of wing–wing interaction depends on stroke trajectory in flapping insect wings.* Journal of Experimental Biology (2007) 210: 1362-1377; DOI: 10.1242/jeb.02746
[3] S. P. Sane, M. H. Dickinson. *The aerodynamic effects of wing rotation and a revised quasi-steady model of flapping flight.* Journal of Experimental Biology (2002) Apr;205(Pt 8):1087-96.
[4] Ch. P. Ellington, C. van den Berg, A. P. Willmott & A. L. R. Thomas. *Leading-edge vortices in*

insect flight. Nature. Vol. 384, pages 626–630 (1996).

[5] R. Godoy-Diana, J. L. Aider, J. E. Wesfreid. Transitions in the wake of a flapping foil. Phys. Rev. E 77, 016308, 2008.

[6] C. Marais, B. Thiria, J. E. Wesfreid, R. Godoy-Diana. Stabilizing effect of flexibility in the wake of a flapping foil. Journal of Fluid Mechanics, Vol. 710, pp. 659–669, 2012.

[7] Michelin, S. and Llewellyn Smith, S. G. Resonance and propulsion performance of a heaving flexible wing. Phys. Fluids. 21, 071902, doi:10.1063/1.3177356., 2009.

[8] Ch. Eloy. *Optimal Strouhal number for swimming animals*. Journal of Fluids and Structures 30 (2012) 205–218. DOI:10.1016/j.jfluidstructs.2012.02.008

[9] Li Jeany Zhang∗,† and Jeff D. Eldredge. *A viscous vortex particle method for deforming bodies with application to biolocomotion*. Int. J. Numer. Meth. Fluids 2009; **59**:1299–1320. DOI: 10.1002/fld.1867

[10] Ch. Gong, J. Han, Z.Yuan et all. *Numerical investigation of the effects of different parameters on the thrust performance of three dimensional flapping wings*. Aerospace and Technology. № 84, p. 431-445, (2019).

[11] L. Schouveilera, F.S. Hoverb, M.S. Triantafyllou. *Performance of flapping foil propulsion*. Journal of Fluids and Structures. V. 20, № 7, p. 949-959, (2005).

[12] M.F. Plazer, K.D. Jones. *Flapping wing aerodynamics: Progress and challenges*. AIAA Journal. V. 46, № 9, p. 2136-2149. (2008). DOI: 10.2514/1.29263

[13] Guvernyuk S.V., Dynnikova G.Ya. *Modeling the flow past an oscillating airfoil by the method of viscous vortex domains*. Fluid Dynamics. 2007, 42, (1), 1–11.

[14] P. R. Andronov, D. A. Grigorenko, S. V. Guvernyuk, and G. Ya Dynnikova. *Numerical simulation of plate autorotation in a viscous fluid flow*. Fluid Dynamics, 42(5):719–731, (2007).

[15] Y. A. Dynnikov, G. Y. Dynnikova, S. V. Guvernyuk. *Simulation of the flexible body moving in viscous fluid.* Proceedings of the ECCOMAS Thematic Conference on Multibody Dynamics 2015. Barcelona, p. 960–967. (2015).

[16] Y.Ogami, T. Akamatsu. *Viscous flow simulation using the discrete vortex method – the diffusion velocity method*. Computers & Fluids. 1991, 19, (¾),.433–441.

[17] G. Ya. Dynnikova, P. R. Andronov. *Expressions of force and moment exerted on a body in a viscous flow via the flux of vorticity generated on its surface*. European Journal of Mechanics, B/Fluids. 2018. 72, (6), 293–300.

[18] Y. A. Dynnikov. *Meshless technology for numerical modeling of viscous fluid interactions and airfoils systems with kinematic and elastic constraints*. Thesis. Moscow. MGTU of N.E. Bauman. (2016) (in Russian)

PARALLEL IMPLEMENTATION OF FAST METHODS FOR VORTEX INFLUENCE COMPUTATION IN VORTEX METHODS FOR 2D INCOMPRESSIBLE FLOWS SIMULATION

DARIA D. LEONOVA[1], ILIA K. MARCHEVSKY[1,2] AND EVGENIYA P. RYATINA[1,2]

[1] Bauman Moscow State Technical University
2-nd Baumanskaya st., 5, 105005 Moscow, Russia

[2] Ivannikov Institute for System Programming of the Russian Academy of Sciences
Alexander Solzhenitsyn st., 25, 109004 Moscow, Russia

daria.denisovna9713@gmail.com, iliamarchevsky@mail.ru, evgeniya.ryatina@yandex.ru

Key words: Vortex Methods, Incompressible Media, Vortex Influence Calculation, Fast Methods, Barnes — Hut-type Method, Fast Fourier Transform, OpenMP, MPI

Abstract. Vortex methods are a powerful tool for solving engineering problems of incompressible flow simulation at small subsonic speeds. The main idea is to consider vorticity as a primary computed variable. Vorticity distribution is simulated by a set of elementary vorticity carriers — vortex elements. Their velocity in the flow is a sum of the convective and diffusive ones. The simplest way to compute the convective velocity of each vortex element is to summarize the influences of all the other vortices, it should be done at every time step. Such problem is similar to the N-body gravitational problem, its computational complexity is proportional to N^2 (N is number of vortices). This fact restricts significantly the applicability of vortex methods.

Two approximate fast methods of logarithmic ($N \log N$) computational complexity are implemented and investigated. The first method is analogous of the Barnes — Hut fast method for the gravitational N-body problem; the second one is based on the possibility of convolution integral fast calculation through Fast Fourier Transform (FFT) technique with further results correction, which permits to take into account the influence of closely-spaced vortices. Sequential and parallel implementations of both methods are developed. Numerical experiments show that the FFT-based method is more efficient in comparison to the Barnes — Hut method; it provides the acceleration of about 1000 times for the velocities calculation for $N = 500\,000$ vortex elements (in comparison to the direct "point-to-point" calculation). The number of mesh cells doesn't effect the method accuracy, however it determines the computational complexity of the algorithm. It is found that the mesh size should be chosen according to the derived estimation of the algorithm's numerical complexity and available computational resources.

1 INTRODUCTION

For many problems of two-dimensional outer gas and fluid flows simulation the Lagrangian vortex methods [1, 2] can be very efficient in comparison to well-known mesh methods. Their range of applicability is limited by incompressible flows, however for some engineering applications the compressibility can be neglected. We consider pure Lagrangian meshless modification of vortex methods, namely Viscous Vortex Domains method [3]; its main idea is considering the vorticity as a primary computed variable. The vorticity in the flow moves with the velocity which is a sum of the convective velocity and diffusive one caused by the viscosity influence. The vorticity distribution $\boldsymbol{\Omega} = \Omega\,\boldsymbol{k}$ is simulated by a set of elementary vorticity carriers — vortex elements, characterised by their positions in the flow domain $\boldsymbol{r}_i$ and circulations Γ_i, which remain constant:

$$\Omega(\boldsymbol{r}) = \sum_{i=1}^{N} \Gamma_i \delta(\boldsymbol{r} - \boldsymbol{r}_i),$$

where N is number of vortex elements, which simulate the vortex wake, $\delta(\boldsymbol{r})$ is two-dimensional Dirac delta-function, $\boldsymbol{k}$ is the unit vector orthogonal to the flow plane.

The convective velocity of the vortex elements is calculated through known vorticity field and incident flow velocity $\boldsymbol{V}_\infty$ according to the Biot — Savart law (we consider flows without streamlines surfaces, however all the presented results can be transferred to more general cases):

$$\boldsymbol{V}_{conv}(\boldsymbol{r}, t) = \boldsymbol{V}_\infty + \int_S \underbrace{\frac{\boldsymbol{k} \times (\boldsymbol{r} - \boldsymbol{\xi})}{2\pi |\boldsymbol{r} - \boldsymbol{\xi}|^2}}_{\boldsymbol{Q}(\boldsymbol{r}-\boldsymbol{\xi})} \Omega(\boldsymbol{\xi}, t) dS_\xi = \boldsymbol{V}_\infty + \sum_{i=1}^{N} \Gamma_i \boldsymbol{Q}(\boldsymbol{r} - \boldsymbol{r}_i). \qquad (1)$$

The vortex influence calculation by direct summation according to (1) is the most time-consuming operation in the vortex method algorithm [4]. The computational complexity is proportional to N^2, and is similar to the gravitational N-body problem. In practice the number of elements N can reach 10^5, so it takes about 10^{10} operations only for the sum (1) calculation. Note, that such sum should be calculated at every time step while the number of steps can has order of tens thousands. So, the direct calculation of the sum (1) becomes impossible in a reasonable time.

This problem can be partially solved using the modern graphic accelerators (GPU). As for all the particle methods, implementation of the vortex methods by using the Nvidia CUDA technology is very efficient [4]. However this approach doesn't solve the mentioned problem fundamentally, because the computational complexity remains squared and computations for more than $3 \cdot 10^5$ vortex elements again require unacceptable time.

The computational complexity of the problem can be reduced significantly by implementing of the approximate fast methods. In this paper we consider the Barnes — Hut-type method [5], initially developed for N-body problem, and the method based on the fast Fourier transform and further correction procedure [7]. Both methods have logarithmic computational complexity (proportional to $N \log N$); their sequential and parallel implementations are developed.

2   THE BARNES — HUT-TYPE METHOD

The main idea of this method is that the influence of the groups of closely adjacent vortex elements on another such groups located far apart, can be calculated approximately using linearized formulae [5]. For this purpose the hierarchical tree-structure of rectangular space domains (cells) is constructed in the flow domain. The zero-level cell contains all the vortex elements, and then it is divided across its long side into two first-level cells, each is reduced horizontally and vertically according to its vortices in order to exclude empty area. Next, similarly the second-level cells are constructed, etc. Such procedure is continued until the target level is achieved or the cell contains single vortex. The whole algorithm consists of the following stages:

1. Zero-level cell formation which contains all the vortex elements.

2. Tree structure construction.

3. Calculation of the necessary tree-cells parameters (centers of positive and negative vorticity and total circulations).

4. For every terminal tree-cell the following operations are performed:

   a) tree traversal and determination of the far-spaced cells according to chosen proximity criteria;

   b) accumulation of the linear expansion coefficients for all far-spaced cells;

   c) exact calculation of the influence from the vortices in cells from neighboring zone according to (1);

   d) summation of the influences calculated approximately and exactly.

The numerical experiments were performed for different time-consuming problems (Fig. 1) and the results (time of computations) are in a good agreement with theoretical estimation (logarithmic computational complexity).
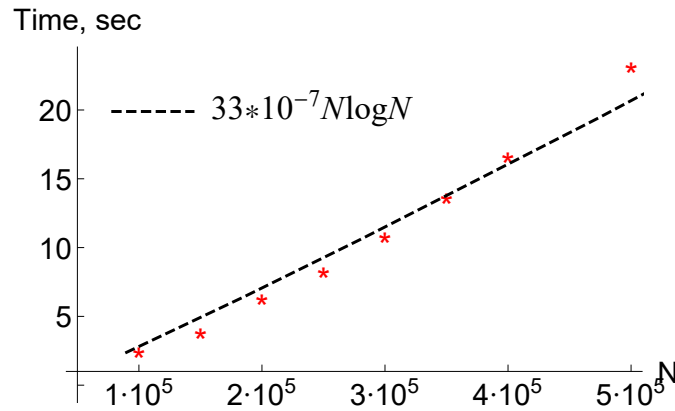
Figure 1: Time of computations for different number of vortex elements N

The method has two adjustable parameters: the proximity parameter θ and number of tree levels k (tree depth).

The first parameter allows changing ratio between the accuracy and computational complexity. All numerical results, presented in the paper, are obtained with relative error not exceeding 0.2% comparing with the "direct" calculation according to the (1). The number of tree levels effects only the computational complexity, and for every particular problem there is an optimal value, which provides the minimal computational cost.

3 PARALLEL IMPLEMENTATION OF THE BARNES — HUT METHOD

The parallel implementations of the method are developed using both OpenMP and MPI technologies. The terminal cells are split between MPI-processes (or/and OpenMP threads). The stages 1–3 are performed in sequential mode simultaneously by all MPI-processes due to their small contribution in all algorithm.

3.1 Efficiency of the parallel implementation for shared memory system

The first numerical experiment was performed for 18-cores CPU Intel Core i9-7980XE using both OpenMP and MPI technologies. The achieved acceleration is shown in Fig. 2 for the time-consuming problem with large number of vortex elements ($N = 1\,000\,000$).
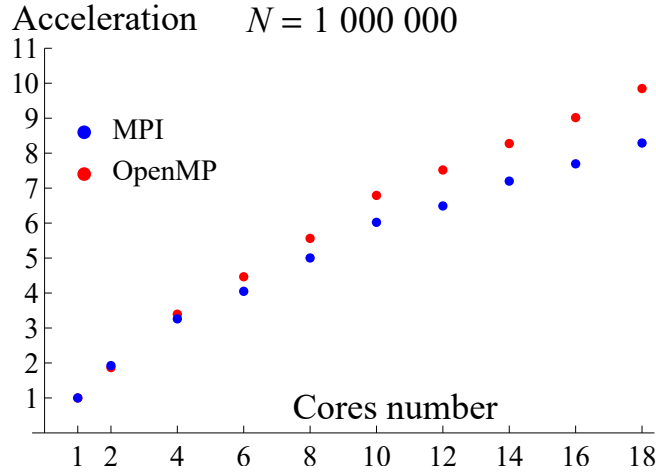
Figure 2: Acceleration of the Barnes — Hut-type method algorithm

It is seen that OpenMP-implementation is more efficient for shared memory systems. Its efficiency for 18 cores is about 55% while MPI-implementation efficiency is 46%. Obtained results correspond to the Amdahl's law with 5% and 7% of sequential code (for OpenMP and MPI technologies, respectively).

3.2 Efficiency of the parallel implementation for cluster system

For the cluster system there is a possibility of simultaneous usage of both OpenMP and MPI technologies. The numerical results for 3-nodes cluster system with 4-cores processors Intel Core i7-940 are shown in Table 1 for the same problem.

Table 1: Time of computations and acceleration of the Barnes — Hut-type method algorithm for the cluster system

Nodes number	1 OpenMP thread per node		4 OpenMP threads per node		4 MPI process per node	
	Time, sec	Acceleration	Time, sec	Acceleration	Time, sec	Acceleration
1	106.13	1.00	30.84	3.44	33.58	3.16
2	54.02	1.96	16.82	6.31	18.20	5.83
3	36.67	2.89	12.11	**8.76**	13.17	**8.06**

It is seen that the usage of both OpenMP and MPI technologies is more efficient in comparison to the only MPI technology. The efficiency of parallel implementation on 12-cores cluster system is 73 %. Note, that for this case total acceleration comparing to the "direct" sequential algorithm is about 1000 times.

The Barnes — Hut-type method is satisfactory scalable, at the same time its sequential implementation is not very efficient itself. The fact is that this method initially had been developed for the gravitational N-body problem, but we consider two-dimensional problem statement. While in 3D problems the influence of a body on another decreases proportionally to squared distance between them, in 2D case it is inversely proportional to the first degree of the distance only. That's the reason of the other method implementation, which is more efficient for 2D problems.

4 THE FFT-BASED METHOD

This method is based on the possibility of the convolution integral in (1) calculation using Fast Fourier Transform (FFT) technique [6]. As it is shown in [7], the usage of this method "directly" leads to the significant error caused by inaccurate calculated influence from vortex elements located in some neighboring zone. So, the special correction procedure is required. It is based on the linear dependency between the velocity and nodal circulations through some correction matrix $\{V\} = [C]\{\Gamma\}$. In such a way it is possible to exclude the inaccurately calculated influence from the neighboring zone of each cell and add the accurate one, calculated directly using the Biot — Savart law. It was found in numerical experiment, that the optimal neighboring zone size is 3 cell layers [7]. In this case the relative error level is less than 0.2 %; it is acceptable for most applications.

In the flow domain rectangular uniform mesh is introduced, which for simplicity contains $M \times M$ nodes ($M \ll N$). The FFT-based algorithm can be split into 3 blocks:

1. Q_1 — nodal circulations calculation (by using the Monaghan's operator M_4 [8]) and correction velocities calculation (which afterwards should be subtracted).

2. Q_2 — convolution integral calculation using the FFT technique.

3. Q_3 — velocities interpolation from the mesh nodes onto the vortex elements and addition the accurately (exactly) calculated vortex influence from the neighboring zone of each cell using the Biot — Savart law.

Note, that the coefficients of the correction matrix $[C]$ depend only on the cell size, so it can be calculated only once at the beginning of the calculation procedure.

The ratio of the operations Q_1, Q_2 and Q_3 significantly depends on the mesh size. Herewith for fixed number of vortex elements N there is some optimal mesh size M when computational complexity of the method is the lowest. The optimal ratio is shown in Fig 3, a. But in practice such ratio almost can't be reached due to well-known fact, that for the optimal performance of the fast Fourier transform subroutines the mesh size should be chosen as $M = 2^d$, $d \in \mathbb{N}$. This fact limits the variability of value M, so the real optimal ratio for each problem is deviates from the ratio in Fig. 3, a. The examples for two different problems with $N = 100\,000$ and $N = 500\,000$ are shown in Fig. 3, b, c.

a) Theoretical estimation   b) $N = 100\,000$, $M = 128$ c) $N = 500\,000$, $M = 512$
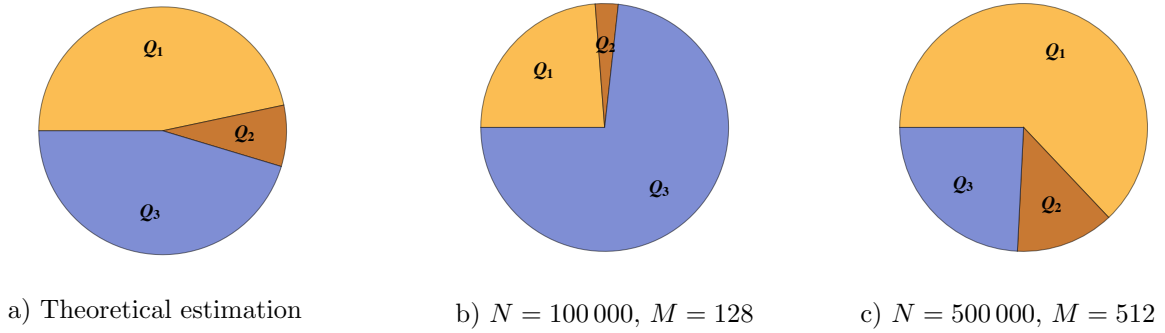
Figure 3: An optimal ratios of the FFT-based algorithm operations

Assuming that the number of vortex elements increases in time, it is important to determine when the mesh size should be doubled. The time of calculations for different time-consuming problems is shown in Fig. 4. The calculations were performed for two mesh sizes: $M = 256$ and $M = 512$.
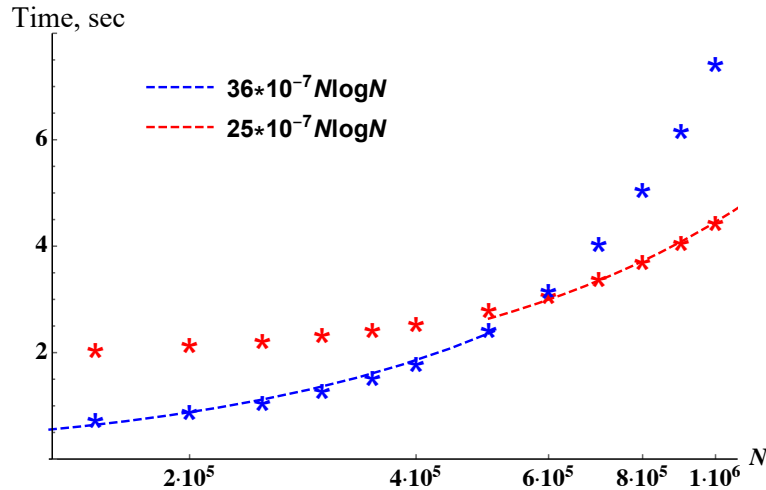
Figure 4: Computational time for different problems (number of vortex elements N); blue asterisks correspond to calculations with $M = 256$; red ones — with $M = 512$

It is seen that the FFT-based method has logarithmic computational complexity $O(N \log N)$, when the mesh size is optimal; the change-over of the mesh size should be performed from $M = 256$ to $M = 512$ when $N > 500\,000$.

If the number of vortex elements is large ($N = 1\,000\,000$), the vortex influence calculation using the "direct" method takes about 3 hours (at one time step); the Barnes — Hut-type method takes 60 seconds and the FFT-based method takes only 4.5 seconds. Thus, we obtain the acceleration more than 2000 times.

5   PARALLEL IMPLEMENTATION OF THE FFT-BASED METHOD

The simulation of the vortex elements movement requires the velocities calculation at every time step. Besides the fact that the number of vortex elements in real problems can exceed hundreds of thousands, the number of time steps can also be tens or even hundreds of thousands, therefore any possible acceleration of calculations is required. For this purpose, assuming that all modern processors are multi-core, the parallel implementation of the above mentioned fast method algorithm is developed.

5.1   Parallel implementation using OpenMP technology

The following stages of the algorithm are implemented in parallel mode using OpenMP technology:

1. Mesh cells initialization.

2. Calculation of the matrix $\{\Gamma\}$ of nodal circulations.

3. Velocities interpolation from the mesh nodes onto vortex elements.

4. Calculation of the influence in the neighboring zone directly according to the Biot — Savart law.

5. Summation of the influences calculated approximately and exactly.

As noted earlier, the mesh size M significantly effects the numerical complexity of operations Q_1, Q_2 and Q_3 of the FFT-based method. The operation Q_2 is implemented sequentially, and it takes the most part of the sequential code in the whole algorithm. Its numerical complexity depends only on the mesh size, so the ratio of sequential code can vary. The parallel implementations of the operations Q_1 and Q_3 are developed.

There is an relationship between these two blocks of operations: increasing contribution of one of them leads to decreasing of the other. For small values of M the operation Q_3 preponderates (since in this case the neighboring zone is rather large and it contains large number of vortex elements). Therefore, the acceleration of this operation should increase for coarser mesh and decrease at the mesh refinement. For the operation Q_1 the situation is opposite. So, for optimal mesh size the acceleration will be quite moderate. The numerical results for the problem with $N = 1\,000\,000$ vortex elements prove these estimations (Fig. 5). Here Q' is total numerical complexity of the parallelized operations Q_1 and Q_3. All calculations were performed for the 12-cores CPU Inter Core i9-7980XE.

a) $M = 256$ b) $M = 512$
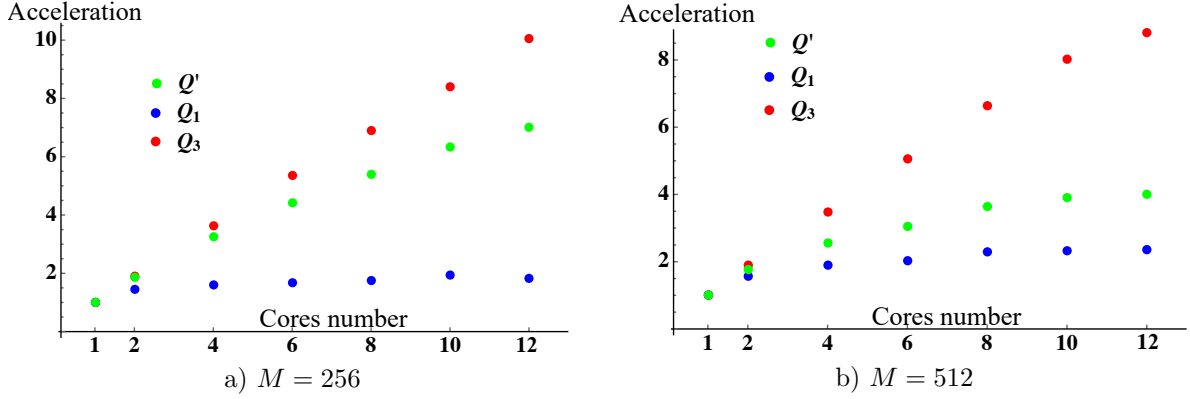
Figure 5: Different operations accelerations obtained using OpenMP-implementation

It is seen that total acceleration (green points) located somehow between accelerations of operations Q_1 and Q_3, approaching to the most time-consuming one. The highest acceleration and the lowest calculation time are achieved for non-optimal mesh $M = 256$ (Table 2). Here Q_{tot} includes all the operations (Q_1, Q_2 and Q_3).

Table 2: Calculation time and acceleration of the FFT-based method operations using OpenMP

	Acceleration			Time, sec		
	M = 256	$M = 512$	$M = 1024$	**M = 256**	$M = 512$	$M = 1024$
Q_1	1.81	2.35	2.79	0.36	0.56	1.69
Q_3	10.05	8.82	7.69	0.61	0.19	0.10
Q'	7.00	4.00	3.12	0.97	0.75	1.79
Q_{tot}	**6.57**	3.05	2.08	**1.05**	1.12	3.24

In sequential mode the optimal mesh consists of $M = 512$ nodes for such problem, however now we obtain the best result for $M = 256$. It means that the mesh choice depends on available computing resources. Obtained accelerations for the mesh $M = 256$ have a good agreement to the Amdahl's law with 7% of sequential code.

5.2 Parallel implementation using MPI technology

In parallel implementation of the FFT-based method using MPI technology the computational domain is split vertically into rectangular bands; number of such bands corresponds to the number of MPI-processes.

The MPI-implementation includes the following parts:

a) parallel code (every MPI-process performs this code for its mesh domain):

    1. Cells initialization.

    2. Calculation of the circulation matrix $\{\Gamma\}$ at mesh nodes.

    3. Correction velocities calculation.

4. Velocities interpolation from the mesh nodes onto vortex elements.

5. Calculation of the neighboring zone influence using the Biot — Savart law.

6. Summation of the influences calculated approximately and exactly.

b) data exchange:

1. Transferring the information from the shadow edges. It includes nodal circulations $\{\Gamma\}$ (1 cell layer) and correction velocities (3 cell layers).

2. Gathering all nodal circulations on the master-process for the convolution integral calculation using the FFT (non-blocking data transfer is used).

3. Transferring of the vortex elements data for boundary cells of each process for correct calculation of the vortex influence in neighboring zone of such cells.

c) sequential code:

1. Convolution integral calculation using the Fast Fourier Transform technique.

The numerical results are similar to the previous section (OpenMP implementation). They are shown in Fig. 6 for the same problem with $N = 1\,000\,000$ vortex elements.
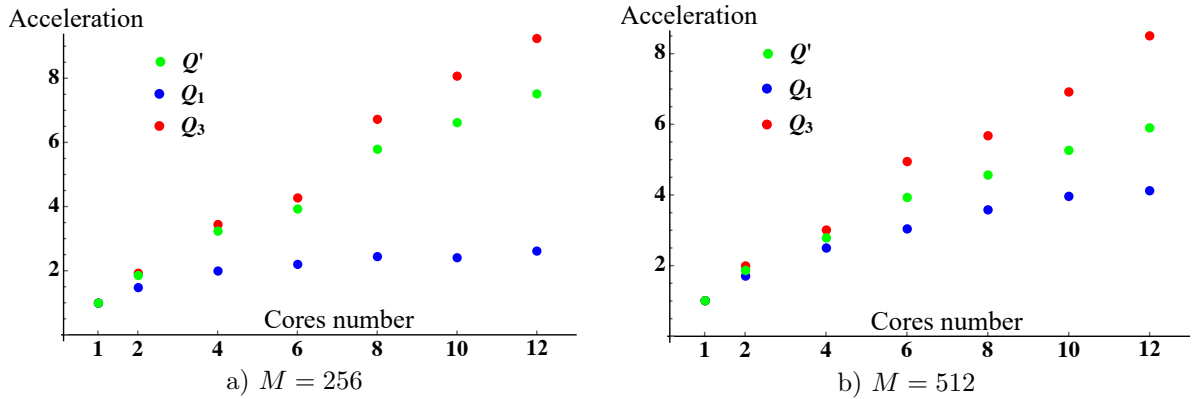
Figure 6: Different operations accelerations obtained using MPI-implementation

It is seen again, that the total acceleration for $Q' = Q_1 + Q_3$ (green points) is located somehow between accelerations for Q_1 and Q_3; the highest acceleration is again achieved on the coarser mesh ($M = 256$), but in this case computational time is less on the optimal mesh for considering problem ($M = 512$). The resulting acceleration and computational time are shown in Table 3. Comparing with the similar results shown in Table 2, it can be seen that the MPI technology is more efficient from the computational time point of view, so it is preferable even for the systems with shared memory.

Numerical experiment results for the mesh with the best acceleration ($M = 256$) are in good agreement with Amdahl's law with $6\,\%$ of sequential code.

Table 3: Calculation time and acceleration of the FFT-based method operations using MPI

	Acceleration			Time, sec		
	M = 256	$M = 512$	$M = 1024$	$M = 256$	**M = 512**	$M = 1024$
Q_1	2.59	4.12	6.81	0.24	0.31	0.58
Q_3	9.24	8.51	7.78	0.66	0.21	0.11
Q'	7.49	5.89	6.96	0.90	0.51	0.68
Q_{tot}	**6.97**	3.69	2.50	0.98	**0.92**	2.65

5.3 Efficiency of the parallel implementation for cluster system

For the cluster system both OpenMP and MPI technologies can be applied simultaneously. The numerical results for 3-nodes cluster system with 4-cores CPU Intel Core i7-940 are shown in Table 4 for the same problem.

Table 4: Computational time and acceleration of the FFT-based method on cluster system

Nodes number	1 OpenMP thread per node		4 OpenMP threads per node		4 MPI processes per node	
	Time, sec	Acceleration	Time, sec	Acceleration	Time, sec	Acceleration
1	4.46	1.00	2.57	1.73	1.77	2.52
2	2.80	1.59	1.80	2.47	1.49	2.99
3	2.23	2.00	1.56	**2.86**	1.41	**3.16**

As it was discussed in the previous section, the MPI technology is more efficient. So, despite the data transfer, the maximal acceleration (and minimal time) is obtained using only the MPI technology.

6 COMPARISON WITH THE "DIRECT" METHOD

As noted earlier, the "direct" method is highly scalable. Thus, the calculation with usage GPU Tesla V100 takes about 10 seconds (for $N = 1\,000\,000$), while the direct velocities computation takes about 3 hours. The calculation using the Barnes — Hut-type method in sequential mode takes about 60 seconds, while the FFT-based method in sequential mode takes only 4.5 seconds. Thus, the FFT-based method is more efficient even in sequential mode than "direct" method, been running on the most powerful graphic accelerator nowadays. Considering the parallel implementations of both fast methods, we obtain that for the same problem the Barnes — Hut-type method, being run on multicore CPU requires nearly the same time, that the direct method on GPU. At the same time, the FFT-based method on the same CPU is 10 times faster (it takes only 0.9 seconds).

The numerical experiment was performed for 12-cores CPU Intel Core i9-7980XE. The computational time for "direct" and FFT-based method is shown in Fig. (7). It is seen that for 12 cores the FFT-based method becomes more efficient for $N > 150\,000$. If only 4 cores are used (which the most modern processors have) the FFT-based method is comparable with the "direct" GPU-implementation already for $N = 200\,000$.
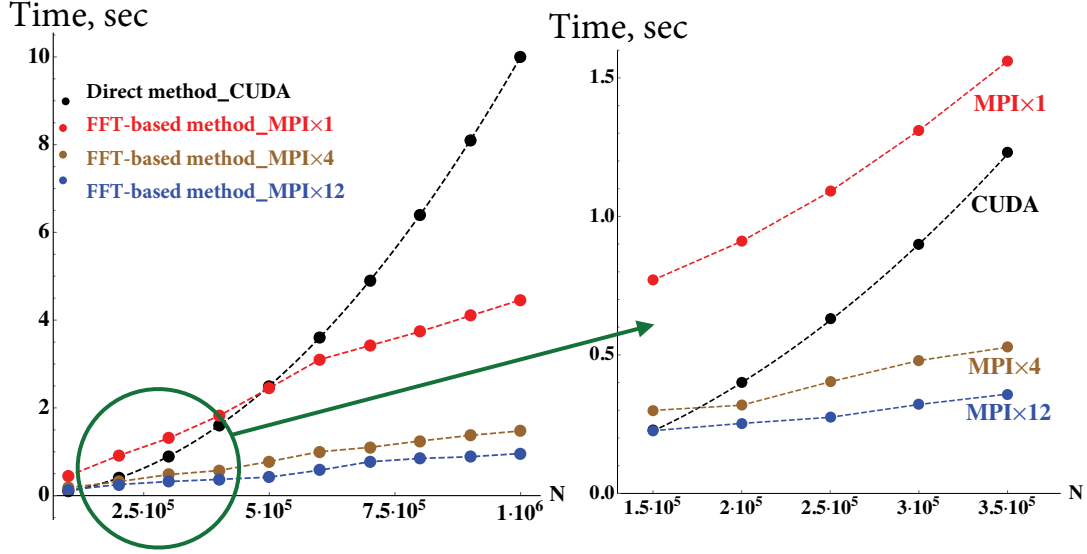
Figure 7: Time of calculations for the FFT-based and "direct" methods

7 CONCLUSIONS

The problem of computational complexity reduction in the algorithms of vortex methods is considered. Two fast approximate methods for vortex influence computation are implemented. Both methods have a logarithmic computational complexity instead of the squared one. Their sequential and parallel implementations are developed. Acceptable relative error for all numerical experiments is less than 0.2%.

The first method is an analogue of the Barnes-Hut fast method for the gravitational N-body problem. The efficiency of this method for 2D problems is lower in comparison to 3D problems, however, it is scalable and can be parallelized rather easily. For the sequential code the acceleration in comparison to the "direct" (the Biot — Savart law-based) method for the problem with 10^6 vortex elements is about 180 times. Using the OpenMP technology it is possible to achieve additional 10 times acceleration for 18-cores Intel i9-7980XE CPU. For MPI-implementation the acceleration is slightly lower.

The other considered fast method is based on the possibility of convolution integral fast calculation by using the Fast Fourier Transform (FFT) technique with further results correction on the coarse mesh for correct influence accounting of closely-spaced vortex elements. For sequential implementation this method is about 10 times more efficient in comparison to the previous one. For 10^6 vortex elements it is more than $2\,000$ times faster in comparison to "direct" calculation. At the same time the efficiency of its parallelization is lower, the maximal achieved acceleration for 12-cores CPU is about 6 times (for all the operations, excluding the FFT transform itself).

Even for sequential version the FFT-based method is faster than the "direct" approach, being implemented for GPU architecture for the most powerful graphical accelerator Tesla V100 for number of vortices $N > 500\,000$. Parallel implementation of the FFT method (12 cores) makes it possible to perform one time step for 10^6 vortices within 0.9 seconds, while for Tesla V100 about 10 seconds is required.

Acknowledgement

REFERENCES

[1] Cottet, G.H. and Koumoutsakos, P.D. *Vortex methods. Theory and practice.* Cambridge University Press (2000).

[2] Lewis, R.I. Vortex element methods for fluid dynamic analysis of engineering systems. Cambridge University Press (2005).

[3] Anronov, P.R., Guvernuk, S.V. and Dynnikova, G.Ya. *Vortex Methods for Computation of Unsteady Hydrodynamic Loads.* Moscow State University Press (2006).

[4] Kuzmina, K.S., Marchevsky, I.K. and Ryatina, E.P. On CPU and GPU parallelization of VM2D code for 2D flows simulation using vortex method. *Proceedings of the 6th European Conference on Computational Mechanics (ECCM 6) and 7th European Conference on Computational Fluid Dynamics (ECFD 7)* (2018): 2390–2401.

[5] Dynnikova, G.Ya. Fast technique for solving the N-body problem in flow simulation by vortex methods. *Computational Mathematics and Mathematical Physics* (2009) **49**:1389–1396.

[6] Nussbaumer, H.J. *Fast Fourier Transform and Convolution Algorithms.* Springer-Verlag (1982).

[7] Morgenthal, G. and Walther, J.H. An immersed interface method for the Vortex-In-Cell algorithm. *Computers and Structures* (2007) **85**:712–726.

[8] Monaghan, J.J. Extrapolating B-splines for interpolation. *Journal of Computational Physics* (1985) **60**:253-262.

Simulation of butterfly flapping with the method of dipole domains

Galina Ya. Dynnikova*, Sergey V. Guvernyuk*, Dmitry A. Syrovatskiy*

* Lomonosov Moscow State University
Instiue of Mechanics,
Michurinsky pr. 1, 119192, Moscow, Russia
e-mail: dyn@imec.msu.ru, guv@imec.msu.ru, talismanium@gmail.com

ABSTRACT

A numerical mesh-free method of dipole domains [1,2] is used for simulation of a butterfly flapping model. This method is based on the representation of a vortex field by the set of dipole particles. The vector function D describes density of dipole moments in accordanse with Navier-Stokes or Euler equations [3]. The butterfly model consists of two flat plates with a common edge performing harmonic oscillations in two planes. New mechanism of the thrust performing is proposed.

Key words: Mesh-free numerical method, three dimensional flow, dipole particles, butterfly model, mechanism of the thrust performance.

1. INTRODUCTION

The mesh-free particles-based methods are effective for modeling the flows with intensively changing boundaries. In the grid based methods two strategies are usually utilized: morphing grids and overset grids. The first approach is not applicable when the computational domain variation is large. The overset grid technology suffers from the low accuracy of computations which is caused by non conservative character of the interpolation between grids. Mesh-free methods could be a good alternative to grid based techniques for such problems.

Among the mesh-free methods, the vortex methods have an advantage in modeling incompressible flows in an unbounded space, since the region with essentially non-zero vorticity has a small volume. In addition, the boundary conditions at infinity are automatically provided.

Simulation of 3D vortex flow in 3-D space has the problem of the representation of three-dimensional vortex field by discrete elements. This field must be divergence-free as a curl of velocity field. But when the discrete vortex particles are used, this property can be destroyed. The velocity field which the vortex particle induces in accordance with Biot-Savart formula has non-zero vorticity in the whole space but not only in the localization of the particle. If the set of the vortex particles does not form a divergence-free vector field then the rotor of the induced velocity field does not coincide with this vector field. This leads to errors in the calculation if special measures are not taken. Therefore hybrid methods are often applied with combination of the Eulerian and Lagrangian approaches [4]. After the particles have been moved, their intensities are recalculated at Euler mesh for recovering the solenoidality at each step. This procedure enforces to build grids, and can increase the numerical viscosity.

In this work the dipole particles are used for simulating of the 3-D vortex field. This representation provides a solenoidality of the vortex field. The fully lagrangian method of Dipole Domains (DD) is developed in [1]. Dipole distributions are widely used in hydrodynamics to calculate the potential flows (double-layer potential). The idea to construct a numerical method based on the dipole particles was suggested by Yanenko, Veretentsev and Grigoriev [5]. However, numerical implementation hasn't been performed. Chefranov [6] used the point dipoles to model the vorticity in an ideal fluid for analyzing the mechanisms of turbulence and turbulent viscosity. It has been shown that interaction of the point dipoles in an ideal fluid can lead to explosive growth of localized vorticity. The vortex dipoles were applied in papers [7-9] for the simulation of the inviscid vortex flow and analyzing of the turbulence. In the method of Dipole Domains the smooth dipole particles are used. Viscous interaction of the particles can be taken into account.

2. GOVERNING EQUATIONS

The method of dipole domains is based on the equation for the vector function **D** called as density of dipole moments

$$\frac{\partial \mathbf{D}}{\partial t} = \mathbf{V} \times \boldsymbol{\Omega} + \nu \nabla^2 \mathbf{V} - \nabla\left(\mathbf{VD} - \nu \nabla \mathbf{D}\right), \tag{1}$$

where **V** is fluid velocity, $\boldsymbol{\Omega} = \nabla \times \mathbf{V}$, $\nabla \cdot \mathbf{V} = 0$, , ν is kinematic viscosity. Applying curl to equation (1) one can see that evolution of the field $\nabla \times \mathbf{D}$ obeys the same equation as the vorticity $\boldsymbol{\Omega}$. Hence at the equivalent boundary conditions $\nabla \times \mathbf{D} = \boldsymbol{\Omega}$. The velocity field **V** is a divergence-free part of **D**. It can be expressed via **D** with the help of Biot-Savarat formula. In infinite space τ it has the form

$$\mathbf{V}(\mathbf{R}) = \frac{1}{4\pi} \int \frac{\mathbf{r} - \mathbf{R}}{|\mathbf{r} - \mathbf{R}|^3} \times \left(\nabla \times \mathbf{D}\right) d\tau + \mathbf{V}_\infty, \quad \mathbf{r} \in \tau. \tag{4}$$

Expression (4) can be transformed to following

$$\mathbf{V}(\mathbf{R}) = \frac{2}{3}\mathbf{D}(\mathbf{R}) + \frac{1}{4\pi} \int \left(-\frac{\mathbf{D}}{|\mathbf{r} - \mathbf{R}|^3} + \frac{3(\mathbf{r} - \mathbf{R})((\mathbf{r} - \mathbf{R}) \cdot \mathbf{D})}{|\mathbf{r} - \mathbf{R}|^5} \right) d\tau. \tag{5}$$

Here the integral is taken in the principal value. The integrand is the velocity which the point dipole located in **r** induces in the point **R**. That is why we call function **D** as dipole density.

The use of the field **D** has an advantage over the natural variables because the numerical scheme can be constructed in such a way that **D** will have a non-zero value mainly in the wakes behind the bodies. The advantage over the vortex methods is that the solenoidality of the vorticity field is provided automatically.

For the hydrodynamic force calculation we use expression of the hydrodynamic impulse of the flow via **D**. In accordance with [10] in the case of the infinite space and finite distribution of the vorticity, the hydrodynamic impulse I is equal to

$$\mathbf{I} = \frac{1}{2} \int \mathbf{r} \times \boldsymbol{\Omega} \, d\tau$$

Taking into account $\nabla \times \mathbf{D} = \boldsymbol{\Omega}$ and applying the general Stokes theorem we obtain

$$\mathbf{I} = \frac{1}{2} \int \mathbf{r} \times \left(\nabla \times \mathbf{D}\right) d\tau = \frac{1}{2} \oint_{S_\infty} \mathbf{r} \times \left(\mathbf{n} \times \mathbf{D}\right) dS - \frac{1}{2} \int \left(\mathbf{D} \times \nabla\right) \times \mathbf{r} \, d\tau =$$
$$= -\frac{1}{2} \int \left(\mathbf{D} \cdot \nabla\right) \mathbf{r} \, d\tau + \frac{1}{2} \int \mathbf{D}\left(\nabla \cdot \mathbf{r}\right) d\tau = \int \mathbf{D} \, d\tau \tag{6}$$

Formulas (5), (6) are also valid in the case of flows around infinitely thin bodies, if they are represented as the distribution of **D**. The hydrodynamic force acting on the body is equal to

$$\mathbf{F}_H = -\frac{d\mathbf{I}}{dt}$$

3. NUMERICAL METHOD

In this work we use the simplified model of the ideal incompressible flow around infinitely thin bodies. The field **D** is represented by the set of dipole particles with dipole moments ς_i. Each particle is smoothed by function

$$\mathbf{D}_i(\mathbf{r}) = \begin{cases} \dfrac{\varsigma_i}{\varepsilon_i^3} f(\xi_i), & \xi < 1, \\ 0, & \xi \geq 1, \end{cases} \qquad \xi = \frac{|\mathbf{r} - \mathbf{r}_i|}{\varepsilon_i}, \quad f(\xi_i) = \frac{105}{16\pi}(1 + 3\xi)(1 - \xi)^3. \tag{7}$$

Equation (1) is transformed to the following form

$$\frac{\partial \mathbf{D}}{\partial t} + \left(\mathbf{V}\cdot\nabla\right)\mathbf{D} = -\left(\mathbf{D}\cdot\nabla\right)\mathbf{V} - \mathbf{D}\times\mathbf{\Omega}$$

This equation corresponds to the particle movement at the velocity $\mathbf{V}$ with changing dipole moment

$$\frac{\partial \varsigma_i}{\partial t} = -\left(\varsigma_i\nabla\right)\mathbf{V} - \varsigma_i\times\mathbf{\Omega}.$$

The discrete formulas for the velocity are:

$$\mathbf{V}(\mathbf{R}) = \sum_n\left(-\frac{\varsigma_n a}{r'^3} + \frac{3b\left(\varsigma_n\mathbf{r}'\right)\mathbf{r}'}{r'^5}\right) + \mathbf{V}_\infty,$$

$$\mathbf{r}' = \mathbf{R} - \mathbf{r}_n, \quad a = \eta_n - \sigma_n, \quad b = \eta_n - \frac{\sigma_n}{3},$$

$$\eta_n = \int_0^{r'/\varepsilon}\xi^2 f\left(\xi\right)d\xi, \quad \sigma_n = \frac{r'^3}{\varepsilon^3}f\left(\frac{r'}{\varepsilon}\right).$$

The rate of the dipole moment changing has the following discrete form

$$\frac{d\varsigma_i}{dt} = \sum_n\delta_{in},$$

$$\delta_{in} = \left(\frac{\left(\varsigma_i\varsigma_n\right)\left(3a - a'r'\right)}{r'^5}\mathbf{r}' + \frac{3b\left(\left(\varsigma_i\mathbf{r}'\right)\varsigma_n + \left(\varsigma_n\mathbf{r}'\right)\varsigma_i\right)}{r'^5} - \frac{3\left(5b - b'r'\right)\left(\varsigma_n\mathbf{r}'\right)\left(\varsigma_i\mathbf{r}'\right)}{r'^7}\mathbf{r}'\right).$$

One can see that $\delta_{in} = -\delta_{ni}$, that is hydrodynamic impulse $\mathbf{I} = \sum_i\varsigma_i$ conserves if the bodies and external forces are absent in the flow.

The infinitely thin plates are simulated by the attached dipole particles. They have to provide the boundary non-flow condition. New free dipole particles shed into the wake from trailing edge satisfying the Kutta-Zhukovcky condition.

4. RESULTS AND DISCUSSION

The method is applied for simulation of the ideal incompressible flows around the model of butterfly wings. The particles are generated at the plates and detach from the trailing edges.
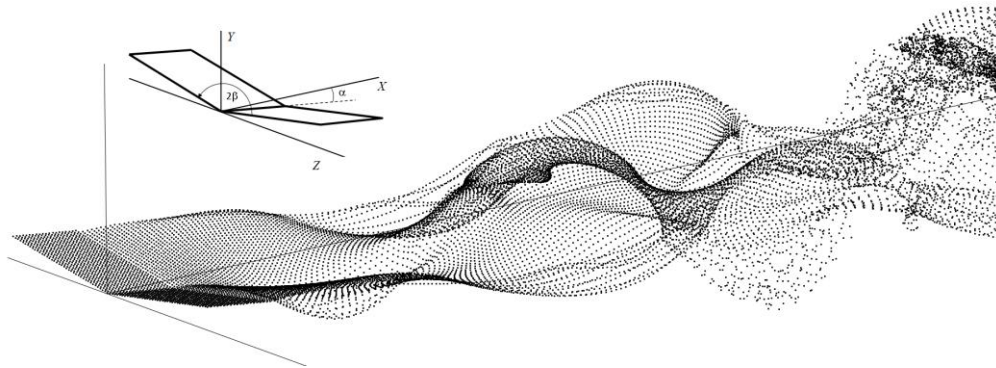
Figure.1 The wake behind the flapping wings of the butterfly model

The model of the butterfly wings consists of two plates with the common edge (see Fig.1). The plates

perform angular oscillations about this edge according to law $\beta = \pi/2 - \gamma(t)$, where $\gamma = \gamma_0\sin(2\pi ft)$. In addition, the entire system performs angular oscillations about the Z axis $\alpha = \alpha_1 + \alpha_0\sin(2\pi ft+\varphi)$. A vortex wake behind the wings is shown In fig. 2 at $\alpha_0 = 10°$, $\alpha_1 = -5°$, $°\gamma_0 = 10°$, $\varphi = -150°$, Strouhal number Sh = 0.15. The time dependencies of the coefficients Cx, Cy, and the angles α and β are presented in fig.2. It can be seen that the average lifting force in this mode is positive, and the average resistance is negative, i.e. there is a propulsive force towards the flow.
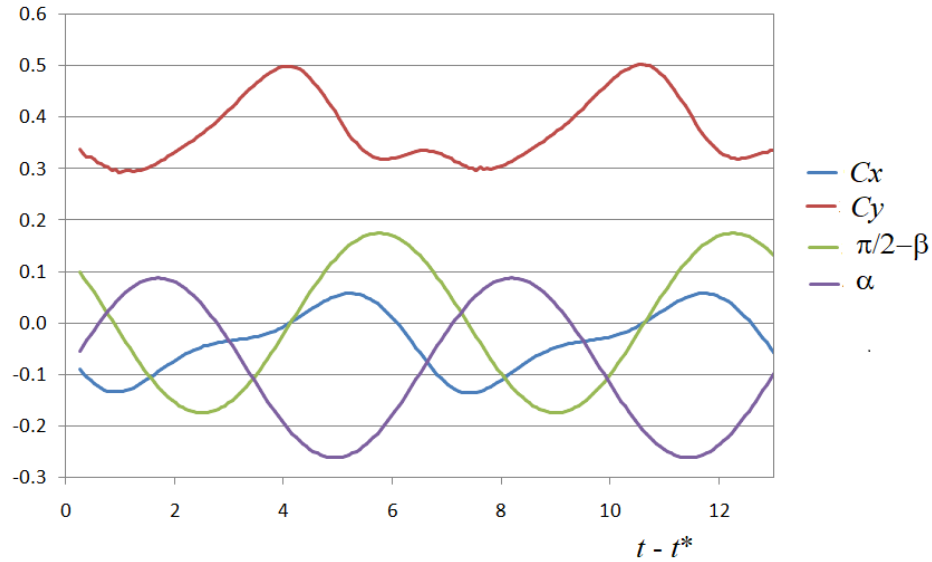
Figure 2. Time dependencies of the coefficients Cx, Cy, and the angles α and β

Most of investigators studying flapping wings find the reason of thrust performance in the vortex structures arising near the bodies such as reversive vortex street and vortex ring [11-16]. But it is more credible that these structures are not a cause but a consequence of thrust. We think that the reason of thrust is accelerated wing movement at an appropriate angle of attack. Let us consider the combined oscillations of a two-dimensional plate consisting of translational oscillation along Y-axis (see fig. 3) $y = y_0 \sin\left(\dfrac{2\pi}{T}t\right)$ and angular oscillation $\alpha = \alpha_0 \sin\left(\dfrac{2\pi}{T}t\right)$ around the leading edge (the left point).
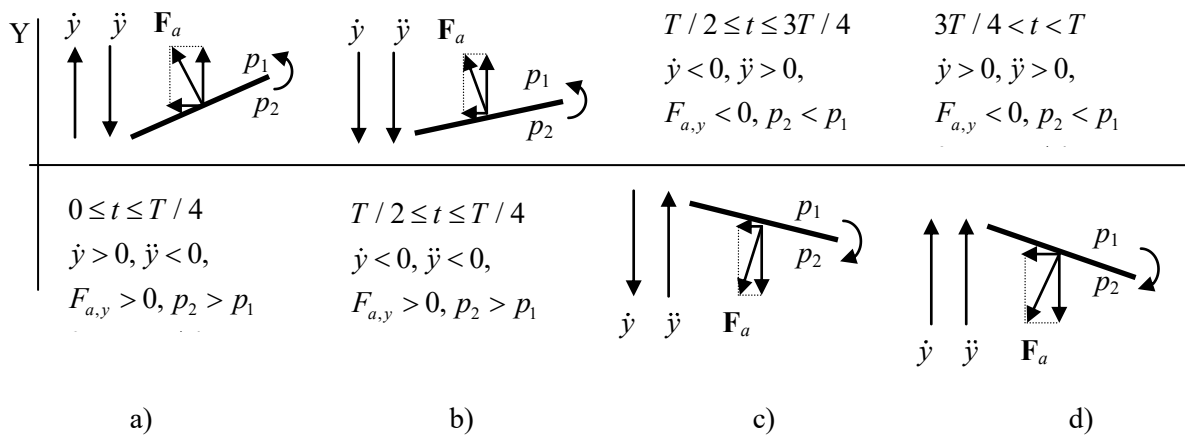
Figure 3. Scheme of the vectors directions in different oscillation phase

In the first quarter of the period, the plate moves up, but the acceleration is directed downwards (fig. 3a). When the body moves with acceleration, a force $\mathbf{F}_a$ arises associated with the added mass of fluid. This force is directed against acceleration, i.e. in this case, upwards. If the acceleration is large enough, this force dominates. This means that the pressure on the lower side of the plate is higher than on the top. The horizontal component of $\mathbf{F}_a$ is directed from the right to the left. The counter clock-wise vortex sheds from the trailing edge. In the second quarter of the period, the acceleration is also directed downward. The horizontal component of the force $\mathbf{F}_a$ is also directed from the right to the left. In the second half of the period, the acceleration changes sign. The angle of the plate changes the sign also. As a result, the horizontal component of the force conserves direction. Thus the interaction of the plate with the added mass of fluid creates a propulsion force. The pressure difference between the lower and upper sides of the plate determines the sign of the vortex shedding from the trailing edge. In the first half of the period this is the counter-clock-wise vortices, and clock-wise in the second half. In such a way a reversive vortex street arises.

4. CONCLUSIONS

The mesh-free dipole particles-based methods is developed and applied for simulation of the insect flapping wings. It is shown that the main cause of the thrust performance is interaction of wings with an added mass of fluid at the wings acceleration.

ACKNOWLEGMENT

REFERENCES

[1] Dynnikova G.Ya..*Calculation of three-dimensional flows of an incompressible fluid based on a dipole representation of vorticity*, Doklady Physics. Vol. 56, no. 3, p. 163–166 (2011).

[2] Syrovatskiy D., Dynnikova G., Guvernyuk S., Arutunyan G. *Using the dipole particles for simulation of 3d vortex flow of a viscous incompressible fluid*, IV International Conference on Particle-based Methods – Fundamentals and Applications PARTICLES 2015 Barcelona, Spain, 2015. p. 692–701.Cottet, G.H. and Koumoutsakos, P.D. *Vortex Methods: Theory and Practice.* Cambridge University Press, (2000).

[3] Oseledets, V.I., *On a new way of writing the Navier-Stokes equation. The Hamiltonian formalism*, Russ.Math.Surveys, 44, 210-211 (1989).

[4] Cottet, G.H. and Koumoutsakos, P.D. *Vortex Methods: Theory and Practice.* Cambridge University Press, (2000).

[5] Yanenko, N.N., Veretentsev, A.N. and Grigoryev, Yu.N., *In: Numerical methods of Mechanics of continuous medium*. Novosibirsk, Vol. 10, p. 144, (1979), in Russian.

[6] Chefranov, S.G., *The dynamics of point vortex dipoles and spontaneous singularities in three-dimensional turbulent flows.* Journal of Exp. And Theor. Phys. (ISSN 0044-4510), Vol. 93, pp. 151-158, (1987), in Russian.

[7] Buttke, T.F. and Chorin, A.J., *Turbulence calculations in magnetization variables*, Appl. Numer. Math., 12 (1993), pp. 47–54.

[8] Cortez, R., *On the accuracy of impulse methods for fluid flow*. SIAM J. Sci. Comput. Vol. 19, No. 4, pp. 1290–1302, July (1998).

[9] Newton, P.K., *The dipole dynamical system.*Discret and continuous dynamical systems. Supplement Volume (2005) pp. 692-699.

[10] Saffman, P. G., *Vortex Dynamics,* Cambridge University Press, (1992).

[11] Gong Ch., Han J.,.Yuan Z et all. *Numerical investigation of the effects of different parameters on the thrust performance of three dimensional flapping wings*. Aerospace and Technology. № 84, p. 431-445, (2019).

[12] Cros A., Llamas B. F., Hernández E. S., *Vortical patterns generated by flapping foils of variable*

ratio chord-to-thickness. Experiments in Fluids (2018) 59:152 https://doi.org/10.1007/s00348-018-2604-2

[13] Bomphrey R., Godoy-Diana R. *Insect and insect-inspired aerodynamics: unsteadiness, structural mechanics and flight control*. Elsevier, 2018, 30 (Décembre 2018), pp.26-32. <10.1016/j.cois.2018.08.003>. <hal-01972623>

[14] Godoy-Diana R., Aider J. L., Wesfreid J. E. *Transitions in the wake of a flapping foil*. Phys. Rev. E 77, 016308, (2008).

[15] Wang Sh., He G., and Liu T. *Estimating lift from wake velocity data in flapping flight*. J. Fluid Mech. (2019), vol. 868, pp. 501-537. doi:10.1017/jfm.2019.181

[16] Fuchiwaki, M., Kuroki, T., Tanaka, K. and Tabata, T., *Dynamic Behavior of the Vortex Ring Formed on a Butterfly Wing*, Exp. Fluids, (2013), 54:1450, 2013.

VORTEX PARTICLE INTENSIFIED LARGE EDDY SIMULATION - VπLES

S. Samarbakhsh[1] and N. Kornev[2]

Chair of modeling and simulation
University of Rostock
Rostock, Germany
[1]e-mail: sina.samarbakhsh@uni-rostock.de

[2] e-mail: nikolai.kornev@uni-rostock.de

Key words: LES, subgrid model, meshless method, free jet, hybrid Eulerian/Lagrangian method

Abstract. This paper presents a novel Large Eddy Simulation approach with a direct resolution of the subgrid motion of fine concentrated vortices. The method, proposed first by [10], is based on combination of a grid based and the grid free computational vortex particle (VPM) methods. The large scale flow structures are simulated on the grid whereas the concentrated structures are modeled using VPM. Due to this combination the advantages of both methods are strengthened whereas the disadvantages are diminished. The procedure of the separation of small concentrated vortices from the large scale ones is based on LES filtering idea. The flow dynamics is governed by two coupled transport equations taking two-way interaction between large and fine structures into account. The fine structures are mapped back to the grid if their size grows due to diffusion. Algorithmic aspects specific for three dimensional flow simulations are discussed. Validity and advantages of the new approach are illustrated for a well tried benchmark test of the decaying homogeneous isotropic turbulence using the experimental data of [4] and free turbulent jet flow using experiments of [8, 2, 15].

1 INTRODUCTION

Insufficient resolution of fine vortex structures in turbulent flows is one of the key problems in Computational Fluid Dynamics (CFD). The most advanced and popular technique to resolve multi scale flow structures is the Large Eddy Simulation (LES) which is based on the idea of scale decomposition into large and small ones. While the large eddies are directly resolved on the grid, the effect of small vortices is taken into account through a subgrid stress (SGS) model.

The subgrid motion is not resolved in LES but rather it is modelled using different functional and structural approaches. However, there are many problems which require direct representation of the subgrid motion to simulate, for instance, mixing or particle

dynamics in turbulent flows. In our previous papers (see [9], [10], [11], [16]]), we proposed a simulation technique resembling LES with an effort to directly reproduce the subgrid motion at least in the statistical sense. It is suggested to apply a hybrid grid and particle based method, utilizing a combination of the finite volume and computational vortex particle (VPM) (see [5]) methods. The large scale field is represented on the grid like in LES, whereas the small scale one (subgrid field) is calculated using the VPM. The new method called VπLES is a purely Lagrangian one for small structures and purely grid based one for large scale structures.

The method is based on the decomposition of the velocity $\mathbf{u}$ and vorticity fields $\boldsymbol{\omega}$ into the distributed large scale (upper index 'g') and concentrated small scale (upper index 'v') fields:

$$\mathbf{u}(\mathbf{x}, t) = \mathbf{u}^g(\mathbf{x}, t) + \mathbf{u}^v(\mathbf{x}, t), \boldsymbol{\omega}(\mathbf{x}, t) = \boldsymbol{\omega}^g(\mathbf{x}, t) + \boldsymbol{\omega}^v(\mathbf{x}, t) \tag{1}$$

The fine vortex detection procedure utilizes the Large Eddy Simulation (LES) filtration applied to the grid based velocity field $\mathbf{u}^g$:

$$\overline{\mathbf{u}}^g(\mathbf{x}, t) = \int\limits_{-\infty}^{\infty} \mathbf{u}^g(\mathbf{s}, t) F(\mathbf{x} - s) d\mathbf{s} \tag{2}$$

where $F(\mathbf{x} - \mathbf{s})$ is a certain filter function. The small scale velocity field $\mathbf{u}'$ calculated as the difference between the original and filtered fields

$$\mathbf{u}'(\mathbf{x}, t) = \mathbf{u}^g(\mathbf{x}, t) - \overline{\mathbf{u}}^g(\mathbf{x}, t) \tag{3}$$

should be approximated by vortex particles in regions of concentrated vortices which are detected using any vortex identification criteria, for instance, λ_{ci} ([1]). The cells with $\lambda_i > \lambda_{ci,min}$ contain the vortices which in principle can be converted to vortex particles. Such cells are marked as active ones using the $\lambda_{i,active}$ field:

$$\lambda_{i,active} = \begin{cases} 1, & \text{if } \lambda_{ci} > \lambda_{ci,min} \\ 0, & \text{otherwise} \end{cases} \tag{4}$$

where $\lambda_{ci,min}$ is a certain small value introduced in order to limit the number of particles.

To keep the required computational resources on an acceptable level, only small vortices with size proportional to the local cell size Δ are to be converted to single vortex particles. Neighboring cells which all have $\lambda_{i,active} = 1$ form large vortices. For them it is supposed that the larger vortices with scales of a few Δ can accurately be represented on the grid. Therefore the next task is to detect cells with fine vortices. According to the algorithm, all neighboring cells of the $i - th$ cell are checked for the condition $\lambda_{ci} > \lambda_{ci,min}$. If all neighbors fulfill this condition, we identify a cell cluster which remains on the grid and all its cells become non- active $\lambda_{i,active} = 0$. Only vortices in cells with $\lambda_{i,active} = 1$ are to be replaced by vortex particles.

At each cell with $\lambda_{i,active} = 1$ the new vortex particle is introduced at the cell center if the permissible number of vortex particles per cell N_{pt} is not exceeded. Otherwise,

the new vortex replaces the cell's weakest one. The number N_{pt} was introduced to keep the total number at a reasonable level. This restriction is conform with the concept that the largest contribution to the subgrid kinetic energy is made by a small fraction of the strongest vortices. The radius of the new vortex is set as $\sigma = \beta Vol_i^{1/3}$, where β is the overlapping ratio which is taken as $\beta = 2$ and Vol_i is the volume of the i-th cell. A thorough analysis of the influence of N_{pt} and $\lambda_{ci,min}$ for the jet case is given in [11] in Sec. 4.3.5. The vortex particle strength is calculated as

$$\boldsymbol{\alpha} = Vol_i \boldsymbol{\omega}^v = Vol_i(\nabla \times \mathbf{u}') \tag{5}$$

The velocity $\mathbf{u}^v(\mathbf{x}, t)$, induced by the vortex particles, is calculated at grid points $\mathbf{x}$ using the Biot-Savart law

$$\mathbf{u}^v(\mathbf{x}, t) = \frac{1}{4\pi} \nabla \times \int_{FlowVolume} \frac{\boldsymbol{\omega}^v(\boldsymbol{\xi}, t)}{|\mathbf{x} - \boldsymbol{\xi}|} dV(\boldsymbol{\xi})$$

and subtracted from the grid velocity $\mathbf{u}^{g,new} = \mathbf{u}^g - \mathbf{u}^v$. Thus, the total velocity at grid points $\mathbf{u}^{g,new} + \mathbf{u}^v = \mathbf{u}^g$ remains constant after the vortex particle generation procedure.

2 GOVERNING EQUATION

The evolution of vortex particles and large scale flow represented on the grid is described by a system of two coupled transport equations derived in [9, 10, 11] for incompressible isothermal flows:

$$\frac{\partial \mathbf{u}^g}{\partial t} + (\mathbf{u}^g \cdot \nabla)\mathbf{u}^g = -\frac{1}{\rho}\nabla p^g + \nu\Delta\mathbf{u}^g + \overline{\mathbf{u}^v \times \boldsymbol{\omega}^g} \tag{6}$$

$$\frac{d\boldsymbol{\omega}^v}{dt} = (\boldsymbol{\omega}^v \cdot \nabla)(\mathbf{u}^v + \mathbf{u}^g) + \nu\Delta\boldsymbol{\omega}^v + \nabla \times [\mathbf{u}^v \times \boldsymbol{\omega}^g - \overline{\mathbf{u}^v \times \boldsymbol{\omega}^g}], \tag{7}$$

The sum of the curl of the first equation and the second equation retrieves the original Navier Stokes equation written in the form of the vorticity transport equation. The first equation (6) is coupled with the second one (7) through the additional term $\overline{\mathbf{u}^v \times \boldsymbol{\omega}^g}$ whereas the coupling of the second equation with the first one is due to the terms $(\mathbf{u}^g \cdot \nabla)\boldsymbol{\omega}^v$, $(\boldsymbol{\omega}^v \cdot \nabla)\mathbf{u}^g$ and $\nabla \times [\mathbf{u}^v \times \boldsymbol{\omega}^g - \overline{\mathbf{u}^v \times \boldsymbol{\omega}^g}$. The equations (6) and (7) are solved sequentially. The first equation is solved on the grid whereas the second one uses the grid free Vortex Particle Method (VPM) [5]. The physical meaning of the coupling term $\overline{\mathbf{u}^v \times \boldsymbol{\omega}^g}$ is explained in [10].

The vortex particle displacement is calculated from the trajectory equation

$$\frac{d\mathbf{r}_i}{dt} = \mathbf{u}_i^g + \mathbf{u}_i^v, \tag{8}$$

where i is the particle number. Computation of the velocity induced by vortex particles $\mathbf{u}^v$ is performed with the direct summation of the Bio-Savart law taking into account one or two layers of neighboring cells. Only induction of the neighboring points is taken into account because the velocity $\mathbf{u}^v$ is much less than $\mathbf{u}^g$ and it is mostly determined

by interaction of neighboring particles lying at a short distance. The justification of this simplification presented in [11] is that the correlation between neighboring small scale vortices is weak and they are well separated. This simplification can be considered as a kind of model which results in a very fast computational procedure of a local character suitable for parallel calculations.

The velocity induced by a vortex particle can be calculated from the formula

$$\mathbf{u}_p^v = \frac{1}{4\pi} \frac{\boldsymbol{\alpha} \times \boldsymbol{\xi}}{\xi^3} (1 - e^{-\xi^3/\sigma^3}) \tag{9}$$

proposed by [14]. Here α and σ are the strength and the radius of a vortex particle, which are defined below. The velocity induced by a set of particles $\mathbf{u}^v$ is calculated as the sum of $\mathbf{u}_p^v$. It should be noted that the technique presented here is independent of any specific choice of vortex particles. Particularly, a set of functions introduced in [12] can be used within the present method.

2.1 Numerical solution of the equations (7) and (8) using the VPM

Instability of numerical solution of the equation (7) caused by the stretching term $(\boldsymbol{\omega} \cdot \nabla)\mathbf{u}$ is the most important problem of the VPM along with the computation of the velocity $\mathbf{u}^v$. In grid based methods with low and moderate order schemes, the action of the stretching is effectively counterbalanced by the numerical viscosity which is very low in Langrangian vortex particle methods. Theoretically, a stable VPM solution can be obtained by increasing the accuracy of the stretching and diffusion simulation which can be attained by a high number of vortex particles and high temporal resolution. Both make the method impractical at least for high Reynolds numbers. After many efforts the authors settled on the algorithm which was originally proposed by [7] and modified in [11]. This algorithm consists of the following substeps:
• Calculation of the change of the vorticity strength magnitude

$$\frac{d|\boldsymbol{\omega}^v|}{dt} = \frac{d\sqrt{\boldsymbol{\omega}^v \cdot \boldsymbol{\omega}^v}}{dt} = \frac{\boldsymbol{\omega}^v}{|\boldsymbol{\omega}^v|} \cdot \frac{d\boldsymbol{\omega}^v}{dt} \tag{10}$$

where $\frac{d\boldsymbol{\omega}^v}{dt}$ is calculated from (7) without the viscous diffusion term. The term $(\boldsymbol{\omega}^v \cdot \nabla)\mathbf{u}^v$ is calculated taking into account adjacent vortex particles located only within one or two layers of neighboring cells.
• Calculation of the particle length from the equation of the elementary section dl transported in inviscid flow

$$\frac{dl}{dt} = \frac{l}{|\boldsymbol{\omega}^v|} \frac{d|\boldsymbol{\omega}^v|}{dt} \tag{11}$$

• Calculation of the particle core radius from the equation describing the transport of an elementary tube with length l and radius σ in inviscid flow

$$\frac{d\sigma}{dt} = -\frac{\sigma}{2l} \frac{dl}{dt} \tag{12}$$

- Consideration of the viscosity influence using the core spreading method (CSM) (see [5]). The particle core radius is increased by $\Delta\sigma$:

$$\Delta\sigma = \sqrt{4\nu\Delta t} \tag{13}$$

- Calculation of the new particle orientation

$$\boldsymbol{\omega}^* = \boldsymbol{\omega}^v(t) + \frac{d\boldsymbol{\omega}^v}{dt}\Delta t \tag{14}$$

- Calculation of the particle strength magnitude from [7]

$$|\boldsymbol{\alpha}(t+\Delta t)| = |\boldsymbol{\alpha}(t)|\frac{\sigma(t+\Delta t)}{\sigma(t)} \tag{15}$$

- Calculation of the new strength vector

$$\boldsymbol{\alpha}(t+\Delta t) = |\boldsymbol{\alpha}(t+\Delta t)|\frac{\boldsymbol{\omega}^*}{|\boldsymbol{\omega}^*|} \tag{16}$$

In the original version proposed by [7] the next step should be the redistribution of particles whose length has doubled. According to our experience the redistribution results in an avalanche-like increase of the vortex particles number in areas of strong stretching. To prevent this [7] proposed a special elimination procedure based on a knowledge of a threshold for the dissipation rate which is difficult to set in a general flow case. To develop a robust code, to obtain a stable solution and to keep the particle number in a reasonable range we avoid the redistribution procedure in our computations. Thus, the smallest vortices are removed. This reduces the range of scales that must be resolved in a numerical calculation. Such a reduction, as pointed out by [3], is an immanent part of every turbulence model.

There is a permanent exchange between the small vortices and large scale ones represented on the grid. Large scale vortices become small due to stretching and are converted to particles. If particles grow due to viscosity and flow stagnation and exceed some size they are mapped back to the grid. The simple Euler method is used for the integration of the differential equations. The flowchart of the whole algorithm is presented in [11].

The present method has the same error sources as every LES model [6]. Two comments should be made on the filtering errors. First, the applicants understand that the models relying on the small scales comparable with cell sizes can suffer from the filter aliasing errors inherently presented in each numerical method. For instance, such errors most strongly affect dynamic type models which rely heavily on the smallest scales to determine SGS properties [6].Second, since our algorithm does not use commutation of differencing and filtering operators which is the big difficulty in LES formalism and represents the second part of the filtering errors, the commutation error is not present.

3 RESULT AND DISCUSSION

3.1 Summary of previous result

Validation and verification is performed for wall free flows including decaying isotropic turbulence (DIT) [4] and free turbulent jet [8, 2] test cases. Results revealed that the effect of the term $\overline{\mathbf{u}^v \times \boldsymbol{\omega}^g}$ in the equation (7) is similar to that of a LES subgrid model. The term $\overline{\mathbf{u}^v \times \boldsymbol{\omega}^g}$ behaves as an energy drain transferring the energy of the grid based motion into the fine scale energy. At coarse resolutions, it acts as a diffusive Large Eddy Simulation subgrid model resulting in a LES-like behavior of the whole method.

The additional term $\overline{\mathbf{u}^v \times \boldsymbol{\omega}^g}$ is automatically switched off when the resolution increases, the present method is consistent and converges to the Direct Numerical Simulation. The energy back scattering is also captured by the present method. As mentioned in [16], the intensification of the turbulent kinetic energy due to back scattering is proved to be very important to properly reproduce the jet breakdown and transition to turbulence close to the nozzle without any artificial turbulence forcing at the nozzle. The Reynolds stresses of the velocity field induced by particles possess the pronounced anisotropy which is space dependent. It was also shown that the model for the jet case can be sufficiently reduced by neglecting the inner interaction between particles. This results in a drastic reduction of the computational time. Some additional result on the model reduction and anisotropy Reynolds stresses are given in the next section. The result are obtain for the free jet at the Reynolds number $Re = 10^4$. More details about grid properties and set up of the simulation are thoroughly described in [16].

3.2 Model reduction

As shown in [11] the equations 7 and 8 can sufficiently be reduced by neglecting inner interaction between vortex particles without a significant loss of the simulation accuracy. The reduced equations take the form:

$$\frac{\partial \boldsymbol{\omega}^v}{\partial t} + (\boldsymbol{u}^g \cdot \nabla)\boldsymbol{\omega}^g = (\boldsymbol{\omega}^v \cdot \nabla)\mathbf{u}^g + \nu\Delta\boldsymbol{\omega}^v, \tag{17}$$

and the r.h.s of the trajectory equation (18) contains only the grid based velocity

$$\frac{d\mathbf{r}_i}{dt} = \mathbf{u}_i^g \tag{18}$$

As seen in [11], the influence of inner interactions on spatially averaged kinetic energy and scalar dissipation rate is relatively weak and can be neglected in the calculation. Thereby the computations can be done sufficiently faster.This model is further referred to as the passive vortices model. Within the next simplification step the influence of the grid based solution on the evolution of vortex particles strengths is neglected. The equations describing the vortex particle evolution take the simplest form:

$$\frac{\partial \boldsymbol{\omega}^v}{\partial t} + (\boldsymbol{u}^g \cdot \nabla)\boldsymbol{\omega}^g = \nu\Delta\boldsymbol{\omega}^v, \tag{19}$$

179
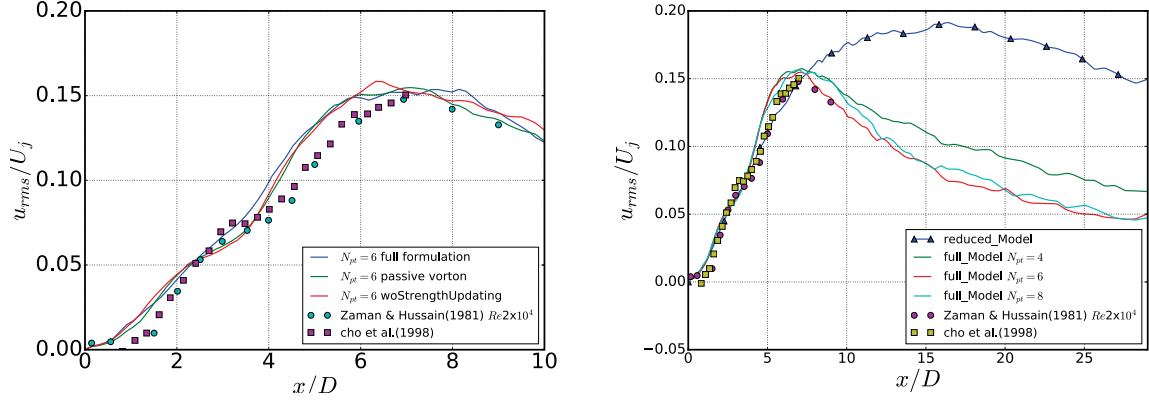
(a) influence of ignoring inner interaction between vortex particles

(b) influence of considering vortex particles only in the curretn time step

Figure 1: Influence of the interaction between vortex particles and grid on the evolution of u_{rms}

$$\frac{d\mathbf{r}_i}{dt} = \mathbf{u}_i^g \tag{20}$$

Figure 1-a demonstrates results for the r.m.s. of the axial velocity obtained using the full model equations 7 and 8, passive vortices model equations 17 and 18 and the model without influence of the grid based flow on vortex particles strengths equations 19 and 20. The difference between results is negligible pointing out that vortex particles serve just as triggers or intensifiers of turbulence and their inner interaction doesn't contribute sufficiently to the flow evolution. Hence the name of the method is the LES intensified by the vortex particles or VπLES .

In the next step of model reduction only the influence of vortex particles generated in the current time step are considered and vortex particles generated in the previous time step were mapped back to the grid. In this case the time of computations is less than full model since we only deal with a vortex particles in the current time step. As can be seen in Figure 1-b the result shows that the vortex particles trigger the turbulence and have a good agreement with experiment in the near jet exit region while in far field region decay of kinetic energy is not physical. It can be interpreted in this way that the energy drain of fine scale motion from large scale motion is not high enough and accumulation of kinetic energy on the grid flow motion happens. Concluding, not only new generated vortices but also the whole set of vortices including those generated upstream in previous time steps have a significant influence on the turbulence development downstream. With other words, the fine scale vortices model (7) and (8) can be reduces but not neglected.

3.3 Anisotropy of fine scale structures induced by vortex particles

Since a deterministic prediction of a turbulent flow as mentioned in the definition of the turbulent motion by Lesieur [13] is practically impossible, the task of every SGS model is to reproduce the subgrid motion only in the statistical sense. The following features of the

(a) total velocity $(u^g + u^v)$

(b) fine scale velocity u^v
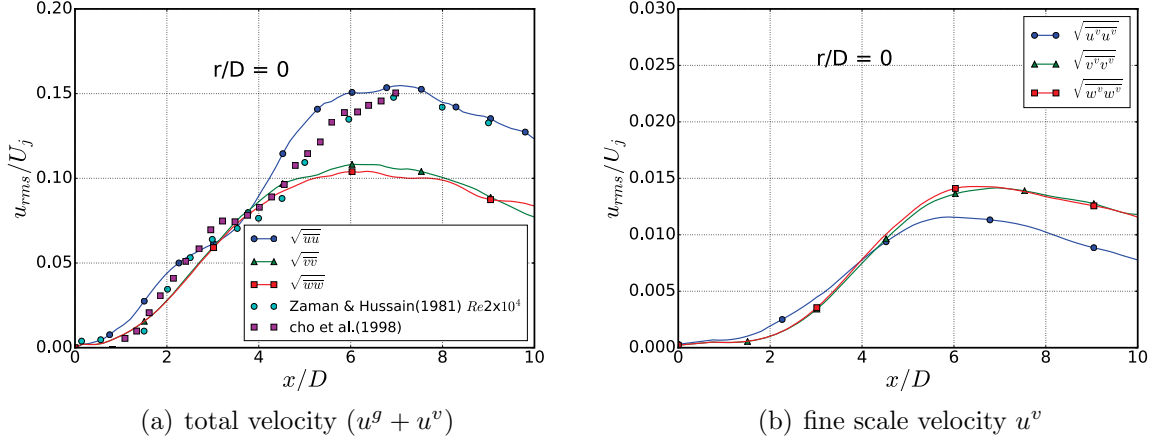
Figure 2: Distribution of the diagonal Reynolds stresses components for the total and fine scale velocity along the jet axis

subgrid motion should be captured by a proper subgrid model: non-equilibrium effects including laminar-turbulent zone, energy backscatter and anisotropy of fine scale motion. In this subsection the anisotropy of velocities induced by fine vortices is discussed.

The total flow shows a well pronounced anisotropy with the dominance of the axial fluctuations on the jet centerline (see Fig. 2-a). Reynolds stresses R_{ii}^v of the velocity field $\mathbf{u^v}$ shows also a clear anisotropy which is space-dependent. On the center line at $x/D > 5$ two diagonal stresses are equal to each other $R_{22}^v \approx R_{33}^v$ and dominate over R_{11}^v (see Fig. 2-b). To explain this effect, we consider stochastic distribution of the statistically independent axis-symmetric vortex particles on the centerline with strengths aligned with the x-axis. They induce velocities $u_x^v = 0$ and $u_y^v \neq 0$, $u_z^v \neq 0$. Due to axis symmetrical character of each vortex the spatially averaged squares of velocities u_y^v and u_z^v are equal, i.e. $\overline{(u_y^v)^2} = \overline{(u_z^v)^2}$. Precession of vortices around their spins causes the appearance of the longitudinal velocities u_x^v which are much smaller than u_y^v and u_z^v. Thus, the jet axis area at $x/D > 5$ is populated by vortex particles with axes predominantly oriented along the jet propagation or mean flow direction. At $x/D < 5$ on the centerline and $r/D = 0.25$ the fine scale turbulence is nearly isotropic $R_{11}^v \approx R_{22}^v \approx R_{33}^v$ in the beginning of the jet development (see Fig. 3-a), i.e. this area is populated with vortex particles with orientations uniformly distributed around a sphere. Further downstream the same anisotropy takes place as that on the jet axis. At the jet boundary the fine scale turbulence becomes anisotropic with a clear dominance of the radial fluctuations $R_{22}^v > R_{11}^v \approx R_{33}^v$ (see Fig. 3-b), i.e. the dominating fluctuations are in the direction of the dominating large scale entrainment motion. Figures 4 shows the p.d.f of vortex axes orientation where L_x, L_y and L_z are defined as $Lx = \frac{\boldsymbol{\alpha}_x}{|\boldsymbol{\alpha}|}$, $Ly = \frac{\boldsymbol{\alpha}_y}{|\boldsymbol{\alpha}|}$, $Lz = \frac{\boldsymbol{\alpha}_z}{|\boldsymbol{\alpha}|}$.

4   CONCLUSION

The paper presents validation and verification study of a novel VπLES method which is based on the decomposition of the flow structures in large scale ones, resolved on the grid,
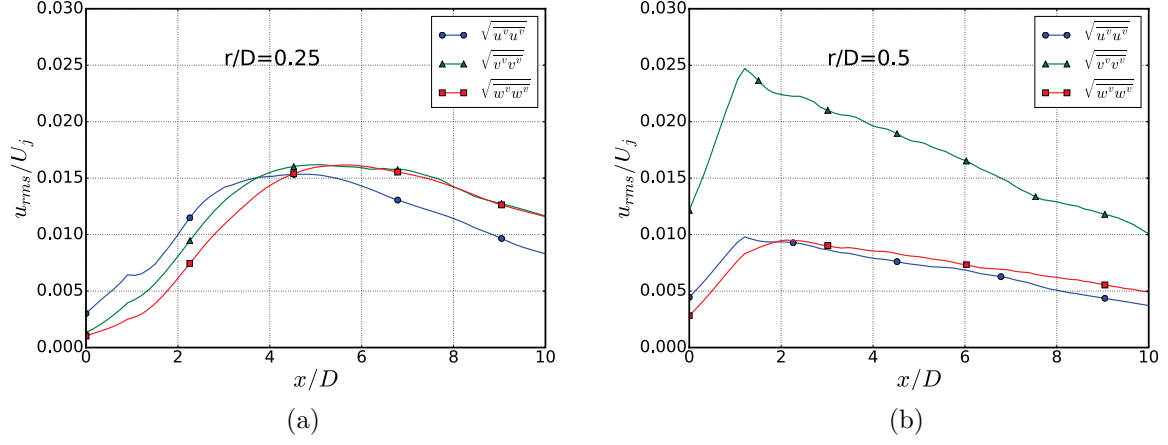
Figure 3: Distribution of the diagonal Reynolds stresses components for the fine scale velocity u^v along the line $r/D = 0.25$ and $r/D = 0.5$
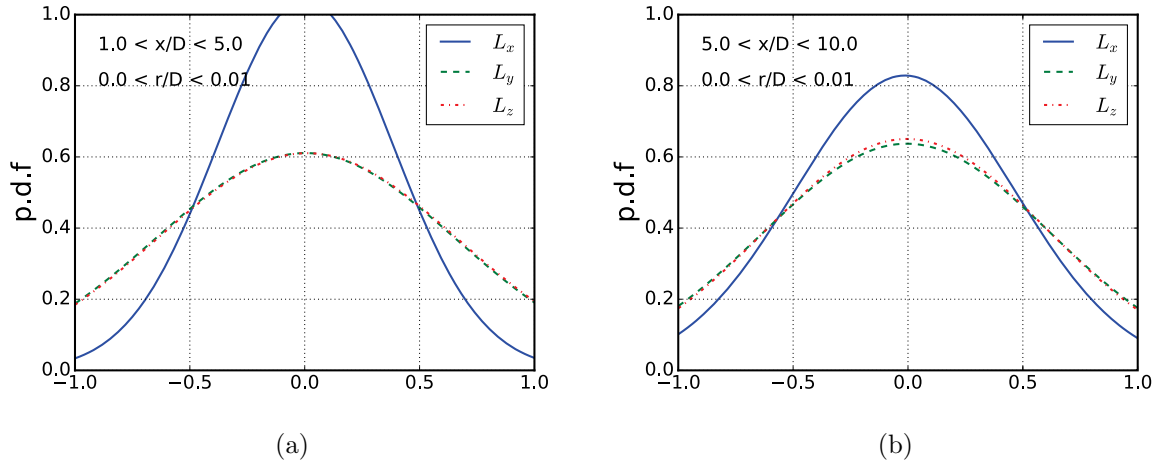
Figure 4: p.d.f of vortex axes orientation line $r/D = 0$

and small scale ones, represented by vortex particles ([10] and [11]). In this paper it was shown that the model can be sufficiently reduced. However, the reduction has a certain limit. The inner interaction between vortices and the influence of large scales on strengths of fine vortices can be neglected. This results in a very efficient and fast computational procedure. However, velocity field induced by particles possesses a pronounced anisotropy which is space dependent. The future work is the validation of VπLES for wall bounded flows.

REFERENCES

[1] Chakraborty, P., Balachandar, S., and Adrian, R. On the relationships between local vortex identification schemes. *Journal of Fluid Mechanics 535* (2005), 189–214.

[2] Cho, S. K., Yoo, J. Y., and Choi, H. Vortex pairing in an axisymmetric jet using two- frequency acoustic forcing at low to moderate Strouhal numbers. *Experiments in Fluids 25*, 4 (1998), 305–315.

[3] Chorin, A. *Vorticity and turbulence.* Springer, 1994.

[4] Comte-Bellot, G., and Corrsin, S. Simple Eulerian time correlation of full- and narrow-band velocity signals in grid-generated, isotropic turbulence. *Journal of Fluid Mechanics 48*, 2 (1971), 273–337.

[5] Cottet, G., and Koumoutsakos, P. *Vortex Methods: Theory and Practice.* Cambridge University Press, 2000.

[6] de Villiers, E. *The Potential of Large Eddy Simulation for the Modeling of Wall Bounded Flows.* PhD thesis, Imperial College of Science, Technology and Medicine, 2006.

[7] Fukuda, K., and Kamemoto, K. Application of a redistribution model incorporated in a vortex method to turbulent flow analysis. In *Proceedings of the 3rd International Conference on Vortex Flows and Vortex Models (ICVFM2005)* (Yokohama, Japan, 2005).

[8] Hussain, A. F., and Zaman, K. B. M. Q. The preferred mode of the axisymmetric jet. *J. Fluid Mech. 110* (1981), 39–71.

[9] Kornev, N. Improvement of vortex resolution through application of hybrid methods. In *Proceedings of the 6th International Conference on Vortex Flows and Vortex Models, Nagoya, Japan* (2014).

[10] Kornev, N. Hybrid method based on embedded coupled simulation of vortex particles in grid based solution. *Computational Particle Mechanics 5*, 3 (2018), 269–283.

[11] Kornev, N., and Samarbakhshl, E. Large Eddy Simulation with direct resolution of subgrid motion using a grid free vortex particle method. *International Journal of Heat and Fluid Flow 75* (2019), 86–102.

[12] Leonard, A., and Winckelmans, G. Contribution to vortex particle methods for the computation of three-dimensional incompressible unsteady flows. *J. Comput. Phys., 109* (1993), 247–273.

[13] Lesieur, M. *Turbulence in fluids.* Kluwer Academic Publishers, Dordrecht, 1997.

[14] Mosher, M. A method for computing three dimensional vortex flows. *Zeitschrift für Flugwissenschaften 9*, 3 (1985), 125–133.

[15] Russ, S., and Strykowski, P. Turbulent structure and entrainment in heated jets: The effect of initial conditions. *Physics of Fluids A: Fluid Dynamics 5*, 12 (1993), 3216–3225.

[16] Samarbakhsh, E., and Kornev, N. Simulation of the free jet using the vortex particle intensi

ed LES (VπLES). *International Journal of Heat and Fluid Flow submitted* (2019).

VORTICITY DYNAMICS PAST AN INCLINED ELLIPTICAL CYLINDER AT DIFFERENT RE NUMBERS: FROM PERIODIC TO CHAOTIC SOLUTIONS

O. Giannopoulou*, D. Durante†, A. Colagrossi†◇ and C. Mascia*

* Department of Mathematics - Sapienza University of Rome, Rome, Italy
e-mail: giannopoulou@mat.uniroma1.it

†Consiglio Nazionale delle Ricerche - Istituto di iNgegneria del Mare (CNR - INM), Rome, Italy

◇ Ecole Centrale Nantes, LHEEA res. dept. (ECN and CNRS), Nantes, France

Key words: Vortex Particle Methods, Flow past ellipse, Chaotic system

Abstract. Vortex methods offer an alternative way for the numerical simulation of problems regarding incompressible flows. In the present paper, a Vortex Particle Method (VPM) is combined with a Boundary Element Method for the study of viscous incompressible planar flow around solid bodies. The method is based on the viscous splitting approach of Chorin [3] for the Navier-Stokes equations in vorticity-velocity formulation and consists of an advection step followed by a diffusion step. The evaluation of the advection velocity exploits the Helmholtz-Hodge Decomposition (HHD), while the no–slip condition is enforced by an indirect boundary integral equation. In order to deal with the problem of disordered spacial distribution of particles, caused by the advection along the Lagrangian trajectories [1], in the present method the particles are redistributed on a Regular Point Distribution (RPD) during the diffusive step. The RPDs close to the solid bodies are generated through a packing algorithm developed by [4], thanks to which the use of a mesh generator is avoided. The developed Vortex Particle Method has been called Diffused Vortex Hydrodynamics (DVH) and it is implemented within a completely meshless framework, hence, neither advection nor diffusion requires topological connection of the computational nodes. The DVH has been extensively validated in the past years (see *e.g.* [8]) and is used in the present article to study the vorticity evolution past an inclined elliptical cylinder while increasing the Reynolds number from 200 up to 10,000 in a 2D framework. The flow evolution is characterized by a periodic behaviour for the lower Reynolds numbers which is gradually lost to give its the place to a chaotic behaviour.

1 INTRODUCTION

Two dimensional studies of flow past bluff bodies is long researched problem due to the importance and utility of flow separation, its immediate impact on the forces on the both in aerodynamic and hydrodynamic applications. While most of the studies are concentrated on the circular cylinders, applications require the study of a less symmetric geometry in order

to be more realistic as for is the case of an elliptical cylinder which can exhibit richer flow characteristics.

Studies of the dynamical characteristics on two dimensional flows past elliptic cylinders involve mostly works at *low Reynolds regimes*. The questions addressed at these regimes include establishing the critical Reynolds for separation to occur and their dependence from different aspect ratios (see for example [14], [11], [7], [12], [20]). At these Reynolds it is possible to study the inception of instabilities using *analytic or semi-analytic* tools as in [10], [15].

Additionally, a large part of the studies performed concern the near wake characteristics. On the other hand, also the far wake analysis may reveal important qualities of the flow for the relevant applications (for example acoustics or sound propagation). Regarding the far wake wake studies of elliptic cylinders, these also refer to low to moderate Reynolds numbers (< 1000), for varying both the angle of incidence and the Reynolds number.

In the current work, the goal is to extend the study of the flow past an elliptic cylinder at incidence to Reynolds between 200 and 10000 and to study the characteristics of the wake using tools from non linear dynamical systems such as Lyapunov theory. Moreover, the numerical simulations are performed using a VPM, which allows to study the more realistic unbounded problem without enforcing any unphysical boundary condition on the computational domain.

Vortex Particle methods are Lagrangian methods for the numerical simulation of unsteady viscous flow problems (see *e.g.* [6]) where the fluid is discretized into vortex elements. These methods have the definite advantage of eliminating the pressure, requiring no CFL condition, and the implicit fulfillment of the far field conditions.

The Vortex Particle Method described in this work is called Diffused Vortex Hydrodynamics (DVH), recently developed and tested on numerous benchmark tests (see [16–18], [5] and [8]). This approach yield an accurate evaluation of both near and far flow fields. In the numerical simulations considered, high spatial resolutions are used for the near field around the body as well as for the wake region. Furthermore, computations were carried out for very long time, in order to achieve stable regime values of average forces and of their oscillating part.

In the present paper, the study of the flow past an ellipse at incidence is discussed. The Reynolds number is changing from 200 up to 10000, whereas the angle of attack remains constant at 20°. The main goal of the paper is to study the effect of the Reynolds on the drag and lift forces and also to reveal the way in which the periodic behaviour of the solution leads to the inception of a chaotic regime.

The paper is organized as follows: in section 2 the essential features of the methodology followed in this work are reported, whereas in section 3 the evolution from periodic to non periodic of the lift and drag coefficients is investigated for increasing Reynolds numbers.

2 Brief description of DVH algorithm

In this section, the main characteristics of the vortex particle method (DVH) used for simulations are briefly discussed; further details can be found in [16–18].

The vorticity formulation of the two-dimensional, incompressible Navier-Stokes equations is used and the evolution of the flow field is solved through an operator splitting.

By following [2], an advection step and a diffusion step are defined. The advection step is:

$$\begin{cases} \dfrac{D\omega}{Dt} &= 0 \\[2mm] \dfrac{D\mathbf{x}}{Dt} &= \mathbf{u}(\mathbf{x},t) \end{cases} \qquad \text{with} \qquad \nabla^2\mathbf{u} = -\nabla \times \omega \qquad (1)$$

where $\mathbf{u}(\mathbf{x},t)$ is the velocity field of the material point $\mathbf{x}$ at time t and $\omega = |\omega|$ is the vorticity modulus. The right equation in (1) is the Poisson equation linking the vorticity with the velocity field.

The velocity field is decomposed through a HHD in a curl-free (potential) part $\mathbf{u}_\phi$ and a divergence–free (non potential) part $\mathbf{u}_\omega$. The velocity component due to the free stream $\mathbf{u}_\infty$ is also added. The $\mathbf{u}_\omega$ component is obtained through the Biot–Savart law in a 2D framework for an unbounded domain. Indeed this law is a free solution of the Poisson equation (1). The enforcement of the no-slip boundary condition on ∂D_B is performed with the $\mathbf{u}_\phi$ solution using an Indirect Boundary Element Method (IBEM). The IBEM solution also provide the circulation density distribution γ used as source term during the diffusion-step.

The latter consists in the diffusion of the vorticity due to the viscosity which is a phenomenon governed by the linear heat equation:

$$\begin{cases} \partial_t\omega &= \nu\nabla^2\omega, \qquad \mathbf{x} \in D \\[2mm] \nu\dfrac{\partial\omega}{\partial n} &= -\dot{\gamma}, \qquad \mathbf{x} \in \partial D_B \end{cases} \qquad (2)$$

where γ is the circulation density on ∂D_B which, as stated above, is exploited to enforce the no-slip condition on the solid boundary (for details see [9])

In order to discretize the above PDEs, the vorticity field is discretized by a collection of N_v discrete vortices as:

$$\omega(\mathbf{x},t) = \sum_{j=1}^{N_v} \Gamma_j(t)W_\epsilon(\mathbf{x}-\mathbf{x}_j(t)), \qquad (3)$$

where Γ_j is the circulation of the j-th particle and W_ϵ is the kernel function, which is a smoothed Dirac function with parameter $\epsilon > 0$.

3 Flow past ellipse with angle of attack $\alpha = 20°$ for different Reynolds numbers

The geometry considered for this test case is an ellipse set at incidence $\alpha = 20°$, with a Reynolds number spanning from 200 to 10000. The axes ratio is $b/a = 0.4$, a and b being the major and minor axes respectively; in order to be consistent with the usual definition for an airfoil, the Reynolds number is defined as Re $= Ua/\nu$, where U is the modulus of the free stream velocity and ν is the kinematic viscosity.

From the vorticity fields (see figure 2), a very smooth arrangement of the wake dipoles is evident for Re up to 3000, whereas it appears definitely chaotic for higher Reynolds numbers (figure 3).

This behaviour is in agreement with [19], where, by changing the Reynolds number at fixed incidence, the vorticity wake pattern changes with the Reynolds number becoming even more

187
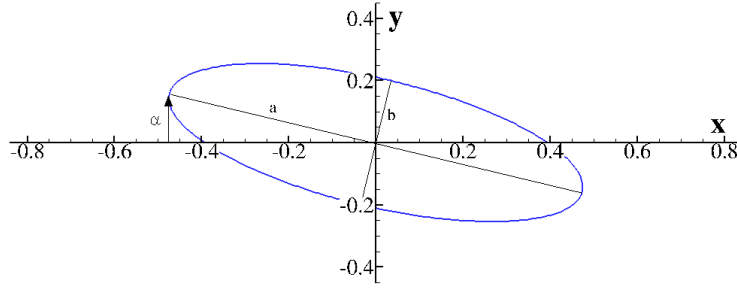
Figure 1: Ellipse geometry. a, b are the major and minor axes, respectively, and α is the angle of attack

chaotic with its increasing. Accordingly, the lift time histories (in figure 4) are very regular for $Re \leq 3000$ and the Fourier transforms (in figure 5) show one greater evident peak corresponding to the Strouhal shedding frequency; at $Re = 4000$ subharmonic modulations are manifested in the time signal and reflected in the Fourier spectrum where peaks at lower intensity appear almost symmetrically respect to the dominant one. From $Re = 5000$ to $Re = 10000$ the spectra become continuous without the evidence of a single dominant peak and similarly the wakes do not exhibit an ordered arrangement of the vorticity cores anymore.

Regarding the time-averaged values of C_L and C_D, the figure 6 shows the variation of the force coefficients with the Reynolds number.

For $200 \leq Re \leq 1000$, the ellipse manifests a drag force greater than the lift, while a sudden increase of the lift force is evident for Re up to 4000. For $Re = 5000$ the lift drops down, although it rise up again for $Re = 6000$ and then lowers with the increasing of the Reynolds number. The figure 7 shows the maximum Lyapunov exponents variation with the Reynolds number. The exponents are calculated for every lift time history according the Wolf algorithm [21]. The Lyapunov exponent of a dynamical system is a quantity characterizing the rate of separation of infinitesimally close trajectories, so that it represents a measure of the sensitivity of the system to become unstable under certain initial conditions. Positive values of the exponent may indicate an evolution of the system toward a chaotic behaviour, although it does not represent a sufficient condition (see for example [13]). From 200 to 3000, coherently with the vorticity wake field and with the Fourier transforms, the Lyapunov exponents are very low, meaning that the system is in a equilibrium condition. At $Re = 4000$ the exponents start to increase and at $Re = 5000$ assume the greatest value, when the system moves toward a chaotic condition. After $Re = 5000$ the exponents lower with the increasing of the Reynolds number. In figure 8, the phase portraits diagram $C_L - \dot{C}_L$ are shown and coloured with an intensity increasing with the time. A single and sharp orbit is visible for Re up to 4000, where a large number of orbits appears.
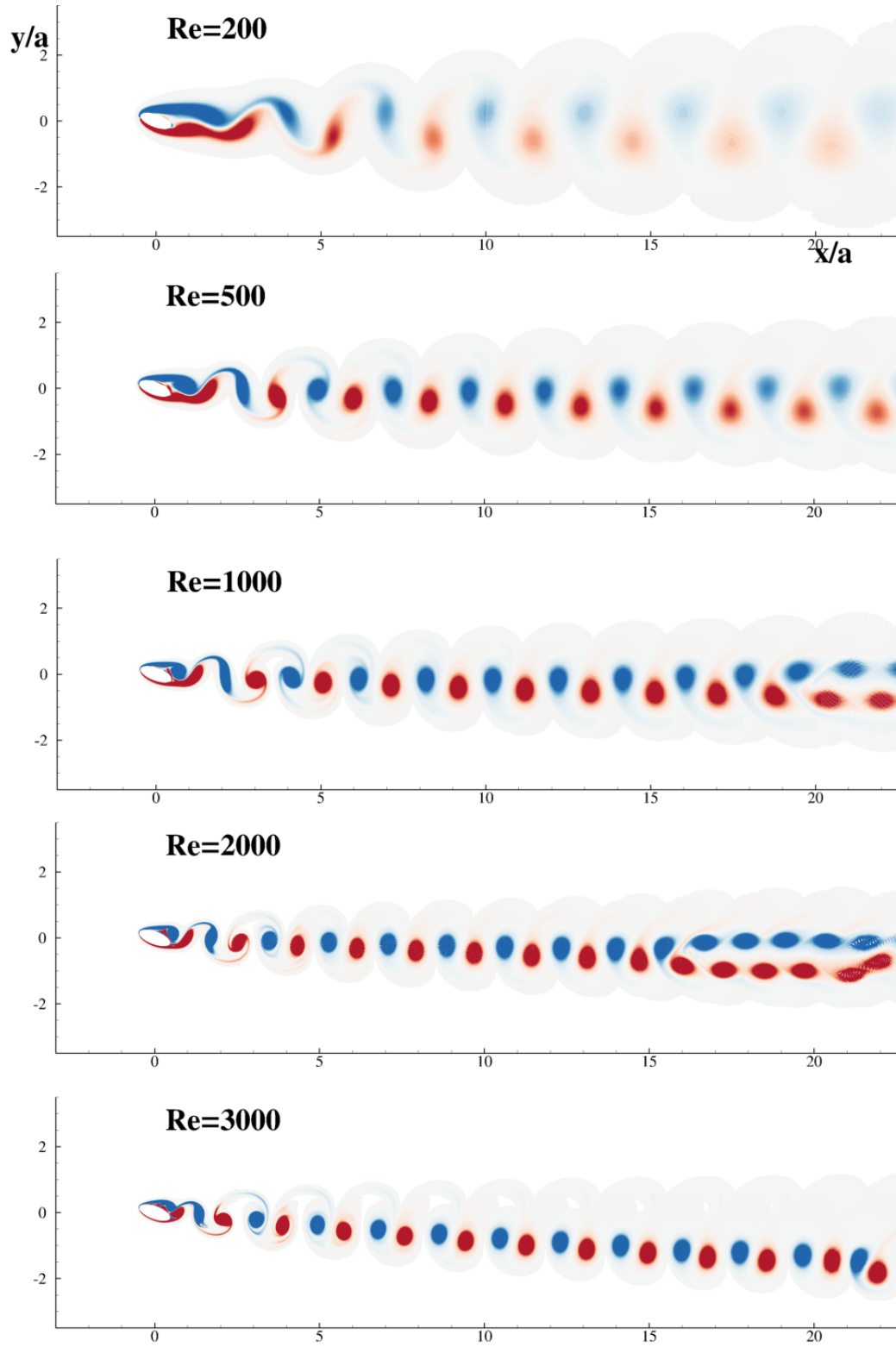
Figure 2: Vorticity fields for the flow past an ellipse from *Re* = 200 to *Re* = 3000. Dimensionless vorticity $\omega a/U$ scales from -2 (blue) to 2 (red).
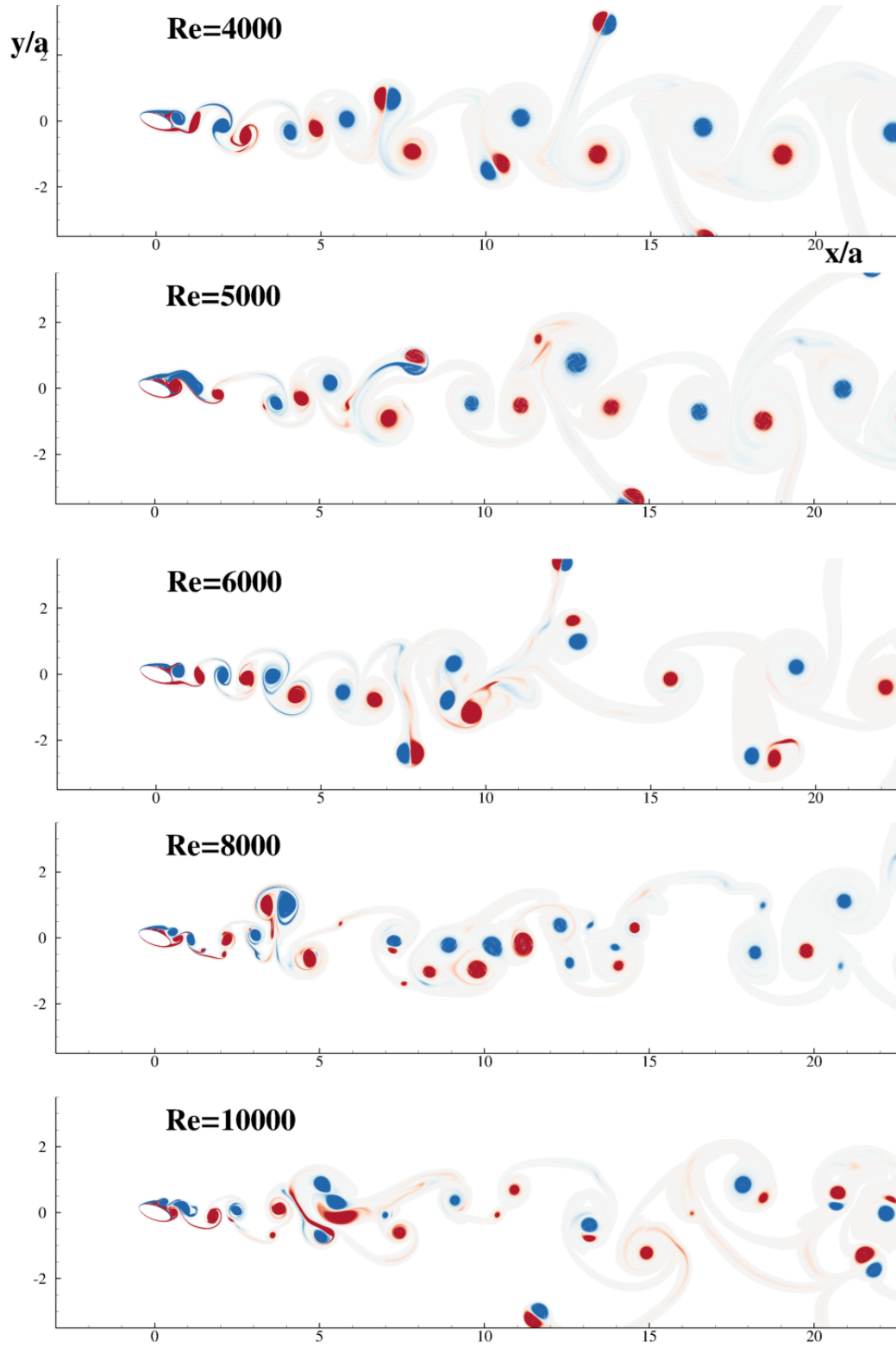
Figure 3: Vorticity fields for the flow past an ellipse from $Re = 4000$ to $Re = 10000$. Dimensionless vorticity $\omega a/U$ scales from -2 (blue) to 2 (red).
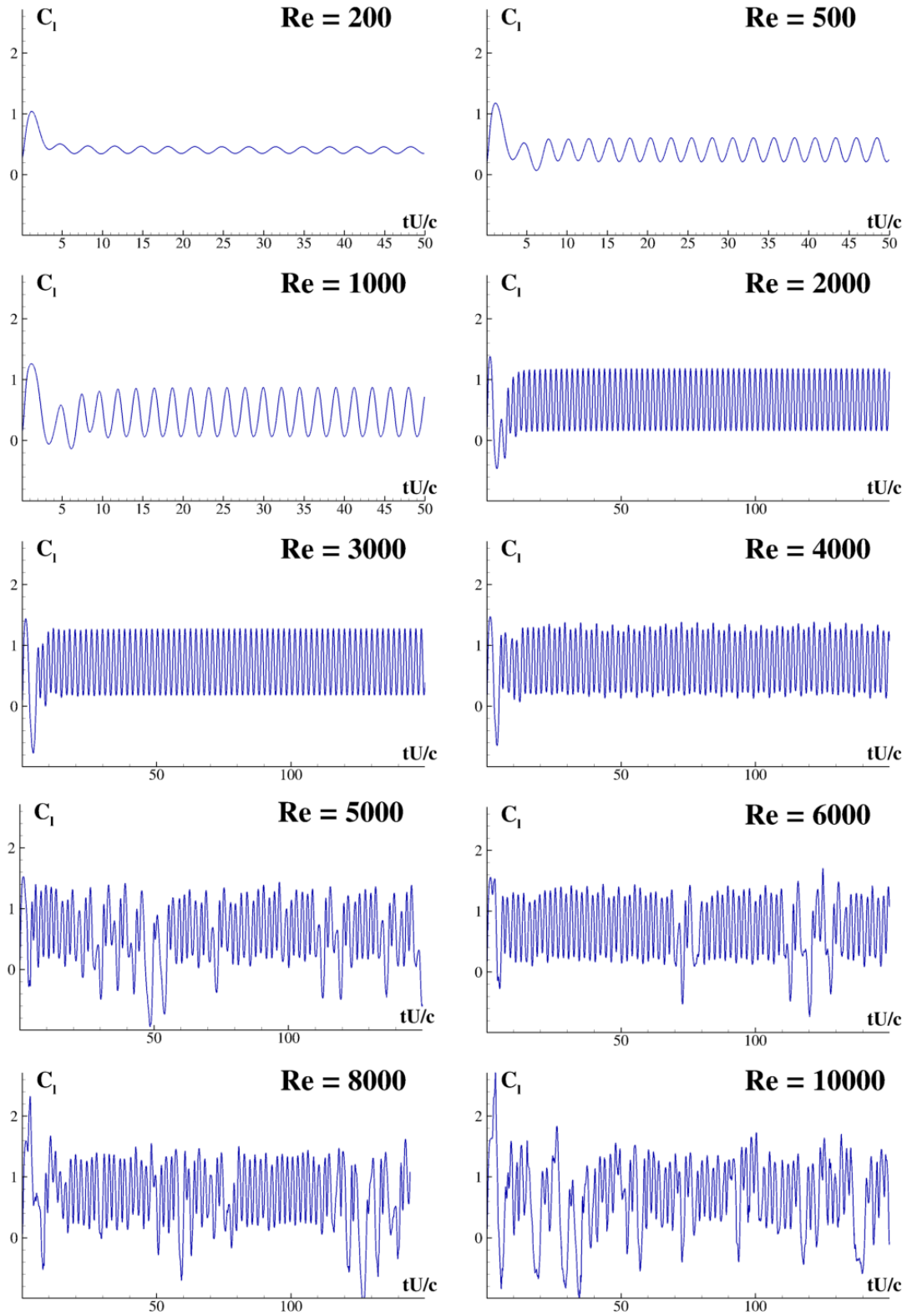
Figure 4: Time history of the lift coefficients for the Reynolds numbers simulated.
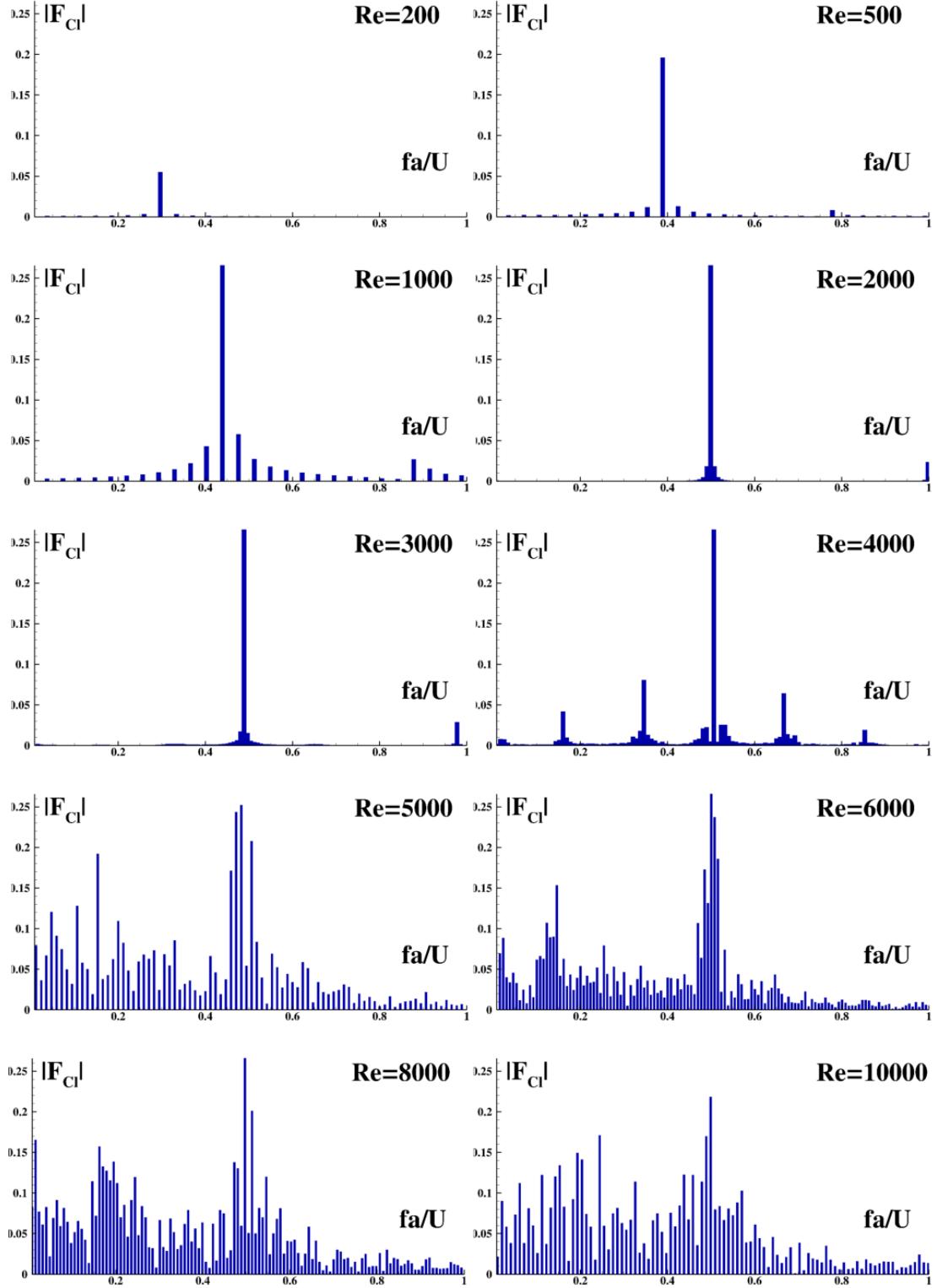
Figure 5: Fourier coefficients for the lift time history for the Reynolds numbers under study
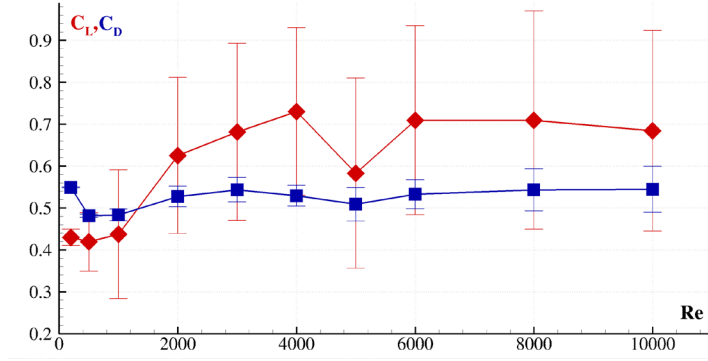
Figure 6: Time averaged Lift $\bar{C}_L$ and Drag $\bar{C}_D$ coefficients versus *Re* number. The error bars corresponding to standard deviations are also indicated.

The chaotic time histories of the lift force for $Re \geq 5000$, portrayed in figure 4, are immediately related to the impossibility for the system to find a stable limit cycle. As shown in figure 7, from $Re = 5000$ the system passes toward a chaotic state that persists for higher Reynolds numbers.
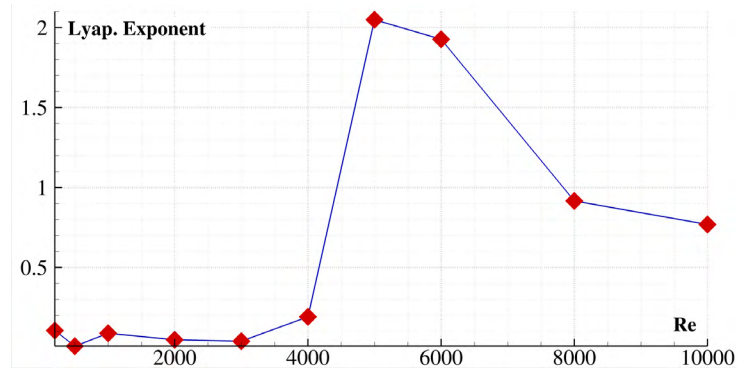
Figure 7: Maximum Lyapunov exponents of the lift coefficients, for each Reynolds number studied.

4   Conclusion and perspectives

In the present work, the flow past an ellipse at $20°$ is investigated for varying Reynolds number. The vorticity wake field, as well as the lift force are analysed. In particular, the Fourier transform and the $C_L - \dot{C}_L$ maps are sketched and exploited for the analysis of the system stability. The maximum Lyapunov exponents of the lift force are also calculated and their behaviour with the Reynolds number has been reported. In order to get a better insight on the dynamical system, a wider number of simulations must be performed, clustering them within the interval $4000 - 5000$, where the chaotic behaviour take place. Moreover, the effect of the thickness of the ellipse at fixed Reynolds number may be interesting and should be analysed in the extended version of the present paper.
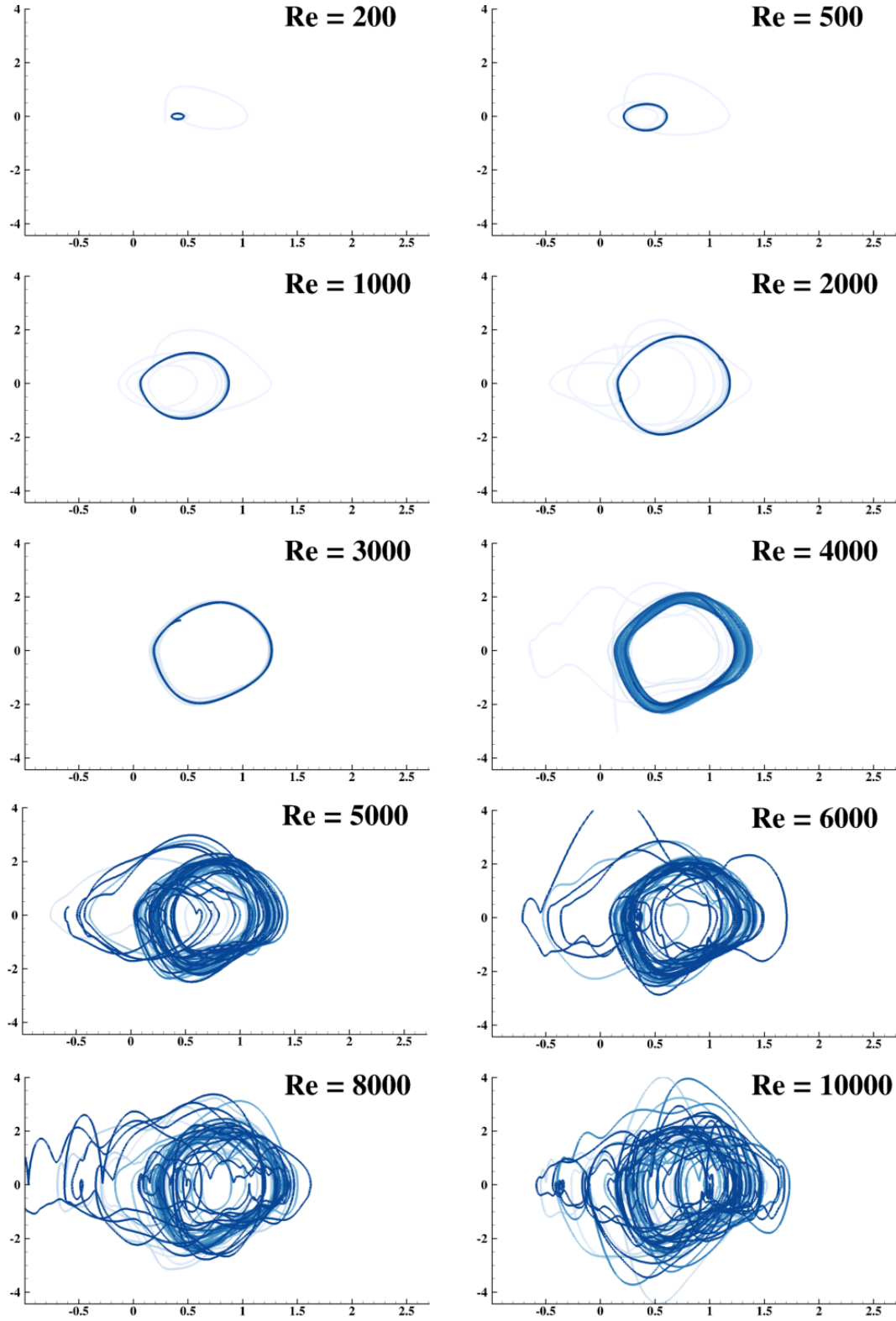
Figure 8: $C_L - \dot{C}_L$ maps for the Reynold numbers simulated.

REFERENCES

[1] L. Barba, A. Leonard, and C. Allen. Vortex method with fully mesh-less implementation for high-reynolds number flow computations. *European Congress on Computational Methods in Applied Sciences and Engineering ECCOMAS*, pages 24–28, 08 2004.

[2] A. J. Chorin. A numerical method for solving incompressible viscous flow problems. *Journal of computational physics*, 2(1):12–26, 1967.

[3] A. J. Chorin. Numerical solution of the Navier-Stokes equations. *Mathematics of computation*, 22(104):745–762, 1968.

[4] A. Colagrossi, B. Bouscasse, M. Antuono, and S. Marrone. Particle packing algorithm for SPH schemes. *Computer Physics Communications*, 183(8):1641–1653, 2012.

[5] A. Colagrossi, E. Rossi, S. Marrone, and D. Le Touzé. Particle Methods for Viscous Flows: Analogies and Differences Between the SPH and DVH Methods. *Communications in Computational Physics*, 20(3):660–688, 2016.

[6] G.-H. Cottet, P. D. Koumoutsakos, D. Petros, et al. *Vortex methods: theory and practice*. Cambridge university press, 2000.

[7] S. Dennis and P. Young. Steady flow past an elliptic cylinder inclined to the stream. *Journal of engineering mathematics*, 47(2):101–120, 2003.

[8] D. Durante, E. Rossi, A. Colagrossi, and G. Graziani. Numerical simulations of the transition from laminar to chaotic behaviour of the planar vortex flow past a circular cylinder. *Communications in Nonlinear Science and Numerical Simulation*, 48:18–38, 2017.

[9] O. Giannopoulou, A. Colagrossi, A. D. Mascio, and C. Mascia. Chorins approaches revisited: Vortex particle method vs finite volume method. *Engineering Analysis with Boundary Elements*, 106:371388, 2019.

[10] C. Jackson. A finite-element study of the onset of vortex shedding in flow past variously shaped bodies. *Journal of fluid Mechanics*, 182:23–45, 1987.

[11] S. Johnson, M. Thompson, and K. Hourigan. Flow past elliptical cylinders at low reynolds numbers. In *Proc. 14th Australasian Fluid Mechanics Conference, Adelaide University, South Australia, Dec*, pages 9–14, 2001.

[12] M.-S. Kim and A. Sengupta. Unsteady viscous flow over elliptic cylinders at various thickness with different reynolds numbers. *Journal of mechanical science and technology*, 19(3):877–886, 2005.

[13] G. A. Leonov and N. V. Kuznetsov. Time-varying linearization and the perron effects. *International journal of bifurcation and chaos*, 17(04):1079–1107, 2007.

[14] J. K. Park, S. O. Park, and J. M. Hyun. Flow regimes of unsteady laminar flow past a slender elliptic cylinder at incidence. *International Journal of Heat and Fluid Flow*, 10(4):311–317, 1989.

[15] V. Patel. Flow around the impulsively started elliptic cylinder at various angles of attack. *Computers & Fluids*, 9(4):435–462, 1981.

[16] E. Rossi, A. Colagrossi, B. Bouscasse, and G. Graziani. The Diffused Vortex Hydrodynamics method. *Communications in Computational Physics*, 18(2):351–379, 2015.

[17] E. Rossi, A. Colagrossi, D. Durante, and G. Graziani. Simulating 2d viscous flow around geometries with vertices through the diffused vortex hydrodynamics method. *Computer Methods in Applied Mechanics and Engineering*, 302:147–169, 2016.

[18] E. Rossi, A. Colagrossi, and G. Graziani. Numerical Simulation of 2D-Vorticity Dynamics using Particle Methods. *Computers and Mathematics with Applications*, 69(12):1484–1503, 2015.

[19] E. Rossi, A. Colagrossi, G. Oger, and D. LeTouzé. Multiple bifurcations of the flow over stalled airfoils changing the Reynold numbers. *Journal of Fluid Mechanics*, 846:356–391, 2018.

[20] S. Sen, S. Mittal, and G. Biswas. Steady separated flow past elliptic cylinders using a stabilized finite-element method. *Computer Modeling in Engineering & Sciences(CMES)*, 86(1):1–27, 2012.

[21] A. Wolf, J. B. Swift, H. L. Swinney, and J. A. Vastano. Determining lyapunov exponents from a time series. *Physica D: Nonlinear Phenomena*, 16(3):285–317, 1985.

NUMERICAL MODEL OF THE MECHANICAL BEHAVIOR OF COATED MATERIALS IN THE FRICTION PAIR OF HIP RESURFACING ENDOPROSTHESIS

GALINA M. EREMINA², ALEXEY YU. SMOLIN¹

¹ National Research Tomsk State University (TSU)
pr. Lenina 36, 634050, Tomsk, Russia
E-mail: asmolin@ispms.tsc.ru , web page: http://www.tsu.ru

² Institute of Strength Physics and Materials Science (ISPMS)
Siberian Branch of Russian Academy of Sciences
pr. Akademicheskii 2/4, 634055, Tomsk, Russia
E-mail: rector@tsu.ru , web page: http://www. ispms.ru

Key words: hip resurfacing endoprosthesis, coatings, scratch test, friction, simulation, movable cellular automaton method, Movable Cellular Automata, Particle-Based s.

Abstract. The paper is devoted to the theoretical study of the mechanical behavior of materials in the friction pair of hip resurfacing endoprosthesis. The investigation was based on three-dimensional computer simulation by the movable cellular automaton (MCA) method, which is a representative of the methods of particles in the mechanics of materials. The results indicate the promising use of metallic alloys with biocompatible ceramic coatings in friction pairs to increase the service life of hip resurfacing.

1   INTRODUCTION

For the treatment of pathologies of the hip joint in the modern world, endoprosthesis (EP) are widely used. Two types of endoprosthesis are used for hip: total hip replacement and hip resurfacing arthroplasty. For the treatment of osteoporosis and other diseases of the hip joint, a hip resurfacing arthroplasty is preferable. The advantage of using hip resurfacing is the possibility of maintaining healthy bone and the possibility of revision operations [1].

An important factor affecting the durability of the hip joint endoprosthesis is wear in pair of friction "acetabular cup-femur head". In the case of resurfacing, just the surface of the femur head is replaced by the cap, which is specially shaped like a mushroom [2-3]. The difference in the diameters of the hip resurfacing cup and the acetabular cup averages about 2 mm [4]. Polyethylene-metal friction pairs were the first generation of a pair of materials used in a friction pair of hip resurfacing endoprosthesis, however, a large degree of wear led to look for other materials suitable for use in the friction pair [5]. Metal friction pairs based on cobalt-chromium alloys are suitable for the manufacture of endoprosthesis even for young physically active people, since due to their mechanical behavior they are able to withstand high dynamic loads. However, during wear, metal endoprosthesis excrete particles that induce inflammatory processes in the surrounding tissues [6–7]. The use of titanium alloys is a good alternative to the use of cobalt-chromium alloys due to its biocompatible properties, however, these alloys are prone to increased wear. Another group of materials with good

biocompatibility are ceramic products, however, this type of prosthesis is applicable mainly to people with low and medium physical activity due to their tendency to brittle failure under high dynamic loads. Therefore, at present, the directions of hip resurfacing endoprosthesis based on metallic titanium alloys with ceramic coatings [8], which combine good biocompatibility and wear resistance, are being actively developed.

Endoprosthesis testing of has two main stages: preclinical and clinical trials. Clinical trials are carried out by installing the endoprosthesis in a living human body. However, when conducting clinical trials there is a danger that poor-quality or incorrectly chosen endoprosthesis may adversely affect the patient's health, therefore, great attention is paid to preclinical trials in the development of endoprosthesis. Preclinical studies of the mechanical behavior of the endoprosthesis can be divided into experimental and theoretical. Experimental studies are tests using a technological installation that simulates the dynamic loading experienced by the endoprosthesis. Theoretical studies of the mechanical behavior of the endoprosthesis using computer simulation make it possible to investigate the mechanical behavior of endoprosthesis taking into account the influence of various factors.

Most of the work on modeling the mechanical behavior of materials in friction pairs is devoted to total hip replacement. Works on modeling hip resurfacing are mainly devoted to studying the mechanical behavior of a single-component endoprosthesis and the system "bone-endoprosthesis" under dynamic loads without rotation in a friction pair [9-11]. In [12], a force action scheme with rotation of the head in the acetabular cup with and without friction is presented. However, there is no work to simulate the rotational motion of the resurfacing cap in the acetabulum; therefore, it is important to build a numerical model for the rotation of the resurfacing cap in the acetabulum consisting of one-component and two-component materials.

This paper proposes a numerical study of the mechanical behavior of contacting elements of a friction pair consisting of a homogeneous material and a material with a coating during rotational motion using the method of movable cellular automata.

2 METHOD OF MOVABLE CELLULAR AUTOMATA

MCA is a new efficient numerical method in particle mechanics that is different from methods in the traditional continuum mechanics [13,14]. Within the frame of MCA, it is assumed that any material is composed of a certain amount of elementary objects (automata) which interact among each other and can move from one place to another and rotate, thereby simulating a real deformation process. The automaton motion is governed by the Newton-Euler equations:

$$
\begin{cases}
m_i \dfrac{d^2 R_i}{dt^2} = \sum_{j=1}^{N_i} F_{ij}^{\text{pair}} + F_i^{\Omega}, \\
\hat{J}_i \dfrac{d\omega_i}{dt^2} = \sum_{j=1}^{N_i} M_{ij}
\end{cases}
\tag{1}
$$

where $\mathbf{R}_i$, $\boldsymbol{\omega}_i$, m_i and $\hat{J}_i$ are the location vector, rotation velocity vector, mass and moment

of inertia of ith automaton respectively, F_{ij}^{pair} is the interaction force of the pair of ith and jth automata, F_i^{Ω} is the volume-dependent force acting on ith automaton and depending on the interaction of its neighbors with the remaining automata. In the latter equation, $M_{ij} = q_{ij}\left(n_{ij} \times F_{ij}^{pair}\right) + K_{ij}$, here q_{ij} is the distance from the center of ith automaton to the point of its interaction ("contact") with jth automaton, $n_{ij} = \left(R_j - R_i\right)/r_{ij}$ is the unit vector directed from the center of ith automaton to the jth one and r_{ij} is the distance between automata centers, K_{ij} is the torque caused by relative rotation of automata in the pair.

The forces acting on automata are calculated using deformation parameters, i.e. relative overlap, tangential displacement and rotation, and conventional elastic constants, i.e. shear and bulk moduli. A distinguishing feature of the MCA method is calculating of forces acting on the automata within the framework of multi-particle interaction [15,16], which provides for an isotropic behavior of the simulated medium regarded as a consolidated body rather than a granular medium. Moreover, stress tensor components can be calculated for the automaton taking into account all the forces acting on the automaton [15-17], which enables the realization of various models of the plastic behavior of materials developed in the frame of continuum mechanics.

A pair of elements might be considered as a virtual bistable cellular automaton, which permits simulation of fracture and cracks healing and micro welding by the MCA. In this work, a fracture criterion based on the threshold value of von Mises stress was used [15,16]. A criterion based on the threshold value of plastic work was used for making a new bond between contacting automata [16]. Switching of a pair of automata from bonded to non-bonded state and vice versa would result in a changeover in the forces acting on the elements; in particular, non-bonded automata would not resist moving away from one another.

3 DESCRIPTION OF THE MODEL

3.1 Material characterization

From the literature [18] we chose the following values for the material properties of the titanium alloy Ti6Al4V: density $\rho = 4420$ kg/m^3, shear modulus $G = 41$ GPa, bulk modulus $K = 92$ GPa, Young's modulus $E = 110$ GPa, yield stress $\sigma_y = 0.99$ GPa, ultimate strength $\sigma_b = 1.07$ GPa and ultimate strain $\varepsilon_b = 0.10$. The mechanical properties of the TiN coating [19]: density $\rho = 5220$ kg/m^3, shear modulus $G = 104$ GPa, bulk modulus $K = 129$ GPa, Young's modulus $E = 258$ GPa, yield stress $\sigma_y = 3.00$ GPa, ultimate strength $\sigma_b = 3.5$ GPa and ultimate strain $\varepsilon_b = 0.075$.

3.2 Geometry of the model and scheme of loading

In the case of a one-component material, the geometric model consists of a hemisphere simulating the resurfacing cap for femur head, with an external diameter D_ext_cap=36 mm and an interior diameter D_int_cap=33 mm, a hemisphere simulating the acetabulum cup insert, with an outer diameter of D_ext_insert=41 mm and an iterior diameter of D_int_insert=38 mm, and also a prismatic shell for the insert imitating the surrounding bone tissue (fig. 1). In the case of a two-component coated material, hollow hemispheres are additionally specified for the resurfacing cap with an outer diameter of 35.9 mm and an inner

diameter of 33.1 mm (fig.2, a).
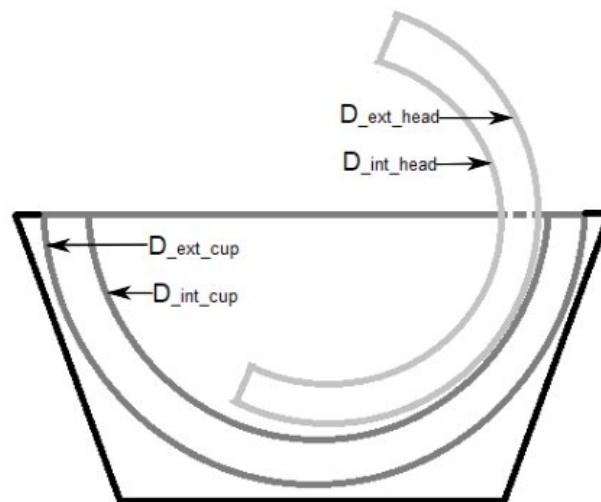
Figure 1. Schematic representation of the model of friction pair of the resurfacing endoprosthesis in cross-section

The load is applied by specifying the translational and rotational velocity of the resurfacing cap automata, corresponding to its rotation as an absolutely rigid body around the axis of symmetry of the corresponding sphere and parallel to the axis X.

a   b
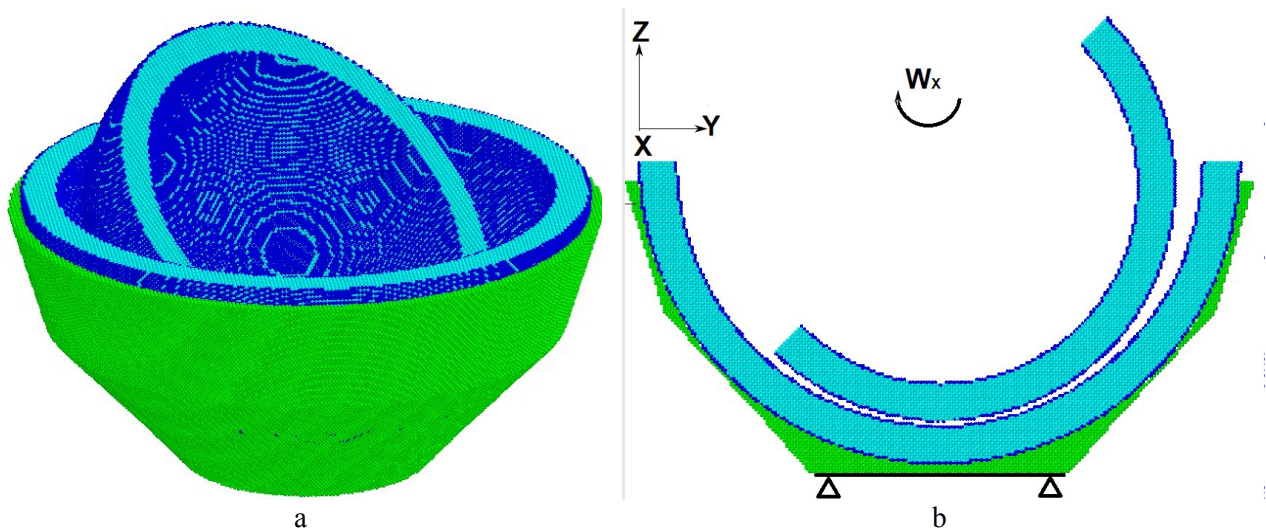
Figure 2. General view of the model for friction pair of hip resurfacing endoprosthesis (a) and its cross-section with loading parameters (b), represented by automata packing

In this case, the value of the corresponding rotational velocity gradually increases from 0 to 10 1/s. The bottom layer of the automata of the cylindrical shell of the bone tissue is rigidly fixed (fig 2, b).

4   SIMULATION RESULTS

When simulating a single rotational cycle, the maximum reaction force was not greater than 3000 kN, which corresponds to the load of a walking man, and the angle of rotation of the resurfacing cap was 120°, which is typical for standard daily physical activities for an ordinary healthy person.

a

b
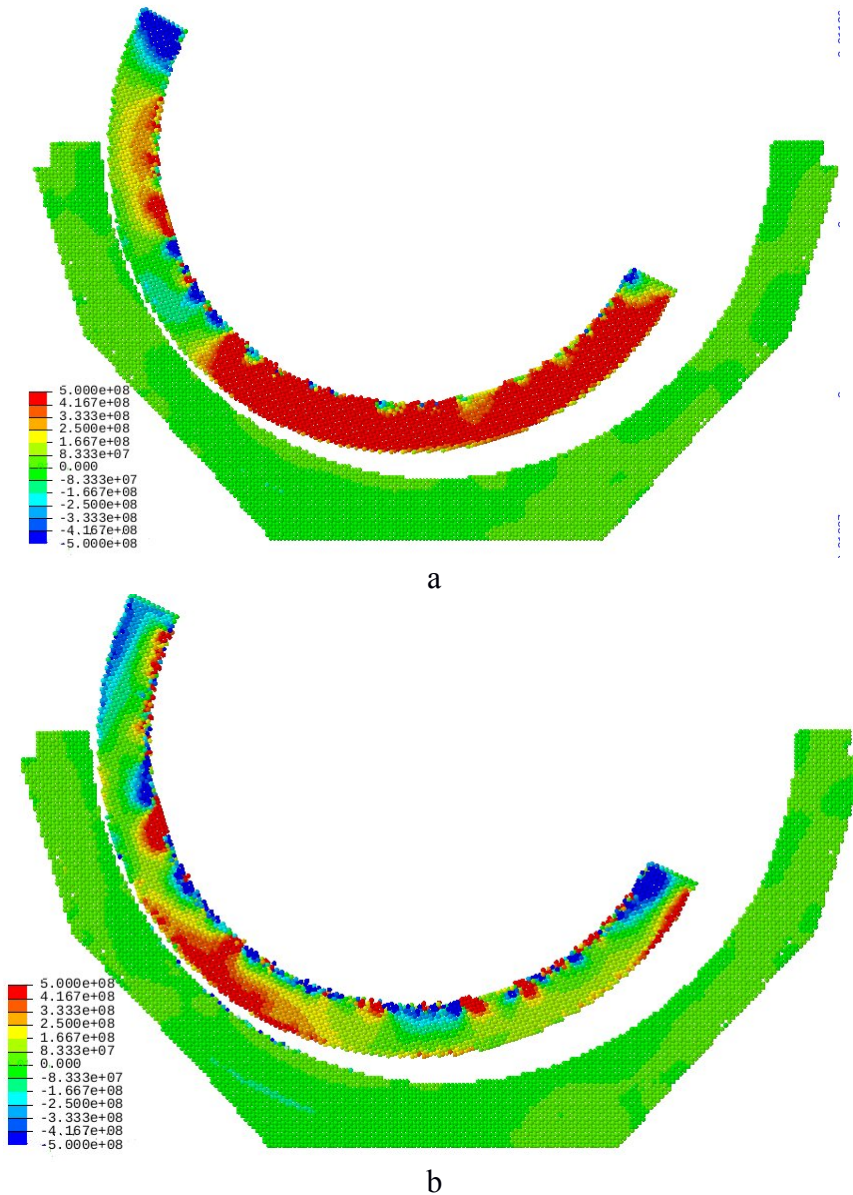
Figure 3: Distributions of mean stress in the friction pair of the hip resurfacing endoprosthesis of titanium alloy (a) and titanium alloy with TiN coating (b)

The simulation results showed that in the case of a friction pair of a homogeneous material in the zone of contact interaction of the acetabulum insert and resurfacing cap and behind it at extreme positions (edge of the acetabulum) a large are of tensile stress with a maximum value

not reaching 990 MPa appeared in the cap. Such a load exceeds the yield strength and, therefore, can lead to rapid wear of the surface of the resurfacing cap of the femur head of the joint (fig.3, a). These results are consistent with the data on the stress distribution in the metal head obtained in [20]. At the same time, the stress in the acetabulum insert did not exceed 100 MPa.

In the case of a coated endoprosthesis, a zone of tensile stresses with a maximum value of 1.1 GPa was observed in the contact zone, but this area was significantly smaller and concentrated mainly in the coating (fig.3, b). In addition, when using two-component materials in the friction pair, there was no noticeable increase in stress values in the cap when it was in the extreme positions. Consequently, the use of titanium alloys with a ceramic coating allows avoiding premature wear at the extreme positions of the femur head in the acetabulum. In the insert consisting of titanium alloy and coating, the value of compressive stresses reached 300 MPa. It should be noted that the magnitude of such stresses is not critical for the coating.

In general, the results of the numerical simulations suggest that the use of coated materials in the friction pair of hip resurfacing endoprosthesis can help avoiding premature wear of the endoprosthesis.

5   CONCLUSIONS

A three-dimensional model of the mechanical behavior of materials in a friction pair of hip resurfacing endoprosthesis during rotational motion is presented based on the method of movable cellular automata. The obtained simulation results allow us to draw the following conclusions.

The greatest value of tensile stresses in the cap made of titanium alloy during rotation is observed at the extreme positions of the resurfacing cap, in the case of the cap made of TiN coated titanium, this tendency is avoided.

The use of a hardening coating would help to avoid premature wear of the contacting elements of the hip resurfacing endoprosthesis.

6   ACKNOWLEDGMENTS

REFERENCES
[1] Vendittoli, P.A., Lavigne, M., Girard, J., Roy A.G. A randomised study comparing resection of acetabular bone at resurfacing and total hip replacement. *J Bone Joint Surg Br* (1994) **88B**: 997-1002 (2006).
[2] Dunstan, E., Sanghrajka, A.P., Tilley, S., Unwin, P., Blunn, G., Cannon, S.R. et al. Metal ion levels after metal-on-metal proximal femoral replacements: a 30-year follow-up. *J Bone Joint Surg Br* (2005) **87**: 628-631.
[3] Campbell, P., De Smet, K., Case studies of suspected metal allergy in hip resurfacing. *The Hip Resurfacing Handbook* (2013) 479-487.
[4] Campbell P., De Smet K., Design issues and comparison of hip resurfacing prostheses *The Hip*

Resurfacing Handbook (2013) 88-109.

[5] Shimmin, A.V, Beaulé, P.E., Campbell, P., Metal-on-Metal Hip Resurfacing Arthroplasty. *The Journal of Bone and Joint Surgery-American* (2008) **90(3)**: 637–654.

[6] Smith, A.J., Dieppe, P., Howard, P.W., Blom, A.W. Failure rates of metal-on-metal hip resurfacings: analysis of data from the National Joint Registry for England and Wales. *Lancet* (2012) **380**: 1759-1766.

[7] Olmedo-Garcia, N.I., Zagra, L. High risk of complications using metal heads after ceramic fracture in total hip arthroplasty. *HIP Int.* (2019) **29(4)**: 373-378.

[8] Hamelynck, K.J., Woering, R.G., The advanced ceramic coated implant systems (ACCIS) hip resurfacing prosthesis. *The Hip Resurfacing Handbook,* Woodhead Publishing (2013) 3-10.

[9] Todo, M. Biomechanical Analysis of Hip Joint Arthroplasties using CT-Image Based Finite Element Method. *Journal of Surgery and Research* (2018) **1**: 34-41.

[10] Stempin, R., Dragan, S.Ł., Kulej, M., Filipiak, J., Dragan, S.F. Effect of elliptical deformation of the acetabulum on the stress distribution in the components of hip resurfacing surgery. *Acta of bioengineering and biomechanics* (2017) **19(4)**: 35-41.

[11] Zienkiewicz O.C., Taylor R.L., Zhu J.Z. *The Finite Element Method: Its Basis and Fundamentals. 7th ed*. United Kingdom: Butterworth-Heinemann 2013.

[12] Puccio, F.D., Mattei, L. Biotribology of artificial hip joints. *World J Orthop* (2015) **6(1):** 77-94.

[13] Psakhie, S.G., Moiseyenko, D.D., Smolin, A.Yu., Shilko, E.V., Dmitriev, A.I., Korostelev, S.Yu., Tatarintsev, E.M. The features of fracture of heterogeneous materials and frame structures. Potentialities of MCA design. *Comp. Mater. Sci*. (1999) **16**: 333-343.

[14] Dmitriev, A.I., Smolin, A.Yu., Popov, V.L., Psakhie, S.G. A multilevel computer simulation of friction and wear by numerical methods of discrete mechanics and a phenomenological theory. *Phys. Mesomech.* (2009) **12(1-2)**: 11-19.

[15] Smolin, A.Yu., Eremina, G.M., Sergeyev, V.V., Shilko, E.V., Psakhie, S.G. Three-dimensional MCA simulation of elastoplastic deformation and fracture of coatings in contact interaction with a rigid indenter. *Phys. Mesomech.* (2014) **17**: 292-303.

[16] Smolin, A.Yu., Shilko, E.V., Astafurov, S.V., Kolubaev, E.A., Eremina, G.M., Psakhie, S.G., Understanding the mechanisms of friction stir welding based on computer simulation using particles. *Defence Technology* (2018) **14**: 643–656.

[17] Grigoriev, A.S., Shilko, E.V., Skripnyak, V.A., Psakhie, S.G. Kinetic approach to the development of computational dynamic models for brittle solids. *Int. J. Impact Eng.* (2019) **123**: 14-25.

[18] Material Datasheet: TIMETAL 6-4s, Titanium Metals Corporation, 2000.

[19] Bonello, T., Avelar-Batista Wilson, C., Housden, J., Gutmanas, E.Y., Gotman, I., Matthews, A., Leyland, A., Cassar, G. Evaluating the effects of PIRAC nitrogen-diffusion treatments on the mechanical performance of Ti–6Al–4V alloy. *Mat. Sci. & Eng. A* (2014) **619:** 300-311.

[20] Xia, Z., Kwon, Y.M., Mehmood, S., Downing, C., Jurkschat, K., Murray, D.W. Characterization of metal-wear nanoparticles in pseudotumor following metal-on-metal hip resurfacing. *Nanomedicine* (2011) 7: 674-681.

Numerical modelling of bed sediment particle tracking in open channel with skewed box-culvert

Israel E. Herrera-Díaz*[†], Mariano López-Amezcua[††], Noe Saldaña-Robles[†] and Javier Zavala Sandoval[†]

[†] Depto. Ingeniería Agrícola, DICIVA, Campus Irapuato-Salamanca, Universidad de Guanajuato, México e-mail: eherrera@ugto.mx, saldanar@ugto.mx, web page: http://www.ugto.mx/campusirapuatosalamanca/

[††] Programa de Ingeniería Civil, DCSI, Campus Celaya-Salvatierra, Universidad de Guanajuato, México, e-mail: m.lopezamezcua@ugto.mx, web page: http://www.ugto.mx/campus-celaya-salvatierra

ABSTRACT

A particle tracking model was applied to estimate the bed sediment transport in open channel with skewed box-culvert in rivers in Mexico, for which purpose the calculation of the hydrodynamics of the study channel was determined the three-dimensional velocity field [1], later, the calculation of particle transport was obtained, which was determined in any direction of the space caused by the velocity field and the turbulent dispersion (random movement of the Brownian type). The dispersion and re-suspension mechanisms of the particles used were represented by stochastic models, which describe the movement by means of a probability function [2]. The validation of the model was previously carried out by [3], obtaining average relative errors of less than 4.8%.

Three numerical scenarios were calculated including different alternatives and its behaviour at the entrance, interior and exit of the water flow in the construction to determine which is the best option to be used on the skewed multi barrel crossings. In order to accomplish this, a variable slope channel and 1: 60 scale models of box culverts with 10, 22 and 45 degrees of skewedness were used.

The results observed in the multi-eyed box culverts were favourable, due to the fact that the speed spans are low increase inside and outside of them, which favours the hydrodynamic behaviour and minimize the accumulation of sediment into structure in the river.

INTRODUCTION

The analysis and design of culvert for the flow of water through bridges, roads or road infrastructure works are important to minimize environmental problems and environmental impact on rivers and streams in the area of construction and civil engineering.

The behavior of these culverts has been studied in relation to the number and placement of these in the bridges or crossings over rivers and streams, all depending on the geographical, hydrological and construction characteristics, always with the purpose of minimizing the natural channel and associated environmental processes such as sediment transport.

For the study of these structures that facilitate the transit of water through roads and bridges, the use of numerical models is necessary to test different arrangements and configurations before the hydraulic scenarios that occur in the area at different times of the year.

Various results have been proposed by works related to the hydrodynamics of rivers, irrigation channels and control works to regularize fluid flow and flow measurement.

The numerical computational model developed in this work for the transport of the particles is governed by the Lagrangian approach, where the particles are located following a concentration exponential law or randomly located in the space. The advantage of using Lagrangian models to estimate sediment transport and some temporal changes in the morphology of the bottom lies in the

computational speed of using a previously calculated hydrodynamic field for the movement of particles. These allow the approximation of the temporal concentration of sediments contemplating the density of the material and using the PIC method to quantify the sediment transport associated with the displacement of the particles near the bottom.

The Lagrangian approach is widely used in the study of the trajectories of movement of solid particles in fluid environments. This is due to the fact that it is possible to track the movement for each specific particle in more detail, in comparison with determining average concentration for grid cells. However, in practice, the most difficult part to use a Lagrangian based method is the strong dependence on the performance of computational resources, such as the amount of memory required for the particles.

The Lagrangian mathematical approximations, based on methods of random movement, are well established tools for the calculus of sediment transport and pollutant discharges into aquatic environments. The discharges are treated as a finite number of particles; these particles move under the influence of the previously established flow field.

The results of the hydrodynamic calculation correspond to a stable field and converged in time, which indicates that the velocity fields and their turbulent parameters can be assumed as constants, but with an important spatial variation, in this way the simulation of the transport of particles is performed for times greater than those obtained in the hydrodynamic simulation. Therefore, for the transport of particles, the same hydrodynamic field can be used repeatedly, for all time intervals, (Dt) as many times as required, until the simulation period is completed. The velocities of the particles are obtained by linearly interpolating the velocities around the particle in the three-dimensional mesh. An advantage of separating the hydrodynamic simulation from the simulation of particle movement, allows us to develop large numbers of transport simulations [4], in this way we can simulate particle movements with: different locations and types of sources, several simulation durations, different transport parameters and different physical properties of the particles (specific weight and diameter), all this based on a hydrodynamic velocity simulation.

According to some current review papers regarding the Lagrangian modelling of Saltating Sediment Transport [5, 6], a model for the transport of sediment has to include mainly the motion of saltating grains, diffusion of particles, and calculation of bedload transport rate and to improve the motion of particles representing more natural shapes. And, for rivers, it must consider the nonuniform character of sand, distribution of particle saltation lengths, and excursion lengths may be more important in determining the morphodynamic behavior of the channel bed than the average particle motion.

The application problem was to estimate the bed sediment transport in open channel with skewed box-culvert in rivers in Mexico, the study was in specific three different scenarios with a variable slope channel laboratory and 1:60 scale models of box culverts with 10, 22 and 45 degrees of skewedness were used, all conditions were controlled on flow rate and velocities to get the hydrodynamics field.

Three sediment particle diameters were considered in all domain, shape regular and sand material properties in all simulation time; the seeded of 700,000 particles is homogeneous throughout the domain, 3 different diameters D15, D50 and D90 are included with a percentage distribution of 40, 40 and 20 respectively of the total particles.

METODOLOGY

The governing equation hydrodynamical model

The Navier-Stokes equations in free surface flow, in cartesian coordinates; use the hypothesis of hydrostatic pressure and considering the postulates of Reynolds [7].

$$\frac{\partial u}{\partial t} + u\frac{\partial u}{\partial x} + v\frac{\partial u}{\partial y} + w\frac{\partial u}{\partial z} = -g\frac{\partial \eta}{\partial x} + div\left(v_e \overrightarrow{grad}(u)\right)$$

$$\frac{\partial v}{\partial t} + u\frac{\partial v}{\partial x} + v\frac{\partial v}{\partial y} + w\frac{\partial v}{\partial z} = -g\frac{\partial \eta}{\partial x} + div\left(v_e \overrightarrow{grad}(v)\right)$$

$$\frac{\partial \eta}{\partial t} = -\frac{\partial}{\partial x}\left(\int_{-zf}^{\eta} u\, dz\right) - \frac{\partial}{\partial y}\left(\int_{-zf}^{\eta} v\, dz\right)$$

(1)

where $\boldsymbol{v_e}$ effective viscosity coefficient, obtained by adding the turbulent and molecular viscosity coefficient $\boldsymbol{v_e} = \boldsymbol{v_t} + \boldsymbol{v_m}$, [8] proposes the following model to solve the turbulent viscosity:

$$v_t = \left\{\ell_h{}^4\left[2\left(\frac{\partial u}{\partial x}\right)^2 + 2\left(\frac{\partial v}{\partial y}\right)^2 + \left(\frac{\partial v}{\partial x} + \frac{\partial u}{\partial y}\right)^2\right] + \ell_v{}^4\left[\left(\frac{\partial u}{\partial z}\right)^2 + \left(\frac{\partial v}{\partial z}\right)^2\right]\right\}^{\frac{1}{2}}$$

(2)

where the vertical length scale $\boldsymbol{\ell_v} = \boldsymbol{\kappa}(\boldsymbol{z} - \boldsymbol{z_b})$ for $\frac{(z-z_b)}{\delta} < \frac{\lambda}{\kappa}$ and $\boldsymbol{\ell_v} = \boldsymbol{\lambda\delta}$ for, $\frac{\lambda}{\kappa} < \frac{(z-z_b)}{\delta} < \boldsymbol{1}$ $\boldsymbol{\kappa}$ is the von Kármán constant typically 0.41, $(\boldsymbol{z} - \boldsymbol{z_b})$ is the distance from the wall, $\boldsymbol{\delta}$ is the boundary-layer thickness and $\boldsymbol{\lambda}$ is a constant, typically 0.09. In the case of shallow-water flows, due to a steady current, the boundary-layer thickness may be assumed to be equal to the water depth h. The horizontal length scale is usually different than the vertical length scale, and the simplest assumption is to assume direct proportionality defined by $\boldsymbol{\ell_h} = \boldsymbol{\beta\ell_v}$. The constant $\boldsymbol{\beta}$ has to be determined experimentally.

Free surface and bottom conditions

$$\tau_x^{fondo} = v_e\left.\frac{\partial u}{\partial z}\right|_{fondo} = \frac{g\sqrt{u^2 + v^2}}{Cz^2}\,(u)$$

$$\tau_y^{fondo} = v_e\left.\frac{\partial v}{\partial z}\right|_{fondo} = \frac{g\sqrt{u^2 + v^2}}{Cz^2}\,(v)$$

(3)

where $\boldsymbol{Cz}$ is the Chezy friction coefficient. The velocity components are taken from values of the layer adjacent to the sediment-water interface.

$$\boldsymbol{\tau_x^{sup}} = \boldsymbol{v_e}\left.\frac{\partial \boldsymbol{u}}{\partial \boldsymbol{z}}\right|_{superficie} = -\frac{\boldsymbol{\rho_{aire}}}{\boldsymbol{\rho_{agua}}}\boldsymbol{a_{viento}}\boldsymbol{\omega_x}|\boldsymbol{\omega_x}|$$

$$\boldsymbol{\tau_y^{sup}} = \boldsymbol{v_e}\left.\frac{\partial \boldsymbol{v}}{\partial \boldsymbol{z}}\right|_{superficie} = -\frac{\boldsymbol{\rho_{aire}}}{\boldsymbol{\rho_{agua}}}\boldsymbol{a_{viento}}\boldsymbol{\omega_y}|\boldsymbol{\omega_y}|$$

(4)

where $\boldsymbol{\rho_{aire}} = 1.29$ kg/m3, $\boldsymbol{\omega_x}$ y $\boldsymbol{\omega_y}$ are the horizontal components at x and y respectively of the wind speed at 10 m altitude. The unidimensional coefficient $\boldsymbol{a_{viento}}$ can be obtained using the equation given by [9].

$$a_{viento} = 0.565 \times 10^{-3}; \quad si \; |\vec{\omega}| \leq 5 \, m/s$$

$$a_{viento} = (-0.12 + 0.137|\vec{\omega}|)10^{-3}; \\ si \; 5 \leq |\vec{\omega}| \leq 19.22 \, m/s$$

$$a_{viento} = 2.513 \times 10^{-3}; \quad si \; |\vec{\omega}| \geq 19.22 \, m/s$$

$$(5)$$

The governing equation particle tracking model

The numerical model for particle transport is given under a Lagrangian approach; the particles are placed following an exponential law of concentrations or by an initial position in three-dimensional space [10]. For the movement of particles, a stochastic model is considered and discretized in three dimensions (Fig. 1), considering the specific weight of each particle as well as the fall velocity of the same [11] and it is verified if these are within the domain study for a single time step (Dt) from (n) to (n + 1) is given by:

$$x_i^{n+1} = x_i^n + u_{i,j,k}(\Delta t) \pm (2rand(iseed) - 0.5)\sqrt{\left(2\upsilon t_{i,j,k}\Delta t\right)}$$

$$y_i^{n+1} = y_i^n + v_{i,j,k}(\Delta t) \pm (2rand(iseed) - 0.5)\sqrt{\left(2\upsilon t_{i,j,k}\Delta t\right)}$$

$$z_i^{n+1} = z_i^n + w_{i,j,k}(\Delta t) \pm (2rand(iseed) - 0.5)\sqrt{\left(2\upsilon t_{i,j,k}\Delta t - w_s\Delta t\right)}$$

$$(6)$$
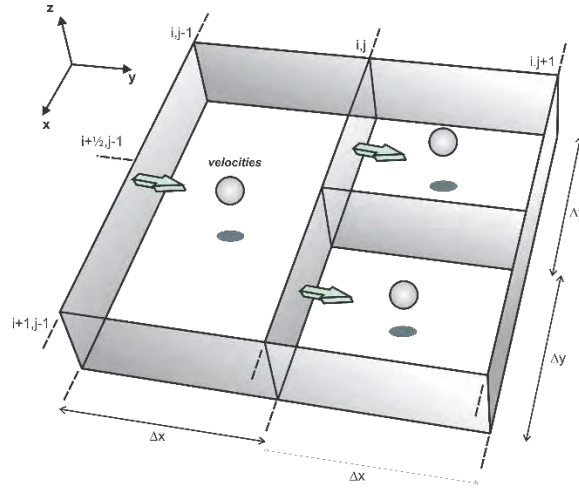
Fig. 1. Location in the three-dimensional space of the particle and its associated velocities

where (x_i^n, y_i^n, z_i^n) is the position of the particle in time (t), (u, v, w) are the average velocities in (i, j, k), (υ_t) is the turbulent viscosity coefficient, (Dt) is the Lagrangian time step and (w_s) is the velocity of sediment falling. The tracking of the particles is using the Eq. (6), therefore each particle is subject to a spatial displacement of magnitude $\pm (2rand(iseed) - 0.5)\sqrt{\left(2\upsilon t_{i,j,k}\Delta t\right)}$, in any direction of the domain, the sign is positive or negative depending on the sense of its location. In that moment of time the velocity field acts on each particle, in this way the movement has a sense in function of the main movement, given by the velocity fields. The term (υ_t) is found over the entire domain, represented by a field of positive scalars, which possesses information of turbulent intensities.

The shear forces in a turbulent flow, along its depth (z), can be written as:

$$\tau_i = \rho \upsilon \frac{dU}{dz} - \rho \overline{u_\iota w} \qquad\qquad (7)$$

where: (τ_i) bottom shear stress, (ρ) fluid density, (υ) cinematic viscosity coefficient, (U) mean fluid velocity and $(\overline{u_\iota w})$ bottom double correlation.

The critical shear stress that perform on the particles, is written:

$$\tau_{critico} = 0.03(\rho_s - \rho)gd_{50} \qquad (8)$$

where: (ρ_s) solid density, (ρ) water density, (g) gravitational constant and (d50) particle diameter 50%.

The probability function for the deposition of the particles is determined with the following equation:

$$P_{depósito} = \begin{Bmatrix} 0 \\ \left(1 - \dfrac{\tau_{x,y}}{\tau_{critico}}\right) \end{Bmatrix}, \begin{matrix} \tau_{x,y} \geq crítico \\ \tau_{x,y} < crítico \end{matrix} \qquad (9)$$

And the probability function for the resuspension of the particles is established in the following way:

$$P_{depósito} = \begin{Bmatrix} 0 \\ \left(1 - \dfrac{\tau_{critico}}{\tau_{x,y}}\right) \end{Bmatrix}, \begin{matrix} \tau_{x,y} \leq crítico \\ \tau_{x,y} > crítico \end{matrix} \qquad (10)$$

Velocity fall of sediment

To determine the velocity fall of sediment particles, these are considered to have non-spherical shape, so the effect of the shapes have a considerable influence on their velocity, mainly on relatively large particles (>300μm), the expressions that determine the magnitude of velocity fall [12] are expressed below.

$$w_s = \frac{(S-1)gd^2}{0.8\nu}; \quad 1 < d \leq 100\mu m$$

$$w_s = \frac{10\nu}{d}\left[\left(1 + 0.01\frac{(S-1)gd^3}{\nu^2}\right)^{0.5} - 1\right]; 100 < d \leq 1000\mu m$$

$$w_s = 1.1\left((S-1)gd^2\right)^{0.5}; \quad d > 1000\mu m$$

$$(11)$$

where (d) diameter of particle, (S) specific gravity, (ν) kinematic viscosity coefficient y (g) gravitational constant.

RESULTS AND APPLICATION

The physical scale open channel (Fig.2) had 2.32 m length, 0.18 m depth and 0.25 m width; the flow rate was 0.0019 m3/s, slope 0.006 and three skewed multi barrel crossings with 0, 10, 22 and 45 degrees.

| Open channel scheme | Open channel laboratory |
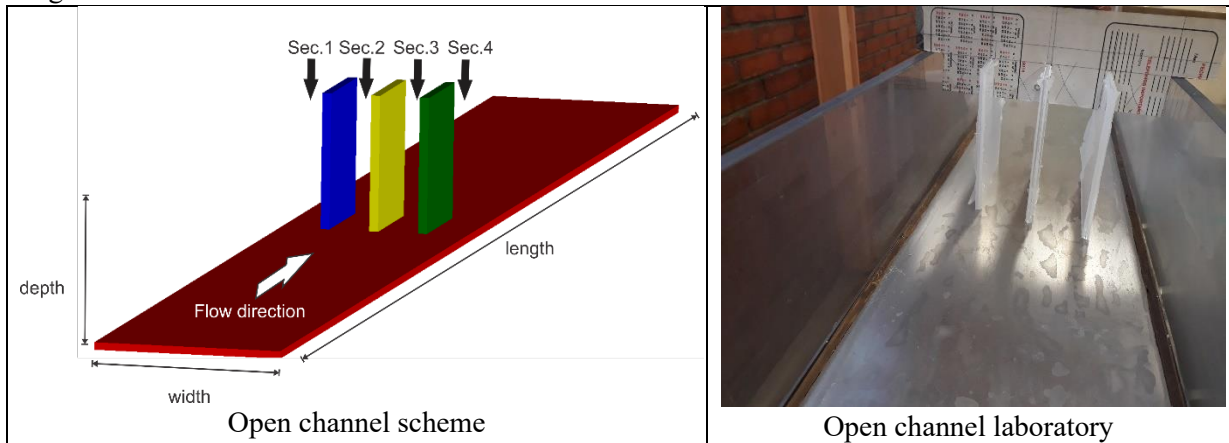
Fig. 2. Open channel domain

The numerical model was worked with a mesh in finite elements (Fig. 3) the first scenario contained 8986 nodes and 17280 triangles to zero degrees of skewedness; the second scenario contained 7730 nodes and 14816 triangles to ten degrees of skewedness; the third scenario was 2034 nodes and 3736 triangles to twenty-two degrees of skewedness; and the last scenario was 8178 nodes and 15712 triangles to forty-five degrees of skewedness were simulated with increments of Dt = 0.01 s and total time of 1500 s.

Scenario 1: zero degrees of skewedness

Scenario 2: ten degrees of skewedness

Scenario 3: twenty-two degrees of skewedness

Scenario 4: forty-five degrees of skewedness
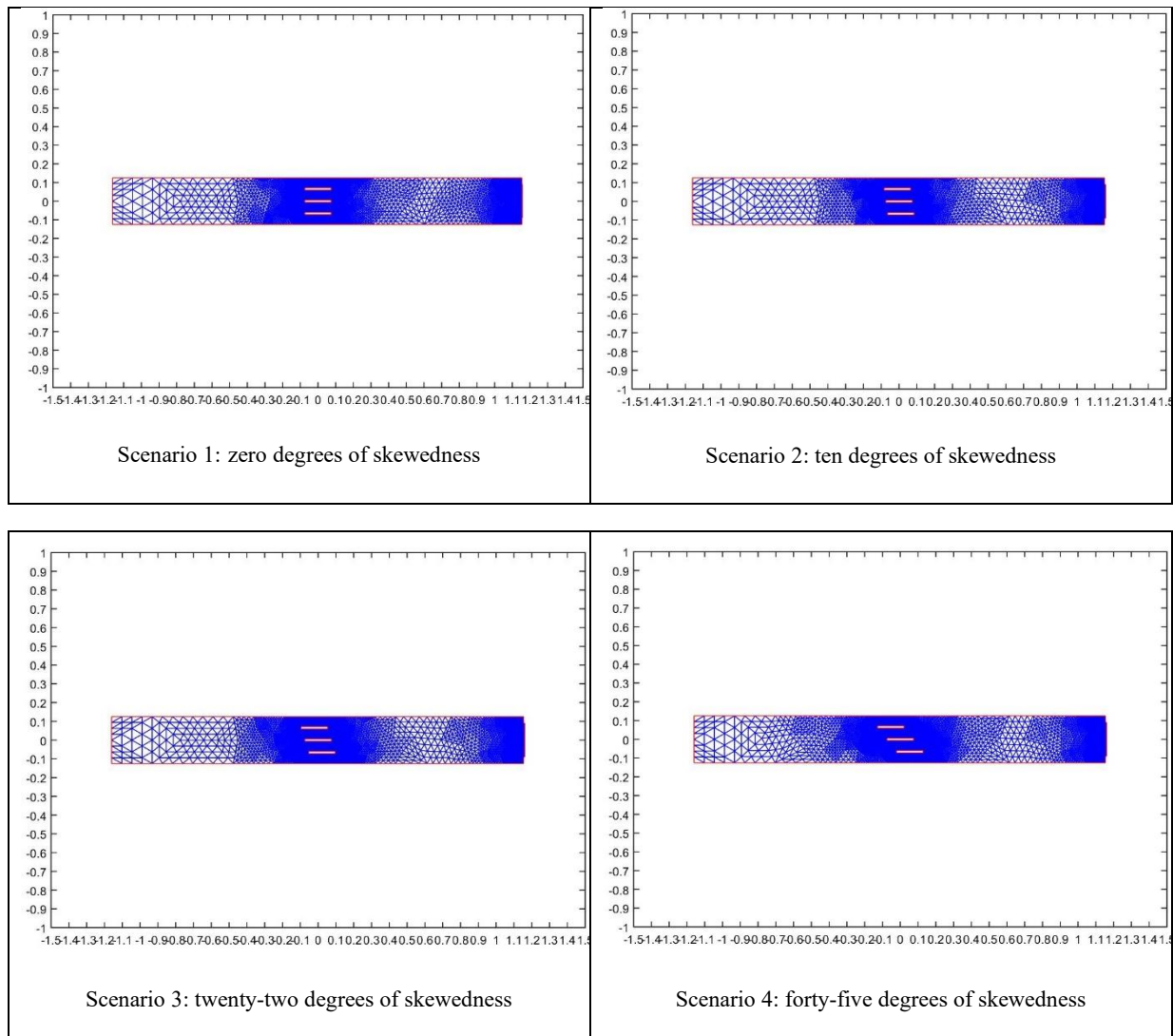
Fig. 3. Finite element mesh in different degrees of skewedness

The hydrodynamic model was used to generate the velocity field corresponding to 1500 s., taking as force the magnitude of flow rate in all scenarios.

In the Fig. (4 to 7) the results of the behavior of the hydrodynamic in laboratory channel are presented, it is observed that the velocity magnitude had change in each scenario, especially near to the box-culvert.

Velocity magnitude (m/s)

Field velocity vector (m/s)
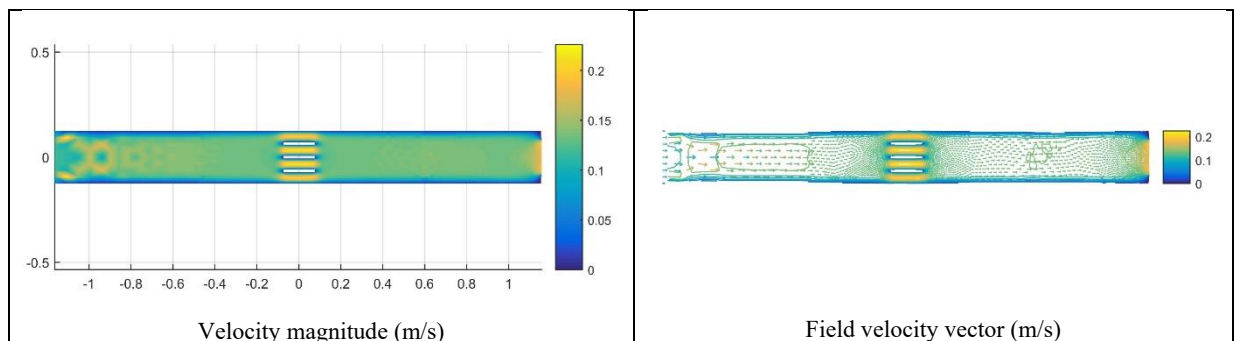
Fig. 4. Hydrodynamic field in zero degrees of skewedness (m/s)

| Velocity magnitude (m/s) | Field velocity vector (m/s) |
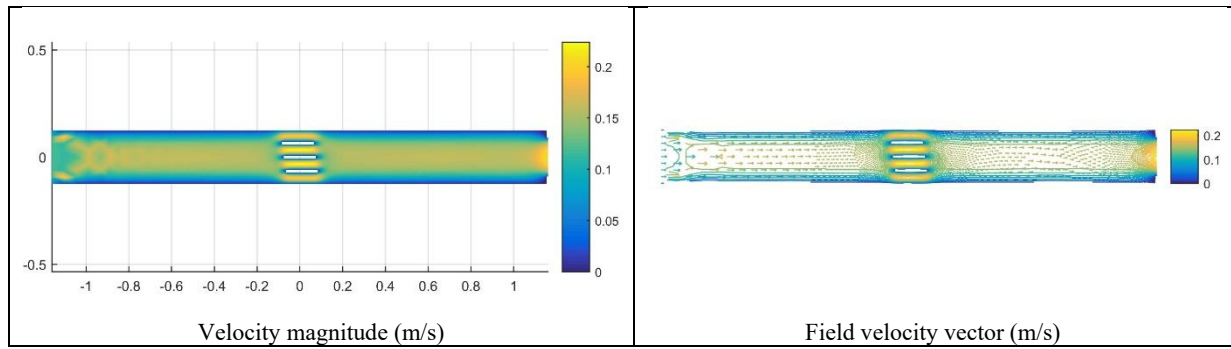
Fig. 5. Hydrodynamic field in ten degrees of skewedness (m/s)

| Velocity magnitude (m/s) | Field velocity vector (m/s) |
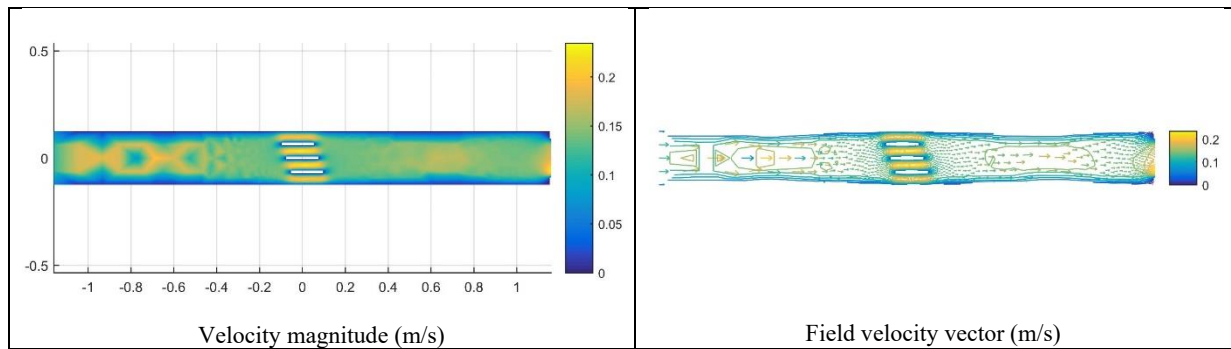
Fig. 6. Hydrodynamic field in twenty-two degrees of skewedness (m/s)

| Velocity magnitude (m/s) | Field velocity vector (m/s) |
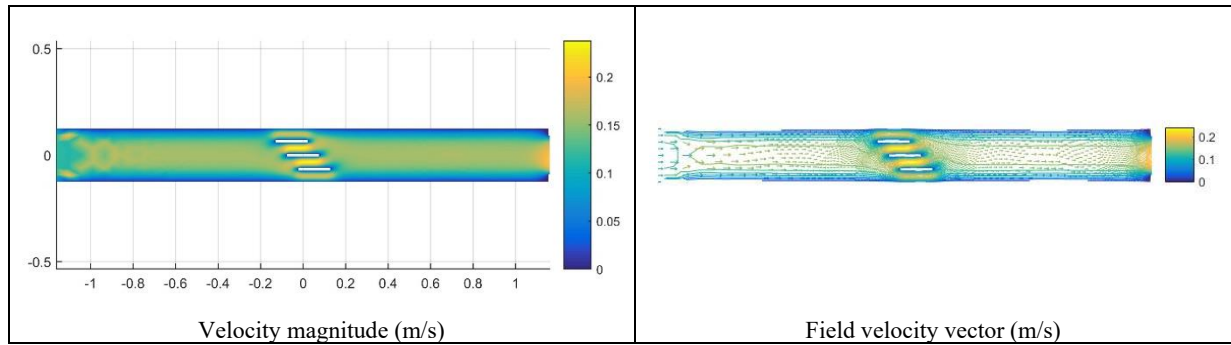
Fig. 7. Hydrodynamic field in forty-five degrees of skewedness (m/s)

Once the velocity field has been obtained, the seeding of sediment particles is placed at the bottom, the characteristic diameters of the sediment in the study area, which feed the sediment model are mentioned in the table (1), the material is constituted in 87% sand and the remaining 13% is distributed in coarse and bulky material.

Table 1. Characterization of bottom sediments

Grid	Sand particle diameter (mm)	Bulky particle diameter (mm)
D15	0.19	1.25
D50	0.28	1.65
D90	0.42	1.80

The seeding of sediment particles in the bottom of laboratory channel was established with an approximation by the PIC method (Particle in Cell), generalizing an initial concentration of sediments in a moment of time zero with 700,000 particles in this case. The concentration in an individual cell is obtained dividing the total mass in the cell by its volume.

The Fig. (8) presents the results of sediment transport for 1500 s in zero degrees of skewedness, in these images observed at different times (500, 1000 and 1500 s) the evolution of the transport in the bottom and consequently, the areas of sediment accumulation before and after the box culverts.
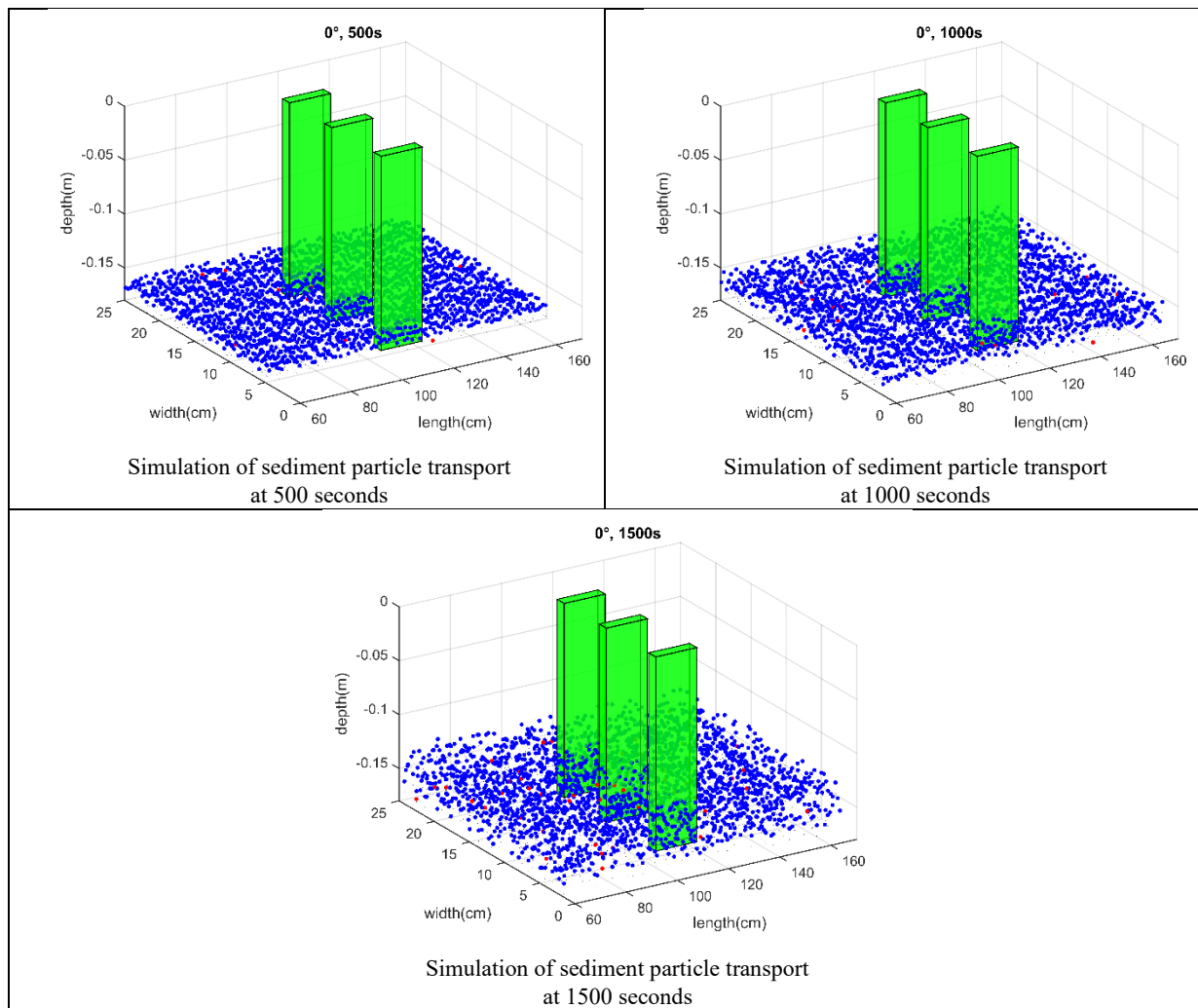
Fig. 8 Simulation of cloud evolution sediment particle transport to zero degrees of skewedness

The Fig. (9) presents the results of sediment transport in ten degrees of skewedness, we observed the different distribution by the hydrodynamic field near to bottom box culvert inlet, the areas of sediment accumulation were increased.

211
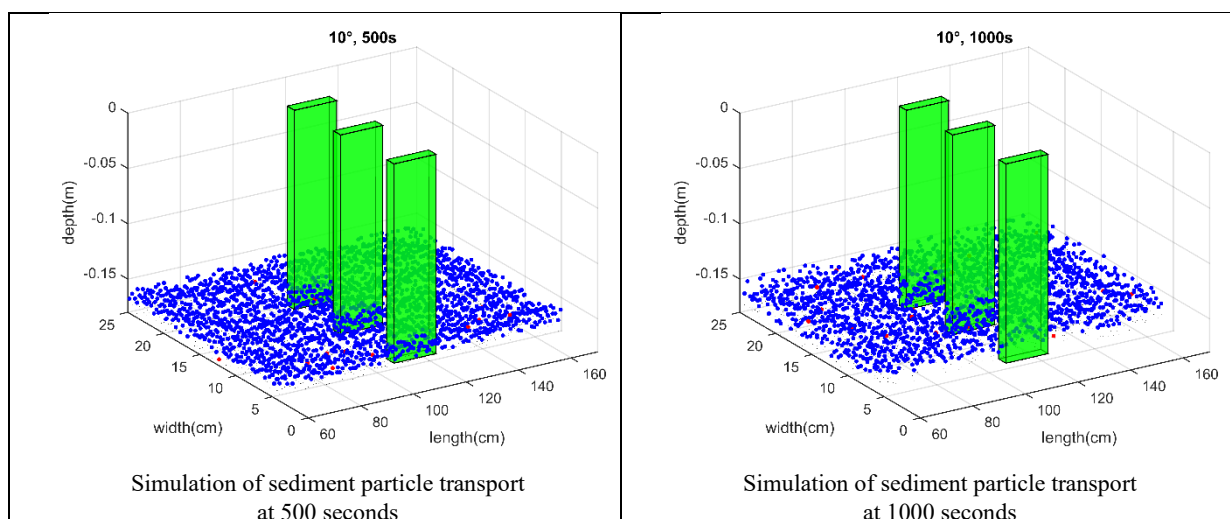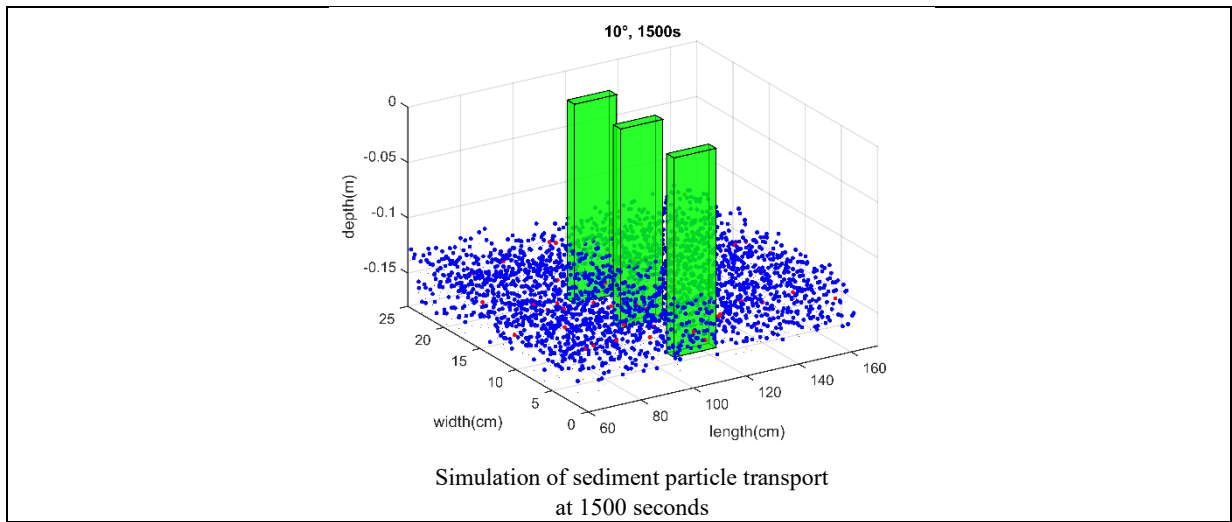
Fig. 9 Simulation of cloud evolution sediment particle transport to ten degrees of skewedness

In twenty-two degrees of skewedness, the Fig. (10) presented low behaviour in distribution of the particle transport in the bottom, the areas of sediment accumulation were reduced by angle increment of box culvert position.
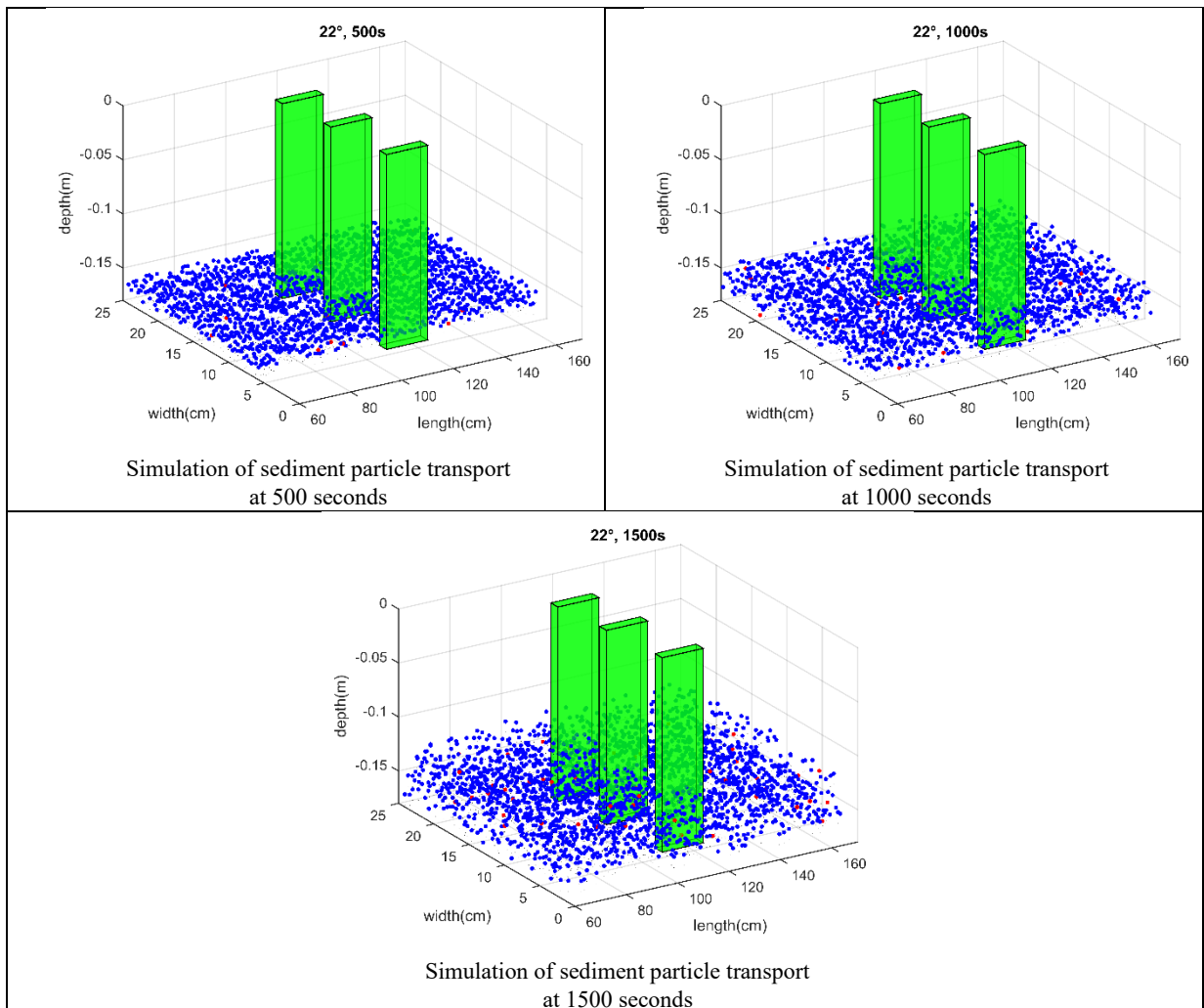
Fig. 10 Simulation of cloud evolution sediment particle transport to twenty-two degrees of skewedness

The Fig. (11) presents the results of sediment transport for 1500 s in forty-five degrees of skewedness, in these images observed at different times (500, 1000 and 1500 s) the evolution of the

212

transport in the bottom and consequently, the areas of sediment accumulation before and after the box culverts.

Simulation of sediment particle transport at 500 seconds

Simulation of sediment particle transport at 1000 seconds

Simulation of sediment particle transport at 1500 seconds

Fig. 11 Simulation of cloud evolution sediment particle transport to forty-five degrees of skewedness

To visualize the behavior of the distribution of the number of particles of the three different diameters (D15, D50 and D90), in Fig. (12) the results of the distribution of the particles in the evolution of the simulation time are shown.

Results to zero degrees of skewedness

Results to ten degrees of skewedness

| Results to twenty-two degrees of skewedness | Results to forty-five degrees of skewedness |
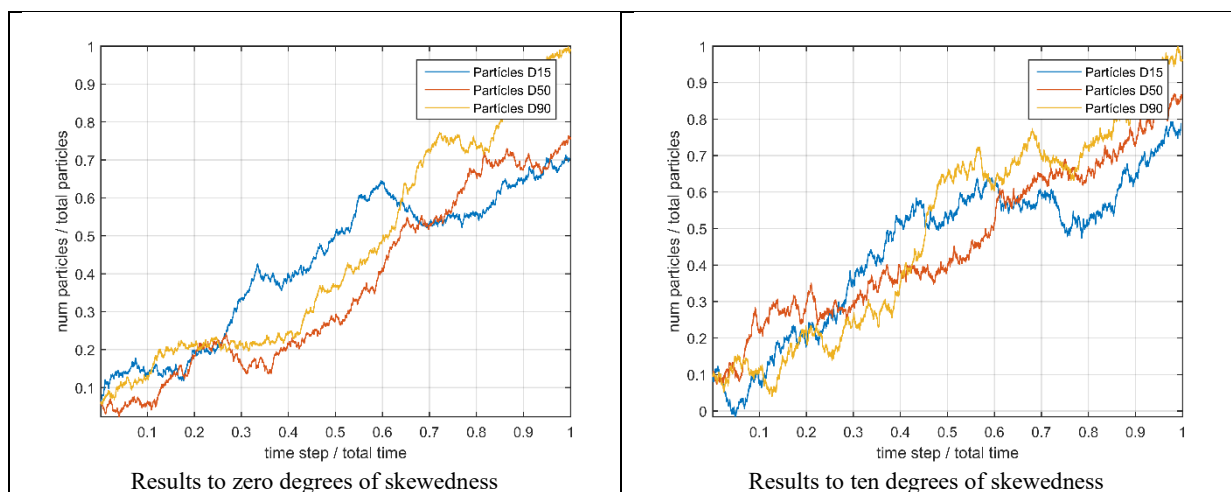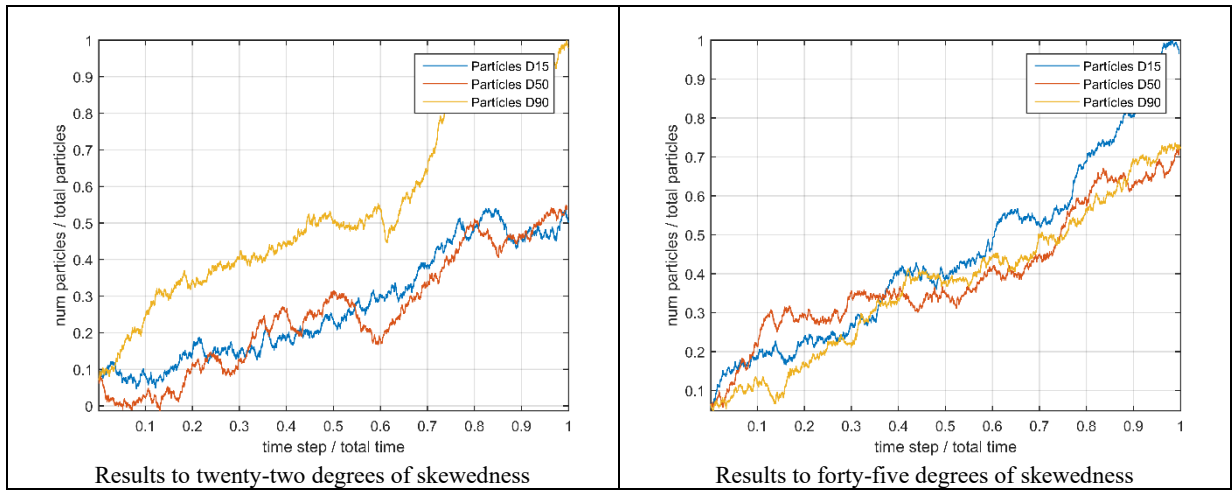
Fig. 12 Number of sediment particle diameters to different degrees of skewedness along to time simulation

The Fig. (13 to 16) shows the distribution of particles at the midpoint of sections A, B, C and D as a function of the number of particles in the water column represented as sediment concentration.

For the configuration of zero degrees of deflection, the results of the distribution of water column particles in the center of each section are shown in Fig. (13), the suspension of the background particles produced by the velocities of the flow in each section of the channel.

| Section A | Section B |
| Section C | Section D |
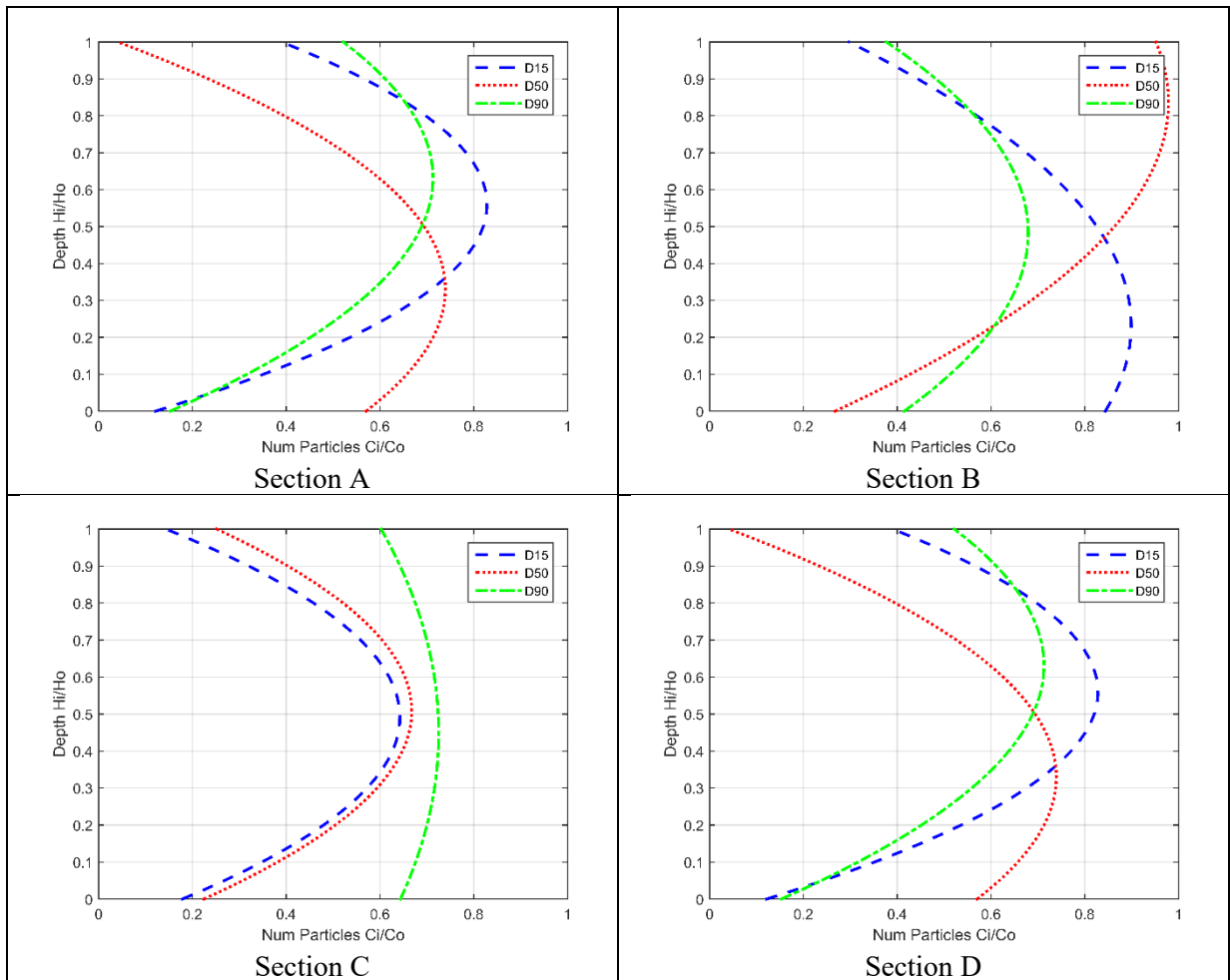
Fig. 13 Concentration profiles in all sections in zero degrees of skewedness at final time simulation

For ten degrees of skewed, in Fig. (14) the results of the concentrations of particles in each section are observed, sections B and C show values in D15 with representative changes in their concentration

214

in water column, due to the randomness of the functions used and the speed field through these sections.
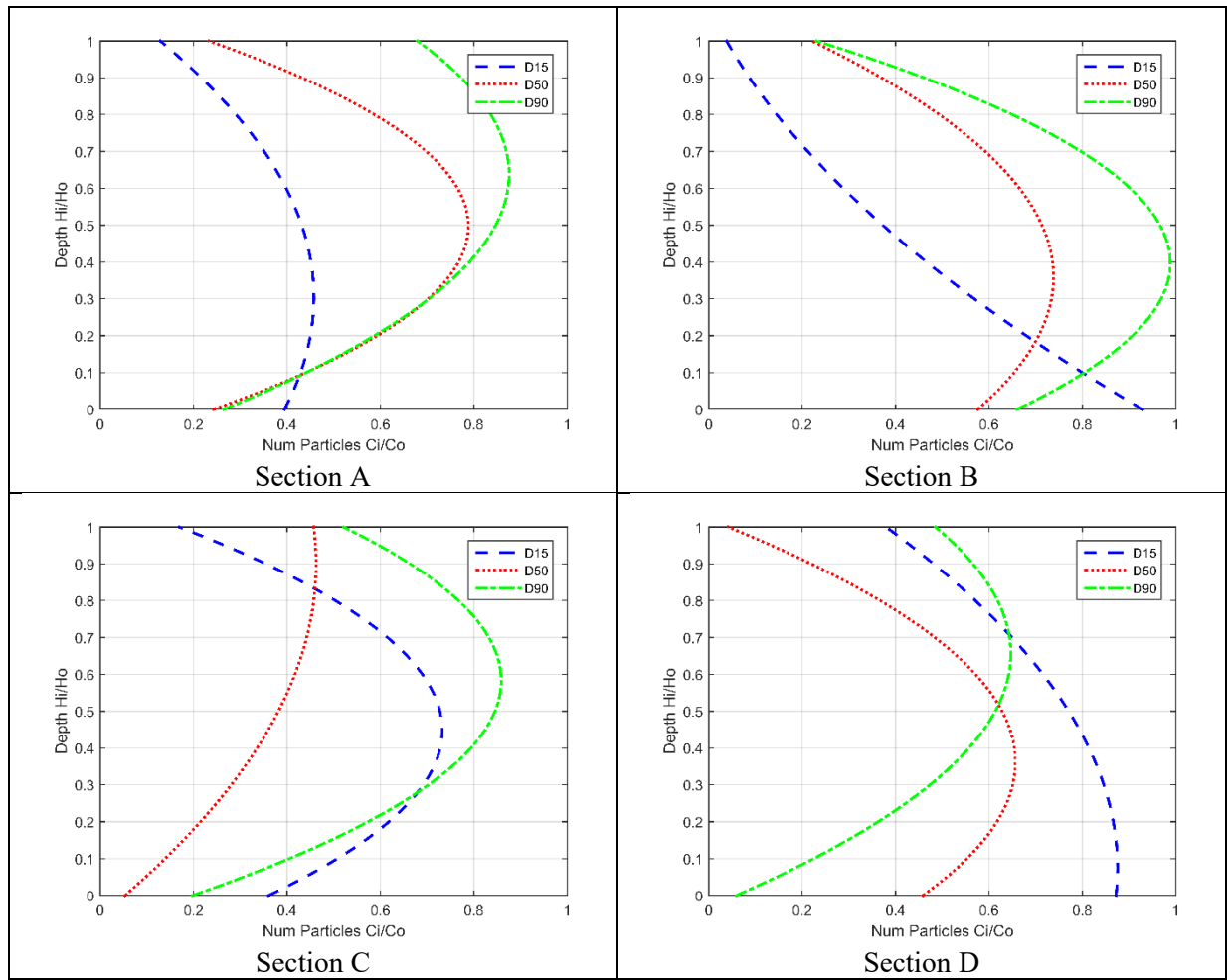
Fig. 14 Concentration profiles in all sections in ten degrees of skewedness at final time simulation

Similarly, in Fig. (15), we show the results for twenty-two degrees of skewed, where in section D, it presents a different behavior in the representative D15 in its concentration in water column, in relation to the other sections, It is estimated that it is due to the velocity field that passes through this section.

215
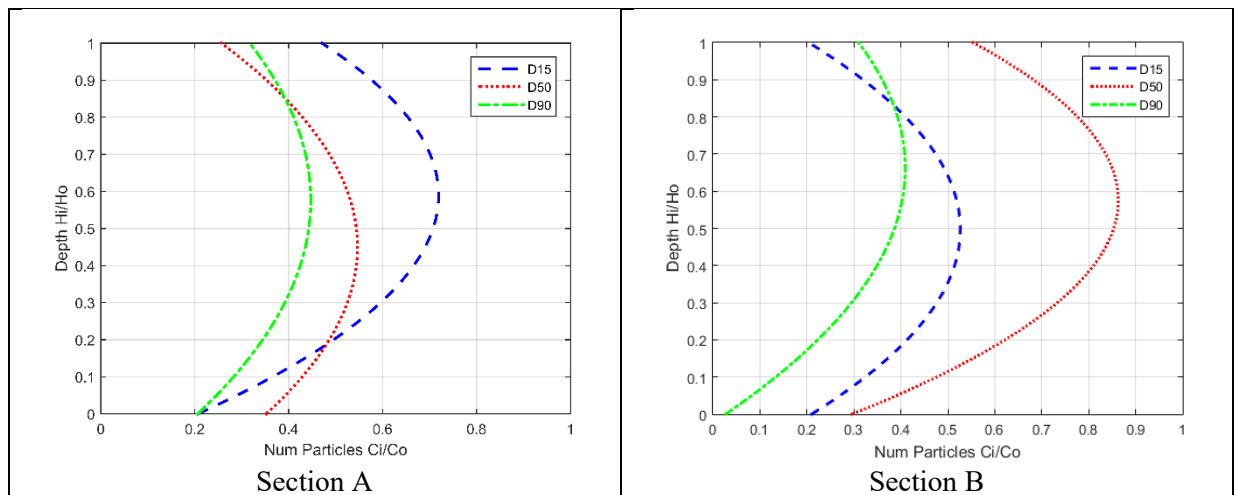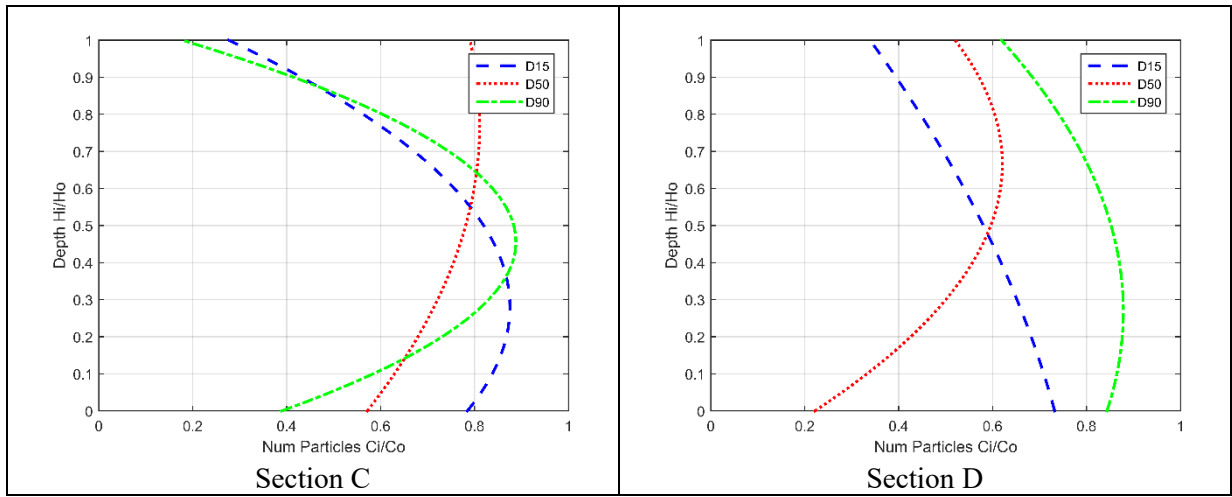
Fig. 15 Concentration profiles in all sections in twenty-two degrees of skewedness at final time simulation

Finally, in Fig. (16), the results for forty-five degrees of skewed are shown, where it is observed that the values of the concentration of particles in water column increase their value in suspension due to the velocity field that is presented in this configuration.
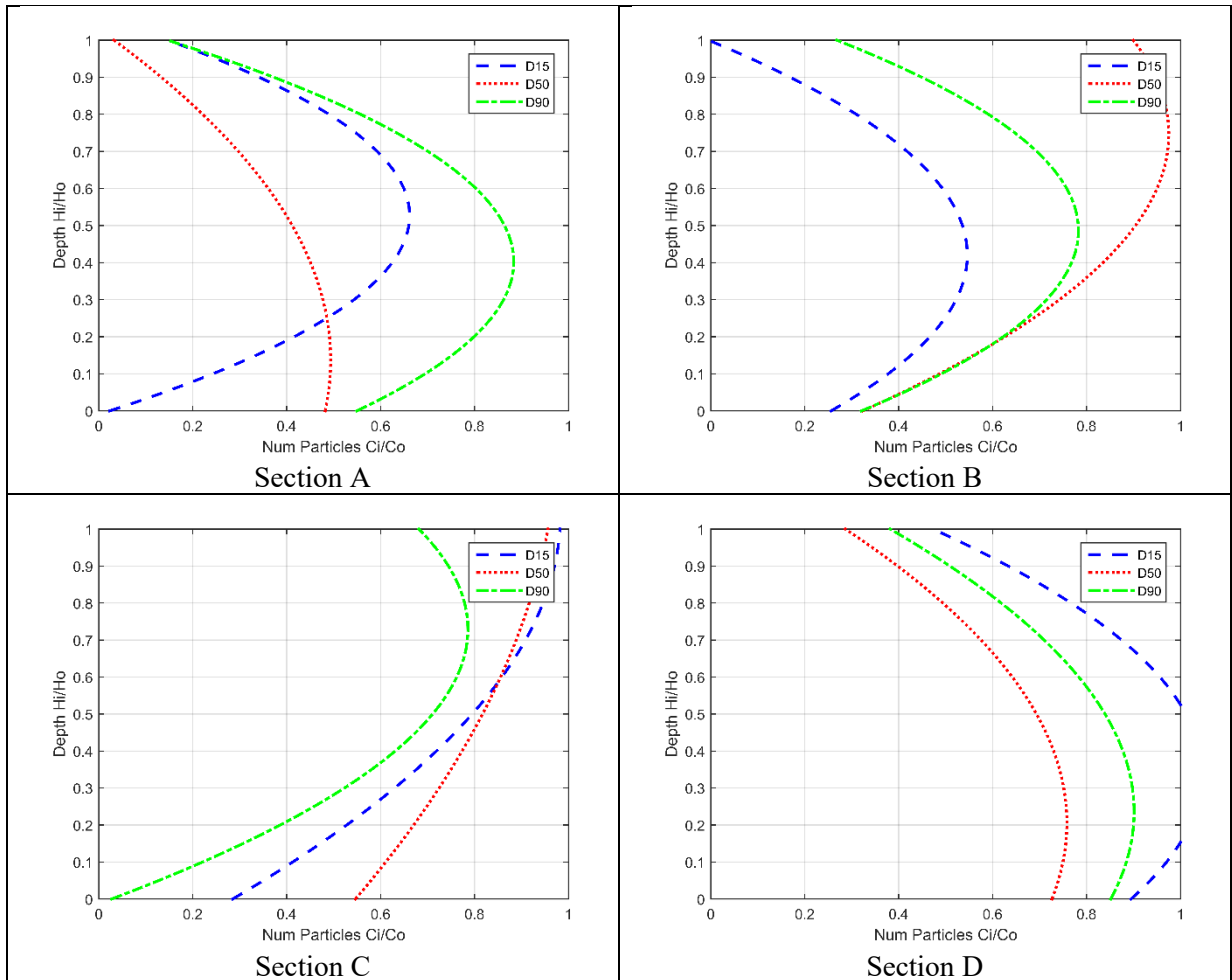
Fig. 16 Concentration profiles in all sections in forty-five degrees of skewedness at final time simulation

The results show that, for different degrees of skewed, they cause a different behavior of the particles in the water column, especially in those sections such as C and D which are further away from sections A and B which are the ones that they have a first contact with the flow.

CONCLUSIONS

A general model for the sediment transport and dispersion of pollutants has been developed, based on a Lagrangian formulation. The model allows to describe the evolution of tracer cloud both in the near and far-field.

The introduction of random motion to the equations of the particle movement produces good results by simplifying the equations of particle motion, thus producing a model that can withstand a large number of particles without consuming too many computational resources.

The model has the capacity to simulate 700,000 particles, limited only by the memory of the computer that is used. In this case, the evolution of tracer cloud is a function of the velocity field of the open channel and sediment process.

The results of the distribution of particles show considerable changes in the magnitude of concentration or number of particles in suspension that can be measured in a water column; due to the increase in the angle of skewed and the number of multi-barrel that are placed in the cross section, as well as the dimensions of each section and its geometry.

Actually, we are calibrating the numerical model with PIV measurements to 4 different scenarios of skewed multi barrel crossings.

Therefore, it may be concluded that sediment particle transport allows estimate which is the better configuration of skewed box-culvert to minimize suspension sediment particles and erosion in each cross section.

REFERENCES

[1] Rodríguez C., Couder C., Flores E., Herrera I.E., Cisneros R., "Modelling shallow water wakes using a hybrid turbulence model", Journal of Applied Mathematics, Vol. 2014, pp.1-10.

[2] Herrera I.E., Rodríguez C., Couder C., Gasca J.R., "Modelación numérica hidrodinámico-hidrológica en zonas de inundación con presencia de infraestructura", Tecnología y Ciencias del Agua, Vol. VI, Num. 1 Ene-Feb. 2015, pp. 139-152.

[3] Herrera I.E., Torres F.M., Moreno J.Y., Rodriguez C., Couder C., "Light particle tracking model for simulating bed sediment transport load in river areas", Mathematical Problems in Engineering, Hindawi Publishing, Vol. 2017, pp.1-15

[4] Gu H.B., Causon D.M., Mingham C.G. and Qian L., "A Fast-Marching Semi-Lagrangian level set method for free surface flows", Proc. of the Nineteenth International Offshore and Polar Enginnering Conference (ISOPE) 2009.

[5] R. J. Bialik, "Lagrangian modelling of saltating sediment transport: a review," in Rivers physical, Fluvial and Environmental Processes, GeoPlanet: Earth and Planetary Sciences, pp. 427–441, Springer International, Cham, Switzerland, 2015.

[6] S. Naqshband and B. McElroy, "Sediment transport at grain scale: a review, future research and morphological implications," in River Flow 2016, pp. 914–918, CRC Press, Boca Raton, Fla, USA, 2016.

[7] Broomans, P. "Numerical accuracy in solutions of the shallow-water equations", Master thesis, 2003, TU Delf & WL, Delf Hydraulics.

[8] Stansby, P. "A mixing-length model for shallow turbulent wakes", Journal of Fluid Mechanics, Vol. 495, 2003, pp. 369-384.

[9] Flather R.A., "Results from surge prediction model of the North-West European continental shelf for April, November and December", Institute of Oceanographic (UK), Report number 24, 1976.

[10] Robinson M., Monaghan J., and Mansour J. "SPH simulation of 2d wall-bounded turbulence", SPHERIC, Smoothed Particle Hydrodynamics European Research Interest Community, Second International Workshop 2007, 107–110pp.

[11] Hernandez I., "Modelos euleriano-lagrangeanos en flujos a superficie libre: Aplicación al transporte de partículas suspendidas y al crecimiento de microorganismos", Tesis Maestría, 2003, DEPFI, UNAM.

[12] Van-Rijn L.C., Walstra D.J. and Van-Ormondt M. "Unified view of sediment transport by currents and waves IV: Application of Morphodynamic model", Journal of Hydraulic Engineering 2007, 133-7:776– 793pp.

A METHODOLOGY OF A SENSITIVITY ANALYSIS IN DEM EXPERIMENTS

Momme Jahn[1] and Martin Meywerk [2]

[1]Helmut-Schmidt-University
Chair of Automotive Engineering
Holstenhofweg 85, 22043 Hamburg, Germany
e-mail: momme.jahn@hsu-hh.de

[2] Helmut-Schmidt-University
Chair of Automotive Engineering
Holstenhofweg 85, 22043 Hamburg, Germany
e-mail: martin.meywerk@hsu-hh.de

Key words: DEM, Sobol' Indices, Metamodels, Sensitivity Analysis, Particle Pile, Oedometer Test, Force-Controlled Plate, Angle Of Repose

Abstract. In this publication a sensitivity analysis for DEM modelparameters with respect to the pile- and the oedometer experiment is described. The analysis is performed with Sobol' indices. Since the huge computational effort of the corresponding DEM models different metamodels are used to determine these indices. The (RSM) metamodels are established by using Latin Hypercube sampling points.
A three-dimensional ansatz for the determination of the angle of repose as well as the algorithm of a force-controlled plate is described in order to get results for the pile- and the oedometer experiment.

1 INTRODUCTION

The Discrete-Element-Method (DEM) is a capable method to investigate huge deformations in granular media [23]. These could occur e.g. in tire-soil-interactions [7, 9], the flow of particles through hoppers [5].
A very important and challenging point is the identification of DEM-parameters. A common way for the parameter identification is the calibration of experiments. An often used experiment is the calibration of granular piles [2]. The angle of repose could be used to determine the accordance between the numerical pile and the experimental one. Another experiment is the oedometer test, which is a one-dimensional compression test where the horizontal displacement of the soil is prevented [16, 10]. This test is used to investigate the stress-displacement behavior [13, p. 252]. Often the calibration process is done with a trial-and-error procedure despite its disadvantages with the high number of parameters [11, p. 73]. A more appropriate calibration process could be performed if the influence of parameters and their interactions are known [2, p. 333] e.g. if some parameters have a negligible influence, they could be neglected in

the parameter calibration process. In order to determine the influence of parameters and their interactions a sensitivity analysis is performed with Sobol' indices [3, p. 1]. Sobol's indices are a common used for sensitivity measurements[17, p. 964].

The determination of the angle of repose is performed in [11, p. 74] with an image processing algorithm. In [6, p. 375] a two dimensional approach is used. In this work a three dimensional ansatz is used. The first step is the searching of boundary particles of the pile. Then straight lines are positioned with the minimization of the distance of the line to the boundary particles. The angle of repose is achieved with the average of all the angles corresponding to these lines. In [16, 13] the oedometer experiment is performed with non-spherical particles. The influence of the particle size for spherical particles is investigated in [10]. One result of the latter work is that particle assemblies with a good graduation have a denser packing density and are less compressible [10, p. 52]. A common way for the oedometer-test is that the plate for the compression is velocity-driven. In [16, p. 422] the velocity is controlled to reduce the difference between the measured and the simulated forces.

In this work a force-driven plate was implemented. With this plate a static case is simulated for four load-steps. The implemented force-plate prevents incorrect simulation conditions where the resultant force of the particles is huger than the actual load-step.

2 DEM

Each particle is identified by the index $I \in \mathbb{M}_P$ where $\mathbb{M}_P$ is the set of all particle-identifiers. Each particle has a mass m_I and a radius R_I. The location of the center of mass is denoted by $\underset{I}{\boldsymbol{S}}(t)$ and the rotational velocity by $\underset{I}{\dot{\boldsymbol{\theta}}}(t)$. The units which are used in this work are listed in table 1.

Quantity	Used units	SI-units
Mass	mg	10^{-6}kg
Length	mm	10^{-3}m
Time	ms	10^{-3}s

Table 1: Summary of the used units

In the following paragraphs the contact-displacement law is shown. Let $\mathbb{T}_C = [t_s, t_e]$ be a time interval in which the two particles are in contact. Shortly before t_s and after t_e the two particles are not in contact.

The material parameters for all particle are identical. Hence a tupel

$$P = (E, \nu, \mu_{PP}, \mu_{PW}, e_r, \mu_{R,PP}, \mu_{R,PW}) \tag{1}$$

is introduced, where the components are the Young's modulus E, Poisson ratio ν, the coefficient of friction between two particles μ_{PP}, the coefficient of friction between a particle and a wall μ_{PW}, the coefficient of restitution e_r, the coefficient of rolling resistance between two particles $\mu_{R,PP}$ and between a particle and a wall $\mu_{R,PW}$, respectively. In order to determine the force-displacment law for contact between particle I and J the equivalent radii, mass and Young's-

and shear modulus (cf. [9, p. 233-235]) must be determined with[1]

$$\underset{IJ}{R} := \frac{\underset{I}{R}\,\underset{J}{R}}{\underset{I}{R}+\underset{J}{R}} \quad , \quad \underset{IJ}{m} := \frac{\underset{I}{m}\,\underset{J}{m}}{\underset{I}{m}+\underset{J}{m}} \quad , \quad \overset{*}{E}(P) := \frac{E}{2\,(1-\nu^2)} \quad \text{and} \quad \overset{*}{G}(P) := \frac{G}{2\,(2-\nu)} \quad , \quad (2)$$

respectively [18, p. 242]. A nonlinear spring-dashpot model is used for the contact-displacement law [4, p. 985]. The stiffness and the viscous-damping in the normal direction is determined (cf. [9, p. 234]) with

$$\underset{IJ_\mathrm{N}}{K}(P) := \frac{4}{3}\overset{*}{E}(P)\sqrt{\underset{IJ}{R}} \quad \text{and} \quad \underset{IJ_\mathrm{N}}{\gamma}(t,\underset{IJ_\mathrm{N}}{\delta},P) := \beta(P)\sqrt{\underset{IJ}{m}\,\underset{IJ_\mathrm{N}}{K}(P)}\,\sqrt[4]{\underset{IJ_\mathrm{N}}{\delta}(t)} \quad , \quad (3)$$

$$\text{with} \quad \beta(P) := \ln(e_\mathrm{r})\sqrt{\frac{5}{\ln^2(e_\mathrm{r})+\pi^2}} \quad , \quad (4)$$

where e_r is the coefficient of restitution and $\underset{IJ_\mathrm{N}}{\delta}(t)$ the overlap of the particles in the normal direction. The contact-force in the normal direction equals (cf. [18, p. 242])

$$\underset{IJ_\mathrm{N}}{F}(t,\underset{IJ_\mathrm{N}}{\delta},\underset{IJ_\mathrm{N}}{\dot{\delta}},P) := -\underset{IJ_\mathrm{N}}{K}(P)\,\underset{IJ_\mathrm{N}}{\delta}(t)^{\frac{3}{2}} - \underset{IJ_\mathrm{N}}{\gamma}(t,\underset{IJ_\mathrm{N}}{\delta},P)\,\underset{IJ_\mathrm{N}}{\dot{\delta}}(t) \quad . \quad (5)$$

The stiffness and the viscous-damping in the tangential direction (cf. [9, p. 234]) equals

$$\underset{IJ_\mathrm{T}}{K}(P) := 8\overset{*}{G}\sqrt{\underset{IJ}{R}} \quad \text{and} \quad \underset{IJ_\mathrm{T}}{\gamma}(t,\underset{IJ_\mathrm{T}}{\delta},P) := 2\beta(P)\sqrt{\frac{1}{6}\underset{IJ_\mathrm{T}}{K}(P)}\,\sqrt[4]{\underset{IJ_\mathrm{T}}{\delta}(t)} \quad , \quad (6)$$

respectively and the corresponding force could be determined with

$$\underset{IJ_\mathrm{T}}{F}(t,\underset{IJ_\mathrm{T}}{\delta},\underset{IJ_\mathrm{T}}{\dot{\delta}},\underset{IJ_\mathrm{N}}{F},P) := \min\left(\left(\left|\underset{IJ_\mathrm{T}}{K}(P)\,\underset{IJ_\mathrm{T}}{\delta}(t) + \underset{IJ_\mathrm{T}}{\gamma}(t,\underset{IJ_\mathrm{T}}{\delta},P)\,\underset{IJ_\mathrm{T}}{\dot{\delta}}(t)\right|\right),\left|\mu_\mathrm{PP}\underset{IJ_\mathrm{N}}{F}(t,\underset{IJ_\mathrm{N}}{\delta},\underset{IJ_\mathrm{N}}{\dot{\delta}},P)\right|\right) \quad , \quad (7)$$

where μ_PP is the coefficient of the Coloumb friction and $\underset{IJ_\mathrm{T}}{\delta}(t)$ is the tangential overlap (see [22, p. 155]).

2.1 Rolling friction

Rolling friction is introduced to decrease the translational and rotational velocity of a particle. In reality the particle velocity decreases during the movement. In order to achieve this behavior in the simulation rolling resistance is introduced (cf. [21, p. 540]). The used rolling friction model is Method-B from [21, p. 539]

$$\underset{I_\mathrm{R}}{\boldsymbol{M}}(t,P,\underset{IJ_\mathrm{N}}{F}) := -\mu_\mathrm{R,PP}\left\|\underset{IJ}{\dot{\boldsymbol{\theta}}}(t)\right\|\underset{IJ_\mathrm{N}}{F}(t,\underset{IJ_\mathrm{N}}{\delta},\underset{IJ_\mathrm{N}}{\dot{\delta}},P)\frac{\underset{I}{\dot{\boldsymbol{\theta}}}(t)}{\left\|\underset{I}{\dot{\boldsymbol{\theta}}}(t)\right\|} \quad , \quad (8)$$

where $\underset{IJ}{\dot{\boldsymbol{\theta}}}(t)$ is the relative angular velocity at the contact point.

---

[1]Usually the equivalent Young's modulus and the shear modulus are determined with specific values of Poisson Ratio and Young modulus.

3   COMPUTATIONAL MODEL FOR THE PILE

In this section the computational model of the dynamic simulation of the pile is described. Different ways for generating piles can be found in [2]. The simulation in this work is treated similar to the dynamic investigation of a hopper. In order to investigate only the influence of the material parameters with regard to the angle of repose the model must only depends on the material parameters. Hence the initial position of each particle must be identical for each simulation.

The sensitivity analysis is performed for two different particle sets in order to compare the sensitivity of two different particle size distributions. The particle radii for both assemblies are created by means of a normal distribution. In table 2 the interval for the restriction of the particle radii $R_I \in [r_L; r_U]$, the mean values, the standard deviation and the number of particles of the two assemblies are shown.

Particle-set	Interval for radii	Mean value	Standard deviation	Number of particles
1	$[1; 3.5]$mm	2mm	0.5mm	6000
2	$[0.8; 2.5]$mm	1.5mm	0.35mm	8000

Table 2: Summary of parameters for the particle generation

3.1   Particle positioning

The particle assembly consists of discs with a radius of $r_{fu} = 20$mm in which particles are positioned like it is depicted in Fig. 2a. One of such discs is depicted in Fig. 1a.

The generation of these disc is performed with an algorithm which fills sequential annuli (see. Fig. 1a). The vertical position of the discs starts with $h = r_U$. For the following discs the vertical position is increased by $2r_U$ until the maximal height of h_{fu} is reached (see Fig. 2a). Then all following in sequence generated discs get the height h_{fu}.
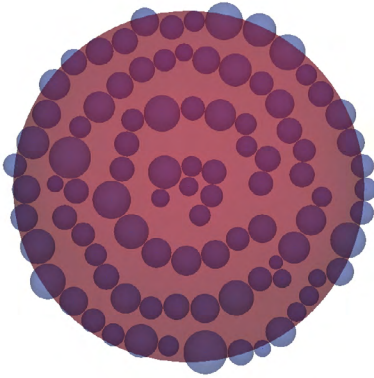
(a) Illustration of a disk of spheres for the pile investigation

(b) Measurement of the angle of repose

Figure 1: Particle-positioning for the pile assemblies

(a) Initial stage of the simulation

(b) Simulation of the pile
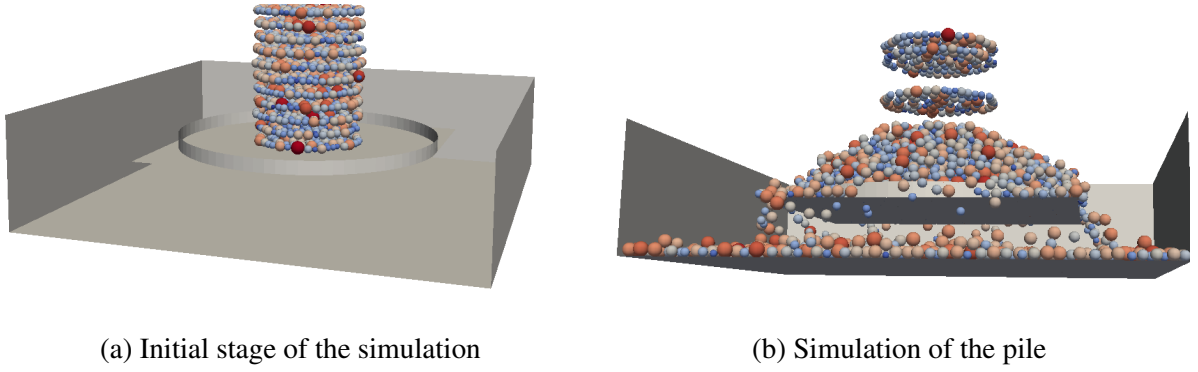
Figure 2: Simulation of the pile

(a) Simulated pile after the ralaxation

(b) Heap after the filter process
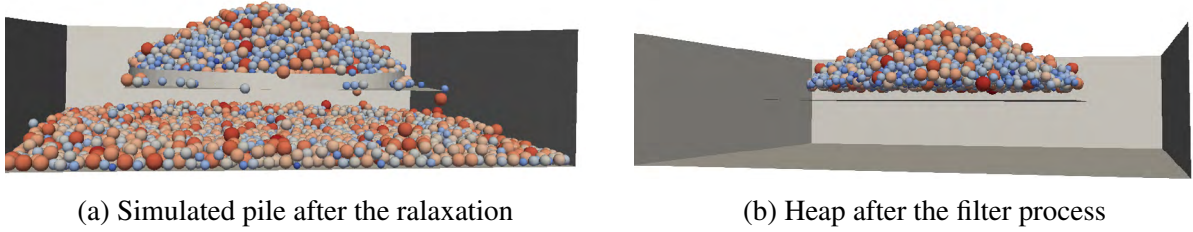
Figure 3: Finished simulation of the pile

3.2 Simulation

In order to lower the influence of the interaction between the particles and the plane a cylinder is introduced (cf. [2, p. 318]). It has a radius of $r_{cy} = 50$mm and height of $h_{cy} = 5$mm. In the initial stage of the simulation all particles of the discs with a height below $h_{fu} = 100$mm are treated, like it is depicted in Fig. 2a. In the following steps the simulation is performed for $t = \sqrt{\dfrac{4 r_U}{\|g\|}}$, thus the upper discs covers a distance of $2 r_U$. Then the treated particles are appended by the next disk with a height of h_{fu} (see Fig. 2b). These steps are repeated until all particles are treated.

In order that the last inserted particles find a stable position at the end a simulation is carried out for $t = 600$ms. The state after this integration is shown in Fig. 3a. Then a filter process is performed. All particles in the box or below the upper edge of the cylinder are removed, like it is depicted in Fig. 3b. During the filter-process the height of the pile h_P is determined.

3.3 Determination of the steepest angle of repose

A picture, in which the the steepest angle of repose of a real sandpile is measured, is shown in Fig. 1b. It can be seen that the top of the pile is rounded while the boundary of the remaining part is formed like a truncated cone. In order to determine the steepest angle of repose a cylindrical coordinate system is introduced. The origin of the coordinate system is placed at the bottom in the middle of the rounded base area of the pile. The angle of the polar axis is divided into

(a) Boundary particles

(b) Visualization of the truncated cone
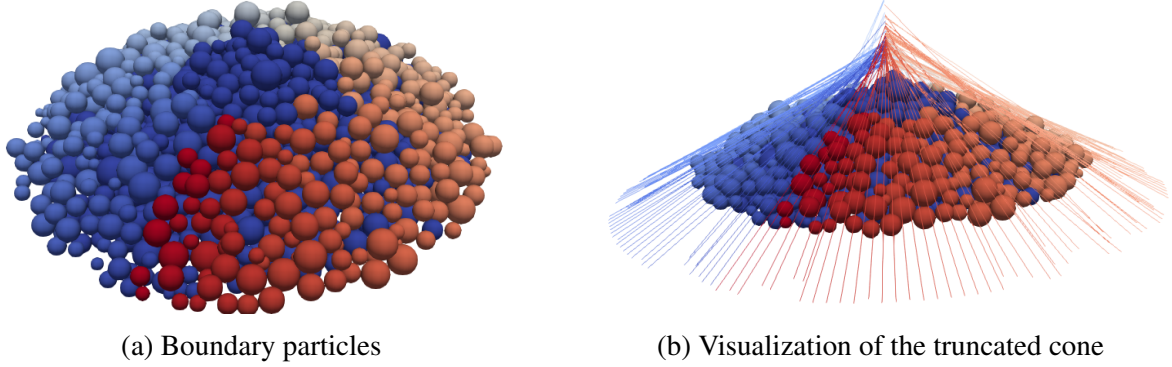
Figure 4: Approximation of the angle of repose

$\phi_N = 180$ parts. These direction vectors are given with

$$\boldsymbol{e}_{i_\phi} := \begin{pmatrix} \cos(\phi_{i_\phi}) \\ -\sin(\phi_{i_\phi}) \end{pmatrix} \qquad \text{with} \qquad \phi_{i_\phi} := \frac{360}{\phi_N} i_\phi \qquad , \qquad (9)$$

where $i_\phi = 0, \ldots, i_{\phi_N} - 1$ holds. In each direction several equidistant level of heights between $0.2 h_P$ and $0.75 h_P$ are defined in which the particle with the largest radial distance is searched. In Fig. 4a the particles which lie on the boundary are marked with the color which changes from red to blue with increasing i_ϕ. The dark blue particles are particles which doesn't lie on the boundary.

A line for each $\boldsymbol{e}_{i_\phi}$ is fitted with the minimization of the orthogonal distance between the particles and the line. The average angle ϕ of all these lines is the approximated angle of repose[2]. In Fig. 4b the line elements on the marked particles are shown.

The values of the measured angle of repose (see Fig. 1b) are $32°$ and $35°$. The goodness of the fit $E_\phi(P) = (\hat{\phi} - \phi(P))^2$ is determined with the average $\hat{\phi} = 33.5°$.

4 OEDOMETER

The oedometer test is a one-dimensional compression test [19, p. 115 ff.]. A soil sample is put inside a box. On top of the soil sample a load-plate is installed on which different loads are applied. The used box has a base area of $10\,\text{cm} \times 10\,\text{cm}$ and a height of $10\,\text{cm}$. This box prevents horizontal deformation of the soil sample. The average of six oedometer experiments is shown in Fig. 5. The settlement s is determined with $h_0 - h$ where h is the actual height of the plate and h_0 the height of the plate at the initial load step of $100\,\text{N}$.

The computational model consists of a rigid box which is filled with particles. In Fig. 6a the particle assembly in the box is shown after a compression with $100\,\text{N}$. Two assemblies are investigated. Assembly one consists of 4642 particles and has a void ratio of $e_1 = \frac{V_S}{V_P} = 0.66$, while assembly two consists of 3361 particles and has a void ratio of $e_2 = 0.67$. The quantity V_S is the solid volume taken by the particles and $V_P = 10 \cdot 10 \cdot 5\,\text{cm}^3 - V_S$ the volume of the voids.

---

[2]The implementation was performed in the bachelor thesis "Entwicklung eines Algorithmus zur Approximation des Schüttwinkels und Sensitivitätsanalyse" of Mr. B.Sc. Fabian Pfaff.
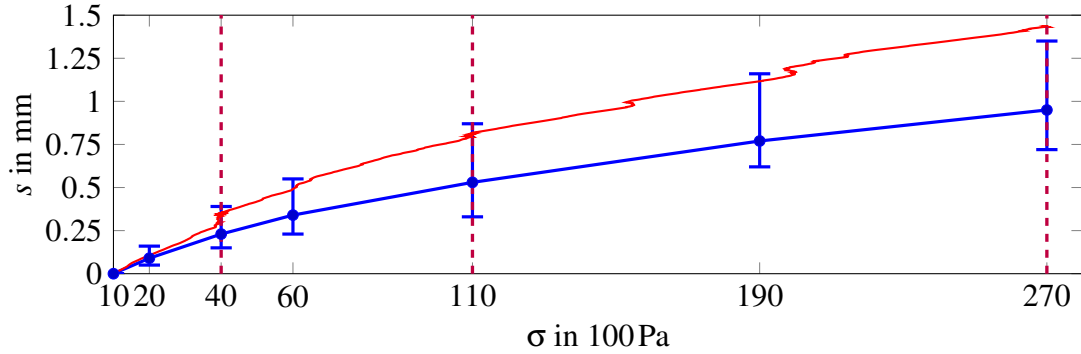
Figure 5: Stress-displacement curve for P_{120}

The force driven plate is applied for four loads L_n with $n \in \{0, 1, 2, 3\}$. The plate iteration starts with the following three steps: The generation of a backup of the particle positions and velocities, the movement of the load-plate downwards by a trial step δ_{Ta} and an integration of $n_s = 15000$ integration-steps.

This procedure is repeated until the resulting particle force of the force plate F_R satisfies the condition $F_R > L_n$. If this condition is fulfilled an integration of $n_L = 80000$ integration-steps is performed in order to relieve the particle force. If the resulting force F_R falls below L_n, the procedure with the short integrations and the backups is performed again. If the resulting force F_R after a long integration of n_L integration steps exceeds L_n, the backup of the last valid trial-step is loaded and the corresponding height of the force plate is applied. If this case occurs the trial step δ_{Ta} is reduced in each following trial-step with $\delta_{Ta} \leftarrow \delta_{Ta} m_T$, where $m_T = 0.95$ is a reduction factor. The reduction of the trial step considers the amount of the residuum $R = |F_R - L_n|$, so that m_T is adjusted to the residuum. It is also considered that the trial step does not fall below a critical value of $0.05\delta_{T0}$. The trial step is initialized with $\delta_{Ta} \leftarrow \delta_{T0} = 0.0075$. If the absolute value of the residuum is lower than the precision $R_{pr} = 30$ which equals $0.03\,\text{N}$ the iteration is finished.

With this procedure static states for the loading steps are simulated. Incorrect simulation conditions where the resulting force exceeds the plate force do not occur, since in such situations the backup of the last valid simulation state is loaded.

The simulation is performed with four loading steps $L_0 = 100\,\text{N}$, $L_1 = 400\,\text{N}$, $L_2 = 1100\,\text{N}$ and $L_3 = 2700\,\text{N}$. In Fig. 6b the iteration for the load-step L_0 is shown. The achieved precision for this load step is $(100000 - 100017.59)10^{-3}\,\text{N} \approx 0.017\,\text{N}$. The corresponding settlement $s_0 = 2.433\,795\,2\,\text{mm}$ is used as a reference value for settlements of the following load-steps (see Fig. 5). The experimental settlement for the initial load-step was much smaller. The reason for this could be that the packing density must be much higher. This could be achieved with lower particle radii or/and a good graduation [10, p. 52]. In Fig. 5 the displacement-stress curve of the load-steps $L_1 = 400\,\text{N}$, $L_2 = 1100\,\text{N}$ and $L_3 = 2700\,\text{N}$ is shown. In Fig. 5 and 6b the purple dashed lines marks the simulated load-steps L_i, the blue curve is the average of the measurements while the red one is the simulated curve. The error-bar in Fig. 5 represents the lowest and the highest measured values of the settlement. The quality of the simulation is quantified with the error

(a) Particle assembly after a compression with 100N

(b) Iteration of the load-plate with 100N for P_{120}
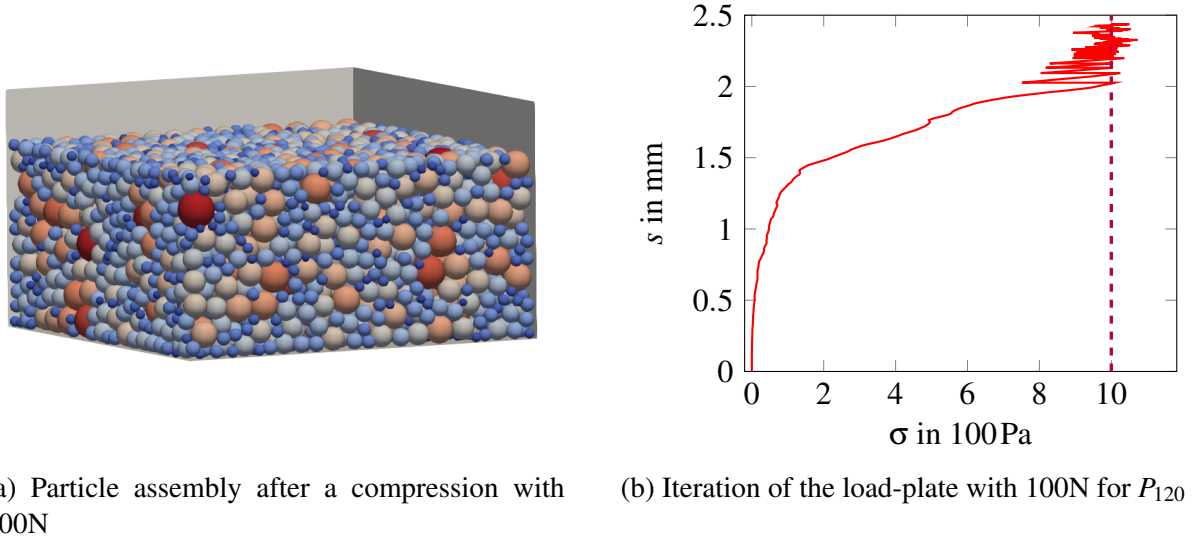
Figure 6: Oedometer test sample 120

measure $E_0 := \sqrt{\sum_{i=1}^{3}(\widetilde{s}_i - s_i)^2}$. which treats only the deviation of the settlements, since the deviation of the forces are negligible small due to the precision $R_{\mathrm{pr}} = 0.03$N.

5 DESIGN OF EXPERIMENTS AND METAMODELS

Since the numerical models for the investigation of the pile and the oedometer test are time expensive the sensitivity analysis should be performed using metamodels. The numerical model of the pile described in section 3 assigns each DEM-input parameters P (see (1)) a corresponding approximation of the angle of repose $\phi(P)$. The numerical model for the oedometer-test described in section 4 is investigated with respect to the failure measure E_0. Hence both models assign each parameter tuple with a scalar for the quality of the fit with the experimental measurement.

The DOE is performed with the Latin-Hypercube-sampling (LHS) (cf. [8, p. 240]) with 160 points for the pile and 200 for the oedometer test. In Tab. 3 the investigated interval[3] for each element of P (see (1)) is shown.

On this basis four different meta-models are generated. A quadratic and a cubic polynomial response surface method (cf. [1, p. 2123]) is used. The quality of the metamodel could be determined with the regression coefficient $R^2 = \dfrac{\mathrm{SSE}}{\mathrm{SST}}$ where SSE is the sum of square error and SST the total square error [1, p. 2123]. In [1, p. 2123] it is mentioned that generally with increasing R^2 the quality of the fit is rising. The quadratic polynomials have a poor quality of fit for the pile- and the oedometer model in comparison to the cubic ones. An interpolating metamodel is generated as well with radial basis functions (RBF). A cubic (triharmonic) ansatz function[4] $\psi_{\mathrm{T}}(r) = r^3$ [20, p. 55] and the thin-plate ansatz $\psi_{\mathrm{P}}(r) = r^2 \log(r^2)$ is used [1, p. 2124].

---

[3]The inverval for $\mu_{\mathrm{R,PP}}$ and $\mu_{\mathrm{R,PW}}$ for the oedometer experiment is $[5 \cdot 10^{-5}, 0.01]$.

[4]The parameter c which is used in [1, p. 2124] is equal to one in this work.

Quantity	Interval
Young's modulus E	$E \in [10^5, 10^6]$
Poisson's ratio ν	$\nu \in [0.2, 0.4]$
Coefficient of friction between particles μ_{PP}	$\mu_{\text{PP}} \in [0.7, 1.9]$
Coefficient of friction between particles and the wall μ_{PW}	$\mu_{\text{PW}} \in [0.4, 1.9]$
Coefficient of restitution e_{R}	$e_{\text{R}} \in [0.2, 0.6]$
Coefficient of rolling resistance between particles μ_{RPP}	$\mu_{\text{RPP}} \in [0.45, 4.5]$
Coefficient of rolling resistance between particles and the wall μ_{RPW}	$\mu_{\text{RPP}} \in [0.8, 5]$

Table 3: The DOE interval for the sensitivity analysis

6 Sobol' indices for the angle of repose

The global sensitivity-analysis is used to determine the influence of input variables or their combinations on the output of a system [14, p. 271]. Sobol' indices are often used since they are appropriate for the most models [17, p. 964]. A disadvantage is, that $2^n = 128$ terms [12, p. 259] must be determined for $n = 7$ input parameters. In this work the first and second order Sobol' indices are calculated for the pile and the oedometer experiments. Since the high computational effort of the numerical models the Sobol' indices are determined with the metamodels. In order to determine the Sobol' indices the input space must be defined in a n-dimensional unit cube [3, p. 3]. Hence the 7-dimensional input space (see tab. 3) for the parameter-tuple P must be transformed in a 7-dimensional unit cube $\widehat{\mathcal{P}} = [0,1]^7$. The investigated models are the quadratic and the cubic polynomial RSM, the thin-plate - and the cubic RBF of the pile experiment as well as the oedometer experiment. Each investigated model $f(\hat{P})$ with $\hat{P} \in [0,1]^7$ is decomposed in 2^n summands of different dimensions based on the Fourier-Haar series [15, p. 408] hence

$$f(\widehat{P}_1, \cdots, \widehat{P}_n) = f_0 + \sum_{i=1}^{n} f_i(\widehat{P}_i) + \sum_{i=1}^{n-1} \sum_{j=i+1}^{n} f_{ij}(\widehat{P}_i, \widehat{P}_j) + \cdots + f_{1,\ldots,n}(\widehat{P}_1, \cdots, \widehat{P}_n) \quad (10)$$

holds with $\widehat{P} = (\widehat{P}_1, \cdots, \widehat{P}_n)$. If $\widehat{P}$ is a uniform distributed random variable in $[0,1]^n$, then $f(\widehat{P})$ and the summands $f_{i_1,\ldots,i_s}(\widehat{P}_{i_1}, \cdots, \widehat{P}_{i_s})$ are random variables, too. The corresponding variances are D and $D_{i_1 \cdots i_s} = \int_{(\hat{P}_{i_1}, \cdots, \hat{P}_{i_s}) \in [0,1]^s} f_{i_1,\ldots,i_s}(\hat{P}_{i_1}, \cdots, \hat{P}_{i_s})^2 \mathrm{d}(\hat{P}_{i_1}, \cdots, \hat{P}_{i_s})$, respectively [14, p. 272].

In order to determine the variance eq. (10) could be rewritten with

$$D = \int_{\hat{P}_{\text{S}} \in [0,1]^n} f(\hat{P}_{\text{S}})^2 \mathrm{d}\hat{P}_{\text{S}} - f_0{}^2 = \sum_{i=1}^{n} \int_{\hat{P}_i \in [0,1]} f_i(\hat{P}_i)^2 \mathrm{d}\hat{P}_i + \sum_{i=1}^{n} \sum_{j=1}^{n} \int_{(\hat{P}_i, \hat{P}_j) \in [0,1]^2} f_{ij}(\hat{P}_i, \hat{P}_j)^2 \mathrm{d}(\hat{P}_i, \hat{P}_j) + \cdots$$

$$(11)$$

The Sobol' indices are determined [14, p. 272] with $S_{i_1,\ldots,i_s} := \dfrac{D_{i_1,\ldots,i_s}}{D}$. The second order Sobol' indices are lower than 0.05. Hence, they are negligible small. In Tab. 4 and 5 the first order

metamodel	E	ν	μ_{PP}	μ_{PW}	e_r	$\mu_{R,PP}$	$\mu_{R,PW}$	Res
RSM quad.	0.0166	0.0087	0.0370	0.0102	$3.7E{-}5$	0.8961	0.0040	0.035
RSM cub.	0.030	$9.4E{-}4$	0.0165	0.0132	$7.8E{-}6$	0.5302	0.0066	0.4483
RBF th. pl.	0.0419	0.0260	0.0091	0.0160	0.008	0.701	0.0215	0.1938
RBF cub.	0.0429	0.0275	0.0163	0.0185	0.019	0.547	0.0299	0.3302

Table 4: First order Sobol'indices for the pile experiment with assembly one

metamodel	E	ν	μ_{PP}	μ_{PW}	e_r	$\mu_{R,PP}$	$\mu_{R,PW}$	Res
RSM quad.	0.0072	0.022	0.003	0.0297	$2.3E{-}5$	0.9118	$7.5E{-}4$	0.0405
RSM cub.	0.014	0.054	0.0241	$5.5E{-}4$	$1.3E{-}6$	0.5065	0.0208	0.4096
RBF th. pl.	0.013	0.0218	0.0048	0.0015	0.020	0.759	0.010	0.2463
RBF cub.	0.016	0.019	0.0069	0.010	0.0194	0.6642	0.0207	0.3489

Table 5: First order Sobol'indices for the pile experiment with assembly two

Sobol' indices for the pile experiment are shown. The Sobol' indice for the parameter $\mu_{R,PP}$ has by far the biggest influence for all metamodels and both particle assemblies. In Tab. 6 and 7 the first order Sobol' indices for the oedometer experiment are shown. The most significant parameter of the oedometer model is by far the Young's modulus E. The sum of all indices should not exceed one. This isn't achieved in Tab. 7 for the quadratic polynomial RSM and the cubic RBF due to numerical errors.

7 CONCLUSION

In this work a sensitivity analysis with Sobol' indices is performed for the pile- and the oedometer experiment. Since the computational models of the two treated experiments are very time consuming sampling-points are generated with the Latin Hypercube sampling. On this basis four different metamodels are used to determine the first- and second order Sobol' indices. The second order Sobol' indices are negligible. The influence of the rolling friction parameter between particles is by far the most significant parameter in the pile experiment. For the oedometer experiment the Young's Modulus is by far the most significant parameter. With this information a more appropriate parameter fitting could be performed with an optimization of these parameters. A three dimensional ansatz was described to determine the angle of

metamodel	E	ν	μ_{PP}	μ_{PW}	e_r	$\mu_{R,PP}$	$\mu_{R,PW}$	Res
RSM quad.	0.9877	0.0058	0.0060	0.0018	$7.1E-6$	0.0011	0.0077	0.0103
RSM cub.	0.981	0.0017	0.0050	0.0057	$1.6E-5$	0.0059	0.0085	0.0416
RBF th. pl.	0.892	0.0011	0.0042	0.0029	0.0214	0.0026	0.0031	0.0885
RBF cub.	0.879	0.0029	0.0040	0.0049	0.0193	0.0012	0.0019	0.1066

Table 6: First order Sobol'indices for the oedometer experiment with assembly one

metamodel	E	ν	μ_{PP}	μ_{PW}	e_r	$\mu_{R,PP}$	$\mu_{R,PW}$	Res
RSM quad.	1.00	0.0094	0.0070	0.0017	$1.2E-5$	$1.8E-4$	0.0038	0.0250
RSM cub.	0.9314	0.0018	0.0067	0.0048	$2.4E-6$	0.0029	0.0069	0.0587
RBF th. pl.	0.9373	$3.4E-4$	0.0036	0.0084	0.0082	0.0021	$4.0E-4$	0.0444
RBF cub.	1.00	0.0093	0.0070	0.0017	$1.2E-5$	1.894	0.0038	0.025

Table 7: First order Sobol'indices for the pile experiment with assembly two

repose as well as a force-driven plate, which prevents incorrect simulation conditions where the resulting particle force exceeds the load-step.

REFERENCES

[1] Fang, H. and Rais-Rohani, M. and Liu, Z. and Horstemeyer, M.F. A comparative study of metamodeling methods for multiobjective crashworthiness optimization. *Computers & Structures* (2005) **83**:2122–2136.

[2] Grima, A. P. and Wypych, P. W. Discrete element simulations of granular pile formation: Method for calibrating discrete element models. *Engineering Computations* (2011)**28**:314–339.

[3] Homma, T. and Saltelli, A. Importance measures in global sensitivity analysis of nonlinear models *Reliability Engineering & System Safety* (1996) **52**:1–17.

[4] Hu, G. and Hu, Z. and Jian, B. and Liu, L. and Wan, H. On the determination of the damping coefficient of non-linear spring-dashpot system to model Hertz contact for simulation by Discrete element method *JOURNAL OF COMPUTERS* (2011) **6**:984–988.

[5] Langston, P. A. and Tüzün, U. and Heyes, D. M. Discrete element simulation of granular flow in 2D and 3D hoppers: dependence of discharge rate and wall stress on particle interactions. *Chemical Engineering Science* (1995) **50**:967–987.

[6] Lee, J. and Herrmann, H. J. Angle of repose and angle of marginal stability: Molecular dynamics of granular particles. *Journal of Physics A: Mathematical and General* (1993) **26**:373–383.

[7] Li, H. *Analysis of Off-Road Tire-Soil Interaction through Analytical and Finite Element Methods*. PhD dissertation Technischen Universität Kaiserslautern (2013).

[8] McKay, M. D. and Beckman, R. J. and Conover, W. J. Comparison of three methods for selecting values of input variables in the analysis of output from a computer code. *Technometrics* (1979) **21**:239–245.

[9] Michael, M. and Vogel, F. and Peters, B. DEM–FEM coupling simulations of the interactions between a tire tread and granular terrain. *Computer Methods in Applied Mechanics and Engineering* (2015) **289**:227–248.

[10] Minh, N. H. and Cheng, Y. P. A DEM investigation of the effect of particle-size distribution on one-dimensional compression. *Géotechnique* (2013) **63**:44-53.

[11] Rackl, M. and Hanley, K. J. A methodical calibration procedure for discrete element models. *Powder technology* (2017) **307**:73–83.

[12] Saltelli, A. and Annoni, P. and Azzini, I. and Campolongo, F. and Ratto, M. and Tarantola, S. Variance based sensitivity analysis of model output. Design and estimator for the total sensitivity index. *Computer Physics Communications* (2010) **181**:259–270.

[13] Skuodis, Š. *Modeling and Simulation in Engineering Sciences*. IntechOpen, (2016) 245–264.

[14] Sobol, I. M. Global sensitivity indices for nonlinear mathematical models and their Monte Carlo estimates. *Mathematics and computers in simulation* (2001) **55**:271–280.

[15] Sobol, I. M. Sensitivity estimates for nonlinear mathematical models. *Mathematical modelling and computational experiments* (1993) **1**:407–414.

[16] Stahl, M. and Konietzky, H. Discrete element simulation of ballast and gravel under special consideration of grain-shape, grain-size and relative density. *Granular Matter* (2011) **13**:417–428.

[17] Sudret, B. Global sensitivity analysis using polynomial chaos expansions. *Reliability engineering & system safety* (2008) **93**:964–979.

[18] Tsuji, Y. and Tanaka, T. and Ishida, T. Lagrangian numerical simulation of plug flow of cohesionless particles in a horizontal pipe *Powder technology* (1992) **71**:239–250.

[19] Verruijt, A. *An Introduction to Soil Mechanics*. Springer Switzerland Vol. 30, (2017).

[20] Yaghouti, M. and Azarboni, H. R. Determining optimal value of the shape parameter c in RBF for unequal distances topographical points by Cross-Validation algorithm. *Journal of Mathematical Modeling* (2017) **5**:53–60.

[21] Zhou, Y. C. and Wright, B. D. and Yang, R. Y. and Xu, B. H. and Yu, A. B. Rolling friction in the dynamic simulation of sandpile formation *Physica A: Statistical Mechanics and its Applications* (1999) **269**:536–553.

[22] Haff, P. K. *Granular Matter: an interdisciplinary approach* Springer New-York (1994)

[23] Jahn, M. and Meywerk, M. On the transformation laws for the macro to micro transformation *PAMM* (2019) accepted for puclication.

Atomistic submodel implementation and application within microstructure analysis by molecular dynamics

Ivan Trapić [1]*, Robert Pezer [2] and Jurica Sorić [1]

[1] University of Zagreb, Faculty of Mechanical Engineering and Naval Architecture,
Ivana Lučića 5, 10 000 Zagreb, Croatia
e-mail: ivan.trapic@fsb.hr, jurica.soric@fsb.hr, web page: www.fsb.unizg.hr/lnm/staff/

[2] University of Zagreb, Faculty of Metallurgy, Aleja narodnih heroja 3, 44 103 Sisak, Croatia
e-mail: rpezer@simet.hr, web page: www.simet.unizg.hr/hr/o-fakultetu/Members/rpezer

ABSTRACT

Classical continuum mechanics faces substantial difficulties for adequately describe stress and strain distributions around microstructural material discontinuities such as crystallographic defects, voids, and grain boundaries. One way to improve the microstructural model is the development of the atomistic submodel that provides a minimal increase in the amount of atomistic data, but provides more accurate stress predictions without time consuming calculation of full atomistic model. In the proposed approach continuum model, discretized by finite elements, provides a displacement field for atoms on the edge of the simulation cell of the the atomistic submodel driven by molecular dynamics. The final result is the utilization of the best from both worlds, calculation speed of the constinuum mechanics using finite elements method and informing it with relevant material properties inferred from atomistic simulations by using molecular dynamics where it is the necessary.

1 INTRODUCTION

One way to improve the continuum mechanics (CM) material model is the development of the atomistic, *ab initio*, atomistic submodel (AS) for atomic dynamics that underline material strength under the temperature and stress loading. Molecular dynamics (MD) is a prominent theoretical tool of choice used to investigate responses of different materials at the nanoscale. With the advent of access to the high-speed computer throughout recent decades, there has been a substantial advance in the atomistic simulation applications. However, as soon as one tries to tackle with a vast quantity of information that arises at that scale, even tiny macro scale piece of real material, usually force us to use multiscale (MS) approach. Coupling of the two models poses significant challenges as described in [1], [2]. In the essence difficulty reconciling the CM and MD approach is caused by the very different nature of the underlining theories. Discrete chunky nature of atomistic reality features phenomena that are very hard to connect with some CM features. For example, the crack tip propagation is a process that simultaneously involves many different scales at ones. This fact of the crack propagation brings us to the high interest in the development of MS models tuned up for a specific purpose. Many examples of a MS approach aiming to couple atomistic and continuum models have been proposed, among many, in the following reviews [2-6].

One route to go around that problem is a combination of the standard finite elements method (FEM) techniques and the MD approach. Microstructural objects like defects, micro porosities, impurities, or misorientation in crystalline systems very often cause long-range effects, far beyond immediate atomistic neighborhood where they are [7]. From the physical point of view, we also do not need an

immense quantity of information that is provided by MD simulation. Important types of nanoscale defects in material typically involve many atoms and are identified as critical individual objects that describe material properties. Atomistic to CM models coupling methods are used to mutually exchange of information between atomistic and continuum systems. If this coupling is a successful one can describe nanosized effects in great detail within the unified model.

2 MULTISCALE MODELING

2.1 Molecular dynamics

Modeling of materials by MD starts with a description of the atom dynamics within MD where they are material points without internal degrees of freedom. By this approach, we are left with a system of multiple point particles which position and velocities can be calculated using Newton's laws of motion. However apparent simplicity of general idea hides complexities and nonlinearity of the coupled partial differential equations that are second-order and nonlinear. Also of the complexity of the system of equations are even further scaled up with the sheer number of atoms and dimensionality of the problem. Therefore the system is far from trivial to solve and even more difficult to accurately interpret from the macroscopic point of view. The central question is how to reconcile immense complexity and data redundancy given by atomistic degrees of freedom with standard CM physical quantities. For a recent review, see an in-depth discussion of the subject provided by Admal and Tadmor [8].

For atomistic simulation, we use field *de facto* standard software suite known as LAMMPS (stands for **L**arge-scale **A**tomic/**M**olecular **M**assively **P**arallel **S**imulator) as described in [9]. LAMMPS is a classical MD simulation code that is capable to effectively solve the system with millions of Newtonian equations for different macro phases of matter including solid material. To be predictive, it needs information about particles interactions and external forces. A significant effort of the community in recent decades resulted in many realistic potentials that can be used in modeling tasks. One of the prominent projects along those lines that we use here is OpenKIM framework [10-11] that gives us reproducible and reliable realistic interaction potential input for atomistic simulation.

2.2 Atomistic to continuum coupling

MS modeling incorporates forming of a material model that spans over several orders of magnitude in the time and length scale. Usually, MS methods are used to connect the fine scale of atoms and more coarse scale of CM. By this coupling, one can, in the same model, study nanostructure in the localized region of particular interest where dynamics of an individual atom is relevant and use computation less expensive CM in the area, where deformation is more homogenous and smooth. Usualy the atomistic model described by using MD is surrounded by finite element (FE) mesh. Model space is therefore divided into two parts: one dominated by discrete atomistic features like chemical bonding and the rest of the area where computationally less demanding CM approach is applied. Depending on the type of transitions between two regions, different computational strategies are developed. Frequently used methods are *Quasicontinuum* (QC) method developed by Tadmor, Ortiz, and Phillips [12] and *Bridging Domain* (BD) developed by Belytschko and Xiao [13]. In QC coupling of the atomistic and continuum model is achieved by refining FE mesh in the area of interest until one node corresponds to one atom. In BD to achieve a smooth transition from atomistic into the CM so-called handshake region is introduced, where atomistic and continuum models are simultaneously present.

The first problem to be solved is the identification of the parts of the model space where MD calculation is to be applied. This way, atomistic submodel can used only around the areas where

continuum models are about to fail. Significant problem visible in such a composite model is the correspondence of the continuum and atomistic quantities like stress, strain and displacement. In our approach, we have chosen a path inspired by already developed MS methods and couple the AS by imposing displacement boundary conditions. Simulations run separately on different scales and by using FEM we have implied that one FE contains many atoms. This is similar to QC and that the displacement of atoms follows the movement of FE edges (in accordance with Cauchy-Born rule [14]). Since the goal is to get the entire stress field, there has been no necessity to impose any kind of model overlapping since beyond the stress concentration area there is an agreement of stress field of FEM and MD.

2.3 Atomistic stress analysis

Here we briefly outline the procedure for atomistic stress calculation. For the AS we go along the same lines as in [7] for microscopic stress calculation, which can be broken down into four steps:

1) define a representative set of points in space,
2) choose one point and identify all atoms within the averaging radius r_{ave} around that point,
3) add up all stress contributions per chosen atoms (equation (1)),
4) divide the obtained cumulative stress with the total volume (area in our 2D case) summing the volumes per identified atoms (equation (2)).

For calculating stress per atom we use standard expression available in LAMMPS:

$$\tilde{\sigma}_{ij} = -\left[m v_i v_j + \frac{1}{2}\sum_{\kappa=1}^{N_p}\left(r_i^{\kappa,1}f_j^{\kappa,1} + r_i^{\kappa,2}f_j^{\kappa,2}\right) + \frac{1}{3}\sum_{\zeta=1}^{N_a}\left(r_i^{\zeta,1}f_j^{\zeta,1} + r_i^{\zeta,2}f_j^{\zeta,2} + r_i^{\zeta,3}f_j^{\zeta,3}\right) + ...\right] \quad (1)$$

where interaction potential takes care of atoms present within the defined cutoff range that contributes to the stress.
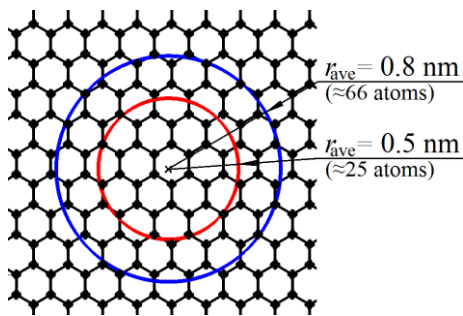
Figure 1, Determination of the averaging radius (all atoms within the circle are taken into account for the stress averaging procedure) [7]
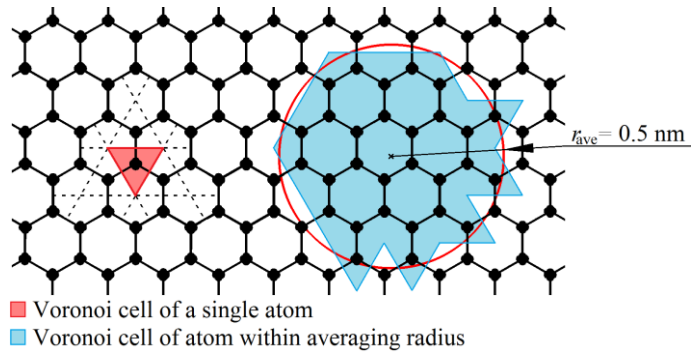
Figure 2, Representation of the Voronoi tessellation used for volume per atom determination [7]

Once the stress for each atom in a given region is calculated, we obtain spatially averaged stress for this region using the standard expression for N atoms:

$$\boldsymbol{\sigma}(r) = \frac{\sum_{\alpha=1}^{N}\tilde{\boldsymbol{\sigma}}^{\alpha}}{\sum_{\alpha=1}^{N}\Omega^{\alpha}} \quad (2)$$

N is the number of particles within the area we examine, while Ω^{α} is volume associated with the particular atom obtained using Voronoi tessellation. The process is shown in Figure 1 and Figure 2.

In addition to spatial stress also averaging include time averaging by conducting stress averaging procedure on snapshots of atomistic configuration every 1 ps, so local thermal excitement of atoms is washed out which result in the correct stress field. Time averaging is a simple mean value of averaged stress for the same point in space. In both cases (whole model and AS) configuration snapshots are taken after the system thermalizes for at least 10 ps.

3 MODELS

3.1 1D system

For the demonstration purposes, we outline the main idea in the case of a 1D system, as shown in Figure 3. To be as simple as possible but keep the main features, we analyze the standard mechanical problem of truss fixed at one end and loaded with some force on the other one. When translated into the atomistic picture, we get a chain of atoms connected with nonlinear elastic springs. As is well known realistic atomistic interaction like here, Lennard-Jones contains nonlocal contributions coming from distant atoms. Despite rapid decay of the force magnitude with distance and screening effects, this introduces a noticeable difference in calculated response to the external loading.
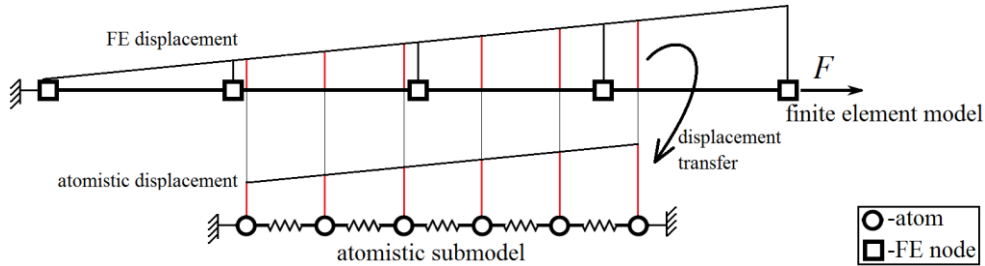
Figure 3, Atomistic submodel within full model space
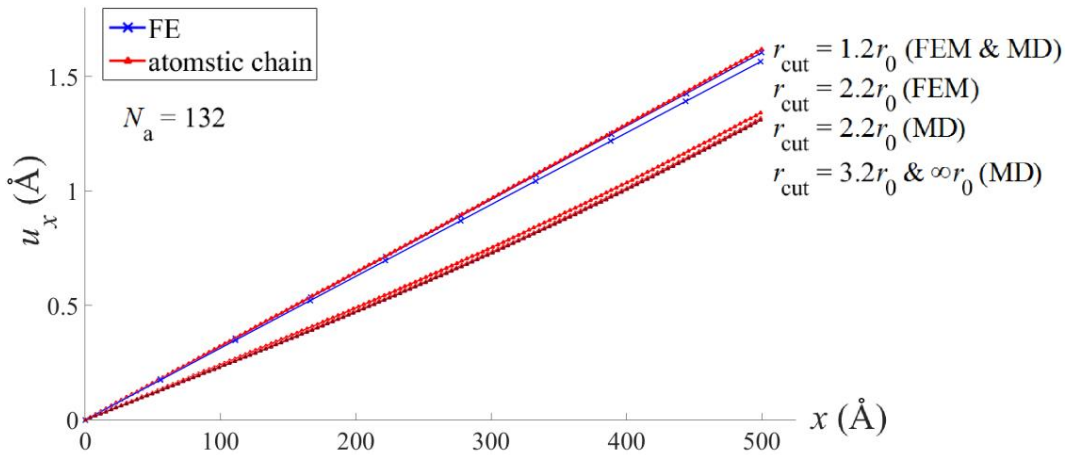
Figure 4, Comparison of atomistic chain analysis by FEM and MD for different cutoff radii

In Figure 4 we show the main results in the 1D case with the dependency of the displacement from the equilibrium position and coordinate along the full chain. The main message to be drawn from this is that we see a noticeable difference between MD and CM results. This difference gives a clear indication of how nonlinear and long-range interaction contribution influence results even in elastic regime. Namely, for CM and MD results to agree it is not enough to stay in elastic regime during loading but also cut off radii r_{cut} has to be small including just nearest-neighbor interatomic interactions. So this result demonstrates clearly that physical modeling in regions of high-stress

concentration even in topologically trivial 1D case calls for caution in the proper account for relevant physical quantities.

3.2 2D system

Our strategy following these results from the 1D model is to devise a combined model taking the CM results far from the hole and impose deformation as boundary conditions to the AS. This limited region is identified based on atomistic to CM stress ratio as criteria following the prescription given in [7]. Basic configuration in a 2D system that is the main objective of the present paper is shown in Figure 5. One of the results that we have obtained is that it is unimportant what is the shape of the submodel region as long as we are far away from the high values of stress gradients. We have chosen the square because of computational simplicity. According to the external loading, we first calculate deformation within the CM framework by standard FE discretization in the system.
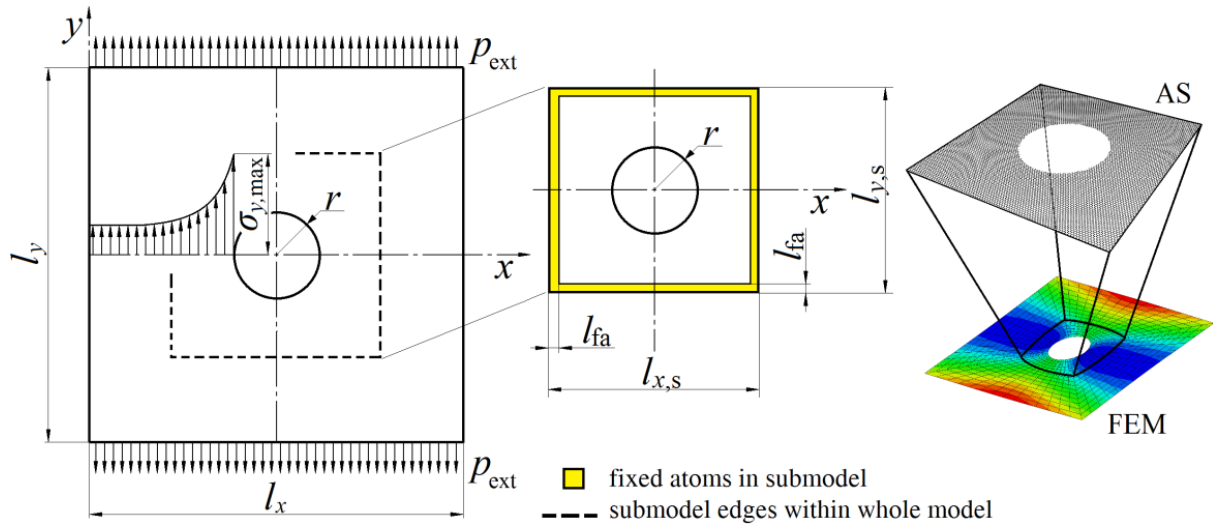
Figure 5, The geometry of the 2D sheet with the position of a circular hole

Table 1, Model parameters follow labeling symbols in Figure 5

	full model	submodel
sheet size (before loading)	l_x = 168.4 nm	$l_{x,s}$ = 39,86 nm
	l_y = 169.9 nm	$l_{y,s}$ = 40,91 nm
the thickness of fixed atoms in the atomistic submodel	/	l_{fa} = 2 nm
hole radius	r = 9 nm	
imposed deformation	ε_y = 0.025	/
2D elasticity modulus	3300 GPa/Å	/
Poisson ratio	0.16	/
temperature	T = 300 K	
initial thermalization time	t_{therm} = 10 ps	
stretching time	t_{load} = 100 ps	/
equilibration time	t_{eq} = 10 ps	t_{eq} = 30 ps
number of atoms	1,116,371	53,611
averaging radius	r_{ave} = 2 nm	
the average number of atoms within an average radius	$N_{ave} \approx 473$	
number of time frames for averaging	10	
the span between time frames	1 ps	
calculation time	660.42 h	5.17 h

In the region depicted in Figure 5 by yellow color (narrow square strip) we impose deformation on atoms as obtained from FE calculation. Using MD simulation, we let the subsystem equilibrate and calculate stress distribution using equations (1) and (2). For relevant simulation parameters, see Table 1. For atomistic simulation, we have used AIREBO (**A**daptive **I**ntermolecular **R**eactive **E**mpirical **B**ond **O**rder potential) potential, developed by Stuart et al. [15], from OpenKIM repository for carbon giving us account for graphene sheet with a topology defined in Figure 5. AIREBO potential is an upgrade to REBO (**R**eactive **E**mpirical **B**ond **O**rder potential) initial developed by Brenner et al. [16]. Using such a realistic description of interaction gives us the confidence to faithfully reproduce experimentally relevant elastic properties and strength, as presented in [17]. In the case of full atomistic model calculations are conducted using thermostating procedure in the isobaric-isothermal (NpT) ensemble at a zero pressure and temperature of 300 K (provided by LAMMPS thermostating facility) with periodic boundary conditions were used along x and y axsis with imposed deformation in with imposed deformation in y direction.

First, we solve the CM problem using standard FEM procedures for linear static analysis and elements are first order four nodes 2D FEs. After FEM analysis, deformation is imposed faraway from hole (yellow square edge of the AS) to the atomistic system. Boundary conditions for AS are fixed edge atoms. Bulk atoms are subjected to the Canonical ensemble and left to thermalize for 30 ps.

4   RESULTS

Figure 6 is the result of the AS output. Stress averaging has been performed spatially using the averaging radius r_{ave} of 2 nm. Since boundary atoms of the AS are fixed and unaffected by relaxation, their contribution to the stress distribution is not affected by thermalization of the system and therefore should not be taken into account. The results of stress averaging on the AS are shown in Figure 6 with leaving out the parts of the model space with unmovable atoms.
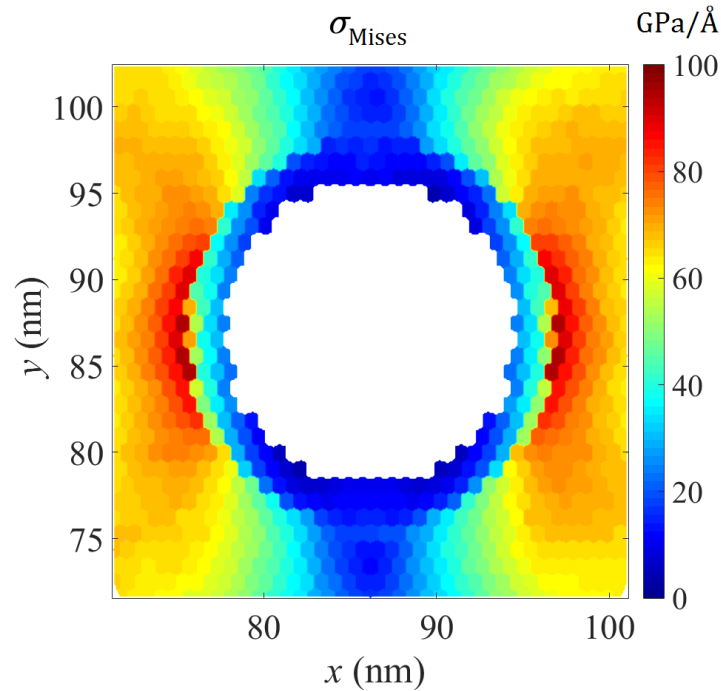
Figure 6, Spatially averaged atomistic stress distribution within AS

The stress distribution calculated using the atomistic model by the spatial and time averaging procedure is used to inform the full model in the concurrent region. Figure 7 shows stress distribution

through the model space with CM stress far away from the hole, and atomistic averaged stress around the opening. To visualize the final results more clearly in Figure 7, we show a series of the stress distribution results from the CM model on the left figure and averaged atomistic on the right one. In the Figure 7 right, we have inserted instead of CM results values obtained from AS. Connecting criteria is that the displacement of the atoms and CM media agree in the joint region as inspired by the Cauchy-Born approximation. This way, we have obtained a composite multiscale solution which combines the calculation speed of CM with accuracy and realistic properties of MD. With the natural implementation of boundary effects around the hole and with a substantial reduction of computer processing time.
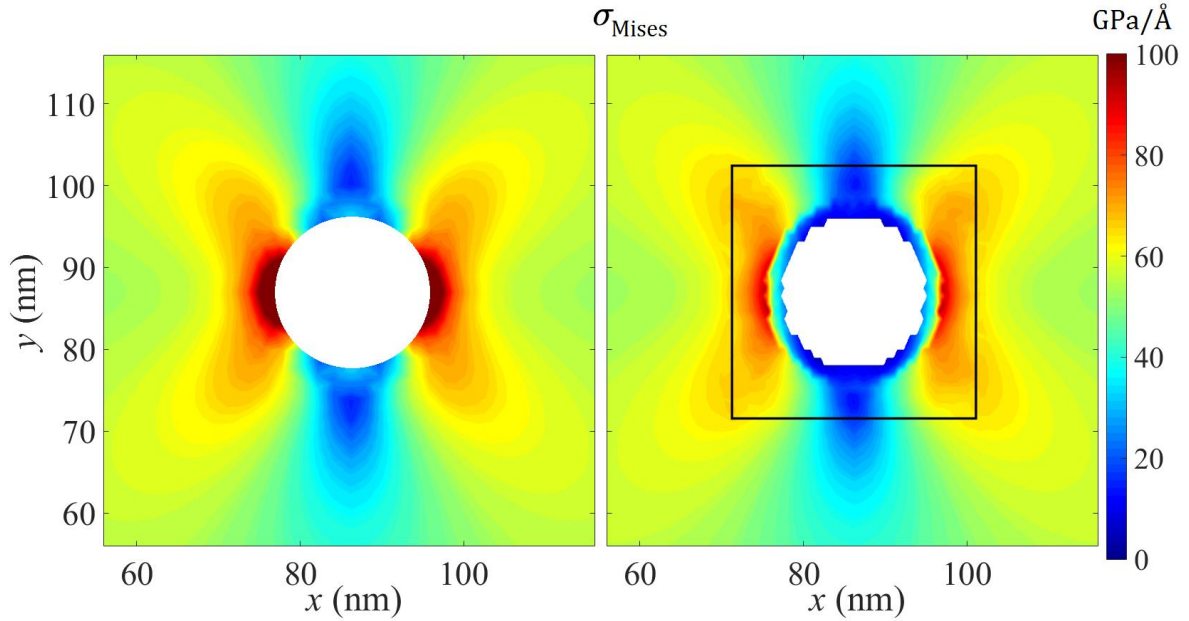
Figure 7, Stress distribution around the hole as seen from the full model only by FEM (left) and with submodel correction (right),

5   CONCLUSION

In this paper, we report on the simple yet effective way to unite CM and atomistic approach for the case of 1D and 2D system under external loading. First, we have shown a simple 1D academic example that examined key differences between atomistic and CM models and possible difficulties we might face in connecting the two approaches. In the second part, we show how we can effectively deal with the 2D problem of a graphene sheet with a circular hole under the uniaxial tension. We present an effective procedure of how one can use atomistic MD simulation in regions where the CM model is about to fail without proper account for near the edge stress distribution. Precise calculations of the stress distribution were atomistic discrete nature of matter plays a decisive role is of great importance with nanosized structures similar to the ones presented here. We have also outlined the main difficulties in developing proper physical MS connections of the CM system with the AS.

6   REFERENCES

[1]   E. B. Tadmor, R. E. Miller: *Modeling Materials*. Cambridge University Press, Cambridge, 2011,

[2]   W.A. Curtin, R.E. Miller: *Atomistic/continuum coupling methods in multi-scale materials modeling*, Modeling and Simulation in Materials Science and Engineering, 11(3):R33-R68, 2003,

[3]   S. Li, S. Urata, *An atomistic-to-continuum molecular dynamics: Theory, algorithm, and applications*, Computer Methods in Applied Mechanics and Engineering, Volume 306, Pages 452-478, 2016,

[4]   P. Bochev, R. Lehoucq, M. Parks, S. Badia, M. Gunzburger: *Blending Methods for Coupling Atomistic and Continuum Models*, In: Jacob Fish, eds., Multiscale Methods: Bridging the Scales in Science and Engineering, 151-177. Oxford University Press, Inc. New York, 2009

[5]   D. W. Brenner, O. A. Shenderova, J. A. Harrison, S. J. Stuart, B. Ni, S. B. Sinnott: *A second-generation reactive empirical bond order (REBO) potential energy expression for hydrocarbons*, J. Phys.: Condens. Matter 14, P. 783–802, 2002

[6]   J. Fish.: *Bridging the scales in nano engineering and science*, J. Nanopart. Res., 8:577-594, 2006

[7]   I. Trapić, R. Pezer, J. Sorić, *Atomistic Modelling of 2D Stress Distribution Around Discontinuities*, Transactions of FAMENA (1333-1124) 42, 3; 47-60, 2018,

[8]   N. C. Admal, E. B. Tadmor: *The non-uniqueness of the atomistic stress tensor and its relationship to the generalized Beltrami representation*, Journal of the Mechanics and Physics of Solids, 93, 72-92, 2016.

[9]   S. Plimpton: *Fast Parallel Algorithms for Short-Range Molecular Dynamics*, J Comp Phys 1995, 117 1-19. DOI: 10.1006/jcph.1995.1039, (http://lammps.sandia.gov)

[10] E. B. Tadmor, R. S. Elliott, S. R. Phillpot, S. B. Sinnott, NSF Cyberinfrastructures: *A New Paradigm for Advancing Materials Simulations*, Current Opinion in Solid State & Materials Sciences, 17, 298-304, 2013. (https://openkim.org/)

[11] E. B. Tadmor, R. S. Elliott, J. P. Sethna, R. E. Miller, C. A. Becker: *The Potential of Atomistic Simulations and the Knowledgebase of Interatomic Models*, JOM, 63, 17, 2011.

[12] E. B. Tadmor, M. Ortiz, R. Phillips: *Quasicontinuum analysis of defects in solids*, Philosophical Magazine A, 73:1529{1563, 1996

[13] T. Belytschko,, S. P. Xiao: *Coupling methods for continuum model with molecular model*, International Journal for Multiscale Computational Engineering, 1:12, 2003

[14] F. Milstein: *Crystal elasticity, Mechanics of solids*, edited by H. G. Hopkinks and M. J. Sewel, 417:452, Pergamon, Oxford, 1982

[15] S. J. Stuart, A. B. Tutein, J. A. Harrison: *A reactive potential for hydrocarbons with intermolecular interactions*, Journ. of Chem. Phys., V 112,14, p. 6472-6486, 2000

[16] D. W. Brenner, O. A. Shenderova, J. A. Harrison, S. J. Stuart, B. Ni, S. B. Sinnott: *A second-generation reactive empirical bond order (REBO) potential energy expression for hydrocarbons*, J. Phys.: Condens. Matter 14, P. 783–802, 2002

[17] L. Changgu, W. Xiaoding, Kysar, W. Jeffrey, J. Hone: *Measurement of the Elastic Properties and Intrinsic Strength of Monolayer Graphene*, Science, 321, 385-388, 2008

DEM MODELING OF ROCKFALL REBOUND ON PROTECTIVE EMBANKMENTS

G. LA PORTA[1], S. LAMBERT[2] AND F. BOURRIER[2]

Politecnico di Torino
Corso Duca degli Abruzzi, 24, 10129 Torino
e-mail: giulia.laporta95@gmail.com

[2] Univ. Grenoble Alpes, Irstea
ETNA, 38000 Grenoble, France
e-mail: Stephane.Lambert@irstea.fr

Key words: Rockfall, Protective Structures, DEM.

Abstract. Design of Rockfall Protection Embankments and estimation of their capacity to control the trajectory of rock boulders are complex issues, which give considerable room for research and improvement. A lack of detailed models for the simulation of block rebound in the embankment vicinity is mainly due to the large number of parameters that influences the phenomenon. Therefore, the evaluation of the embankment efficiency in satisfactorily acting on the block trajectory, as a function of the site characteristics and boulder kinematics, is still precluded to design engineers.

In the present paper, the open-source code YADE, based on a discrete element method (DEM), is used to model the bouncing of a rock block on the embankment face, while taking into account a certain number of parameters with influence on the impact.

By contrast with previously developed models (DEM, FEM or coupled approaches), the aim is here to propose a model with limited computation cost. In this purpose, the embankment is modelled as a membrane interacting with the rock block. The embankment body is not represented because it would require a large number of particles, and, consequently, a high computational time. Various elements implemented in YADE are used to model the embankment surface, with the aim of mimicking the mechanisms involved during the rock boulder rebound. The validity of the approach is addressed comparing simulation results with the few experimental data available from the literature. The influence of characteristics of the impacting block (radius and weight) and kinematic parameters (impact angle and velocity) on the restitution coefficients is explored. In particular, the normal (R_n), tangential (R_t) and energetic (R_{TE}) coefficients of restitution are monitored. The goal of defining an efficient model in a realistic range of these parameters is pursued.

1 INTRODUCTION

Rockfall protection embankments are massive civil engineering structures, built in elevation with respect to the ground to intercept large falling rocks. They are typically 3 to 7 m high and up to a few hundred meters long. On a functional point of view, the design of an embankment aims in assessing the ability of the structure in adequately modifying the blocks trajectories. This is particularly related to the way the blocks bounce on the embankment's face. Such a rebound appears to be extremely complex as it depends on many parameters related to the block shape, velocity (translational, rotational), to the impact point location and to the embankment characteristics (constitutive materials and geometry).

Different studies have addressed numerically the impact response of embankments (Peila et al. [10], Plassiard and Donzé [12], Breugnot et al. [2]). The block rebound and its post-impact trajectory have been investigated by Plassiard and Donzé only ([12]). It is worth highlighting that, as shown by Lambert et al. [7], simulation tools used by design engineers for modelling the trajectory of rock blocks down natural slopes are not appropriate for modelling the rebound after impact on rockfall protection embankments.

The purpose in this study is to create a model that can properly reproduce the block bouncing, accounting for the relative influence of each parameter, structural or mechanical. The main interest is to develop a model, inexpensive in terms of computational time, which permits a calibration as simple as possible. This model is developed using YADE [14], an open source software based on a discrete element method (DEM).

The impacted surface is modelled considering a physical idea and a design that strictly simulate the response of the real structure. Its body is not considered in the representation because of the large dimension and, consequently, large number of particles that would be required in the modelling, and the computational time. The model is calibrated and the response is verified using experimental data and empirical relations.

2 PHYSICAL MECHANISM

Embankments are designed in order to limit the there that the block jumps or rolls over the structure after bouncing on the structure face. This risk depends on many parameters.

It is increased if (1) the uphill face inclination is insufficient (inclination higher than 65° are sometimes recommended for avoiding any 'springboard effect'), (2) the block trajectory before impact is oriented upward and (3) the incident rotational velocity of the block is high. The shape of the block can influence its behaviour post impact: a shape with edges can favour bouncing over the structure while a spherical one will favour rolling over.

Bouncing also depends on the energy dissipation occurring in the embankment during the impact. The impact by the block induces a high stress in the vicinity of the impacted area, with compaction and particle crushing inducing energy dissipation. These mechanisms are associated to longer impact durations (up to 300 ms) depends on the embankment fill materials characteristics.

The developed model aims at proposing a tool to be used by design engineers and accounting for the influence of all these parameters on the post-impact trajectory of the block.

3   THE STRUCTURE

3.1 The model – Physical idea

The aim of this work is to develop a computationally-efficient model of the block rebound on embankments uphill face. The main mechanisms controlling the block-structure interaction are the penetration (in terms of force and deformation) and the friction at the block/face interface. It is proposed to model this interaction via a membrane located at the embankment face. This membrane is supported by simple mechanical systems as shown in Figure 1. This physical model is based on vertical elements supporting a surface with frictional characteristics. These elements can reflect a combined behaviour of springs, dampers, sliders, etc., simulating the overall structure's behaviour.
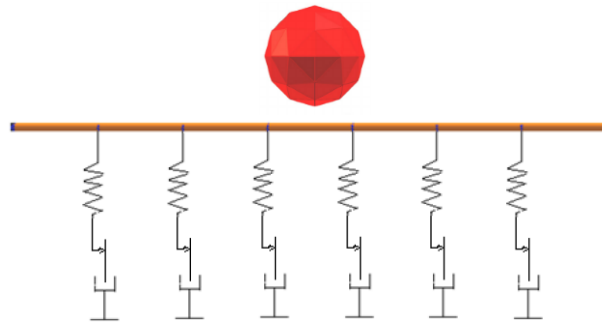
Figure 1: Physical model considered for the structure modelling.
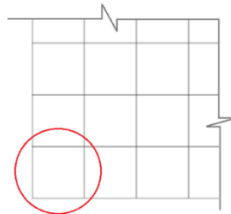
Figure 2: Scheme of the elementary structure (circled in red), reproduced to create the overall structure.

3.2 Model construction

The surface is built reproducing a square elementary structure (Figure 2). The surface's edges are blocked, in order to maintain the overall position of the surface in the modelling space during the impact. The vertical elements are calibrated in order to control the behaviour of the structure during the penetration.
Some points are crucial:
- The surface has to be large enough in order to avoid any influence of the boundary conditions on the block-surface interaction.

- The dimension of the elementary structure has to be small with respect to the radius of the impacting block, to ensure a contact as continuous as possible between these two bodies during impact. For this reason, a dimension of 1/5 the radius was chosen.
- The expected maximum penetration being 1.5 m, a length of the vertical elements of 2 m is used.

As for the surface mass, two cases have been tested: (1) constant surface mass, even changing the dimensions of the boulder and (2) surface mass proportional to the boulder mass. Simulations showed that the two cases led to the same maximum penetration values. However, an irregular behavior of the surface during deformation was observed when its mass was too high compared to the boulder mass. Some areas of the surface showed temporarily an unexpected and non realistic deformation. Therefore, choice was made to give the surface a mass proportional to the boulder mass.

The study of the penetration focuses on the impact moment having a duration typically less than 300ms. Gravity was not considered in the modelling, due to its very limited influence on the block trajectory over such a short period of time.

3.2.1 The elementary structure

The elementary structure is built using available elements from YADE: nodes (Grid Nodes), cylinders (Grid Connections), and PFacets.

Figure 3: Elements of Yade - cylinders, spheres, Pfacets.

PFacets are used to manage the friction between the boulder and the surface. These were preferred over the so-called Facets elements, because these latter did not allow creating a continuous surface, due to discontinuities from one element to the other. This problem was overcome considering PFacets inside a triangular configuration between physical elements: nodes (Grid Nodes) in the angles, and cylinders (Grid Connections) connecting them. In this way the space between two of these elements in contact is occupied by the cylinders, which guarantee continuity in the structure.

Two different configurations for the elementary structure were tested (Figure 4). The elementary structure was created using 2 or 4 PFacets. In Figure 4, PFacets are the triangular elements, the Grid Nodes appear in yellow and the Grid Connections appear in orange. Using 4 PFacets an additional node is located in the structure centre and the radius of Nodes and Grid Connections is smaller than in the previous case.
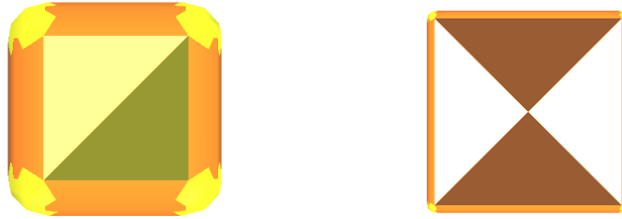
Figure 4: The two types of elementary structures tested (2 and 4 Pfacets, left and right, resp.)

The behaviour of the model with the first elementary structure resulted problematic. The response of the surface to the impact was not symmetric with respect to the impact point in case of a normal impact. This problem was attributed to the fact that the mass of PFacets is concentrated on the nodes at the edges of the triangle. In fact these elements were originally developed for fixed configurations, while in the proposed application these elements are mobile and experience large and fast displacements. The proposed solution to overcome this problem was to use the second type of elementary structure, with 4 PFacets.

In the case of the model built reproducing the second elementary structure, with 4 PFacets, the number of vertical elements is twice that of the previous case, because all the central elements of the elementary structures are clumped to vertical units. The overall surface is now symmetric with respect to each axis crossing the central node. Therefore, the response of this model to the impact is regular and symmetric.

4   ELASTO-PLASTIC MODEL

The membrane mechanical response to impact is mainly governed by the vertical elements, which response governs the penetration (including dissipation) and rebound.   Vertical elements consist of Yade's elements named cylinders (Grid Connections) which were attributed the law developed by I. Olmedo et al. [9]. This interaction law allows the input of an elasto – plastic constitutive law, specifying parameters like the elastic deformation modulus, the deformation modulus in the plastic phase, or the unloading one, the yielding point (Figure 5). Nevertheless, these elements only work in tension, while it is supposed to work in compression in this application. As a solution, the trick consisted in placing these elements on the same side as the projectile (green lines on Figure 6) while making them invisible to the projectile so that there was no interaction between these two body types.

Each vertical element is connected, on one side to the surface thanks to a Clump with each Node of the elementary structures and to a fix point on the other side. In Figure 6, the boundary nodes of the surface are coloured in blue because these are fix compared to other nodes from the surface.

The parameters of these elements were calibrated, in combination with the characteristics of the surface, in order to have a response in terms of deformation vs the impact force as realistic as possible. The parameters reported in Table 1 were considered for the boulder and the embankment materials.

242
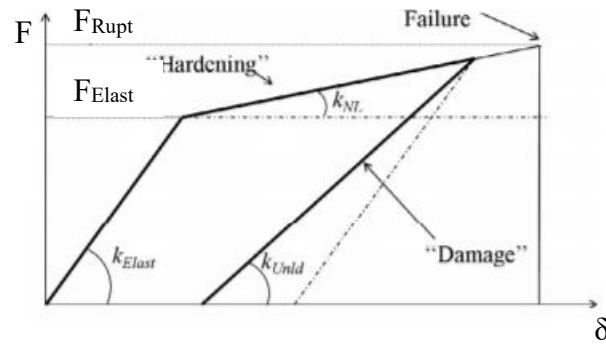
Figure 5: Scheme of the trilinear hysteresis.
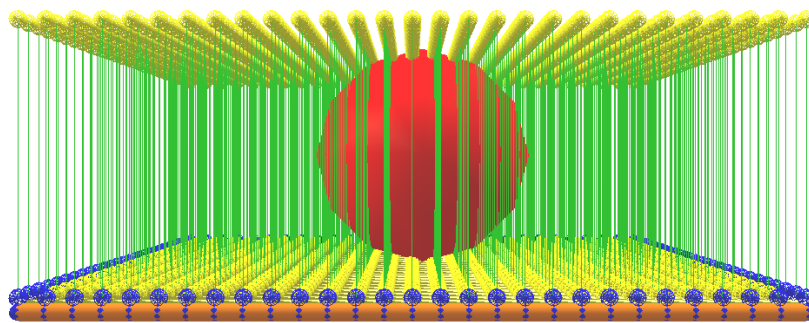
Figure 6: Overall structure (vertical elements in green).

Table 1: Model average parameters.

Young's Modulus [Pa]	4.00E+07
Poisson's Modulus [-]	0.3
Density [kg/m3]	2650
Friction Angle [°]	20
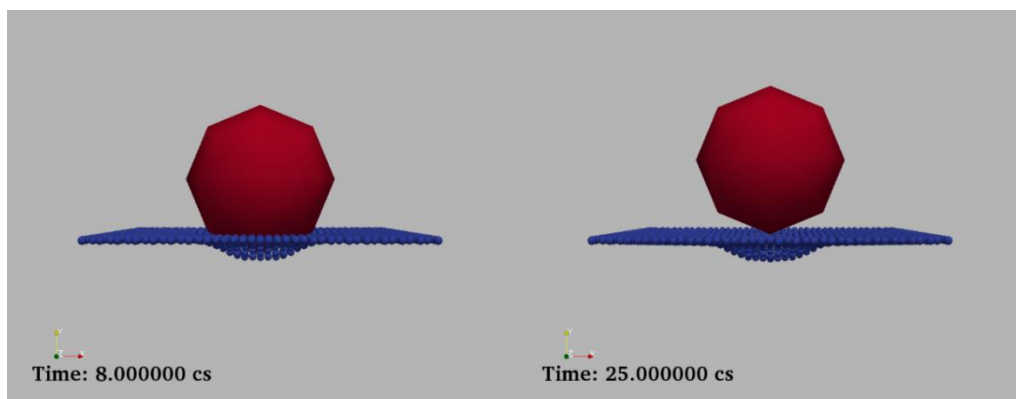
Figure 7: Impact simulation in the elasto-plastic model. Velocity of the rock block: (0,10,0) m/s.

4.1 Model calibration

The calibration was conducted with the aim of making the model able to approach realistic values for the penetration and impact force, considering existing knowledge from different sources. This calibration is not conducted for a specific study case. The values reported in Table 2 were used to calibrate the developed model, referring to an impact of a sphere 1 m in radius, and 11100 kg in mass, translational velocity perpendicular to the surface and rotational one null.

Table 2: Values used for the calibration of the model.

Boulder's velocity	10 m/s	25 m/s
Impact force	4000 kN	12000 kN
Max penetration	0.40 m	0.75 m
Duration	55 ms	45 ms

The maximum impact force was calculated by the Montani's equation [8].

$$F_i \, [kN] = 1.35 * exp\left(\frac{r}{3t}\right) * r^{0.2} * M_E^{0.4} * (tan\phi)^{0.2} * \left(m * H_c * \frac{g}{10^3}\right)^{0.6} \tag{1}$$

With:
- r: radius of the projectile [m];
- t: soil layer thickness [m];
- M_E : impacted material static elastic modulus [kPa];
- ϕ : friction angle of the impacted material;
- m: mass of the projectile [kg];
- H_c : projectile free falling height [m];
- g: gravity [m/s].

Then the penetration was evaluated, using the simplified formulae:

$$p = \frac{mv^2}{F_i} \tag{2}$$

The penetration was also compared to an equation derived from the work by Calvetti and di Prisco (2007) [3]:

$$p = 0.027 * r * v + 0.24 \tag{3}$$

with *r* the radius of the impacting block and *v* its velocity.

Finally, the duration of the impact (penetration until the maximum value) was evaluated through the relation:

$$\Delta t = \frac{2mv}{F_i} \tag{4}$$

Regarding the penetration, it was decided to consider an average value between the values calculated from Montani's, and Calvetti and di Prisco's relations.

5   MODELLING APPROACH RELEVANCY

The model was tested varying the boulder's radius, impact angle, and impact translational and rotational velocity with aim of assessing the relevancy of the proposed modeling approach in mimicking the block rebound.

Maximum penetration trend - impacts perpendicular to the surface

The first comparison concerns impacts perpendicular to the surface, varying the impact velocity. Calvetti and di Prisco [3] established trends between the maximum penetration and the projectile free falling height, considering different values of boulder's radius. The application case was a concrete gallery covered with a granular layer from 1 to 2 meters, and an impacted by block of mass 850 kg. Based on numerical simulations, they proposed the chart presented in the Figure 8, on the left. A regular increase of the maximum penetration with the falling height is observed. Additionally, the slope of the curves increases with the boulder's radii.
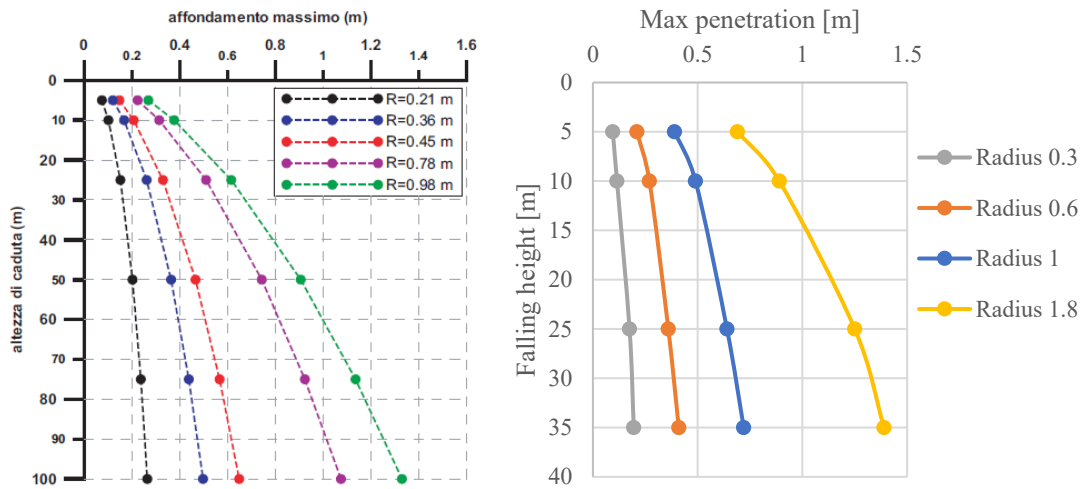
Figure 8: On the left, maximum penetration trend by Calvetti and di Prisco (2007) [3]. On the right, maximum penetration trend of the developed model.

In the developed model, the test was conducted in order to verify the regularity in the response of the system. Simulation results presented in the Figure 8, on the right, reveal similar trends. It means that, even though the model parameters were calibrated a rough way,

the system reacts to the variations of the simulation conditions in a satisfactory way, varying the initial velocity and block radius.

Influence of the incidence angle and impact velocity

The model was then tested in the case of inclined impacts and compared with the state of the art and the experimental results presented in Heidenreich in 2004 [6] with the aim, again, at evaluation the relevancy of the modeling approach in reproducing established trends.

One way to study the rebound evolution with the incidence angle is to consider the normal, tangential and energetic coefficients of restitutions:

$$R_t = \frac{v_{t,r}}{v_{t,i}} \tag{5}$$

$$R_n = \left| \frac{v_{n,r}}{v_{n,i}} \right| \tag{6}$$

$$R_{TE} = \frac{E_{TOT,r}}{E_{TOT,i}} \tag{7}$$

$$R_\omega = \frac{\omega_r}{\omega_i} \tag{8}$$

Where:
- v_t and v_n: respectively tangential and normal components of the velocity;
- ω: angular velocity;
- "indices" i and r: incident and rebound elements, characterizing the velocity and the energy before and after the impact;
- E_{TOT}: total energy, sum of E_t and E_R, defined as

$$E_t = 0.5 * m * \left(v_x^2 + v_y^2 \right) \tag{9}$$

$$E_r = 0.5 * \Theta * \omega^2 \tag{10}$$

With m the boulder mass, Θ the inertia moment and ω its rotational velocity (rad/s).

These coefficients allow quantifying the variation in the velocity components and the energy dissipation during the impact. Additionally, these restitution coefficients allow highlighting couplings between the different component of the generalized velocity vector (ex: After an inclined impact by a block without rotation, the rotational velocity is not null anymore).

The influence of the impact angle and the impact translational velocity (the rotational velocity, in this case, is imposed equal to zero) on the block rebound is studied considering two spheres, with radii of 0.3 and 1 m, and correspondent masses of 300 and 11100 kg. In this way, even the influence of the boulder's mass, directly linked to the boulder's radius, is showed.
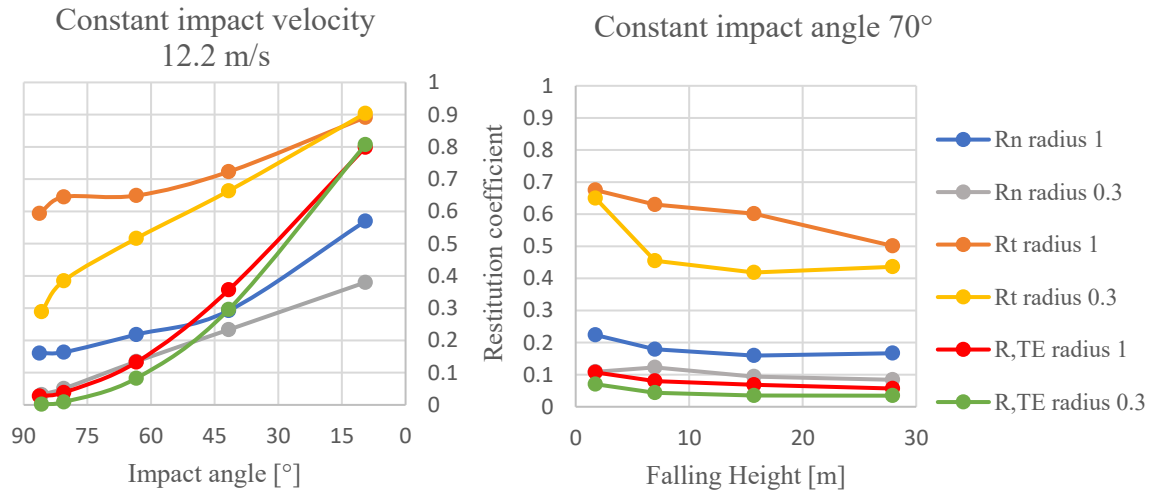
Figure 9: Influence of the impact velocity and the impact angle on the restitution coefficients.

In order to schematize the observations on the graphs, the trends are explained by arrows, indicating with the symbol ↗ an increasing, and with the symbol ↘ a decreasing.

➢ *Influence of the parameters related to the kinematics:*
- Maintaining the falling height constant (and, consequently, the impact velocity), and decreasing the impact angle
$$R_n ↗, R_t ↗, R_{TE} ↗↗$$
- Maintaining the impact angle constant, and increasing the falling height (and, consequently, the impact velocity)
$$R_n ↘, R_t ↘, R_{TE}↘.$$
It is possible to observe an initial increasing of R_n for the block with a radius of 0.3 m.

➢ *Influence of the parameters related to the block:*
- Increasing the block radius and, therefore, the weight
$$R_n ↗, R_t ↗, R_{TE} ↗$$

The trends may be compared to trends cited in the literature ([6]):
- Ritchie [13], in 1963, and Gerber [4], in 1995, basing on in situ observations, affirmed that the characteristics of the slope influence the blocks' kinematics. They observed that increasing the impact angle, the loss of energy becomes bigger.
- Habib [5], in 1977, declared that the normal coefficient of restitution is not only related to the ground material, but it is also a function of the block's kinematics, the mass and the shape.
- Bozzolo and Pamini (1986) [1], noticed that the R_{TE} depends on the impact angle: the energy dissipated rises with the growth of the impact angle, till a maximum value for an impact perpendicular to the surface.
- Pfeirrer and Bowen (1989) [11] perceived that faster blocks dissipate more energy than slower ones, during impact.

o B. Heidenreich (2004) [6] explained what happens during the impact: the translational energy decreases quickly, and the rotational one rises due to friction between block and slope.

Additionally, B. Heidenreich observed that for falling heights between 5 and 10 m, R_t grows slightly with the coupled raise of mass and radius of the boulder. Even R_n shows a growing in this context.

Finally, for increasing falling heights (so, impact velocities), she ascertained that R_t decreases greatly, while R_n and R_{TE} present, generally, a slower decreasing. In the half – scale experiments context (block with a radius of 0.3 m, in our case), she observed an initial increasing of the R_n with the falling height, that she justified in the way explained below. For small values of falling heights, the block rolling imposes the rebound direction (fairly tangential, so R_n results little, and R_t assumes a high value). For increasing falling heights, the growing slope ground resistance in front of the block provokes a more normal rebound, with respect to the slope (R_n initially rises, while R_t decreases strongly).

The comparison highlights that the trends from the model are consistent with test results obtained considering different experimental conditions.

Unfortunately, no real – scale data were available to check the behavior of the model considering a block radius of 1 m. However, in the hypothesis of good functioning of the system, that simulations would be useful to extend the study to more serious cases.

6 CONCLUSIONS

A simple block-soil interaction model has been proposed for modeling the rebound of rockfall on the uphill face of embankments. This simplified model relies on the substitution of the structure body by a surface, located on its impacted face, in order to save computation costs.

Different DEM strategies were considered for developing such a model using Yade's elements. The optimum consisted in a membrane made of the repetition of elementary structures made of 4 PFacets, supported by cylinder elements. The proposed model allows accounting for plasticity of soil associated to compaction and for friction at the block-surface interface.

A first comparison with previous studies confirmed the relevancy of the proposed modeling approach. In case of normal-to-the membrane impacts, observed trends concerning the penetration are in line with previously described ones. Varying the angle of incidence of the rock block also shows similar trends as those observed in the past. However, some limitations rose when addressing the influence of the block angular velocity (not shown here). Indeed, the latter appeared to have a moderate influence on the restitution coefficients, contrary to what was expected. This point will be improved.

REFERENCES

[1]   Bozzolo, D., Pamini, R. (1986). *Simulation of Rock Falls down a Valley Side*.

[2]   Breugnot, A., Lambert, S., Villard, P., Gotteland, P. (2015). *A Discrete/ Continuous Coupled Approach for Modeling Impacts on Cellular Geostructures*.

[3]   Calvetti, F., di Prisco, C. (2007). *Linee guida per la progettazione di gallerie paramassi*.

[4]   Gerber, W. (1995). Auswertung von Feldversuchen. Unterlagen zum FAN-Kurs der Forstlichen Gruppe Naturgefahren zum Thema "*Steinschlag*".

[5]   Habib, P. (1977). *Note sur le rebondissement des blocs rocheaux*. Proceedings Meeting on Rockfall dynamics and protective works effectiveness.

[6]   Heidenreich, B. (2004). *Small- and half-scale experimental studies of rockfall impacts on sandy slopes*.

[7]   Lambert, S., Bourrier, F., Toe, D. (2013). *Improving three-dimensional rockfall trajectory simulation codes for assessing the efficiency of protective embankments*. International Journal of Rock Mechanics and Mining Sciences, Vol. 60, p. 26-36.

[8]   Montani, S. (1998). *Sollicitation dynamique de la couverture des galeries de protection lors de chutes de blocks*. PhD thesis, EPFL Lausanne, Switzerland.

[9]   Olmedo, I., Bourrier, F., Bertrand, D., Berger, F., Limam, A. (2016). *Discrete Element model of the dynamic response of fresh wood stems to impact*.

[10]   Peila, D., Oggeri, C., Castiglia, C., Recalcati, P., Rimoldi, P. (2002). *Testing and modelling geogrid reinforced soil embankments subject to high energy rock impacts*.

[11]   Pfeirrer, T., Bowen, T. (1989). *Computer Simulation of Rockfalls.* Bulletin of the Association of Engineering Geologists.

[12]   Plassiard, J., Donzé, F. (2010). *Optimizing the design of rockfall embankments with a discrete element method*.

[13]   Ritchie, A. M. (1963). *Evaluation of rockfall and its control*.

[14]   Smilauer, V., Catalano, E., Chareyre, B., Dorofeenko, S., Duriez, J., Dyck, N., … Yuan, C. (2015). *Yade Documentation 2nd ed.* Zenodo. http://doi.org/10.5281/zenodo.34073.

DEM SIMULATION OF TRIAXIAL TESTS OF RAILWAY BALLAST FOULED WITH DESERT SAND

PABLO JIMÉNEZ[1], JOSÉ ESTAIRE[2], CLARA ZAMORANO[1], ALEJANDRO DE BENITO[1] AND IGNACIO G. TEJADA[1]

[1] ETSI Caminos, Canales y Puertos - Universitad Politécnica de Madrid (UPM)
C/ Profesor Aranguren 3, 28040 Madrid, Spain
e-mail: pablo.jimenez@upm.es
[2] CEDEX Laboratorio de Geotecnia

Key words: Railway Ballast, DEM

Abstract. Some high-speed rail lines go through desert zones where sand particles transported by winds may foul track ballast layers. This fouling can be troublesome since it increases the stiffness of the layer and reduces its capacity to absorb vibrations from the rolling stock.

We are studying this phenomenon through both laboratory and numerical experiments. In the laboratory, we performed two kinds of experiments: 9 inches triaxial tests and physical modelling in the CEDEX Track Box testing facility. The latter is a unique 1:1 model of railway track section (of dimensions 21 m ×5 m ×4 m) that has been built to model high-speed rail lines (with passenger and freight trains passing at velocities of up to 400 km/h). The laboratory experiments allowed us to measure the change of stiffness with the fouling level (represented through the void contaminant index, VCI). Numerical simulations are being performed with the Discrete Element Method, reproducing drained triaxial test conditions. Due to the considerable different size of railway ballast and sand grains, we are using idealized packings of spherical particles to study this phenomenon. We are paying particular attention to the sample size effects and are registering the evolution of the stiffness with the fouling level up to high values of VCI. The results obtained from these idealized systems will be contrasted to the laboratory experiments carried out with real railway ballast and sand.

1 INTRODUCTION

The railway track is a layered foundation made of several layers: railway ballast, compacted sub-ballast and form layer, followed by an embankment or formation soil. Railway ballast is an uniformly graded coarse granular material that is placed underneath and between track sleepers. The purpose of railway ballast is to provide drainage and structural support for the loading applied by trains. Rock type, quality, size distribution, and particle shape are among the major considerations in ballasted railway track design. Usually, the ballast is produced by crushing locally available rocks such as granite or basalt.

One of the challenges found in ballasted tracks is the fouling, *i.e.* the contamination with thinner granular materials, which increases the stiffness of the layer and can make it loose its capacity to absorb vibrations. The fouling may be caused by ballast breakdown, by the migration of subgrade particles or by the deposition of coal dust, among others. In railway lines crossing desert zones, the sand carried by the wind can foul the ballast.

In this context, the CEDEX conducted some studies to analyze the phenomenon of ballast fouling with sand [1]. These studies were mainly experimental and consisted on large triaxial tests and the measurement of track stiffness in a 1:1 scale model of a railway track built in CEDEX Track Box. In these tests, ballast was fouled with fine sand in different levels to determine its influence in the ballast mechanical properties. Both tests presented very good agreement. The study concluded that the stiffening is only noticeable at high levels of contamination and also helped to quantify the effect.

In the light of these results, we are now setting up a series of numerical simulation with the Discrete Element Method [2]. This method may help to understand the behavior of railway ballast [3, 4, 5, 6, 7, 8] or phenomena caused by the fouling [3] The purpose of this on-going work is twofold: to quantify the uncertainty of the measurements and to explain the stiffening curve that has been observed in the laboratory. The main advantage of numerical modeling is that the experiments can be massively repeated, something imposible in the laboratory because of the difficulties to handle such amount of railway ballast, the duration of the tests and the specific needs. Although some DEM models reproduce much better the complex shape of the particles with clumps [3, 5] or contact models [8], fouling phenomena need a lot of particles and considerably simplifications are necessary. In fact, the modelling of the fouling needs the inclusion of so many particles that these have to be pretty simple to make numerical experiments computationally feasible.

2 METHODOLOGY

2.1 Theoretical background

Fouling degree: several index have been proposed to quantify the degree of fouling [9]. We have used the Void Contaminant Index [10], which is defined as:

$$VCI = \frac{1 + e_\mathrm{f}}{e_\mathrm{b}} \frac{G_\mathrm{b}}{G_\mathrm{f}} \frac{M_\mathrm{f}}{M_\mathrm{b}} = \frac{V_{\mathrm{f},t}}{V_{\mathrm{b},void}} \,, \tag{1}$$

being e_f, e_b the void ratios, G_f, G_b the relative gravity and M_f, M_b the masses of fouling material, f, and railway ballast, b, respectively. $V_{\mathrm{b},void}$ is the volume of the voids in the clean railway ballast and $V_{\mathrm{f},t}$ is the total volume occupied by the fouling material. Therefore the definition of VCI actually corresponds to a saturation degree, which ranges from 0 (clean ballast) to 1 (completely fouled ballast).

Mechanical behavior of clean railway ballast: if the railway ballast was supposed to be a homogeneous, isotropic and lineal elastic material, under drained triaxial testing conditions, the next relationship between deviatoric stress and axial strain would be found (after the isotropic compression of the sample):

$$\sigma_1 = E_0 \varepsilon_1 \,, \tag{2}$$

where E_0 is the Young's modulus of the material. σ_3 is assumed to not change during the application of the deviatoric load.

The linear model is useful only for low stress (or strains) levels. When this is not the case, a more advanced constitutive relationship is needed. A well-known model, which is widely used to reproduce the relationship between deviatoric stress and axial strain in drained triaxial compression tests, is the celebrated hyperbolic model [11]:

$$\sigma_1 - \sigma_3 = \frac{\varepsilon_1}{\frac{1}{E_0} + \frac{\varepsilon}{(\sigma_1 - \sigma_3)_{\mathrm{ult}}}} \, . \tag{3}$$

The elastic tangent modulus E_0 and the ultimate deviatoric stress $(\sigma_1 - \sigma_3)_{\mathrm{ult}}$ are the two parameters that scale this model. For small strains and constant σ_3, Eq. 2 approximates Eq. 3.

Mechanical behavior of fouled railway ballast: when the ballast is fouled with a material made of much smaller grains, because of gravity, most of the fouling material goes down and saturates the bottom of the sample, while the rest of the sample remains clean. As a result, the mechanical behavior is that of a bilayered material. A simplistic approximation to the bilayered material would be a sample of height H that is made of two layers of different materials, of heights H_1 and $H - H_1$ and whose corresponding Young's moduli are E_1 and E_2 (with $E_1 > E_2$). An elastic 1D approximation to the drained triaxial conditions, would lead to a relationship like Eq. 2, with an equivalent Young's modulus given by:

$$\frac{1}{E_{\mathrm{eq}}} = \frac{H_1}{H} \frac{1}{E_1} + \frac{(H - H_1)}{H} \frac{1}{E_2} \, . \tag{4}$$

If the Young's modulus of a railway ballast fully saturated with sand is $E_{\mathrm{b+f}}$ and that of the clean ballast is E_{b} and $H_1 = VCI \cdot H$, this simplistic approximation would give:

$$\frac{1}{E_{\mathrm{eq}}} = \frac{VCI}{E_{\mathrm{b+f}}} + \frac{(1 - VCI)}{E_{\mathrm{b}}} \, . \tag{5}$$

Equation 5 predicts that the equivalent Young's modulus should progressively increase from E_{b} ($VCI = 0$) to $E_{\mathrm{b+f}}$ ($VCI = 1$), with a higher rate as $VCI \to 1$.

2.2 Laboratory experiments

Several laboratory tests were performed with real railway ballast. More details are found in [1]. Ballast grains were composed of an andesite that came from an authorized quarry for railway ballast in high speed lines in Spain. Ballast sieve sizes ranged between 25 and 60 mm, with $D_{50} = 40$ mm and a coefficient of uniformness $C_u = 1.48$. The sand used to evaluate the effects of railway ballast fouling was composed mainly by quartz, with $D_{50} = 0.4$ mm and $C_u = 1.6$. The relative density of the sand was $G_f = 2.65$ and it presented maximum and minimum densities of $1.64 \cdot 10^3$ and $1.44 \cdot 10^3$ kg/m^3. These values correspond to porosities of $n_{\min} = 0.37$ and $n_{\max} = 0.46$.

2.2.1 Triaxial testing

The mechanical behavior of the fouled ballast was studied through large triaxial testing. Clean and fouled specimens were tested (with corresponding VCIs of 0.0, 0.15, 0.30, 0.45, 0.62, 0.80 and 1.00). This was done by pouring a certain weight of of sand into the cell containing the ballast. The sand went down and filled the void from the bottom of the specimen. The dimensions of the cell were 230 mm diameter and 460 mm high. The ballast was compacted in five layers with vibratory hammer until reach a porosity of $n_b = 0.39$. The maximum particle size in the sample was 60 mm so the ratio cell diameter to particle size was 3.85, a little below the recommended value 5.0 [12]. The confinement pressure was 150 kPa. The deviatoric vs axial strains curves were fitted with a hyperbolic model to obtain a value of the initial tangent modulus E_0 for each VCI.

2.2.2 Physical modeling

The CEDEX Track Box (CTB) is a unique physical model of high speed railway track. This 21 m long, 5 m wide and 4 m deep model allow to test, at the real scale, complete railway track sections of conventional and high speed lines for passenger and freight trains, at speeds up to 400 km/h [1]. The simulation of the effect of the approaching, passing-by and departing of a train in a test cross-section is achieved by applying loads that are adequately unphased as a function of the train velocity. Forces are applied by three pairs of servo-hydraulic actuators (each of them can apply a maximum load of 250 kN at a frequency of 50 Hz), placed on each rail and 1,5 m longitudinally separated. Two piezoelectric actuators can apply loads up to 20 kN at 300 Hz to reproduce wheel or trach defectives. The railway track response, in terms of displacements, velocities and accelerations, is collected from a great number of LVDTs, geophones, accelerometers and pressure cells installed both inside the embankment and the bed layers (ballast, sub-ballast and form layer) of the track.
Quasi-static loading tests were performed to assess the mechanical behavior of the track fouled with sand at different levels of VCI. The tangent elastic modulus was estimated from the deformations.

2.3 DEM simulation

The discrete element method [2], implemented in YADE-DEM [13][1] is used to get more insights into the stiffening of the railway ballast fouled with sand. The toy-models are made of spherical particles. The interaction between spheres is frictional-Hookean, with normal stiffness $k_n = 2E\bar{R}$ and $1/\bar{R} = 1/R_1 + 1/R_2$ (being R_1 and R_2 the radii of interacting particles). The introduction of small particles may considerably increase the computational cost of simulations since the number of particles is much larger and the critical timestep is reduced. As the computer performance is undoubtedly limited, not all VCI levels can be simulated. We have set up a simulation plan including two main stages:

---

[1] https://yade-dem.org/.

1. **Determination of the representative cell size for clean railway ballast**: the first step is the establishment of the lowest number of large spheres that have to be included in the simulation box to get accurate measurement of the parameters for the hyperbolic model. To do that, several samples of almost equal sized spheres were compressed at scaled rates to reach the confinement isotropic stress. Then a deviatoric load was applied in one of the direction while the stress was maintained in the perpendicular ones. The deviatoric strain vs axial strain curve was fitted by a least squares procedure to get the parameters for the hyperbolic model in each case. This process was repeated several times for each number of large spheres to generate a statistical sample. The confidence interval of the measured parameters are $E_o \pm \Delta E_0$ and $(\sigma_1 - \sigma_3)_{\mathrm{ult}} \pm \Delta (\sigma_1 - \sigma_3)_{\mathrm{ult}}$ were established -after expecting that the values follow a normal distribution- from the following equation:

$$\Delta x = t_{\alpha, \mathcal{N}-1} \frac{S_x}{\sqrt{\mathcal{N}}} \, , \tag{6}$$

where $\mathcal{N}$ is the number of tests, S_x is the squared root of the unbiased sample variance and $t_{\alpha, \mathcal{N}-1}$ is the double side t-distributed value corresponding to a confidence level α. A coefficient of variation has been defined as

$$CoV = \frac{\Delta x}{x} \, . \tag{7}$$

CoV is expected to decrease with the number of large spheres N_{b} in the simulation box. The critical value $N_{b,\mathrm{c}}$ is that on which boundary or other effects have no influence on the results. This will be precisely the number of large spheres that we will use in simulations with fouled samples.

2. **Triaxial testing of fouled samples:** Once $N_{b,\mathrm{c}}$ is known, we follow the same triaxial testing procedure that we followed with clean samples. However, when the sample has been isotropically compressed and right before the application of the deviatoric load, a set of small spheres is introduced within the voids. We would desire to include as many, and as small, as possible spheres to approximate the real conditions but this is not always possible. As the large sphere to small sphere ratio increases, the number of small spheres explodes. This has been illustrated in Figure 1. These data have been obtained after assuming that the coarse fraction reaches a random close packing [14] with porosity $n = 0.36$ and that the small fraction is packed with the same porosity within the voids created by the coarse packing. The total number of spheres in the simulation will be $N_{\mathrm{b,c}} \cdot \left(1.0 + \frac{N_{\mathrm{f}}}{N_{\mathrm{b}}} \right)$. Size ratios below 10.0 are undesired because small particles could block the throats between the voids. Much higher sizes ratios would make simulations unfeasible. For example, in the laboratory experiments (section 2 above), $D_{50,\mathrm{b}}/D_{50,\mathrm{f}} = 100$, and this means that $360,000$ small spheres should be included per each large one to reach a VCI of 1.0.
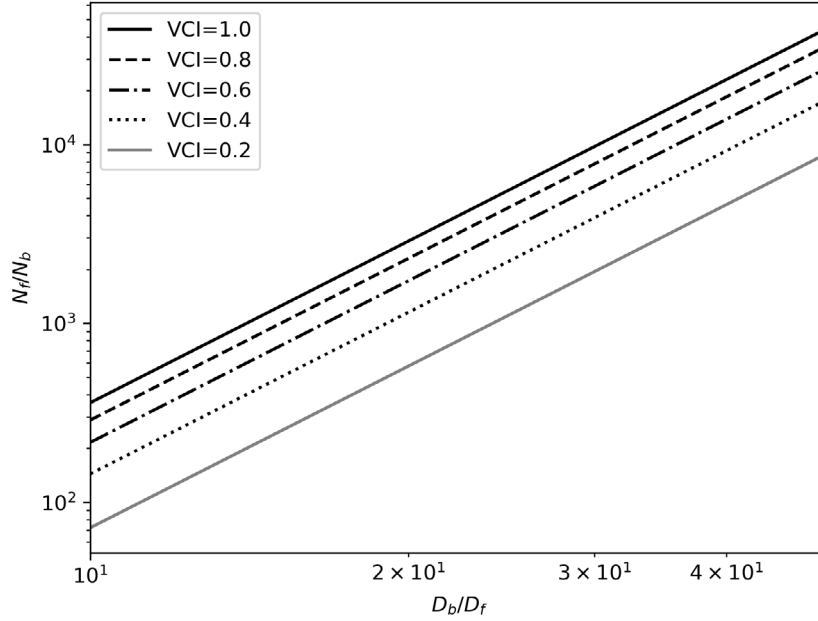
Figure 1: Number of small spheres to be included in the simulation of each large to small particle size ratio and VCI.

Table 1: Parameters used in the DEM numerical simulations to generate ensemble samples.

Mean diameter	D	0.1	m
Diameter variation	$\frac{\Delta D}{D}$	0.2	-
Young's modulus	E	$1.5 \cdot 10^7$	Pa
Particle density	ρ_{s}	$2.6 \cdot 10^3$	kg.m^{-3}
Interparticle friction	Φ	$\pi/6$	rad
Confinement pressure	σ_3	50.0	kPa

The parameters used in the simulations are included in Table 1. Packings were generated by slowly compressing a loose cloud of particles until the confinment pressure is reached. The cell is surrounded by elastic walls, which are moved to reduce or increase the cell size and hence increase or reduce the stress. Both the size of the initial cell and the applied strain rates were scaled with $N_{\mathrm{b}}^{1/3}$ factors. The diameters of the spheres uniformly laid within the interval $D_{\mathrm{b}} \pm \Delta D_{\mathrm{b}}$. After the isotropic compression, two opposite walls were moved at constant rate until produce an axial strain of $\varepsilon_1 = 0.2$. The walls parallel to direction 1 were moved to keep the value of the confinement pressure constant.

3   RESULTS

Laboratory triaxial tests and the DEM simulation of these are showing a nonlinear deviatoric stress vs. axial strain curve that can be approximated by a hyperbolic model. In Figure 4 these curves are shown for different experiments performed with 5000 particles.
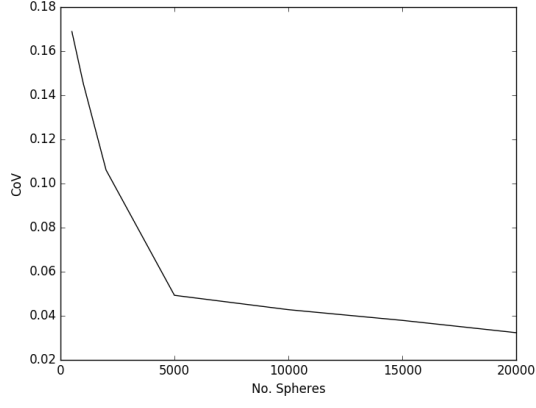
(a) Coefficient of Variation
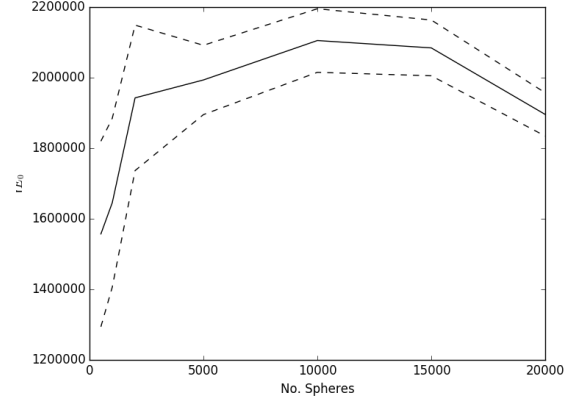
(b) Mean value and % 95 confidence interval.

Figure 2: Initial tanget modulus E_0
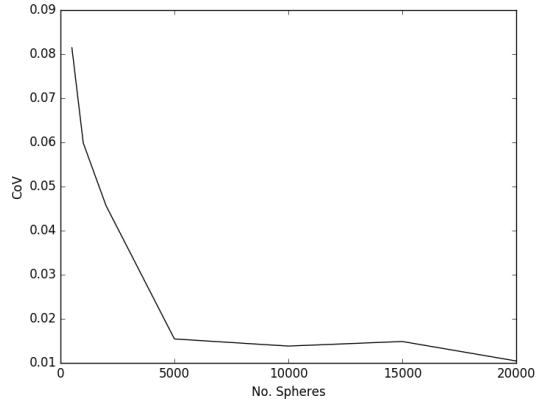
(a) Coefficient of Variation
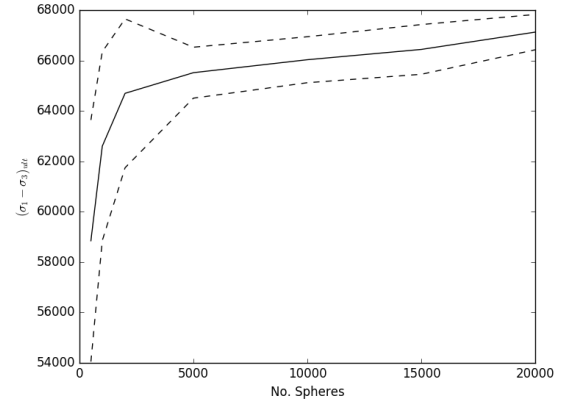
(b) Mean value and % 95 confidence interval.

Figure 3: Asymptote, $(\sigma_1 - \sigma_3)_{\mathrm{ult}}$.
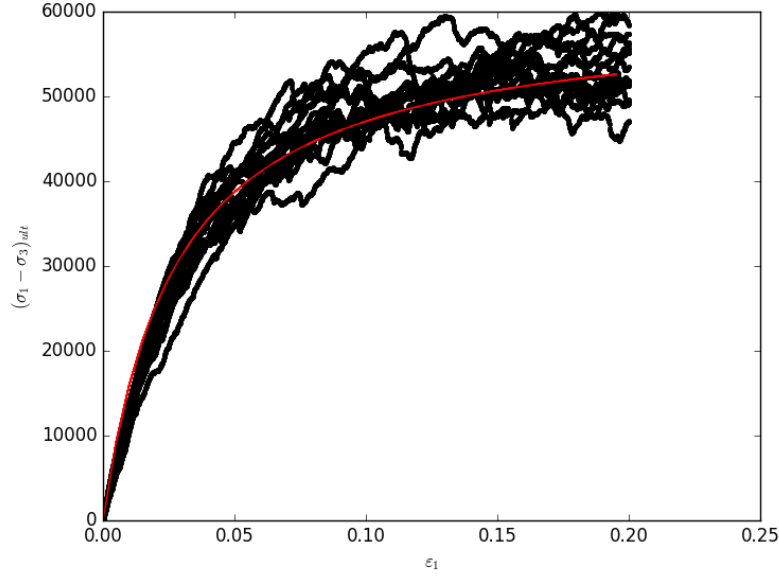
Figure 4: Deviatoric stress vs. axial strain simulated with DEM for 2000 spheres.

5000 is precisely the number that we take as $N_{b,c}$, according to what is shown in Figures 2 and 3.

In Figure 5 the first values of E_{b+f}/E_b obtained from DEM at low VCIs are compared to those obtained in the laboratory. A value of $D_b/D_f = 10$ was used. A few set of data have been produced to the date, so the uncertainty is high and conclusions cannot be yet established.

4 CONCLUDING REMARKS

- Laboratory experiments (large triaxial testing and physical 1:1 model) had shown an increase of the stiffness of railway ballast fouled with sand characterized by a bimodal behavior: no stiffening below a threshold VCI and almost linear increase over that value. However the variation of the data is considerable and the data set is reduced.

- We are investigating if an idealized DEM model made of almost uniform spherical particles contaminated with smaller spheres may help to understand how the stiffness changes at different levels of VCI. In particular we aim to understand if the curve stiffening vs VCI is actually bi-modal or not.

- The on-going DEM simulation campaign first tries to establish the confidence intervals to reduce as much as possible the number of coarse particles included in the simulation. An additional analysis on whether or not the critical number of large particles could be reduced for high VCI values will be performed.

257
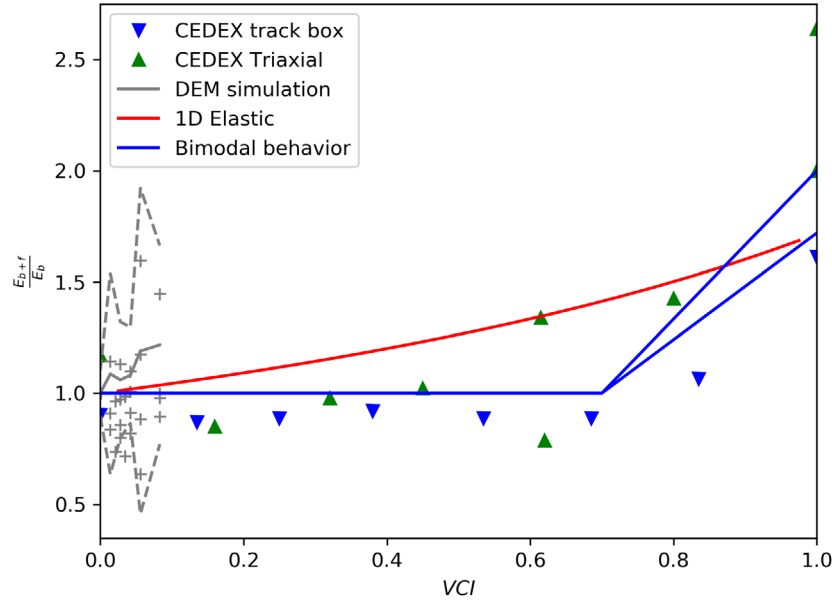
Figure 5: Stiffening as a function of the VCI.

- Once the confidence intervals are properly established, the bi-modal or continuously growing shape of the stiffening curve would be more clearly understood.

REFERENCES

[1] J. Estaire, V. Cuéllar, and M. Santana. Track stiffness in a ballast track fouled with desert. In *GEORAIL International Symposium*, 11 2017.

[2] P. A. Cundall and O. D. L. Strack. A discrete numerical model for granular assemblies. *Géotechnique*, 29(1):47–65, 1979.

[3] B. Indraratna, N. Trung Ngo, C. Rujikiatkamjorn, and J. S. Vinod. Behavior of fresh and fouled railway ballast subjected to direct shear testing: Discrete element simulation. *International Journal of Geomechanics*, 14(1):34–44, 2014.

[4] Z. Wang, G. Jing, Q. Yu, and H. Yin. Analysis of ballast direct shear tests by discrete element method under different normal stress. *Measurement*, 63.

[5] E. Mahmoud, A.T. Papagiannakis, and D. Renteria. Discrete element analysis of railway ballast under cycling loading. *Procedia Engineering*, 143:1068 – 1076, 2016. Advances in Transportation Geotechnics III.

[6] N. Trung Ngo, B. Indraratna, and C. Rujikiatkamjorn. Micromechanics-based investigation of fouled ballast using large-scale triaxial tests and discrete element modeling. *Journal of Geotechnical and Geoenvironmental Engineering*, 143(2):04016089, 2017.

[7] J. Irazábal. Numerical analysis of railway ballast behaviour using the discrete element method, 2017.

[8] J. Irazábal, F. Salazar, and E. Onate. Numerical modelling of granular materials with spherical discrete particles and the bounded rolling friction model. application to railway ballast. *Computers and geotechnics*, 85:220 – 229, 2017.

[9] B. Indraratna, L. Su, and C. Rujikiatkamjorn. A new parameter for classification and evaluation of railway ballast fouling. *Canadian Geotechnical Journal*, 48(2):322–326, 2011.

[10] N. Tennakoon, B. Indraratna, C. Rujikiatkamjorn, S. Nimbalkar, and T. Neville. The role of ballast-fouling characteristics on the drainage capacity of rail substructure. *Geotechnical Testing Journal*, 35(4):629–640, 2012.

[11] J.M. Duncan and C.Y. Chang. Nonlinear analysis of stress and strain in soils. *J. of the Soil Mech. And Found. Div*, 96:1629–1653, 1970.

[12] B. Indraratna. The effect of normal stress-friction angle relationship on the stability analysis of a rockfill dam. *Geotechnical & Geological Engineering*, 12(2):113, Jun 1994.

[13] V. Šmilauer et al. Reference manual. In *Yade Documentation 2nd ed.* The Yade Project, 2015. http://yade-dem.org/doc/.

[14] J. D. Bernal and J. Mason. Co-ordination of randomly packed spheres. *Nature*, 188:910–911, 1960.

EXPERIMENTAL AND NUMERICAL INVESTIGATIONS ON PARAMETERS INFLUENCING ENERGY DISSIPATION IN PARTICLE DAMPERS

Niklas Meyer[1], Robert Seifried[1]

[1] Institute of Mechanics and Ocean Engineering, Hamburg University of Technology
Eißendorfer Straße 42, 21073 Hamburg, Germany
n.meyer@tuhh.de/robert.seifried@tuhh.de, www.tuhh.de/mum

Key words: Particle damping, Complex power, Energy dissipation, DEM

Abstract. Particle damping has become a favorable passive damping technique for lightweight structures, however, its complex dimensioning process hinder its wide use in technical applications. An experimental based model and a numerical model are developed in order to investigate the energy dissipation of the dampers regardless of the underlying structure. The experimental model consists only of the particle box with a free-free boundary condition, which is excited by a harmonic force. Via the complex power, the loss factor and the energy dissipation are obtained. A corresponding numerical discrete element model is developed. With these models, a large frequency and acceleration range is analyzed. Different filling ratios of the particle box are investigated, indicating the high potential of particle dampers for different excitation ranges. First comparisons of experiments and simulations showing a good qualitative agreement, enabling the simulation as a future design tool for particle dampers.

1 Introduction

One favorable passive tool to reduce vibrations of technical applications is the utilization of particle dampers being a derivative of impact dampers. Instead of using only one impact object, dozens or even thousands of particles might be included in a single particle damper. Thus, the particle size normally ranges from the micrometer scale to the millimeter scale. Either a box or a hole in the vibrating structure serves as a particle container. The structural vibrations are transferred via the container walls onto the particles. Interactions between particles and between particles and the container walls cause an energy dissipation by impacts and frictional phenomena, resulting in vibration attenuation.

Particle dampers show several advantages when compared to other existing passive damping techniques [1]. However, despite the efficiency of particle dampers, they have been used only in a few different engineering applications so far mostly designed for a very specific system. This might be due to the fact, that the physical processes in the particle dampers are complex and highly nonlinear. These processes are not fully understood yet

and depend on a variety of different influence parameters, like the excitation frequency, the vibration amplitude, the filling ratio of the container and the used materials. These dependencies make the optimal design of particle dampers so far very burdensome and time intensive due to empiric parameter tuning.

Particle dampers might be analyzed utilizing a specific underlying vibrating structure [2]. Instead, in this paper investigations are performed concerning the energy dissipation of particle dampers directly, by excluding the underlying structure. The obtained experimental and numerical results and insights provide a tool for a target-oriented particle damper design. Therefor, an experimental based model and a numerical model for the particle damper are introduced. Both models consist only of the particle box with a free-free boundary condition, which is excited by a harmonic force. The complex power is calculated by the velocity signal and the excitation signal. Via the complex power, the loss factor and the energy dissipation are obtained. A large frequency range ($40\,\mathrm{Hz}$ - $1\,\mathrm{kHz}$) and acceleration range ($10\,\mathrm{m/s}^2$ - $400\,\mathrm{m/s}^2$) is investigated.

For the numerical model the discrete element method is used. The simulations help to identify the interdependent parameters affecting the energy dissipation of particle dampers. Particles are considered as unconstrained moving bodies only influenced by their interactions. The experiments are compared with the numerical results. The influence of the different contact parameters are analyzed. A good qualitative agreement is achieved by using a velocity dependent coefficient of restitution and sliding friction.

2 Experimental model

In [2] particle dampers are analyzed utilizing an underlying vibrating structure. Here, the energy dissipation of particle damper alone is investigated, i.e. without an underlying structure. Thus, a corresponding testbed is developed, see also [3]. A systematic representation and a picture of these are shown in Fig. 1. The concept of the testbed is a particle box with a free-free boundary condition and excited by a controlled harmonic force via a shaker. The excitation force is controlled such, that the frequency and acceleration magnitude of the box stays constant. Via the measured velocity of the box and the measured force of the shaker, the complex power is determined [4]. By the complex
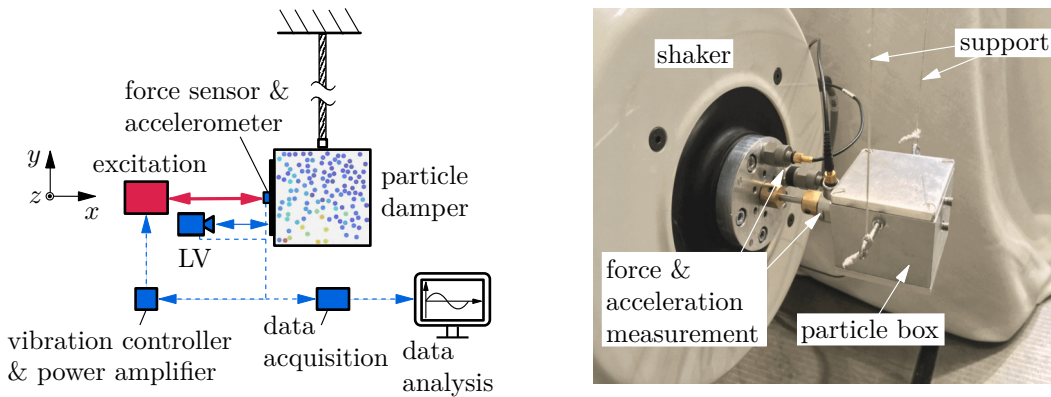
Figure 1: Systematic representation (left) and picture (right) of the testbed.

power, the energy dissipation and the loss factor can be calculated.

The box is made of aluminum with a cubical shape and an inner edge length of 4 cm. The free-free boundary condition is accomplished by two ropes. The force sensor, the accelerometer, and the control system are from BRÜEL & KJAER. While the box is excited by the LDS V455 shaker, its acceleration is controlled via the LDS Comet system. Due to the impacting particles on the box walls, the acceleration signal is very noisy. In order to use this acceleration signal in the control of the excitation, the accelerometer is additionally equipped with a mechanical low-pass filter. It consists of a plastic tube with a Young's modulus of $86\,\mathrm{N/mm^2}$. This filter element is designed in a way that its eigenfrequency ω is at $2.5\,\mathrm{kHz}$. Hence, the single particle impacts on the box walls are filtered efficiently, as their contact frequency is normally significantly above $5\,\mathrm{kHz}$. Simultaneously, frequencies up to the measurement range of $1\,\mathrm{kHz}$ are only little influenced.

The velocity of the particle box is measured via a laser vibrometer (LV), the PSV-500, from POLYTEC. The data acquisition of the velocity and force signals are accomplished by the Front-End of the PSV-500 with a sampling frequency of $250\,\mathrm{kHz}$. The second accelerometer, seen in Fig. 1 (right), is not equipped with a filter as it is only used for triggering the measurement. The feasible measurement range of the system is between $40\,\mathrm{Hz}$ till $1\,\mathrm{kHz}$ and between $10\,\mathrm{m/s^2}$ till $400\,\mathrm{m/s^2}$. The measurement range is divided into a logarithmic grid of 108 points. Nine frequencies and twelve acceleration values are used and each combination is measured for $2.5\,\mathrm{s}$.

3 Complex power

For the determination of the dissipated energy and the loss factor, the complex power P, introduced for particle damper analysis by Yang [4], is used and briefly summarized here. Given a harmonic excitation, the complex power follows to

$$P = \frac{1}{2}FV^*. \tag{1}$$

Hereby, F denotes the fast Fourier transform (FFT) of the force signal and V^* the conjugate FFT of the velocity signal. The dissipated power P_{diss} and the maximum power stored in a cycle P_{max} follow from the complex power as

$$P_{\mathrm{diss}} = \mathrm{Real}(P) = \frac{1}{2}|F||V|\cos(\phi_{\mathrm{F}} - \phi_{\mathrm{V}}), \tag{2}$$

$$P_{\mathrm{max}} = \mathrm{Imag}(P) = \frac{1}{2}|F||V|\sin(\phi_{\mathrm{F}} - \phi_{\mathrm{V}}). \tag{3}$$

The phase angles of the force and velocity signals are denoted by ϕ_{F} and ϕ_{V} respectively. To obtain the dissipated energy per radiant E_{diss} the dissipated power is divided by the excitation frequency Ω as

$$E_{\mathrm{diss}} = \frac{P_{\mathrm{diss}}}{\Omega}. \tag{4}$$

The loss factor η is defined as the ratio of the dissipated power to the maximum power stored in a cycle as

$$\eta = \frac{P_{\text{diss}}}{P_{\text{max}}} = \frac{\text{Real}(P)}{\text{Imag}(P)}. \tag{5}$$

4 Discrete Element Method

The Discrete Element Method (DEM) is a discrete simulation method for granular materials. The DEM has been developed by Cundall and Strack [5] for the simulation of systems consisting of discs and spheres. Its general concept can be used for any system of many unconstrained particles where the system behavior is governed by the contacts between these particles [6]. While in general the particles can have an arbitrary shape, for efficiency purpose mostly spherical particles are used in the simulations. Every particle is considered as an unconstrained moving body only influenced by applied forces. The dynamics are obtained by setting up Newton's and Euler's equation of motion for every particle [7]. For spherical particles, this reads

$$m_i \ddot{\boldsymbol{x}}_i = \boldsymbol{F}_i, \quad \boldsymbol{I}_i \dot{\boldsymbol{\omega}}_i = \boldsymbol{M}_i \quad (i = 1, ..., N), \tag{6}$$

with $\ddot{\boldsymbol{x}}_i$ and $\dot{\boldsymbol{\omega}}_i$ being the translational and rotational accelerations. The particle mass is denoted by m_i and its diagonal inertia tensor by $\boldsymbol{I}_i$, whereby all three entries of $\boldsymbol{I}_i$ are identical. The applied forces and moments are denoted by $\boldsymbol{F}_i$ and $\boldsymbol{M}_i$, and N is the total number of particles. The Eq. (6) is in general a coupled nonlinear differential equation with $6N$ degrees of freedom for 3D simulations. Particle systems often contain a large number of particles (up to thousands or millions). During the time integration, all existing contacts need to be detected and resolved in every time step. Therefore, efficient detection algorithms and contact laws are needed. Also, the choice of an appropriate time integration scheme is crucial [6]. In this research, the algorithms presented in [2] are used and only shortly introduced.

4.1 Contact forces

In DEM simulations, particle-particle and particle-wall continuous contacts occur. The contact partners are treated as rigid, thus only touching in a single point. In continuous contact modeling, the contact partners i and j are allowed to overlap, and virtually connected by unilateral springs and dampers, as shown in Fig. 2. Hereby, the corresponding contact forces occur which counteract the overlap δ_{ij}. For the calculation of the contact forces, various models have been developed [8, 9, 10]. The contact law of Hertz [8] is widely used for a sphere-sphere contact, as it is based on physical parameters, namely the Young's modulus $E_{i/j}$ and the Poisson's ratio $\nu_{i/j}$. Later on, the result of Hertz was extended by a dissipative term [9, 10]. In the simulations, the formula of Gonthier [10] for the normal contact force is used, which reads,

$$F_{\text{N},ij} = k_{ij} \delta_{ij}^{3/2} \left(1 + \frac{\bar{d}}{e} \frac{\dot{\delta}}{\bar{\delta}_{\text{a}}} \right). \tag{7}$$
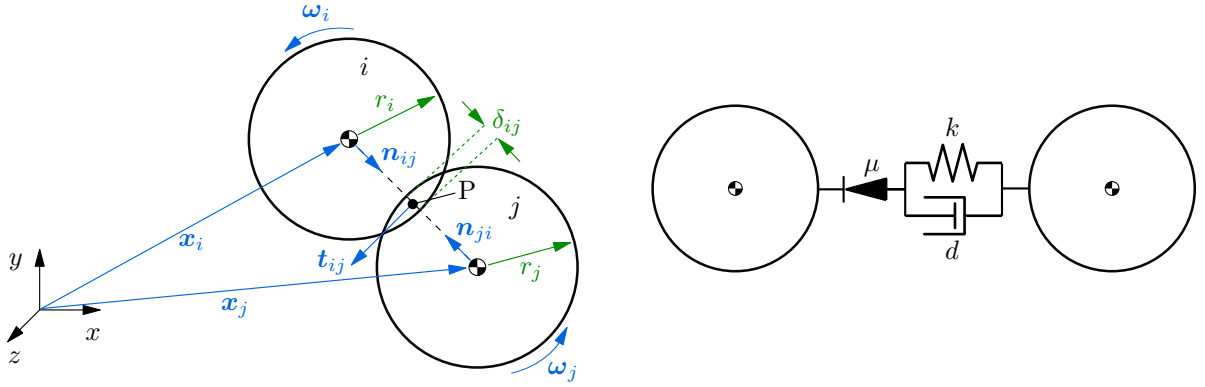
Figure 2: Contact states (left) and contact model (right) of two spheres.

Hereby, the contact stiffness and the material parameters are given as

$$k_{ij} = \frac{4}{3\pi(h_i + h_j)}\sqrt{\frac{r_i r_j}{r_i + r_j}}, \tag{8}$$

$$h_{i/j} = \frac{1 - \nu_{i/j}^2}{\pi E_{i/j}}. \tag{9}$$

The penetration velocity and the initial penetration velocity in normal direction are denoted as $\dot{\delta}$ and $\dot{\delta}_a$ respectively. The coefficient of restitution e ($0 < e < 1$) controls the amount of energy dissipation during the contact. In contrast to other contact models, e.g. Lankarani [9], the formula of Gonthier (7) can be applied to nearly the complete range of e. The nonlinear parameter $\bar{d}$ is only depending on e and can be solved once offline [10]. For spherical particles, the tangential forces result only from sticking and sliding friction, whereas the resistance of the surface is described by the coefficient of friction μ. For highly dynamical systems the sticking friction can be neglected [6]. When only sliding friction is considered, a smoothing hyperbolic tangent function can be used, in order to avoid jumps in the friction forces at zero velocity, see [11]. The sliding friction reads

$$\boldsymbol{F}_{\mathrm{R},ij} = -\mu|F_{\mathrm{N},ij}|\boldsymbol{t}_{ij}\tanh(\tau|\boldsymbol{v}_{\mathrm{P},ij}^{\mathrm{t}}|), \tag{10}$$

with $\boldsymbol{v}_{\mathrm{P},ij}^{\mathrm{t}}$ being the relative, tangential velocity at the boundary point P and τ as the smoothing parameter. The tangential direction is denoted by $\boldsymbol{t}_{ij}$. The resulting torques on the particles are only depending on the friction forces, as the normal forces are always pointing towards the center of mass of the particles. For comparison also sticking friction is implemented, see [12]. However, in the simulation this model is much more time consuming.

4.2   Contact detection and time integration

Another very important component of the DEM is the contact detection. All existing contacts have to be determined in every time step. A variety of algorithms have been developed for this task, such as sort-based, cell-based, or tree-based ones, decreasing the

complexity to an optimum of $\mathcal{O}(N)$. In the program, the verlet list in combination with the link cell algorithm is used [7].

Also, the time integrator has a big influence on the simulation speed and the overall stability. As the contact detection and evaluation of the contact forces are most time-consuming in DEM simulations, the numerical effort for the time integrator itself is often negligible. But, its choice has a big influence on the number of evaluations of the equation of motion. In this research, good results with the fifth order Gear predictor-corrector algorithm [13] have been achieved.

4.3 Coefficient of restitution calculation using FEM

In DEM simulations often a constant coefficient of restitution (COR) is used. Indeed, this is in reality not the case, as the COR depends on a variety of influence parameters. These influence parameters are mainly associated with the energy dissipation effect. For the used metals (S235 and Al6060) in this work, the energy dissipation comes mainly from plastic deformations in the contact zone. Thus, the impact velocity has a big influence on the COR. There exist different investigations on the COR, as for instance in [14, 15, 16]. In this work, the FEM-approach and material data from [16] are used. Metals often behave elastic-viscoplastic. This means, that the plastic flow also depends on the strain-rate. For the material description the Perzyna model [17] is used. This model relates the dynamic yield stress σ_{d} by a factor β with the quasi-static yield stress σ_{y} and the effective plastic strain-rate $\dot{\varepsilon}$ by

$$\sigma_{\mathrm{d}} = \beta\sigma_{\mathrm{y}} \quad \text{with} \quad \beta = 1 + \left(\frac{\dot{\varepsilon}}{\gamma}\right)^{m}. \tag{11}$$

The material viscosity parameter is denoted by γ, and the strain-rate hardening parameter by m. Both parameters have to be obtained from the Split Hopkinson pressure bar test.

In Fig. 3 the quasi-static yield stress for S235 and Al6060 are shown. In Tab. 1 the corresponding material data and Perzyna coefficients are listed. Finite Element simulations of two impacting particles are performed to determine the COR. A schematic representation
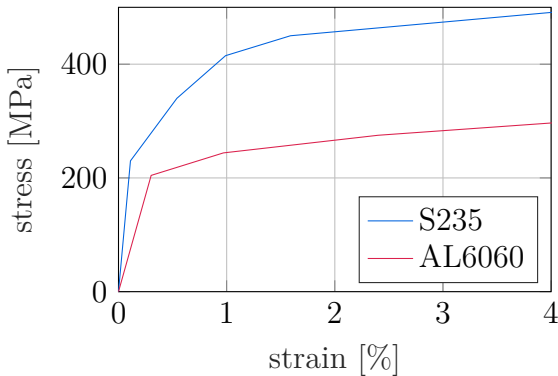
Figure 3: Quasi-static stress-strain curves.

Table 1: Material parameters.

Material	E [GPa]	ν [-]	ρ [kg/m^3]
S235	208	0.3	7800
Al6060	67.7	0.33	2702

σ_{y} [MPa]	γ [-]	m [-]
230	305	0.403
205	5548	1

of the sphere-sphere model is shown in Fig. 4 (left). The spheres have an initial radius of 5 mm, which can be scaled for different sizes. Each sphere consists of 6093 axis symmetric 2D elements, in ABAQUS called CAX4R. The element size varies between 0.5 mm till 0.015 mm. Both spheres are assigned with half the collision velocity ($\dot{\delta}_a$) with opposed signs.

The kinematic COR is evaluated by the normal velocities of the spheres before (0) and after (1) the collision of sphere I and II, reading

$$e = \frac{v_{\mathrm{I}}^1 - v_{\mathrm{II}}^1}{v_{\mathrm{I}}^0 - v_{\mathrm{II}}^0}. \tag{12}$$

The velocities before impact are priori known. The velocities after impact are evaluated at the reference points of the spheres. The mean value of the last 200 time steps is taken, as the velocity is oscillating a little bit due to mechanical vibrations of the spheres, which are induced thru the collision. If instead of a sphere-sphere contact a sphere-wall contact is simulated one sphere is replaced by a wall. The wall is modeled as a cylinder with its diameter and length being the diameter of the sphere. The contour of the cylinder is completely clamped. In the later DEM simulations steel spheres of 5 mm radius will be used. The box is made of aluminum. For these settings, the COR is shown in Fig. 4 (right). A high dependency on the impact velocity is observed. For both settings the COR is close to one for small impact velocities. When the impact velocity increases the COR starts to decrease rapidly. For high velocities the COR drops to 0.5 till 0.4.

5 Experimental and numerical investigations

To check the experimental measurement system the empty particle box is analyzed first. As only minor damping effects, arising from the boundary condition or material damping, exist the energy dissipation is very small. The mean value of the loss factor is about 0.01. In the next step, particles are filled in the box. Unhardened, steel balls made of V2A, which are used in the hardened form for ball bearings, are utilized. These have a high degree of roundness and accurate material parameters are available for the later simulation purposes. For the first setup, 58 of 62 maximum possible particles with a radius of 5 mm are used. The total weight of the particles is 241 g.

The energy dissipation and loss factor for this setting are shown in Fig. 5. From the loss factor a high energy dissipation over a big area of the measurement range can be observed. The mean loss factor is 0.18, which is eighteen times higher than in the empty case. The loss factor is especially high for medium frequencies (60 Hz - 150 Hz) or medium accelerations (20 m/s^2 - 70 m/s^2) with an value up to 0.7. Only at high frequencies (>200 Hz) and high accelerations (>100 m/s^2) the dissipation is comparatively small. The minimum value of the loss factor is here only 0.03. In the area of high frequencies ($\approx$800 Hz) and low accelerations ($\approx$10 m/s^2) the loss factor becomes unrealistic high. However, in this area the energy of the system is very low and inaccuracies in the force signal have a bigger effect on the result. At the lower border of the frequency range (<60 Hz) and acceleration range (<20 m/s^2) the loss factor starts to drop, showing that here another ineffective area of the particle damper starts.
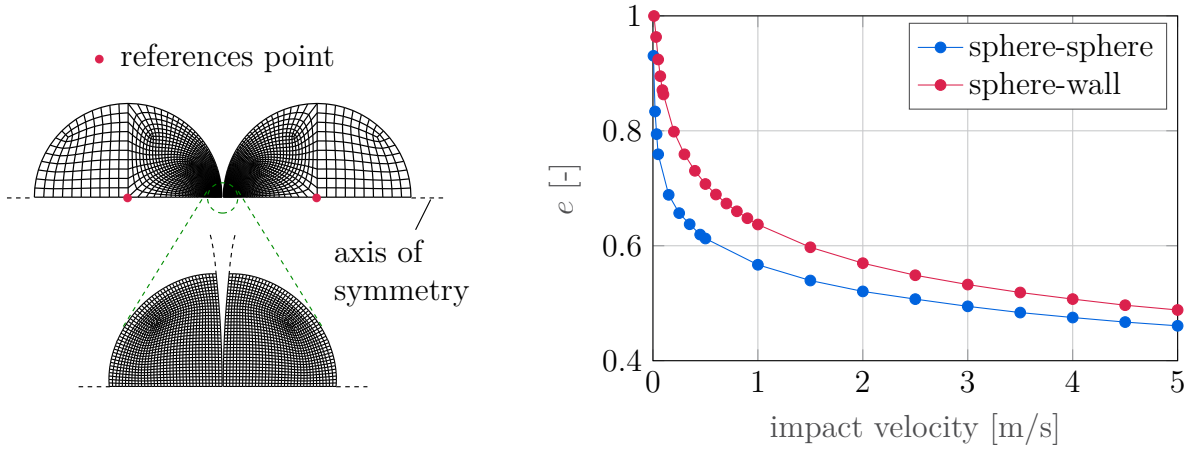
Figure 4: Left: Schematic representation of the FEM model of two impacting spheres.
Right: Velocity dependent COR for a sphere-sphere and sphere-wall contact with a size of 10 mm.
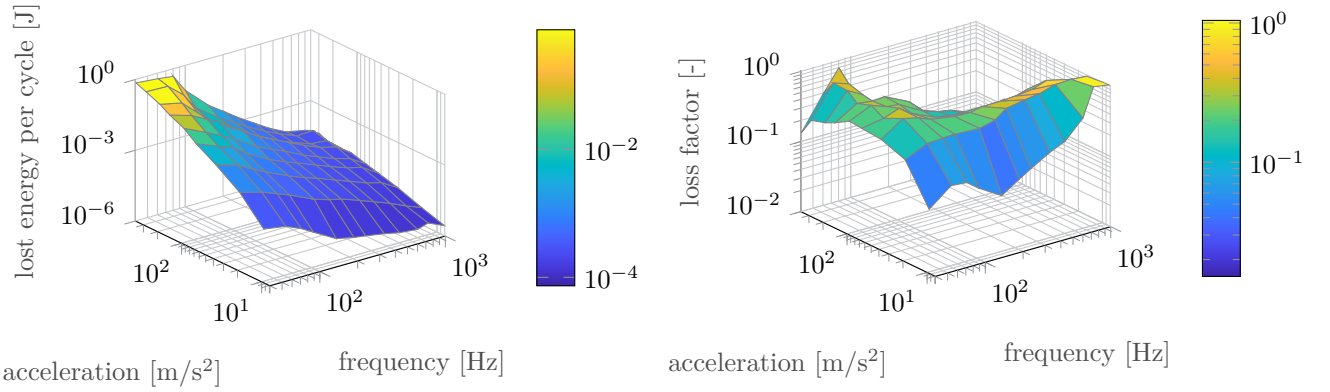
Figure 5: Measured energy dissipation (left) and loss factor (right) with 58 particles of 5 mm radius.

5.1 Numerical investigations of the contact parameters

In the following, the DEM simulation results are compared with the measurements. In order to do so, the measured frequencies and acceleration values are simulated. Each grid point is simulated for 25 periods, whereas the first five periods are cut off to remove the irregular movement of the particles introduced by the initial conditions. The main adjustment parameters are the force laws and their parameters. As normal force the formula of Gonthier (Eq. (7)) is chosen, whereby a constant COR as well as the velocity dependent COR from Fig. 4 are utilized. Indeed, not the exact same materials for the particles are used in the experiment (V2A) as in the FEM simulation (S235), but their characteristics are very similar. For the friction force no friction, sliding friction, see Eq. (10), and sticking friction [12] are analyzed.

The best result between experiment and simulation is achieved with the velocity dependent COR and the sliding friction with $\mu = 0.1$. The relative mean difference of the energy dissipation is 0.36. This setting is thus used for all following simulations. If instead a

constant COR is used, the relative mean difference is 0.44, and the best COR has to be found by excessive tuning. By neglecting friction the minimal relative mean difference becomes 0.43. Taking the sticking friction algorithm the relative mean difference is 0.36, but the simulation time is much higher as with the sliding friction algorithm.

In Fig. 6 the simulation results for the chosen contact parameters are compared to the measured results. The biggest differences occur at low accelerations ($<20\,\mathrm{m/s^2}$) and high frequencies ($>250\,\mathrm{Hz}$). Indeed, this area is also prone to measurement inaccuracies of the force signal. Also, around $400\,\mathrm{m/s^2}$ and $100\,\mathrm{Hz}$ there is a small area where the difference is much bigger as in the surroundings. In this area an offset in the energy dissipation curves is observed and out-

Figure 6: Comparison of experimental and numerical results for the energy dissipation.

side this area both curves agree well. This shows that the simulations meet the qualitative characteristics of the energy dissipation very well, with some quantitative differences in its magnitude. However, besides the quantitative discrepancies the simulations are very useful to give qualitative insights on the complex dynamics inside the damper.

One special characteristic of particle dampers is the complex movement of the particles. In the following, it is analyzed by simulation how this movement and the contact parameters are affecting the energy dissipation of the dampers for different periods. For this purpose, the energy dissipation is directly calculated by the given force laws. In Fig. 7 (left) the relative standard deviation of the energy dissipation is given for the four edge points of the measurement range for one and for 20 periods. For only one period the relative standard derivation is comparably high. Especially at high frequencies this is the case. However, combining 20 periods reduces the standard deviation significantly. Thus, in the simulations 20 periods are used for the calculation of the complex power.

Figure 7: Left: Relative standard deviation of energy dissipation for one (■) and 20 (■) periods. Right: Ratio of dissipated energy of normal contacts to frictional contacts.

In Fig. 7 (right) the ratio of the energy dissipation of normal contacts to frictional contacts is shown. There exist three major regions, i.e. the energy dissipation is dominated by the normal contacts, by friction or is on the same scale. For low frequencies ($<100\,\mathrm{Hz}$) and low accelerations ($<40\,\mathrm{m/s^2}$) the dissipation is dominated by friction by a factor up to two. When the acceleration is increased, the dissipation becomes dominated by the normal contacts up to a factor of three. For high frequencies ($>250\,\mathrm{Hz}$), independent of the acceleration, both dissipation effects are on the same scale. Especially in this area the highest standard deviations for the energy dissipation are determined, as seen in Fig. 7 (left).

5.2 Filling ratio of the particle box

In the next step, different filling ratios of the particle box are analyzed using the experiment and simulation. In addition, to the 58 particles, 40 and 62 particles are utilized, with 62 being the maximum possible particle number. Here as well, a good qualitative agreement between simulation and experiment is obtained. An extended frequency and acceleration range is investigated using the simulation with 20 grid points for the frequency and acceleration values. The frequency varies between $10\,\mathrm{Hz}$ till $1\,\mathrm{kHz}$ and the acceleration between $10\,\mathrm{m/s^2}$ till $1000\,\mathrm{m/s^2}$. The results for the lost energy are shown in Fig. 8. Comparing, 40 with 58 particles in Fig. 8 (left), one can see that the 58 particles perform better for frequencies above $70\,\mathrm{Hz}$. For frequencies below $70\,\mathrm{Hz}$ there is a strong dependency on the acceleration. The 40 particles are here especially suited for the higher accelerations. The energy dissipation in this area is dominated by the normal contacts, which dissipate up to five times more energy as the frictional losses. A similar behavior is seen by comparing 58 with 62 particles in Fig. 8 (right), but with shifted values. For frequencies below $70\,\mathrm{Hz}$, the 58 particles perform always better as the 62 particles. For higher frequencies indeed, a high dependency on the acceleration is observed again. Here, the 62 particles are especially suited for medium to high accelerations ($>40\,\mathrm{m/s^2}$), whereby the energy dissipation by the normal and tangential forces in this area is on the same scale. The different dissipation values can be explained by the varying particle activities [18]. The higher the particle activity is, the higher is the energy dissipation.
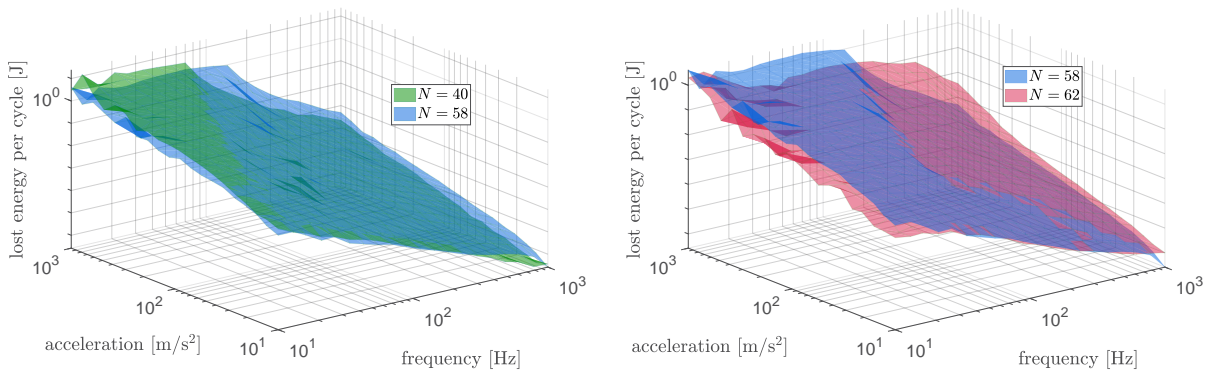
Figure 8: Simulated energy dissipation for 40 vs. 58 particles (left) and 58 vs. 62 particles (right).

Important factors seem to be amongst others the excitation frequency and acceleration, the particle inertia, the available space to move for the particles and their material.

6 Conclusion

An experimental based model and a numerical model for the determination of the energy dissipation and the loss factor of particle dampers alone are presented. Excluding the underlying vibrating structure and concentrating on the particle damper, enables to make general statements about the energy dissipation effects in a single particle damper. Thereby, a large frequency and acceleration range is analyzed. A significant energy dissipation is determined with a high loss factor for specific excitations showing the high potential of particle dampers. A good agreement between experiment and simulation is achieved. The dissipation effect varies between normal contacts and frictional effects, depending on the given excitation. Also, the filling ratio of the particle box showing a big influence on the dissipation energy, as for different frequency areas different filling ratios are better suited. With this parameter, a particle damper can be tuned for a specific excitation, and thus maximizing the damping of the underlying structure. First comparisons of experiments and simulations showing a good qualitative agreement, enabling the simulation as a future design tool for a target-oriented particle damper design. Though, some quantitative differences remain and are focus of future research.

REFERENCES

[1] H. Panossian, Structural damping enhancement via non-obstructive particle damping technique, Journal of Vibration and Acoustics 105 (114).

[2] N. Meyer, R. Seifried, Numerical and experimental investigations in the damping behavior of particle dampers attached to a vibrating structure, Preprint Reihe des SPP 1897 Calm, Smooth, Smart (7).

[3] N. Meyer, R. Seifried, An experimental model for the analysis of energy dissipation in particle dampers, PAMM 19 (1), accepted.

[4] M. Y. Yang, G. A. Lesieutre, S. Hambric, G. Koopmann, Development of a design curve for particle impact dampers, Noise Control Engineering Journal 53 (2005) 5–13.

[5] P. A. Cundall, O. D. L. Strack, Discrete numerical model for granular assemblies, International Journal of Rock Mechanics and Mining Sciences and Geomechanics 16 (4) (1979) 77.

[6] F. Fleissner, T. Gaugele, P. Eberhard, Applications of the discrete element method in mechanical engineering, Multibody System Dynamics 18 (1) (2007) 81–94.

[7] T. Pöschel, Computational Granular Dynamics: Models and Algorithms, Springer, Berlin, 2005.

[8] H. Hertz, The principles of mechanics : presented in a new form, new dover ed; unabridged and unaltered republication of the 1. ed. Edition, Dover books, Dover Publ, New York, NY, 1956.

[9] H. M. Lankarani, P. E. Nikravesh, A contact force model with hysteresis damping for impact analysis of multibody systems, Journal of Mechanical Design 112 (3) (1990) 369–376.

[10] Y. Gonthier, J. McPhee, C. Lange, J.-C. Piedbœuf, A regularized contact model with asymmetric damping and dwell-time dependent friction, Multibody System Dynamics 11 (3) (2004) 209–233.

[11] S. Andersson, A. Söderberg, S. Björklund, Friction models for sliding dry, boundary and mixed lubricated contacts, Tribology International 40 (4) (2007) 580–587.

[12] A. Di Renzo, F. P. Di Maio, An improved integral non-linear model for the contact of particles in distinct element simulations, Chemical Engineering Science 60 (5) (2005) 1303–1312.

[13] C. W. Gear, The numerical integration of ordinary differential equations of various orders, Mathematics of Computation 21 (98) (1967) 146.

[14] W. Goldsmith, Impact: The Theory and Physical Behavior of Colliding Solids, Edward Arnold Publishers, London, 1960.

[15] T. Pöschel, N. V. Brilliantov, Extremal collision sequences of particles on a line: Optimal transmission of kinetic energy, Physical Review E 63 (2).

[16] R. Seifried, H. Minamoto, P. Eberhard, Viscoplastic effects occurring in impacts of aluminum and steel bodies and their influence on the coefficient of restitution, Journal of Applied Mechanics 77 (4).

[17] P. Perzyna, Fundamental problems in viscoplasticity, in: Advances in Applied Mechanics, Vol. 9, 1966, pp. 243–377.

[18] C. Gnanasambandham, M. Stender, N. Hoffmann, P. Eberhard, Multi-scale dynamics of particle dampers using wavelets: Extracting particle activity metrics from ring down experiments, Journal of Sound and Vibration 454 (2019) 1–13.

Laboratory and numerical investigation of direct shear box test

Dániel Horváth*, Tibor Poós† and Kornél Tamás+

*†Department of Building Services and Process Engineering
Budapest University of Technology and Economics (BME), Faculty of Mechanical Engineering
Bertalan Lajos street 4-6. Building D110, H-1111 Budapest, Hungary
*e-mail: horvath.daniel@mail.bme.hu, † e-mail: poos@mail.bme.hu
web page: https://www.epget.bme.hu/en/

+Department of Machine and Product Design
Budapest University of Technology and Economics (BME), Faculty of Mechanical Engineering
Bertalan Lajos street 4-6. Building MG300, H-1111 Budapest, Hungary
e-mail: tamas.kornel@gt3.bme.hu, web page: http://www.gt3.bme.hu/en/

ABSTRACT

In agriculture, food, chemical, plastic and pharmaceutical industries for designing and operating machines, it is essential to determine the mechanical parameters of the processed granular materials. In most cases, these characteristics are the internal friction angle, the contact cohesion developed by the surface moisture and the apparent cohesion occurred by the shape of the granular material. Further physical quantities are required to characterize the motion state of the particles, which were determined by laboratory measurements in this study. Hulled millet was used for the measurements because its geometric shape can be modeled as sphere in the numerical investigations with good approximation. The porosity, the particle and bulk density of the hulled millet were determined by means of an air pycnometer in case of several moisture content. Using laboratory direct shear box test, under standard conditions, the shear strength of the cohesive liquid bridges and the internal friction angle in the bulk were determined. The results obtained were used for input parameters of a discrete element model. The aim of this research was to determine the micromechanical parameters by simulation, based on the macromechanical results of the hulled millet bulk during laboratory measurements.

1. INTRODUCTION

In the industry, it is necessary to know the physical and mechanical properties of the processed materials in order to operate and design different machines. Such parameters can be, for example, the angle of repose and the internal friction angle of the materials in agriculture and food industry, as well as their bulk and particle density. It is important to distinguish between dry and wet material bulks, as the moisture content of the surface and the material can greatly affect the movement and behavior of the bulk. Nowadays, various design and operation tasks are supported by computerized numerical models. Discrete Element Method (DEM) is a solution for modeling the movement of granular materials, which builds up a particle assembly from discrete elements with their own micromechanical parameters during the simulations [1]. Thus, we can distinguish between the mechanical parameters of the macro- and micromechanical, ie. the bulk-level and the one-particle only. The former is used for operational planning and operation, and the latter for computer modeling and other grain processing operations (eg. hulling, seed separation, cleaning, grinding, etc.).
C. J. Coetzee (2016) [2] described the steps of a DEM model calibration procedure and the effects of the particle shape. In his research, he determined some macromechanical material properties of crushed stones of less than 40 mm size by laboratory measurements and calibrated each micromechanical material parameters with DEM simulations. The internal friction angle was determined between particle-particle with direct shear box tests and angle of repose tests. He pointed out that the internal friction angle values obtained by the angle of repose tests

should be handled with care because they may prove to be low in other applications. In the DEM simulations, a particle model of linear springs, viscous dampings and Coulomb friction was used to model the real processes.

In the research of Tamás K. *et al.* (2015) [3], mechanical properties of rapeseed were determined by measurements and DEM simulations, in which a particle contact model consisting of liner springs, viscous dampings and Coulomb friction was also used to describe the collisions between the particles. In addition, the adhesion forces created by the surface moisture between the particles were modeled by cohesive bonds. In their research, direct shear box test was used, but the effect of the moisture content was not investigated.

J. Horabik and M. Molenda (2016) [4] collected micromechanical parameters of agricultural crops and different DEM contact models used in the studies of other researchers. Considering the absorbent effects of each material, ranges were given for each material properties, but based on the parameters collected in this way, it is not possible to determine the range and function characteristics of the domains depending on the moisture content.

In this study, DEM numerical simulations were carried out using cohesive-frictional contact model [5]. After developing the model of the direct shear box test and using the macromechanical parameters obtained from the laboratory measurements, micromechanical parameters were determined. These were the rolling and twisting resistance coefficients and the normal and shear strengths of the cohesive bonds depending on the moisture content of the material. The aim of this research was to determine the micromechanical parameters by simulations, based on the macromechanical results of the hulled millet bulk during laboratory measurements.

2. MATERIAL AND METHOD

2.1. Material

In this research, hulled millet (Panicum miliaceum L.) was used, which is illustrated in Fig. 1.

Figure 1. Hulled millet (Panicum miliaceum L.)

Before the measurements, the impurities and the broken particles were removed by the wind classification device, and the nearly homogeneous distribution of particles was created in the examined bulk. The material was wetted in a uniquely made rotating drum unit, into which a certain amount of millet and water was loaded. The drum was operated for 4 hours and it mixed the material at 10 minutes intervals for 2 minutes. The method for determining the moisture content of the hulled millet is to dry a sample from the bulk to constant weight at 105±5 °C which takes generally about 24–48 h. By weighing the wet sample before drying

(m_{wm}) and after drying (m_{dm}), the moisture content on wet basis of the material could be calculated:

$$x = \frac{m_{wm} - m_{dm}}{m_{wm}} \cdot 100\% \qquad (1)$$

The typical diameter of the hulled millet was $d = 1.8\ mm$, which was determined by sieve analysis and the moisture content-dependent particle density by air pycnometer [6].

2.2. Experimental method

Using direct shear box tests, geotechnical investigations can be carried out primarily, but nowadays, with the widespread use of discrete element modeling, researchers are also using it for investigating larger granular materials [2], [3], [7], [8]. The operation of the equipment is based on the shearing of the particulate material bulk and the measurement of the resulting shear force at different normal direction loads which produces the normal stresses. The standard rectangular device used in laboratory measurements is illustrated in Fig. 2.
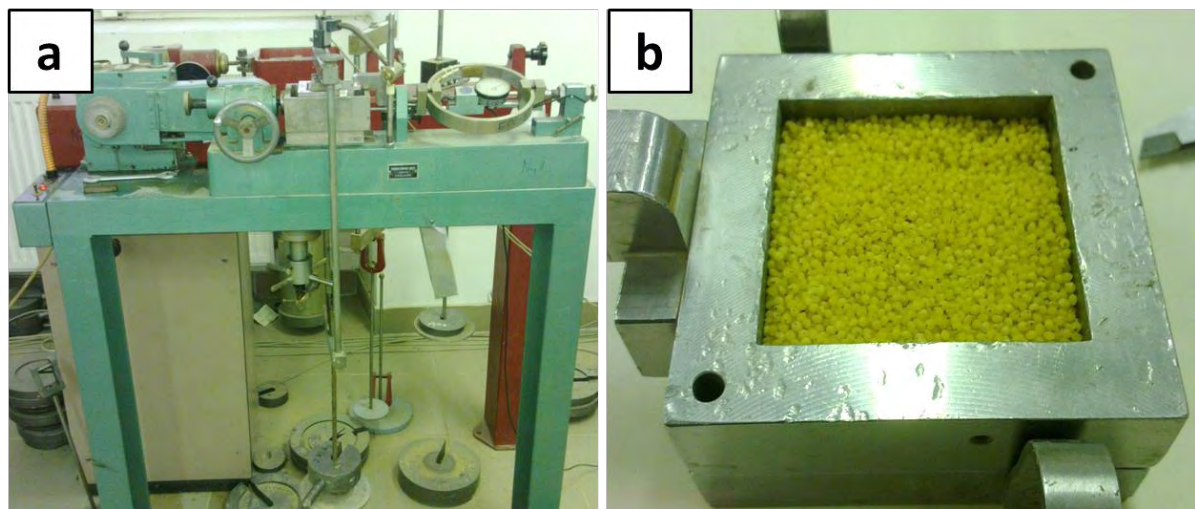
Figure 2. The laboratory direct shear box (a), and the shear box filled with hulled millet (b)

The standard laboratory direct shear box apparatus had an inner size of 60×60×30 mm where the granular material could be loaded. The shear speed of $v_{shear} = 0.02\ mm/s$ and shear displacement of $h = 6 - 9\ mm$ were set based on [9]. During the measurements, shear tests were carried out using $\sigma_{load} = 11.96; 19.61; 29.42\ kPa$ normal loads, and the evaluation was performed according to standard [8]. The shear force, shear displacement and time were recorded during the measurement. For a given normal load, by knowing the shear cross-section ($A = 60 \cdot 60 = 3600\ mm^2$) and the measured maximum shear force ($F_{shear,max}$), the maximum shear strength of the granular material could be determined:

$$\tau_{shear,max} = \frac{F_{shear,max}}{A} \qquad (2)$$

By illustrating the maximum shear strength (τ_{max}) and the normal load (σ) point pairs and then fitting a linear trend line, the failure envelope of the granular assembly can be obtained. The slope of the failure envelope defines the internal friction angle ($\varphi\ '$), and the axis section to the macromechanical apparent and contact cohesion shear strength of the particle assembly ($\tau_{coh,ma}$).

2.3. Discrete element method

For numerical simulations, the Yade open-source discrete element software [10] was used, in which the model building can be done using *python* programming language. Cohesive-frictional particle contact model (CohFrictMat) illustrated in Fig. 3 was utilized to model the rheological processes between the particles, in which the tensile forces resulting from the interparticle liquid can be modeled with bonds [5].
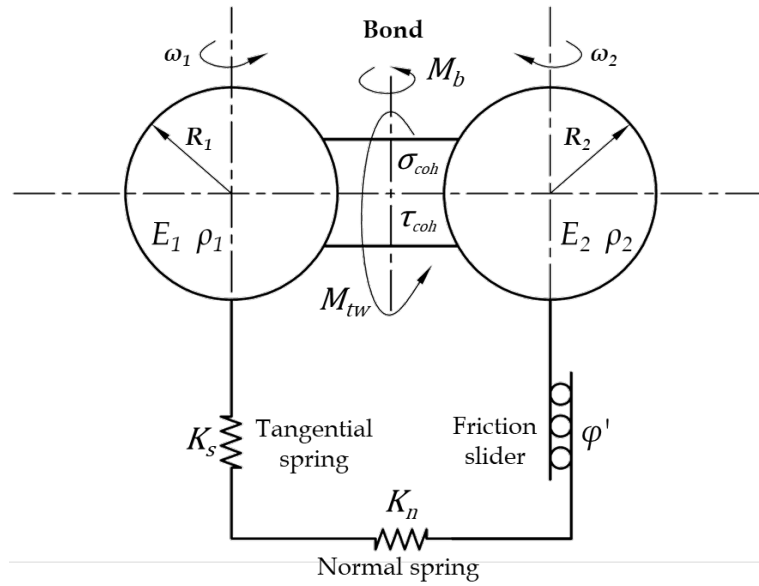
Figure 3. The schematics of the cohesive-frictional contact model (CohFrictMat)

The particle contact model consists of a normal and a tangential linear spring and a friction slider modeling the Coulomb friction. Cohesive bond can be modeled as a rigid beam behavioral element that can break due to tensile force in normal direction. In case of a particle collision, the normal contact stiffness (K_n) can be calculated from the modulus of elasticity of the colliding particles (E_1; E_2) and the radius of the particles (R_1; R_2), taking the harmonic average of the parameters:

$$K_n = 2\frac{E_1 R_1 E_2 R_2}{E_1 R_1 + E_2 R_2} = 2\frac{k_{n1}k_{n2}}{k_{n1}+k_{n2}} \tag{3}$$

The tangential contact stiffness (K_s) can be given by a proportional factor (v), which can be used to control the Poisson ratio indirectly:

$$K_s = vK_n = 2\frac{E_1 R_1 v_1 E_2 R_2 v_2}{E_1 R_1 v_1 + E_2 R_2 v_2} = 2\frac{k_{s1}k_{s2}}{k_{s1}+k_{s2}} \tag{4}$$

The normal force vector occurring during the collision of the particles can be calculated from the normal contact stiffness, the normal overlap of the particles (u_n) and the normal vector ($\underline{n}$) perpendicular to the collision plane:

$$\underline{F_n} = K_n u_n \underline{n} \tag{5}$$

The resulting shear force vector can be calculated from the tangential contact stiffness, the tangential velocity ($\underline{v_s}$), and the time step (Δt) using incremental formulation that takes into account the value of one time step earlier:

$$\underline{F_s}^t = \underline{F_s}^{t-\Delta t} + K_s \underline{v_s} \Delta t \tag{6}$$

The maximum shear force can be determined from the normal force, the internal friction angle (φ') and the shear strength of the cohesive bond ($F_{coh,s}$) which is zero if there is no cohesive bond between the colliding particles:

$$F_{s,max} = |\underline{F_n}| \tan(\varphi') + F_{coh,s} \tag{7}$$

If the arising shear force during the collision exceeds the maximum allowed for elasticity, ie. $|\underline{F_s}| > F_{s,max}$, the shear force must be limited to meet the elasticity conditions and to slip:

$$\underline{F_s}^{limited} = \underline{F_s} \frac{F_{s,max}}{|\underline{F_s}|} \tag{8}$$

Based on these, the force vector arising in the contact point during the collision is:

$$\underline{F} = \underline{F_n} + \underline{F_s} \tag{9}$$

The normal ($F_{coh,n}$) and shear force ($F_{coh,s}$) of the cohesive bonds can be calculated from the normal (σ_{coh}) and the shear strength (τ_{coh}) using the radiuses of the particles in contact:

$$F_{coh,n} = \min(\sigma_{coh,1}; \sigma_{coh,2}) \min(R_1; R_2)^2 \tag{10}$$

$$F_{coh,s} = \min(\tau_{coh,1}; \tau_{coh,2}) \min(R_1; R_2)^2 \tag{11}$$

If the arising normal force exceeds the normal-direction cohesive force, ie. $|\underline{F_n}| > F_{coh,n}$, the cohesive bond breaks between the two particles. There are two options for activating the cohesive bonds in the software. One is the '*setCohesionNow*' command [11], which is used to activate the cohesive bonds between the overlapping ($u_n > 0$) particles at the given time step, and not after the bond breaking at later time steps. The other command is '*setCohesionOnNew-Contacts*' [11], which, after activation, creates cohesive bond at any later time step in case of particle overlapping. In the presence of cohesion bonds, the particles cannot roll freely and cannot twist freely, and in reality the shape of the particles is not a perfect sphere. In this way, bending and twisting torques have been introduced to adjust the above-mentioned aspects. To determine the torques, first, the relative angular velocity vector is required, which can be calculated from the angular velocity vector ($\underline{\omega}_1; \underline{\omega}_2$) of the two colliding particles:

$$\underline{\omega}_{rel} = \underline{\omega}_2 - \underline{\omega}_1 \tag{12}$$

The rolling component of the relative angular velocity vector can be defined as follows:

$$\underline{\omega}_{rel,b} = \underline{\omega}_{rel} - \underline{\omega}_{rel,tw} \tag{13}$$

Twisting component of relative angular velocity vector:

$$\underline{\omega}_{rel,tw} = (\underline{\omega}_{rel} \cdot \underline{n})\underline{n} \tag{14}$$

The rolling stiffness can be given by a proportionality factor (α_{kr}) relative to the radius of the particles and the tangential contact stiffness:

$$K_r = R_1 R_2 K_s \alpha_{kr} \tag{15}$$

It should be noted that recent literature [12] has shown that the rolling stiffness should be compared to normal contact stiffness instead of tangential contact stiffness. Similarly, the twisting stiffness can be calculated with another proportionality factor (α_{ktw}) as the rolling stiffness:

$$K_{tw} = R_1 R_2 K_s \alpha_{ktw} \tag{16}$$

Finally, the bending (M_b) and the twisting torque (M_{tw}) can be determined using an incremental formulation that takes into account the previous value of one time step:

$$\underline{M_b}^t = \underline{M_b}^{t-\Delta t} - K_r \underline{\omega}_{rel,b} \Delta t \tag{17}$$

$$\underline{M_{tw}}^t = \underline{M_{tw}}^{t-\Delta t} - K_{tw} \underline{\omega}_{rel,tw} \Delta t \tag{18}$$

The maximum allowable bending ($M_{b,max}$) and twisting torque ($M_{tw,max}$), which still satisfy the elasticity conditions, can be calculated using the rolling (η_r) and the twisting resistance coefficient (η_{tw}):

$$M_{b,max} = |\underline{F_n}| \min(\eta_r R_1; \eta_r R_2) \tag{19}$$

$$M_{tw,max} = |\underline{F_n}| \min(\eta_{tw} R_1; \eta_{tw} R_2) \tag{20}$$

Similarly to the determination of the rolling stiffness, it is advisable to determine the maximum twisting torque with shear force instead of the normal force, based on literature [12]. If the resulting bending torque exceeds the maximum value, it must be controlled to meet the elasticity conditions:

$$\underline{M_b}^{limited} = \underline{M_b} \frac{M_{b,max}}{|\underline{M_b}|} \tag{21}$$

Similar to bending torque, the twisting torque must also be limited:

$$\underline{M_{tw}}^{limited} = \underline{M_{tw}} \frac{M_{tw,max}}{|\underline{M_{tw}}|} \tag{22}$$

The critical time step calculated by the software is used to select the appropriate time step. The critical time step is given by the smallest value calculated from the particle radius, the particle density, and the modulus of elasticity, which calculation is done using all (i) particles [10], [13]:

$$\Delta t_{crit} = \min_i R_i \sqrt{\frac{\rho_{p,i}}{E_i}} \tag{23}$$

Since there is no speed-dependent damping in the presented contact model, numerical (artificial) damping (λ_d) can be used to dissipate the kinetic energy of the particles. This is done by reducing the $\underline{F_i}$ forces which increase the speed of the particles by ΔF_d force, taking into account the speed ($\underline{v_i}$) of the particles and their acceleration ($\underline{a_i}$) [9]:

$$\frac{\Delta F_d}{F_i} = -\lambda_d \text{sgn}\underline{F_i}\left(\underline{v_i} + \frac{a_i \Delta t}{2}\right) \tag{24}$$

Based on these, the damping mechanism is not a physical but an artificial quantity, because the damping is done with a component that is not invariant with respect to the coordinate system rotation. The resting state of the examined particle assembly can be measured with the unbalanced force ratio during the simulations. This parameter specifies the ratio of the average of all forces exerted on the bodies and the magnitude of the average force in the contacts. In case of perfect static equilibrium, the total exerted force on the bodies is zero, so the ratio tends to zero. Meanwhile, the discrete elements of the simulation are stabilized and thus come to resting state. However, the ratio never takes zero value because of the finite precision computation.

2.4. Discrete element model

The DEM model of the direct shear box test was built on 1:1 scale based on the laboratory equipment. The two part of the shear box and the load plate were modeled as structure walls. The lower box was open at the top and the upper box was open at the top and the bottom side. The material parameters of the structure walls were taken from the material properties of steel [4]. The steel had a density of 7750 kg/m³, a modulus of elasticity of 200 GPa, a proportional parameter between normal and tangential contact stiffness of 0.3, and an internal friction angle of 40.1°. To fill the boxes with particles, gravity deposition was used, to which a bottom side open box was placed in our model over the upper shear box so that the particles did not fall out during the process. Due to the wall thickness of the boxes, square shapes were used in the shear direction to prevent the particles from falling out of the boxes during the simulations. In order to provide the normal load, an infinitely wide structure wall was used. It did not have a

mass, but at a given speed, it moved as a servo drive at the top of the particle set in the same or opposite direction as the gravity acceleration. This was necessary because, during the laboratory measurements, the load plate moved upwards too in the vertical direction as a result of shearing. The appropriate normal load was set by measuring the force exerted by the particles on the element modeling the load plate. The DEM model of the direct shear box and the simulation steps are illustrated in Fig. 4.
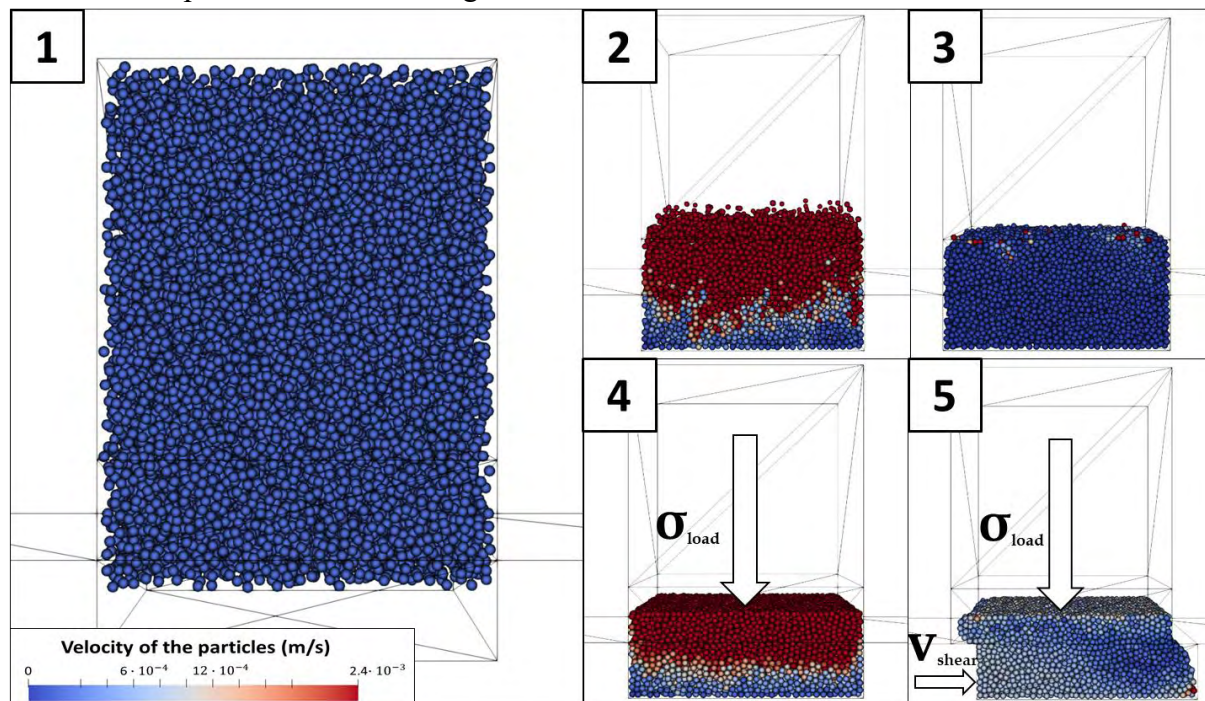
*Figure 4. DEM model of the direct shear box test and the steps of the simulation
(1. generating particles; 2. gravity deposition of the particles; 3. activating cohesive bonds;
4. application of load plate; 5. start of shearing)*

The first step of the simulation was the generation of the particles (Fig. 4/1) followed by the gravity deposition (Fig. 4/2). After the stabilization of the particle set, when the unbalanced force ratio dropped below 0.001, the cohesive bonds were activated using the '*setCohesionNow*' command (Fig. 4/3). This was followed by the application of the normal load (σ_{load}) (Fig. 4/4), then at the speed of $v_{shear} = 1 \frac{mm}{s}$, the shearing was started by moving the lower shear box (Fig. 4/5). The increase in the shear velocity compared to the laboratory measurements ($v_{shear} = 0.02 \, mm/s$) was used to reduce the computational time requirement. It was assumed that the increase in shear speed does not affect the maximum shear force value but only the position of it at the shear length [9]. The resulting shear force was measured on the right-hand side of the upper shear box illustrated in Fig. 4/1 at a sampling interval of 0.1 s. The hulled millet particles were modeled with spheres with a normal distribution of $d = 1.8 \pm 0.1 \, mm$, The particle density (ρ_p) of the hulled millet was chosen based on preliminary air pycnometer measurements, the elasticity modulus ($E = 20 \, MPa$) and the proportional parameter between normal and tangential contact stiffness ($\upsilon = 0.2$) were selected from the literature [4] and the internal friction angle (φ') was set based on previous simulation experience. The additional values of the setting parameters are summarized in Table 1.

Table 1. DEM material parameters of hulled millet

No.	Measured x [%]	Selected ρ_P [kg/m³]	Measured φ' [°]	Set Δt [s· 10^{-6}]
1	11.2	1379	42.2	4.7
2	16.1	1388	42.1	4.8
3	18.7	1393	41.6	4.8
4	23.6	1402	40.5	4.9
5	24.1	1403	38.7	4.9
6	28.2	1410	37.5	5

The time steps used in the simulations were set lower than the critical time step obtained by Eq. (23). The numerical damping value was $\lambda_d = 0.5$ and 21000 particles were modeled. The normal (σ_{coh}) and shear strengths (τ_{coh}) of the cohesive bonds were determined by simulation calibrations, as well as the rolling (η_r) and twisting resistance coefficients (η_{tw}), which are presented in the *Results* section.

3. RESULTS

Fig. 5 illustrates the measurement and simulation results of the direct shear box test where the shear force (F_{shear}) - shear displacement (h) results can be seen at different normal loads ($\sigma_{load} = 11.96\ kPa; 19.61\ kPa; 29.42\ kPa$) for $x = 18.7\%$ moisture content hulled millet.
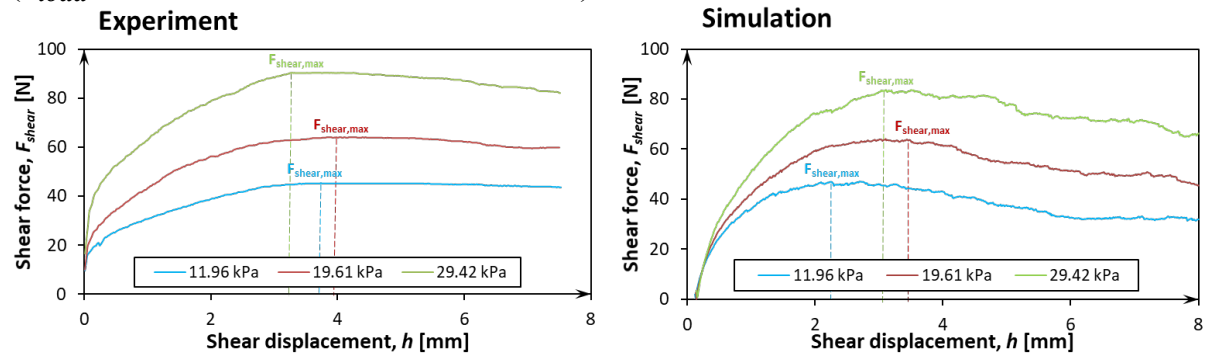
Figure 5. The measured (left side) and simulated (right side) shear force as a function of shear displacement at different normal loads for x=18.7% moisture content hulled millet

In the simulation results - compared to the measurements -, the steeper reductions in the forces seen after the maximum shear forces were due to the use of artificial damping and higher shear speed [9]. However, the results showed a good match as the maximum shear forces occurred at almost the same shear displacement for $\sigma_{load} = 19.61\ kPa; 29.42\ kPa$ normal loads. By calculating the shear stresses from the maximum shear forces, and illustrating them as a function of the associated normal loads, the failure envelopes shown in Fig. 6. could be plotted.
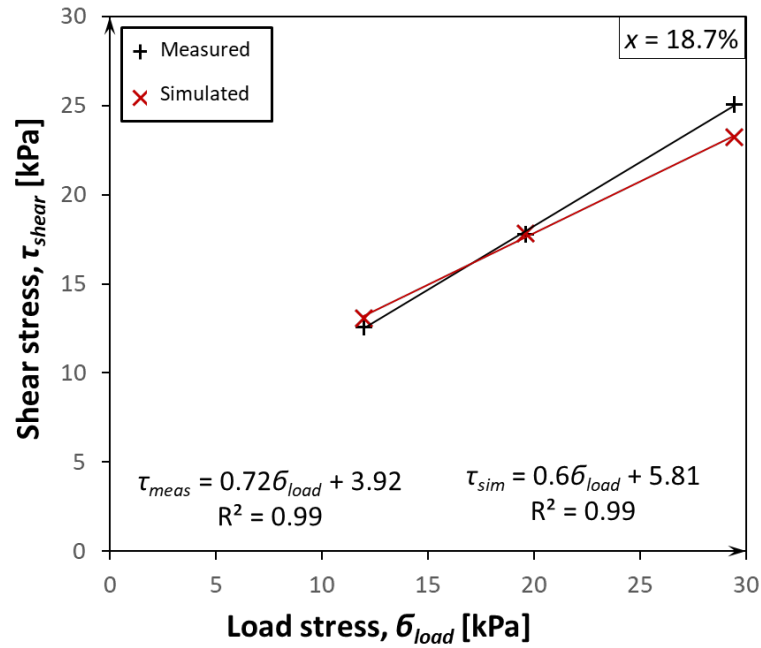
Figure 6. The failure envelopes in case of x=18.7% moisture content hulled millet, obtained by measurements and DEM szimulations

In the simulation calibrations, the unknown micromechanical cohesive normal and shear strengths were set equally for a specific moisture content based on own simulation experience. The values of the rolling and twisting resistance coefficients were also treated equally, but they gave a value of $\eta_r = \eta_{tw} = 0.05$ regardless of the moisture content. In the simulation results, the cohesive strengths could be used to change the axis section of the failure envelopes, but by changing the resistance coefficients, the slopes of the lines could be influenced. The calibrated micromechanical cohesive normal and shear strengths are plotted against the moisture content in Fig. 7.
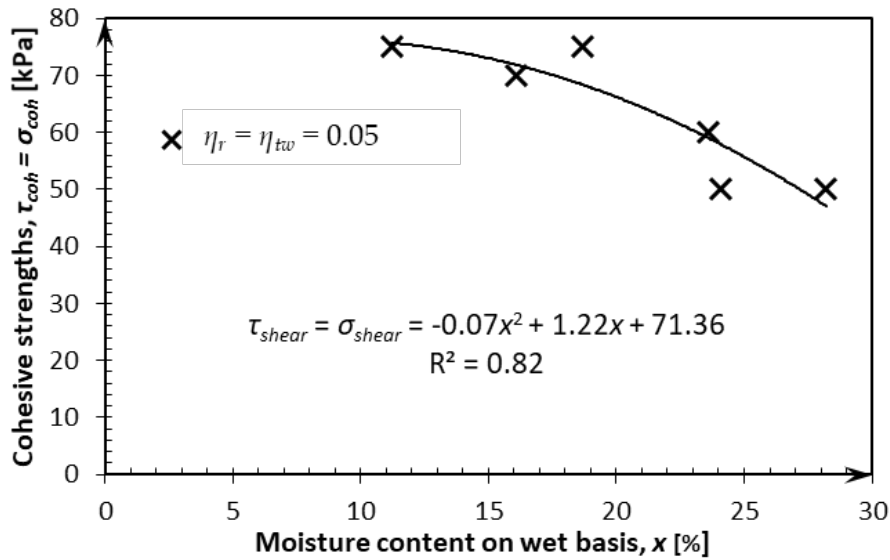
Figure 7. The micromechanical cohesive strengths of the bonds obtained by DEM simulations as a function of the moisture content of the hulled millet for $\eta_r = \eta_{tw} = 0.05$ resistance coefficents

The function fitted to the data showed a second order polynomial nature, which means that it is not enough to specify a domain for each micromechanical parameter, but also to define the function nature so that it can be used more accurately for later DEM simulations. The accuracy of the simulation results was characterized by the relative errors between the measured

280

($\tau_{shear,measured}$) and simulated shear strengths ($\tau_{shear,simulated}$), which were calculated as follows:

$$Relative\ error = \left| \frac{\tau_{shear,simulated} - \tau_{shear,measured}}{\tau_{shear,measured}} \right| 100\% \qquad (25)$$

The measured and simulated maximum shear strengths for different moisture contents and normal loads, and the relative errors are summarized in Table 2.

Table 2. Measured and simulated maximum shear strengths, moisture contents, normal loads and the calculated relative errors

No.	x [%]	σ_{load} [kPa]	$\tau_{shear,measured}$ [kPa]	$\tau_{shear,simulated}$ [kPa]	Relative error [%]
1		11.96	14.42	13.86	3.9
2	11.2	19.61	17.42	17.92	2.9
3		29.42	25.47	23.53	7.6
4		11.96	14.42	13.22	8.3
5	16.1	19.61	18.61	18.69	0.4
6		29.42	24.86	25.14	1.1
7		11.96	12.58	13.06	3.8
8	18.7	19.61	17.78	17.83	0.3
9		29.42	25.06	23.22	7.3
10		11.96	11.97	12.28	2.6
11	23.6	19.61	17.11	17.08	0.2
12		29.42	24.11	23.11	4.1
13		11.96	10.19	11.28	10.6
14	24.1	19.61	16.25	16.14	0.7
15		29.42	22.89	21.81	4.7
16		11.96	10.31	10.19	1.1
17	28.2	19.61	15.19	15.06	0.9
18		29.42	21.97	20.61	6.2

The highest relative error (10.6%) between the measured and simulated results was at $x = 24.1\%$ moisture content and 11.96 kPa normal load. In other cases, the results of the laboratory measurements were modeled with relative error less than 10% using the previously defined DEM micromechanical parameters.

4. CONCLUSION

In this research, direct shear box tests were performed using hulled millet in case of different moisture contents. The discrete element model of the laboratory equipment was created, using a cohesive-frictional particle contact model to model the collisions of the particles and the cohesive forces resulting from the surface moisture of the material. The main goal was to determine the micromechanical parameters describing the cohesion relationships and their moisture-dependent behavior. These were the cohesive normal and shear strengths, and the rolling and twisting resistance coefficients that were less dependent of the moisture content. By varying the former two parameters equally, the axis section of the failure envelopes - obtained by the direct shear box simulations - could be changed, while the latter two variables could be used to influence the slopes. Based on these, it was possible to simulate the measurement results with just one parameter set combination in case of a moisture content. Cohesive strengths were determined at moisture content range of $11.2 - 28.2\%$. The points thus obtained were described by a second-degree polynomial function with good accuracy and can be used for future DEM simulations.

REFERENCES

[1] Cundall, P. A., Strack, O. D. L.: *Discrete numerical model for granular assemblies.* Geotechnique, vol. 29, no. 1, pp. 47–65, 1979.

[2] Coetzee, C. J.: *Calibration of the discrete element method and the effect of particle shape*. Powder Technol., vol. 297, pp. 50-70, 2016.

[3] Tamás, K., Földesi, B., Rádics, J. P., Jóri, I. J., Fenyvesi, L.: *A Simulation Model for Determining the Mechanical Properties of Rapeseed using the Discrete Element Method.* Period. Polytech. Civ. Eng., vol. 59, no. 4, pp. 575–582, 2015.

[4] Horabik, J., Molenda, M.: *Parameters and contact models for DEM simulations of agricultural granular materials: A review*. Biosyst. Eng., vol. 147, no. Supplement C, pp. 206–225, 2016.

[5] Bourrier, F., Kneib, F., Chareyre, B., Fourcaud, T.: *Discrete modeling of granular soils reinforcement by plant roots*. Ecol. Eng., vol. 61, no. Part C, pp. 646–657, 2013.

[6] Szabó, V.: *Fluidizációs szárítás hő- és anyagátadási folyamatainak modellezése (Modeling of heat and mass transfer in fluidized bed dryers)*. PhD dissertation, Budapest University of Technology and Economics, Budapest, Hungary, 2019.

[7] Suhr, B., Six, K.: *On the effect of stress dependent interparticle friction in direct shear tests.* Powder Technol., vol. 294, no. Supplement C, pp. 211–220, 2016.

[8] Yang, H., Xu, W.-J., Sun, Q.-C., Feng, Y.: *Study on the meso-structure development in direct shear tests of a granular material*. Powder Technol., vol. 314, no. Supplement C, pp. 129–139, 2017.

[9] Saadat, M., Taheri, A.: *A cohesive discrete element based approach to characterizing the shear behavior of cohesive soil and clay-infilled rock joints.* Comput. Geotech., vol. 114, p. 103-109, 2019.

[10] Šmilauer, V. *et al.*: *Dem formulation. In Yade Documentation 2nd ed.* Yade Proj., p. 37, 2015.

[11] Šmilauer, V., Gladky, A., Kozicki, J., Modenese, C., Stránský, J.: *Using and programming. In Yade Documentation 2nd ed.* Yade Proj., p. 149, 2015.

[12] Jiang, M., Shen, Z., Wang, J.: *A novel three-dimensional contact model for granulates incorporating rolling and twisting resistances*. Comput. Geotech., vol. 65, pp. 147–163, 2015.

[13] Chareyre, B., Villard, P.: *Dynamic Spar Elements and Discrete Element Methods in Two Dimensions for the Modeling of Soil-Inclusion Problems.* J. Eng. Mech., vol. 131, no. 7, pp. 689–698, 2005.

LARGE DEFORMATION ANALYSIS OF GROUND WITH WALL MOVEMENT OR SHALLOW FOUNDATION UNDER EXTREMELY LOW CONFINING PRESSURE USING PIV

K. SATO*, H. AKAGI*, T. KIRIYAMA† AND K. ESAKI*

* Department of Civil and Environmental Engineering
Waseda University
58-205, 3-4-1, Ohkubo, Shinjuku-ku, Tokyo, 169-8555, Japan
e-mail :adjl@fuji.waseda.jp, web page : https ://www.f.waseda.jp/akagi/index_e.html

† Institute of Technology
Shimizu Corporation
3-4-17, Etchujima, Koto-ku, Tokyo, 135-0044, Japan
e-mail :kiriyama@shimz.co.jp, web page : https ://www.shimz.co.jp

Abstract. Large-scale natural disasters have occurred frequently in recent years. In such disasters, large ground deformation has been a recurring phenomenon. As it directly affects the structure, has dureable design is necessitated to minimize the damages. Additionally, the fracture process zones are predicted using numerical analysis, and thereafter, the results of the analysis are validated after comparison with the experimental ones. In this study, image analysis is performed using particle image velocimetry (PIV), and subsequently, the analysis results are validated by the comparison. We herein aim to improve the precision of the image-analysis results, and examine the experimental or analytical condition of reproducing the deformation .

1 INTRODUCTION

In the recent years, there are growing concerns about geohazards triggered by earthquakes and heavy rainfalls in Japan. Geohazards, such as slope failure and landslide, have caused heavy damages to social infrastructures. Taking an example of the 2016 Kumamoto Earthquakes, which occurred on 16th April 2016, slope failures, landslides and debris flow occurred mainly around the Mt. Aso area. In particular, large-scale (deep) landslides occurred in Minami-Aso village Tateno area, and Aso Bridge collapsed completely by this slope failure. In order to minimize the risk of such damages, it is desirable to understand the ground collapse process, scale and range. However, large deformation problem of ground that ranges more than tens of meters has mainly been based on case studies such as literature surveys and ground surveys. Along with these investigations, it is necessary to simulate the destruction process by numerical analysis, and the analysis should be evaluated by practical engineering or physical evaluation.

In order to validate the numerical method, the tracking of the deformation of laboratry test results is performed. A deformation measurement method based on Particle Image Verocimetry (PIV) has been used for a tool to geotechnical testing. In the paper, the deformation of ground model with laminated aluminium bars is analyzed with the PIV method. Applying the PIV

method to the model tests, the distribution of displacement can be obtained with higher resolution than that of the method using target markers.

By using PIV, accurate results of deformation analysis in model test, that manages the bearing capacity of shallow footing or deformation analysis on retaining wall movement tests, can be obtained. Also comparing the result of PIV with the numerical analysis, the validity of numerical analysis about large deformation problem is evaluated from shear strain and load settlement relationship in the ground. Through the examination and comparision of the results of both model test analysis and numerical analysis, the study aims to the approximation of reproducing the actual phenomena based on numerical analysis such as DEM, FEM or other methods.

2 DEFORMATION ANALYSIS OF MODEL TESTS USING PIV

2.1 Mechanism of Particle Image Velocimetry

Particle image velocimetry (PIV), which is an image analysis method used in this experiment, is a fluid measurement method that can obtain instantaneous velocity of multiple points in a flow field without contact, using two temporally continuous images, the luminance distribution in a minute area in the first time image and the luminance in the area in the second time image. The fluid displacement is calculated by finding the similarity of the pattern and estimating the displacement that is the maximum value as the average displacement vector in the inspection area. The similarity between the luminance patterns of the image at t = t and the image at t = t + Δt is calculated by the following equation ;

$$R(\xi,\eta) = \frac{\sum_0^{M-1}\sum_0^{N-1}\{f(m,n)-f_{av}\}\{g(m+\xi,n+\eta)-g_{av}\}}{\sqrt{\sum_0^{M-1}\sum_0^{N-1}\{f(m,n)-f_{av}\}^2}\sqrt{\sum_0^{M-1}\sum_0^{N-1}\{g(m+\xi,n+\eta)-g_{av}\}^2}} \qquad (1)$$

where f (m, n) and g (m, n) represent the intensity distribution at time t = t and t = t + Δt, M and N are the tracking mesh size, ξ and η are the mesh movement amount.

In which

$$f_{av} = \frac{\sum_0^{M-1}\sum_0^{N-1}f(m,n)}{MN} \qquad (2)$$

$$g_{av} = \frac{\sum_0^{M-1}\sum_0^{N-1}g(m+\xi,n+\eta)}{MN} \qquad (3)$$

Equation (2) and (3) are an average value of the luminance inside each tracking meshes.

From the equation, the displacement of the particle group is determined by (ξ, η) where the similarity R (ξ, η) is the highest. These operations are applied to all meshes to calculate the inter-image displacement vector of the whole image. Based on the calculated displacement vector, the shape functions are adopted and the strain is determined.

2.2 Deformation tests on ground model with aluminum bar laminate

To conduct deformation tests on the aluminum bar laminate using PIV, sequent pictures of the deforming laminate are taken, with the equipment moving in equal intervals. To make the particle size distribution as equal as that of Toyoura sand, the aluminum bars are blended with radius 1.6 mm and 3.0 mm at a mass ratio of 2:1. Moreover, to give a wide luminance distribution on PIV analysis, a side of the aluminum bars is multi-colored. Pictures are taken from the side of the aluminum bar laminate in each deformation intervals, and deformation analysis based on PIV is conducted.

In the analysis, analysis mesh is set on the deformation target. The mesh size is 5 mm (to give the luminance variation within the mesh squares).
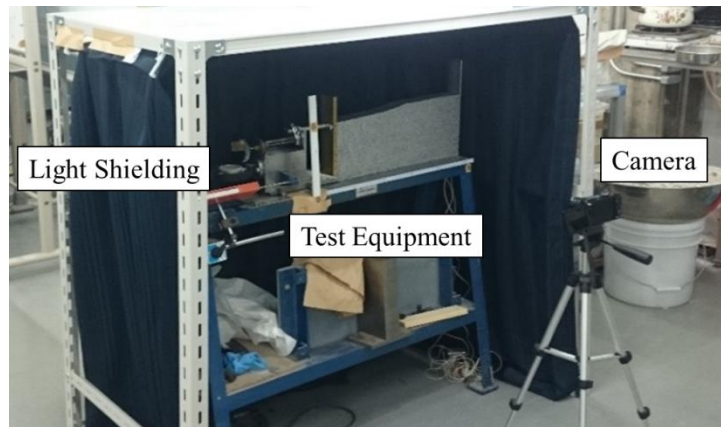
Figure 1: Viewing of deformation test condition
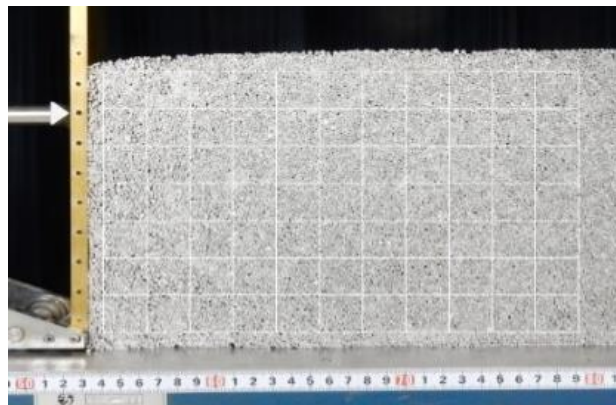
Figure 2: Example of analysis mesh arrangement

2.3.1 Deformation tests on retaining wall movement

The retaining wall test equipment consists of retaining wall and aluminum bar laminated ground that simulates the ground behind the retaining wall. The retaining wall is made by a brass rigid material with a height of 200 (mm), a width of 10 (mm) and a depth of 50 (mm), which can be controlled by the handle to a horizontal displacement of 95 (mm) in active earth pressure direction.

The equipment of the wall model is shown in Figure.3, and the dimensions of the retaining wall test equipment are as shown in Table 1. The ground is tightly packed, and aluminum bars are laid as densely as possible. The test is done with running the wall parallel to the active earth pressure direction. The velocity of wall is set as the deformation is regarded as quasi-static state. The experimental procedure follows as configuration conditions described in Table 2. To avoid the image error due to the setting of camera, filming is done with manual mode, and configurations are shown in Table 3. From the captured pictures, PIV analysis is conducted and confirming the deformation of laminated ground.
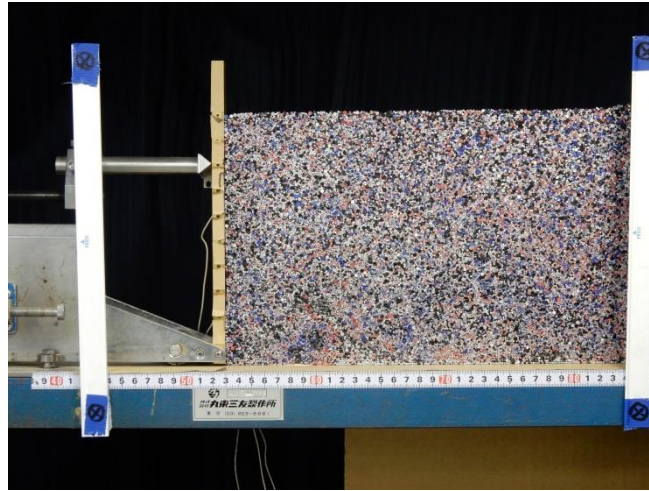
Figure 3: Arrangement of retaining wall test equipment

Table 1: Dimensions of ground model (retaining wall test)

Height (mm)	Depth (mm)	Width(Wall) (mm)	Width(laminate) (mm)
200	50	10	400

Table 2: Configuration of model test (retaining wall test)

Maximum displacement (mm)	Wall movement speed (mm/min)	Filming interval (sec)
60	2	30

Table 3: Configuration of filming condition (retaining wall test)

Pixels	ISO sensitivity	Camera Height	Distance Camera-Model	Shutter speed	Diaphragm value
4608×3456	125	855	1370	1/8	F5.3

2.3.2 PIV analysis results (retaining wall test)

PIV analysis is conducted under the conditions described above, and selection of maximum shear strain contour distribution, which displacements are 10mm and 60mm, is shown in Figure 4. Experimental results are shown with fixed contour, which range is set as 0 to 0.25.

As shown in Figure 4, strain due to the wall movement is clearly captured consistently. It is obvious that there is local large deformation at the bottom of the wall and the contact of slip line and ground surface. The deformation analysis results, which use target markers, are also shown in Figure 5.
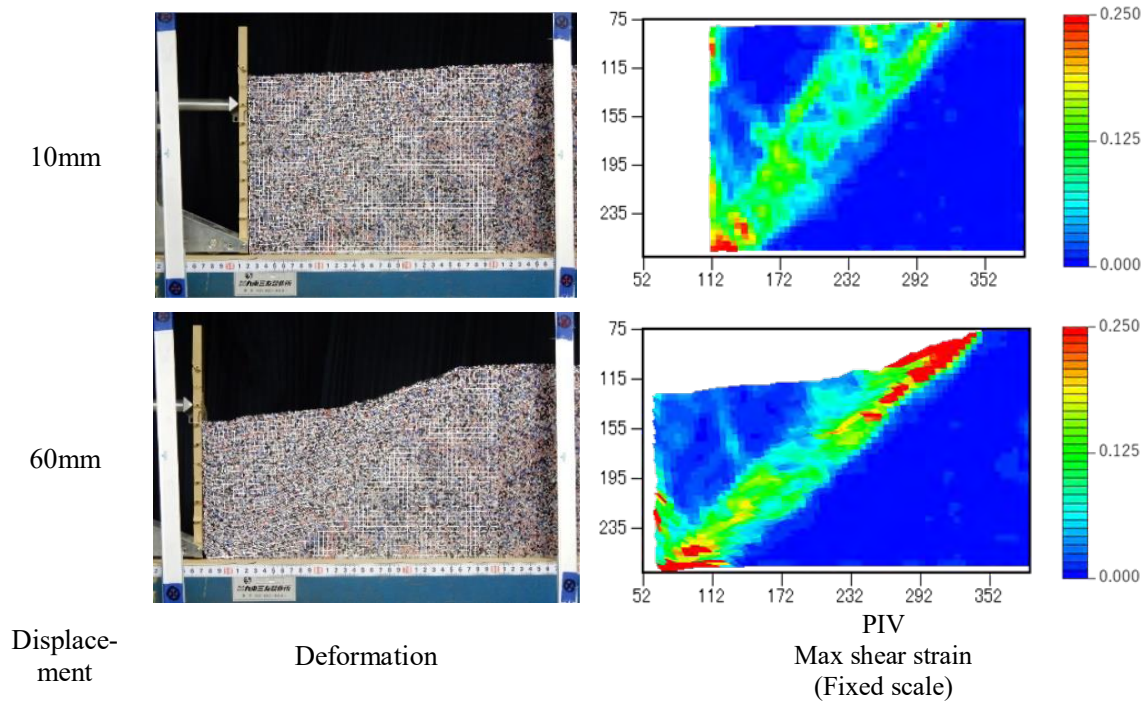
Figure 4 : Results of deformation analysis on retaining wall test using PIV (Selection)
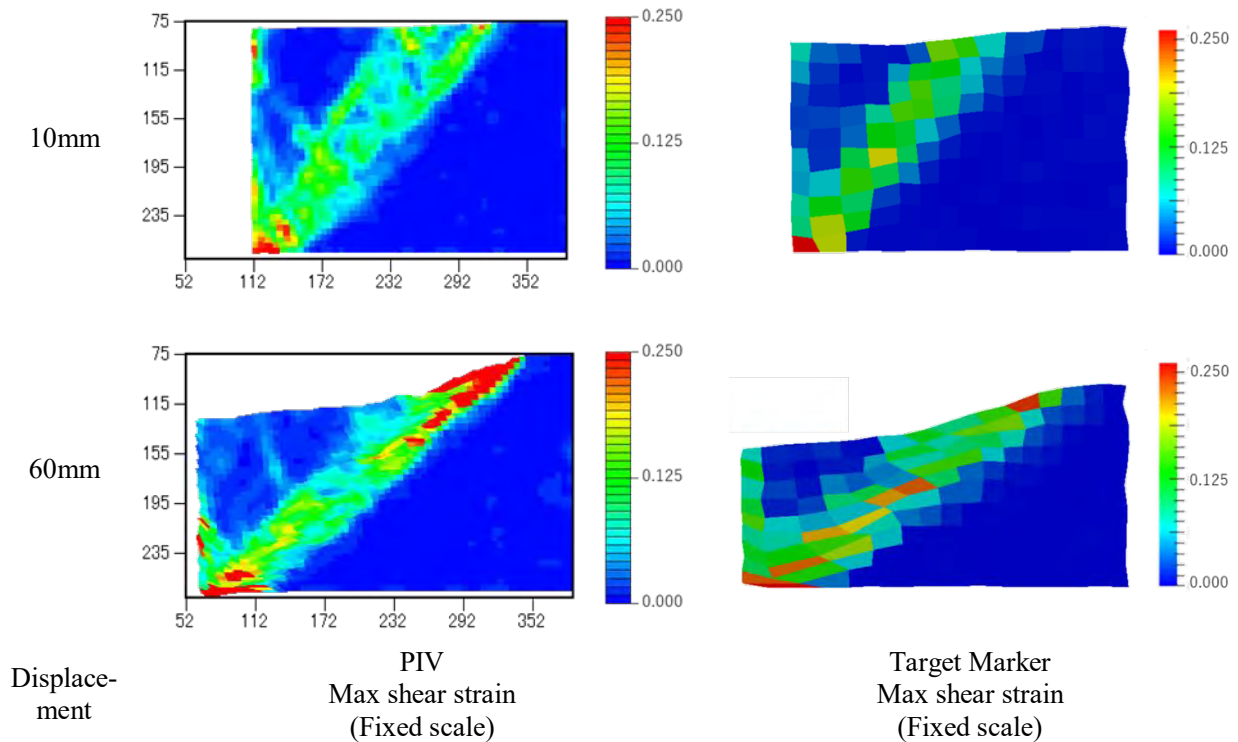
Figure 5 : comparisons of results of deformation analysis (Target marker / PIV)

2.4.1 Deformation tests on shallow foundation loading

The loading test equipment consists of foundation and aluminum bar laminated ground that simulates the ground under the foundation. The foundation is made by a brass rigid material with a height of 60 (mm), a width of 80 (mm) and a depth of 50 (mm), which can be controlled by the handle to a vertical displacement of 30 (mm) from the top of the ground surface. Through experiment, the loading pressure is also measured simultaneously, and obtains a relationship of loading versus displacement.

The equipment of the wall model is shown in Figure.6, and the dimensions of the foundation loading test equipment are as shown in Table 4. The ground is tightly packed, and aluminum bars are laid as densely as possible. The experimental procedure follows as configuration conditions described in Table 5. Filming configurations are also shown in Table 6.

Figure 6 : Arrangement of shallow foundation loading test equipment

Table 4: Dimensions of ground model (foundation loading test)

Height (mm)	Depth (mm)	Width(laminate) (mm)
200	50	523

Table 5: Configuration of model test (foundation loading test)

Maximum displacement (mm)	Foundation loading speed (mm/min)	Filming interval (sec)
25	1	30

Table 3: Configuration of filming condition (foundation loading test)

Pixels	ISO sensitivity	Camera Height	Distance Camera-Model	Shutter speed	Diaphragm value
6000×4000	200	830	1350	1/8	F8.0

2.4.2 PIV analysis results (shallow foundation loading test)

PIV analysis is conducted under the conditions described above, and selection of maximum shear strain contour distribution, in which foundation displacements are 5mm and 22mm, is shown in Figure 7. Experimental results are shown with fixed contour, which range is set as 0 to 0.15. The relationship between loading pressure and displacement of foundation is also shown in Figure 8.

| Displace-ment | Deformation | PIV Max shear strain (Fixed scale) |
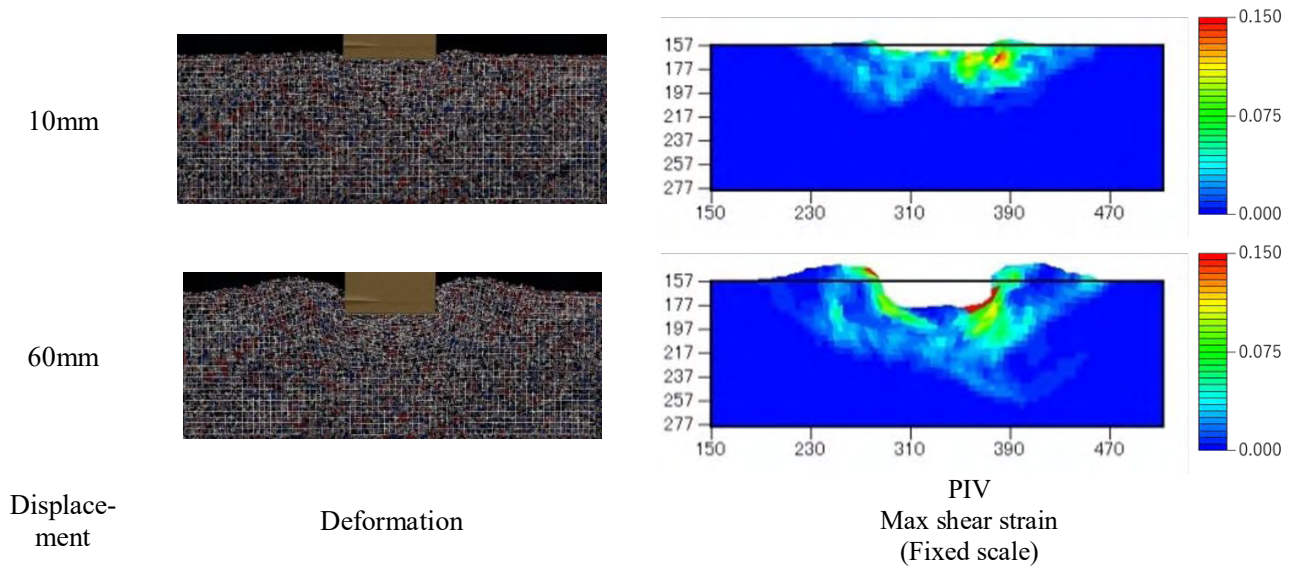
Figure 7: Results of deformation analysis on foundation loading test using PIV (Selection)
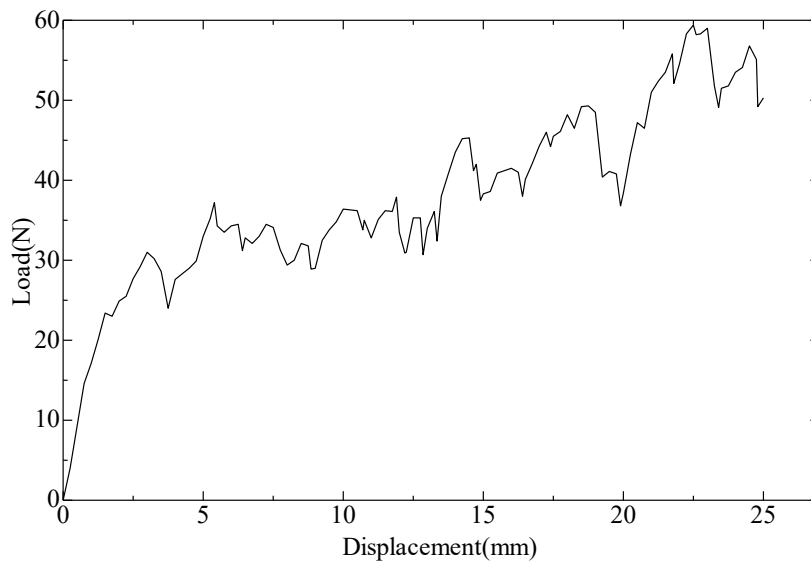
Figure 8: chart of loading versus displacement in foundation test

2.5 Discussions

The higher-resolution deformation tracking in PIV is used as opposed to target markers (Figure 5) since slip surfaces (at 10 mm displacement) are not visible in the latter method. This phenomenon is due to the continuous failure and deformation. Furthermore, the contour range in PIV is higher than that of target marker; strain localization is more clear and easier to capture (Figure 9).

In the foundation loading test, the deformation shape resembles the rupture curve based on Prandtl's theory (Figure 10). However, according to the superposition of PIV results and theoretical curve, the foundation width that matches the captured deformation is smaller than the one derived from Prandtl's theory. As the stress distribution under the foundation is not uniform, it is assumed that the aluminum laminate deforms locally at the edge of foundation. Figure 8 shows the plastic state during the displacement 0-5 mm, and load stress gradually rises with minor fluctuation during the displacement 5-25 mm). Focusing on the minor fluctuation of load with comparing PIV results and chart of loading versus displacement, the deformation spread while loading decreases. As shown in Figure 11, the distribution of the value of the maximum shear strain exceeding 0.075 is increased as the whole ground as compared with the region (a).

PIV
Max shear strain
(Auto scale)

Target Marker
Max shear strain
(Auto scale)
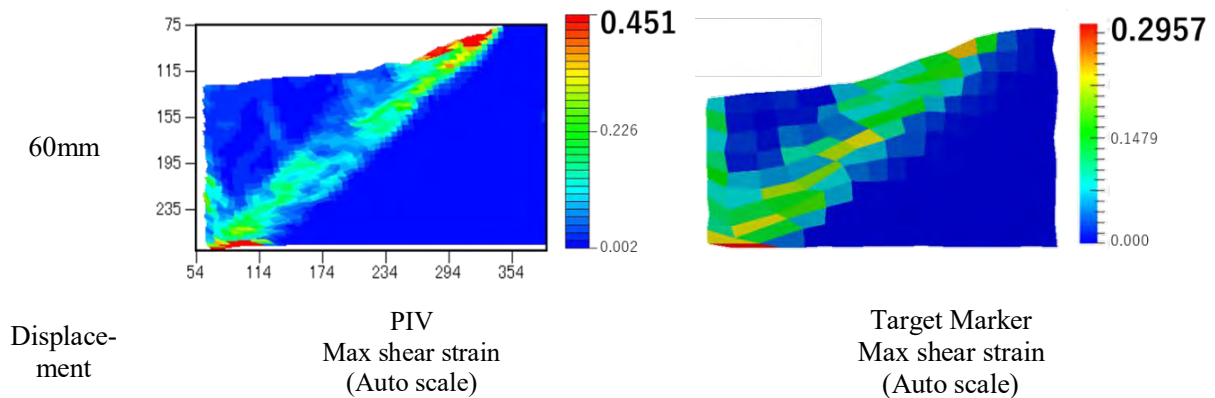
Figure 9: difference of contour range (PIV / target marker) [From Figure. 5]
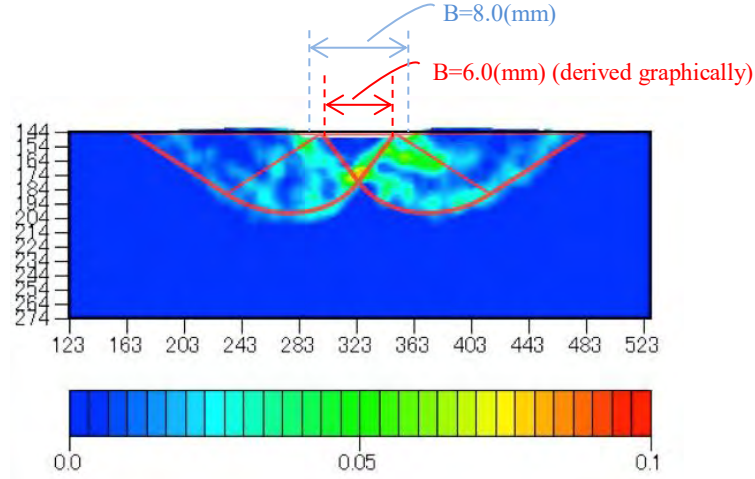
Figure 10: Superposition of PIV result (d=3.5~4.0mm) and Prandtl mechanism
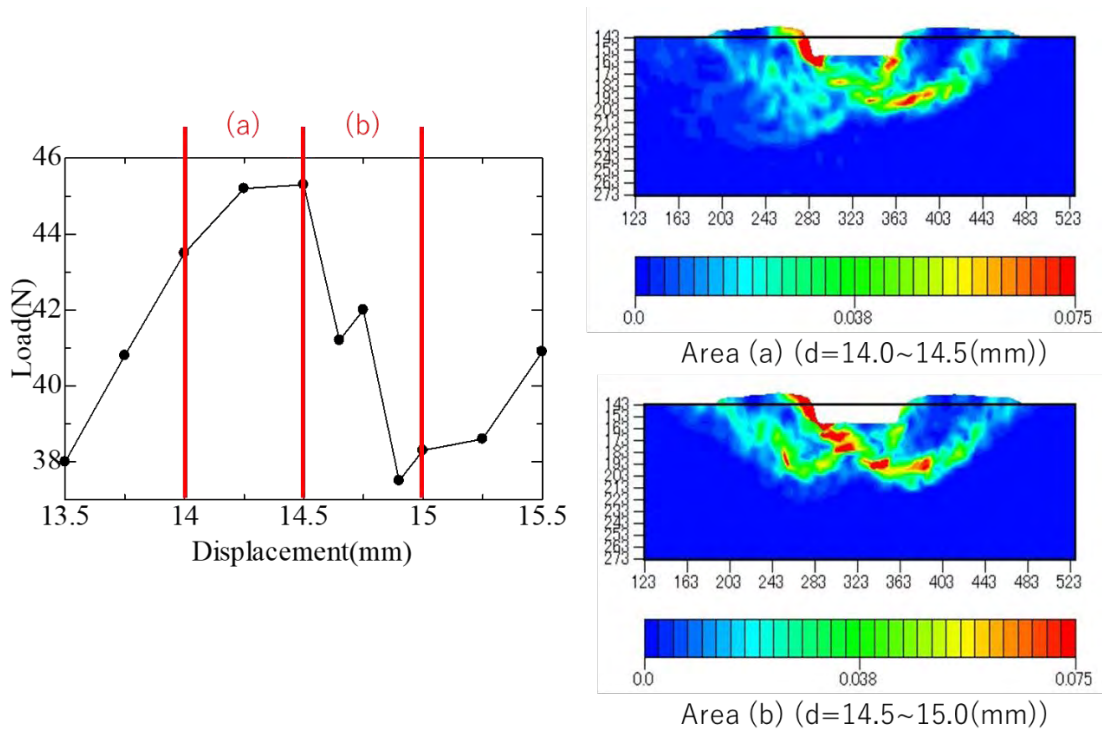
Figure 11: Example of comparison of PIV results and chart of loading versus displacement

5   CONCLUSION

In this paper, the experiments (retaining wall test and foundation loading test) were conducted that to observe ground deformation. This study demonstrates that the PIV analysis captures the deformation more accurately than target markers. Furthermore, evaluating the deformation and experimental values such as loading stress, experimental value is also reexamined based on the PIV analysis results. Therefore, it is shown that detailed phenomenon in ground model can be grasped by utilizing PIV method.

The main finding of this study was that utilizing the PIV method shown above, the criteria for validity of any numerical deformation analysis are confirmed. Large deformation, such has not been explained in formula, is reproduced in numerical analysis, therefore the experimental deformation results are needed. Thus the aforementioned method is more efficient and numerical analysis can be properly evaluated.

REFERENCES

[1] DJ White, WA Take and MD Bolton, Soil deformation measurement using particle image velocimetry (PIV) and photogrammetry, Ge´otechnique 53, No. 7, 619–631, 2003

[2] Prandtl, L.: "On the penetrating strength (hardness) of a plastic construction materials and the strength of cutting edges", Zeit. angew. Math. Mech., 1. No.1,1921

[3] T. Miura, H. Akagi and T. Kiriyama (2016). Experimental study on large deformation behaviors of the ground behind retaining walls, The 71st Japan Society of Civil Engineers Conference, 177-178 (in Japanese).

[4] S. Sreng and K. Ueno (2004). Deformation behavior and bearing capacity of sand under two adjacent foundations, Japan Society of Civil Engineers, Vol.7, 65-74 (in Japanese)

[5] R.F. Scott：Principles of Soil Mechanics, Appendix B, 1965

MODELING THE SOIL HETEROGENEITY IN THE DISCRETE ELEMENT MODEL OF SOIL-SWEEP INTERACTION

Kornél Tamás*, Márton F. Tóth[†]

[*] Department of Machine and Product Design
Budapest University of Technology and Economics (BME), Faculty of Mechanical Engineering
Bertalan Lajos street 4-6. Building MG300, H-1111 Budapest, Hungary
e-mail: tamas.kornel@gt3.bme.hu, web page: http://www.gt3.bme.hu/en/

[†] Department of Machine and Product Design
Budapest University of Technology and Economics (BME), Faculty of Mechanical Engineering
Bertalan Lajos street 4-6. Building MG300, H-1111 Budapest, Hungary
e-mail: t.marton95@gmail.com

ABSTRACT

In agriculture the analyse of soil compaction in soil-tool interaction has a significant role. The equipments of agricultural farms are getting bigger and more complicated and it has huge importance to optimize the tillage methods. Two of most frequently investigated factors are the tool's mixing-effect and the draught force on the tool; these results are important for agronomical experts to design tillage tools and cultivation processes. Discrete element method (DEM) is one of the numerical methods to model soil's behaviour and soil-tool interaction. Aim of this study is to develop a 3D DEM model for clay soil and analyse the behaviour of soil-model regarding to non-homogeneous soil condition of agricultural fields. Simulation results will be compared with field test measurements for cone penetration tests. In this paper effects of particle's shape and micromechanical properties will be investigated and simulations will be compared using special particles, so-called clumps in model. Clumps are aggregations that are set of spheres. This study investigates the effect of using clumps instead spheres in simulations and it will be attempted to model the thixotropic behaviour of soil with special kind of particles. Non-homogeneous property and varied compaction of field soil will be modelled with more layers, keep to be comparable the simulation results with field tests. Measurements were set for more moisture content; study investigates appropriate set of micromechanical parameters to simulate the effect of water.

1 INTRODUCTION

In agriculture the role of research about precision plant cultivation is getting bigger and many digital technologies have a great importance in this field. A lot of technologies and methods are used in agriculture and food industry and have some special fields, such as numerical simulations; these used to analyze and improve harvest and food process methods. Another frequently researched area is the analyzing of soil-tool interaction with tests and simulations. Many papers can be found connected to this research, such as in [1, 2, 3] where the mostly and successfully used numerical technique was the discrete element method (DEM).

The [1] study focused on the dynamical behavior of soil and it was analyzed with measurements and simulations. In this research the DEM model included only spherical particles with more distributions of radius. In simulations parallel-bond model was applied and the experiments were soil-bin tests with a sweep tool. Soil-bin tests appeared in [2], and this paper presented a DEM model for soil-tool interaction. This study used only spherical particles with equal radii. In soil model were applied 3 layers with different parameters to model inhomogeneous soil conditions. For calibration were used cone penetration models and tillage data, the calibrated parameters were the particle and bond stiffness. The successful model was used to investigate the influence of tillage-depth for draught force and loosening-efficiency. The paper [3] presents a study about sensitivity analysis. Research focused on soil-thrown effect and draught force while soil-sweep interaction. The influence of micro properties, such particle and bond elasticity, damping coefficient, etc. were investigated and DEM simulations with spherical particles were compared with soil-bin tests. The most sensitive parameter was the Young's modulus according to results of paper. Similar study can be found in [8], paper investigated the role of parallel bond model and viscous damping parameter in a soil-sweep DEM model. Conclusion of research showed, the bond radius has an important role in modeling of soil moisture content and the viscous damping need to be decreased at higher speeds in model to keep it comparable with measurements.

The most of studies was able to investigate soil-bin tests and publications focused mainly on this art of measurements; respectively soil models use always spherical particles. Although, in some cases the DEM models were able to simulate complex fluid mechanics behavior of soil and the soil-tool mixing-effect. On the other hand, in agriculture it has a high importance to make in-situ tests on agricultural fields and develop soil models which can be compared with in-situ results. These measurements usually require high costs and the evaluation of test results are often difficult due to the inhomogeneous structure of soil. The aim of this study is analyzing the results of field tests and improving a 3D DEM model to simulate the heterogeneity of agricultural soil and developed model serves a preparation of investigating of soil-tool interaction. On the one hand, the motivation of this research is the trying to reduce draught force of agricultural processes, because it could require high draught power which means more costs for farmers and more load for cultivator machines. On the other hand, this research can be useful to investigate the soil-degradation phenomenon.

2 MATERIAL AND METHODS

2.1 FIELD EXPERIMENTS

The field tests were set at three different moisture content before tillage in a clay-sandy soil, on the placement of Hungarian Institute of Agricultural Engineering (NARIC). First penetrate measurements were set at ten randomly chosen points on agricultural field (Fig.1). The second

Figure 1: **a**) Placement of field experiments, **b**) first series of cone penetration test [10]

cone penetration test series were set on same placement with same experiment's number, at another time. The third test series was set at same place, it included only 3 measurements. For measurements was used a penetrometer, this device measures the vertical resistant force and the volumetric moisture content of soil. It is available as a complete set suitable for measurements up to a depth of 80 cm. The cone penetrometer itself consists of a penetrologger housing with GPS and a control panel. The logger is contained in a water-resistant housing with electrically insulated grips. Cone is screwed onto the bottom end of a bipartite probing rod. Depending on the application and the expected resistance to penetration different cones can be attached. The cones supplied have 60º top angle and various projected areas. At field tests was used a cone with 60º top angle and 1 cm^2 area. The resistant force is divided by projected area of conehead and averaging all measurements at each test series, so, can be given a curve that express stress values, the Cone Penetration Resistance (CPR) of soil. As could be observed, there are large deviations from average but values can define one exact curve. The test results are compared at different moisture contents, it shows Fig. 2. The penetrometer recorded the soil moisture content at all measurements, at first series was the soil driest, at second series soil contained the most moisture and the third test showed a medial moisture content, as can be seen in Table 1.

Table 1: moisture content at each cone penetration measurement

	Moisture content, V/V%										Mean values
1. Test series:	9	6	5	4	9	7	7	8	4	7	**6.6**
2. Test series:	24	21	23	21	20	21	23	22	24	22	**22.1**
3. Test series:	13	14	13								**13.3**
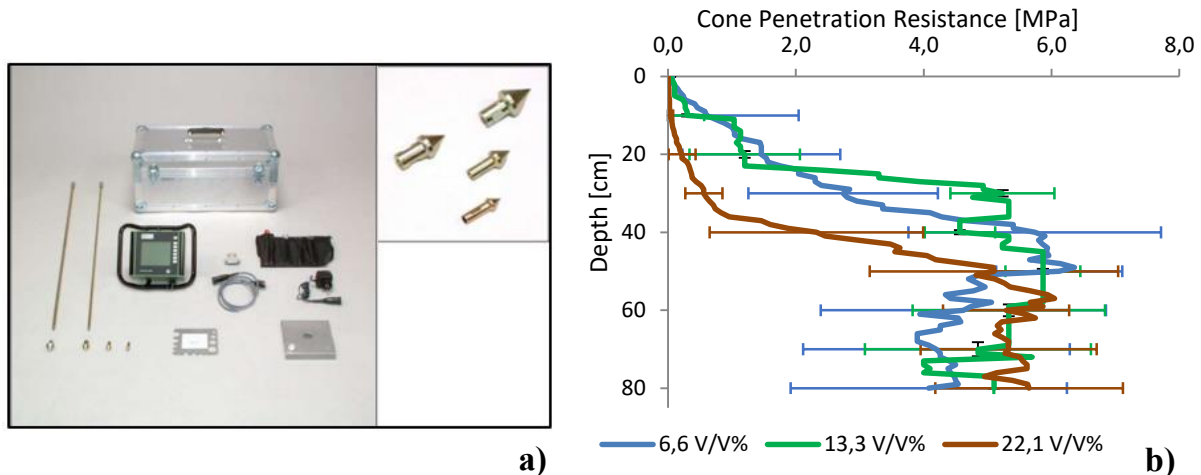
Figure 2: **a)** complete penetrologger set and cone heads for field tests **b)** averaged cone penetration resistance of soil at different moisture contents with standard deviations

It can be seen on Fig. 2, drier soils have larger resistance, similar to [4], and the peak at each curve is given between 50 and 60 cm deep from the top of soil. Cone resistance depends on soil compaction, bulk density, moisture content; and higher resistance is associated with higher bulk density [5,6]. Test results will be used for further simulations with soil model and have high role in calibration process. After each cone penetration test, began the tillage process with a tractor, as can be seen on Fig. 3. For this process was used a cultivator sweep tool, and during tillage the draught force was recorded with a 50 Hz sample frequency. The distances of measurements were between 60-90 meter, the average velocity was 9.1 km h^{-1} and the work-

Figure 3: **a)** cultivator tools, the piece in the middle was used for tillage experiments **b)** the tractor
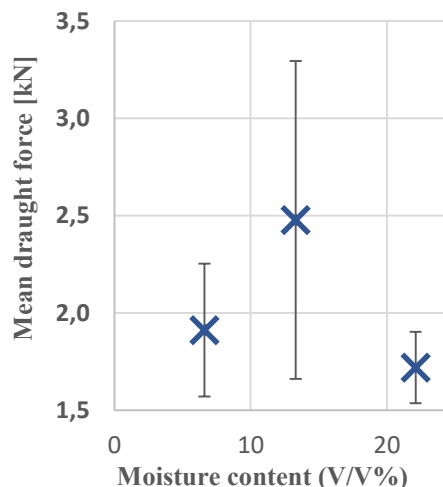
Figure 4: Mean draught force with standard deviations by tillage at each moisture content

depth was at each experiment 10-15 cm. Fig. 4 shows, soil with medium moisture content (13.3 V/V%) produced the highest draught force, and the smallest mean force was observed by the soil with the highest moisture content (22.1 V/V%). Results are similar to cone resistant experiments, where the driest and medial moisture content soil produced largest resistant and the soil with less wet shows the smallest cone penetration resistance (CPR) until 50 cm depth.

2.2 DISCRETE ELEMENT MODEL

For the simulation of soil behavior was used DEM and applied YADE DEM software. The DEM is able to model some effect of soil-tool interaction but there are some numerical parameters which need to calibrate a model. The most frequently used method for that is the
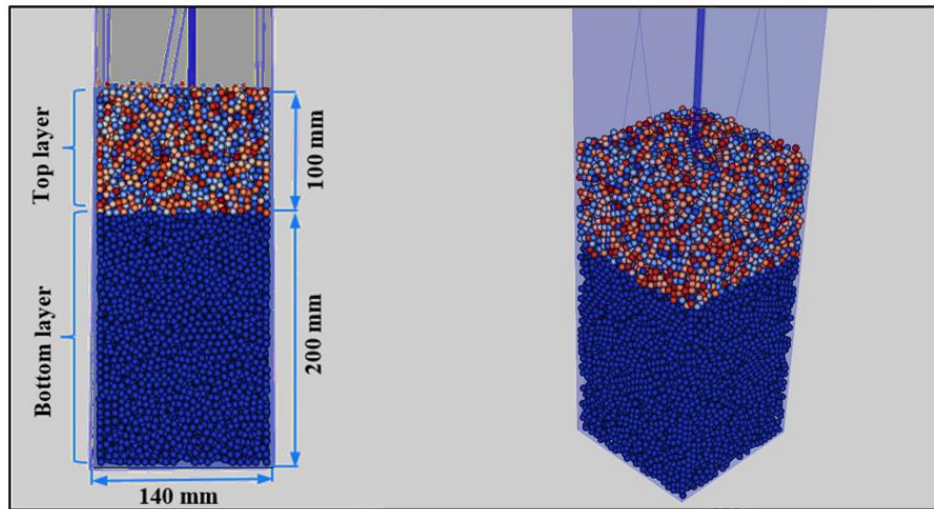
Figure 5: the two layers of soil DEM model and the rod with conehead

parameter sensitivity analysis. The most sensitive parameters in soil models usually are the Young's modulus [3], normal and shear cohesion, and the friction. But its notable, many studies were developed using only spherical particles and parallel-bond model in simulations. Other techniques to find appropriate parameters are systematic methods and optimization processes [2,7]. In this paper, the energy dissipation was modeled with particle's shapes using clumps. Three types of clumps were applied in model with different portions, these can be seen on Fig. 6. Finding appropriate microparameters a sensitivity analysis was applied, based on mentioned and similar studies. The 3D discrete element model was set up for conical tests, and it was developed with 2 layers. Previous paper [4] used same technique to model soil with different layers, but there were 3 layers in one penetrometer. For conical simulations was set up a 140×140×1000 mm box and the cone model was used with 1.5 cm^2 projected area and 60° cone angle. Speed of penetrometer was at each case 0.1 m s^{-1}. Other parameters of model are showed in Table 2.

The soil model consisted three types of clumps, as can be seen on Fig.6: so-called dyad by two, peanut by three and stick by four spheres. Particle distribution was set with these clumps with 5-5-90% ratio and the greatest size of these elements was between 13.9- and 24.1-mm. Damping between particles was not applied.

Figure 6: clumps built by spheres; **a)** dyad, **b)** peanut and **c)** stick elements

Soil model for cone penetration test included 9700 elements and it reached 0.3 m height. The cone moved 0.3 m deep in soil model with the mentioned constant speed and only vertical force was recorded during simulation. Regarding to inhomogeneous structure and compaction of field soil DEM model was divided along vertical two layers: top layer was set with 0.1 m and the bottom layer with 0.2 m. It was possible to set up different soil parameters for each layer and it was one device to the effective calibration. The two layers in model and the cone are visualized on Fig. 5.

Table 2: physical properties of soil for cone penetrate model

Parameters	Unit	Value
Particle density, ρ_p	kg m^{-3}	2700
Young modulus, E_Y	Pa	$5 \cdot 10^6$
Particle friction, μ_p	-	Calibrated
Wall friction angle, μ_w	deg	40
Cohesion, σ, τ	Pa	Calibrated
Poisson ratio, ν_p	-	0.4

3. RESULTS

As seen the results of cone field tests it would be required to make more soil layers in DEM model and add different parameters. At first simulations the cohesion of top and bottom layers was modified and the other parameters were still constants. The previous results showed, it is considerable to set up higher cohesion at bottom layer, and the cohesion values could be selected in range from 10^3 to $\mathbf{5 \cdot 10^6}$ Pa according to previous simulations and based other studies. During simulations normal and shear cohesions were set as equal. Particle friction will be usually expressed as friction angle; it was the other varied property.

At the next parameter sensitivity test the effect of particle friction was investigated. In this model both layers had constant $5 \cdot 10^4$ Pa cohesion and the friction coefficient has varied in both layers. It can be observed, with higher friction coefficient the cone resistance profile is similar to drier soil, and with low particle friction coefficient the results of simulations are closer to higher moisture content, so, the curve of model results is getting steeper. As can be seen on Fig. 7. the set #1.3 and #1.4 had the best match with driest soil and #1.1 and #1.2 were the closest to the soil with most moisture content. Parameter set #1.3 was closest to soil with medium moisture content at top section, and the set #1.5 passed to this soil at deeper section. It was observed, friction values had significant influence to cone index and the increasing of CPR was almost proportional with increase of friction coeficient. At the next simulation series, the cohesion of layers was varied with constant frictions; parameters are showed in Table 4. Best matches were achieved due to different cohesion at case of dry soil with set of #2.1 and #2.2. It can be seen on Fig. 8., that influence of particle friction is same as in earlier parameter series, curves shifted to higher cone resistance while increase friction. Interestingly, with change of

cohesion's size ratio between layers there was not large deviation between layer's resistance. It is supposed, the influence of larger cohesion at bottom layer appears in top of soil, so cone resistance does not decrease instead lower cohesion at top layer. So, with change of cohesion's ratio, CPR profiles shifted almost parallel and profile curves were get steeper and followed worse test results than previous parameter set.
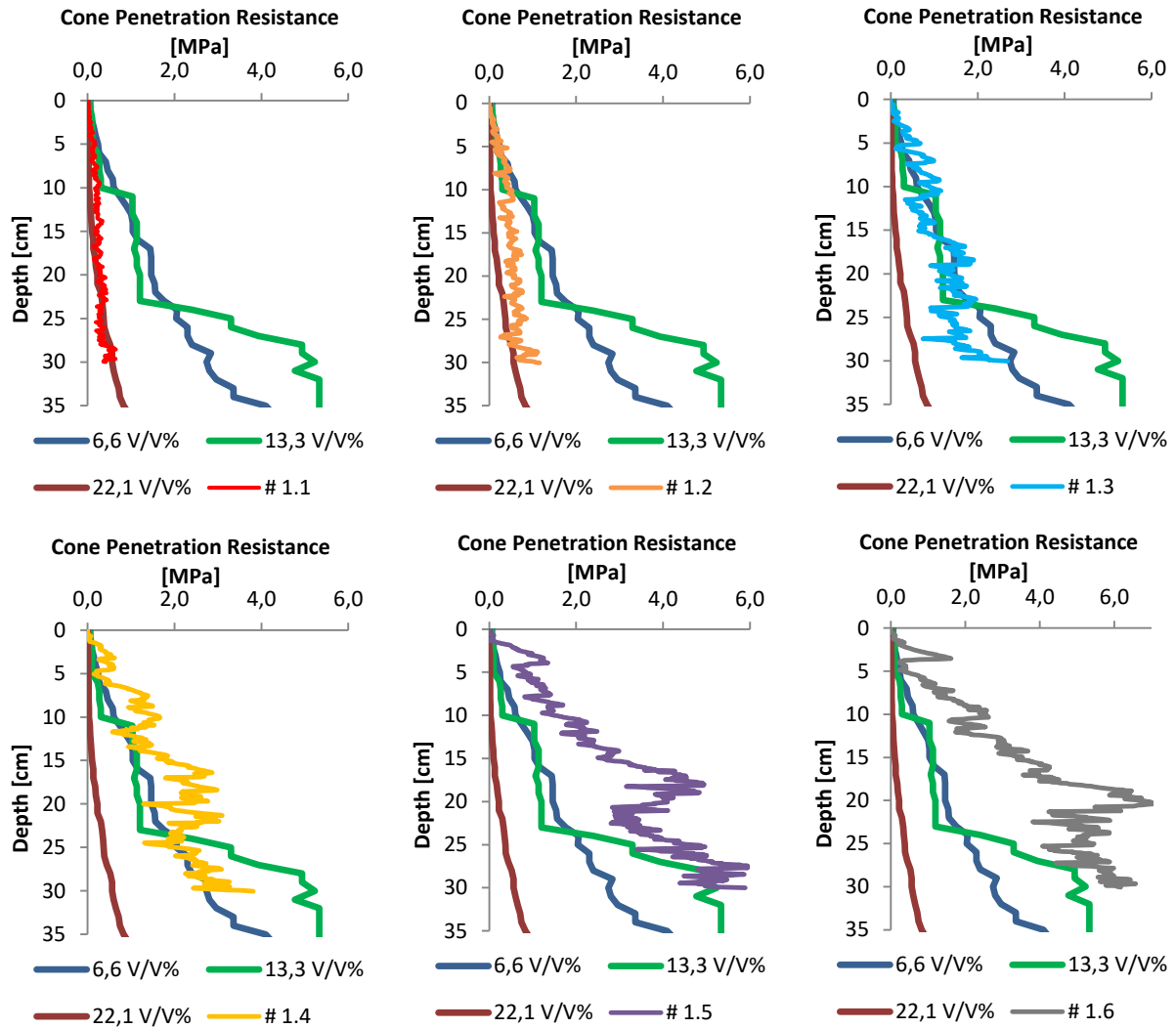
Figure 7: simulation and test results compared at first parameter series

Table 3: Parameter set of soil for cone penetrate model at first parameter sensitivity test

Parameter set	Friction angle	Cohesion at each layer
	deg	Pa
#1.1	10	
#1.2	15	
#1.3	25	$5 \cdot 10^4$
#1.4	30	
#1.5	40	
#1.6	45	

Higher cohesion at bottom layer laid to higher cone penetration resistant, as Fig. 8. shows in left and middle charts. By parameter set #2.5 and #2.6 results are not totally consistent with trend of second parameter series, but the curves shifted next to higher penetration resistance as effect of higher friction.
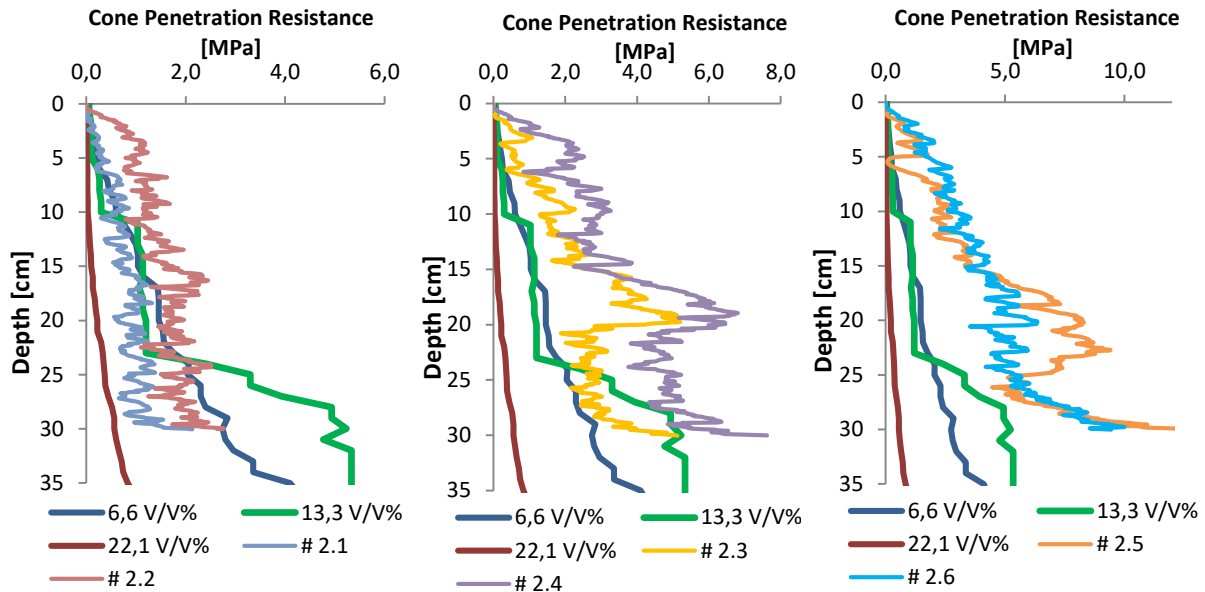
Figure 8: simulation and test results compared at second parameter series

Table 4: Parameter set of soil for cone penetration model at second parameter sensitivity analises

Parameter set	Cohesion at top layer	Cohesion at bottom layer	Friction angle
	Pa	Pa	deg
# 2.1	$5 \cdot 10^5$	$5 \cdot 10^4$	20
# 2.2	$5 \cdot 10^4$	$5 \cdot 10^5$	
# 2.3	$5 \cdot 10^5$	$5 \cdot 10^4$	35
# 2.4	$5 \cdot 10^4$	$5 \cdot 10^5$	
# 2.5	$5 \cdot 10^5$	$5 \cdot 10^4$	45
# 2.6	$5 \cdot 10^4$	$5 \cdot 10^5$	

At another parameter sensitivity analise at all set of properties was the cohesion at the bottom layer higher, regarding to earlier results. The effect of particle friction coefficient was same as the other penetration simulations and it could be observed, the lower cohesion at top layer and the higher cohesion at bottom layer led to gently sloped curves, when difference was enough between cohesions. So some of these results followed better the deeper section of soil's cone resistance, but at most of these simulation results CPR was extremly overestimated along full depth instead very low cohesion in top layer and low friction value. At some parameter sets could be observed a peak of curve like at set #1.5 and #1.6. These peaks appeared obviously only by high friction value and between 15 and 20 cm depth of soil.
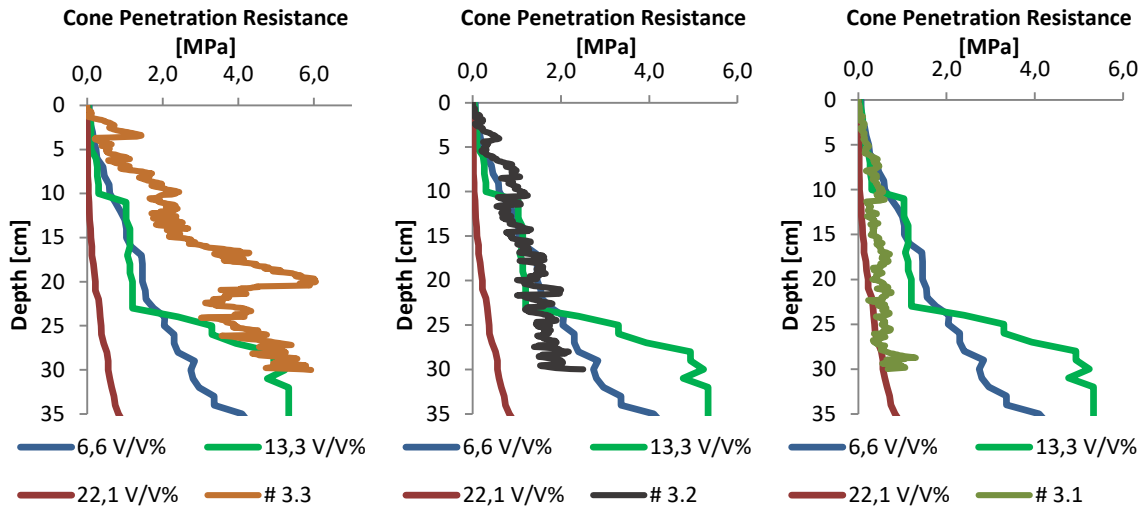
Figure 9: simulation and test results compared at third parameter series

Table 5: Parameter set of soil for cone penetration model at third parameter sensitivity analises

Parameter set	Friction angle at top layer	Friction angle at bottom layer	Cohesion
	deg	deg	Pa
# 3.1	10	15	
# 3.2	10	25	$5 \cdot 10^4$
# 3.3	10	40	

Fig. 9. shows the results of simulations with third parameter series. As can be seen in Table 5., the friction was a constant and low value at top layer, but friction in bottom layer was increased, while constant and equal cohesions were applied at each layer. The profiles and behavior of cone resistance were similar to first series, but the match at deeper soil'layers was better with these parameters. As can be seen set #3.3 it follows only deep section of soil CPR with medium moisture content and instead low friction it exceeds the CPR of top layer. One simulation was set over and above with medial top layer friction (25°) and higher friction coefficient (40°) at the bottom layer.

The resulted curve with these properties was very similar to set of #3.3 but it overestimated the deeper section of CPR too. To compare objectively the model and test penetrate results, it was considerable to calculate relative error (RE) between simulated and test values [9]. Its calculation form was given as:

$$\text{RE} = \frac{1}{n} \cdot \sum_{1}^{n} \frac{CPR_{DEM} - CPR_{Test}}{CPR_{Test}} \cdot 100 \ (\%) \tag{1}$$

RE was calculated with use of trend-line values by model results and it was averaged at top and bottom layer and along full depth. Mean values are represented in Table 6.

Table 6: parameter set with the least mean relative errors between model and test results

Moisture content	Parameter set	Mean RE at top layer	Mean RE at bottom layer	Mean RE at full layer
V/V%		%	%	%
6.6	# 1.4	59.1	9,4	**27.0**
	# 2.2	46.8	9.9	**22.9**
	# 3.2	57.5	30.9	**40.3**
13.3	# 1.2	34.1	62.8	**52.7**
	# 2.1	64.4	40.4	**49.9**
	# 3.2	115.9	28.6	**59.6**
22.1	# 1.1	394.2	71.1	**163.4**

4. CONCLUSIONS

The 3D DEM model for cone penetration tests was successfully developed and with the variation of parameters were given several cone penetration test results. The comparation of simulations and test results were successful and some of these parameter sets were able to model the soil behavior. According to mentioned results of simulations, the range of friction coefficient and cohesion values is compliance to investigate appropriate model for the analyzed agriculture soil. In some cases, the mean problem was generally the overestimation by top layer and underestimation by bottom layer between test and model values. At first parameter series it succeeds to adjust the steep of curves respectively by dry and mostly wet soil using friction coefficient value as variable. At second series it was concluded, using different cohesion at each layer resulted very steep CPR curves, because bottom layer with higher cohesion influences top layer, so, it seemed difficult to calibrate appropriately using different cohesion. At third parameter series friction value was varied at each layer and these sets resulted also good matches but it was failed to follow the soil with medial moisture content and relative error by soil with most wet content stayed relatively high. It could be observed; the relative errors were highest always at top layer and the largest error appeared by soil with most moisture content. By driest soil least RE was for full depth 23%, by 13.3 V/V% moisture content it was 50% and by 22.1% it reached 163%. For calibration of models using cohesion as variable was one opportunity but friction coefficient seemed more effective to get an appropriate soil model, and it seemed not necessary to apply more layers at each case. Although, in favor to get better matches its considerable to set up simulations with another thick of layers. The analyzed soil model can be a good preparation of further simulations of soil-tool interaction.

5. ACKNOWLEDGEMENT

REFERENCES

[1] Milkevych, V., Munkholm, L.J., Y Chen, Y., Nyord, T. *Modelling approach for soil displacement in tillage using discrete element method.* Soil and Tillage Research 183, 60-71 (2018)

[2] Zeng, Z., Chen, Y., Zhang, X. *Modelling the interaction of a deep tillage tool with heterogeneous soil.* Computers and electronics in agriculture 143, 130-138 (2017)

[3] Sadek, A., Chen, Y. *Feasibility of using PFC3D to simulate soil flow resulting from a simple soil-engaging tool.* Transactions of the ASABE 58 (4), 987-996 (2015)

[4] Sadek, M.A., Tekeste, M., Naderi, M. *Calibration of soil compaction behavior using Discrete Element Method (DEM).* ASABE Annual International Meeting, 1 (2017)

[5] Lipiec, J., Hatano, R. *Quantification of compaction effects on soil physical properties and crop growth.* Geoderma 116 (1-2), 107-136 (2003)

[6] Tekeste, M.Z., Raper, R.L. Schwab, E. *Soil Drying Effects on Soil Strength and Depth of Hardpan Layers as Determined from Cone Index Data.* Agricultural Engineering International: the CIGR Ejournal, X, 1-17. (2008)

[7] Asaf, Z., Rubinstein, D., Shmulevich, I., *Determination of discrete element model parameters required for soil tillage.* Soil & Tillage Research 92 227-242 (2007)

[8] Tamás, K. *The role of bond and damping in the discrete element model of soil-sweep interaction.* Biosystem engineering 169 57-70 (2018)

[9] Sadek, M. A., Ying Chen, and Jude Liu., *Simulating shear behavior of a sandy soil under different soil conditions.* Journal of Terramechanics 48.6: 451-458. (2011)

[10] www.google.com/maps , June 2019

PRELIMINARY NUMERICAL AND EXPERIMENTAL TESTS FOR THE STUDY OF VIBRATION SIGNALS IN DRY GRANULAR FLOWS

FRANCESCO ZARATTINI[1], ANTONIO POL[1], LUCA SCHENATO[2], PIA R. TECCA[2], ANDREA M. DEGANUTTI[2], ANDRÉS GARCIA-RUIZ[4], MIGUEL SORIANO-AMAT[4], MIGUEL GONZÀLEZ-HERRÀEZ [4], HUGO F. MARTINS[5], ALESSANDRO PASUTO[2], LUCA PALMIERI[3], FABIO GABRIELI[1]

[1] Department of Civil, Environmental and Architectural Engineering, University of Padova, Italy
francesco.zarattini@studenti.unipd.it

[2] Research institute for Geo-hydrological Protection, National Research Council, Padova, Italy

[3] Department of Information Engineering, University of Padova, Italy

[4] Department of Electronics, University of Alcalá, Madrid, Spain

[5] Istituto de Òptica, Consejo Superior de Investigaciones Cientificas, Madrid, Spain

Key words: vibrations, debris flows, DEM, granular materials, distributed optical fiber sensing, distributed vibration sensing.

Abstract. Debris flows are one of the most important hazards in mountainous areas because of their paroxysmal nature, the high velocities, and energy carried by the transported material. The monitoring of these phenomena plays a relevant role in the prevention of the effects of these events. Among different possibilities, fiber optical sensors appear well-suited for this purpose thanks to their fair cheapness (with the exception of the interrogator), the robustness to electromagnetic interferences, the adaptability in extreme harsh conditions (no power supply is required), the possibility of locating the interrogator many kilometers far away from the monitored site, and the unique feature to provide very-dense multipoint distributed measurements along long distances. In this work, the vibro-acoustics signal produced by these phenomena has been focused as a possible source of information for the prediction of incipient movement, and the tracking of their path, velocity and thickness. Few literature works investigate these aspects, and for this reason, a preliminary laboratory and numerical campaign have been carried out with dry granular flume tests on an inclined chute. The discrete element method has been used to simulate the tests and to synthesize the signal measured on an instrumented mat along the channel. The grain shapes of the granular material used in simulations have been obtained by a photogrammetric tridimensional reconstruction. The force-time signal has been also analyzed in time-frequency domain in order to infer the features of the flow. The numerical activity has been preparatory for the experiments carried out by instrumenting the flume with an optical fiber distributed vibration sensing system.

F. Zarattini, A. Pol, L. Schenato, P. R. Tecca, A. M. Deganutti, A. Garcia-Ruiz, M. Soriano-Amat, M. Gonzàlez-Herràez, H. F. Martins, A. Pasuto, L. Palmieri, F.Gabrieli

1   INTRODUCTION

Debris flows are particularly hazardous slope instability phenomena due to the high speeds and high amount of energy that the transported material carries [1, 2]. Structures such as weirs and deposit areas are solutions that sometimes do not provide precautionary values of the safety factor. Therefore, monitoring plays a fundamental role in the prevention and mitigation of the effects produced by these flows. In addition to traditional methods (echometers, geophones, estensimeters), recent studies suggested the possibility of using distributed fiber optic sensors (DFOS) to monitor the flows [3, 4].

The DFOS technology employed in this study is the so-called distributed acoustic sensor (DAS), that is a promising sensing platform for many different applications in structural health monitoring, leak detection in pipelines, seismic wave detection, and many more geophysical applications.

With this technology, the fiber is probed by a coherent laser pulse and the DAS interrogator tracks the changes in the phase of the optical backscattered signal in time. The longitudinal strain exerted to the fiber is proportional to the recorded optical phase shifts between pulses and therefore, that shift can be mapped into the dynamic distributed strain field across a given fiber segment by integration.

In regard to the specific application addressed here by DAS technology, the optical fibre behaves as an equivalent array of many concatenated geophones (hundreds per kilometre of fibre length) capable of detecting acoustic perturbations and vibration in real time, over a frequency range up to a few kilohertz. As in other DFOS, the optical fibre acts here as both the communication channel and the sensing element. This unique feature of DOFS enables the reduction of the system complexity in particular for those applications requiring many hundreds of sensing points.

Furthermore, the DAS used in this study implements a novel interrogation scheme based on highly chirped probe pulses [5]. This technique is more robust than conventional DAS scheme, as it offers localised detection of the perturbation with the same spatial resolution and acoustic/vibration bandwidth of traditional implementation, where instead the perturbation effects cumulate along the fibre.

In this work, first step of a wider study, some tests on a channel with granular material were simulated using the discrete elements method (DEM). From the simulations the seismic signal produced by the passage of the material above a control plate placed on the bottom of the channel was obtained. Considering a priori significant the shape of the grains on the signal produced, this has been reproduced through rigid aggregates of spheres (clumps). The shape of an individual clump derives from a previous tridimensional scanning phase of some sample grains taken from the material used in the laboratory tests.

The goal of this study is to obtain preliminary information (numerically and experimentally) about the signal produced by a granular flow, in terms of vibrations, number of interactions, force and strain vs time and of their frequency content.

F. Zarattini, A. Pol, L. Schenato, P. R. Tecca, A. M. Deganutti, A. Garcia-Ruiz, M. Soriano-Amat, M. Gonzàlez-Herràez, H. F. Martins, A. Pasuto, L. Palmieri, F.Gabrieli

2 NUMERICAL SIMULATIONS

2.1 The geometry of the model

The simulated geometry is the same used in the subsequent laboratory tests but, in order to reduce the computational time and the amount of data storage (which has been collected for more than 350000 timesteps), the informations about the flow were collected only along one section along the channel, just above a measurement plate (Figure 1). The channel is 1.55 m long, 0.30 m large and inclined of 38° with respect to the horizontal plane. The measurement plate is 20 cm long and located 64.5 cm far away from the gate of the upper tank.

Initially the release mass is poured in the upper tank; then the lateral wall of the tank is removed and the granular material strats to flow. A larger box is used as deposit base as presented in Figure 1.
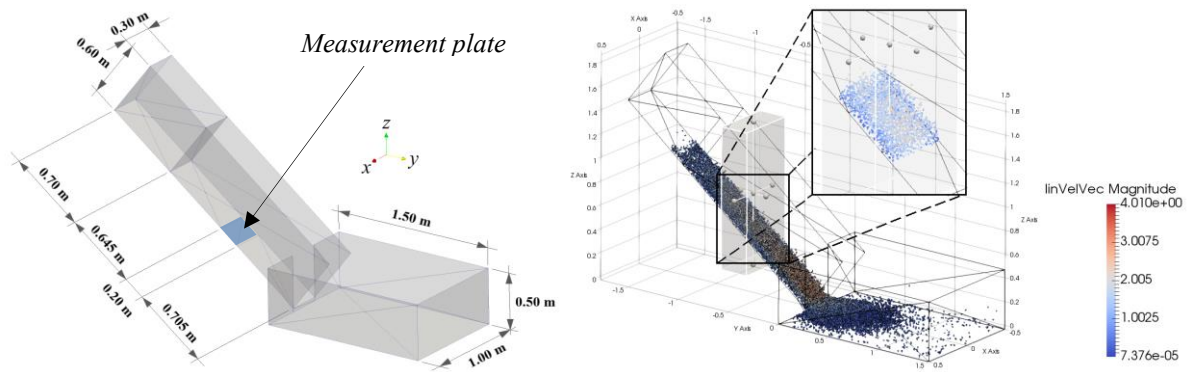
Figure 1: Geometry used for the numerical simulation of the dry granular flow.

A fixed granular volume of 0.027 m^3 is used in each test; the initial porosity is 0.45 for ~ 40 kg of mass. All simulations are performed using the open-source code Yade [6].

2.2 The granular material

Clumps of 4, 8, 16 spheres have been used in order to better mimic the real shape of the grains used in the experimental tests. For this purpose, 16 samples of grains were scanned through a stereo-photogrammetrical method based on the "Structure from motion" (SfM) ([7, 8]), the *Meshlab* software [9], and using a rotating platform.

The discretization of the mesh via polar spheres was performed with *Power Crust* [10] which implements the median axis approach. In Figure 2 an example of a reconstructed grain, discretized with a different number of spheres, is reported.

(a)   (b)   (c)
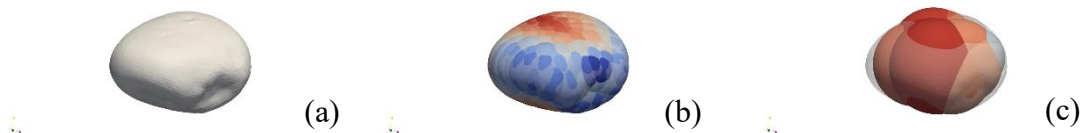
Figure 1: Example of clump generation: from (a) the surface mesh reconstruction, to a (b) 395 spheres and (c) 16 spheres representation.

F. Zarattini, A. Pol, L. Schenato, P. R. Tecca, A. M. Deganutti, A. Garcia-Ruiz, M. Soriano-Amat, M. Gonzàlez-Herràez, H. F. Martins, A. Pasuto, L. Palmieri, F.Gabrieli

The contact model was Hertz-Mindlin in normal direction, while the Mindlin theory was adopted in the tangential one [11]. The rolling and twisting resistance were neglected since their effect has been substituted by the better description of the grain shapes.

The Young modulus and the Poisson's ratio at the contact were set E=10^8 Pa, ν=0.2 for both the clumps and the walls. The contact friction angle was 40° while the normal and tangential restitution coefficient of the contact sphere-sphere and wall-sphere were 0.8 and 0.4 respectively.

2.3 Numerical results

The registration of the data started at time t_0 when one particle crossed the control volume above the measurement plate.

After that, at each time step, impact force components along the three axes have been recorded, as well as the number of clump-plate interactions. Moreover, every 0.025 s the coordinates of the centers of each sphere in the volume above the plate, and their linear (v_x, v_y, v_z) and angular velocities (ω_x, ω_y, ω_z), have been stored.
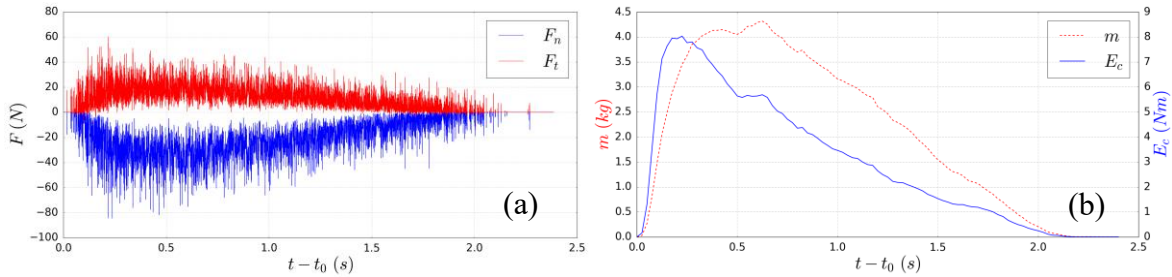
Figure 3: (a) Trends of normal and tangential forces and (b) of the mass and translational kinetic energy above the measurement plate.

From the collected data it is possible to obtain the seismic signal transmitted from the dry granular flow, its spectrogram, together with kinetic energies obtained from the velocities.

For the sake of brevity we refer here only to the results of the simulation obtained with the smooth pebbles of 11.2-16 mm diameter, and represented with 16 spheres per clump.

The trend of the normal force F_n and the tangential force F_t with the time is reported in Figure 3(a), while the mass and the translational kinetic energy on the control volume above the plate, are showed in Figure 3(b).

The high variability of the force signals is due to the continuous creations and destructions of contact force chains [12] between the particles and the measurement plate. The mean force signal presents a peak at 0.5 seconds while the peak of kinetic energy precedes the peak of mass: it occurs at $t - t_0$=0.25 s and in correspondence of the maximum variability of the forces.

F. Zarattini, A. Pol, L. Schenato, P. R. Tecca, A. M. Deganutti, A. Garcia-Ruiz, M. Soriano-Amat, M.
Gonzàlez-Herràez, H. F. Martins, A. Pasuto, L. Palmieri, F.Gabrieli
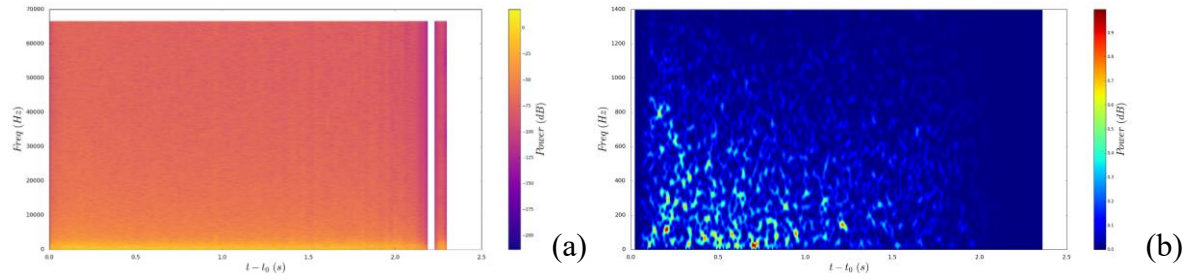
Figure 4: (a) Spectrogram obtained from the normal impact forces F_n and (b) PSD spectrogram of the same force, limited to the frequency of 1.4 kHz.

In Figure 4(a) and (b) the spectrograms of the signal generated by F_n are reported. The maximum frequency detected is almost 70 kHz. But, if a narrower frequency range is investigated (up to 1.4 kHz), it can be observed that the higher power of the signal is concentrated within this range (see Figure 4(b)). These numerical results have been used to set the spatial and temporal resolution of the DAS system used in the experimental tests.

3   EXPERIMENTAL TESTS

The laboratory setup consists of a chute of the same dimensions of the one used for the numerical simulations (the geometry is reported in §2.1). An engineered mat, embedding the optical fiber, has been opportunely designed and placed at the bottom of the flume: the mat is constituted by high-density polyethylene foam and embeds 20 PVC mandrels (diameter 5 cm, height 2 cm) – each coiled with approximately 40 m of optical fiber and the surface of the mat, exposed to the debris, is protected by a 3 mm rubber sheet. Overall, approximately 800 m of fiber are embedded in the mat.

The 20 mandrels are arranged in two sets of 10, at the right and left side of the flume, at 8 cm from the lateral walls. Along the flume, from bottom to the top, the coils of the two sets are at 15, 27.5, 40, 57.5, 75, 91.6, 108.2, 125, 145 and 165 cm.

Having a spatial sampling of 2 meters, 20 sampling points per each coils are measured. Please note that the DAS spatial resolution is 4 m, and correspondingly, each coil corresponds to an equivalent array of 10 geophones, while the signals collected in the entire mat correspond to an equivalent array of 200 geophones. The signal collected by the DAS, is expressed as the variation of axial strain inside the optical fiber with respect to the time, given the sampling frequency f_s of 1 kHz. The amount of data collected per each experiments is very huge and it is still under analysis: here, some preliminary results will be presented, mainly to show the feasibility of the approach and the great potential of the DAS technology.

For example, Figure 5 shows the signals collected at the coil on the right side, 75 cm from the bottom of the flume, during the flow test with sharp-edges grains of dimensions 11.2-16 mm. Such coil is situated approximately in the same position of the measurement plate in the numerical simulations.

F. Zarattini, A. Pol, L. Schenato, P. R. Tecca, A. M. Deganutti, A. Garcia-Ruiz, M. Soriano-Amat, M. Gonzàlez-Herràez, H. F. Martins, A. Pasuto, L. Palmieri, F.Gabrieli
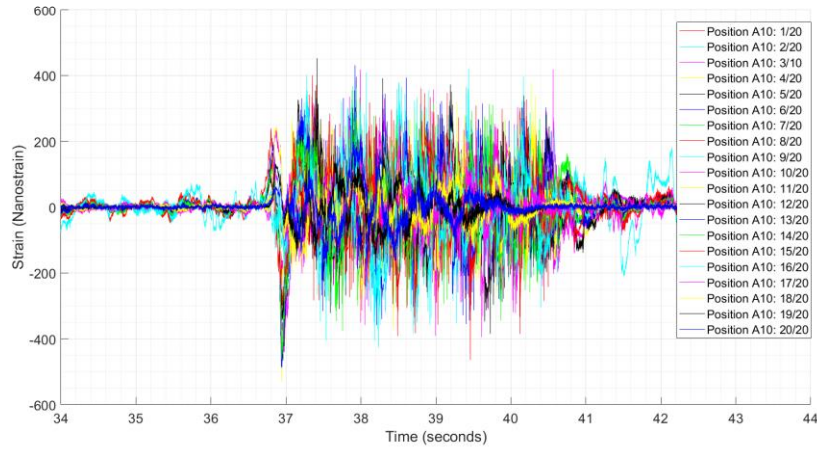
Figure 5: Strain in the 20 sampling points of one coil during the test with angular grains and grain size 11.2-16mm.

In order to measure the velocity of the flow, the energy carried by the signal has been considered. The energy of the debris obtained from a coil has been considered as the average of the energies detected by every single sampling point.

In Figure 6 the mean energy of the debris in correspondence of each coil with respect to the time is reported. By analyzing its evolution, it is possible to identify the instant at which the front of the flow reaches each coil: the black spots in Figure 6(b) report the instants in which the energy of the signal is considered to be representative of the front of the flow of the material. Finally, in Figure 7 the instants in which every coil is reached by the front of the flow are reported. The data shows a position-time trend, with a quite constant front velocity in the considered section.
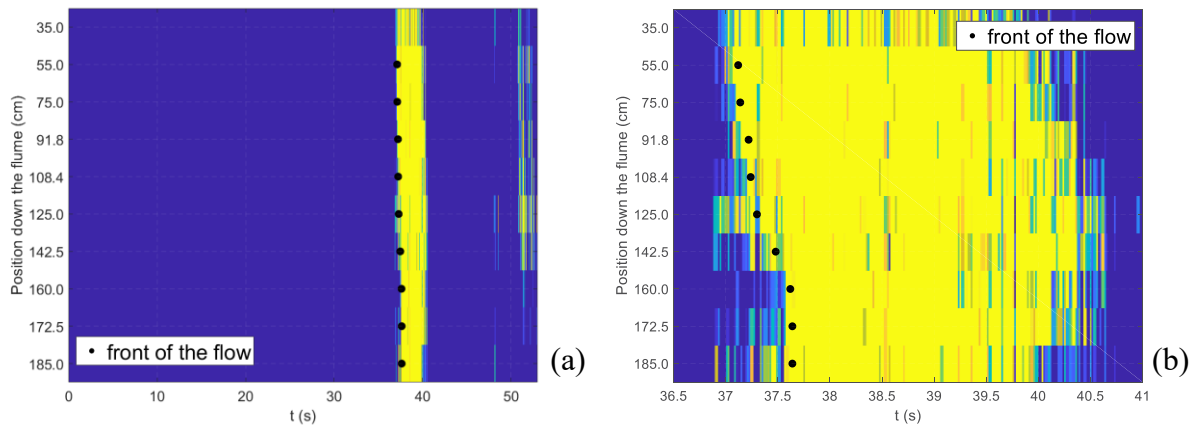
Figure 6: Mean energy measured by each coil on the right side along the chute with respect to the whole acquisition time, (b) with respect to the flow event.

310

F. Zarattini, A. Pol, L. Schenato, P. R. Tecca, A. M. Deganutti, A. Garcia-Ruiz, M. Soriano-Amat, M. Gonzàlez-Herràez, H. F. Martins, A. Pasuto, L. Palmieri, F.Gabrieli
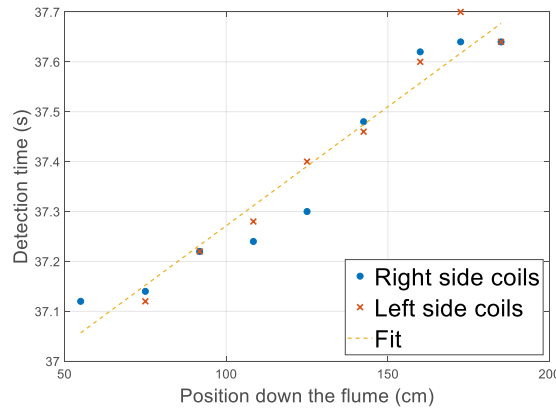
Figure 7: Instants in which the front reaches the left and the right sides coils along the flume.

4 CONCLUSIONS

From the preliminary numerical results highlighted in this work, it was shown that the signal generated by a granular flow is given by two contributions: one is related to the mass of the flow and one is related to its kinetic energy. The two contributions do not present simultaneous peaks in a given section: in our test, the first is the peak of kinetic energy which corresponds to the peak of force fluctuation. The peak of the mass instead is related to the thickness of the flow and it arrives after the front.

Moreover, observing the spectrograms, two different behaviours in terms of power emitted at different frequencies can be seen: a high power concentrated within a narrow frequency range; a low power spread in a wide frequency range. This means that the seismic signal is given by a sum of a low frequency signal – due to the mass of the material, that can be expressed as the thickness of the flow on the recording plate – and a high frequency signal, which is generated by the collisions. This preliminary analysis made it possible to reconstruct, although in a simplified manner, the signal produced by a granular flow.

This information has been used for the parameters used in the fiber optic measurement tool, based on Distributed Acoustic Sensing technology.

By the analysis of the signal recorded by the DAS, some preliminary results were obtained: in particular, evaluating the mean debris energy on each coil, it was possible to detect the kinematic of the front flow.

ACKNOWLEDGEMENTS

REFERENCES

[1] Iverson, R., Reid, M. & LaHusen, R. (1997), Debris-flow mobilization from landslides.

F. Zarattini, A. Pol, L. Schenato, P. R. Tecca, A. M. Deganutti, A. Garcia-Ruiz, M. Soriano-Amat, M. Gonzàlez-Herràez, H. F. Martins, A. Pasuto, L. Palmieri, F.Gabrieli

Earth and Planetary Science Letters, 85-138.

[2] Iverson, R. (1997), The Physics of Debris Flow. Reviews of Geophysics, 245–296.

[3] Michlmayr, G.; Chalari, A.; Clarke, A.; Or, D. Fiber-optic high-resolution acoustic emission (AE) monitoring of slope failure. Landslides 2017, 14, 1139–1146.

[4] Schenato, L. A Review of Distributed Fibre Optic Sensors for Geo-Hydrological Applications. Appl. Sci. 2017, 7, 896.

[5] J. Pastor-Graells, H. F. Martins, A. Garcia-Ruiz, S. Martin-Lopez, and M. Gonzalez-Herraez, "Single-shot distributed temperature and strain tracking using direct detection phase-sensitive OTDR with chirped pulses," Opt. Express 24, 13121-13133 (2016)

[6] Šmilauer, V. et al. (2015), Yade Documentation 2nd ed. The Yade Project. DOI 10.5281/zenodo.34073 (http://yade-dem.org/doc/).

[7] Wu, C., Agarwal, S., Curless, B. and Seitz, S. M. (2011), Multicore Bundle Adjustment, CVPR.

[8] Wu, C. (2013), Towards Linear-time Incremental Structure From Motion, 3DV.

[9] Ranzuglia, G., Callieri, M., Dellepiane, M., Cignoni, P., Scopigno, R. (2013), MeshLab as a complete tool for the integration of photos and color with high resolution 3D geometry data, *CAA 2012 Conference Proceedings*, page 406-416.

[10] Amenta, N., Choi, S., Kolluri, R. K., The Power Crust, University of Texas at Austin.

[11] Johnson, K. L., Contact mechanics, *Cambridge University Press*, *Cambridge*, *UK*, 1985.

[12] Lingran, Z., Nho Gia Hien Nguyen, Lambert S., Nicot F., Prunier F. & Djeran-Maigre I. (2016), The role of force chains in granular materials: from statics to dynamics, *European Journal of Environmental and Civil Engineering, DOI*.

OPTIMAL PACKING OF POLY-DISPERSE SPHERES IN 3D: EFFECT OF THE GRAIN SIZE SPAN AND SHAPE

William F. Oquendo-Patiño[*]**, Nicolas Estrada-Mejia**[†]

[*] Department of Mathematics, Physics and Statistics
Faculty of Engineering, Universidad de la Sabana
Km 7 Autopista Norte, Chia 140013, Colombia
e-mail: william.oquendo@unisabana.edu.co

[†] Department of Civil and Ambiental Engineering
Universidad de los Andes, Bogota 111171, Colombia
e-mail: n.estrada22@uniandes.edu.co

Key words: Granular Materials, DEM, Packing, Density, Polydispersity

Abstract. In this work, we explore the effect of the grain size distribution (gsd) on the packing of 3D granular materials composed of spheres, and find the optimal packing with the highest density as a function of the gsd parameters.

1 INTRODUCTION

Granular media are materials composed of interacting bodies with many types of possible microscopic parameters that impact the global response of the system under given external conditions. In particular, poly-dispersity, which characterizes the differences in size for the constituent grains and can be described by the grain size distribution (gsd), has been shown to strongly influence the packing properties of the system.

In this work, the gsd is modeled as a truncated power law that can be characterized by its shape (exponent, η) and its size span (ratio of the larger to the smaller particle size, λ), and is defined as

$$\rho = \left(\frac{d - d_{\min}}{d_{\max} - d_{\min}} \right)^{\eta} = \left(\frac{\frac{d}{d_{\min}} - 1}{\lambda - 1} \right)^{\eta}, \tag{1}$$

where $d_{\min}$ ($d_{\max}$) is the minimum (maximum) diameter in the sample, and ρ is the fraction of volume occupied by particles of diameter d. This distribution arises as a result of the previous works of Fuller, Thompson, and Talbot [1, 2, 3] (experimental) and those by Furnas [4, 5] (theoretical) between 1907 and 1931.

One common and important question is if there is an optimal gsd that generates the best packing measured in terms of some packing variables such us the packing fraction (or density), the local connectivity [6, 7] and anisotropy [8, 9, 10], the force distributions and so on. For instance, Fuller and Thomson found [1], more than a century ago, than an

optimal packing with the densest state could be obtained with an exponent of $\eta \simeq 0.5$. This has been verified [11, 12] in 2D simulations comprising systems with large size spans, up to $\lambda = 32$.

Large size spans in three dimensions are hard to simulate due, in part, to the large computational resources involved. Previous work had focused in 2D [13, 14] ($\lambda \simeq 8$), [15] ($\lambda = 3$), and with special mention to the works of Voivret where really large size spans where explored for discs ($\lambda \simeq 20$) [16, 17] and polygonal particles [18, 19], and recent works with larger λ [11, 12, 20] and in 3D [21].

In this work we explore very large three-dimensional samples composed of frictionless spheres under isotropic compression and with different gsd. The shape of the distribution was in the range $\eta \in [0.1, 0.2, \ldots, 0.9, 1.0]$, while the size span was changed as $\lambda \in [2, 4, 8, 12, 16, 24, 32]$. These values include common distributions and explore some regions not commonly simulated. For instance, $\eta = 1.0$ corresponds to a uniform by volume distribution. For large λ and small η, the systems were composed of up to 400000 particles to represent the gsd accurately (maximum difference less than 5%). Some of those systems, when compressed, also generated more than one million contacts. Simulations were performed using the LIGGGHTS [22] package on a multicore server. Figure 1 shows snapshots of the 3D systems for fixed $\eta = 0.5$ and $\lambda = [4, 32]$. Only the particles away from the walls by $1.5\langle d \rangle$ were used for processing.
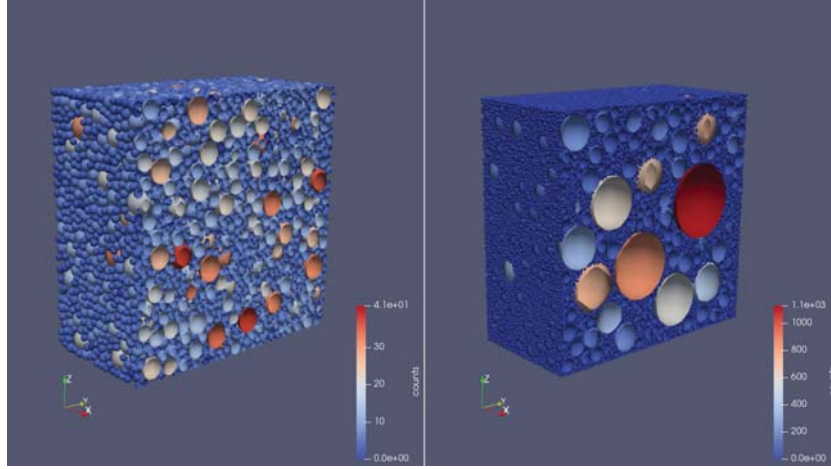
Figure 1: Screenshot for $\eta = 0.5$, and (left) $\lambda = 4$ and (right) $\lambda = 32$. The systems were cut in half to show the inner particles. Color represents the number of contacts. For the $\lambda = 32$ system, the larger particles could have more than 1000 contacts.

We found that values around $\eta = 0.5$ produce packings with the highest densities, which is in agreement with the century-old Fuller-Thomson distribution. Also, the proportion of floating particles could reach values as high as 90% for large λ, while the mean coordination number decreases drastically. These results allows, for instance, to design packings which could be better densified and connected just by controlling its generating gsd. Finally, the very high number of floating particles, or, equivalently, the very low mean coordination number, means that some systems could fracture under some mechanical conditions since

the forces will be focused on a small number of particles.

The paper is structured as follows: in section 2, we describe the numerical method and the sample setup. In section 3, we show the main results for the density and the local ordering as functions of the gsd. Finally, in section 4, we present some conclusions and suggestions for future work.

2 Numerical method

Simulations were carried out by using the soft-particle discrete element method. Here the particles are modeled as bodies that deform a little (given the Young modulus) when touching each other, and the repulsion force is proportional to a power of that deformation. In particular, we used the so called Hertz model [22, 23, 24, 25]. The particles were spherical, without friction, and compressed isotropically on a cubic domain.
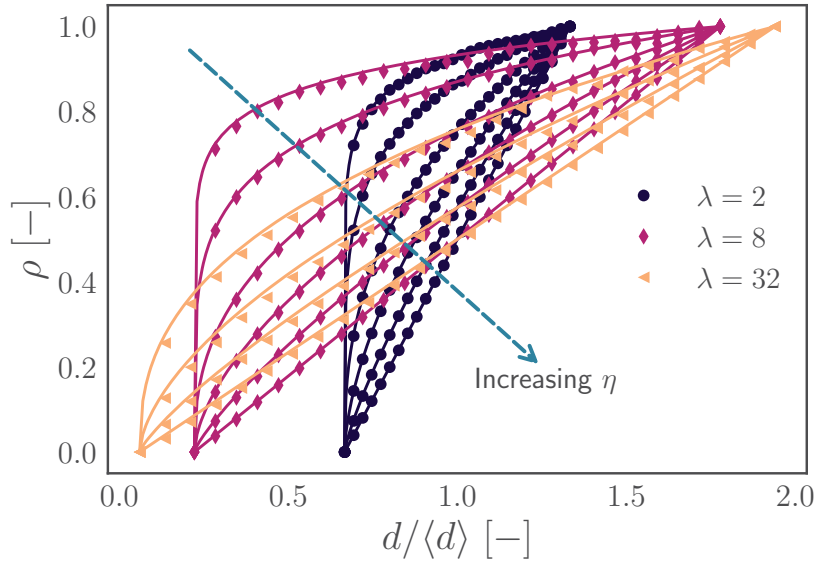
Figure 2: Grain size distribution (1) for some values of λ and all η. In all cases, the average diameter $\langle d \rangle = 0.5(d_{\min} + d_{\max})$ was fixed to the same value.

We randomly generated radius according to the gsd (1) and accepted configurations only when the maximum difference between the numerical and the theoretical gsd was smaller than 5%. The generated sample was equilibrated inside a cubic box and then compressed isotropically, slowly, until reaching mechanical equilibrium. The simulation was stopped when the cundal parameter, defined as the sum of the net force per particle over the sum of the net force per contact was smaller than 0.001, which indicated mechanical equilibrium. Data processed to extract the results shown below was filtered to be one mean diameter away from the walls and, when needed, excluding the floating particles, defined as particles with only 0 or 1 contact.
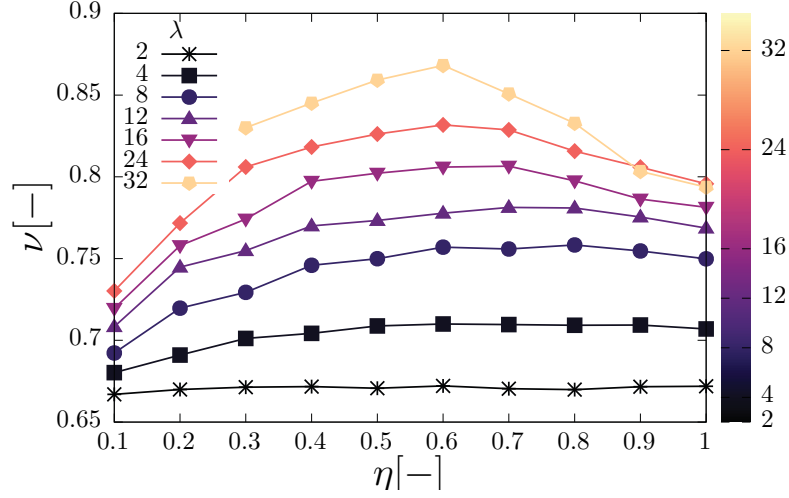
Figure 3: Packing fraction ν for several λ and η, after an isotropic compression.

3 Density and connectivity

Figure 3 shows the packing fraction ν (volume of particles over volume of the packing)

$$\nu = \frac{V_p}{V}, \tag{2}$$

as a function of both λ and η. We can see that for all λ, there is always and optimal $\eta \simeq 0.5$ where the packing fraction is the largest, and this is more notorious for larger λ. This result agrees with the Fuller and Thomson finding, giving it support now for 3D. This shows that, to maximize the density it is not enough to have a large λ, but also and intermediate value of η. Allowing to increase the proportion of small particles helps filling the voids left but the larger particles, but when η is too large then the space filling is not optimal again.

One measure of the connectivity of the system corresponds to the proportion of floating particles, or, equivalently, the mean coordination number, which is the mean number of contacts per particle. Both of them give a first order idea on how well connected is the system to distribute the external forces among the particles.

The proportion of floating particles, κ, is defined as

$$\kappa = \frac{N_f}{N_p}, \tag{3}$$

where N_f is the number of floating particles and N_p is the total number of particles. A particle is defined as a floating particle if its number of contacts is 0 or 1, so it cannot be a part of a force bearing chain inside the sample.

Figure 4 shows the percentage of floating particles as a function of both λ and η. This proportion can reach values of up to 90%, which in turns decreases the mean coordination number to values around 0.5, when all particles are included in the computation. In fact, when the floating particles are excluded, the mean coordination fluctuates around 6,
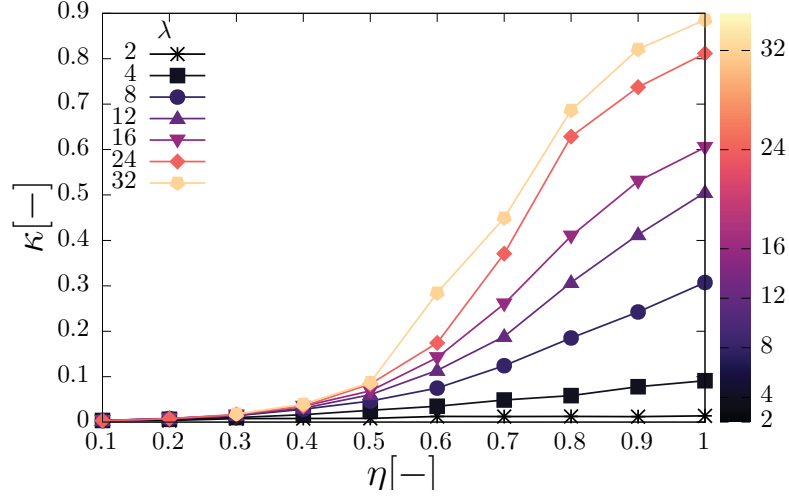
Figure 4: Proportion of floating particles, κ, for several λ and η, after an isotropic compression.

as expected for the isostatic condition. This high percentage of floating particles looks surprising, and has some mechanical implications. For instance, it implies that the forces inside the packing are distributed among a small subset of the particles. This makes this kind of systems more likely to fracture.

4   Summary and conclusions

We have studied three-dimensional frictionless systems with very large polydispersities characterized by the grain size distribution (1) with shape $\eta = [0.1, 0.2, \ldots, 1.0]$, and size span $\lambda = [2, 4, 8, 12, 16, 24, 32]$. The systems were compressed isotropically until mechanical equilibrium was reached.

We found an optimal packing where the density is maximum and correspond to eta = 0.5, which is Fuller and Thomson.

The density of the system, measured by the packing fraction ν, depends strongly on λ and η. In particular, we found that for almost all system, specially large λ, there is always an optimal packing with the largest density around $\eta \simeq 0.5 - 0.6$, which is close to the Fuller-Thomson distribution and confirms that this shape parameters generates the densest packing.

Furthermore, after these optimal η values, the proportion of floating particles κ increases strongly, reaching values of up to 90%. This implies that $\eta \simeq 0.5 - 0.6$ corresponds not only to the densest packing but also marks the transition from a well connected packing to a packing where a small subset of particles participate on the force bearing networks. The high percentage of floating particles make the systems more fragile since they might be more likely to fracture the grains.

The present results support the design of granular packings from the actual gsd, choosing λ and η to reach a target density and connectivity. This can be extended to systems with friction, or with different mechanical solicitations, like simple shear or triaxial tests.

REFERENCES

[1] William B Fuller and Sanford E Thompson. The laws of proportioning concrete. *Transactions of the American Society of Civil Engineers*, 59(2):67–143, 1907.

[2] Frederick W Taylor and Sanford E Thompson. *A Treatise on Concrete, Plain and Reinforced.* John Wiley & Sons, 1919.

[3] Arthur Newell Talbot and Frank Erwin Richart. The strength of concrete-its relation to the cement, aggregates and water. Bulletin 137, University Of Illinois, University of Illinois, Urbana, October 1923.

[4] CC Furnas. Report of Investigations. Technical Report Serial No. 2894, Department of Commerce, Bureau of Mines, Report of Investigation Serial No. 2894, 1928, 1929.

[5] CC Furnas. Grading aggregates-I.-Mathematical relations for beds of broken solids of maximum density. *Industrial & Engineering Chemistry*, 23(9):1052–1058, September 1931.

[6] Ivana Agnolin and Jean-Noel Roux. Internal states of model isotropic granular packings. II. Compression and pressure cycles. *Physical Review E (Statistical, Nonlinear, and Soft Matter Physics)*, 76(6):061303, 2007.

[7] Ivana Agnolin and Jean-Noel Roux. Internal states of model isotropic granular packings. III. Elastic properties. *Physical Review E (Statistical, Nonlinear, and Soft Matter Physics)*, 76(6):061304, 2007.

[8] Mohamed Hassan Khalili, Jean-Noël Roux, Jean-Michel Pereira, Sébastien Brisard, and Michel Bornert. Numerical study of one-dimensional compression of granular materials. II. Elastic moduli, stresses, and microstructure. *Phys. Rev. E*, 95(3):032908, March 2017.

[9] H. Troadec, F. Radjai, S. Roux, and JC Charmet. Model for granular texture with steric exclusion. *Physical review. E, Statistical, nonlinear, and soft matter physics*, 66(4 Pt 1):041305, 2002.

[10] F. Radjai, J.-Y. Delenne, E. Azéma, and S. Roux. Fabric evolution and accessible geometrical states in granular materials. *Granular Matter*, 14(2):259–264, 2012. 10.1007/s10035-012-0321-8.

[11] Nicolas Estrada. Effects of grain size distribution on the packing fraction and shear strength of frictionless disk packings. *Physical Review E*, 94(6):062903, 2016.

[12] Nicolas Estrada and W. F. Oquendo. Microstructure as a function of the grain size distribution for packings of frictionless disks: Effects of the size span and the shape of the distribution. *Phys. Rev. E*, 96(4):042907, October 2017.

[13] S. G. Bardenhagen, J. U. Brackbill, and D. Sulsky. Numerical study of stress distribution in sheared granular material in two dimensions. *Physical Review E*, 62(3):3882, 2000.

[14] M Reza Shaebani, Mahyar Madadi, Stefan Luding, and Dietrich E Wolf. Influence of polydispersity on micromechanics of granular materials. *Physical Review E*, 85(1):011301, 2012.

[15] Maya Muthuswamy and Antoinette Tordesillas. How do interparticle contact friction, packing density and degree of polydispersity affect force propagation in particulate assemblies? *Journal of Statistical Mechanics: Theory and Experiment*, 2006(09):P09003, September 2006.

[16] C. Voivret, F. Radjaï, J.-Y. Delenne, and M. S. El Youssoufi. Space-filling properties of polydisperse granular media. *Phys. Rev. E*, 76(2):021301, August 2007.

[17] C. Voivret, F. Radjaï, J.-Y. Delenne, and M. S. El Youssoufi. Multiscale force networks in highly polydisperse granular media. *Phys. Rev. Lett.*, 102(17):178001, April 2009.

[18] Duc-Hanh Nguyen, Émilien Azéma, Farhang Radjai, and Philippe Sornay. Effect of size polydispersity versus particle shape in dense granular media. *Physical Review E*, 90(1):012202, 2014.

[19] Duc-Hanh Nguyen, Emilien Azéma, Philippe Sornay, and Farhang Radjai. Effects of shape and size polydispersity on strength properties of granular materials. *Physical Review E*, 91(3):032203, 2015.

[20] Emilien Azéma, Sandra Linero, Nicolas Estrada, and Arcesio Lizcano. Does modifying the particle size distribution of a granular material (ie, material scalping) alters its shear strength? In *Powders and Grains 2017*, 2017.

[21] David Cantor, Emilien Azéma, Philippe Sornay, and Farhang Radjai. Rheology and structure of polydisperse three-dimensional packings of spheres. *Physical Review E*, 98(5), November 2018.

[22] Christoph Kloss, Christoph Goniva, Alice Hager, Stefan Amberger, and Stefan Pirker. Models, algorithms and validation for opensource DEM and CFD–DEM. *Progress in Computational Fluid Dynamics, an International Journal*, 12(2-3):140–152, 2012.

[23] S. Luding. Cohesive, frictional powders: Contact models for tension. *Granular Matter*, 10(4):235–246, 2008.

[24] H. Hertz. Über die berührung fester elastiches körper. *J. Reine angewandte Mathematik*, 92:156–171, 1882.

[25] Nikolai V. Brilliantov, Frank Spahn, Jan-Martin Hertzsch, and Thorsten Pöschel. Model for collisions in granular gases. *Phys. Rev. E*, 53(5):5382–5392, May 1996.

PARAMETER IDENTIFICATION FOR DISCRETE ELEMENT SIMULATION OF VERTICAL FILLING: IN-SITU BULK CALIBRATION FOR REALISTIC GRANULAR FOODS

Stefan Kirsch[1,2]

[1] Technische Universität Dresden

[2] Bosch Packaging Technology B.V.
Postbus 16, 6000AA Weert, The Netherlands
stefan.kirsch2@bosch.com

Key words: Vertical filling, Granular foods, Tubular bagger, DEM, CFD, Air Resistance

Abstract. Vertical filling of granular media is influenced by resistance of the surrounding medium, especially in the case of a dilute process with relatively large distances between particles and relatively low particle densities. Discrete Element simulations were carried out to calibrate models of such a filling process for two granular food goods. The aim was to perform bulk calibration in-situ, meaning in the process of interest itself, rather than a second setup. To account for the air drag but keep computational cost practical, the computationally cheap free fall was modeled with the Schiller-Naumann correlation for drag force. The predictions where compared to simulations without fluid influence. The results show that the predictive quality of the models was increased with the simple drag model. It is shown that with the expanded model, calibration can be performed in the filling process itself, which might be useful especially for industry application.

1 INTRODUCTION

Vertical filling is a staple in the industrial packaging of granular foods, such as candy, cereal, nuts and pasta. The most common example is the vertical form, fill and sealing process (VFFS), which is capable of producing and filling over a hundred bags per minute. The process is shown schematically in figure 1a.

After a dosing unit has filled the collection bucket with a defined amount of good, the particles are released and fall through the forming tube. The latter is surrounded by a downwards moving film tube. As the sealing jaws close, they seal both the bottom of the current bag as well as the top of the last bag. The bag production rate is often limited by the falling behavior of the bulk good. This is due to the fact that in each cycle, all particles must entirely fall past the sealing jaws which are only open for a limited amount of time between sealing events. The maximum time allowed for filling t_{fill}, must thus be longer than the time between the first and the last particle to leave the tube at the bottom. The relationship between the events of each bag production cycle are shown in
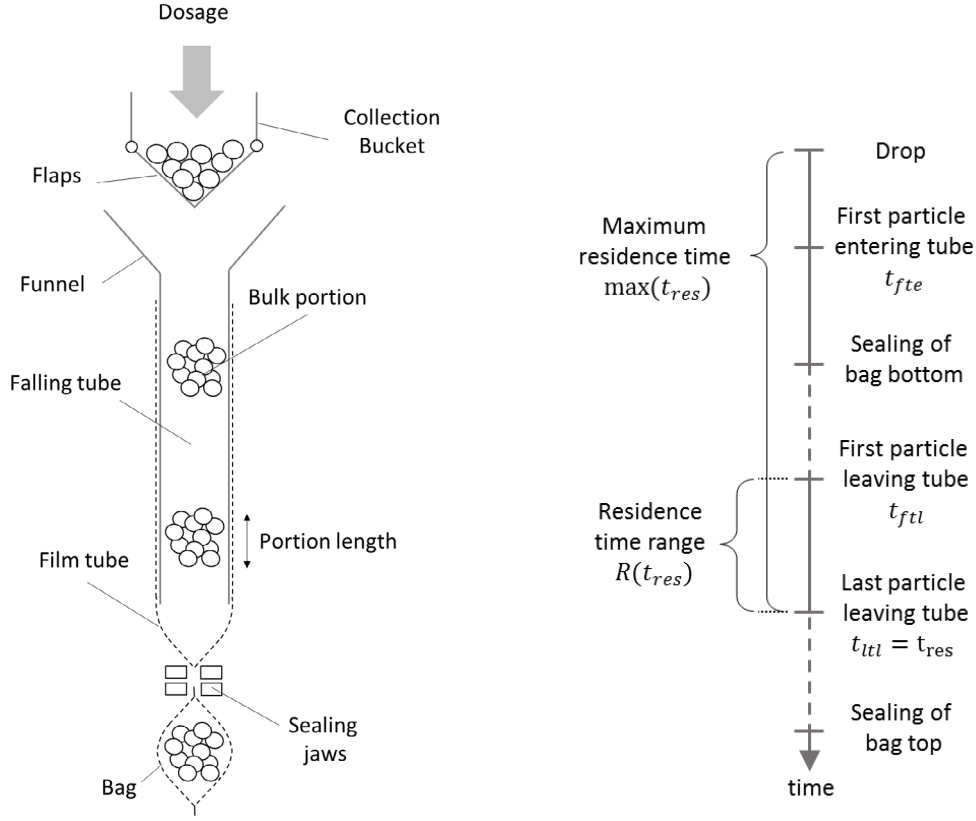
(a) Schematic filling in a vertical tubular bagger (VFFS). Adapted from[1].

(b) Events in each cycle of bag filling. The dashed lines represent indicate variable buffer times which are necessary to accomodate random variation. From [2].

Figure 1: Overview of the vertical filling process.

figure 1b. The time allowed for filling t_{fill} must be longer than the range of the particle residence time $R(t_{res})$, i.e. the residence time of the last particle to leave the tube t_{ltl} minus the residence time of the first particle to leave the tube t_{ftl}.

$$t_{fill} \overset{!}{>} R(tres) = t_{ltl} - t_{fte} \tag{1}$$

To accommodate random variation in the falling behavior of the particles, the sealing jaws must be kept open at least for the mean of $R(t_{res})$ plus a certain buffer time. In each cycle, if one or more particles are delayed more than that buffer time, there is a risk of the particle getting caught by the sealing jaws, which is often detrimental to the quality of the seam. Choosing overly long buffer times however, increases cycle time and therefore reduces bag output. In order to achieve optimal profitability, it is therefore crucial to accurately estimate the residence time range $R(t_{res})$ and its variation between cycles.

The falling behavior of the bulk material largely depends on the kinetics of contacts between particle-particle and particle-wall contacts [3]. Furthermore, the particles experi-

ence air resistance during the fall. Frank et al. showed that the vertical filling process can be described numerically with the Discrete Element Method (DEM) [4]. However, their model did not consider air resistance and required a separate test for model calibration. Kirsch showed that model calibration can be performed in the filling process itself but he also did not include air resistance. [1]

Coupling the DEM with computational fluid dynamics (CFD) is a widely used technique to account for the interaction between fluid and particles [5]. However, sophisticated CFD methods significantly increase computational cost compared to the DEM alone [6]. The aim of this study was to evaluate, if a much simpler formulation for drag can improve the DEM model enough to accurately describe the filling process. For this purpose, experiments and simulations were conducted for two different granular foods. Firstly, we obtained parameters from bulk calibration according to the state of the art, using a funnel discharge test, where the air influence was assumed to be negligible. The obtained parameters were validated in three different scenarios of a vertical drop, which revealed notable deviation from the experimental references, especially for the good with lower particle density.

In order to improve the physical accuracy of the model, a simple relation for air drag was introduced characterizing the free fall of a single particle. While this method fails to capture swarm effects, it is computationally cheap. In order to account for the slipstream effect of particles behind the bulk front, the drag correlation was turned off after the bulk front left the bottom of the tube. The model validation was repeated with he air drag model. While with high solid density, the simulations showed good agreement with the experimental references, the prediction was poorer for lower solid density. Finally, the calibration was repeated in the drop process itself (in-situ calibration) with the drag model. The predictions from the re-calibrated models are in good agreement with the experiment with a maximum of 5% deviation of the average and median of $R(t_{res})$. This indicates the validity of the chosen drag model for the presented cases, despite its simplicity.

2 DISCRETE ELEMENT SIMULATION

2.1 Contact formulation

Granular dynamics are largely determined by contacts between the particles. Particle contacts cause fairly complex elastic and plastic deformations, which are impractical to describe in full detail if a large quantity of particles is to be included in a simulation. The Discrete Element Method simplifies contacts to save numerical cost. Since the deformations are often much smaller than the particles' dimensions, they are neglected with regard to particle shape. The particles are thus considered as rigid bodies, often spheres. However, the particles are allowed to overlap upon contact. The normal and tangential forces resulting from contact are then described by empirical relations between overlap and force magnitude and direction. For the present study, the elastic-plastic linear hysteresis model was used [8], which follows Hooke's spring law but uses a higher spring constant for the relaxation after contact, to account for the energy dissipation due to plastic deformation.

2.2 Contact parameter identification

DEM simulations require a series of contact parameters, such as friction and restitution coefficients. These parameters are difficult to determine experimentally, since no standard tests are available. Furthermore, due to the empirical nature of the DEM contact laws, the physically accurate parameters may fail to compensate model errors, which often makes it necessary to use nonphysical "effective" parameter values. [9, 10] In practice, the contact parameters are thus often not measured but "calibrated" by iteratively tuning their values so that the DEM simulation reproduces a certain outcome of an experiment with the bulk good [7, 9, 11, 12, 10].

For model calibration, most studies rely on a dedicated lab-scale calibration test, which allows quick tests and is usually simpler to reproduce in the simulation than the actual process. However, only parameters that play a significant role in determining the calibration trials outcome can be determined this way [13]. The actual process however might be sensitive to additional parameters. A way to achieve identical parameter sensitivity in the calibration test and the actual process, is to perform the calibration in-situ, i.e. in the process of interest itself. Kirsch compared in-situ calibration in the drop process to calibration in a separate trial and showed both methods provided good model fidelity [1].

2.3 Effects of model shortcomings

Model calibration is an example for inverse approach and as such is sensitive to incomplete physics in the simulations [14]. In the case of vertical filling, DEM-only simulations neglect the influence of air drag on the particles. If the influence of drag is significant, this will introduce a bias to the solver. The parameter set with the lowest error is then only apparently optimal, and will, to some degree, differ from the actual optimal parameter set. Thus, the question is, if the influence of air significantly affects the falling behavior of the bulk. It has been shown that the speed of particle clusters falling in a vertical tube exceed the terminal velocity of a single particle [15]. This is an indication that a clustered drop resembles more a fall in vacuum. However the authors stated, that this is only to be assumed for drops with a low void fraction.

3 PARAMETER IDENTIFICATION

3.1 Experimental setups

The experiments were performed with two sample goods: near spherical bite-size chocolate candy and puffed rice. Their dimensions, bulk densities and sample masses used are noted in table 1.

Two different experimental setups were used in this study: a funnel discharge test with a dense particle flow [1] and a dilute drop test mimicking the industrial filling process [16]. The funnel setup was constructed from transparent polycarbonate. This allowed tracking the bulk's motion over time upon release. The experiments were filmed with a high speed camera at 100 frames/second. The videos were processed with the Matlab® Image Processing Toolbox™, so that the visible area of particles was extracted (figure 2). The experiments were each repeated five times and the resulting time signals were

Table 1: Set bulk good parameters.

Material	Parameter	Value	Sample masses
Chocolate Candy	Young's Modulus Bulk density Particle diameter d	10^7 m $662 \, \text{kg/m}^3$ $11.2 \, \text{mm}$	$2000 \, \text{g}^\nabla$, $300 \, \text{g}$, $500 \, \text{g}$, $700 \, \text{g}^*$
Puffed Rice	Young's Modulus Bulk density Particle diameter d Particle length l	10^7 m $129 \, \text{kg/m}^3$ $4.8 \, \text{mm}$ $9.0 \, \text{mm}$	$230 \, \text{g}^\nabla$, $50 \, \text{g}^*$, $100 \, \text{g}$, $200 \, \text{g}$
Polycarbonate	Young's Modulus	10^7 m	–

∇ Funnel discharge calibration

$*$ Drop test calibration

averaged.

(a) Original frame.
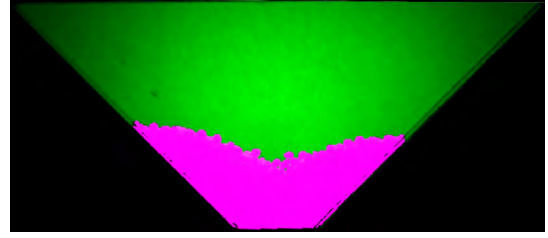
(b) Result of binarization.

Figure 2: Experimental funnel discharge test and image processing to obtain visible particle surface.

The drop test setup is shown schematically in figure 3a. Before each experiment, the sample bulk was placed in the sample bucket. The drop was then initiated by opening the motor-driven flaps. The drop experiments were filmed with a high-speed camera at 1024 frames/second. The videos were then processed using the Matlab® Image Processing Toolbox™ similar to the funnel test, so that the 2-dimensiona particle area could be extracted (figure 3b). This allowed calculating and tracking the virtual center of mass of the 2-dimensional projection over time [2]. Additionally, the time stamps t_{ftl} and t_{ltl} of the first and last particle to leave the tube at the bottom were extracted. Each test was conducted at least seven times and the resulting curves and the time stamps were averaged.

The experimental setup and the operation conditions were transferred into the DEM environment Rocky DEM. From every simulation run, a video mimicking the experimental videos was exported and analyzed analogously.

(a) Drop setup, measures in mm. The bulk sample can be released with motor-driven flaps. Adapted from [16].

(b) Original and processed example video frames of the drop process. The asterisk shows the location of the 2D center of mass. From [2].
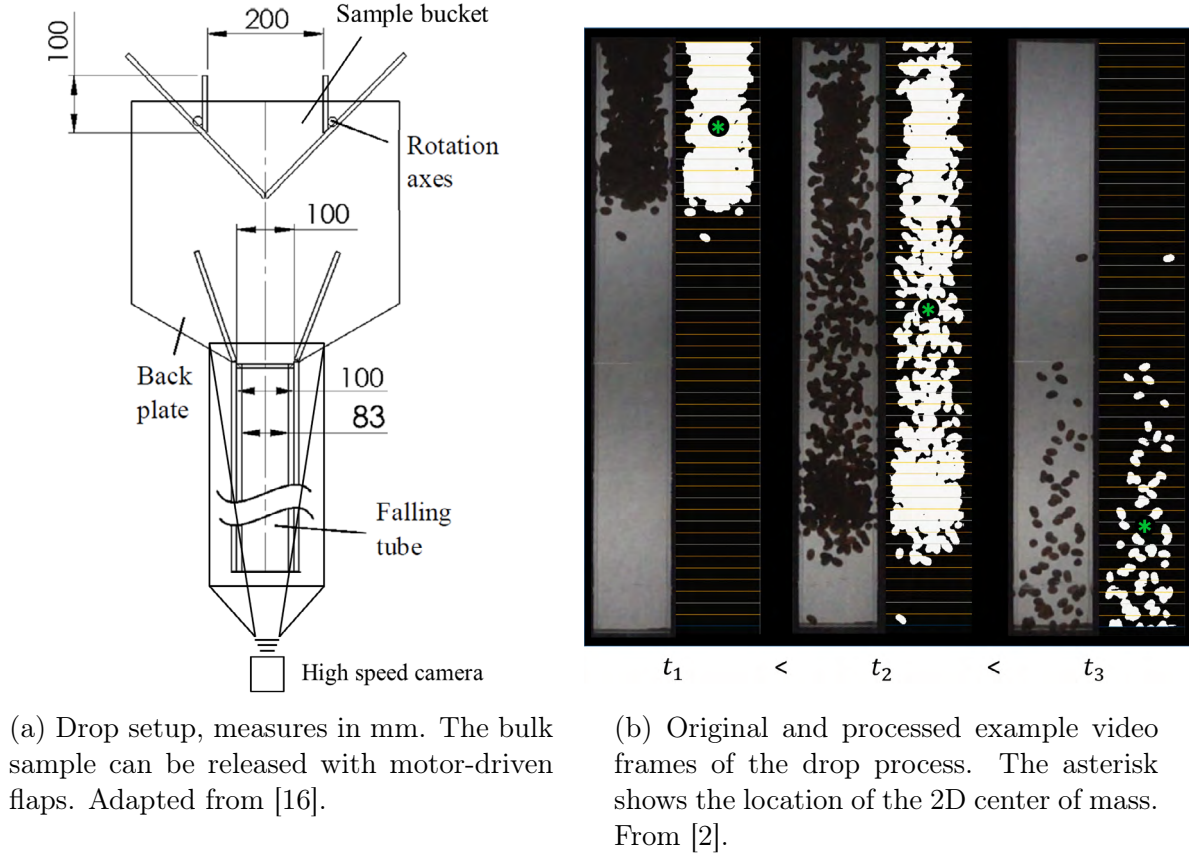
Figure 3: Experimental drop setup and image processing.

3.2 Parameter variation and regression of solver response

The aim of the calibration is to find the parameter set $\vec{x}_{opt}$ where the error between simulation and experimental reference becomes minimal. The error function $E(\vec{x})$ varied between calibration scenarios (see 3.3). Iterative calibration is numerically expensive, since every parameter combination tested requires one solver run. The development of efficient and reliable calibration procedure has gained the attention of several groups [1, 17, 13, 18]. Rackl et al. and Kirsch performed the calibration on a meta model, which was constructed from the responses of a predetermined number of solver calls at different parameter sets which were obtained from Latin Hypercube sampling (LHC) [1, 13, 19, 20]. The benefit of the meta model is, that it is much cheaper to evaluate than the DEM solver and thus allows for faster search of an optimal parameter set. Additionally, the regression is capable of smoothing out some random variation (solver noise), which makes optimization more efficient [21].

The parameter variation and optimization scheme is shown in figure 4 [1]. It was implemented using the optimization software package Optislang®. The scheme features an iterative adaptive approach where samples are added in the regions where the error function is low, to increase local resolution. Optislang® offers a measure for the fidelity

of the regression in the coefficient of prognosis [22]. The process was stopped if the coefficient of prognosis did not further increase. In all cases, a minimum of six iterations were performed. After the last sampling iteration, the parameter set with the lowest error between simulation and reference was identified. The resulting parameter set $\vec{x}_{opt}$ was then used for validation.
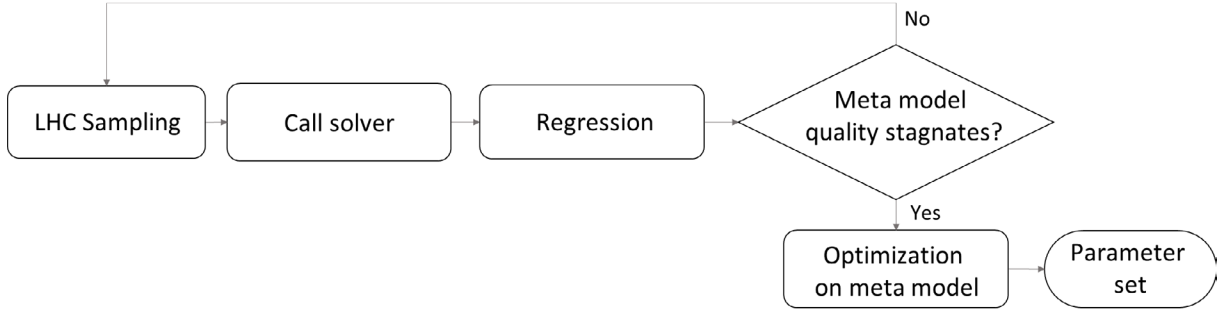
Figure 4: Workflow for DEM input contact parameter calibration (Adapted from [1]).

3.3 Calibration scenarios

The scheme described in section 3.2 was performed for two calibration scenarios and for both sample goods. The first scenario was the funnel discharge test as described above. The error function $E(\vec{x})$ was defined as the averaged absolute point-wise deviation between reference and simulation. Secondly, the drop test as described above was used for calibration. The error function $E(\vec{x})$ was the root mean square error (RMSE) of the virtual center of mass in longitudinal direction between reference and simulation [2]. For the second calibration, a CFD model was used to account for air drag.

Accurate descriptions of air resistance, for example FEM methods, describe the element-wise interaction between particles and the surrounding medium. This makes calculations significantly more expensive and would lead to impractical run times for model calibration. In order to avoid this issue, a much simpler approach for air drag was attempted for this study. It was reasoned that due to the dilute nature of the drop process, the air drag could be approximated by the case of a single particle falling through an unconstrained fluid domain (free fall). The drag force F_D in this case follows the relationship

$$F_D = \frac{1}{2}\rho v^2 C_D A_p \tag{2}$$

where ρ is the particle density, v the particle's velocity, and A_p it's cross sectional area. The drag coefficient C_D depends on the particle shape and on the Reynold's number. Many empirical relations for C_D can be found in literature. A commonly used relation for C_D based on the original formulation of Schiller and Naumann is given by [23, 24]:

$$C_D = max\left[\frac{24}{Re}\left(1 + 0.15Re^{0.687}\right), 0.44\right] \tag{3}$$

With this simple relationship for air drag, the effect of particle velocity is incorporated in the model, while the local particle concentration and the history of air displacement by leading particles is neglected. The latter slipstream effect results in particles behind the leading front to experience less air drag. In order to include this into the model, the air drag model was only used in the first half of every simulation until the particle front left the tube at the bottom. After this, the drag model was switched off, assuming a fall in vacuum. Due to the simplicity of the model, the air drag introduced should not be viewed as an expansion of the physics model, but rather as an empirical correction factor for the DEM simulations. Such an approach is only considered viable, as long as the influence of air drag is overall low compared to the influence of the particle contacts, which was first to be tested on the DEM models calibrated to the funnel experiment.

4 RESULTS AND DISCUSSION

4.1 Calibration to funnel test

The predictions of the DEM models calibrated to the funnel discharge test are shown in a box plot in figure 5. On the ordinate, the mass of the bulk sample and the source of the data are given (experimental reference, simulation in vacuum or simulation with CFD). The vertical line in the box plot marks the median and the box edges indicate the first and third quartile. The whiskers indicate the most extreme observations that still fall within 1.5 times the interquartile range. All other observations are marked with a plus sign and indicate outliers.

(a) Residence time range $R(t_{res})$ of chocolate candy.

(b) Residence time range $R(t_{res})$ of puffed rice.
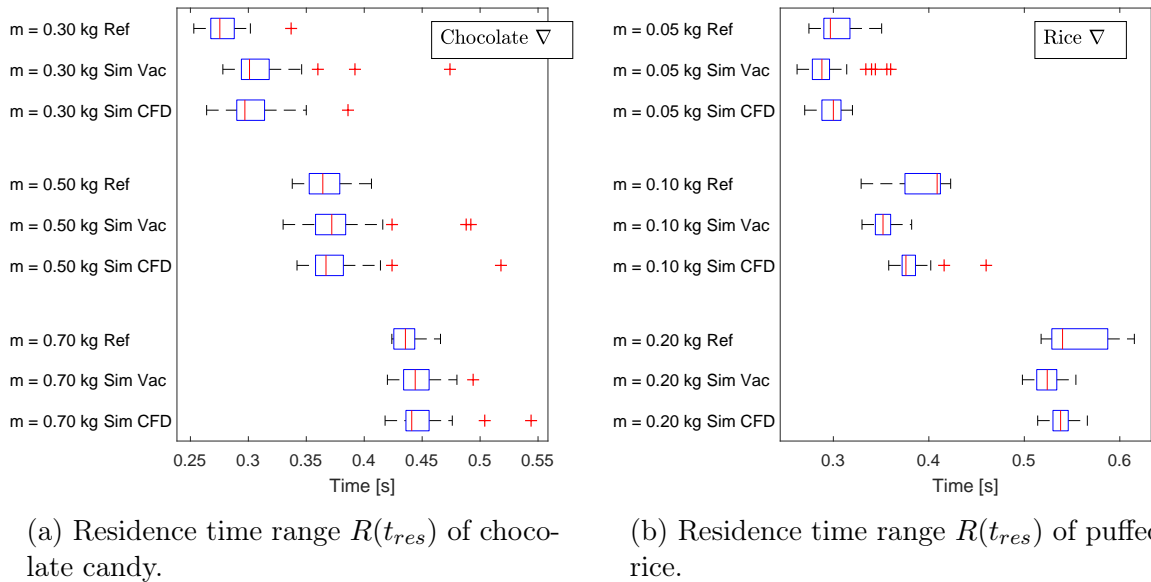
Figure 5: Validation of the models calibrated in the funnel discharge test.

We find a notable deviation between the experimental data and the simulations, which varies from case to case. Furthermore, we find that the drag model has little impact for the

chocolate candy, but notably influences the simulations with puffed rice. In the latter, the drag model improves the prediction of the simulation, by reducing the underestimation of the residence time range. These results give an indication that the chosen CFD model is a viable correction factor for air drag.

4.2 Calibration to drop test with drag model

Based on the previous findings, a new set of two calibration runs with the drag model was performed in the drop test with the bulk masses indicated in table 1. The results of the validation of the calibrated models are shown in figure 6.

(a) Residence time range $R(t_{res})$ of chocolate candy.

(b) Residence time range $R(t_{res})$ of Puffed rice.
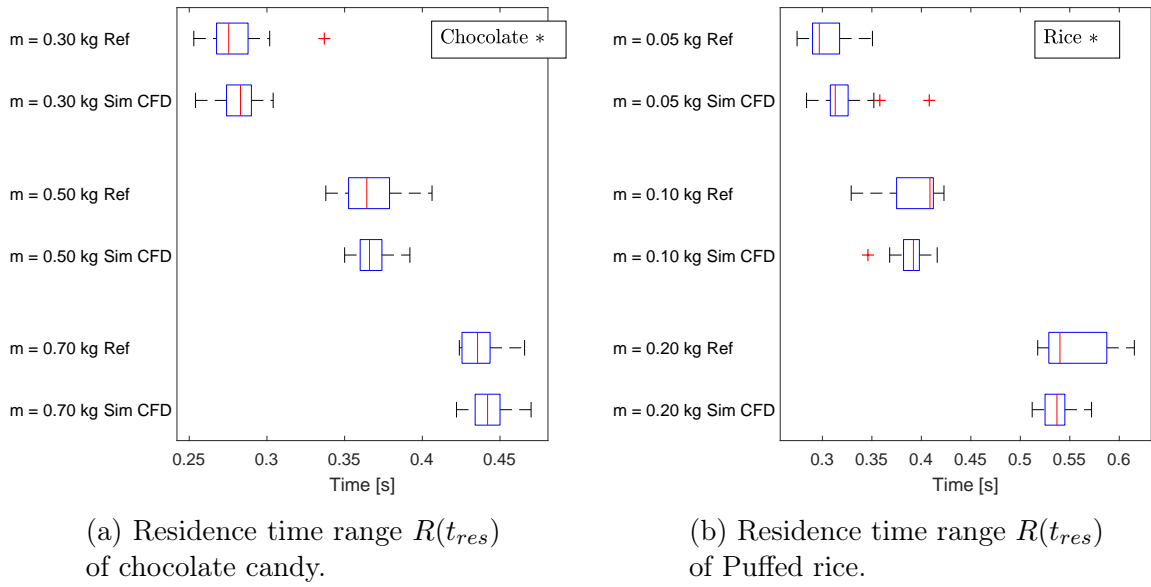
Figure 6: Validation of the models calibrated in the drop test with CFD model.

For the chocolate candy, we find a better agreement between reference and simulation (figure 6a) than in the validation of the model calibrated to the funnel test before. (figure 5a). More specifically, the prediction of the median is more accurate and more consistent over the sample mass. Secondly, the location and distance of the first and third quartile show a much better agreement between reference and simulation than in figure 5a. This is an indication, that the model could also be used to make statistical predictions. This would be of especially high importance for industry application, since the filling process is intrinsically random. Thus, if a model is capable of predicting "worst cases", i.e. abnormally long $R(t_{res})$, and their likelihood, one could infer economically beneficial settings of the filling process, considering earnings for bags output versus cost for possible machine downtime when a particle was caught between the sealing jaws.

For the DEM-CFD for puffed rice (figure 6b), we find a comparable prediction accuracy as in the model calibrated to the funnel test (figure 5b). We find notable deviation in the median of a maximum up to 5% for the cases with lower sample mass, which could

still be considered acceptable for practical use. The predictions for statistical spread now also show notable deviation. This would make the model for puffed rice less reliable for predictions in an industrial context. A reason for the deviation is that the impact of air resistance seems to be larger than for the chocolate candy (figure 5). This is explainable by the lower density of the puffed rice particles, which could mean that the real air flow plays a larger role. Thus, these simulations might require a more sophisticated drag model.

5 CONCLUSION

The aim of this study was to find a computationally cheap CFD model, capable of correcting the DEM model's shortcomings regarding air drag for the simulation of the industrial vertical filling process. We showed in a simplified drop setup that a fairly simple relationship for air drag was capable of providing a plausible correction to DEM models so that their predictive capability was improved. Furthermore, the CFD model was implemented in an in-situ calibration approach, meaning that the DEM parameters were calibrated in the process of interest itself. The calibrated models show good agreement with the median observation from the measurements and even predict the statistical spread fairly reliably for denser particles. Both are important for industrially relevant choices regarding machine operation.

REFERENCES

[1] Kirsch, S. DEM model calibration for vertical filling: Selection of adequate trials and handling randomness. *Weimar Optimization and Stochastic Days* (2018).

[2] Kirsch, S. Stochastic discrete element modelling of granular filling processes for industry application: Can we formulate a standardized approach? *7th International Computational Modelling Symposium* (2019).

[3] Pöschel, T and Schwager, T. *Computational Granular Dynamics: Models and Algorithms.* Springer-Verlag Berlin Heidelberg, (2005).

[4] Frank, M. and Holzweißig, J. Simulation-based optimization of geometry and motion of a vertical tubular bag machine. *Research report, Sächsische Landesbibliothek.* (2016).

[5] Zhu, H.P., Zhou, Z.Y., Yang, R.Y. and Yu, A.B. Discrete particle simulation of particulate systems: A review of major applications and findings. *Chem. Eng. Science* (2008) **63**(23):5728–5770.

[6] Zhu, H.P., Zhou, Z.Y., Yang, R.Y. and Yu, A.B. Discrete particle simulation of particulate systems: Theoretical developments. *Chem. Eng. Science.* (2007) **62**(13):3378–3396.

[7] Markauskas, D. and Kacianauskas, R. Investigation of rice grain flow by multi-sphere particle model with rolling resistance. *Granular Matter* (2010) **13**(2):143–148.

[8] Luding, S. Collisions and contacts between two particles. *Physics of Dry Granular Media* **350**:285–304.

[9] Coetzee, C. J. Review: Calibration of the discrete element method. *Powder Technol.* (2017) **310**:104–142.

[10] Barrios, G.K.P., de Carvalho, R.M. and Kwade, A. and Tavares, L.M. Contact parameter estimation for DEM simulation of iron ore pellet handling. *Powder Technol.* (2013) **248**:84–93.

[11] Roessler, T. and Katterfeld, A. DEM parameter calibration of cohesive bulk materials using a simple angle of repose test. *Particuology* (2018) **343**:803—812.

[12] Coetzee, C. J. Calibration of the discrete element method and the effect of particle shape. *Powder Technol.* (2016) **297**:50–70.

[13] Rackl, M. and Hanley, K.J. A methodical calibration procedure for discrete element models. *Powder Technol.* (2017) **307**:73–83.

[14] Pernot, P. and Cailliez, F. A critical review of statistical calibration/prediction models handling data inconsistency and model inadequacy. *Transport Phenomena and Fluid Mechanics* (2017) **63**.

[15] Nakashima, K., Johno, Y. and Shigematsu, T. Free fall characteristics of particle clusters in a vertical pipe. *Journal of Physics: Conference Series* (2009) **147**(1).

[16] Kirsch, S. and Philipp, A. Simulation of vertical filling processes of granular foods for typical retail amounts. *9th Conference Processing Machines and Packaging Technology Dresden* (2018).

[17] Benvenuti L., Kloss C. and Pirkera S. Identification of DEM simulation parameters by artificial neural networks and bulk experiments. *Powder Technol.* (2016) **291**:456–465.

[18] Roessler, T., Richter, C., Katterfeld, A. and Will, F. Development of a standard calibration procedure for the DEM parameters of cohesionless bulk materials – part I: Solving the problem of ambiguous parameter combinations. *Powder Technol.* (2018) (343):803–812.

[19] McKay, M. D., Beckman, R. J. and Conover and W. J. A comparison of three methods for selecting values of input variables in the analysis of output from a computer code. *Technometrics* (1979) **21**(2):239–245.

[20] Helton, J.C. and Davis, F.J. Latin hypercube sampling and the propagation of uncertainty in analyses of complex systems. *Reliab. Eng. Syst. Safe.* (2003) **81**:23–69.

[21] Barton, R.R. and Meckesheimer, M. Metamodel-based simulation optimization. *Handbooks in Operations Research and Management Science* (13):535–574 Elsevier (2006).

[22] Most, T. and Will J. Metamodel of optimal prognosis - an automatic approach for variable reduction and optimal metamodel selection. *Weimar Optimization and Stochastic Days* (2008).

[23] Schiller, L. and Naumann A. A drag coefficient correlation. *Zeitschrift des Vereins Deutscher Ingenieure* (1935) (77):318–320.

[24] *Fluent Theory Guide* ANSYS, Inc., (2013).

PARAMETER IDENTIFICATION FOR SOIL SIMULATION BASED ON THE DISCRETE ELEMENT METHOD AND APPLICATION TO SMALL SCALE SHALLOW PENETRATION TESTS

Jonathan Jahnke[1,*], Stefan Steidel[1], Michael Burger[1], Salomi Papamichael[2], Andreas Becker[2] and Christos Vrettos[2]

[1] Department Dynamics, Loads and Environmental Data
Division of Mathematics for Vehicle Engineering
Fraunhofer Institute for Industrial Mathematics ITWM
Fraunhofer-Platz 1, 67663 Kaiserslautern, Germany
e-mail: [jonathan.jahnke, stefan.steidel, michael.burger]@itwm.fraunhofer.de

[2] Division of Soil Mechanics and Foundation Engineering
Technical University Kaiserslautern
Erwin-Schrödinger-Straße, 67663 Kaiserslautern, Germany
e-mail: [salomi.papamichael, andreas.becker, christos.vrettos]@bauing.uni-kl.de

Key words: Granular Materials, Discrete Element Method, Parametrization, Triaxial Compression Test, Shallow Penetration Test

Abstract. The Discrete Element Method (DEM) is well-established and widely used in soil-tool interaction related applications. As for all simulation tools, a proper calibration of the model parameters is crucial. In this contribution, we present the parametrization procedure of the DEM software *GRAnular Physics Engine* (GRAPE), developed and implemented at Fraunhofer ITWM, and attempt to use two parametrized soil samples for the simulation of small scale shallow penetration tests. The results are compared to laboratory measurements.

1 Introduction

In recent years, the Fraunhofer ITWM has developed and implemented a software solution entitled *GRAnular Physics Engine* (GRAPE) for modeling and simulating soil and soil-tool interaction based on investigations in [1, 2, 3]. GRAPE is based on the Discrete Element Method (DEM) with a focus on the accurate prediction of draft forces with heavy construction equipment. The particles are represented by three-dimensional rigid spheres with three translational degrees of freedom and scale-invariant linear particle interaction forces in which the corresponding parametrization is based on a triaxial compression test, see Section 2 and 3. In particular, GRAPE is validated in real application scenarios among others in cooperation with Volvo Construction Equipment, cf. [4, 5].

The parametrization process for soil simulation is a challenging task. Cone penetrometer tests in the context of vehicle engineering have been studied in [6] using *Smoothed Particle Hydrodynamics*. Shallow hemiball and toroid penetrometers have been simulated using a *Large Deformation Finite Element Method* in [7] to find fitting equations for in situ evaluation and soil identification. Cone penetrometer tests, together with plate sinkage and shear tests have been used in an optimization routine to estimate DEM model parameters [8]. It was found that the combination of several in situ tests is sufficient for the calibration of their model. Small scale shallow penetration experiments using different materials have been conducted and evaluated in [9].

In this contribution, we illustrate the parameter identification process for two types of soil, namely a poorly graded sand (A) and a well graded sand-silt mixture (B) with mean grain diameter $d_{50}(A) = 0.290$ mm and $d_{50}(B) = 0.036$ mm, respectively. In Section 2 we describe the Discrete Element Method and explicate the specifics of our model. Thereafter, the experimental procedure on triaxial compression and shallow cone pentration test is shortly presented in Section 3. We determine the respective soil and particle interaction parameter sets $\mathcal{P}(A)$ and $\mathcal{P}(B)$ to match the observed strain-stress behavior in the corresponding triaxial compression tests, see Section 4. Subsequently, we discuss the applicability of these identified parameter sets – that reflect the triaxial test – to reproduce small scale shallow penetration tests performed in the soil mechanics laboratory, see Section 5. Finally, we summarize our results in Section 6.

2 Fundamentals of the DEM model

In this section, we briefly describe the Discrete Element Method in general and our efficient and soil-specific model in more detail [1, 10, 4, 11]. The DEM dates back to the 1970s [12] and with the rise of computing power as predicted by Moore's law, the method gained practical relevance in the 1990s until today. Zhu et al. [13] present a still ongoing boom referring to the number of particle simulation related publications. The main idea of the DEM is to consider soft-sphere particles and their interaction leading to granular bulk behavior. The decision on the shape of the particles and on how to model the inter particle contact law has to be taken with care. The physically most accurate contact law seems to be the Hertzian contact model with additions due to Mindlin and Deresievicz to account for cohesion [14]. Much more efficient but less physical is a linear-elastic Hookean model. However, when it comes to soil and granular matter with complex shapes, the error due to regularized geometries is much more relevant than the error owing to the linear contact law [15]. Due to the fact, that we are interested in the soil-tool interaction forces and usually do not focus on the micro-mechanical behavior of particle interaction, we choose the simplest geometry, namely spheres and a linear contact law. In our model, we neglect the rotational degrees of freedom, and solely rely upon an accurate parametrization in order to obtain physical bulk behavior, e.g. a realistic strain stress behaviour and angle of friction.

2.1 Normal interaction

The particle dynamics relies upon Newton's second law

$$m_i \ddot{\mathbf{x}}_i = \mathbf{f}_i. \tag{1}$$

Here m_i denotes the mass of the i-th particle, $\mathbf{x}_i$ its position, $\dot{\mathbf{x}}_i$ its velocity and $\ddot{\mathbf{x}}_i$ its acceleration vector. If two particles interact, that is the overlap $\delta_{ij} = r_i + r_j - \|\mathbf{x}_i - \mathbf{x}_j\|$ is non-negative, r_i denoting the radius of the i-th particle, a linear damped spring

$$F_{ij}^N = k_{ij}^N \delta_{ij} + d_{ij}^N \dot{\delta}_{ij} \qquad \text{and} \qquad \mathbf{f}_{ij}^N = F_{ij}^N \mathbf{n}_{ij}, \tag{2}$$

is activated. Here, the normal unit vector at the contact point is defined by

$$\mathbf{n}_{ij} = \frac{\mathbf{x}_i - \mathbf{x}_j}{\|\mathbf{x}_i - \mathbf{x}_j\|}.$$

The stiffness and damping coefficients k_{ij}^N and d_{ij}^N depend upon the particle radius.

Scale invariance and normal stiffness The terminology of scale-invariant contact laws is due to Feng [16]. Let us consider physical grains with radius r_P and larger model particles with radius r_M.

Definition 1 *We say that a model is scale-invariant, if and only if for radii r_P and r_M it holds $\sigma_P = \sigma_M$ for $\epsilon_P = \epsilon_M$.*

Lemma 1 *An n-dimensional contact law of the form $F = cr^\alpha \delta^\beta$ is scale-invariant if and only if $\alpha + \beta = n - 1$.*

This result is shown in [16]. Considering two particles as a stiff beam, with mean radius $r_{ij} = \frac{1}{2}(r_i + r_j)$ and mean area $A_{ij} = \pi r_{ij}^2$. The length of the beam corresponds to $L_{ij} = 2r_{ij}$. Considerung the normal stress σ and strain ε

$$\sigma = \frac{F_{ij}}{A_{ij}} = \frac{k_{ij}^N \delta_{ij}}{\pi r_{ij}^2} \qquad \text{and} \qquad \varepsilon = \frac{\delta_{ij}}{2r_{ij}}, \tag{3}$$

we obtain for the Young modulus

$$E_N = \frac{\sigma}{\varepsilon} = \frac{k_{ij}^N \cdot 2r_{ij}}{\pi r_{ij}^2} \qquad \text{thus} \qquad k_{ij}^N = \frac{E_N \pi r_{ij}}{2} \tag{4}$$

Hence the presented model, neglecting the damping term, describing a 3-dimensional contact law with $n = 3$ and $\alpha = \beta = 1$, is scale-invariant.

Normal Damping Furthermore, we set the inter-particle damping

$$d_{ij}^N = D_N \cdot 2 \cdot \sqrt{k_{ij}^N m_{ij}}, \qquad \text{where} \qquad m_{ij} = \frac{m_i \cdot m_j}{m_i + m_j}. \tag{5}$$

The effective mass m_{ij} stems from the consideration of two particles as one damped oscillator. The parameter D_N controls the desired percentage of the critical damping.

2.2 Tangential interaction

If two particles overlap, the initial contact points $\mathbf{c}_i = \mathbf{c}_j$ coincide and are saved in local coordinates of particle i and j. If the particles translate with respect to each other, the local contact points differ. We project them into the tangential contact plane and consider the resulting vector $\boldsymbol{\xi}_{ij}$ as tangential elongation. The tangential spring then reads

$$\mathbf{f}_{ij}^T = -k_{ij}^T \boldsymbol{\xi}_{ij} - d_{ij}^T \dot{\boldsymbol{\xi}}_{ij} \qquad \text{and} \qquad F_{ij}^T = \|\mathbf{f}_{ij}^T\|. \tag{6}$$

The parameters k_{ij}^T and d_{ij}^T are defined similarly to the normal interaction.

2.3 Coulomb friction

If the tangential elongation becomes large, we need to account for friction. We don't distinguish sticking and sliding friction and use the Coulomb friction model. We restrict the absolute value of the tangential force with respect to the normal force introducing the local stiffness parameter μ, that is $F_{ij}^T \leq \mu F_{ij}^N$. Otherwise slipping friction occurs and we reset the tangential elongation to

$$\boldsymbol{\xi}_{ij}' = \frac{\mu F_{ij}^N}{k_{ij}^T \|\boldsymbol{\xi}_{ij}\|} \boldsymbol{\xi}_{ij}. \tag{7}$$

3 Relevant experiments

We shortly describe the experimental setup of the triaxial compression test, needed for parameter identification. Thereafter, we focus on the small scale shallow penetration test.

3.1 Triaxial compression test

The triaxial compression test is a well-established laboratory test which has been developed in the first half of the 20th century. It serves as a method to quantify a material's strain-stress characteristic. For this study, displacement-controlled triaxial tests are carried out according to the specifications of DIN 18137. Dry samples of 100 mm in diameter and 120 mm in height are prepared using a standardized procedure. Confining pressure in the triaxial cell is applied using water in order to allow measurement of specimen volume change. Axial load is measured outside the cell. Piston friction is assessed by a calibration procedure. Volumetric strain is determined by measuring the volume change of the water in the triaxial cell from the differential movement of a piston. Strains are defined positive in compression. Loading of the sample is applied at a constant displacement rate of 0.1 mm/min. The variation of the axial load and of the volumetric strain are recorded at gradually increasing axial strain. Assuming a linear Mohr–Coulomb failure criterion, the shear strength parameters of the soil, i.e. angle of internal friction ϕ and cohesion c, are determined from the peak values of the strain-stress curves at three distinct levels of the cell pressure.

Two materials (A) and (B) are tested. They are classified as sand and sandy-silt, respectively. The porosity of the samples amounts to $n_A = 0.34 - 0.48$ for (A) and $n_B = 0.45 - 0.60$ for (B). The shear strength parameters, namely the angle of friction ϕ

and the amount of cohesion c for sand (A) and silt (B) as determined from the tests amount to $\phi_A = 39.5°, c_A = 2.1$ kPa and $\phi_B = 42.5°, c_B = 0.5$ kPa. For the parametrization we use the entire stress vs. strain and volume change vs. strain curves obtained from the tests as depicted in Figure 4.
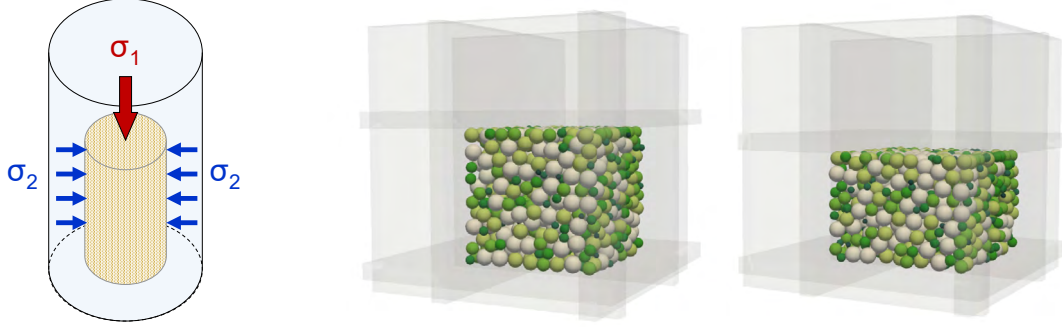
Figure 1: Visualization of the Triaxial Compression Laboratory Test (left) and the respective simulation at the beginning (middle) and in the end (right)

3.2 Shallow penetration test

The tests are carried out in a cylindrical container of a diameter of 290 mm and a height of 200 mm with a steel rod penetrometer of 10 mm diameter with a flat base. During the test, the penetration force and the corresponding displacement are measured for a total depth of 30 mm. The shallow penetration test is performed under a constant displacement rate of 1.2 mm/min. The force needed to penetrate the bar is continuously recorded by an appropriate load cell.
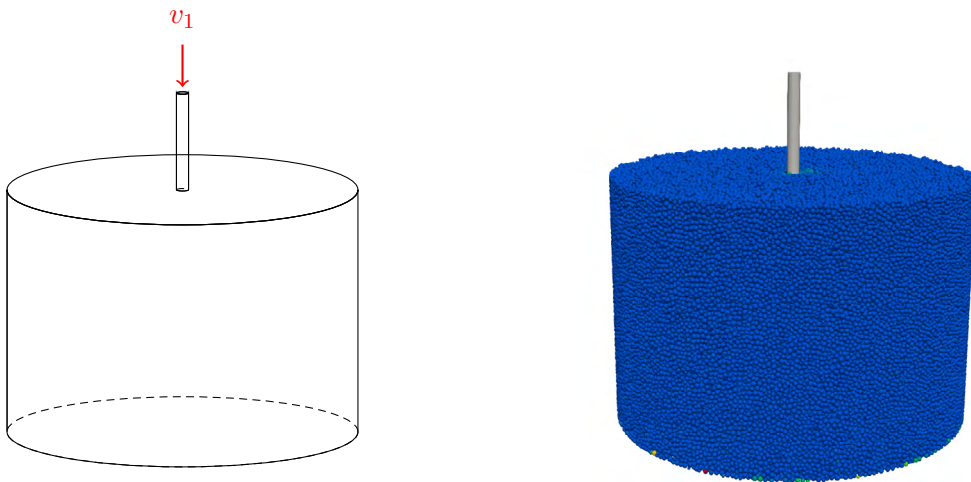
Figure 2: Visualization of the shallow cone penetration experiment and the respective simulation

Parameter	Symbol	Unit	sand $\mathcal{P}$(A)	silt $\mathcal{P}$(B)
Sample generation				
radii	r_i	[mm]	2	0.5-2.5
porosity	n	[-]	0.34-0.53	0.37-0.54
density	ρ	[kg/m^3]	2650	2700
Triaxial compression test				
Young modulus	E_N	[N/m^2]	1.2e8	1.2e7
tangential stiffness parameter	E_T	[N/m^2]	1e8	1e7
local friction coefficient	μ	[-]	0.2	0.25

Table 1: Parameters $\mathcal{P}$(A) and $\mathcal{P}$(B) as determined for the two materials

4 Parametrization via triaxial compression test

In this section, we describe the calibration procedure of our DEM model, as developed in [1, 10]. The parametrization of a GRAPE model is based on a triaxial test, see also Section 3, and implies the appropriate choice of the most influencing simulation parameters. First of all, we decide for the particle size distribution r_i that may represent a scaling of the real grain-size distribution due to the scale-invariant force law, see Section 2.1. The model parameters are the porosity n, the normal stiffness E_N and damping D_N, the tangential stiffness E_T and damping D_T and the local friction coefficient μ. The parameters of the virtual experiment are determined to reflect the soil's characteristic strain-stress behavior in the corresponding real experiment performed in the soil mechanics laboratory.

4.1 Sample generation

In a first step, we study the grain-size distribution and decide for suitable particle radii. Due to the scale-invariance, it is possible to use larger particles which reduces the simulation time, but limits the micro-mechanical modeling fidelity. The first choice is a monodisperse particle sample, which also simplifies the numerical calculation, because the particle stiffness and damping remain constant for all particles. The porosity of the material has to be estimated from the experimental minimal and maximal values. The particle density, corresponding to the mass equals to the density of the soil grain and can be measured in laboratory experiments. A list of all relevant parameters with the determined parameters for sand and silt is given in Table 1.

According to the desired grain-size distribution, the particles are loosely assembled on a regular lattice and slightly disturbed in a random direction. Thereafter, outer sidewalls compress the particles until the desired porosity is reached. This basic sample can then be replicated and cut in order to obtain a desired particle pile. For our study, we use mono-disperse particles of radius 2 mm for the poorly graded material (A). For the sandy-silt (B), we try to approximate the grain-size distribution using seven different particle radii between 0.5 and 2.5 mm, see Figure 3. The porosity of the material's basic sample corresponds to $n_A = 0.34$ and $n_B = 0.37$ for the triaxial compression test. The porosity for silt is underestimated with respect to the measurements. We focussed on reproducing the
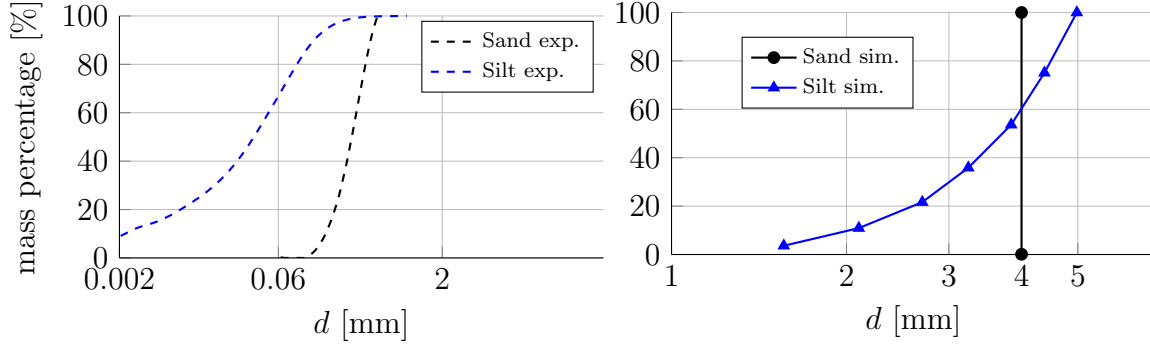
Figure 3: (left) Grain size distribution for two different materials: poorly graded sand (black) and well-graded sand-silt mixture (blue), which we denote by silt; (right) Particle size distribution within the simulation.

grain size distribution, which leads to a denser particle pile density. But when generating the cylindrical sample, we replicate the basic sample and consolidate it under the influence of gravity. The porosity then corresponds to $n_A = 0.53$ for material (A) and $n_B = 0.54$ for material (B).

4.2 Triaxial test simulations

The basic sample obtained in Section 4.1 is loaded in a triaxial test simulation. Instead of using a cylinder-shaped geometry, we use a cube, see Figure 1. The side-walls in horizontal and lateral direction are pressure-controlled. The bottom wall remains constant. The top wall is moved downwards at constant velocity, then the side-walls displace until an equilibrium between the desired side-wall pressure and the particles pressure is reached. The axial displacements ε_1, in vertical direction and ε_2 and ε_3 in horizontal and lateral direction, the volumetric strain ε_v and the top wall pressure σ_1 in vertical direction are recorded. Graphically, this leads to a strain-stress curve and a volumetric strain, axial strain curve, see Figure 4 and 5. The axial stress versus strain behavior demonstrates good accordance. The volumetric strain of silt behaves slightly different with respect to the simulation. The damping constants D_N and D_T are chosen as 0.1.

In this step, the stiffness and friction parameters are estimated. A useful concept is the stiffness number, which gives a rough estimate for the inter-particle stiffness [1]. Different authors have reported a connection between normal and tangential stiffness [17]. As discussed by Obermayr [10], we assume the ratio of $E_N/E_T = 1.2$. If a reasonable particle-particle stiffness yields good results within the triaxial compression test simulation, in terms of fitting the measured strain-stress relation for a specific side-wall pressure, we fine tune the strain-stress curves with the local stiffness constant μ. The parametrization may not be unique and is only valid in a certain pressure range.

5 Numerical results of shallow penetration test

First, we summarize the procedure to optimize the total time for the penetration simulation. The laboratory experiments are performed in a total time frame of about 25
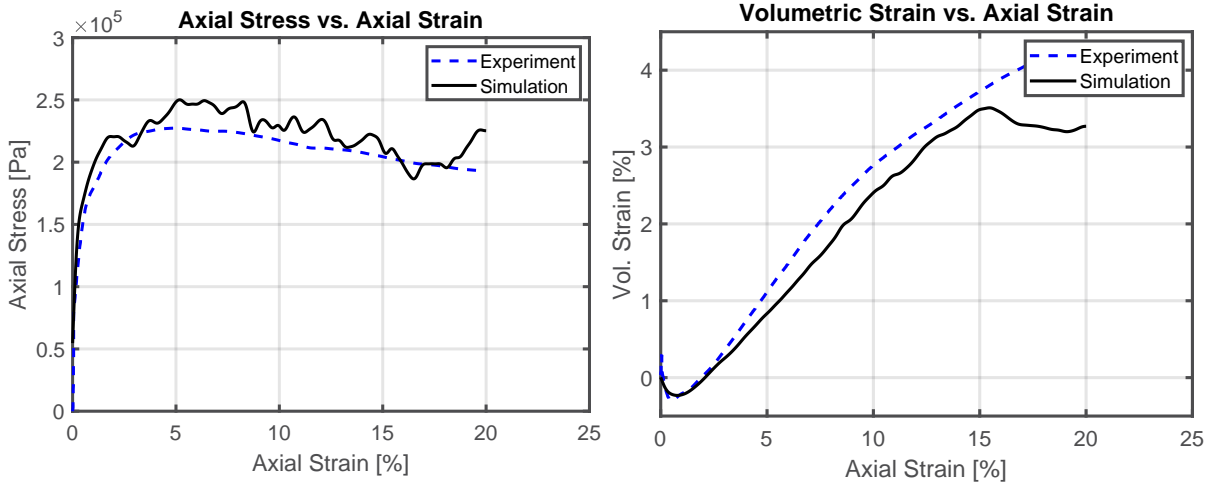
Figure 4: Simulation results of triaxial compression test and comparison to measurement for sand $\mathcal{P}(A)$, the side-wall pressure corresponds to $\sigma_2 = \sigma_3 = 50$ kPa.
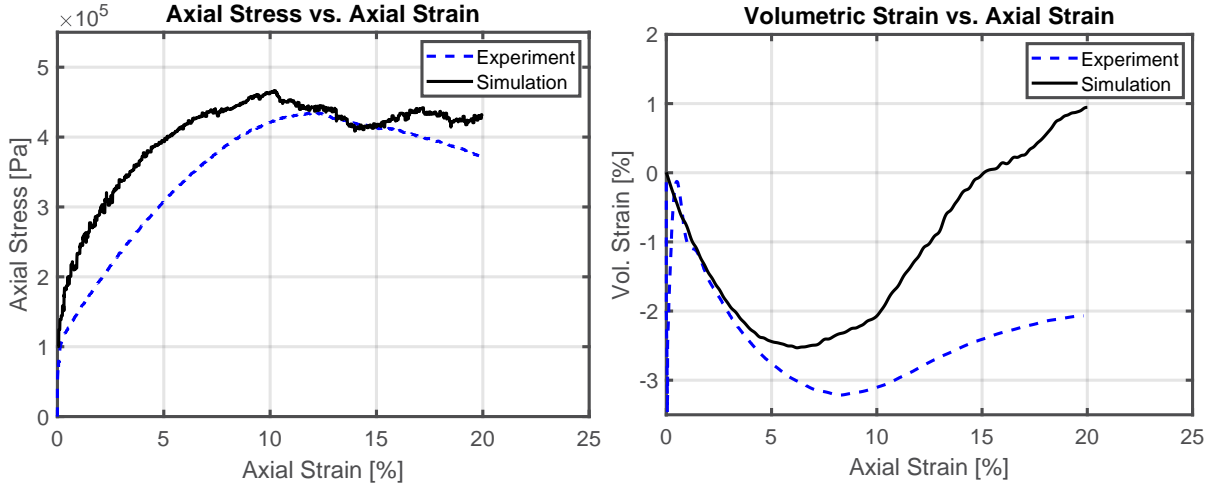
Figure 5: Simulation results of triaxial compression test and comparison to measurement for silt $\mathcal{P}(B)$, the side-wall pressure corresponds to $\sigma_2 = \sigma_3 = 80$ kPa.

minutes. This is not feasible in the simulation. We started with a simulation time of 30 to 60 seconds. As an estimate for the total time, we use the concept of the inertia number as introduced by [14] and [10]. More specifically, we consider the dimensionless number

$$ I = 2\dot{\gamma}r\sqrt{\frac{\rho_g}{p}}, \tag{8} $$

where $\dot{\gamma}$ denotes the shear velocity, in our case we assume it to account for the amount of penetration distance per time, r the particle radius, ρ_g the density of the granular material and p the typical pressure. Da Cruz et al. [10, 18] report that the inertia number should not exceed 10^{-2} in order to remain in the quasi-static regime. The inertia number for our shallow penetration simulations suggest, that also smaller total time intervals lead to quasi-static simulations. The experimental time is in the range of 25 minutes, whereas

for the total simulation time we chose $t = 1$ s. Internal studies have shown that the simulation time does not seem to have a big influence on the total force output in vertical z-direction, working with quasi-static loads. Here, we simulate soil sample geometries of the same size as in the experiment, that is of height 200 mm and diameter of 290 mm. To save computation time it might be sufficient to have at least ten particles in each direction in order to obtain a good approximation of the bulk behavior. It should thus suffice to shrink the container, depending on the particle radius. We consider virtual soil samples for (A) and (B) with interaction parameters $\mathcal{P}(A)$ and $\mathcal{P}(B)$, simulate the corresponding penetration tests and compare the resulting particle reaction forces on the penetrator with the measured reaction forces in the experiment. The results show that
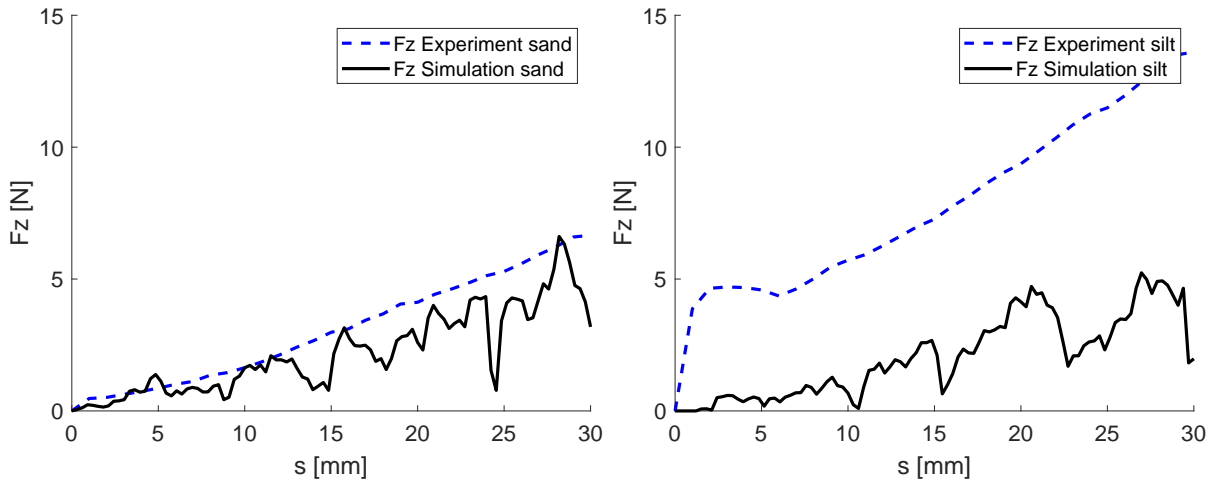
Figure 6: Force results with respect to the penetratration depth s of the shallow small scale penetration test; we obtain the penetration depth of 30 mm in a total simulation time of 1 second.

the reproduction of the observed behavior for the penetration in sand is satisfactory, see Figure 6 (left). In contrast, the simulated values for the indentation resistance in the silt-sand mixture are considerably lower than those observed in the tests. The latter show a sudden increase immediately after the start of the test, followed by a plateau and a monotonic increase in resistance. It seems that for this type of fine-grained material the DEM modeling is not capable in accurately reproducing both the triaxial compression test and the penetration test. Bear in mind that the shallow penetration of the flat-ended rod induces stress-singularity along the edge of the base contact area that considerably complicates matters. The unsteady nature of the simulated force reaction curve may arise because of the enlarged particle radii. The flat surface of the rod tip gives room for a limited number of particles. Each particle-tool interaction leads to a force jump. For large tool geometries such as plates and excavation tools, we expect some averaging effect, but for the small area of the rod, these impacts clearly influence the force output.

6 Discussion and conclusion

The procedure outlined in this presentation delivers a calibrated set of parameters that is validated on a boundary value problem. The force amplitude matches the result

obtained from the measurement on sand. The oscillations in the simulation results as shown in Figure 6, may be due to the larger particle radii. Thus only few particles collide with the tool which leads to unsteady force output.

The simulation underestimates the force response of the finer material. Here, our DEM model seems to have reached its limitations. Mainly three difficulties come into play. First, the fine-grained nature of silt is difficult to reproduce with the DEM. Scaling the grain-size distribution is challenging. Second, although the measured cohesion of $c_B = 0.5$ kPa is relatively low, it still maybe inaccurate to ignore it. And third, the surface effects of the shallow cone penetration test seem very difficult to model and the Discrete Element Method may not be able to capture this behavior.

The parametrization procedure relies upon simulation and careful selection of the interaction parameters. An automated procedure would be favorable. The collected data, generated during the simulation process may be used to find a good initial guess regarding future soil parametrizations.

Acknowledgement

REFERENCES

[1] Obermayr, M., Dressler, K., Vrettos, C. and Eberhard, P. Prediction of draft forces in cohesionless soil with the Discrete Element Method. *Journal of Terramechanics* (2011) **48(5)**:347–358.

[2] Obermayr, M., Dressler, K., Vrettos, C. and Eberhard, P. A bonded-particle model for cemented sand. *Computers and Geotechnics* (2013) **49**:299–313.

[3] Obermayr, M., Vrettos, C., Eberhard, P. and Däuwel, T. A discrete element model and its experimental validation for the prediction of draft forces in cohesive soil. *Journal of Terramechanics* (2014) **53**:93–104.

[4] Balzer, M., Burger, M., Däuwel, T., Ekevid, T., Steidel, S. and Weber, D. Coupling DEM Particles to MBS Wheel Loader via Co-Simulation . In *Proceedings of the 4th Commercial Vehicle Technology Symposium, Kaiserslautern* (2016):479–488.

[5] Burger, M., Dressler, K., Ekevid, T., Steidel, S. and Weber, D. Coupling a DEM material model to multibody construction equipment. In *Proceedings of the ECCOMAS Thematic Conference on Multibody Dynamics 2017* (2017):417–424.

[6] Goodin, C. and Priddy, J. D. Comparison of SPH simulations and cone index tests for cohesive soils. *Journal of Terramechanics* (2016) **66**:49–57.

[7] Stanier, S. A. and White, D. J. Shallow Penetrometer Penetration Resistance. *J. Geotech. Geoenviron. Eng.* (2015) **141(3)**:04014117.

[8] Asaf, Z., Rubinstein, D. and Shmulevich, I. Determination of discrete element model parameters required for soil tillage. *Soil and Tillage Research* (2007) **92(1)**:227–242.

[9] Vrettos, C., Becker, A., Merz, K. and Witte, L. Penetration Tests in a Mold on Regolith Quasi-Analogues at Different Relative Densities. In *Earth and Space 2014: Engineering for Extreme Environments* (2014):10–15.

[10] Obermayr, M. *Prediction of Load Data for Construction Equipment using the Discrete Element Method.* PhD thesis, Universität Stuttgart, Shaker Verlag (2013).

[11] Jahnke, J., Steidel, S., Burger, M. and Simeon, B. Efficient Particle Simulation Using a Two-Phase DEM-Lookup Approach. In *Proceedings of the ECCOMAS Thematic Conference on Multibody Dynamics 2019* (2019).

[12] Cundall, P. and Strack, O. A discrete numerical model for granular assemblies. *Geotechnique* (1979) **29**:47–65.

[13] Zhu, H., Zhou, Z., Yang, R. and Yu, A. Discrete particle simulation of particulate systems: Theoretical developments. *Chemical Engineering Science* (2007) **62(13)**:3378–3396.

[14] O'Sullivan, C. *Particulate Discrete Element Modelling.* CRC Press (2011).

[15] Renzo, A. D. and Maio, F. P. D. Comparison of contact-force models for the simulation of collisions in DEM-based granular flow codes. *Chemical Engineering Science* (2004) **59(3)**:525–541.

[16] Feng, Y., Han, K., Owen, D. and Loughran, J. On upscaling of discrete element models: similarity principles. *Engineering Computations* (2009) **26(6)**:599–609.

[17] Belheine, N., Plassiard, J., Donze, F., Darve, F. and Seridi, A. Numerical simulation of drained triaxial test using 3D discrete element modeling. *Computers and Geotechnics* (2009) **36**:320–331.

[18] da Cruz, F., Emam, S., Prochnow, M., Roux, J.-N. and Chevoir, F. Rheophysics of dense granular materials: Discrete simulation of plane shear flows. *Phys. Rev. E* (2005) **72**:021309.

PARTICLE-STRUCTURE INTERACTION USING CAD-BASED BOUNDARY DESCRIPTIONS AND ISOGEOMETRIC B-REP ANALYSIS (IBRA)

T. Teschemacher[1], M. A. Celigueta[2], G. Casas Gonzalez[3], R. Wüchner[4] and K.-U. Bletzinger[5]

[1] Technical University of Munich (TUM)
Arcisstr. 21
80333 Munich, Germany
tobias.teschemacher@tum.de
[4]wuechner@tum.de
[5]kub@tum.de

[2] International Centre for Numerical Methods in Engineering (CIMNE)
CIMNE - Edifici C1
Campus Nord UPC C/
Gran Capità, S/N
08034 Barcelona, Spain
maceli@cimne.upc.edu
[3]gcasas@cimne.upc.edu

Key words: CAD-integrated analysis, Isogeometric Analysis (IGA), DEM, FEM, Contact Problems

Abstract. The procedure and the properties with the use of NURBS-described CAD models in particle-structure interaction are presented within this contribution. This implies the needed entities of those models and the description of trimmed multipatches to discretize analysis suitable numerical models. Finally, the properties will be shown with some test cases in comparison to analytical benchmarks and simulations with FEM as boundary description.

1 INTRODUCTION

The integration of design in the simulation process became progressively important to allow more advanced monitoring, designing and modeling processes and higher qualities in solutions. Thus, the development of so called isogeometric methods raised and gained significance in science and industry. Those methods allow to bridge the gap between computer aided design (CAD) and numerical simulation without meshing or surface tesselation. Thus, no additional model error is introduced and the solution quality and convergence rate can be increased.

The given properties of the so called isogeometric B-Rep Analysis (IBRA) [1] can additionally be taken into account for different numerical methods in multiphysic simu-

(a) Rendered perspective view of CAD model.

(b) Untrimmed patches in transparent.

(c) Exploded view of multi-patches.
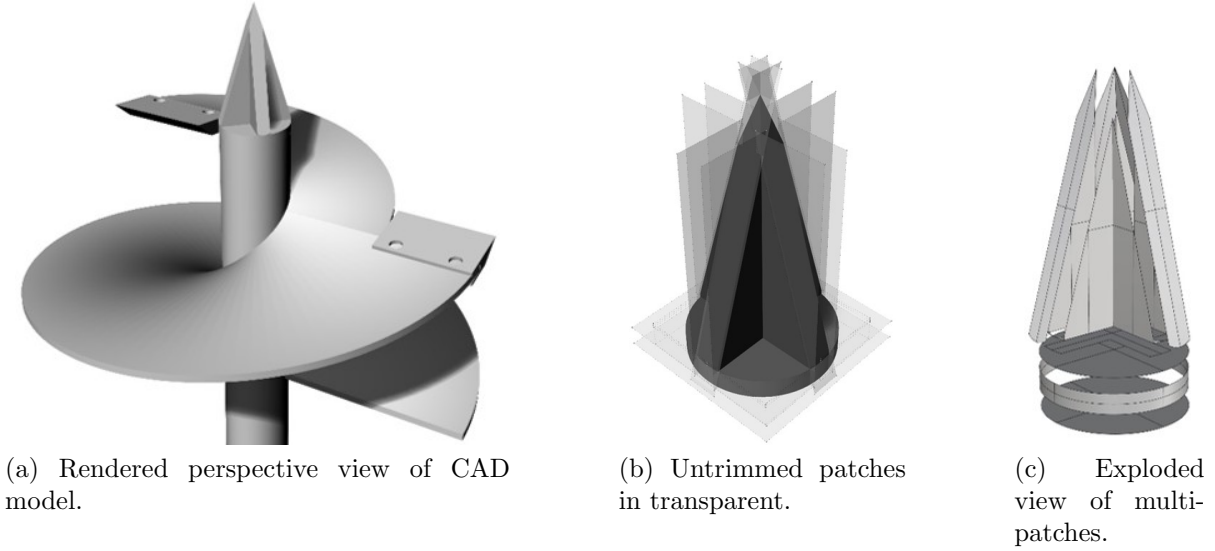
Figure 1: NURBS-based B-Rep CAD model of a soil driller. The hat of the driller is displayed once with the untrimmed patch descriptions and once with the exploded view of the trimmed patches of the structure.

lations. In those coupled approaches, the isogeometric description can be used as spatial delineation of boundaries but the structure can also interact and move with the external impacts. This means that using isogeometrically described structures in interaction with discrete particles, can provide more accurate results and allows to use the modeling advantages given due to the CAD integration.

2 ISOGEOMETRIC B-REP ANALYSIS (IBRA)

The *Isogeometric B-Rep Analysis* [1] can be seen as an extension to the *Isogeometric Analysis* (IGA) [3]. It enhances the approach with the spacial delineation of the NURBS-described geometry objects. IGA focuses on the use of surfaces (called patches) and curves, whereas IBRA allows to use cut, trimmed and coupled entities.

2.1 CAD model and Boundary Representation (B-Rep)

In Computer Aided Design, B-Rep is an approach to describe physical objects using their boundaries. It is containing to parts:

- *geometry* - defines the shape and the spatial position, curvature, ...

- *topology* - allows to link between geometrical entities and to enhance additional geometrical and physical information.

The three main topology entities are the *faces*, *edges* and *vertices*. That means, solids are described by a set of enclosing surfaces, faces by a surface and a set of underlying curves and edges by a curve and the boundary points. With this data type complex shapes can be described efficiently. In figure 1 is shown a advanced CAD-model which

344

(a) One surface

(b) Trimmed surface
boundary edge

(c) Multiple
projections

(d) Multiple
surfaces

(e) One surface and one
boundary
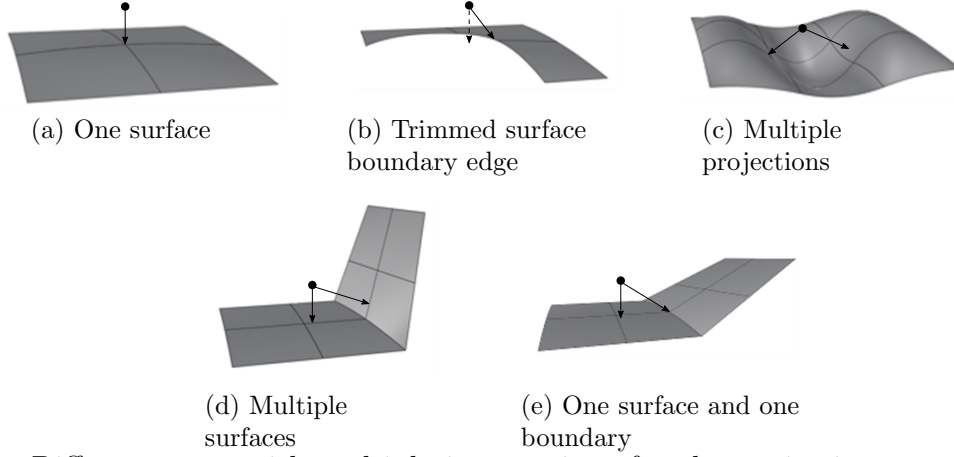
Figure 2: Different cases with multiple intersections for the projection towards B-Rep described NURBS-surfaces.

its respective components. Further information about how CAD-integrated simulations can be performed for structural analysis can be found in [1, 2]. Here are shown the requirements for analysis suitable CAD models.

2.2 Intersection with DEM-particles

Considering the high complexity of CAD models, many possible scenarios need to be considered. The most important cases are shown in figure 2.

(a) shows the standard case, of an interface within the middle of a surface.

(b) shows that the case not the closest point towards the surface is relevant because with trimmed patches, the closest point could be cut off.

(c-e) show special cases with multiple intersections. Here, more contact projections need to be performed.

With those intersections the needed interfaces can be formulated. Those need to transfer forces from the DEM particles to the IBRA geometries and obtain in return the distance, the relative displacement of the contact point within the last time step and the velocity of it. In IBRA one can not obtain the interface values directly on the degree of freedoms, thus, those have to be applied related to the shape functions of the location. The displacement and velocity at the interface point are computed as following. Those values are mapped to the discrete elements:

$$\mathbf{u}^j = \sum_{i=0}^{n_{cp}} N^i \cdot \mathbf{u}_{cp}^i; \quad \dot{\mathbf{u}}^j = \sum_{i=0}^{n_{cp}} N^i \cdot \dot{\mathbf{u}}_{cp}^i \qquad (1)$$

3 ANALYTICAL BENCHMARKS

In the following some benchmarks shall be described, to see, that with the use of the continuous NURBS-background the solution quality can be improved significantly. First, an example on a flat surface will be compared to the analytical solution and to a FEM simulation within the same solver framework. Second, an example on a curved shape will be either simulated on the exact geometry of the background and on a linearized discretization.

3.1 Sliding and Rolling Sphere

The following example has a particle rolling and sliding with an initial velocity over a flat plate. After a certain time the ball will slow down and keeps on rolling. The description of this problem is shown in figure 3. The simulation results are shown in figure 4. The comparison between IBRA, FEM and anyltical solution is described in table 1. The properties and the analytical solution of this simulation are adapted from [5]. With decreasing the time step, especially in the critical point, when the sliding stops and only rolling occurs, the results can be improved significantly.

To prove the generality of this approach different surface discretizations are tested with the same example. The surfaces were varied with a distortion of the control points and with multiple overlapping, coupled and trimmed patches. Some of the tested cases are shown in figure 5. It was possible to prove that the solution is not dependent on the modeling, as it is with finite elements, check table 1. As the solutions are identical, the results are not displayed separately.

Physical Properties:
- Initial velocity: 5 $\frac{m}{s}$
- Radius r: 0.3m
- Friction coefficient: 0.3
- Young's modulus: 1e10
- Poisson's Ratio: 0.0
- Gravitiy: [0.0, 0.0, -9.81]

Solver Properties:
- Time step: 1e-5 s
- Neighbour search freq.: 1
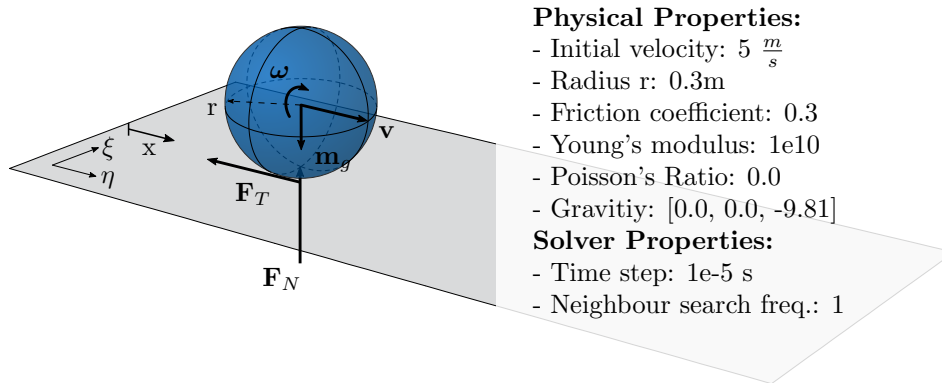
Figure 3: Description with physical and solver properties of ball rolling and sliding on plate.

3.2 Sphere Rolling on Brachistochrone

The Brachistochrone is one of the oldest optimization problems. It optimizes the shape of a surface on which a ball rolls the fastest from a higher point to lower one. The outcome is a curved surface with a new lowest point. For the chosen problem, the shape of the
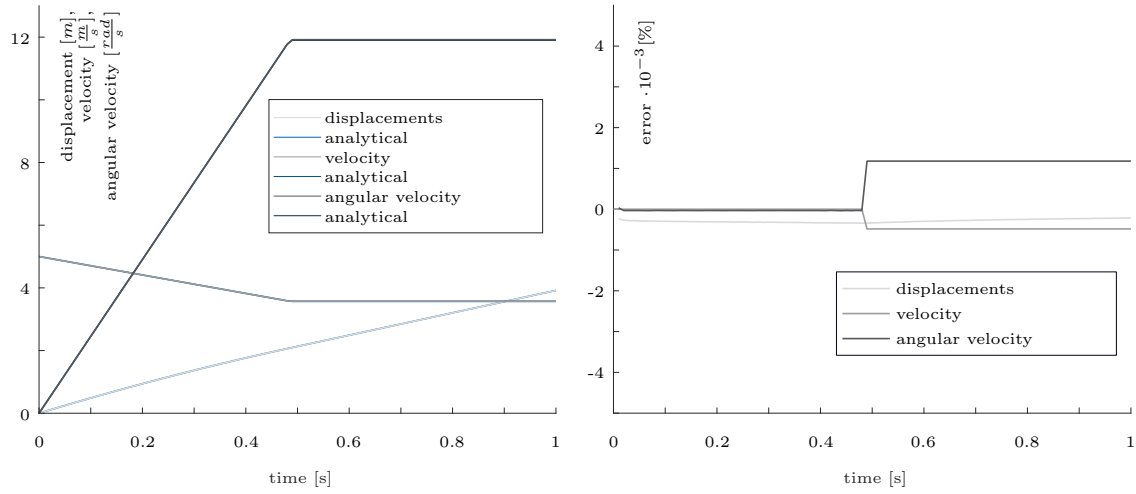
Figure 4: Comparison of analytical solution with coupled IBRA simulation.

	distance [m]	velocity $\left[\frac{\mathrm{m}}{\mathrm{s}}\right]$
Analytical solution	3.9182	3.5714
Quadrilateral mesh [5]	3.9021	3.5410
Triangle mesh [5]	3.9022	3.5410
IBRA	3.9173	3.5697

Table 1: Comparison of IBRA, 2 FEM discretizations and the analytical solution for sliding and rolling sphere on plate.
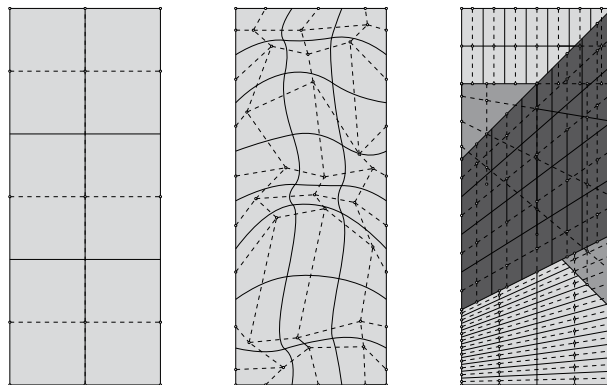
Figure 5: Different surface discretizations with same shape.
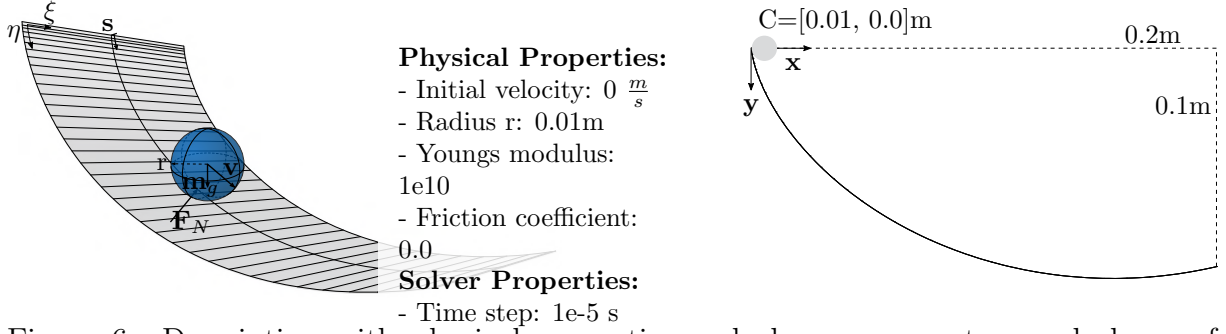
Figure 6: Description with physical properties and chosen parameters and shape of Brachistochrone.
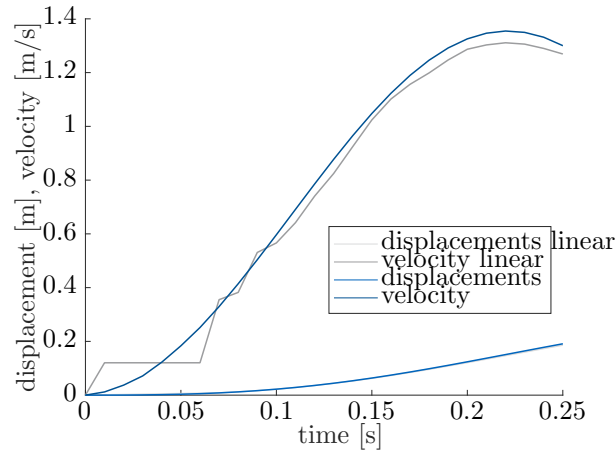
Figure 7: Comparison of displacement and velocity between the two discreizations: linear (gray) and high order (blue).

surface is described by:

$$x(s) = r(s - \sin s)$$
$$y(s) = r(1 - \cos s) \tag{2}$$

In figure 6 is shown the surface and all the chosen parameters for the simulation. This example is adapted from [5]. This example is an ideal showcase to see that with a linearized surface, as a mesh, the solution weakens significantly in comparison to the exact geometry of the NURBS-surface.

In figure 7 is shown the comparison of the two different boundary walls. It can be seen that the sphere is jumping away after each section, within the linearized shape. This error can be reduced, by reducing the youngs modulus, however, this is not preferred in this case as then, the model would be modified. In this case one can see the advantages of using the exact surface as boundary delineation.

4 CONCLUSIONS

In this contribution the IBRA part was used as fixed boundary, however, it can also be extended in a multiphysics environment with a physical counter part on the IBRA surfaces, as for examples in [4]. Further, the complexity of the CAD models can also be improved, which was already tested and will be shown in upcoming publications.

The displayed approach, to use IBRA as boundary walls for DEM, eases the simulation process, the modeling procedure and can increase the solution quality and the stability of the simulation. The advantages of using IBRA are summarized as following:

- No additional model, as linearized FEM-meshes need to be introduced. This allows a direct cast from CAD to the solver.

- Keeping the geometry description and the high-order shape avoids to introduce modeling errors. This is essential for simulations, where a high accuracy is needed. The advantages of NURBS can be seen especially with e.g. bearings, curve shapes as cones, ...

- The continuous shape needs less contact interfaces and thus less evaluation of interface areas. At the mesh boundaries special treatment need to be done to keep physical correctness. IBRA keeps the full patches which are generally bigger and thus, not that many cell jumps are occurring. For some simulation this can lead to a higher stability and a better quality.

Disadvantages with the use of CAD models:

- Higher complexity of CAD model in comparison to linearized meshes. Models need to be included with the entire CAD topology and have to be treated accordingly. However, this additional information can also be advantageous in certain parts of the simulation.

- CAD models which are used for design can come with a not sufficient quality for numerical analyses. The same problem occurs if those need to be meshed, however, sometimes mesh cleaning can be simpler than CAD model cleaning.

- Depending on the model, higher computational costs for projections, including special treatment of the contact interface points (see figure 2). Need of considering multiple local optima in one boundary object for the contact to the DEM-particles.

REFERENCES

[1] Breitenberger, M.; Apostolatos, A.; Philipp B.; Wüchner R. and Bletzinger K.-U., Analysis in computer aided design: Nonlinear isogeometric b-rep analysis of shell structures. *Computer Methods in Applied Mechanics and Engineering*, (2015) **284**:401–457.

[2] Teschemacher, T.; Bauer, A.M.; Oberbichler, T.; Breitenberger, M.; Rossi, R.; Wüchner, R. and Bletzinger K.-U., Realization of CAD-integrated shell simulation based on isogeometric B-Rep analysis. *Advanced Modeling and Simulation in Engineering Sciences*, (2018) **5**:19.

[3] Hughes, T.J.R.; Cottrell, J.A.; Bazilevs, Y., Isogeometric analysis: CAD, finite elements, NURBS, exact geometry and mesh refinement. *Computer Methods in Applied Mechanics and Engineering*, (2005) **194**:4135–4195.

[4] Casas, G.; Mukherjee, D.; Celigueta, M.A., Zohdi, T.I., Oñate, E., A modular, partitioned, discrete element framework for industrial grain distribution systems with rotating machinery. *Computational Particle Mechanics*, (2017) **4**:181–198.

[5] Santasusana, M., Irazábal, J., Oñate, E. and Carbonell J. M., The Double Hierarchy Method. A parallel 3D contact method for the interaction of spherical particles with rigid FE boundaries using the DEM. *Computational Particle Mechanics*, (2016) **3**:407–428.

REBOUND CHARACTERISTICS OF COMPLEX PARTICLE GEOMETRIES

PAUL PIRCHER[1], ERIC FIMBINGER[2]

[1] Chair of Mining Engineering and Mineral Economics -
Conveying Technology and Design Methods
Montanuniversität Leoben (University of Leoben)
Franz Josef-Straße 18, 8700 Leoben
e-mail: paul.pircher@unileoben.ac.at
webpage: https://bergbaukunde.unileoben.ac.at/en/

[2] Chair of Mining Engineering and Mineral Economics -
Conveying Technology and Design Methods
Montanuniversität Leoben (University of Leoben)
Franz Josef-Straße 18, 8700 Leoben
e-mail: eric.fimbinger@unileoben.ac.at
webpage: https://bergbaukunde.unileoben.ac.at/en/

Key words: DEM, Complex Particle Geometries, Primitive Forms, Rebound Behaviour

Abstract. Digital analysation method for the characterisation of rebound effects of non-spherical DEM-particles:

For the modelling of bulk material in DEM-simulations spherical particles are usually used. Due to their simple form and regarding the computational effort, such spherical particles offer an efficient modelling of bulk material with sufficient accuracy. However, spherical particles may lead to falsified results, especially in the case of highly non-spherical bulk materials (e.g. cylindrical pellets) or when certain effects are analysed in detail (e.g. rebound directions of particles). In general, the contact behaviour of complex particles is very different from the behaviour of idealised, spherical shaped particles. In this project a method was developed to analyse and compare the diverging rebound behaviours of different particle shapes: Particles with complex geometry are moved against a plane surface and the resulting rebound directions are detected. These directions are processed and the distinct rebound direction distribution characterises the analysed particle geometry. This method allows the analysation of rebound characteristics of bulk material concerning the scattering effects of the bulk. Subsequently, this allows a particle geometry definition in DEM-simulations in such a way, that a simple geometry (e.g. ellipsoids or cylinders) depicts the real bulk material (e.g. grain, hot briquetted iron etc.) in terms of rebound behaviour with high accuracy. Another approach is the modification of spherical particles by repositioning their centre of mass or by adjustment of their mass moment of inertia, so that the modified particle behaves like a particle with a more complex geometry. This method enables the analysation of rebound characteristics due to the particles' geometry

and allows the modelling of complex bulk materials with simplified digital geometries. Efficient simulations with complex particle behaviour are thus made possible.

1   INTRODUCTION

Nowadays the Discrete Element Method (DEM) has a wide area of application ranging from mining industry over agriculture all the way up to pharmaceutical industry. In all those fields the DEM can be used to predict the possible outcome of conveying systems or filling procedures. For simplicity and speed of the simulation a common approach is to use spherical particles. The choice is obvious as the sphere is a natural geometry that can be easily described in terms of contact detection and force calculation. However, there are aspects that could lead to falsified results as real bulk material will almost never have a perfectly spherical shape. [1]

Therefore, the usage of complex shaped particles was needed and became more popular or rather possible. There are four ways to form a complex particle in DEM simulations:

1. Multi-spheres: In this method many spheres with different sizes are stuck together to form a complex shape. The more spheres are used, the more accurate the real shape of the material can be represented as seen below in Figure 1 [2].

Figure 1: Multispherical Particles [3]

2. Primitive forms: Calculation-optimised common geometries (ellipsoids, cylinders, cubes etc.) offer an easy way to simulate material behaviour that is different to spheres. Some examples can be seen in Figure 2.
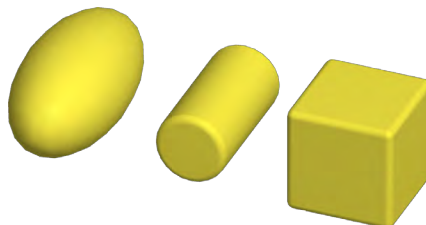
Figure 2: Primitive Forms [4]

3. Complex hybrid: Even more complex shapes can be realised if spheres and primitive shapes are combined to a new geometry. In Figure 3, a complex hybrid particle is shown. To achieve the geometry of a nail for example, a combination of two cylinders can be used.
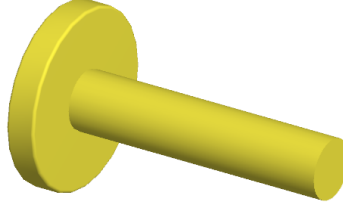
Figure 3: Compound/Complex-Hybrid Particle [4]

4. Fully complex particles: 3D-scanned particles or geometries designed in CAD-software can be implemented and used for simulation. In Figure 4, a designed flange can be seen that was imported and recalculated as a triangle mesh.
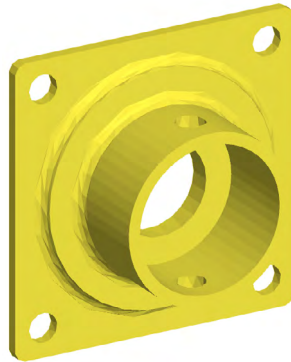
Figure 4: A flange as a DEM particle [4].

The calculation time and the computational power required to simulate more complex shapes rises significantly with the complexity of the particles.

There are a lot of differences how the particles behave if they are built up differently in the simulation [5]. For instance, if complex shaped particles are moved against a plane surface in a DEM simulation, they will rebound in a certain direction. This is due to the contact model for movement calculation that represents real particle behaviour. In the Hertz-Mindlin contact model it is built with a spring-damper system for each particle connected via a friction model [6]. As an example, the spring-damper-friction contact-system for an ellipsoid is shown in Figure 5 [7].

In Figure 6, the exact moment of contact of a particle with a part is shown for a sphere and an ellipsoid. For a sphere, the reaction force F will always be in a line with the gravitational force G. For ellipsoids this is not always the case. Depending on the

353
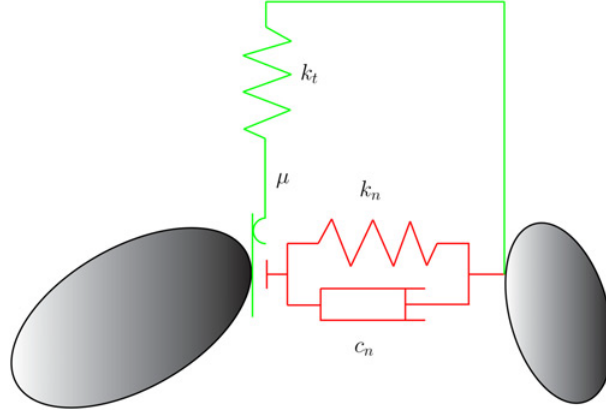
Figure 5: Mechanical contact system of two interacting ellipsoids [7]

distance r between the reaction force F and the gravitational force G of the particle, a torque momentum is initiated. Among other factors this leads to a change of rebound direction. This generated momentum of the particle has a strong influence on it's rebound behaviour. Friction between particle and surface is mandatory here (just as a tire of a car needs friction to move the car forward). That is why a strong deviation compared to spheres is expected for different geometries.
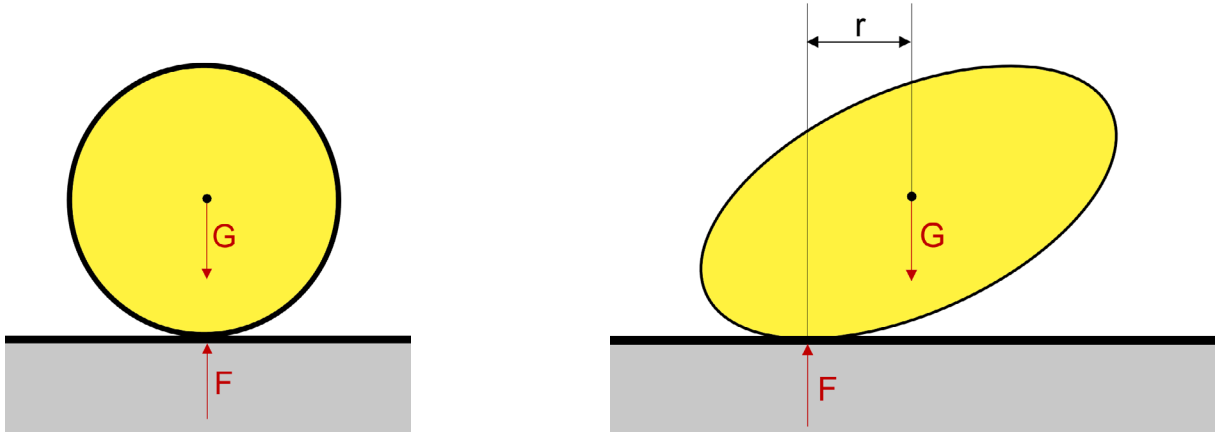
Figure 6: Generated momentum by the distance between centre of gravity and point of contact

2 Approach

The idea of this research project was to spotlight primitive forms and to determine how differently they behave compared to spheres by using the software *ThreeParticle/CAE* [4]. The focus in this project lies in the particle's rebound characteristics. As mentioned before, the entry angle of the falling particles is different to the exit angle after the rebound. To compare primitive forms to each other, shapes, that are similar to a sphere, were taken into consideration. The decision was made to examine cylinders and boxes

with rounded edges as well as ellipsoids. Spheres with a dislocated centre of mass were also studied. To actually compare those shapes, they need to have the same size. Therefore, the volume of a sphere with a certain diameter was calculated and the other shapes were then formed with the same volume.

2.1   The Parameters

To compare different particle geometries, it is required, that all simulation parameters are identical for all analysed shapes. In order to achieve this, it is mandatory to find the right value for those parameters as several of them have a strong impact on the outcome.

The general material parameters (density, shear modulus and poisson's ratio) are all attributes that need to be set to a certain value for the simulation to work. It is common to set the value for the shear modulus smaller than the real material value. This enhances the simulation speed and still provides the needed accuracy, but in this case, it should not be too small. The reason: It strongly affects the rebound angle. If the value is too small, it becomes hard to distinguish a different rebound angle as almost all particles will rebound straight up again. One can imagine this behaviour by thinking about dropping a sharp-edged cube in the middle of a trampoline. No matter how different the cube is shaped compared to a sphere, it will not affect the rebound angle significantly.

For our research the Hertz-Mindlin contact model was chosen. In *ThreeParticle/CAE* [4] three parameters can be set for this model: Restitution, static friction and rolling friction. Restitution normally has a value between zero and one and it describes the energy that is conserved after a collision of a particle with a part or another particle. It is important that it is not equal to zero as a fully elastic impact is required. For friction this works the same way. The value for static friction needs to be above zero, otherwise the momentum generated by the impact of non-spherical particles will not lead to a change of the rebound direction. As for the shear modulus mentioned above static friction has a strong influence on the rebound angle and should be chosen wisely. Rolling friction plays a minor role and can be neglected in this test. If all other parameters in DEM simulations are the same for each analysed particle, the resulting rebound direction distribution of the test characterises those analysed shapes, which can be compared to others.

2.2   The Test

To test the rebound behaviour and to receive the final rebound direction distribution, a method was developed where the difference of the rebound can be seen directly. The test consists of a generation plane, a rebound plane and a half dome as visualised in Figure 7. The generation plane of the simulation was modelled as small as possible, but still large enough so every particle can be created, in order to minimise inaccuracy. Below this plane, one particle after another is created and given an initial speed. This way the particles are moved against the rebound plane with which they interact. After their contacty they move in a certain direction in a straight line as shown in Figure 8, as gravity is disabled in this simulation. For measuring, the half dome is made up by small cone shells. Each cone shell represents a one degree interval. Each particle will touch one cone shells of

the half dome after their rebound. Here, every contact is counted for the corresponding cone shell. If the number of particles is high enough this leads to a rebound direction distribution for each analysed complex particle.
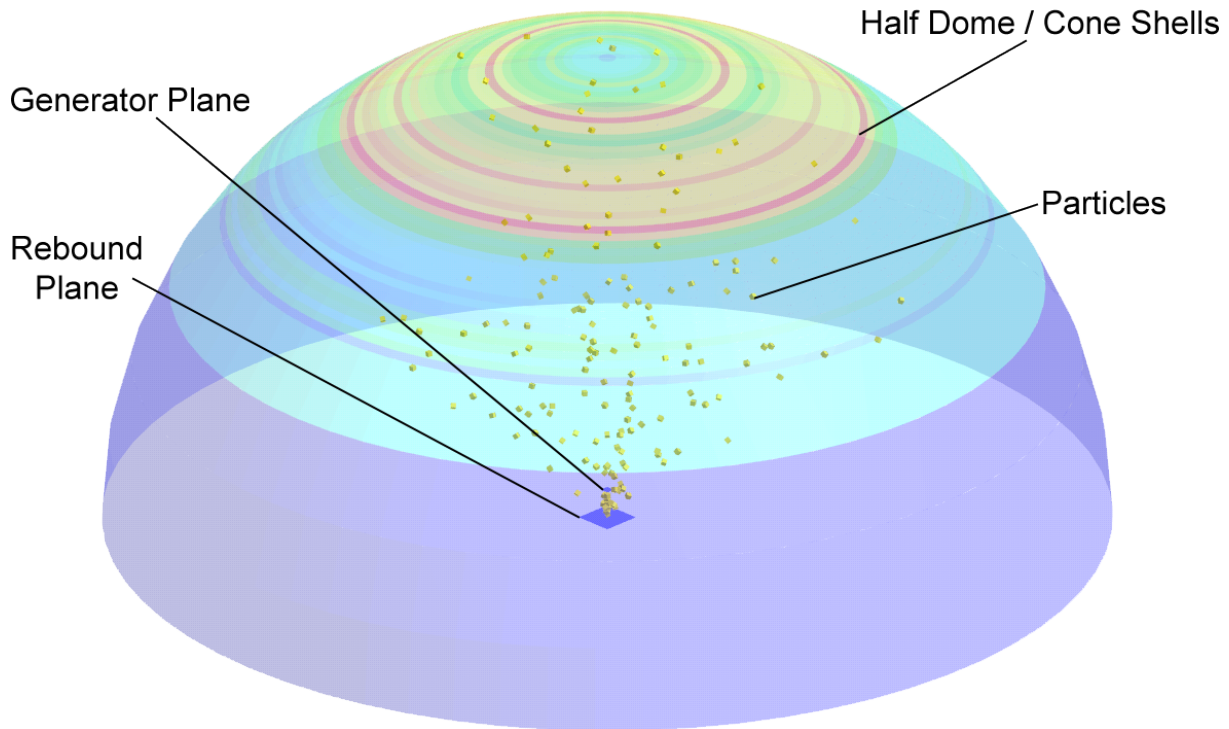
Figure 7: The test setup

3 CONCLUSION

A method was developed to receive characteristic rebound direction distributions for primitive forms of particles in DEM simulations. This way the deviation of the rebound direction compared to a spherical shaped particle can be analysed. After multiple different primitive forms have been examined, it is made possible to analyse differences in the rebound behaviour of various particle shapes. As primitive forms are relatively new to be used in common DEM software, this will be useful for the simulation of bulk material. A lot of minerals are nowadays pressed into cylindrical shapes also known as pellets or in pharmaceutical industries the ellipsoid or capsule shape are found all over the market. If precise results are required in DEM simulations it is needed to design complex particles and it is good to know in advance how they will influence the computed simulation results.

Another idea is to compare spheres with a dislocated centre of mass to primitive forms. The distance between the centre of volume and the centre of mass of a sphere can be adjusted to result in a distribution that is similar to the distribution of a complex shaped particle. The complex particle can then be exchanged in the simulation for a modified sphere. This will lead to faster simulations without neglecting complex particle behaviour.
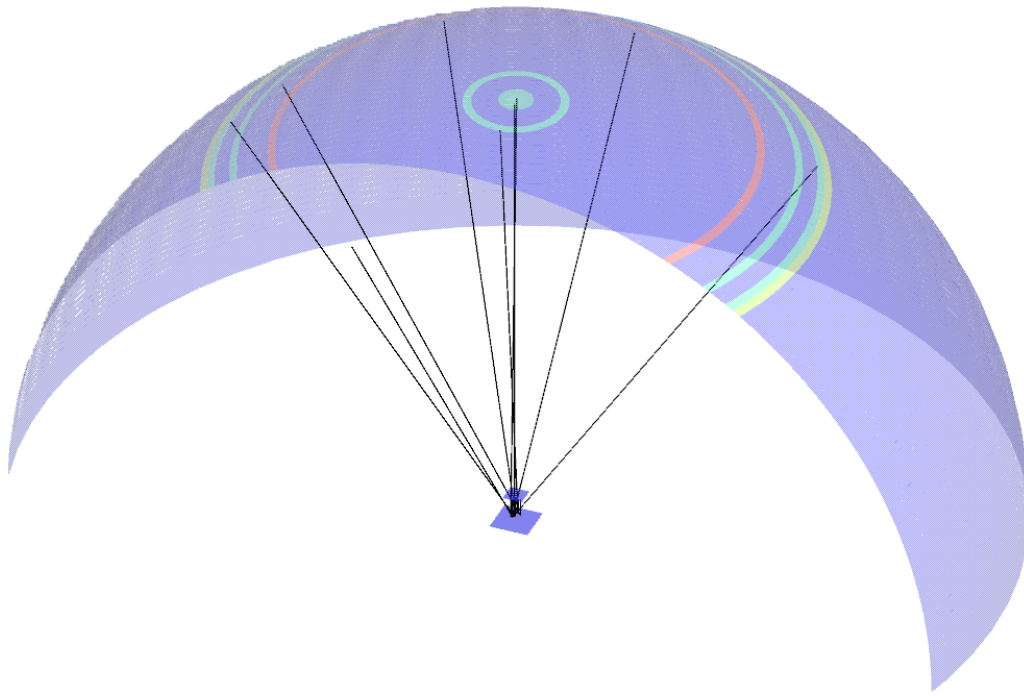
Figure 8: The streamlines of the particles

For future research, a more precise analysis method with the help of the built-in API (application programming interface) of *ThreeParticle/CAE* [4] will be developed to minimise inaccuracy as far as possible. It will then be possible to receive precise distributions for each particle and further influences of complex shaped particles in DEM simulations can be researched.

REFERENCES

[1] Ferellec, J. -F. and McDowell, G. R.(2008) *A simple method to create complex particle shapes for DEM*,Geomechanics and Geoengineering, 3:3, 211-216

[2] Peter Böhling *Modeling of non-spherical particles in the Discrete Element Method (DEM) simulations* TU Graz 2014

[3] Mathew Price, Vasile Murariu, Garry Morrison *Sphere clump generation and trajectory comparison for real particles* 2007.

[4] ThreeParticle/CAE - Multiphysics simulation software including DEM. *https://www.becker3d.com/*

[5] Christoph Pieper, Georg Maier, Florian Pfaff, Harald Kruggel-Emden, Robin Gruna, Benjamin Noack, Siegmar Wirtz, Viktor Scherer, Thomas Längle, Uwe D. Hanebeck, Jürgen Beyerer *Numerical modelling of the separation of complex shaped particles in an optical belt sorter using a DEM-CFD approach and comparison with experiments* Particles 2017 E-Book (2017).

[6] EDEM - Discrete Element Method Software. *https://www.edemsimulation.com/news/edem-for-teaching-dem-solutions-announces-launch-of-edem-classroom-edition/*

[7] Beichuan Yan, Richard A. Regueiro and Stein Sture, *Three-dimensional ellipsoidal discrete element modeling of granular materials and its coupling with finite element facets* in Engineering Computations February 2009

List of Figures

DEM SLOPE- FAILURE ANALYSIS OF THE MINAMI- ASO / TATENO AREA DURING THE 2016 KUMAMOTO EARTHQUAKES

K. ESAKI[1], H. AKAGI[1], T. KIRIYAMA[2], AND K. SATO[1]

[1] Waseda University, Department of Civil and Environmental Engineering
58-205, 3-4-1, Ohkubo, Shinjuku-ku, Tokyo, 169-8555, Japan
e-mail :esakikoichi@akane.waseda.jp, web page :
https ://www.f.waseda.jp/akagi/index_e.html

[2] Shimizu Corporation, Institute of Technology
3-4-17, Etchujima, Koto-ku, Tokyo, 135-0044, Japan
e-mail :kiriyama@shimz.co.jp, web page : https ://www.shimz.co.jp

Key words: Discrete Element Method, Kumamoto earthquakes

Abstract. The Kumamoto earthquakes, which occurred on April 16, 2016, included deep large-scale landslides in the Minami-Aso village / Tateno area; the Aso Bridge collapsed completely because of this slope failure. Aso Bridge is considered to have collapsed for various reasons, e.g., fault displacements, earthquake accelerations, and landslide sediment depositions on the bridge. In this study, the possibility of landslide-sediment depositions on the bridge was assessed as a reason for the bridge collapse using the discrete element method (DEM), and the landslides at Aso Bridge were reproduced. An experiment and analysis were conducted on the large deformation of aluminum-bar laminated ground with wall movement, to confirm the applicability of DEM to large ground-deformation problems. Next, the Aso Bridge slope-failure analysis was carried out, based on different analysis conditions, and the sediment distribution was compared with field observation results from qualitative and quantitative viewpoints. It was concluded that sediment deposition on the bridge was not a cause of the Aso Bridge failure.

1 INTRODUCTION

In recent years, concerns have been growing about geohazards triggered by earthquakes and heavy rainfall in Japan. Geohazards, e.g., slope failures and landslides, have caused heavy damage to social infrastructures. For example, the 2016 Kumamoto earthquakes that occurred on April 16, 2016, caused slope failures, landslides, and debris flow, mainly around the Aso area, and did considerable damage. Particularly, deep large-scale landslides occurred in the Minami-Aso village / Tateno area, and the Aso Bridge collapsed completely by this slope failure.

To minimize the risk of such damage, it is desirable to understand the ground-collapse process, scale, and range. However, large ground-deformation problems that range more than tens of meters have mainly been based on case studies, e.g., literature surveys and ground surveys. Along with these investigations, it is necessary to simulate the destruction process using numerical analyses, and the analyses should be evaluated using practical engineering or a physical evaluation.

The Aso Bridge might have collapsed for various reasons, e.g., fault displacements, earthquake accelerations, and landslide sediment depositions on the bridge. The definitive causes of the bridge collapse have not been determined. In this study, the possibility of landslide-sediment depositions on the bridge is assessed as a cause of the bridge collapse, using numerical analyses and reproducing the landslides at the Aso Bridge.

Finite element methods are used in engineering to evaluate the mechanical behavior of continua. However, in these methods, the mesh collapses when the ground deforms intensively in landslide simulations. Therefore, in this research, the discrete element method (DEM), which is a numerical analysis method of discrete bodies, is adopted as an analysis method. DEM was developed by Cundall [6] as a method of analyzing ground discontinuities. The applicability of the numerical analysis was evaluated from the viewpoint of large geomaterial deformations.

In this paper, an Aso Bridge slope-failure analysis is conducted. Based on Geographical Survey Institute (GSI) reports and elevation data, a 2D slope model was created of the area before the earthquake occurred. The collapse analysis was based on different analysis conditions, and the sediment distribution was compared from the qualitative and quantitative viewpoints.

2 KUMAMOTO EARTHQUAKES AND ASO BRIDGE SLOPE FAILURE

2.1 Kumamoto earthquakes in 2016

A 6.5-magnitude earthquake occurred at 9:26 pm on April 14, 2016, at a depth of about 10 km, with the Kumamoto area as the hypocenter. A seismic intensity of 7 was recorded in Mashikimachi town, Kumamoto. Then, at 1:25 am on April 16, a 7.3-magnitude earthquake occurred at a depth of about 10 km, again with the Kumamoto area as the epicenter. A seismic intensity of 7 was recorded in Mashikimachi town. The Japan Meteorological Agency identified the first as a foreshock and the second as the main earthquake.

In the foreshock on April 14, the Takano-Shirahata section of the Hinagu fault zone moved. The focal mechanism was a lateral-slip fault type with a tension axis in the north-northwest– south-southeast direction. The hypocenter fault, estimated from the aftershock distribution and focal mechanism of the earthquake, was a right-lateral slip fault extending in the north-northeast–south-southwest directions.

In the main shock on April 16, the Futagawa fault in the Futagawa fault zone moved, and the focal mechanism was a lateral-slip fault type with a tension axis in the north–south direction. The hypocenter fault estimated from the aftershock distribution and the focal mechanism of the earthquake was a right-lateral slip fault extending in the northeast–southwest direction, which included normal fault components. This Kumamoto earthquake caused construction-site runoff, river-embankment settlements, ground settlements in Aso Caldera, etc. In addition, many slope failures occurred in the Kumamoto area, including a major landslide that caused the Aso Bridge to collapse.

2.2 Slope failure of Minami Aso Tateno area

The Minami-Aso / Tateno area is located at the outer edge of the Aso Caldera, which is at the northeast end of the Futagawa fault. The eastern slope of the mountain collapsed (755.8 (m) above sea level); it is part of the Aso Caldera outer-ring mountain near Minami-Aso / Tateno.

The slope collapsed from near the top; National Road No. 57 and the main JR Hohi railway line were buried, and soil flowed into the Kurokawa River. The scale of the landslides in the Minami-Aso / Tateno area, shown in Figure 1, is estimated to be about 700 (m) in length, 200 (m) in width, 25 (m) in maximum depth, and about 500,000 (m^3) in landslide material.

The collapse range includes the JR Hohi main line, Route 57, and Route 325, which crosses the Aso Bridge over the Kurokawa River. The center of the sediment-inflow range to the river section was slightly offset from the Aso Bridge, and sediment flowed into the upper stream of the Kurokawa River. Geologically, the surface material is volcanic-ash clay (black and red) and the bedrock consists of hard andesite and semi-soft pyroclastic rock, belonging to the pre-Aso volcanic rocks. In addition, the hard andesite was confirmed to have developed fractures. The upper end of the slope was about 35 degrees steep, and the lower part was a low-gradient slope, around 15 degrees, and used as a field.
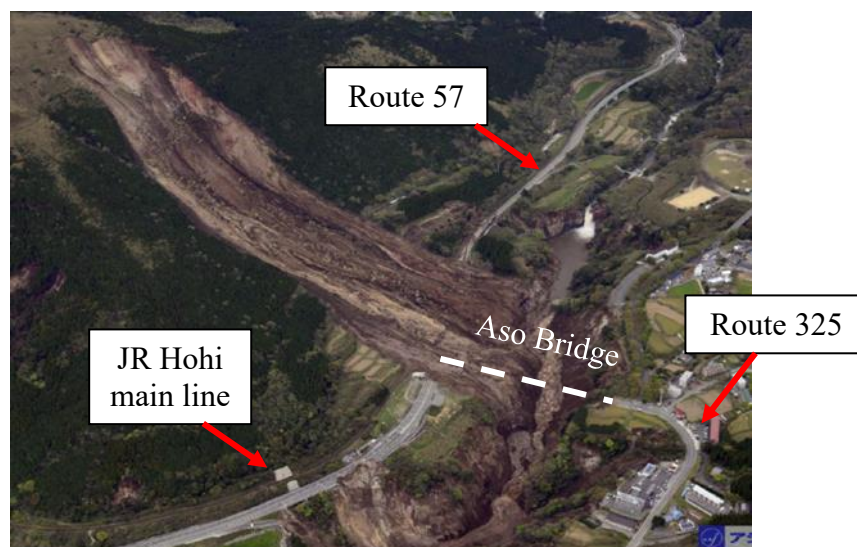
Figure 1: Slope failure of Minami Aso Tateno area [1]

3 LARGE DEFORMATION OF ALUMINUM- BAR LAMINATED GROUND WITH WALL MOVEMENT

The Aso Bridge slope was a large-scale slope failure. Thus, in this paper, the authors adopt a discrete element method (DEM) suitable for large ground-deformation analyses as a numerical analysis method. It was necessary to confirm the applicability of the DEM coded by the authors to large deformation problems. The applicability was shown by carrying out deformation experiments on aluminum-bar laminated ground with wall movement—which is a large ground-deformation problem—and comparing the experimental results with the analysis results.

3.1 Experimental apparatus and procedure

The retaining-wall test setup consists of a retaining wall and aluminum-bar laminated ground, which simulates the ground behind the retaining wall. The retaining wall is made of a rigid brass material with a height of 200 (mm), a width of 10 (mm) and a depth of 50 (mm); it can

be controlled by a handle to a horizontal displacement of 95 (mm) in the active-earth-pressure direction.

The experimental procedure is as follows. First, 200 (mm) × 50 (mm) aluminum bars are stacked. During the ground preparation, mark points for evaluating the deformation shapes are installed in the ground at 10 (mm) intervals in length and width. The ground is tightly packed, and the aluminum bars are laid as densely as possible. The aluminum bar is 50 (mm) in length, 1.6 (mm) in diameter, and 3 (mm) in circular cross section. The aluminum bars were prepared by mixing aluminum bars at a mass ratio of 2:1.

Figure 2 shows the arrangement of the retaining wall and the aluminum-bar laminated ground before the experiment. After the model ground was prepared, the retaining wall was horizontally displaced to 95 (mm) at a speed of 2 (mm/min) in the active-earth-pressure direction. The state of the experiment at that time was shot by a camera from the front of the device. From the captured video, the mark points were connected to confirm the deformation shape of the aluminum-bar laminated ground.
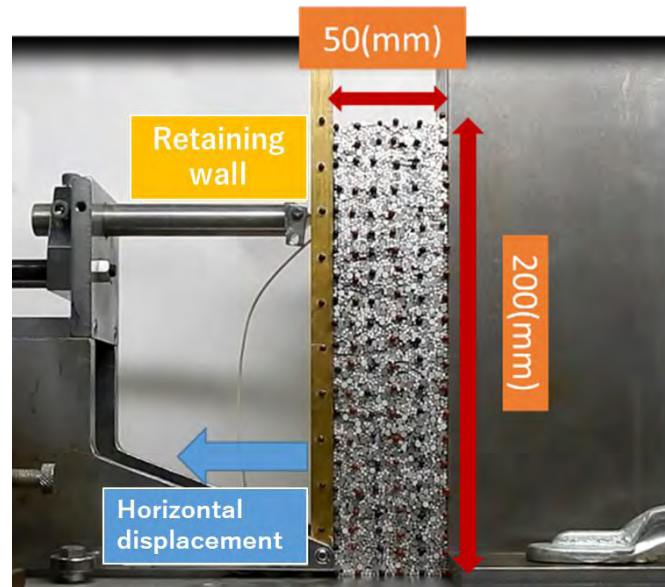
Figure 2: Retaining wall and aluminum- bar laminated ground before deformation

3.2 Analysis conditions and procedure

The DEM numerical analysis was conducted under the conditions shown in Table 1. The normal stiffness, viscous damping constant, local damping constant, and constant by which the rotational stiffness was multiplied were determined by trial calculation, considering the calculation stability. The shear stiffness was determined by introducing a reduction rate of 0.25 to the normal stiffness. The friction angle between aluminum-bar particles was shown to be 16 (°) by Matsuoka [2]. The internal friction angle was 23.5 (°) when the direct-shear test of the aluminum-bar laminated ground was conducted in previous studies [3].

In this experiment, it can be expected that the friction angle between particles will be 16 (°) or more because the friction angle between the particles changes as the granular soil changes, depending on the particles' stress state. Considering the above, the friction angle between the particles under analysis was set to 20 (°) (coefficient of friction $\mu = 0.36$). To prepare the ground

for analysis, the particles were filled using a gravity-packing method. After filling, the retaining wall was displaced at a speed of 5 (mm/s) in the active-earth-pressure direction to a displacement of 95 (mm) on analysis. The behavior of the granular material was then confirmed by visualizing. As in the experiment, mark points were installed in the ground at 10 (mm) intervals in length and width, and connected to confirm the deformation shape of the aluminum-bar laminate ground.

Table 1: Physical property values in DEM

Variable	Unit	Value
Integration time interval Δt	s	0.000002
Particle density d	g/cm^3	2.7
Normal stiffness k_n	N/m	20000000
Shear stiffness k_s	N/m	5000000
Viscous damping constant h	-	0.05
Local dumping constant α	-	0.12
Coefficient of friction μ	-	0.36
Constant- k_r by which the rotational stiffness is multiplied	-	300000

3.3 Experimental and analysis results

The analysis results were compared with experimental results. The red frame in Figure 3 is the outline of the aluminum-bar laminated ground. From the deformed figure in Figure 3, it is clear that the experimental and the analytical results correspond well at displacements of 65 (mm), 80 (mm), and 95 (mm). On the other hand, at displacements from 5 (mm) to 35 (mm), it is clear that the outline of the granular soils in the analysis result is smaller than the outline of the experimental result. This is due to the use of gravity packing to prepare the ground for analysis.

When the ground was prepared for the experiment, the aluminum bars were laid as densely as possible; however, in the gravity-packing method, the particles were not packed as densely as in the experiment. With the movement of the retaining wall, the ground volume tended to expand in the experiment and contract in the analysis. The effects of the volume expansion and contraction decreased with the movement of the retaining wall, and the outline of the experimental results and the analytical results were gradually approximated for displacements of 80 (mm) and 95 (mm), whose deformations were large.

From these results, the authors qualitatively evaluated and demonstrated the applicability of DEM to large deformation problems.

Displacement 5(mm)   Displacement 65(mm)

Displacement 20(mm)   Displacement 80(mm)

Displacement 35(mm)   Displacement 95(mm)

(a) Calculation   (b) Experiment   (c) Calculation   (d) Experiment
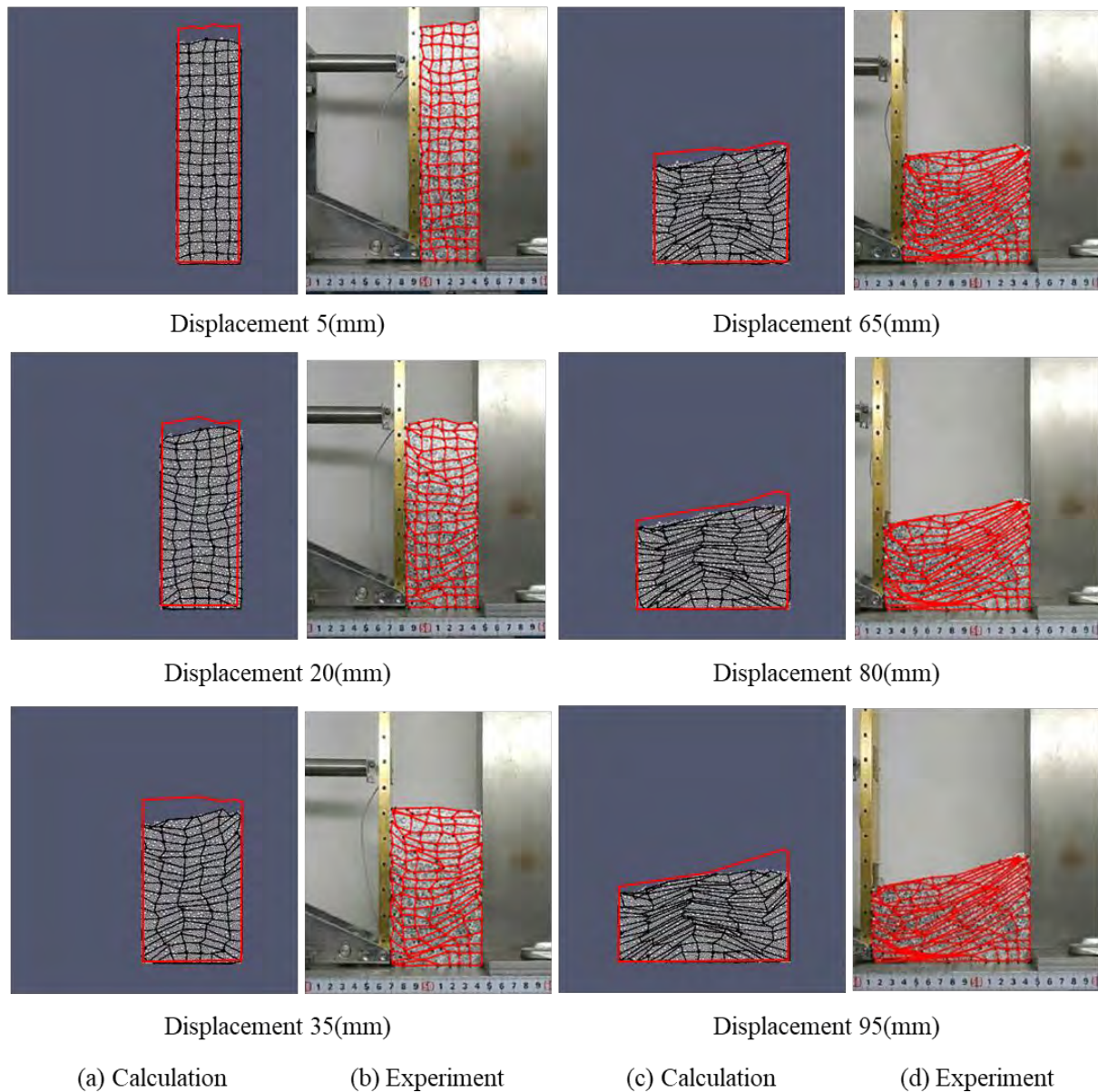
Figure 3: Comparison of deformation between analysis and experiment

4   NUMERICAL ANALYSIS OF ASO BRIDGE SLOPE FAILURE

4.1 Creation of analysis model

The field-survey report about the slope failure that occurred in the Minami-Aso / Tateno area [1] confirmed that part of the soil that collapsed on the west side of the Aso Caldera wall, which is at the top of the slope, was deposited in the middle of the slope, and most of the remainder flowed into the Kurokawa River. The scale of the collapse was about 700 (m) in length, 200 (m) in maximum width, 25 (m) in maximum depth, and 500,000 (m^3) in landslide material.

Based on the report and elevation data from the Geographical Survey Institute (GSI), a 3D

CAD model of before the earthquake occurred was created, and the flow range was estimated by comparing aerial photographs from after the earthquake with the 3D CAD model (Figure 4). Under this condition, a two-dimensional cross section in the longitudinal direction was extracted. In this section, based on the report data [3], the slope width and depth were set to 200 (m) and 25 (m), respectively (Figure 5), and the ground-surface shape was estimated, assuming the arc slip surface. A two-dimensional slope was determined (Figure 6), which approximated the estimated soil volume of 500,000 (m^3) by calculating the total soil volume on the arc-slip surface by adding the area of the small trapezoid from the slope coordinates and the coordinates of the set arc lower limit. This is the surface shape of the 2D slope-failure model used for the DEM analysis.

Longitudinal direction of flow range
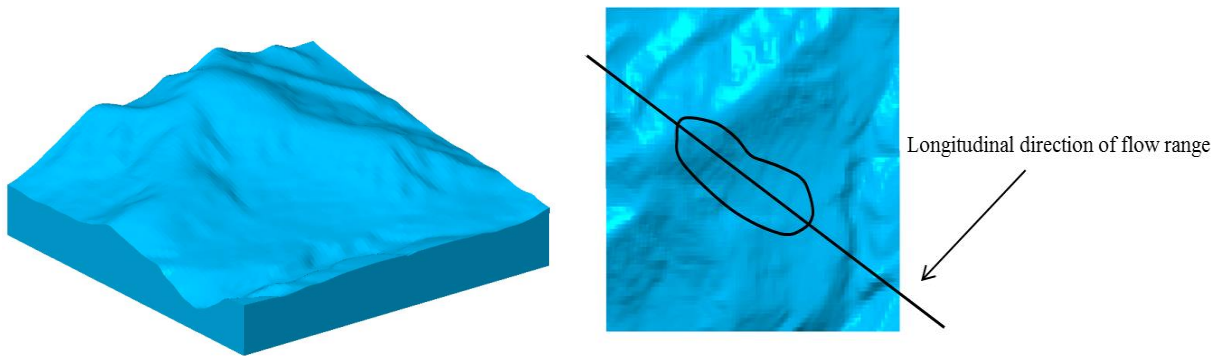
Figure 4: 3D CAD before the Kumamoto earthquake and Estimation of flow range
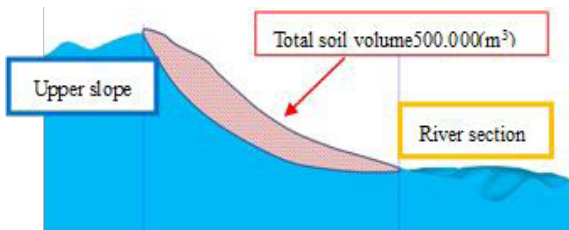
Figure 5: Estimation of slope shape by arc slip   **Figure 6**: Surface shape in analysis model
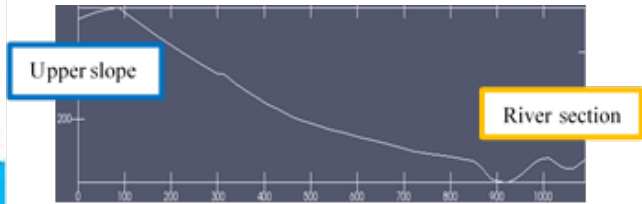
4.2 Determination of parameters and case studies

First, 0.25 (m)-diameter particles were packed using gravity packing into the collapse area in the determined ground-surface shape. A slope-failure analysis was performed, on the assumption that the filled particles reached downstream in 100 (s) by their own weight.

The physical properties used for the DEM analysis are shown in Table 2. The viscosity coefficient and the local damping constant were determined by parametric studies, considering the stability of the calculation. In this paper, the deposition shapes and flow tendency are compared for three cases by considering the cohesion force and coefficient of friction during the slope failure. The DEM analysis was performed for large (Case 1), intermediate (Case 2), and small values (Case 3). Table 3 shows the physical property values of the three cases. The analysis results were compared, and the influence of the physical property values during the slope failure in the DEM analysis was investigated.

Table 2: Physical property values used for DEM analysis

Variablle	Unit	Value
Integration time interval Δt	s	0.00002
Particle density d	g/cm^3	1.6
Normal stiffness (between particles)k_n	N/m	1.0×10^7
Shear stiffness (between particles) k_s	N/m	2.5×10^6
Normal stiffness (between particle walls)k'_n	N/m	1.0×10^8
Shear stiffness (between particle walls) k'_s	N/m	2.5×10^7
Viscosity coefficient h	$N \cdot s/m$	1.0
Local dumping constant α	-	0.05

Table 3: Physical property values of three cases

Variable	Unit	Case1	Case2	Case3
Coefficient of friction μ	-	0.58	0.27	0.18
Cohesive force k_r	kPa	10	5	2

4.3 Discussions

The analysis results of Cases 1 through 3 are compared. Figure 7 shows the initial deposition shape of the particles in the DEM analysis. The particles placed at the upper part of the slope flow onto the slope with the passage of time, are deposited on the middle part of the slope, and flow into the river. The DEM simulation results confirmed that the flow tendency, e.g., the speed in reaching the river area, and the shape of the deposition differ depending on the coefficient of friction and the cohesive force. Particularly, the greater the cohesion force and coefficient of friction, the lower the flowability, and the particles tend to stay upstream of the slope.

This tendency is evaluated by the difference in sediment distribution. As shown in Figure 8, the slope was divided into four areas (upper section, middle section 1, middle section 2, and river section), and Figure 9 shows the sediment distribution in each case. It was confirmed that the sediment distribution on the slope is different in each case.

In Case 1, the sediment flowed slowly, and most of it was deposited in the upper section and middle section 1. At 100 (s), 270,000 (m³) were deposited in the upper section, 220,000 (m³) in middle section 1, and 996 (m³) flowed into the river section.

In Case 2, the sediment passed through the upper section by 40 (s), and then was gradually deposited in the middle section. At 100 (s), about 350,000 (m³) were deposited in the upper section, 290,000 (m³) in middle section 1, 170,000 (m³) in middle section 2, and 3,675 (m³) flowed into the river section.

In Case 3, the sediment flowed quickly, and most sediment passed through the upper section by 20 (s) and converged to the final sediment-deposition state by 50 (s). About 113,000 (m³) of sediment was deposited in middle section 2, and the rest of the sediment, 380,000 (m³), flowed into the river section.

From these results, it was confirmed that the speed of the sediment arriving in the river and the deposition shape differed, depending on the coefficient of friction and the cohesion force. The disaster report [1] confirmed that, in the actual slope failure in the Minami-Aso / Tateno area, the majority (about 500,000 m^3) of the sediment that collapsed in the upper section was deposited in middle section 2 and flowed into the river section. Therefore, the authors judged Case 3 to be an appropriate analysis result, considering the sediment distribution.

Regarding the inflow sediment around the Aso Bridge, it was confirmed that the majority of the inflow sediment flowed into the upstream side of the Kurokawa River. Therefore, in Case 3, not all of the 380,000 (m^3) of sediment that flowed into the river section was deposited on the Aso Bridge. In other words, the sediment deposition on the Aso Bridge was relatively modest. Estimating from the analysis results, it was concluded that sediment deposition was unlikely to be the main reason for the collapse of the Aso Bridge.
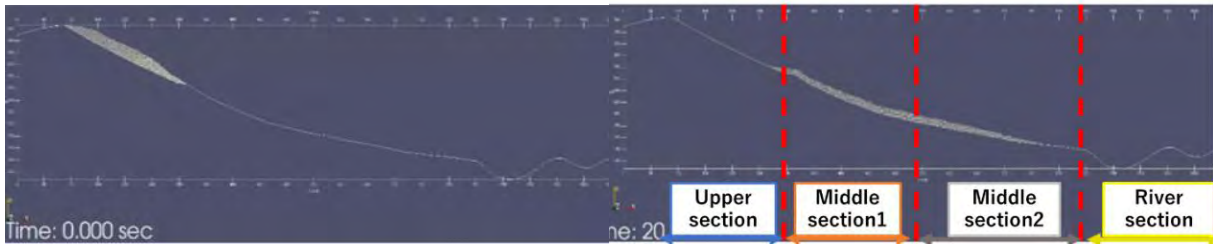
Figure 7: Initial deposition shape of DEM analysis

Figure 8: Division of slope area
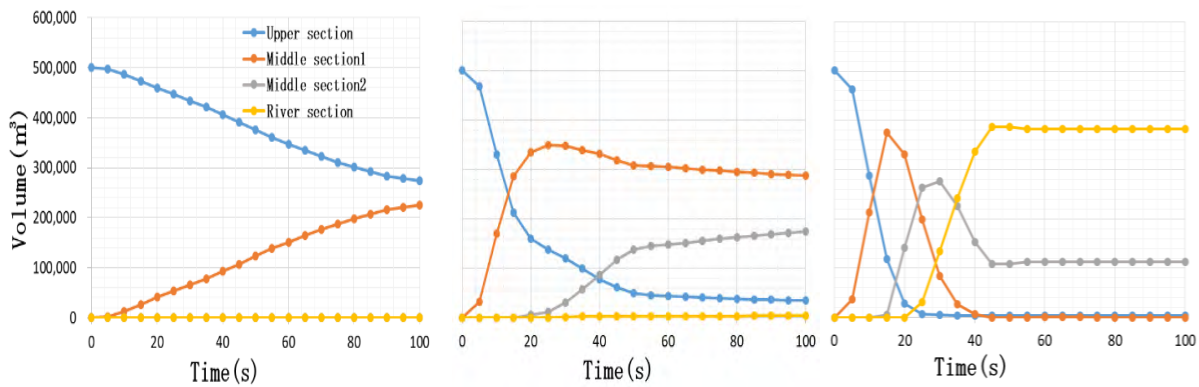
Figure 9: Sediment volume change over time at each section

367

Time 20(s)

Time 40(s)

Time 60(s)

| Case 1 | Case 2 | Case 3 |
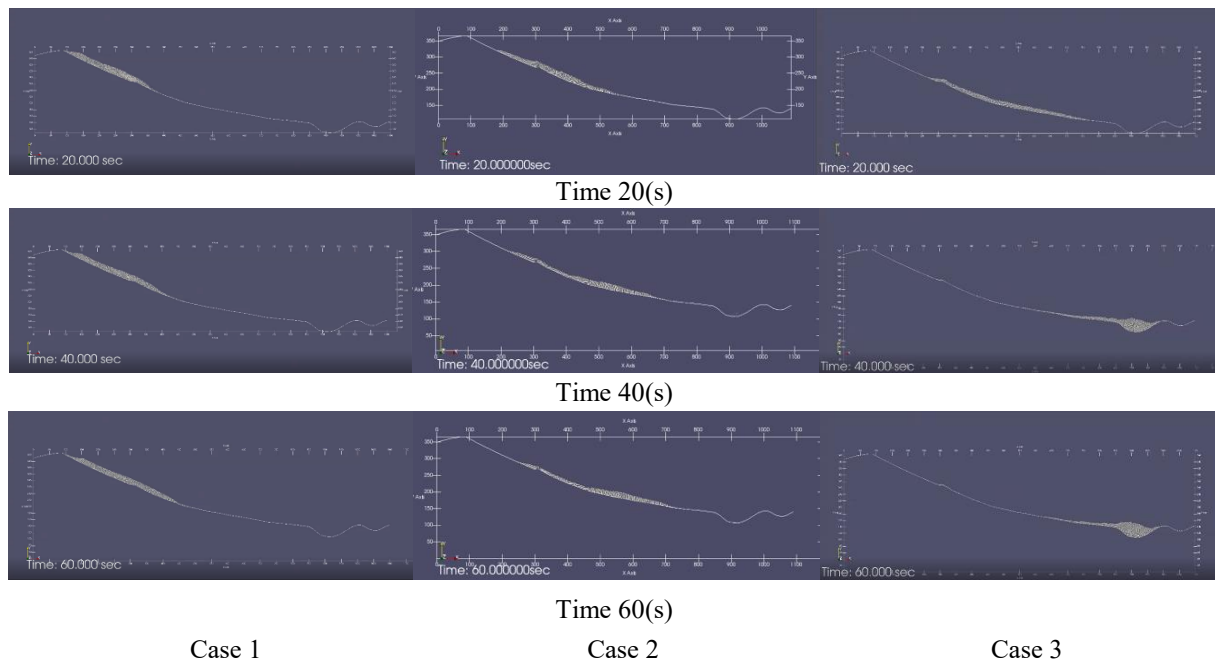
Figure 10: Sediment distribution situations

5 CONCLUSION

In this paper, the slope failure in the Minami-Aso / Tateno area during the 2016 Kumamoto earthquakes was analyzed using DEM. The deposition shape and flow tendency, due to the difference in the coefficient of friction and the adhesion force failure, were confirmed, and these tendencies were quantitatively compared and considered, regarding the difference in sediment distribution. From the final sediment deposition on the slope and the inflow to the river, Case 3, with a relatively low coefficient of friction and cohesion force, was judged to be a highly reproducible analysis result. From the estimated sediment distribution amount, the authors concluded that sediment deposition on the bridge was not a cause of the Aso Bridge failure.

A future issue is the re-examination of the sediment arrival speed in Case 3. Case 3 converges to the final deposition shape at 50 (s); however, in the actual slope failure, the sediment-flow velocity was slow. It is necessary to reexamine the viscosity coefficient and the local damping constant related to the analytical stability calculation.

REFERENCES

[1] Earth and sand disaster emergency investigation team pertaining to the 2016 Kumamoto earthquake (2016). Emergency investigation report on earth and sand disaster due to the 2016 Kumamoto earthquake, Japan Society of Erosion Control Engineering, 15–24 (in Japanese).

[2] 2016 Kumamoto Earthquake Geotechnical Disaster Investigation Team (2017). Field survey report on slope disaster caused by the 2016 Kumamoto earthquake, The Japanese Geotechnical Society (in Japanese).

[3] H. Matsuoka, K. Saiki (1992). A Measurement Method of Interparticle Friction Angle (φ_μ) of Two-Dimensional Granular Body (Round Bar), The 27th Geotechnical Engineering Conference, 579–580 (in Japanese).

[4] ITASCA (2002). PFC2D Online Manual, Table of Contents—Theory and Background—Section 1: General Formulation.

[5] Structure and landslide disaster investigation team (2016). 2016 Kumamoto earthquake survey report, International Research Institute of Disaster Science (in Japanese).

[6] P. Cundall (1987). Distinct element models of rock and soil structure, Analytical and Computational Methods in Engineering Rock Mechanics, Ch. 4, 129–163. E.T. Brown, ed., London: Allen & Unwin.

[7] K. Imada, H. Akagi, A. Saito, T. Kiriyama (2018). Slope Failure Analysis of Minami Aso Tateno District due to Kumamoto Earthquake Using DEM, The 73rd Japan Society of Civil Engineers Conference, 589–590 (in Japanese).

[8] K. Esaki, H. Akagi, A. Saito, T. Kiriyama (2018). Large deformation analysis of aluminum bar model ground with wall movement by using Discrete Element Method, The 73rd Japan Society of Civil Engineers Conference, 743–744 (in Japanese).

MICROSCOPIC CALIBRATION OF ROLLING FRICTION TO MIMIC PARTICLE SHAPE EFFECTS IN DEM

RICCARDO RORATO[1], MARCOS ARROYO[2], ANTONIO GENS[3] AND EDWARD ANDÒ[4]

[1] Universitat Politècnica de Catalunya (UPC)
Department of Civil and Environmental Engineering, 08034 Barcelona (Spain)
riccardo.rorato@upc.edu

[2] Universitat Politècnica de Catalunya (UPC)
Department of Civil and Environmental Engineering, 08034 Barcelona (Spain)
marcos.arroyo@upc.edu

[3] Universitat Politècnica de Catalunya (UPC)
Department of Civil and Environmental Engineering, 08034 Barcelona (Spain)
antonio.gens@upc.edu

[4] Université Grenoble Alpes, CNRS
Grenoble INP, 3SR, F-38000 Grenoble (France)
edward.ando@3sr-grenoble.fr

Key words: Granular Materials, DEM, Particle Shape, Rolling Resistance, Contact Problems.

Summary. *It is widely recognised that particle shape influences the mechanical response of granular materials [1-2]. Rolling resistance elasto-plastic contact models are frequently used to approximate particle shape effects in simulations using the Discrete Element Method (DEM) [3-4]. Such contact models require calibration of several micro-parameters, most importantly a rolling resistance coefficient. In this work, the rolling resistance has been calibrated to reproduce the triaxial tests – in terms of mechanical and kinematic responses – of two different sands: Hostun and Caicos sands. The value of rolling resistance is directly linked to true sphericity, a basic measure of grain shape, as originally proposed in Rorato et al. (2018) [5]. When shape measurements are performed [6], this link enables independent evaluation of the rolling resistance coefficient for each particle. It does also allow the characteristic shape variability of natural soils to be easily taken into account.*

1 INTRODUCTION

Much work has been done to characterise granular shape and to understand its influence on overall soil behavior. Thus, Wadell (1932) [7] introduced the concept of "sphericity" that quantifies how a particle differs from a sphere, in terms of surface area. Krumbein (1941) [8] presents the first chart to visually estimate shape from the grain lengths ratios.

There is much evidence showing that particle shape is relevant for mechanical responses of soils. Andò (2013, 2012) [1], [9] tested in triaxial conditions different sands with shape ranging from very angular to rounded. Using Digital Image Correlation, he showed that angular sands exhibited a larger shear band thickness compared to rounded sands. Rorato *et al.* (2019) [10] demonstrated that a rounded sand (Caicos ooids) exhibits higher grains rotations compared to an angular sand (Hostun sand).

In this work, we propose a new procedure for an optimal calibration of the DEM contact model parameters that is able to mimic the effect of particle shape without dramatically increase the computational time. In particular, our approach aims to (1) limit the number of free parameters requested, (2) respect the mechanical and kinematic triaxial responses of the sheared granular materials and (3) maintain low the computational time. The Particle Flow Code (PFC5) developed by Itasca Inc. has been used.

2 DESIGN AND ANALYSIS

The most widely used shape used in DEM is the sphere, because it allows straightforward and computationally efficient contact detection. Unfortunately, soil particles are not spheres. Some researchers has tried to tackle this challenge by introducing *non-spherical* elements, like clumps (*e.g.,* [11], [12]), polyhedrons (*e.g.,* [13], [14]) or grain-shape-inspired particles (*e.g.*, [15], [16]), at the price of increasing dramatically the complexity of the contact detection and computational time. Other researchers (*e.g.*, [3], [4], [17]) have proposed the introduction of a resisting moment (*i.e.*, rolling resistance) into the contact law, beside normal and shear forces, in order to consider the influence of flat (*i.e.,* not punctual) contacts between real grains.

In this work, a simplified version - as implemented in the PFC5 software - of the Iwashita & Oda contact model [3] has been used under the following assumptions:
(1) The *rolling stiffness* (k_r) is defined as the Iwashita & Oda's original contact model:

$$k_r = k_s R_r{}^2 \tag{1}$$

where k_s is the contact *shear stiffness* and R_r the *effective radius* defined as

$$R_r = \frac{1}{R_1} + \frac{1}{R_2} \tag{2}$$

being R_1 and R_2 the radii of the two particles in contact.
(2) The moment-rotational contact law is implemented as an elastic-perfectly plastic model with the yielding moment (M^*) defined as:

$$M^* = \mu_r F_n R_r \tag{3}$$

where μ_r is defined as *rolling friction coefficient* and F_n is the normal contact force.

This paper exploits a novel approach to relate the particle shape with the rolling resistance applied at the contacts, extending the model that was originally proposed in Rorato *et al.*

(2018) [5]. In particular, it is hypothesized that the *degree of true sphericity* [1](ψ), of one particle is univocally related with its *coefficient of rolling friction*, through a relation

$$\mu_r = F(\psi) = F\left(\frac{S_n}{S}\right) \tag{4}$$

valid for all the spherical particles participating in the DEM simulation. Therefore, if the statistical distribution of sphericity is known for one particular sand, it is possible to extract infinite values so that one measure of ψ can be assigned to each sphere of the numerical specimen, and therefore the *rolling friction coefficients* can distributed through all the discrete elements. The histograms of true sphericity for three different sands (Hostun, Caicos and Ticino sands), computed as in Rorato *et al.* (2019) [6], are showed in Figure 1.
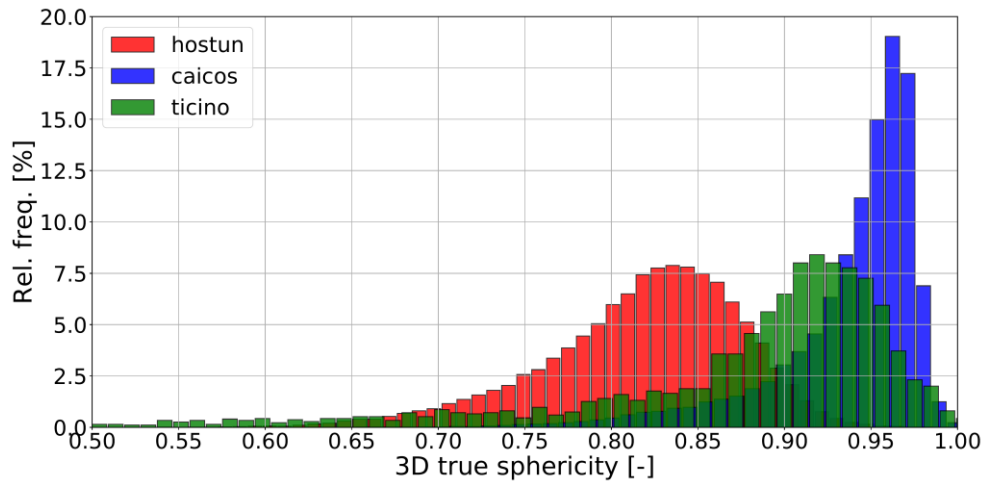
Figure 1: Statistical distributions of 3D true sphericity for Hostun, Caicos and Ticino sands.

The question then is what shape function $F(\psi)$ might take. We tried to find the equation of $F(\psi)$ that could best match the experimental triaxial tests performed on Hostun sand (specimen "HNEA01") and Caicos ooids (specimen "COEA01"). The calibration procedure here proposed aims to fit the conventional macro-mechanical responses together with kinematic measures. In particular, the histories of the cumulated grain rotations are known for each grain from the experiments have been measured and the particles rolling frictions have been adjusted to reproduce similar kinematic responses inside the shear bands of the numerical specimens. It is indeed well known from past DEM studies [18]–[21] that the same macroscopic friction angle can be obtained from several couples of *sliding friction coefficient* (μ) and *rolling friction coefficient* (μ_r). Both parameters contribute to the shear resistance of the numerical sample, and their influence is coupled. However, the rotational information - from the experimental measures of grains rotations - provides a unique numerical solution.

---

[1] Defined by Wadell (1932) [7] as the ratio between the surface area (S_n) of the equivalent sphere (*i.e.,* same volume as the grain) and the surface area (S) of the particle.

3   RESULTS AND DISCUSSION

The equation of $F(\psi)$ has been finally chosen, after an iterative procedure, according to a power law written as

$$\mu_r = 0.1963(\psi)^{-8.982} \tag{5}$$

with an upper bound fixed at $\psi = 1$ (perfect sphere).

This relationship allows a good fit of the macro-mechanical responses (*i.e.,* stress-volumetric-strain) of HNEA01 and COEA04 sand specimens and the mean rotations inside the shear bands (*i.e.,* the kinematics at failure) throughout the execution of the triaxial test.

Particles belonging to the shear bands, in both the physical and numerical specimens, have been identified according to a procedure originally proposed by Catalano [22] and detailed in Rorato *et al.* (2019) [10] for the two sand considered in this study.

The proposed approach has been then tested for validation in three different situations, achieving successful results, (1) at higher confining pressures, (2) testing a third type of sand (Ottawa sand) for which the statistical distribution of 3D sphericity was known and (3) testing a fourth type of sand (Ticino sand) for which the distribution of 3D sphericity was not known. Regarding the third case, an innovative method is exploited to determine the statistical distribution of the *degree of true sphericity* (3D shape parameter) from 2D measures, as originally proposed by Rorato *et al.* (2019) [6]. In particular, a table scanner has been used to obtain an "oriented" projection of thousands of sand grains laying on their *plane of greatest stability*. The 2D outlines of all the particles thus obtained, can be then studies by image analysis techniques in order to extrapolate[2] the statistical distribution of ψ, and therefore of μ_r, according to Eq. 5.

The values of rolling frictions obtained from Eq. (5) have been compared to the ones computed using a completely different -geometrical- approach originally proposed by Wensrich & Katterfeld (2012) [20] and then improved in [21]. In particular, they claimed that rolling resistance is originated at the micro-scale level by the eccentricity of the contact, as shown in Figure 3.
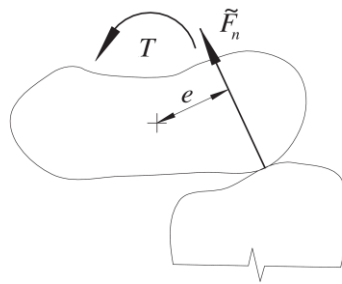
Figure 3: Contact of un-spherical particles producing a torque (*T)* due to the eccentricity (*e*) of the normal contact force (F_n) [20]

---

[2] It is known from [6] that the degree of true sphericity (ψ) is highly correlated with the *perimeter sphericity*, 2D shape parameter, after "oriented" particle projection (*i.e.,* perpendicularly to the minor particle length).

Assuming the magnitude of the torque T at the contact equal to

$$|T| = e|F_n|$$

and being M^* the limiting value of from the contact model (Eq. 3), Wensrich & Katterfeld supposed that a good estimation of the rolling friction is obtained imposing $|T| = M^*$, that leads to

$$\mu_r = \frac{\langle e \rangle}{R_r}$$

where $\langle e \rangle$ is the average eccentricity of contact over all possible contacts and R_r is the rolling radius.

In this work, we compute the values of μ_r using this approach for all the grains of HNEA01 and COEA04, and we compare them with the values obtained from Eq. 5. The average eccentricity and the rolling radius of each grain are computed numerically exploiting the vertices of the surface mesh created by the Marching Cubes algorithm implemented in the Scikit-image python library [23]. The comparison between the two approaches is shown in Figure 4.
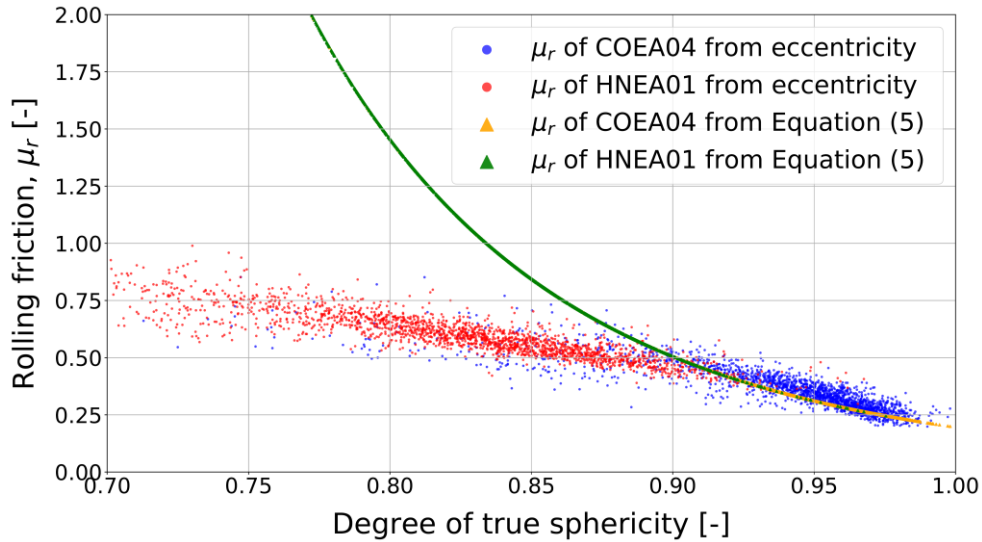
Figure 4: Rolling frictions of all particles involved in the simulation obtained from both eccentricity calculation and Equation 5. For high values of particle sphericity (*i.e., ψ*>0.90) the two approaches provide similar values.

It is evident from Figure 4 that both approaches provide values of rolling frictions that decrease with particle sphericity, as expected. It is somehow surprising that the two approaches, although conceptually completely different, provide similar rolling frictions values, especially at higher values of particle sphericity (*i.e., ψ*>0.90). Both approaches suggest that even for very spherical grains, a coefficient of rolling friction of about 0.20 should be assigned. However, the results start diverging when the grains become more angular. It worth reminding that Eq. (5) has been design to match the experimental material responses. Therefore, if the rolling frictions from the eccentricity calculations were assigned in the DEM simulation, the numerical response would be weaker compared to the experiments, especially for specimen HNEA01. It means that the geometrical description of

particle shape is not sufficient to capture all of the contributions provided by shape to the shearing material resistance. However, some other contributions (*e.g.,* grain interlocking, adhesion), which are not directly related to shape as a geometric property of one single particle, are somehow included in the proposed relationship described by Eq. (5).

4   CONCLUSIONS

This paper presents an innovative technique to relate univocally the degree of true sphericity of each grain contained in a sand sample with the coefficient of rolling friction to apply to its numerical avatar of spherical shape. The main advantage of the proposed model is that it reduces the number of free parameters to set by trial-and-error procedures when performing DEM simulations, albeit respecting the grains kinematics at failure. Indeed, if the statistical distribution of sphericity is known, either from experiments either from the literature, the resisting rolling moment is entirely determined since all the parameters involved in the contact model are known or predictable.

The contact detection remains economical and advanced algorithms are not required, maintaining low the computational time. This will open new frontiers to the use DEM for studying engineering applications at larger scales, especially in geotechnical problems in which the particulate nature of the soil cannot be ignored.

5   REFERENCES

[1]   E. Andò, "Experimental investigation of microstructural changes in deforming granular media using x-ray tomography," PhD Thesis. Université de Grenoble, 2013.

[2]   J. Santamarina and G. Cho, "Soil behaviour: The role of particle shape," in *Advances in Geotechnical Engineering. Proceedings of the Skempton Conference*, 2004, pp. 1–14.

[3]   K. Iwashita and M. Oda, "Rolling resistance at contacts in simulation of shear band development by DEM," *J. Eng. Mech.*, vol. 124, no. 3, pp. 285–292, 1998.

[4]   M. J. J. Jiang, H.-S. Yu, and D. Harris, "A novel discrete model for granular material incorporating rolling resistance," *Comput. Geotech.*, vol. 32, no. 5, pp. 340–357, 2005.

[5]   R. Rorato, M. Arroyo, A. Gens, E. Andò, and G. Viggiani, "Particle shape distribution effects on the triaxial response of sands: a DEM study," in *micro to MACRO Mathematical Modelling in Soil Mechanics, Trends in Mathematics*, 2018, pp. 277–286.

[6]   R. Rorato, M. Arroyo, E. Andò, and A. Gens, "Sphericity measures of sand grains," *Eng. Geol.*, vol. 254, no. April, pp. 43–53, 2019.

[7]   H. Wadell, "Volume, Shape, and Roundness of Rock Particles," *J. Geol.*, vol. 40, no. 5, pp. 443–451, 1932.

[8]   W. C. Krumbein, "Measurement and Geological significance of shape and roundness of sedimentary particles," *J. Sediment. Petrol.*, vol. 11, no. 2, pp. 64–72, 1941.

[9]   E. Andò, S. A. Hall, G. Viggiani, J. Desrues, and P. Bésuelle, "Grain-scale experimental investigation of localised deformation in sand: A discrete particle tracking approach," *Acta Geotech.*, vol. 7, no. 1, pp. 1–13, 2012.

[10]   R. Rorato, M. Arroyo, E. Andò, A. Gens, and G. Viggiani, "Linking shape and rotation of grains during triaxial compression of sand," *Geotechnique*, p. (submitted), 2019.

[11] J. Katagiri, T. Matsushima, Y. Yamada, J. Katagiri, T. Matsushima, and Y. Yamada, "Simple shear simulation of 3D irregularly-shaped particles by image-based DEM," *Granul. Matter*, vol. 12, pp. 491–497, 2010.

[12] M. Lu and G. R. McDowell, "The importance of modelling ballast particle shape in the discrete element method," *Granul. Matter*, vol. 9, no. 1–2, pp. 69–80, 2007.

[13] J. Elias, "DEM simulation of railway ballast using polyhedral elemental shapes," in *PARTICLES 2013 - III International Conference on Particle-based Methods – Fundamentals and Applications*, 2013, pp. 1–10.

[14] P. Langston, J. Ai, and H.-S. Yu, "Simple shear in 3D DEM polyhedral particles and in a simplified 2D continuum model," *Granul. Matter*, vol. 15, pp. 595–606, 2013.

[15] A. X. Jerves, R. Y. Kawamoto, and J. E. Andrade, "Effects of grain morphology on critical state: A computational analysis," *Acta Geotech.*, vol. 11, no. 3, pp. 493–503, 2016.

[16] R. Kawamoto, E. Andò, G. Viggiani, and J. E. Andrade, "All you need is shape: Predicting shear banding in sand with LS-DEM," *J. Mech. Phys. Solids*, vol. 111, pp. 375–392, 2018.

[17] H. Sakaguchi, E. Ozaki, and T. Igarashi, "Plugging of the Flow of Granular Materials during the Discharge from a Silo," *Int. J. Mod. Phys. B*, vol. 7, no. 09–10, pp. 1949–1963, 1993.

[18] N. Estrada, A. Taboada, and F. Radjaï, "Shear strength and force transmission in granular media with rolling resistance," *Phys. Rev. E*, vol. 78, no. 2, pp. 1–11, 2008.

[19] K. Cheng, Y. Wang, Q. Yang, Y. Mo, and Y. Guo, "Determination of microscopic parameters of quartz sand through tri-axial test using the discrete element method," *Comput. Geotech.*, vol. 92, pp. 22–40, 2017.

[20] C. M. Wensrich and A. Katterfeld, "Rolling friction as a technique for modelling particle shape in DEM," *Powder Technol.*, vol. 217, pp. 409–417, 2012.

[21] C. M. Wensrich, A. Katterfeld, and D. Sugo, "Characterisation of the effects of particle shape using a normalised contact eccentricity," *Granul. Matter*, vol. 16, no. 3, pp. 327–337, 2014.

[22] E. Catalano, B. Chareyre, and E. Barthélémy, "Pore-scale modeling of fluid-particles interaction and emerging poromechanical effects," *Int. J. Numer. Anal. Methods Geomech.*, vol. 38, no. 1, pp. 51–71, Jan. 2014.

[23] S. van der Walt *et al.*, "scikit-image: image processing in Python," *PeerJ*, vol. 2:e453, 2014.

INFLUENCE ON UNCERTAINTY OF EARTHQUAKE RESPONSE ANALYSIS RESULTS BY INITIAL PARTICLE ARRANGEMENTS AND COHESION PARAMETERS IN EXTENDED DISTINCT ELEMENT METHOD

- PARTICLES 2019

TAIKI. YOSHIDA[1], HITOSHI. TOCHIGI[2]

[1] Central Research Institute of Electric Power Industry (CRIEPI)
Earthquake Engineering Sector Civil Engineering Research Laboratory
1646 Abiko, Abiko-sh, Chiba 270-1194 JAPAN
taiki@criepi.denken.or.jp and https://criepi.denken.or.jp/

[2] Central Research Institute of Electric Power Industry (CRIEPI)
Earthquake Engineering Sector Civil Engineering Research Laboratory
1646 Abiko, Abiko-sh, Chiba 270-1194 JAPAN
tochigi@criepi.denken.or.jp and https://criepi.denken.or.jp/

Key words: EDEM, Impact Force, Uncertainty, Cohesion.

Abstract Following the occurrence of extremely large earthquakes, such as the Great East Japan Earthquake, the level of design for earthquake ground motion in nuclear power plants has been enhanced. Additionally, the quantitative evaluation of the seismic performance of critical facilities, such as nuclear power plants, and earthquake-induced failure of surrounding slopes are becoming increasingly important as deterministic approaches in regulation. However, evaluation of other aspects besides the design for earthquake ground motion in probabilistic risk assessment (PRA) needs to be conducted voluntarily by the corporation.

For the earthquake response analysis, including the seamless transition of the slope from continuum to dis-continuum, the extended distinct element method (EDEM) is an effective approach; however, EDEM is characterised by initial particle arrangement uncertainty. Therefore, we investigated the uncertainty in the EDEM results with respect to failure timing and region. Although essential in the evaluation of impact force in the PRA framework, there are few researches regarding the uncertainty of impact force on the wall of the reactor building after slope failure caused by numerous initial particle arrangements. Furthermore, reducing the computational time is crucial in PRA. Hence, the parameters that do not have an influence on the EDEM results can be omitted, resulting in their dispersion and a reduction in the computational time.

This research aims to investigate the impact force uncertainty caused by initial particle arrangements and the influence of cohesion uncertainty. For the former, we conducted 50 numerical simulations for the uncertainty of EDEM results caused by the initial particle arrangements. For the latter, we conducted 50 numerical simulations with two uncertainty factors, namely, cohesion and initial particle arrangement.

The simulation results revealed that the largest and second largest loads on the wall occurred in two cases, namely, when there were single particles impacting the wall and when there were group particles impacting the wall. Additionally, the uncertainty caused by cohesion was less than that caused by the initial particle arrangement when the coefficient of variation was 0.1. Thus, the cohesion uncertainty can be ignored if it is somewhat small.

1 INTRODUCTION

Following the occurrence of extremely large earthquakes, such as the Great East Japan Earthquake, the level of design for earthquake ground motion in nuclear power plants has been enhanced. Additionally, the quantitative evaluation for the seismic performance of critical facilities, such as nuclear power plants, and earthquake-induced failure of surrounding slopes are becoming increasingly important as deterministic approaches in regulation. However, the evaluation of other aspects besides the design for earthquake ground motion in probabilistic risk assessment (PRA) needs to be voluntarily conducted by the corporation.

The seismic stability of the surrounding slopes on the basis of ground displacement is often determined using the finite element method (FEM). For example, the Central Research Institute of Electric Power Industry (CRIEPI) recommends a time history nonlinear analysis for evaluating the stability of slopes, including post-earthquake residual displacement, and predicting a failure range when large deformations and displacements occur [1].

For the evaluation of rock mass displacement, once the failure of the slope model has been confirmed by FEM, the distinct element method (DEM) is often used. This is a discontinuous analysis method [2], which can easily evaluate large deformations or failures in comparison with FEM.

Moreover, the earthquake response analysis of the slope, including its seamless transition from continuum to dis-continuum can be better than the method, which is divided into two steps which are the stability evaluation by FEM and the one of rock mass displacement by DEM.

The extended distinct element method (EDEM) may be effective for developing such a seamless analytical approach [3]. In the EDEM, a pore spring exists among the soil pores for cohesion between particles. By setting the tensile strength and shear strength between particles and turning off the pore spring when the pore force exceeds the tensile and shear strengths, the progressive failure of the slopes can be modelled.

EDEM is characterised by the initial particle arrangement uncertainty. Therefore, we investigated the uncertainty in EDEM results with respect to failure timing and region [4,5]. The probability distribution of the inclination angle was similar to the normal distribution when a slope fails and most of the slip lines defined in the analysis were near the slip lines in the experiment. Yoshida et al. investigated the influence of initial particle arrangements using the moving particle simulation (MPS) [6].

Although essential in the evaluation of impact force in the PRA framework, there are few studies on the uncertainty of impact force on the wall of a reactor building after slope failure caused by several initial particle arrangements. Furthermore, reducing the computational time is critical in PRA. Thus, the parameters that do not have any influence on the EDEM results can be omitted, resulting in their dispersion and a reduction in the computational time.

This research has two purposes, which are to investigate the impact force uncertainty caused by initial particle arrangements and the influence of cohesion uncertainty. For the former, we conducted 50 numerical simulations for the uncertainty of EDEM results caused by initial particle arrangements. Additionally, for the latter, we conducted 50 numerical simulations with two uncertainty factors, namely, cohesion and initial particle arrangement.

2   SHAKING TABLE MODEL TEST

The geo-materials used to construct the slope model comprised stainless particles, iron sand, and water, which were mixed in the ratio of 40:30:1. The physical parameters were obtained from laboratory results of a plane strain compression test, cyclic tri-axial test, and uniaxial tension test, as presented in Table 1 (σ indicates the confining pressure).

Table 1: Physical properties of geo-materials

Physical property	Value
Wet unit weight [kg/m^3]	4.20×10^3
Poisson ratio [-]	9.00×10^{-2}
Static elastic modulus [MPa]	$1.36 \cdot \sigma^{1.03}$
Initial shear elastic modulus [MPa]	$34.44 \cdot \sigma^{0.32}$
Tensile strength [kPa]	0.5
Peak shear strength [kPa]	$7.0 + \sigma \cdot \tan 40.9°$
Residual shear strength [kPa]	$2.05 \cdot \sigma^{0.69}$

The scale of the slope model, with a slope gradient of 1:0.5, is illustrated in Figure 1.
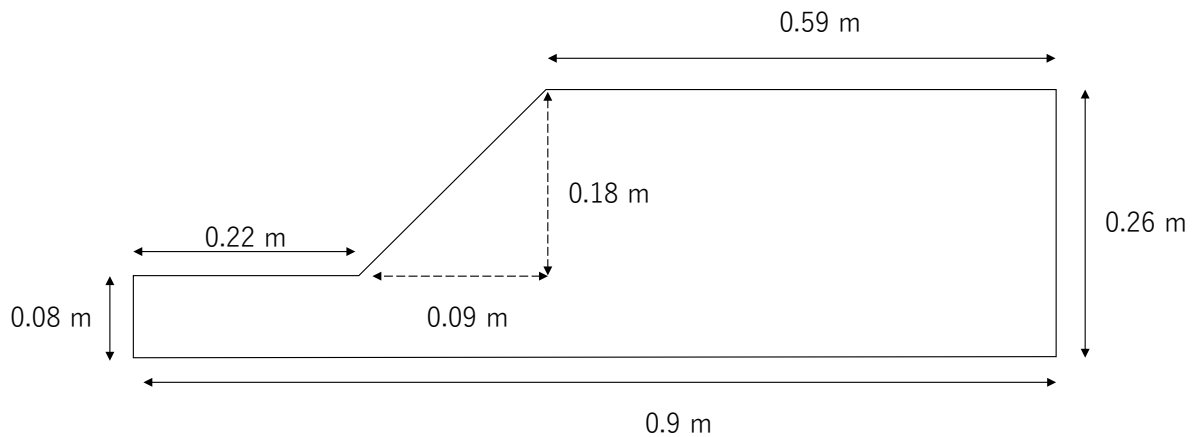
Figure 1: Scale of slope model

The model was shaken in 16 stages at input accelerations. The input acceleration was a sinusoidal waveform, with the main section consisting of 20 waves at a frequency of 20 Hz. The horizontal acceleration waveform measured at the bottom of the soil bin in this test is illustrated as an example in Figure 2.
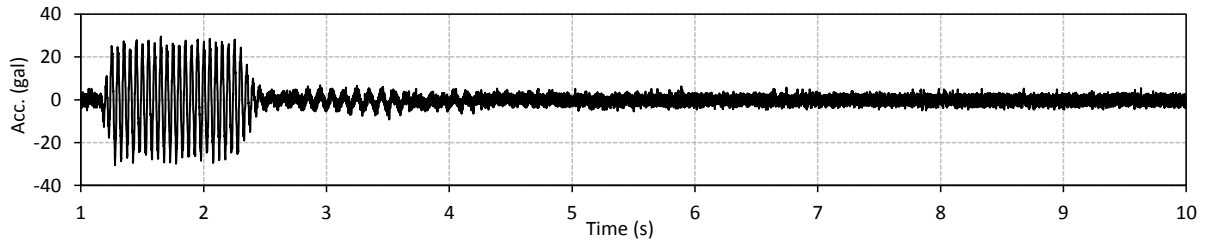
Figure 2: Horizontal acceleration measured at the bottom of the soil bin during the third stage of the shaking table model test

3   DISTINCT ELEMENT METHOD (DEM) FOR SOFT ROCK

For the numerical simulation, we used Itasca PFC3D code and constrained particles that were moving out from the plane direction to model the granular materials as a 2D analysis. When calculating the force between the particles, a spring coefficient was used to obtain the contact force, a viscous damping coefficient was used to determine the energy attenuation, a divider was used to ignore the tensile force, and a slider was used to determine the dynamic frictional force. The initial particle cohesion was modelled as a parallel bond, and the motion of each particle is expressed as follows:

$$\frac{d\boldsymbol{P}}{dt} = \sum \boldsymbol{F} \tag{1}$$

$$\frac{d\boldsymbol{L}}{dt} = \sum \boldsymbol{N} \tag{2}$$

Here, $\boldsymbol{P}$ represents the linear momentum, $\boldsymbol{F}$ represents the force acting on the soil element, $\boldsymbol{L}$ is the angular momentum, and $\boldsymbol{N}$ is the torque acting on the soil element.

To classify the material properties depending on confining pressure, we divided the slope model vertically into three layers, as depicted in Figure 4, where the red area represents 1.78 kPa, the blue area represents 5.35 kPa, and the green area represents 8.92 kPa in terms of confining pressure.
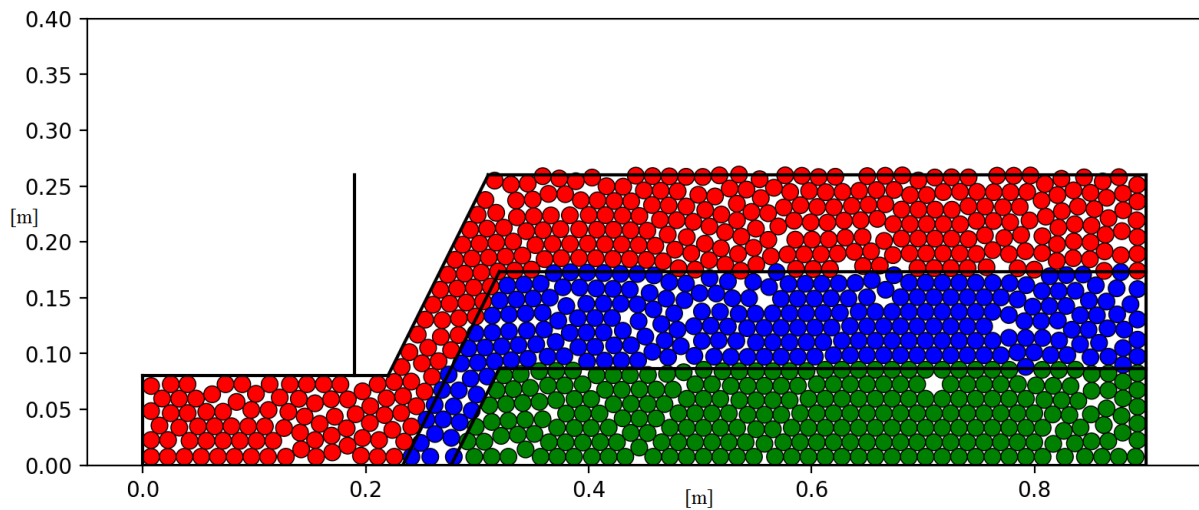
Figure 3: Example of analytical model of slope

For the boundary condition, the front and back of the slope were modelled as a rigid wall and the particles at the bottom of the soil bin, indicated in purple in Figure 3, were fixed.

Fifty models with varying initial particle arrangements were prepared. Each model was composed of particle whose diameter were 15 mm.

The DEM parameters for the contact force are listed in Table 2. The spring coefficient, pore spring coefficient, and shear strength were determined using the plane strain compression test, whereas the dynamic friction coefficients were determined using the cyclic tri-axial test. The tensile strength was obtained by the uniaxial tension test.

Table 2: DEM parameters for contact force

Layer number	First	Second	Third
Wet unit weight [kg/m^3]		4.20×10^3	
Normal spring coefficient [N/m]	4.25×10^7	5.51×10^7	6.51×10^7
Tangential spring coefficient [N/m]	1.92×10^7	2.48×10^7	2.93×10^7
Normal pore spring coefficient [N/m]	1.28×10^5	1.65×10^7	1.95×10^7
Tangential pore spring coefficient [N/m]	5.76×10^4	7.44×10^4	8.79×10^4
Normal damping ratio [%]		3	
Tangential damping ratio [%]		3	
Inter-particle friction angle [°]		34	

Inertial force was added to the centre of the particles using horizontal acceleration waveforms measured at the bottom of the soil bin in the shaking table model test. The shaking started only from the third stage in the numerical simulation because there was white noise excitation and a low response from the slope in the first two stages.

4 RESULTS AND DISCUSSION

4.1 Impact force

The impact force P can be calculated based on the elastic contact theory in EDEM analysis as follows:

$$P = \kappa \delta^n \tag{3}$$

$$\kappa = \frac{4}{3} E_0 \sqrt{R_0} \tag{4}$$

$$E_0 = \frac{1}{\frac{1-v_1^2}{E_1} + \frac{1-v_2^2}{E_2}} \tag{5}$$

$$R_0 = R \tag{6}$$

Here, P represents the impact force, κ represents the force acting on the soil element, δ is the amount of overlap, n is 1.5, E_0 is defined in equation (5), v_1 is the Poisson's ratio of the wall, E_1 is the elastic modulus of the wall, v_2 is the Poisson's ratio of the rock mass, E_2 is the elastic modulus of the rock mass, R_0 is defined in equation (6), and R is the particle radius depicted in Figure 4.
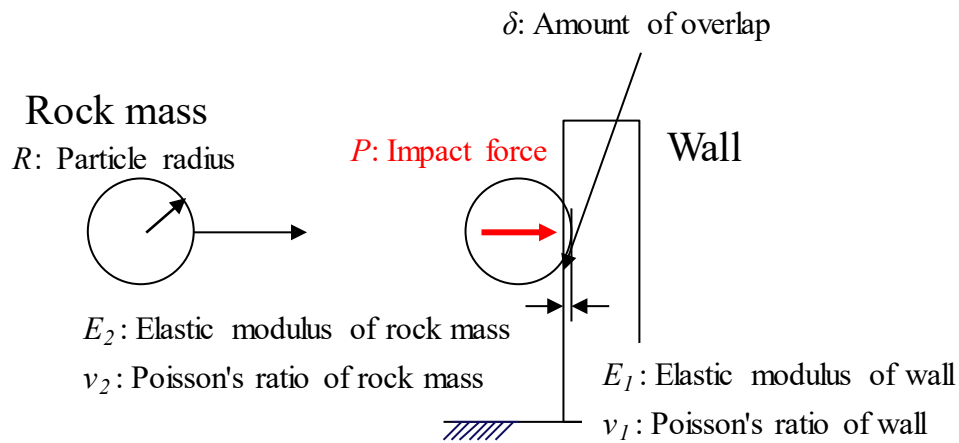
Figure 4: Parameters for impact force

The virtual rigid wall is located 3 cm away from the foot of the slope, as illustrated in Figure 3. Fifty numerical simulations were conducted with varying initial particle arrangements. Figure 5 illustrates the histogram of the maximum load on the wall.
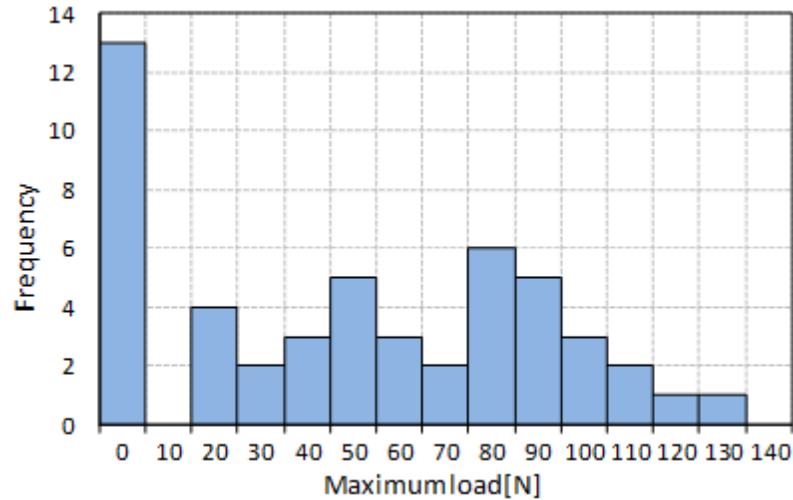
Figure 5: Histogram of maximum load on the wall

It can be observed from Figure 5 that the largest load is approximately 125 N in case 44 and the second largest load is approximately 117 N in case 22. It is important to clarify how features there are when the impact force is so large from these analytical results.

Figure 6 depicts the timing when the maximum load on the wall occurs in case 44, in which a single particle impacts the wall.
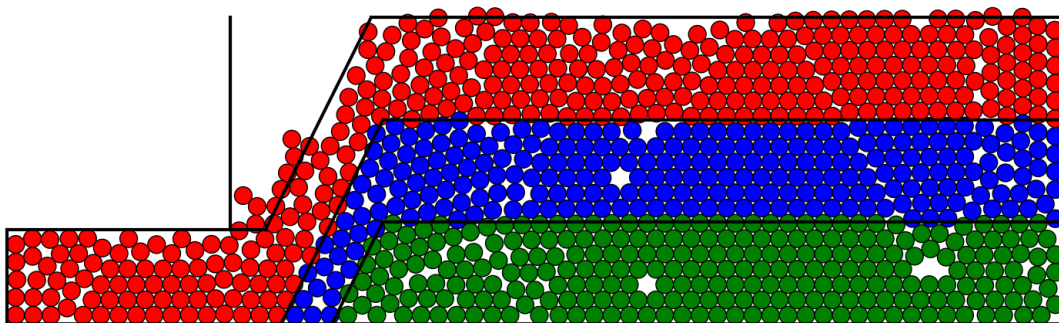
Figure 6: Timing of maximum load on the wall in case 44

On the other hand, Figure 7 depicts the timing when the maximum load on the wall occurs in case 22, in which a particle group impacts the wall.
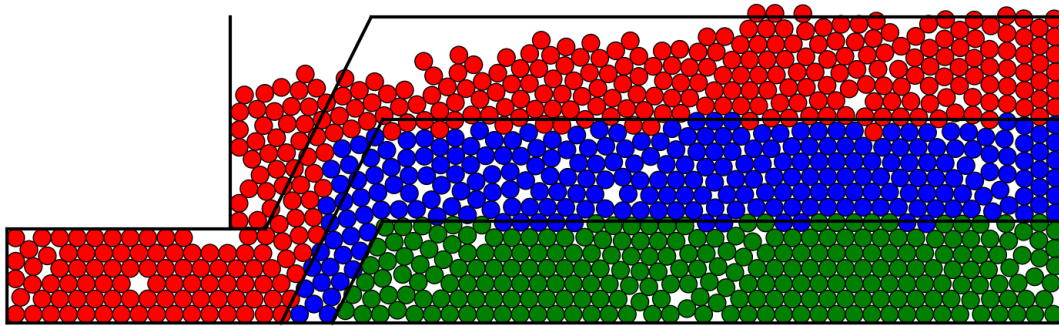
Figure 7: Timing of maximum load on the wall in case 22

According to the theoretical consideration, the impact force depends on the kinematic energy of the rock masses, as expressed in equation (5).

$$E = \frac{1}{2}MV^2 \tag{5}$$

Here, **M** represents the mass of the rock and **V** represents the velocity of the rock.

In cases when the kinematic energy is high, there are two possibilities: the mass M can be extremely large or the velocity V is extremely high. Case 44 is interpreted as the former, and case 22 is interpreted as the latter.

4.2 Influence of initial particle arrangement on uncertainty

The frequency line graph of the numerical simulation results are depicted in Figure 8. In this analysis, failure timing is defined as the time when the average movement of particles near the top of the slope exceeds the threshold set for particle displacement.
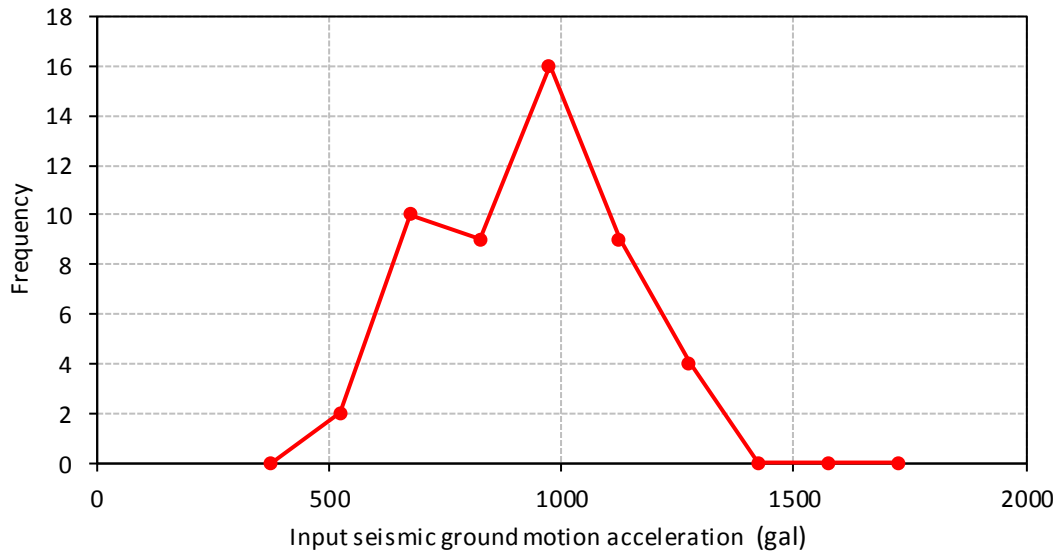
Figure 8: Frequency line graph of numerical simulation result

Based on the $\chi-$square test, the theoretical probability distribution is determined as a normal distribution. The average value of input seismic ground motion acceleration is approximately 902 gal and the coefficient of variation is 0.22.

4.3 Influence of cohesion and initial particle arrangement on uncertainty

Fifty numerical simulations were conducted with both cohesion parameters and initial particle arrangements. The purpose was to investigate the influence of the cohesion parameters on the uncertainty by comparing the results of only the initial particle arrangements with those of the cohesion parameters and initial particle arrangements.
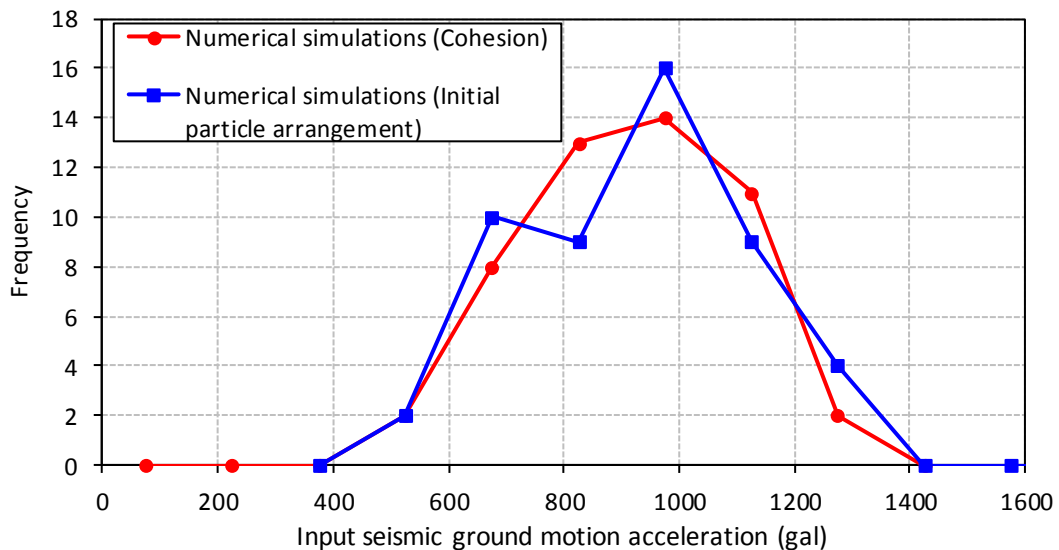
Figure 9: Frequency line graphs of two numerical simulation results from 50 cohesion parameters, whose coefficient of variation is 0.1, and initial particle arrangements
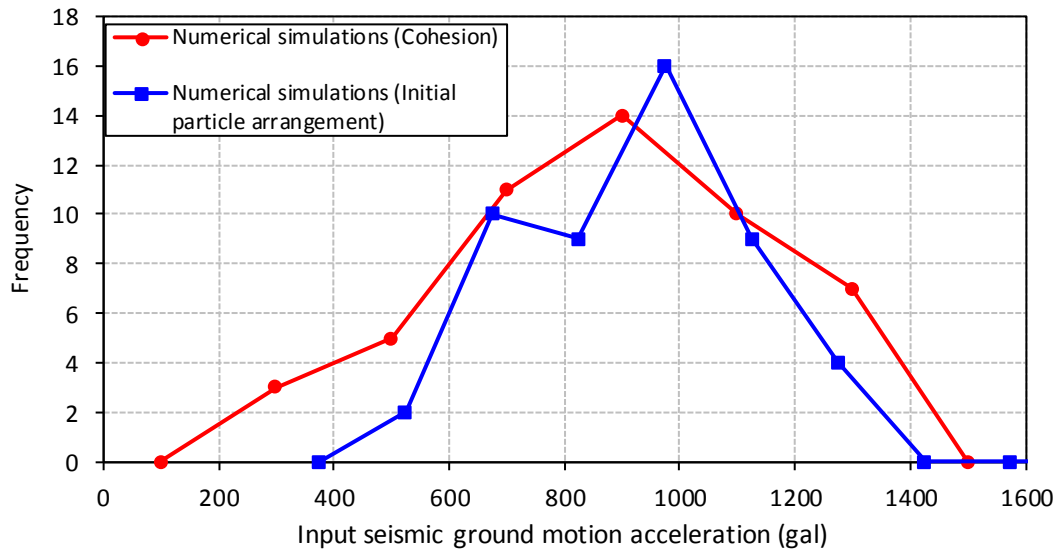
Figure 10: Frequency line graphs of two numerical simulation results from 50 cohesion parameters, whose coefficient of variation of 1.0, and initial particle arrangements

Figure 9 illustrates the frequency line graphs of the numerical simulation results with a coefficient of variation of 0.1. The average value of the input seismic ground motion acceleration is approximately 899 gal and the coefficient of variation from numerical simulations is 0.20.

On the other hand, Figure 10 depicts the frequency graph of the numerical simulation results with a coefficient of variation of 1.0. The average value of the input seismic ground motion acceleration is approximately 858 gal and the coefficient of variation from numerical simulations is 0.33.

In comparison with the results in Figure 9, the coefficient of variation is larger in Figure 10. It is also clarified that the coefficient of variation from the numerical simulations of the cohesion parameters and initial particle arrangements in Figure 9 is less than that of only the initial particle arrangements in Figure 8.

Based on these results, it can be concluded that the uncertainty of cohesion can be ignored if the coefficient of variation is somewhat small.

12 CONCLUSIONS

This research clarified two cases when the impact force is large. It is concluded that there are two possibilities: the mass M can be extremely large or the velocity V is extremely high. Additionally, the cohesion uncertainty was investigated. The results confirm that the influence of cohesion uncertainty can be ignored when its coefficient of variation is somewhat small.

In the future, we aim to clarify the range of the coefficient of variation, in which the influence of cohesion uncertainty can be ignored, and conduct the same investigation using other parameters.

REFERENCES

[1] Ishimaru, M., Okada, T., Nakamura, H., Kawai, T., Kazama, M. "*Modelling of strength and deformation characteristics after shear failure of soft rock and application to evaluation of seismic stability of slopes against sliding*," J. Jpn. Soc. Civil Eng. Ser. C, 73(1), pp. 23-38, (2017). (in Japanese)

[2] Tochigi, H., Nomura, Y., Ozawa, K. "*DEM analysis of falling rocks' reaching distance providing that surrounding slope in nuclear power plant facility failures*," (*Proc. Annu. Conf JSCE*), (2018). (in Japanese).

[3] Hakuno, M. "*Simulation of rupture-tracing rupture by an extended distinct element method*," Tokyo: Morikita Publishing Co., Ltd. (1997).

[4] Yoshida, T., Tochigi, H. "*Numerical Simulation on Inclining Model Experiment by Extended Distinct Element Method*," *Proceedings of the 52nd Japan National Conference on Geotechnical Engineering*, 0861, pp. 1719-1720, (2017). (in Japanese)

[5] Yoshida, T., Nakajima, M., Tochigi, H. "*Studying parameters for changing the initial particle arrangements of distinct element analysis in earthquake response based on slope analysis*," *Proceedings of 14th International Conference on Probabilistic Safety Assessment and Management (PSAM14)*, (2018).

[6] Yoshida, I. "*Basic study on failure analysis with using MPS method*," J. Jpn. Soc. Civil Eng. Ser. C, 73(1), pp. 93-104, (2011). (in Japanese)

Role of inter-particle friction in granular materials under three dimensional conditions — PARTICLES 2019

Shuhan. Yang[1], Wei. Zhou[1], Jiaying. Liu[1], Tianqi. Qi [1], Gang. Ma[1]

[1] State Key Laboratory of Water Resources and Hydropower Engineering Science
Wuhan University
8 Donghu South Road, 430072 Wuhan, China
E-mail: yang-sh@whu.edu.cn(Shuhan Yang); zw_mxx@whu.edu.cn (Wei Zhou)

Key words: DEM, Inter-particle Friction, True Triaxial Tests, Strong and Weak Contact System, Coordination Number, Anisotropy.

Abstract. The inter-particle friction is known to be an important contributor to the strength and deformation characteristics in granular materials. The mechanism of inter-particle friction to the macroscopic responses can be explained by microscopic investigations. Based on the discrete element method (DEM), a series of true triaxial tests for the cubic granular assembly are carried out and the effects of inter-particle friction coefficient (μ) on the evolutions of macro- and micromechanical parameters of granular materials are studied. The macroscopic stress, the distribution of coordination numbers and contact force with regard to strong and weak contact networks are concerned, as well as the corresponding fabric tensor and anisotropies. Findings indicate that increasing inter-particle friction sharpens the peak value of deviatoric stress and enhances the degree of dilatancy of the granular assembly at the macroscopic level. From the microscopic perspective, the distribution of the coordination number of the weak contact system varies dramatically, while the number of particles with smaller coordination number in the strong contact system changes little with different μ. Besides, the difference between strong and weak contact networks is enlarged, and anisotropy indicators are significantly enhanced, which strengthen the bearing ability of anisotropic stresses in granular materials.

1 INTRODUCTION

Granular materials are closely linked to our daily life. Many important infrastructures concerning the quality and safety of our everyday life, such as rockfill dams, dikes and foundations, are built with geotechnical friction-dissipative granular materials. The performance of granular materials under external loads directly affects the design, construction and operation of these structures [1]. Under shear, granular materials exhibit extremely complex mechanical behaviors at the macroscopic level while the typical multi-scale features contribute a lot to the overall complexity [2]. The granular materials are composed of discrete particles whose macroscopic responses are vitally interrelated to their interaction. Inter-particle friction as one of the key factors affecting the interplay between particles, may significantly contribute to the macro- and micro-responses of granular materials.

DEM (Discrete Element Method) has demonstrated its ability in reproducing the

macroscopic responses and exploring the microscopic mechanism of granular materials [3]. Based on DEM simulations of granular assemblies, contact orientation [4, 5], force transmission [6, 7], contact networks [14] are regarded as the important characterization of the microstructure. Besides, the fabric tensor [9, 10, 11, 12] has been defined to measure the intensity and orientation of the contact texture anisotropy.

The interplay between particles is the intrinsic factor that causes the macroscopic responses of granular materials. To figure out the effects of inter-particle friction on granular materials, Rothenburg et al. [13] observed the relationship between void ratio and coordination number along different inter-particle friction by biaxial tests. Huang et al. [14] evaluated the sensitivity of critical state behaviors to inter-particle friction. Maya et al. [15] identified that increasing inter-particle friction promotes the formation of straighter chains and a greater degree of branching in the force chain network by two-dimensional simulations. Antoy et al. [16] investigated how particle-scale friction affect the mechanism of mobilization of macroscopic shear strength by conventional triaxial tests. However, true triaxial tests are rarely used in these simulations, which can reflect the real situation in nature or engineering.

The main purpose of this paper is to investigate the effects of inter-particle friction on the characteristic behaviors of granular materials under true triaxial tests. The stress–strain relationships and peak state of deviatoric stress are presented. From the view of strong-weak contact network, the micro-responses are explored, including the coordination number, the contact force, the fabric tensors and the anisotropies. The contribution of micro-investigations to macro-mechanical properties is further discussed.

2 DEM SIMULATIONS OF TRUE TRIAXIAL TESTS

2.1 Stress-strain invariants

The stress invariants describing true triaxial stress state are generalized shear stress q, average hydrostatic pressure p and Lode angle θ_σ:

$$p = \frac{\sigma_1 + \sigma_2 + \sigma_3}{3} \tag{1}$$

$$q = \frac{1}{\sqrt{2}} \sqrt{(\sigma_1 - \sigma_2)^2 + (\sigma_2 - \sigma_3)^2 + (\sigma_3 - \sigma_1)^2} \tag{2}$$

$$\tan\theta_\sigma = \frac{\sqrt{3}b}{2-b}, \quad b = \frac{\sigma_2 - \sigma_3}{\sigma_1 - \sigma_3} \tag{3}$$

The intermediate principal stress ratio b responses the relative magnitude of the intermediate principal stress σ_2 between the minor principal stress σ_3 and the major principal stress σ_1. The range of b is $0 \leq b \leq 1$. The Lode angle θ_σ defines the angle between the major principal stress and the deviatoric part of stress in the principal stress space. The true triaxial test with $b = 0.0$ represents the triaxial compression test ($\sigma_2 = \sigma_3$, $\theta_\sigma = 0$) and $b = 1.0$ indicates the traxial extension test ($\sigma_1 = \sigma_2$, $\theta_\sigma = \pi/3$).

2.2 Sample preparation and loading paths

The numerical sample is composed of 31 253 non-contacting spherical particles with Gaussian distribution in a 400mm×400mm×400mm cube. The minimum and maximum

particle sizes are 2 and 8.5 mm, respectively. Fig.1 shows the particle size distribution (PSD). In order to generate isotropic samples in the initial fabrics, we use the displacement control to compress the samples with a constant-speed in all directions until the target size. After that, isotropic consolidation is carried out and three-dimensional isobaric stress is applied to the specimen until the desired confining pressure 0.5 MPa is reached. Finally, the initial void ratio of the specimen is 0.582. The Hertz–Mindlin contact model is adopted. The inter-particle friction coefficient μ during loading process is set as 0.05, 0.1, 0.2, 0.3, 0.4 and 0.5, respectively, and other numerical parameters are shown in Table 1.
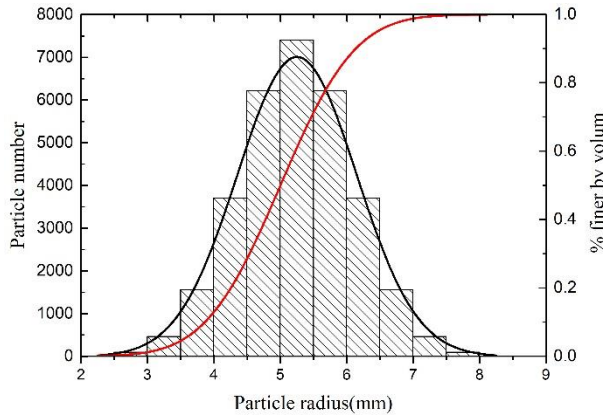
Fig.1 Radius distribution   **Fig.2** Stress path under true triaxial tests
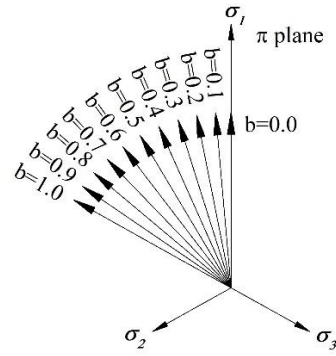
Table1: Microscopic parameters of numerical simulation

Parameters	Value
Density ρ/(kg/m^3)	2600
Particle radius d/mm	2-8.5
Young's modulus E/GPa	65.0
Poisson's ratio v	0.4
coefficient of restitution e	0.95
sliding friction coefficient μ	0.05,0.1,0.2,0.3,0.4,0.5

In this paper, a series of true triaxial tests are under the constant-p and constant-b loading condition, and the stress paths are shown in Fig.2. In order to eliminate the boundary influence and avoid the occurrence of strain localization, these tests are carried out with periodic boundary. The stress in each direction of the specimen is controlled by the migration rate of periodic boundary. The intermediate principal stress σ_2 and minor principal stress σ_3 can be estimated from Eq. (4) and Eq. (5) respectively:

$$\sigma_2 = b\sigma_1 + (1-b)\frac{3p - \sigma_1(1+b)}{(2-b)} \tag{4}$$

$$\sigma_3 = \frac{3p - \sigma_1(1+b)}{(2-b)} \tag{5}$$

3   MACRO-SCALE RESPONSES

For various inter-particle friction, the evolution curves of generalized shear stress q and volumetric strain ε_v along deviatoric strain ε_d are shown in Fig. 3 (the positive volumetric strain represents contraction, negative value represents dilation). Increase in inter-particle friction μ steadily raises the shear strength of a granular assembly (the peak deviatoric stress) while the peak value occurs at a similar strain level (about 6%) irrespective of various μ. The deviatoric stress changes to a downward trend after reaching the peak value, which means strain softening. The larger inter-particle friction can enhance the strain softening behavior. In addition, diverse μ values lead to different volume responses of a granular assembly. Specifically, after a small compression deformation, the specimens are all in the dilatation condition. The particle assembly with large inter-particle friction starts the dilatation state earlier and shows a more evident dilatation degree at later stage of loading.
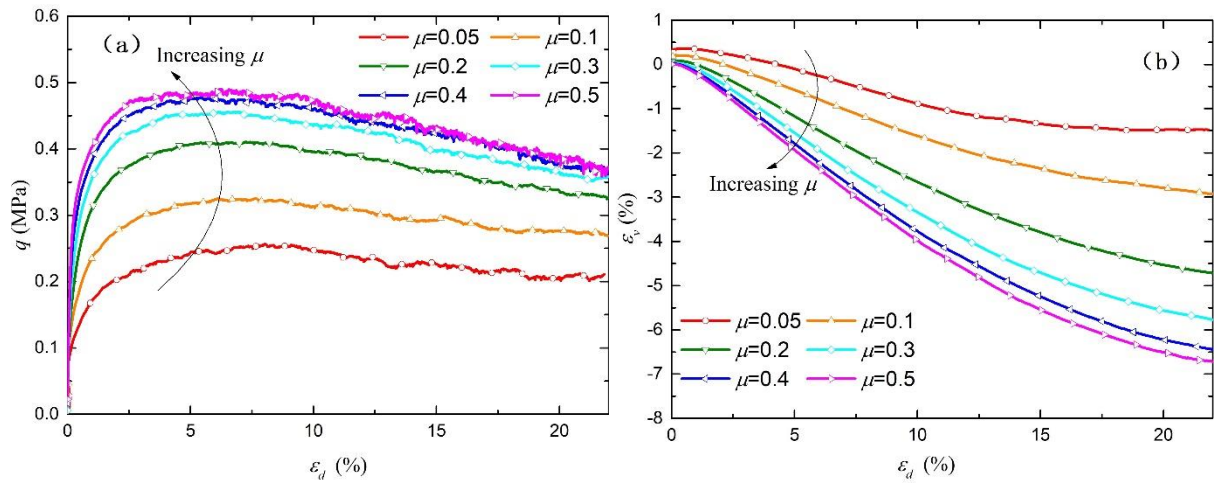
Fig.3 Macroscopic response of granular assemblies with different inter-particle friction: evolution of deviatoric stress (a) and volumetric strain（b）versus deviatoric strain ε_d
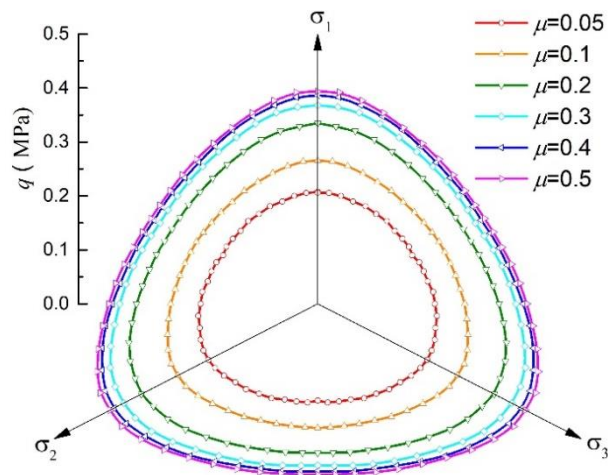
Fig.4 Peak state of deviatoric stress along different friction coefficients

Corresponding to different inter-particle friction, the three-dimensional stress surfcae in π plane is plotted in Fig. 4. For each given μ, the curve presents similar shape like triangular cone but differs from one another in size. The stress evolution in π plane reflects the peak deviatoric stress of the granular assmebly at different b and μ values. It can be seen that, the peak deviatoric stress decreases with the increase of b but improves with the increase of μ. Moreover, the sensitivity of the specimen to inter-particle friction debases along with μ, for the smaller increaseing extent of deviator stress. The stress characteristics shown in Fig. 4 conform to the general rule of true triaxial test and are also consistent with the conclusions of other numerical tests [16, 17, 18].

4   COORDINATION NUMBER

The geometric stability of a granular assembly under mechanical loading is generally studied in the matter of its apparent coordination number Z (i.e., average number contacts of per particle) at a given stage of loading. As a mesoscopic scalar index of granular materials, average coordination number Z_t is given by $2N_c/N_p$ where N_c and N_p are the total number of contacts and particles in the specimen respectively. It can also reflect the overall volume change of a granular assembly. In generally, higher average coordination number is corresponding to smaller porosity, closer interaction between particles, and more stable/isotropic internal structure. On the contrary, the degree of anisotropy increases.

Radjai et al. [5] divided the whole contact network into two complementary sub-contact nectworks, a strong contact subnetwork and a weak contact network that carry normal contact forces larger and less than the average. The two contact networks have different mechanisms for the geometric stability of granular materials. In presenting the results, we have hereby separated the contributions of the weak contact network from the strong contact network, along with the total value. The strong contact network is denoted by Γ_{strong}, the part from the weak contact network by Γ_{weak}, and the entire contact network by Γ_{total}. Fig. 5 shows difference performance among the three contact networks in terms of the relationship between the average coordination number and the inter-particle friction in the triaxial compression condition. Under the given loading path, each contact network presents a law that Z_t decreases with the increase of μ, which confirms the macroscopic phenomenon that the dilatation degree of the specimen is more obvious with large μ. Besides, average coordination number in Γ_{weak} is larger than that of Γ_{strong}, reflecting stronger internal stability and higher isotropy of Γ_{weak}. Considering the relationship between the average coordination number and the volume deformation of granular materials, it indirectly shows that the weak contact network contributes greater to the deformation of a granular assembly.

In a granular media, the coordination number Z_t indicates an average over particles within contact networks while the number of contacts neighbors n varies from particle to particle. Bratberg et al. [19] recognized that the connectivity of a granular assembly should be given by the fraction P_n, defined by particles having n contact neighbors. From the study of Liu et al. [20], particles with fewer coordination numbers are in lower degree of restraint condition, corresponding to higher anisotropy. Conversely, particles are more stable and show isotropy feature.

From the distribution of coordination number at stress peak state in Fig. 6, the coordination number Z in accordance with the abscissa denotes P_n, and the corresponding ordinate refers to

the number of n adjacent particles in contact with a single particle. In the total contact network (Fig.6a), the maximum particle content changes from P_5 to P_4, meanwhile, all distribution curves seem to move left entirely with the increase of μ value. Evidently, some particles with $n \geq 5$ contacts lose neighbor contacts, causing the number of particles with $n \leq 4$ contacts increase. The distribution of coordination number within weak contact network (Fig.6b) is similar to that of the total contact network, while the maximum particle content moves from P_4 to P_3. From that, the anisotropy feature of Γ_{weak} is stronger than that of Γ_{total} and both of them diminish owing to the increase of μ.

It is interesting to take a quantitative look at the strong contact network (Fig.6c) whose distribution of coordination number is quite different from that of the total contact network. Thanks to the increase of μ value, the number of particles ($P_n \geq P_3$) decreases. However, μ value appears to have little effect on the number of particles whose coordination number is 1 and 2, whereas P_1 and P_2 constitute the end and main body of the force chain in the contact network. It shows that the number of particles forming the force chain accounts for 1/3 of the total number and does not fluctuate with the change of μ value, as if satisfying the most advantageous condition of particulate distribution. This demonstrates that the shear resistance of granular assembly can be mobilized by selecting relatively few benificial oriented contacts to transmit the greater than average contact force.

Compared with strong, weak and total contact network (Fig.6d), the three curves can be roughly considered as the left translation of the total contact network curve. For the total contact network, the weak contact network makes more contribution to the coordination number distribution than the strong contact network. The influence of inter-particle friction on coordination number distribution of Γ_{weak} is greater than that of Γ_{strong}. The weak contact network tends to be isotropic, balancing hydrostatic pressure of the granular media, dominating overall volume deformation; while the strong contact network has obvious anisotropic feature, and bear most of the deviatoric stress of the granular assembly (shown in next chapter).
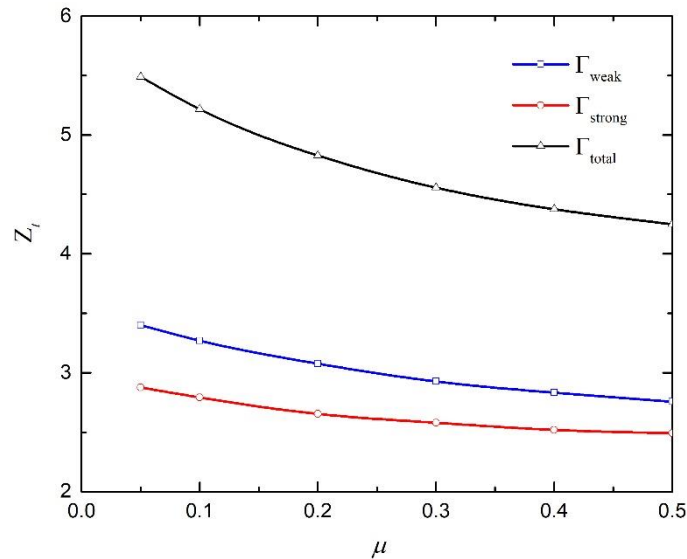
Fig.5 The relationship between the average coordination number and the inter-particle friction
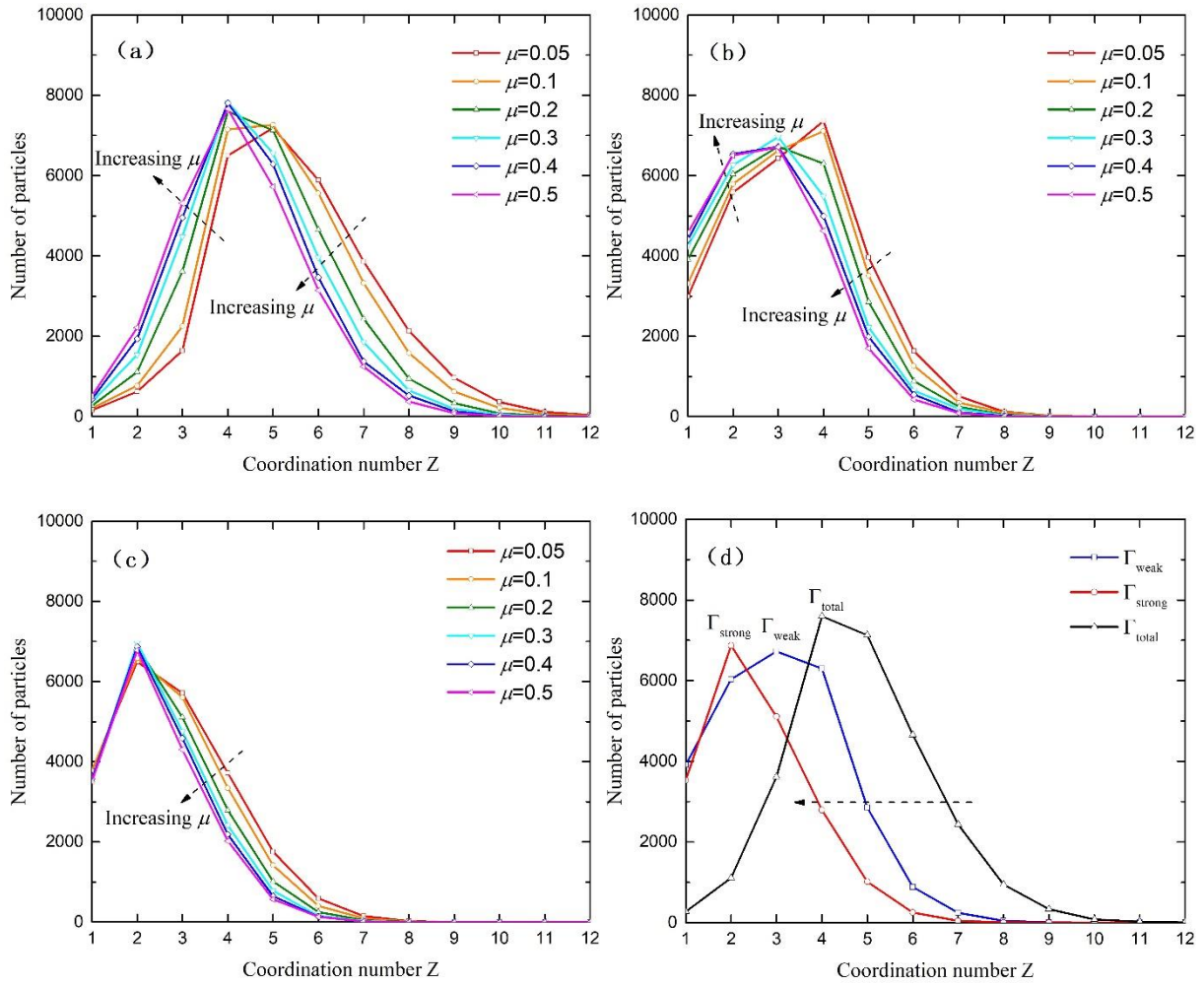
Fig.6 The distribution of coordination number at stress peak state: Number distribution of coordination number Z in the total contact network (a) the weak contact network (b) the strong contact network (c) and the comparison (d) while μ=0.2

5   FABRIC TENSOR AND ANISTROPY

5.1 Contact force

Radjai et al. [6] pointed out that the strong and weak contact network in a granular media have different mechanical mechanisms. Strong contacts have a decisive influence on the contribution of macro-mechanics. Fig. 7 shows the evolution of the average normal contact force and tangential contact force in the strong, weak and total contact network during true triaxial loading. The average normal contact force is much larger than the tangential contact force, indicating it's leading position. There is great disparity between the average normal contact force of strong and weak contact network, and the numerical relationship between them is about 4 times. For the total contact network, the evolution contribution of the average normal contact force is dominated by the strong contact network. With the increase of μ value, the normal contact force and tangential contact force in each contact network increase

obviously, while the average coordination number of them decreases. This reasonably explains the increase in the mechanic anisotropy feature of the granular assmebly (see Fig. 8), and highlights the supporting effect of the strong contact network on balancing external load.
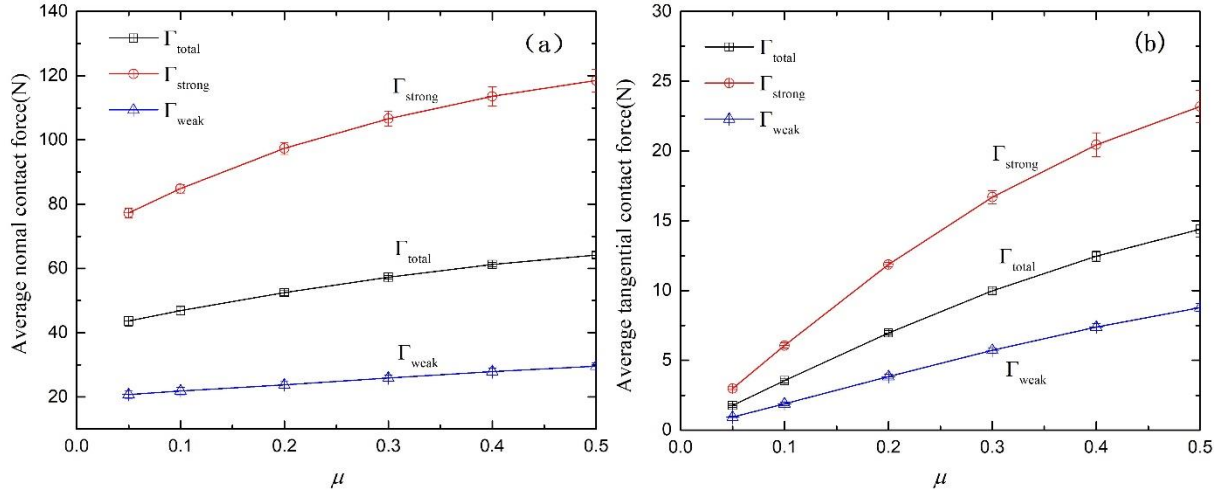
Fig.7 The relationship between contact force and inter-particle friction (a) Normal contact force (b) Tangential contact force

5.2 Definition of Contact Fabric Tensor

Based on the work of Yimsiri et al. [21] in quantitatively analyzing the anisotropy of a particle assembly, two classes of anisotropy with different mechanisms are differentiated: geometric anisotropy and mechanical anisotropy. The geometrical anisotropy is defined by the local orientation of contact plane which can be expressed by the distribution of contact normals and branch vectors. The mechanical anisotropy, however, is mainly created by the external forces and can be splited into normal force anisotropy (caused by normal contact forces) and tangential force anisotropy (induced by tangential contact forces). This paper adopts the following expression of fabric tensor proposed by Satake [22] and Oda [23]:

$$\Phi_{ij} = \int_{\Theta} E(\Theta) n_i n_j d\Theta \tag{6}$$

where n is the unit vector along the normal direction of the contact surface. Θ characterizes the orientation of n relative to the global coordination system. $E(\Theta)$ is the distribution probability density function, which can be expressed in terms of the second-order Fourier expansion:

$$E(\Theta) = \frac{1}{4\pi}(1 + a_{ij}^c n_i n_j) \tag{7}$$

where the second-order anisotropy tensor a_{ij}^c is deviatoric and symmetric, which characterizes the geometrical anisotropy induced by normal contact.

$$a_{ij}^c = 15/2\Phi_{ij}' \tag{8}$$

where Φ_{ij}' is the deviatoric part of the fabric tensor Φ_{ij}.

Only when the particle system is composed of non-spherical particles, the branch vector contributes greater to geometric anisotropy. The distribution of branch vectors can be expressed in the way similar to formula (7) and formula (8):

$$d_{ij} = \frac{1}{4\pi} \int_\Theta \overline{d}(\Theta) n_i n_j d\Theta \qquad (9a)$$

$$\overline{d}(\Theta) = \overline{d}^0 (1 + \mathrm{a}_{ij}^l n_i n_j) \qquad (9b)$$

where $\mathrm{a}_{ij}^l = 15/2 \ (d_{ij}' / \overline{d}^0)$ is the contribution value of branch vectors to the geometric anisotropic tensor. $\overline{d}^0 = d_{ii}$ is the average length of branch vectors in the domain Θ and d_{ij}' is the deviatoric part of d_{ij} .

The distribution function of normal contact force and tangential contact force are expressed respectively as (10b) and (11b). Correspondingly, the normal contact force tensor and the tangential contact force tensor are defined by equation (10a) and (11a).

$$\chi_{ij}^n = \frac{1}{4\pi} \int_\Theta \overline{f}^n(\Theta) n_i n_j d\Theta \qquad (10a)$$

$$\overline{f}^n(\Theta) = \overline{f}^0 (1 + \mathrm{a}_{ij}^n n_i n_j) \qquad (10b)$$

and $$\chi_{ij}^t = \frac{1}{4\pi} \int_\Theta \overline{f}^t(\Theta) t_i n_j d\Theta \qquad (11a)$$

$$\overline{f}_i^t(\Theta) = \overline{f}^0 \left[a_{ik}^t n_k - (a_{kl}^t n_k n_l) n_i \right] \qquad (11b)$$

wherein $a_{ij}^n = \dfrac{15}{2} \dfrac{\chi_{ij}'^n}{\overline{f}^0}$, $a_{ij}^t = \dfrac{15}{2} \dfrac{\chi_{ij}'^t}{\overline{f}^0}$

$\overline{f}^0 = \chi_{ii}^n$ is the average normal force in the domain Θ. The second-order anisotropy tensors $a_{ij}^c, a_{ij}^l, a_{ij}^n, a_{ij}^t$ are deviatoric and symmetric, then, the degree of anisotropy can be quantified by using the second invariants of the three anisotropy tensors defined above:

$$a_* = \sqrt{\frac{3}{2} a_{ij}^* a_{ij}^*} \qquad (12)$$

where the sub/super-script * stands for contact normal, c, branch vector, l, normal contact force, n, and tangential contact force, t, respectively.

5.3 Characteristics and Evolution of Anisotropy

The characteristics of anisotropy and its evolution during the loading process are depicted in Fig.8. Owing to the use of spherical particles with a relatively narrow size distribution, the branch vector is almost in the same direction as contact normal vector and contributes so little to the total strength that can be ignored. The anisotropic coefficient of the initial specimen increases rapidly with the increase of the deviation strain, and the increase rate becomes more sharply with larger inter-particle friction. It can be seen evidently that the peak value of the normal contact force anisotropy a^n (about 3% of the deviatoric strain) comes earlier than that of the contact normal anisotropy a^c (about 6% of the deviatoric strain), and the peak value is higher than the latter. With the increase of μ value, the difference is more obvious. Interestingly, the contact tangential force anisotropy a^t reaches its peak within 1% of the

deviatoric strain, then decreases slightly and remains stable. Compared with the two mechanical anisotropy coefficients, the contribution of the tangential contact force anisotropy a^t to the anisotropy of the whole system is significantly less than that of the normal contact force anisotropy a^n.
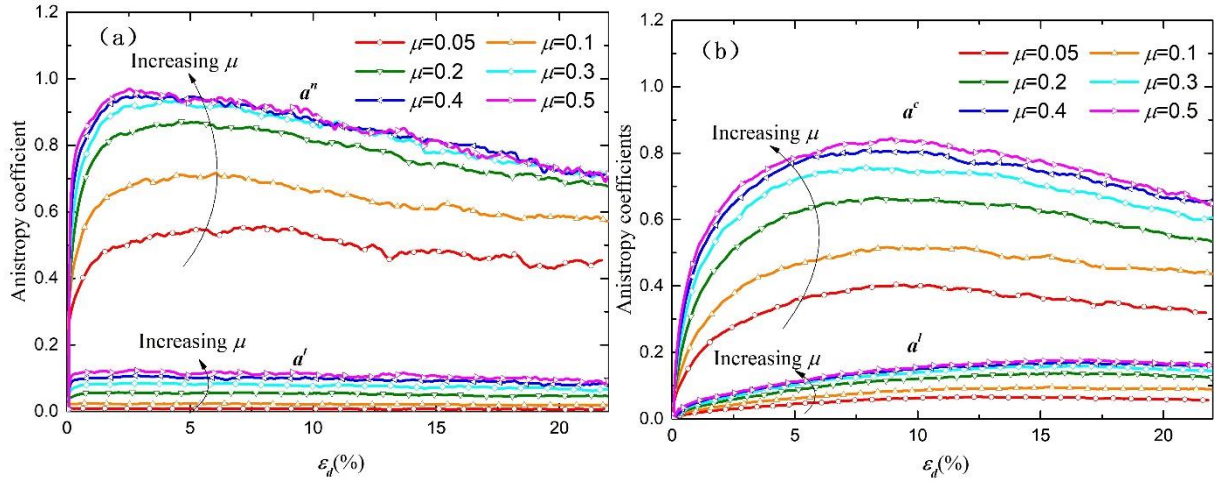
Fig.8 Anisotropy coefficient evolution curve (a) geometric anisotropy (b) mechanical anisotropy

The initial state, loading path and final size of the granular assembly are all the same under the true triaxial tests. Because of different inter-particle friction, great changes happen in the contact structure of the granular assembly. The average coordination number Z_t decreases, while the contact force enlarges, and the degree of anisotropy increases. The stark contrast between strong and weak contact forces is more striking, which effectively stimulates the anistropy of strong contact network and mobilizes shear strength to banlance external loads. Meanwhile, larger inter-particle friction makes the tangential contact point more difficult to destroy, which is conducive to the formation of the strong normal support to ensure that the granular assembly has a close contact state and maintain stability.

6   CONCLUSIONS

This paper has made a contribution to advance fundamental understanding of granular material response by considering the effects of inter-particle friction on the material response. Using DEM simulations of true triaxial tests, we have presented alternative ways to link the evolution of micro-mechanical parameters to the macro-scale behaviour of granular materials. The primary findings drawn from this qualitative study are the followings:

- In the constant-p and constant-b true triaxial tests, the macro stress-strain relationship of the granular assembly conforms to the existing physical and numerical results. With the increase of inter-particle friction, the peak deviatoric stress increases, the dilatancy state comes more rapidly, and the degree of dilatancy is more obvious.
- The influence of inter-particle friction on the coordination number of the strong and weak contact networks varies greatly. In the peak deviatoric stress state, the coordination number distribution of the weak contact network is similar to that of the total contact network and greatly affected by μ, while the number of particles forming

the force chain in the strong contact network does not fluctuate. The average coordination number of Γ_{weak} is larger than that of Γ_{strong}, with different inter-particle friction. It can be deduced that the weak contact network contributes greatly to the deformation of granular materials.

- The inter-particle friction has a significant effect on the micro-mechanical properties of the granular assembly, enhancing the contact force between particles and the overall stability. The increase in inter-particle friction results in the decrease of the relative slip behavior between particles, the increasing difference of contact forces between strong and weak contact networks, and the enchanced anisotropy feature of the total network. These phenomena stimulate the strong contact network to strengthen the shear strength to balance the external loads and enhance the ability of the granular assembly to bear macro-stress anisotropy.

REFERENCES

[1] K. Been, M. Jefferies. *Soil Liquefaction: A Critical State Approach.* Taylor & Francis, New York, (2006).

[2] Zhao J, Guo N. A new definition on critical state of granular media accounting for fabric anisotropy[C]// AIP Conference Proceedings. American Institute of Physics, (2013).

[3] Wei Z, Lifu Y, Gang M, et al. Macro-micro responses of crushable granular material in simulated true triaxial test. *Granular Matter* (2015) **17(4)**:497-509.

[4] L. Rothenburg, R. J. Bathurst. Analytical study of induced anisotropy in idealized granular materials. *Géotechnique* (1989), **39**:601-614.

[5] Wei Z, Jiaying L, Gang M, et al. Macroscopic and microscopic behaviors of granular materials under proportional strain path: a DEM study. *International Journal for Numerical and Analytical Methods in Geomechanics* (2016) **40(18)**:2450-2467.

[6] F. Radjai, D. E. Wolf, M. Jean, et al. Bimodal Character of Stress Transmission in Granular Packings. *Physical Review Letters* (1998) **80(1)**:61-64.

[7] F. Radjai, M. Jean, J. J. Moreau, et al.Force Distributions in Dense Two-Dimensional Granular Systems. *Physical Review Letters* (1996) **77(2)**:274-277.

[8] K. Hanley, X. Huang, C. O'Sullivan, et al. Temporal variation of contact networks in granular materials. *Granular Matter* (2014) 16(1):41-54.

[9] Jiaying L, Gang M, Wei. Z et al. Three-dimensional critical state and dilatancy of granular materials based on DEM. Journal of Hydraulic Engineering, (2017) **48(9)**:1107-1117.

[10] Wei Z, Wei W, Gang M, et al. Study of the effects of anistropic consolidation on granular materials under complex stress paths using the DEM. *Granular Matter* (2017) **19(4)**:76.

[11] Zhao J, Guo N. Rotational resistance and shear-induced anisotropy in granular media. *Acta Mechanica Solida Sinica* (2014) **27(1)**:1-14.

[12] Jiaying L, Gang M, Wei Z et al. Contact fabric characteristics of granular materials under three dimensional stress paths. *Chinese Journal of Theoretical and Applied Mechanics* (2019) **51(1)**:34-43.

[13] L. Rothenburg, N. P. Kruyt. Critical state and evolution of coordination number in simulated granular materials. *International Journal of Solids and Structures* (2004) **41(21)**:5763-5774.

[14] Huang X, K. J. Hanley, C. O'Sullivan, et al. Exploring the influence of interparticle friction on critical state behaviour using DEM. *International Journal for Numerical and Analytical Methods in Geomechanics* (2014) **38(12)**.

[15] M. Muthuswamy, A. Tordesillas. How do interparticle contact friction, packing density and degree of polydispersity affect force propagation in particulate assemblies?. *Journal of Statistical Mechanics: Theory and Experiment*, (2006), **2006(09)**:P09003-P09003.

[16] Antony S J, Kruyt N P. Role of interparticle friction and particle-scale elasticity in the shear-strength mechanism of three-dimensional granular media. *Physical Review E* (2009) **79(3)**:031308.

[17] V. Richefeu, M. S. E. Youssoufi, E. Azéma, et al. Force transmission in dry and wet granular media. Powder Technology (2009), 190(1):258-263.

[18] Xing H, K. J. Hanley, C. O'Sullivan, et al. Exploring the influence of interparticle friction on critical state behaviour using DEM. *International Journal for Numerical and Analytical Methods in Geomechanics* (2014) **38(12)**: 1276-1297.

[19] I. Bratberg, F. Radjai, A. Hansen. Dynamic rearrangements and packing regimes in randomly deposited two-dimensional granular beds. *Physical Review E* (2002) **66(3)**:031303.

[20] Jiaying L, Wei Z, Gang M, et al. Strong contacts, connectivity and fabric anisotropy in granular materials: a 3D perspective. *Powder Technology*. Submitted.

[21] S. Yimsiri, K. Soga. DEM analysis of soil fabric effects on behaviour of sand. *G´eotechnique* (2010) **60(6)**:483-495.

[22] M. Satake. The role of the characteristic line in static soil behavior. *IUTAM symposium on Deformation and Failure of Granular Materials* (1982): 63-68.

[23] M. Oda. Fabric tensor for discontinuous geological materials. *Soils and Foundations* (1982) **22(4)**: 96-108.

SIMULATION OF GEOLOGICAL FAULTS WITH DISCRETE ELEMENT METHOD

VADIM V. LISITSA[1,2], VLADIMIR A. TCHEVERDA[2] AND DMITRY R. KOLUYKHIN[2]

[1] Sobolev Institute of Mathematics SB RAS
4 Koptug ave., Novosibirsk, Russia, 630090
lisitsavv@ipgg.sbras.ru

[2] Institute of Petroleum Geology and Geophysics SB RAS
3 Koptug ave., Novosibirsk, Russia, 630090
cheverdava@ipgg.sbras.ru

Key words: DEM, Geological Faults

Abstract. We present an algorithm for simulation of the Earth's crust tectonic movements and formation of the geological faults and near-fault damage zones. The algorithms are based on the Discrete Elements Method, and it is implemented using CUDA technology. We used to simulate faults formation due to different scenarios of tectonic movements. We considered the displacements with dipping angles varied from 30 to 90 degrees; i.e., up to vertical throw. For each scenario, we performed simulations for some statistical realizations. To characterize the simulated faults and damage zones, we consider the strains distribution and apply data clustering and Karhunen-Loeve analysis to distinguish between different forms of the fault zones. In particular, clustering analysis shows that displacements with high and low dip angles form completely different geological structures. Nearly vertical displacements, high dip angles, form wide V-shaped deformation zones, whereas the at displacements cause narrow fault-cores with rapidly decreasing strains apart from the fault core. Results of the presented simulations can be used to estimate mechanical and seismic properties of rocks in the vicinity of the faults and applied further to construct models for seismic modeling and interpretation, hydrodynamical simulations, history of matching simulation, etc.

1 INTRODUCTION

A typical interpretation of geological faults from seismic data is a planar surface where the signal phase is discontinuous. Further on this representation of the faults is used in geological modeling to construct a model of the Earth's crust. As the result, faults are considered as a structural discontinuities in a model, whereas studies of the outcrops show that the faults and near-fault damage zones have more complex structure [1], [2]. In particular, damage zone may be highly fractured, thus, permeable especially for carbonates

[3], or it can be an impermeable due to the presence of deformation bonds which is typical for the sandstones [4]. Such differences of the local permeability near faults may strongly affect the reservoir performance. Thus a detailed representation of the fault and damage zone is required for efficient oil and gas exploration.

To study the fault formation due to tectonic motions, we suggest using numerical simulation. Simulation of finite deformations in solids and, in particular, in the geomaterials, geostructures, core samples, and Earth's crust can be done by either grid-based methods such as finite differences [5], finite elements [6], boundary elements [7] or by meshless approaches also known as discrete elements method (DEM) [8], [9]. The letter is preferred because no predefined crack or fault geometry is needed for simulation. However, particle-based methods are more computationally intense and require calibration of the particle properties to match the mechanics of the whole body [9], [10]. Despite this, the particle-based methods are incredibly flexible and can be used to generate multiple statistical realizations of the fault zones and study statistical features of the strongly deformed and highly-distorted zones. This opens a possibility to analyze the correlations between the peculiarities in the fault structure and their responses to the seismic waves. Moreover, use of the graphical processor units (GPU) significantly reduces the computational time making the DEM simulations an efficient and flexible tool.

In our opinion, meshless methods of geological faults formation simulations can be used to generate faults geometries in realistic environments. After that simulated faults can be introduced in geological models which are used for seismic modeling and imaging [11], [12], [13], moreover use advanced simulation techniques such as local mesh refinement [14], [15] allow studying seismic responses of the fine structure of near-fault damage zones.

The paper has the following structure. In the section 2, we describe the discrete element method, discuss its features, and present the algorithm for fault formation simulation by DEM. Description of the numerical experiments, cluster analysis, and statistical Karhunen–Loeve analysis is provided in section 3.

2   DISCRETE ELEMENT FORMULATION

To simulate the tectonic movements causing finite deformations and geological fault formation in the Earth's crust we use the discrete element method, following [16], [17], [18]. In this approach, the media is represented as an assembly of individual particles with a particular geometry and physical properties. Each particle is characterized by the coordinate of its center $\vec{x}^j$, radius R_j, repulsion and attraction bulk moduli K_r^+ and K_r^- respectively, tangential sliding stiffness K_s, and two friction coefficients μ_s is the static one and μ_d is the dynamic friction coefficient. Having set these parameters, one may define the interaction forces between two adjoint particles.

2.1 Computation of forces

Consider two particles with the numbers i and j, with the coordinates $\vec{x}^i$ and $\vec{x}^j$ and radii R^i and R^j respectively. Particle j acts on particle i with the normal elastic forces:

$$\vec{F}_n^{ji} = \begin{cases} K_r^- (R^i + R^j - \|\vec{X}^{ji}\|)\vec{n}^{ji}, & R^i + R^j - \|\vec{X}^{ji}\| > 0, & repulsion, \\ K_r^+ (R^i + R^j - \|\vec{X}^{ji}\|)\vec{n}^{ji}, & 0 \leq R^i + R^j - \|\vec{X}^{ji}\| \leq r_0, & active\ bond, \\ 0, & R^i + R^j - \|\vec{X}^{ji}\| > r_0, & no\ bond, \end{cases} \tag{1}$$

where r_0 is the bond length, typically chosen equal to $0.05(R_i + R_j)$, vector $\vec{X}^{ji} = \vec{x}^i - \vec{x}^j$ connects the centers of the particles and directed from particle j to particle i, vector $\vec{n}^{ji} = \vec{X}^{ji}/\|\vec{X}^{ji}\|$ is the unit vector directed from the centers of particle j to the center of particle i or normal vector, because it is normal to the contact plane. Note, that we use the model of linear elastic particles interaction and assume that the repulsion and attraction bulk moduli coincide, which is mainly valid for geomaterials across a wide range of scales.

Additionally frictional forces are taken into account if two particles are in a contact [18]:

$$\vec{F}_t^{ji} = \begin{cases} -K_s \delta_t \vec{t}^{ji}, & K_s \delta_t \leq \mu^s \|\vec{F}_n^{ji}\|, & static\ friction, \\ -\mu^d \|\vec{F}_n^{ji}\|\vec{t}^{ji}, & K_s \delta_t > \mu^s \|\vec{F}_n^{ji}\|, & dynamic\ friction, \end{cases} \tag{2}$$

where K_s is the tangential sliding stiffness, usually considered to be equal to bulk modulus; i.e., $K_s = K_r$, vector $\vec{t}^{ji}$ is the unitary tangential vector directed along the projection of the relative velocity onto the contact plane of two particles; i.e.,

$$\vec{t}^{ji} = \frac{\vec{v}^{ji} - (\vec{v}^{ji}, \vec{n}^{ji})\vec{n}^{ji}}{\|\vec{v}^{ji} - (\vec{v}^{ji}, \vec{n}^{ji})\vec{n}^{ji}\|}, \quad \vec{v}^{ji} = \vec{v}^i - \vec{v}^j. \tag{3}$$

In this notations $\vec{v}^{ji}$ is the relative velocity of the particle i with respect to particle j. Parameter δ^{ji} denotes the tangential displacement of the contact point from its initial position. Tangential forces provided by formula (2) satisfy the Coulombs law; i.e., the static friction governs the particles interaction if the forces as below a critical value. If the tangential forces exceed the critical dynamical friction proportional to normal force is applied. Typically the static friction is much higher than the dynamical one.

Additionally, an artificial dissipation is introduced in the system to prevent elastic waves from propagating through the model and ensuring the media to remain stable at infinite instants:

$$\vec{F}_d^i = -\nu\vec{v}^i, \tag{4}$$

where ν is an artificial viscosity.

The Earth's crust also remains under gravitational forces which are accounted as

$$\vec{F}_g^i = M_i g \vec{e}_3, \tag{5}$$

where $g = 9.8$ m/s is the gravitational constant, $\vec{e}_3 = (0, 0, 1)^T$, and M_i is the mass of the considered particle.

To compute the total forces acting at a particle one need to account the forces due to interactions with all the neighbors, plus artificial dissipation, plus gravitational forces, as a result, one gets:

$$\vec{F}^i = \sum_{j \in J(i)} \left[\vec{F}_n^{ji} + \vec{F}_t^{ji} \right] + \vec{F}_d^i + \vec{F}_g^i, \tag{6}$$

where $J(i)$ is the set of indexes of the neighbors of i-th particle.

2.2 Time integration

Having computed all external forces acting at j-th particle one may recompute its position using classical mechanics principles:

$$M^i \frac{d^2 \vec{x}^i}{dt^2} = \vec{F}^i \left(t, \vec{x}^i, \vec{x}^j, \frac{d\vec{x}^i}{dt}, \frac{d\vec{x}^j}{dt} \right), \tag{7}$$

where dissipative $\vec{F}_d^i$ and frictional forces $\vec{F}_t^{ji}$ explicitly depend on the particles velocities $\vec{v}^i = \frac{d\vec{x}^i}{dt}$.

To numerically resolve system of equations (7) we use the Verlet-like scheme with the velocity half-step [17], [19]. Assume coordinates, velocities, and thus forces of all particles are known at instant $t = t^n = \tau \cdot n$, then they can be updated to the instant t^{n+1} by the rule:

$$\begin{aligned}
\frac{(\vec{v}^i)^{n+1/2} - (\vec{v}^i)^n}{\tau/2} &= \frac{1}{M^i} \vec{F}^i \left(t^n, (\vec{x}^i)^n, (\vec{x}^j)^n, (\vec{v}^i)^n, (\vec{v}^j)^n \right), \\
\frac{(\vec{x}^i)^{n+1} - (\vec{x}^i)^n}{\tau} &= (\vec{v}^i)^{n+1/2}, \\
\frac{(\vec{v}^i)^{n+1} - (\vec{v}^i)^{n+1/2}}{\tau/2} &= \frac{1}{M^i} \vec{F}^i \left(t^{n+1}, (\vec{x}^i)^{n+1}, (\vec{x}^j)^{n+1}, (\vec{v}^i)^{n+1/2}, (\vec{v}^j)^{n+1/2} \right), \\
j &\in J(i).
\end{aligned} \tag{8}$$

In case of no explicit dependence of forces on the velocities the scheme is the second order accurate, however if applied to the equation of motion for DEM, this scheme possesses only the first order of approximation.

To ensure the stability of the finite-difference scheme we use the time step as suggested in [17], [19]

$$\tau \leq 0.2 \frac{D_{min}}{V_{max}}, \tag{9}$$

where R_{min} is the minimum diameter of the particles, and V_{max} is the maximal velocity of perturbation propagation in the system. In the case on no artificial viscosity, the maximal velocity is the wave-speed of the longitudinal wave in the media, where the normal stresses and strains are related as $\sigma_{nn} = K_r \varepsilon_{nn}$, where K_r is exactly the attractions/repulsion bulk modulus used in the simulation. If there is a nontrivial artificial viscosity, the velocity will increase, however, this effect is compensated by the constant 0.2. The discussion can be found in [18].

Note, that the implementation of the algorithm is based on the use of Graphic Processor Units with the help of domain decomposition to band limit the dependency matrix. Discussion of the implementation can be found in [20].

2.3 Boundary conditions

Proper implementation of the boundary conditions is a challenging task for the particles-based methods. In our research, we deal with two types of boundary conditions. First, we impose the rigid boundary condition; i.e., the surface Γ_s is fixed, or its movement is prescribed. Moreover, it is stiff; thus the particles cannot penetrate through it. Formally, this type of boundary condition can be stated as follows. Assume a boundary $\Gamma_s = \{\vec{x}|x_2 = x_2^B\}$. If a particle is close enough to the boundary; i.e., if for the j-th particle $|x_2^j - x_2^b| \leq R^j$, then $F_2^{jB} = K_r^-(R^j - |x_2^j - x_2^b|)$.

However, numerical implementation of this condition requires extra conditional operators. Thus it is worth implementing stiff-boundary as a series of particles, to make the simulation uniform either in the interior of the domain or near the boundary. To do so, we introduced the "boundary" particles with the same physical properties as those of the interior particles. However, we do not compute the forces acting on the "boundary" particles but allow the "boundary" particles to move according to a prescribed law. We specify the particular movement laws in the section 3.

The second type of the boundary conditions is $P_{over} = const$. This condition ensures the constant overburden pressure. Note that, condition P_{over} assumes that external forces act at the upper boundary of the domain $\Gamma_p(t)$ along the normal direction to the boundary. This boundary is flexible, and it evolves in time; thus, to impose the boundary condition we need to follow the elements which form the upper boundary. This can be done, for example, by computing Voronoi diagrams for upper elements. However, such procedures are computationally intense. To overcome this difficulty, we suggest using the flexible membrane at the upper boundary [21], [22]. The idea of the approach is to introduce a layer of discrete elements so that the membrane elements are affected only by the normal forces.

If two adjoint membrane elements are interacting

$$\vec{F}_n^{m,m\pm 1} = K_r(R^{m\pm 1} + R^m - \|\vec{X}^{m,m\pm 1}\|)\vec{n}^{m,m\pm 1}, \tag{10}$$

if membrane element interacts with other elements

$$\vec{F}_n^{mi} = K_r(R^i + R^m - \|\vec{X}^{mi}\|)\vec{n}^{mi}, \quad R^i + R^m - \|\vec{X}^{mi}\| > 0. \tag{11}$$

It means that the adjoint membrane elements are bonded, and these bonds never bake, however no bonds of friction are considered when membrane elements interact with elements of other types. The membrane elements are ordered; thus it is easy to approximate constant pressure condition. If a membrane element with number m is considered then additional force, due to the pressure is

$$\vec{F}_p^m = 2PR^m\vec{n}, \tag{12}$$

where $\vec{n}$ is the vector normal to the boundary, which can be computed as:

$$\vec{n} = (x_2^{m-1} - x_2^{m+1}, x_1^{m-1} - x_1^{m+1})^T,$$

the direction of the normal vector is defined uniquely due to the ordering of the membrane elements.

2.4 Output parameters

Numerous parameters can be obtained as a result of discrete elements simulations. If rock properties are studied using uniaxial and triaxial stress tests, then the primary attention is paid to the distribution of the braked bonds [23], [24], stresses, and normal forces distribution [25] However, at the scale of the geological bodies a reliable parameter to determine fault zones is the strains distribution [26], [16], [17], [27], [11]. These strains can be further translated to the changes of physical parameters of rocks using the experimental laboratory measurements.

To estimate the strains distribution one may compute the relative displacements element-wise, after that the strain tensor components can be computed and interpolated to a regular grid. A detailed discussion of the strains estimation can be found in [26].

3 NUMERICAL EXPERIMENTS

In this paper, we focus our attention on the effect of the direction and amplitude of tectonic movement on the geometry of the fault and damage zone. DEM-based simulations include uncertainties due to the particle's positions and radii distributions. It means that for each scenario of the tectonic movements we need to perform a series of numerical simulations for different statistical realizations of the particles geometry distribution.

In all the experiments presented below, we use the following set of parameters. The size of the computational domain is 4000 m in horizontal and 500 m in the vertical direction. The repulsion/attraction modulus is 16 GPa, and same value is used for the tangential sliding stiffness. The coefficient of static friction is 0.8, which is typical for the majority of geomaterials, whereas the dynamic friction coefficient is 0.3, which is close to that of sandstone and limestone. We consider the bonds length proportional to the radii of the adjoint particles; i.e., $r_0 = 0.05(R_j + R_i)$. We assume that the formation is buried at 3000 m; thus the overburden pressure of 10^7 Pa is applied at the top boundary of the model. The particles radii are homogeneously distributed from 1.25 to 2.5 m. So, the total number of elements is 390000.

We consider several scenarios of dipping normal tectonic movements with the dip angles equal to 90°, 75°, 60°, 45°, 30°. Maximal vertical displacement is 100 m.

For each tectonic movement we simulate ten statistical realizations of the particles distributions; thus, 10 simulations are performed for each scenario. Also, we computed extra 20 realizations for the most common movement scenario with the dip angle equal to 60°. Each simulation consists of two stages. First, the elements should be compacted under the overburden pressure and gravitational forces. This step takes about 60 % of the computational time. Second, the tectonic movements are applied. The total simulation time for one experiment (one realization) is about 8.7 hours by a single GPU (NVIDIA Tesla M 2090).

We provide the strains distribution for displacement with dip angle equal to 30°, 60°, 90° in figures 1-3. The main trend observed from the presented figures is that for big dip angles; i.e., for nearly vertical displacements no narrow fault cores are formed. When the dip angle gets smaller fault cores are formed (figure 1) and they are located within

Figure 1: A single realizaton of hydrostatic (top) and shear (bottom) strains distribution in the fault zone for the displacement dip equal to 30°.

a narrow zone. Moreover, for low dip angles the form of the fault and its inclination is similar, thus might depend mainly on the medium properties rather than on the direction of tectonic movements. To verify this assumption, we perform clustering of the results and their statistical analysis in the following section.

3.1 Clustering of the results

According to the figures 1-3 fault zones formed after tectonic movements with low dip angles are similar. To quantify this observation, we applied k-means clustering of the computed strains distribution. Before processing to the formal analysis, we need to point out, that we performed two additional series of simulations (9 realizations in each series) corresponding to the tectonic movement dip angle equal to 60°. In total we have 27 statistical realizations corresponding to this scenario; however, we will still consider them as three independent series in our statistical analysis.

We start with the determination of the optimal number of clusters in which the data can be partitioned. To do so, we use the Calinski-Harabasz Index [28] which measures the ratio of the total inter-clusters variance to total within-cluster variance for all possible data subdivision. According to this criterion the optimal number of clusters is two. Then we applied k-means clustering technique to our data. We constructed clusters for each component of the strain tensor separately, as well as for all of them together. The panels in figure 4 represents the clustering results in two clusters. In these experiments we applied clustering to the all components of the strain tensor. One may note that the displacement scenarios with dip angles equal to 75° and 90° form one cluster, whereas all others form the second cluster. We consider the within-cluster sum of squares (WCSS); i.e., the functional which is minimized by the k-means algorithm:

$$D = \sum_{i=1}^{k} \sum_{e \in S_i} \| e - <e>_i \|,$$

where k is a number of clusters, S_i is the i-th cluster, a subset of the considered dataset,

Figure 2: A single realizaton of hydrostatic (top) and shear (bottom) strains distribution in the fault zone for the displacement dip equal to 60°.
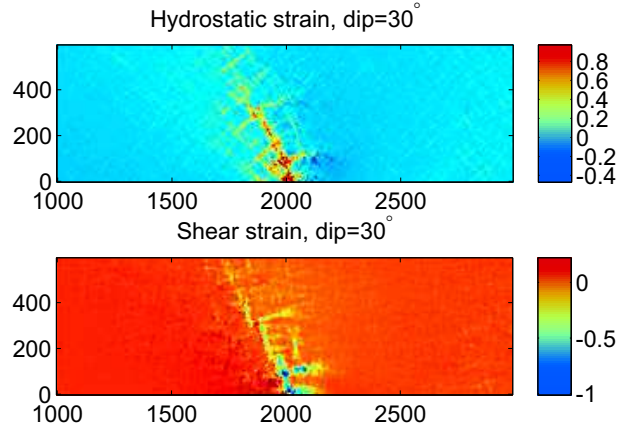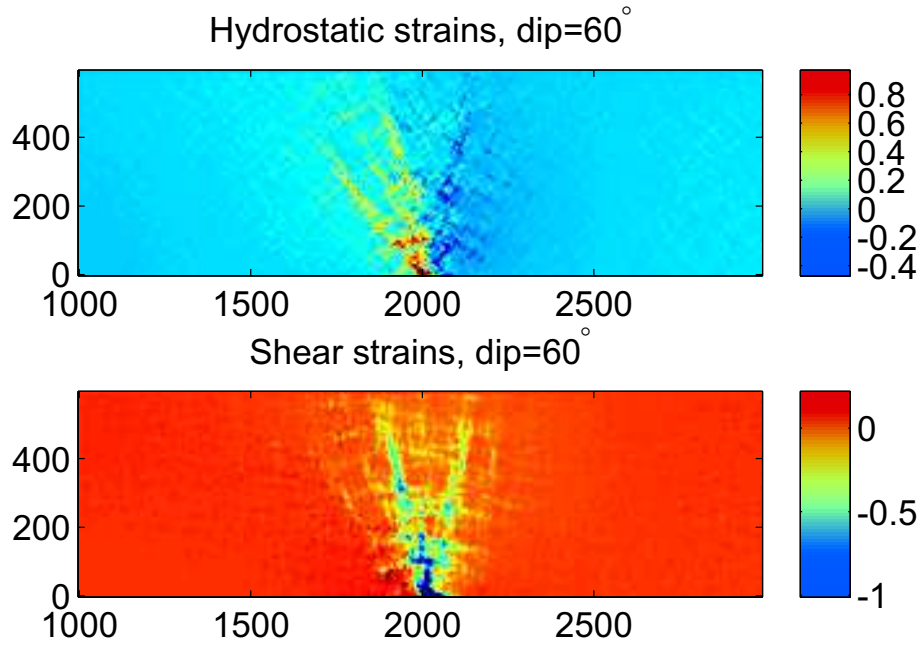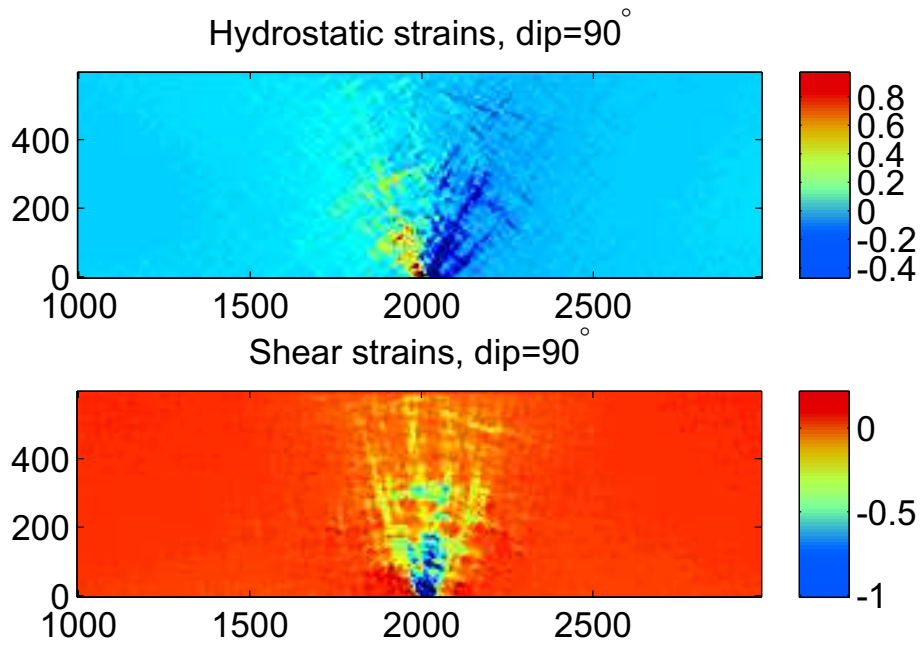

Figure 3: A single realizaton of hydrostatic (top) and shear (bottom) strains distribution in the fault zone for the displacement dip equal to 90°.
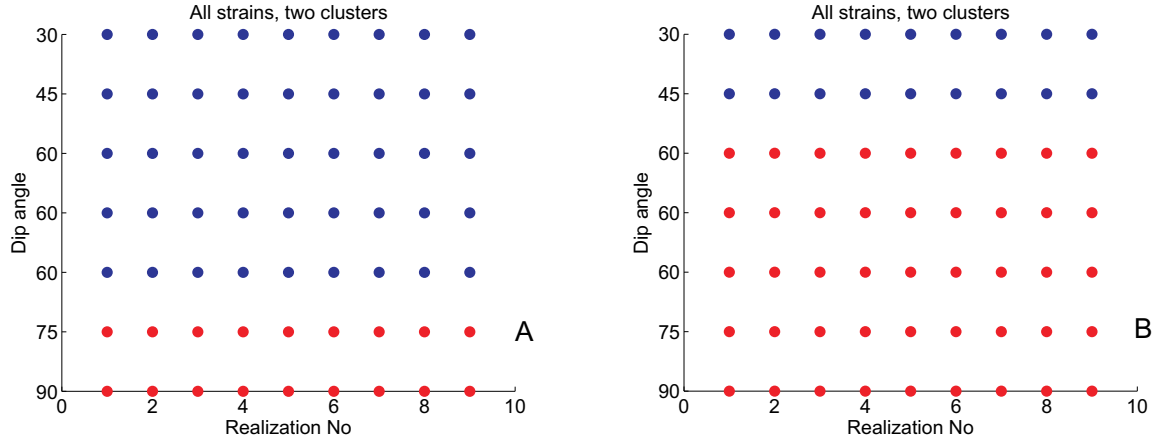
Figure 4: Panels representing data clustering (two clusters) for all components of strain tensor. Left panel (A) corresponds to the optimal clustering with minimal distance, right panel (B) represents a case of local minimum of k-means functional. Different colors correspond to different clusters.

$< e >_i$ is the mean value of the elements from i-th set S_i. There are different options to define the norm; however, in this work, we deal with the L^2 norm of vectors. So, the optimal clustering delivers $D_{all} = 3692$ respectively. However, there is another local minimum of the WCSS functional which leads to the clustering where strains for the tectonic displacements with dip angles equal to 30° and 45° form one cluster, whereas solutions corresponding to the subvertical movements go to the other cluster (figure 4 B). In the second case, the WCSS is $D_{all} = 3753$. The difference in the within-cluster distances between the two scenarios is less than 1%, and these two cases are hardly distinguishable. It means that the displacements with dipping angle equal to 60° can either form a wide deformation zone, same as subvertical displacements, or narrow inclined fault cores, same as in case of flat tectonic movements.

4   CONCLUSIONS

We presented an algorithm for simulation of the Earth's crust tectonic movements and formation of the geological faults and near-fault damage zones. The algorithms are based on the Discrete Elements Method, and it is implemented using CUDA technology. We used to simulate faults formation due to different scenarios of tectonic movements. We considered the displacements with dipping angles varied from 30 to 90 degrees; i.e., up to vertical throw. For each scenario, we performed simulations for some statistical realizations. To characterize the simulated faults and damage zones, we considered the strains distribution and applied data clustering to distinguish between different forms of the fault zones. In particular, clustering analysis shows that displacements with high (75° and 90°) and low (30° and 45°) dip angles form completely different geological structures. Nearly vertical displacements, high dip angles, form wide V-shaped deformation zones, whereas the flat displacements cause narrow fault-cores with rapidly decreasing strains apart from the fault core. Results of the presented simulations can be used to estimate mechanical and seismic properties of rocks in the vicinity of the faults and applied further

to construct models for seismic modeling and interpretation, hydrodynamical simulations, history of matching simulation, etc.

5   ACKNOWLEDGMENTS

REFERENCES

[1] Choi J.-H., Edwards P., Ko K., and Kim Y.-S. Definition and classification of fault damage zones: A review and a new methodological approach. *Earth-Science Reviews.* (2016) **152**:70–87.

[2] Peacock D. C. P., Dimmen V., Rotevatn A., and Sanderson D. J. A broader classification of damage zones. *Journal of Structural Geology.* (2017) **102**:179–192.

[3] Hausegger S., Kurz W., Rabitsch R., Kiechl E., and Brosch F. J. Analysis of the internal structure of a carbonate damage zone: Implications for the mechanisms of fault breccia formation and fluid flow. *Journal of Structural Geology.* (2010) **32**:1349–1362.

[4] Fossen H., Schultz R. A., Shipton Z. K., and Mair K. Deformation bands in sandstone: a review. *Journal of the Geological Society.* (2007) **164**:755–769.

[5] González G., Gerbault M., Martinod J., Cembrano J., Carrizo D., Allmendinger R., and Espina J. Crack formation on top of propagating reverse faults of the Chuculay fault system, northern Chile: Insights from field data and numerical modelling. *Journal of Structural Geology.* (2008) **30**:791–808.

[6] Guiton M. L. E., Sassi W., Leroy Y. M., and Gauthier B. D. M. Mechanical constraints on the chronology of fracture activation in folded devonian sandstone of the western moroccan anti-atlas. *Journal of Structural Geology.* (2003) **25**:1317–1330.

[7] Resor P. G. and Pollard D. D. Reverse drag revisited: Why footwall deformation may be the key to inferring listric fault geometry. *Journal of Structural Geology.* (2012) **41**:98–109.

[8] Gray G. G., Morgan J. K., and Sanz P. F. Overview of continuum and particle dynamics methods for mechanical modeling of contractional geologic structures. *Journal of Structural Geology.* (2014) **59**(Supplement C):19–36.

[9] Lisjak A. and Grasselli G. A review of discrete modeling techniques for fracturing processes in discontinuous rock masses. *Journal of Rock Mechanics and Geotechnical Engineering.* (2014) **6**:301–314.

[10] Alassi T.H. and Holt R. Relating discrete element method parameters to rock properties using classical and micropolar elasticity theories. *International Journal for Numerical and Analytical Methods in Geomechanics.* (2012) **36**:1350–1367.

[11] Botter C., Cardozo N., Hardy S., Lecomte I., and Escalona A. From mechanical modeling to seismic imaging of faults: A synthetic workflow to study the impact of faults on seismic. *Marine and Petroleum Geology.* (2014) **57**:187–207.

[12] Kolyukhin D. R., Lisitsa V. V., Protasov M. I., Qu D., Reshetova G. V., Tveranger J., Tcheverda V. A., and Vishnevsky D. M. Seismic imaging and statistical analysis of fault facies models. *Interpretation* (2017) **5**:SP71–SP82.

[13] Vishnevsky D. M., Kolyukhin D. R., Lisitsa V. V., Protasov M. I., Reshetova G. V., Tcheverda V. A., Qu D., and Tveranger J. Correlation analysis of statistical facies fault models. *Doklady Earth Sciences.* (2017) **473**:477–481.

[14] Kostin V., Lisitsa V., Reshetova G., and Tcheverda V. Local time-space mesh refinement for simulation of elastic wave propagation in multi-scale media. *Journal of Computational Physics.* (2015) **281**:669–689.

[15] Lisitsa V., Reshetova G., and Tcheverda V. Finite-difference algorithm with local time-space grid refinement for simulation of waves. *Computational Geosciences.* (2012) **16**:39–54.

[16] Hardy S. and Finch E. Discrete-element modelling of detachment folding. *Basin Research.* (2005) **17**:507–520.

[17] Hardy S., McClayc K., and Munozb J. A. Deformation and fault activity in space and time in high-resolution numerical models of doubly Vergent thrust wedges. *Marine and Petroleum Geology.* (2009) **26**:232–248.

[18] Luding S. Introduction to discrete element methods. *European Journal of Environmental and Civil Engineering.* (2008) **12**:785–826.

[19] Mora P. and Place D. Simulation of the frictional stick-slip instability. *Pure and Applied Geophysics.* (1994) **143**:61–87.

[20] Lisitsa V. V., Tcheverda V. A., and Volianskaia V. V. GPU-based implementation of discrete element method for simulation of the geological fault geometry and position. *Supercomputing Frontiers and Innovations.* (2018) **5**:46–50.

[21] Wang Y. and Tonon F. Modeling triaxial test on intact rock using discrete element method with membrane boundary. *Journal of Engineering Mechanics.* (2009) **135**:1029–1037.

[22] Bono J. de, Mcdowell G., and Wanatowski D. Discrete element modelling of a flexible membrane for triaxial testing of granular material at high pressures. *Géotechnique Letters* (2012) **2**:199–203.

[23] Cundall P. A. and Strack O. D. L. A discrete numerical model for granular assemblies. *Géotechnique* (1979) **29**:47–65.

[24] Li Z., Wang Y. H., Ma C. H., and Mok C. M. B. Experimental characterization and 3D DEM simulation of bond breakages in artificially cemented sands with different bond strengths when subjected to triaxial shearing. *Acta Geotechnica* (2017) **12**:987–1002.

[25] Duan K., Kwok C. Y., and Ma X. DEM simulations of sandstone under true triaxial compressive tests. *Acta Geotechnica* (2017) **12**:495–510.

[26] O'Sullivan C., Bray J. D., and Li S. A new approach for calculating strain for particulate media. *International Journal for Numerical and Analytical Methods in Geomechanics.* (2003) **27**:859–877.

[27] Abe S., van Gent H., and Urai J. L. DEM simulation of normal faults in cohesive materials. *Tectonophysics.* (2011) **512**:12–21.

[28] Calinski T. and Harabasz J. A dendrite method for cluster analysis. *Communications in Statistics.* (1974) **3**:1–27.

STOCHASTIC SOLUTION OF GEOTECHNICAL PROBLEMS IN TRULY DISCRETE MEDIA

Ignacio G. Tejada[1]

[1] Departamento de Ingeniería y Morfología del Terreno - ETSI Caminos, Canales y Puertos
Universidad Politécnica de Madrid (UPM)
C/ Profesor Aranguren 3, 28040 Madrid, Spain
e-mail: ignacio.gtejada@upm.es

Key words: Granular Materials, DEM, Statistical Mechanics

Abstract. This research deals with the solution of geotechnical problems on intermediate length scales, i.e. when the length scale of interest is larger than the size of the grains of the soil (or rockfill) but the medium cannot be considered as a continuous body. This is because on such scales, despite the large number of involved grains, the volumetric average stress fluctuates around the mean value and the fluctuation is due to the truly discrete nature of the soil. Then, the smooth stress field that would be predicted by continuum mechanics approaches is replaced by a stochastic system of interparticle forces forming force chains. The forces can be transformed into equivalent stresses by means of homogenization techniques, but the obtained fields are again non-smooth and stochastic. A classical statistical mechanics framework is followed to anticipate the probability distribution functions of equivalent (extensive) stresses according to the macroscopic constraints of the problem. In particular, we get stochastic models for two seminal problems in geotechnics: the at rest lateral earth pressure acting on a retaining wall and the vertical stress at a given point in the soil that is caused by a vertical surface load. The theory is validated through massive numerical simulation with the Discrete Element Method.
Mesoscale geotechnical analysis can find its main applications in the case of rockfill or other very coarse granular materials. However, it could be useful as well for laboratory, numerical and theoretical researches that are approached on small length scales. This theoretical framework contributes to fill the gap between micro and macro geotechnics and the resulting stochastic models may be useful for reliability analyses.

1   INTRODUCTION

There is a class of problems in soil mechanics that deals with the estimation of the stress field caused by the application of a certain load on the soil. The stress field is needed to verify whether these stresses can be withstood by the soil or to determine the deformations of the soil, which must usually remain limited.
In many seminal problems in soil mechanics the stress field was computed in the framework of the theory of elasticity [1]. For example, for the case of a vertical surface load,
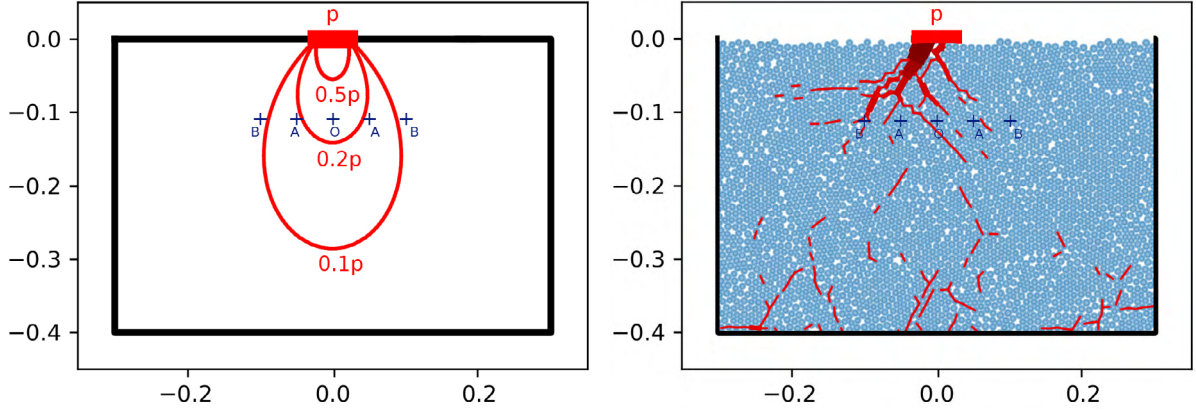
(a) The solution in a continuous, homogeneous, isotropic and lineal elastic half-space obtained from continuum mechanics.

(b) A solution in a half-space made of discrete and elastic particles obtained from DEM simulation.

Figure 1: Flamant's problem (with uniform load of magnitude p on a strip of width $2a$).

Boussinesq [2], Flamant [3], Newark, etc. provided solutions by the end of the XIXth century. In all these cases the soil is supposed to be a half-space that is continuous, homogeneous, isotropic and linear elastic. Although this behavior may be a quite severe approximation, it can be sometimes useful as it gives reasonably accurate solutions. When this is not possible, rather complicated constitutive relationships are needed. Many constitutive models have been proposed to capture the inhomogeneous, anisotropic, non-linear or non-elastic behavior of soils [4]. These phenomenological laws are calibrated from laboratory experiments and, as common numerical methods are capable for using them, many geotechnical problems can be solved with noteworthy success. However it is not yet clear how geotechnical problems can be solved when the truly discrete nature of the soils cannot be ignored. Although such situation is not very common (since most of the time the length scale of interest is much larger than the typical size of soil particles and it behaves as a continuous body) there is no clear procedure to estimate the stresses (and their variability) in such circumstances. This could be the case of large particles (e.g. rockfill, rock blocks) or micromechanical approaches in which both length and grain scales come together and the particulated nature of soil has consequences. The most direct one is the existence of fluctuations of stresses (or forces [5]), with local values that may be much higher than the average.

Stress fluctuations are possible because the voids interrupt the continuity of the stress field from particle to particle. The support of the own weight or of any external load is provided by a system of interparticle forces, which form force chains [6, 7, 8, 9, 10, 11, 12, 13, 14]. The next two significant features invalidate continuum based approaches:

1. the stress field may sharply change from a particle to its immediate neighbors,

2. the problem is stochastic: if particles are packed in a different way, a new equilibrium is reached with a completely different system of interparticle forces.

This is the reason why the equivalent stress field of a particle can only be anticipated with some uncertainty. This work aims at establishing the statistical distribution of stress values expected at a given position, what will make it possible to get expected values with uncertainty intervals. This is done by following a statistical mechanics approach that is presented in section 2. Then this approach is applied to two seminal problems in geotechnics and verified trough numerical simulation (section 3). Results are shown in section 4 and discussed in section 5.

2   STATISTICAL MECHANICS

Statistical mechanics is the branch of physics that deals with systems made of a large number of constituents [15]. Although it was originally developed for thermal systems, several applications for granular media have been sought for [16, 17, 18, 19, 20, 21], starting from first Edward's model in 1989. Some of these approaches have been set up by considering the role played by the extensive stress (*i.e.* the product of the volumetric average of the stress within a region by the volume of that region) [19, 20, 21]. Following these ideas, a theoretical model for geotechnical applications has been set up [22]. This model is outlined in the following paragraphs:

1. There is vast number of ways of packing a granular system in static equilibrium objected to some body forces and boundary conditions. Each new random realization of an experiment will end up with one of these solutions. In the absence of any further information all the solutions are supposed to be equally likely.

2. Each packing can be partitioned into domains according to a Voronoi diagram. Each cell includes the space occupied by the particle and an associated part of void space.

3. The volumetric average of the stress field within a cell can be obtained from the interparticle forces that keep the corresponding particle in static equilibrium [23]:

$$\langle \sigma_{ij}^m \rangle = \frac{1}{V^m} \int \sigma_{ij}^m dV^m = \frac{1}{V^m} \sum_l x_i^{mn} F_j^{mn}, \qquad (1)$$

where V^m is the volume of the cell associated to particle m, F_j^{mn} is the j-component of the interaction force between particles m and n and x_i^{mn} is the i-component of the point of application of the force. The tensor product of forces by positions is the so-called extensive stress $\Sigma_{ij}^m = \sum_l x_i^{mn} F_j^{mn}$. This tensor is equal to the volumetric average of the stress field multiplied by the volume of the cell, $\Sigma_{ij}^m = \langle \sigma_{ij}^m \rangle V^m$. The extensive stress is expressed in energy units and is additive (the extensive stress of a composite body is equal to the sum of the extensive stress of its components).

4. The volumetric average of the stress field within a control volume V^c ($< V^m$) located at $\mathbf{x}^c$, in the cell of particle m is supposed to be equal to the volumetric average of the stress of the cell. This assumption becomes true as V^c approximates V^m.

5. A statistical ensemble is an idealization consisting of a large number of virtual copies of the system randomly generated and driven according to the same procedure. Statistical samples can be generated by gathering the values of the extensive stress Σ_{ij} of a control volume V^c that is located at $\mathbf{x}^c$.

6. Normal extensive stresses $(\Sigma_{xx}, \Sigma_{yy}, \Sigma_{zz})$ are supposed to take any positive value provided that the average value over an ensemble is finite and corresponds to the solution of the equivalent boundary value problem (this is the value of the corresponding stress multiplied by the control volume: $\mu_{\Sigma ii} = \sigma_{ii} V^c$). Values obtained from different packings are uncorrelated and the three normal and shear components are uncorrelated from each other. Shear extensive stresses take any positive or negative value, provided that the distribution has a specified variance.

7. Under these constraints, the most probable statistical distribution of extensive normal components is an exponential distribution (similar to that of the Maxwell-Boltzmann statistics but with the extensive stress playing the role of energy):

$$f_{(\Sigma_{ii})} = \frac{1}{\mu_{\Sigma ii}} e^{-\Sigma_{ii}/\mu_{\Sigma ii}}. \tag{2}$$

For shear stresses, this model is incomplete. If either positive or negative values were possible and the variance was defined, then a normal distribution $\mathcal{N}_{(\mu_{\Sigma ij}, \sigma_{\Sigma ij})}$ would be expected, because this is the PDF of maximum entropy under such constraints. However a procedure to anticipate of such variance in a given problem is still missing.

3 METHODOLOGY

3.1 Estimation of the expected probability distribution function in two geotechnical problems

Two seminal problems in geotechnics have been analyzed in 2D, x-z plane, for the lack of simplicity: a half-space made of almost equal sized disks under its own weight and the same space supporting a vertical finite surface load.

Gravity: The gravity causes a stress field that at any point can be determined from the weight of the overlying material:

$$\sigma_{zz,\mathrm{g}} = \gamma z, \tag{3}$$

where γ is the unitary weight (in kN/m^3) and z is the depth. $\gamma = (1-n)\,\rho_{\mathrm{s}}\mathrm{g}$, ρ_{s} is the density of the material of the particles, g is the gravitational acceleration and n is the average porosity of the overlying packing.

The horizontal stress also increases with depth, but it does at a rate given the at-rest coefficient of lateral earth pressure:

$$\sigma_{xx,\mathrm{g}} = K_0 \sigma_{zz,\mathrm{g}}. \tag{4}$$

Just by the action of the gravity, vertical and horizontal stresses are aligned with principal stresses,

$$\sigma_{xz,\mathrm{g}} = 0.0. \tag{5}$$

Vertical surface load: The stress field caused by a vertical surface load is obtained from classical solutions (e.g. Boussinesq and Flamant problems, explained in [1]). In both cases the stresses depend not only on the depth but also on the horizontal distance to the applied load. In 2D, the stresses caused by a surface load p are given by:

$$\sigma_{zz,\mathrm{p}} = \frac{p}{\pi} \left[(\theta_1 - \theta_2) + \sin \theta_1 \cos \theta_1 - \sin \theta_2 \cos \theta_2 \right], \tag{6}$$

$$\sigma_{xx,\mathrm{p}} = \frac{p}{\pi} \left[(\theta_1 - \theta_2) - \sin \theta_1 \cos \theta_1 + \sin \theta_2 \cos \theta_2 \right], \tag{7}$$

and

$$\sigma_{xz,\mathrm{p}} = \frac{p}{\pi} \left[\cos \theta_2{}^2 + \cos \theta_1{}^2 \right], \tag{8}$$

with $\theta_1 = \arctan (x - X_1)/z$ and $\theta_2 = \arctan (x - X_2)/z$ and X_1, X_2 the left and right limits of the surface load.

Gravity + Vertical surface load: As the material is supposed to be elastic, both solutions can be superposed in such a way that $\sigma_{ij} = \sigma_{ij,\mathrm{g}} + \sigma_{ij,\mathrm{p}}$. For any stress state, a shear indicator can be defined as the ratio of the maximum shear stress to the mean stress $s = (\sigma_1 - \sigma_3) / (\sigma_1 + \sigma_3)$.

Once the expected values of stresses are known, the PDFs of extensive stresses can be established. The mean values at any control volume are given by $\mu_{\Sigma ij} = \sigma_{ij} V^c$. For normal components, these values set the scale of the exponential distributions. Regarding extensive shear stresses, the PDF remains unknown.

Finally, when only the gravity acts, the at-rest coefficient of lateral pressure would follow the next ratio distribution:

$$f_{(K_0)} = \frac{\mu_{K0}}{(\mu_{K0} + K_0)^2}, \tag{9}$$

whose expected value would be $\mu_{K0} = \mu_{\Sigma xx}/\mu_{\Sigma zz}$.

3.2 Numerical validation

A series of numerical experiments were performed with the discrete element method [24], implemented in YADE-DEM [25][1]. A common frictional-Hookean DEM approach was followed. Two types of numerical experiments were performed: Case 1 (gravity) and Case 2 (gravity + surface load). The parameters used in the simulations are included in Table 1.

---

[1] https://yade-dem.org/.

Table 1: Parameters used in the DEM numerical simulations to generate ensemble samples.

Parameter		Case1	Case2	Units
Number of particles	N	5000		-
Number of experiments	#	1812	5324	-
Simulation width	L	1.0	1.0	m
Mean diameter	D	0.01		m
Diameter dispersion	$\frac{\Delta D}{D}$	0.05		-
Young's modulus	E	$1.0 \cdot 10^7$		kPa
Material density	ρ_{s}	$2.6 \cdot 10^3$		kg.m^{-3}
Interparticle friction	Φ	$\pi/6$	0	rad
Loading width	$2a$	-	0.045	m
Surface load	p	-	44.4	kPa
Control point O	$(x^{\mathrm{O}}, z^{\mathrm{O}})$	$(0.00, 0.29)$	$(0.00, 0.10)$	m
Control point A	$(x^{\mathrm{A}}, z^{\mathrm{A}})$	-	$(0.08, 0.10)$	m
Control point B	$(x^{\mathrm{B}}, z^{\mathrm{B}})$	-	$(0.15, 0.10)$	m

Packings were generated by randomly pouring 5000 particles within a 1.0 m wide domain and waiting for an almost complete dissipation of the kinetic energy. The diameters of disks uniformly laid within the interval $D \pm \Delta D$. Gravity acted downwards with g = 9.81 m/s^2. Surface loads were applied by gently and vertically (downwards) moving a rigid body of length $2a$ and centered at $x = 0.0$. The simulation was stoped when the vertical reaction of the soil on the rigid element was equal to $2ap$.

A statistical sample of extensive stress values was measured at different control positions (see 1). In Case 1 the control point was located in the middle of the simulation box at a depth $z^c \pm \Delta z^c$ from the surface. In Case 2, three control points were considered: point O -right below the center of the surface load- and points A and B -located at the same depth than O but horizontally shifted (leftwards and rightwards) a certain distance-. These points were selected because the total stress induced there by the surface load $\sigma_{zz,\mathrm{p}}$ is noticeable, with respective ratios $\sigma_{zz,\mathrm{p}}/\sigma_{zz,\mathrm{g}}$ of 4.59, 2.15 and 0.65. The simulation box was large enough to ensure that the stress field caused by the surface loading p is below $0.05p$ at the boundaries. The control volume was $V^c = 2.5 \cdot 10^{-5}$ m$^2 \simeq D^2/4$.

As the average height of the half-space H (and hence the porosity n) as well as the final position of the footing H_{f} slightly changed with the realization of the experiment, there are some uncertainties in the measurement. $H \pm \Delta H$ and $n \pm \Delta n$ were computed after performing a linear regression of the vertical stress with the depth (Eq. 3, with $z = H - h_i$). The final position of the footing and the actual surface load, with their variation intervals, are directly measured during the numerical experiments. An additional source of uncertainty is caused by the fact that the position of the control point may separate up to a distance $\simeq D/2$ from the center of the particle used to compute the extensive stress of the cell.
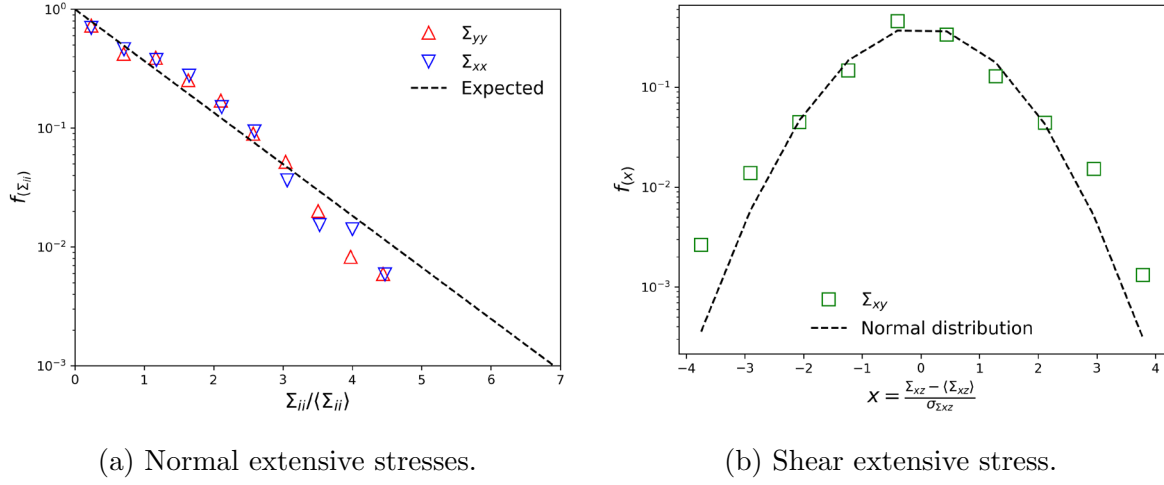
(a) Normal extensive stresses.
(b) Shear extensive stress.

Figure 2: Expected and measured statistical distribution of extensive stresses in Case 1.

4 RESULTS

The obtained height of the half-space after pouring the particles under the action of gravity was $H = 0.49 \pm 0.01$ (average porosity $n = 0.22 \pm 0.01$) for interparticle friction angle $\phi = \pi/6$ and $H = 0.46 \pm 0.02$ m ($n = 0.15 \pm 0.03$) for frictionless particles. In Case 1, the measured at-rest coefficient of lateral earth pressure (sample mean) was $\langle K_0 \rangle = 0.83$. The expected vertical extensive stress was $\Sigma zz = (19.68 \pm 0.42) \cdot 10^{-2}$ Jul and the measured sample mean was $\langle \Sigma_{zz} \rangle = 19.42 \cdot 10^{-2}$ Jul, perfectly lying within the incertitude interval. In Fig 2 the statistical distribution of vertical and horizontal extensive stresses of the ensemble are compared to the expected exponential distributions.

In Case 2, $\langle K_0 \rangle = 0.95$ after the gravity deposition. The action of the surface load increased shear ratios from $s_O = s_A = s_B = 0.023$ to $s_O = 0.693$, $s_A = 0.614$ and $s_B = 0.466$ and rotated the principal stressess $33.9°$ and $51.6°$ in points A and B, respectively, and did not rotate them in point O. The expected vertical extensive stress at points O, A and B were $\Sigma_{zz}^O = (33.17 \pm 1.00) \cdot 10^{-2}$ Jul, $\Sigma_{zz}^A = (18.73 \pm 1.40) \cdot 10^{-2}$ Jul and $\Sigma_{zz}^B = (9.81 \pm 1.01) \cdot 10^{-2}$ Jul. The sample mean at the control points were $\langle \Sigma_{zz}^O \rangle = 32.6 \cdot 10^{-2}$ Jul, $\langle \Sigma_{zz}^O \rangle = 17.8 \cdot 10^{-2}$ Jul and $\langle \Sigma_{zz}^B \rangle = 8.9 \cdot 10^{-2}$, lying within the interval in all the cases. In Fig. 4 the PDFs are plotted. In the three cases, the distributions seem to follow the exponential distribution predicted by the proposed model. The fitting with the exponential distribution is better in Case 2 than in Case 1, something that could be related to the higher shear ratios and the stress rotation.

5 DISCUSSION

The statistical distributions of extensive stress measured with DEM fit quite well those that were predicted under certain hypotheses: exponential distributions for extensive normal stresses and normal distribution for extensive shear stresses. The fitting is better

(a) Normal extensive stresses. The dotted line corresponds to the mean K_0 value.

(b) At-rest coefficient of earth trust. The doted line is the expected ratio distribution resulting from two independiently exponentially distributed normal stresses
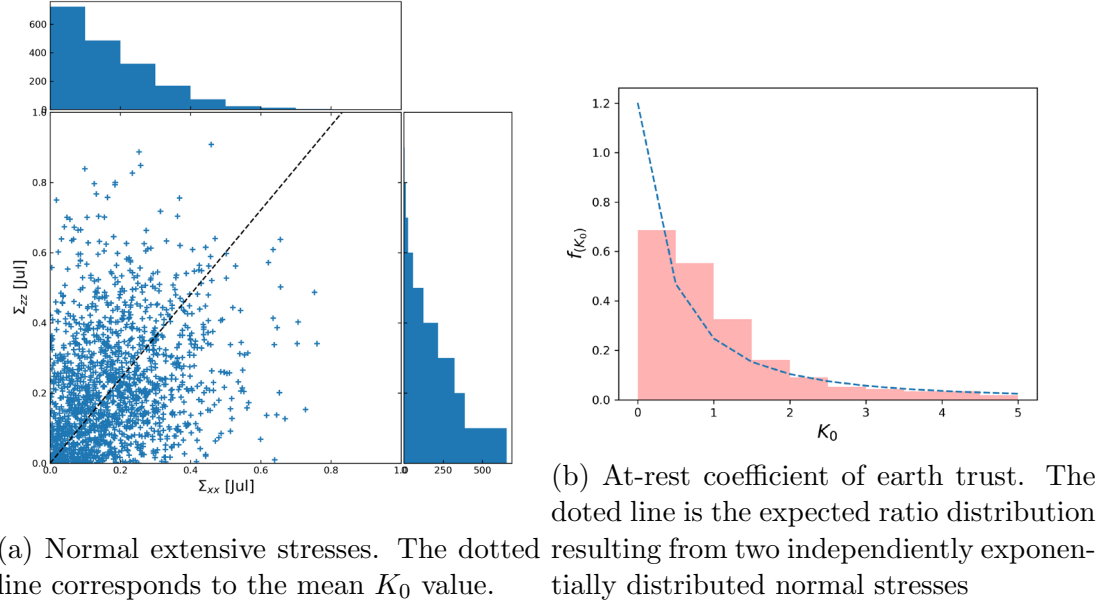
Figure 3: Measured normal extensive stresses and K_0 in Case 1.
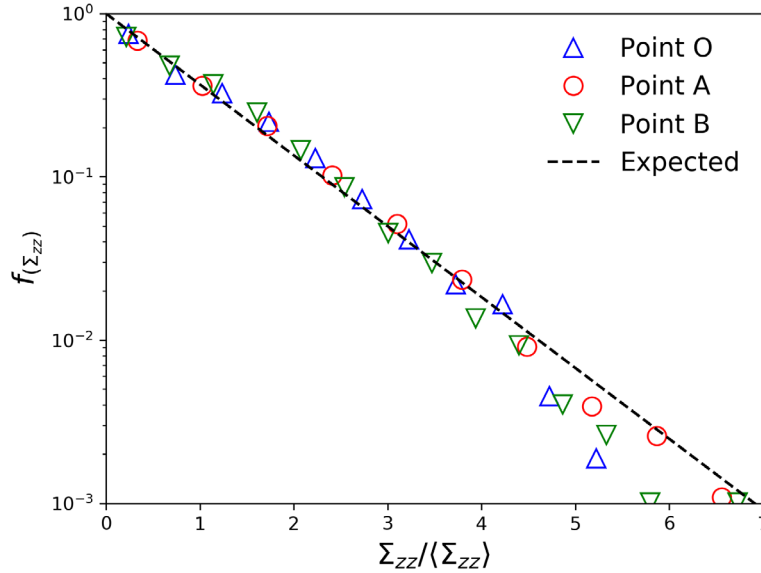

Figure 4: Expected and measured statistical distribution of vertical extensive stress in Case 2.

when a vertical surface load is acting after the deposition by gravity than in the the case that there is no such load. This could have to do with the fact that the stresses obtained after the gravity deposition were asymmetrically increased and modified during the application of the surface load. This higher level of shear and the stress rotation could have driven the distribution of forces and stresses towards the expected PDFs.

These result are interesting for geotechnical applications since they provide a way to solve geotechnical problems when particle and length scale of interest are close. For example, let be a rigid rectangular framework of width L covered with a layer of coarse granular fill (of depth H). Continuum based approaches would predict[2] that the total load on the top of the framework would correspond to the weight of the overlaying material γHL, being γ the unitary weight of the fill. However if the discrete nature of the filling is considered, the total load will fluctuate around the mean, especially when the number of particles interacting with the framework ($\mathcal{N} = L/D$) is small. The model here presented would anticipate that, with 100 particles interacting with the top of the framework, in 5% of cases the total pressure would be 20% higher than the mean value. Another example of interest could be the estimation of the total horizontal force acting on a block of an earth retaining wall that is supporting a rockfill.

6   CONCLUSIONS

- The solution of geotechnical problems in truly discrete media needs a stochastic model that provides interval estimations of the stress at a given point, rather than a point estimation.

- A simplistic model based on classical statistical mechanics has been set up to anticipate the probability distribution function of the extensive stresses (this is the average vertical stress field of a domain multiplied by its volume).

- This approach has been used to determine the PDFs of extensive stresses in two cases: an elastic half-space under its own weight and the same case with a vertical finite surface load. The mean value of the stresses is got from classical solutions.

- The model predicts that the PDF of normal components is an exponential distribution, while that of the shear extensive stresses could be normally distributed.

- Massive DEM simulation have been used to generate statistical samples of values of extensive stresses at several control points. The matching between expected and obtained PDFs is good, especially for practical purposes.

- Anticipating the PDF of extensive stresses can be very useful when the size of the discrete particles and the length scale of the problem come close. For example, this approach could provide the probability of finding stresses that double the value obtained from the corresponding continuum approach.

---

[2]Provided that the stiffness of the fill and framework are the same.)

- This research fills a gap between discrete and continuum geotechnical models and opens a way to treat other seminal problems in geotechnics.

REFERENCES

[1] Arnold Verruijt and Stefan Van Baars. *Soil mechanics*. VSSD Delft, the Netherlands, 2007.

[2] Joseph Boussinesq. *Application des potentiels à l'étude de l'équilibre et du mouvement des solides élastiques: principalement au calcul des déformations et des pressions que produisent, dans ces solides, des efforts quelconques exercés sur une petite partie de leur surface ou de leur intérieur: mémoire suivi de notes étendues sur divers points de physique, mathematique et d'analyse*, volume 4. Gauthier-Villars, 1885.

[3] A Flamant. Sur la répartition des pressions dans un solide rectangulaire chargé transversalement. *CR Acad. Sci. Paris*, 114:1465–1468, 1892.

[4] Poul V Lade. Overview of constitutive models for soils. In *Soil constitutive models: Evaluation, selection, and calibration*, pages 1–34. 2005.

[5] A. Drescher and G. de Josselin de Jong. Photoelastic verification of a mechanical model for the flow of a granular material. *Journal of the Mechanics and Physics of Solids*, 20(5):337–340, 1972. cited By 438.

[6] C. h. Liu, S. R. Nagel, D. A. Schecter, S. N. Coppersmith, S. Majumdar, O. Narayan, and T. A. Witten. Force fluctuations in bead packs. *Science*, 269(5223):513–515, 1995.

[7] H. M. Jaeger and S. R. Nagel. Granular solids, liquids, and gases. *Reviews of Modern Physics*, 68(4):1259–1271, 1996.

[8] S. N. Coppersmith, C. h. Liu, S. Majumdar, O. Narayan, and T. A. Witten. Model for force fluctuations in bead packs. *Phys. Rev. E*, 53:4673–4685, May 1996.

[9] Farhang Radjai, Michel Jean, Jean-Jacques Moreau, and Stéphane Roux. Force distributions in dense two-dimensional granular systems. *Phys. Rev. Lett.*, 77:274–277, Jul 1996.

[10] Daniel M. Mueth, Heinrich M. Jaeger, and Sidney R. Nagel. Force distribution in a granular medium. *Phys. Rev. E*, 57:3164–3169, Mar 1998.

[11] Farhang Radjai, Stéphane Roux, and Jean Jacques Moreau. Contact forces in a granular packing. *Chaos: An Interdisciplinary Journal of Nonlinear Science*, 9(3):544–550, 1999.

[12] T. S. Majmudar and R. P. Behringer. Contact force measurements and stress-induced anisotropy in granular materials. *Nature*, 435(7045):1079–1082, 2005.

[13] J. F. Peters, M. Muthuswamy, J. Wibowo, and A. Tordesillas. Characterization of force chains in granular material. *Phys. Rev. E*, 72:041307, Oct 2005.

[14] Farhang Radjai. Modeling force transmission in granular materials. *Comptes Rendus Physique*, 16(1):3 – 9, 2015. Granular physics / Physique des milieux granulaires.

[15] Radu Balescu. *Equilibrium and nonequilibrium statistical mechanics*. John Wiley & Sons Inc, 1975.

[16] S.F. Edwards and R.B.S. Oakeshott. Theory of powders. *Physica A*, 157(3):1080–1090, 1989.

[17] S.F. Edwards, D.V. Grinev, and J. Brujić. Fundamental problems in statistical physics of jammed packings. *Physica A*, 330:61–76, 2003.

[18] S.F. Edwards. The full canonical ensemble of a granular system. *Physica A*, 353:114–118, 2005.

[19] S. Henkes, C. S. O' Hern, and B. Chakraborty. Entropy and temperature of a static granular assembly: An ab initio approach. *Phys. Rev. Lett.*, 99(3):1–4, 2007.

[20] S. Henkes and B. Chakraborty. Statistical mechanics framework for static granular matter. *Phys. Rev. E*, 79, 2009.

[21] Ignacio G. Tejada. Ensemble theory for slightly deformable granular matter. *The European Physical Journal E*, 37(9):81, Sep 2014.

[22] Ignacio G. Tejada. Boussinesq-like problems in discrete media. *arXiv:1812.08424*, 2018.

[23] Katalin Bagi. Stress and strain in granular assemblies. *Mechanics of Materials*, 22(3):165 – 177, 1996.

[24] P. A. Cundall and O. D. L. Strack. A discrete numerical model for granular assemblies. *Géotechnique*, 29(1):47–65, 1979.

[25] V. Šmilauer et al. Reference manual. In *Yade Documentation 2nd ed.* The Yade Project, 2015. http://yade-dem.org/doc/.

ASSESSMENT OF NEIGHBOR PARTICLES SEARCHING METHODS FOR DISCRETE ELEMENT METHOD (DEM) BASED SIMULATIONS

LUIS ANGELES[1], CESAR CELIS[2]

[1]Department of Engineering, Pontificia Universidad Católica del Perú (PUCP)
Av. Universitaria 1801, San Miguel, Lima 32, Peru
langelesr@pucp.edu.pe

[2]Mechanical Engineering Section, Pontificia Universidad Católica del Perú (PUCP)
Av. Universitaria 1801, San Miguel, Lima 32, Peru
ccelis@pucp.edu.pe

Key words: Discrete element method (DEM), Neighbor particles, Searching methods.

Abstract. The performance of discrete element method (DEM) simulations is highly dependent on the requirements of the associated algorithms in terms of computer memory usage and CPU time. In particular, computer CPU time heavily depends on the identification of neighbor particles and the computation of particle-particle interactions. Over the years several neighbor particles searching methods have been developed. Accordingly, in this work the performance of two of well-known searching methods, linked cell and Verlet tables algorithms, are assessed in the context of the development of a new DEM-based tool. More specifically, the neighbor searching methods performance and related computational costs are parametrically analyzed and an assessment of their suitability for carrying the intended numerical simulations is provided. The referred numerical simulations are performed accounting for a canonical configuration used for the verification of the algorithms included in the new computational tool under development. The referred tool incorporating state of the art physical and numerical models will be used for modelling following a CFD-DEM approach mineral transport and grinding processes present in concentrator plants.

1 INTRODUCTION

Particulate flows (two-phase liquid-solid flows) known as pulp or slurry are common in both industry and nature. The pulp transport and wet milling processes present in the mining industry are difficult to characterize experimentally. Numerical models based on computational fluid dynamics (CFD) for instance allows getting a better understanding of the associated phenomena occurring in such flows. There are two main approaches commonly used for the modeling of particulate flows, Eulerian-Eulerian and Eulerian-Lagrangian. The approaches focused on the modeling of the referred flows can be also divided according to the treatment of the particulate's phase, continuous and discrete [1]. The continuous approach models large amounts of particles as an artificial continuous medium. One disadvantage of this approach is that the local behavior of individual particles is not accounted for. This modeling approach is closely related to the Eulerian-Eulerian one since usually the continuous approach relies on Eulerian treatments. The discrete approach in turn describes the movement and contact of each particle individually. The discrete element method (DEM) is one of the most important methodologies relying on a discrete approach. Compared to the continuous approach, the main disadvantage of the discrete one relates to its relatively high computational cost. The use of Lagrangian based techniques for tracking the transport and contact of the particles present in the flow is the main responsible for such high costs.

In the past pulps have been mainly simulated using Eulerian approaches [2] for both the solid phase and the transporting fluid. Eulerian methods are indeed able to accurately reproduce the particle concentration and velocity profiles, as well as they are capable of handling a large number of particles with a relatively low computational cost [3]. The main disadvantage of such approaches is that the detailed information at the macroscale and mesoscale is compromised by the approximations used. Contrarily, Lagrangian methods [4] are able to provide detailed information on the interactions between particle-particle, particle-fluid and particle-solid, but their computational costs are high. The referred costs are highly dependent on the number of Lagrangian particles being transported. Numerical simulations involving large numbers of particles generally requires the use of high performance computing (HPC).

The discrete element method (DEM) is one of the most important particle-based simulation methods that has been used for applications in several fields including chemical engineering, pharmaceutics, agriculture, energy, mining, environment and geological engineering [1]. The performance of DEM simulations is highly dependent on computer memory usage and CPU time [5]. The computer memory requirements come usually from the memory size used for storing both the mesh and the particle neighbor related information. Computer CPU time heavily depends in turn on the identification of neighbor particles and the computation of particle-particle interactions. Selecting the adequate neighbor particles searching methods and adjusting their associated parameters is thus criterial for the performance of DEM simulations.

There are several neighbor searching methods that have been tried in the past. They include for instance the linked cell [6] and the Verlet tables [7] ones. This work assesses the performance of these two searching methods in the context of the development of a new DEM-based tool. In particular, the neighbor searching methods performance and related computational costs are parametrically analyzed, and an assessment of their suitability for

carrying the intended numerical simulations is provided. The referred numerical simulations are performed accounting for a canonical configuration used for the verification of the algorithms included in the new computational tool under development. Accordingly, Section 2 briefly describes the general context in which this work has been carried out. Some specifics about the two several neighbor searching methods studied here are highlighted in Section 3. Finally, Sections 4 and 5 discuss, respectively, the main results obtained from the parametric assessments carried out and the main conclusions drawn from them. Notice that the DEM-based tool under development incorporating state of the art physical and numerical models will be used for modelling following a CFD-DEM approach mineral transport and grinding processes present in concentrator plants.

2   WORK CONTEXT

The neighbor particles searching methods assessed in this work constitutes one set of algorithms of the several ones composing a new DEM-based tool, the so-called CFLOWSS (Complex FLOWS Solver), currently under development. The development of this tool for the modeling of inert and reactive complex flows is continuous. Its modules, models and numerical algorithms are constantly updated in order to improve the accuracy of the flow modeling processes undertaken with its aid. The referred DEM-based tool (CFLOWSS) incorporating state of the art physical and numerical models will be used for modelling complex flows such as those involving mineral transport and grinding processes present in concentrator plants.

3   NEIGHBOR SEARCHING METHODS

The interaction between pairs of particles has to be evaluated during DEM-based simulations. A general algorithm accounting for all $N(N - 1)/2$ interactions between the N particles involved in a given simulation constitutes the most basic particles searching method. In terms of computational effort, this base algorithm has an overall order of O(N2). There are of course other more time-efficient particles searching methods. Two of these methods, the linked cell algorithm (neighborhood tables) [6] and the Verlet tables [7], are studied here.

3.1 Linked cell algorithm

The linked cell algorithm [6], also called the neighborhood tables one, is based on the creation of a "mesh" of cells, where the cell size is a function of the particles sizes. The potential interacting pairs of a particle belonging to a given particular cell are determined from those ones belonging to the surrounding cells. Briefly, following this particles searching method, the algorithm first creates a mesh of a specified cell size and assigns each particle to its corresponding cell. The algorithm searches next the interacting pairs for a particle located at a given cell by analyzing the particles located in the surrounding cells. In order to avoid counting twice a given particle pair, the particle search processes are carried out from left to right and from bottom to top as shown in Figure 1. As highlighted in this figure, more than one line of neighbor cells around a given cell can also be accounted for during the neighbor particles searching processes.
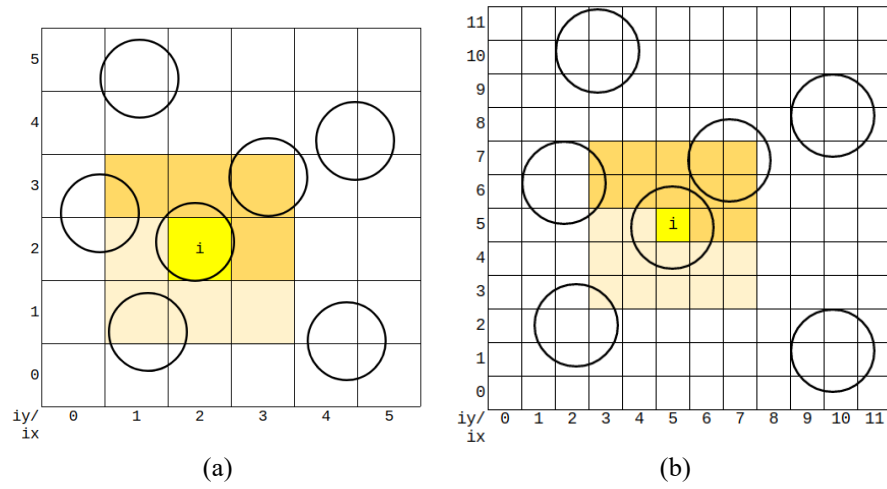
Figure 1: Linked cell algorithm with a uniform grid. The cell under analysis is shown in yellow, the neighbor cells considered for determining the interacting pairs are shown in strong orange, and the cells disregarded during the analyses are shown in light orange. Systems of monodisperse particles accounting for (a) one (1) line and (b) two (2) lines of neighbor cells around cell i.

3.2 Verlet tables algorithm

The Verlet tables algorithm is based on the original Verlet method [7]. This algorithm considers an imaginary sphere of radius R_{nbr} around a particle i, which contains the potential interacting particles. A pair of the round particles i and j is added to the neighborhood list of particle i if [1],

$$\left\| \bar{X}_i - \bar{X}_j \right\| < R_{nbr} = s + r_i + r_j \, , \tag{1}$$

where $\bar{X}$ is the particles position vector, s is the Verlet or skin parameter, and r is the particle radius. For a constant time step Δt and a maximum particle velocity V_{max}, the number of time steps in which the Verlet table is valid is computed from,

$$N_{verlet} = \frac{s}{2\, V_{max}} \, . \tag{2}$$

Following this algorithm thus, a Verlet table is initially created, which is used for N_{verlet} time steps. After this time has elapsed, the Verlet table is updated and a new N_{verlet} is computed. This process is repeated until reaching the end time.

4 RESULTS AND DISCUSSIONS

The numerical modeling of multiple packs of particles is useful for studying some of the physical phenomena characterizing mineral grinding processes and transport of dense slurries. In this work thus, numerical simulations of a dam break-like configuration are carried out in order to compare the performance of two different neighbor particles searching methods used in DEM-based approaches.

426

4.1 General description

As highlighted in Section 3, in addition to the general one, two neighbor particles searching methods, the linked cell algorithm (neighborhood tables) [6] and the Verlet tables [7], have been analyzed here. These algorithms have been implemented in the DEM-based tool under development (CFLOWSS) using C++ as the main programing language. In order to reduce the associated computational cost and to carry out several parametric studies, only two-dimensional simulations of a dam break-like configuration have been performed. For particle-particle and particle-wall interactions, normal elastic forces without damping (no tangential forces) were accounted for only. Three particle arrangements were tested varying the number of particles along the horizontal and vertical directions, 10 x 10, 16 x 16 and 22 x 22. The simulations were run on a single computer core of an Intel(R) Core(TM) i7-8700 CPU @ 3.20GHz processor.

Five dam-break related cases have been simulated considering a time step equal to 1E-6 s, from a physical time between 0 and 1 s. The particle governing equations are integrated using SUNDIALS/CVODE and the Adams scheme [8]. Two lines around a cell have been considered for the linked cell method (Figure 1b), and a skin factor equal to four (4) times the radius for the Verlet tables one. Elastic constants equal to 4000 and 40000 have been considered for the particle-particle and particle-wall contacts, respectively. The radius of the particles is equal to 0.5. For particular cases assessed here, some of the parameters highlighted before have been modified. The first case was simulated using the parameter values as just described. The CVODE solver based on Backward Differentiation Formulas (BDF) was used in the second case. Time steps equal to 2E-6 and 4E-6 are analyzed in the third and fourth cases, respectively. Finally, the skin factor used in the Verlet tables method has been varied in the fifth case. The skin factor variations ranged from 1 to 64 times the particles radius. The main results obtained from the simulations of the five cases highlighted above are discussed in the following section.

4.2 Results

Figure 2 shows as a function of the number of particles the CPU time associated with the general search algorithm and the two studied neighbor searching methods. As noticed from this figure, the CPU time is significantly reduced when neighbor searching algorithms are utilized. In addition, when compared each other the linked cell and the Verlet tables algorithms, the former is slightly less time consuming. This particular outcome has been observed in all results obtained in this work.

The results associated with the use of two different numerical schemes present in the CVODE solver utilized here are highlighted in Figure 3. It is noticed in particular from these results that for relative small time steps the Adams scheme is slightly more time efficient than the BDF one. The referred differences in CPU time increase with the increase in the number of particles accounted for in the numerical simulations.

In Figure 4, the CPU times as a function of the number of particles characterizing the first, third and fourth cases are shown. These results indicate that the CPU time is proportionally reduced when the time step is doubled. It is worth noticing that, as shown in Figure 7, the results do not differ when increasing the time step size. This means that the impact of the numerical errors associated with the use of these bigger time steps on the particles transport is negligible.
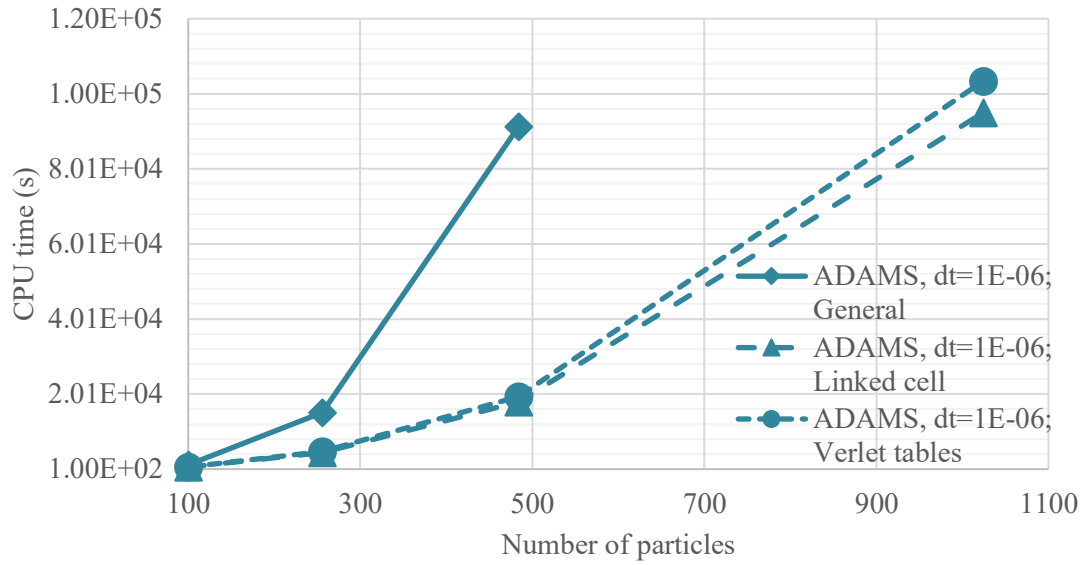
Figure 2: CPU time comparison between neighborhood searching methods for Case 1 (ADAMS, dt=1E-06).
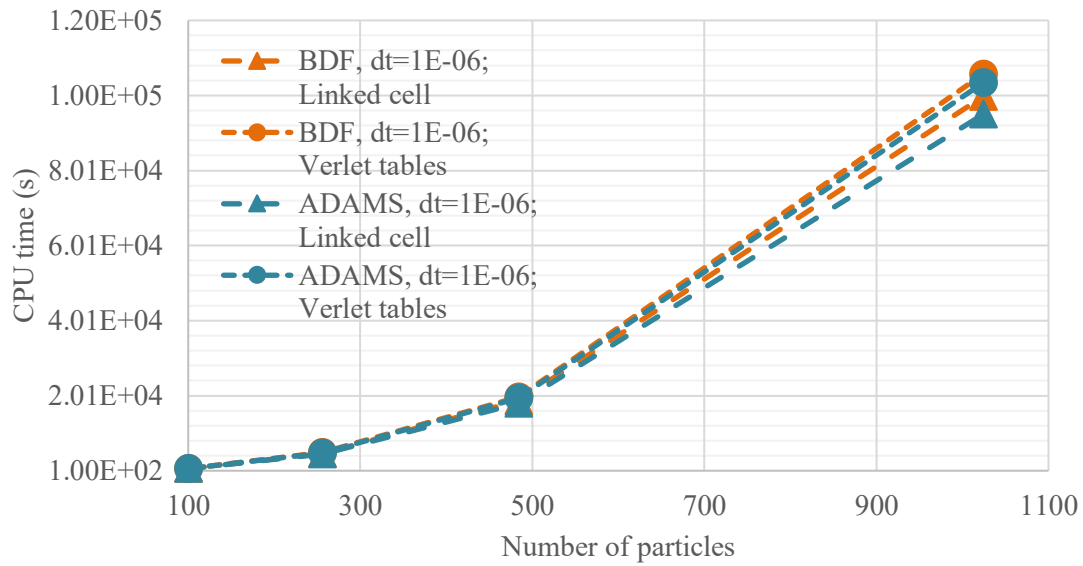
Figure 3: CPU time comparison between Case 1 (ADAMS, dt=1E-06) and Case 2 (BDF, dt=1E-06).

The influence of the skin factor s on the CPU time (Case 5) is highlighted in Figure 5. As noticed on this figure, the CPU time is the lowest when the skin factor takes a value equal to one (1), i.e., equal to the particle radius. In addition, the CPU time increases with the increase in the skin factor values. The highest CPU time that can be obtained by increasing the skin factor is theoretically equal to that characterizing the general algorithm (15114 s). This last

aspect is reflected in the essentially constant CPU time values obtained for skin factors higher than 32 times the particle radius. Finally, Figure 8 compares the results obtained with a $s = 4r$ (Case 1) and $s = r$ (Case 5). The similarity of the results shown in this figure indicates that the implemented algorithms work without any detection problems with the skin factor modifications analyzed here.
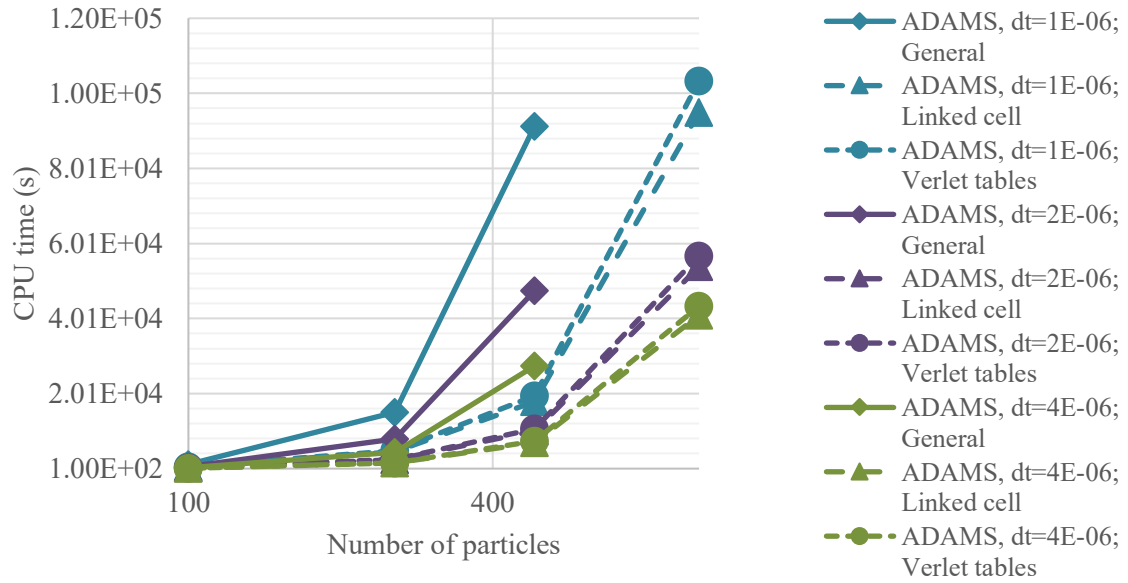
Figure 4: CPU time comparison between Case 1 (ADAMS, dt=1E-06), Case 3 (ADAMS, dt=2E-06) and Case 4 (ADAMS, dt=4E-06).
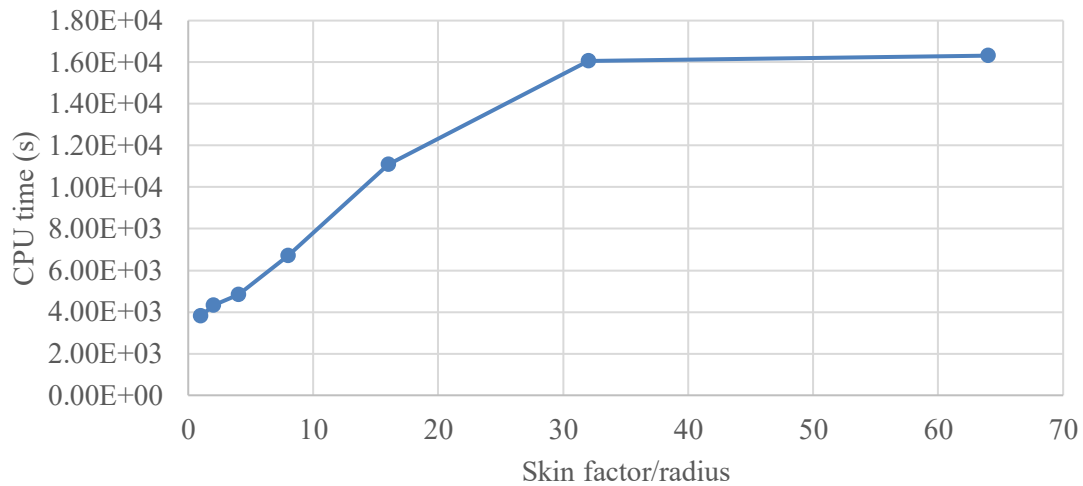
Figure 5: CPU time as a function of the ratio between skin factor and particles radius (Case 5).
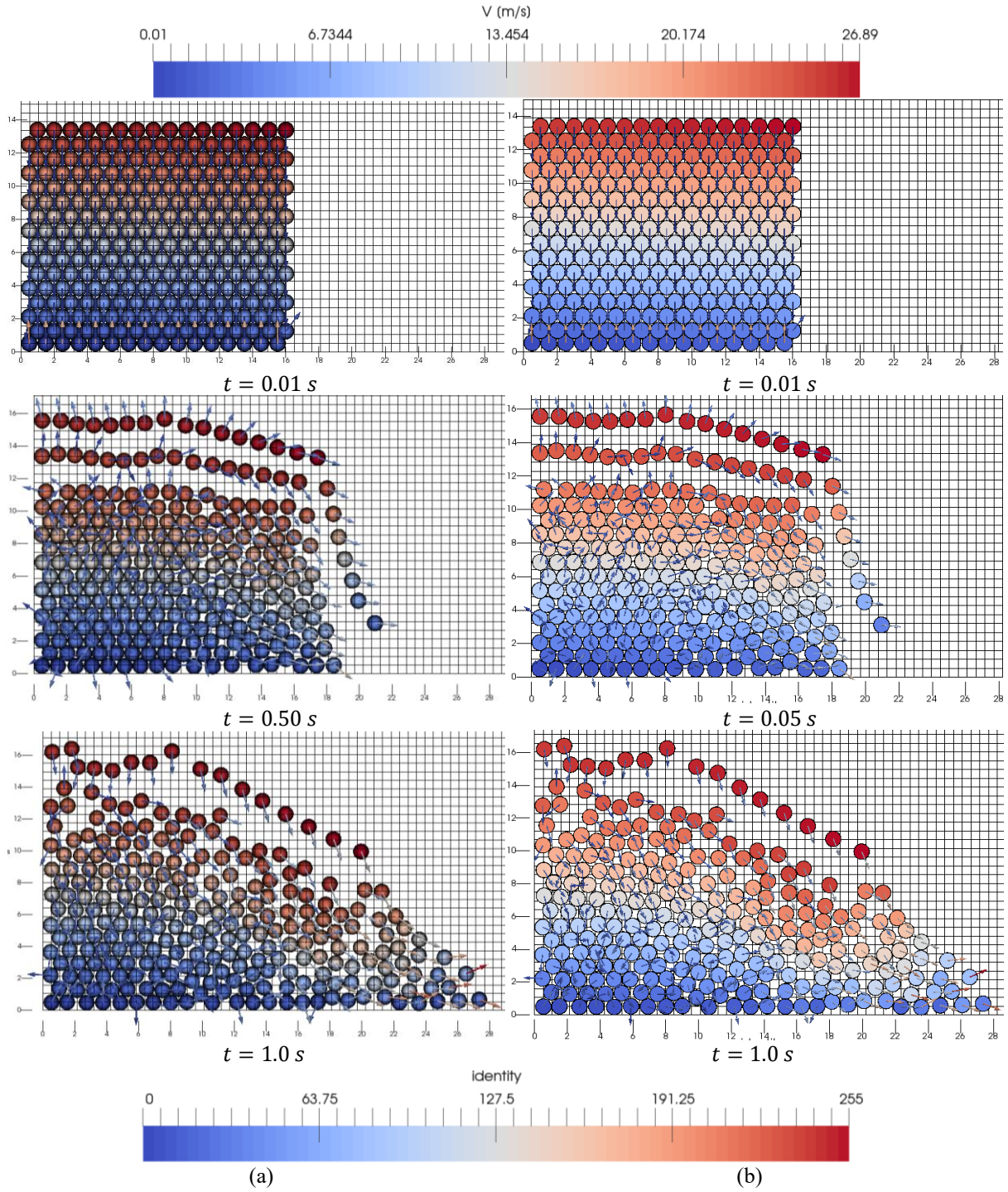
Figure 6: (a) Time evolution comparison between (a) Case 1 (ADAMS, dt=1E-06) and (b) Case 2 (BDF, dt=1E-06) using the Verlet tables algorithm for a dambreak having an initial 16 x 16 (256 particles) arrangement.
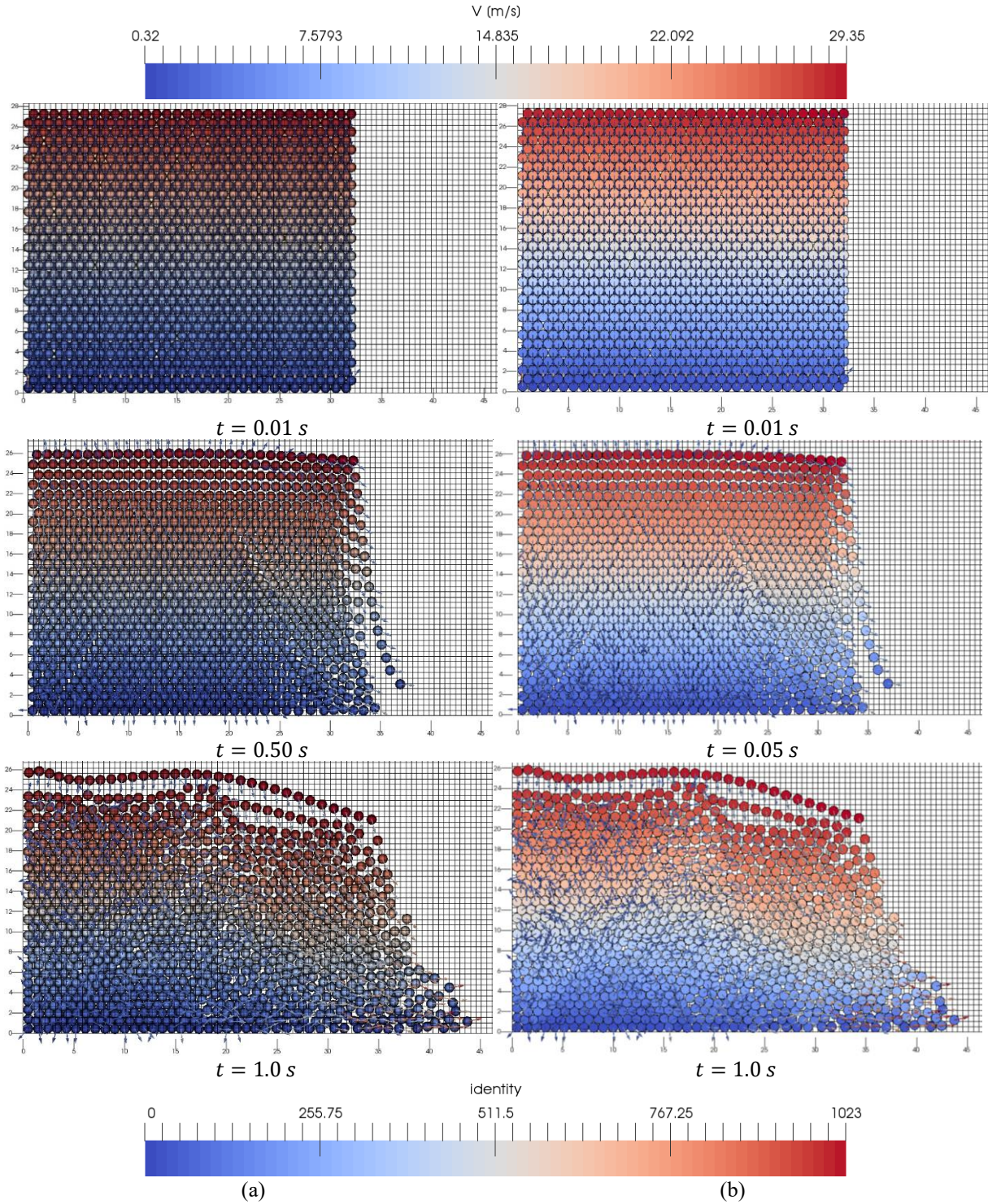
Figure 7: Time evolution comparison between (a) Case 1 (ADAMS, dt=1E-06) and (b) Case 4 (ADAMS, dt=4E-06) using the Linked cell algorithm for a dambreak having an initial 32 x 32 (1024 particles) arrangement.
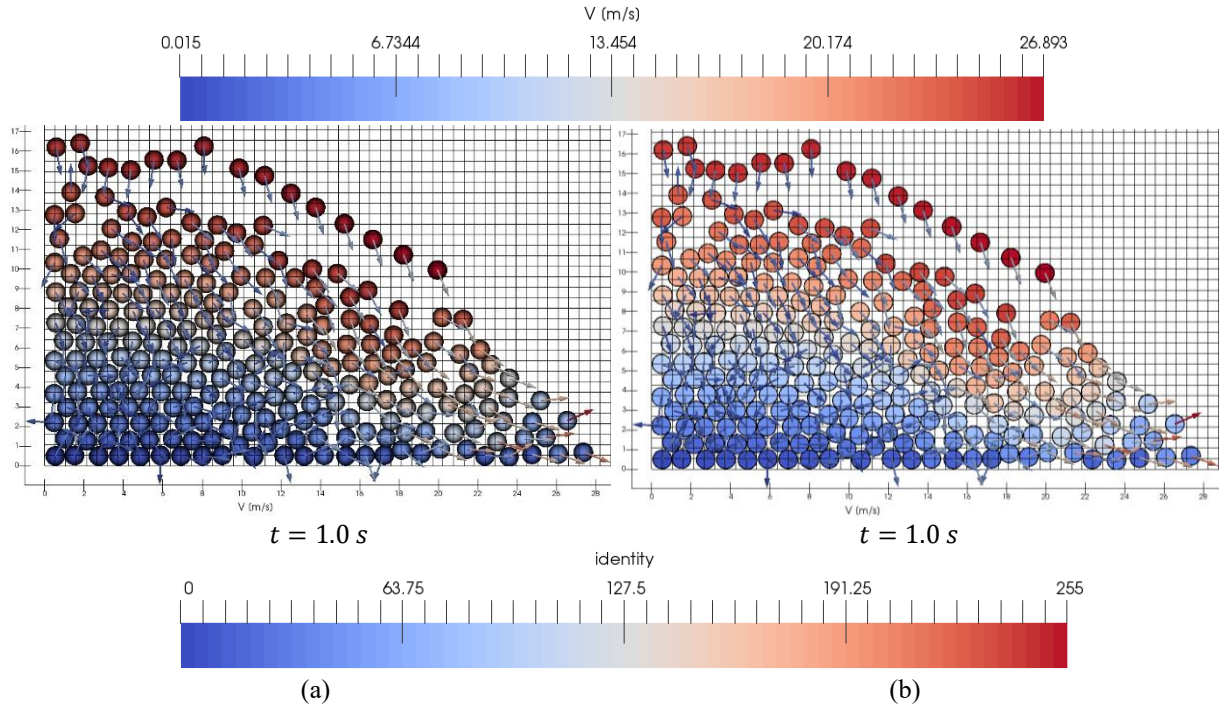
Figure 8: Time evolution comparison between (a) Case 1 (ADAMS, dt=1E-06) with $s = 4r$ and (b) Case 4 (ADAMS, dt=4E-06) with $s = r$ using Verlet tables for a dambreak having an initial 16 x 16 (256 particles) arrangement.

5 CONCLUSIONS

Two classical neighbor particles searching methods, Linked cell algorithms and Verlet tables, have been implemented in a new DEM-based tool, the so-called CFLOWSS. A two-dimensional dam break-like configuration has been numerically simulated using the referred two algorithms and the general searching method. Different number of particles and skin factors for the Verlet tables have been studied. The main results indicate that the Linked cell algorithms and Verlet tables present as expected lower CPU times compared to the general searching method. In addition, there are no significant differences in terms of CPU time when using Adams or BDF solver schemes. Increasing the time step from 1E-06 to 2E-06 and 4E-06 leads to savings in CPU time and there are no noticeable differences in the associated numerical results. Finally, the Verlet tables show great dependence on the skin factor and a value for this parameter equal to the particle radius do not result in particle pair detection problems.

6 ACKNOWLEDGEMENTS

REFERENCES

[1] C. Kloss, C. Goniva, A. Hager, S. Amberger y S. Pirker, «Models, algorithms and validation for opensource DEM and CFD-DEM,» *Progress in Computational Fluid Dynamics,* vol. 12, nº 2/3, 2012.

[2] L. Chen, Y. Duan, W. Pu y a. C. Zhao, «CFD simulation of coal-water slurry flowing in horizontal pipelines,» *Korean J. Chem. Eng.,* vol. 26, nº 4, pp. 1144-1154, 2009.

[3] J. Capecelatro y O. Desjardins, «Eulerian–Lagrangian modeling of turbulent liquid–solid slurries in horizontal pipes,» *International Journal of Multiphase Flow,* vol. 55, pp. 64-79, 2013.

[4] W. Zhong, X. L. Aibing Yu, Z. Tong y H. Zhang, «DEM/CFD-DEM Modelling of Non-spherical Particulate Systems: Theoretical Developments and Applications,» *Powder Technology,* vol. 302, pp. 108-152, 2016.

[5] R. Cai, L. Xu, J. Zheng y Y. Zhao, «Modified cell-linked list method using dynamic mesh for discrete element method,» *Powder Technology,* vol. 340, pp. 321-330, 2018.

[6] H.-G. Matuttis y J. Chen, Understanding the Discrete Element Method, Singapore: John Wiley & Sons, 2014.

[7] L. Verlet, «Computer "Experiments" on Classical Fluids. I. Thermodynamical Properties of Lennard-Jones Molecules,» *Physical Review,* vol. 159, nº 1, pp. 98-103, 1967.

[8] Lawrence Livermore National Laboratory, Center for Applied Scientific Computing (2016), «CVODE v4.1.0».

DEM POWDER SPREADING AND SPH POWDER MELTING MODELS FOR ADDITIVE MANUFACTURING PROCESS SIMULATIONS

CLAAS BIERWISCH

Fraunhofer IWM
Wöhlerstr. 11, 79108 Freiburg, Germany
e-mail: claas.bierwisch@iwm.fraunhofer.de, www.simpartix.com

Key words: Additive manufacturing, laser-powder bed fusion, surface tension, Marangoni currents, DEM, SPH.

Abstract. Particle-based numerical methods enable different process simulations for powder bed additive manufacturing. Two examples are the simulation of powder spreading and the simulation of melting and re-solidification. From these simulations, several material properties can be extracted such as packing density after spreading, porosity and surface properties after re-solidification and, ultimately, indicators for the strength of the component. In this work simulations of powder spreading using the Discrete Element Method (DEM) as well as simulations of the melt pool dynamics by means of Smoothed Particle Hydrodynamics (SPH) are presented. Surface tension material properties are varied and the influence on the resulting surface shape is discussed. The occurrence of different surface roughness patterns can be addressed to certain dimensionless numbers, namely the Capillary number, the Marangoni number and the ratio of the laser scan speed to a characteristic Marangoni current surface velocity.

1 INTRODUCTION

Simulations of the powder spreading process were reported by Parteli et al. [1]. They carried out DEM simulations of the application of a new layer of powder with a counter-rotating roller. The grain shape is modelled by a multi-sphere approach. The key finding of this work is an increase of the roughness of the surface with the square of the translation speed of the roller. Interestingly, a powder without fines shows less roughness.

Continuum mechanical modeling studies of the melting and re-solidification process, which take into account the heat input by the laser, the heat transfer and the phase transformation of the bulk material, were carried out using the finite element method (FEM) as well as the lattice Boltzmann method (LBM). The studies can be distinguished based on whether the powder was considered explicitly as individual particles or in a homogenized bulk representation. A brief survey is given below.

1.1 Homogenized models without explicit representation of the powder

Gusarov et al. present a model describing laser absorption and heat transport for laser powder bed fusion (L-PBF) in combination with the thermodynamics during melting and re-solidification [2]. The occurrence of so-called balling, i.e., the formation of spherical

structures in the melt pool, was described in this model by a Plateau-Rayleigh instability which can be avoided by low scanning speeds. Hodge et al. present a thermomechanical continuum model for the L-PBF process [3]. They demonstrate that the energy input in a new layer leads to renewed heating and associated expansions in deeper layers. Riedlbauer et al. use FEM simulations and experiments to study the electron beam melting (EBM) process [4]. They find very good agreement for the dependencies of melt pool lifetime on line energy and on scan speed as well as of melt pool width on scan speed.

1.2 Models with explicit representation of the powder

Körner et al. describe the simulation of the energy absorption, the heat transfer and the melting and re-solidification of a powder bed in 2D using the LBM, taking into account the size distribution of the particles [5]. A key result of this work is that the powder volume fraction has a strong influence on the homogeneity of the melt pool. A high volume fraction supports the formation of a well-defined half-circle shaped pool while for a low volume fraction the pool geometry becomes sensitive to the local powder arrangement. Furthermore, the authors could derive a process diagram relating the melt track appearance to the parameters beam power and scan speed based on simulations and complementary experiments. This work was continued in Körner et al. [6] and Bauereiß et al. [7] by simulating the subsequent melting and re-solidification of several layers. The particles of a new layer are applied by a trickling algorithm rather than by a powder spreading process simulation. A key message of these works is that the stochastic properties of the powder bed in combination with wetting and capillary effects have a strong influence on defect formation during the building process.

Gürtler et al. developed a 3D continuum mechanical model for the L-PBF process [8]. By means of the volume of fluid approach, individual particles of the powder bed were represented. In comparison with experiments, basic phenomena such as porosity formation under unfavorable process conditions could be reproduced. Khairallah et al. also use a FEM continuum mechanical description of the L-PBF process in 3D [9]. By using free surfaces, individual particles in the powder bed and their distribution could be modeled. Furthermore, irregular solidification patterns could be predicted by the model. In a subsequent study, Khairallah et al. include a temperature-dependent surface tension which causes Marangoni currents as well as recoil pressure during vaporization [10]. This model allows for analyses of the complex dynamics of the melt pool with emphasis on pore formation mechanisms.

2   NUMERICAL METHODS

DEM simulations are used to study the powder spreading process. The powder particles are modeled as spheres with a finite size distribution. The particles interact through Hertzian repulsion, viscous damping, cohesion, sliding friction and rolling friction. Details of the simulation method are given in [11].

The main focus of this study is melt pool dynamics which is simulated using the SPH method. To do so, the continuity equation,

$$\frac{D\rho}{Dt} = -\rho\, \nabla \cdot \boldsymbol{u}\,,\qquad(1)$$

as well as the Navier-Stokes momentum equation,

$$\rho \frac{D\boldsymbol{u}}{Dt} = -\boldsymbol{\nabla} p + \mu \, \boldsymbol{\nabla}^2 \boldsymbol{u} + \boldsymbol{f}_\Sigma + \rho \, \boldsymbol{g} \, , \tag{2}$$

are solved. Here, $\boldsymbol{u}$ is the velocity, ρ is the mass density, p is the hydrostatic pressure, μ is the dynamic viscosity, $\boldsymbol{f}_\Sigma$ is the volumetric surface tension force and $\boldsymbol{g}$ is the acceleration due to gravity. Bold face symbols denote vector quantities.

The hydrostatic pressure is given by an equation of state,

$$p = \frac{\rho_0 \, s^2}{\gamma} \left[\left(\frac{\rho}{\rho_0} \right)^\gamma - 1 \right] , \tag{3}$$

where ρ_0 is the equilibrium density, s is the speed of sound and γ is the isentropic exponent.

The melt rheology is modeled by means of a temperature-dependent viscosity. The viscosity changes depending on the state of matter of the material. Here, we differentiate three states: fully solid (S) below the solidus temperature T_S, fully liquid (L) above the liquidus temperature T_L and an intermediate state in between,

$$\mu(T) = \begin{cases} \mu_L \, , & T \geq T_L \, , \\ \mu_S + (\mu_L - \mu_S) \dfrac{T - T_S}{T_L - T_S} \, , & T_S < T < T_L \, , \\ \infty \, , & T \leq T_S \, . \end{cases} \tag{4}$$

The surface tension force,

$$\boldsymbol{f}_\Sigma = (-\sigma_N \, \kappa \, \boldsymbol{n} + \sigma_T \, \boldsymbol{\nabla}_\Sigma T) \, \delta_\Sigma \, , \tag{5}$$

is composed of a contribution normal to and a contribution tangential to the local surface. Here, σ_N is the surface tension, κ the surface curvature and $\boldsymbol{n}$ the surface unit normal vector. σ_T is the Marangoni coefficient describing the variation of surface tension with temperature and $\boldsymbol{\nabla}_\Sigma T$ is the gradient of the surface temperature field. δ_Σ is a delta function marking the location of the surface in space. Details of the SPH surface tension model are given in [12].

The balance equation for the thermal energy per unit mass e,

$$\rho \frac{De}{Dt} = k \, \boldsymbol{\nabla}^2 T - \varepsilon \, \sigma_B (T^4 - T_0^4) \, \delta_\Sigma + \frac{dI}{dz} \tag{6}$$

is composed of contributions from heat conduction, Stefan-Boltzmann radiation and absorbed laser energy. Here, k is the thermal conductivity, ε is the emissivity, σ_B is the Stefan-Boltzmann constant, T_0 is the ambient temperature and I is the local intensity of the laser radiation.

The absorption of the laser radiation along the vertical coordinate z is described by the Lambert-Beer law with an attenuation coefficient a,

$$\frac{dI}{dz} = a \, I \, . \tag{7}$$

The relation between temperature T and thermal energy per unit mass e is given by the following expression which takes into account the specific heat capacity c and the latent heat of melting H,

$$
T(e) = \begin{cases} T_L + \dfrac{e - e_L}{c}, & e \geq e_L, \\[2ex] T_S + \dfrac{e - e_S}{c + \dfrac{H}{T_L - T_S}}, & e_S < e < e_L, \\[2ex] \dfrac{e}{c}, & e \leq e_S. \end{cases} \tag{8}
$$

Here, $e_S = c\, T_S$ is the solidus thermal energy per unit mass and $e_L = c\, T_L + H$ is the liquidus thermal energy per unit mass.

The laser radiation is described by a Gaussian intensity profile in 2D,

$$
I(x) = \frac{P}{\sqrt{2\pi}\, 6\, w^2} \exp\left[-\frac{(x - x_0)^2}{2w^2} \right], \tag{9}
$$

or in 3D,

$$
I(x, y) = \frac{P}{2\pi\, w^2} \exp\left[-\frac{(x - x_0)^2 + (y - y_0)^2}{2w^2} \right], \tag{10}
$$

with the power P, the characteristic width w and the laser spot center coordinates x_0 and y_0.

3 RESULTS

The systems simulated in this study are represented by the capillary number,

$$
\mathrm{Ca} = \frac{\mu\, u}{\sigma_N}, \tag{11}
$$

which describes the ratio of viscosity and surface tension and the Marangoni number,

$$
\mathrm{Ma} = -\frac{\sigma_T\, \Delta T\, l\, \rho_0\, c}{\mu\, k}, \tag{12}
$$

which quantifies the strength of the thermal convection at the surface. Here, u is a characteristic fluid velocity in the melt pool, l is a characteristic melt pool diameter and ΔT is a characteristic temperature difference along the melt pool.

3.1 Two-dimensional simulations

First, we study the two-dimensional simulation of a simple lattice of three layers of powder particles which is traversed by a laser producing heat. Selected snapshots of the temperature field are shown in Figure 1 for three test cases: No surface tension, surface tension and Marangoni convection. In the case without surface tension (left column), a largely homogenous surface sets after re-solidification, which still reveals the positions of the original powder particles. With surface tension (middle column), the surface is better smoothed. On the other hand, Marangoni convection currents at the surface caused by a temperature-dependent surface tension (right column) lead to a very irregular surface, which is significantly rougher than the original particle distribution.
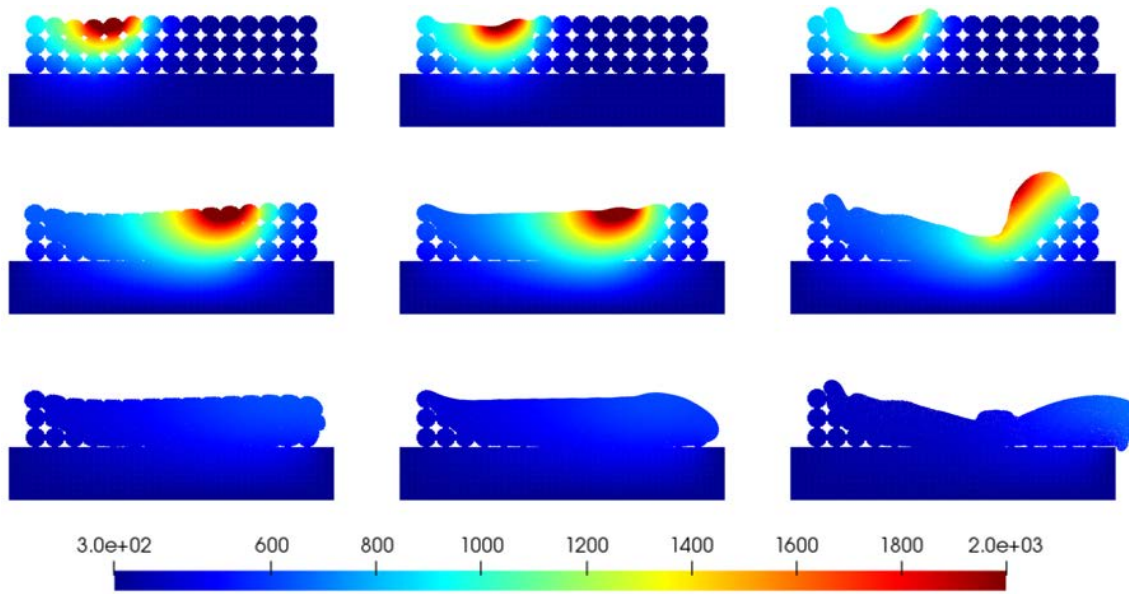
Figure 1: 2D SPH simulation of melting and re-solidification. The laser moves to the right at constant speed. The temperature field in Kelvin is color-coded. The rows represent different points in time. Left column: without surface tension ($Ca = \infty$, $Ma = 0$); middle column: with surface tension ($Ca = 1$, $Ma = 0$); right column: with Marangoni currents ($Ca = 1$, $Ma = 150$).
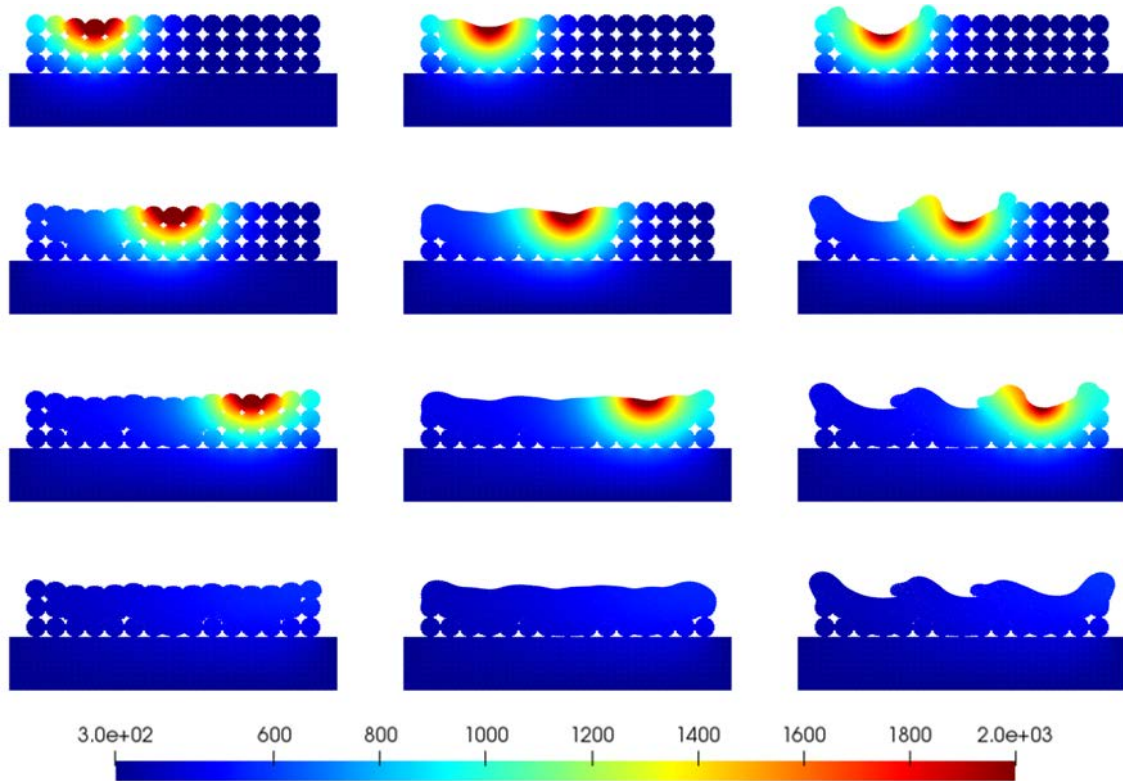
Figure 2: Like Figure 1, however, the laser remains for a certain time at one position and then changes to the next position. As a result, laser tracks into the plane of observation are approximated.

Complementary to the previous situation, laser motion into the plane of observation is now simulated. For this purpose, the position of the laser source remains constant for a certain time in the 2D simulation and then changes abruptly. The results are summarized in Figure 2. Again, in the case without surface tension (left), the initial arrangement of the powder particles is still easily recognizable. The surface tension leads to a smoothing of the surface, while still a slight ripple with a wavelength which corresponds approximately to the distance of the laser positions remains (middle). The Marangoni currents lead again to the most irregular surface (right).

3.2 Three-dimensional simulations

To create a realistic spatial powder arrangement prior to melting, a DEM simulation is performed in which a new powder layer is applied by spreading with a counter-rotating roller moving at a constant speed (see Figure 3). A section of the powder bed is then prepared using a finer spatial discretization for the following melt pool simulation (see Figure 4).
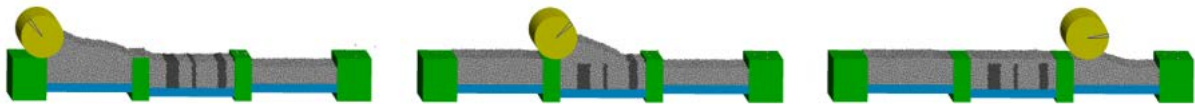
Figure 3: 3D DEM simulation of the spreading process with a counter-rotating roller.
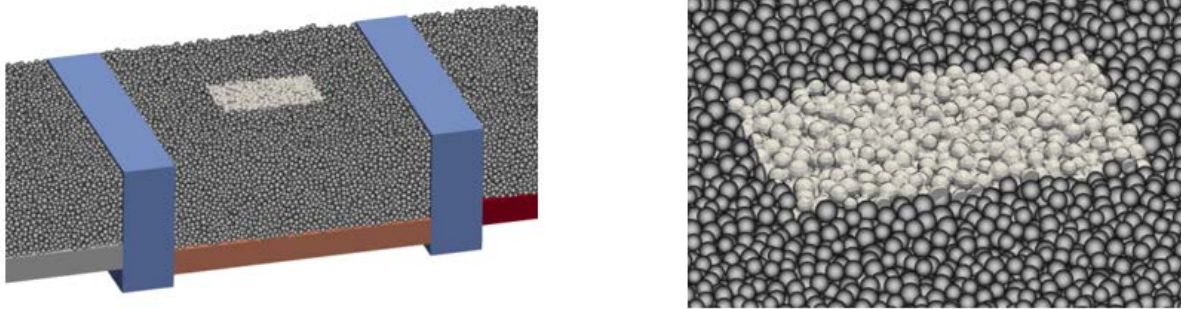
Figure 4: Particle distribution after the spreading simulation in two magnifications. Shown in light gray is the region used for the following melt pool simulation.

Three-dimensional simulations of melting and re-solidification are again performed using the SPH method. The laser beam traverses three adjacent tracks. Figure 5 summarizes the results. For all parameter variations, the powder particles are melted along the laser tracks. Differences can be found in the occurring maximum temperatures. Without surface tension (left), the temperature is highest, while it is lowest in the case of temperature-dependent surface tension (right). This observation can be explained by the fact that without surface tension the convective heat transport is the lowest and the introduced heat is almost only removed by conduction and radiation. Surface tension enhances convective transport and Marangoni currents maximize it.
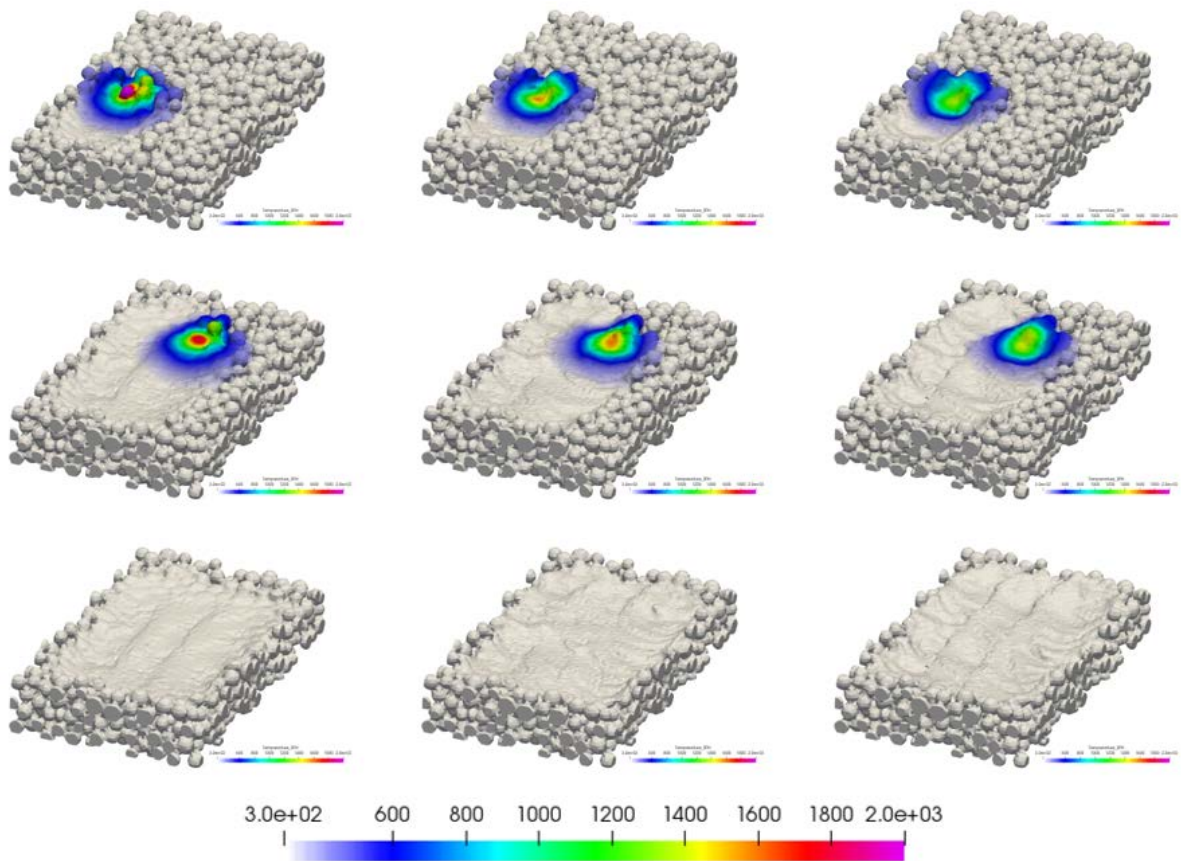
Figure 5: 3D SPH simulation of the melting and re-solidification of the arrangement of particles from the spreading simulation. The laser moves at constant speed along three equidistant tracks. The temperature field in Kelvin is color-coded. The rows represent different points in time. Left column: without surface tension (Ca = ∞, Ma = 0); middle column: with surface tension (Ca = 0.1, Ma = 0); right column: with Marangoni currents (Ca = 0.1, Ma = 15).

To analyze the resulting surface after re-solidification, Figure 6 shows the corresponding color-coded height profiles. In all profiles, the laser tracks are still visible. In the case without surface tension (left), the profile has the greatest depression approximately at the end of the first third of each track. With surface tension (center), additional scale-like structuring occurs along the laser tracks. These scale structures are most pronounced in the case of the Marangoni currents (right). Also, the height differences in the profile are the largest in that case.

The Marangoni currents in the case of a temperature-dependent surface tension are further studied by means of the surface velocity profiles in the melt pool. Figure 7 shows the velocity components along and perpendicular to the laser scan direction in addition to the height profile. For better visibility of each scan track the hatch spacing between the tracks in increased compared to the simulations shown before and, thus, only two tracks are included in the simulation.
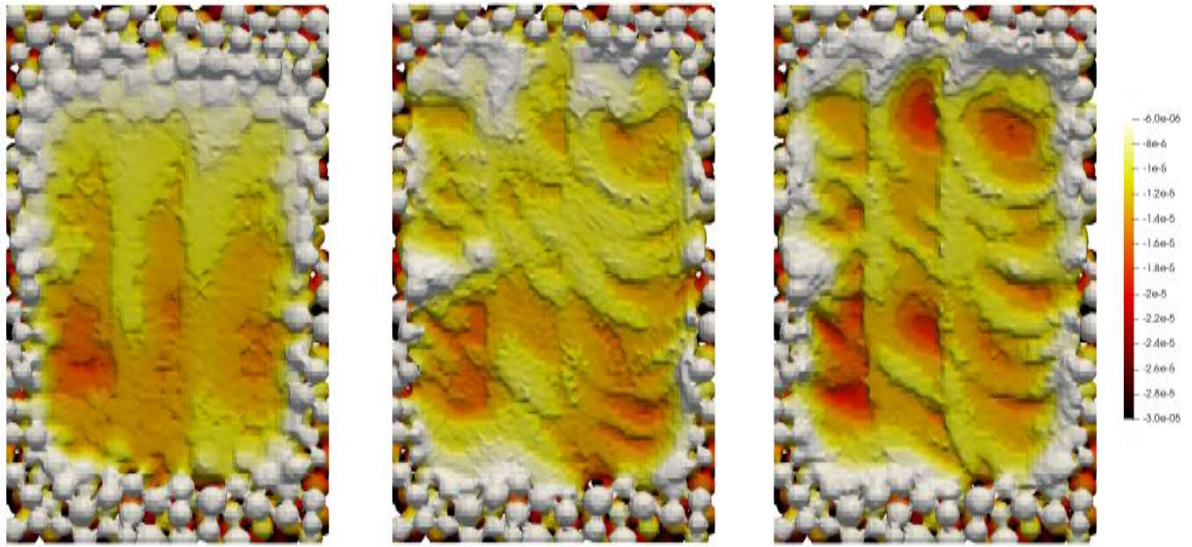
Figure 6: Color-coded height profiles in meters (red: bottom, white: top) of the simulations from Figure 5.
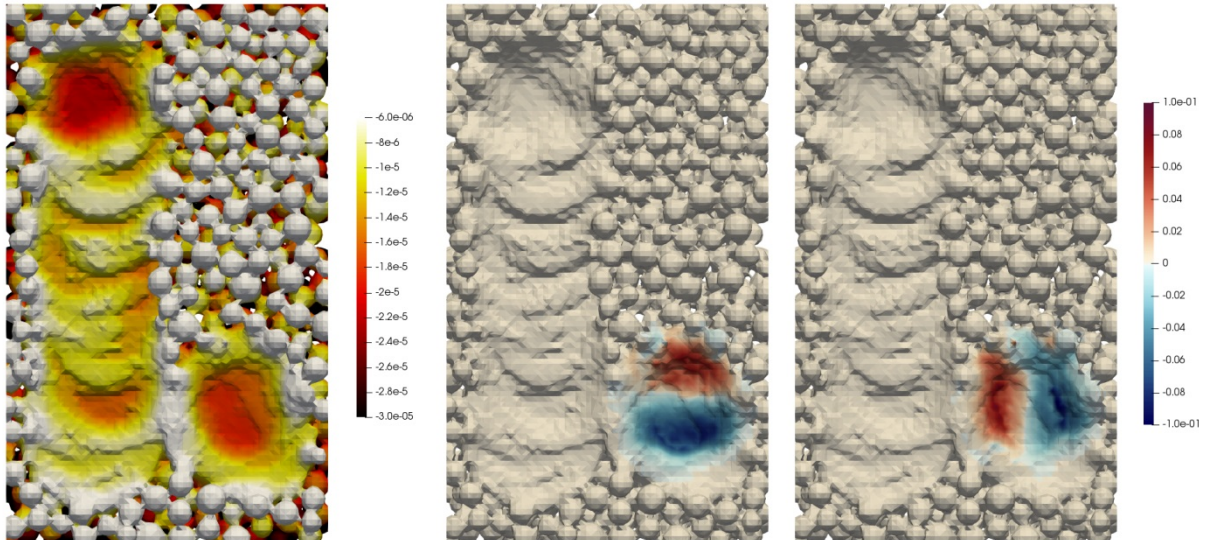
Figure 7: Height profile (left) and velocity components parallel (middle) and perpendicular (right) to the laser scan track during a simulation with a ratio of laser scan speed to Marangoni current surface velocity of 1.

It is found in both 2D and 3D simulations that the maximum Marangoni current surface velocity in the melt pool can be expressed as

$$u_S \approx -\frac{\sigma_T \, \Delta T}{20 \, \mu}.$$

(13)

In order to investigate the formation of the scale structures in more detail further simulations with variations of the laser scan speed c_L are carried out. In particular, the ratio of the scan speed and the surface velocity of the Marangoni current in the melt pool is analyzed. Figure 8 shows simulated height profiles using velocity ratios c_L/u_S between 1 and 10. In the case of a velocity ratio of 1 the scale pattern is clearly pronounced and rather regular. For a ratio of 3 the pattern in still discernible but less pronounced. For a ratio of 10 the scale pattern does not appear any more. This observation hints that an upper bound for the laser scan speed above which scale patterns do not occur can be expressed as

$$c_{L,\max} \approx -\frac{\sigma_T \, \Delta T}{2 \, \mu}.$$

(14)
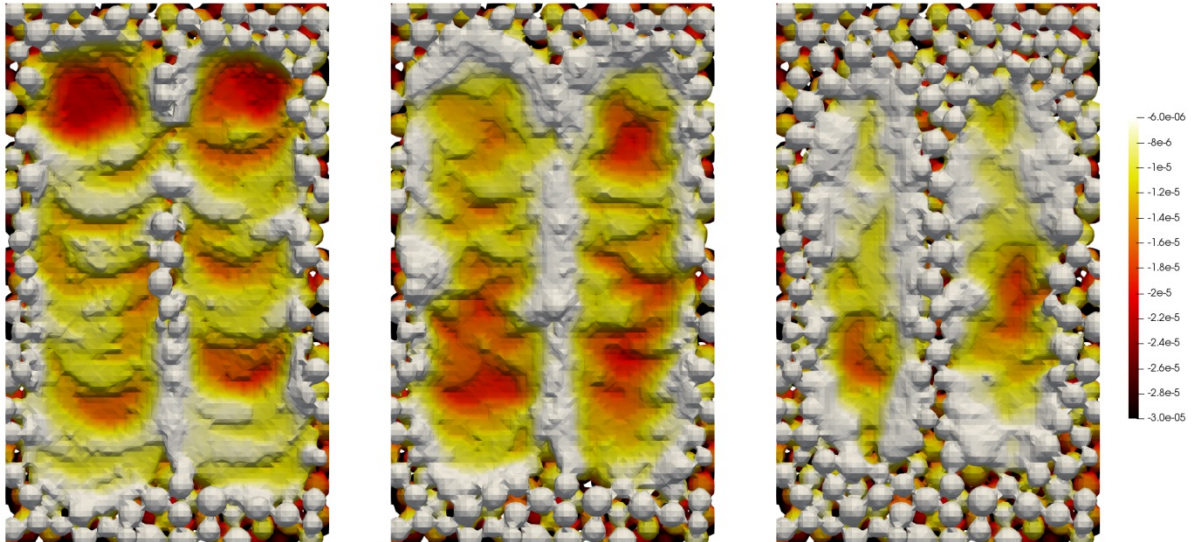
Figure 8: Color-coded height profiles of simulations with different ratios of laser scan speed to Marangoni current surface velocity. Left: $c_L/u_S \approx 1$; middle: $c_L/u_S \approx 3$; right: $c_L/u_S \approx 10$.

4   CONCLUSIONS

Particle-based simulations provide detailed insights into melt pool dynamics and are particularly suitable for the systematic investigation of the influence of process and material parameters on the process result. In this work, relations between surface tension effects and the resulting surface profile in 2D and 3D simulations are investigated as examples. It is shown that, on the one hand, surface tension can have a smoothing effect. On the other hand, especially Marangoni currents can cause a pronounced surface roughness. Dimensionless numbers allow for characterization of the emerging surface profiles based on material properties and process parameters.

5 ACKNOWLEDGEMENTS

REFERENCES

[1] Parteli, E.J.R. and Pöschel, T. Particle-based simulation of powder application in additive manufacturing. *Powder Technol.* (2016) **288**:96–102.

[2] Gusarov, A.V., Yadroitsev, I., Bertrand, Ph. and Smurov, I. Heat transfer modelling and stability analysis of selective laser melting. *Appl. Surf. Sci.* (2007) **254**(4):975–979.

[3] Hodge, N.E., Ferencz, R.M. and Solberg, J.M. Implementation of a thermomechanical model for the simulation of selective laser melting. *Comput. Mech.* (2014) **54**(1):33–51.

[4] Riedlbauer, D., Scharowsky, T., Singer, R.F., Steinmann, P., Körner, C. and Mergheim, J. Macroscopic simulation and experimental measurement of melt pool characteristics in selective electron beam melting of Ti-6Al-4V. *Int. J. Adv. Manuf. Technol.* (2017) **88**:1309–1317.

[5] Körner, C., Attar, E. and Heinl, P. Mesoscopic simulation of selective beam melting processes. *J. Mater. Process. Technol.* (2011) **211**(6): 978–987.

[6] Körner, C., Bauereiß, A. and Attar, E. Fundamental consolidation mechanisms during selective beam melting of powders. *Modelling Simul. Mater. Sci. Eng.* (2013) **21**(8):085011.

[7] Bauereiß, A., Scharowsky, T. and Körner, C. Defect generation and propagation mechanism during additive manufacturing by selective beam melting. *J. Mater. Process. Technol.* (2014) **214**(11):2522–2528.

[8] Gürtler F.-J., Karg. M., Leitz, K.-H. and Schmidt, M. Simulation of laser beam melting of steel powders using the three-dimensional volume of fluid method. *Physics Procedia* (2013) **41**:881–886.

[9] Khairallah, S.A. and Anderson, A. Mesoscopic simulation model of selective laser melting of stainless steel powder. *J. Mater. Process. Technol.* (2014) **214**:2627–2636.

[10] Khairallah, S.A., Anderson, A.T., Rubenchik, A. and King, W.E. Laser powder-bed fusion additive manufacturing: Physics of complex melt flow and formation mechanisms of pores, spatter, and denudation zones. *Acta Materialia* (2016) **108**:36–45.

[11] Bierwisch, C., Kraft, T., Riedel, H. and Moseler, M. Three-dimensional discrete element models for the granular statics and dynamics of powders in cavity filling. *J. Mech. Phys. Solids* (2009) **57**:10–31.

[12] Bierwisch, C. A surface tension and wetting model for the δ^+-SPH scheme. In: *Proceedings of the 13th SPHERIC International Workshop 2018.* Quinlan, N.J., Tong, M., Moghimi, M.H. and McLoone, M. (Eds.). National University of Ireland, Galway, Ireland (2018) 95–102.

[13] http://www.simpartix.com

NUMERICAL INVESTIGATION OF SCREW DESIGN INFLUENCE ON SCREW FEEDING IN A ROLLER COMPACTOR

Kumari S. Awasthi[1,*], Srikanth R. Gopireddy[2], Regina Scherließ[1] and Nora A. Urbanetz[2]

[1]Department of Pharmaceutics and Biopharmaceutics
Christian-Albrechts-University Kiel, Grasweg 9a, 24118 Kiel, Germany
e-mail: sawasthi@pharmazie.uni-kiel.de, rscherliess@pharmazie.uni-kiel.de

[2]Daiichi-Sankyo Europe GmbH
Pharmaceutical Development, Luitpoldstr. 1, 85276 Pfaffenhofen, Germany
e-mail: Srikanth.Gopireddy@daiichi-sankyo.eu, Nora.Urbanetz@daiichi-sankyo.eu

Key words: Screw design, Particle conveying, Cohesive powder.

Abstract. Roller compaction refers to a dry granulation process where fine particulate feed is fed to the counter rotating rolls of a roller compactor to form ribbons which are further milled to produce free flowing agglomerates. For the continuous production of ribbons, there needs to be an adequate supply of powder by the screw to the rolls without any interruptions. In general, screws used in roller compactors are designed to convey powders of all types (cohesive, bulky, compressible, etc.), whereby usage of different screw designs for different powder types may be avoided. However, using such single screw type roller compactors for poor flowing powders may be challenging. On the other hand, the selection of the right screw for a given powder can only be done based on a combination of prior experience and trial-and-error experimentation. Empirical correlations exist to predict the draw down rate of screw feeders depending on their design, however, these correlations assume that there is continuous supply of powder by the screw, which limits its application to free-flowing powders only. To address this, in this study numerical simulations are performed based on discrete element method (DEM) to investigate the impact of screw design on the powder supply to rolls for cohesive and poorly flowing powders.

The geometry considered includes a hopper, horizontal feeding screw below the hopper, and two counter-rotating rolls at the end of the screw. Two different screw designs are investigated where the main difference between them is the pitch length. The influence of scraper speed is investigated. Additionally, the influence of material attribute such as cohesion is studied. For both designs, the simulation results calculated include the rate of powder supply by the screw, velocity of particles in the screw etc. The simulation results of powder supply rate are also compared with results obtained based on empirical correlation. Overall, this simulation approach helps in selecting appropriate screw design for the given cohesive powder.

1   INTRODUCTION

Roller compaction is a dry granulation process designed to compact fine powders i.e. densifying the powder blend by application of pressure, to produce ribbons which are further processed to yield granules and pertains to continuous manufacturing procedure [1]. Roller

compaction process has significant effect on flowability, homogeneity, compressibility of active pharmaceutical ingredients and excipients and thus can affect post compression parameters of tablet [2]. Therefore, it is necessary to optimize the process parameters to obtain good quality granules.

A typical roll compactor consists of a hopper connected to a single rotating screw, which feeds the material into the gap between two counter-rotating rolls and cheek plates on the sides to avoid leakage which is represented in Figure 1. Experimental studies on screws have been conducted by Bates [3] to match different screws and material in hopper in order to investigate flow pattern.

It is frequently found that a mechanical discharging apparatus in a roll compactor is virtually essential for handling cohesive powder. One such method is the screw feeder which comprises a helical screw blade or "flight" on a horizontal shaft (Figure 2). The construction of the screw may be of uniform or varied geometry [3].

Theoretical models have also been proposed by Yu and Arnold [4] for a uniform flow pattern based on the pitch characteristic of screws, and Roberts [5] for uniform drawdown used to predict the flow patterns generated in hoppers for a given screw. However, screw shear and power draw can be affected by the forces acting on the screw which varies along the screw length [6].

Moysey and Thompson developed a new 3-D model for solids conveying in a single screw extruder using DEM. The model has been shown to be an excellent tool for studying solids flow within the screw channel [7][8]. Further, Fernandez et al. studied the influence of screw design on the particle mass flow rate, evenness of particle drawdown from the hopper and power consumption [6]. However, in all these studies, the hopper used did not had any scraper or impeller attached to it and it is one of the useful process attribute for handling cohesive material.

In this study, the impact of screw shape on the discharge from hopper on cohesive material is explored. Also, DEM is used to investigate the effect on total mass flow rate out of the screw, mass holdup, velocity of particles inside screw zone. Finally, the results are compared for different cohesion case. The screws in this study is one of commonly found designs having variation in screw pitch spacing. Also, the study aims to evaluate the relative performance of screws and to establish the accuracy of the continuum based analytic model. Further, prediction from this study is compared to theoretical study of discharge prediction from Roberts [5][9].

2   MATERIAL AND METHODS

2.1   Discrete Element Method (DEM)

The DEM is a numerical method based on Newton's laws of motion and was introduced by Cundall and Strack (1979) [10]. It is a Lagrangian method i.e. all particles in the computational domain are tracked by explicitly solving their trajectories [11]. The details of modeling using DEM can be found in [12] and various industrial application of DEM in [13].

In this work all the computations were performed using the open source DEM software known as LIGGGHTS [17]. LIGGGHTS stands for LAMMPS improved for general granular and granular heat transfer simulations. It is a parallel C++ DEM code based on the Molecular Dynamics (MD) code LAMMPS [14] distributed by the developers via the GNU public license [11] and in this study LIGGGHTS version 3.7 is used. The models chosen in this study include Hertz and Mindlin & Deresiewicz theories for the calculation of normal and tangential forces,

respectively [15]. The cohesion is included through the simplified Johnson-Kendall-Roberts model [16] which adds an additional normal force contribution and this is successfully implemented in our previous study [17]. The other non-contact force considered includes gravity.

The current study aims at using the well-developed models of DEM to capture the particle flow in the hopper of a roller compactor under different material and process attributes.

2.2 Geometry

The hopper design including scraper, screw and rolls are shown in Figure 1. Two different geometries of same design are used in this paper for performing simulations. Figure 1a shows the complete roll compactor geometry , Figure 1b shows the same geometry but only half of the screw is considered for simulations (to optimize simulation time and discharge behavior of the particles) and Figure 1c is the x-z plane view of the same geometry as shown in Figure 1b.
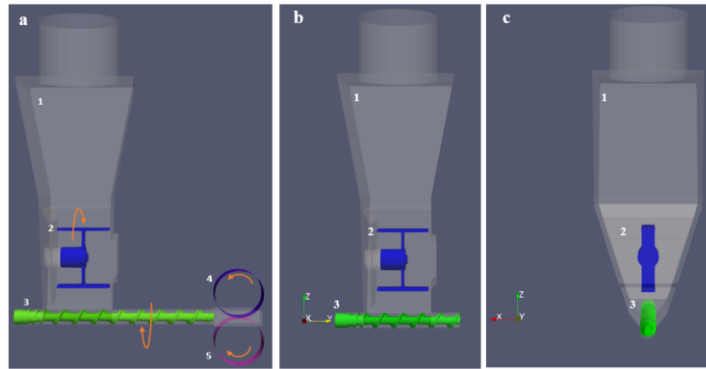
Figure 1 Roll compactor geometry (a) including rolls (b) no rolls included, y-z plane view and (c) no rolls included, x-z plane view
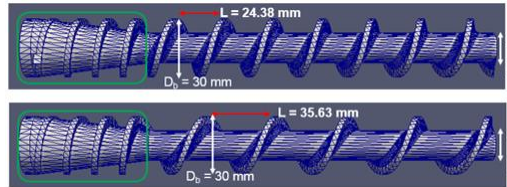
Figure 2 Screw designs

The hopper is marked as 1 in the Figure 1. Here, the hopper is selected such that the walls are steep enough and have friction low enough to let the material slide in a mass flow manner to the screw zone. Location 2 is the scraper used inside the hopper, one of the reason is to handle cohesive powder so that the powder is continuously fed to the screw zone. Location 3 is the screw, 4 and 5 are the upper roll and lower roll respectively. The roll gap can be adjusted according to required final ribbon density in addition to the force applied by the rolls on the material and screw speed.

The screws are one of the basic types of feeders used in roller compaction process. They play an important role in particle feeding to the rollers. With different screw types, the consolidation of particles in the compaction zone might differ. The main difference between

the two screws is the pitch. Screw 1 has lower pitch with 24.38 mm as compared to screw 2 with 35.63 mm.

2.3 Particle size selection

Three-dimensional simulations done with DEM are recognized to be extremely CPU-intensive, requiring from a few hours to several days in the case of systems involving a large number of particles. The current hopper system has a volume of about 3000 cm^3. In this volume, a typical pharmaceutical dry granulation blend having about 200 μm particle diameter, could contain about 3 x 10^9 particles. To address this, typical procedure is to consider enlarged particle size in simulation but keeping the bulk behavior of powder closer to reality. In this study, particles with radius of 2.0 mm were selected and considered for simulations which has in total particles of about 170,000 within the hopper.

2.4 Material property calibration
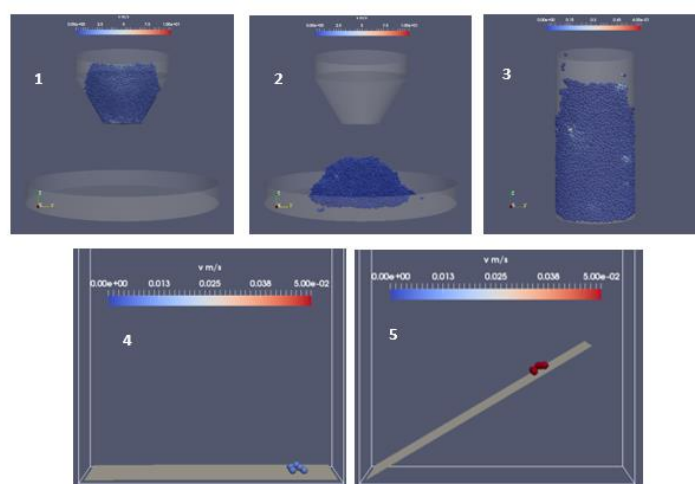
Figure 3 Calibration screenshots (1) Angle of repose at filled state (2) Angle of repose at final state (3) Bulk density for particles filled inside the cylinder (4) Angle to start flow filled state (only 5 particles are used) (5) Angle to start flow final state i.e. angle at which the particles start to roll from the surface.

After the particle size is selected, different microscopic particle properties which enter as input parameters in DEM simulations are calibrated based on bulk properties available through experimental data. This results in increased accuracy and validity of the discrete element modeling work. The different material properties calibrated include cohesion energy density, rolling friction and particle density using the angle of repose, initiation of flow over an inclined plate and bulk density, respectively. The standard calibration procedure is followed as described e.g. by Jensen et al. [18] and by Coetzee and Els [19], which is also depicted in Figure 3.

The rationale for calibrating the particle density, rolling friction and cohesion energy density is due to the observation that these properties influence the powder flow behavior in hoppers [20], [21]. The measured data of bulk density, angle of repose and initiation angle of particles to slide on inclined plate for the considered powder blend are 0.24 g/mL, 57° and 30°, respectively. The final calibrated values of particle density, cohesion energy density and rolling

friction for particle size 2 mm is given in Table 1. The other microscopic particle properties which are not calibrated, however taken from literature [17].

Table 1 Final values of particle properties after calibration

Property (DEM input parameter)	Particle radius of 2.0 mm	Property used for calibration
Particle density / g/mL	0.613	Bulk density
Cohesion (particle-particle) / J/m^3	90000	Angle of repose
Cohesion (particle-wall) / J/m^3	6000	Angle of repose
Rolling friction (particle-wall) / -	0.54	Angle to start flow

2.5 Initialization of simulations

With the finalized values of DEM input parameters after calibration, simulation of hopper with screw conveying is performed with the selected particle sizes of 2 mm. The typical simulation procedure is that for the selected particle size, using the particle properties defined in Table 1, the particles are filled into the hopper during which the scraper and the screw is idle. Once complete filling of particles and their subsequent settling is achieved, which is observed through the total particle kinetic energy and rotational kinetic energy, the filling is said to be complete. With this filled state, the process parameters such as screw speed and scraper speed are set and simulations as per the plan given in Table 2 is started.

3. RESULTS AND DISCUSSION

At first, a base case is considered to define basic result that are studied in this paper to evaluate the differences. The results are then organized at first to find the differences in screw type considering different process parameter such as scraper speed. Following which the impact of cohesion on the discharge rate is studied.

3.1 Base case

The calibrated value of material properties for 2 mm particle size is taken to describe the basic results extracted from the details generated by the DEM simulation for all the particles at every time step.

The particle size of 2.0 mm is filled inside the hopper every 0.5 second till 20 s to achieve uniform filling. Appropriate time is allotted to particles after insertion so that the particles are settled inside the hopper aptly. During the filling, scraper, screw and rolls are idle. Once the filling is done, the particles are colored in the direction of positive y axis as can be seen in Figure 4.

Table 2 Simulation details including process parameters

Run.	Geometry	Screw type	Particle radius	Cohesion (J/m^3)		Scraper Speed (rpm)	Screw Speed (rpm)
				Particle - particle	Particle-wall		
1	Full	Screw 2	2.0 mm	90000	6000	15	90
2	Half	Screw 2	2.0 mm	120000	1200	5	90
3	Half	Screw 1	2.0 mm	120000	1200	5	90
4	Half	Screw 2	2.0 mm	120000	1200	20	90
5	Half	Screw 1	2.0 mm	120000	1200	20	90
6	Half	Screw 2	2.0 mm	120000	1200	15	90
7	Half	Screw 1	2.0 mm	120000	1200	15	90
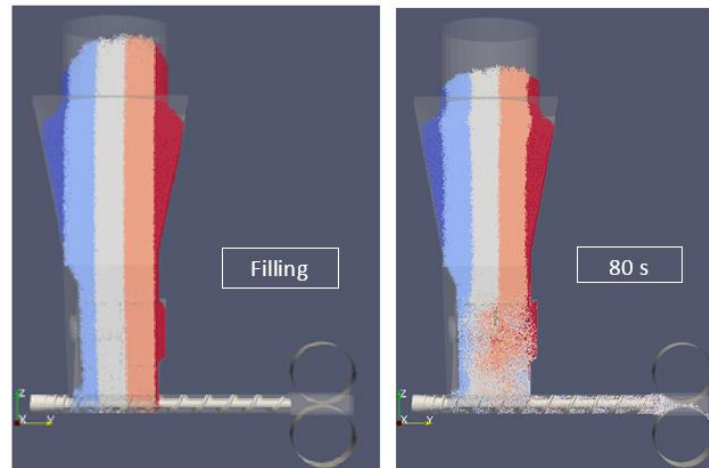
Figure 4 Geometry of screenshot at filling state and 80 s of discharge

After filling is complete, the scraper, screw and rolls are rotated at the speed of 15 rpm, 90 rpm and 10 rpm respectively. Figure 4 shows the flow state at filling and 80 s of discharge. The mixing of particles in the scraper zone can be seen at 80 s. Also, the particles are seen to be

completely filled in the screw zone as the rolls rotate and discharge takes place. However, mass flow behavior is observed i.e. the powder seems to discharge smoothly without any obstruction in flow. Following this, various aspects such as mass holdup, throughput and velocity of particles in screw zone is studied to observe the particles behavior.

3.1.1 Mass holdup in screw zone

Mass holdup refers to the weight of particles in kilograms inside the screw zone. The achievement of steady state is explained through the mass holdup inside the screw zone. As the screw rotates, the particles are drawn from the hopper, inside the screw zone and is conveyed through the screw towards the rolls.
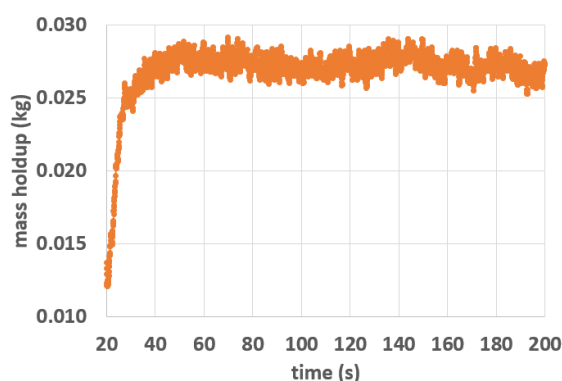
Figure 5 Mass holdup inside the screw zone

Figure 5 shows the escalation of mass of powder inside the screw zone. It can be seen from Figure 4, filling state that there is already presence of some particles inside the screw zone, therefore, the ordinate in Figure 5 starts from value other than 0 at 20 seconds. As the time progresses, the mass holdup inside the screw zone increases and reaches a constantly fluctuating value signifying the steady state achievement and the average mass holdup inside the screw zone is 0.027 kg. However, the mass holdup might vary if the screw speed is changed from 90 rpm to other value.

3.1.2 Discharge behavior study

To study the discharge behavior of particles, factors such as throughput and velocity acting on particles in the screw zone are studied.

Throughput

Throughput is defined as the mass of powder coming out of the system considered per unit time. Figure 6 represents the throughput of the system. While looking at the abscissa, it can be observed that initially, the mass discharge is almost zero. This is the time frame that particles took to travel from outlet of the hopper to the point where particles come out of the system. After which, the graph follows linearly increasing trend which represents achievement of constant throughput. Here, the slope of the graph represents the throughput which is around

0.0026 kg/s and 9.35 kg/h corresponds to packing fraction of 0.26 in screw zone (explained in next section based on calculation from equation 1 from Roberts [5]).
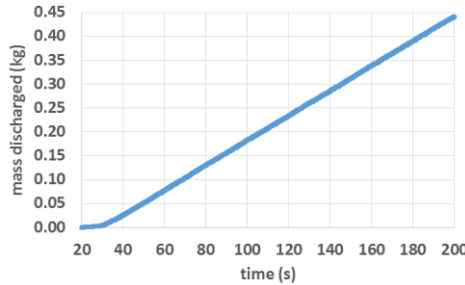
Figure 6 Throughput of the process

Velocity of particles inside screw zone
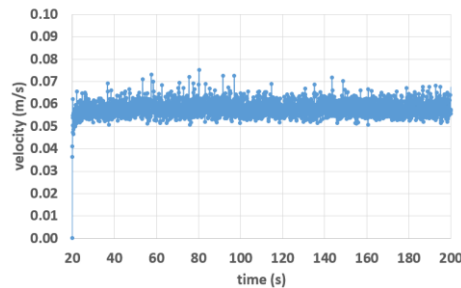
Figure 7 Velocity of particles inside the screw zone

Velocity of particles inside the screw zone is shown in Figure 7 will help to analyze the cohesive behavior of powder particles inside the screw zone. A cuboidal box is considered to mark the x, y and z bound in the region belonging to screw zone and velocity of particles at every 0.05 seconds is calculated. For the particle size of 2 mm, the average velocity of particles inside the screw zone is 0.058 m/s. The rotational speed of screw is 90 rpm, which is 0.137 in linear velocity. The velocity of particles is lower than the tip speed of screw which can be attributed to the presence of a lot of particles inside the screw zone, where only limited number of particles near to the screw surface are in contact with the screw. This result would help to compare the behavior of cohesive particles in different process conditions and material properties.

3.2 Comparison of screw design

For comparing screw designs, the half geometry as shown in Figure 1b and 1c is considered in order to reduce the overall simulation time. The two screw geometries considered are shown in Figure 2. The particle size of 2 mm with higher particle-particle cohesion and lower particle wall cohesion is considered to observe how the cohesive blend would behave to the change in process parameter such as scraper speed (5 rpm, 15 rpm and 20 rpm). Also, the mass discharged from the screw is calculated over time.

451

Table 3 shows the respective throughput and mass holdup data in the screw zone for different screw type and scraper speed. The throughput for comparing the two screw designs with scraper speed of 5 rpm, 15 rpm and 20 rpm are as shown below in Table 3:

Table 3 Study of screw 1 and screw 2 design on mass discharge and mass holdup in screw zone

Run	Screw type	Scraper speed (rpm)	Throughput (kg/h)	Mass holdup in screw (kg)
2	2	5	11.5	0.012
3	1	5	10.5	0.013
4	2	15	12.6	0.014
5	1	15	11.2	0.015
6	2	20	12.6	0.014
7	1	20	11.1	0.015

It is interesting to observe that the mass discharge rate out of the hopper is higher for the cases with screw 2 as compared to screw 1. This observation can also be compared to the theoretically calculated throughput from the equation 1 from Roberts [5], [9] as following:

$$m = \pi\rho\varphi\omega L(D_b^2 - D_s^2)/4 \qquad (1)$$

Where, m is the throughput in kg/s, ρ is the bulk density in kg/m³, φ is the packing density in screw, ω is the screw speed in round per second (rps), L is the screw pitch in meter, D_b is the blade diameter in meter and D_s is the shaft diameter in meter.

The Figure 8 is prepared from equation 1 for the two different screws 1 and 2 respectively differing in screw pitch. It can be perceived that with changing packing density of particles inside the screw zone, the flow rate increases and is higher for screw 2 as compared to screw 1. This observation is well in agreement with the DEM simulation observation where screw 2 shows higher discharge in all the coupled cases of different scraper speed.

Mass holdup in screw zone

The packing fraction of particles inside the screw zone is 0.24 and the volume of empty space to be filled with particle inside the screw zone is 83 ml which gives the volume of particles inside the screw zone to be ~ 20 ml. The maximum consolidation inside the screw should be 60 % of available empty space which is ~50 ml (packing fraction is 0.6). Therefore, the particles inside the screw zone is in safe operation mode to move freely and interact with the surrounding

particles and wall. The mass holdup in screw column of Table 3 shows the respective mass holdup in the screw zone for respective cases.
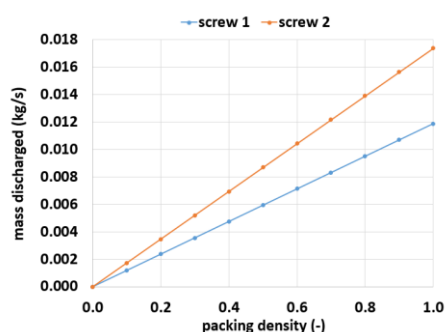
Figure 8 Mass discharged vs time based on correlation proposed by Robert

It is interesting to observe that the mass holdup in case of screw 2 is lower as compared to the screw 1. This effect can be attributed to the smaller pitch in screw 1 which can consolidate higher number of particles therefore, larger mass. Furthermore, the effect of scraper speed can also be observed in mass holdup inside the screw zone. It can be compared that the higher scraper speed of 15 rpm and 20 rpm shows higher mass holdup in the screw zone as compared to lower scraper speed of 5 rpm. The same mass holdup in screw zone for 15 rpm and 20 rpm scraper speed can be another reason for the similar discharge rate out of the screw. The mass holdup during the discharge time zone is constant all over for all the cases but differs in magnitude which can be attributed to scraper speed.

Velocity of particles in screw zone

The average velocity of particles for the case of screw 2 is 0.049 m/s in the screw zone and that for screw 1 is 0.039 m/s. The speed of screw is 90 rpm in both the screw geometries which is 0.137 m/s when converted to linear velocity. Higher velocity of particles in screw 2 case can be attributed to lower mass holdup in screw 2 as compared to screw 1.

Comparison of scraper speed

When the scraper speed is kept constant, the discharge is merely dependent on the screw shape (or pitch) see Table 3. The reason being the similar supply of powder from the scraper zone to the screw zone in both the cases i.e. different screw shape. However, as the scraper speed is increased, the flow rate is also seen to increase. This could happen because more number of particles per unit time are loosened with the scraper and are forced towards the screw zone. Further, when the scraper speed is increased from 15 rpm to 20 rpm, almost no increase in mass discharge rate is observed for both the screw cases. One reason could be the threshold of powder loosening is achieved in the scraper zone o that there is no further increase in powder mass flow rate from scraper zone to the screw zone. The other reason is the screw speed which is constant at 90 rpm, which would impact the throughput if changed.
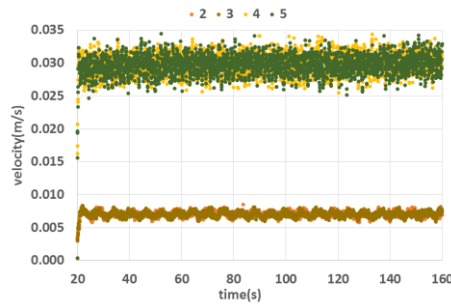
Figure 8 Velocity of particles in scraper zone

Figure 8 shows the velocity of particles in the scraper zone. The velocity of scraper is 5 and 20 rpm for cases 1, 2 and 3, 4 respectively. It can be observed in the Figure 8 that the average velocity of particles is 0.007 m/s for the case 1 ad 2 (there is only difference in screw type and the scraper speed is kept at 5 rpm). Similarly, the average velocity of particles for case 3, 4 in the scraper zone are also same at 0.029 m/s. The velocity of particles in scraper zone are not influenced by the change in screw type. Also, with four times increase in scraper speed, average velocity in scraper zone is also increased by four times for both the screws signifying similar loosening of blend.

3.3   Impact of cohesion on flow pattern

This simulation was performed with screw 2. The cohesion energy density (reflecting cohesion in J/m^3) value of particle-particle interaction is increased from 90000 (case 1) to 120000 (case 6) and particle-wall interaction is decreased from 6000 (case 1) to 1200 (case 6). The influence is the change in average particle velocity in the screw zone i.e. from 0.058 m/s to 0.066 m/s (see Figure 12). There is a little but not significant change in particle velocity in this zone, as on one side, the particle-particle cohesion increase restricts the particles to move freely with respect to each other whereas, decrease of particle wall cohesion tends the particles to move freely and not stick to the wall.

Mass discharge out of the hopper

The mass discharge rate for case 6 and case 1 are compared and it is observed that the mass discharge for case 6 is 8.02 kg/h and for case 1 is 9.35 kg/h which is expected as the particle - particle cohesion is lower in case 1 as compared to case 6 which leads to lower interaction in between particles and hence higher discharge rate out of the screw.

4.   CONCLUSION

A comparison of flow from two different type of screws are performed with DEM simulations. The mass discharge rate calculated from theoretical equations are compared to the simulations and are found to be well in agreement suggesting screw 2 to be better than screw 1. Further, impact of scraper speed is also investigated for the throughput. Overall, a vision is emerged to investigate different screw designs. Further, the impact of particle size, particle shape and process parameters change can be applied in order to evaluate its influence on the

flow. The findings are useful for comparing the screw designs and operation of screw feeders for handling cohesive powder.

REFERENCES

[1]   A. Mazor, L. Orefice, A. Michrafy, A. de Ryck, and J. G. Khinast, "A combined DEM & FEM approach for modelling roll compaction process," *Powder Technol.*, vol. 337, pp. 3–16, 2018.

[2]   P. Srikant, J. Akash, D. Mahesh, and S. Astik, "Roller compaction design and critical parameters in drug formulation and development: Review," *Int. J. PharmTech Res.*, vol. 7, no. 1, pp. 90–98, 2015.

[3]   L. BATES, "Entrainment Patterns of Screw Hopper Dischargers," *J. Eng. Ind.*, pp. 295–302, 1969.

[4]   . Yu, Y. and Arnold, P., C., "The influence of screw feeders on bin flow patterns, Powder technology," vol. 1, no. 88, pp. 81–87, 1996.

[5]   A. W. Roberts, "The influence of granular vortex motion on the volumetric performance of enclosed screw conveyors," *Powder Technol.*, vol. 104, no. 1, pp. 56–67, 1999.

[6]   J. W. Fernandez, P. W. Cleary, and W. Mcbride, "Effect of screw design on hopper draw down by a horizintal screw feeder," *Prog. Comput. Fluid Dyn. An Int. J.*, no. December, pp. 1–6, 2009.

[7]   P. A. Moysey and M. R. Thompson, "Investigation of solids transport in a single-screw extruder using a 3-D discrete particle simulation," *Polym. Eng. Sci.*, vol. 44, no. 12, pp. 2203–2215, 2004.

[8]   P. A. Moysey and M. R. Thompson, "Modelling the solids inflow and solids conveying of single-screw extruders using the discrete element method," *Powder Technol.*, vol. 153, no. 2, pp. 95–107, 2005.

[9]   Q. F. Hou, K. J. Dong, and A. B. Yu, "DEM study of the flow of cohesive particles in a screw feeder," *Powder Technol.*, vol. 256, pp. 529–539, 2014.

[10]   P. A. Cundall and O. D. L. Strack, "A discrete numerical model for granular assemblies," *Géotechnique*, vol. 29, no. 1, pp. 47–65, 1979.

[11]   C. Kloss, C. Goniva, A. Hager, S. Amberger, and S. Pirker, "Models, algorithms and validation for opensource DEM and CFD-DEM," *Prog. Comput. Fluid Dyn. An Int. J.*, vol. 12, no. 2/3, p. 140, 2012.

[12]   H. P. Zhu, Z. Y. Zhou, R. Y. Yang, and A. B. Yu, "Discrete particle simulation of particulate systems: Theoretical developments," *Chem. Eng. Sci.*, vol. 62, no. 13, pp. 3378–3396, 2007.

[13]   P. W. Cleary, "Large scale industrial DEM modelling," *Eng. Comput. (Swansea, Wales)*, vol. 21, no. 2–4, pp. 169–204, 2004.

[14]   S. Plimpton, "Fast parallel algorithms for short-range molecular dynamics," *J. Comput. Phys.*, vol. 117, pp. 1–19, 1995.

[15]   A. Di Renzo and F. P. Di Maio, "Comparison of contact-force models for the simulation of collisions in DEM-based granular flow codes," *Chem. Eng. Sci.*, vol. 59, no. 3, pp. 525–541, 2004.

[16]   K. L. Johnson, K. Kendall, and A. D. Roberts, "Surface Energy and the Contact of Elastic Solids," pp. 301–313, 1971.

[17]   S. R. Gopireddy, C. Hildebrandt, and N. A. Urbanetz, "Numerical simulation of powder flow in a pharmaceutical tablet press lab-scale gravity feeder," *Powder Technol.*, vol. 302, pp. 309–327, 2016.

[18]   A. Jensen, K. Fraser, and G. Laird, "Improving the Precision of Discrete Element Simulations through Calibration Models," pp. 1–12, 2014.

[19]   C. J. Coetzee and D. N. J. Els, "Calibration of discrete element parameters and the modelling of silo discharge and bucket filling," *Comput. Electron. Agric.*, vol. 65, no. 2, pp. 198–212, 2009.

[20]   A. Anand, J. S. Curtis, C. R. Wassgren, B. C. Hancock, and W. R. Ketterhagen, "Predicting discharge dynamics from a rectangular hopper using the discrete element method (DEM)," *Chem. Eng. Sci.*, vol. 63, pp. 5821–5830, 2008.

[21]   A. Anand, J. S. Curtis, C. R. Wassgren, B. C. Hancock, and W. R. Ketterhagen, "Predicting discharge dynamics of wet cohesive particles from a rectangular hopper using the discrete element method (DEM)," *Chem. Eng. Sci.*, vol. 64, no. 24, pp. 5268–5275, 2009.

OPENFOAM-INTERACTIVE (OFI): AN INNOVATIVE UNIVERSAL INTERFACE TO CONTROL SOLVERS IN OPENFOAM

ARPIT SINGHAL†*, RAPHAEL SCHUBERT†, ADHAM HASHIBON†

† Fraunhofer-Institut für Werkstoffmechanik IWM
Wöhlerstraße 11,
79108 Freiburg im Breisgau,
Germany
E-Mail: arpit.singhal@iwm.fraunhofer.de

Key words: OpenFoam-Interactive, Particle simulation, Interface Wrappers

Abstract. We present a new method for coupling fluid and particle systems that works by directly manipulating the flow field variables, mimicking the presence of solid particles rather than adding additional force terms in the governing equations as, e.g., in the traditional immersed boundary method (IBM). We demonstrate an implementation based on the open source OpenFOAM [2] package. The OpenFOAM-Interactive (OFI) presented here gives access to all internal field variables of the governing equations. This ease and facilitates complex computational and seamless data exchange and manipulation of the field variable. OFI contributes to reducing the time needed in creating the initial geometry and enables readily re-creating the geometry for the basic computational fluid dynamics (CFD) simulation steps. The presented methodology is verified for a reference simple problem (i) obstruction to flow with bluff bodies. The verified methodology is then applied as an example to demonstrate a realistic problem of heat transfer to a gas through particle bed [1]. The particle bed is created "on the fly" with OFI, this will facilitate studying fluid behavior over different particle configurations in particle beds (i.e. porosity variation) more efficiently in future.

1 INTRODUCTION

Computation fluid dynamics (CFD) is applied in various applications ranging from environmental studies to design the functionality of heat exchangers to aerodynamics applications and so on [1]–[3]. CFD works on the basic principle of dividing the entire system domain into several grids or cells and solving the governing equations of flow by numerically discretizing the partial differential equations (PDE) of the fluid phase in these small grid elements [4], [5]. The development in computational resources CFD simulations have gained quite a limelight, even simulations at resolved scales are possible today [6], [7]. Many commercial packages (like Fluent [8], Star CCM+ [9]) and open source package (like OpenFOAM [10], CFDEM Coupling [11]) exists in the current scenario.

Open Source Field Operation and Manipulation (OpenFOAM) [10], [12] is the most used open source suite of C++ libraries to CFD problems. It was first released in 1980, since then it

has grown more mature to handle different complexities in physics (from macroscopic level to microscopic level). The best feature being the accessibility to the flexible framework to build your own applications as required. Different methods and algorithms are being added in every release with the help of a big community of users using OpenFOAM to back the continuous growth. These are being shared on online Git version controlled repositories (like GitHub [13], GitLab [14], etc.).

The flexibility in the OpenFOAM framework has led to many developments/improvements in solving CFD problems by developing new solvers pertaining to the specific industrial or academic question by improving the previous numerical schemes [15]–[18] or by adding features to solve addition problem domain[19]–[23].

The recent demands from industries to parametrize studies in order to optimize product and system geometries, requiring the intrinsic approach has led towards efficient automatization mechanisms. In a typical CFD case, mostly a small change in the geometry requires careful and intricate re-meshing. This limits the automation specifically and especially due to the lack of existing meshing tools in open source world.

There have been developments in the field of automating the whole procedure of running a case with OpenFOAM through python scripts which are used to serve as interface to pre and post process OpenFOAM (specifically, pyFoam and pyFlu)[24], [25]. These packages demand too many changes deep in the code to create a library interface for OpenFOAM. They offer excellent automation schemes for the cases which do not require re-creation and re-meshing of the geometry.

In this work we develop the access to OpenFOAM field variables i.e. volume scalar and volume vector fields using the client server architecture along with complete access to the OpenFOAM objects of mesh and runtime. Thus, this enables us to control and manipulate OpenFOAM operations such as Run, Edit, Print, Search, and Rerun with static meshing i.e. create objects, run and edit the cases rapidly.

In general, any OpenFOAM or any CFD associated problem consists of three stages (i) pre-processing (ii) solver and (iii) post-processing, the purpose of the work is to reduce the dependability or efforts towards pre-processing as much as possible with minimal change or duplicity required to the original OpenFOAM solvers. The aim is to introduce dynamic features to reduce the dependence on complex re-meshing and expensive dynamic meshing to work with the server client architecture in order to create, mesh and manipulate the domain variable easily. At this stage, this paper is the benchmark in this direction for our future works, where a more detailed numerical scheme behind the functionality of the OFI will be presented and applied to more physical problems.

The paper has been structured as follows, we first introduce the literature in Section 1, and we lay down the methodology implied to OpenFOAM-Interactive (OFI) in Section 2, we then add on to present the verification and results in Section 3 and in the end, we conclude with possible future outcomes from the work in Section 4.

2 METHODOLOGY

To give an idea of the overall methodology that we employ to render OpenFOAM-Interactive (OFI) to control OpenFOAM (v2.4.0 to v5.0.x tested in this paper, though we already have implementation supporting OF up to version 6.0) solvers through an interface wrapper is presented. The aim is to introduce minimal changes to the source code of OpenFOAM solver and make use of already well-established suite of the OpenFOAM framework. A schematic of representation of the workflow is shown in Fig. 1. This paper explains SimPhony OpenFoam Wrapper from Fig 1.

The main concept is shown schematically in Figure 3. OpenFOAM consists of a main loop over time or solver iterations. After each such iteration a condition is evaluated to determine whether convergence is achieved. OFI intercepts these calls and replaces them with additional machinery allowing changing the internal state of the case while it is running. Client-server architecture is designed and implemented to allow the user to send arbitrary commands to OpenFoam that are to be performed in these intercepts. These changes include: read and write cell value for scalar/vector volume fields, set up and fix a value at every time step, run for specific time, finding cells etc. While this may seem not very useful initially, an adept user can change the field values in order to exert or mimic various complex conditions e.g., simulating the presence of a rigid or flexible solid object within fluids, multiphase dynamics, chemical reactions, and arbitrary geometrical objects, to name but a few.

Key to the success of this method is the physical and mathematical soundness of the commands and variations induced by the user. The kind of changes and how to employ them is indeed not trivial and is the subject of a follow up publication. Here we demonstrate the method and some of its possibilities focusing on the software engineering aspects.

2.1 Approach and Implementation Detail

As shown in Fig. 1 any solver and any version of OpenFOAM package can be made to work with OFI. In this verification study, we consider as an example a case of incompressible Newtonian fluid in laminar flow regime for demonstrating the proposed method. The straightforward way to solve the problem of an incompressible Newtonian fluid in laminar regime with SimpleFoam solver given in Fig. 2 (a) includes, (i) creating a geometry, (ii), solution to the problem, followed by, (iii) visualizing the results. The complexity of each of these steps depends on the actual problem, and may range from being as trivial as shown in Fig. 2(b), or as complex as shown in Fig. 2(c).

If the problem is extended to behave as shown in Fig.2 (b), i.e. an obstacle to the flow has to be created (considering No-slip conditions); all the above-mentioned steps would have to be redone. This is due to the need to re-create and re-mesh of the geometry. The intention behind OFI is to reduce the efforts in doing so, i.e. to enable directly encoding the obstacle in the mesh without directly re-creating and re-meshing the whole geometry all over again. In fact, using OFI both cases in Fig. 2(a), Fig. 2(b) or Fig. 2(c) become equally easy.
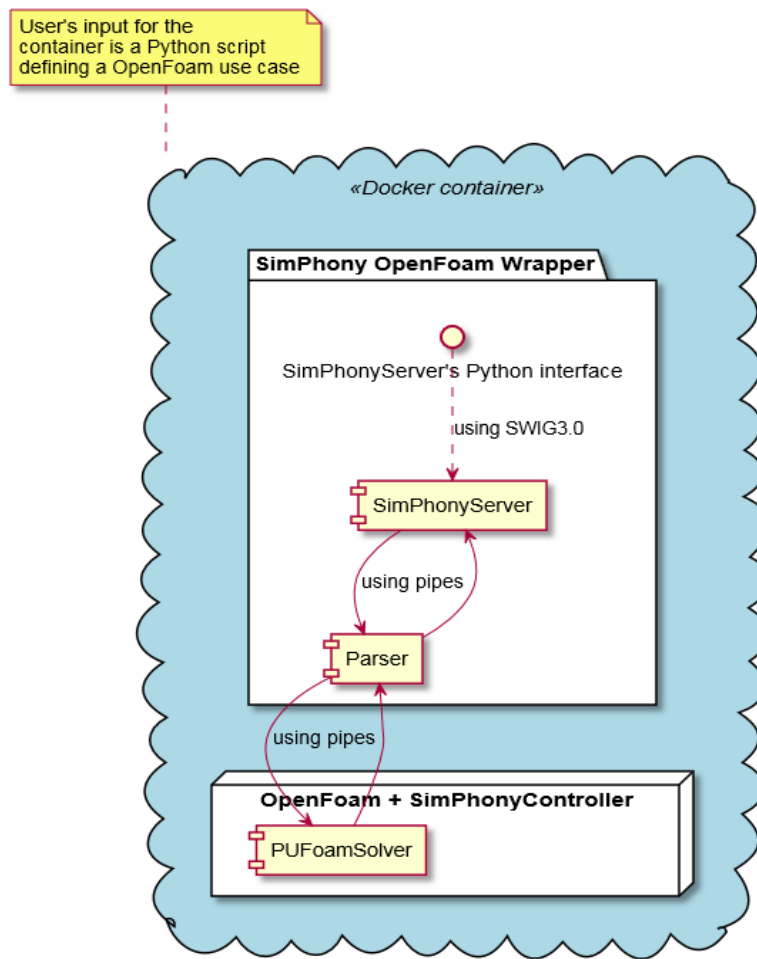
Figure 1: A schematic representation of the OFI architecture.   A think controller layer is embedded in the main loop of the OF solver which intercepts the execution of OF and alters the state seamlessly. The controller communicates through a pipe socket to the Parser which parses commands from the client. The parser in turn communicates through a socket with the client part where currently the user can make changes and issue commands. The Controller converts these commands into actions. There is python interface to this SimPhonyServer which makes the description of the use case in Python.

2.2 Treatment of obstacle in a flow with OFI

The obstruction to flow as shown in Fig. 2(b) is directly emulated by making the velocity of the cells in the region (i.e. the obstacle zone) fixed to zero in each iteration of the solver. In pictorial terms it is explained in Fig. 3, the case following the boundary conditions and initial conditions is prepared in OFI. In a typical SIMPLE algorithm, the previous iteration values in the cells provide as the initial values for the next iteration or current iteration. In OFI, the solver is forced to stop at each iteration and is reset (or re-initialized) with the constant value (in this case zero velocity) in cells (emulated as an obstacle). This makes the cells (in an emulated zone) behave as on obstruction zone.
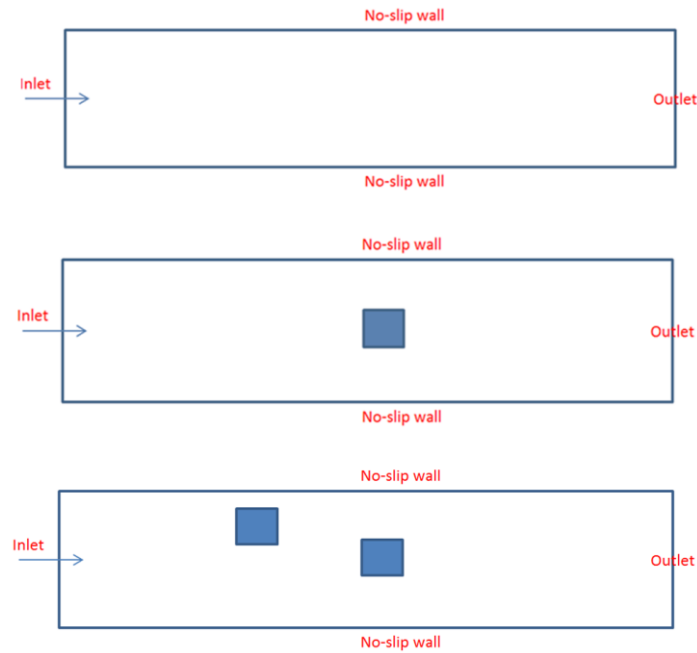
Figure 2: 2D schematic flow diagram of the problem solved in this work with OpenFOAM-Interactive (OFI) (bottom) and without OpenFOAM-Interactive, but with basic steps of any CFD setup (top). The square obstacle is created with OpenFOAM-Interactive and also with the basic step of re-creating the geometry and re-meshing for OpenFOAM-2.4.0.
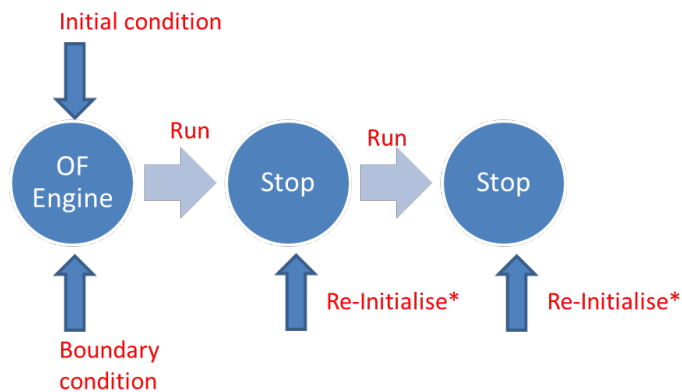
Figure 3: Pictorial representation of the re-Initializing steps for the cells in region* (obstruction) required to act as obstruction. OF-Engine represents the complete OpenFOAM-Interactive suite.

3   RESULTS

In this section, the proposed methodology of OpenFOAM Interactive (OFI) is applied to a case with SimpleFoam solver i.e. a 2D channel flow with two square obstacles disarranged to the flow. The fluid is considered to be of steady incompressible Newtonian in nature and within laminar regime (Reynolds number Re 100 and Re 50). The description of the geometry and flow parameters is listed in Table 1. The purpose of the comparison of the OFI SimpleFoam with OF-2.4.0 SimpleFoam solver is based on boundary resistance and velocity structure

representation of the flow. Hence the sole criterion for comparison is velocity magnitude (in m/s).

This study is a one to one comparison between a case solved by OFI using the SimpleFoam solver and one solved entirely with the native OF SimpleFoam solver. That is, we compare the solution of an obstacle using the built in OpenFOAM methodology and compare it to a solution where in effect OpenFOAM is ran on a system without any obstacles internally (simple uniform mesh) but the obstacle is emulated by an external manipulation of cells directly using OFI. This is done to validate both the approach and the implementation. The goal is to demonstrate the capability of OFI solver to predict basic flow behavior with precision. Moreover, we consider only the hydrodynamics entrance region in this work to create the geometry; the fully developed region was not considered significant in this comparison.

The complexity used for comparison in this section is simulated with similar solver setting and geometry as previously explained in Table 1. Also, note that neither the numerical sensitivity analysis (like, grid independence) nor the solver sensitivity analyses are considered here, for a full validation there will be a follow up publication. The focus of this work is to demonstrate the capability of OFI solver to give corresponding results with similar flow and solver parameters as would be the case with the OpenFOAM-2.4.0 solver.

3.1 Results for Two square obstructions disoriented in arrangements

As an example, disoriented square obstacles to the flow were considered. This is quite a challenging problem in literature, and it is influenced by different numerical and solver accuracy parametrizations. This is because of the flow from the first obstacle creating a wake region with vortexes which hinders the inflow for the second obstacle and so on.

For similar numerical accuracy, solver parameters and Reynolds numbers (Re 100 and Re 50), the contour plots for velocity magnitude (in m/s; in Fig. 4) shows the ability of OFI to capture the flow behavior with much accuracy compared with OF-2.4.0. To have a thorough comparison of the flow profiles obtained from both approaches, 3 different regions (i.e. Lines L1, L2, L3) in the simulated geometry (all in different flow regimes) were analyzed as shown in Fig. 5. The results obtained for velocity magnitude fluctuations are within the acceptable error margin (within 5% difference margin).

3.2 Result of flow over a 2D representation of packed particle bed

In the previous section obstacles to flow is emulated to see the velocity fluctuation to the flow. A more complex case with simulation parameters from Table 2 and having a real application with multiple blocked cells portrayed as a packing of a packed bed is simulated in this section to extract the temperature profile. This happens without re-meshing for the particles and by recalibrating the values of temperature in the cells to behave as the particles of constant heat source. We emphasize that this is a first step towards a more detailed analysis of particle-fluid and solid-fluid interaction based on OpenFOAM-Interactive (OFI).

It is shown in Figure 6 that the 2D representation of the cells behaving as the constant heat source (573K) is heating the fluid (at 473K) till they reach an equilibrium temperature.
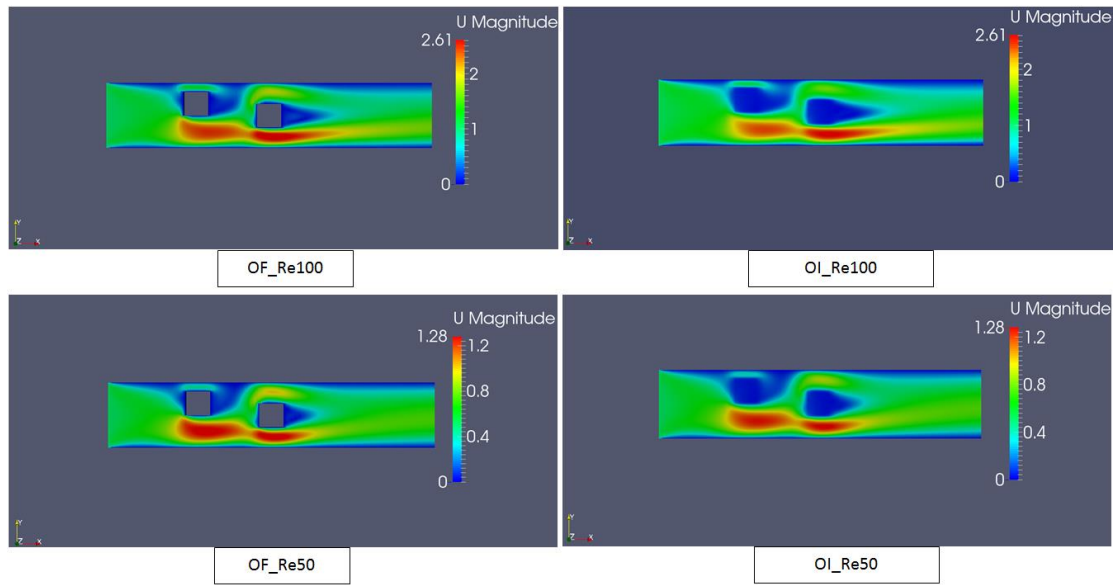
Figure 4: Velocity contour graphs for disoriented square obstruction to flow from OpenFOAM-Interactive (OFI) (right) and OpenFOAM-2.4.0 (OF) (left); SimpleFoam solver for a flow at Re100 and Re50 [NOTE: the scale is in (m/s); also, the dimensions of the square obstacles are 0.141m^2].

Table 1. Details of the parameters used in simulation. *The OFI is compatible with all versions of OpenFOAM

Parameter	Value
Length of the 2D channel (m)	5
Width of the 2D channel (m)	1
Mesh resolution	40x40
Number of mesh elements	1600
Reynolds number (Re)	100; 50
Solver used	SimpleFoam
OpenFOAM version*	5.0.x

Table 2. Details of the parameters used in simulation. *The OFI is compatible with all versions of OpenFOAM

Parameter	Value
Length of the 2D channel (m)	2
Width of the 2D channel (m)	5
Mesh resolution	40x100
Number of mesh elements	4000
Reynolds number (Re)	10
Solver used	byoyantBoussinesqSimpleFoam
OpenFOAM version*	5.0.x
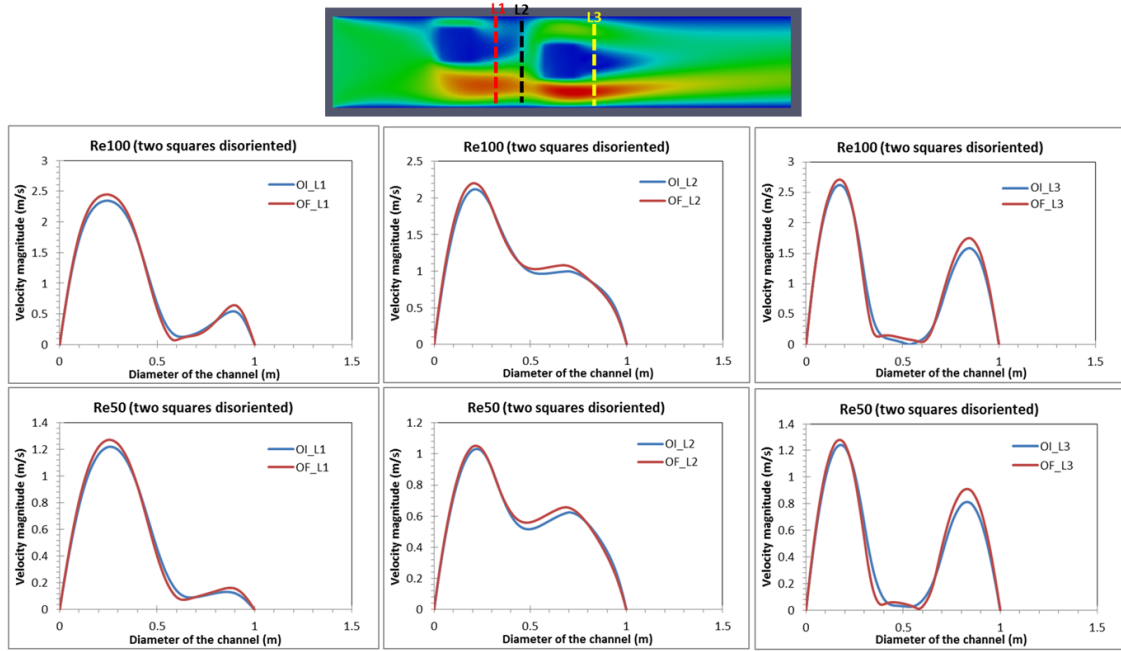
Figure 5: The comparison of velocity magnitude (m/s) profiles obtained for Re100, Re50 between OpenFOAM-Interactive (OFI) and OpenFOAM-2.4.0 (OF) for double disoriented square obstruction of similar sizes. The velocity data profiles are plotted over lines (L1, L2 and L3) from bottom wall of the channel to the top wall).
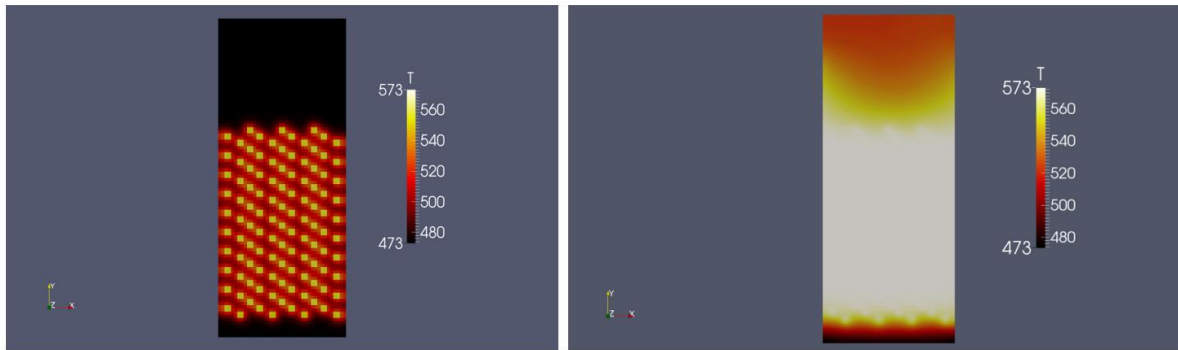
Figure 6: Temperature contour plots for 2D particle bed generated with OFI as cells of constant heat source. [left] is the profile at the first iteration showing the temperature in the cells manipulated to behave at 573K. [right] shows the evolution of the temperature profile in the geometry domain after the temperature has reached an equilibrium.

4 CONCLUSIONS

We present an innovative simple yet efficient means to control OpenFOAM with minimal changes to the code by manipulating directly the control flow. The proposed method allows enhanced automation and provides new means of performing complex CFD modelling, in particular it enables alteration of the numerical domain without re-meshing.

The concept introduced in this paper laid a path forward to utilizing server client architecture to completely control OpenFOAM and similar tools. This will form an integral part of an open

simulation platform and is planned to be offered as a service and APP on the upcoming Materials Modelling MarketPlace (https://www.the-marketplace-project.eu/), which is a framework of integrating simulation frameworks in a semantic and interoperable environment facilitated by the common universal data structure (CUDS). The unique feature of the presented methodology i.e. OpenFOAM-Interactive (OFI) is the adaptability to the change in OpenFOAM versions. It is flexible to plug-in it to any OpenFOAM versions.

The presented package OFI has been applied to solve an interesting problem from literature i.e. bluff bodies to the flow. Our presented methodology helps scale the steps of re-creating and re-meshing the geometry when and if required according to the change in the simulated problem. The results obtained were within the error margin of 5% which demonstrates that our developed OFI suite works well.

Following that the methodology is applied to imitate a particle packing simulation. The validation and verification of the detailed heat transfer analysis resulting from the change in porosities and validation from the literature pertaining to more real-time engineering problems with packed beds will be a part of the future studies.

REFERENCES

[1] B. Sanderse, S. P. Pijl, and B. Koren, "Review of computational fluid dynamics for wind turbine wake aerodynamics," *Wind Energy*, (2011), **14**, 7, 799–819.

[2] M. M. Aslam Bhutta, N. Hayat, M. H. Bashir, A. R. Khan, K. N. Ahmad, and S. Khan, "CFD applications in various heat exchangers design: A review," *Appl. Therm. Eng.*, (2012), **32**, 1–12.

[3] H. Wang, H. Wang, F. Gao, P. Zhou, and Z. (John) Zhai, "Literature review on pressure–velocity decoupling algorithms applied to built-environment CFD simulation," *Build. Environ.*, (2018), **143**, 671–678.

[4] Y. Lim and S. B. Jørgensen, "Partial Differential Equations (PDE) and Computational Fluid Dynamics (CFD)," (2006), **Chapter 1.**, 2006, 35-106 BT-Computer Aided Process & Products Eng.

[5] P. F. Galpin, J. P. Van Doormaal, and G. D. Raithby, "Solution of the incompressible mass and momentum equations by application of a coupled equation line solver," *Int. J. Numer. Methods Fluids*, (2018), **5**, 7, 615–625.

[6] A. Singhal, S. Cloete, S. Radl, R. Quinta-Ferreira, and S. Amini, "Heat transfer to a gas from densely packed beds of monodisperse spherical particles," *Chem. Eng. J.*, (2017), **314**, 27–37.

[7] A. Singhal, S. Cloete, S. Radl, R. Quinta-Ferreira, and S. Amini, "Heat transfer to a gas from densely packed beds of cylindrical particles," *Chem. Eng. Sci.*, (2017), **172**, 1–12.

[8] "ANSYS® Academic Research Mechanical, Release 18.1, Help System, Coupled Field Analysis Guide, ANSYS, Inc." .

[9] "STAR CCM+ Users Manual. http://www.cd-adapco.com/products/star-ccm/documentation." .

[10] H. G. Weller, G. Tabor, H. Jasak, and C. Fureby, "A tensorial approach to computational continuum mechanics using object-oriented techniques," *Comput. Phys.*, (1998), **12**, 6, 620–631.

[11]   C. Goniva, C. Kloss, N. G. Deen, J. A. M. Kuipers, and S. Pirker, "Influence of rolling friction on single spout fluidized bed simulation," *Particuology*, (2012), **10**, 5, 582–591.

[12]   "OpenFOAM." .

[13]   Http://en.wikipedia.org/wiki/GitHub, "Github." [Online]. Available: http://github.com/.

[14]   https://en.wikipedia.org/wiki/GitLab, "GitLab." [Online]. Available: https://about.gitlab.com/.

[15]   G.-H. Kim and S. Park, "Development of a numerical simulation tool for efficient and robust prediction of ship resistance," *Int. J. Nav. Archit. Ocean Eng.*, (2017), **9**, 5, 537–551.

[16]   M. V. Kraposhin, E. V. Smirnova, T. G. Elizarova, and M. A. Istomina, "Development of a new OpenFOAM solver using regularized gas dynamic equations," *Comput. Fluids*, (2018), **166**, 163–175.

[17]   C. Goniva, C. Kloss, A. Hager, and S. Pirker, *An open source CFD-DEM perspective*, (2010). 2010.

[18]   C. Fernandes, F. Habla, O. Carneiro, O. Hinrichsen, and J. M. Nobrega, *Development of a new 3D OpenFOAM® solver to model the cooling stage in profile extrusion*, (2016). 2016.

[19]   S. M. Longshaw *et al.*, "mdFoam+: Advanced molecular dynamics in OpenFOAM," *Comput. Phys. Commun.*, (2018), **224**, 1–21.

[20]   C. White *et al.*, *DsmcFoam+: An OpenFOAM based direct simulation Monte Carlo solver*, (2017). 2017.

[21]   H. Jasak and M. Beaudoin, *OpenFOAM turbo tools: From general purpose CFD to turbomachinery simulations*, (2011), **1**. 2011.

[22]   P. Horgue, C. Soulaine, J. Franc, R. Guibert, and G. Debenest, "An open-source toolbox for multiphase flow in porous media," *Comput. Phys. Commun.*, (2015), **187**, 217–226.

[23]   L. Orgogozo *et al.*, "An open source massively parallel solver for Richards equation: Mechanistic modelling of water fluxes at the watershed scale," *Comput. Phys. Commun.*, (2014), **185**, 12, 3358–3371.

[24]   B. F. W. Gschaider and A. Arbor, "Automatic case setup with pyFoamPrepareCase," (2015)June, 1–185.

[25]   B. F. W. Gschaider, "Automatization with pyFoam - How Python helps us to avoid contact with OpenFOAM," *5th OpenFOAM Work.*, (2010)June, 1–80.

PARTICLE-BASED METHOD FOR INVESTIGATION OF THE PHYSICAL PROCESSES IN THE COMPLEX INDUSTRIAL TASKS

KRAPOSHIN M.[1], EPIKHIN A.[1, 2], MELNIKOVA V.[1, 2] AND STRIJHAK S.[1]

[1]Ivannikov Institute for System Programming of the Russian Academy of Sciences
Solzhenitsyna str. 25, 109004, Moscow, Russia
E-mail: vg-melnikova@yandex.ru, strijhak@yandex.ru web page: http://www.ispras.ru/en

[2]Bauman Moscow State Technical University
Baumanskaya 2-ya str., 5, 105005, Moscow, Russia

Key words: particle, FVM, OpenFOAM, Euler-Lagrange approach, water droplets, injection, jet, wind farm, wind turbines, solvers.

Abstract. The main task of this paper is improved of modeling accuracy and understanding of the physical process which arises in complex industrial tasks using Euler-Lagrange approach. There were two cases under the study. The first one was aimed to study the dynamics of self-organized turbulent structures. A first qualitative insight into the entrainment process in wind farm is obtained through particle tracking. The second case is focusing on developing the Euler-Lagrange approach for the understanding of the physical processes occurring the water droplets injection into a jet. The water droplets, coming out of the special sockets, are simulated by packages (parcels) of particles of a certain mass and size according to the specified flow rate. Parcels moving in the flow, breakup at high speeds, heating and evaporation are investigated.

1 INTRODUCTION

Currently, many of the known basic models (including implemented in commercial foreign packages) use assumptions and methods based on the transfer of single particles or multi-liquid approaches that are convenient for modeling some phenomena but not suitable for describing complex transient processes. Also, the investigations are underway to combine different approaches for expanding the use of models that describe the multiphase flow — for example, models that include the transfer of the interphase boundary and transfer of individual droplets. However natural and experimental estimation, usually, represent significant difficulties and a quite high cost in the case of study of complex physical phenomena. As a result, there is a need for the use of numerical modeling tools and the development of hybrid models of solvers that combine continuum (Euler) and discrete (described in Lagrange variables) systems. This approach provides additional information about the flow pattern and structure and in many cases serves as confirmation or refutation of the hypothesis describing a physical phenomenon.

In this paper, we consider the use of hybrid (Euler-Lagrange) approach for solving two industrial problems. The open source package OpenFOAM has been chosen as the main platform. The first task is devoted to the dynamics of self-organized turbulent structures around wind turbines, where the use of this approach allows conducting research of the phenomenon of ejection. The second is the development and implementation of a hybrid (Euler-Lagrange) approach for modeling the process of interaction water droplets and a high-temperature gas jet.

2 WATER DROPLETS INJECTION INTO A JET

Currently, one of the critical tasks in the rocket and space field is to reduce the acoustic noise from the working engines jets. Various passive and active methods are used to solve this problem at present. One of these methods is the water jets supply in the area of the hot gas propulsion jet. This approach has been the subject of research, which is reflected in a number of papers by various authors [1-5]. A detailed study of gas-dynamic and acoustic processes arising from the use of this technology in real conditions is a significantly complex and expensive task. The heterogeneity of the region in terms of Mach number, multiphase, splashing of water jets, the presence of physical and chemical processes, the possible interaction and reflection of shock waves, etc. - all these features necessitate the use of numerical modeling tools and the development of a hybrid model of the solver capable of correctly reproducing and predicting the phenomena described above.

The solution of such a problem requires an accounting of the droplet propagation in the supersonic flow. To do this, it is necessary to divide the description of the gas-droplet flow into two systems: continuous (Euler) and discrete (Lagrangian).

2.1 Government equations

Taking into account the currently accepted assumptions, the mathematical model consists of three-dimensional Navier-Stokes equations for turbulent super -, trans- and subsonic flows of a compressible gas-droplet mixture, including the mass, momentum and energy conservation equations; turbulent transfer equation, components of the mixture transfer equations, droplets transfer equation, description of the mechanisms of interaction of water and gas flows (evaporation, momentum exchange). The basis for the continuum system was the pimpleCentralFoam solver [6], which is based on a hybrid method of approximation of convective terms and the Kurganov-Tadmor Scheme.

For the Lagrangian (droplet) part as a base was used an OpenFOAM cloud model sprayCloud. This model used a for representation of a gathering of real particles. This construction is plainly made because that it is almost always too computational demanding to simulate all the real particles.

A sphere particle defined by its position x_p, diameter D_p, velocity U_p and density ρ_p. The mass of the particle $m_p = \frac{1}{6}\rho_p\pi D_p^3$. The particle motion is solved by integrating the force balance. The force represents the sum of all relevant forces: drag force from the fluid phase (F_D) and gravity force (F_G).

$$\frac{dx_p}{dt} = U_p \tag{1}$$

$$m_p\frac{dU_p}{dt} = \sum F_i = F_D + F_G = m_p\frac{U - U_p}{\tau_p} + m_p g \tag{2}$$

The relaxation time of the particles (the time it takes for a particle to respond to changes in the local flow velocity):

$$\tau_p = \frac{4}{3}\frac{\rho_p D_p}{\rho * C_D * |U - U_p|} \tag{3}$$

The drag coefficient C_D calculated via function in the dependency of the particle Reynolds number (Re):

$$C_D = \begin{cases} 0.424 * Re, & Re > 1000 \\ 24 * (1 + Re^{2/3}/6), & Re \leq 1000 \end{cases}$$

Below are the basic equations, special models modifications (injection and phase change models) and its investigation (heat transfer model, breakup model) to create a hybrid Euler-Lagrange approach for simulating the interaction of gas jets with water are proposed.

2.2 Injection Models

In OpenFOAM, there are several different tools for introducing particles in the fluid flow, according to settings specified by the user. These tools are properly called injectors. Several injection models already exist in OpenFOAM, such as cone nozzle, manual injection, patch injection, and others, but water spray socket may have a different shape. Most often, the holes for the flow of water drops represent a slit and there is a hole with a rotating screw at the end of the socket. Two own models of particle injection have been developed: cone nozzle curling injection model and slit injection model.

Cone Nozzle Curling Injection. Model of cone nozzle injection with curling set by next parameters: time start of injection; total mass of parcels for duration of injection; type of initial velocity; injection number of parcels per second; position, radius R_p and direction of the nozzle injection, angle of injection, rotation frequency ω and direction (clockwise, counterclockwise) and parcels size distribution type.

The full initial parcel injection velocity:

$$\overline{U} = \omega * R_p * \overline{curlDir} + U_{mag} * \overline{dir} \tag{4}$$

$\overline{curlDir}$ – the velocity tangential direction vector; $\overline{dir}$ – the velocity direction vector.

The normal parcel velocity depending from the setting type:

- constantVelocity

$$U_{mag} = constant \tag{5}$$

- flowRateAndDischarge

$$U_{mag} = \frac{\dot{m}}{\rho_p * A} \tag{6}$$

- pressureDrivenVelocity

$$U_{mag} = \sqrt{\frac{p_{inj} - p}{\rho_p}} \tag{7}$$

$\dot{m}$ – mass flow rate of water, kg/s; p_{inj}- injection pressure, Pa.; $A = \pi * R^2$ - area of the outlet, m².

On Figure 1 the water particles injection with the next parameters: mass flow rate $\dot{m} = 0.2$ kg/s, injection parcels per second – 10^5, clockwise curling, angle of injection – 30 degrees, outer diameter – 1 mm, omega – 1000 rad/s, particles size from 0.1 to 0.15 mm - in air with pressure $p = 101325$ Pa and temperature $T = 293$ K. is shown.
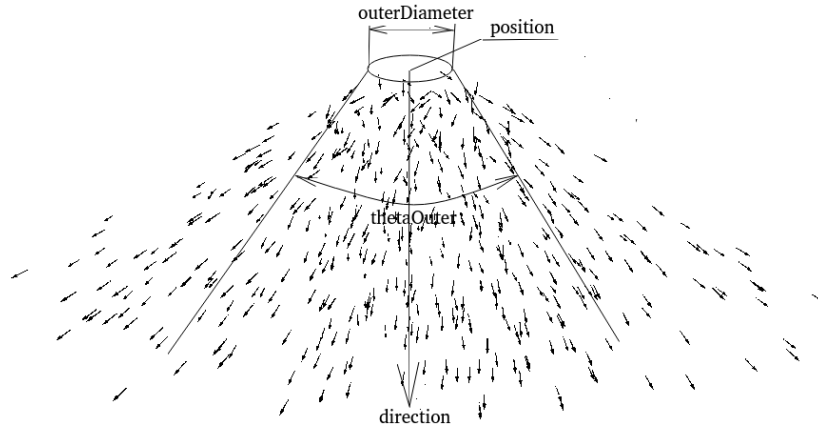
Figure 1: Particles and it's velocity during cone nozzle curling injection

Slit Injection. As the initial parameters for slit injection, besides total mass of parcels, duration, flow type and number parcels per second parameters, using two vectors (*limitDirection 1* and *2*) that determines the spray direction, position of the slit center, slit width (*sW*) and height (*sH*).

The full initial parcels velocity calculated by equation:

$$\overline{U} = U_{mag} * \overline{dir} \tag{8}$$

$\overline{dir}$ randomly choose between vectors *limitDirection1* and *limitDirection2, A = sW * sH*.

The particle injection with the next parameters: mass flow rate $\dot{m} = 1.0$ kg/s, parcels per second – 10^5, sW = 140 mm, sH = 1 mm, particles size from 0.1 to 0.15 mm – in environment with pressure p = 101325 Pa and temperature 293 K is shown on Figure 2.
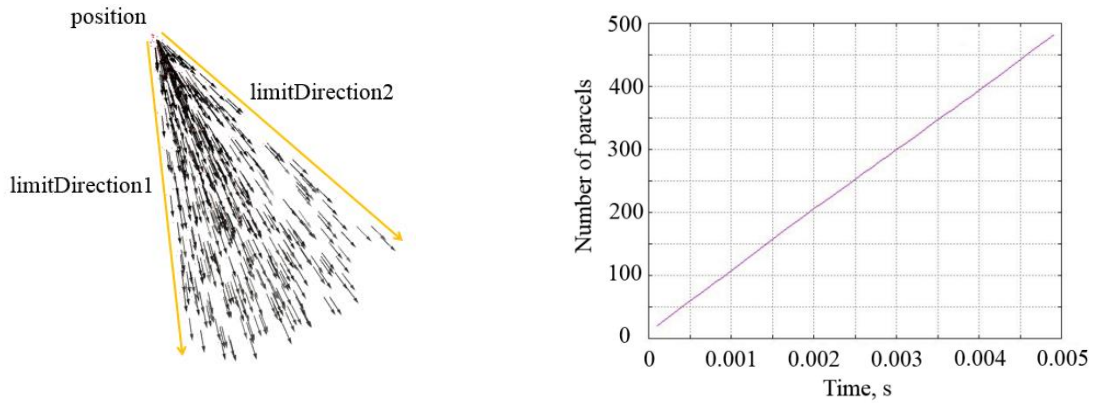
Figure 2: Particles and it's velocity during slit injection.

2.3 Heat Transfer Model

For the calculation of heat transfer from a spherical particle to the surrounding gas, the Ranz Marshall model [7] is used. The Nusselt number can be written:

$$Nu = 2 + 0.6 * \sqrt{Re} * \sqrt[3]{Pr} \tag{9}$$

The test case was made with water parcel with particles 100 μm diameter, mass – $5.2*10^{-9}$ kg and initial temperature 293 K situated in air with the temperature 380 K and 101325 Pa pressure. Gravitational and drag force off. Two variants with motion and steady parcels were considered. The graph on Figure 3 shows that in both cases the system comes to thermodynamic equilibrium, the temperature of the parcels reaches the 373 K and stops. Mass of the parcel, the number of particles and its diameter did not change. When the particles have an initial velocity (U_p=1 m/s), its heating occurs faster.
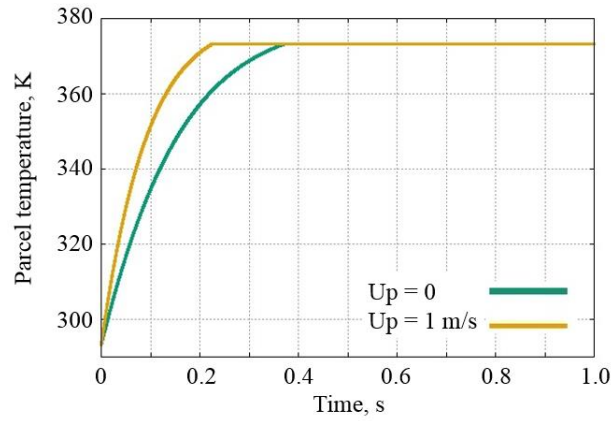
Figure 3: Temperature dependence during time.

2.4 Phase Change Model

The phase change model responds for the evaporation of the droplet. Two models were investigated during simulation. One of them liquidEvaporation model already implemented in OpenFOAM and another one – Spalding model, described in [8], was integrated. Below you can see the verification tests for these models.

Spalding model. The Spalding model realization compared with [8]. According to analytical solution the time of droplet vaporization directly proportional the square of the droplet radius (d^2 law):

$$R_p = \sqrt{R_{p0} - kt} \tag{10}$$

$$k = 2 * \frac{\rho_p}{\rho} * D_{ab} * ln(1 + B_m) \tag{11}$$

R_{p0} – initial particle radius, m; t – time, s; ρ - gas density, kg/m³; D_{ab} - vapor diffusivity, m²/s; B_m - Spalding mass transfer coefficient.

The following case was made to confirm it. The unmoved water droplet (diameter - 0.0017 m, mass – $2571*10^{-9}$ kg) evaporates with constant environment temperature 293 K and pressure 101300 Pa. The result is presented at Figure 4.

The changes of the one water droplet temperature in time were compared with simulation and experimental results in [8] (Figure 5). The water droplet with the temperature 301.45 K free fall. The environment temperature is 301.45 K and pressure is 101300 Pa with air relative humidity 0.22. Two variants of saturated pressure calculation were considered: by OpenFOAM

library and by Clausius-Clapeyron equation:

$$pSat = p * Exp[-\frac{H}{R} * (\frac{1}{T_p} - \frac{1}{Tvap})] \tag{12}$$

H - enthalpy of evaporation, $40.7*10^6$ Дж/(моль*К); $Tvap$ - temperature of vaporization, 373 K; T_p – particle temperature, K; p – environment pressure, Pa.
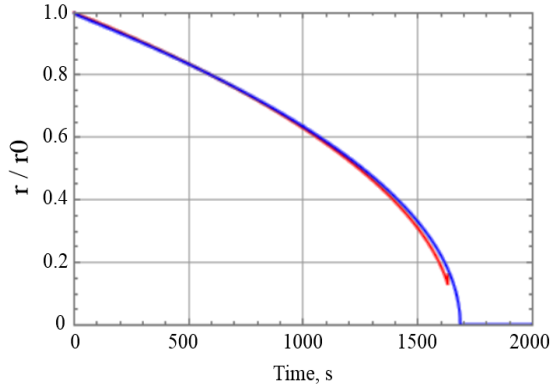
Figure 4: Particle size dependence during time
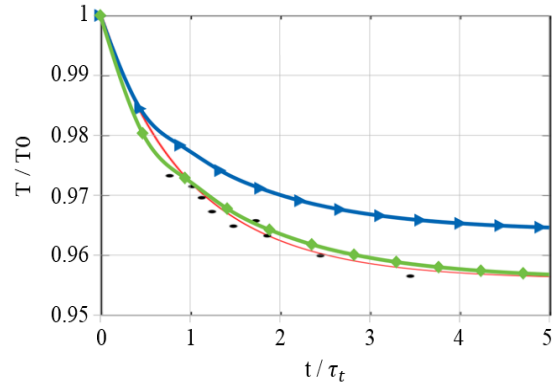
Figure 5: Temperature dependence during time (test 2)
red line – simulation in [2], black dots – experiment [2], green line – simulation (saturated pressure calculated by Clausius-Clapeyron equation), blue line – simulation (saturated pressure calculated in OpenFOAM library)

OpenFOAM liquidEvaporation model. Liquid evaporation model - uses ideal gas assumption. As the test case was chosen the evaporation of the one water parcel with the dimension 100 μm, mass - $5.2*10^{-9}$ kg and temperature 293 K. The environment temperature – 10000 K and pressure 101325 Pa. Two variants were considered when the particle is unmoved and moving with the velocity 1 m/s. The gravitational and drag forces off.

The graphs on Figure 6 show that the particle heats to the evaporation temperature, particle mass and diameter decrease during time. When the particle have the initial velocity ($U_p = 1$ m/s), it heating and respectively evaporation occurs faster.
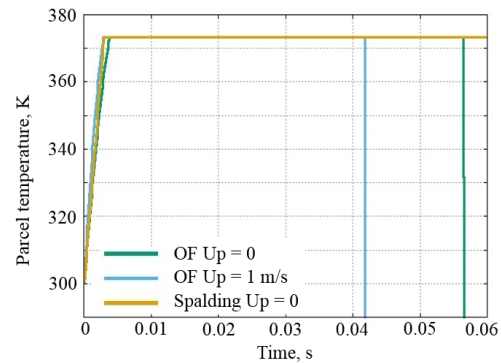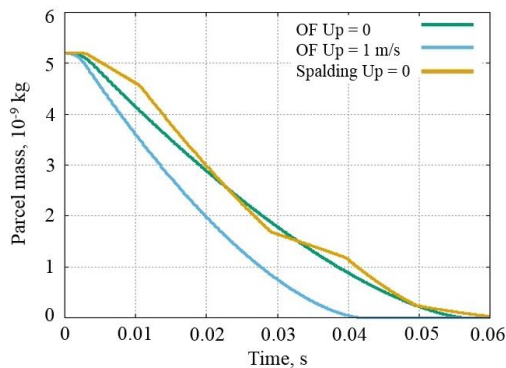
Figure 6: Water mass and maximum particle temperature dependence during time

2.5 Breakup Model

Also, the breakup model was investigated. In our simulations we used a Taylor Analogy Breakup (TAB) Model [9]. This method is based upon Taylor's analogy between an oscillating and distorting droplet and a spring mass system. With the increasing speed of the parcel, the number of droplets should become more, but drops should be a smaller diameter, and respectively evaporates faster. The number by which the drop is divided depends on the Number of Weber.

From the Figure 7 you can see that with the increase of the critical Weber number the mass of the evaporated gas is reduced, a large critical Weber number is similar to disabling a model of the drops breakup.
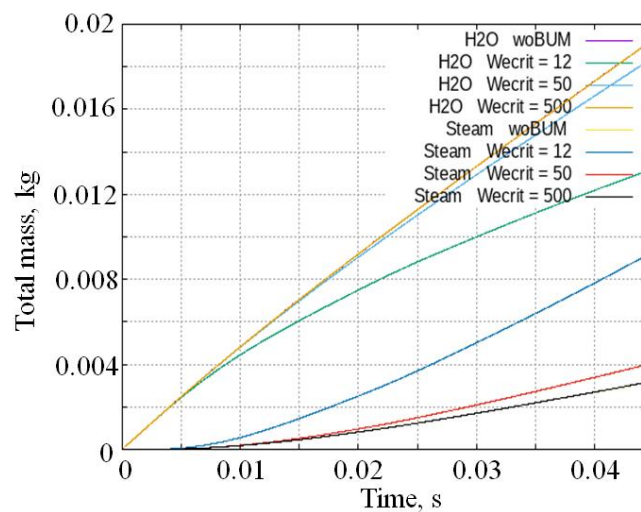
Figure 7: Water and steam phase change in the system with different critical Weber number

3 DYNAMICS OF SELF-ORGANIZED TURBULENT STRUCTURES AROUND WIND TURBINES

Wind energy is an important part of renewable energy sources in many countries. The development of the wind energy industry in Russian Federation (RF) involves the design and operation of new wind power plants and turbines. Wind farms can operate in various climate conditions on the vast territory of RF (Ulyanovsk Oblast, Republic of Adygea, Taman Peninsula, Arctic Region). The first one with 28 wind turbines was constructed in 2017-2018 in Ulyanovsk Oblast. The second one with 3 wind turbines was built in Tiksi in 2018. The new wind farms are building now in Republic of Adygea and in Azov area, and are planned to be built in Krasnodar, Rostov, Stavropol Regions, Republic of Kalmykia till 2022.

The community of researches is normally focused on studying behavior and performance of wind farms, spectral contents of the power fluctuations, different methods of quantifying effects of turbulence-generated loads on wind turbine blade, influence of atmospheric turbulence on the fatigue loads. The turbulent wakes dynamics and wind turbines performance in wind farms

are the questions of the great interest now for the scientific community [10]. Large-eddy simulation (LES) has recently been well applied in the context of numerical simulation of a flow over wind turbines on flat and complex terrains.

The phenomenon of ejection plays a positive role and allows to restore the velocity's deficit in the wake of the wind turbine, therefore, affect the wind capacity of wind farm. The phenomenon of ejection can be studied using the motion of solid particles.

3.1 Computation setup

The open source library SOWFA (Simulator for On/Offshore Wind Farm Application) based on the OpenFOAM is used in this research work. SOWFA includes several incompressible solvers and utilities, being now used actively by the research community, and applies the Large-Eddy Simulation (LES) approach using the finite volume method to solve the governing equations, with different sub-grid-scale (SGS) models relevant for Atmospheric Boundary Layer (ABL) [11]. For instance, the Lagrangian dynamic Smagorinsky model for SGS viscosity can be applied, with an extra constraint on the dynamic Smagorinsky constant C_S used to avoid its negative values which may occur in calculations. The buoyancy effect is inserted by the separate term in the momentum equation in Boussinesq approximation. Effects of topography, environment stratification, Earth rotation, thermal flux changes are all taken into account to compute flow parameters.

The terms in the governing equations, for quantities defined in the mesh cell center, are approximated with the first and second order of accuracy on time and space. The improved iterative PISO algorithm is implemented to solve the system of discretized algebraic equations, using the predictor-corrector procedure and the iterative method of conjugate gradients with a preconditioner for velocity, pressure, potential temperature, stress tensor, and SGS model parameters.

LES with finite volume method for the solution of the main equations reflecting conservation laws was used. The following equations are considered: the continuity equation, the momentum equation, the transport of scalar value - potential temperature equation and other equations for the SGS stress tensor, turbulent viscosity.

The subgrid-scale models are an important part of LES [12]. The SGS stress tensor was raised from the filtering of the Navier-Stokes equations. The Boussinesq approximation for buoyancy force is included with the separate term in the momentum equation.

The Gauss linear Scheme was used for approximation of the convective terms, the Gauss linear corrected scheme was used for approximation of laplacian terms. To solve linear system equations the PBiCG method with DILU preconditioner was used for velocity, temperature and the GAMG method was used for pressure.

The main idea of new solver with the Euler-Lagrange approach, developed in ISPRAS, is based on adding a new KinematicCloud class to the ABLSolver LES solver, which describes a kinematic cloud of particles with equations (1)-(3).

An example of solving an applied wind energy problem for a model wind farms with 12 or 14 wind turbines will be investigated. To determine the initial distribution of parameters, we used the neutral atmospheric boundary layer approximation, calculated using the method Precursor, implemented in the ABLSolver solver. The mathematical modeling of the flow parameters in the wind farm was done using the pisoFoamTurbine solver and the Actuator Line

Model.

3.2 Definition of the problem

The 12 wind turbines in model wind farm were considered in case with SOWFA library. The diameter of rotor for wind turbine was equal to $D = 0.416$ m. The reference velocity was set to $U_{ref} = 1.5$ m/s. Atmospheric Boundary Layer model was introduced to represent experimental conditions. The parameters of Neutral ABL, used in our simulation, are listed in Table 1 of work [13].

Each of the prototype wind turbines had 3 blades with constant cross section. The blade was made of carbon fibre with a shape of a twisted thin flat plate of 0.8 mm thickness, without using any aerofoil cross-section [14]. Operating tip-speed ratio (TSR) was set to 6.

The value of numBladePoints for the case with 12 wind turbines was set to 40, the epsilon value was set to 5.0. The data on velocity profile and wind direction were taken from the weather station and the free report in Internet.

The domain with following dimensions was selected: 6.5 m x 5.5 m x 1 m in width (x-), transverse (y-), and height (z-) directions. The resulting unstructured mesh for the test with 12 wind turbines counted 2, 4, 6 millions of cells. After constructing the primary mesh with blockMesh tool the central zone with the turbines array inside was refined twice and an additional refinement was done around each turbine. The final mesh had 6 millions of cells. The pisoTurbineFoam solver was tested on famous Blind-test tutorial with 2 model wind turbines [15] and 12 wind model turbines in climatic tunnel [13, 16].

3.3 Results of simulations

Figure 8 shows distribution of the vorticity field. Propagation of the velocity along the sequence of wind turbines is illustrate in Figure 9. Figure 10 shows normalized mean velocity in different sections of the computation domain.
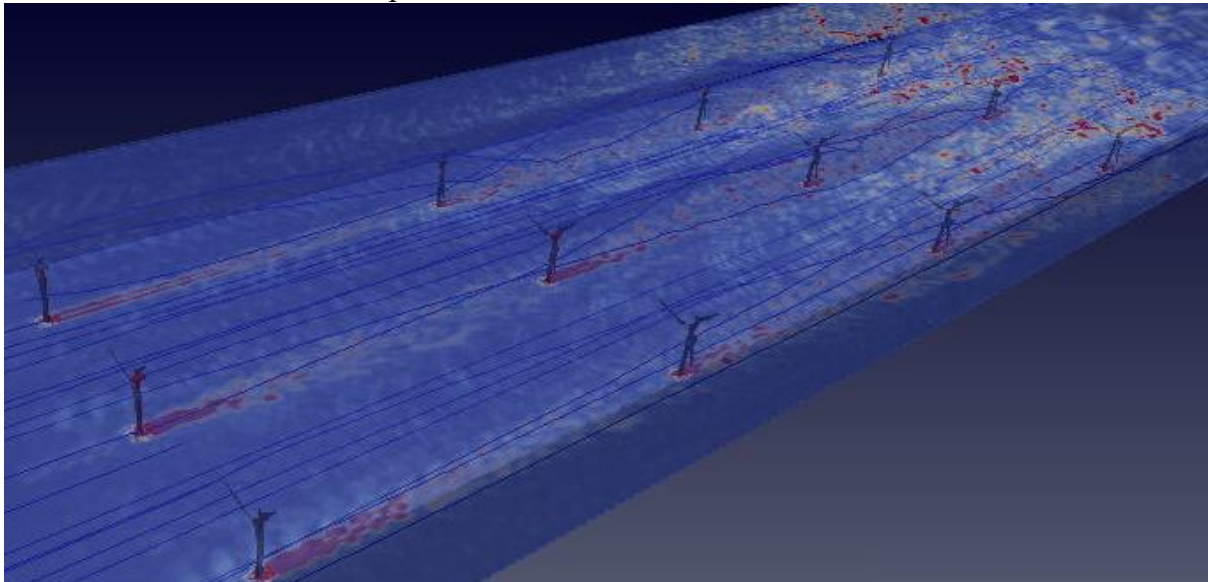
Figure 8: Vorticity field at $T_{end} = 20$ seconds
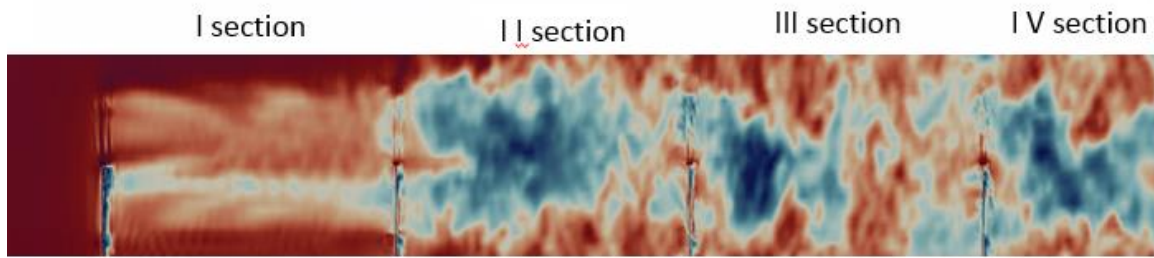
Figure 9: Propagation of the velocity along the sequence of wind turbines
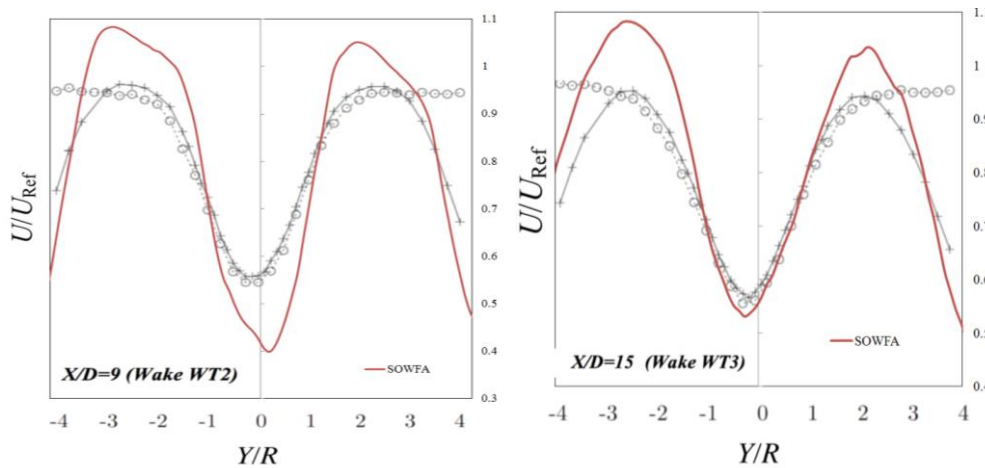
Figure 10: Normalized mean velocity profile

Particles application. The standard injection models in OpenFOAM, such a manual injection, and patch injection were used at the inlet. Solid parcel with the dimension $1*10^{-5}$ m, mass - $1*10^{-8}$ kg and temperature 285 K. The environment temperature – 285 K and pressure 98000 Pa. A first qualitative insight into the entrainment process in wind farm is obtained through particle tracking, where passive particles are released into the flow for every 200th time step. The particles are advected according to the local velocity at each time step. It was defined that there was a high degree of mixing and the initial colour partitioning was broken after turbines 1–2 for both seeding positions. There were also areas, where the particles have essentially been flushed away by the turbulent fluctuations, e.g. between turbines 7–12. The distribution of particles changes significantly over time as they are advected through the wind farm. The distribution of particles from each seeding height is counted within 'imaginary' cylindrical tubes between the turbines.

4 CONCLUSIONS

A study of two developed solvers based on the OpenFOAM package and using the Euler-Lagrange approach was conducted. Validation of the proposed models was carried out with analytical and experimental data. A particle of spherical shape and various models of their injections to the computational domain were considered.

REFERENCES

[1] Tam, C.K.W., Viswanathan, K., Ahuja, K.K., Panda, J. The sources of jet noise: experimental evidence. *Journal of Fluid Mechanics* (2008) **615**: 253-292.

[2] Tam, C.K.W., Golebiowsky, M., Seiner, J.M. On the two components of turbulent mixing noise from supersonic jets. *AIAA-Paper 96-1716* (1996).

[3] Rajput, P., Kumar, S. Jet noise reduction by downstream fluidic injection: effect of injection pressure ratio and number of injection ports. *2018 AIAA Aerospace Sciences Meeting* (2018).

[4] Crighton, D.G. Basic principles of aerodynamic noise generation. *Progress in Aerospace Sciences* (1975) **16, Iss. 1**: 31-96.

[5] Kandula, M., Vu, B. On the scaling laws for jet noise in subsonic and supersonic flow. *NASA Preprint No. KSC-2003-040* (2003).

[6] Kraposhin, M.V., Banholzer, M., Pfitzner, M., Marchevsky, I.K. A hybrid pressure- based solver for nonideal single- phase fluid flows at all speeds. *Int. J. for Num. Meth. In Fluids* (2018) **88, Iss. 2**: 79-99.

[7] Aissa, A., Abdelouahab, M, Noureddine, A., Elganaoui, M., Pateyron, B. Ranz and Marshall correlations limits on heat flow between a sphere and its surrounding gas at high temperature. *Thermal Science* (2015) **19**: 1521-1528.

[8] Barba, F.D., Picano, F. Evaporation of dilute droplets in a turbulent jet: clustering and entrainment effects. *arXiv:1703.0927v1 [physics.flu-dyn]* (2017).

[9] O'Rourke, P. J. and Amsden, A. A. The Tab Method for Numerical Calculation of Spray Droplet Breakup. International Fuels and lubricants meeting and Exposition. United States. 1987.

[10] Andersen, S.J., Sørensen, J.N., Mikkelsen, R.F. Turbulence and entrainment length scales in large wind farms. *Phil. Trans. R. Soc.* (2017) **A 375**: 20160107.

[11] Churchfield, M.J., Lee,S, J. Michalakes, J., Moriarty, P.J. A numerical study of the effects of atmospheric and wake turbulence on wind turbine dynamics. *Journal of Turbulence* (2012) **13, No. 14**: 1–32.

[12] Epikhin, A. S. and Kalugin, V. T. Features of numerical simulation of the unsteady vortex flow around aircraft considering airbrake. *IOP Conference Series: Materials Science and Engineering* (2018) 468(1).

[13] Hancock, P.E. and Farr, T.D. Wind-tunnel simulations of wind-turbine arrays in neutral and non-neutral winds. *Journal of Physiscs: Conference Series* (2014) **524**: 012166.

[14] Hancock, P. E. and Pascheke, F. Wind-Tunnel Simulation of the Wake of a Large Wind Turbine in a Stable Boundary Layer: Part 2, the Wake Flow. *Boundary-Layer Meteorology* (2014) **151**: 23–37.

[15] Kryuchkova, A., Tellez-Alvarez, J., Strijhak, S., Redondo, J. M. Assessment of Turbulent Wake Behind two Wind Turbines Using Multi-Fractal Analysis. *2017 Ivannikov ISPRAS Open Conference (ISPRAS), Moscow, Russia*. (2017): 1-7.

[16] Strijhak, S.V., Koshelev, K.B., Kryuchkova A.S. Studying parameters of turbulent wakes for model wind turbines. *AIP Conference Proceedings.* (2018). **2027. # 030086**: 1-8.

A LATTICE BOLTZMANN METHOD IN GENERALIZED CURVILINEAR COORDINATES

J. A. Reyes Barraza[1] and R. Deiterding[2]

[1] Aerodynamics and Fluid Mechanics Research Group
Engineering and Physical Sciences Faculty
University of Southampton
Highfield Campus, Southampton SO17 1BJ, UK
Email: j.a.reyes@soton.ac.uk

[2] Aerodynamics and Fluid Mechanics Research Group
Engineering and Physical Sciences Faculty
University of Southampton
Highfield Campus, Southampton SO17 1BJ, UK
Email R.Deiterding@soton.ac.uk, Web page: http://rdeiterding.website/

Key words: LBM, Generalized Curvilinear Coordinates, Finite Difference

Abstract. A second-order central time-explicit method is implemented to solve the Lattice Boltzmann Equation in generalized curvilinear coordinates in order to simulate fluid flows with non-uniform grids and curved boundaries. Several test cases are used for verification, including the Taylor-Green vortex in two-dimensions, the square lid-driven cavity and the 2D circular cylinder. The Taylor-Green vortex is a classical benchmark test that is compared with the analytical solution using a non-uniform grid. The 2D lid-driven cavity is solved for moderate Reynolds numbers, where a clustering function is employed to stretch the mesh and increase the resolution in the cavity corners. The boundary conditions for these two test-cases are relatively straightforward to implement since there are no curved walls. Therefore, the 2D circular cylinder is used to demonstrate the capacity of the present method to perform steady and unsteady simulations with curved boundaries. Our results have been compared with the literature available, and the outcomes of this method are consistent with other results, confirming the feasibility of the implemented scheme. In addition, the present method has been compared to our own standard Cartesian lattice Boltzmann solver with adaptive mesh refinement for the 2D circular cylinder problem.

1 INTRODUCTION

The lattice Boltzmann method (LBM) is a relatively new development, that has emerged as a powerful computational method for the study of fluid dynamic problems. Instead of approximating the Navier-Stokes equations, the approach is based on solving a simplified version of the Boltzmann equation in a specific discrete space. It can be shown via the Chapman-Enskog expansion that the LBM recovers the Navier-Stokes equations in the nearly incompressible flow limit [1]. The simplicity of the lattice Boltzmann algorithm can lead to dramatic reductions in computational time compared to traditional computational fluid dynamics (CFD) solvers. On uniform grids and unsteady flow simulations, it can easily show performance gains up to two orders of magnitude [2], which has made the approach certainly popular in recent years.

In the standard LBM, the discretisation of the physical space is coupled with the discretisation of momentum space [3]. The advantage of this scheme is the exact treatment of the advection term, therefore it does not have any numerical diffusion. On the other hand, this condition results in a numerical method that is restricted to Cartesian grids. This aspect of the standard LBM limits its application and solving problems with curved geometries and thin boundary layers become troublesome. For realistic geometries and aerodynamic investigations, the usage of uniform Cartesian meshes is impractical, since the boundary layer flow needs to be adequately resolved for a good representation of the physics. It is somewhat straightforward to apply isotropic mesh adaptation to the standard LBM, and thereby resolving laminar boundary layers is relatively easy [4]. However, this approach can become remarkably expensive for capturing boundary layers of turbulent flows, and therefore it is impractical for most technically relevant problems in aerodynamics.

The discretisation of the physical space does not necessarily require to be coupled with the moment space [5]. Therefore, it is possible to implement standard numerical techniques on the LBM to use non-uniform and body-fitted meshes. In recent years, several efforts have been made to overcome this shortcoming in order to make LBM a practical computational fluid dynamics tool. Some authors have taken different approaches toward the same issue. Some of them have used interpolation schemes [6] and others have applied traditional numerical methods used in CFD mainly, finite differences [7] and finite volume [8]. Therefore, we propose an implementation of the LBM in generalized curvilinear coordinates, so the LBE can be solved with non-Cartesian grids. Various test cases were used for verification, including the Taylor green vortex, the 2D lid-driven cavity and the 2D circular cylinder. Clustering functions are employed on all test-cases to stretch the mesh and increase resolution on certain regions of the domains. This study shows that this implementation deals with curved boundary walls more accurately and efficiently than the Cartesian method.

2 METHODOLOGY

In this paper, the implementation is done on the classical D2Q9 LBM-BGK model [1]. Hence, the LBE with a simplified collision operator can be written as

$$\frac{\partial f_\alpha}{\partial t} + \mathbf{e}_\alpha \cdot \nabla f_\alpha = -\frac{1}{\tau}\left(f_\alpha - f_\alpha^{eq}\right). \tag{1}$$

The latter can be transformed into a generalized curvilinear coordinate system, in which the physical and computational planes are represented by (x, y) and (ξ, η), respectively,

$$\begin{aligned} \xi &= \xi(x, y), \\ \eta &= \eta(x, y). \end{aligned} \tag{2}$$

To transform the LBE from the physical plane (x, y) to the computational plane (ξ, η) we must apply

$$\begin{aligned} \frac{\partial}{\partial x} &= \frac{\partial}{\partial \xi}\frac{\partial \xi}{\partial x} + \frac{\partial}{\partial \eta}\frac{\partial \eta}{\partial x}, \\ \frac{\partial}{\partial y} &= \frac{\partial}{\partial \xi}\frac{\partial \xi}{\partial y} + \frac{\partial}{\partial \eta}\frac{\partial \eta}{\partial y}. \end{aligned} \tag{3}$$

The physical domain is related to the computational domain by the following condition

$$\begin{bmatrix} \xi_x & \xi_y \\ \eta_x & \eta_y \end{bmatrix} = \frac{1}{J}\begin{bmatrix} y_\eta & -x_\eta \\ -y_\xi & x_\xi \end{bmatrix}, \tag{4}$$

where J is the Jacobian of the transformation defined as

$$J = x_\xi y_\eta - x_\eta y_\xi. \tag{5}$$

The convection term in Eq. (1) can be rewritten as

$$\begin{aligned} \mathbf{e}_\alpha \cdot \nabla f_\alpha &= e_{\alpha x}\frac{\partial f_\alpha}{\partial x} + e_{\alpha y}\frac{\partial f_\alpha}{\partial y} \\ &= e_{\alpha x}\left(\frac{\partial f_\alpha}{\partial \xi}\frac{\partial \xi}{\partial x} + \frac{\partial f_\alpha}{\partial \eta}\frac{\partial \eta}{\partial x}\right) + e_{\alpha y}\left(\frac{\partial f_\alpha}{\partial \xi}\frac{\partial \xi}{\partial y} + \frac{\partial f_\alpha}{\partial \eta}\frac{\partial \eta}{\partial y}\right) \\ &= \left(e_{\alpha x}\frac{\partial \xi}{\partial x} + e_{\alpha y}\frac{\partial \xi}{\partial y}\right)\frac{\partial f_\alpha}{\partial \xi} + \left(e_{\alpha x}\frac{\partial \eta}{\partial x} + e_{\alpha y}\frac{\partial \eta}{\partial y}\right)\frac{\partial f_\alpha}{\partial \eta} \\ &= \tilde{e}_{\alpha\xi}\frac{\partial f_\alpha}{\partial \xi} + \tilde{e}_{\alpha\eta}\frac{\partial f_\alpha}{\partial \eta}, \end{aligned} \tag{6}$$

where

$$\tilde{\mathbf{e}}_\alpha = (\tilde{e}_{\alpha\xi}, \tilde{e}_{\alpha\eta}) = (e_{\alpha x}\xi_x + e_{\alpha y}\xi_y, e_{\alpha x}\eta_x + e_{\alpha y}\eta_y). \tag{7}$$

Therefore, the LBE in the computational domain can be written as

$$\frac{\partial f}{\partial t} + \tilde{e}_{\alpha\xi}\frac{\partial f_\alpha}{\partial \xi} + \tilde{e}_{\alpha\eta}\frac{\partial f_\alpha}{\partial \eta} = -\frac{1}{\tau}\left(f_\alpha - f_\alpha^{eq}\right). \tag{8}$$

Equation (8) can be solved using any appropriate numerical procedure. The spatial derivatives are discretised by the second-order central difference and the temporal term is integrated by the explicit multistage Runge-Kutta. The right hand side of Eq. (8) can be rewritten as

$$
R_{\alpha_{(i,j)}} = -\left(\tilde{e}_{\alpha\xi_{(i,j)}} \frac{f_{\alpha_{(i+1,j)}} - f_{\alpha_{(i-1,j)}}}{2\Delta\xi} + \tilde{e}_{\alpha\eta_{(i,j)}} \frac{f_{\alpha_{(i,j+1)}} - f_{\alpha_{(i,j-1)}}}{2\Delta\eta} \right) - \frac{1}{\tau}\left(f_{\alpha_{(i,j)}} - f^{eq}_{\alpha_{(i,j)}} \right).
$$

(9)

Now, the solution is advanced in the time by using the standard fourth-stage Runge-Kutta scheme as follows,

$$
\begin{aligned}
f^1_\alpha &= f^t_\alpha, \\
f^2_\alpha &= f^1_\alpha + \frac{\Delta t}{4} R^1_\alpha, \\
f^3_\alpha &= f^1_\alpha + \frac{\Delta t}{3} R^2_\alpha, \\
f^4_\alpha &= f^1_\alpha + \frac{\Delta t}{2} R^3_\alpha, \\
f^{t+\Delta t}_\alpha &= f^1_\alpha + \Delta t R^4_\alpha.
\end{aligned}
$$

(10)

Central schemes can be unstable when non-linearities are present. Therefore a fourth-order artificial dissipation is added in Eq. (9) as

$$
D = -\epsilon \left((\Delta\xi)^4 \frac{\partial^4 f_\alpha}{\partial\xi^4} + (\Delta\eta)^4 \frac{\partial^4 f_\alpha}{\partial\eta^4} \right),
$$

(11)

in order to stabilize the solution [9]. The order of the numerical scheme does not change since the artificial dissipation has a higher order than the formal scheme.

3 COMPUTATIONAL RESULTS

Numerical computations are carried out to show that the second-order central time-explicit method implemented is an accurate, stable and reliable option to solve the LBE in curvilinear coordinates. Also, to demonstrate its superior capabilities to resolve the flow in the vicinity of the wall when using curved geometries.

3.1 Taylor-Green vortex

The Taylor-Green vortex decay problem has been widely used for the verification of incompressible flow solvers. This problem has an exact solution of the incompressible Navier-Stokes equations and the set-up is straightforward, since it only has a set of initial conditions and periodic boundaries. This benchmark test is done to demonstrate the accuracy of the scheme, and the capacity of the present methodology to use non-uniform

grids. The exact solution of this unsteady problem is given by

$$u(x, y, t) = -u_o \cos(k_x x) \sin(k_y y) e^{-k^2 \nu t},$$

$$v(x, y, t) = \frac{k_x}{k_y} u_o \sin(k_x x) \cos(k_y y) e^{-k^2 \nu t},$$

$$P(x, y, t) = P_0 - 0.25 \rho_0 u_o^2 \left[\cos(2k_x x) + \left(\frac{k_x}{k_y} \right)^2 \cos(2k_y y) \right] e^{-2k^2 \nu t}, \tag{12}$$

where u_o is the initial velocity magnitude, ν is the kinematic viscosity of the fluid, $k_x = 2\pi/L_x$ and $k_y = 2\pi/L_y$ are the wave numbers in x and y directions, $k = \sqrt{k_x^2 + k_y^2}$, The initial conditions for the velocity and pressure fields are obtained by setting $t = 0$.

A clustering function has been selected to stretch the mesh in both directions, x and y. The stretched grid can be obtained with:

$$x = H \frac{(2\alpha + \beta)[(\beta + 1)/(\beta - 1)]^{(\xi - \alpha)/(1 - \alpha)} + 2\alpha - \beta}{(2\alpha + 1)\left(1 + [(\beta + 1)/(\beta - 1)]^{(\xi - \alpha)/(1 - \alpha)}\right)}, \tag{13}$$

$$y = H \frac{(2\alpha + \beta)[(\beta + 1)/(\beta - 1)]^{(\eta - \alpha)/(1 - \alpha)} + 2\alpha - \beta}{(2\alpha + 1)\left(1 + [(\beta + 1)/(\beta - 1)]^{(\eta - \alpha)/(1 - \alpha)}\right)}, \tag{14}$$

where β is the clustering parameter, α defines where the clustering takes place, and H is the length. If $\alpha = 0.5$, the clustering is distributed equally, and if $\alpha = 0$ the clustering takes place at H. Herein, all the computations are performed with $\alpha = 0.5$ and $\beta = 1.2$.
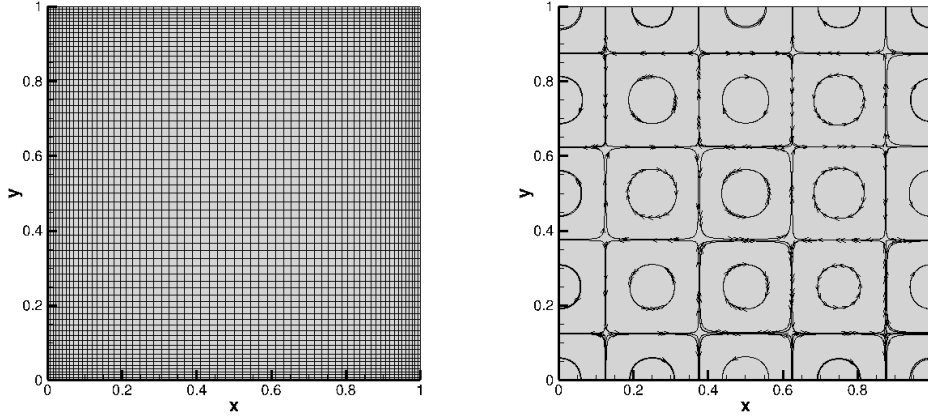
Figure 1: Left: Non-uniform mesh. Right: Streamlines for the Taylor-Green Vortex at the initial conditions.

Figure (1) shows the non-uniform grid, namely (65×65), that can be obtained by applying the clustering functions described, and the initial flow field shown by streamlines. The present methodology is compared with the analytical solution and shown in Figure (2) at a dimensionless time of 0.2. For this simulation a grid of (128×128) was used, the reference velocity u_o is 0.02 and a Reynolds number of 100 was selected.
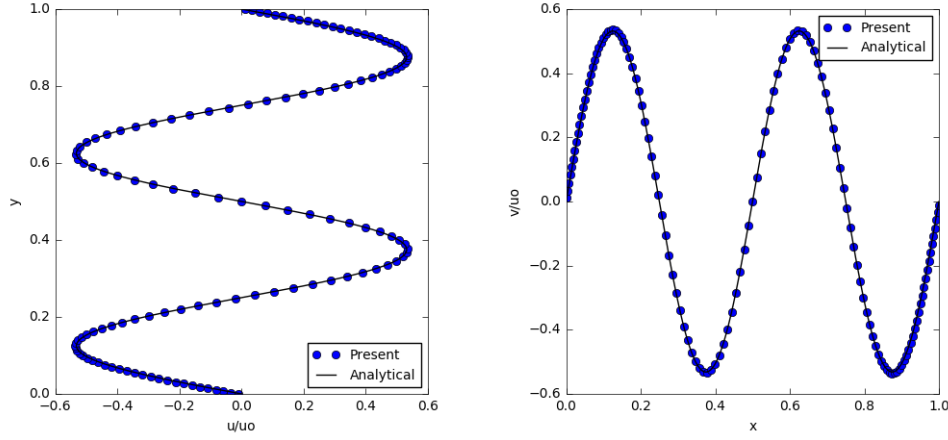
Figure 2: Left: u-velocity along the vertical centreline. Right: v-velocity along the horizontal centreline.

3.2 2D lid-driven cavity

The 2D lid-driven cavity is a classical benchmark test, thanks to its simple geometry and complex flow physics [10]. It consists of the movement of the top-lid at a constant velocity (u_o) and three stationary walls ($u = v = 0$). The geometry normally is a square of aspect ratio one, but this may be different. The same grid (cf. Fig. 1) used for the Taylor-Green vortex is also used for this test case. The numerical computations are carried out with $u_o = 0.1$ and the results are shown for two different Reynolds numbers, Re = 1000 and Re = 3200. The grid sizes used are (257×257) and (513×513) respectively.
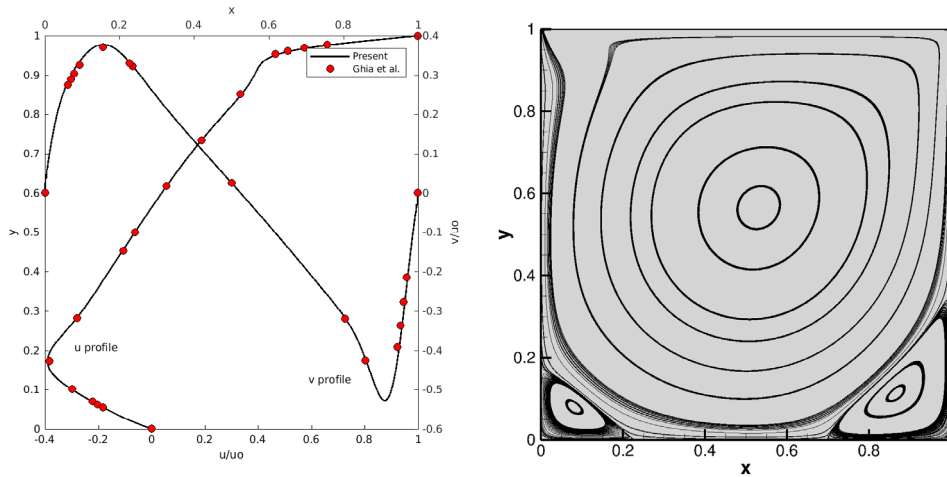
Figure 3: Re = 1000. Left: u-velocity along the vertical centreline and v-velocity along the horizontal centreline. Right: Flow field exhibited by streamlines.

There is no exact solution for the 2D cavity flow, because of this we need to compare our results with a comprehensive study, such as the one done by Ghia et al. [10]. The
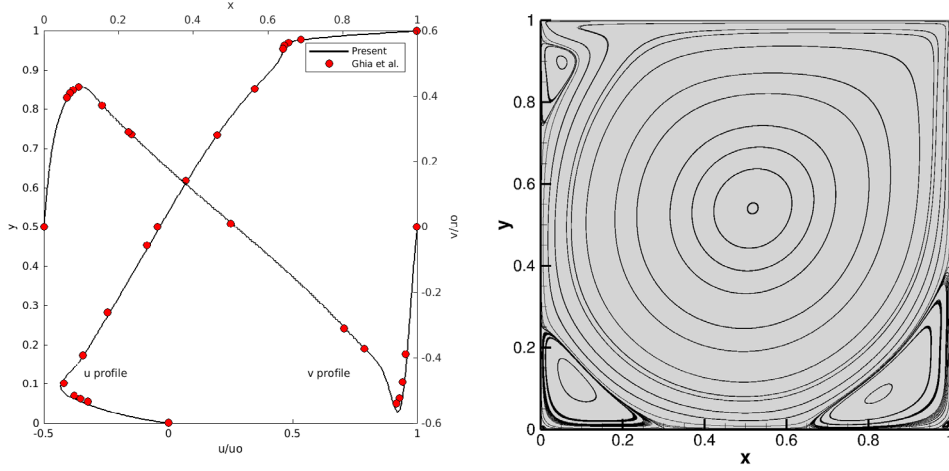
Figure 4: Re = 3200. Left: u-velocity along the vertical centreline, v-velocity along the horizontal centreline. Right: Flow field exhibited by streamlines.

u-velocity profile along the vertical centre line, the v-velocity profile along the horizontal centre line and the streamlines for the two different Reynolds numbers are shown in Figures 3 and 4. This shows that our results have an excellent agreement with the reference [10], and the streamlines show a correct flow behaviour in the entire domain. It is known that the corners are singularity points, and our results do not exhibit any issue in this regions, demonstrating the capability of the current methodology and the proper application of the stretching function on the grid.

3.3 2D circular cylinder

The wall-boundary treatment of the previous test cases is relatively straightforward since there are no curved walls. Therefore, the 2D circular cylinder is used to demonstrate the capacity of the present method to perform steady and unsteady simulations with curved surfaces. In addition, proper stretching functions have been implemented to increase the resolution in the proximity of the wall and in the wake region. Our results have been compared with the literature available, and the outcomes of the present method are consistent with other results, supporting the proposed scheme. In addition, the present method is compared to our own standard Cartesian LBM solver [2], AMROC (Adaptive Mesh Refinement in Object-oriented C++).

The following function is used for the stretching in the wall normal direction

$$y_n = \delta \frac{(1-\beta)\left(\frac{\beta+1}{\beta-1}\right)^{1-\xi} + (\beta+1)}{\left(\frac{\beta+1}{\beta-1}\right)^{1-\xi} + 1} + r, \quad 0 \leq \xi \leq 1, \tag{15}$$

where δ is the radial distance between the body and the outer boundary, β is the clustering parameter which has been set to 1.007 for these simulations and r is the radius of the cylinder. The grid clustering function shown in Eq.(14) was used to increase the resolution

behind the cylinder. The clustering parameter used for the wake is 1.045.
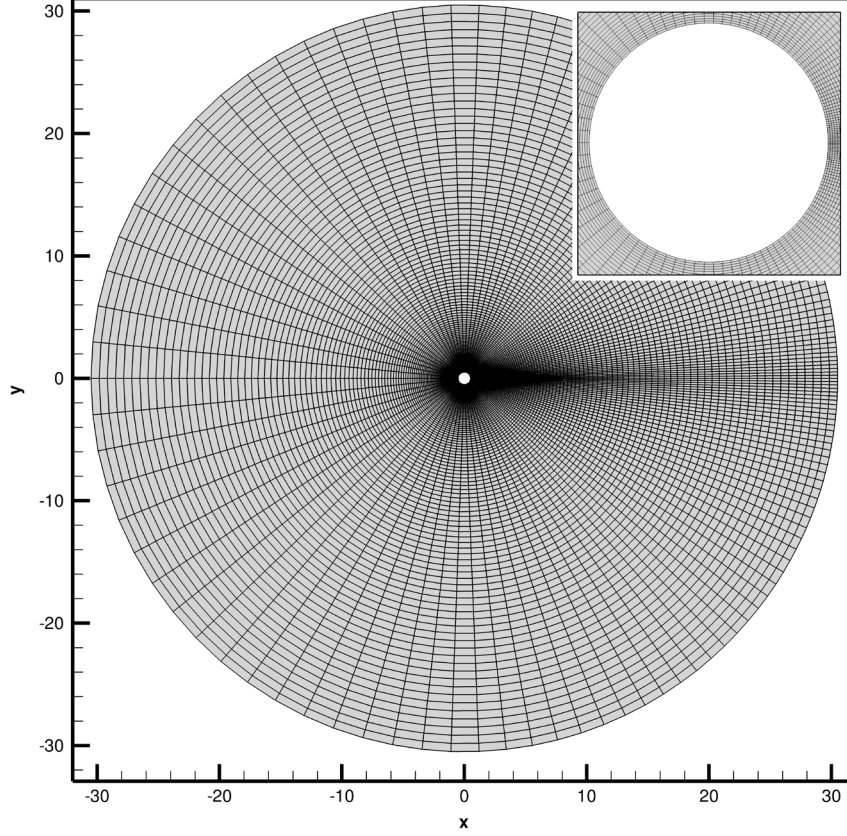
Figure 5: O-Grid for the 2D cylinder mesh. Overlaid on the upper-right is a close-up of the body-conforming mesh around the cylinder.

All the computations for the cylinder test-case using the proposed methodology were carried out on a grid size of (257×257) with an outer diameter 30 times bigger than the inner diameter (cf. Fig. 5). The simulations carried out using the Cartesian LBM with adaptive mesh refinement were performed on a domain size of $[-16D \times 48D] \times [-16D \times 16D]$ with the axis located at $(x, y) = (0, 0)$ and using a grid size of (640×320) at its coarsest level (for the steady-state cases). The adaptive mesh refinement is set to 3 additional levels with a refinement factor of 4.

Two Reynolds number were selected for the steady-state simulations, 20 and 40. At this flow regime a stationary recirculation region appears for both cases behind the cylinder, and the wake increases in length as the Reynolds number increases, as it can be seen in Figure 6. The literature shows that the recirculating regions appear around $5 < \text{Re} < 47$. Anything under Reynolds number 5 the flow will remain attached and above the critical Reynolds, which is 47, the solution produced will be unsteady.

The comparison of the steady-state results are shown in Table 1. The references used are quite vast and they include the numerical solutions of the Navier-Stokes equations from

Table 1: Effects of the Reynolds number on steady flow over the circular cylinder

Re	Author(s)	C_d	$C_p(0)$	$C_p(180)$	$2L/D$
20	Tritton [11]	2.10	-	-	-
	Henderson [12]	2.06	-	-0.60	-
	Dennis and Chang [13]	2.05	1.27	-0.58	1.88
	Hejranfar and Ezzatneshan [5]	2.02	1.25	-0.59	1.84
	AMROC-LBM	1.98	1.26	-0.59	1.85
	Present	2.02	1.31	-0.55	1.85
40	Tritton [11]	1.59	-	-	-
	Henderson [12]	1.55	-	-0.53	-
	Dennis and Chang [13]	1.52	1.14	-0.50	4.69
	Hejranfar and Ezzatneshan [5]	1.51	1.15	-0.48	4.51
	AMROC-LBM	1.45	1.19	-0.49	4.66
	Present	1.51	1.19	-0.46	4.60
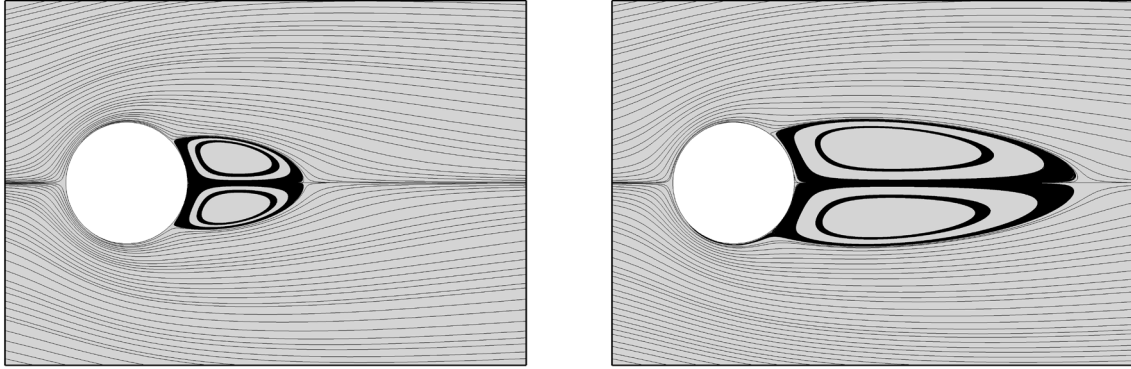
Figure 6: Flowfield for steady flow over the 2D circular cylinder shown by streamlines using the implemented methodology. Left: Re = 20. Right: Re = 40.

Henderson [12], Dennis and Chang [13], compact-finite difference LBM from Hejranfar and Ezzatneshan [5] and the experimental data from Tritton [11]. The variables presented are drag coefficient C_d, the pressure coefficient at the stagnation point $C_p(0)$ and at the rear-point $C_p(180)$, the normalized length of the wake $2L/D$, where L is the actual length of the wake and D is the diameter of the cylinder. Table 1 shows that our results exhibit good agreement with diverse references.

For the unsteady test-case, two laminar flows at 100 and 200 Reynolds number were selected. These simulations demonstrate the capacity of the presented method to simulate time-dependent flows around geometries with curved boundaries. At these flow conditions, the recirculation bubbles behind the cylinders become unstable, and time-periodic vortex-shedding solutions appear. The dimensionless number used to characterize this phenomenon is the Strouhal number that is defined as $St = f_q D/u_o$, where f_q is the

shedding frequency. The Strouhal number can also be written as $St = D/u_o T_p$, where T_p is the peak-to-peak period of the lift coefficient.
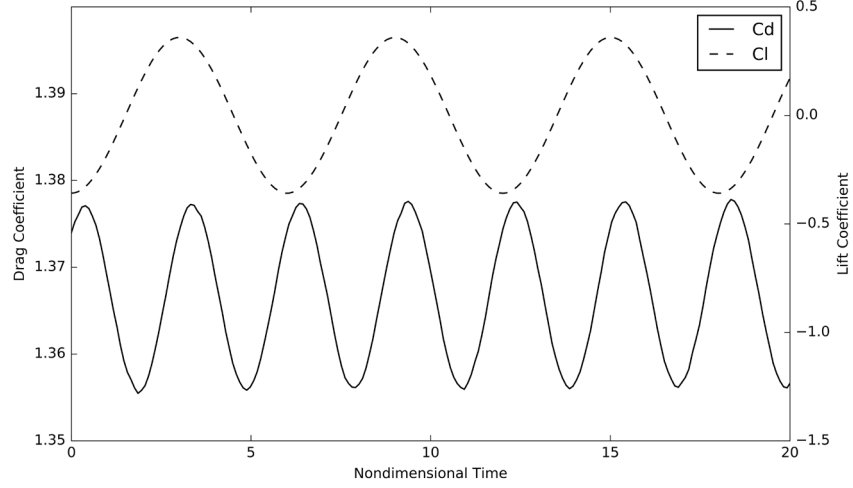
Figure 7: Drag and lift coefficient trends for the time periodic flow over the circular cylinder at Re = 100.
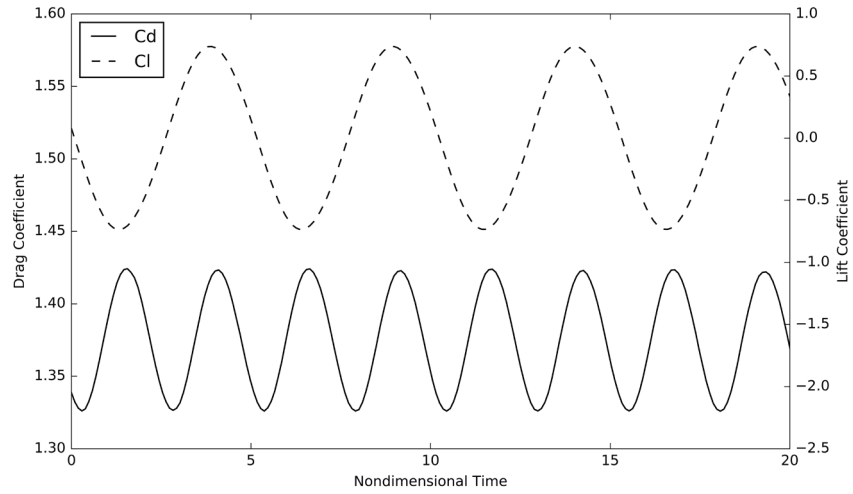
Figure 8: Drag and lift coefficient trends for the time periodic flow over the circular cylinder at Re = 200.

The lift and drag coefficient with respect to the non-dimensional time are shown in Figures 7 and 8, after the simulations have reached a stable periodic solution. These plots show the capacity of the central-scheme implemented to predict correctly the vortex-shedding phenomenon within these Reynolds numbers. Table 2 compares the present time-depended solutions with the reference selected and as well as with the results obtained using AMROC-LBM. The Navier-Stokes solutions from Chiu et al. [14] are used as a

Table 2: Strouhal number for different authors

Re	Author(s)	St	$\overline{C_d}$	C_l'
100	Chiu et al. [14]	0.167	1.35	0.30
	AMROC-LBM	0.165	1.25	0.30
	Present	0.165	1.36	0.35
200	Chiu et al. [14]	0.198	1.37	0.71
	Present	0.196	1.37	0.73

reference. The variables compared are the Strouhal number, the average drag coefficient $\overline{C_d}$ and the lift coefficient amplitude C_l'. The results produced by the LBM in generalized curvilinear coordinates have an excellent agreement with the references for all the variables compared. The results obtained by AMROC-LBM also have a good agreement with the variables compared. However, in this case it was necessary to increase the resolution to (960×480) at its coarsest level, the domain and the mesh adaptation settings remained the same, in order to get convergence.

4 CONCLUSIONS

It is noticeable that the Cartesian solver requires a significantly higher number of grid points in order to obtain a converged solution, given its inability to represent curved geometries accurately and its lack of flexibility to have meshes of diverse sizes. On the other hand, it is possible to apply isotropic mesh adaptation and to benefit from it. In this study, it has been shown that the second-order scheme implemented is accurate, stable and capable of solving the LBE in generalized curvilinear coordinates. The results obtained by the present methodology and AMROC-LBM exhibit good agreement with all references. However, the current implementation deals with curved boundary walls more accurately and efficiently than the Cartesian method.

The test cases in this paper are relevant to the literature and serve well to validate the current implementation. However, it is within our scope to solve more technically challenging problems. Hence as a next step, it is planned to solve the flows around aerofoils, which require a high-level of mesh stretching for properly resolving the boundary layer.

5 ACKNOWLEDGEMENTS

References

[1] S. Chen, G. D. Doolen, Lattice Boltzmann method for fluid flows, Annual Review of Fluid Mechanics 30 (1998) 329–364.

[2] R. Deiterding, S. L. Wood, Predictive wind turbine simulation with an adaptive

lattice Boltzmann method for moving boundaries, Journal of Physics: Conference Series 753 (2016).

[3] X. He, L.-S. Luo, Theory of the lattice Boltzmann method: From the Boltzmann equation to the lattice Boltzmann equation, Physical Review E 56 (1997) 6811–6817.

[4] Z. Guo, C. Shu, Lattice Boltzmann Method and its Applications in Engineering, World Scientific, 2013.

[5] K. Hejranfar, E. Ezzatneshan, Implementation of a high-order compact finite-difference lattice Boltzmann method in generalized curvilinear coordinates, Journal of Computational Physics 267 (2014) 28–49.

[6] X. He, G. Doolen, Lattice Boltzmann method on curvilinear coordinates system: Flow around a circular cylinder, Journal of Computational Physics 134 (1997) 306–315.

[7] R. Mei, W. Shyy, On the finite difference-based lattice Boltzmann method in curvilinear coordinates, Journal of Computational Physics 143 (1998) 426–448.

[8] S. Succi, G. Amati, R. Benzi, Challenges in lattice Boltzmann computing, Journal of Statistical Physics 81 (1995) 5–16.

[9] K. Hejranfar, M. Hajihassanpour, Chebyshev collocation spectral lattice Boltzmann method in generalized curvilinear coordinates, Computers and Fluids 146 (2017) 154–173.

[10] U. Ghia, K. N. Ghia, C. T. Shin, High-resolutions for incompressible flows using Navier-Stokes equations and a multigrid method, Journal of Computational Physcis 48 (1982) 387–411.

[11] D. Tritton, Experiments on the flow past a circular cylinder at low Reynolds numbers, Journal of Fluid Mechanics 6 (1959) 547–567.

[12] R. D. Henderson, Details of the drag curve near the onset of vortex shedding, Physics of Fluids 7 (1995) 2102–2104.

[13] S. C. R. Dennis, G. Chang, Numerical solutions for steady flow past a circular cylinder at Reynolds numbers up to 100, Journal of Fluid Mechanics 42 (1970) 471–489.

[14] P. H. Chiu, R. K. Lin, T. W. Sheu, A differentially interpolated direct forcing immersed boundary method for predicting incompressible Navier Stokes equations in time-varying complex geometries, Journal of Computational Physics 229 (2010) 4476–4500.

SHSLBM Simulation of Hybrid Nanofluid Thermal Convection at High Rayleigh Numbers

Yuan Ma[a,b,*] and Zhigang Yang[a,b,c,*]

[a] Shanghai Automotive Wind Tunnel Center, Tongji University, No.4800, Cao'an Road, Shanghai, China, 201804
[b] Shanghai Key Lab of Vehicle Aerodynamics and Vehicle Thermal Management Systems, No.4800, Cao'an Road, Shanghai, China, 201804
[c] Beijing Aeronautical Science & Technology Research Institute, Beijing, China, 102211

*Corresponding author. E-mail address: 1510812@tongji.edu.cn (Yuan Ma), zhigang.yang@sawtc.com (Zhigang Yang)

ABSTRACT

A new method called simplified and highly stable lattice Boltzmann method (SHSLBM) was used to simulate the hybrid nanofluid natural convection and heat transfer in a square enclosure with a heating obstacle at high Rayleigh numbers. There are four fins on the heating obstacle to affect the flow pattern and heat transfer performance. SHSLBM is based on the lattice Boltzmann framework. The effects of Rayleigh number ($10^6 \leq Ra \leq 10^9$), nanoparticle volume fraction ($0 \leq \phi \leq 0.05$) and length of fin ($0.1 \leq h \leq 0.3$) on the flow pattern, temperature distribution and heat transfer characteristics were illustrated and analyzed. The benchmark simulation results were performed to the method of validation. Three kinds of flow patterns (steady symmetry, unsteady symmetry and unsteady asymmetry) can be observed at various Rayleigh number. At $\phi = 0.01$, when the Ra increases from 1×10^6 to 1×10^9, the transitions of flow regime from steady symmetry state to unsteady asymmetry state occur. The ϕ and h also affects the flow pattern significantly. At higher ϕ, the flow inside the enclosure is steadier and the effect of h on the flow pattern varies at different Ra.

Keywords: SHSLBM; High *Ra*; Nanofluid; Fin; Natural convection; Heat transfer

1. Introduction

Thermal convection in an enclosure has been a significant subject of numerical simulations in the past several decades.[1,2,3] The flow pattern and heat transfer characteristics have comprehensive application in the engineering applications such as electronic equipment systems, heat exchangers, solar energy systems and chemical reaction systems.[4] Bhardwaj et al.[5] analyzed the natural convection and heat transfer in a porous two-dimensional right-angled triangular cavity with undulatoy walls. It has been observed that the maximum Nusselt number of the left wall increases 53% at $Ra = 10^6$ comparing with the no-undulation case. Esfe et al.[6] numerically investigated the natural convection in a trapezoidal cavity. They found that the average Nusselt number (Nu) increases by decreasing the inclination angle (γ) at low Rayleigh numbers ($Ra \leq 10^4$). However, at $Ra = 10^6$, the average Nu increases firstly and then decreases and obtains the maximum value at $\gamma = 30$.

Ma et al.[7] studied the effects of nanofluid and aspect ratio (AR) on the flow pattern and heat transfer characteristics in a baffled U-shaped enclosure in the presence of a magnetic field. It can be obtained that the change of AR cannot affect the flow pattern and the average Nu increases by increasing AR. Haghighi et al.[8] experimentally studied the natural convection in plate-fin based heat sinks. Six different types of fins are conducted in their study. They found that the thermal resistance increases as decreasing the gap between the fins. Besides, the plate cubic pin-fin heat sinks have a better heat transfer performance.

Recently, nanofluid has been studied to enhance the rate of heat transfer due to its high heat transfer performance.[9,10] Ma et al.[11] numerically studied the Ag-MgO/water hybrid nanofluid convection and heat transfer in a channel with active heaters and coolers in the presence of magnetic field. They found that the average Nusselt number is increasing function of nanoparticle volume fraction and Reynolds number, but a decreasing function of Hartmann number. Hatami and Safari[12] performed a numerical simulation to investigate the nanofluid natural convection and heat transfer in an enclosure with wavy walls and an inside heating cylinder. The results showed that the heat transfer performance is best when the obstacle is located on the center for all the

volume fraction of nanoparticles.

Lattice Boltzmann method has been widely used to simulate the problem of fluid flow and heat transfer due to its advantages such as easy to implement, natural parallel and easy to deal with the complex boundaries. Recently, many new methods based on the LBM have been developed. Chikatamarla and Karlin[13] proposed a new model named entropic lattice Boltzmann method (ELBM) to simulate the multiphase flows. They found that the ELBM is suitable for the high Reynolds number and high Weber numbers for two-phase flows. A high-order simplified thermal lattice Boltzmann method (HSTLBM) is developed by Chen et al.[14] to study the incompressible thermal flows accurately and efficiently. After the validation of benchmark simulations, HSTLBM is treated as an efficient method to solve the thermal convection at high Rayleigh numbers. Jami et al.[15] developed a new thermal MRT-LBM for simulating the convection. They examined the different convection cases when the Rayleigh number is less than 10^8. After the comparison and validation, the method is proved to solve the similar problems. Chen et al.[16] developed a new method named simplified and highly stable lattice Boltzmann method (SHSLBM) to solve the fluid flow problems. The method showed a very nice stability characteristic in high Reynolds number.

The literature shows that the nanofluid flow and heat transfer at high Rayleigh numbers did not get enough attention. Thus, the first objective of the present work is to study the flow pattern and heat transfer characteristics of nanofluid natural convection at high Rayleigh numbers. Four fins are mounted on the heating obstacle in the storage unit to enhance the heat transfer rate and the effects of fins on the flow regime and heat transfer are investigated, which is the second objective of the work. Moreover, in the present work, the SHSLBM is developed into the thermal filed and used to solve the governing equations of the present simulations. The effects of Rayleigh number ($10^6 \leq Ra \leq 10^9$), nanoparticle volume fraction ($0 \leq \phi \leq 0.05$) and length of fin ($0.1 \leq h \leq 0.3$) on the flow pattern, temperature distribution and Nusselt number are investigated.

2. Mathematical formulation

2.1. Problem definition

The Ag-TiO$_2$/water hybrid nanofluid flow and heat transfer in a thermal energy storage with four fins are considered in Fig. 1. Table 1 illustrates the thermophysical properties of pure water and nanoparticles. In this finned heat storage unit, the four fins are mounted on the four walls of the square obstacle and their temperature is fixed at $T_h = 1$. The four walls of the heat storage unit have a constant temperature (T_c) which is lower than T_h. P$_1$ and P$_2$ are two monitoring points inside the finned heat storage unit.
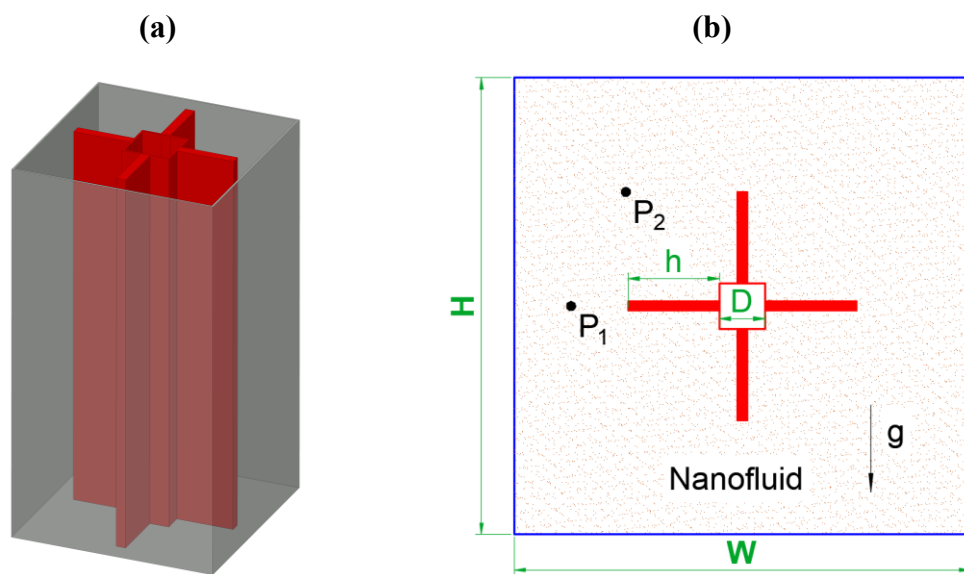
Fig. 1 3D and 2D schematic diagram under consideration in the present work.

Table 1. Thermophysical properties of pure water and nanoparticles at 25° C.

Property	Pure water	Ag (nanoparticles)	TiO$_2$ (nanoparticles)
C_p (J/kg K)	4179	235	686.2
ρ (kg/m^3)	997.1	10500	4250
K (W/m k)	0.623	429	8.9538
$\beta \times 10^5$ (K^{-1})	21	1.89	0.9
$\mu \times 10^4$ (kg/m s)	8.55	-	-

2.2. Standard LBM

The standard thermal LBM of D$_2$Q$_9$ model[17] is firstly introduced in this section.

For the flow field:

$$f_i(x + e_i\delta_t, t + \delta_t) = f_i(x,t) + \frac{\delta_t}{\tau_v}[f_i^{eq}(x,t) - f_i(x,t)] + \Delta t e_i F_i \tag{1}$$

For the thermal field:

$$g_i(x + e_i\delta_t, t + \delta_t) = g_i(x,t) + \frac{\Delta t}{\tau_c}[g_i^{eq}(x,t) - g_i(x,t)] \tag{2}$$

f_i^{eq} and g_i^{eq} denotes the equilibrium distribution function.

$$f_i^{eq} = w_i\rho[1 + \frac{e_i u}{c_s^2} + \frac{1}{2}\frac{(e_i u)^2}{c_s^4} - \frac{1}{2}\frac{u^2}{c_s^2}] \tag{3}$$

$$g_i^{eq} = w_i T[1 + \frac{e_i u}{c_s^2}] \tag{4}$$

where ρ is the lattice fluid density, T is the lattice fluid temperature and the weight function w_i has the value of $w_0 = 4/9$, $w_{1-4} = 1/9$, $w_{5-8} = 1/36$. The force term in Eq. (1) is:

$$F_i = 3w_i\rho g_y\beta(T - T_m) \tag{5}$$

where ρ, g_y, β, T, T_m stand for local density, gravitational acceleration vector, thermal expansion coefficient, local temperature and the average temperature $T_m = (T_h + T_c)/2$, respectively.

v and α are kinetic viscosity and thermal diffusivity, respectively. The relaxation time for the flow and temperature fields, τ_v and τ_c, can be defined as

$$\tau_v = 0.5 + v\frac{1}{\delta t c_s^2} \tag{6}$$

$$\tau_c = 0.5 + \alpha\frac{1}{\delta t c_s^2} \tag{7}$$

where $c_s = c/\sqrt{3}$ is the speed of sound.

The macroscopic variables (density, momentum and temperature) can be calculated with the following formula:

$$\rho = \sum_i f_i, \quad \rho u = \sum_i e_i f_i, \quad T = \sum_i g_i \tag{8}$$

2.2. SHSLBM

Based on the thermal LBM above, thermal SHSLBM was reported and used in the current research. Formulations of thermal SHSLBM includes two steps, which are as follows:

Predictor step:

$$\rho^* = \sum_i f_\alpha^{eq}(\boldsymbol{r} - \boldsymbol{e}_i\delta_t, t - \delta_t) \tag{9}$$

$$\rho^*\boldsymbol{u}^* = \sum_\alpha \boldsymbol{e}_i f_i^{eq}(\boldsymbol{r} - \boldsymbol{e}_i\delta_t, t - \delta_t) \tag{10}$$

$$\rho^* e^* = \sum_i g_i^{eq}(\boldsymbol{r} - \boldsymbol{e}_i\delta_t, t - \delta_t) \tag{11}$$

Corrector step:

$$\rho(\boldsymbol{r}, t) = \rho^* \tag{12}$$

$$\rho(\boldsymbol{r}, t)\boldsymbol{u}(\boldsymbol{r}, t) = \rho^*\boldsymbol{u}^* + (\tau_v - 1)\sum_i \boldsymbol{e}_i f_\alpha^{eq}(\boldsymbol{r} + \boldsymbol{e}_i\delta_t, t) - (\tau_v - 1)\rho(\boldsymbol{r}, t - \delta_t)\boldsymbol{u}(\boldsymbol{r}, t - \delta_t) + F_E\delta_t \tag{13}$$

$$\rho(\boldsymbol{r}, t)e(\boldsymbol{r}, t) = \rho^* e^* + (\tau_c - 1)\sum_i g_i^{eq}(\boldsymbol{r} + \boldsymbol{e}_i\delta_t, t) - (\tau_c - 1)\rho(\boldsymbol{r}, t - \delta_t)e(\boldsymbol{r}, t - \delta_t) \tag{14}$$

$$F_E = \rho g_y \beta(T - T_m) \tag{15}$$

2.4. Nanofluid thermo-physical properties

The density, specific heat capacity at constant pressure and thermal expansion coefficient of the hybrid nanofluid are calculated as follows:

$$\rho_{nf} = \phi_1 \rho_{s_1} + \phi_2 \rho_{s_2} + (1 - \phi)\rho_f \tag{16}$$

$$(\rho c_p)_{nf} = \phi_1(\rho c_p)_{s_1} + \phi_2(\rho c_p)_{s_2} + (1 - \phi)(\rho c_p)_f \tag{17}$$

$$(\rho\beta)_{nf} = \phi_1(\rho\beta)_{s_1} + \phi_2(\rho\beta)_{s_2} + (1 - \phi)(\rho\beta)_f \tag{18}$$

where ϕ_1, ϕ_2, ρ_{s1}, ρ_{s2}, $(c_p)_{s1}$, $(c_p)_{s2}$, $(\beta)_{s1}$, $(\beta)_{s2}$ are the volume fraction, density, specific heat capacity at constant pressure and thermal expansion coefficient of the two different nanoparticles, respectively. Also, ϕ is the overall volume fraction of two types of nanoparticles in hybrid nanofluid and is determined by

$$\phi = \phi_1 + \phi_2 \tag{19}$$

The effective thermal conductivity and effective viscosity of nanofluid are obtained by:

$$k_{nf} = \frac{(k_{hs} + 2k_f) - 2\phi(k_f - k_{hs})}{(k_{hs} + 2k_f) + \phi(k_f - k_{hs})} k_f \tag{20}$$

with

$$k_{hs} = \frac{\phi_1 k_{s_1} + \phi_2 k_{s_2}}{\phi} \tag{21}$$

The viscosity of nanofluid can be calculated as:

$$\mu_{nf} = \frac{\mu_f}{(1-\phi)^{2.5}} \tag{22}$$

The nanofluid thermal diffusivity and Prandtl number are determined as

$$\alpha_{nf} = \frac{k_{nf}}{(\rho c_p)_{nf}} \tag{23}$$

$$\text{Pr}_{nf} = \frac{(\mu c_p)_{nf}}{k_{nf}} \tag{24}$$

The local Nusselt number of the horizontal boundary can be calculated by

$$Nu_{loc} = -\left(\frac{k_{nf}}{k_f}\right)\left(\frac{\partial T}{\partial y}\right) \tag{25}$$

Finally, the average Nusselt number can be calculated by the integrating of the local Nusselt number along the heater and the cooler.

3. Verification of the simulation

In this section, the SHSLBM results are verified by well-know cases in the literature. Fig. 2 shows the streamlines and isotherms inside a square enclosure at different Rayleigh numbers. The temperature of the left wall of the enclosure is fixed as $T_h = 1$ and the right wall is set as a low temperature $T_c = 0$. The top and bottom walls of the enclosure are adiabatic. It can be seen that the obtained results from the present code are in good agreement with those in the previous papers[18,19].

$Ra = 10^6$ $Ra = 10^7$ $Ra = 10^8$
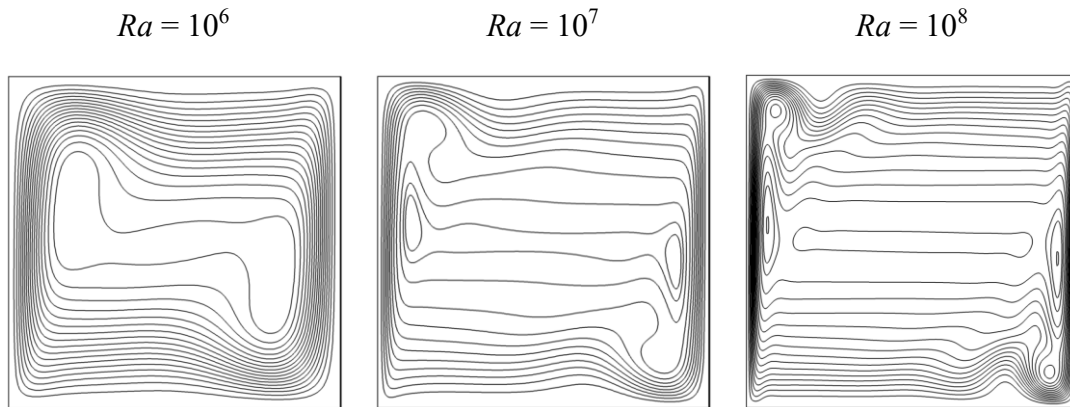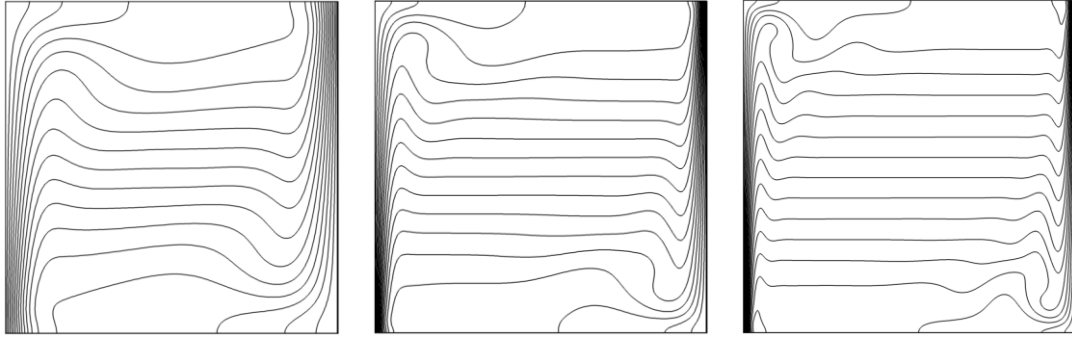
Fig. 2 The streamlines (top) and isotherms (bottom) of two-dimensional natural convection at $Ra = 10^6$, 10^7 and 10^8.

4. Results and discussion

4.1. Bifurcation map

Fig. 3 shows the bifurcation map for different Rayleigh number and the length of fins. There are three different types of flow patterns (steady symmetry, unsteady symmetry and unsteady asymmetry) can be observed in the figure. At relatively low Rayleigh number (10^6), the fluid inside the enclosure keeps the flow regime of steady symmetry and dose not vary with the increase of h. As for relatively high Rayleigh numbers (10^8-10^9), the unsteady asymmetry can be always observed regardless of the fin length. When the Rayleigh number increases from 2.5×10^6 to 1.0×10^7, the transitions of three different flow regimes occur for different Ra and h. For a certain h, as increasing the Rayleigh number from 10^6 to 10^9, the fluid flow changes from steady and symmetry to unsteady and symmetry firstly, and then changes to unsteady asymmetry flow regime. We focus on the nanofluid flow and heat transfer characteristics in these flow pattern. Therefore, the streamlines, temperature distribution and Nusselt number are illustrated in the following sections.
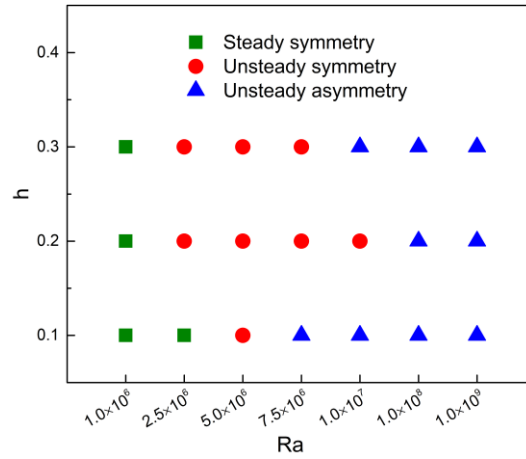
Fig. 3 Bifurcation map for different Rayleigh numbers and h at $\phi = 0.01$.

4.2. Steady symmetry

Fig. 4 shows the comparison of streamlines and isotherms between the pure water and nanofluid in the steady symmetry flow regime. As seen in Fig. 4(a), at $Ra = 2.5 \times 10^6$ and $h = 0.1$, two vortices can be found inside the enclosure which are in clockwise and anticlockwise directions, respectively. The magnitude of fluid flow increases by adding the nanoparticles into the pure water which strengthens the transport energy of the fluid. As a result, the absolute value of maximum of stream function increases with increasing the solid volume fraction. Moreover, it can be observed in Fig. 4(b) that the isothermal lines adjacent to the heating obstacle and four fins cover the shape of them. One thermal plume can be clearly observed above the heat source. The addition of nanoparticles into the base fluid leads to the thickness of thermal boundary layer increases, which causes the decrease of temperature gradient.

(a)   **(b)**

497
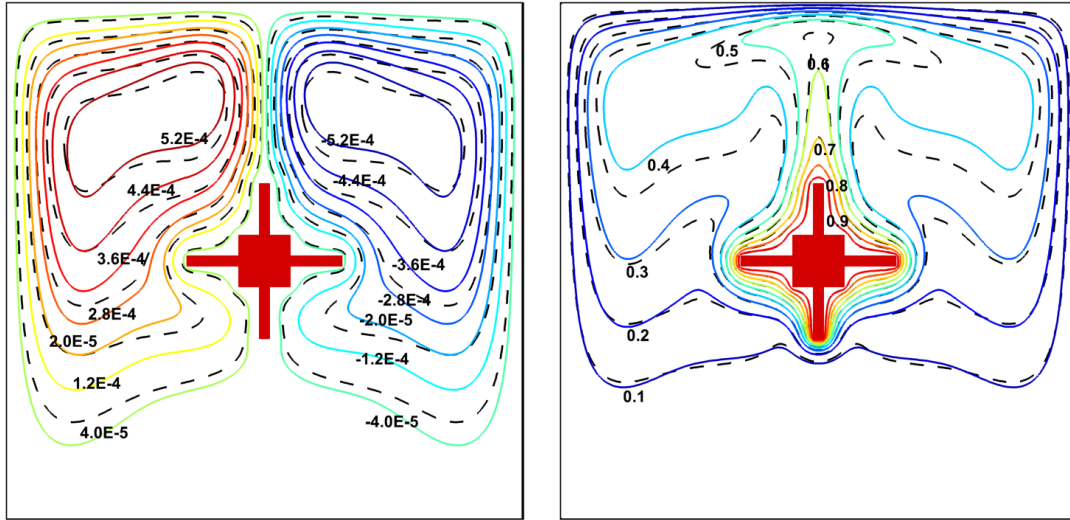
$|\Psi_{\max}|_f = 0.00048$, $|\Psi_{\max}|_{nf} = 0.00071$

Fig. 4 Comparison of streamlines and isotherms at $Ra = 2.5 \times 10^6$ and $h = 0.1$ between the pure water (dashed lines) and nanofluid (solid lines).

The Streamlines in the steady symmetry flow pattern at $\phi = 0.01$ for different Rayleigh number and length of fins. In this pattern, the flow is steady and the streamlines are symmetrical about the central line. The fluid around the hot source is heated and goes up due to the buoyancy force. For $Ra = 10^6$, at $h = 0.1$, two recirculation cells form on the left and right sides inside the enclosure, respectively. The clockwise vortex is on the right of the anticlockwise vortex. When the length of fins increases to 0.2, the streamlines are squeezed by the longer fins, and this effect is more significant in the horizontal direction. Still, the pattern of streamlines inside the enclosure does not change as increasing the h from 0.1 to 0.2. However, when the h increases to 0.3, the pattern of streamlines changes significantly. Two primary vortices can be observed inside the cavity and each vortex occupies half of the zone. Two secondary vortices are established in one primary vortex due to the small gap between the horizontal fin and the side wall. The directions of two secondary vortices are same to their primary vortex, respectively. Hence the existence of fins impedes and controls fluid flow motion. When the Rayleigh number increases to 2.5×10^6 and at $h = 0.1$, the flow pattern is also steady symmetry. Comparing with the pattern of streamlines at $Ra = 10^6$ and $h = 0.1$, it changes distinctly. The two primary vortices at $Ra = 2.5 \times 10^6$ and $h = 0.1$ are similar to that at

$Ra = 10^6$ and $h = 0.1$. However, two small secondary vortices form inside each primary vortex at $Ra = 2.5 \times 10^6$ and $h = 0.1$. This is because the increase of Rayleigh number leads to the enhancement of natural convection.

(a)　　　　　　　　　　　　　　**(b)**

(c)　　　　　　　　　　　　　　**(d)**
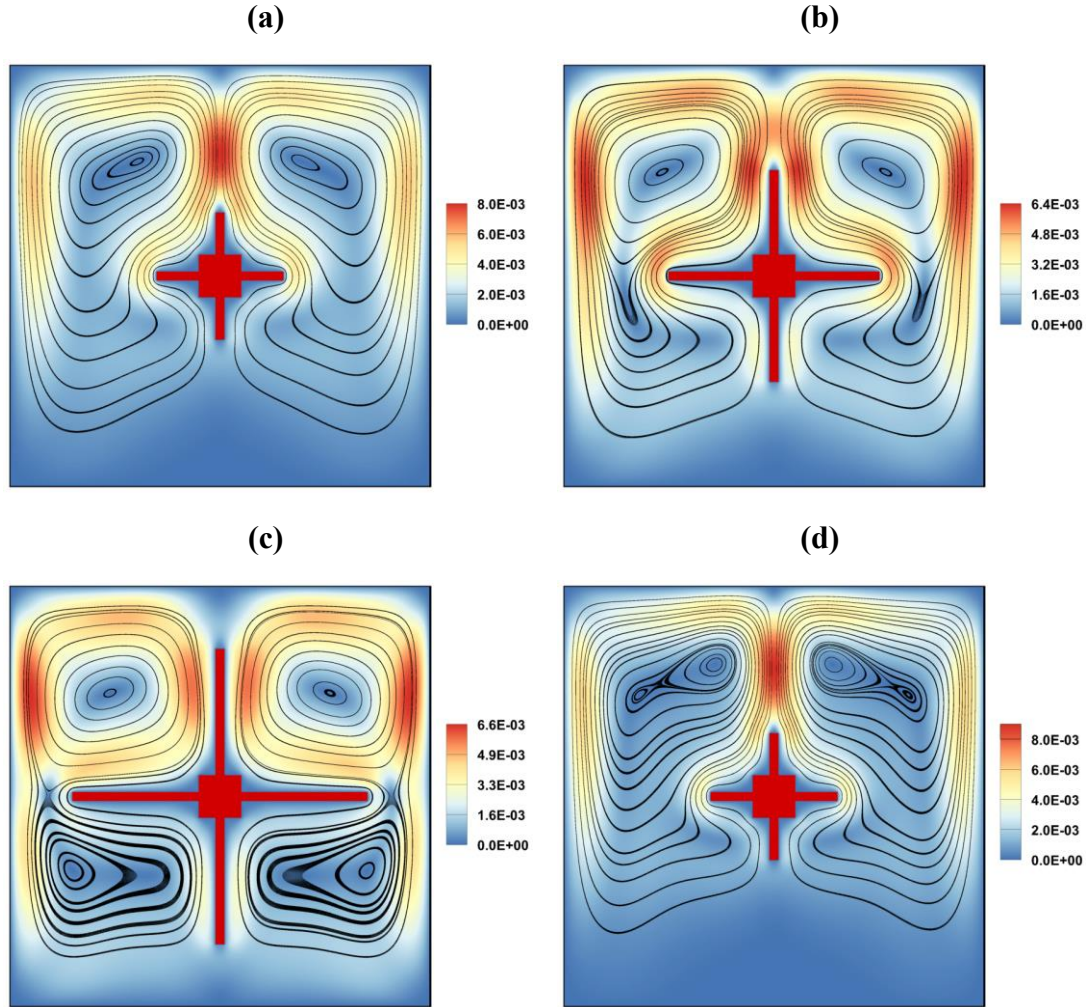
Fig. 5 Streamlines at $\phi = 0.01$ for **(a)** $Ra = 10^6$, $h = 0.1$; **(b)** $Ra = 10^6$, $h = 0.2$; **(c)** $Ra = 10^6$, $h = 0.3$; **(d)** $Ra = 2.5 \times 10^6$, $h = 0.1$.

Fig. 6 despites the temperature distribution of nanofluid inside the enclosure at different Rayleigh number and h. The isothermal lines below the hot source is packed more closely to the hot source than those above the hot source. As seen in Fig. 6(a)-(c), the temperature of each node inside the enclosure increases by increasing the length of fins. This is due to the fact that the increase of h leads to the expansion of heating obstacle surface area. As a result, the cold fluid inside the cavity can be heated much

more easily.
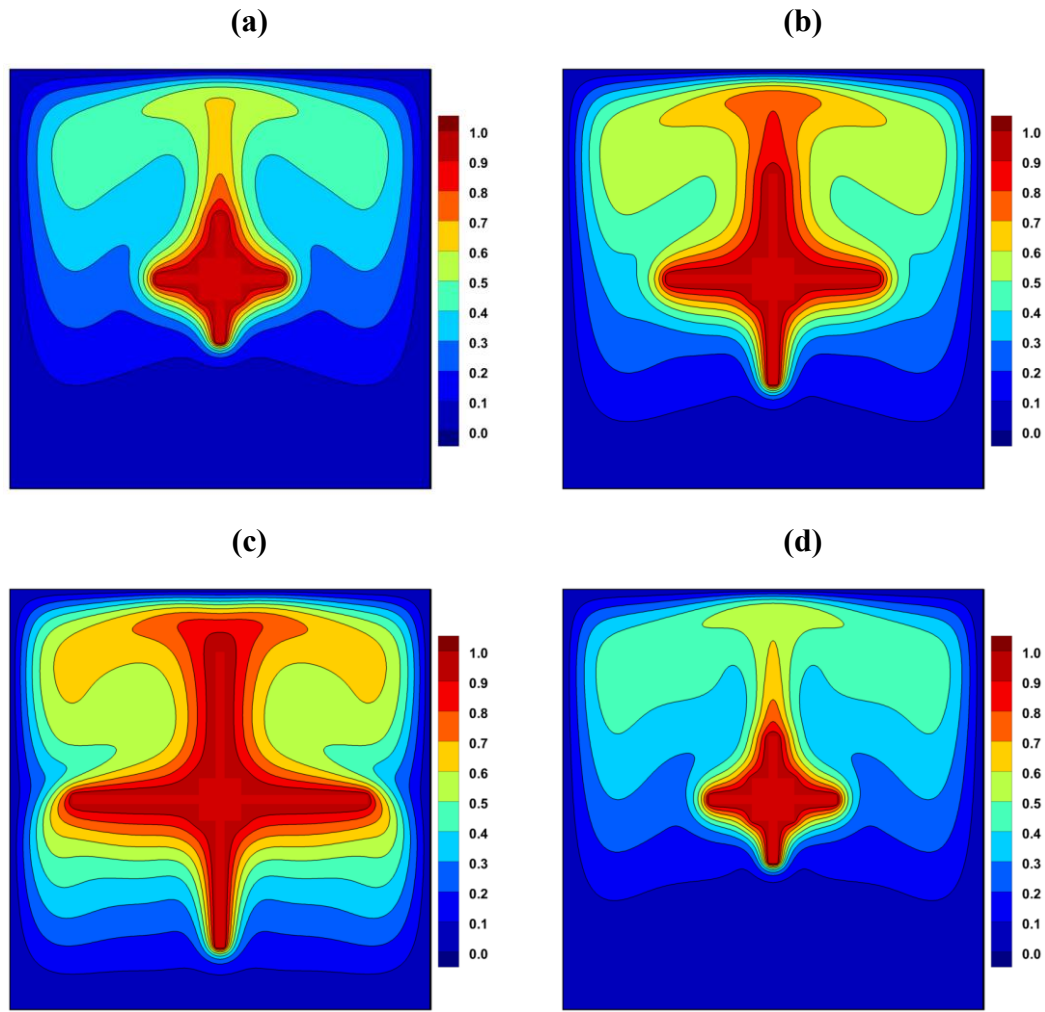
Fig. 6 Isothermal lines at $\phi = 0.01$ for **(a)** $Ra = 10^6$, $h = 0.1$; **(b)** $Ra = 10^6$, $h = 0.2$; **(c)** $Ra = 10^6$, $h = 0.3$; **(d)** $Ra = 2.5 \times 10^6$, $h = 0.1$.

4.3. Unsteady symmetry

As seen in Fig. 3, when the Rayleigh number is larger than 2.5×10^6, the flow pattern of unsteady symmetry can be observed. For $\phi = 0.01$, it can be found that the flow pattern is unsteady symmetry at $Ra = 5 \times 10^6$ for any fin length. Fig. 7 shows the average Nusselt number versus LB time at $Ra = 5 \times 10^6$ and $\phi = 0.01$ for different h. It can be found clearly that the three curves about average Nusselt number have the characteristic of periodicity. At $h = 0.1$ or 0.3, the curves are sinusoidal shape. Moreover, as h increases from 0.1 to 0.3, the mean value of average Nusselt number decreases.
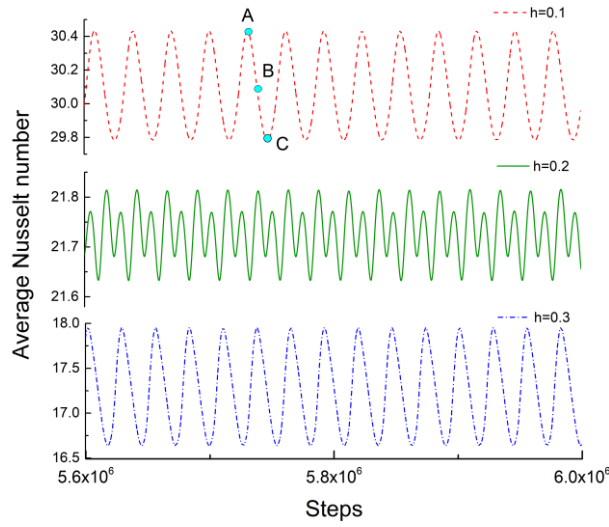
Fig. 7 Average Nusselt number versus steps at $Ra = 5{\times}10^6$ and $\phi = 0.01$ for different h.

In order to illustrate the evolution of the flow and temperature fields in the unsteady symmetry flow regime, the instantaneous streamlines and isotherms in one period are reported. Fig. 8 shows the instantaneous streamlines and isotherms at three moments ($t = A$, B and C, see Fig. 7) for $Ra = 5{\times}10^6$, $h = 0.1$ and $\phi = 0.01$. It can be observed from the streamlines that at $t = A$, only two primary vortices form inside the enclosure and the average Nusselt number achieves the maximum value. When the time is $t = B$, the vortex inside the primary vortex breaks into two secondary vortices and the upper cell is larger than the lower one. As for $t = C$, the two secondary vortices vary and the upper cell become lower than the lower one. Also, at this moment, the average Nusselt number reaches the minimum value.

(a)

501
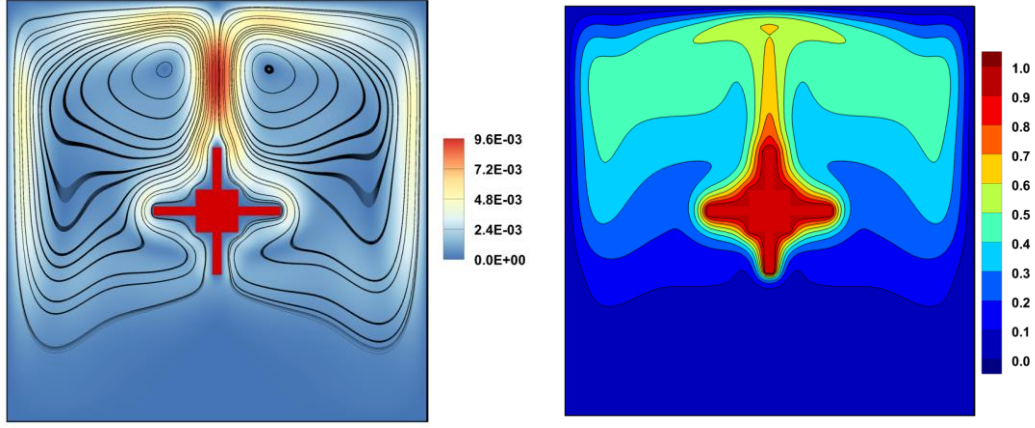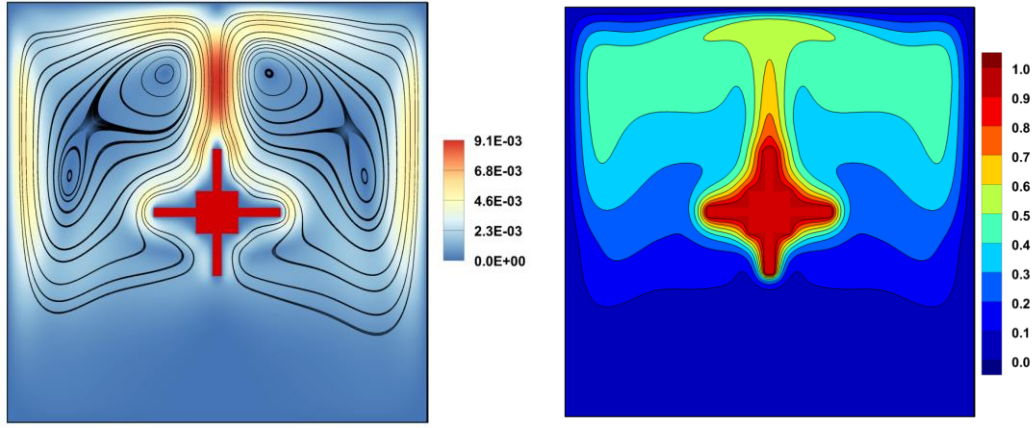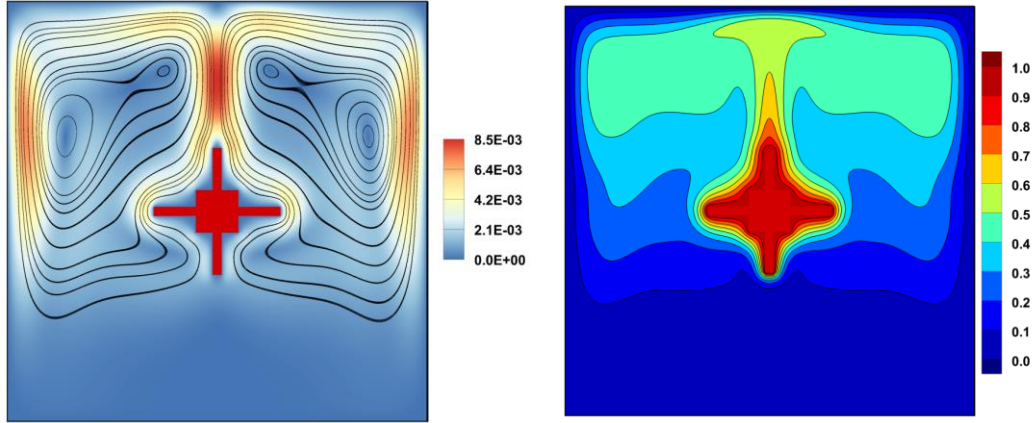
Fig. 8 Streamlines and isotherms at $Ra = 5\times10^6$, $h = 0.1$ and $\phi = 0.01$ at **(a)** $t = $ A; **(b)** t = B; **(c)** $t = $ C.

Fig. 9 presents the fast Fourier transform of average Nusselt number at $Ra = 5\times10^6$ and $\phi = 0.01$ for different h (see Fig. 7), which expresses the power spectrum. It can be found that there is one frequency for $h = 0.1$ and 0.3. However, at $h = 0.2$, two different

frequencies can be observed.

(a)

(b)

(c)
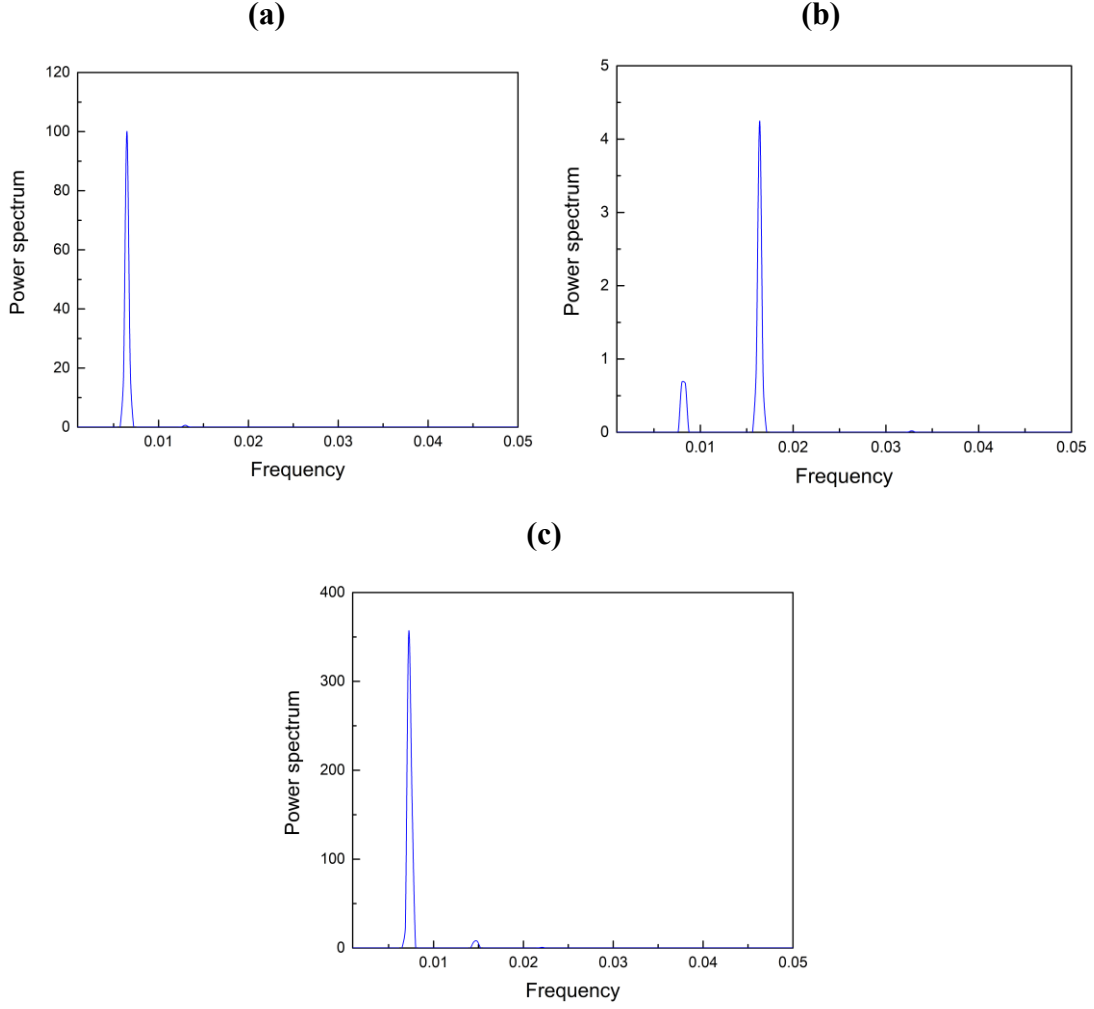
Fig. 9 Fast Fourier transform of *Nu* signals $Ra = 5 \times 10^6$ and $\phi = 0.01$ for **(a)** $h = 0.1$;

(b) $h = 0.2$ **(c)** $h = 0.3$.

To verify the existence of the periodicity in the present flow pattern, the phase diagrams of two monitoring points (P_1 and P_2, see Fig. 1) are shown in Fig. 10 and Fig. 11. In these phase diagrams, the signal of velocity in the horizontal and vertical directions (U and V) are plotted along the horizontal and vertical axis (X and Y), respectively. After long time, the curves in the phase diagrams become enclosed shapes, which illustrates the periodic behavior of the fluid in the flow pattern of unsteady symmetry.
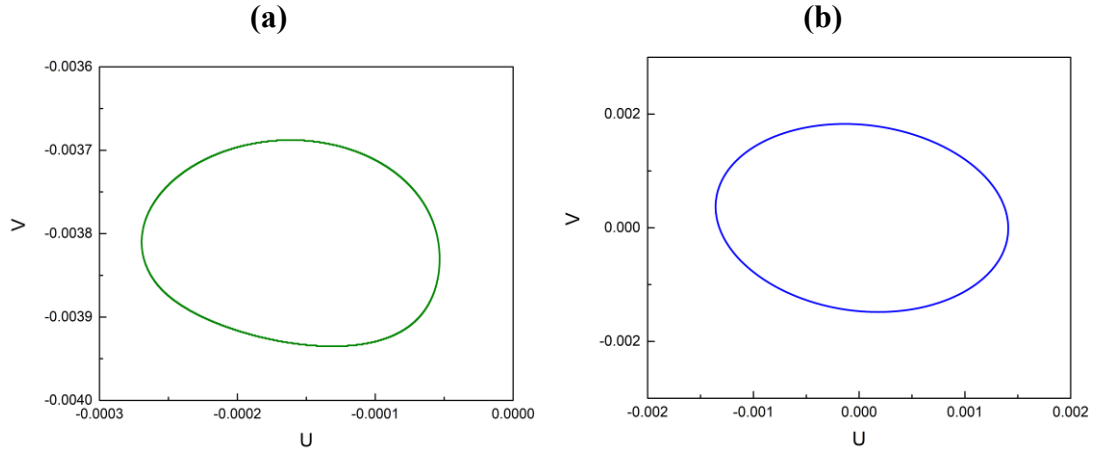
Fig. 10 Phase diagrams at $Ra = 2.5 \times 10^6$, $h = 0.2$ and $\phi = 0.01$ on **(a)** P_1; **(b)** P_2.
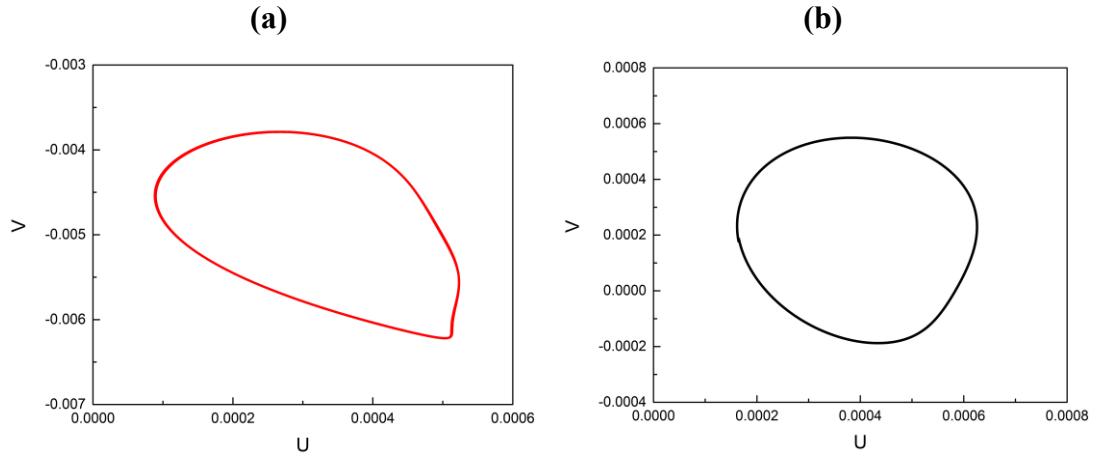
Fig. 11 Phase diagrams at $Ra = 5 \times 10^6$, $h = 0.3$ and $\phi = 0.01$ on **(a)** P_1; **(b)** P_2.

Fig. 12 shows the effect of nanoparticle volume fraction on the average Nusselt number at $Ra = 5 \times 10^6$ and $h = 0.1$. The variation of mean value of average Nusselt number indicates that the average Nu increases by increasing the solid volume fraction. Moreover, the amplitude of average Nu is a decrease function of the nanoparticle volume fraction. Especially at $\phi = 0.05$, the average Nu becomes a constant value and the flow pattern accordingly becomes steady symmetry.
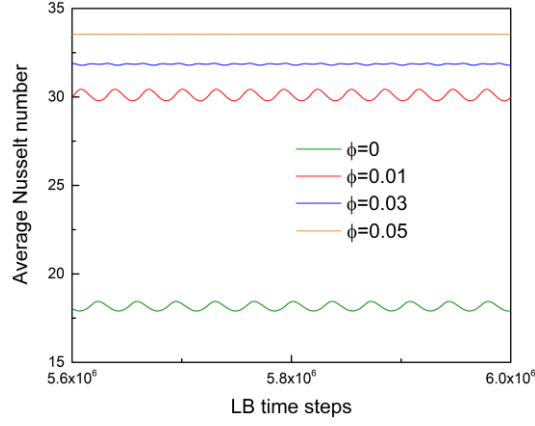
Fig. 12 Effect of nanoparticle volume fraction on the average Nusselt number at $Ra = 5 \times 10^6$ and $h = 0.1$.

4.4. Unsteady asymmetry

When the Rayleigh number is large enough for certain h and ϕ, the flow pattern evolves into the unsteady asymmetry mode. Fig. 13 shows the instantaneous velocity contour, streamlines and isothermal lines at $Ra = 1 \times 10^9$, $\phi = 0.01$ and $h = 0.2$, which is the unsteady asymmetry flow pattern. Both the streamlines and isotherms are very complicated, disordered, asymmetrical and hard to anticipate. Due to the high Rayleigh number, the convection heat transfer is enhanced and a number of recirculation cells can be discovered inside the enclosure.

(a) **(b)**
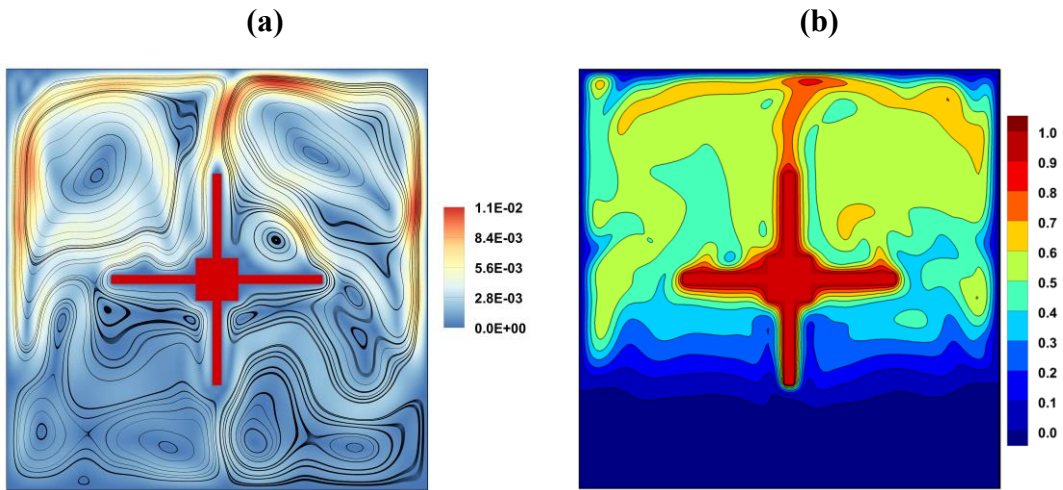
Fig. 13 Instantaneous velocity contour, streamlines and isotherms at $Ra = 1 \times 10^9$, $\phi = 0.01$ and $h = 0.2$.

505

The phase diagram on the point of P$_1$ at $Ra = 10^9$, $h = 0.2$ and $\phi = 0.01$ is depicted in Fig. 14. It's not hard to find that the curve is disorganized and the characteristics of periodicity occurs in the phase diagram, which illustrates the aperiodic unsteady feature of the flow pattern.
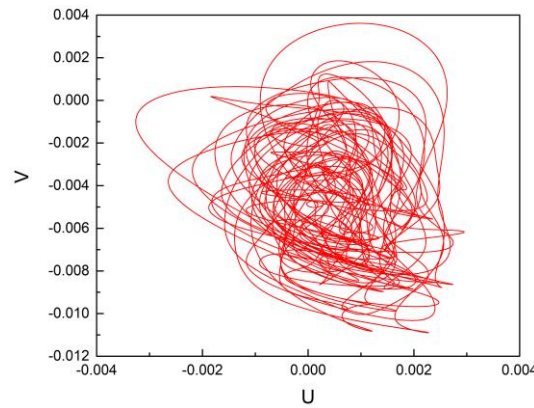
Fig. 14 Phase diagram on P$_1$ at $Ra = 10^9$, $h = 0.2$ and $\phi = 0.01$.

5. Conclusion

In the present paper, a new method (SHSLBM) developed from lattice Boltzmann method was used to simulate hybrid nanofluid flow and heat transfer in a thermal energy storage with four fins at high Rayleigh numbers ($10^6 \leq Ra \leq 10^9$). The effects of Rayleigh number, nanoparticle volume fraction and length of fin on the flow pattern, temperature distribution and heat transfer characteristics were reported. The following remarks can be obtained:

- SHSLBM is an especially promising approach for solving the problems of turbulent flow and heat transfer.

- Three kinds of flow patterns (steady symmetry, unsteady symmetry and unsteady asymmetry) can be observed at various Rayleigh number.

- When the Ra increases from 1×10^6 to 1×10^9, the transitions of flow regime from steady symmetry state to unsteady asymmetry state occur, through the unsteady symmetry flow pattern. The steady symmetry flow pattern cannot change to unsteady asymmetry directly by increasing Ra.

- The ϕ affects the flow pattern significantly. For instance, at $Ra = 5 \times 10^6$ and $h = 0.1$, the flow inside the enclosure is steadier at higher ϕ.

- The length of fins also affects the flow pattern. The effect of h on the flow pattern varies at different Ra. In the same flow pattern, i.e. at $Ra = 5 \times 10^6$ and $\phi = 0.01$, there is one frequency for $h = 0.1$ and 0.3, but two different frequencies at $h = 0.2$.

- For different h and ϕ, the critical Rayleigh number where the flow pattern changes from steady symmetry to unsteady asymmetry is different.

References

[1] Das D, Roy M, Basak T. Studies on natural convection within enclosures of various (non-square) shapes–A review. International Journal of Heat and Mass Transfer. 2017 Mar 1;106:356-406.

[2] Dawood HK, Mohammed HA, Sidik NA, Munisamy KM, Wahid MA. Forced, natural and mixed-convection heat transfer and fluid flow in annulus: A review. International Communications in Heat and Mass Transfer. 2015 Mar 1;62:45-57.

[3] Öztop HF, Estellé P, Yan WM, Al-Salem K, Orfi J, Mahian O. A brief review of natural convection in enclosures under localized heating with and without nanofluids. International Communications in Heat and Mass Transfer. 2015 Jan 1;60:37-44.

[4] Amber I, O'Donovan TS. Natural convection induced by the absorption of solar radiation: A review. Renewable and Sustainable Energy Reviews. 2018 Feb 1;82:3526-45.

[5] Bhardwaj S, Dalal A, Pati S. Influence of wavy wall and non-uniform heating on natural convection heat transfer and entropy generation inside porous complex enclosure. Energy. 2015 Jan 1;79:467-81.

[6] Esfe MH, Arani AA, Yan WM, Ehteram H, Aghaie A, Afrand M. Natural convection in a trapezoidal enclosure filled with carbon nanotube–EG–water nanofluid. International Journal of Heat and Mass Transfer. 2016 Jan 1;92:76-82.

[7] Ma Y, Mohebbi R, Rashidi MM, Yang Z, Sheremet MA. Numerical study of MHD nanofluid natural convection in a baffled U-shaped enclosure. International Journal of Heat and Mass Transfer. 2019 Mar 1;130:123-34.

[8] Haghighi SS, Goshayeshi HR, Safaei MR. Natural convection heat transfer enhancement in new designs of plate-fin based heat sinks. International Journal of Heat and Mass Transfer. 2018 Oct 31;125:640-7.

[9] Ma Y, Mohebbi R, Rashidi MM, Yang Z. Study of nanofluid forced convection heat transfer in a bent channel by means of lattice Boltzmann method. Physics of Fluids. 2018 Mar;30(3):032001.

[10] Ma Y, Mohebbi R, Rashidi MM, Yang Z. Effect of hot obstacle position on natural convection heat transfer of MWCNTs-water nanofluid in U-shaped enclosure using lattice Boltzmann method. International Journal of Numerical Methods for Heat & Fluid Flow. 2019 Jan 7;29(1):223-50.

[11] Ma Y, Mohebbi R, Rashidi MM, Yang Z. MHD convective heat transfer of Ag-MgO/water hybrid nanofluid in a channel with active heaters and coolers. International Journal of Heat and Mass Transfer. 2019 Jul 1;137:714-26.

[12] Hatami M, Safari H. Effect of inside heated cylinder on the natural convection heat transfer of nanofluids in a wavy-wall enclosure. International Journal of Heat and Mass Transfer. 2016 Dec 1;103:1053-7.

[13] Chikatamarla SS, Karlin IV. Entropic lattice Boltzmann method for multiphase flows. Physical review letters. 2015 May 1;114(17):174502.

[14] Chen Z, Shu C, Tan D. High-order simplified thermal lattice Boltzmann method for incompressible thermal flows. International Journal of Heat and Mass Transfer. 2018 Dec 1;127:1-6.

[15] Jami M, Moufekkir FA, Mezrhab A, Fontaine JP, Bouzidi MH. New thermal MRT lattice Boltzmann

method for simulations of convective flows. International Journal of Thermal Sciences. 2016 Feb 1;100:98-107.

[16] Chen Z, Shu C, Tan D, Wu C. On improvements of simplified and highly stable lattice Boltzmann method: Formulations, boundary treatment, and stability analysis. International Journal for Numerical Methods in Fluids. 2018 Jun 10;87(4):161-79.

[17] Mohamad A A, Kuzmin A. A critical evaluation of force term in lattice Boltzmann method, natural convection problem[J]. International Journal of Heat and Mass Transfer, 2010, 53(5-6): 990-996.

[18] de Vahl Davis G. Natural convection of air in a square cavity: a bench mark numerical solution. International Journal for numerical methods in fluids. 1983 May;3(3):249-64.

[19] Chen Z, Shu C, Tan D. A simplified thermal lattice Boltzmann method without evolution of distribution functions. International Journal of Heat and Mass Transfer. 2017 Feb 1;105:741-57.

VERIFICATION AND VALIDATION OF A LATTICE BOLTZMANN METHOD COUPLED WITH COMPLEX SUB-GRID SCALE TURBULENCE MODELS

CHRISTOS GKOUDESNES[1] AND RALF DEITERDING[2]

[1] Aerodynamics and Fluid Mechanics Research Group
Engineering and Physical Sciences Faculty
University of Southampton
Highfield Campus, Southampton SO17 1BJ, UK
e-mail: C.Gkoudesnes@soton.ac.uk, web page: http://be.linkedin.com/in/christosgkoudesnes

[2] Aerodynamics and Fluid Mechanics Research Group
Engineering and Physical Sciences Faculty
University of Southampton
Highfield Campus, Southampton SO17 1BJ, UK
e-mail: R.Deiterding@soton.ac.uk, web page: http://rdeiterding.website/

Key words: Lattice Boltzmann, LES, Isotropic Turbulence, Taylor Green Vortex

Abstract. In this paper, we present our recent work on single relaxation Lattice Boltzmann method and Large Eddy Simulation (LES) models, namely the dynamic Smagorinsky and wall-adapting local eddy-viscosity (WALE). Initially, forced and decaying homogeneous isotropic turbulence cases were run to compare direct numerical simulations with LES. Moreover, the Taylor-Green vortex was employed to further test the performance of the turbulence models under transition to turbulence. The main purpose of this work was the verification for wall-free simulations of the two newly-implemented LES models in the in-house AMROC framework.

1 INTRODUCTION

Two Large Eddy Simulation (LES) models, namely the Dynamic SMAgorinsky (DSMA) and the Wall-Adapting Local Eddy-viscosity (WALE), have been recently implemented in the in-house solver based on the Single Relaxation Time (SRT) Lattice Boltzmann Method (LBM) [1]. The LBM solver [2, 3, 4, 5] is part of the AMROC framework (Adaptive Mesh Refinement in Object-oriented C ++) [6]. In this paper, we verify them under wall-free circumstances by employed the test cases of Decaying Homogeneous Isotropic Turbulence (DHIT), Forced Homogeneous Isotropic Turbulence (FHIT) and Taylor-Green Vortex (TGV). For the case of FHIT, the forcing scheme of [7] was applied due to its low implementation complexity and, particularly, the ability to start a simulation with the fluid at rest. For the FHIT and TGV, the results are also compared against the Constant SMAgorinsky (CSMA) model.

2 LATTICE BOLTZMANN METHOD

In the standard finite difference SRT-LBM scheme the numerical step is divided into two sub-steps. The first one, called streaming, deals with exchange of information with a number of neighbour cells depending on the LBM model in use. In the current work the D3Q19 models was used. The second sub-step, namely collision, occurs locally per cell and reads

$$f_\alpha(\mathbf{x}, t + \Delta t) = \check{f}_\alpha(\mathbf{x}, t) + \frac{\Delta t}{\tau_L}(\check{f}_\alpha^{eq}(\mathbf{x}, t) - \check{f}_\alpha(\mathbf{x}, t)) + \frac{\Delta t \, w_\alpha(\mathbf{e}_\alpha \cdot \mathbf{F})}{c_s^2}. \tag{1}$$

The notation $\check{f}_\alpha$ refers to values of the distribution function after the streaming and before the collision. The equilibrium distribution function f_α^{eq} is truncated to second order. $\mathbf{e}_\alpha$ are the 19 lattice velocities with w_α the coefficients of the LBM model. Δt is the time step, τ_L is the relaxation time and c_s is the speed of sound with value $1/\sqrt{3}$. The macroscopic variables, density, velocities and pressure, can be estimated from the moments of the distribution function.

The incorporation of an LES model into AMROC-LBM is achieved through the alteration of the discrete relaxation time τ_L and its replacement by an effective discrete relaxation time $\tau_L^\star$ [8]. The difference is the addition of the eddy viscosity ν_t computed as

$$\nu_t = (C\Delta)^2 OP_{LES}, \tag{2}$$

where C is a constant depending on the employed model; Δ is the spatial step size, and OP_{LES} is a function expressing the characteristic timescale of each LES model.

2.1 The external force for FHIT

The last term in the right side of Eq. (1) is the contribution of the external force $\mathbf{F}$. In the case of the FHIT, the force of [7] was used, defined as

$$\begin{aligned}
F_x &= 2\rho A\Big(\frac{\kappa_y \kappa_z}{|\kappa|^2}\Big) G(\kappa_x, \kappa_y, \kappa_z, \phi), \\
F_y &= -\rho A\Big(\frac{\kappa_x \kappa_z}{|\kappa|^2}\Big) G(\kappa_x, \kappa_y, \kappa_z, \phi), \\
F_z &= -\rho A\Big(\frac{\kappa_x \kappa_y}{|\kappa|^2}\Big) G(\kappa_x, \kappa_y, \kappa_z, \phi),
\end{aligned} \tag{3}$$

where ρ is the density and A the acceleration with value 10^{-4} for all the simulations. The force was applied to the range of low wavenumbers $1 \leq \kappa_i \leq 2$, where $i \in x, y, z$ with magnitude $|\kappa|$. Finally, the phase of the force is given by the function

$$G(\kappa_x, \kappa_y, \kappa_z) = \sin\left(\frac{2\pi x}{L}\kappa_x + \frac{2\pi y}{L}\kappa_y + \frac{2\pi z}{L}\kappa_z + \phi\right), \tag{4}$$

with ϕ the random phase estimated by an equidistance distribution and L the length of the domain which in this case was a cube with value 2π.

2.2 CSMA

For the case of CSMA the eddy viscosity is computed as

$$\nu_t = (C_S\Delta)^2|\overline{S}|, \tag{5}$$

where C_S is a global user-defined variable and $|\overline{S}| = \sqrt{2\overline{S}_{ij}\overline{S}_{ij}}$ is the intensity of the strain rate. The notation $\overline{X}$ describes an LES filtered variable. In the LBM framework the strain rate can be computed locally per cell avoiding the use of finite differences as

$$\overline{S}_{ij} = -\frac{1}{2\rho c_s^2 \tau_L^\star} \sum_\alpha \mathbf{e}_{\alpha i}\mathbf{e}_{\alpha j}(\overline{f}_\alpha - \overline{f}_\alpha^{\,eq}). \tag{6}$$

After some algebra, τ_L^* can be also calculated locally.

2.3 DSMA

The implementation of the dynamic Smagorinsky in AMROC-LBM is based on the work of Premnath *et al.* [9] and follows the idea of Germano *et al.* [10], including the modification of Lilly [11]. The same formula of CSMA, Eq. (5), is also applied here for the estimation of ν_t. In this case, C is a local per cell variable that is computed before the streaming as

$$C^2 = -\frac{1}{2}\frac{\langle L_{ij}M_{ij}\rangle}{\langle M_{ij}M_{ij}\rangle}. \tag{7}$$

The two tensors L_{ij} and M_{ij} can be calculated as

$$L_{ij} = \widehat{\overline{u_i\overline{u}_j}} - \widehat{\overline{u}}_i\widehat{\overline{u}}_j,$$
$$M_{ij} = \widehat{\overline{\Delta}}^2|\widehat{\overline{S}}|\widehat{\overline{S}}_{ij} - \overline{\Delta}^2\widehat{|\overline{S}|\overline{S}_{ij}}, \tag{8}$$

where $\widehat{\overline{x}}$ denotes a test-filtered value computed through the employment of a discrete trapezoidal filter. In Eq. (7), $\langle\cdot\rangle$ means averaging in homogeneous directions and, if the problem is statistically stationary, in time, too. In AMROC the averaging takes place locally in each cell and per time step. This has the potential of introducing local extrema with unphysical values of C [11]. To alleviate this problem, C is truncated as $0 \leq C \leq 0.23$. Compared to the CSMA, the application of the test-filter impose the use of central finite differences leading to non-local calculations.

2.4 WALE

In the WALE model a more advanced timed scale is employed to handle effectively the damping of the eddy viscosity in the vicinity of the wall [12]. The new operator is a function both of the strain rate S_{ij} and the rotation rate Ω_{ij} and reads

$$OP_{WALE} = \frac{(\mathcal{J}_{ij}\mathcal{J}_{ij})^{\frac{3}{2}}}{(\overline{S}_{ij}\overline{S}_{ij})^{\frac{5}{2}} + (\mathcal{J}_{ij}\mathcal{J}_{ij})^{\frac{5}{4}}}, \tag{9}$$

where $\mathcal{J}_{ij}$ is

$$\mathcal{J}_{ij} = \overline{S}_{ik}\overline{S}_{kj} + \overline{\Omega}_{ik}\overline{\Omega}_{kj} - \frac{1}{3}\delta_{ij}(\overline{S}_{mn}\overline{S}_{mn} - \overline{\Omega}_{mn}\overline{\Omega}_{mn}). \tag{10}$$

The constant of the model C is always equal to 0.5. To compute the two rates, central finite differences are used for the derivatives. Compared to DSMA, the WALE model does not need truncation corrections besides the situation where all the velocities are zero, i.e. during the initialisation of the flow field, in which scenario ν_t is set to zero.

3   FORCED HOMOGENEOUS ISOTROPIC TURBULENCE

The computational domain for the FHIT, DHIT and TGV test cases was a periodic cube of a 2π length. The initial conditions for the FHIT were a zero velocity field and unit density. The value of viscosity ν was used to alter for a specific resolution the value of $Re_\lambda = u'\lambda/\nu$, where u' is the root mean square of the velocity and λ the Taylor length scale. After a transient time Δt_t, the external energy due to the force equilibrates with the viscous dissipation and a statistically steady state is achieved for a duration of Δt_a. The library FFTW [13] was employed to perform the essential Fourier transforms. The end of the transient time was decided by examining the evolution of the kinetic energy k and particularly the dissipation rate ε. Figure 1 presents an example of their evolution for a specific simulation. The time has been normalised by the eddy turnover time $\tau_e = L_{11}/u'$, where L_{11} is the integral length scale.

Initially, Direct Numerical Simulations (DNS) for a variety of resolutions and viscosity value equals to $5 \cdot 10^{-5}$ were simulated to validate the LBM solver. As a benchmark, the model spectrum of [14] has been used. Simultaneously, the performance of the applied force to be used as a verification tool was evaluated. Table 1 shows some parameters and the measured statistics of four simulations with different resolutions. In this table, we also report the Kolmogorov scales, η the Kolmogorov length scale, u_η the Kolmogorov velocity scale and τ_η the Kolmogorov time scale. For more information on the computation of the mentioned turbulent statistics the interested reader can refer to [14].
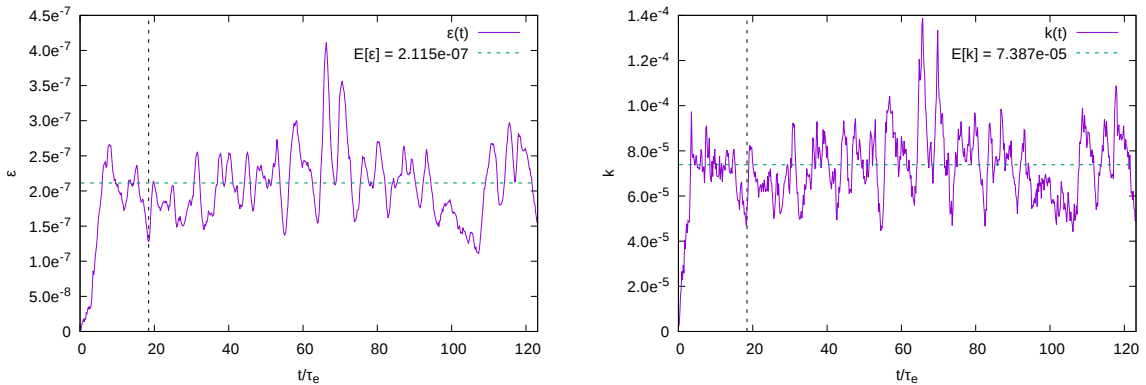
Figure 1: Time evolution of dissipation rate ε (left) and turbulent kinetic energy k (right) for DNS of resolution of 128^3 cells and $\nu = 5 \cdot 10^{-5}$. The vertical dashed line shows the onset of the averaging time. The horizontal dashed line is the averaged value.

Table 1: Turbulent statistics and simulation parameters for LBM DNS for the FHIT case.

N^3	32^3	128^3	256^3	512^3
Δt	2 x 10^{-1}	4.9 x 10^{-2}	2.5 x 10^{-2}	1.2 x 10^{-2}
Re_λ	47	59	66	69
k	2.6 x 10^{-5}	7.4 x 10^{-5}	1.2 x 10^{-4}	1.5 x 10^{-4}
ε	4 x 10^{-8}	2.1 x 10^{-7}	4.3 x 10^{-7}	6.2 x 10^{-7}
$\kappa_{max}\eta$	6.8 x 10^{-1}	1.8	3	5.4
η	4.2 x 10^{-2}	2.8 x 10^{-2}	2.3 x 10^{-2}	2.1 x 10^{-2}
λ	5.7 x 10^{-1}	4.2 x 10^{-1}	3.7 x 10^{-1}	3.5 x 10^{-1}
L_{11}	1	9.3 x 10^{-1}	9 x 10^{-1}	8.8 x 10^{-1}
$L(= k^{3/2}/\varepsilon)$	3.2	3	3	2.9
u_η	1.2 x 10^{-3}	1.8 x 10^{-3}	2.1 x 10^{-3}	2.4 x 10^{-3}
u'	4.1 x 10^{-3}	7 x 10^{-3}	8.9 x 10^{-3}	9.9 x 10^{-3}
τ_η	35.9	15.7	11	9
k/ε	632.1	349.3	274.4	238.9
τ_e	250.51	132.94	101.6	88.5
$\Delta t_a/\tau_e$	63.88	104.68	68.5	19.1
$\Delta t_t/\tau_e$	15.68	18.46	12.08	8.32
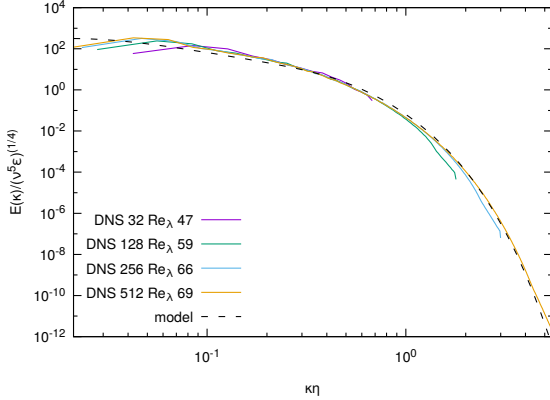
Figure 2: Time-averaged Kolmogorov energy spectra of LBM DNS for four resolutions (solid) and the model spectrum (dashed) [14] for $\nu = 5 \cdot 10^{-5}$.
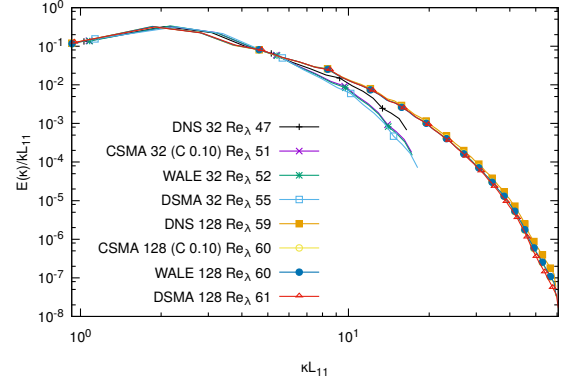
Figure 3: Time-averaged energy spectra normalised by k and L_{11} of LBM DNS and LES for two resolutions and a value of $\nu = 5 \cdot 10^{-5}$.

Comparing the turbulent statistics in Table 1, it is evident that there is a resolution dependence for the input energy due to the current forcing scheme affecting the other turbulent statistics, too. However, by applying Kolmogorov normalisation for the spectra, it is possible to compare them, as one can see in Fig. 2. Due to the different Re_λ per resolution the spectra do not collapse in the lower wavenumbers. On the other hand, it is the numerical dissipation that prevents the spectra from aligning with the model one, besides the highest resolution of 512^3 cells or $\kappa_{max}\eta > 5$.

The results and particularly the energy spectra of DNS have validated the AMROC-LBM solver to deal with elementary turbulent flows. Moreover, this DNS database was used for comparison for the verification of the LES models. Table 2 shows the measured

Table 2: Turbulent statistics and simulation parameters for LBM LES simulations for two resolutions of the FHIT test case.

	CSMA ($C = 0.1$)		DSMA		WALE	
N^3	32^3	128^3	32^3	128^3	32^3	128^3
Δt	2×10^{-1}	4.9×10^{-2}	2×10^{-1}	4.9×10^{-2}	2×10^{-1}	4.9×10^{-2}
Re_λ	51	60	55	61	52	60
k	2.5×10^{-5}	7.3×10^{-5}	2.5×10^{-5}	7.3×10^{-5}	2.5×10^{-5}	7.4×10^{-5}
ε	3.1×10^{-8}	2×10^{-7}	2.7×10^{-8}	1.9×10^{-7}	3×10^{-8}	2×10^{-7}
$\kappa_{max}\eta$	7.2×10^{-1}	1.8	7.5×10^{-1}	1.8	7.3×10^{-1}	1.8
η	4.5×10^{-2}	2.8×10^{-2}	4.7×10^{-2}	2.9×10^{-2}	4.5×10^{-2}	2.8×10^{-2}
λ	6.3×10^{-1}	4.3×10^{-1}	6.8×10^{-1}	4.4×10^{-1}	6.4×10^{-1}	4.3×10^{-1}
L_{11}	1.08	9.3×10^{-1}	1.13	9.5×10^{-1}	1.08	9.3×10^{-1}
L	4	3.1	4.6	3.3	4.1	3.2
u_η	1.1×10^{-3}	1.8×10^{-3}	1.1×10^{-3}	1.8×10^{-3}	1.1×10^{-3}	1.8×10^{-3}
u'	4.1×10^{-3}	7×10^{-3}	4×10^{-3}	7×10^{-3}	4.1×10^{-3}	7×10^{-3}
τ_η	40.4	16.1	44	16.4	41.3	16.1
k/ε	796.1	363.6	928.8	380.8	823	367.7
τ_e	264.47	133.47	280.63	136.29	267.14	133.18
$\Delta t_a/\tau_e$	60.51	113.09	57.02	98.15	59.9	100.44
$\Delta t_t/\tau_e$	14.8	9.19	14	21.61	14.7	22.11

statistics of LBM LES for two resolutions, namely 32^3 and 128^3 cells. To assist the discussion, Fig. 3 presents the energy spectra of the LES models and DNS for this two resolutions. The spectra are normalised by the turbulent kinetic energy k and the integral length scale L_{11}. Under this normalisation the spectra should collapse in the energy-containing range, which is verified by the plot. The lowest resolution is under-resolved based on the previous data, $\kappa_{max}\eta = 0.68$, while the other one is well-resolved, $\kappa_{max}\eta = 1.8$. Therefore, we can examine the behaviour of the LES models for both scenarios.

First of all, in the case of the well-resolved resolution, the spectra of all three LES models have collapsed to the one of DNS. This behaviour can be also identified by comparing Table 1 and Table 2 for the resolution of 128^3 cells. The turbulent statistics are identical for all simulations. This indicates the shut-down of the LES models in well-resolved meshes as it is expected.

On the other hand, for the lowest resolution, all LES models have diverged for the DNS spectrum in the higher wavenumbers, showing increased dissipation in this range. In this way, by reducing the energy of the small scales, the turbulence models stabilise the simulation. Indeed, all three LES models have estimated higher values of $\kappa_{max}\eta$ compared to their DNS counterpart. This behaviour is highly important for running high Re number flows with a low dissipation scheme such as the SRT-LBM. Moreover, by further examining the data, the CSMA with $C = 0.1$ had identical results as the WALE. Considering the isotropy of this test case, this was expected. On the contrary, the DSMA returned the highest value of $\kappa_{max}\eta$ with the smallest estimated dissipation rate ε. These results indicate increased values of eddy viscosity compared to the other models and thus a more dissipative behaviour.
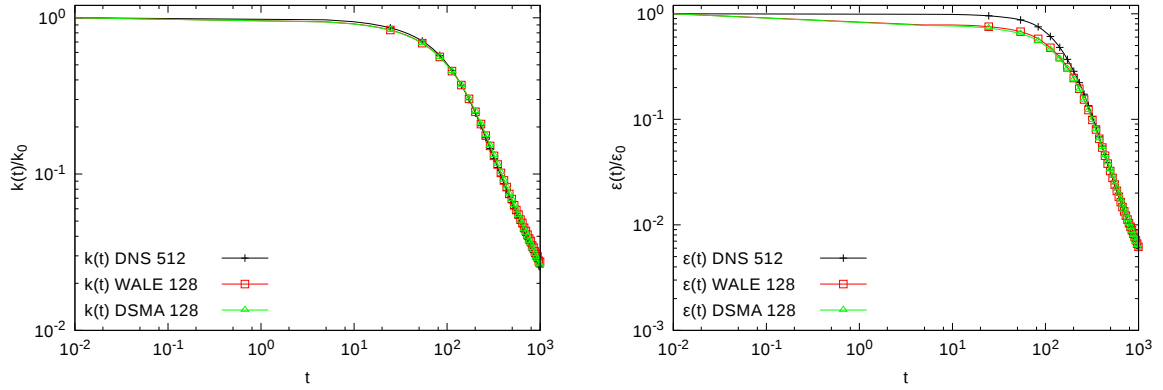
Figure 4: Evolution of the turbulent kinetic energy k (left) and dissipation rate ε (right) for DNS of 512^3 against DSMA and WALE of 128^3 cells resolution.

4   DECAYING HOMOGENEOUS ISOTROPIC TURBULENCE

To further exploit the above mentioned set-up, we restarted the DNS simulation of 512^3 resolution from the final saved time step without the forcing scheme. Simultaneously, by appropriately locally volume-averaging the same initial data, we run DSMA and WALE simulations of a resolution of 128^3 cells, again without the employment of the force. Under this set-up, one can examine DHIT. We have also tried to initialise a DNS of 128^3 cells using the same procedure but it crashed.

Figure 4 shows the evolution of the turbulent kinetic energy k and the dissipation rate ε for the three simulations. Their initial values have been used to normalise both variables. All simulations were run for 1000 time units. It is evident that all three simulations have estimated similar behaviour for the evolution of the turbulent kinetic energy k. On the other hand, the LES models have deviated from the DNS solution in the case of the dissipation rate ε for the first 300 time units. However, after this initial period, their solution collapsed with the DNS data. At this point, it is important to mention that we have not experienced the deviations reported in [15], where the DSMA model of 32^3 cells resolution was compared against DNS of 64^3 for a similar case. Moreover, another vital difference is that the Multi Relaxation Time (MRT) collision model was used instead of the SRT in our case.

To further evaluate the LES models, Fig. 5 shows the energy spectra for the three models after 100 and 1400 iterations, at $t = 4.91$ and $t = 68.72$, respectively. Both of these times lie in the initial period of the deviation in the dissipation rate ε. It is clear that the spectra in both times collapse in the energy-containing range and they only deviate in higher wavenumbers due to the lower resolution and the application of the filtering due to LES. We have also plotted the spectra at $t = 1000$ (not shown here), and the situation was identical. This is a strong indication of the expected behaviour of the implemented models.

Finally, Fig. 6 shows the vorticity field of the three models for the two previously mentioned times. First of all, both LES models have predicted similar flow fields. On
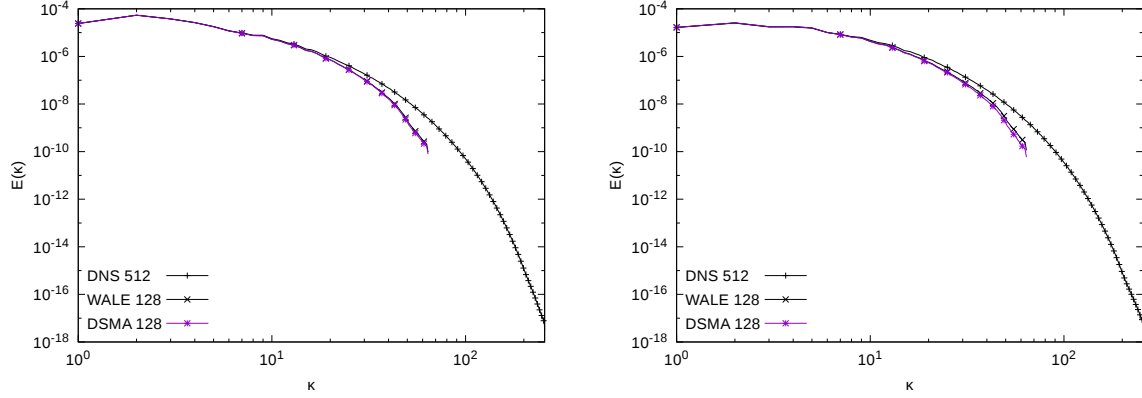
Figure 5: Energy spectra at $t = 4.91$ (left) and at $t = 68.72$ (right) for DNS of 512^3 against DSMA and WALE of 128^3 cells resolution.
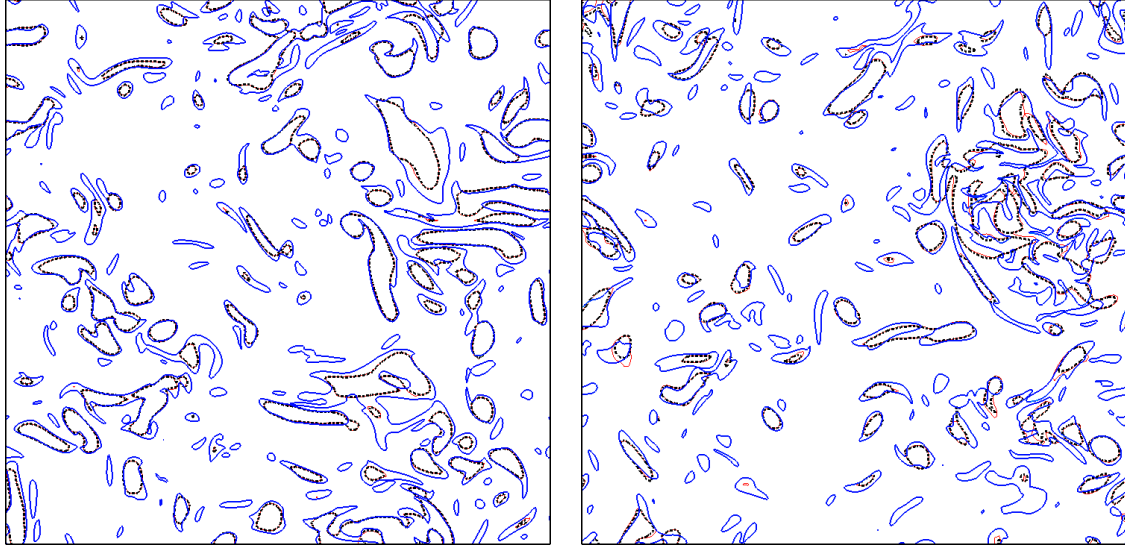
Figure 6: Contours of vorticity magnitude ($|\omega| = 0.18$) at $t = 4.91$ (left) and $t = 68.72$ (right) for DNS (thin blue lines) of 512^3 against DSMA (dotted black lines) and WALE (thick red lines) of 128^3 cells resolution.

the other hand, the DNS solution of the higher resolution has captured much finer scales. However, the LES models were able to simulate the majority of large eddies appearing in the DNS.

5   TAYLOR GREEN VORTEX

The TGV case was chosen as the final wall-free benchmark for the newly implemented LES models. Again the domain was a periodic cube with a length equal to $2\pi L$, where $L = 1$. There is no external force, while the initial conditions read
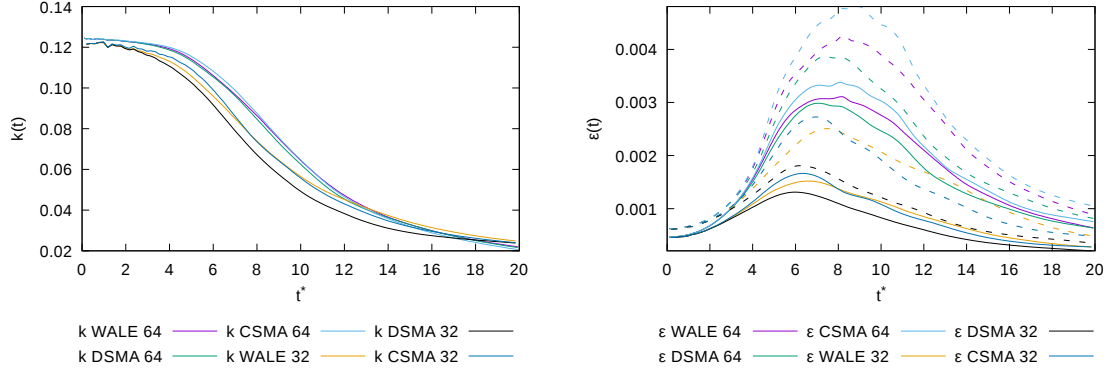
Figure 7: Evolution of kinetic energy (left) and kinetic energy dissipation rate (dashed) against dissipation rate based on enstrophy (solid) (right) of LES for two resolutions.

$$u(\mathbf{x}, t_0) = U_0 \sin\left(\frac{x}{L}\right) \cos\left(\frac{y}{L}\right) \cos\left(\frac{z}{L}\right), \quad v(\mathbf{x}, t_0) = -U_0 \cos\left(\frac{x}{L}\right) \sin\left(\frac{y}{L}\right) \cos\left(\frac{z}{L}\right),$$

$$w(\mathbf{x}, t_0) = 0, \qquad \rho(\mathbf{x}, t_0) = \rho_0 + \frac{\rho_0 U_0^2}{16c_s^2} \left[\cos\left(\frac{2x}{L}\right) + \cos\left(\frac{2y}{L}\right)\right]\left[\cos\left(\frac{2z}{L}\right) + 2\right]. \quad (11)$$

In the above, $\rho_0 = 1$ and $U_0 = 0.1$ leading to Ma ≈ 0.17. To achieve Re $= U_0 L/\nu = 1600$, the viscosity ν was set to $6.25 \cdot 10^{-5}$. Due to the imposed initial conditions, large scale vortices appear initially in the flowfield. As the time passes, they will start to break into smaller eddies that finally will be dissipated. Therefore, this test case has an initial inviscid part that is followed by transition to turbulence and finishes with the decay of turbulence. The above procedure imposes new challenges for the new models.

To test them, two resolutions of 32^3 and 64^3 cells were simulated for WALE, DSMA and CSMA, with $C = 0.1$, while their DNS counterparts crashed. The left plot in Fig. 7 shows the evolution of the turbulent kinetic energy k for these simulations. Firstly, for the lowest resolution some oscillations can be detected in the initial part for all three models indicating insufficient number of cells. For $t^* > 3$, the lines predicted by the three models are diverged, with DSMA has the largest diversion. On the contrary, the WALE is able to recover and for $t^* > 7$ returns similar values to CSMA. This diversion indicates that both WALE and, particularly, DSMA have added extra dissipation during the transition phase compared to CSMA, with $C = 0.1$. The extra dissipation has led to the appearance of fewer small eddies and thus reduction in the peak of the kinetic energy dissipation rate, as one can see in the right plot of Fig. 7. The WALE has predicted a lower peak compared to CSMA. However, it has a smoother slope for the rest of the time showing that was able to adjust better during the phase of decay of turbulence. Moreover, in this plot, the difference between the two dissipations is a measure of the numerical dissipation. In that respect, DSMA had the best performance.

For the highest resolution, there are no apparent discrepancies in the evolution of the turbulent kinetic energy k for the three models. Examining the evolution of the dissipation rates, again both WALE and DSMA have exaggerated the dissipation during
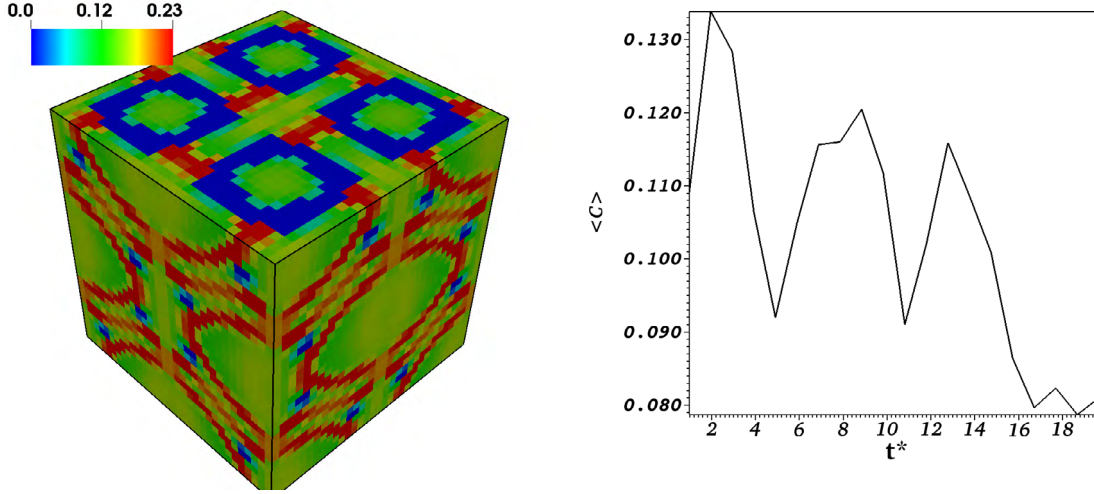
Figure 8: The Smagorinsky constant C estimated at $t^* \approx 3$ (left) and its volume averaged evolution (right) for the DSMA for the resolution of 32^3 cells.

the transition phase, though in this resolution the difference was smaller. Similarly, the CSMA has performed better during the transition phase but the steeper slope in the dissipation rates during the decay phase denotes overestimated dissipation.

To further analyse the behaviour of the DSMA, the left plot of Fig. 8 shows the instantaneous estimation of the constant C over the domain for the lowest resolution at $t^* \approx 3$. Around this moment, the transition to turbulence is initiated. This is also the time when DSMA started to diverge from the other models. It is evident from the plot that the model was able to identify the inviscid large vortices, the square blue regions with a value close to zero, while a value around 0.1 was estimated in the majority of the domain. However, the constant C reached the maximum available value of 0.23 in regions where the vortices interacted. In an attempt to further examine this issue, the same simulation was rerun without trimming the maximum value. The outcome was regions with overestimated values of C, even above 1, indicating that the trimming is necessary. This behaviour is the result of calculating C, Eq. (7), locally and not averaging in homogeneous directions, which are all three in this case. This approximation tends to lead to local maxima [11]. However, a complicated and rather expensive algorithm would be needed to identify the homogeneous directions in a real engineering application and is thus avoided. Finally, the right plot in Fig. 8 presents the evolution of the volume averaged values of C. The maximum peak is located during the first inviscid part and it is around 35% higher than the value for CSMA, explaining the more dissipative behaviour during this phase. Afterwards, as the time passes its value was reduced, as it is anticipated, due to the gradual depletion of the kinetic energy. During the final phase of decay, it reached values below the one of CSMA ($C = 0.1$) leading to the smoother shape of the dissipation rates.

6 CONCLUSIONS

In this paper, we present an easily to implement methodology to verify and evaluate LBM-LES models under wall-free circumstances. To achieve this, initially, we employed the test case of FHIT. For its realisation, the force scheme of [7] was applied, having the important advantage that no initialisation of the velocity field is needed. The disadvantage of this force is the appearance of a resolution-dependent Re_λ. To deal with this issue, one can still compare the energy spectra of different resolutions by applying suitable non-dimensionalisation [14]. Moreover, having a solution of FHIT case, it is trivial to run DHIT by deactivating the external force. In this way, one can compare different resolutions with the same Re_λ, by using the same initial data and appropriately locally volume-average them. In the end, the test case of TGV can challenge the models for the situation of an inviscid flowfield transitioning to turbulence and final decay.

By applying the above procedure, we have verified the two newly implemented models, DSMA and WALE. In the case of FHIT and DHIT, we have examined their performance to deal with a fully developed turbulent field showing an expected behaviour. We present that under a reasonably well-resolved mesh, they could be deactivated. On the other hand, in an under-resolved simulation, they estimated a more depleted dissipation range compared to DNS, improving the stability. In comparison with the CSMA, the WALE had identical behaviour while the DSMA seemed to be slightly more dissipative. In the case of DHIT, they managed to capture accurately the large scales of a DNS of higher resolution. Finally, by running the TGV case, we show that both of them tend to overestimate the eddy viscosity during transition to turbulence. The DSMA had the worst performance, particularly in highly under-resolved meshes. However, they were able to adjust their extra dissipation in the final phase of the decay. As for the DSMA, we conclude that the localisation of the calculation of the constant C leads to local maxima and thus a more dissipative behaviour compared to the other models.

Acknowledgements

REFERENCES

[1] Succi, S. *The Lattice Boltzmann Equation for Fluid Dynamics and Beyond*, OUP Oxford, Oxford, New York, 2001.

[2] Deiterding, R. and Wood, S. L. An adaptive lattice Boltzmann method for predicting wake fields behind wind turbines, in: A. Dillmann, G. Heller, E. Krämer, C. Wagner, C. Breitsamter (Eds.), *New Results in Numerical and Experimental Fluid Mechanics X*, Vol. 132 *of Notes on Numerical Fluid Mechanics and Multidisciplinary Design*, Springer, 2016, pp. 845–857.

[3] Deiterding, R. and Wood, S. L. Predictive wind turbine simulation with an adaptive lattice Boltzmann method for moving boundaries, *J. Phys. Conf. Series* 753 (2016) 082005.

[4] Deiterding, R. and Domingues, M. O. Simulation of the flow around an oscillating cylinder with adaptive lattice Boltzmann methods, *in: P. Ivanyi, B. H. V. Topping, G. Varady (Eds.), Proc. 5th Int. Conf. on Parallel, Distributed, Grid and Cloud Computing for Engineering*, Civil-Comp Press, 2017, p. paper 19.

[5] Feldhusen, K., Deiterding, R. and Wagner, C. A dynamically adaptive lattice Boltzmann method for thermal convection problems, *J. Applied Math. and Computer Science* 26 (2016) 735–747.

[6] Deiterding, R. Block-structured Adaptive Mesh Refinement - Theory, Implementation and Application, *ESAIM: Proceedings* 34 (2011) 97–150.

[7] Abdel Kareem, W., Izawa, S., Xiong, A.-K. and Fukunishi, Y. Lattice Boltzmann simulations of homogeneous isotropic turbulence, *Computers & Mathematics with Applications* 58 (5) (2009) 1055–1061.

[8] Hou, S., Sterling, J., Chen, S. and Doolen, G. D. A lattice Boltzmann subgrid model for high Reynolds number flows, *in: A. T. Lawniczak, R. Kapral (Eds.), Pattern formation and lattice gas automata, Vol. 6, Fields Inst Comm*, 1996, pp. 151–166.

[9] Premnath, K. N., Pattison, M. J. and Banerjee, S. Dynamic subgrid scale modeling of turbulent flows using lattice-Boltzmann method, *Physica A: Statistical Mechanics and its Applications* 388 (13) (2009) 2640–2658.

[10] Germano, M., Piomelli, U., Moin, P. and Cabot, W. H. A dynamic subgridscale eddy viscosity model, *Physics of Fluids A: Fluid Dynamics* 3 (7) (1991) 1760–1765.

[11] Lilly, D. K. A proposed modification of the Germano subgridscale closure method, *Physics of Fluids A: Fluid Dynamics* 4 (3) (1992) 633–635.

[12] Nicoud, F. and Ducros, F. Subgrid-scale stress modelling based on the square of the velocity gradient tensor, *Flow, Turbulence and Combustion* 62 (1999) 183–200.

[13] Frigo, M. A fast Fourier transform compiler, *in: ACM Sigplan Notices, Vol.* 34, ACM, 1999, pp. 169–180.

[14] Pope, S. B. *Turbulent flows*, Cambridge University Press, Cambridge; New York, 2000.

[15] Orphee, J., Gungor, A., Sanchez-Rocha, M. and Menon, S. Direct and large-eddy simulation of decaying and forced isotropic turbulence using lattice Boltzmann method, *in: 36th AIAA Fluid Dynamics Conference and Exhibit*, American Institute of Aeronautics and Astronautics, San Francisco, California, 2006.

A CONSISTENT BOUNDARY METHOD FOR THE MATERIAL POINT METHOD – USING IMAGE PARTICLES TO REDUCE BOUNDARY ARTEFACTS

STEPHAN SCHULZ[1], GODEHARD SUTMANN[1,2]

[1] Interdisciplinary Centre for Advanced Materials Simulation (ICAMS)
Ruhr-University Bochum
D-44801 Bochum, Germany
e-mail: stephan.schulz-x2q@rub.de, web page: http://www.icams.de

[2] Jülich Supercomputing Centre (JSC)
Forschungszentrum Jülich GmbH
D-52425 Jülich, Germany
e-mail: g.sutmann@fz-juelich.de - Web page: http://www.fz-juelich.de

Key words: material point method, particle methods, boundary conditions, materials science, Euler-Lagrangian method

Abstract. The Material Point Method (MPM) is a continuum-based numerical method which discretises the object as material points. It is particularly well suited for and has shown great success in the community for large deformations. Even though it has been widely adopted, there are still fundamental questions to be addressed.

In MPM the material properties are carried on the material points and the dynamics is calculated on an overlaid grid. Afterwards, the material points are integrated according to the grid values using an explicit time integration scheme. The explicit boundary methods are applied on the grid values, such as setting the grid momentum to zero for grid nodes inside a fixed wall. This can cause artefacts in the stress as seen for an object in touch with the wall. These distort the stress multiple grid lengths into the object.

In this paper we propose a novel consistent boundary method to reduce these artefacts. The method is based on image particles, an approach originally developed for electrostatic problems. This concept allows a consistent formulation for the momentum field on both the grid and particles. We demonstrate a way of optimization that makes the explicit construction of mirror particles unnecessary.

The explicit boundary method and image particle method are then compared using numerical examples featuring stress induced by simple shear and body forces.

These numerical examples show a significant reduction of boundary artefacts using the image particle method.

1 INTRODUCTION

Materials science simulations have evolved into a powerful branch which complements experiment and theory and provides additional insight into, e.g., structure and mechanical properties on different length scales. On the macroscopic level, continuum methods based on Eulerian methods, e.g., finite element techniques (FEM) had a great success in describing mechanical, thermodynamic or elasto-plastic properties of materials. Alternatively, Lagrangian methods, e.g., smoothed particle hydrodynamics (SPH) have been adopted to overcome the computational overhead in administrating complex meshes in system set ups, involving either complex geometries or time dependent deformation [1], and presenting an alternative approach to FEM. However, problems in terms of momentum and/or energy conservation, appearance of dynamical artefacts or computational overheads due to neighbour searches poses, for certain simulation scenarios, limits on quantitative comparison with, e.g., FEM. To overcome in part some problems of SPH and to improve some features of FEM, an alternative approach, the materials point method (MPM), has been suggested, which is an Eulerian-Lagrangian method, i.e., transporting physical properties in time on particles but performing computations on a mesh. This approach gains flexibility in adjusting to complex scenarios by self adaptation through the use of particles and avoiding the need of re-meshing the computational grid in cases of large deformation by filling the space with particles, which are mapped onto a regular mesh, that is simple to administrate. Since its development, the method has been applied to a growing number of application scenarios.

For simulations of deformations, MPM has been applied to systems, such as snow [2], foam [3] or sand [4]. It has also been applied to cold spraying of particles [5], simulation of tunnelling induced deformations [6], sliding contact ploughing [7] or micro milling [8].

MPM originates from fields of particle simulation methods, applied to systems where the detailed short range nature of interactions is coarse grained and known as Particle In Cell (PIC) method [9]. A number of variants were later on developed which were based on similar assumptions, but modified details to better conserve quantities, e.g., energy, momentum or angular momentum. E.g., the Fluid Implicit Particle (FLIP) method consists of a modification to better simulate fluids [10]. For materials science, MPM was the first approach to solve the specific underlying equations on the continuum level [11], which was later on improved by versions respecting rotational invariants (RPIC) or affine fields (APIC) [12]. Although, MPM as been further developed towards an alternative to FEM, some problems have still not been sufficiently considered and are often suppressed in discussions about the method. One important aspect is the consistent treatment of boundary conditions, which affect slip-, no-slip or prescribed force- or velocity boundary conditions. E.g., in the stress field of a material, often an artificial oscillatory behaviour is observed, which might lead to instabilities or error propagation. The present article is a contribution to increase awareness to this type of artefacts in MPM and to provide a method to avoid such artefacts in materials simulations.

2 THE ALGORITHM

We are using the APIC method by Jiang et al. [12] and Jiang, Schroeder, and Teran [13] with a few additions shown in this section and explicit time integration.

The simulation is initialised with the particles and their corresponding material properties. First the momentum is transferred onto the grid. Then the internal state, the strain and deformation gradient, as well as stress of the particles, is updated followed by the internal forces based on the particles' stress and external forces. The resulting forces on the grid are then used to integrate the momentum of the grid nodes calculating the dynamics. These are then transferred back onto the particles and their velocities, positions, strains, deformation gradients are updated, propagating the material properties. Boundary conditions are omitted here, because they are described later in subsection 2.3.

In the following we will index quantities on nodes with i and on particles with p. If all variables of an equation are from the same time step n it will be omitted.

2.1 Damped dynamics

In some cases a fully dynamic simulation is unnecessary and can lengthen the simulation time needed to reach equilibrium, if at all possible. For these cases we implement a simple reduction of dynamics by dissipating the kinetic energy in every time step. This is done by setting the grid momentum to zero after transferring the particle properties to the grid. The following integration is then just a relaxation of the particles along the gradient of the force.

2.2 Force description

To apply forces on (selected) particles an acceleration is applied. The total force is thereby given as

$$\boldsymbol{F} = \int \rho \, \boldsymbol{b} \, \mathrm{d}V \tag{1}$$

$$= \sum_p m_p \boldsymbol{b}_p \tag{2}$$

$$= \sum_{i,p} m_p \boldsymbol{b}_p w_{ip}. \tag{3}$$

For a constant acceleration $\boldsymbol{b}_p$ and particle mass m_p this results in

$$\boldsymbol{F} = N_p m_p \boldsymbol{b}_p. \tag{4}$$

Here ρ is the mass density and $\boldsymbol{b}$ acceleration of the material. Because the acceleration $\boldsymbol{b}_p$ is weighted by the particle mass, the resulting force is independent of the number of particles and only depends on the total mass of the accelerated object.

2.3 Boundary conditions

When simulating most systems, their boundaries must be treated specifically. For some we prescribe a desired velocity, for others a certain force acting on objects on contact with

the boundary. Here we will focus on no-slip boundaries, where no relative motion is desired between the boundary and objects in touch with it, slip boundaries, where only motion parallel to the boundary is desired and a force based boundary, that also applies a certain force on the object in contact.

We will see that the commonly used boundary conditions induce stress artefacts as visible in Figure 1 for example. In section 3 we investigate the artefacts closer for two example set ups.

2.3.1 Explicit no-slip

To apply the no-slip boundary a straightforward method is to set the node momentum and acceleration of nodes within the boundary to zero [14]. It is important to not only set $q_i = 0$ after the particle to grid transfer, but also to set the total force $\dot{q}_i = 0$. Otherwise, particles can slowly move into the boundary under a continuous force.

2.3.2 Explicit slip

To enforce full slip boundaries a similar method is used, but only the momentum and acceleration perpendicular to the boundary are set to 0. So for a boundary with the normal $\hat{n}$ we modify the momentum as

$$q' = q - q_\perp (= q_\parallel) \tag{5}$$
$$= q - \hat{n}(\hat{n} \cdot q). \tag{6}$$

2.3.3 Boundary object

The image particle treatment as described above does not include additional external forces or a force based boundary. What we can do instead is use a boundary layer of particles which are accelerated and have no slip with regards to the original object. The boundary layer should have a certain thickness and can also be wider than the object. Note, since the boundary is defined using the acceleration of the boundary layer particles, the thickness and width changes the total force acting on the object. Care must be taken when setting up the system to get the desired forces.

2.3.4 Image particles

When running simulations using the above mentioned boundary conditions certain artefacts appear in the stress distribution as visible on the left in Figure 1. To mitigate these artefacts we propose a new method to implement boundary conditions.

This new method originates from electrostatics and is known as image charges [15]. Mirroring an electric charge on a plane with a sign change causes a constant electric field of $0\,\mathrm{V\,m^{-1}}$ at the plane. The same can be done for the particles' properties in MPM.

For a particle shown as a cross in Figure 2 near a planar boundary, we create an image particle at the same distance on the opposite side of the wall. With the vector d
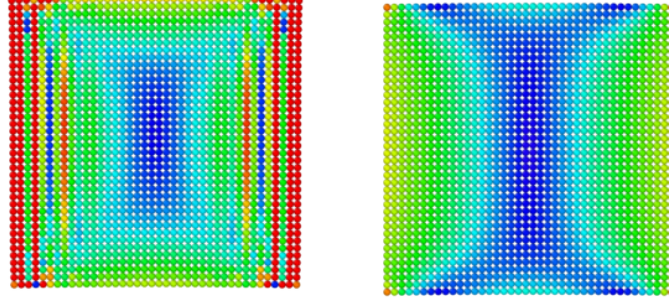
Figure 1: An example of the artefacts introduced by the explicit boundary conditions. The left figure shows the von Mises stress for the explicit boundary conditions and the right figure with the proposed image particle method. This set up is further investigated in section 3.
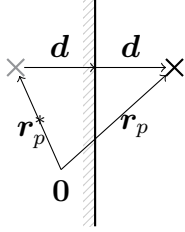
Figure 2: The particles and its image counterpart are separated by $2d$. That vector is perpendicular to the boundary. An arbitrary origin $\mathbf{0}$ is shown in the figure.
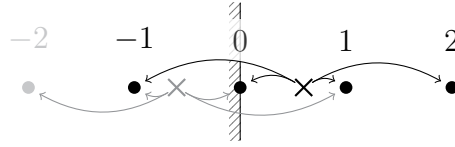
Figure 3: Shown are a particle (black cross) its virtual counterpart (grey cross) the grid nodes (circles) and to which grid nodes quantities are contributed. The light grey grid node does not contribute to the original particle and can be ignored.
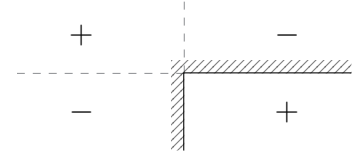
Figure 4: The sign changes of the mirrored quantities are shown for a positive quantity in the lower right quadrant. Each mirroring changes the sign.

describing the shortest distance from the boundary to the particle at $\mathbf{r}_p$ the image particle is positioned at

$$\mathbf{r}_p^* = \mathbf{r}_p - 2\mathbf{d}. \tag{7}$$

This process has to be repeated for each boundary, as seen in Figure 4. The particle is represented with a positive quantity in the lower right quadrant. It is then mirrored to the lower left quadrant with a negative quantity. For multiple boundaries we have to mirror image particles as well. So both of these particles are then mirrored into the upper quadrants with their respective sign changes. The order of the mirroring does not change the result, but for clarity we are first treating x direction, then y and lastly z.

A particle with respect to the grid nodes is shown in Figure 3. We see the four nodes to which properties are transferred to, indicated with black arrows. The nodes $i \leq 0$ are boundary nodes. Node -2 can safely be ignored, because it does not transfer its

quantities onto any real particles, if we assume the material stays outside the boundary. The contributions of the image particles are shown with grey arrows.

The purpose of this set up is to reach a no-slip condition at the boundary, which means the momentum and force of the boundary node should be 0. The question arises, if we can simply change the sign of the properties that are being transferred. The desired result is, that the contribution of the particle to grid node i is counteracted by the image particles contribution. In the case of the grid momentum a change of sign in the particle velocity almost suffices as can be seen from the particle to grid transfer of the momentum

$$\boldsymbol{q}_i = \sum_p w_{ip} m_p \boldsymbol{v}_p + \sum_p w_{ip} m_p \mathbf{B}_p (\mathbf{D}_p)^{-1} (\boldsymbol{r}_i - \boldsymbol{r}_p). \tag{8}$$

In the case of APIC the affine matrix $\mathbf{B}_p$ has to be treated as well. For this we look at the behaviour when the relative position $\Delta \boldsymbol{r}_{ip}$ changes sign in one component. The transfer function is symmetric, so

$$w_{ip} = w_{ip}^*. \tag{9}$$

Mirrored properties will be indexed with a star. The second term of the momentum contains $(\boldsymbol{r}_i - \boldsymbol{r}_p)$ $(= -\Delta \boldsymbol{r}_{ip})$ which changes sign only in the component the particle is mirrored against. This means the affine matrix has to change in all columns except the one we mirror in. Using Greek indices for the components and the Kronecker delta we can write this as

$$B_{p,\alpha\beta}^* = -B_{p,\alpha\beta} + 2B_{p,\alpha\beta}\delta_{\beta\kappa} \tag{10}$$

for the mirror direction κ. The mass will be untouched and the particle acceleration can simply change its sign.

As an example let's mirror in the y direction, so $\kappa = 2$. Then we have

$$\Delta \boldsymbol{r}_{ip}^* = \begin{pmatrix} \Delta r_{ip,1} \\ -\Delta r_{ip,2} \\ \Delta r_{ip,3} \end{pmatrix} \tag{11}$$

and the mirrored affine matrix must be constructed as

$$\mathbf{B}_p^* = \begin{pmatrix} -B_{p,11} & B_{p,12} & -B_{p,13} \\ -B_{p,21} & B_{p,22} & -B_{p,23} \\ -B_{p,31} & B_{p,32} & -B_{p,33} \end{pmatrix} \tag{12}$$

so the resulting mirrored velocity is

$$\boldsymbol{v}_p^* = -\boldsymbol{v}_p. \tag{13}$$

The treatment of the particle state, that will result in the opposite internal force contribution, is more complex. Even for the simple Hooke's Law this is not necessarily easy. However, in general we have to invert the constitutive equation to know how to

transform the strain or deformation gradient. This follows from the definition of the internal force on the grid nodes

$$\boldsymbol{f}_i^{(\mathrm{i})} = -\sum_p V_p \sigma_p \cdot \boldsymbol{\nabla} w_{ip} \tag{14}$$

where the particle stress is used to calculate the internal force. To see how the stress has to transform we first look at the transfer function gradient. Similar to the relative distance earlier only the component of mirroring changes sign. The internal force is the dot product of the stress and the gradient, so, as with the affine matrix, all components of the stress not inverted by the transfer function gradient have to be inverted. This means

$$\sigma_{p,\alpha\beta}^* = -\sigma_{p,\alpha\beta} + 2\sigma_{p,\alpha\beta}\delta_{\beta\kappa}. \tag{15}$$

For a Poisson ratio of 0 and Hooke's Law this applies to the strain as well, since it is a linear relationship.

Luckily, the exact properties of the image particle are not needed, because we only need the contributions of it. This means we can simply calculate the contributions of our particle and add the negative of those to the appropriate grid nodes the image particle would transfer to. For this to work we have to assume the transfer function has the same value for both particle node pairs. This is only given if the particle is mirrored exactly at a plane parallel to two axes and aligned on the node positions. Taking Figure 3, the transfer function between the particle and node 0 is then the same as between the image particle and node 0. The same holds between the particle and node 1, and the image particle and node -1.

Image charges work, because of the anti symmetry in the resulting field. This ensures the field at the boundary, the symmetry plane, is always zero. If a second plane is introduced, a second boundary, it must also be anti symmetric to the first plane. This can only be satisfied for a perpendicular plane. Therefore, complex boundaries are not supported, but only boxes.

Unaligned boundaries are also possible, albeit with a bit more computational effort. Assuming unaligned boundaries that are still parallel to the axis planes, instead of just adding the corresponding value of the particle to the image particles grid node, the weight is recalculated. So the particle property has to be reused at a new position, the mirror particle's position. This means additional evaluation of the transfer function and its gradient. This also causes additional bookkeeping effort for the caching of these values as is done for the normal particles as well.

3 THE SIMULATION SET UP

We will consider two types of boundaries. First, no-slip boundaries where the material should not move relative to the boundary. Second, slip boundaries with a constant force acting on the material parallel to the boundary. In both cases the boundary itself is fixed. The simulations are done in three dimensions with the material block as a cube. The relevant simulation parameters are shown in Figure 1. These parameters result in

64 000 particles. The method supports a wide variety of constitutive equations for the material, such as neo-Hookean, or Drucker-Prager based elastoplastic [4] materials. Only the calculation of the internal force is needed, for which the stress of the particle is used. Here we will use Hooke's Law to calculate the stress from the strain

$$\sigma = \mathbf{C}\varepsilon \tag{16}$$

with the stiffness tensor $\mathbf{C}$. The Young's modulus Y and Poisson ratio ν are used as material properties.
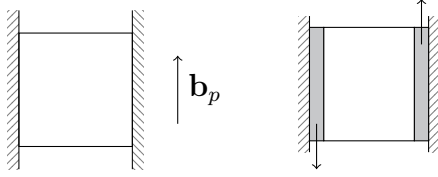
Figure 5: On the left a body force is acting on the material and the left and right walls are no-slip. On the right a simple shear is created by applying a constant force to the left and right boundary layers. The two walls are full slip.

Table 1: Simulation parameters used for the example set ups.

Δt	$1 \times 10^{-4}\,\mathrm{s}$
Δh	$0.05\,\mathrm{m}$
N_p/cell	8
Y	$1 \times 10^4\,\mathrm{Pa}$
ν	0
L	$1\,\mathrm{m}$
b_p	$100\,\mathrm{m\,s^{-2}}$
$|b_{p,\mathrm{boundary}}|$	$400\,\mathrm{m\,s^{-2}}$
L_{bd}	$0.5\Delta h$

For comparisons, we will look at the von Mises stress defined as

$$\sigma_v = \left(\frac{1}{2} \big((\sigma_{xx} - \sigma_{yy})^2 + (\sigma_{yy} - \sigma_{zz})^2 + (\sigma_{zz} - \sigma_{xx})^2 \big) \right.$$
$$\left. + 3\big(\sigma_{xy}^2 + \sigma_{yz}^2 + \sigma_{zx}^2 \big) \right). \tag{17}$$

3.1 No-slip boundary

In the first case we induce a strain in the material by applying a constant acceleration $\boldsymbol{b}_p$ parallel to the boundary as seen on the left in Figure 5. The left and right boundaries should result in no-slip and the other boundaries are open.

Using the explicit no-slip boundary conditions from subsubsection 2.3.1, the stress shows very large oscillations at the no-slip boundaries on the left and right. The resulting von Mises stress distribution is shown in Figure 6 on the left. These oscillations are quite wide and reach multiple grid widths into the material. In these simulations the particles are half a grid width apart.

These oscillations are on the length scale of a few grid widths which can be seen for a higher resolution simulation in the second image of Figure 6. There the same set up has been used, but the grid width was reduced by a factor of five to $\Delta h = 0.01\,\mathrm{m}$, resulting in 8 000 000 particles. The stress distribution is now correctly modelled inside the object, but due to the additional computation time reducing the grid width not a valid option.
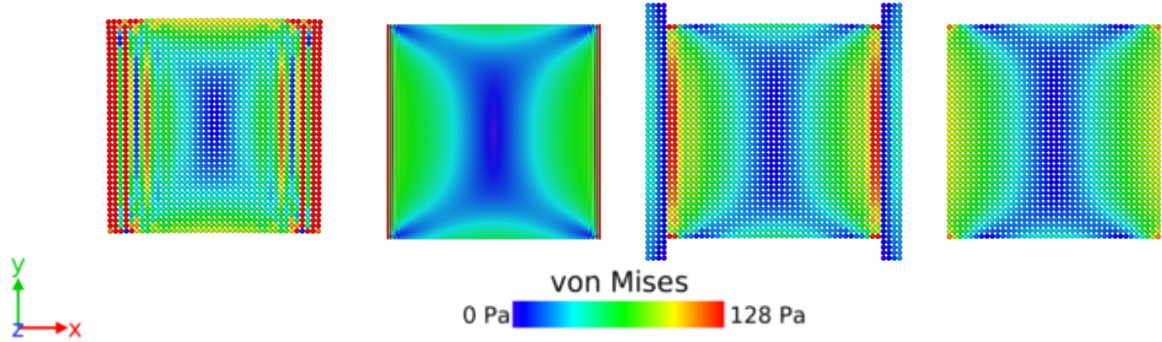
Figure 6: The no-slip set up for the different boundary conditions. From left to right they are the explicit method in normal and higher resolution and a boundary object, followed by our proposed image particle method. The boundary artefacts appear on the length scale of grid widths at the left and right boundary. For the image particle method only small artefacts in the corners are visible.

These artefacts are reduced if a buffer object is introduced between the material and the boundary as shown in the third image of Figure 6. Here the buffer object is two grid widths deep, which equals the penetration of the used transfer function. A very clear difference to the unbuffered method is also visible at the top and bottom boundaries. Except for the one grid width wide area at the left and right boundary, the expected stress is computed quite well. The drawback for this method is the additional computational effort for the buffer objects, which is non negligible.

These artefacts are further reduced with our image particle method from subsubsection 2.3.4. The result is shown on the right in Figure 6. No artefacts can be seen at any boundary. Only the corners show an aberration as small as a grid cell. Although the image particles require additional computational effort as well, with optimizations this can be very small and limited to simple additions.

Another aspect of interest is the time the simulations take to reach a steady state. The explicit boundary condition has not converged after 1000 time steps (0.1 s), with the main change still occurring in the boundary region of large artefacts. The buffer objects decreases this time to about 250 time steps (0.025 s), whereas the image particles cause a fast convergence in about 100 time steps (0.01 s).

The run time of these simulations shows the inefficiency of the buffer object method. That method took about 50 % longer to run than the explicit method. This is mainly caused by the introduction of new particles by the buffer object, which actually are not needed for the image particles, since we just duplicate the transfer from particle to grid. The difference of run time between the image particle method and the explicit method is within the margin of error.
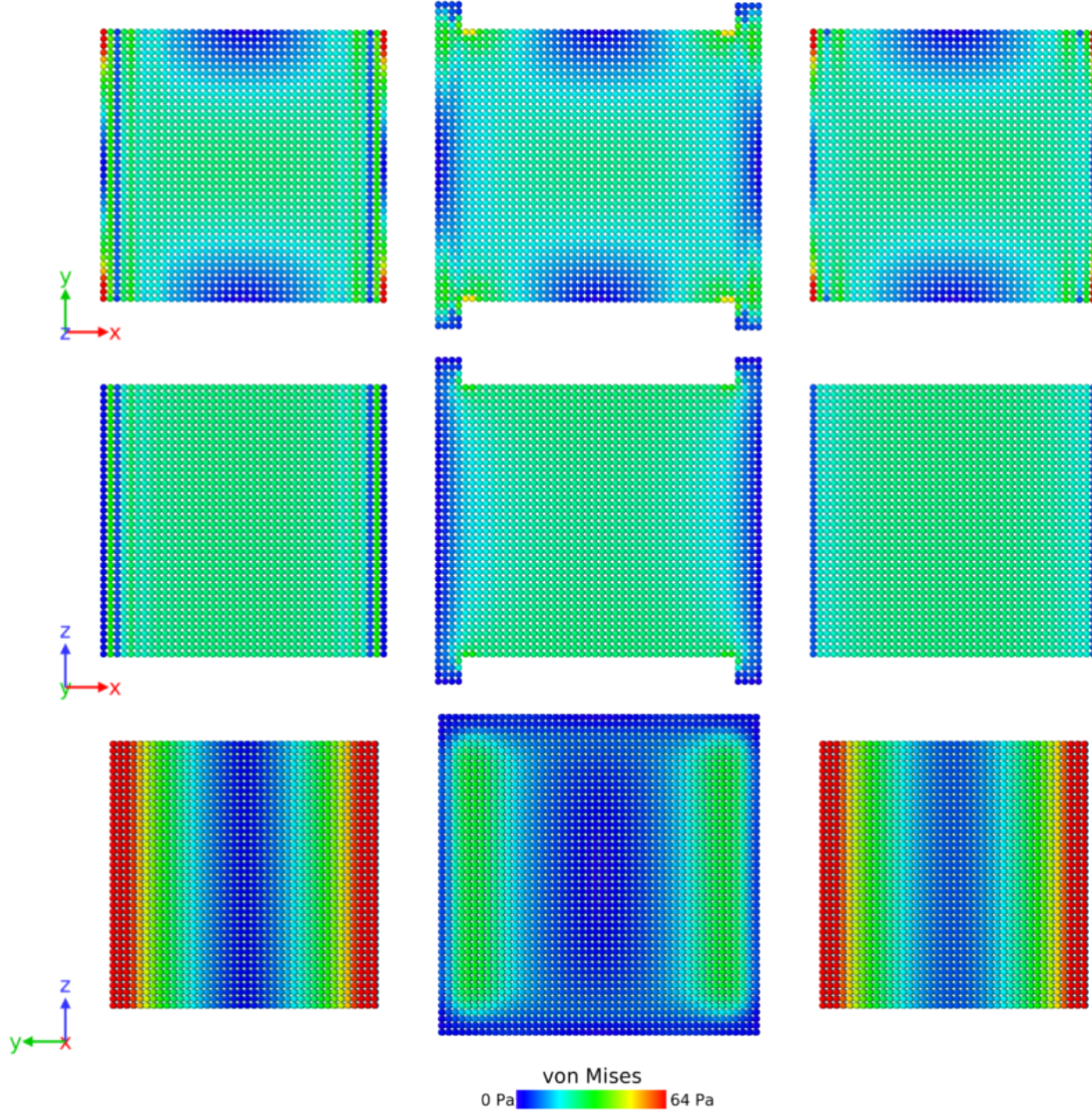
Figure 7: Three methods are shown in columns. The first two are the explicit method with a single and respectively four particle layer boundary object. The last one also has a single layer boundary object, but uses the image particle method. The rows show different views of the stress distribution of the systems. The first row shows the stress in the middle of the system with the external shear forces applied on the left and right towards positive and negative y direction. The second row has the forces on the left and right into and out of the page. The last row shows the boundary layer from the left.

3.2 Constant force boundary

To study force based boundaries a simple shear set up as shown in Figure 5 on the right is used. The shear is induced by an acceleration b_p acting on the object between the material and the slip boundary.

For a boundary object with one particle thickness the von Mises stress is shown in the first column of Figure 7. The artefacts from the no-slip case are much less pronounced, but still visible. They also still reach a few grid widths into the material.

For an increased thickness of the boundary object of two grid lengths, the depth of the transfer function, we see much less of the oscillating artefacts. The results are shown in the second column in Figure 7. The stress distribution is smooth inside the material and across into the boundary object. The edges along z direction show up in the upper figure in the corners as yellow. The stress is, however, much improved compared to the thin object. Due to the larger boundary object, this simulation takes about 23 % longer to run. However, the image particle method and explicit method have about the same run time.

The boundary artefacts can also be reduced by using the image particle method, modified to provide a slip boundary, and a one particle boundary layer. This results in the stress shown on the right in Figure 7. The artefacts are much smaller than for the explicit boundary method, but still more pronounced than for the thick boundary object.

In other particle based simulation methods, such as SPH, similar boundary effects are observed as have Ma and Hartmaier [1].

4 CONCLUSION AND FURTHER WORK

We have shown that the image particle method efficiently removes the high frequency boundary oscillations in the stress for a no-slip and slip boundary. In a simple shear set up induced by boundary objects with forces, the stress field is more accurately represented than in the case of the normal boundary condition. Although small artefacts remain in the extreme case of a thin, one particle layer, boundary object.

The image particle method can be highly optimized for planar boundaries aligned with node positions. Unaligned boundaries are also possible, but require additional computational effort, chiefly because the transfer weights have to be recomputed.

An additional force acting directly on the image particles and propagating onto the grid is easy to implement, but more difficult to control. The total force acting on the system depends on both the volume of image particles and whether the grid nodes onto which the image particles contribute to, have an effect on real particles.

The method shown does not include boundaries with a limited extent, but assumes unbounded planes. It can also be adapted for walls and boundaries with limited extent, but a few additional considerations have to be made. Further work into this direction will be conducted, since it is required for the simulation of more complex environments, such as equal channel angular pressing. Furthermore, the parameters such as the thickness and extent of the boundary object can be further optimized.

References

[1] Ma, A. and Hartmaier, A. A crystal plasticity smooth-particle hydrodynamics approach and its application to equal-channel angular pressing simulation. *Model. Sim. Mat. Sci. Eng.* **24** (2016), 085011.

[2] Stomakhin, A., Schroeder, C., Chai, L., Teran, J., and Selle, A. A material point method for snow simulation. *ACM Trans. Graph.* **32** (2013), 102.

[3] Ram, D., Gast, T., Jiang, C., Schroeder, C., Stomakhin, A., Teran, J., and Kavehpour, P. A material point method for viscoelastic fluids, foams and sponges. *Proceedings of the 14th ACM SIGGRAPH/Eurographics Symposium on Computer Animation.* ACM. 2015, 157–163.

[4] Klár, G., Gast, T., Pradhana, A., Fu, C., Schroeder, C., Jiang, C., and Teran, J. Drucker-prager elastoplasticity for sand animation. *ACM Trans. Graph.* **35** (2016), 103.

[5] Liu, Y. and Xu, C. Investigating the cold spraying process with the material point method. *Int. J. Mech. Mat. Design* **15** (2019), 361–378.

[6] Fern, E. J. Modelling tunnel-induced deformations with the material point method. *Comp. Geotechnics* **111** (2019), 202–208.

[7] Mishra, T., Ganzenmüller, G. C., Rooij, M. de, Shisode, M., Hazrati, J., and Schipper, D. J. Modelling of ploughing in a single-asperity sliding contact using material point method. *Wear* **418** (2019), 180–190.

[8] Leroch, S., Eder, S., Ganzenmüller, G., Murillo, L., and Ripoll, M. R. Development and validation of a meshless 3D material point method for simulating the micro-milling process. *J. Mat. Proc. Tech.* **262** (2018), 449–458.

[9] Harlow, F. H. The Particle-In-Cell Method for Numerical Solution of Problems in Fluid Dynamics. *Experimental Arithmetic, High Speed Computing and Mathematics.* American Mathematical Society, 1963, 269–288.

[10] Brackbill, J. U., Kothe, D. B., and Ruppel, H. M. FLIP: a low-dissipation, particle-in-cell method for fluid flow. *Comp. Phys. Commun.* **48** (1988), 25–38.

[11] Sulsky, D., Zhou, S.-J., and Schreyer, H. L. Application of a particle-in-cell method to solid mechanics. *Comp. Phys. Commun.* **87** (1995), 236–252.

[12] Jiang, C., Schroeder, C., Selle, A., Teran, J., and Stomakhin, A. The affine particle-in-cell method. *ACM Trans. Graph.* **34** (2015), 51.

[13] Jiang, C., Schroeder, C., and Teran, J. An angular momentum conserving affine-particle-in-cell method. *J. Comput. Phys.* **338** (2017), 137–164.

[14] Buzzi, O., Pedroso, D. M., and Giacomini, A. Caveats on the implementation of the generalized material point method. *Comp. Model. Eng. Sci.* **31** (2008), 85–106.

[15] Jackson, J. D. *Classical Electrodynamics.* 3rd ed. Wiley, 1998.

NUMERICAL MODELLING OF VAL D'ARÁN LANDSLIDE WITH MATERIAL POINT METHOD

Gaia Di Carluccio[1]*, Núria M. Pinyol[2], Pau Perdices[2], Marcel Hürlimann[2]

[1]Centre Internacional de Mètodes Numèrics en Enginyeria (CIMNE), Barcelona, Spain
e-mail:gaia.di.carluccio@upc.edu

[2]Department of Civil and Environmental Engineering, Barcelona, Spain
Universitat Politècnica de Catalunya (UPC), Barcelona, Spain
e-mail:nuria.pinyol@upc.edu
pau.perdices@estudiant.upc.edu
marcel.hurlimann@upc.edu

Key words: Landslide, Runout, Constitutive modelling, Material point method.

Abstract. *Flow-like landslides in mountainous areas can cause extensive damages due to their high velocity and long run-out distance. This work presents a real case of landslide occurred on 11 May 2018 in Val d'Arán (Catalonia, Spain). It involved about 50.000 m^3 of glacial and colluvial material, travelling about 250 m until the valley floor and climbing about 100 meters on the opposite hillside. With the aim to assess the capabilities of the Material Point Method (MPM) [1,2] plane strain analyses with the 2-phases 1-point formulation [3,4] are conducted on a representative section. First, the slope material is described with the Mohr-Coulomb criterion. Second, a constitutive model based on the critical state theory (Ta-Ger [5,6]), is adopted. The simulations results led to conclude that an advanced constitutive model, able to simulate the strength loss of the material during the movement, is required to reproduce flow-like landslides and to obtain realistic results in terms of long run-out distance.*

1 INTRODUCTION

Velocity and run-out of landslides are key factors determining the damage induced by landslide. Estimation of the initiation and post-failure behaviour is essential for evaluating the risk and quantifying the magnitude of consequences. The prediction of both run-out distances and velocity was investigated experimentally through flume laboratory tests [7]–[11] and numerically in the framework of the continuum [12]–[16] and discontinuous methods [17]. However, its numerical modelling is still challenging mainly because it involves large deformations, dynamic factors and requires a proper constitutive model able to reproduce the transitional behaviour between solid and fluid.

The landslide investigated in this work occurred on 11 May 2018 in Val d'Arán (Catalonia, Spain) after a period of significant rainfall. It involved about 50.000 m^3 of glacial and colluvial material, travelling about 280 m until the valley floor and climbing about 100 meters on the opposite hillside [18]. Based on field observation and laboratory tests conducted, both materials can be classified as clayey sands. Although the evolution of groundwater level and

pore water pressures prior the failure is unknown, one of the hypotheses that could explain the failure triggering is the soil saturation induced by the water table rising. If the soil is susceptible to liquefaction, excess pore water pressure can be generated with the associated decrease of effective stress, affecting the velocity and post-failure behaviour of the landslide.

2 METHODOLOGY

The numerical method adopted in this study is the Material Point Method (MPM). It was developed to represent fluid dynamics [19] and extended to soil mechanics problems [1,2]. The method is intermediate between particle-based methods and finite element methods. The continuum media is described by a set of Lagrangian materials points that can move with the material and a computational mesh that remains fixed through the calculation and covers the whole domain. Each point represents a portion of the domain and carries all the information of the material while the governing equations are solved at the nodes of the computational background. This double discretization can simulate large deformations without problems associated with mesh distortion, which are typical in conventional finite element methods.

In this study, plane strain analyses with the MPM 2-phases 1-point formulation [3,4] are conducted on a representative section by using the Anura3D software, developed by the MPM Research Community (www.anura3d.com).

The failure triggering was probably due to the soil saturation induced by the water table rising. With the aim of evaluating the initiation of the movement, different hypotheses of phreatic levels are considered by modelling the slope material with the Mohr-Coulomb criterion. Then, the strength loss of the failed mass and its effect on the run-out distance are investigated by introducing a softening behaviour of the material. Finally, the limitations of the previous analyses are discussed and the advanced constitutive model Ta-Ger [5,6] is adopted to reproduce the flow-like landslide.

The objective is to ascertain if this model is able to track the triggering of the movement and the post-failure behaviour by reproducing the strength loss due to the propagation of pore water pressure, allowing the landslide mass to travel a long distance.

3 NUMERICAL MODEL

The geometry of the problem and the computational mesh are given in Figure 1. Plane strain conditions are imposed by means of the boundary conditions restricting out-of-plane deformation and horizontal displacements along the vertical contours. The computational mesh is generated by using a 3D mesh of linear tetrahedral elements with a size of 5 m. A thin slice of one element thickness is considered to simulate 2D conditions. Initially, four material points are distributed within each element in the position of Gauss points.

From a geological point of view, the slope is characterized by a layer of colluvium material on the top of a deposit of glacial origin with irregular thicknesses. The bedrock is located at a depth of about 25 m and is modelled as linear elastic as it is not involved in the failure. In order to simplify the geological model, the colluvial and glacial layers are represented as a unique material. This assumption can be accepted since the results of laboratory tests provided similar properties for both materials. In particular, a friction angle $\phi_{res}' = 33°$, obtained from ring shear tests, is assumed in the simulations.

For a given phreatic level, the material above is defined as dry material, while the one below is considered fully saturated. A more accurate analysis may be performed by modelling the slope as a 3-phase unsaturated material, however, in this work, a simplified simulation is presented.
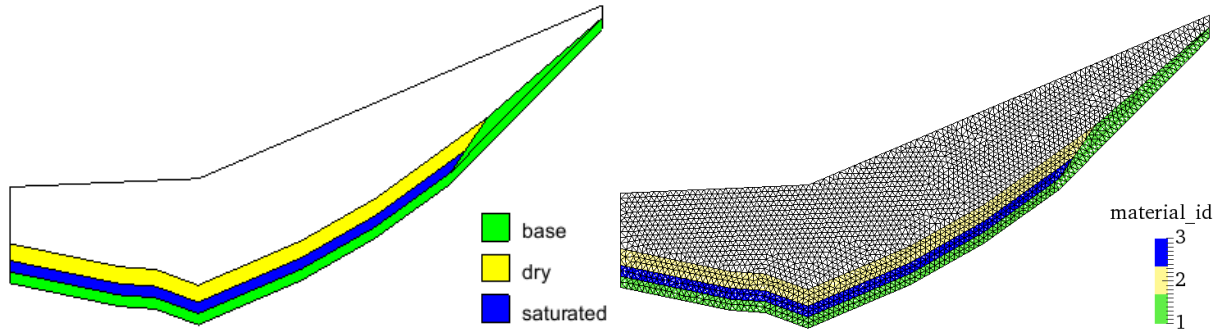
Figure 1: Geometry and computational mesh for the phreatic level located at -15 m of depths from the upper surface.

4 RESULTS

4.1 Drained analysis with Mohr-Coulomb

As a first approximation, the Mohr-Coulomb constitutive model is used to model the colluvial and glacial layers and drained conditions are considered for the saturated material, thus no excess pore water pressures are computed. The material properties are summarized in Table 1. The simulation is carried out in two stages. Stresses are initialized by applying a quasi-static gravity loading. A homogeneous local damping factor $\alpha = 0.75$ is applied to reach a quasi-static equilibrium state in a faster way allowing a considerable reduction in the computational time. In the second stage, the full dynamic behaviour of the soil is analysed and a small local damping factor $\alpha = 0.05$ is used in order to simulate the natural energy dissipation of the material.

Table 1. Mohr-Coulomb model parameters.

Parameter	Symbol	Unit	Value
Initial porosity	n	-	0.48
Young Modulus	E	kPa	10000
Poisson ratio	ν	-	0.33
Friction angle	ϕ'	°	33
Cohesion	c'	kPa	5

Figure 2 shows the results of the numerical simulations for the different assumption in the depth of the phreatic levels. In drained conditions, the water table rising leads to an increase in the destabilizing forces but they are not sufficient to accelerate the slide and reach the observed run-out. This result seems to indicate that during the movement the resistance offered by the mobilized mass significantly reduced. In order to investigate this aspect, in the second simulation, the slope material is described with Mohr-Coulomb with strain softening model.
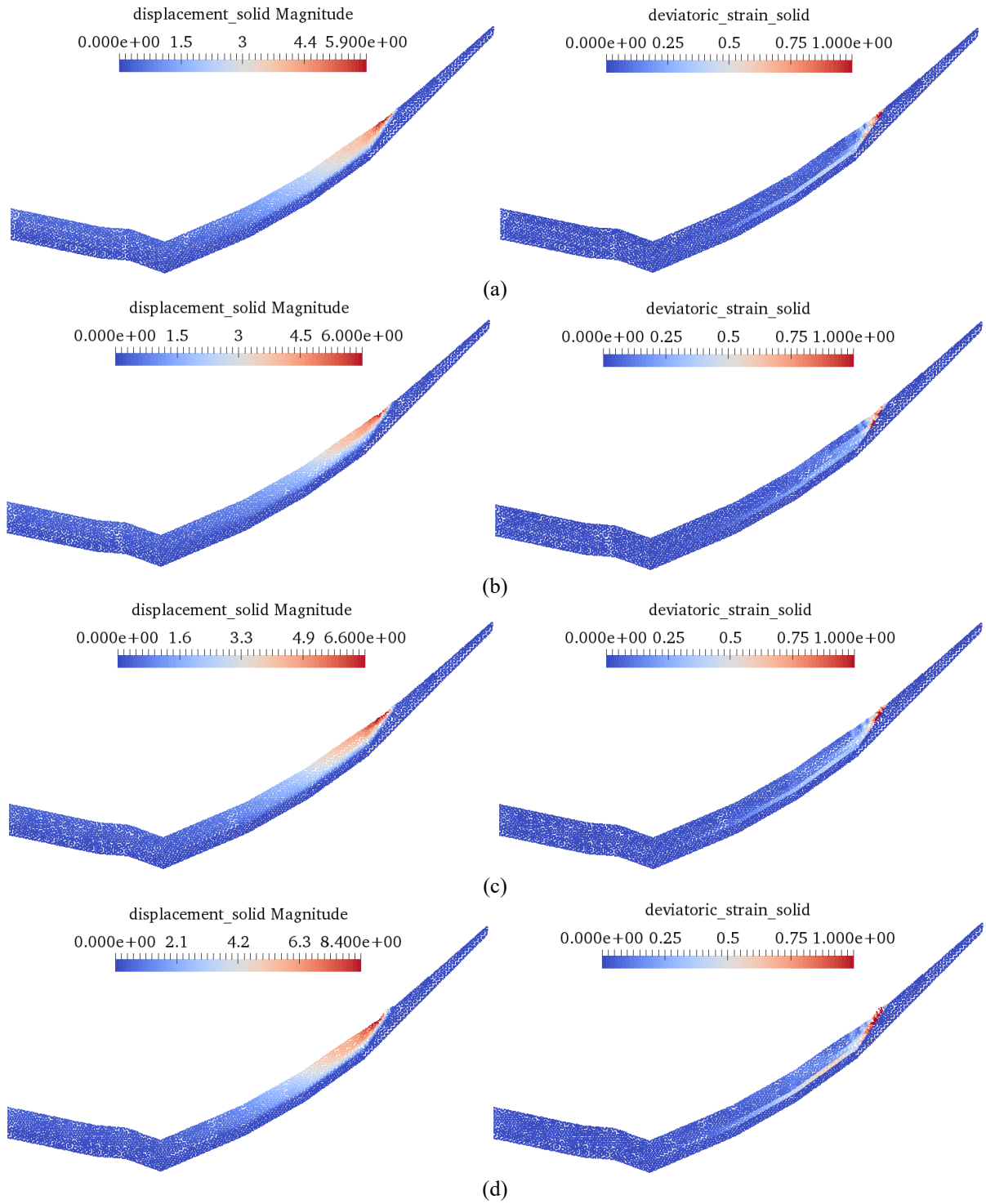
Figure 2: Total displacement and accumulated deviatoric strain results (after 10 seconds) for different depths of phreatic levels (PL) by using the Mohr-Coulomb model. (a) PL = −15m; (b) PL = −10m; (c) PL = −5m; (d) PL = 0 m.

4.2 Drained analysis with Mohr-Coulomb Strain Softening

The softening behaviour of the soil is introduced by reducing the effective strength parameters with the accumulated equivalent plastic strain. The strength loss of the material after the landslide triggering can generate a progressive failure phenomenon and facilitates the acceleration of the failed mass. For the case of phreatic level located at the surface, the residual values of cohesion and friction angle that needed to simulate the long run-out distance are shown in Table 2. The table also indicates the rest of the model parameters. The shape factor is an additional parameter that controls the rate of strength decrease with shear displacement. The simulation is carried out in two stages as described in the previous section.

Table 2: Mohr-Coulomb with Strain Softening model parameters.

Parameter	Symbol	Unit	Value
Initial porosity	n	-	0.48
Young Modulus	E	kPa	10000
Poisson ratio	ν	-	0.33
Peak friction angle	ϕ'_{peak}	°	33
Residual friction angle	ϕ'_{res}	°	10
Peak cohesion	c'_{peak}	kPa	5
Residual cohesion	c'_{res}	kPa	1
Shape factor	β	-	50

As shown in Figure 3, the post-failure mechanism and the long run-out can be quite well simulated by imposing a softening behaviour to the soil. However, the residual values of friction angle and cohesion that are needed are not compatible with the geotechnical characterization of the material.
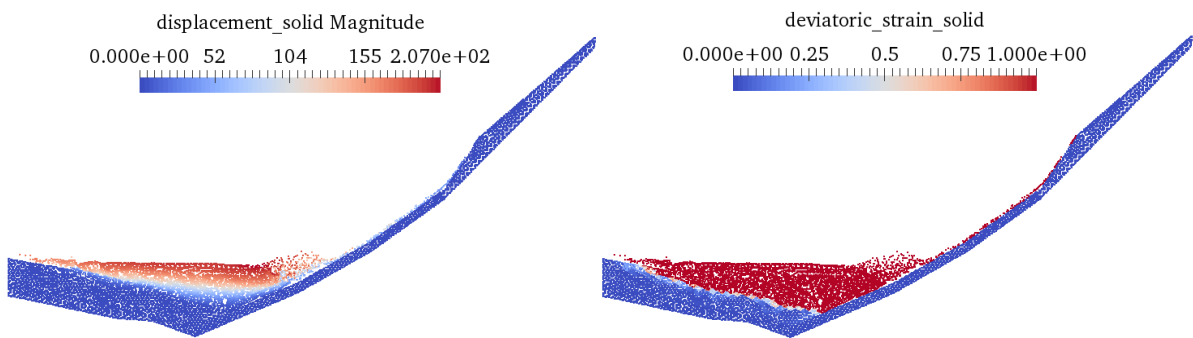
Figure 3: Total displacement and accumulated deviatoric strain results (after 40 seconds) for the case of the phreatic level at the surface by using the Mohr-Coulomb with strain softening model.

4.3 Undrained analysis in effective stresses with Ta-Ger

In the last simulation, the strength loss of the material is attributed to the excess pore water pressure generated during motion, which induces an effective stress decrease and, consequently, loss of frictional strength [20]. The loss of strength is being modelled in order to understand the long run-out observed. In the numerical calculation, the water table raising is assumed so fast that there is a significant generation of excess pore pressure, but negligible

relative movement between solid and fluid phase, therefore pore pressure dissipation is neglected. The slope material is described with the Ta-Ger constitutive model [5,6]. It is an elastoplastic model based on the critical state theory and developed with the aim of reproducing the behaviour of soil under different types of loading, drainage conditions and initial stresses, without the need to recalibrate its parameters. A material that exhibits a contractive behaviour is considered.

In order to characterize the mobilized soil, drained and undrained triaxial compression tests are simulated for samples consolidated isotropically to 100, 150 and 200 kPa prior to shearing. The model parameters are summarized in Table 3. Figure 4 shows the results of the simulation in drained and undrained conditions. It can be observed that, when the drainage conditions are prevented and the soil is contractive, the mean effective stress decreases as a consequence of growing positive excess pore water pressure. The reduction in mean effective stress is accompanied by the reduction in deviatoric stress and hence the sample softens.
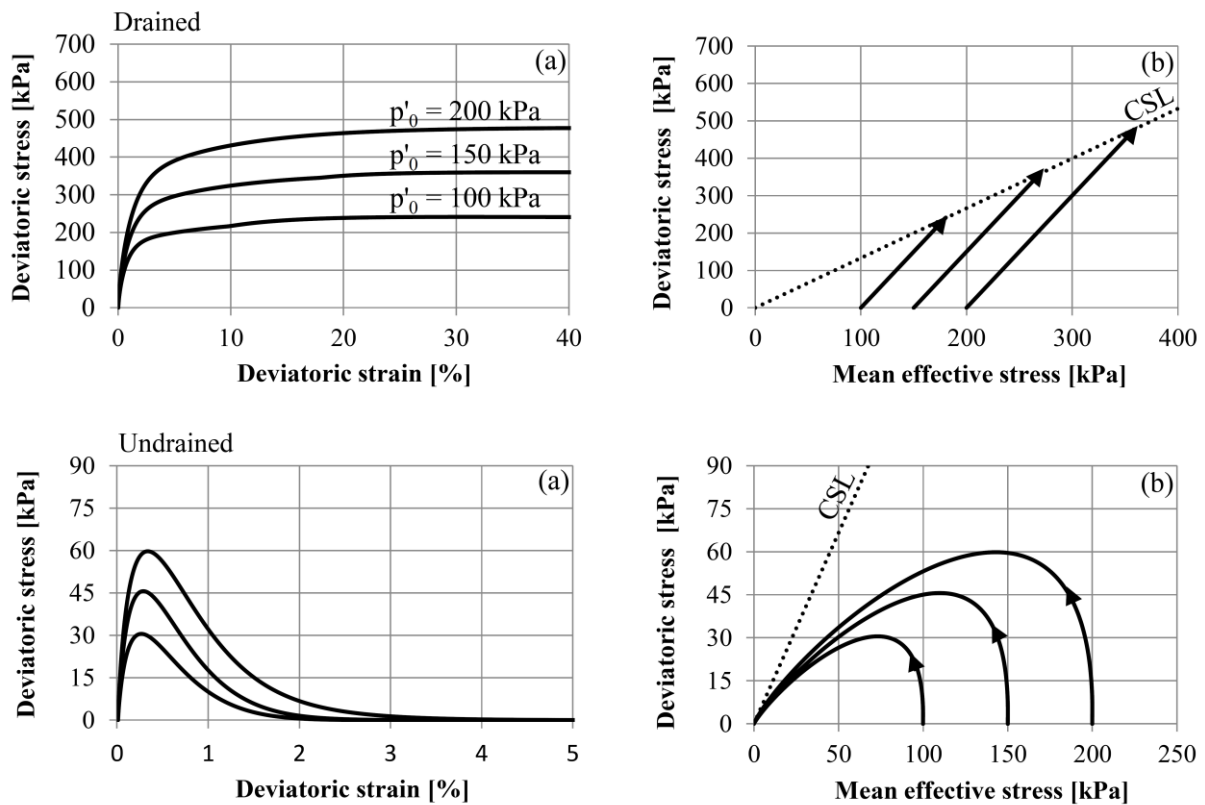
Figure 4: Drained and undrained triaxial compression simulations at different confining pressures. (a) Deviatoric stress-deviatoric strain relationship; (b) stress path in the triaxial plane.

The simulation is carried out in two phases: (1) Stresses are initialized by quasi-static gravity loading ($\alpha = 0.75$); (2) the full dynamic behaviour of the soil is analysed and undrained conditions are imposed to the material ($\alpha = 0.05$).

Table 3: Ta-Ger model parameters.

| Parameter	Symbol	Unit	Value
Shear modulus constant	G_0	-	2500
Shear modulus exponent	m	-	0.4
Poisson ratio	ν	-	0.33
Friction angle at critical state	ϕ'_{cs}	°	33
Hardening exponent	n	-	0.5
Initial value of bounding stress ratio	M_{s0}	-	1.11
Bounding and Phase transformation coefficient	c	-	6
Initial void index	e_0	-	0.93
Minimum void index	e_{min}	-	0.597
Maximum void index	e_{max}	-	0.977
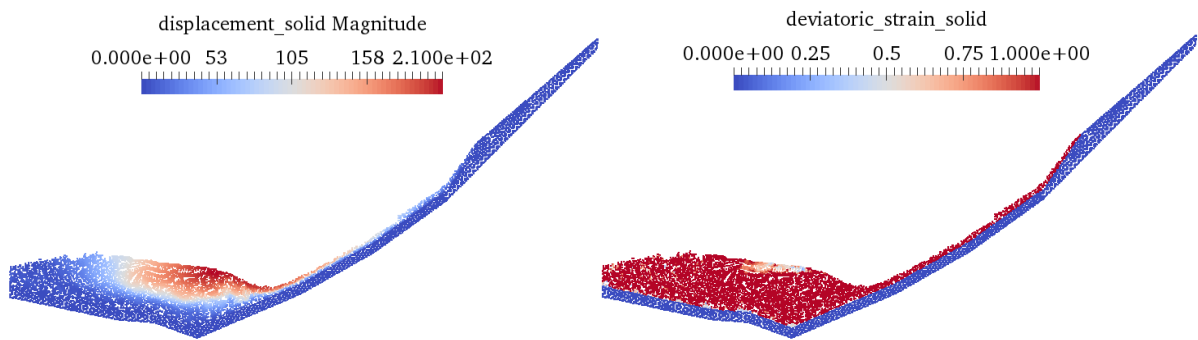
Figure 5: Total displacement and accumulated deviatoric strain results (after 20 seconds) for the case of the phreatic level at the surface by using Ta-Ger model with undrained conditions.

Figure 5 shows the total displacement and accumulated deviatoric strain at the end of the simulation period for the case of the phreatic level located at the surface. The dynamics of the movement and the large run-out is well reproduced. It can be seen that the generation of excess pore water pressure is fundamental to trigger the mechanism of flow-like landslides.

5 CONCLUSIONS

A flow-like landslide can be generated by several mechanisms such as the saturation of the soil involved in the failure and its susceptibility to liquefaction. The high velocity of the failed mass and the long run-out distances characterize its post-failure behaviour.

Table 4: Results comparison (the run-out observed in the field is 380 m).

Phreatic level	MC		MCSS		Ta-Ger	
	Run-out	Duration	Run-out	Duration	Run-out	Duration
-15 m	5.9 m	10 s				
-10 m	6.0 m	10 s				
-5 m	6.6 m	10 s				
0 m	8.4 m	10 s	207 m	40 s	210	20 s

The classical elasto-plastic constitutive models such as the Mohr-Coulomb and the Mohr-Coulomb with strain softening are not able to reproduce the real behaviour of the soil including the strength loss due to the propagation of the pore water pressures in the post-failure stage.

The hypothesis of a generation of excess pore pressures in undrained conditions, together with the advanced constitutive model Ta-Ger, allowed to capture the general characteristic of the flow-like failure and the large run-out.

In Table 4 are summarized the results of the simulations in terms of run-out and duration of the movement.

ACKNOWLEDGEMENTS

REFERENCES

[1] D. Sulsky, Z. Chen, and H. L. Schreyer, "A particle method for history-dependent materials," *Comput. Methods Appl. Mech. Eng.*, vol. 118, no. 1–2, pp. 179–196, 1994.

[2] D. Sulsky, S. Zhou, and H. L. Schreyer, "Application of a particle-in-cell method to solid mechanics," *Comput. Phys. Commun.*, vol. 87, pp. 236–252, 1995.

[3] F. Zabala and E. E. Alonso, "Progressive failure of Aznalcóllar dam using the material point method," *Géotechnique*, vol. 61, no. 9, pp. 795–808, 2011.

[4] I. Jassim, D. Stolle, and P. Vermeer, "Two-phase dynamic analysis by material point method," *Int. J. Numer. Anal. Methods Geomech.*, vol. 37, no. 15, pp. 2502–2522, 2013.

[5] P. Tasiopoulou and N. Gerolymos, "Constitutive modelling of sand: a progressive calibration procedure accounting for intrinsic and stress-induced anisotropy," *Géotechnique*, vol. 66, no. 9, pp. 754–770, 2016.

[6] P. Tasiopoulou and N. Gerolymos, "Constitutive modelling of sand: Formulation of a new plasticity approach," *Soil Dyn. Earthq. Eng.*, vol. 82, pp. 205–221, 2016.

[7] G. Wang and K. Sassa, "Factors affecting rainfall-induced flowslides in laboratory flume tests," *Géotechnique*, vol. 51, no. 7, pp. 587–599, 2001.

[8] G. Wang and K. Sassa, "Pore-pressure generation and movement of rainfall-induced landslides: effects of grain size and fine-particle content," *Eng. Geol.*, vol. 69, pp. 109–125, 2003.

[9] Y. Okura, H. Kitahara, and H. Ochiai, "Landslide fluidization process by flume experiments," *Eng. Geol.*, vol. 66, pp. 65–78, 2002.

[10] L. Olivares, E. Damiano, R. Greco, L. Zeni, L. Picarelli, and A. Minardo, "An Instrumented Flume to Investigate the Mechanics of Rainfall-Induced An Instrumented Flume to Investigate the Mechanics of Rainfall-Induced Landslides in Unsaturated Granular Soils," *Geotech. Test. J.*, vol. 32, no. 2, 2009.

[11] M. B. De Groot, D. R. Mastbergen, J. Lindenberg, and G. A. Van den Ham, "Liquefaction flow slides in large flumes," *Int. J. Phys. Model. Geotech.*, pp. 1–17, 2018.

[12] G. Crosta, "Numerical modelling of large landslides stability and runout," *Nat. hazards*

earth Syst. Sci., vol. 3, pp. 523–538, 2003.

[13] G. B. Crosta, S. Imposimato, and D. G. Roddeman, "Continuum numerical modelling of flow-like landslides," in *Landslides from Massive Rock Slope Failure*, Springer, 2006, pp. 211–232.

[14] M. Pastor, B. Haddad, G. Sorbino, S. Cuomo, and V. Drempetic, "A depth-integrated, coupled SPH model for flow-like landslides and related phenomena," *Int. J. Numer. Anal. Methods Geomech.*, vol. 33, pp. 143–172, 2009.

[15] L. Cascini, S. Cuomo, M. Pastor, and G. Sorbino, "Modeling of Rainfall-Induced Shallow Landslides of the Flow-Type," *J. Geotech. Geoenvironmental Eng.*, vol. 136, no. 1, pp. 85–98, 2010.

[16] Y. Huang, W. Zhang, Q. Xu, P. Xie, and L. Hao, "Run-out analysis of flow-like landslides triggered by the Ms 8.0 2008 Wenchuan earthquake using smoothed particle hydrodynamics," *Landslides*, no. 9, pp. 275–283, 2012.

[17] F. Calvetti, G. Crosta, and M. Tatarella, "Numerical simulation of dry granular flows: from the reproduction of small-scale experiments to the prediction of rock avalanches," *Riv. Ital. di Geotec.*, vol. 21, no. 2, pp. 21–38, 2000.

[18] Institut Cartogràfic I Geològic De Catalunya, "Nota tècnica de la visita realitzada al flux ocorregut a «Era Abelha» de la Val de Valarties," Arties, Val d'Aran, 2018.

[19] F. H. Harlow, M. A. Ellison, and J. H. Reid, "The particle-in-cell computing method for fluid dynamics," *Methods Comput. Phys.*, vol. 3, no. 3, pp. 319–343, 1964.

[20] K. Sassa, "Mechanism of flows in granular soils," Invited paper. In *GeoEng2000*, vol. 1, pp. 1671–1702, 2000.

NUMERICAL STUDY ON LOAD-SETTLEMENT RELATIONSHIPS OF SHALLOW FOUNDATION UNDER EXTREMELY LOW CONFINING PRESSURE

H. AKAGI[1] K. SATO[1] AND T. KIRIYAMA[2]

[1] Waseda University, Department of Civil and Environmental Engineering
58-205, 3-4-1, Ohkubo, Shinju-ku, Tokyo, 169-8555, Japan
e-mail: akagi@waseda.jp, web page: http://www.f.waseda.jp/akagi/index_e.html

[2] Shimizu Corporation, Institute of Technology
3-4-17, Etchujima, Koto-ku, Tokyo, 135-0044, Japan
e-mail: kiriyama@shimz.co.jp, web page: https://www.shimz.co.jp/en/

Key words: Material Point Method, Shallow Foundation, Large Deformation

Abstract. In order to investigate the ground behavior under shallow foundation with extremely low confining pressure, numerical analysis has been performed using the Material Point Method. Material Point Method is one of particle-based methods but it still uses numerical grid. It has been applied to many problems of geomaterial since it was proposed for the first time. The authors focus on the robustness of the method under large deformation problem and applied it to the shallow foundation problem of geomaterial. In this paper, the formulation and implementation of Material Point Method are described, followed by verification and validation for the implemented code. Then, the parametric investigations on ground behavior under shallow foundation have been carried out.

1 INTRODUCTION

Foundation stone has been employed for thousands of years to support historical structures. The foundation stone support system is basically composed of a base ground, foundation stones, and an upper structure. Self-weight of an upper structure is transferred from structural columns to a base ground through foundation stones. In this support system, main purpose of foundation stones is to distribute a concentrated column force in a foundation stone body, relaxing stress concentration at the bottom of columns.

In this support system, foundation stones often penetrate into a base ground once they are undergoing additional external forces such as earthquakes because surface grounds around foundation stones don't have enough bearing capacity due to an extremely low confining pressure condition. Conventional bearing capacity theory is employed when it can be regarded as it be under the small deformation condition whereas it becomes difficult to evaluate bearing capacities and to predict settlements under the large deformation condition such in case of foundation stones. The conventional method is based on an assumption of rigid-plastic behaviour and it focuses on a bearing capacity at an ultimate state. Therefore, the same approach cannot be applied to the case under large deformation conditions, which include geometrical nonlinearity.

In order to assess the support system behaviour under extremely low confining pressure,

experimental and numerical study are the main options to be chosen. Experimental testing is performed and reported in the companion papers by the same authors, demonstrating that a load-settlement relationship under large deformation condition shows much higher bearing capacity than the case of small deformation condition, demanding incremental external force for a footing to settle. In this paper, the demonstration of the applicability of numerical simulation is to be focused, employing a particle-based numerical method, which have been applied to geomaterial literally [1]. A shallow foundation model is set up numerically, in which footing foundation is modelled as elastic and a base ground is modelled as elasto-plastic material with Mohr-Coulomb failure criteria. Then, the support system behaviour is assessed by comparing the experimental results with the simulation results.

From comparison between experimental and numerical results, the load-settlement relationship by both methods gives a good agreement to each other, meaning particle-based numerical method is capable of simulating the behaviour of the support system under extremely low confining pressure.

2 MATERIAL POINT METHOD

The Material Point Method (MPM), which is originally proposed by Sulsky et al. [1], is a derivative of Particle-In-Cell (PIC) [2], in which a particle has all physical quantities but the equation of motion is solved at grid point. PIC is formulated based on for Fluid Mechanics while MPM is based on Solid Mechanics. Physical quantities at material point are transferred to grid point by using interpolation functions. After equation of motion is solved at grid point, the solution is going back to material point by using interpolation function again. The transferring of physical quantities by using interpolation function is repeated at every numerical step. The first Material Point Method, call original MPM in this paper, uses 4-node shape function for the interpolation function in two-dimensional problems. However, the numerical oscillation occurs when material point crosses the numerical grid because the derivative of the shape function flips its value from plus to minus or vice versa. In order to overcome the numerical oscillation, Generalized Interpolation Material Point (GIMP) method is proposed by Bardenhagen and Kober [3], in which the interpolation function is averaged over its control domain. Hereafter, many interpolation functions have been reported on Material Point Method while most of them are derivative of GIMP method. In this section, the formulation of original MPM and GIMP method are described. The simulation of verification and validation are performed with both original MPM and GIMP method.

2.1 Formulation of Material Point Method

In the following equations, superscript k is the time step and subscript g and p are the physical quantities at the grid point and material point, respectively. The grid point mass is extrapolated from the material point mass as

$$m_g^k = \sum_{i=1}^{n_p} m_{p,i} S_{p,i} \tag{1}$$

in whici m_g, m_p, S_p, n_p are the mass of the grid point, the mass at the material point, the interpolation function value at the material point, and the number of material points in the

reference cell, respectively. The grid point internal force is calculated by integrating the stresses of the reference material points as

$$f_g^{int,k} = -\sum_{i=1}^{n_p} \frac{m_{p,i}^k}{\rho_{p,i}^k} G_{p,i}^T \sigma_{p,i}^k \tag{2}$$

in which f_g^{int}, ρ_p, G_p, σ_p, are the grid point internal force, the density of material point, interpolation function derivative value at the material point and the stress of the material point, respectively. The grid point external force is calculated as

$$f_g^{ext,k} = m_g^k \cdot g^k \tag{3}$$

in which f_g^{ext} is the grid point external force and g is the gravitational acceleration. Eqs. (1)-(3) yields the equation of motion in each direction(x and y) of the grid point as

$$a_g^k = \frac{1}{m_g^k} \left(f_g^{int,k} + f_g^{ext,k} \right) \tag{4}$$

in which a_g is the acceleration of the grid point. The material point coordinates are updated as

$$x^{k+1} = x^k + \Delta t \cdot \sum_{i=1}^{n_g} v_{g,i}^k S_{p,i}^k \tag{5}$$

in which x, v, Δt, n_g are the material points coordinates, the grid point velocity, the incremental time, and the number of grid points in the cell to which the reference material point belongs. The material point displacement(u), acceleration(a_p) and velocity(v_p) are updated as

$$u^{k+1} = u^k + \Delta t \cdot \sum_{i=1}^{n_g} v_{g,i}^k S_{p,i}^k \tag{6}$$

$$a_p^k = \sum_{i=1}^{n_g} a_{g,i}^k S_{p,i}^k \tag{7}$$

$$v_p^{k+1} = v_p^k + \Delta t \cdot a_p^k \tag{8}$$

The grid point velocity(v_g) is updated as

$$v_g^k = \sum_{i=1}^{n_p} \frac{S_{p,i} m_{p,i}}{m_g^k} v_p^k \tag{9}$$

The material point strains(ε_p) are updated as

$$\Delta \varepsilon_p^k = \frac{\Delta t}{2} \cdot \sum_{i=1}^{n_p} \left(G_{p,i} v_g^k + \left(G_{p,i} v_g^k \right)^T \right) \tag{10a}$$

$$\varepsilon_p^{k+1} = \varepsilon_p^k + \Delta\varepsilon_p^k \tag{10b}$$

in which $\Delta\varepsilon_p$ is the incremental strain during a time step (Δt). The material point stresses are updated as

$$\Delta\sigma_p^k = K \cdot \Delta\varepsilon_p^k \tag{11a}$$

$$\sigma_p^{k+1} = \sigma_p^k + \Delta\sigma_p^k \tag{11b}$$

in which $\Delta\sigma$ is the incremental stress during time step Δt. As seen in Eq. (10), the stress and strain objectivities are not satisfied. They are assumed to increase linearly during time step Δt, which is set to be very small (e.g., 1.0×10^{-5}(s)). The volume (*Volume*) and density (ρ) of the material point are updated as

$$Volume^{k+1} = Volume^k \cdot (1 + \Delta\varepsilon_v^k) \tag{12}$$

$$\rho^{k+1} = \frac{\rho^k}{(1 + \Delta\varepsilon_v^k)} \tag{13}$$

When using GIMP method, in which the particle control domain is considered, the widths of the material points(l_p) are updated as

$$l_p^{k+1} = l_p^k \cdot (1 + \Delta\varepsilon_i^k) \tag{14}$$

The widths of material points are often not updated for practical reason. Then, the method, which updates the widths, is called contigous particle GIMP (cpGIMP) method whereas the method, which does not update the widths, is called unchanged/uniform GIMP (uGIMP) method.

The numerical procedure from Eq.(1) to Eq.(13) corresponds to one cycle of the MPM algorithm, and the incremental time is Δt. To solve time interval t, the procedure above cycles for the number of time steps, which becomes $t/\Delta t$ times.

3 VERIFICATION AND VALIDATION OF THE METHOD

In order to confirm the integrity of the implemented code, the verification and validation for the code is performed. The importance of the verification and validation (V&V) has been increased as the numerical simulation is more applied in practical engineering use. In this section, the implementations of GIMP method are verified by using the theoretical solution and validated by comparison with the experimental result.

3.1 Verification using one dimensional solution under large deformation

For the investigation of shallow foundation problem under large deformation, the total stress formulation is employed. Then, the formulation is verified by comparing the numerical solution with the total stress theoretical solution under large deformation condition. Zhang et al. [4] proposed the theoretical solution for one-dimensional column under gravitational force by assuming that the potential energy is kept constant based on the finite deformation theory. Theoretical stress and displacement of Zhang's 1D column are described as follows.

$$\sigma(x) = \sigma(0) \frac{(1 - x/h_0) + \kappa(x/h_0)}{1 - \kappa(1 - \kappa)(x/h_0)}, \text{where } \kappa = \frac{\sigma(0)}{2E} \tag{33}$$

$$X - x = \kappa[2 - \kappa - (1 - \kappa) \, x/h_0]/[1 - \kappa(1 - \kappa)/(x/h_0)] \tag{34}$$

in which X and x are the initial and the current coordinates from the bottom of column, respectively. h_0 is the length of the column. $\sigma(x)$ is the stress at the coordinate of x. E is Young's Modulus.

For the verification problem, the numerical model for the one-dimensional column is prepared. 50 particles are lined with the length of 1 m, meaning each particle has 2 cm wide control domain. Column is discretized with 50 cells of numerical grid, in which one particle is arranged in each cell. Young's modulus and unit weight of particles are 10,000 kPa and 9.8 kN/m^3, respectively. The gravitational force is applied to the column incrementally with the damping coefficient [5] of 0.8 in order to obtain the quasi-static equilibrium solution. Figure 1 shows the comparison between numerical results and theoretical solutions. The numerical solutions give a good agreement to the theoretical one under 1G gravitational force (Fig. 1(a)). Original MPM begins to show the oscillation under 10G condition while uGIMP and cpGIMP method still give a good agreement to the theoretical one (Fig. 1(b)). Under 20G condition, uGIMP begins to show the oscillation, which becomes much more under 50G condition while cpGIMP still shows a good agreement to the theoretical solution (Fig. 1(c), (d)). The uGIMP solution is oscillate around the theoretical one. In the elastic problem the solution by uGIMP method may acceptable in case that only deformation is focused. However, in case of nonlinear problem, only cpGIMP solution is applicable because unexpected deformation occurs if particles reach yield surface during their stress oscillation.

3.2 Validation by comparing numerical result with experimental results

In order to validate the numerical simulation method, numerical results are compared with the experimental results of load-settlement relationship and strain distribution in the ground. The experiments are performed in physical simulation of shallow foundation, in which the ground and the foundation are modeled by aluminum bar and brass block as a rigid footing, respectively. The footing is controlled by displacement, penetrating into the ground while the load and the displacement are monitored by load-cell and displacement sensor, both of which are attached to the footing. The digital camera, which is located besides the physical model, captures snap shots of deformed ground during the loading. By using Particle Image Velocimetry (PIV) technique, displacement and maximum shear strain distribution inside the ground are visualized at every 5 mm penetration.

The numerical procedure, which simulates the experiment, is described below. Fig. 2 shows the initial configuration of the model and boundary condition. The numerical model is a half model by using the geometrical symmetry, in which the left side is the symmetric center. 4 particles are arranged regularly in one cell. The spacial resolution of the numerical model is defined as 5 mm, which is the same as the resolution of image analysis (PIV) in the experiment, which enables the direct comparison of strain. Table 1 and 2 show material properties and numerical conditions, respectively. During the simulation, the density of the loading block is changed gradually, which generates the increase in contact force and induce the ground
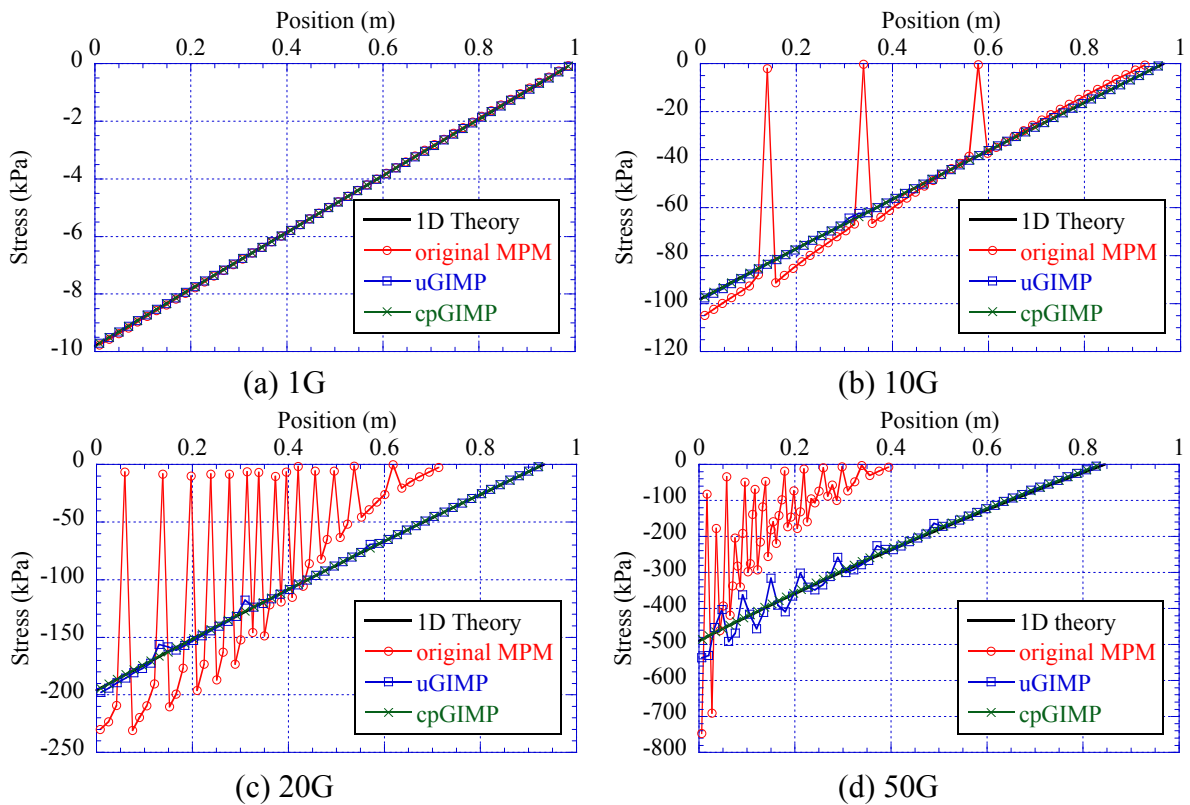
Figure 1. Comparison between numerical result and theoretical solution

deformation. The numerical load-settlement relationship is calculated by monitoring both the self-weight and the penetration of the loading block. Fig. 3 shows the load-settlement relationship obtained from both experiment and numerical simulation, which give a quite similar relationship. Fig. 4 shows the vertical displacement of the ground at the footing penetration of 5, 15, and 25 mm. The vertical displacements by both experiments and simulation also give a good agreement to each other. These comparison of load-settlement relationship and
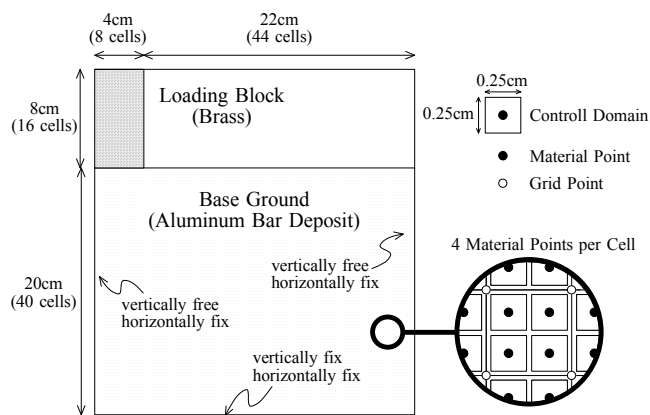
Figure 2. Numerical model of shallow foundation experiments

Table 1. material properties

E (kPa)	v	ρ (g/cm³)	ϕ (deg)	c (kPa)
1000	0.3	2.43	20	0

Table 2. numerical condition

Items	Values
Particles Per Cell	4
Dimensions(H x W)	0.26 m x 0.28 m
Width of cell	0.005 m
Time increment	0.000015
Damping factor	0.8
Number of Particles	
Ground	8,320
Footing	512

deformations inside the ground validate that the simulation result are evaluated as applicable for shallow foundation problems.
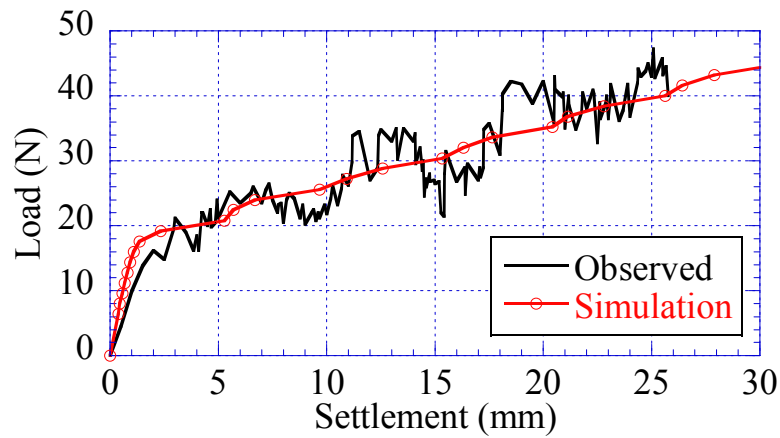
Figure 3. Comparison of load-displacement relationship between experimental and numerical results

(i) observed   (ii) simulation

(a) settlement=5mm

(i) observed   (ii) simulation

(b) settlement=15mm

(i) observed   (ii) simulation

(c) settlement=25mm
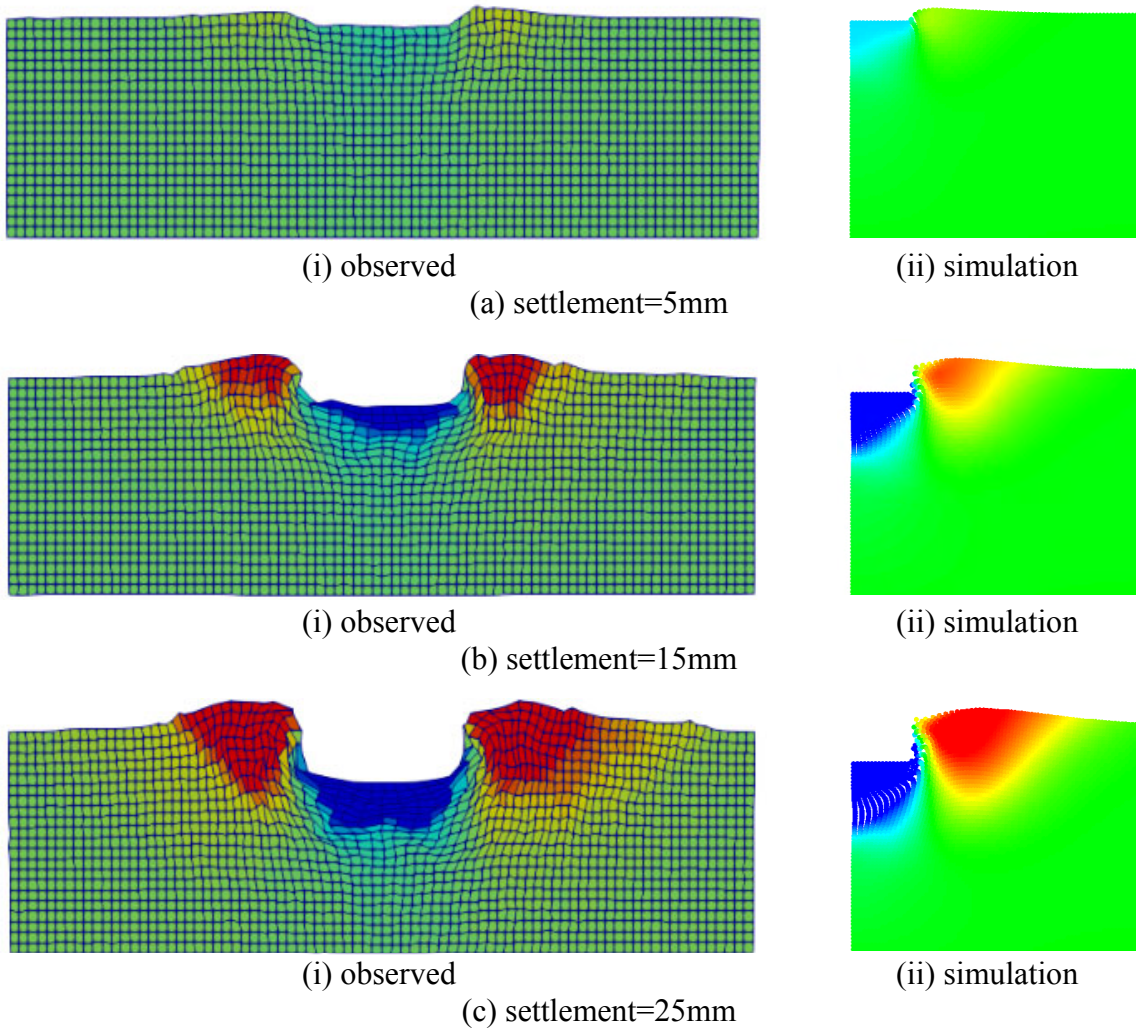
Figure 4. Comparison of settlement between experimental and numerical results

(i) observed   (ii) simulation
(a) settlement=5mm

(i) observed   (ii) simulation
(b) settlement=15mm

(i) observed   (ii) simulation
(c) settlement=25mm
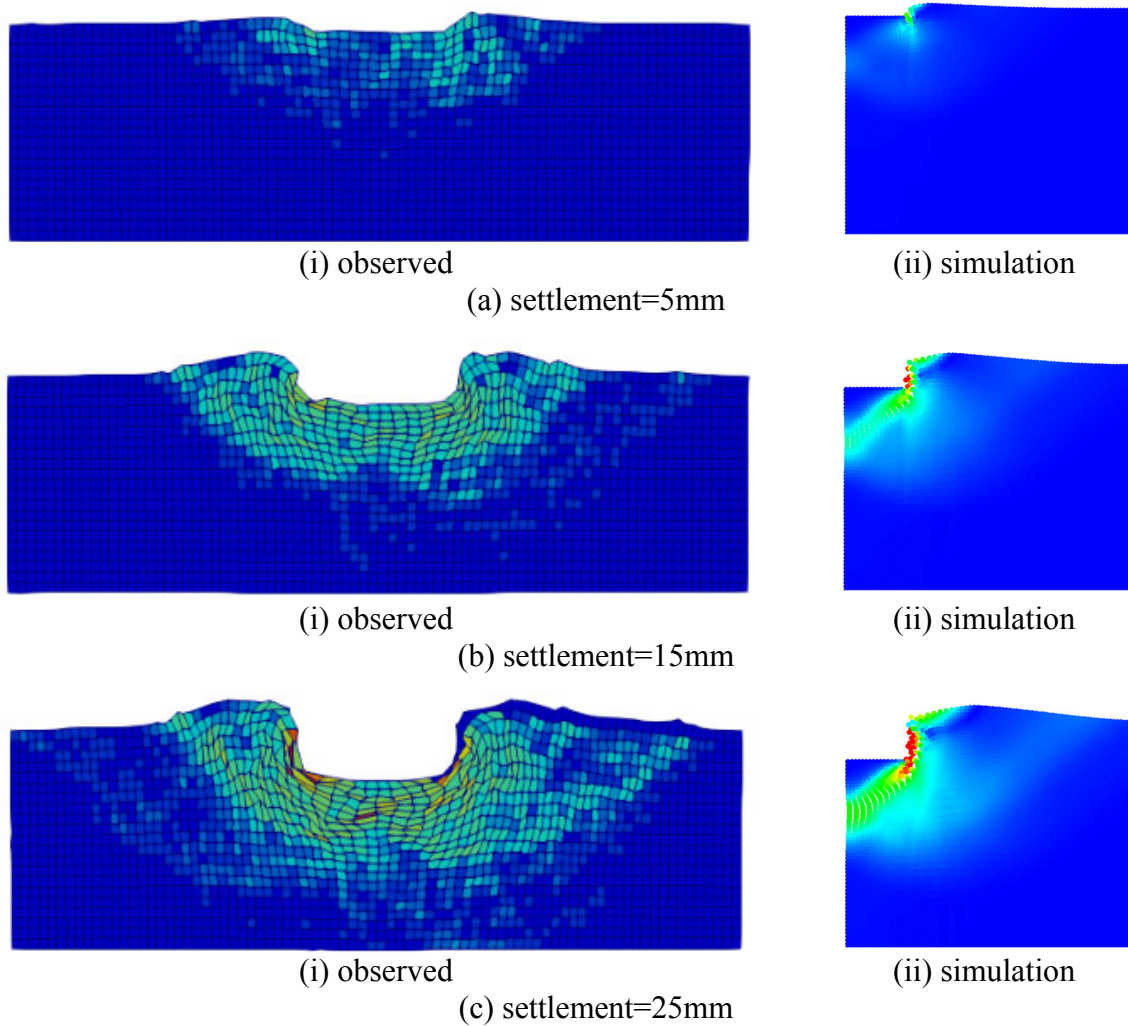
Figure 5. Comparison of maximum shear strain between experimental and numerical results

4   SHALLOW FOUNDATION BEHAVIOR UNDER LOW CONFINING PRESSURE

In order to understand the ground behavior under shallow foundation, parametric study using Material Point Method is performed. The same numerical model in previous section is employed with different material strength, which is changed as frictional or cohesive material to make it simple to understand the ground behavior. Table 3 shows material strength in the simulation. Cases from 1 to 3 are for understanding the behavior with frictional soil and cases from 4 to 6 are for cohesive soil. The load-settlement relationships and deformation inside the ground are obtained from the series of simulations, which are explained below.

4.1 Ground behavior of frictional soil under shallow foundation

Fig. 6 shows the load-settlement relationship obtained from soil condition with three different internal frictional angles of 15, 20 and 25(degree). The curves in Fig. 6 indicate two

Table 3. Material strength

Case	E (kPa)	ρ (kN/m^3)	Poisson's ratio v	ϕ (deg)	c (kPa)
1				15.0	0.0
2			0.3	20.0	0.0
3	1000	20.0		25.0	0
4				0.0	0.5
5			0.4	0.0	1.0
6				0.0	2.0

phases. The first phase shows hardening behavior with different initial stiffness, which is seen in Fig. 6. The second phase shows the ultimate behavior, which is corresponding to the practical bearing capacity. It is quite difficult for the practical use to determine the initial stiffness every time only strength parameter changes. In the previous chapter, the initial stiffness has been determined by calibrating the material properties. It is also difficult to determine soil stiffness without any geotechnical investigation prior to the assessment. Then, geotechnical investigation is strongly recommended before assessing the frictional soil behaviors. Fig. 7 shows the total displacement and maximum shear strain, in which the punching type failure mechanism is observed in the first phase (Fig. 7(a)-(i),(b)-(i)) while the Terzaghi's bearing capacity theory
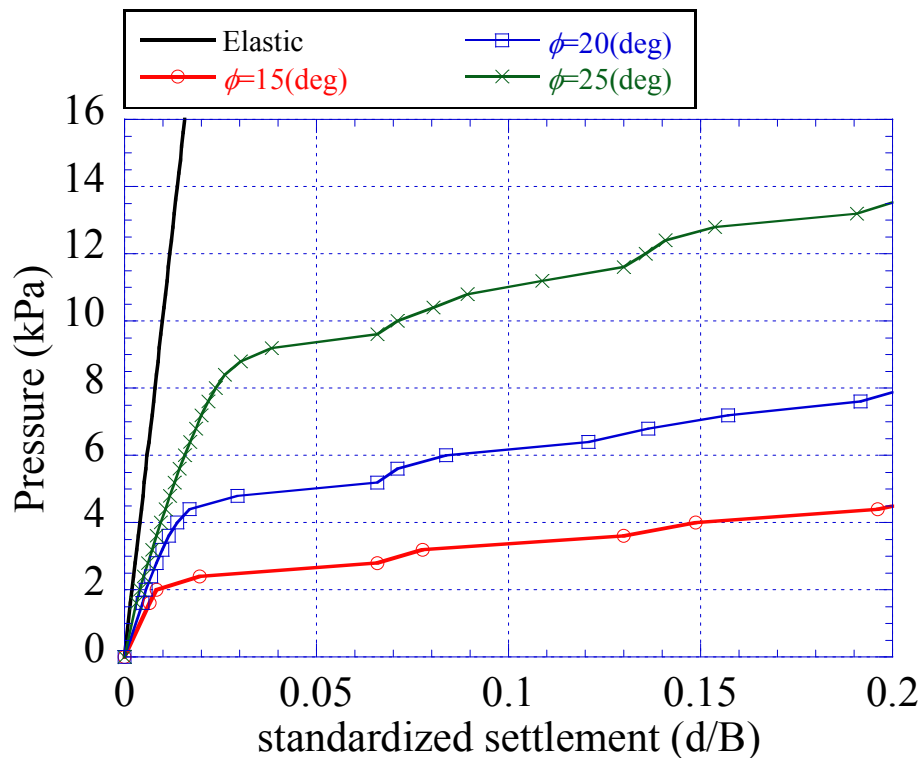
Figure 6. Load-settlement relationship of the frictional material ground

(i) Pressure=4(kPa)   (ii) Pressure=10(kPa)   (iii) Pressure=13.2(kPa)

(a) Total displacement

(i) Pressure=4(kPa)   (ii) Pressure=10(kPa)   (iii) Pressure=13.2(kPa)

(b) Maximum shear strain
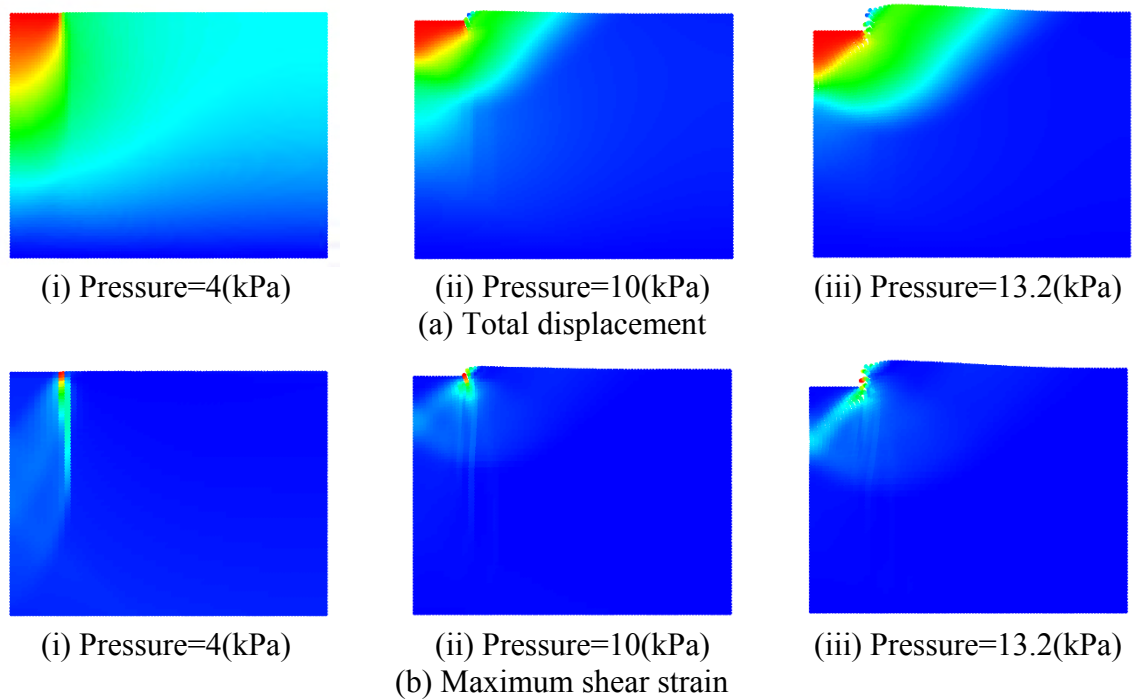
Figure 7. Deformation inside the frictional material ground (Case3: ϕ=25(deg))

type failure mechanism is observed in the second phase (Fig. 7(a)-(ii),(iii),(b)-(ii),(iii)). The bearing capacities in Fig. 7 exceed the Terzaghi's theory. This is mainly due to the embedded effect under large deformation condition. In the theory, the embedded effect act only as an additional resistance but it extends the sliding line under large deformation, resulting in the more effect on the bearing capacity than the Terzaghi's theory.

4.2 Ground behavior of cohesive soil under shallow foundation

Fig.11 shows the load-settlement relationship obtained from soil condition with three different cohesions of 1.0, 2.0 and 3.0(kPa). The curves in Fig.11 indicate three phases. The first phase shows elastic behaviors, in which all the material shows the same line. The second phase shows the hardening behavior, which is a transient phase from elastic status to the ultimate status. The third phase shows the ultimate behavior, which is corresponding to the practical bearing capacity. Fig. 8 shows the total displacement and maximum shear strain, in which the elastic behavior is observed in the first phase, forming the displacement bubble (Fig. 8(a)-(i),(b)-(i)), followed by the second phase in which the punching type failure mechanism is observed(Fig. 8(a)-(ii),(b)-(ii)), and the third phase in which the Terzaghi's bearing capacity theory type failure mechanism is observed(Fig. 8(a)-(iii),(b)-(iii)). The bearing capacities in Fig.11 exceed the Terzaghi's theory. As seen in the result of frictional material, this is also due to the embedded effect under large deformation condition. The importance of considering the geometrical nonlinearity is recognized from the results.
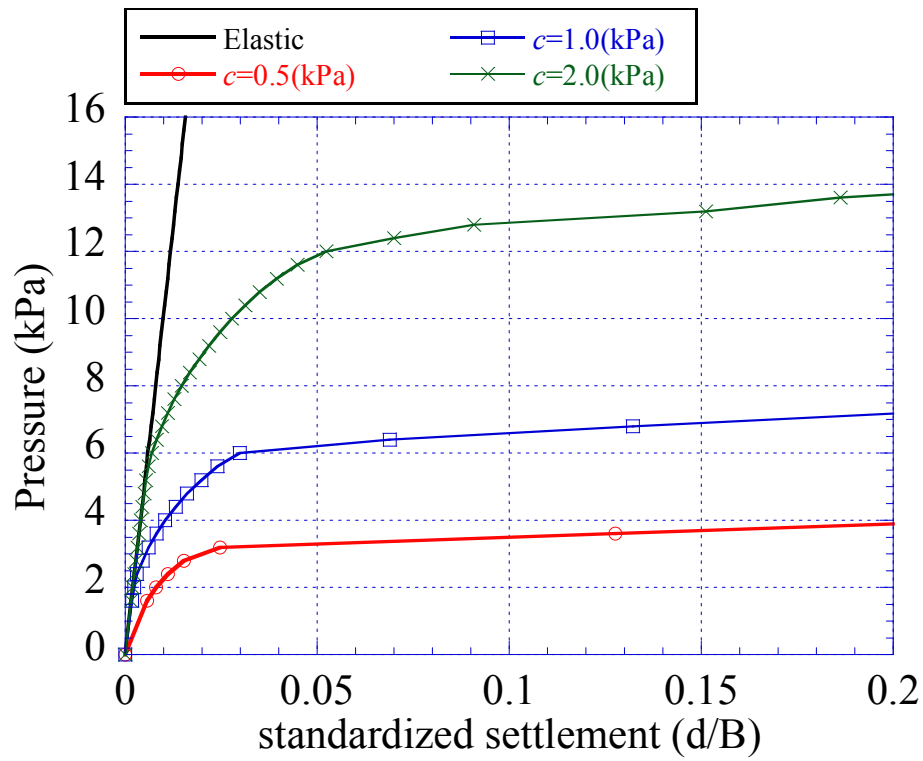
Figure 8. Load-settlement relationship of the cohesive material ground

(i) Pressure=4(kPa) (ii) Pressure=10(kPa) (iii) Pressure=13.2(kPa)

(a) Total displacement

(i) Pressure=4(kPa) (ii) Pressure=10(kPa) (iii) Pressure=13.2(kPa)

(b) Maximum shear strain
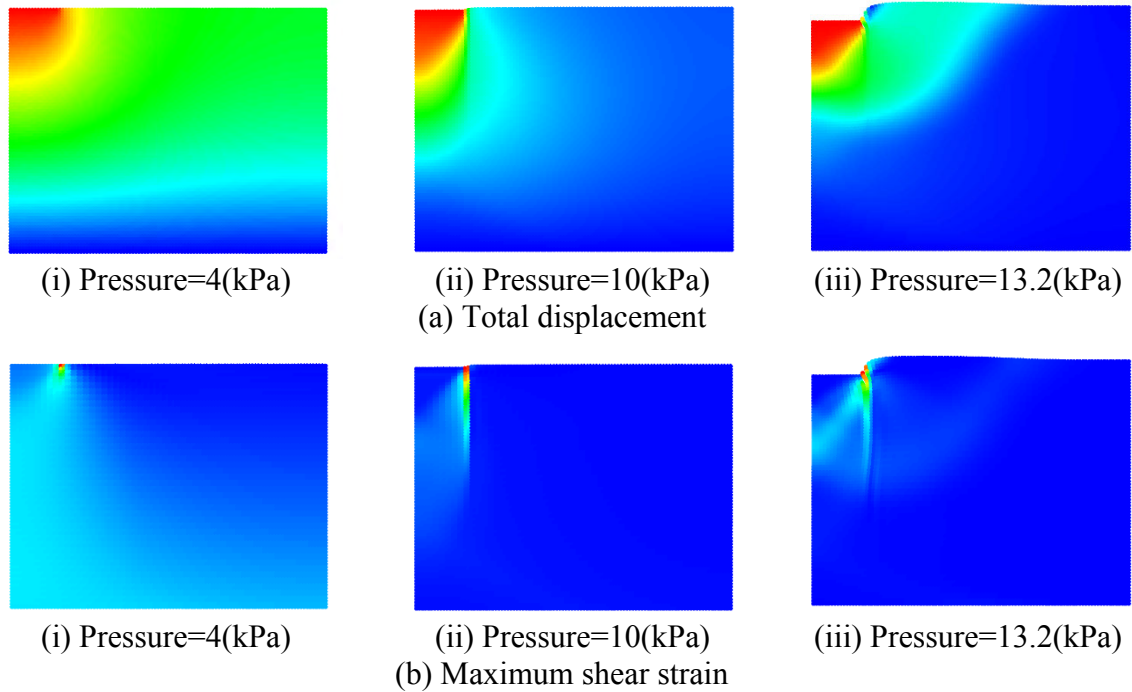
Figure 9. Deformation inside the cohesive material ground (Case6:c=2(kPa))

5   CONCLUTION

In this paper, the formulation, verification and validation of the Material Point Method are reviewed, in which the difference of the formulation are scribed and the oscillation of the original MPM are demonstrated while the GIMP does not show any numerical oscillation. In the validation simulation, the numerical simulation results are compared with the experimental results. The load-settlement relationship and the deformation of the ground obtained from both simulation and experiment shows a good agreement to each other, showing the validity of the numerical method. After that, the parametric studies on the ground behavior are reported, in which ground behavior with different material strength are simulated. The ground behavior with frictional material shows the load-settlement curve with two phases, which are the foundation punching behavior in the first phase and Terzaghi's type sliding behavior in the second phase. The ground behavior with cohesive material shows the load-settlement curve with three phases, which are the elastic response in the first phase, followed by the punching and Terzaghi's type sliding in second and third phase respectively.

REFERENCES

[1] D. Sulsky, Z. Chen and H.L. Schreyer, (1994). A particle method for history-dependent materials, Computer Methods in Applied Mechanics and Engineering, 118, 179-196.

[2] Harlow, F.H., (1956). A Machine Calculation Method for Hydro-dynamic Problems. Los Alamos Scientific Laboratory re-port LAMS.

[3] Bardenhagen, S. G. & Kober, E. M. (2004). The generalized interpolation material point method, Computer Modeling in Engineering and Science 5(6), 447-495.

[4] Zhang, D.Z., Ma, X. and Giguere, P.T., (2011). Material point method enhanced by modified gradient of shape function, Journal of Computational Physics, Vol.230, pp.6379-6398.

[5] Cundall, P. A. (1987). Distinct element models of rock and soil structure, analytical and computational methods in engineering rock mechanics, Ch.4, 129-163. E.T. Brown, ed. London : Allen & Unwin.

TIME INTEGRATION ERRORS AND ENERGY CONSERVATION PROPERTIES OF THE STORMER VERLET METHOD APPLIED TO MPM

Martin Berzins[*]

[*] Scientific Computing and Imaging Institute
University of Utah
Salt Lake City, UT 84112 USA
e-mail: mb@sci.utah.edu, web page: http://www.sci.utah.edu

Key words: MPM, Time Integration, Stormer Verlet Method, Energy Conservation Accuracy

Abstract. The success of the Material Point Method (MPM) in solving many challenging problems nevertheless raises some open questions regarding the fundamental properties of the method such as the energy conservation since being addressed by Bardenhagen and by Love and Sulsky. Similarly while low order symplectic time integration techniques are used with MPM, higher order methods have not been used. For this reason the Stormer Verlet method, a popular and widely-used symplectic method is applied to MPM. Both the time integration error and the energy conservation properties of this method applied to MPM are considered. The method is shown to have locally third order accuracy of energy conservation in time. This is in contrast to the locally second order accuracy in energy conservation of the methods that are used in many MPM calculations. This third accuracy accuracy is demonstrated both locally and globally on a standard MPM test example.

1 INTRODUCTION

The Material Point Method (MPM) is often described as a solid mechanics method that is derived [10, 11] from the fluid implicit particle, FLIP and PIC methods. MPM has been very successful when applied to very many large deformation problems. However some of the properties of the method are still not as well-understood as they might be in areas such as time integration and conservation of energy. For example energy conservation is considered by Bardenhagen [1] and it is shown that the standard MPM method gives second order energy conservation over a timestep or first order overall. The analysis of Love and Sulsky [8] extends these results and shows that energy conservation is possible if a full mass matrix is used. The same authors also show that using a lumped mass matrix gives second order locally energy conservation. Other improved time integration methods based upon a central difference approach are considered by [12]. The relationship between MPM time integration and symplectic time integration methods is considered by [3]. Such symplectic methods have good conservation properties [6]. Furthermore the Stormer-Verlet [6] method has third order accuracy locally. This method is symplectic and very widely used in many applications [7] such as molecular dynamics and planetary orbits

and even dates back to Newton as was demonstrated by Feynman see [6]. The intention here is to apply the Stormer-Verlet method to MPM and to determine its accuracy and conservation properties. It is shown that the time continuity properties of the spatial methods used play an important role in time accuracy and in conservation. Furthermore it is shown that it is helpful for the basis functions to possess a commutative property so that a discrete version of integration by parts may be used. Although a model one dimensional problem is considered the results are more broadly applicable to higher dimensions. Section 2 describes the MPM method and the model problem used, while Section 3 explains how the Stormer Verlet method may be applied to MPM. Section 4 provides an analysis of the timestepping errors of the Stormer Verlet method and MPM while Sections 5 and 6 derives the energy conservation error of the method. Numerical experiments comparing the aproaches on a model problem used by [5] are reported in Section 7, and show show that the Stormer Verlet method has better accuracy and conservation properties than the method considered in [1].

2 MPM MODEL PROBLEM AND METHOD

The description of MPM used here follows [5] in that the model problem used here is a pair of equations connecting velocity v, displacement u and density ρ (here assumed constant):

$$\frac{Du}{Dt} = v, \tag{1}$$

$$\rho \frac{Dv}{Dt} = \frac{\partial \sigma}{\partial x} + b(x,t), \tag{2}$$

with a linear stress model $\sigma = E \frac{\partial u}{\partial x}$ for which Young's modulus, E, is constant, a body force b, which is initially assumed to be zero, and with appropriate boundary and initial conditions. For convenience a mesh of equally spaced $N+1$ fixed nodes X_i with intervals $I_i = [X_i, X_{i+1}]$, on on the interval $[a,b]$ is used where

$$a = X_0 < X_1 < ... < X_N = b, \tag{3}$$

$$h = X_i - X_{i-1}. \tag{4}$$

Theses fixed nodes are referred to as the i points. It will also be assumed that periodic boundary conditions exist in that

$$\sigma(a)v(a) = \sigma(b)v(b) \tag{5}$$

together with appropriate initial conditions. While the analysis of MPM for time integration error and energy conservation uses the model problem above it does apply more generally and in multiple space dimensions with a few obvious modifications. It will also be assumed that are n_p particles between each pair of nodes, situated at x_p^n points where at each time step, $t^n = \delta t * n$, where n is the nth time step, and the computed solution at the pth particles will be written as $u_p^n = u(x_p^n, t^n)$. Suppose that the particles in interval i lie between X_i and X_{i+1} and have positions $x_{im+j}, j = 1,..,m$. The calculation of the internal forces in MPM at the nodes requires the calculation of the volume integral of the divergence of the stress [12] using

$$f_i^{int} = -\sum_p D_{pi}(x_p^n)\sigma_p V_p \tag{6}$$

In this case the subscript *pi* represents a mapping from particles *p* to node *i*. The subscript *ip* would represent a mapping from nodes *i* to particles *p*. The negative sign arises as a result of using integration by parts [5]. The mass at node *i* is defined by

$$m_i = \sum_p m_p S_{pi}(x_p^n) \tag{7}$$

It is important to note that the coefficients $D_{pi}(x_p^n)$ and $S_{pi}(x_p^n)$ depend explicitly on the background mesh and the particle positions and that they also be chosen to reproduce derivatives of constant and linear functions exactly [5]. It should also be noted that mappings from particles to derivatives on grids e.g.D_{pi} may possibly be very different from forming derivatives at particles using nodal values as denoted by D_{ip}. Similar comments apply to interpolating from particles to grids as denoted by the coefficients S_{pi} and from nodes to grids as denoted by S_{ip}. The initial volume of the particles is uniform for the n_p particles in an interval. The particle volumes are defined using the deformation gradient, F_p^n, and the initial particle volume,V_p^0,

$$V_p^n = F_p^n V_p^0, \text{ where } V_p^0, = \frac{h}{n_p}, \text{ where } F_p^0 = 1 \tag{8}$$

From (7) the acceleration equation in the MPM method in this simple case is

$$a_i(t) = \frac{-1}{m_i} \sum_p D_{pi}(x_p(t))\sigma_p(t)F_p(t)V_p^0 \tag{9}$$

The equation to update velocity at the nodes, as denoted by v_i^n is then given by

$$\dot{v}_i = a_i \tag{10}$$

The equation for the update of the particle velocity is then

$$\dot{v}_p = a_p \tag{11}$$

Where the value of the acceleration at a point x_p^n is given by interpolation based upon nodal values of acceleration

$$a_p = \sum_i S_{ip}(x_p(t))a_i \tag{12}$$

The equation for the particle position update is

$$\dot{x}_p = v_p \tag{13}$$

The update of the deformation gradients is given using,

$$\frac{\partial v}{\partial x}(x_p(t)) = \sum_i D_{ip}(x_p(t))v_i \tag{14}$$

The displacement update equation is

$$\dot{F}_p = \frac{\partial v}{\partial x}(x_p(t),t)F_p \tag{15}$$

While the stress update equation is, using the appropriate constitutive model and Young's Modulus, E,

$$\dot{\sigma}_p = E\frac{\partial v}{\partial x}(x_p(t)) \tag{16}$$

3 THE STORMER VERLET TIME INTEGRATION METHOD

In solving the system of equations defined above by equations (6) to (16) one standard approach used is to order the equations in a certain order and then to solve them in turn using explicit methods. Differences in how the equations are solved corresponds to whether or not the stress is updated first or last in a timestep, a choice that is discussed at length by [1] and [4]. These two different choices are related to the use of the semi-implicit Euler A or B method, [7], [3]. An alternative approach of Hairer et al.[6] defines a method with better time integration properties. Applying the method of p. 407 of [6] requires one extra step over the symplectic Euler Stress Last or Stress First methods [3, 1] to define both nodal and particle velocities, and spatial points at half timestep values. This approach applied to MPM will now be described. On the very first step the nodal accelerations and velocities have to be calculated.

$$v_i^n = \sum_p S_{pi}(x_p^n) \frac{m_p}{m_i} v_p^n \tag{17}$$

$$a_i^n = \frac{-1}{m_i} \sum_p D_{ip}(x_p^n) \sigma_p^n F_p^n V_p^0 \tag{18}$$

The equation to update velocity at the nodes is then given by

$$v_i^{n+1/2} = v_i^n + \frac{dt}{2} a_i^n \tag{19}$$

The value of the acceleration at a point x_p^n is given by interpolation based upon nodal accelerations is

$$a_p^n = \sum_i S_{ip}(x_p^n) a_i^n \tag{20}$$

The equation for the update of the particle velocity is then

$$v_p^{n+1/2} = v_p^n + \frac{dt}{2} a_p^n \tag{21}$$

Similarly the equation for the particle position update is

$$x_p^{n+1/2} = x_p^n + \frac{dt}{2} v_p^n \tag{22}$$

The velocity gradients at particles are calculated using

$$\frac{\partial v}{\partial x}(x_p^{n+1/2}, t_{n+1/2}) = \sum_i D_{ip}(x_p^{n+1/2}) v_i^{n+1/2} \tag{23}$$

These velocity gradients are used to update the stress and deformation gradients at particles

$$F_p^{n+1} = F_p^n + \frac{dt}{2} \frac{\partial v}{\partial x}(x_p^{n+1/2}, t_{n+1/2})(F_p^n + F_p^{n+1}) \tag{24}$$

While stress is updated using the appropriate constitutive model and Young's Modulus, E,

$$\sigma_p^{n+1} = \sigma_p^n + dt E \frac{\partial v}{\partial x}(x_p^{n+1/2}, t_{n+1/2}) \tag{25}$$

and the acceleration is updated with these two values which are the updated stresses and deformation gradients at the current grid points, but at the next time level t^{n+1}.

$$a_i^{n+1} = \frac{-1}{m_i} \sum_p D_{ip}(x_p^{n+1/2}) \sigma_p^{n+1} F_p^{n+1} V_p^0 \tag{26}$$

The equation to update velocity at the nodes is then given by

$$v_i^{n+1} = v_i^n + \frac{dt}{2} \left(a_i^{n+1} + a_i^n \right) \tag{27}$$

The value of the acceleration at a point x_p^n is given by interpolation based upon nodal accelerations:

$$a_p^{n+1} = \sum_i S_{ip}(x_p^{n+1/2}) a_i^{n+1} \tag{28}$$

The final equation for the update of the particle velocity is then

$$v_p^{n+1} = v_p^n + \frac{dt}{2} \left(a_p^{n+1} + a_p^n \right) \tag{29}$$

while the equation for the particle position update is

$$x_p^{n+1} = x_p^n + \frac{dt}{2} \left(v_p^{n+1} + v_p^n \right) \tag{30}$$

The conservation of energy analysis below will assume that the updated spatial position are substituted into equation (26) so that the nodal and particle accelerations and velocities at time t^{n+1} reflect the correct values of the spatial mesh points.

4   Local Errors in Stormer-Verlet applied to MPM

In evaluating the local error in a step of the Stormer Verlet method it is important to note that the method consists of a half step using a forward Euler method. The values computed from this are substituted into what may be described as a Trapezoidal rule or Midpoint rule, before a final update that appears like part of a second-order Runge-Kutta Method. Considering the Forward Euler half step, the first error is that in the nodal velocity equation (19). In this case if this error is denoted as LEV_i its value is given by the standard Forward Euler local error as

$$LEV_i^{n+1/2} = \frac{dt^2}{8} \frac{da_i^n}{dt} + h.o.t \tag{31}$$

$$= \frac{dt^2}{8} \frac{d}{dt} \left(\frac{-1}{m_i} \sum_p D_{ip}(x(t)) \sigma_p(t) F_p(t) V_p^0 \right) + h.o.t. \tag{32}$$

This obviously require differentiability of the coefficients $D_{ip}(x(t))$, even when particles cross grid boundaries. Similarly at the particles

$$LEV_p^{n+1/2} = \frac{dt^2}{8} \sum_p \frac{d}{dt}(S_{ip}(x(t)) a_i(t)) + h.o.t. \tag{33}$$

For the particle update the local error as denoted by $LEx_p^{n+1/2}$ is given by

$$LEx_p^{n+1/2} = \frac{dt^2}{8} \sum_p \frac{d}{dt}(S_{ip}(x(t))V_i(t)) + h.o.t. \tag{34}$$

Second order accuracy requires that the coefficients $S_{ip}(x(t))$ are differentiable in time. The local errors in the updates of the deformation gradient as defined in (24) is similar to that of the Trapezoidal Rule and is given by

$$LEF_p^{n+1} = \frac{dt^3}{12} \frac{d^2}{dt^2}\left(F\frac{\partial v}{\partial x}(x_p(t),t)\right) + h.o.t. \tag{35}$$

Stress is updated using the appropriate constitutive model and Young's Modulus, E, at the mid point and so $LE\sigma_p^{n+1}$ is the stress local time error obtained from the mid-point rule

$$LE\sigma_p^{n+1} = \frac{Edt^3}{24} \frac{d^2}{dt^2}\left(\frac{\partial v}{\partial x}(x_p(t),t)\right) + h.o.t. \tag{36}$$

Again the differentiability of the coefficients D is required. The full local errors including those carried from the velocity calculation at the half step are given by

$$leF_p^{n+1} = LEF_p^{n+1} + dtF\sum_q \frac{\partial}{\partial x_q}\left(\frac{\partial v}{\partial x}(x_q(t),t)\right) LEx_q^{n+1/2} + h.o.t. \tag{37}$$

and

$$le_p\sigma_p^{n+1} = LE\sigma_p^{n+1} + dtE\sum_q \frac{\partial}{\partial x_q}\left(\frac{\partial v}{\partial x}(x_q(t),t)\right) LEx_q^{n+1/2} + h.o.t. \tag{38}$$

When updating the velocity and position at the particles the nodal errors are carried by interpolation. For the final velocity update at nodes the local error as denoted by LEV_i^{n+1} is given by

$$LEV_i^{n+1} = \frac{dt^3}{12} \frac{d^2}{dt^2}(a_i(t)) + h.o.t. \tag{39}$$

The full local error in the equation to update velocity at the nodes (29) is then given by

$$lev_i^{n+1} = dtlea_i^{n+1} + LEV_i^{n+1} \tag{40}$$

where the propagated error from the stress and deformation gradients in the acceleration is (ignoring products of these errors) given by

$$lea_i^{n+1} = \frac{-1}{m_i}\left[\sum_p D_{ip}(x_p^{n+1/2} + LEx_p^{n+1/2})(\sigma_p^{n+1} + LE\sigma_p^{n+1})(F_p^{n+1} + LEF_p^{n+1})V_p^0\right.$$

$$\left. -\sum_p D_{ip}^{n+1/2}\sigma_p^{n+1}F_p^{n+1}V_p^0\right] \tag{41}$$

$$lea_i^{n+1} \approx \frac{-1}{m_i}\left[\sum_p D_{ip}(x_p^{n+1/2})(LE\sigma_p^{n+1}F_p^{n+1} + LEF_p^{n+1}\sigma_p^{n+1})\right.$$

$$\left. +\sum_p \frac{\partial D_{ip}(x_p(t))}{\partial x_p(t)}LEx_p^{n+1/2}F_p^{n+1}\sigma_p^{n+1})\right]V_p^0 \tag{42}$$

The time local error in the value of the acceleration at a point x_p^n as defined by (28) is given by interpolating nodal acceleration errors

$$lea_p^{n+1} = \sum_i S_{ip}(x_p^n) lea_i^{n+1} \tag{43}$$

The equation for the full local time error in the update of the particle velocity as defined by (29) is then

$$lev_p^{n+1} = dt lea_p^{n+1} + LEV_p^{n+1} \tag{44}$$

where the Trapezoidal rule-like error is given by

$$LEV_p^{n+1} = \frac{dt^3}{12} \sum_p \frac{d^2}{dt^2}(S_{ip}(x_p(t))a_i(t)) + h.o.t. \tag{45}$$

For the particle update the local error, as denoted by LEx_p^{n+1}, is given by

$$LEx_p^{n+1} = \frac{dt^3}{12} \sum_p \frac{d^2}{dt^2}(S_{ip}(x_p(t))V_i^n) \tag{46}$$

The equation for the full local time error in the particle position update as given by (30) is

$$lex_p^{n+1} = dt lev_p^{n+1} + LEx_p^{n+1} \tag{47}$$

In summary, even after taking into account the propagated errors from the different MPM stages, the local error appears to be third order, providing that the coefficients of the MPM method $S_{ip}(x(t))$ and $D_{ip}(x(t))$ are sufficiently differentiable.

5 ENERGY CONSERVATION OF MPM

The focus here is on the energy of the particles as this corresponds to the points moved in computation and solution values that used and displayed. The starting point is, for the moment, to ignore the body forces and then to use the approach of [1].

5.1 Grid Point Kinetic Energy of MPM

The change in kinetic energy as denoted by $\Delta K\mathcal{E}_{grid}$ on the points is given by [1]

$$\Delta K\mathcal{E}_{pts} = \frac{1}{2} \sum_p m_p(v_p^{n+1})^2 - \frac{1}{2} \sum_p m_p(v_p^n)^2 \tag{48}$$

where m_p is the mass at particle point x_p. Hence the grid Kinetic energy is also given by

$$\Delta K\mathcal{E}_{pts} = \frac{1}{2} \sum_p m_p(v_p^{n+1} - v_p^n)(v_p^{n+1} + v_p^n) \tag{49}$$

This may be written in terms of the acceleration as

$$\Delta K\mathcal{E}_{grid} = \frac{dt}{4} \sum_p m_p(a_p^{n+1} + a_p^n)(v_p^{n+1} + v_p^n) \tag{50}$$

Substituting for the acceleration at a point using (12) gives

$$\Delta K \mathscr{E}_{grid} = \frac{dt}{4} \left[\sum_p m_p(v_p^{n+1} + v_p^n) \left(\sum_i S_{ip}(x_p^{n+1/2})a_i^{n+1} + \sum_i S_{ip}(x_p^n)a_i^n \right) \right] \tag{51}$$

and again for the nodal acceleration using (9) gives

$$\Delta K \mathscr{E}_{grid} = \frac{-dt}{4} \sum_p (v_p^{n+1} + v_p^n) \left[\sum_i S_{ip}(x_p^{n+1/2}) \frac{m_p}{m_i} \sum_q D_{qi}(x_q^{n+1/2}) \sigma_q^{n+1} F_q^{n+1} V_q^0 \right.$$
$$\left. + \sum_i S_{ip}(x_p^n) \frac{m_p}{m_i} \sum_q D_{qi}(x_q^n) \sigma_q^n F_q^n V_q^0 \right] \tag{52}$$

Using the extension to define velocities and accelerations at the final particle positions x_p^{n+1} gives

$$\Delta K \mathscr{E}_{grid} = \frac{-dt}{4} \sum_p (v_p^{n+1} + v_p^n) \left[\sum_i S_{ip}(x_p^{n+1}) \frac{m_p}{m_i} \sum_q D_{qi}(x_q^{n+1}) \sigma_q^{n+1} F_q^{n+1} V_q^0 \right.$$
$$\left. + \sum_i S_{ip}(x_p^n) \frac{m_p}{m_i} \sum_q D_{qi}(x_q^n) \sigma_q^n F_q^n V_q^0 \right] \tag{53}$$

5.2 Strain Energy of MPM

The rate of change of strain energy is given by (28) in [1]. Hence integrating this equation from t^n to t^{n+1} and using the Trapezoidal rule gives

$$\Delta S \mathscr{E} = \frac{dt}{2} \sum_p \left(\sigma_p^{n+1} F_p^{n+1} \frac{\partial v_p^{n+1}}{\partial x} + \sigma_p^n F_p^n \frac{\partial v_p^n}{\partial x} \right) V_p^0 + O(dt^3) \tag{54}$$

This expression is different from that derived by Bardenhagen [1] using piecewise linear approximations for σ and for F. The error in equation (54) is $\frac{dt^3}{12} \frac{\partial t^2}{\partial t^2}(\sigma F \frac{\partial V_p}{\partial x})$, while the error in Bardenhagen's expression is about a factor of three larger. Substituting for the spatial derivatives in equation (54) gives

$$\Delta S \mathscr{E} = \frac{dt}{2}$$

$$\sum_p \left(\sigma_p^{n+1} F_p^{n+1} \sum_i D_{ip}(x_p^{n+1}) \sum_q S_{qi}(x_q^{n+1}) v_q^{n+1} \frac{m_q}{m_i} + \sigma_p^n F_p^n \sum_i D_{ip}(x_p^n) \sum_q S_{qi}(x_q^n) v_q^n \frac{m_q}{m_i} \right) V_p^0 \tag{55}$$

Changing the order of summation gives

$$\Delta S \mathscr{E} = \frac{dt}{2} \left(\sum_q v_q^{n+1} \sum_i S_{qi}(x_q^{n+1}) \frac{m_q}{m_i} \sum_p D_{ip}(x_p^{n+1}) \sigma_p^{n+1} F_p^{n+1} V_p^0 + \right.$$
$$\left. \sum_q v_q^n \sum_i S_{qi}(x_q^n) \frac{m_q}{m_i} \sum_p D_{ip}(x_p^n) \sigma_p^n F_p^n V_p^0 \right) \tag{56}$$

The two symmetry relations mentioned in the introduction are now needed

$$S_{qi}(x_q(t)) = S_{iq}(x_q(t)) \tag{57}$$

and

$$D_{qi}(x_q(t)) = D_{iq}(x_q(t)) \tag{58}$$

to be able to write equation (56) as

$$\Delta S\mathscr{E} = \frac{dt}{2}$$

$$\left(\sum_q v_q^{n+1} \sum_i S_{iq}(x_q^{n+1}) \frac{m_q}{m_i} \sum_p D_{pi}(x_p^{n+1}) \sigma_p^{n+1} F_p^{n+1} V_p^0 + \sum_q v_q^n \sum_i S_{iq}(x_q^n) \frac{m_q}{m_i} \sum_p D_{pi}(x_p^n) \sigma_p^n F_p^n V_p^0 \right)$$

6 Energy Conservation Error of the Stormer Verlet Scheme

Combining the kinetic and strain energy expressions gives the energy conservation error

$$\Delta\mathscr{E}\mathscr{E}_{err} = \frac{-dt}{2} \left(\sum_p \frac{(v_p^{n+1} + v_p^n)}{2} \right) \left[\sum_i S_{ip}(x_p^{n+1}) \frac{m_p}{m_i} \sum_q D_q(x_q^{n+1}) \sigma_q^{n+1} F_q^{n+1} V_q^0 \right.$$

$$\left. + \sum_i S_{ip}(x_p^n) \frac{m_p}{m_i} \sum_q D_{qi}(x_q^n) \sigma_q^n F_q^n V_q^0 \right] -$$

$$\left(\sum_q v_q^{n+1} \sum_i S_{iq}(x_q^{n+1}) \frac{m_q}{m_i} \sum_p D_{pi}(x_p^{n+1}) \sigma_p^{n+1} F_p^{n+1} V_p^0 + \sum_q v_q^n \sum_i S_{iq}(x_q^n) \frac{m_q}{m_i} \sum_p D_{pi}(x_p^n) \sigma_p^n F_p^n V_p^0 \right)$$

Assuming for the moment that the D and S values are updated to have the final velocities this may now be simplified to be

$$\Delta\mathscr{E}\mathscr{E}_{err} = \frac{dt}{2} \left(\left(\sum_q (v_q^{n+1} - \frac{(v_q^{n+1} + v_q^n)}{2}) \sum_i S_{iq}(x_q^{n+1}) \frac{m_q}{m_i} \sum_p D_{pi}(x_p^{n+1}) \sigma_p^{n+1} F_p^{n+1} V_p^0 \right. \right.$$

$$\left. \left. + \sum_q (v_q^n - \frac{(v_q^{n+1} + v_q^n)}{2}) \sum_i S_{iq}(x_q^n) \frac{m_q}{m_i} \sum_p D_{pi}(x_p^n) \sigma_p^n F_p^n V_p^0 \right) \right) \tag{59}$$

and again to

$$\Delta\mathscr{E}\mathscr{E}_{err} = \frac{dt}{2} \sum_q \left(\frac{(v_q^{n+1} - v_q^n)}{2} \right)$$

$$\left(\sum_i S_{iq}(x_q^{n+1}) \frac{m_q}{m_i} \sum_p D_{pi}(x_p^{n+1}) \sigma_p^{n+1} F_p^{n+1} V_p^0 - \sum_i S_{iq}(x_q^n) \frac{m_q}{m_i} \sum_p D_{pi}(x_p^n) \sigma_p^n F_p^n V_p^0 \right) \tag{60}$$

Using (18,20,25) and (28) this may now be written as

$$\Delta\mathscr{E}\mathscr{E}_{err} = \frac{dt}{2} \sum_q \left(\frac{(v_q^{n+1} - v_q^n)}{2} \right) m_q \left(a_q^{n+1} - a_q^n \right) \tag{61}$$

It follows that if all the components of the above equation are differentiable then

$$\Delta\mathscr{E}\mathscr{E}_{err} = O(dt^3) \tag{62}$$

6.1 Contribution from the Body Forces

The body forces may be divided by nodal mass to get body accelerations at the nodes, denoted here by $\hat{b}_i$. The body accelerations at the particles are denoted by $\hat{b}_p$. It is then routine to show that the energy error due to the body forces, $\Delta \mathscr{E} \mathscr{E}_{err}^B$ is given by

$$\Delta \mathscr{E} \mathscr{E}_{err}^B = \frac{-dt}{2} \left(\sum_p \frac{(v_p^{n+1} + v_p^n)}{2} \Big[\sum_i S_{ip}(x_p^{n+1/2})\hat{b}_i^{n+1} + \sum_i S_{ip}(x_p^n)\hat{b}_i \Big] - \sum_q v_q^{n+1}\hat{b}_q^{n+1} - \sum_q v_q^n \hat{b}_q^n \right)$$

Using the expression

$$\hat{b}_p^n = \sum_i S_{ip}(x_p^n)\hat{b}_i^n + (\hat{b}_p^n - \sum_i S_{ip}(x_p^n)\hat{b}_i^n)) \tag{63}$$

allows the above equation to be written as

$$\Delta \mathscr{E} \mathscr{E}_{err}^B = \frac{dt}{2} \left(\sum_q (v_q^{n+1} - \frac{(v_q^{n+1} + v_q^n)}{2})\hat{b}_q^{n+1} + \sum_q (v_q^n - \frac{(v_q^{n+1} + v_q^n)}{2})\hat{b}_q^n + ERR_b \right) \tag{64}$$

and as

$$\Delta \mathscr{E} \mathscr{E}_{err}^B = \frac{dt}{2} \left(\sum_q (\frac{(v_q^{n+1} - v_q^n)}{2})(\hat{b}_q^{n+1} - \hat{b}_q^n) + ERR_b \right) \tag{65}$$

where the term ERR_B is given by

$$ERR_B = \frac{dt}{2} \left(\sum_p \frac{(v_q^{n+1} - v_q^n)}{2}(b_p^n - b_p^{n+1} + \sum_i S_{ip}^{n+1}b_i^{n+1} - \sum_i S_{ip}^n b_i^n) \right) \tag{66}$$

Again all these terms are $O(dt^3)$ if there is sufficient smoothness in time.

6.2 Energy Conservation Errors of The Stress First/Last Schemes

The above analysis may easily be extended to the stress first and stress last schemes discussed by [1]. In the case of Stress First this gives, in terms of the particular Stress First accelerations and velocities [?], the energy conservation error

$$\Delta \mathscr{E} \mathscr{E}_{err}^{first} = \frac{-dt}{2} \sum_q v_q^n m_q \left(a_q^{n+1} - a_q^n \right) \tag{67}$$

While in the case of Stress Last the sign is reversed. It follows that both these errors are $O(dt^2)$.

7 COMPUTATIONAL EXPERIMENTS

In order to illustrate the above results the model 1D bar problem used by [5] and [3] is used. The cell width is $h = 10^{-2}$, the material density is $\rho_0 = 1$ and the time interval is [0,1]. The initial spatial discretization uses two evenly spaced particles per cell with the spatial domain being $[0, 1]$. The Young's modulus values are $E = 256$ and $E = 64$. The maximum displacement is $A = 0.015$, and $A = 0.05$ and the time step values used are $dt = 10^{-6}, 10^{-5}, 10^{-4}, 10^{-3}$. In

both these cases for the values given of *A* it should be noted that with the use of the above parameters particles will cross from one cell to another.

Experiments were undertaken with the MPM GIMP method [9] These experiments were run with fixed time steps as shown in Table 1 in which the time step, *dt* is varied appropriately. The number of grid crossings varies greatly, see [3]. Roughly speaking the case with $A = 1.5e-2$ has about half the grid crossings of the case when $A = 5.0e-2$. The results in Table 1 show for the maximum over th timesteps of the sum of squares of energy and displacement errors that the Stormer Verlet method is much better at conserving energy that a standard MPM approach, as indeed the theoretical results suggest. Moreover the theoretical local second and third order accuracies also in this case give rise to global second and third order accuracy.

8 CONCLUSIONS

This approach addresses the conservation properties of the MPM method by deriving the conservation properties of the Stormer Verlet Method and by contrasting it in experiments with the Stress First and Stress Last methods discussed by [1]. The Stormer Verlet method appears to have superior energy conserving properties.

REFERENCES

[1] Bardenhagen S., Energy conservation error in the material point method for solid mechanics, *Journal of Computational Physics*, 180, 2002, 383-403.

[2] Bardenhagen s. and Kober E., The generalized interpolation material point method, *Computer Modeling in Engineering and Science*, 5 (2004), 477-495.

[3] Berzins M. Nonlinear stability and time step selection for the MPM method, *Computational Particle Mechanics*, Jan, 2018.

[4] Buzi O., Pedroso D.M. and Giacomini A. Caveats on the Implementation of the Generalized Material Point Method. *CMES.* vol 31, 2, 85-106, 2008

[5] Gritton C.E. and Berzins M., Improving Accuracy In the MPM Methods by Using a Null Space Filter, *Computational Particle Mechanics* 2017, 4 131-142.

[6] Hairer E., Lubich C., and Wanner G., Geometric numerical integration illustrated by the Stormer-Verlet Method. *Acta Numerica* 2003, pp.399-450, Cambridge University Press.

[7] Leimkuhler B.and Reich S., *Simulating Hamiltonian dynamics*. Cambridge Monographs on Applied and Computational Science. Cambridge University Press 2004.

Table 1: Maximum Energy and Maximum Displacement Errors over Timesteps

	A=1.5e-2	E = 256			A=5e-2	E =256	
dt	Method	Energy Error	Displacement Error	dt	Method	Energy Error	Displacement Error
1e-3	GIMP	3.2e-2	5.2e-5	1e-3	GIMP	4.5e-4	2.4e-3
	SVGP	7.5e-6	7.8e-5		SVGP	2.4e-4	3.0e-3
1e-4	GIMP	2.3e-4	2.2e-5	1e-4	GIMP	7.0e-3	2.9e-3
	SVGP	7.7e-9	2.1e-5		SVGP	1.0e-6	3.0e-3
1e-5	GIMP	2.5e-6	2.3e-5	1e-5	GIMP	1.0e-4	2.8e-3
	SVGP	8.5e-12	2.3e-5		SVGP	1.5e-9	2.8e-3
1e-6	GIMP	2.5e-8	2.3e-5	1e-6	GIMP	1.0e-6	2.7e-3
	SVGP	9.0e-15	2.3e-5		SVGP	1.6e-12	2.7e-3
	A=1.5e-2	E = 64			A=5e-2	E =64	
dt	Method	Energy Error	Displacement Error	dt dt	Method	Energy Error	Displacement Error
1e-3	GIMP	1.2e-3	1.8e-5	1.e-3	GIMP	1.9e-2	9.3e-4
	SVGP	2.0e-7	2.5e-5		SVGP	7.9e-6	6.3e-4
1e-4	GIMP	1.2e-5	6.2e-6	1e-4	GIMP	2.5e-4	7.0e-4
	SVGP	1.7e-10	6.5e-6		SVGP	1.3e-8	6.9e-4
1e-5	GIMP	1.4e-7	7.4e-6	1e-5	GIMP	2.8e-6	7.3e-4
	SVGP	2.0e-13	7.4e-6		SVGP	1.8e-11	7.3e-4
1e-6	GIMP	1.5e-9	7.5e-6	1e-6	GIMP	2.9e-8	7.3e-4
	SVGP	2.0e-16	7.5e-5		SVGP	2.0e-14	7.0e-4

[8] Love, E and Sulsky, D. An energy consistent material point method for dynamic finite deformation plasticity. *International Journal for Numerical Methods in Engineering*. 65. 1608 - 1638, 2006.

[9] Steffen M., Wallstedt P.C., Guilkey J.E. , Kirby R.M. and Berzins M., Examination and analysis of implementation choices within the Material Point Method (MPM), *Computer Modeling in Engineering & Sciences*, 2008, 31, 2, 107-127.

[10] Sulsky D., Chen Z. and Schreyer H.L. A particle method for history-dependent materials. *Computer Methods in Applied Mechanics and Engineering* 118 (1994):179-196.

[11] Sulsky D., Zhou S.-J. and Schreyer H.L. Application of a particle-in-cell method to solid mechanics. *Computer Physics Communications* 87 (1995):236-252 .

[12] Wallstedt P.C. and Guilkey J.E., An evaluation of explicit time integration schemes for use with the generalized interpolation material point method. *Journal of Computational Physics* 2008, 227, 22, 9628-9642.

APPLICATION OF MIXED MESHLESS SOLUTION PROCEDURES FOR DEFORMATION MODELING IN GRADIENT ELASTICITY

BORIS JALUŠIĆ[1], TOMISLAV JARAK[1] AND JURICA SORIĆ[1]

[1]University of Zagreb, Faculty of Mechanical Engineering and Naval Architecture
Ivana Lučića 5, 10002 Zagreb
boris.jalusic@fsb.hr; tomislav.jarak@fsb.hr, jurica.soric@fsb.hr; www.fsb.hr/lnm

Key words: Mixed MLPG methods, fourth-order differential equation, gradient elasticity

Abstract. The present study is related to the utilization of the mixed Meshless Local Petrov-Galerkin (MLPG) methods for solving problems in gradient elasticity, which are governed by fourth-order differential equations. Here, three different numerical MLPG methods are presented, where the continuity requirements for the approximation functions are lowered by applying different mixed procedures to improve the numerical accuracy and efficiency. The first one is based on the direct solution of the problem, where the primary variable (displacement) and its independently chosen higher-order variables are approximated separately. The global discretized system of equations consists of appropriate equilibrium and compatibility equations written for each node and the solution vector contains all unknown independent nodal variables. Such approach demands only the first-order continuity of meshless approximation functions. The second and third procedures are both based on the displacement-based operator-split approach, where the original gradient elasticity problem is solved as two uncoupled problems governed by the second-order differential equations. Herein, in both uncoupled problems only primary variable (displacement) and its first derivative (strain) are approximated independently. In these procedures the original problem is solved by a staggered approach, where the solution of the first uncoupled equation is utilized as an input in the second equation. The main difference in the second and third procedure is that the one is based on the solution of the local weak forms of the governing equations, while the other is based on solution of the strong forms of the same equations. The accuracy of the presented computational methods is compared to analytical solutions and demonstrated on a one-dimensional benchmark problem of axial bar in gradient elasticity.

1 INTRODUCTION

The solution of the fourth-order differential equations using the Finite Element Method (FEM) results is complicated formulations [1]. When solved using primal FEM, where only primary variable (displacement) is approximated, the C1 continuous shape functions are a necessity, which results in complexity even for two-dimensional problems [2]. On the other hand, if mixed FEM procedures [3] are utilized, the well-known Ladyzhenskaya–Babuška–Brezzi (LBB) conditions [4] need to be satisfied to ensure the stability of the method, and a large number of unknown nodal variables appear. Alternatively, meshless methods have attracted attention due to simple manner of construction of high-order continuity approximations [5]. Nevertheless, the calculation of high-order meshless approximation

functions and their derivatives is still a major drawback due to its high computational costs. This can be easily seen in early papers where primal C1 formulations of meshless methods are applied for solving thin beams [6] and plates [7]. Furthermore, weak form primal meshless methods suffer from a further computational deficiency due to the inaccurate integration of the weak forms containing the derivatives of meshless functions [8]. This deficiencies are here alleviated to a certain extent by using the mixed MLPG method paradigm [9].

In this contribution, three different mixed MLPG methods for solving problems in gradient elasticity are proposed. For simplicity, here the proposed approaches are presented only for one-dimensional elasticity, but they can readily be extended to higher dimensional problems. In the first method, the displacement and the higher-order independent variables are approximated separately by the same functions. The governing equations are based on the local weak form of the original strain gradient equation and the compatibility conditions between the approximated variables. In the standard Galerkin weak forms, the Heaviside functions are chosen as the test function leading to the mixed Meshless Finite Volume Method (mMFVM) [10]. Therein, the use of the mixed stratagem lowers the continuity on trial functions and enables the use of lower polynomial bases, which improves numerical stability and reduces computational costs. In this formulation, only the values of nodal shape functions need to be calculated in order to assemble the nodal stiffness matrix. The second and third considered formulations are based on the operator-split solution procedure, where the original gradient elasticity fourth-order differential equation is first decomposed in an uncoupled two sets of the second-order differential equations [11], for the purpose of decreasing the continuity requirement on the trial functions. Hence, two different boundary value problems, local (classical) and non-local (gradient), are being solved, where the solution of the former problem is used as an input in the latter one. The continuity requirements for trial functions are further lowered by separately approximating displacements and their first derivatives in each decoupled equation set. In the second procedure which is based on the use of the local weak forms of the governing equations the application of the operator-split solution scheme [12], utilizing the mixed meshless approach, results in a C0 meshless formulation. Hence, within this approach only the values of nodal shape functions need to be computed to assemble coefficient matrices. In comparison, in the third procedure where the strong forms of the governing equations are being used the calculation of the first-order derivatives of shape functions is necessary in order to assemble the coefficient matrices.

The paper is organized as follows: Section 2 is related to the overview of the governing equations for one-dimensional gradient elasticity for three different solution procedures being considered. The brief description of the utilized Interpolating Moving Least Squares (IMLS) approximation [13] and the derivation of the applied mixed meshless methods are presented in Section 3. One numerical example of axial bar subjected to force in gradient elasticity is analyzed in Section 4. In the last section, concluding remarks on the presented solution procedures are given.

2 GOVERNING EQUATIONS

2.1 Mixed Meshless Finite Volume Method (mMFVM)

In order to present the proposed mixed meshless finite volume procedure, here a general governing equation for a homogeneous axial bar in gradient elasticity

$$Eu'' - l^2 Eu'''' + q = 0, \quad \text{in} \ \Omega, \tag{1}$$

is considered. In equation (1), the unknown variable is the displacement u, and the primed symbols denote its derivatives, while q denotes the axial continuous load per unit length. In order to solve the problem, boundary conditions (BCs) on the outer global boundary Γ need to be satisfied. These BCs can be written as

$$u = \bar{u} \ \text{on} \ \Gamma_u, \ P = \bar{t} \ \text{on} \ \Gamma_P, \ \Gamma = \Gamma_P \cup \Gamma_u, \ \Gamma_P \cap \Gamma_u = \varnothing,$$

$$R = \bar{R} \ \text{on} \ \Gamma_R, \ Du = \overline{u_{,1}} = \bar{\varepsilon} \ \text{on} \ \Gamma_{Du}, \ \Gamma = \Gamma_R \cup \Gamma_{Du}, \ \Gamma_R \cap \Gamma_{Du} = \varnothing, \tag{2}$$

where $u_{,1} = \varepsilon$ is the first-order displacement gradient, i.e. strain, and P and R are the tractions and double tractions, respectively, while $\Gamma_u, \Gamma_P, \Gamma_{Du}$ and Γ_R denote parts of Γ with the prescribed values for the displacements, strains, tractions and double tractions, respectively. These tractions are defined as

$$P = t = n(\sigma + \mu) = n(\sigma - \tau_{,1}) = n\tilde{\sigma}, \ R = nT = nn\tau = \tau. \tag{3}$$

Herein, t and T stand for the "true" tractions and double tractions, while P and R are their generalized "mathematical" counterparts emerging from the variational formulation of the considered problem. Note that in general the above equality between the "true" and generalized loading variables is not valid, see e.g. [3] for a detailed discussion on that subject. n denotes the outward unit normal vector on the global boundary, and $\tilde{\sigma} = \sigma + \mu$ stands for the true stress, with $\mu = -\tau_{,1}$ is the second-order stress, and τ denotes the double stress. Here it is important to note that the value of R is completely defined by the value of τ, e.g. $\Gamma_R = \Gamma_\tau$.

In this contribution, a simple constitutive law with only one microstructural parameter l is employed. Hence, $\sigma = E\varepsilon = Eu_{,1}$ is the Cauchy stress, and $\tau = l^2 \nabla \sigma = l^2 Eu_{,11}$ is the double stress, with E as the Young's modulus. According to the mixed MLPG strategy, the primal displacement u and the variables depending on the displacement gradients may all be regarded as independent variables and approximated separately [9]. In this contribution, the set of variables is chosen so that it simplifies the integrals of the weak form as much as possible, while preserving a clear physical overview. These set of chosen independent variables are as follows

$$u_1 = u, \ u_2 = \varepsilon = u', \ u_3 = \eta = u'', \ u_4 = \mu = -l^2 Eu'''. \tag{4}$$

For simplification the substitutions $\{u, \varepsilon, \eta, \mu\} = \{u_1, u_2, u_3, u_4\}$ are employed in the further text. By using the set of independent variables (4), the original governing equation (1) may be recast into the following system of equations

$$\begin{aligned} u' - \varepsilon &= 0, & \Rightarrow & \quad u_1' - u_2 = 0, \\ \varepsilon' - \eta &= 0, & \Rightarrow & \quad u_2' - u_3 = 0, \\ \tau_{,1} + \mu &= 0, & \Rightarrow & \quad l^2 Eu_3' + u_4 = 0, \\ (\sigma + \mu)_{,1} + q &= 0, & \Rightarrow & \quad Eu_2' + u_4' + q = 0, \end{aligned} \tag{5}$$

where the fourth equation is the equilibrium equation written in terms of stresses, and the first three equations represent the compatibility equations between various independent variables. The local weak forms of the governing equations (5) may now be written for each node as

$$\int_{\Omega_S} v_1 \left(u_1' - u_2 \right) \mathrm{d}x = 0, \qquad \int_{\Omega_S} v_2 \left(u_2' - u_3 \right) \mathrm{d}x = 0,$$

$$\int_{\Omega_S} v_3 \left(l^2 E u_3' + u_4 \right) \mathrm{d}x = 0, \qquad \int_{\Omega_S} v_4 \left(E u_2' + u_4' + q \right) \mathrm{d}x = 0. \tag{6}$$

In all the above equations the Heaviside functions are chosen as the test functions v_i, $i = 1, 2, 3, 4$, leading to the mixed meshless finite volume method (mMFVM).

2.2 Mixed Meshless Finite Volume Operator Split Method (mMFVOSM)

In the second procedure the original fourth-order governing equation (1) is solved as an uncoupled sequence of two differential equations of the second-order. According to [12] the original problem is split into classical (local) governing equation

$$E u_c'' + q = 0, \quad \text{in } \Omega, \tag{7}$$

and the gradient (non-local) governing equation

$$u_g - l^2 u_g'' = u_c, \quad \text{in } \Omega. \tag{8}$$

Herein and in the following, the indices c and g denote the variables and objects referring to the classical (7) or gradient problem (8), respectively. The problem stated by (7) and (8) can be solved in a staggered manner. Firstly the classical problem (7) is solved and thereafter its solutions are used as input in the gradient problem (8). Due to the operator-split procedure the BCs of the original problem (2) have to be modified [11]. The BCs that need to be satisfied when solving (7) and (8) are

$$u_c = \bar{u}_c \ \text{ on } \Gamma_{cu}, \quad t_c = \sigma_{c11} n_c = \bar{t}_c \ \text{ on } \Gamma_{ct}, \quad \Gamma_c = \Gamma_{cu} \cup \Gamma_{ct},$$

$$u_g = \bar{u}_g \ \text{ on } \Gamma_{gu}, \quad t_g = l^2 u_g' n_g = \bar{t}_g \ \text{ on } \Gamma_{gt}, \quad \Gamma_g = \Gamma_{gu} \cup \Gamma_{gt}, \tag{9}$$

where Γ_{cu} and Γ_{gu} denote parts with the prescribed values of essential BCs of displacements u_c and u_g, while Γ_{ct} and Γ_{gt} are the parts where natural BCs are applied. These natural BCs include prescribed values of classical traction t_c and the second-order traction t_g. The local weak forms of the governing equations of the classical (7) and gradient problem (8), after the integration by parts, are written as

$$\int_{\Omega_S} v_c' E u_c' \mathrm{d}x \ - \int_{\Gamma_S \cup \Gamma_{cu}} v_c t_c \mathrm{d}x = -\int_{\Omega_S} v_c q \mathrm{d}x + \int_{\Gamma_{ct}} v_c \bar{t}_c \mathrm{d}x,$$

$$\int_{\Omega_S} v_g u_g \mathrm{d}x + \int_{\Omega_S} l^2 v_g' u_g' \mathrm{d}x \ - \int_{\Gamma_S \cup \Gamma_{gu}} v_g t_g \mathrm{d}x = \int_{\Omega_S} v_g u_c \mathrm{d}x + \int_{\Gamma_{gt}} v_g \bar{t}_g \mathrm{d}x. \tag{10}$$

In the considered operator-split procedure, a mixed meshless paradigm as in [9] is utilized in the classical problem (the first equation in (10)), and the gradient problem is discretized in analogous manner (the second equation in (10)). Accordingly, the classical or gradient displacements and their first-order derivatives (strains), u_c and $\varepsilon_c = u_c'$, or u_g and $\varepsilon_g = u_g'$, respectively, are chosen as the unknown system variables, depending on the equation being solved. All the unknown variables are approximated separately using the same approximation

functions. Again, in the weak forms in (10) the Heaviside function may be used as the test function in order to reduce computational costs and to improve the numerical accuracy and stability. It is then obvious that all the natural BCs ($t_c = \bar{t}_c$ on Γ_{ct} and $t_g = \bar{t}_g$ on Γ_{gt}) are enforced in the weak sense. The unknown displacements and the first order derivatives are connected via well-known compatibility equations $\varepsilon_c = u_c'$, $\varepsilon_g = u_g'$. They can be enforced for each node in a weak form over the local subdomain as in mMFVM, see (6), or by means of collocation at the nodes, as in [9]. In the latter case, the size of the global equation system can be reduced relatively easily by eliminating the values of nodal strains from the equations (10), see [8] or [9] for more details. Then, the essential BCs ($u_c = \bar{u}_c$ on Γ_{cu} and $u_g = \bar{u}_g$ on Γ_{gu}) can be satisfied directly as in FEM.

2.3 Mixed Meshless Collocation Operator Split Method (mMCOSM)

The third considered procedure is similar to the second one and is also based on the previously described staggered solution scheme. If the standard Galerkin weak forms of the equations (7) and (8) are written we obtain the local forms of the classical (local)

$$\int_{\Omega_S} v_c \left(Eu_c'' + q \right) dx = 0, \quad \text{in} \quad \Omega, \tag{11}$$

and gradient (non-local) governing equation

$$\int_{\Omega_S} v_g \left(u_g - l^2 u_g'' - u_c \right) dx = 0, \quad \text{in} \quad \Omega. \tag{12}$$

In the above equations the Dirac delta function is chosen as the test function leading to meshless collocation method [14]. In that way, the strong for of the governing equations only at the collocation nodes are obtained

$$Eu_c''(x_I) + q(x_I) = 0, \quad \text{in} \quad \Omega, \tag{13}$$

$$u_g(x_I) - l^2 u_g''(x_I) - u_c(x_I) = 0, \quad \text{in} \quad \Omega. \tag{14}$$

Solution procedure remains the same as in the second procedure, however there is no need for numerical integration. In the utilized solution procedure the mixed meshless collocation paradigm [15] is used. Herein, the chosen unknown system variables in the solution procedure of the classical problem are u_c and $\varepsilon_c = u_c'$, while in the gradient problem they are u_g and $\varepsilon_g = u_g'$. In order to connect the approximated variables the compatibility equations $\varepsilon_c = u_c'$, $\varepsilon_g = u_g'$ are enforced at the nodes using the collocation method. Furthermore, due to the used staggered solution procedure the BCs of the original problem according to [11] have to be changed. Thus, the BCs that need to be satisfied are

$$u_c = \bar{u}_c, \quad \text{on} \ \Gamma_{cu}, \quad t_c = \sigma_{c11} n_c = \bar{t}_c, \quad \text{on} \ \Gamma_{ct}, \tag{15}$$

$$u_g = \bar{u}_g \quad \text{on} \ \Gamma_{gu}, \quad t_g = n_g^2 u_g'' = \bar{t}_g, \quad \text{on} \ \Gamma_{gt}. \tag{16}$$

The essential BCs are here again enforced directly as in FEM, while the natural BCs are discretized using mixed meshless collocation and satisfied at the collocation nodes as in [16].

3 NUMERICAL IMPLEMENTATION

3.1 Discretization

The global domain Ω in both procedures is discretized by a set of N nodes $x_I, I = 1, 2, ..., N$. Around each node I a local sub-domain Ω_S^I is defined, bounded by a local boundary Γ_S^I, as displayed in Fig.1.
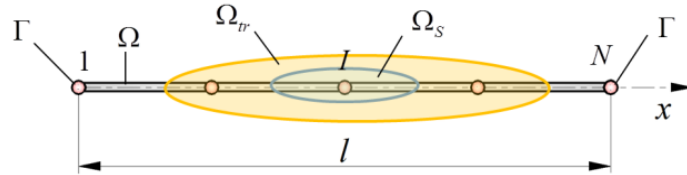

Figure 1: Discretization model

The local weak forms of equations (6) or (10) are written for each Ω_S^I. All the considered unknown variables are approximated using the same meshless approximation scheme. In the first procedure (mMFVM), independently chosen variables u_i from (4) are considered as the unknown variables in (6). Within the mMFVOSM, in the local problem the classical displacement u_c and the classical strain ε_c are approximated, while in the non-local problem gradient displacement u_g and gradient strain ε_g are utilized as unknown variables. Here, the IMLS approximation is used, written as

$$\varphi(x) = \sum_{J=1}^{N} \phi_J(x)(\hat{\varphi})_J. \tag{17}$$

In (17), ϕ_J and $(\hat{\varphi})_J$ represent the one-dimensional (1D) nodal shape function and the nodal value of the approximated variables at node J, respectively. According to [17, 18], the nodal shape function $\phi_J(x)$ can be written as

$$\phi_J(x) = \mathbf{p}^T(x) \left[\mathbf{A}^{-1}(x) \mathbf{B}(x) \right]_J. \tag{18}$$

In equation (18) the momentum matrix $\mathbf{A}(x)$ is

$$\mathbf{A}(x) = \sum_{J=1}^{n} W_J(x) \mathbf{p}(x_J) \mathbf{p}^T(x_J), \tag{19}$$

while the matrix $\mathbf{B}(x)$ is written as

$$\mathbf{B}(x) = \left[W_1(x)\mathbf{p}(x_1) \quad W_2(x)\mathbf{p}(x_2) \quad \cdots \quad W_J(x)\mathbf{p}(x_J) \quad \cdots \quad W_n(x)\mathbf{p}(x_n) \right]. \tag{20}$$

In order to improve the conditioning of the momentum matrix $\mathbf{A}(x)$, the complete monomial basis $\mathbf{p}$ is written in terms of local normalized coordinates [19]. Within (19) and (20) $W_J(x)$ represents the weight function associated with node J. In this contribution the regularized weight function [20] is utilized to ensure the Kronecker delta property, $\phi_J(x_I) \approx \delta_{JI}$. It

should be stated that the node I influences the values of the approximated variables only at the points within the weight function support domain Ω_{tr}^I.

In the first considered procedure (mMFVM), by inserting approximations defined by (17) into the local weak forms (6), the system consisting of four linear algebraic equations obtained for each node. In the operator split procedure, by using the approximations (17) within the weak forms (10) only one algebraic equation is obtained for a given node in each of the problems considered (local and gradient). For both procedures, a global system of equations is achieved by writing the equations in node-by-node principle [18].

3.2 Discretized equations of the mMFVM

Analogously to the formulation in [10], all the test functions v_i in (6) are chosen to be Heaviside functions. Hence, a form of mixed Meshless Finite Volume Method (mMFVM) is obtained. In order to derive the discretized system of equations for each node, firstly the integration by parts and divergence theorem is applied in all weak forms (6). Secondly, the discretization of the chosen independent variables using IMLS functions [20] is done leading to the final system of equation for the node I

$$\sum_{J=1}^{N} \mathbf{K}_{IJ}\, \hat{\mathbf{U}}_J = \mathbf{R}_I, \tag{21}$$

where $\mathbf{K}_{IJ}$ is the contribution of the node J to the stiffness of the local subdomain of the node I, Ω_S^I. In (21) $\hat{\mathbf{U}}_J$ denotes the vector consisting of nodal variables at the node J, while $\mathbf{R}_I$ is the nodal force vector at node I. For the chosen independent variables vector $\mathbf{R}_I$ is defined as

$$\mathbf{R}_I = \left[-\int_{\Gamma_u^I} n\, \bar{u}_1 \,\mathrm{d}\Gamma \quad -\int_{\Gamma_{Du}^I} n\, \bar{u}_2 \,\mathrm{d}\Gamma \quad -\int_{\Gamma_R^I} \bar{T} \,\mathrm{d}\Gamma \quad -\int_{\Omega_S^I} q \,\mathrm{d}\Gamma - \int_{\Gamma_P^I} \bar{t} \,\mathrm{d}\Gamma \right]^{\mathrm{T}}. \tag{22}$$

In the above equation, n represents the outward unit normal vector to the global boundary, and the prescribed values are defined as

$$\begin{aligned}
&\bar{u}_1 = \bar{u}, \qquad \bar{u}_2 = \bar{\varepsilon} = \bar{u}', \\
&\bar{T} = n\, \bar{\tau} = n\, l^2 E\, \bar{u}'' = n\, l^2 E\, \bar{u}_3, \\
&\bar{t} = n\, \bar{\tilde{\sigma}} = n\left(\bar{\sigma} + \bar{\mu} \right) = n\left(E\, \bar{u}' - l^2 E\, \bar{u}''' \right) = n\left(E\, \bar{u}_2 + \bar{u}_4 \right).
\end{aligned} \tag{23}$$

Note that the double traction $\bar{R}$ is completely defined by the known value of the double stress $\bar{\tau}$, according to (3). From (22), it is obvious that in this method all BCs are satisfied in a weak form, without the need to introduce special procedures for enforcing BCs, which can be a problem in meshless methods [18]. In addition, all non-zero terms of the matrix $\mathbf{K}_{IJ}$ are integrals over Ω_S^I and the parts of local boundary Γ_S^I, and contain only nodal shape functions. Therefore, the stiffness matrix can be computed without the need of performing costly and inaccurate numerical integration of the derivatives of nodal shape functions.

3.3 Discretized equations of the mMFVOSM

Here again the test functions in both classical v_c and gradient problem v_g are chosen to be Heaviside functions in order to obtain a form of the mMFVOSM. According to the mixed MLPG strategy the local weak forms (10) are firstly discretized by using the approximation (17) for ε_c and ε_g. Next, to obtain the discretized systems of equations with only the classical u_c and gradient u_g displacements as unknowns, the compatibility between the approximated strains and displacements is enforced via the collocation method at the nodes of the model. By employing the compatibility conditions in the discretized form of the local weak forms (10) the nodal strains are eliminated. This nodal elimination can be performed efficiently during the node-by-node assembly of the global system of equations for both the classical and gradient problems. Firstly, the classical problem is assembled and solved, and thereafter, the solution of the classical problem is utilized in the assembly of the gradient system of equations, where the obtained classical displacements appear as the input term in the gradient nodal force vector. The final systems of equations in this procedure can be written as

$$\sum_{J=1}^{N} \mathbf{K}_{IJ}^{c} \, \hat{\mathbf{U}}_{J}^{c} = \mathbf{R}_{I}^{c},$$

$$\sum_{J=1}^{N} \mathbf{K}_{IJ}^{g} \, \hat{\mathbf{U}}_{J}^{g} = \mathbf{R}_{I}^{g}, \tag{24}$$

where $\mathbf{K}_{IJ}^{c}$ and $\mathbf{K}_{IJ}^{g}$ are the contributions of the node J to the coefficient matrices associated with the local subdomains of node I in the classical and gradient problem, respectively, while the nodal vectors $\hat{\mathbf{U}}_{J}^{c}$ and $\hat{\mathbf{U}}_{J}^{g}$ consist of unknown classical and gradient displacements. Furthermore, the nodal vectors on the right-hand side at node I are equal to

$$\mathbf{R}_{I}^{c} = \left[\int_{\Omega_S^I} q \, \mathrm{d}\Gamma + \int_{\Gamma_{ct}^I} \overline{t}_c \, \mathrm{d}\Gamma \right],$$

$$\mathbf{R}_{I}^{g} = \left[\int_{\Omega_S} u_c \mathrm{d}\Gamma + \int_{\Gamma_{gt}} \overline{t}_g \mathrm{d}\Gamma \right]. \tag{25}$$

As can be seen from (25), the natural BCs are satisfied in the weak sense, similar to the first procedure. Due to the interpolation property of the meshless approximation functions, in both uncoupled problems the essential BCs can be easily imposed, just as in FEM.

3.4 Discretized equations of the mMCOSM

Since the Dirac delta function in chosen as the test function in both classical v_c and gradient problem v_g the form of mMCOSM is achieved. Here, related to the mixed collocation strategy in [16] the strong forms (13) and (14) are firstly discretized utilizing (17) for ε_c and ε_g. Furthermore, in order to obtain the closed solvable systems of equations with only the classical u_c and gradient displacements u_g as unknowns, the compatibility between the approximated strains and displacements in enforced using the collocation method. As in

the second procedure, the classical problem is firstly assembled and solved. The solution of the classical problem is then used as input in the subsequent assembly and solution of the gradient problem. The obtained final system of equations in this procedure can also be written analogous to equations given by (24). In addition, at the nodes where the natural boundary conditions are present the system equations are replaced by discretized boundary conditions at the node I. The BCs are discretized using mixed collocation and can be written as

$$\mathbf{R}_I^{\text{c}} = nE\sum_{J=1}^{N}\mathbf{B}_{IJ}^{\text{c}}\ \hat{\mathbf{U}}_J^{\text{c}},$$

$$\mathbf{R}_I^{\text{g}} = n^2\sum_{K=1}^{N}\mathbf{H}_{FK}^{\text{g}}\sum_{J=1}^{N}\mathbf{G}_{KJ}^{\text{g}}\ \hat{\mathbf{U}}_J^{\text{g}}. \tag{26}$$

From (26) it is evident that all the natural BCs are satisfied in the strong sense, no numerical integration is used in the procedure. Therein, the matrices $\mathbf{B}$, $\mathbf{H}$ and $\mathbf{G}$ are compatibility matrices consisting of first-order derivatives of shape functions. Since the IMLS approximation is used the essential BCs are satisfied by a standard procedure as in FEM.

4 NUMERICAL EXAMPLE

4.1 AXIAL BAR

In order to verify the presented methods a benchmark example of the bar in gradient elasticity subjected to the axial load, displayed in Fig. 2, is considered. The problem of gradient elasticity is governed by the differential equation (1). The bar has the cross-section surface $A=1$ and the length $L=1$. The Young's modulus is taken as $E=1$. The left side of the bar is clamped, while on the right side the force $P_0=1$ is applied, as seen in Fig. 2. For the mixed Meshless Finite Volume Method (mMFVM) the utilized BCs are $u(0)=0$, $R(0)=-l^2Eu''(0)=0$, $u'(L)=\varepsilon_o=0.5$ and $P(L)=Eu'(L)-l^2Eu'''(L)=P_0$. Here, P and R stand for the generalized tractions and double-tractions, respectively.
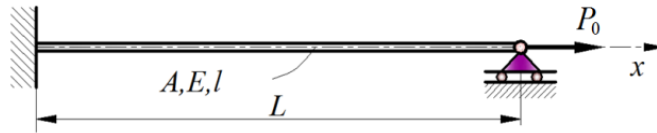

Figure 2: Axial bar in gradient elasticity

In the mMFVOSM and mMCOSM, BCs are modified. Herein, the gradient elasticity problem is governed by second-order differential equations (7) and (8). Therein, the BCs of the classical problem are defined as $u_{\text{c}}(0)=0$ and $t_{\text{c}}(L)=P_0$, while the BCs of the gradient problem are $u_{\text{g}}(0)=0$ and $u_{\text{g}}(L)=u_{\text{g}}^{\text{AN}}$. Herein, the value of the gradient displacement at the right-hand-side of the bar, at $x=L$, is dependent on the parameter l and is calculated from the analytical solution [21]. Numerical calculations using presented mixed meshless procedures have been done. For the approximation of the unknown variables only the first-order basis in the IMLS functions is used. For computing purposes, discretizations using

uniformly distributed nodes are applied. The influence of the parameter l on the deformation responses of the bar has been investigated and the obtained distributions for the displacement and strain are compared with the analytical solutions [21] as portrayed in Fig. 3 and Fig. 4.
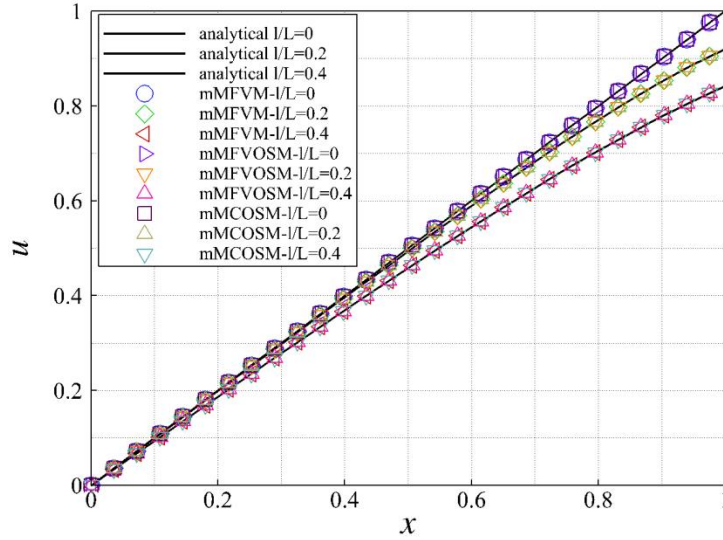

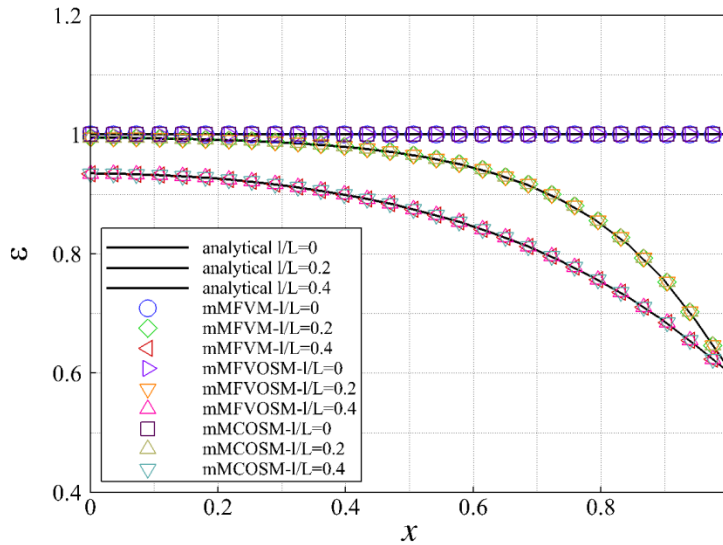**Figure 3**: Axial bar - distribution of displacement

Figure 4: Axial bar - distribution of strain

As evident, the obtained results are accurate and analytical distributions are captured correctly using all the presented mixed meshless procedures. Thus, these methods show considerable potential for applications in high dimensional structures, where gradient elasticity is a necessity. Some of these phaenomena include the modeling of size effects in structures and capturing accurate stress distributions near the crack tip in fracture problems.

5 CONCLUSION

Three different meshless methods based on the mixed MLPG stratagem for solving gradient elasticity have been proposed and applied for solving simple problems in 1D gradient elasticity. In first two mixed meshless methods, the Heaviside function is chosen as the test function leading to the forms of the mixed Meshless Finite Volume Method (mMFVM). In the third method the Dirac delta function is utilized as the test function leading to a mixed meshless collocation method. The first method (mMFVM) is based on the modification of the original fourth-order governing equation of the gradient elastic bar by employing a mixed approach, where displacements and the higher-order gradients are approximated separately, while the second (mMFVOSM) and third (mMCOSM) method are based on the application of the operator split procedure and a staggered solution of the original problem. For the approximation of all unknown field variables IMLS is utilized. In mMFVM, all BCs are satisfied in the weak sense, while in mMFVOSM a reduction of the equation system is performed, and the essential BCs are imposed directly, as in FEM. In the mMCOSM all the BCs are enforced in the strong form at the collocation nodes. The presented mixed meshless methods have been tested on one benchmark example dealing with the axially loaded bar with gradient elasticity and it has been shown that all methods yield very accurate responses even for the first-order meshless approximation functions. The obtained results imply that the proposed mixed MLPG strategies have considerable potential for solving engineering problems governed by high-order differential equations. It is to note that the application of the mixed MLPG strategy lowers the continuity requirements on the trial functions, which in general reduces the computational time and increases numerical robustness. Thus, in future research the presented methods will be extended and utilized for solving gradient elasticity problems in higher-dimensions.

REFERENCES

[1] G. Engel, K. Garikipati, T.J.R. Hughes, M.G. Larson, L. Mazzei, R.L. Taylor, Continuous/discontinuous finite element approximations of fourth-order elliptic problems in structural and continuum mechanics with applications to thin beams and plates, and strain gradient elasticity, Computer Methods in Applied Mechanics and Engineering, 191 (2002) 3669-3750.

[2] P. Fischer, J. Mergheim, P. Steinmann, On the C1 continuous discretization of non-linear gradient elasticity: A comparison of NEM and FEM based on Bernstein–Bézier patches, International Journal for Numerical Methods in Engineering, 82 (2010) 1282-1307.

[3] E. Amanatidou, N. Aravas, Mixed finite element formulations of strain-gradient elasticity problems, Computer Methods in Applied Mechanics and Engineering, 191 (2002) 1723-1751.

[4] A. J. Salgado, J. Guzmán, F.-J. Sayas, A Note on the Ladyzenskaja-Babuska-Brezzi Condition, Journal of Scientific Computing, 56 (2012) 219-229.

[5] G.R. Liu, Y.T. Gu, An Introduction to Meshfree Methods and Their Programming, Springer, Dordrecht, The Netherlands, 2005.

[6] P. Krysl, T. Belytschko, Analysis of thin plates by the element-free Galerkin method, Computational Mechanics, 17 (1995) 26-35.

[7] S.N. Atluri, J.Y. Cho, H.-G. Kim, Analysis of thin beams, using the meshless local Petrov–Galerkin method, with generalized moving least squares interpolations, Computational Mechanics, 24 (1999) 334-347.

[8] T. Jarak, J. Soric, Analysis of rectangular square plates by the mixed Meshless Local Petrov-Galerkin (MLPG) approach, CMES: Computer Modeling in Engineering & Sciences, 38 (2008) 231-261.

[9] S.N. Atluri, Z.D. Han, A.M. Rajendran, A New Implementation of the Meshless Finite Volume Method, Through the MLPG "Mixed" Approach, CMES: Computer Modeling in Engineering & Sciences, 6 (2004) 491-514.

[10] M.R. Moosavi, F. Delfanian, A. Khelil, The orthogonal meshless finite volume method for solving Euler–Bernoulli beam and thin plate problems, Thin-Walled Structures, 49 (2011) 923-932.

[11] H. Askes, I. Morata, E.C. Aifantis, Finite element analysis with staggered gradient elasticity, Computers & Structures, 86 (2008) 1266-1279.

[12] C.Q. Ru, E.C. Aifantis, A simple approach to solve boundary-value problems in gradient elasticity, Acta Mechanica, 101 (1993) 59-68.

[13] T. Most, C. Bucher, A Moving Least Squares weighting function for the Element-free Galerkin Method which almost fulfills essential boundary conditions, Structural Engineering and Mechanics, 21 (2005) 315-332.

[14] H.-Y. Hu, A.H.-D. Cheng, Radial basis collocation methods for elliptic boundary value problems, Computers & Mathematics with Applications, 50 (2005) 289–320.

[15] S.N. Atluri, H.T. Liu, Z.D. Han, Meshless local Petrov-Galerkin (MLPG) mixed collocation method for elasticity problems, CMES: Computer Modeling in Engineering & Sciences, 14 (2006) 141-152.

[16] B. Jalušić, Meshless numerical method for modeling of heterogeneous structures, Faculty of Mechanical Engineering and Naval Architecture, Zagreb, 2016.

[17] G.R. Liu, Mesh Free Methods: Moving beyond the Finite Element Method, CRC Press, Boca Raton,USA., 2003.

[18] S.N. Atluri, The Meshless Method (MLPG) for Domain & BIE Discretization, Tech Science Press, Forsyth, USA, 2004.

[19] T. Jarak, J. Soric, J. Hoster, Analysis of shell deformation responses by the meshless local Petrov-Galerkin (MLPG) approach, CMES: Computer Modeling in Engineering & Sciences, 18 (2007) 235-246.

[20] T. Most, C. Bucher, New concepts for moving least squares: An interpolating non-singular weighting function and weighted nodal least squares, Engineering Analysis with Boundary Elements, 32 (2008) 461-470.

[21] S. Papargyri-Beskou, D. Beskos, Static Analysis of Gradient Elastic Bars, Beams, Plates and Shells, 2010.

DIFFICULTIES IN IMPLEMENTATION OF VISCOSITY MODELS IN THE FRAGMENTON-BASED VORTEX METHODS

OLEG S. KOTSUR, GEORGY A. SHCHEGLOV

Bauman Moscow State Technical University
2-nd Baumanskaya, 5, 105005, Moscow, Russia
e-mail: oskotsur@gmail.com, shcheglov_ga@bmstu.ru

Key words: vortex methods, viscous fluid, fragmenton, PSE, DVM, splitting

Abstract. Fragmenton-based lagrangian vortex methods showed their effectiveness for inviscid fluid dynamics problems. However the attempts to extend these methods to viscous flows simulation meet difficulties resulting from nonfulfillment of the Helmholtz theorems of vorticity motion. Direct implementation of the viscosity models used in particle-based vortex methods leads to fragmenton "splitting" problem and accumulation of numerical errors. In this paper we discuss in details the essence of splitting problem on the examples of a classical Particle Strength Exchange (PSE) method and a hybrid DVM-PSE scheme, adapted to a fragmenton-based vortex method.

1 INTRODUCTION

Simulation of viscous fluid with vortex methods has been intensively investigated over the last 40 years. Wide range of approaches has been created to account for the diffusion term in the vorticity evolution equation, starting from the stochastic "random-walk" model of Chorin, particle strength exchange (PSE) [1], diffusion velocity method (DVM) [2], hybrid DVM-PSE schemes [3] and ending with hybrid particle-mesh methods, where the diffusion term is discretized on the mesh [4].

In all mentioned approaches vorticity is discretized over pointwise singular or regularized vortex particles (vortons), somehow distributed in the flow [5]. From the physical point of view this sight is not "natural". Vorticity field is solenoidal and it is best represented with the notion of vortex tubes, which intensity must be conserved in any flow, both viscous and inviscid. Vortex particles are mostly mathematical objects than physical ones and do not constitute a solenoidal field. This may lead to accumulation of approximation errors during the simulation. Though using hybrid particle-mesh approaches one can resolve this issue, the method itself stops being pure lagrangian anymore.

Instead of pointwise particles we consider vortex line fragments (fragmentons) [6]. They can be used either independently or connected into close filaments, making fragmentons also the basis of vortex filament method [7, 8]. Fragmenton-based vortex methods showed to be more effective in some specific inviscid cases in terms of the amount of vortex

elements needed for a stable simulation [9]. Pure lagrangian vortex fragmenton methods also showed their effectiveness for the inviscid fluid-structure interaction (FSI) problems [10], where the use of a mesh is undesirable or leads to extensive computational costs.

The good performance of fragmenton-based methods for the simulation of inviscid flows motivates to expand them also to viscous flows. However the direct application of the particle-based viscosity approaches (like PSE or DVM-PSE) to the fragmenton-based methods leads to the problem of "vorticity splitting". This problem appears due to nonfulfilment of the Helmholtz theorems that state that the material lines, initially chosen as vortex lines, stay vortex lines during their evolution in an inviscid flow, that is generally not true for the viscous flows.

It the following sections we give a brief review of the fragmenton vortex method and discuss the implementation of the classical PSE model, DVM and the hybrid DVM-PSE approach suggested by Mycek et al. [3], for the fragmenton-based vortex methods. We explain in detail the essence of the splitting problem and show that the both viscosity concepts lead to excessive splitting in the test problem of vortex oval evolution in viscous fluid.

2 FRAGMENTON-BASED VORTEX METHODS

Consider vorticity evolution equation for a tree-dimensional incompressible viscous fluid without bodies and frontiers

$$\frac{\partial \boldsymbol{\omega}}{\partial t} + (\boldsymbol{V} \cdot \nabla) \boldsymbol{\omega} = (\boldsymbol{\omega} \cdot \nabla) \boldsymbol{V} + \nu \Delta \boldsymbol{\omega}, \tag{1}$$

where $\boldsymbol{V} = \boldsymbol{V}(\boldsymbol{x}, t)$, $\boldsymbol{\omega} = \nabla \times \boldsymbol{V}$ are velocity and vorticity fields ν – kinematic viscosity.

The classical vortex methods suggest approximate the continuous vorticity field $\boldsymbol{\omega}$ with a set of pointwise vortex particles (vortons):

$$\boldsymbol{\omega}(\boldsymbol{x}, t) \approx \sum_{k=1}^{N} \boldsymbol{\alpha}_k(t) \delta(\boldsymbol{x} - \boldsymbol{x}_k),$$

where δ is the Dirac delta function and $\boldsymbol{\alpha_k}$ is the intensity of k-th vorton, which can be treated as the amount of vorticity concentrated in a point with the position $\boldsymbol{x}_k$.

Fragmenton-based vortex methods approximate the vorticity field with a set of fragments of vortex lines [6]. Each fragment (fragmenton) can be mathematically interpreted as integrals of delta function over the material vector $2\boldsymbol{h}_k$ (fig. 1):

$$\boldsymbol{\omega}(\boldsymbol{x}, t) \approx \sum_{k=1}^{N} \boldsymbol{\gamma}_k \int_{-1}^{1} \delta\big(\boldsymbol{x} - (\boldsymbol{x}_k + s\boldsymbol{h}_k)\big) ds, \tag{2}$$

where $\boldsymbol{\gamma}_k = \gamma_k \boldsymbol{h}_k$, γ_k is the k-th fragmenton scalar intensity, which can be treated as circulation of a vortex filament; $\boldsymbol{x}_k$ is fragmenton's center position (marker). It should be emphasized that $\boldsymbol{\gamma}_k$ must stay collinear to material vector $\boldsymbol{h}_k$ in the simulation. Violating this requirement may lead to stability problems caused by breakdown of the solenoidity of the vorticity field and accumulation of numerical errors.
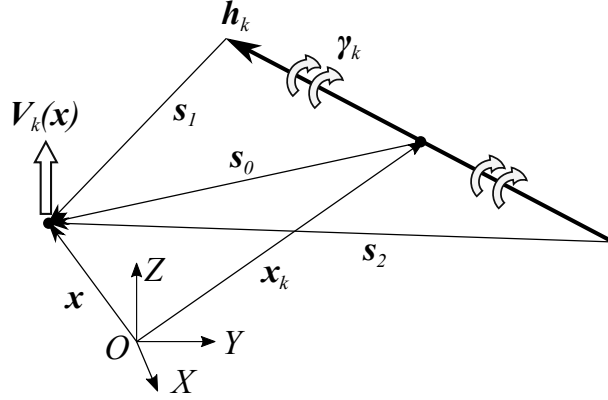
Figure 1: Fragmenton model

Velocity field, induced with the set of fragmentons (2), can be recovered by integrating (2) with the Biot-Savart kernel, that gives [6]

$$\boldsymbol{V}(\boldsymbol{x},t) \approx \sum_{k=1}^{N} \frac{\gamma_k}{4\pi} \frac{\boldsymbol{h}_k \times \boldsymbol{s}_0}{|\boldsymbol{h}_k \times \boldsymbol{s}_0|^2} \left[\left(\frac{\boldsymbol{s}_2}{|\boldsymbol{s}_2|} - \frac{\boldsymbol{s}_1}{|\boldsymbol{s}_1|} \right) \cdot \boldsymbol{h}_k \right],$$

which is also only true when $\boldsymbol{\gamma}_k$ and $\boldsymbol{h}_k$ are collinear. This formula gives singularities upon reaching the axis of a fragmenton and can be regularized as described in [6].

For the case of inviscid fluid ($\nu = 0$) substitution of (2) into the vorticity evolution equation (1) gives the system of the ODEs for the fragmenton parameters: $\boldsymbol{x}_k$, $\boldsymbol{h}_k$ and $\boldsymbol{\gamma}_k$:

$$\begin{cases} \dfrac{d\boldsymbol{x}_k}{dt} = \boldsymbol{V}(\boldsymbol{x}_k), \\[2mm] \dfrac{d\boldsymbol{h}_k}{dt} = \boldsymbol{h}_k \cdot \nabla \boldsymbol{V}(\boldsymbol{x}_k), \\[2mm] \dfrac{d\boldsymbol{\gamma}_k}{dt} = \boldsymbol{\gamma}_k \cdot \nabla \boldsymbol{V}(\boldsymbol{x}_k). \end{cases} \tag{3}$$

The last equation of (3) has the same form as the equation for $\boldsymbol{h}_k$ and therefore can equivalently be written as $\frac{d\gamma_k}{dt} = 0$, and $\boldsymbol{\gamma}_k = \gamma_k \boldsymbol{h}_k$.

Analysis of (3) shows that fragmenton markers $\boldsymbol{x}_k$ follow the velocity field $\boldsymbol{V}$. Material vector $\boldsymbol{h}_k$ and intensity vector $\boldsymbol{\gamma}_k$ change their length and direction with the velocity gradient tensor $\nabla \boldsymbol{V}$, while the fragmenton intensities γ_k stay constant in time. This behavior is aligned with the Helmholtz theorems of motion of vortex filaments in inviscid fluid, that state that

- vortex filaments conserve their strength in time;

- vortex filaments move and deform with the material lines that carry them.

The latter statement in terms of fragmenton method means that $\boldsymbol{\gamma}_k$ and $\boldsymbol{h}_k$ always stay collinear in time, which is particularly important to correctly reconstitute velocity field.

Nonzero viscosity ν results in a nonzero diffusion term in the vorticity evolution equation (1) and in nonfulfilment of the Helmholtz theorems. Physically it means that vortex filaments generally do not move and deform as the material lines, that initially carried them. This fact does not cause any problem for the hybrid particle-mesh methods, where the velocity field is found as the solution of Poisson equation [4]. However for pure lagrangian fragmenton-based methods it becomes a challenge in as much as $\boldsymbol{\gamma}_k$, which we associate with vorticity vector, and $\boldsymbol{h}_k$, which we associate with material vector, should stay collinear.

In what follows we call *splitting* the fact of misalignment of the vectors $\boldsymbol{\gamma}_k$ and $\boldsymbol{h}_k$ that potentially may occur in the simulations.

3   VISCOSITY MODELS

The variety of viscosity models created for particle-based vortex methods are all referred to the means to simplify or approximate the diffusion term $\nu\Delta\boldsymbol{\omega}$ [5, 3]. Direct implementation of these approaches to the fragmenton-based methods results in modification of the evolution equations for $\boldsymbol{h}_k$ and $\boldsymbol{\gamma}_k$ of (3) that may cause splitting, as these equations loose their symmetrical form.

Here we discuss three approaches to account for the diffusion term in particle-based vortex methods, applying them for fragmenton-based methods: Particle Strength Exchange, Diffusion Velocity Method and hybrid DVM-PSE scheme proposed by Mycek et al. [3].

3.1   Particle strength exchange

The PSE method was suggested by Degond & Mas-Gallic in [1] who gave its profound analysis in application to numerical solution of advection-diffusion equations with particle methods. The idea of the PSE method is approximation of the diffusion term $\nu\Delta\boldsymbol{\omega}$ with the integral operator of the form

$$Q^\epsilon(\boldsymbol{\omega}) = \frac{\nu}{\epsilon^2} \int_{\mathbb{R}^3} \eta_\epsilon(\boldsymbol{x} - \boldsymbol{y})(\boldsymbol{\omega}(\boldsymbol{y}, t) - \boldsymbol{\omega}(\boldsymbol{x}, t)) dy, \tag{4}$$

where $\eta_\epsilon(\boldsymbol{x}) = \frac{1}{\epsilon^3}\eta\left(\frac{\boldsymbol{x}}{\epsilon}\right)$; $\eta(\boldsymbol{x}) \in L^1(\mathbb{R}^3)$ is kernel function that must satisfy several moment conditions in order to make $Q^\epsilon(\boldsymbol{\omega})$ converge towards $\nu\Delta\boldsymbol{\omega}$ in certain norms when $\epsilon \to 0$. Details on the kernel function choice can be found in [1].

Replacing $\nu\Delta\boldsymbol{\omega}$ with the integral operator (4) and applying the fragmenton approximation (see [11] for details) we get the following set of the ODEs

$$\begin{cases} \dfrac{d\boldsymbol{x}_k}{dt} = \boldsymbol{V}(\boldsymbol{x}_k), \\[2mm] \dfrac{d\boldsymbol{h}_k}{dt} = \boldsymbol{h}_k \cdot \nabla\boldsymbol{V}(\boldsymbol{x}_k), \\[2mm] \dfrac{d\boldsymbol{\gamma}_k}{dt} = \boldsymbol{\gamma}_k \cdot \nabla\boldsymbol{V}(\boldsymbol{x}_k) + \dfrac{\nu}{\epsilon^2}\displaystyle\sum_{q=1}^{N} G_{kq}(\boldsymbol{\gamma}_q S_k - \boldsymbol{\gamma}_k S_q), \end{cases} \tag{5}$$

where S_k is the cross-section area of the vortex tube, associated to the k-th fragmenton at initial time; $S_k = \sigma_k/|2\boldsymbol{h}_k|$, where σ_k is fragmenton's volume that stays constant in time; G_{kq} is the exchange coefficient between the k-th and q-th fragmentons, which depends on their length and mutual orientation:

$$G_{kq} = \int_{-1}^{1} \int_{-1}^{1} \eta_\epsilon(x_k + \tau\boldsymbol{h}_k - \boldsymbol{x}_q - s\boldsymbol{h}_q)dsd\tau.$$

Comparison of (5) and (3) shows that the equations for $\boldsymbol{x}_k$ and $\boldsymbol{h}_k$ stay without change comparing to the equations for $\boldsymbol{x}_k$ and $\boldsymbol{h}_k$ for ideal fluid. The equation for $\boldsymbol{\gamma}_k$ obtained the additional term, responsible for the exchange of intensities between k-th and q-th fragmentons. In two-dimensional problems this additional term causes no splitting as $\boldsymbol{h}_k$ and $\boldsymbol{\gamma}_k$ have the only nonzero component in the direction normal to the symmetry plane, thus they always stay collinear. However for an arbitrary three-dimensional flow this is not true.

3.2 Diffusion velocity method

The general idea of the diffusion velocity method is to find such vector field $\boldsymbol{U}$ that can be considered as the "virtual" velocity field that transfers vortex tubes in a viscous fluid in a way that the Helmholtz theorems are valid. According to the Fridman theorem [12] such $\boldsymbol{U}$ must satisfy the equation

$$\frac{\partial \boldsymbol{\omega}}{\partial t} + (\boldsymbol{U} \cdot \nabla)\,\boldsymbol{\omega} - (\boldsymbol{\omega} \cdot \nabla)\,\boldsymbol{U} + \boldsymbol{\omega}\nabla \cdot \boldsymbol{U} = 0 \tag{6}$$

or, which is the same,

$$\frac{\partial \boldsymbol{\omega}}{\partial t} + \nabla \times (\boldsymbol{\omega} \times \boldsymbol{U}) = 0.$$

In this view there arise two principle questions:

1. Does such vector field $\boldsymbol{U}$ exist for an arbitrary three-dimensional viscous flow?

2. If yes, are there any practical ways to find this field? In that case the splitting problem would be totally fixed.

Markov and Sizykh proved in [13] that for any elementary fragment of a vortex tube there always exist such field $\boldsymbol{U}$, called *Fridman velocity*. Moreover, this field is not unique and is given by

$$\boldsymbol{U} = \boldsymbol{V} + \frac{\boldsymbol{\omega} \times (-\nu\nabla \times \boldsymbol{\omega} - \nabla f + \nabla W)}{\boldsymbol{\omega}^2} + \gamma\boldsymbol{\omega},$$

where W is arbitrary scalar field, constant along vortex filaments, γ – arbitrary scalar field, f is any scalar function satisfying the condition

$$\boldsymbol{\omega} \cdot \nabla f = -\nu\boldsymbol{\omega} \cdot (\nabla \times \boldsymbol{\omega}). \tag{7}$$

Determination of function f from the condition (7) requires integration along the vortex filaments, thus making the numerical algorithm of search of U very impractical. Another contribution in the problem of the practical ways to find Fridman velocity is given in [14]. It is demonstrated on several examples of swirling flows, that there exist such flows for which there are no local expressions of Fridman velocity U, i.e. at any point U cannot be expressed through the flow parameters in the infinitesimal neighborhood of this point. This result, conceivably, concludes the discussions and gives the negative answer on the second posed question for an arbitrary tree-dimensional viscous flow.

For two-dimensional or axisymmetrical flows without swirling determination of Fridman velocity does not require integration along the vortex filaments. For the 2D-flows it reduces to a simple expression

$$U = V + V_d,$$

where

$$V_d = -\nu \frac{\nabla|\boldsymbol{\omega}|}{\boldsymbol{\omega}^2}$$

is traditionally called *diffusion velocity.*

Therefore for two-dimensional viscous flows, vorticity evolution equation (1) can be reformulated in terms of diffusion velocity V_d as follows

$$\frac{\partial \boldsymbol{\omega}}{\partial t} + ((V + V_d) \cdot \nabla)\boldsymbol{\omega} = 0. \tag{8}$$

The fragmenton approximation of (8) gives the following system of ODEs:

$$\begin{cases} \dfrac{d\boldsymbol{x}_k}{dt} = (V + V_d)(\boldsymbol{x}_k), \\ \dfrac{d\boldsymbol{h}_k}{dt} = 0, \\ \dfrac{d\boldsymbol{\gamma}_k}{dt} = 0. \end{cases}$$

Here fragmenton markers $\boldsymbol{x}_k$ follow the Fridman velocity field $V + V_d$, while their intensities $\boldsymbol{\gamma}$ stay constant unlike in the PSE approach, where they constantly change. The DVM became primary viscosity model used in 2D vortex methods like VVD [15, 16] and 2D-codes based on it [17].

3.3 Hybrid DVM-PSE scheme

Although the idea of diffusion velocity is not directly applicable for an arbitrary 3D-flow, one can use it in a hybrid approach where in some sense "dominating" part of the diffusion term is simulated with the DVM, while the resting part is treated with the PSE method. This decomposition can be done in different ways.

Mycek et al. [3] suggested decompose the diffusion tensor $\nu\nabla\boldsymbol{\omega}$ into convective tensor $-V_d \otimes \boldsymbol{\omega}$ and residual tensor $\hat{B}$:

$$\nu\nabla\boldsymbol{\omega} = -\boldsymbol{V}_d \otimes \boldsymbol{\omega} + \hat{B}. \tag{9}$$

Substitution of (9) into (1) gives

$$\frac{\partial\boldsymbol{\omega}}{\partial t} + \nabla \cdot ((\boldsymbol{V} + \boldsymbol{V}_d) \otimes \boldsymbol{\omega}) = (\boldsymbol{\omega} \cdot \nabla)\,\boldsymbol{V} + \nabla \cdot \hat{B}$$

or

$$\frac{\partial\boldsymbol{\omega}}{\partial t} + ((\boldsymbol{V} + \boldsymbol{V}_d) \cdot \nabla)\,\boldsymbol{\omega} = (\boldsymbol{\omega} \cdot \nabla)\,\boldsymbol{V} - \boldsymbol{\omega}\,(\nabla \cdot (\boldsymbol{V} + \boldsymbol{V}_d)) + \nabla \cdot \hat{B}. \tag{10}$$

$\boldsymbol{V}_d$ is chosen in a way to minimize the components of $\hat{B}$ in a least-squares manner (see [3] for details) and is found to be

$$\boldsymbol{V}_d = -\nu\frac{\nabla|\boldsymbol{\omega}|}{|\boldsymbol{\omega}|},$$

and the tensor $\hat{B}$ takes the form convenient to be approximated with the PSE integral operator:

$$\hat{B} = \nu|\boldsymbol{\omega}|\left(\nabla\frac{\boldsymbol{\omega}}{|\boldsymbol{\omega}|}\right).$$

Though the authors of [3] call $\boldsymbol{V}_d$ *diffusion velocity*, strictly speaking, it is unfortunate naming, because vorticity deformation term $(\boldsymbol{\omega} \cdot \nabla)\boldsymbol{V}$ in (10) does not have additional $\boldsymbol{V}_d$ that is required according to the Fridman's theorem (6). For the particle-based vortex methods this is not a principle problem, since the main aim of such decomposition is transformation of the diffusion term $\nu\Delta\boldsymbol{\omega}$ in a convenient way and not the treatment of the vorticity splitting problem. Applying fragmenton approximation to (10) we get the following ODE system

$$\begin{cases} \dfrac{d\boldsymbol{x}_k}{dt} = (\boldsymbol{V} + \boldsymbol{V}_d)(\boldsymbol{x}_k), \\[2mm] \dfrac{d\boldsymbol{h}_k}{dt} = \boldsymbol{h}_k \cdot \nabla(\boldsymbol{V} + \boldsymbol{V}_d)(\boldsymbol{x}_k), \\[2mm] \dfrac{d\sigma_k}{dt} = \sigma_k\nabla \cdot (\boldsymbol{V} + \boldsymbol{V}_d)(\boldsymbol{x}_k), \\[2mm] \dfrac{d\boldsymbol{\gamma}_k}{dt} = \boldsymbol{\gamma}_k \cdot \nabla\boldsymbol{V}(\boldsymbol{x}_k) + \dfrac{\nu}{\epsilon^2}\sum_{q=1}^{N} G_{kq}\dfrac{|\boldsymbol{\gamma}_q|S_k + |\boldsymbol{\gamma}_k|S_q}{2}\left[\dfrac{\boldsymbol{\gamma}_q}{|\boldsymbol{\gamma}_q|} - \dfrac{\boldsymbol{\gamma}_k}{|\boldsymbol{\gamma}_k|}\right], \end{cases} \tag{11}$$

where $\sigma_k = |2\boldsymbol{h}_k|S_k$ is the k-th fragmenton's volume.

As for the PSE scheme, the equations for $\boldsymbol{h}_k$ and $\boldsymbol{\gamma}_k$ in (11) loose their symmetrical form and cause splitting. It should be also emphasized that $\boldsymbol{h}_k$ and $\boldsymbol{\gamma}_k$ have different deformation tensors: $\nabla(\boldsymbol{V} + \boldsymbol{V}_d)$ and $\nabla\boldsymbol{V}$ respectively.
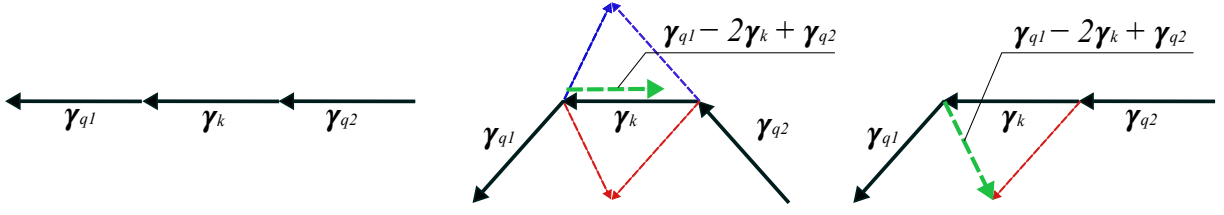
Figure 2: Three fragmenton models and splitting problem

4 "SPLITTING" PROBLEM AND SIMULATION EXAMPLES

The splitting problem that occurs with the PSE and DVM-PSE viscosity models, adapted to the fragmenton-based vortex methods, can be exposed on a simple model. Consider three fragmentons, connected to each other in three different configurations (fig. 2). Every configuration may come up in a real simulation with the vortex filament method, where these fragmentons form a part of a filament. The first case on fig. 2 is associated with the plane-parallel motion (rectilinear vortex tube), the second one — with the axisymmetrical motion (vortex ring) and the third case can be associated with the more general case of 3D-motion, where a rectilinear part merges into a curvilinear part (p.e. a part of a vortex oval).

Let us examine each of suggested configurations in terms of splitting of the vectors $\boldsymbol{h}_k$ and $\boldsymbol{\gamma}_k$ in the PSE and DVM-PSE models. For every fragmenton configuration on fig. 2 we consider $|\boldsymbol{h}_k| = |\boldsymbol{h}_{q1}| = |\boldsymbol{h}_{q2}| = h$, $|\boldsymbol{\gamma}_k| = |\boldsymbol{\gamma}_{q1}| = |\boldsymbol{\gamma}_{q2}| = \gamma$, $S_k = S_{q1} = S_{q2} = S$ and $G_{kq1} = G_{kq2} = G^1$ so that the terms responsible for splitting for k-th fragmenton in the PSE (5) and DVM-PSE (11) models simplify as follows:

$$R_P = \sum_{q=\{q1,q2\}} G_{kq}(\boldsymbol{\gamma}_q S_k - \boldsymbol{\gamma}_k S_q) = GS(\boldsymbol{\gamma}_{q1} - 2\boldsymbol{\gamma}_k + \boldsymbol{\gamma}_{q2}),$$

$$R_{DP} = \sum_{q=\{q1,q2\}} G_{kq}\frac{|\boldsymbol{\gamma}_q|S_k + |\boldsymbol{\gamma}_k|S_q}{2}\left[\frac{\boldsymbol{\gamma}_q}{|\boldsymbol{\gamma}_q|} - \frac{\boldsymbol{\gamma}_k}{|\boldsymbol{\gamma}_k|}\right] = GS(\boldsymbol{\gamma}_{q1} - 2\boldsymbol{\gamma}_k + \boldsymbol{\gamma}_{q2}).$$

As we see, for these particular fragmenton configurations both PSE and DVM-PSE models give the same result for the term $R = R_P = R_{DP}$, responsible for splitting of the central k-th fragmenton.

Analyzing each case separately we see that for the first configuration splitting does not occur as long as $\boldsymbol{\gamma}_{q1} - 2\boldsymbol{\gamma}_k + \boldsymbol{\gamma}_{q2} = 0$ for the k-th fragmenton. For the second configuration on fig. 2 R is nonzero, but it is collinear to $\boldsymbol{\gamma}_k$ and causes decrease of $|\boldsymbol{\gamma}_k|$ without change of its direction (i.e. no splitting). For the third case R tends to change not only the length of $\boldsymbol{\gamma}_k$, but also its orientation, causing splitting.

The first and the second layouts on fig. 2 are the simplified prototypes of plane-parallel and axisymmetrical motions for which both PSE and DVM-PSE models work well, cause no splitting and can be used without problems [18]. But for more general 3D-motion the possible influence of splitting should be analyzed in more proper simulations.

---

[1]Strictly speaking, for the third case $G_{kq1} \neq G_{kq2}$, but we can consider here $G_{kq1} \approx G_{kq2}$ without loss of generality
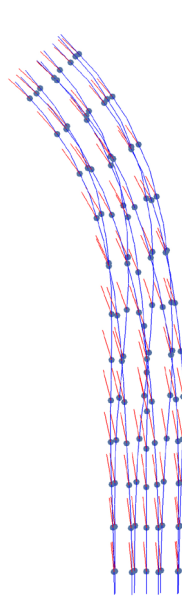
Figure 3: Vortex oval

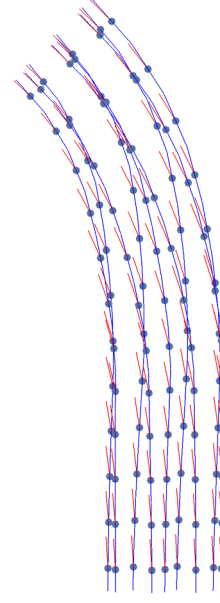**Figure 4**: Splitting with the PSE model

Figure 5: Splitting with the DVM-PSE model

Consider vortex oval with length to width ratio $L/D = 3$ with $D = 2$ (fig. 3). Oval consists in 9 filaments, each divided into 100 fragmentons. Filaments form the oval's core of radius 0.1 and have same intensity so that the oval's overall circulation $\Gamma_0 = 1$. Viscosity $\nu = 0.01$ and Reynolds number is $Re = \Gamma_0/\nu = 100$, PSE cut-off parameter $\epsilon = 0.1$. The problem was simulated with the PSE and DVM-PSE viscosity models, using explicit first order Euler scheme for integrating ODEs (5) and (11) with time step $\Delta t = 0.001$ up to $T = 1$.

At the time T the oval is only on its initial development stage where the circular parts begin rolling over out of the oval's plane, but the fragmentons' splitting is already clearly seen for both models (figures 4 and 5). Fragmentons, that initially formed continuous filaments are now completely separated, though material vectors $\boldsymbol{h}_k$ still form closed structures. This leads to incorrect velocity reconstitution and to imminent breakdown during the following simulation of the oval due to accumulated numerical errors.

5 CONCLUSIONS

Fragmenton-based vortex methods showed to be promising in the simulations of inviscid flows, especially when the use of mesh is inconvenient. Intentions to extend these methods to viscous fluid simulation encouraged the development and adaptation of viscosity models from existing particle-based approaches to the fragmenton-based ones.

The main principal difficulty has physical reasoning that consists in nonfulfillment of the Helmholtz laws for viscous fluid with vorticity, which are crucial for fragmenton-based methods. Every existing viscosity model aimed onto the approximation and discretization between the particles of the diffusion term $\nu\Delta\boldsymbol{\omega}$, faces the problem of misalignment of

vorticity vector and material vector that we call "splitting".

Numerical analysis and simulation examples of a vortex oval demonstrate the splitting problem for the classical PSE approach and the DVM-PSE scheme proposed by Mycek et al. Though 3D diffusion velocity could be a solution for the stated problem, its search is an ill-posed problem and appears to be very impractical for the fragmenton-based methods.

It should also be mentioned about the problems with the general use of PSE-approximation with fragmenton-based methods, as PSE technics needs particles (or fragmentons) to be positioned uniformly, i.e. on the mesh, to maintain approximation accuracy. It is rather difficult to achieve with fragmentons, as they must always form closed structures in a flow.

One should admit that accurate simulation of viscous flow without any assumptions with the fragmenton-based vortex methods seems to be improbable. However, in the sight of the advantageous use of these methods for complicated inviscid FSI problems [10], efforts should be made to the search and elaboration of hybrid DVM-PSE viscosity models that minimize splitting. The second way is to analyze the "no-splitting" assumption, where splitting is suppressed. In this case the DVM part would play the dominating role, and it should be chosen wisely. These problems are the questions of the following authors' research.

REFERENCES

[1] Degond P., Mas-Gallic S. The weighted particle method for convection-diffusion equations. Part1 and Part2. *Math.Comp.*, (1989), Vol. 53, No. 188, pp 485-525.

[2] Lacombe G., Mas-Gallic S. Presentation and Analysis of a Diffusion-Velocity Method. The linear case. *ESAIM: Proceedings*, (1999), Vol. 7, pp 225-233.

[3] Mycek P., Pinon G., Germain G., Rivoalen E. Formulation and analysis of a diffusion-velocity particle model for transport-dispersion equations. *Computational and Applied Mathematics*, (2016), Vol. 35, No. 2, pp 447-473.

[4] Winckelmans G.S. *Chapter Vortex Methods* in *Encyclopedia of Computational Mechanics Second Edition.* John Wiley & Sons, (2017).

[5] Cottet G-H., Koumoutsakos P. *Vortex Methods.* Cambridge: CUP, (2000).

[6] Marchevsky I., Shcheglov G. 3D vortex structures dynamics simulation using vortex fragmentons. *6th European Congress on Computational Methods in Applied Sciences and Engineering (ECCOMAS 2012)*, (2012), pp 5716-5735.

[7] Shcheglov G.A., Dergachev S.A. Hydrodynamic loads simulation for 3D bluff bodies by using the vortex loops based modification of the vortex particle method. *5th International Conference on Particle-Based Methods - Fundamentals and Applications, PARTICLES 2017*, pp. 725-731.

[8] Shcheglov G.A., Dergachev S.A. Vortex Loops Based Method for Subsonic Aerodynamic Loads Calculation. *MATEC Web of Conferences*, (2018), Vol. 221, 05004. DOI: 10.1051/matecconf/201822105004

[9] Bogomolov D.V., Marchevsky I.K., Setukha A.V, Shcheglov, G.A. Numerical simulation of vortex rings pair motion in inviscid fluid using discreet vortex methods. *Engineering physics*, (2008), pp. 8-14. (in Russian)

[10] Korotkiy S.A. Calculation of the design parameters of aerospace system with air launch with account of intensive vortex shedding. *PhD dissertation*, Bauman Moscow State Technical University, Moscow, (2005). (in Russian)

[11] Kotsur O.S., Shcheglov G.A. Implementation of the Particle Strength Exchange Method for Fragmentons to Account for Viscosity in Vortex Element Method. *Herald of the Bauman Moscow State Tech. Univ., Nat. Sci.*, (2018), No. 3, pp. 48-67 (in Russian), DOI: 10.18698/1812-3368-2018-3-48-67

[12] Kochin N.E, Kibel I.A., Roze N.V. *Theoretical Hydromechanics.* John Wiley & Sons, (1964).

[13] Markov V.V., Sizykh G.B. Vorticity evolution in liquids and gases. *Fluid Dynamics*, (2015), Vol. 50, No. 2, pp. 186-192.

[14] Kotsur O.S. On the existence of local formulae of the transfer velocity of vortex tubes that conserve their strengths. *Trudy MFTI*, (2019), Vol. 11, No. 1, pp. 76-85. (in Russian)

[15] Guvernyuk S.V., Dynnikova G.Ya. Modeling the flow past an oscillating airfoil by the method of viscous vortex domains. *Fluid Dynamics*, (2007), Vol. 42, No. 1. pp. 111.

[16] Kuzmina K.S., Marchevsky I.K., Moreva V.S. On the high-accuracy approach to flow simulation aroundthe airfoils by using vortex method. *IOP Conference Series: Materials Science and Engineering*, Vol. 468, No. 1, 012009, DOI: 10.1088/1757-899X/468/1/012009

[17] Kuzmina K.S., Marchevsky I.K., Ryatina E.P. Open Source Code for 2D Incompressible Flow Simulation by Using Meshless Lagrangian Vortex Methods. *Proceedings - 2017 Ivannikov ISPRAS Open Conference*, pp. 97-103. DOI: 10.1109/IS-PRAS.2017.00023

[18] Kotsur O.S., Shcheglov G.A. Viscous fluid simulation with the vortex element method. *31st Congress of the International Council of the Aeronautical Sciences, ICAS 2018*, ICAS2018_0718.

Numerical experiment of the vortex shedding from an oscillating circular cylinder in a uniform flow by the vortex method

Y. Yokoi*

* Department of mechanical engineering, National Defense Academy of Japan (NDA)
1-10-20 Hashirimizu, Yokosuka, Kanagawa, Japan
e-mail: yokoi@nda.ac.jp

ABSTRACT

In this study, the flow features of vortex shedding from a circular cylinder forced-oscillating in the in-line direction were investigated by use of numerical simulation (vortex method) at the Reynolds number Re=500, with varied amplitude ratio and varied frequency ratio. The numerical experiment was performed at the two-dimensional calculation for incompressible and viscous flow. The circular cylinder was divided into 40 panels which distributed the vortices. Every calculation continued to more than non-dimensional time $T = 200$. The main parameters of numerical experiment were the oscillation amplitude ratio $2a/d$ (a: half-amplitude of cylinder motion, d: cylinder diameter), the oscillation frequency ratio f/f_K (f: cylinder oscillation frequency, f_K: natural Karman vortex shedding frequency). The amplitude ratio is three kinds, is 0.0, 0.25 and 0.5, respectively. The oscillation frequency ratio is 15 kinds, is from 0.2 to 3.0 every 0.2 steps. As a result of calculations, two typical flow patterns of the lock-in were shown, and it was confirmed that the calculated flow pattern were reasonable agreement with previous experiment results. The fluid force act on the oscillating cylinder was investigated. It was clarified that the amplitude of the lift coefficient was larger than the amplitude of the drag coefficient in the lock-in of alternate vortex shedding, and the amplitude of the drag coefficient was larger than the amplitude of the lift coefficient in the lock-in of simultaneous vortex shedding.

INTRODUCTION

If a circular cylinder is placed into a steady flow without a time change, vortices will be discharged alternately. And a Karman vortex street is formed behind the circular cylinder. The Karman vortex is a very stable vortex street, and the vortex corresponding to the flow velocity is formed. That can also be said to be a natural synchronous phenomenon. Many of flows which exist really are what is called unsteady flow to which speed is changed in time. When unsteady, it is thinkable that the characteristics of the phenomenon differ compared with the case of being steady. It is industrially important to grasp the fluid force characteristic and the vortex shedding characteristic of the object put on the unsteady flow field. However, in order to realize an unsteady flow with sufficient accuracy, serious troubles are required in a laboratory. In order to experiment simple, in the laboratory, the object which exercises in the direction of flow was installed into the steady flow, so the relative unsteady flow is made. If the circular cylinder which is oscillating in the flow is placed, the vortex shedding which synchronized with circular cylinder oscillating frequency will be observed. This phenomenon was called "lock-in phenomenon" and, as for this "interference of the flow velocity change", research has been done by many researchers [1-4]. It is known that the flow pattern in the lock in state is divided roughly into the "alternate vortex shedding type" and the "simultaneous vortex shedding type". Although there is study which showed the flow pattern at the time of the lock-in, since the experiment is difficult, there is scarcely much study on the fluid force of acting on the body at the time of the lock-in. In order to study the phenomenon, the study which investigates fluid force is interesting, and important. Although the experimental study is difficult therefore, the numerical simulation using a computer is expected.

Since the vortex method which is the Lagrange type flow analyzing method does not need a calculation lattice unlike the region type analyzing method such as finite difference method and finite element method, analysis is easily possible also for the flow of the around of complicated shape. Moreover, since it is the technique of analyzing a flow by following the behaviour of the turbulent flow vortex more than the minimum vortex element size directly in Lagrange, it is possible to reproduce exactly the flow accompanied by large-scale separation and a large-scale reverse flow as

well as the analysis of an unsteady flow. So, it is a technique suitable for cause investigation of phenomena made into a problem in engineering, such as a flow induced vibration excited by the flow. In this study, about the vortex shedding and the fluid force in the case from the circular cylinder which is oscillating in the direction of a flow, a systematic numerical simulation was performed and the time history of fluid force and flow pattern were investigated.

NUMERICAL CALCULATION

The numerical experiment apparatus was consisted of simulation software and a notebook type computer (NEC; LaVie LC958/T) as calculation hardware which are on the market. The software which named 'UzuCrise 2D ver.1.1.3 rev.H (College Master Hands Inc., 2006)' is used. This software used the vortex method which is based on the Lagrangian analysis. Since the vortex method is the grid-less method, it is suitable for the unsteady problem of such moving boundary. The vortex method is a direct viscid-inviscid interaction scheme, and the emanation of velocity shear layers due to boundary layer separation is represented by introduction of discrete vortices with viscous core step by step of time. In the present study, the flow was assumed incompressible and two-dimensional flow field. The configuration of circular cylinder was represented 40 vortex panels using a boundary element method. The separating shear layers were represented the discreet vortices, which were introduced at the separation points. The details of calculation technique of vortex method and accuracy of calculation are shown in Kamemoto [5, 6].

In the present study, the calculations were performed at the two-dimensional flow field for incompressible and viscous flow. A cylinder diameter d and main flow velocity U were determined as 16 mm and 0.04 m/s so that it could compare with the previous experimental result [7]. Since water is assumed as for test fluid, Reynolds number Re becomes 500. The configuration of circular cylinder was represented 40 vortex panels using a boundary element method. Its vortex panels are provided equally. Every calculation continued to until non-dimensional time $T = 200$.

The main parameters of numerical experiment were the oscillation amplitude ratio $2a/d$ (a: half-amplitude of cylinder motion, d: cylinder diameter), the oscillation frequency ratio f/f_K (f: cylinder oscillation frequency, f_K: natural Karman vortex shedding frequency). The oscillation amplitude ratio is three kinds, is 0.0, 0.25 and 0.5, respectively. Here, when the oscillating amplitude ratio is "0.0", it means circular cylinder stationary. The oscillation frequency ratio is 15 kinds, is from 0.2 to 3.0 every 0.2 steps.

The calculation experiment was performed in the following procedures. The case of the stationary circular cylinder is carried out first, and the case where the circular cylinder is oscillating in the direction of a flow after that is carried out. In order to grasp the flow field on the computer, and to determine for the vortex shedding frequency from the stationary single circular cylinder, it needs to be calculated in the case of the stationary circular cylinder. Secondly, the oscillating amplitude ratio is defined, the oscillating frequency ratio is varied, and systematic numerical computation is performed. If a series of numerical computation finishes, the oscillating amplitude ratio will be defined again and the numerical computation will be performed similarly. The arrangement of circular cylinders is shown in Fig. 1.
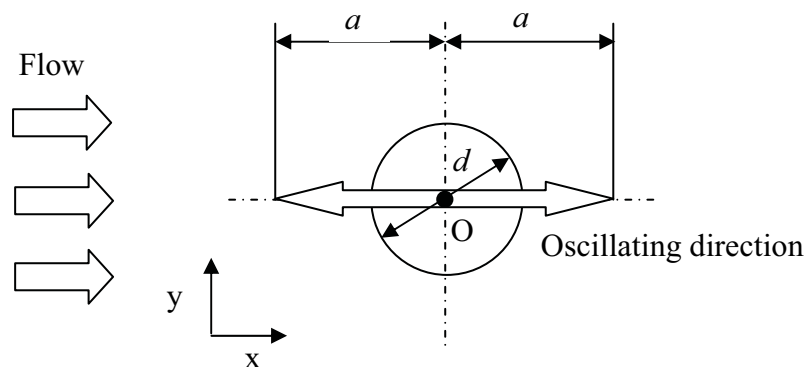

Fig. 1 Coordinate system and definition of symbols (O: the coordinate origin).

RESULTS AND DISCUSSIONS

In order to verify the calculation software to be used, the experimental result and calculation result of a stationary circular cylinder were compared. The time history of the fluid force (a drag component and lift component) of acting on a stationary circular cylinder is shown in Fig. 2. Figure 2 (a) is a time history from the non-dimension time $T = 0$ to $T = 200$, and Fig. 2 (b) expands the section from the non-dimension time $T = 150$ to $T = 200$. The drag oscillation lurking in periodic oscillation and lift oscillation of the lift produced by formation of a Karman vortex street is expressed. The relationship whose oscillation frequency of the drag is twice the oscillation frequency of the lift is shown. The following results were obtained after non-dimension time $T = 150$. Here, the diagram which defines the quantity about the fluid force is shown in Fig. 3. The average value of drag coefficient was $C_{DAVE} = 1.08$ and the root mean square value of amplitude of drag coefficient was $A_{CD} = 0.15$. The average value of lift coefficient was $C_{LAVE} = 0.00$ and the route mean square value of amplitude of lift coefficient was $A_{CL} = 0.73$. The average Strouhal number for which it determined from the lift oscillating period T was $St_{AVE} = 0.26$. The Strouhal number is defined by $St = fd/U = d/\Delta tU = 1/T$. When the Reynolds number is $Re = 500$, it is known that the experimental value of Strouhal number St is about 0.2. Although it seems that this calculation result is highly calculated as compared with an experimental result, it seems that this calculation has obtained the comparatively good calculation result since a two dimensional calculation result becomes higher than an experimental result about 30 to 40%. When the Karman vortex shedding frequency f_K was calculated from the average value of Strouhal number, the Karman vortex shedding frequency was $f_K = 0.65$ Hz.
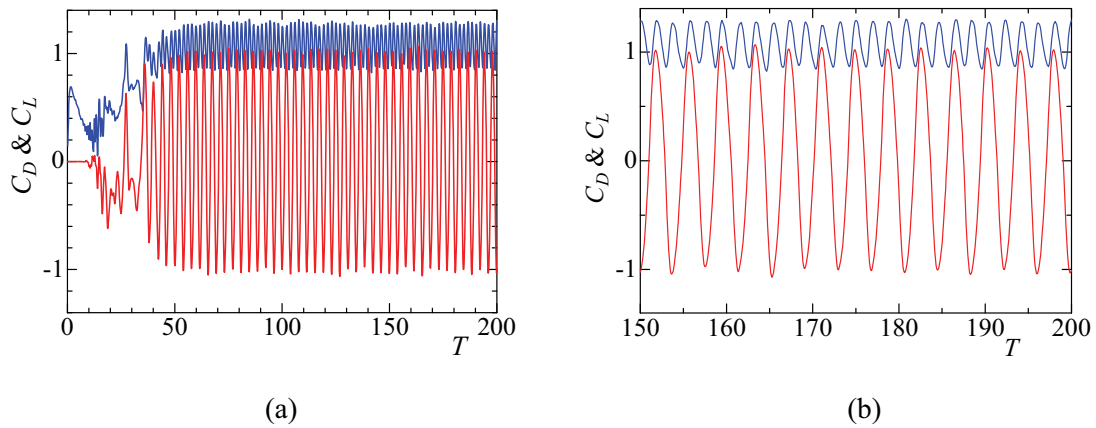

Fig. 2 Time histories of drag and lift coefficients,
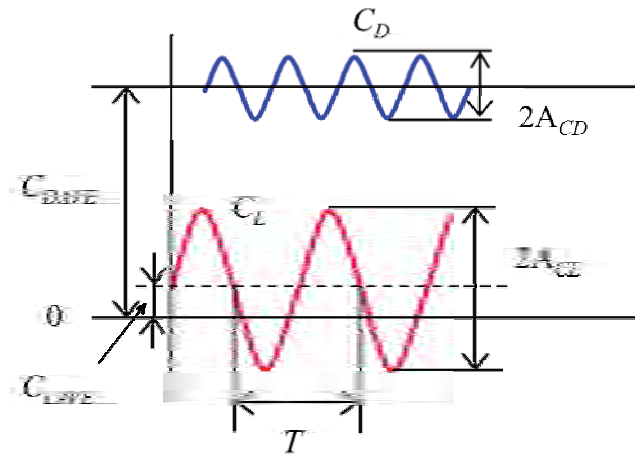(blue and red lines show drag and lift coefficients, respectivery).

Fig. 3 The definition of the magnitude of the drag coefficient or the lift coefficient, and the definition of the oscillating period.

When forced oscillation of the circular cylinder is carried out, it is one of the most interesting things of this study to investigate how fluid force changes. Before performing a systematic numerical experiment, the numerical simulation was performed on the oscillating conditions which the alternate vortex shedding lock-in and the simultaneous vortex shedding lock-in generate. One example of the flow patterns obtained by calculation is shown in Fig. 4. Here, the flow visualization photographs [7] in the similar experimental condition are shown for comparison. Figure 4(a) is simulating the aspect of alternate vortex shedding lock-in. The direction of vortex shedding changes and an aspect that the vortex shedding is performed alternately is shown. An aspect that the vortex discharged from the circular cylinder constitutes a vortex pair which differs in a rotatory direction, respectively, and the vortex street of mushroom shape like the section of a mushroom is formed is expressed well. Figure 4(b) is simulating the aspect of a simultaneous vortex shedding lock-in. An aspect that the vortex of mushroom shape is simultaneously discharged from cylinder both sides, and the characteristic aspects of cylinder wake are shown. Since the characteristic flow patterns by the lock-in are expressed well, the high reliability and the usefulness of this calculation technique are found.

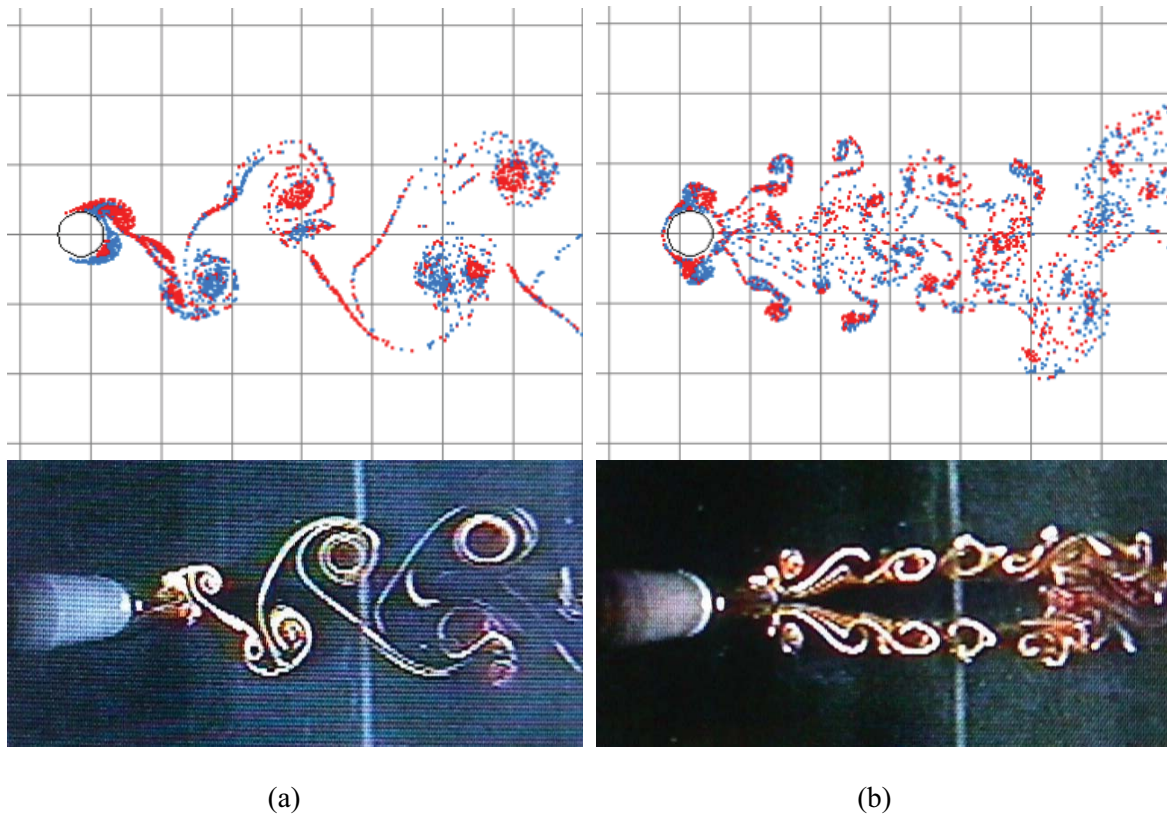(a)   (b)

Fig. 4 Two kinds of lock-in flow patterns, (a) shows an alternate vortex shedding type flow pattern and (b) shows the simultaneous vortex shedding type flow pattern, respectively.

It is the greatest interest matter of this study to investigate change of fluid force. The time histories of the drag coefficient C_D and the lift coefficient C_L in case oscillating amplitude ratios a/d are 0.25 and 0.5 are shown in Fig. 5 and Fig. 6, respectively. As for the time history, the range by the non-dimension time 50-100 is shown, a red line shows the lift coefficient, a blue line shows the drag coefficient, and a black line shows the motion of circular cylinder, respectively. It is found with the increase in the oscillation frequency ratio that change is looked at by the magnitude of the amplitude of the drag coefficient and the magnitude of the amplitude of the lift coefficient. And if the circular cylinder oscillating amplitude ratio becomes large, it will be found that the tendency becomes remarkable. When the oscillation frequency ratio is small, it can be seen that the amplitude of lift coefficient is larger than the amplitude of drag coefficient. On the other hand, when the oscillation frequency ratio is large, the amplitude of drag coefficient is seen be larger than the amplitude of lift coefficient. Here, the "lock-in" is that the vortex shedding frequency from the circular cylinder synchronizes with circular cylinder oscillation frequency. So, it takes notice of the relationship between the waveform of circular cylinder oscillation, the waveform of a drag coefficient, and the
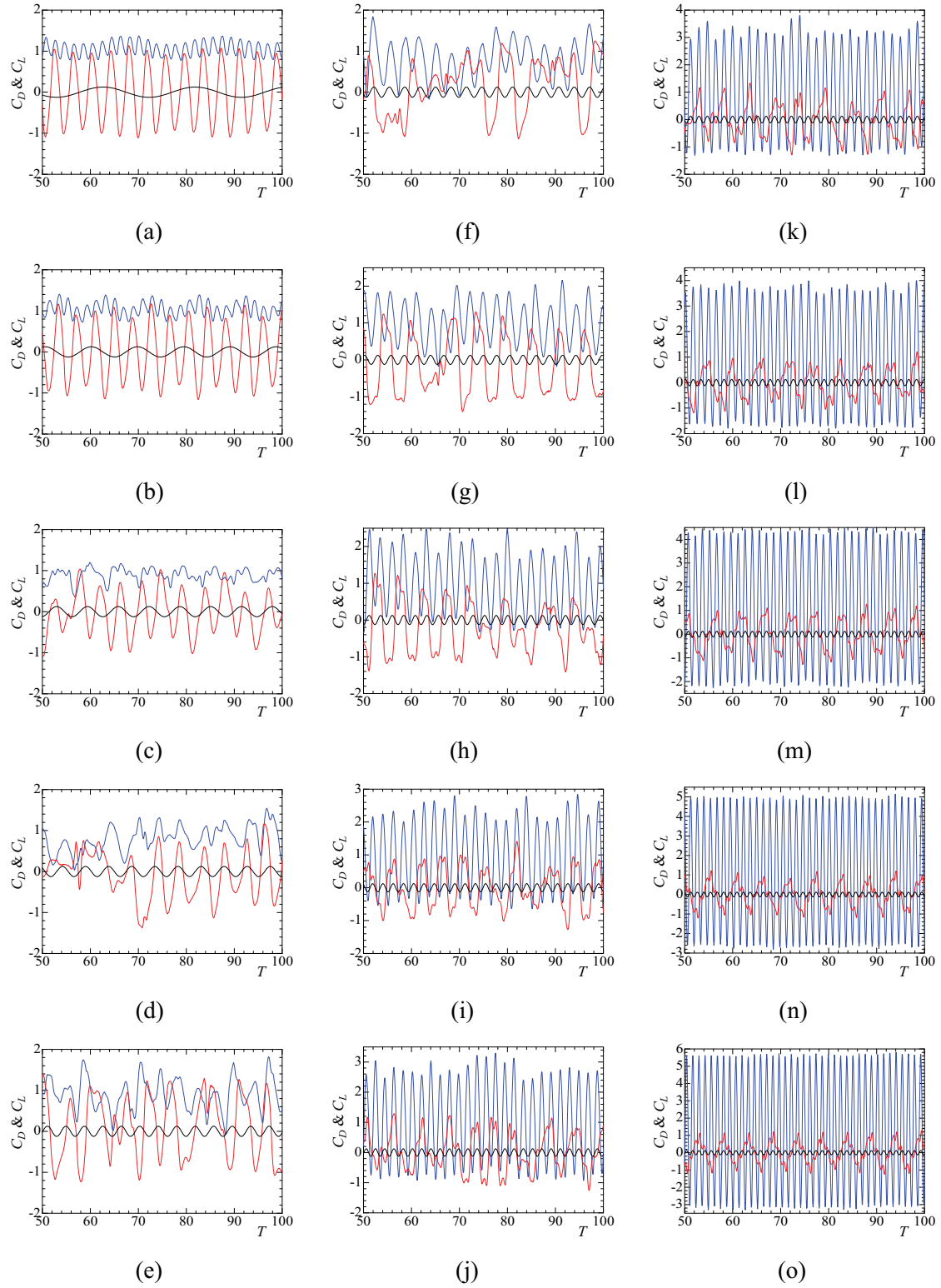
Fig. 5 Time histories of drag and lift coefficients in the case of oscillation amplitude ratio a/d = 0.25 (blue and red lines show drag and lift coefficients, black line is cylinder motion); (a) f/f_K = 0.2, (b) f/f_K = 0.4, (c) f/f_K = 0.6, (d) f/f_K = 0.8, (e) f/f_K = 1.0, (f) f/f_K = 1.2, (g) f/f_K = 1.4, (h) f/f_K = 1.6, (i) f/f_K = 1.8, (j) f/f_K = 2.0, (k) f/f_K = 2.2, (l) f/f_K = 2.4, (m) f/f_K = 2.6, (n) f/f_K = 2.8, (o) f/f_K = 3.0

waveform of a lift coefficient. The case where the lift coefficient is oscillating with the period twice the period of the circular cylinder oscillation is the alternate vortex shedding type lock-in. On the other hand, the case where the drag coefficient is oscillating synchronizing with the period of the circular cylinder oscillation is the simultaneous vortex shedding type lock-in. In the magnitude
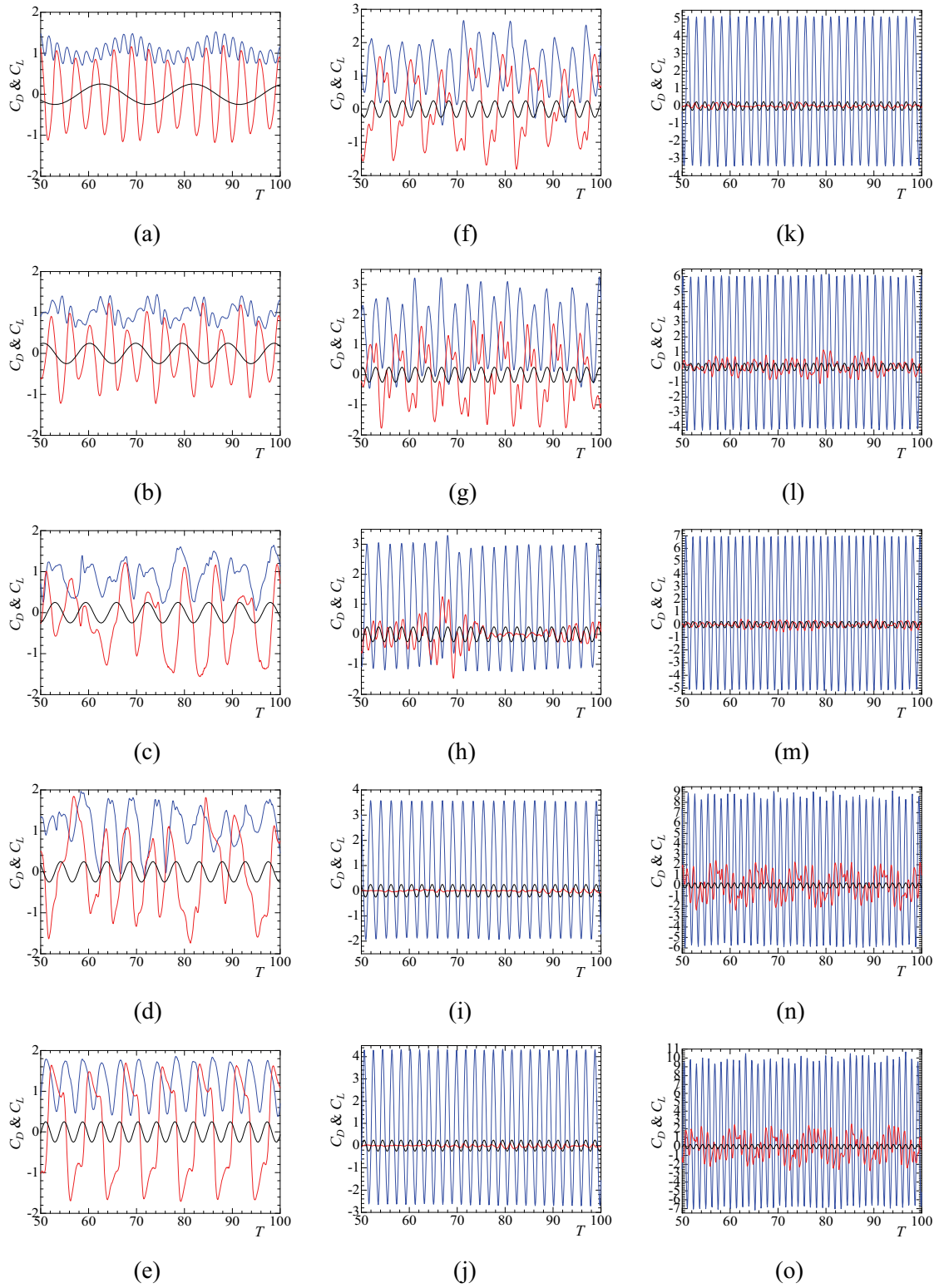
Fig. 6 Time histories of drag and lift coefficients in the case of oscillation amplitude ratio a/d = 0.50 (blue and red lines show drag and lift coefficients, black line is cylinder motion); (a) f/f_K = 0.2, (b) f/f_K = 0.4, (c) f/f_K = 0.6, (d) f/f_K = 0.8, (e) f/f_K = 1.0, (f) f/f_K = 1.2, (g) f/f_K = 1.4, (h) f/f_K = 1.6, (i) f/f_K = 1.8, (j) f/f_K = 2.0, (k) f/f_K = 2.2, (l) f/f_K = 2.4, (m) f/f_K = 2.6, (n) f/f_K = 2.8, (o) f/f_K = 3.0

relationship of the lift coefficient and the drag coefficient, when the amplitude of the lift coefficient is large, it becomes the alternate vortex shedding, and when the amplitude of the drag coefficient is large, it becomes the simultaneous vortex shedding. In Fig. 5, the alternate vortex shedding type lock-in is shown in Fig. 5(g), and the simultaneous vortex shedding type lock-in is shown in Fig. 5(k)
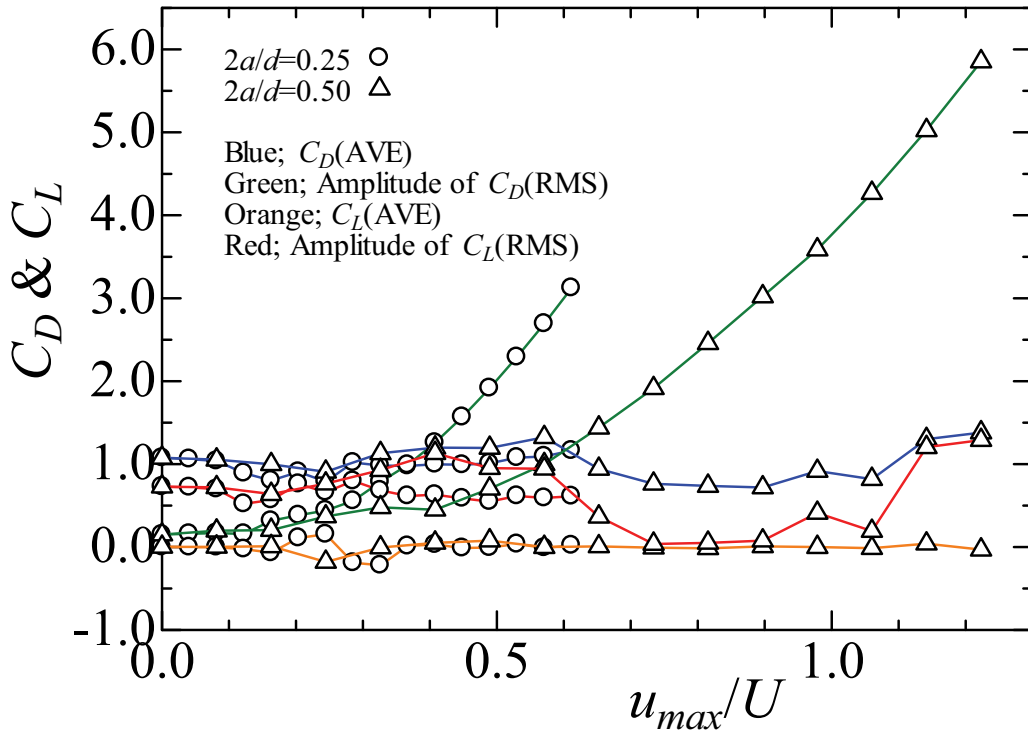
Fig. 7 The variation of fluid force component act on single oscillating cylinder,
$u_{max}/U = 2(a/d)(f/f_K)(\pi St)$

- Fig. 5(o). In Fig. 6, the alternate vortex shedding type lock-in is shown in Fig. 6(e) - Fig. 6(g), and the simultaneous vortex shedding type lock-in is shown in Fig. 6(i) - Fig. 6(o).

The aspects of a variation of fluid force are shown in Fig. 7. An abscissa is the velocity ratio u_{max}/U and an ordinate is each component of fluid force. Here, the velocity ratio defined as $u_{max}/U = 2a/d \cdot f/f_K \cdot (\pi St)$. Since an oscillation frequency ratio f/f_K is constant value, this figure means the variation of the fluid force over the variation of an oscillating amplitude ratio $2a/d$. In the case of low velocity ratio, although the value of drag coefficient C_{DAVE} is smaller than a stationary value, the value of the lift coefficient C_{LAVE} scarcely changes to the stationary value. The value of the amplitude of drag coefficient AC_{DRMS} is increasing while the value of amplitude ratio $2a/d$ increases. On the other hand, although the amplitude of lift coefficient AC_{LRMS} scarcely changed the amplitude ratio to $2a/d = 0.5$, the amplitude of lift coefficient became suddenly small value from velocity ratio $u_{max}/U = 0.65$. In the case of high velocity ratio, the value of drag coefficient C_{DAVE} and the value of lift coefficient C_{LAVE} scarcely change to the stationary case. The value of amplitude of drag coefficient is large and the value of drag coefficient AC_{DRMS} tends to increase with increase of amplitude ratio $2a/d$. However, the value of amplitude of lift coefficient AC_{LRMS} will become smaller than the value of stationary cylinder case at $2a/d = 0.25$ and 0.5, the amplitude of lift coefficient became suddenly large value from the velocity ratio $u_{max}/U = 1.14$.

CONCLUSIONS

A systematic numerical simulation of the flow around a circular cylinder which oscillates in the direction of a flow using the vortex method was performed. The following conclusions were obtained.

(1) The flow pattern of two kinds of lock-in states was well in agreement with the aspect of a previous experiment visualization result.

(2) It is found with the increase in the oscillation frequency ratio that change is looked at by the magnitude of the amplitude of the drag coefficient and the magnitude of the amplitude of the lift coefficient.

(3) In the magnitude relationship of the lift coefficient and the drag coefficient, when the amplitude of the lift coefficient is large, it becomes the alternate vortex shedding, and when the amplitude of the drag coefficient is large, it becomes the simultaneous vortex shedding.

REFERENCES

[1]   O. M. Griffin and M. S. Hall, "Review-Vortex Shedding Lock-on and Flow Control in Bluff Body Wakes", *Trans. of ASME*, **113**, 526-537 (1991).

[2]   R. King, "A Review of Vortex Shedding Research and its Application", *Ocean Engineering*, **4**, 141-171 (1997).

[3]   A Okajima, "Flow-Induced Vibration of a Bluff Body", *Trans. of JSME* Series B, **66**-644,948-953 (2000).

[4]   A Okajima, "Vortical Flow and Fluiddynamic Characteristics of an Oscillating Bluff Body", T*rans. of JSME* Series B, **66**-644, 948-953 (2000).

[5]   K. Kamemoto, "The expandability of the vortex method as a turbulent flow model (the first part: to think a basic of vortex method)", *Computational Fluid Dynamics*, **2**-1, 20-29 (1993).

[6]   K. Kamemoto, "The expandability of the vortex method as a turbulent flow model (the latter part: to lock up the flow by vortex method)", *Computational Fluid Dynamics*, **2**-2, 28-39 (1994).

[7]   Y. Yokoi and K. Hirao, "Vortex Flow Around an In-Line Forced Oscillating Circular Cylinder", *Trans. Japnan Society of Mechanical Engineers Series B*, **74**-746, 2099-2108 (2008).

MESHFREE SIMULATIONS FOR SOLUTION MINING PROCESSES

ISABEL MICHEL[1], TOBIAS SEIFARTH[1] AND JÖRG KUHNERT[1]

[1] Fraunhofer ITWM
Fraunhofer-Platz 1, 67663 Kaiserslautern, Germany
E-mail: contact@meshfree.eu and URL: https://www.meshfree.eu/

Key words: Solution Mining, Meshfree Method, GFDM, FPM, Lagrangian Formulation, Eulerian Formulation

Abstract. Experimental and field investigations for solution mining processes have improved intensely within the last years. Due to today's computing capacities, 3D simulations of potential salt solution caverns can further enhance the process understanding. They serve as a "virtual prototype" of a projected site and support planning in reasonable time. In this contribution, we present a meshfree generalized finite difference method based on a cloud of numerical points that is able to simulate solution mining processes on microscopic as well as macroscopic scales. Focusing on anticipated industrial requirements, Lagrangian and Eulerian formulations including an ALE-approach are considered.

1 INTRODUCTION

Classical simulation methods are meshbased. Moving geometry parts, free surfaces, phase boundaries, or large deformations are difficult to handle or require time-consuming re-meshing algorithms. This is not the case for meshfree methods. They show their advantages especially for these applications. The meshfree Finite Pointset Method (FPM) uses a generalized finite difference method (GFDM) on a cloud of numerical points. There are already successful applications of the method in CFD and continuum mechanics. Examples include water crossing of cars, water turbines, hydraulic valves, soil mechanics, and metal cutting [6, 8, 15, 19]. The current development of the simulation software MESHFREE has eliminated previous shortcomings concerning robust and scalable solutions of sparse, linear systems. MESHFREE combines the advantages of FPM and the fast linear solvers of SAMG [16]. In this contribution, we present its capabilities with respect to the simulation of solution mining processes on microscopic and macroscopic scales.

Originally, a Lagrangian formulation is used, i.e. the point cloud moves according to the flow velocity [6, 9]. Thus, there is an accurate and natural transport of physical information. The basic physical model consists of the conservation equations for mass, momentum, and energy. For solution mining processes, we extend it by the standard k-ε turbulence model and equations for the concentration of the occurring species (see Section 2). The GFDM specific numerics are derived in Section 3 with special focus on

the Lagrangian and Eulerian formulations. The microscopic simulations in Section 4 illustrate a procedure to determine the necessary effective model parameters of a macroscopic problem. For macroscopic simulations, the Lagrangian formulation leads to a significant restriction of the time step size due to the explicit movement of the point cloud. To enable simulations in reasonable time, the Eulerian formulation should be preferred [17]. Thereby, the point cloud is fixed and convective terms represent the transport of physical information. The necessary movement of the boundary of the salt cavern is implemented based on the solution rate. Close to the boundary, interior points are subject to an ALE-approach (Arbitrary Lagrangian-Eulerian) according to [4]. This procedure gives rise to covering the complete life cycle of a salt cavern by a meshfree simulation. We demonstrate the advantages of the Eulerian formulation for a simplified macroscopic example in Section 5, followed by conclusions in Section 6.

2 PHYSICAL MODEL

In this section, we describe the basic physical model and its extensions for solution mining processes. Furthermore, a specific model for the density of a solution is discussed.

2.1 Basic Equations

The basic physical model is given by the conservation equations of mass, momentum, and energy in Lagrangian formulation.

$$\frac{d\rho}{dt} + \rho \cdot \nabla^{\mathrm{T}} \mathbf{v} = 0, \tag{1}$$

$$\frac{d}{dt}(\rho \cdot \mathbf{v}) + (\rho \cdot \mathbf{v}) \cdot \nabla^{\mathrm{T}} \mathbf{v} = (\nabla^{\mathrm{T}} \mathbf{S})^{\mathrm{T}} - \nabla p + \rho \cdot \mathbf{g},$$

$$\frac{d}{dt}(\rho \cdot E) + (\rho \cdot E) \cdot \nabla^{\mathrm{T}} \mathbf{v} = \nabla^{\mathrm{T}} (\mathbf{S} \cdot \mathbf{v}) - \nabla^{\mathrm{T}} (p \cdot \mathbf{v}) + \rho \cdot \mathbf{g}^{\mathrm{T}} \cdot \mathbf{v} + \nabla^{\mathrm{T}} (\lambda \cdot \nabla T),$$

where $\frac{d}{dt} = \frac{\partial}{\partial t} + \mathbf{v}^{\mathrm{T}} \nabla$ denotes the material derivative. Furthermore, we have: nabla operator $\nabla = (\frac{\partial}{\partial x}, \frac{\partial}{\partial y}, \frac{\partial}{\partial z})^{\mathrm{T}}$, density ρ, velocity $\mathbf{v} \in \mathbb{R}^3$, stress tensor $\mathbf{S} \in \mathbb{R}^{3\times3}$ (deviatoric part, i.e. $\mathrm{tr}(\mathbf{S}) = 0$), pressure p, body forces $\mathbf{g} \in \mathbb{R}^3$, total energy $E = c_{\mathrm{v}} \cdot T + \frac{1}{2} \cdot (\mathbf{v}^{\mathrm{T}} \cdot \mathbf{v})$, heat capacity c_{v}, temperature T, and heat conductivity λ. As described in [6, 9], the stress tensor is split into its viscous and solid parts by $\mathbf{S} = \mathbf{S}_{\mathrm{visc}} + \mathbf{S}_{\mathrm{solid}}$. For simplicity, the solid part will be neglected for further analysis. The viscous part is defined by

$$\mathbf{S}_{\mathrm{visc}} = (\eta + \eta_{\mathrm{turb}}) \cdot \left(\nabla \mathbf{v}^{\mathrm{T}} + (\nabla \mathbf{v}^{\mathrm{T}})^{\mathrm{T}} - \frac{2}{3} \cdot (\nabla^{\mathrm{T}} \mathbf{v}) \cdot \mathbf{I} \right), \tag{2}$$

where $\mathbf{I} \in \mathbb{R}^{3\times3}$ is the identity. To incorporate turbulent effects, the standard k-ε turbulence model is considered omitting fluctuating dilatation and source terms, see [14]:

$$\frac{dk}{dt} = \frac{1}{\rho} \cdot \nabla^{\mathrm{T}} \left(\left(\eta + \frac{\eta_{\mathrm{turb}}}{\sigma_k} \right) \cdot \nabla k \right) - \varepsilon + \frac{1}{\rho} \cdot (P_{\mathrm{pr}} + P_{\mathrm{b}}), \tag{3}$$

$$\frac{d\varepsilon}{dt} = \frac{1}{\rho} \cdot \nabla^{\mathrm{T}} \left(\left(\eta + \frac{\eta_{\mathrm{turb}}}{\sigma_\varepsilon} \right) \cdot \nabla \varepsilon \right) - C_{2\varepsilon} \cdot \frac{\varepsilon^2}{k} + \frac{1}{\rho} \cdot C_{1\varepsilon} \cdot \frac{\varepsilon}{k} \cdot (P_{\mathrm{pr}} + C_{3\varepsilon} \cdot P_{\mathrm{b}}),$$

where η is the laminar and $\eta_{\text{turb}} = \rho \cdot C_\eta \cdot \frac{k^2}{\varepsilon}$ is the turbulent viscosity. The turbulent production rate is defined by $P_{\text{pr}} = \eta_{\text{turb}} \cdot \|\nabla \mathbf{v}^{\text{T}}\|_{\text{M}}^2$ with von Mises matrix norm $\| \cdot \|_{\text{M}}$. The turbulent buoyancy is given by $P_{\text{b}} = -\frac{1}{\rho} \cdot \frac{\eta_{\text{turb}}}{\text{Pr}_{\text{turb}}} \cdot \frac{\partial \rho}{\partial T} \cdot (\mathbf{g} \cdot \nabla T)$. For this model, well-established values for the constants are $\sigma_k = 1.0$, $\sigma_\varepsilon = 1.3$, $C_{1\varepsilon} = 1.44$, $C_{2\varepsilon} = 1.92$, $C_{3\varepsilon} = -0.33$, $C_\eta = 0.09$, and $\text{Pr}_{\text{turb}} = 0.85$ (turbulent Prandtl number). In the vicinity of walls, a logarithmic wall function is used. In order to simulate solution mining processes, the model above is extended by convection-diffusion-equations for concentration c_i of species $i = 1, \ldots, N$ with effective diffusion coefficient $D_{i,\text{eff}}$:

$$\frac{dc_i}{dt} + c_i \cdot \nabla^{\text{T}} \mathbf{v} = \nabla^{\text{T}}(D_{i,\text{eff}} \cdot \nabla c_i). \tag{4}$$

In the Eulerian formulation, the material derivative is replaced by its definition.

2.2 Modeling Density, Viscosity, and Heat Capacity

The general form of the equation of state is given by $\rho = \rho(T, c_1, \ldots, c_N)$, i.e. density depends on temperature and concentrations. Based on the formulation in [10, 13], the density of a solution of N species in water is given by

$$\rho_{\text{sol}} = \left(\frac{w_{\text{H}_2\text{O}}}{\rho_{\text{H}_2\text{O}}} + \sum_{i=1}^{N} \frac{w_i}{\rho_{\text{apparent},i}} \right)^{-1}, \tag{5}$$

where $w_{\text{H}_2\text{O}}$ and w_i are the mass fraction of water and species i, respectively. Additionally, $w_{\text{H}_2\text{O}} + \sum_{i=1}^{N} w_i = 1$ has to be satisfied. The density of water is determined by

$$\rho_{\text{H}_2\text{O}} = \frac{(((((A_1 \cdot T + A_2) \cdot T + A_3) \cdot T + A_4) \cdot T + A_5) \cdot T + A_6)}{1 + A_7 \cdot T}, \tag{6}$$

while the apparent density of species i is given by

$$\rho_{\text{apparent},i} = \frac{(C_0^* \cdot (1 - w_{\text{H}_2\text{O}}) + C_1^*) \cdot \exp\left(0.000001 \cdot (T + C_4^*)^2\right)}{(1 - w_{\text{H}_2\text{O}}) + C_2^* + C_3^* \cdot T} \tag{7}$$

with $A_1, \ldots, A_7$ and $C_0^*, \ldots, C_4^*$ according to [13]. The mass fractions w_i are defined by $w_i = \frac{c_i}{\sum_{i=1}^{N} c_i + \rho_{\text{H}_2\text{O}}}$. Similarly, $\eta_{\text{sol}}(T, c_1, \ldots, c_N)$ and $c_{\text{v,sol}}(T, c_1, \ldots, c_N)$ are modeled, see [10, 11, 12].

3 NUMERICS BASED ON GFDM

3.1 Point Cloud Management

The GFDM approach uses a discretization by a cloud of numerical points which compactly covers the computational domain. The density of the point cloud is given by a sufficiently smooth function $h = h(\mathbf{x}, t)$, the so-called interaction radius. There is a direct correlation between the point cloud resolution and the quality of the simulation results

(convergence in h of order 2). Details regarding the initial seeding and quality maintenance of the point cloud are found in [8, 9]. The latter is of utmost importance in the Lagrangian formulation as well as the ALE-approach since the movement of (parts of) the point cloud leads to accumulation or scattering of points which would reduce the quality of the numerical results.

3.2 Differential Operators

We use a specialized weighted moving least squares approach to determine numerical differential operators $\tilde{\partial}^0, \tilde{\partial}^x, \tilde{\partial}^y, \tilde{\partial}^z, \tilde{\Delta}$ for function approximation, x-,y-,z-derivative, and the Laplacian which are independent of the considered function, see [8]. The interaction radius defines the general neighbors of each point. During the least squares operator generation, the ones with the smallest distance to the considered point obtain the highest weight. Furthermore, the numerical operators are defined such that chosen discrete test functions and their derivatives are reproduced exactly. A common choice are monomials up to a certain order and the delta function.

3.3 Time Integration

A strong form discretization of the physical model (Section 2) can be provided based on the numerical differential operators and a chosen time integration scheme. For simplicity, the following considerations are based on first order time integration.

Starting with the Lagrangian formulation, equations (1) can be rewritten as

$$\frac{d\rho}{dt} = -\rho \cdot \nabla^{\mathrm{T}} \mathbf{v}, \tag{8}$$

$$\frac{d\mathbf{v}}{dt} = \frac{1}{\rho} \cdot (\nabla^{\mathrm{T}} \mathbf{S})^{\mathrm{T}} - \frac{1}{\rho} \cdot \nabla p + \mathbf{g},$$

$$(\rho \cdot c_{\mathrm{v}}) \cdot \frac{dT}{dt} = \nabla^{\mathrm{T}} (\mathbf{S} \cdot \mathbf{v}) - (\nabla^{\mathrm{T}} \mathbf{S}) \cdot \mathbf{v} - p \cdot \nabla^{\mathrm{T}} \mathbf{v} + \nabla^{\mathrm{T}} (\lambda \cdot \nabla T).$$

Note that we use $\rho = \rho_{\mathrm{sol}}$ and $c_{\mathrm{v}} = c_{\mathrm{v,sol}}$ to improve readability. Together with equations (2)–(4), this is the starting point of the numerical discretization. The spatial derivatives are replaced by their least squares approximated counterparts. Denoting the future time level by $n+1$ and the current one by n with time step size $\Delta t = t^{n+1} - t^n$, the point cloud is moved according to a second order method by $\mathbf{x}^{n+1} = \mathbf{x}^n + \Delta t \cdot \mathbf{v}^n + \frac{\mathbf{v}^{\mathrm{n}} - \mathbf{v}^{\mathrm{n-1}}}{2 \cdot \Delta t_0} \cdot (\Delta t)^2$ with previous time step size Δt_0 wrt. time levels n and $n-1$, see [18]. A semi-implicit time integration for temperature T^{n+1} reads

$$(\mathbf{I}_T + \mathbf{D}_T) \cdot T^{n+1} = (\rho^n \cdot c_{\mathrm{v}}^n) \cdot T^n + f_T, \tag{9}$$

where $\mathbf{I}_T = \rho^n \cdot c_{\mathrm{v}}^n \cdot \mathbf{I}$, $\mathbf{D}_T = -\Delta t \cdot \tilde{\nabla}^{\mathrm{T}} (\lambda \cdot \tilde{\nabla})$, and $f_T = \Delta t \cdot (\tilde{\nabla}^{\mathrm{T}} (\mathbf{S}^n \cdot \mathbf{v}^n) - (\tilde{\nabla}^{\mathrm{T}} \mathbf{S}^n) \cdot \mathbf{v}^n - p^n \cdot \tilde{\nabla}^{\mathrm{T}} \mathbf{v}^n)$. Equation (9) forms a sparse linear system with unknowns T^{n+1} at each point of the point cloud. For the sake of clarity, the index of the point is omitted. Analogously, a semi-implicit time integration for concentrations c_i^{n+1}, $i = 1, \ldots, N$, can be formed:

$$(\mathbf{I}_{c_i} + \mathbf{D}_{c_i}) \cdot c_i^{n+1} = c_i^n, \tag{10}$$

where $\mathbf{I}_{c_i} = (\mathbf{I} + \Delta t \cdot \tilde{\nabla}^\mathrm{T}\mathbf{v}^n)$ and $\mathbf{D}_{c_i} = -\Delta t \cdot \tilde{\nabla}^\mathrm{T}(D_{i,\mathrm{eff}} \cdot \tilde{\nabla})$. The future density ρ^{n+1}, viscosities $\eta_{\mathrm{sol}}^{n+1}$ and $\hat{\eta}^{n+1} = \eta_{\mathrm{sol}}^{n+1} + \eta_{\mathrm{turb}}^n$, as well as heat capacity c_{v}^{n+1} can be determined according to Section 2.2.

Time integration of the first equation in (8) provides the targeted divergence of velocity $\tilde{\nabla}^\mathrm{T}\mathbf{v}^{n+1}$. To solve for $\mathbf{v}^{n+1}$ and p^{n+1} in an implicit time integration scheme, we use the penalty formulation introduced in [6, 9] which is independent of the Reynolds number. To this end, the pressure is split into its hydrostatic (body forces) and dynamic parts (movement of the fluid) by $p = p_{\mathrm{hyd}} + p_{\mathrm{dyn}}$. For the hydrostatic pressure, we have

$$\tilde{\nabla}^\mathrm{T}\left(\frac{1}{\rho^{n+1}} \cdot \tilde{\nabla}p_{\mathrm{hyd}}^{n+1}\right) = \tilde{\nabla}^\mathrm{T}\mathbf{g}. \tag{11}$$

Defining the preliminary pressure by $\hat{p} = p_{\mathrm{hyd}}^{n+1} + p_{\mathrm{dyn}}^n$, we obtain the following coupled velocity-pressure-system for preliminary velocity $\hat{\mathbf{v}}^{n+1}$ and correction pressure p_{corr}^{n+1}:

$$\left(\mathbf{I} - \frac{\Delta t}{\rho^{n+1}} \cdot \tilde{\psi}_{\hat{\eta}^{n+1}}^{n+1}\right) \cdot \hat{\mathbf{v}}^{n+1} + \frac{\Delta t}{\rho^{n+1}} \cdot \tilde{\nabla}p_{\mathrm{corr}}^{n+1} = \mathbf{v}^n - \frac{\Delta t}{\rho^{n+1}} \cdot \tilde{\nabla}\hat{p} + \Delta t \cdot \mathbf{g}, \tag{12}$$

$$\tilde{\nabla}^\mathrm{T}\left(\frac{\Delta t_{\mathrm{virt}}}{\rho^{n+1}} \cdot \tilde{\nabla}p_{\mathrm{corr}}^{n+1}\right) = \tilde{\nabla}^\mathrm{T}\hat{\mathbf{v}}^{n+1} - \tilde{\nabla}^\mathrm{T}\mathbf{v}^{n+1} \tag{13}$$

with $(\tilde{\psi}_{\hat{\eta}^{n+1}}^{n+1})^\mathrm{T} = \tilde{\nabla}^\mathrm{T}(\hat{\eta}^{n+1} \cdot \tilde{\nabla})(\hat{\mathbf{v}}^{n+1})^\mathrm{T} + (\tilde{\nabla}\hat{\eta}^{n+1})^\mathrm{T} \cdot (\tilde{\nabla}(\hat{\mathbf{v}}^{n+1})^\mathrm{T})^\mathrm{T} + \frac{\hat{\eta}^{n+1}}{3} \cdot (\tilde{\nabla}(\tilde{\nabla}^\mathrm{T}\hat{\mathbf{v}}^{n+1}))^\mathrm{T} - \frac{2}{3} \cdot (\tilde{\nabla}^\mathrm{T}\hat{\mathbf{v}}^{n+1}) \cdot (\tilde{\nabla}\hat{\eta}^{n+1})^\mathrm{T}$ and $\Delta t_{\mathrm{virt}} = A_{\mathrm{virt}} \cdot \Delta t, 0 \leq A_{\mathrm{virt}} \leq 1$. If $A_{\mathrm{virt}} = 1$, the scheme corresponds to an implicit Chorin projection, see [2]. Theoretically, choosing $A_{\mathrm{virt}} = 0$ would give the exact solution. However, the linear system is ill-conditioned and can not be solved in most cases. For $0.001 \leq A_{\mathrm{virt}} \leq 0.1$, conditioning of the linear system is sufficiently good. Furthermore, the resulting preliminary velocity features a divergence which is very close to the targeted one. The update of the velocity and the dynamic pressure are given by $\mathbf{v}^{n+1} = \hat{\mathbf{v}}^{n+1} - \frac{\Delta t_{\mathrm{virt}}}{\rho^{n+1}} \cdot \tilde{\nabla}p_{\mathrm{corr}}^{n+1}$ and $p_{\mathrm{dyn}}^{n+1} = p_{\mathrm{dyn}}^n + p_{\mathrm{corr}}^{n+1}$. The updated stress tensor $\mathbf{S}^{n+1}$ is determined according to (2).

For the k-ε turbulence model, we derive a singularity formulation from (3):

$$\begin{aligned}
\frac{d}{dt}\left(\frac{k}{\varepsilon}\right) =& (C_{2\varepsilon} - 1) + C_\eta \cdot (1 - C_{1\varepsilon}) \cdot \|\tilde{\nabla}\mathbf{v}^\mathrm{T}\|_\mathrm{M}^2 \cdot \left(\frac{k}{\varepsilon}\right)^2 \\
&+ \frac{C_\eta \cdot (C_{1\varepsilon} \cdot C_{3\varepsilon} - 1)}{\rho \cdot \mathrm{Pr}_{\mathrm{turb}}} \cdot \frac{\partial\rho}{\partial T} \cdot (\mathbf{g} \cdot \tilde{\nabla}T) \cdot \left(\frac{k}{\varepsilon}\right)^2 + \frac{1}{\rho} \cdot \tilde{\Delta}_{\eta^*}\left(\frac{k}{\varepsilon}\right),
\end{aligned} \tag{14}$$

$$\begin{aligned}
\frac{d}{dt}\left(\frac{\varepsilon}{k}\right) =& (1 - C_{2\varepsilon}) \cdot \left(\frac{\varepsilon}{k}\right)^2 + C_\eta \cdot (C_{1\varepsilon} - 1) \cdot \|\tilde{\nabla}\mathbf{v}^\mathrm{T}\|_\mathrm{M}^2 \\
&+ \frac{C_\eta \cdot (1 - C_{1\varepsilon} \cdot C_{3\varepsilon})}{\rho \cdot \mathrm{Pr}_{\mathrm{turb}}} \cdot \frac{\partial\rho}{\partial T} \cdot (\mathbf{g} \cdot \tilde{\nabla}T) + \frac{1}{\rho} \cdot \tilde{\Delta}_{\eta^*}\left(\frac{\varepsilon}{k}\right),
\end{aligned}$$

where $\tilde{\Delta}_{\eta^*}\left(\frac{k}{\varepsilon}\right) = \frac{\varepsilon \cdot \tilde{\Delta}_{\eta_k}k - k \cdot \tilde{\Delta}_{\eta_\varepsilon}\varepsilon}{\varepsilon^2}$ and $\tilde{\Delta}_{\eta^*}\left(\frac{\varepsilon}{k}\right) = \frac{k \cdot \tilde{\Delta}_{\eta_\varepsilon}\varepsilon - \varepsilon \cdot \tilde{\Delta}_{\eta_k}k}{k^2}$ with $\tilde{\Delta}_{\eta_k} = \tilde{\nabla}^\mathrm{T}\left(\left(\eta + \frac{\eta_{\mathrm{turb}}}{\sigma_k}\right) \cdot \tilde{\nabla}\right)$ and $\tilde{\Delta}_{\eta_\varepsilon} = \tilde{\nabla}^\mathrm{T}\left(\left(\eta + \frac{\eta_{\mathrm{turb}}}{\sigma_\varepsilon}\right) \cdot \tilde{\nabla}\right)$, respectively. If $k, \varepsilon > 0$ for all $t^n \leq t \leq t^{n+1}$, numerical mean values can be determined from (14): $\frac{k}{\varepsilon}\big|_\mathrm{m} = \frac{1}{\Delta t}\int_{t^n}^{t^{n+1}} \frac{d}{dt}\left(\frac{k}{\varepsilon}\right) dt, \frac{\varepsilon}{k}\big|_\mathrm{m} =$

$\frac{1}{\Delta t} \int_{t^n}^{t^{n+1}} \frac{d}{dt} \left(\frac{\varepsilon}{k} \right) dt$. We use the mean values to avoid singularities in the discretized k-ε turbulence model.

$$
\frac{dk}{dt} = \frac{\tilde{\Delta}_{\eta_k} k}{\rho} - \left. \frac{\varepsilon}{k} \right|_{\mathrm{m}} \cdot k + C_\eta \cdot \left(\|\tilde{\nabla}\mathbf{v}^{\mathrm{T}}\|_{\mathrm{M}}^2 - \frac{1}{\rho \cdot \mathrm{Pr}_{\mathrm{turb}}} \cdot \frac{\partial \rho}{\partial T} \cdot (\mathbf{g} \cdot \tilde{\nabla} T) \right) \cdot \left. \frac{k}{\varepsilon} \right|_{\mathrm{m}} \cdot k, \tag{15}
$$

$$
\frac{d\varepsilon}{dt} = \frac{\tilde{\Delta}_{\eta_\varepsilon} \varepsilon}{\rho} - C_{2\varepsilon} \cdot \left. \frac{\varepsilon}{k} \right|_{\mathrm{m}} \cdot \varepsilon + C_{1\varepsilon} \cdot C_\eta \cdot \left(\|\tilde{\nabla}\mathbf{v}^{\mathrm{T}}\|_{\mathrm{M}}^2 - \frac{C_{3\varepsilon}}{\rho \cdot \mathrm{Pr}_{\mathrm{turb}}} \cdot \frac{\partial \rho}{\partial T} \cdot (\mathbf{g} \cdot \tilde{\nabla} T) \right) \cdot \left. \frac{k}{\varepsilon} \right|_{\mathrm{m}} \cdot \varepsilon.
$$

Consequently, a fully implicit time integration scheme for k^{n+1} reads

$$
k^{n+1} - \frac{\Delta t \cdot \tilde{\Delta}_{\eta_k} k^{n+1}}{\rho} + \Delta t \cdot \left. \frac{\varepsilon}{k} \right|_{\mathrm{m}} \cdot k^{n+1} \tag{16}
$$

$$
- \Delta t \cdot C_\eta \cdot \left(\|(\tilde{\nabla}\mathbf{v}^{n+1})^{\mathrm{T}}\|_{\mathrm{M}}^2 - \frac{1}{\rho \cdot \mathrm{Pr}_{\mathrm{turb}}} \cdot \frac{\partial \rho}{\partial T} \cdot (\mathbf{g} \cdot \tilde{\nabla} T^{n+1}) \right) \cdot \left. \frac{k}{\varepsilon} \right|_{\mathrm{m}} \cdot k^{n+1} = k^n.
$$

Analogously, we have

$$
\varepsilon^{n+1} - \frac{\Delta t \cdot \tilde{\Delta}_{\eta_\varepsilon} \varepsilon^{n+1}}{\rho} + \Delta t \cdot C_{2\varepsilon} \cdot \left. \frac{\varepsilon}{k} \right|_{\mathrm{m}} \cdot \varepsilon^{n+1} \tag{17}
$$

$$
- \Delta t \cdot C_{1\varepsilon} \cdot C_\eta \cdot \left(\|(\tilde{\nabla}\mathbf{v}^{n+1})^{\mathrm{T}}\|_{\mathrm{M}}^2 - \frac{C_{3\varepsilon}}{\rho \cdot \mathrm{Pr}_{\mathrm{turb}}} \cdot \frac{\partial \rho}{\partial T} \cdot (\mathbf{g} \cdot \tilde{\nabla} T^{n+1}) \right) \cdot \left. \frac{k}{\varepsilon} \right|_{\mathrm{m}} \cdot \varepsilon^{n+1} = \varepsilon^n.
$$

The mean values are determined analytically. This is illustrated in detail for $\left. \frac{k}{\varepsilon} \right|_{\mathrm{m}}$. Assuming that the diffusion term $\frac{1}{\rho} \cdot \tilde{\Delta}_{\eta^*} \left(\frac{k}{\varepsilon} \right)$ is negligible as well as defining $x = \frac{k}{\varepsilon}$, $a = C_{2\varepsilon} - 1$, and $b = C_\eta \cdot \left((C_{1\varepsilon} - 1) \cdot \|\tilde{\nabla}\mathbf{v}^{\mathrm{T}}\|_{\mathrm{M}}^2 + \frac{(1 - C_{1\varepsilon} \cdot C_{3\varepsilon})}{\rho \cdot \mathrm{Pr}_{\mathrm{turb}}} \cdot \frac{\partial \rho}{\partial T} \cdot (\mathbf{g} \cdot \tilde{\nabla} T) \right)$, we can rewrite equation (14) as $\frac{dx}{dt} = a - b \cdot x^2$. Thus, we obtain

$$
x^{n+1} = \begin{cases} \sqrt{\frac{a}{b}} \cdot \tanh \left(\Delta t \cdot \sqrt{a \cdot b} + \mathrm{arctanh} \left(\sqrt{\frac{b}{a}} \cdot x^n \right) \right), & x^n < \sqrt{\frac{a}{b}} \\ \sqrt{\frac{a}{b}}, & x^n = \sqrt{\frac{a}{b}} \\ \sqrt{\frac{a}{b}} \cdot \coth \left(\Delta t \cdot \sqrt{a \cdot b} + \mathrm{arccoth} \left(\sqrt{\frac{b}{a}} \cdot x^n \right) \right), & x^n > \sqrt{\frac{a}{b}} \end{cases} . \tag{18}
$$

The updated turbulent viscosity is determined by $\eta_{\mathrm{turb}}^{n+1} = \rho^{n+1} \cdot C_\eta \cdot \frac{(k^{n+1})^2}{\varepsilon^{n+1}}$.

In case of the Eulerian formulation, [17] shows that a second order time integration scheme should be applied to numerically solve transport terms of the form $\mathbf{v}^{\mathrm{T}} \nabla$. For this purpose, the SDIRK2 method is proposed (see [1]). It features the same stability properties as an implicit Euler time integration scheme. Furthermore, an upwind discretization by means of a MUSCL reconstruction with a Superbee limiter is used. For example, the coupled velocity-pressure-system is solved by the following two-step procedure:

$$
\left(\mathbf{I}_{\hat{\mathbf{v}}^{n+\alpha}} - \frac{\alpha \cdot \Delta t}{\rho^{n+\alpha}} \tilde{\psi}_{\hat{\eta}^{n+\alpha}}^{n+\alpha} \right) \cdot \hat{\mathbf{v}}^{n+\alpha} + \frac{\alpha \cdot \Delta t}{\rho^{n+\alpha}} \cdot \tilde{\nabla} p_{\mathrm{corr}}^{n+\alpha} = \mathbf{v}^n - \frac{\alpha \cdot \Delta t}{\rho^{n+\alpha}} \cdot \tilde{\nabla} \hat{p} + \alpha \cdot \Delta t \cdot \mathbf{g}, \tag{19}
$$

$$
\tilde{\nabla}^{\mathrm{T}} \left(\frac{\Delta t_{\mathrm{virt}}}{\rho^{n+\alpha}} \cdot \tilde{\nabla} p_{\mathrm{corr}}^{n+\alpha} \right) = \tilde{\nabla}^{\mathrm{T}} \hat{\mathbf{v}}^{n+\alpha} - \tilde{\nabla}^{\mathrm{T}} \mathbf{v}^{n+\alpha}
$$

with $\mathbf{I}_{\hat{\mathbf{v}}^{n+\alpha}} = (\mathbf{I} + (\widetilde{\mathbf{v}^{\mathrm{T}}\tilde{\nabla}})\hat{\mathbf{v}}^{n+\alpha})$ and $(\tilde{\psi}_{\hat{\eta}^{n+\alpha}}^{n+\alpha})^{\mathrm{T}} = \tilde{\nabla}^{\mathrm{T}}(\hat{\eta}^{n+\alpha} \cdot \tilde{\nabla})(\hat{\mathbf{v}}^{n+\alpha})^{\mathrm{T}} + (\tilde{\nabla}\hat{\eta}^{n+\alpha})^{\mathrm{T}} \cdot$
$(\tilde{\nabla}(\hat{\mathbf{v}}^{n+\alpha})^{\mathrm{T}})^{\mathrm{T}} + \frac{\hat{\eta}^{n+\alpha}}{3} \cdot (\tilde{\nabla}(\tilde{\nabla}^{\mathrm{T}}\hat{\mathbf{v}}^{n+\alpha}))^{\mathrm{T}} - \frac{2}{3} \cdot (\tilde{\nabla}^{\mathrm{T}}\hat{\mathbf{v}}^{n+\alpha}) \cdot (\tilde{\nabla}\hat{\eta}^{n+\alpha})^{\mathrm{T}}$ and, subsequently,

$$\hat{\mathbf{v}}^{n+1} - \Delta t \cdot \alpha \cdot \mathbf{V}(\hat{\mathbf{v}}^{n+1}, p_{\mathrm{corr}}^{n+1}) = \mathbf{v}^n + \Delta t \cdot (1 - \alpha) \cdot \mathbf{V}(\hat{\mathbf{v}}^{n+\alpha}, p_{\mathrm{corr}}^{n+\alpha}), \qquad (20)$$

$$\tilde{\nabla}^{\mathrm{T}}\left(\frac{\Delta t_{\mathrm{virt}}}{\rho^{n+1}} \cdot \tilde{\nabla}p_{\mathrm{corr}}^{n+1}\right) = \tilde{\nabla}^{\mathrm{T}}\hat{\mathbf{v}}^{n+1} - \tilde{\nabla}^{\mathrm{T}}\mathbf{v}^{n+1}$$

with $\mathbf{V}(\hat{\mathbf{v}}^{n+1}, p_{\mathrm{corr}}^{n+1}) = -\frac{1}{\rho^{n+1}} \cdot (\widetilde{\mathbf{v}^{\mathrm{T}}\tilde{\nabla}})\hat{\mathbf{v}}^{n+1} + \frac{1}{\rho^{n+1}} \cdot \tilde{\psi}_{\hat{\eta}^{n+1}}^{n+1} - \frac{1}{\rho^{n+1}} \cdot \tilde{\nabla}\hat{p}^{n+1} + \mathbf{g}$ and $\mathbf{V}(\hat{\mathbf{v}}^{n+\alpha}, p_{\mathrm{corr}}^{n+\alpha}) = \frac{\hat{\mathbf{v}}^{n+\alpha} - \mathbf{v}^n}{\alpha \cdot \Delta t}$ are solved for $\alpha = 1 - \frac{\sqrt{2}}{2}$. Density and viscosity for the intermediate step can for instance be determined by linear interpolation between time level n and $n + 1$.

4 MICROSCOPIC SCALE

In this subsection, we present a general method based on the Lagrangian formulation to identify the effective parameters that are necessary for macroscopic scale simulations. These are effective diffusion coefficient and boundary condition between water and surrounding species. For simplicity, we restrict the following illustration to sodium chloride. Please note that the procedure can directly be transferred to any other species.

4.1 Setup

We consider a cylinder with diameter of 5m and height of 10m which is initially filled with pure water, i.e. $c_{\mathrm{NaCl}}(t = 0) = 0$. During the simulation, the temperature is fixed to $T_0 = 20\,^\circ\mathrm{C}$. The roof of the cylinder acts as inexhaustible supply of sodium chloride which is modeled by applying a Dirichlet condition with saturation concentration $c_{\mathrm{NaCl}}^{\mathrm{s}} = c_{\mathrm{NaCl}}^{\mathrm{s}}(T_0) = 357\frac{\mathrm{kg}}{\mathrm{m}^3}$. For the hull of the cylinder, a homogeneous Neumann condition is applied. Aiming at a quasi-stationary profile, the bottom of the cylinder models an outflow boundary. In the interior, we solve $\frac{\partial c_{\mathrm{NaCl}}}{\partial t} = \nabla^{\mathrm{T}}(D_{\mathrm{micro}} \cdot \nabla c_{\mathrm{NaCl}})$, where $D_{\mathrm{micro}} = D_{\mathrm{laminar}} + D_{\mathrm{turb}}$. The laminar diffusion coefficient for sodium chloride is given by $D_{\mathrm{laminar}} = 1.611 \cdot 10^{-9}\frac{\mathrm{m}^2}{\mathrm{s}}$ (see [3]). For the turbulent part, we have $D_{\mathrm{turb}} = C_\eta \cdot \frac{k^2}{\varepsilon}$. Standard boundary conditions (Dirichlet and Neumann) are prescribed for velocity, pressure, and the turbulent quantities. The simulation runs until a quasi-stationary state is reached.

4.2 Evaluation Strategy

In order to determine the effective quantities, the cylinder is split in z-direction into equal sub-cylinders SC_j, $j = 1, \ldots, J$, which are used to estimate the mass flow. The planes between the sub-cylinders are denoted by HP_j, $j = 1, \ldots, J - 1$. Analogously to the heat flow, the mass flow of sodium chloride is given by $\frac{dm}{dt} = -D_{\mathrm{NaCl,eff}} \cdot \frac{\partial \bar{c}_{\mathrm{NaCl}}}{\partial \mathbf{n}}$, where $\bar{c}_{\mathrm{NaCl}}$ is the mean concentration. The mass flow and the mean concentration in sub-cylinder SC_j are determined by

$$\frac{dm}{dt}(SC_j) = \frac{\int_{SC_j} c_{\mathrm{NaCl}} \cdot v_3 \, dV_{SC_j}}{\int_{SC_j} 1 \, dV_{SC_j}}, \quad \bar{c}_{\mathrm{NaCl}}(SC_j) = \frac{\int_{SC_j} c_{\mathrm{NaCl}} \, dV_{SC_j}}{\int_{SC_j} 1 \, dV_{SC_j}}. \qquad (21)$$

Based on the mean concentration in a sub-cylinder SC_j, we can approximate its normal derivative wrt. the help plane HP_j. This yields the effective diffusion coefficients

$$D_{\text{NaCl,eff}}(SC_j|HP_j) = -\frac{\frac{dm}{dt}(SC_j)}{\frac{\partial \bar{c}_{\text{NaCl}}}{\partial \mathbf{n}}\big|_{HP_j}}, \quad j = 1, \ldots, J-1. \tag{22}$$

As soon as a quasi-stationary state is reached, the values for the different j tend to the desired effective diffusion coefficient for a macroscopic setup (resolution is of the order of the height of the sub-cylinders). To accommodate the "quasi-stationary" character of a simulation, we use a time-averaged effective diffusion coefficient wrt. a small time interval.

In the macroscopic simulation, we use the Robin boundary condition

$$D_{\text{NaCl,eff}} \cdot \frac{\partial c_{\text{NaCl}}}{\partial \mathbf{n}} = \gamma_{\text{NaCl,eff}} \cdot (c_{\text{NaCl}} - c_{\text{NaCl}}^{\text{s}}), \tag{23}$$

where the effective transition coefficient $\gamma_{\text{NaCl,eff}}$ can be derived from the microscopic setup similarly to the effective diffusion coefficient $D_{\text{NaCl,eff}}$:

$$\gamma_{\text{NaCl,eff}}(SC_j) = \frac{\frac{dm}{dt}(SC_j)}{\bar{c}_{\text{NaCl}}(SC_j) - c_{\text{NaCl}}^{\text{s}}}, \quad j = 1, \ldots, J-1. \tag{24}$$

If the quasi-stationary state is reached, the (time-averaged) sub-cylinder specific values tend to the desired value of the effective transition coefficient. With the help of $\gamma_{\text{NaCl,eff}}$, we can define the solution rate of sodium chloride for given temperature T_0 by

$$R_{\text{NaCl}}(T_0) = \gamma_{\text{NaCl,eff}}(c_{\text{NaCl}} - c_{\text{NaCl}}^{\text{s}}). \tag{25}$$

4.3   Numerical Results

The resolution (interaction radius h) in the macroscopic simulation in Section 5 is of the order of meters. Thus, we choose $J = 10$ in the microscopic setup which yields sub-cylinders of height 1m. We consider five levels of resolution with interaction radii $h = 0.30\text{m}, 0.25\text{m}, 0.20\text{m}, 0.19\text{m}, 0.18\text{m}$. The evolution of the concentration for the highest resolution in the time interval $[0\text{s}, 100\text{s}]$ is illustrated in Figure 1. As expected, the flow is characterized by viscous fingering.

Decreasing the interaction radius h, leads to convergence of the estimated effective diffusion and transition coefficients towards $D_{\text{NaCl,eff}} = 0.1 \frac{\text{m}^2}{\text{s}}$ and $\gamma_{\text{NaCl,eff}} = 0.000042 \frac{\text{m}}{\text{s}}$, respectively (see Table 1). According to this, we obtain a solution rate of $R_{\text{NaCl}}(20\,°\text{C}) = -0.0150 \frac{\text{kg}}{\text{m}^2 \cdot \text{s}}$. Compared to the solution rate of $-0.0488 \frac{\text{kg}}{\text{m}^2 \cdot \text{s}}$ for $T_0 = 23\,°\text{C}$ determined in [7] on crystal level, the estimated solution rate is of the correct order of magnitude.

5   MACROSCOPIC SCALE

The effective parameters determined in Section 4 are used in the macroscopic setup below which models a simplified solution mining process. Both the Lagrangian as well as the Eulerian formulation are evaluated, see [17].
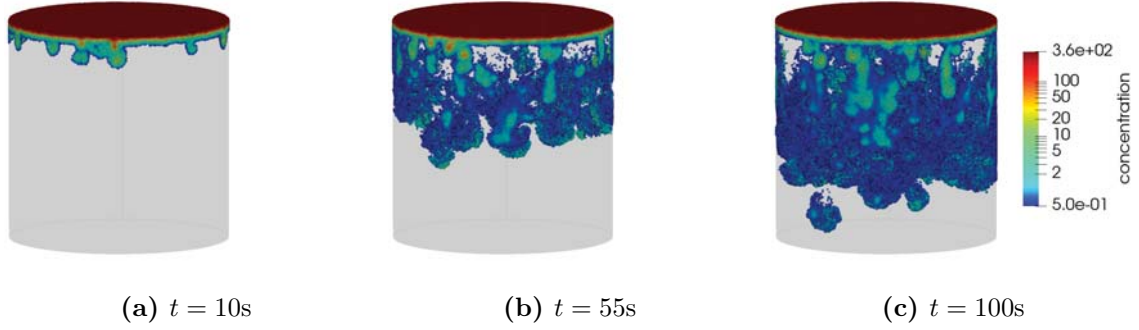
(a) $t = 10$s **(b)** $t = 55$s **(c)** $t = 100$s

Figure 1: Evolution of the microscopic simulation for $h = 0.18$m – concentration.

Table 1: Estimated effective diffusion and transition coefficient, as well as solution rate.

interaction radius	$D_{\text{NaCl,eff}}$	$\gamma_{\text{NaCl,eff}}$	$R_{\text{NaCl}}(20\,^\circ\text{C})$
$h = 0.30$m	$0.1515\frac{\text{m}^2}{\text{s}}$	$0.000184\frac{\text{m}}{\text{s}}$	$-0.0657\frac{\text{kg}}{\text{m}^2 \cdot \text{s}}$
$h = 0.25$m	$0.1558\frac{\text{m}^2}{\text{s}}$	$0.000141\frac{\text{m}}{\text{s}}$	$-0.0504\frac{\text{kg}}{\text{m}^2 \cdot \text{s}}$
$h = 0.20$m	$0.1096\frac{\text{m}^2}{\text{s}}$	$0.000074\frac{\text{m}}{\text{s}}$	$-0.0264\frac{\text{kg}}{\text{m}^2 \cdot \text{s}}$
$h = 0.19$m	$0.1028\frac{\text{m}^2}{\text{s}}$	$0.000050\frac{\text{m}}{\text{s}}$	$-0.0179\frac{\text{kg}}{\text{m}^2 \cdot \text{s}}$
$h = 0.18$m	$0.0999\frac{\text{m}^2}{\text{s}}$	$0.000042\frac{\text{m}}{\text{s}}$	$-0.0150\frac{\text{kg}}{\text{m}^2 \cdot \text{s}}$

5.1 Setup

We are interested in the geometrical evolution of a salt cavern. The initial geometry is given by a small cavern filled with pure water which is surrounded by sodium chloride, see Figure 2. The dimensions of the initial cavern are approximately: width of 90m, height of 50m, and depth of 26m. The sodium chloride deposit is limited in extension which corresponds to impermeable surrounding rock. The pipe on the left side acts as an inlet of fresh water with $|\mathbf{v}_{\text{in}}| = 1\frac{\text{m}}{\text{s}}$, whereas the pipe on the right side acts as the outlet.

In reality, the maximum diameter of the pipes is of the order of 1m. Hence, the
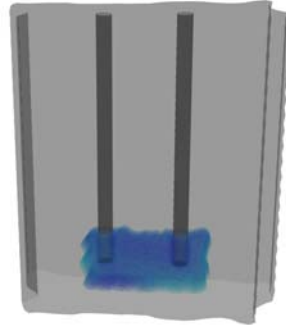
Figure 2: Macroscopic simulation setup – initial geometry, see [17].

606

resolution of the point cloud close to the inlet and the outlet has to be of the order of 0.1m to ensure accurate results. In case of the Lagrangian formulation, this would lead to an extremely small time step size compared to the desired simulation time of several years due to the CFL-condition $\Delta t_{\text{Lag}} \leq CFL_{\text{Lag}} \cdot \frac{h_{\min}}{|\mathbf{v}|}$. Stable results are achieved for $CFL_{\text{Lag}} = 0.15$. Since $|\mathbf{v}| \geq |\mathbf{v}_{\text{in}}|$ and $h_{\min} = \mathcal{O}(0.1\text{m})$, we obtain $\Delta t_{\text{Lag}} = \mathcal{O}(0.1\text{s})$. In order to allow for a comparison of Lagrangian and Eulerian formulation, we consider pipes of diameter 12m and constant interaction radius of $h = 4$m. Furthermore, we fix the temperature to $T_0 = 20\,^\circ\text{C}$ and, subsequently, obtain the corresponding saturation concentration $c_{\text{NaCl}}^{\text{s}} = 357\frac{\text{kg}}{\text{m}^3}$. For simplicity, the following linear relations for density and viscosity of the solution are used as described in [17]: $\rho(c_{\text{NaCl}}) \approx (0.56 \cdot c_{\text{NaCl}} + 1000)\frac{\text{kg}}{\text{m}^3}$, $\eta(c_{\text{NaCl}}) \approx (1.96 \cdot 10^{-6} \cdot c_{\text{NaCl}} + 10^{-3})\frac{\text{Pa}}{\text{s}}$. We use $D_{\text{NaCl,eff}} = 0.1\frac{\text{m}^2}{\text{s}}$ and $\gamma_{\text{NaCl,eff}} = 0.00005\frac{\text{m}}{\text{s}}$.

5.2 Movement of the Boundary

The movement of the boundary of the cavern can be defined by the Stefan condition $\rho v^\star = \gamma_{\text{NaCl,eff}}(c_{\text{NaCl}} - c_{\text{NaCl}}^{\text{s}})$, see [5]. This yields $v^\star = \frac{\gamma_{\text{NaCl,eff}}}{\rho} \cdot (c_{\text{NaCl}} - c_{\text{NaCl}}^{\text{s}})$ and, consequently, a movement of the boundary in normal direction $\mathbf{n}$ with velocity $\mathbf{v}_{\text{boundary}} = v^\star \cdot \mathbf{n}$. To speed up computation, a time lapse procedure can be applied which introduces an additional factor A in the definition of $v^\star$ which is limited by certain stability conditions. For details, the reader is referred to [17].

Due to the movement of the boundary, interior points close to this boundary have to move in the Eulerian formulation also. For this purpose, the ALE-approach presented in [4] is used. Based on current and future position of an affected interior point, the translational velocity $\mathbf{v}_{\text{trans}} = \frac{\mathbf{x}^{n+1} - \mathbf{x}^n}{\Delta t}$ is determined. Due to the explicit movement of these points, the convection terms in the numerical model in Eulerian form in Section 3.3 must refer to the relative velocity $\mathbf{v} - \mathbf{v}_{\text{trans}}$ instead of $\mathbf{v}$. Furthermore, this introduces a CFL-condition of the form $\Delta t_{\text{ALE}} \leq CFL_{\text{ALE}} \cdot \frac{h_{\min}}{v^\star}$. It depends on the boundary velocity $v^\star = \mathcal{O}(0.01\frac{\text{m}}{\text{s}})$ which is considerably smaller than the flow velocity, cf. [17]. Furthermore, $h_{\min}$ is subject to the desired resolution at the moving boundary. At the inlet and the outlet, a coarse resolution is sufficient in this case.

5.3 Numerical Results

Figure 3 illustrates the evolution of the salt cavern in the Eulerian formulation according to $C = c_{\text{NaCl}}$. The need for an ALE-concept is emphasized by the difference in time steps to cover a simulation time of 7200s: in the Lagrangian formulation, 22915 time steps are necessary, whereas only 936 time steps suffice in the Eulerian formulation. This corresponds to a speed-up of approximately 25 in computation time.

6 CONCLUSIONS

In this contribution, we presented the capabilities of the simulation software MESH-FREE regarding solution mining processes on different scales. The developed generalized finite difference approach on a point cloud enables the use of a Lagrangian as well as an Eulerian formulation. On the microscopic scale, we described a procedure to deter-
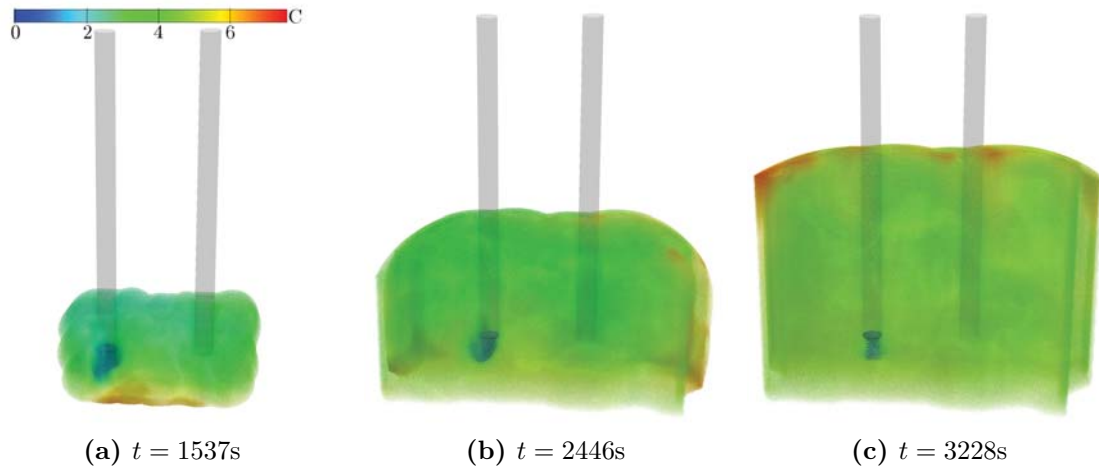
(a) $t = 1537$s **(b)** $t = 2446$s **(c)** $t = 3228$s

Figure 3: Evolution of the macroscopic simulation for $h = 4$m – concentration, see [17].

mine effective diffusion and transition coefficients for an arbitrary species based on the Lagrangian formulation by considering sodium chloride as numerical example. The resulting effective parameters are then used in macroscopic simulations. A comparison of the simulation results for the Lagrangian and the Eulerian formulation (extended by an ALE-approach) illustrate the advantages of the latter one. Aiming at a simulation time of several years, the forecast computation time for a simulation based on the Lagrangian formulation would be of the order of years. In contrast to that, the flexibility of the Eulerian formulation regarding the resolution of the point cloud (local refinement only at the moving boundary) enables meshfree simulations in reasonable time – especially in terms of real applications.

REFERENCES

[1] Alexander, R. *Diagonally Implicit Runge-Kutta Methods for Stiff O.D.E.'s.* SIAM J. Numer. Anal. (1977) **14(6)**:1006–1021.

[2] Chorin, A.J. *Numerical solution of the Navier-Stokes equations.* Math. Comput. (1968) **22**:745–762.

[3] Flury, M. and Gimmi, T. *Solute Diffusion.* In: Dane, J.H. and Topp, G.C. (eds) Methods of Soil Analysis, Part 4, Physical Methods (2002) pp. 1323–1351.

[4] Hirt, C.W. and Amsden, A.A. and Cook, J.L. *An Arbitrary Lagrangian-Eulerian Computing Method for All Flow Speeds.* J. Comput. Phys. (1974) **14(3)**:227–253.

[5] Javierre-Perez, E. *Literature Study: Numerical Methods for Solving Stefan Problems.* Delft University of Technology (2003).

[6] Jefferies, A. and Kuhnert, J. and Aschenbrenner, L. and Giffhorn, U. *Finite Pointset Method for the Simulation of a Vehicle Travelling Through a Body of Water.* In:

Griebel, M. and Schweitzer, M.A. (eds) Meshfree Methods for Partial Differential Equations VII. LNCSE, Vol. 100, Springer, Cham (2015) pp. 205–211.

[7] Karsten, O. *Lösungsgeschwindigkeit von Natriumchlorid, Kaliumchlorid und Kieserit in Wasser und in wässerigen Lösungen.* ZAAC (1954) **276(5-6)**:247–266.

[8] Kuhnert, J. and Michel, I. and Mack, R. *Fluid Structure Interaction (FSI) in the MESHFREE Finite Pointset Method (FPM): Theory and Applications.* In: Griebel, M. and Schweitzer, M.A. (eds) Meshfree Methods for Partial Differential Equations IX, IWMMPDE2017. LNCSE, Vol. 129, Springer, Cham (2019) pp. 73–92.

[9] Kuhnert, J. *Meshfree numerical schemes for time dependent problems in fluid and continuum mechanics.* In: Sundar, S. (ed) Advances in PDE Modeling and Computation, Ane Books, New Delhi (2014) pp. 119–136.

[10] Laliberté, M. *A Model for Calculating the Heat Capacity of Aqueous Solutions, with Updated Density and Viscosity Data.* J. Chem. Eng. Data (2009) **54**:1725–1760.

[11] Laliberté, M. *Model for Calculating the Viscosity of Aqueous Solutions.* J. Chem. Eng. Data (2007) **52**:1507–1508.

[12] Laliberté, M. *Model for Calculating the Viscosity of Aqueous Solutions.* J. Chem. Eng. Data (2007) **52**:321–335.

[13] Laliberté, M. and Cooper W.E. *Model for Calculating the Density of Aqueous Electrolyte Solutions.* J. Chem. Eng. Data (2004) **49**:1141–1151.

[14] Launder, B.E. and Spalding, D.B. *The numerical computation of turbulent flows.* Comput. Methods. Appl. Mech. Eng. (1974) **3**:269–289.

[15] Michel, I. and Bathaeian, S.M.I. and Kuhnert, J. and Kolymbas, D. and Chen, C.-H. and Polymerou, I. and Vrettos, C. and Becker, A. *Meshfree generalized finite difference methods in soil mechanics – part II: numerical results.* Int. J. Geomath. (2017) **8(2)**:191–217.

[16] Nick, F. and Plum, H.-J. and Kuhnert, J. *Parallel Detection of Subsystems in Linear Systems Arising in the MESHFREE Finite Pointset Method.* In: Griebel, M. and Schweitzer, M.A. (eds) Meshfree Methods for Partial Differential Equations IX, IWMMPDE2017. LNCSE, Vol. 129, Springer, Cham (2019) pp. 93–115.

[17] Seifarth, T. *Numerische Algorithmen für gitterfreie Methoden zur Lösung von Transportproblemen.* PhD Thesis, University of Kassel, Fraunhofer Verlag (2018).

[18] Suchde, P. and Kuhnert, J. *Point cloud movement for fully Lagrangian meshfree methods.* J. Comput. Appl. Math. (2018) **340**:89–100.

[19] Uhlmann, E. and Gerstenberger, R. and Kuhnert, J. *Cutting simulation with the meshfree Finite Pointset Method.* Procedia CIRP (2013) **8**:391–396.

Direct Observation and simulation of ladle pouring behaviour in die casting sleeve

T. Sugihara*, M. Fujishiro[†] and Y. Maeda[††]

*Graduate student, Dept. of Mechanical Engineering, Daido University
[†]Dept. of Mechanical Engineering, Daido University
[††] Professor, Dr. Eng., Dept. of Mechanical Engineering, Daido University
10-3 Takiharu-cho, Minami-ku, Nagoya 457-8530 Japan
E-mail: y-maeda@daido-it.ac.jp Web page: https://www.daido-it.ac.jp

Abstract

The ladle pouring process is one part of die casting which has the advantages of high speed, good quality and mass production. The molten metal is quickly poured into the sleeve by tilting the ladle, and immediately injected into the die cavity with high speed and high pressure by advancing the plunger. Since the entrapment of air and the generation of solidified layer in the ladle pouring may cause the defects of cast products, it is necessary to simulate the ladle pouring behavior.

In the present study, the pouring experiment into the sleeve using water and die casting aluminum alloy JIS-ADC12 are carried out to observe the flow behavior by tilting the ladle. The temperature of the dissolved metal is measured using a thermocouple to investigate heat transfer behavior. The flow behaviors in ladle pouring of water and molten aluminum alloy are simulated using Particleworks[TM] of MPS software. The simulation results, when using water are almost the same actual wave behavior. It is difficult to simulate the wave behavior of molten aluminum alloy because there is a difference in wave behavior between water and molten aluminum alloy. On the other hands, it is clear that the molten aluminum alloy is not solidified during wave behavior in the early stage of pouring by the experiments. Therefore, we try to adjust the kinematic viscosity of molten metal and the thermal conductivity of sleeve die. As the result, the wave behavior and temperature of molten aluminum alloy after adjusting the parameters are almost agreed with the actual phenomena. Flow and heat transfer simulation using the MPS method is effective method that ladle pouring of molten aluminum alloy with free surface flow can be simulated accurately.

Keywords: Ladle pouring, Wave behavior, Molten metal, Aluminum alloy, Solidification

1. Introduction

Since the molten metal in die casting process injects to the cavity with high speed and high pressure, it has the advantage of good quality and mass production.[1][2] However, defects are caused by the solidified layer in the sleeve [3][4], air entrainment, the oxide film of the aluminum alloy.[5]-[7] So, it is desirable to suppress the sleeve air entrainment and generation of oxide film in the pouring process [5]-[8].

In this study, the influence of the tilting ladle conditions on the flow behavior in the sleeve is investigated using water and die casting aluminum alloy. The temperature of molten metal is measured using thermocouple in order to investigate the heat transfer behavior. The conditions are three tilting speed and three angle between ladle and sleeve. Also, in recent years, attempts have been made to apply the particle method to the casting field. Mochida et al. Use the SPH method to simulate the die casting process by adopting a model in which the viscosity is changed according to the solid content of the molten metal.[2] Hasuno et.al. is simulated pouring process to sleeve from ladle using MPS method.[5] Kazama et al. Have used the SPH method to reproduce the vibration of the surface of the molten metal during conveyance of the molten metal and to develop an oxide film model of the aluminum alloy, and also obtained good results in analysis.[6][7] Suwa et al. Investigated the validity of the oxide film model when changed the angle and pouring speed of the ladle.[8] There, simulated ladle pouring behavior using by lagrangian MPS particle method software. Further, the flow behaviors in ladle pouring of water and molten aluminum alloy are simulated using Particleworks[TM] of MPS software.[9]

2. Pouring experiment by tilting ladle

2.1 Experimental apparatus

Experimental apparatus consists of tilting ladle, sleeve, automatic pouring machine, recorder and video camera, as shown in Fig.1. The sleeve shape is the rectangular container 300×60×35mm and the front side is the heat-resistant glass wall in order to observe the pouring behavior directlly. It is possible to change the tilting speed and the angle between ladle and sleeve.

The tilting speeds are 0.45,0.37 and 0.28[rad/s]. The angles are 0°, 20° and 40° , as shown in Fig.2. The temperature of molten metal is measured using K-type (Chromel-Alumel) thermocouple in order to investigate the heat transfer behavior.

The measurement points P1, P2, P3 and P4 are located at 1mm from the bottom and at 100,150,200, 250mm from right wall, and P5 is located at 10mm from bottom and on the left wall, as shown Fig.3.

2.2 Experimental procedure

The pouring experiment into the sleeve using water and die casting aluminum alloy JIS-ADC12 are carried out to observe the wave behavior by tilting ladle. The flow behavior is observed using by video camera with 60fps. Table 1 shows the experimental conditions of ladle pouring. Mass of water and aluminum alloy are 250g and 675g, respectively. Those values mean about volume of 250cm^3.

In the experiments, the aluminum alloy are melt in the Muffle furnace, and the sleeve and the ladle are pre-heated at 300°C. When the temperature of molten metal aluminum alloy reaches 700°C, the ladle is tilted by the automatic pouring machine, then the molten aluminum alloy is poured into the sleeve. Number of repetition times is 3 or more taking consideration of reproduciblity.

2.3 Experimental results and discussion

The wave behaviors of water and molten aluminum alloy obtained by experiment in the case of tilting speed 0.45rad/s are shown in Fig.4

Fig.1 Experimental apparatus.

Fig.2 The angle between ladle and sleeve
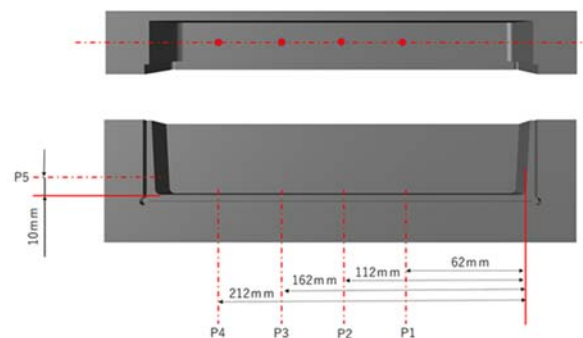
Fig.3 Measurement points for molten metal.

Table 1 Experimental conditions of ladle pouring.

Material	Water	JIS-ADC12
Pouring temp. [°C]	Room temp.	700
Mass of sample [g]	250	675
Ladle angle [°]	0,20,40	
Tilting speed [rad/s]	0.45,0.37,0.28	
Initial temp. of ladle and sleeve [°C]	Room temp.	300

to Fig.7, respectively. The first column shows front view in the case of the ladle angle 0° and the second and third columns show the front and top view in the case of ladle angle 40°. In the case of water, the liquid height rises by bouncing back when the water hits the bottom of the sleeve. Even if the ladle angle varies, the wave behavior of water not almost changed. This tendency is the same in other tilting speeds. The liquid height of molten aluminum alloy is not become high like water. This result is the same trend in other tilting speeds. Further, in the case of water, the tip reaches the left wall at about 2.5 [s], whereas it does not reach in the case of the molten aluminum alloy. Although the kinematic

viscosity of molten aluminum alloy is almost the same with water, it is clarified the different wave behaviors. Please refer to Table 3 and Table 4. Also, in the case of molten aluminum alloy of top view, molten metal is found meandered from Fig.7.

As an example, the temperature cooling curve at P1 in the case of tilting speed 0.45rad/s is shown in Fig.8. Although the result of ladle angle of 20° is a little lower than others, the cooling behavior of molten metal are almost the same tendency. In the case of high tilting speed of 0.45rad/s, the temperatures go down to liquidus temperature about at 5s. From the wave behavior of Fig.5, the flow front of molten metal collides with the left wall at 2.9s, and reaches the front go back to the right wall at 4.2s, and then the wave movement is stopped before the temperature of molten metal reaches the liquidus temperature. Therefore, the solidified layer is not large influenced on the wave movement and is not involved to stop it.
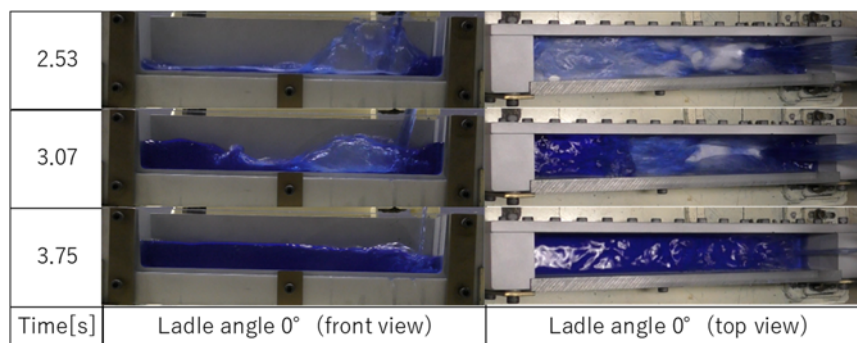
Fig.4 Wave behavior of water obtained by experiment in the case of tilting speed of 0.45rad/s of ladle angle 0°.
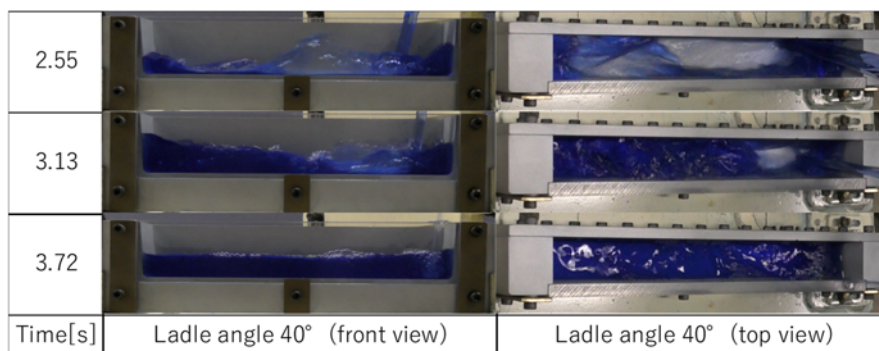
Fig.5 Wave behavior of water obtained by experiment in the case of tilting speed of 0.45rad/s of ladle angle 40°.

Fig.6 Wave behavior of molten aluminum alloy obtained by experiment in the case of tilting speed of 0.45rad/s of ladle angle 0°.

2.57		2.43	
3.13		2.57	
3.88		2.72	
Time[s]	Ladle angle 40° (front view)	Time[s]	Ladle angle 40° (top view)
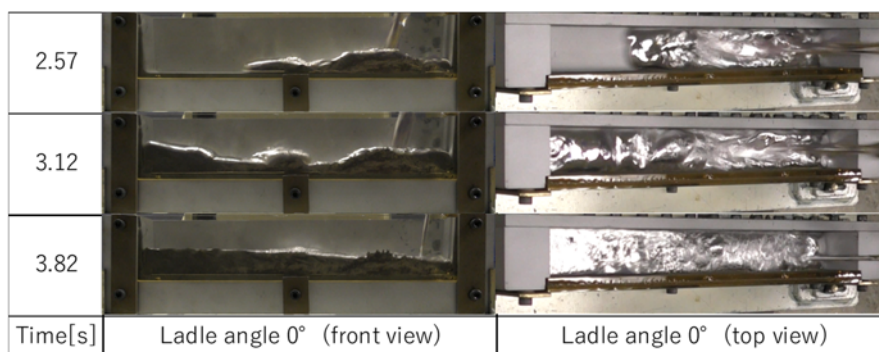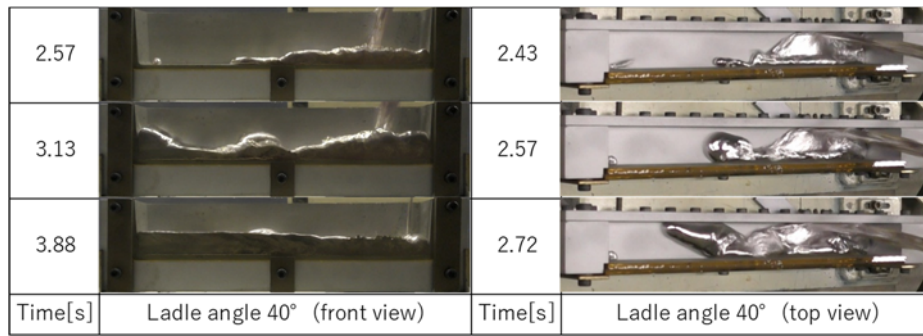
Fig.7 Wave behavior of molten aluminum alloy obtained by experiment in the case of tilting speed of 0.45rad/s of ladle angle 40°.
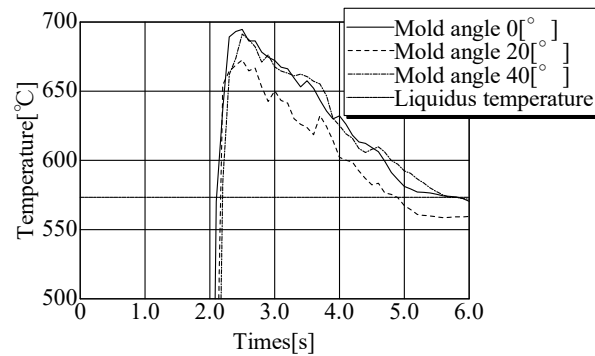
Fig.8 Temperature cooling curve at P1 in the case of tilting speed 0.45rad/s.

3. Particle-based Simulation

It is difficult to simulate the pouring behavior of tilting ladle because the process has the moving boundary of the ladle and free surface boundary of molten metal. [4] Further, in the die casting process, the molten metal is injected from sleeve to the cavity by pushing of plunger. So, the particle-based methods are suitable for the numerical simulation for the die casting process. [5]-[8] In the present study, the ladle pouring behavior is simulated using by the Particleworks^{TM} of MPS software.

3.1 Wave behavior of water

The calculation conditions of present study are shown in Table 2. This speed of sound is not physical property value but also calculation parameter. The physical properties of water shown in Table 3 are used in simulation.

The comparisons of wave behavior between experiment and simulation in the case of the water, the tilting speed of 0.45rad/s and ladle angle of 0° are shown in Fig.9. In the simulation of Fig.9, the color of the fluid is changed by the velocity. Blue indicates that the speed is almost 0m/s, and the speed becomes faster as the color approaches light green. The wave behaviors obtained by simulation are almost agreed with experiments. Fig.8 shows the front view of wave behavior in the case of ladle angle of 40°. Also, Fig.11 shows the flow of top view of water obtained by in the case of ladle angle 40°. The difference in color in the simulation of Fig. 9 is the same as Fig. 10. The

Table 2 Calculation conditions.

Software	Particleworks 6.1.2
Pressure Eq. Scheme	Explicit
Speed of sound [m/s]	7.37
Viscosity condition	Explicit
Surface tension condition	CSF model
Surface tension coefficient	0.90
Particle size [mm]	1.0
Analysis time [s]	6.0
Initial time step [s]	1.25×10^{-4}
Courant number	0.2
Collision distance	0.90
Influence radius	3.1
Interparticle distance	1.0

Table 3 Physical properties of water.

Density [kg/m^3]	1000
Kinematic viscosity coefficient [m^2/s]	1.0×10^{-6}
Surface tension coefficient [N/m]	0.072

613

wave behavior of water can be reproduced even if the angle is changed from Fig.11. The flow front of water obtained by simulation in the case of ladle angle 40° meander like real phenomena. Even if the ladle angle and tilting speed are varied, it possible to simulate in the case of the water the wave behavior reasonably.
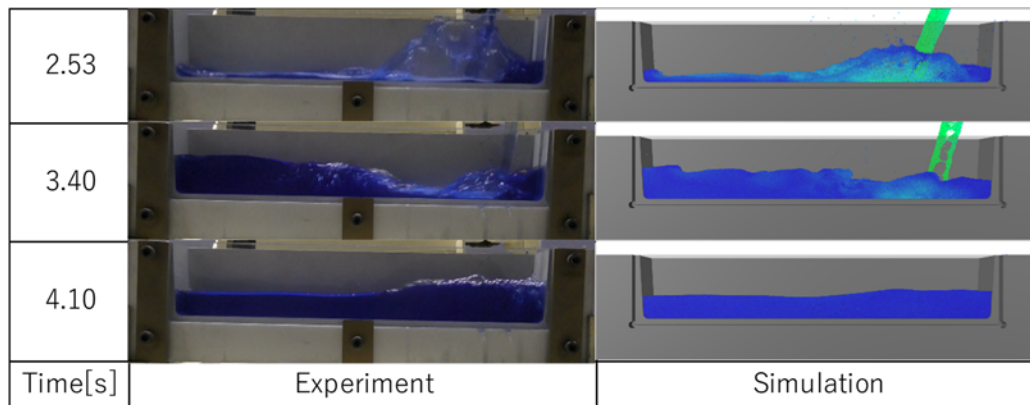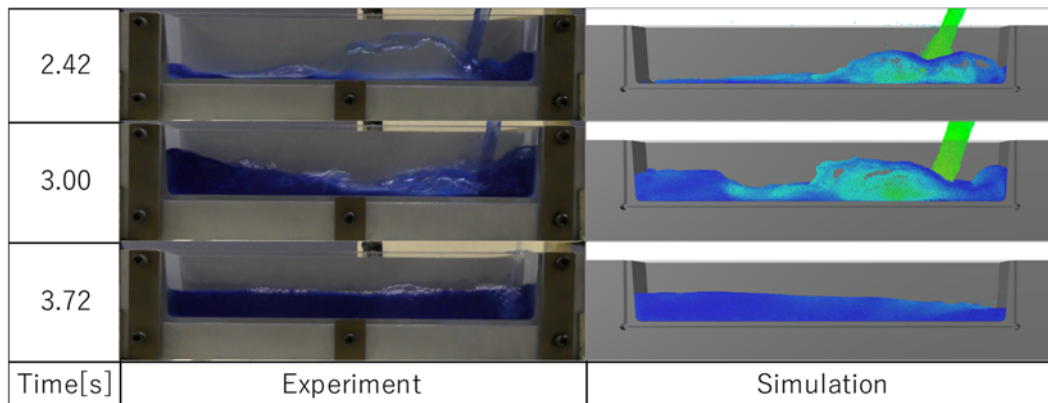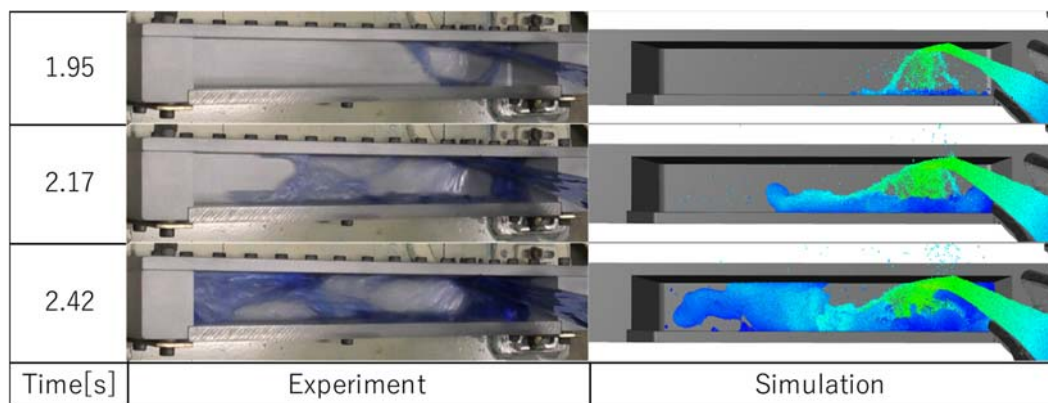

Fig.9 Comparison of front view of wave behavior between experiment and simulation in case of water, tilting speed of 0.45rad/s and ladle angle of 0°.
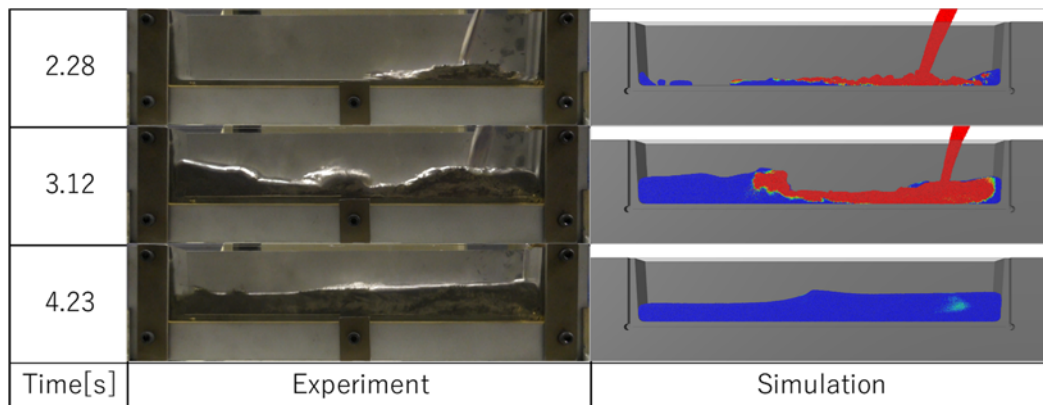

Fig.10 Comparison of front view of wave behavior between experiment and simulation in case of water, tilting speed of 0.45rad/s and ladle angle of 40°.
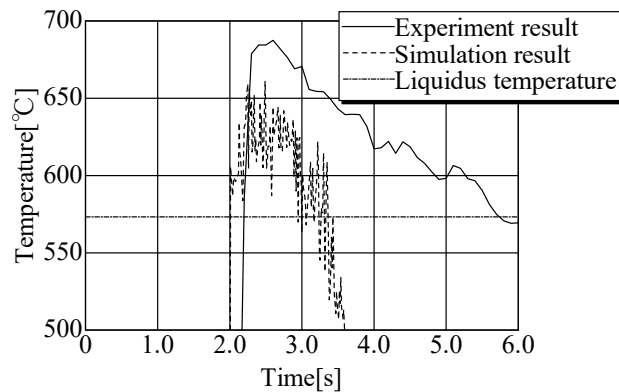

Fig.11 Comparison of top view of wave behavior between experiment and simulation in case of water, tilting speed of 0.45rad/s and ladle angle of 40°.

3.2 Wave behavior of molten aluminum alloy

The physical properties of die casting aluminum alloy JIS-ADC12 are shown in Table 4. The calculation conditions of aluminum alloy are the same of water shown in Table 2 other than the surface tension coefficient for molten aluminum alloy is 0.97. Table 5 shows the physical properties of sleeve made by steel (JIS-SS400).

Table 4 Physical property of aluminum alloy.

Density [kg/m³]	2700
Kinematic viscosity coefficient [m²/s]	1.1×10^{-6}
Surface tension coefficient [N/m²]	0.886
Specific heat [J/(kg·K)]	960
Thermal conductivity [W/(m·K)]	96

Table 5 Physical property of sleeve.

Density [kg/m³]	7850
Specific heat [J/(kg·K)]	4730
Thermal conductivity [W/(m·K)]	51.6

Fig.10 shows the comparison of wave behavior between experiment and simulation in the case of molten aluminum alloy, the tilting speed of 0.45rad/s and ladle angle of 0°. In the simulation, the temperature is changed the color of the fluid. Red indicates the liquidus temperature, blue indicates the solidus temperature, and the other colors indicate the temperature between the liquidus temperature and the solidus temperature. The simulation reproduces the phenomenon close to water and cannot explain the actual wave phenomenon. The reason is considered that it does not taken consideration of specific oxide film of aluminum alloy. Fig.11 shows the comparison of temperature at P1 between experiment and simulation in the case of the molten aluminum alloy, tilting speed of 0.45rad/s and ladle angle of 0°. The calculated temperature decreases rapidly unlike the experiment. The software has not the functions of temperature calculation by heat transfer coefficient and by solidification phenomena.
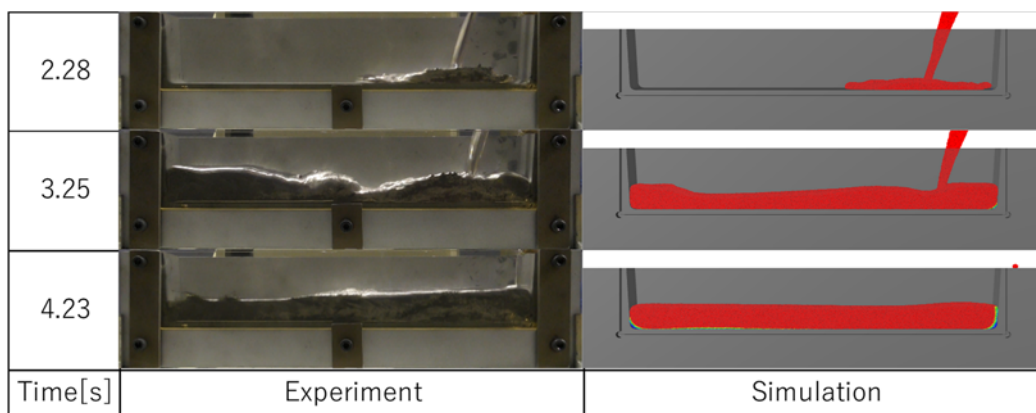

Fig.12 Comparison of wave behavior between experiment and simulation in case of molten aluminum alloy, tilting speed of 0.45rad/s and ladle angle of 0°
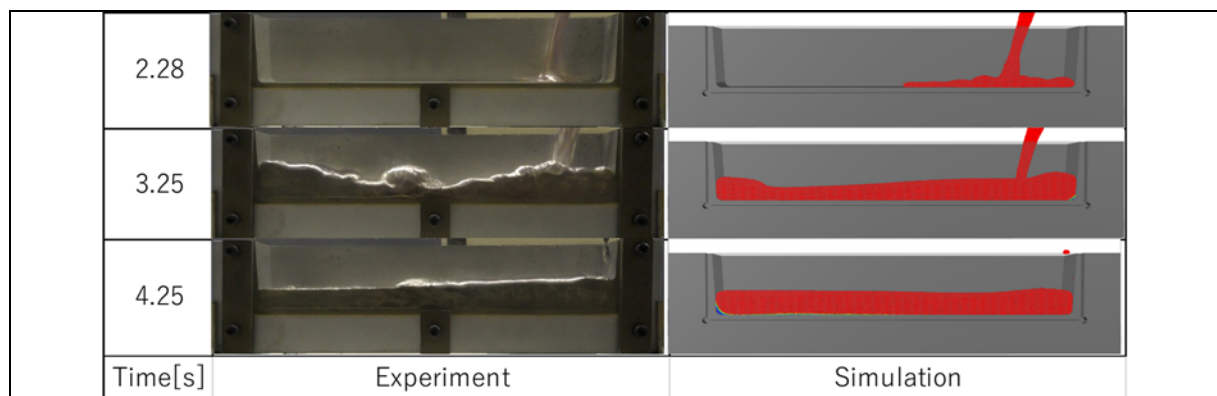

Fig.13 Comparison of temperature at P1 between experiment and simulation in the case of the molten aluminum alloy, tilting speed of 0.45rad/s and ladle angle of 0°

615

3.3 Wave behavior of molten aluminum alloy using adjusted physical properties

Hasuno et.al [5] is adjusted kinematic viscosity coefficient in order to take into consideration of oxide film of aluminum alloy molten. In the present study as well, we tried to adjust kinematic viscosity coefficient unite flow behavior. Regarding heat transfer, the thermal conductivity of sleeve metal is adjusted to match heat transfer behavior.

Fig.14 shows the comparison of wave behavior between experiment and simulation using adjusted parameter in case of molten aluminum alloy, the tilting speed of 0.45rad/s and the ladle angle of 0°. The results in the case of the ladle angle of 40° are shown in Fig.15 and Fig.16. Fig.16 shows the top view of wave behavior. About the difference in the color of the simulation of Fig.14, Fig.15 and Fig.16, it is the same as Fig.12. Fig.17 shows the comparison of temperature at P1 between experiment and simulation using adjusted parameters in the case of the molten aluminum alloy, tilting speed of 0.45rad/s and ladle angle of 0°. From Fig.14 and Fig.15, the simulated result obtained by using adjusted parameters are almost agreed with the experiments. Thermal conductivity behavior obtained by using adjusted parameters as shown in Fig.17 are also the same tendency to the experiment. Although the flow front of molten metal in experiments as shown in Fig.16 goes like a meander, these phenomena cannot simulate in the present study. Because it is considered that the flow front of molten metal goes advance while meandering by repeating of generation and tearing of oxide film. This phenomenon will be simulated in the future study.

Fig.14 Comparison of wave behavior between experiment and simulation using adjusted parameters in case of molten aluminum alloy, tilting speed of 0.45rad/s and ladle angle of 0°.

Fig.15 Comparison of wave behavior between experiment and simulation using adjusted parameters in case of molten aluminum alloy, tilting speed of 0.45rad/s and ladle angle of 40°.

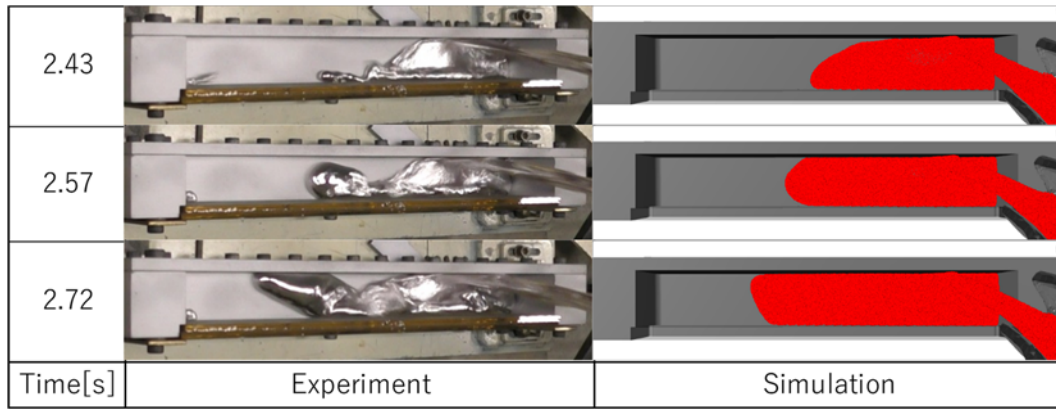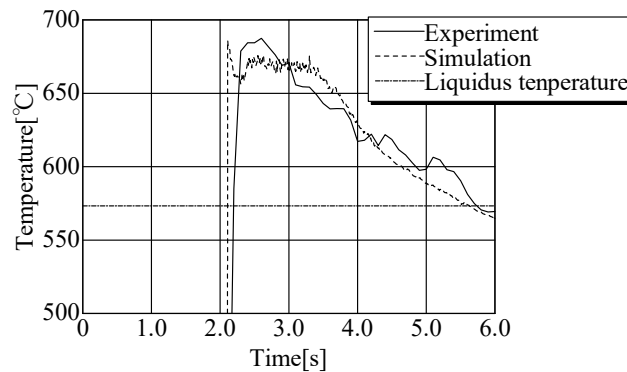| Time[s]	Experiment	Simulation
2.43		
2.57		
2.72		

Fig.16 Comparison of top view of wave behavior between experiment and simulation using adjusted parameters in the case of molten aluminum alloy, tilting speed of 0.45rad/s and ladle angle of 40°

Fig.17 Comparison of temperature at P1 between experiment and simulation using adjusted parameters in the case of the molten aluminum alloy, tilting speed of 0.45rad/s and ladle angle of 0°

4. Conclusion

The pouring experiment of water and molten aluminum alloy by tilting ladle is carried out to observe the wave buhavior in the sleeve and temperature measurement is done. Further, the numerical simulation using MPS software executed to simulate the real phenomena. The following results are obtained.

(1) It is clear that the molten aluminum alloy is not solidified during wave behavior in the early stage of pouring by the experiments in the case of pouring temperature of 700°C.

(2) The ladle pouring simulation used MPS software is good match to experiment result in the case of water.

(3) The simulation result of molten aluminum alloy is not agreed with experimental result. Adjusting the parameters which are the kiematic viscosity of molten metal and the thermal cinductivity of sleeve metal we can get the results coresponding to the real phenomena.

(4) The flow behavior of molten aluminum alloy in the case with ladle angle is observed like a meanber. From the experiment, the flow front of molten metal goes advance while meandering by repeating of generation and tearing of oxide film.

(5) The parameter adjustment is not useful operation for casting CAE. To simulate the real phenomena, it is necessary to develop the new funtional algorithm. There are the oxide film model, heat transfer analysis, solidification analysis and taking into consideration of air gap between mold and melt.

REFERENCES

[1] Japan Foundry Engineering Society : "Die casting", *Research Report No.91*, (2003), p1

[2] Y. Mochida, A. Hasuno, M. Kazama, T. Suwa and Y.Maeda : "Flow analysis of thin-wall die-cast products by particle method", *Journal of Japan Die casting Congress*, (2018), pp.107-110

[3] H. Iwahori, K. Tozawa, T. Asano, Y. Yamamoto, M. Nakamura, M. Hashimoto and S. Uenishi : "Properties of scattered structured included in aluminum die castings", *Journal of Japan Institute of Light Metals*, 34(1984). Pp525-530

[4] Y. Maeda and H. Nomura : "Numerical Experiment of Cold flakes Behavior in Shot Sleeve of Aluminum Alloy Die casting", *Journal of Japan Foundry Engineering Society*, 78(2006), pp.654-660

[5] A. Hasuno, T. Omoto, S. Kami and Y. Maeda : "The simulation of ladle process in die casting", *Journal of Japan Die casting Congress*, (2018), pp.67-70

[6] M. Kazama, T. Suwa, and Y. Maeda : "Modeling of Computation of Molten Aluminum Alloy Flow with Oxide Film by Smoothed Particle Hydrodynamics", *Journal of Japan Foundry Engineering Society*, 90(2018), 2. pp.68-74

[7] M. Kazama, K. Ogasawara, T, Suwa, H. Ito, and Y. Maeda: "Transfer and pouring processes of casting by smoothed particle hydrodynamics method", ICCM2016 (2016), pp.800-807

[8] T. Suwa, M. Kazama, A. Hasuno, Y. Mochida and Y. Maeda : "Ladle pouring simulation of die casting using particle-based method with oxide film model", *Journal of Japan Die casting Congress*, (2018), pp.103-106

[9] Information on https://www.prometech.co.jp

GRANULAR FLOW ANALYSIS CONSIDERING SOIL STRENGTH USING MOVING PARTICLE SIMULATION METHOD

KAZUHIRO KANEDA[1] AND TOMOKI SAWADA[2]

[1] Takenaka R&D Institute
1-5-1 Ohtsuka, Inzai, Chiba 270-1395, Japan
E-mail: kaneda.kazuhiro@takenaka.co.jp website: https://www.takenaka.co.jp/takenaka_e/

[2] Prometech Software, Inc.
34-3, Hongo 3-chome, Bunkyo-ku, Tokyo 113-0033, Japan
E-mail sawada@prometech.co.jp, website: https://www.prometech.co.jp/

Key words: Granular flow analysis; MPM; Soil strength.

Abstract. In recent years, many sediment-related disasters have occurred in Japan. To predict the sediment flow, granular flow analysis was conducted with the moving particle simulation method, using the viscosity term formulated by the Drucker-Prager model. The program code used is Particleworks Ver. 6, developed by Prometech Software. Plastic viscosity is described as a function of (cohesion) c and Φ (the shear resistance angle). Simple problems, such as freestanding height and dam breakage of the simulations were analyzed to assess the accuracy of the particle simulation method with the model.

1 INTRODUCTION

Soil-related disasters occur frequently in Japan. After such occurrences, simulation analysis can be performed on the soil flow area to determine what factors lead to the disaster. The discrete element method (DEM), or particle method, can be employed by assuming soil to be the Bingham model. Dent et al. (1983) simulated an avalanche flow, involving snow and not soil, by assuming snow as the Bingham model. Subsequently, Soussa and Voight (1991) and Moriguchi et al. (2009) applied the particle method to soil flows. Nonoyama et al. (2015) also used simulation, with Smoothed Particle Hydrodynamics (SPH), for soil collapse analysis. Various other numerical analysis methods of collapsed systems are available, each with their own characteristics. In the current study, the collapse analysis was examined with the Moving Particle Simulation (MPS) particle method, originally developed by Koshizuka et al. (1996). This method is known to be able to solve stability for simulation, such as free surface flow. On the other hand, although soil can be assumed as a viscous fluid, such as in the Bingham model, the viscosity is considered inconstant as it can be changed by shear strain and soil constraint pressure. Focusing on this aspect, Moriguchi et al. (2009) proposed a "new" viscosity. Because viscosity changes with stress, it was necessary to modify the basic equation. In this study, therefore, the viscosity proposed by Moriguchi et al. (2009) is used. The basic equation is modified from the original and the behavior was investigated before and after modification.

2 FORMULATION OF THE MATHEMATICAL MODEL

The equivalent viscosity coefficient of the Bingham model proposed by Moriguchi et al. (2009) is as follows:

$$\eta' = \begin{cases} \eta_0 + \dfrac{c + p\tan\phi}{\sqrt{2V_{ij}V_{ij}}} & (\eta \leq \eta_{max}) \\ \eta_{max} & (\eta > \eta_{max}) \end{cases} \tag{1}$$

where V_{ij} is the shear strain tensor.

$$V_{ij} = \frac{1}{2}\left(\frac{\partial u_i}{\partial x_j} + \frac{\partial u_j}{\partial x_i}\right) \tag{2}$$

where c is the cohesion (kPa), ϕ is the shear resistance angle ($^\circ$). The constitutive equation of fluid is as follows:

$$\sigma_{ij} = -p\delta_{ij} + 2\eta'V_{ij} = -p\delta_{ij} + \eta'\left(\frac{\partial u_i}{\partial x_j} + \frac{\partial u_j}{\partial x_i}\right) \tag{3}$$

where p is the pressure (kPa). The conservation of momentum is as follows:

$$\frac{\partial u_i}{\partial t} + u_j\frac{\partial u_i}{\partial x_j} = \frac{1}{\rho}\frac{\partial \sigma_{ij}}{\partial x_i} + g_i \tag{4}$$

where g (m/s) is the gravity acceleration. The uncompressed condition was considered.

$$\frac{\partial u_i}{\partial x_i} = 0 \tag{5}$$

Substitute Equation (4) for (3)

$$\frac{\partial u_i}{\partial t} + u_j\frac{\partial u_i}{\partial x_j} = -\frac{1}{\rho}\frac{\partial p}{\partial x_i} + \frac{1}{\rho}\frac{\partial}{\partial x_j}\left[\eta'\left(\frac{\partial u_i}{\partial x_j} + \frac{\partial u_j}{\partial x_i}\right)\right] + g_i \tag{6}$$

was obtained.

Ignoring the spatial gradient of the viscosity coefficient, it becomes a Navier-Stokes equation. However, in the current research, as a spatial gradient was needed, it was expanded by equation (6). Separate each term as follows:

$$\text{Advection term}: \frac{u_i^* - u_i^n}{\partial t} = -u_j\frac{\partial u_i}{\partial x_j} \tag{7}$$

$$\text{External force term}: \frac{u_i^{**} - u_i^*}{\partial t} = g_i \tag{8}$$

$$\text{Viscous term}: \frac{u_i^{***} - u_i^{**}}{\partial t} = \frac{1}{\rho}\frac{\partial}{\partial x_j}\left[\eta'\left(\frac{\partial u_i}{\partial x_j} + \frac{\partial u_j}{\partial x_i}\right)\right] \tag{9}$$

$$\text{Pressure term}: \frac{u_i^{n+1} - u_i^{***}}{\partial t} = -\frac{1}{\rho}\frac{\partial p}{\partial x_i} \tag{10}$$

Further expansion of the viscosity term is as follows:
X velocity:

$$\frac{1}{\rho}\left[\frac{\partial}{\partial x}\eta\left(\frac{\partial u_x}{\partial x}+\frac{\partial u_x}{\partial x}\right)+\frac{\partial}{\partial y}\eta\left(\frac{\partial u_x}{\partial y}+\frac{\partial u_y}{\partial x}\right)+\frac{\partial}{\partial z}\eta\left(\frac{\partial u_x}{\partial z}+\frac{\partial u_z}{\partial x}\right)\right] \tag{11}$$

$$=\frac{2}{\rho}\frac{\partial\eta}{\partial x}\frac{\partial u_x}{\partial x}+\frac{1}{\rho}\frac{\partial\eta}{\partial y}\left(\frac{\partial u_x}{\partial y}+\frac{\partial u_y}{\partial x}\right)+\frac{1}{\rho}\frac{\partial\eta}{\partial z}\left(\frac{\partial u_x}{\partial z}+\frac{\partial u_z}{\partial x}\right)$$

Y velocity:

$$\frac{1}{\rho}\left[\frac{\partial}{\partial x}\eta\left(\frac{\partial u_y}{\partial x}+\frac{\partial u_x}{\partial y}\right)+\frac{\partial}{\partial y}\eta\left(\frac{\partial u_y}{\partial y}+\frac{\partial u_y}{\partial y}\right)+\frac{\partial}{\partial z}\eta\left(\frac{\partial u_y}{\partial z}+\frac{\partial u_z}{\partial y}\right)\right] \tag{12}$$

$$=\frac{2}{\rho}\frac{\partial\eta}{\partial y}\frac{\partial u_y}{\partial y}+\frac{1}{\rho}\frac{\partial\eta}{\partial x}\left(\frac{\partial u_y}{\partial x}+\frac{\partial u_x}{\partial y}\right)+\frac{1}{\rho}\frac{\partial\eta}{\partial z}\left(\frac{\partial u_y}{\partial z}+\frac{\partial u_z}{\partial y}\right)$$

Z velocity:

$$\frac{1}{\rho}\left[\frac{\partial}{\partial x}\eta\left(\frac{\partial u_z}{\partial x}+\frac{\partial u_x}{\partial z}\right)+\frac{\partial}{\partial y}\eta\left(\frac{\partial u_z}{\partial y}+\frac{\partial u_y}{\partial z}\right)+\frac{\partial}{\partial z}\eta\left(\frac{\partial u_z}{\partial z}+\frac{\partial u_z}{\partial z}\right)\right] \tag{13}$$

$$=\frac{2}{\rho}\frac{\partial\eta}{\partial z}\frac{\partial u_z}{\partial z}+\frac{1}{\rho}\frac{\partial\eta}{\partial x}\left(\frac{\partial u_z}{\partial x}+\frac{\partial u_x}{\partial z}\right)+\frac{1}{\rho}\frac{\partial\eta}{\partial y}\left(\frac{\partial u_z}{\partial y}+\frac{\partial u_y}{\partial z}\right)$$

In addition, the uncompressed condition of the following equation was taken into consideration:

$$\frac{\partial^2 u_z}{\partial x^2}+\frac{\partial^2 u_z}{\partial y^2}+\frac{\partial^2 u_z}{\partial z^2}=0 \tag{14}$$

As can be seen from equations (11) – (13), they are the products of differential coefficients, and the extent of this influence was examined.

In this study, Particleworks Ver. 6 (Prometech Software, Inc. Japan), that introduced MPS, was used.

3   SIMULATION AND DISCUTTION

3.1 Slump test

The influence of the equivalent viscosity coefficient was determined by simulation of the slump test. Figure 1 shows the outline of the slump test. A cone with an inner diameter of 100 to 200 mm, an outer diameter of 166.34 to 266.34 mm, and a height of 300 mm was installed. Soil particles were placed inside the cone and gravity was applied. Subsequently, the cone was raised for 2 seconds. Table 1 shows the simulation cases and the material parameters. In this simulation, the limit of shear velocity was adopted in order to stabilize the analysis. In addition, cases in which the products of the differential coefficients were taken into consideration (termed 'Case A') and not taken into consideration (termed "Case B") were evaluated; as in equations (11) to (13). Table 2 shows the numerical results of the particle spread at 10.0 seconds. Figure 2 shows the state of the average velocity at a steady state(10 seconds). In Case 2, the height is larger and the width smaller than in Case 1. This is because the shear resistance angle is larger than in Case 1. This specimen has the influence of self-sustaining. It is thought that the general behavior of soil can be expressed even as granular matter. A comparison of Case A to Case B indicated less difference between them in this simulation.   The analysis of the products of the differential coefficients solved the Navier-Stokes equation implicitly. However, this term was an explicit analysis method in our simulation that became difficult to converge. Moreover, the procedure is time consuming. It was unnecessary to consider the differential coefficient in this
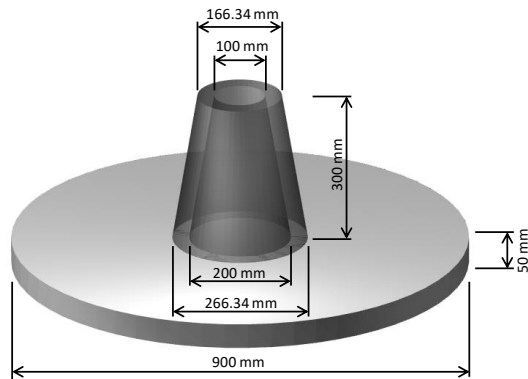
model test.

Figure 1: Layout of slump test

Table 1: Simulation cases and material parameters

	Initial viscosity coefficient η_0	Maximum viscosity coefficient η_{max}	Cohesion c (kPa)	Shear resistance angle ϕ (degrees)	Minimum shear velocity V_{min} (m/s)
Case 1	1.0	10^{100}	100	30	10^{-3}
Case 2	1.0	10^{100}	100	45	10^{-3}

Table 2: Numerical results

		Height (mm)	Width (mm)
Case 1	Case A	62.6	412.3
	Case B	75.8	384.5
Case 2	Case A	64.3	417.7
	Case B	76.5	383.7
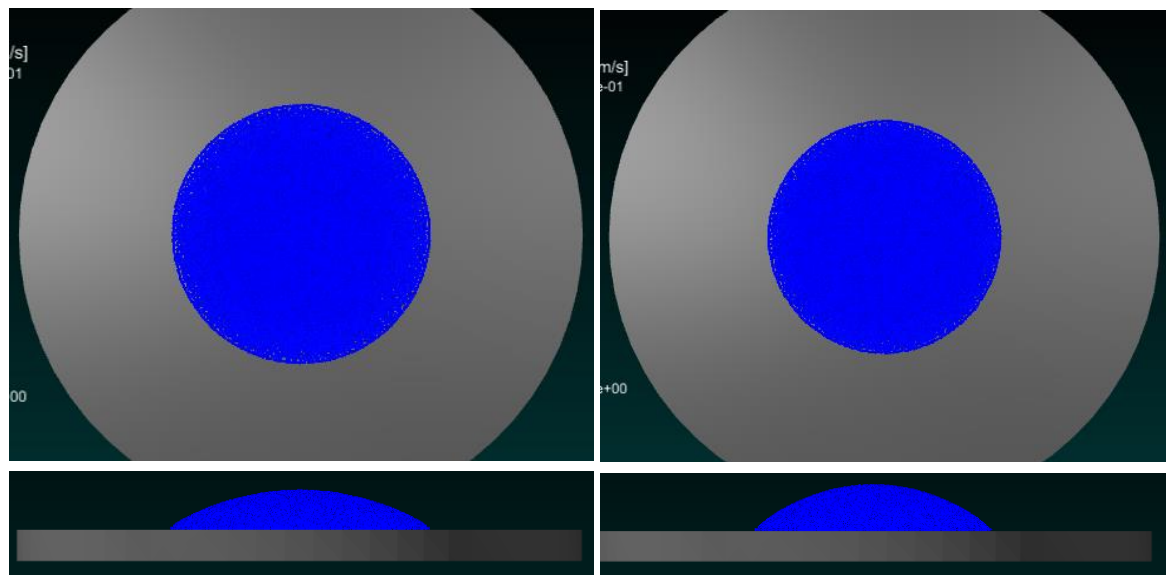
Case 1   Case 2

Case A
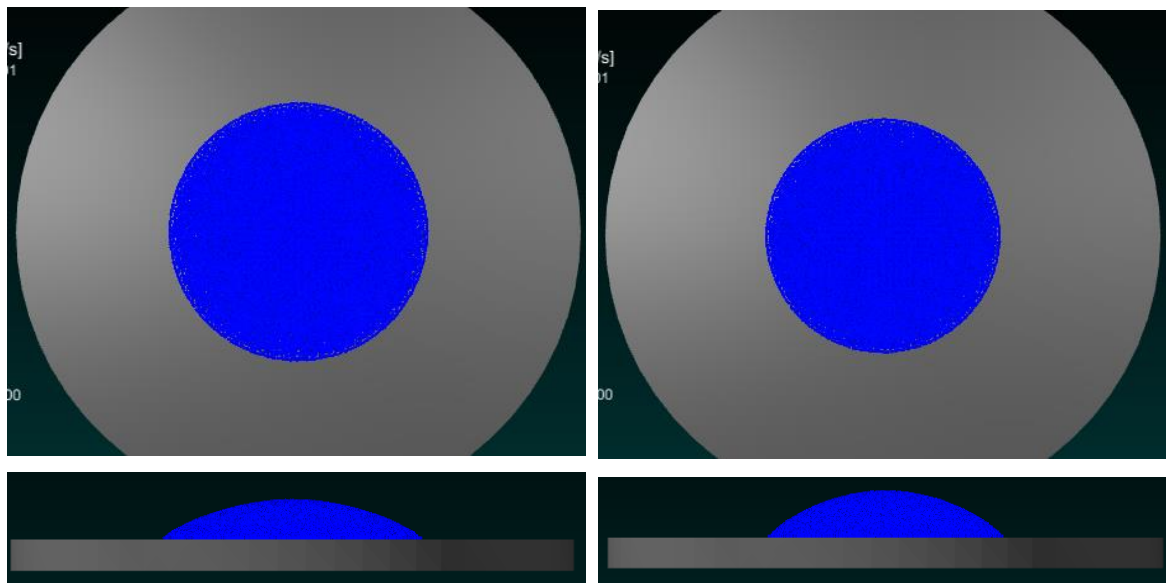
Case 1   Case 2

Case A

Figure 2: Results of the slump test

3.2 Slope flow analysis

The slope flow analysis was performed at a large scale. Figure 3 shows the outline of the slope flow analysis. It was set to the soil height of 50 m and a width of 40 m. The angle of slope is 60 degrees. In the beginning, the wall on the slope surface was set, and then that wall would be removed to begin the flow. The material parameters are the same as in Table 1. Figure 3 shows the shear strain distributions. In the case of a shear resistance angle of 30 degrees (Case 1), at 11 seconds both Case A and Case B are shown. In the case of a shear resistance angle of 40 degrees (Case 2) at 18 seconds Case A is shown, and at 40 seconds Case B is shown. In Case 1, there is less difference between Case A and Case B. The soil particles flow overall, and the especially high shear strain occurred at the surface. In Case 2 and Case A, the soil particle velocity is low, and the slope shape is retained. The shear strain occurs at the surface and then the surface flow can be seen because of a high shear resistance angle. On the other hand, in Case 2 and Case B, at the 40 second mark, the slope shape is retained and surface flow cannot be seen. When the shear resistance angle or coherence is small, the slope becomes more fluid. Once it flows, the shear rate in equation (1) increases and the effects of c and φ become relatively small. As a result, the influence of the spatial gradient of η is reduced. Contrastingly, when the shear resistance angle or coherence is large and the fluid flows slowly, the shear rate of the surface grows larger and the influence of the spatial gradient of η appears. Moreover, it appears that the effect was not as visible in the small model, as shown in Figure 1.

| Case 1 | Case 2 |

Case A

| Case 1 | Case 2 |

Case A
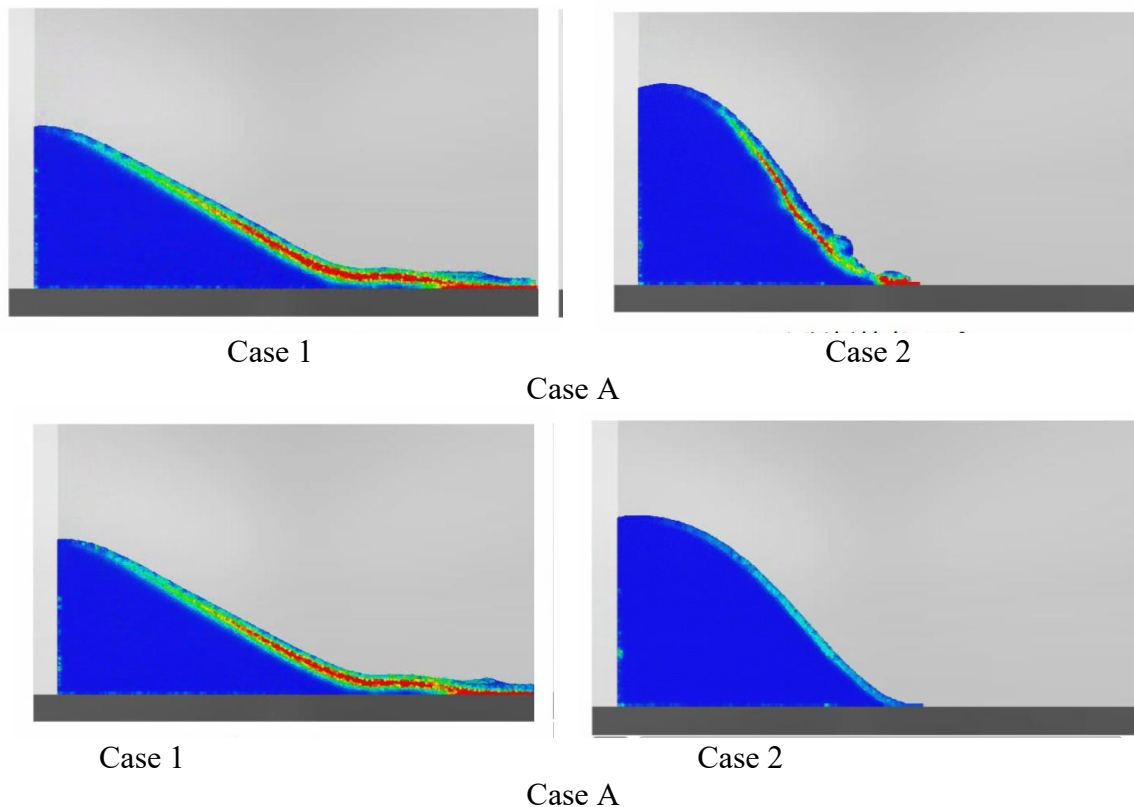
Figure 3: Results of slope flow analysis

4   REMARKS

The moving particle method was employed for the slump test and soil flow analysis. The conclusions are as follows:

- In the slump test as the shear resistance angle increases, the height increases and the width remains wide at a steady state.
- When the slope flow model with a large area is analyzed, the difference in shear resistance angle shows the difference in slope flow. It was also found that the effect of the spatial gradient of η becomes larger as the shear strain at the ground surface becomes larger.

Although aspects of the method need improvement, such as the friction of the bottom surface, the study was able to express the soil flow according to the adhesive strength of the soil and the shear resistance angle.

REFERENCES

[1] Dent JD, Lang TE 1983. A biviscous modified Bingham model of snow avalanche motion. *Ann Glaciol* 4:42–46.

[2] Soussa J, Voight B 1991. Continuum simulation of flow failures. *Geotechnique* 41:515–538.

[3] Nonoyama H, Moriguchi S, Sawada K, Yashima A 2015. Slope stability analysis using (SPH) method. *Soils Found* 55(2):458–470.

[4] Huang Y, Cheng H, Dai Z, Xu Q, Liu F, Sawada K, Moriguchi S, Yashima A 2015. SPH-based numerical simulation of catastrophic debris flows after the 2008 Wenchuan earthquake. *Bull Eng Geol Environ* 74(4):1137–1151.

[5] Koshizuka S, Oka Y 1996. Moving-particle semi-implicit method for fragmentation of incompressible fluid, *Nucl Sci Eng* 123:421–434.

[6] Moriguchi S, Borja R I, Yashima A, Sawada K 2009. Estimating the impact force generated by granular flow on a rigid obstruction. *Acta Geotechica* 4:57–71.

NUMERICAL ANALYSIS OF THE EUTECTIC MELTING AND RELOCATION OF THE B$_4$C CONTROL ROD MATERIALS BY THE MPFI-MPS METHOD

Shota Ueda[*]**, Masahiro Kondo**[†] **and Koji Okamoto**[‡]

[*] Nuclear Technology Research Laboratory
Central Research Institute of Electric Power Industry (CRIEPI)
2-6-1 Nagasaka, Yokosuka-shi, Kanagawa 240-0196, Japan
e-mail: ueda3745@criepi.denken.or.jp - Web page: https://criepi.denken.or.jp/en/index.html
(Formerly, the University of Tokyo)

[†] National Institute of Advanced Industrial Science and Technology (AIST)
1-1-1 Umezono, Tsukuba, Ibaraki 305-8568, Japan
e-mail: kondo.masahiro@aist.go.jp - Web page:
https://unit.aist.go.jp/cd-fmat/ja/teams/igms.html

[‡] Nuclear Professional School
The University of Tokyo
2-22 Shirakata, Tokai-mura, Ibaraki 319-1188, Japan
e-mail: okamoto@n.t.u-tokyo.ac.jp - Web page: http://www.utvis.com

Key words: Eutectic melting, MPS, MPFI, Boron-carbide control rod, Severe accident

Abstract. Eutectic melting and subsequent relocation of the boron-carbide (B$_4$C) control rod materials were simulated by a particle method. In the past, it was difficult to simulate the eutectic melting by a particle method because the melting starts at the interface between two different materials, which leads to the instability of the particle motion due to the small amount of fluid particles and lack of the thermodynamic consistency of the particle system. Thus, the Moving Particle Full Implicit (MPFI)-Moving Particle Semi-implicit (MPS) method was developed and introduced in the current study. Specifically, the MPFI method was introduced for the momentum transfer calculation, and the MPS method was introduced for the heat and mass transfer calculation. The MPFI-MPS method realized the simulation of the eutectic melting and subsequent relocation behaviour.

1   INTRODUCTION

In Fukushima decommissioning, investigation of the boron distribution in the fuel debris is of great significance because it affects the risk of re-criticality[1]. The major source

for the boron species is the boron-carbide B_4C control rod. Thus, the eutectic melting and relocation behavior of B_4C control rod materials receive remarkable attention.

Eutectic melting can occur at the contact interface of several chemical components at lower temperature than melting points of each pure material. B_4C and stainless steel (SS) can have eutectic melting[2] in the B_4C control rod. Liquid phase suddenly appears at the solid interface in eutectic melting, and the complicated multi-component interactions and surface deformation occur. which are challenging for Eulerian direct numerical simulation methods. A particle method, which is one of the Lagrangian methods, is suitable for simulating such complicated flows because it can easily track the motion of thermo-physical properties of eutectic melting, inclusive of solid/liquid phase changes. The Moving Particle Semi-implicit method developed by Koshizuka and Oka[3, 4] is one of such particle methods for the incompressible free surface fluid flow. Eutectic melting model was also developed in MPS framework[5]. However, it was difficult to calculate the initial formation of the liquid phase between the solid phases due to eutectic melting. It is often because the instability of pressure calculation is caused by the too small number of liquid particles between solid phases just after eutectic melting started. Suppressing the numerical oscillations in pressure calculation solves this issue in some cases[6]. Meanwhile, it was reported that modeling a solid phase as very high-viscous fluid can solve the issue because it virtually increases the number of fluid particles used for the pressure calculation[7]. The Moving Particle Full Implicit method[8] is one of the promising method for this kind of issues related with the instability. The MPFI method inherently suppresses the instability of the particle motion because it assures thermodynamic consistency of the particle system after discretization. Thus, it may be expected that adopting the MPFI method [8] for the momentum transfer calculation, and the MPS method [3, 4] for the heat and mass transfer calculation can enjoy the benefits from both the methods to simulate eutectic melting and subsequent relocation; stable calculation and smooth distribution of physical values.

In this study, eutectic melting and subsequent relocation of the B_4C control rod materials were simulated by a particle method. The MPFI-MPS method was developed and introduced in the current simulation. The eutectic melting and relocation processes of the control rod materials were discussed.

2   NUMERICAL METHOD

In this study, we adopted the MPFI method [8] for the momentum transfer calculation, and the MPS method [3, 4] for the heat and mass transfer calculation. The MPFI method suppresses the instability of the particle motion because it assures thermodynamic consistency of the particle system after discretization. Moreover, it conserves angular momentum and makes it possible to simulation rotational motion of fluid. Meanwhile, the heat and mass transfer calculation by the MPS method offers smooth distribution of physical values. We call this method the MPFI-MPS method. In the MPFI method, the particle

interaction models for gradient, divergence and Laplacian operators are formulated as:

$$\nabla\phi = \sum_{j}(\phi^j + \phi^i)\boldsymbol{r}^{ij}\frac{w'^{ij}}{d^{ij}}, \tag{1}$$

$$\nabla \bullet \boldsymbol{A} = \sum_{j}(\boldsymbol{A}^j - \boldsymbol{A}^i)\boldsymbol{r}^{ij}\frac{w'^{ij}}{d^{ij}} \tag{2}$$

and

$$\nabla^2\phi = \sum_{j}(\phi^j - \phi^i)\frac{w'^{ij}}{d^{ij}}. \tag{3}$$

where w'^{ij} is the differential of the weight function shown in Eq. 4:

$$w(d) = \begin{cases} \frac{(r_e - d^{ij})^2}{n_0} & (0 \le r \le r_e) \\ 0 & (r_e \le r) \end{cases} \tag{4}$$

where r_e is an effective radius and d^{ij} is a particle distance. n_0 is a constant to standardize the weight function. The weight function of Eq. 4 is used in the MPFI method. The differential of this weight function is non-zero at $d^{ij} = 0$ so as to keep the particle arrangement uniform.

The following governing equation was adopted:

$$\rho\frac{du_i}{dt} = \frac{\partial}{\partial x_j}\mu\dot{\varepsilon}_{ij} + \frac{\partial}{\partial x_i}(\lambda\dot{\varepsilon}_{kk} + \kappa\varepsilon_{kk}) + \rho g_i. \tag{5}$$

Since this equation becomes the well-known form of incompressible NS equation when we set the parameters λ and κ large enough, it can be used instead of the incompressible NS equation. The first term on the right-hand side is the viscosity term and the second term is equivalent to the pressure term in the general NS equation. Here, the pressure is expressed as:

$$P = -(\lambda\dot{\varepsilon}_{kk} + \kappa\varepsilon_{kk}). \tag{6}$$

The details of the MPFI method are described in the literature [8].

In the MPFI method, the particle interaction models for gradient, divergence and Laplacian operators are formulated as:

$$\nabla\phi_i = \frac{d}{n^0}\sum_{j\neq i}\frac{(\phi_j - \phi_i)(\boldsymbol{r}_j - \boldsymbol{r}_i)}{|\boldsymbol{r}_j - \boldsymbol{r}_i|^2}w(|\boldsymbol{r}_j - \boldsymbol{r}_i|) \tag{7}$$

$$\nabla \cdot \boldsymbol{\phi}_i = \frac{d}{n^0}\sum_{j\neq i}\frac{(\boldsymbol{\phi}_j - \boldsymbol{\phi}_i) \cdot (\boldsymbol{r}_j - \boldsymbol{r}_i)}{|\boldsymbol{r}_j - \boldsymbol{r}_i|^2}w(|\boldsymbol{r}_j - \boldsymbol{r}_i|) \tag{8}$$

$$\nabla^2 \phi_i = \frac{2d}{\lambda n^0} \sum_{j \neq i} [(\phi_j - \phi_i)(w(|\boldsymbol{r}_j - \boldsymbol{r}_i|))] \tag{9}$$

$$\lambda = \frac{\sum_{j \neq i} |\boldsymbol{r}_j - \boldsymbol{r}_i|^2 w(|\boldsymbol{r}_j - \boldsymbol{r}_i|)}{\sum_{j \neq i} w(\boldsymbol{r}_j - \boldsymbol{r}_i)} \tag{10}$$

where, d, n^0 and w denote spatial dimensions and a particle number density. λ is a coefficient to make the statistic increase of deviation consistent to an analytical solution. w denotes the weight function defined as:

$$w(r) = \begin{cases} \frac{r_e}{r} - 1 & (0 \leq r \leq r_e) \\ 0 & (r_e \leq r) \end{cases} \tag{11}$$

where, r denotes a particle distance.
In this study, melting and solidification behavior is expressed with the viscosity change. The solid SS and solid B_4C were modeled as a very high-viscous fluid.

The temperature field is calculated with the heat transfer equation:

$$\frac{Dh}{Dt} = k\nabla^2 T + Q \tag{12}$$

Here, h denotes enthalpy, T denotes temperature, k denotes thermal conductivity and Q denotes heat source. To estimate the temperature from enthalpy, linear relationship between them was assumed in this study. The latent heat was considered with temperature recovery method [9]. Eutectic melting model in the literatures[5, 6] was adopted in the current study. It is mainly composed of two procedures; solving diffusion equation with respect to B_4C and determining the phase of a particle based on Fe–B binary phase diagram. The phase diagram decides whether a particle is solid or liquid by referring to its temperature and mass fraction of B_4C to SS. We assumed that no volumetric change occurs due to the phase change.

3   CALCULATIONS

The eutectic melting of the control-rod materials was simulated in a three-dimensional way to understand their relocation behavior. Figure 1 shows the calculation geometry and initial condition used in the simulation. Two calculation bodies were set in the calculation region. The rod-shaped body at the center (Specimen region) represents the simulated control rod with the physical properties of the control-rod materials. The plates at the sides of the specimen region represent tungsten heaters (W heaters). Thermal radiation was calculated by the S2S thermal radiation model in the simulation. Solid SS and solid B_4C were modeled as a very high-viscous fluid. The bottom half of the specimen was treated with the wall particles. The temperature of heaters was set at 2473 K in this case. The emissivity of the materials was set at 0.23.

Table 1 shows the physical properties used in this study. Here, T denotes the temperature of a particle. The thermal conductivity of B_4C powder bed at the filling rate of 76% was used.

Figure 2 is a representation of solid/liquid particles with respect to viscosity at 60–77 s in a front view. Figure 3 is a front sectional view of Figure 2. The melting at the B_4C-SS interface was successfully calculated. The eutectic melting started from the interface. It was kept inside the specimen until it melted through the SS cladding. After that, it flew down along the SS surface. It was observed that the outer surface of the SS cladding was molten after the contact of the spreading melt (see Figure 3). Some of the eutectic melt solidified because its shape changed while flowing down and heat release to the environment overwhelmed the heat absorption there. Figure 4 and Figure 5 show temperature distribution at 0–68 s and 68–77 s in a front view. The temperature on a upper part of the rod increased by the thermal radiation from the tungsten heaters while that on its bottom part decreased due to the heat release to the environment by thermal radiation. The temperature distribution has approached almost equilibrium before the eutectic melting started. Figure 6 and Figure 7 show B_4C distribution at 0–68 s and 68–77 s in a front view. The B_4C was transferred into the pure SS cladding. In this simulation, temperature distribution reached the steady state firstly, and afterward the rod started to melt when the Fe-B composition in a part of the rod reached the enough value to form a liquid phase in the Fe-B binary phase diagram. The viscosity of the melted part decreased, while that of the solid part remained at the initial high viscosity (Figure 2). The results imply that the eutectic melting from the outer surface of the SS cladding governs the melting speed of the control rod after the eutectic melt penetrates the SS cladding and flow out.

Table 1: Calculation conditions for simulation

|	
Initial particle distance	5.0×10^{-4} m
Density of SS [10]	7.90×10^3 kg/m^3
Density of B_4C[10]	$2.52 \times 10^3/1.33$ kg/m^3
Specific heat capacity of SS[10]	$326.0 - 0.242T + 3.71T^{0.719}$ J/kg/K
Specific heat capacity of B_4C[10]	$563.0 + T(1.54 - 2.94 \times 10^{-4} \times T)$ J/kg/K
Thermal conductivity of SS[10]	$7.58 + 0.0189T$ W/m/K
Thermal conductivity of B_4C[10]	$4.60 + 0.00205T + 26.5\exp(-\frac{T}{448.0})$ W/m/K
Latent heat of fusion	1929 mJ/mm^3
Inter-diffusion coefficient	$2.00 \times 10^{-07}\exp(-\frac{21000 \times 4.184}{8.3 \times T})$ m^2/s
Kinematic viscosity of eutectic melt	1.0 mPa·s
Gravity	9.81 m/s^2
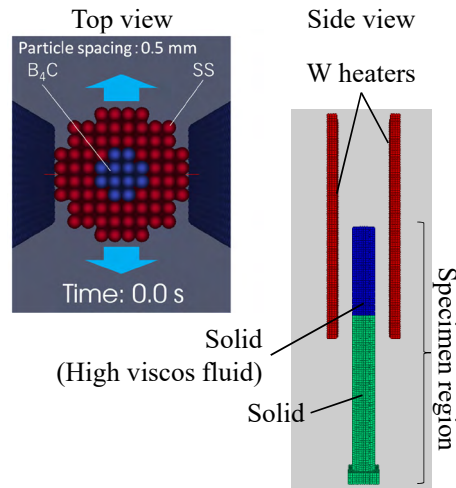
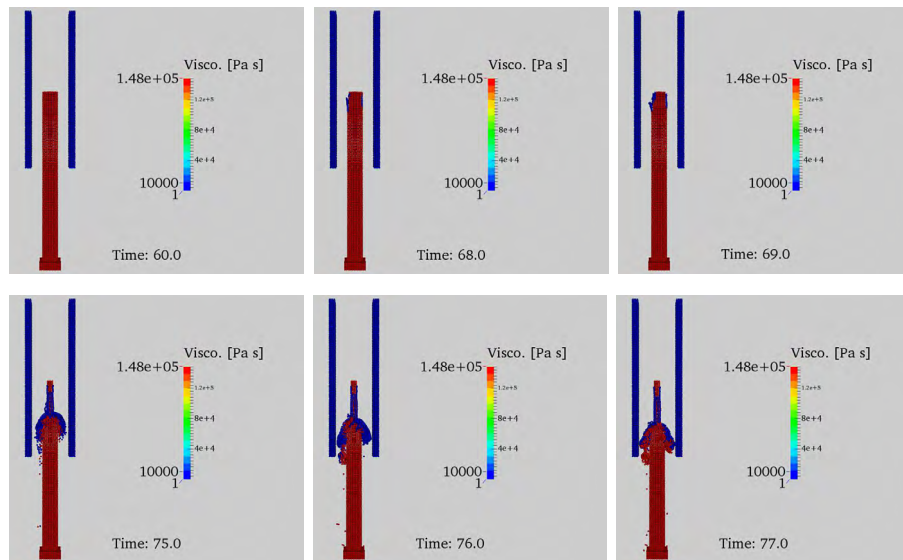**Figure 1**: Calculation geometry and conditions in three-dimensional simulation.

Figure 2: Representation of solid/liquid particles with respect to viscosity at 60–77 s (front view).
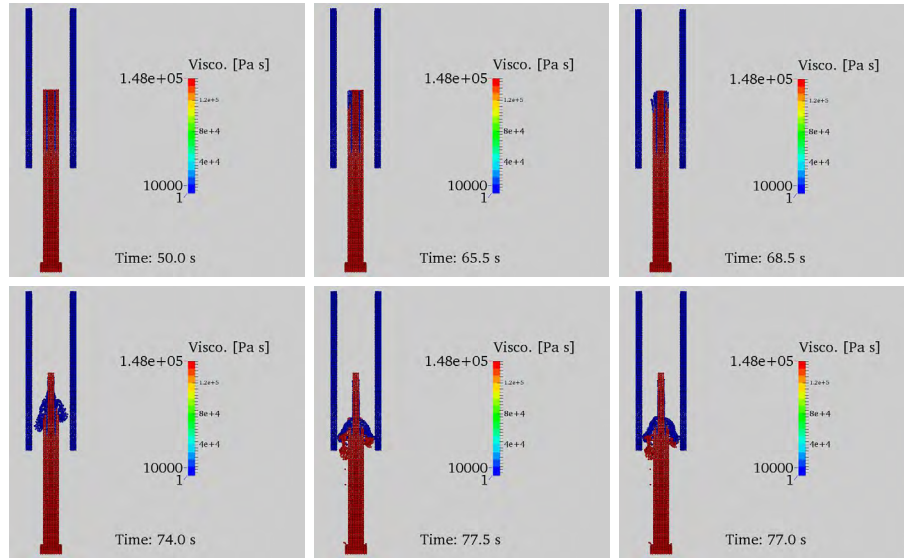
Figure 3: Representation of solid/liquid particles with respect to viscosity at 50–77 s (front sectional view).
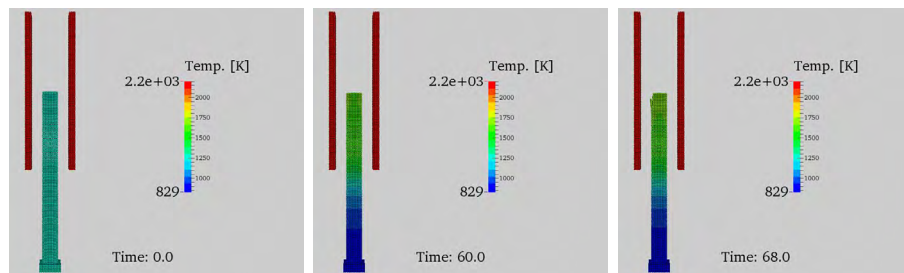

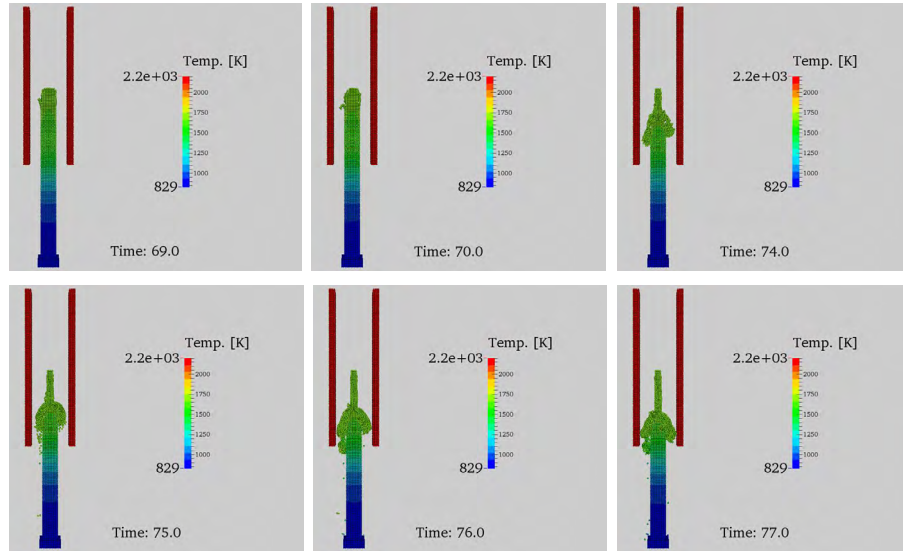**Figure 4**: Temperature distribution at 0–68 s (front view).

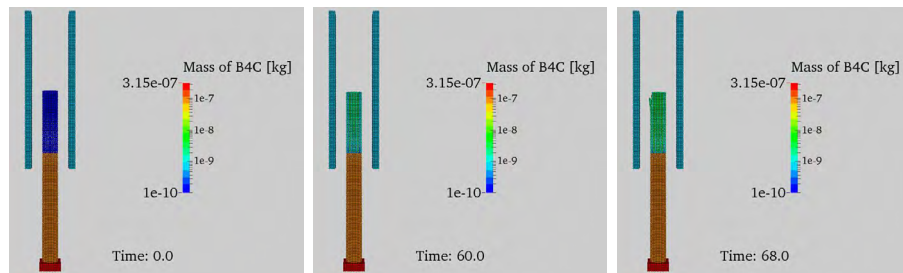**Figure 5**: Temperature distribution at 68–77 s (front view).

Figure 6: B$_4$C distribution with respect to mass [kg] at 0–68 s (front view).
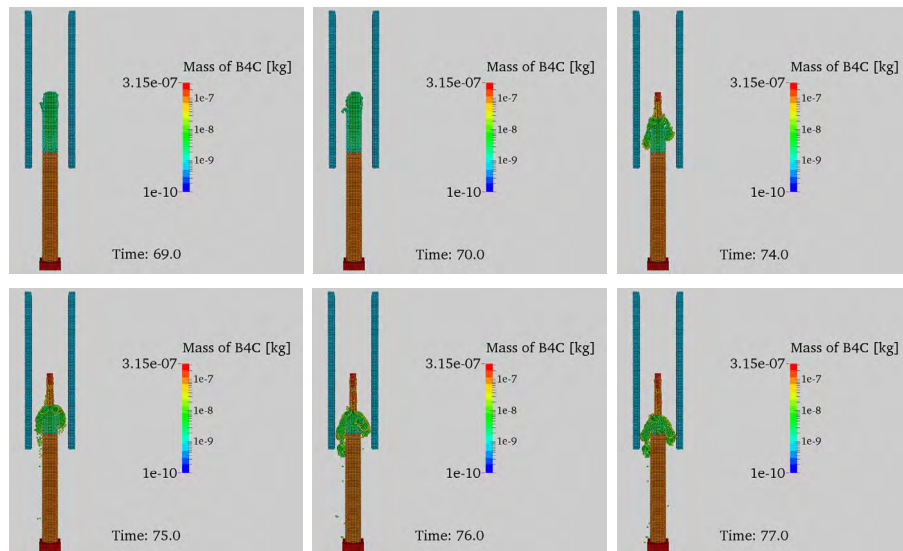
Figure 7: B$_4$C distribution with respect to mass [kg] at 69–77 s (front view).

4 CONCLUSIONS

Eutectic melting and subsequent relocation of the B_4C control rod materials were simulated by a particle method. The MPFI-MPS method was developed and introduced in the current simulation. The numerical analysis of the specimen which simulates the partial length of the B_4C control rod suggested that dominant eutectic-melting interfaces changes before and after the eutectic melting reaches the specimen surface.

ACKNOWLEDGMENTS

REFERENCES

[1] Kasada, R., HA, Y., Higuchi, T. and Sakamoto, K., 2016. Chemical State Mapping of Degradated B4C Control Rod Investigationwith Soft-X-ray Emission Spectrometer in Electron Probe Micro-analysis, *Scientific Reports*, **6**, Article number: 25700.

[2] Gauntt, R., Gasser, R. and Ott, L. J. The DF-4 fuel damage experiment in ACRR with a BWR control blade and channel box. Washington, DC: Division of Systems Research, Office of Nuclear Regulatory Research, U.S. Nuclear Regulatory Commission; 1989, SAND86-1443, NUREG/CR-4671.

[3] Koshizuka, S., Oka, Y. 1996. Moving particle semi-implicit method for fragmentation of incompressible fluid. *Nuclear Science and Engineering*, **123**(3) 421-434.

[4] Koshizuka, S., Shibata, K., Kondo, M. and Matsunaga, T. 2018. Moving Particle Semi-implicit Method: A Meshfree Particle Method for Fluid Dynamics. London: Academic Press.

[5] Mustari, A.P.A., Oka, Y., 2014. Molten uranium eutectic interaction on iron-alloy by MPS method. *Nucl. Eng. Des.* **278**, 387394. doi:10.1016/j.nucengdes.2014.07.028.

[6] Ueda, S., Madokoro, H., Kondo, M. and Okamoto, K., 2018. Numerical Analysis on Eutectic Melting of Boron Carbide Control Rod Materials with a Particle Method. *Transactions of JSCES*, Paper No. 20182002 [In Japanese].

[7] Nagatake, T., Yoshida, H., Takase, K., and Kurata, M., 2015. Development of popcorn code for simulating melting behavior of fuel element; fundamental validation and simulation for melting behavior of simulated fuel rod. Proc. of 23rd Int. Conf. on Nuclear Engineering, Chiba, Japan, May, pp. 1–6.

[8] Kondo, M., Ueda, S. and Okamoto, K., 2017. Melting Simulation Using a Particle Method with Angular Momentum Conservation. 2017 25th International Conference on Nuclear Engineering, July 2–6, Shanghai, China.

[9] Ohnaka, I. 1985. Introduction to Computational Heat Transfer and Solidification Analysis–Application to Casting Process. Tokyo: Maruzen co. [in Japanese]

[10] Siefken, L.J., Coryell, E.W., Harvego, E.A., Honorst, J.K., Matpro -A Library of Materials Properties for Light-Water-Reactor Accident Analysis, Washington, DC: Division of Systems Research, Office of Nuclear Regulatory Research, U.S. Nuclear Regulatory Commission; 2001, NUREG/CR-6150.

Spray Heat Transfer Analysis of Steel Making Process by Using Particle-Based Numerical Simulation

Takao Taya*[†], Norimasa Yamasaki[†] and Atsushi Yumoto[†]

[*] Nippon Steel Corporation (NSC)
Mechanical Engineering Div.
Plant Engineering and Facility Management Center
20-1 Shintomi Futtsu ,Chiba Prefecture(Japan)
e-mail: taya.g7t.takao@jp.nssmc.com, web page: http://www.nssmc.com/

[†]Nippon Steel Corporation (NSC)
Mechanical Engineering Div.
Plant Engineering and Facility Management Center
20-1 Shintomi Futtsu ,Chiba Prefecture(Japan)

Key words: Spray, Steel Making Process, Particle-Based Numerical Simulation, Heat Transfer

ABSTRACT

Spray cooling is often used in the steel manufacturing process, and the steel plate temperature at the time of manufacture affects productivity and quality. Therefore, the spray heat transfer coefficient estimation becomes important when determining manufacturing conditions or when designing manufacturing facilities. The conventional heat transfer coefficient estimation method is obtained by reversely analyzing the temperature of the steel plate when the heated steel plate is cooled by a single nozzle used or an experimental device simulating a real machine manufacturing facility. However, in actual equipment manufacturing facilities, it is difficult to grasp the heat transfer and flow state of heat transfer part details due to the presence of rolls, water staying on steel plates, and spray when a large amount of water is injected, heat transfer by numerical calculation Coefficient prediction has been desired.

In order to calculate the actual physical phenomena even with a single spray, one hundred million droplets of about hundred micrometer diameter are calculated while resolving a few micrometers of vapor film thickness at the time of collision of the steel plates with droplets, so calculation load is huge.Therefore, the authors describe the heat transfer coefficient of the experimental results as a function of the collision pressure because the vapor film is broken and the heat transfer is promoted if the collision pressure of the spray droplets to the steel plate is high [1]. The heat transfer coefficient was calculated by substituting the collision pressure obtained by the numerical calculation into the experimental formula.

The behavior of the spray cooling water includes a complex free interface, but can be calculated by the MPS method, and there is an example [2] where the flow rate of the spray cooling water between rolls of a real steel facility is calculated. In the present examination, the MPS method was similarly used for the prediction of the spray collision pressure, and the

calculated particle diameter was also set to 3 mm as in the case [2]. As a result of examination, the particles were injected from the spray outlet so as to match the actual water density, and the actual droplet size was matched with the actual collision pressure.

1. Introduction

There are various cooling processes using spray in the steel manufacturing process, and play an important role in quality improvement and productivity improvement. In the continuous casting process, solidification non-uniformity caused by cooling non-uniformity of spray water is a problem [2]. In the previous report, it was possible to quantify the macroscopic flow distribution of spray water in a continuous casting machine by numerical analysis. However, the heat transfer coefficient of spray cooling cannot be predicted by numerical analysis, and the solidification state of the entire continuous casting machine was predicted by combining the heat transfer coefficient measurement by experiment and the flow analysis result. In this study, we investigated a method of numerically determining the heat transfer coefficient distribution of spray cooling that could not be predicted by conventional numerical analysis.

2. Impact pressure for cooling capacity estimation

It is difficult to model all physical phenomena by numerical analysis because the spray of the steel cooling process is accompanied by the boiling phenomenon. A steam film is formed between the steel plate and the cooling water, and heat exchange between the steel plate and the cooling water is performed by the steam film having high heat resistance. Therefore, the increase of the water collision pressure makes the vapor film thinner or breaks down, which reduces the thermal resistance and also causes solid-liquid contact phenomenon, thereby promoting heat exchange and improving the heat transfer coefficient (Fig. 1)).
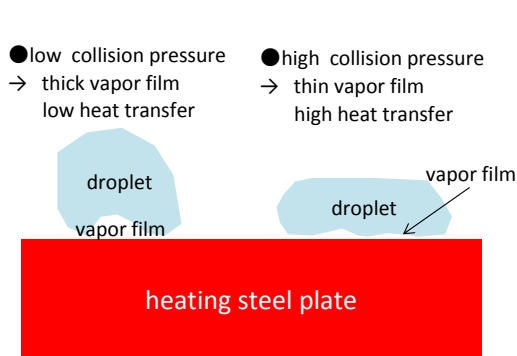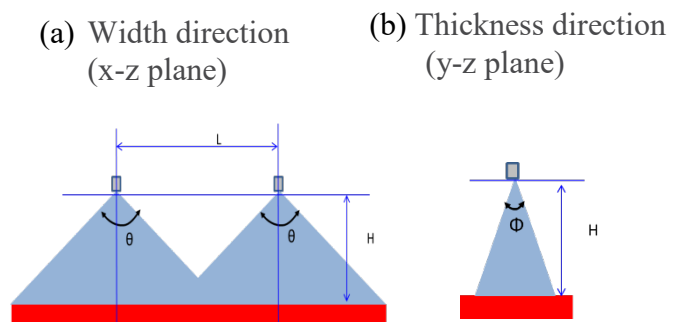

Fig.1. spray heat transfer mechanism

Fig.2   spray injection condtion

From this mechanism, the heat transfer coefficient h of the steel plate surface is a function f using the water density W per unit area, the collision pressure Pc of the droplets onto the steel plate surface, and the steel plate surface temperature Ts after cooling as in equation (1) It is known that it can be formulated [1].

$$h = f(W, Pc, T_s) \tag{1}$$

Since Ts is the surface temperature of steel plate which is the result of cooling, it is necessary to obtain the water density w and the collision pressure Pc in order to predict the heat transfer coefficient by calculation. The water density distribution is the spray performance itself and is relatively easily available from the manufacturer of the spray nozzle. In this paper, we apply the particle method that facilitates free interface handling to flow analysis, model spray injection that can simulate the actual spray water density distribution, and calculate the distribution of collision pressure required for heat transfer coefficient prediction.

We examined whether it was possible to ask. Numerical analysis was performed using general-purpose particle method analysis software "Particleworks". Specifically, two sprays as shown in Fig. 2 are wrapped, and the collision pressure against the steel plate when the spray flow rate, the width direction angle, and the thickness direction angle are changed is compared with the experimental value.
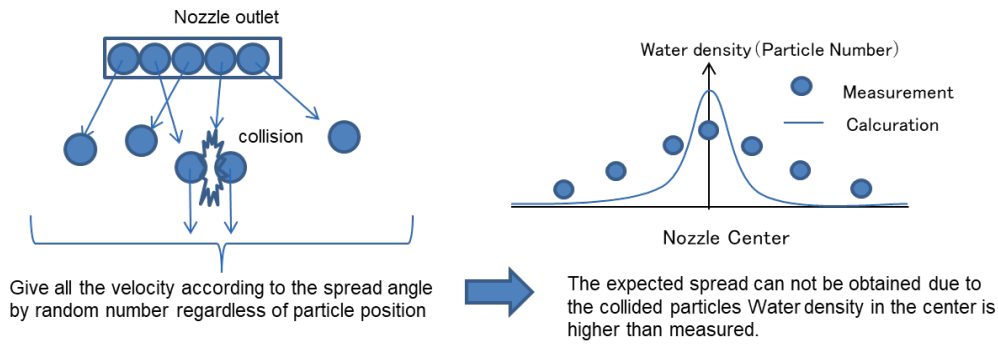
Fig.3   spray injection logic in the standard function of the software

In the standard function of the software, as shown in Fig. 3, random droplet velocity three components Vx, Vy and Vz according to the spray spread angle were given using the equation (2) regardless of the position of the particles.

$$v_x = v_z \tan^{-1}(rand[-H\tan(\theta/2):H\tan(\theta/2)]/H)$$
$$v_y = v_z \tan^{-1}(rand[-H\tan(\phi/2):H\tan(\phi/2)]/H) \qquad (2)$$
$$v_z = Q_n/A_n$$

Here, Qn means the flow rate per nozzle, An means the sectional area of the nozzle outlet, and rand [x0: x1] means that numbers are randomly given in the range of $x0 \leqq x \leqq x1$. However, in this injection logic, the spread of droplets assumed cannot be obtained because the particles collide with each other before reaching the steel plate, and the amount of water is concentrated at the center and there is a problem that it does not match the actually measured water density. Therefore, a spray injection logic as shown in Fig. 4 was considered. The

droplet velocity is given using equation (3). In the improved logic, the initial velocity is given at the injection angle obtained by giving the x coordinate with random numbers to the injection range $x_{i-1} \leqq x \leqq x_i$ obtained from the actually measured water density for the ith particle. By injecting the particles in this manner, the particles do not collide with each other before reaching the steel plate, and the particles can be injected according to the actually measured water density. The implementation of the logic was performed using a user subroutine of general purpose software.

$$v_x^{i} = v_z \tan^{-1}(rand[x_{i-1} : x_i]/H)$$
$$v_y^{j} = v_z \tan^{-1}(rand[y_{j-1} : y_j]/H) \tag{3}$$
$$v_z = Q_n / A_n$$
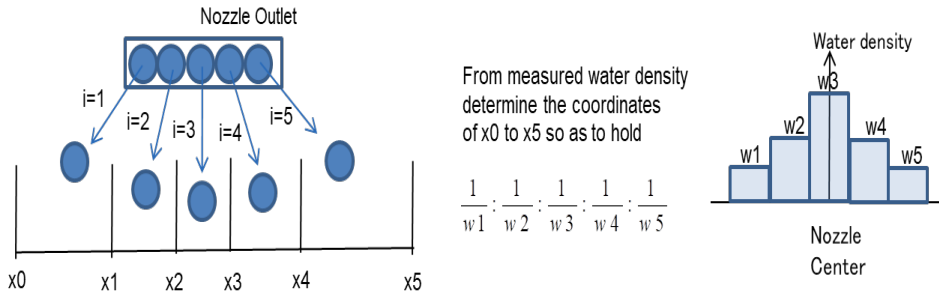
Fig.4.   Spray injection logic improved in this paper
(When coming out 5 pieces in a horizontal row from the discharge port)

The governing equations are discretized using the interparticle interaction model when solving the same continuous equation (Equation (4)) and Navier-Stokes equation (Equation (5)) as in the flow calculation with the finite volume method etc. It is carried out.

$$\frac{D\rho}{Dt} = 0 \tag{4}$$

$$\frac{D\mathbf{u}}{Dt} = -\frac{1}{\rho}\nabla p + \nu\nabla^2\mathbf{u} + \mathbf{f} \tag{5}$$

Here, $\mathbf{u}$ in the equation (5) is a flow velocity vector, p is a pressure, ρ is a density, ν is a kinematic viscosity coefficient, and $\mathbf{f}$ is an external force vector (gravity and surface tension). For the boundary condition of the wall, we used a model in which the wall of Harada et al. [3] is treated as a polygon wall. The collision pressure of the droplets is determined using equation (6) which is a blend of pressure gradient and penalty method when wall particles are used.

$$P_{i,wall}^{press} = f_{i,wall}^{press} / A = m_i [\beta \{ \frac{1}{\rho} \frac{d}{n^0} (P_i^{k+1} - \hat{P}_i^{k+1}) Z_{grad}(r_{iw}) \}$$
$$+ (1-\beta) \{ \frac{l_0/2 - |\vec{r}_{iw}|}{\Delta t^2} \}] \vec{n}(\vec{r}_i) / A \tag{6}$$

Where $P_{i,wall}^{press}$ is the collision pressure, $f_{i,wall}^{press}$ is the force applied when the particle collides with the wall, A is the examination area, m_i is the mass of the particle, $\vec{r}_{iw}$ is the closest distance from the wall to the particle i, and the wall weighting function $Z(\vec{r}_{iw})$ determined by $\vec{r}_{iw}$, P_{wall} is the pressure at the wall , $Z_{grad}(\vec{r}_{iw})$ is the slope of the wall weighting function $Z(\vec{r}_{iw})$ in the wall normal direction, $\vec{n}$ is the normal vector, and β is the weighting parameter.

3. Calculation result of spray injection and collision pressure

When the spray is made to collide with the steel plate under the condition of θ = 110 °, φ = 20 °, H = 145 mm, L = 315 mm according to the definition of Fig. 2 with two nozzles lapped with a flow rate of 24 l / min in Fig.5 . The situation of is compared with experiment and numerical calculation. The particle diameter at the time of calculation was 1 mm. It was confirmed by both experiment and numerical calculation that cooling water collides in the part which two sprays wrap to right and left, and it separates up and down and flows.
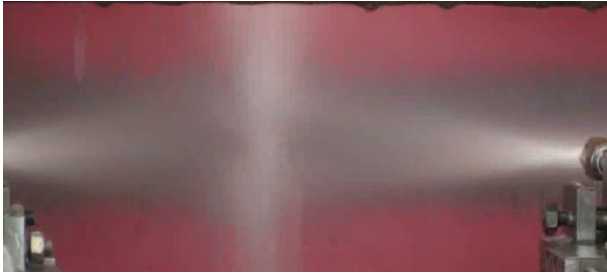
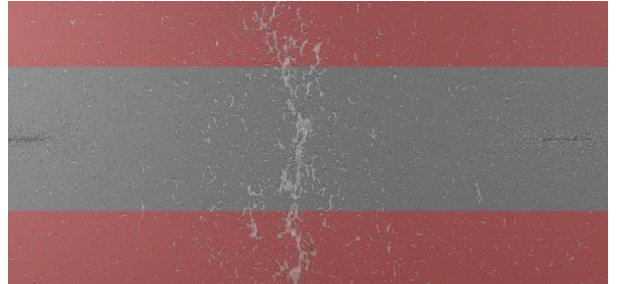(a)experiment   (b)numerical simulation

Fig.5.   State of spray injection
24ℓ/min × 2 ,θ=110°,φ=20°,H=145mm,L=315mm

In Fig. 6, two nozzles with a water volume of 30 l / min were used, and injection was performed under the conditions of θ = 114 °, φ = 10 °, H = 80 mm, L = 100 mm. The water density ratio of the central part of the spray thickness of the The water density is a flow rate per unit area measured by placing a container of 20 mm square on one side at a position separated by 80 mm from the spray. The same method was used for measurement in numerical calculation. According to the method proposed this time, the water density distribution near the actual measurement was calculated from Fig.6.

   Fig. 7 shows the collision pressure at the center of the thickness when the spray is injected under the same conditions as Fig. The calculated value is the collision pressure obtained by the injection logic of equation (3). The collision pressure was measured by attaching a pressure sensor to a plate having a width of 20 mm and a thickness of 100 mm, and moving the plate over the entire spray injection width. As shown in Fig. 7, the phenomenon that the collision pressure becomes large immediately below the nozzle and the collision pressure decreases as it separates from the region below quantitatively coincides with the measured value and the calculated value.
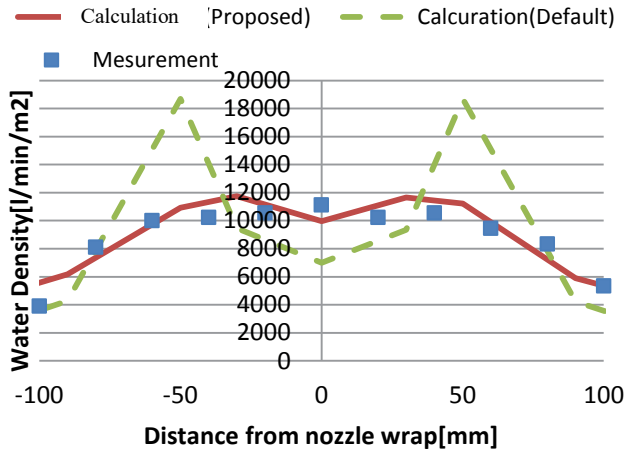
Fig.6. Water density distribution of spray (Thickness center, Frow Rate 30ℓ/min ×2,θ=114°,φ=10°,H=80mm,L=100mm）

Fig.7. Impact pressure distribution of spray (Thickness center, Flow Rate 30ℓ/min ×2 , θ=114°,φ=10°, H=80mm, L=100mm）

4. Heat Transfer Calculation

   Consider numerically predicting the heat transfer coefficient of a single spray. The heat transfer coefficient h of the steel plate surface can be formulated by the function f using the water density W per unit area, the collision pressure Pc of the droplets on the steel plate surface, and the steel plate surface temperature Ts after cooling as in equation (1) It is known [1].

   Based on this finding, first, the spray condition of the spray is set to match the water mass density distribution W of the catalog spec, and the flow of the complex free interface of the spray cooling water is calculated using the particle method. The initial velocity of the particles given by calculation is given from the value obtained by back-calculating the pressure obtained by the PQ diagram of the spray or the value measured by PIV.

   In this paper, we calculate the heat transfer coefficient of the spray by substituting the collision pressure and water density distribution of the steel plate which is the calculation result of the particle method into the equation (1). The spray conditions for the spray were a flow rate of 14.8 L / min, the distance between the spray and the steel plate was 155 mm, the

spread angle in the width direction was 110 °, and the spread angle in the thickness direction was 20 °. The heat transfer coefficients measured in the experiment and the results are compared. The heat transfer coefficient of the experiment was calculated by inversely analyzing the temperature history of the thermocouple embedded in the steel plate after the steel plate was heated to 900 ° C. in a heating furnace. The heat transfer coefficients determined by numerical calculation and the measured heat transfer coefficients are shown in Fig. 8
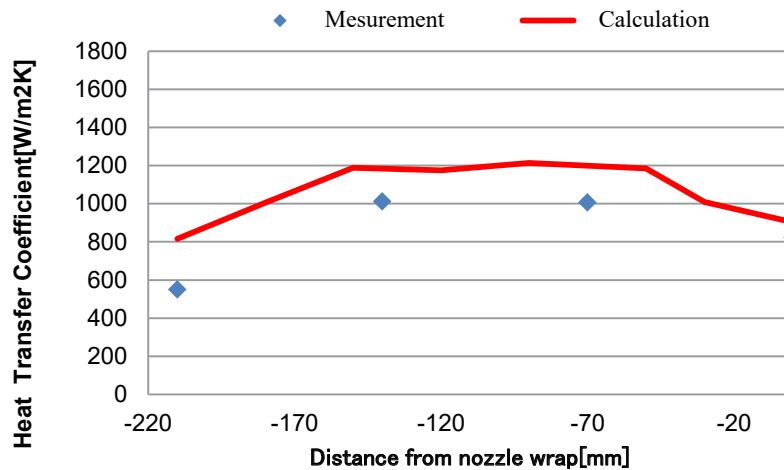

Fig.8　Comparison of Calculated and Measured Spray Heat Transfer Coefficients

5. Conclusion

By calculating the spray injection using the particle method, it becomes possible to calculate the distribution of the collision pressure Pc quantitatively by calculation by combining the water density W with the actual measurement value. From this, it was found that the flow analysis of W, Pc, etc. could predict not only the macro behavior of the spray water but also the heat transfer coefficient h.

REFERENCES

[1]　T. Matsukawa, S. Yuhara, S. Kojima, T. Fujiyama and S. Miyaga:Kawasaki Steel Giho, 19 (1987), 7.

[2]　Norimasa Yamasaki, Shozo Shima, Keiji Tsunenari, Satoru Hayashi, Masahiro Doki , Particle-based Numerical Analysis of Spray Water Flow in Secondary Cooling of Continuous Casting Machines, ISIJ International 2015, 55-5 p. 976-983

[3]　Takahiro Harada, Seiichi Koshizuka, Yoichiro Kawaguchi, Improvement of the Boundary Conditions in Smoothed Particle Hydrodynamics, Computer Graphics & Geometry, Vol. 9, No. 3, 2-15 (2007)

TWO-MASS GYRO-PARTICLE AS THE TOOL
FOR SUPERSONIC AEROELASTICITY ANALYSIS

SERGEY V. ARINCHEV

Bauman Moscow State Technical University (BMSTU)
107005, 2-ya Baumanskaya street, 5/1, Moscow, Russian Federation
arinchev@inbox.ru

Key words: Supersonic Aeroelasticity, Gyro-Particle, Frequency Splitting

Summary. The proposed flutter interpretation is applicable to plasma aeroelasticity analysis. In this case it shall be possible to divide a particle in two, to generate two opposite electric charges and thus ionize the flow. The proposed two-mass gas gyro-particle has the elastic elements and the two pairs of multiple oscillation frequencies. The incident gas gyro-particles interact with the structural particles of the streamlined elastic body. The gas particles start to rotate and pulsate. The multiple oscillation frequencies of the gas particles split. The higher the vehile speed, the larger the gap between the oscillation frequencies of the gas particle. The structural resonance takes place, when the gas-particle pulsation frequency gets into the vicinity of an eigenfrequency of the elastic structure. This resonance is the flutter. Plasma is not considered here. This work is only a preparation step in this direction.

1 INTRODUCTION

Consider the elastic body in the high-speed supersonic flow. From one side, the front of the shock wave gets closer to the body surface. From another side, the turbulent frictional boundary layer of the body gets wider. Assume that these two quantities are commensurable ones. If plasma is available, then the shock wave starts to disintegrate, the flow medium starts to intermix [1,2]. Static equilibrium analysis [3,4] is not satisfactory to solve the flow-and-structure interaction problem. The clearly defined shock-wave-front surface shall be replaced with a specific contact-type vortex-induced formation with uncertain boundaries. The concept of the contact-type vortex-induced formation is introduced by O. Azarova [5]. Her work is available free in the Internet. Possibility of a vortex-type interpretation of the supersonic flow is proved in the work [6].

Nowadays the "piston" theory and its modifications are widely used for solving the supersonic aeroelasticity problem. The important results are obtained [7-9]. The well known vortex-element method [10-12] works properly in the incompressible-liquid medium. The particle approach specified in this issue provides the following calculation facilities: joint analysis of aerodynamic pulsations and oscillations of the elastic body, arbitrary structural-

surface geometry in the incident flow, 3D-motion analysis, gas-compressibility assumption, refinement of the gas-pulsation character, particle disintegration, heating effects, etc. Each particle has its own repulsion-type force characteristic. By changing the force characteristic parameters the subsonic flow may be replaced with the supersonic one. The considered problem is the time-dependent Cauchy one with the given initial conditions.

The concept of the elementary gyro-particle is introduced in [13]. This report considers the so-called two-mass elastic gas gyro-particles with the given repulsion-type force characteristic. The particles are point masses [14,15]. The proposed particle takes the medium elasticity into account. Under the special conditions a separate two-mass particle can be disintegrated in two and thus ionize the incident flow. Each particle interacts with each one. The streamlined elastic body is also made of particles. They are the structural one-mass particles connected by springs. The gas particles interact with the structural ones. This interaction produces the so-called contact-type vortex-induced formation with intensive pulsations. The clearly defined shock-wave-front surface is not available.

The gas particle "rotation intensity" is associated with the its gyro-load parameter. If the gyro-load parameter is zero, then the particle eigenfrequencies are the multiple ones. The higher the gyro-load parameter, the larger the frequency gap. They are the frequencies of the gas pulsations. The system resonance takes place when a gas pulsation frequency gets into the vicinity of the eigenfrequency of the elastic body.

The problem-solution convergence rate (in the number of considered particles) is high [15,16]. Dozens (hundreds) of the particles are quite enough to illustrate the considered aeroelastic effects.

2   DESCRIPTION OF THE TWO-MASS GAS GYRO-PARTICLE

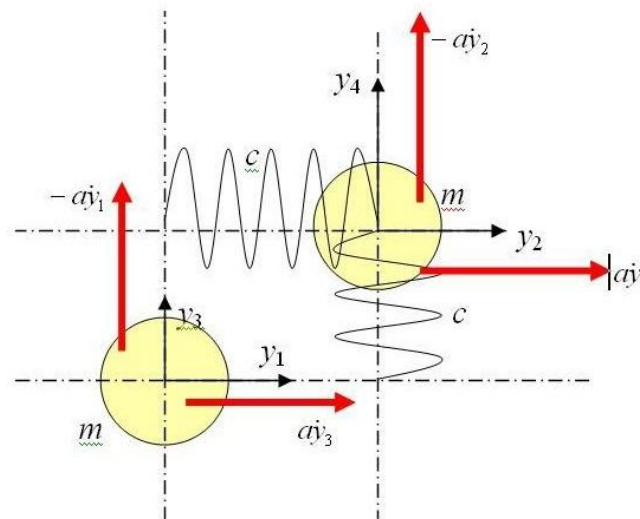The two-mass gas gyro-particle is shown in Figure 1.

Figure 1: The two-mass gas gyro-particle

The particle displacements are translational. Friction is not available. A separate particle (see Figure 1) move in compliance with its dynamics equations:

$$-m\ddot{y}_1 + c(y_2 - y_1) + a\dot{y}_3 = 0$$ (1)
$$-m\ddot{y}_2 - c(y_2 - y_1) + a\dot{y}_4 = 0$$
$$-m\ddot{y}_3 + c(y_4 - y_3) - a\dot{y}_1 = 0$$
$$-m\ddot{y}_4 - c(y_4 - y_3) - a\dot{y}_2 = 0$$

where:

$a -$ is the particle gyro-load parameter associated with its "rotation intensity".

Matrix A of the gyro-load coefficients is the skew-symmetric one:

$$A = \begin{bmatrix} 0 & 0 & a & 0 \\ 0 & 0 & 0 & a \\ -a & 0 & 0 & 0 \\ 0 & -a & 0 & 0 \end{bmatrix}$$ (2)

The particle characteristic eigenvalue equation takes the following form:

$$b_0\lambda^8 + b_2\lambda^6 + b_4\lambda^4 + b_6\lambda^2 = 0$$ (3)
$$b_0 = m^4; b_2 = m^2(4mc + 2a^2); b_4 = 4m^2c^2 + 4a^2mc + a^4; b_6 = 4a^2c^2$$

If the gyro-load parameter $a=0$ (the particle is not "spinned up" yet), then $b_6=0$. In this case the particle has the two pairs of multiple eigenvalues and the two zero (solid-state) ones.
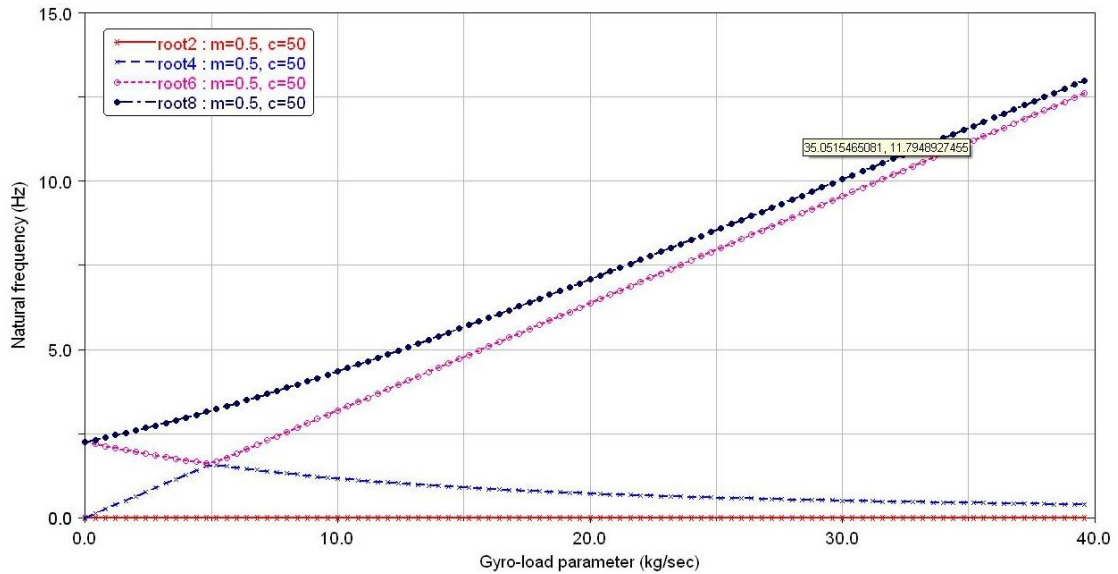

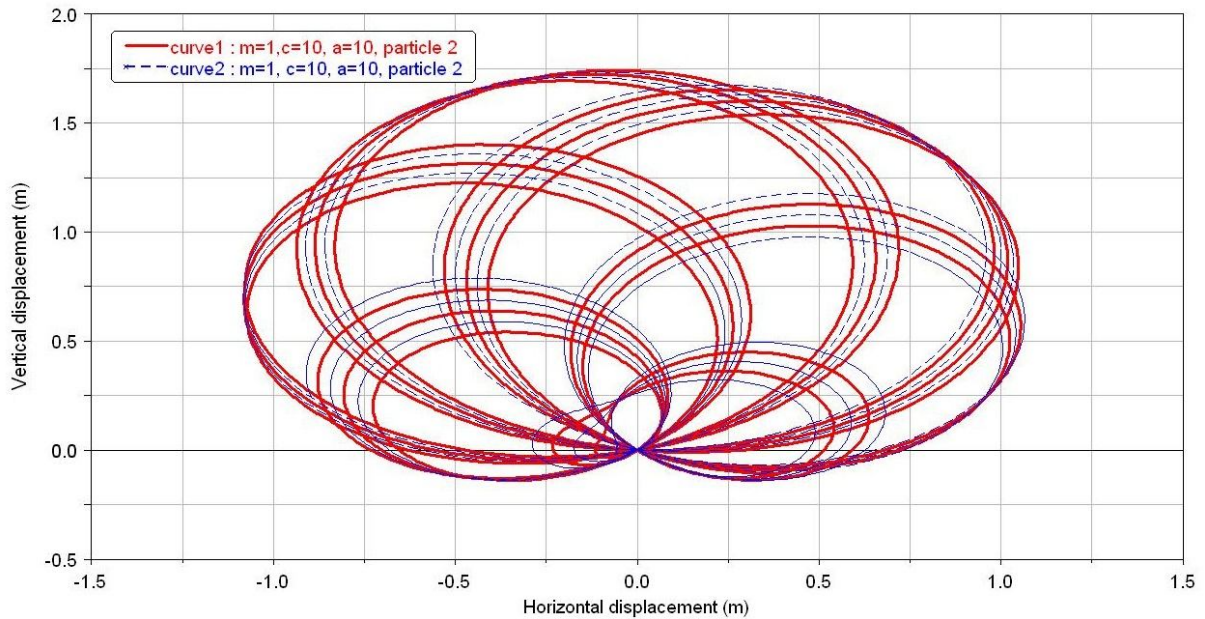**Figure 2:** Splitting of the particle eigenvalues. Loss of one the two zero (solid-state) ones

Figure 3: The particle pulsations induced by the unit impulse (4)

It is shown in Figure 2, that increase of the gyro-load parameter (associated with the particle "rotation intensity") leads: 1) to splitting of the particle eigenvalues, 2) to loss of one of the two zero (solid-state) ones.

Figure 3 specifies the typical pulsation trajectories of the subparticles of the two-mass gyro-particle in its phase plane. It is the dynamic response to the external unit impulse under the following initial conditions:

$$y_1 = ... = y_4 = 0; \dot{y}_1 = 1; \dot{y}_2 = \dot{y}_2 = \dot{y}_3 = 0 \tag{4}$$

One of the two zero (solid-state) eigenvalues is lost. So, displacements of the particle (as a solid body) are constrained.
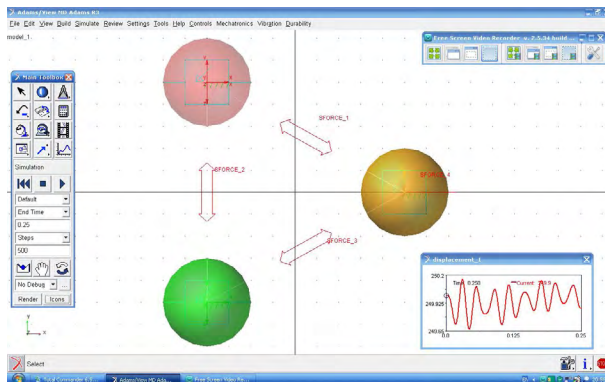

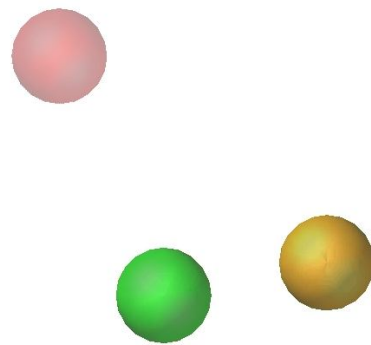**Figure 4a:** The streamlined 3-mass elastic body

Figure 4b: The body 11.2 Hz eigenmode

The report presents the simplified 2D-model of the dynamic interaction of the elastic body with the incident contact-type vortex-induced formation. Figure 4a presents the elastic body. Initially it is the equilateral triangle. Its initial leg is d_1. The 3 structural particles (the m_1 point masses) are in its vertices. The structural particles are connected using the c_1 springs (red arrows in Figure 4a). The structural particles move translationally in the plane. They oscillate. Figure 4b specifies one of the body eigenmodes. Its corresponding eigenfrequency is 11.2 Hz.

The considered gas gyro-particle has two m_2 subparticles (see Figure 1): the main subparticle and the conjugate one. It is assumed that only the main subparticle is active. It takes part in all the interactions. The conjugate subparticle is passive. It just hangs on the main subparticle and hampers its motion. The conjugate subparticles are influenced by inertia forces, elastic springs and gyro forces. The subparticles are connected by the c_2 springs in the coordinate-wise manner.

3   VORTEX CHARACTER OF THE PARTICLE MOTION

The subparticle is a point mass. Its rotation is not available. Its motion is translation under the applied gyro forces. The response trajectory is a polyharmonic one. It has the vortex character. It is the superimposition of rotations (pulsations) in the phase plane. High-frequency weak pulsations are superimposed by the low-frequency strong ones. (The particle numeration scheme is specified later in Figure 7).

The idea is that supersonic character of the flow is defined not by the streamlined-body linear velocity. It is defined by the incident-particle rotation intensity (by the value a of the associated gyro-load parameter). That is why in all the considered examples the body linear velocity is always the same, but the gyro-load parameter a is different. Figures 5a-5b show,
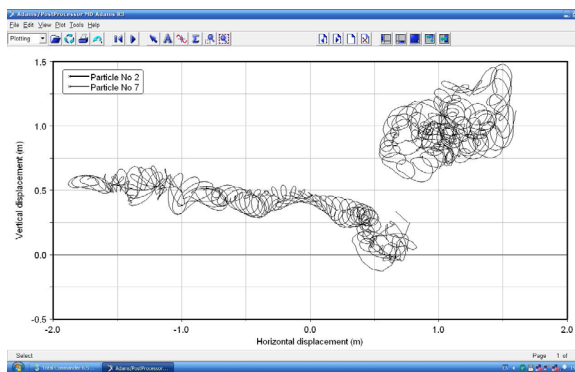

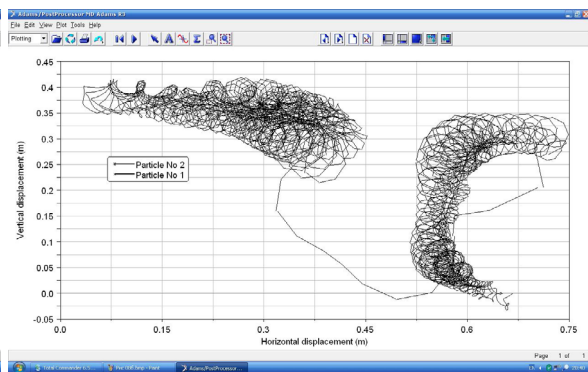**Figure 5a:** Particles Nos.2-7, a=20 (kg/sec)   **Figure 5b**: Particles Nos.1-2, a=50 (kg/sec)

that the higher the particle rotation intensity, the lower the particle pulsation amplitude, the greater the gap between the splitted frequencies.

To the first approximation, Mach number of the incident gas flow can be identified by comparing the considered vortex with the reference one. The reference O. Azarova supersonic vortex (corresponding to M=1.89) is shown in Figure 6a. The reference [5] is available free in the Internet.

The vortex in Figure 6*b* is obtained for *a*=50 (kg/sec). Compare the Figures 6*a* and 6*b*. The considered vortex and the reference one are much alike. So, the gyro-load parameter *a*=50 (kg/sec) of this model corresponds approximately to M≈2.

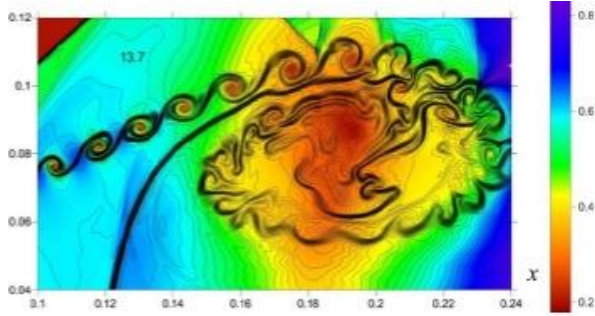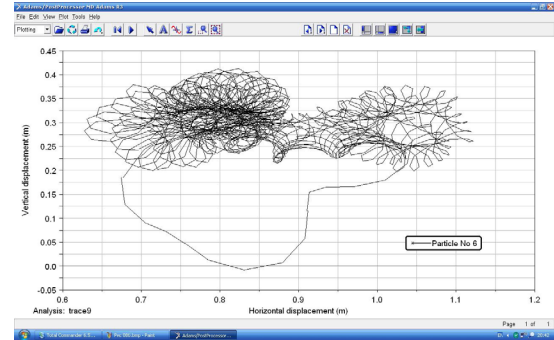**Figure 6*a*:** Reference O. Azarova supersonic vortex [5]

Figure 6*b*: Particle No.6, *a*=50 (kg/sec)

4 FORCE CHARACTERISTIC OF THE GAS GYRO-PARTICLE

Interactions of the gas gyro-particles with each other and interactions of the gas gyro-particles with the structural ones are determined by the repulsion-type force characteristic. Each gas particle repels each one. The force characteristic is the two-particles interaction force depending on the distance between them. It is approximated by the non-positive segment of the shifted parabola:

$$F_{ij}(d_{ij}) = k_{ij}(1/d_2 - 1/d_{ij}) , \; i \neq j \tag{5}$$

If $d_{ij} < d_2$, then $F_{ij} < 0$. If $d_{ij} \geq d_2$, then $F_{ij} = 0$;

where:

k_{ij} − is the compressibility factor; $d_{ij} = \sqrt{(x_j - x_i)^2 + (y_j - y_i)^2}$ − is the distance between the gyro-particles (subparticles); d_2 − is the diameter of the particle influence zone. The compressibility factor controls the flow-disturbance propagation velocity. The particles do not interact, if the distance between them exceeds the diameter of the particle influence zone. Initially the particles are packed closely. The step of the particle initial-distribution grid (in the square of the contact-type vortex-induced formation) is equal to d_2 (see Figure 7).

So, there are 3 structural particles, 16 main gas subparticles and 16 conjugate gas subparticles. The total number of the point masses is 3+16+16=35. To provide effective computer-program cycling, to simplify the formulae derivation, it is taken that all these elements interact with each other. Only some of the compressibility factors k_{ij} are zeroes. The structural particles interact with the main subparticles only. They do not interact with themselves. They do not interact with the conjugate subparticles. The main subparticles do not interact with themselves. They do not interact with the conjugate subparticles (by the repulstion-type force characterisitic). The conjugate subparticles do not interact with other subparticles at all (by the repulstion-type force characteristic).

Let K be the matrix of the specified compression factors. It has $35 \times 35 = 1225$ elements. The factors are entered into the matrix in compliance with the following procedure. At first zero all the matrix elements: $k_{ij} = 0; i = 1,...,35; j = 1,...,35$. Then start to enter non-zero elements. Let k_1 be the compression factors of the structural particles and the main gas subparticles. Let k_2 be the compression factors of the main gas subparticles only. So, the K matrix has the following two corresponding blocks. The first block:

$$k_{ij} = k_1; i = 1,2,3; j = 4,...,19 ; k_{ij} = k_1; j = 1,2,3; i = 4,...,19 \qquad (6)$$

and the second block:

$$k_{ij} = k_2; i = 4,...,19; j = 4,...,19 \qquad (7)$$

The main subparticles do not interact with each other. So, in addition:

$$k_{jj} = 0; j = 4,...,19 \qquad (8)$$

5 DYNAMICS EQUATIONS OF VORTEX-INDUCED FORMATION

The considered equations are nonlinear. The considered aeroelasticity problem is the nonstationary one. The flutter is interpreted as a classic resonance, when the two-mass gas particle pulsation frequency gets into the vicinity of an eigenfrequency of the streamlined elastic body. Friction is not available. These are the X-components of the forces applied to the considered 35 point masses:

$$\ddot{x}_1 = \left[c_1(d_{12} - d_1)\cos\varphi_{12} + c_1(d_{13} - d_1)\cos\varphi_{13} + \sum_{j=4}^{19} F_{1j}(d_{1j})\cos\varphi_{1j} \right] / m_1 \qquad (9)$$

$$\ddot{x}_2 = \left[c_1(d_{23} - d_1)\cos\varphi_{23} + c_1(d_{21} - d_1)\cos\varphi_{21} + \sum_{j=4}^{19} F_{2j}(d_{2j})\cos\varphi_{2j} \right] / m_1$$

$$\ddot{x}_3 = \left[c_1(d_{31} - d_1)\cos\varphi_{31} + c_1(d_{32} - d_1)\cos\varphi_{32} + \sum_{j=4}^{19} F_{3j}(d_{3j})\cos\varphi_{3j} \right] / m_1$$

$$\ddot{x}_4 = \left[c_2(x_{20} - x_4) + a\dot{y}_4 + \sum_{\substack{j=1 \\ j \neq 4}}^{19} F_{4j}(d_{4j})\cos\varphi_{4j} \right] / m_2$$

$$\ldots$$

$$\ddot{x}_{19} = \left[c_2(x_{35} - x_{19}) + a\dot{y}_{19} + \sum_{\substack{j=1 \\ j \neq 19}}^{19} F_{19,j}(d_{19,j})\cos\varphi_{19,j} \right] / m_2$$

$$\ddot{x}_{20} = \left[-c_2(x_{20} - x_4) + a\dot{y}_{20} \right] / m_2$$

$$\ldots$$

$$\ddot{x}_{35} = \left[-c_2(x_{35} - x_{19}) + a\dot{y}_{35}\right]/m_2$$

where: $\cos\phi_{ij} = (x_j - x_i)/d_{ij}$.

The *Y*-components of the forces applied to the considered 35 point masses are much alike.

The initial integration conditions of equations (9) are specified in Figure 7. Initially the two-mass gas gyro-particles are motionless. But the structural particles initially move. *X*-components of their linear velocities are non-zero and equal to v_{x0}. Actually, the elastic body tries to penetrate through the motionless square-type gas formation at the given speed.

The system of 70 equations (9) is integrated using the 4-th order Runge-Kutta procedure. The equation parameters are: a= 0-5000 (kg/sec), m_1=50 (kg), m_2=0.5 (kg), c_1=10^5 (N/m), c_2=50-50000 (N/m), k_1=1000 (N×m), k_2=10 (N×m), v_{x0}=5 (m/sec). Total integration time is T=0.4 (sec). During this time the elastic body penetrates the gas formation completely. The preliminary determined eigenfrequencies of the elastic body (see Figures 4*a*-4*b*) are: 8.72 Hz, 8.74 Hz, 11.2 Hz.

6   THE AEROELASTICITY ANALYSIS RESULTS

The red arrow in Figure 7 specifies the initial v_{x0} velocity direction of the streamlined triangular body. Red lines are the trajectories of its structural particles. The elastic body moves into the motionless 1×1 (m^2) square contact-type vortex-induced formation. This
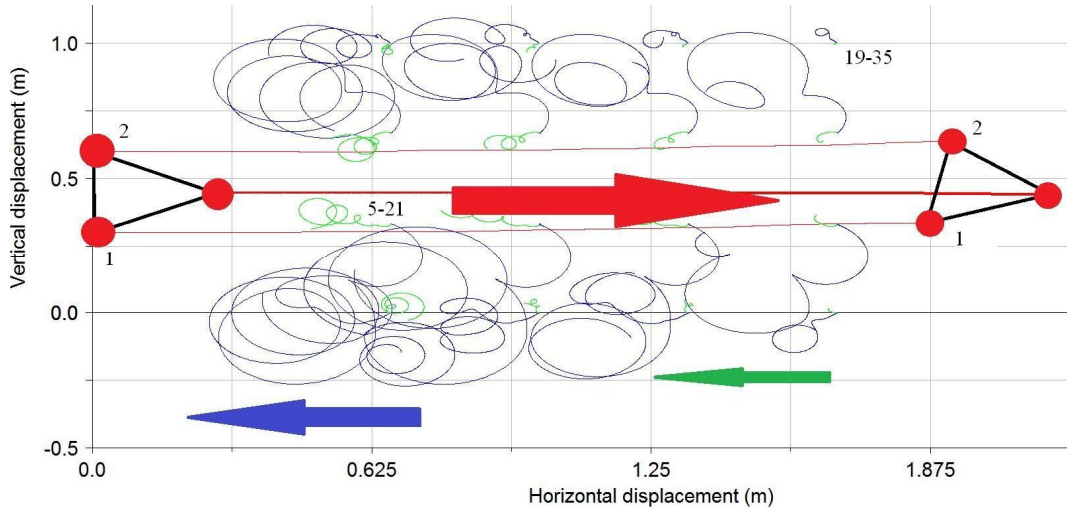

Figure 7: The triangle elastic body penetrates through the contact-type vortex-induced formation

square-shape formation is occupied with 16 two-mass gas gyro-particles. Their initial distribution grid is uniform, d_2 – is the grid step. It is assumed that supersonic character of the incident flow is determined not by the body linear velocity, but by gas particle rotation intensity (by the gyro-load *a* parameter). Initially all the gas gyro-particles are motionless, but they are spinned up strongly. The gyro-loads are applied, $a\neq0$. Rotation intensity of all the particles is the same. If the gyro-particles are arranged from the opposite sides of the streamlined body, then they are spinned up in different directions. Gyro-load parameter of the

upper particles is positive, gyro-load parameter of the lower particles is negative.

Trajectories of the main subparticles are blue. Trajectories of the conjugate subparticles are green. The main trajectory and the conjugate trajectory of the two mass particle start from the same point at the initial time moment. Figure 7 is overloaded. So, not all the particles are numbered. The numbering scheme is: 1) 3 structural particles Nos. (red trajectories) are from 1 to 3, 2) 16 main subparticles Nos. (blue trajectories) are from 4 to 19, 3) 16 conjugate subparticles Nos. (green trajectories) are from 20 to 35. So (see Figure 7), designation 5-21 specified the initial positions of the main subparticle No.5 and its conjugate particle No.21. Note that the applied gyro-loads carry the gas particles down the flow (see the green arrow and the blue arrow at the bottom of Figure 7). The disturbances do not go up the flow. This effect characterises the supersonic nature of the model. It is seen in Figure 7 that the elastic body (in the right) has already penetrated through the gas formation, but motion of the 19-35 gyro-particle has hardly started. In other words, the elastic-body motion velocity exceeds the flow-disturbance propagation velocity.

Traditionally [13] flutter is considered as a solution of the corresponding boundary problem. Unlike the traditional approach in this report flutter is a resonance. Increase of the gyro-load a parameter (gas particle rotation intensity) provides the gas gyro-particle eigenfrequency splitting (see Figure 3). These are the pulsation frequencies of the gas-particle. The resonance takes place when a flow pulsation frequency gets into the vicinity of an eigenfrequency of the elastic body.

Figure 8 specifies the surge of amplitude of relative displacements $y_2 - y_1 - d_1$ of the structural particles in the gyro-load a parameter interval from 30 to 40 (kg/sec).

It is shown in Figure 2, that for a=35.05 (kg/sec) the gas particle pulsation frequency is 11.79 (Hz). Figure 4b specifies the 11.2 (Hz) elastic-body eigenmode. So, it is the resonance, because the gas pulsation frequency has got into the vicinity of the elastic-body eigenvalue.
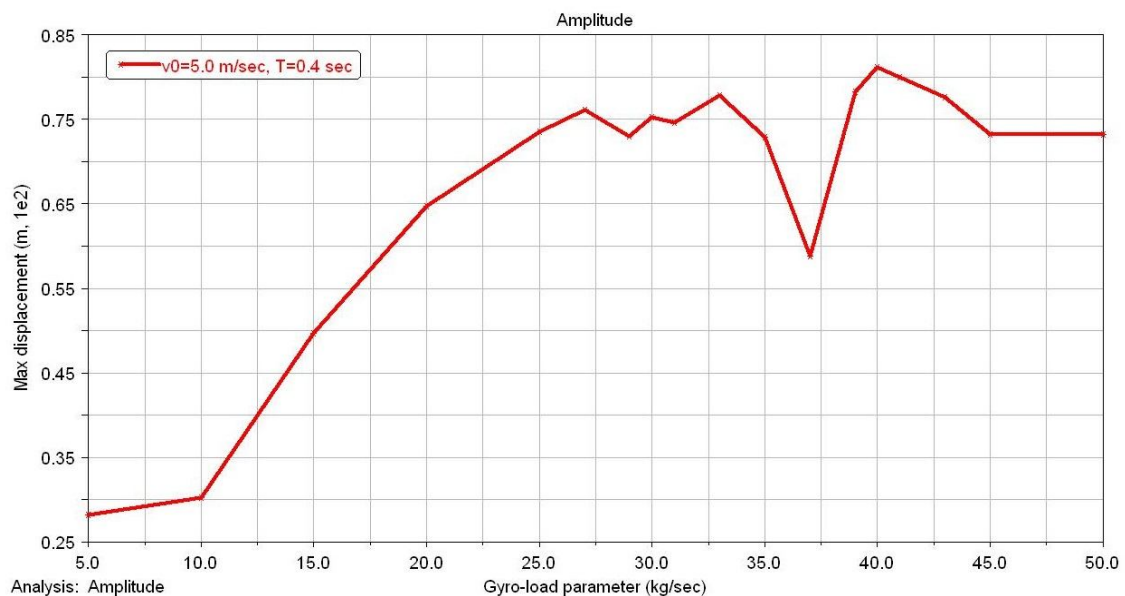

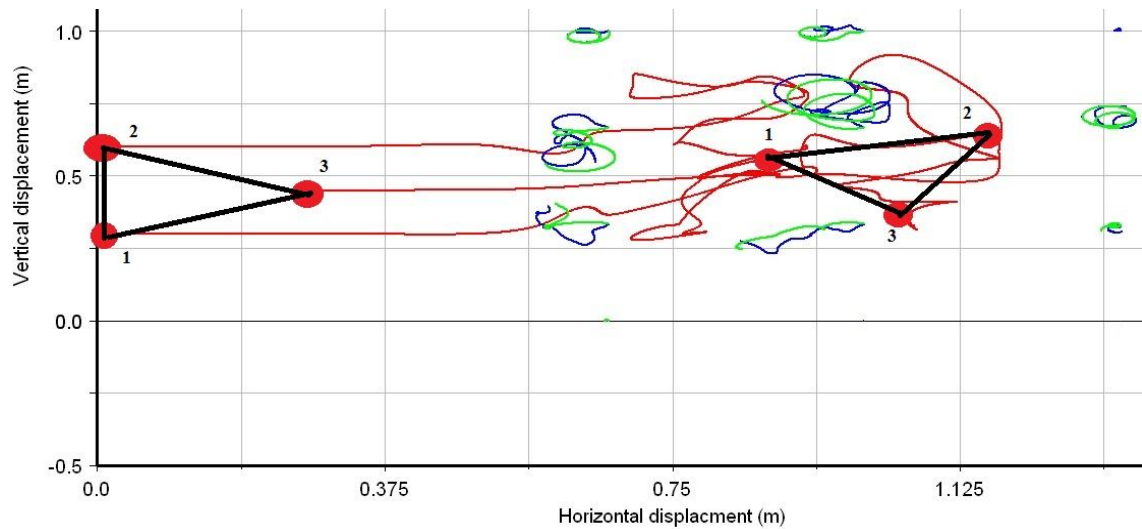**Figure 8:** Resonance (flutter) of the streamlined elastic body

Figure 9: Quarter turn (divergence) of the streamlined elastic body, a=5000 (kg/sec)

Note that further increase of the gyro-load a parameter (gas-particle rotation intensity) is accompanied with growth of aerodynamic drag. Figure 9 illustrates the case, when a is high enough. In this case, the streamlined body runs against the contact-type vortex-induced formation, oscillates chaotically and makes a counter-clockwise quarter turn. This is the aeroelastic divergence.

7 CONCLUSIONS

- The two-mass gyro-particle is proposed as the tool for modeling the plasma-containing supersonic flow. This particle can be divided in two oppositely-charged single gyro-particles and thus ionize the incident flow. Plasma is not considered here. This work is only a preparation step in this direction.
- It is shown that the supersonic flow character may be determined not by linear velocity of the streamlined body, but by rotation intensity of the incident gas gyro-particles.

REFERENCES

[1] T.A. Lapushkina, A.V. Erofeev, O.A. Azarova, O.V. Kravchenko. Interaction of a plane shock wave with an area of ionization instability of discharge plasma in air. *Aerospace Science and Technology* (2019)**85**:347-358.

[2] Артеха С.Н. Определение параметров плазмы с учетом локальных вращений. *Russian Federation, Журнал технической физики* (2011), Vol. 81, **1**:65-68.

[3] Булгаков В.Н., Котенев В.П., Сапожников Д.А. Моделирование сверхзвукового обтекания затупленных конусов с учетом разрыва кривизны образующей тела. *Russian Federation, Математическое моделирование и численные методы* (2017)**2**:81-91.

[4] Котенев В.П., Сысенко В.А. Аналитические формулы повышенной точности для расчета распределения давления на поверхности выпуклых, затупленных тел вращения произвольного очертания. *Russian Federation, Математическое моделирование и численные методы* (2014)**1**:68-81.

[5] Азарова О.А. *Неустойчивости и контактно-вихревые структуры в задачах сверхзвукового обтекания с внешними источниками энергии.* Диссертация на соискание ученой степени доктора физико-математических наук по специальности 01.02.05 «Механика жидкости, газа и плазмы». Москва, (2012).

[6] Борисов В.Е., Давыдов А.А., Константиновская Т.В., Луцкий А.Е., Шевченко А.М., Шмаков А.С. Моделирование сверхзвукового течения в следе за крылом при *M=2−4. Russian Federation, Препринты ИПМ им. М.В. Келдыша* (2018)**50**:1-19. DOI: 10.20948/prepr-2018-50, URL: http://library.keldysh.ru/preprint.asp?id=2018-50.

[7] Ватрухин Ю.М., Мензульский С.Ю., Никопоренко А.В. Определение аэроупругих характеристик гиперзвукового летательного аппарата с точки зрения безопасности авиаперевозок. *Russian Federation, Специальная техника* (2010)**4**:41-46.

[8] Мезульский С.Ю. Методика расчета динамических аэроупругих характеристик конструкции, обтекаемой гиперзвуковым потоком воздуха. *Russian Federation, Известия ВУЗов, Машиностроение* (2011)**2**:16-22

[9] B.J. Thuruthimattan, P.P. Friedmann, J.J. McNamara, and K.G. Powell. Aeroelasticity of a generic hypersonic vehicle. *Proceedings of the 43d AIAA/ASME/ASCE/AHS/ASC Structures, Structural Dynamics and Materials Conference.* Denver, Colorado, (22-25 April 2002):1-14

[10] Щеглов Г.А., Коцур О.С. Реализация метода обмена интенсивностями вортон-отрезков для учета вязкости в методе вихревых элементов. *Russian Federation, Вестник МГТУ имени Н.Э. Баумана, Естественные науки* (2018)**3**:48-67. DOI: 10.18698/1812-3368-2018-3-48-67, http://vestniken.ru/catal…th/compmath/818.html

[11] Щеглов Г.А., Марчевский И.К. Моделирование эволюции переплетенных вихревых нитей методом вихревых элементов. *Russian Federation, Известия Российской Академии Наук, Механика твердого тела* (2016)**3**:131-139.

[12] Marchevskii I.K., Shcheglov G.A. On the dynamic stability of an elastically fixed high-drag airfoil under vortical parametric excitations // Mechanics of solids (2016), Vol. 51, **1**:165-176. DOI: 10.3103/S0025654416030122, http://link.springer.com/…%2FS0025654416030122

[13] Аринчев С.В. *Теория колебаний неконсервативных систем.* Moscow, Publishing House of Bauman Moscow State Technical University, (2002).

[14] Sergey V. Arinchev. Simulation of reversed torsion of the AlMg6 aluminium bar using the macro-molecule approach. *International Center for Numerical Methods in Engineering (CIMNE), Proceedings of the XIII International Conference on Computational Plasticity. Fundamentals and Applications, COMPLAS XIII, Polytechnic University of Catalonia (UPC), Barcelona, Spain, 1-3 Septemper 2015, EbookComplas2015,* (2015):429-439. http://congress.cimne.com/complas2015/frontal/default.asp

[15]   Sergey V. Arinchev. Back from the solid temperature to kinetic energy of its macro-molecules. *International Center for Numerical Methods in Engineering (CIMNE), Proceedings of the IV-th International Conference on Particle-Based Methods. Fundamentals and Applications. Polytechnic University of Catalonia (UPC), Barcelona, Spain 28-30 September, 2015, E-book_PARTICLES_2015*, (2015):909-920. http://congress.cimne.com/particles2015/frontal/doc/E-book_PARTICLES_2015.pdf

EFFECT OF PARTICLE DIAMETER ON AGGLOMERATION DYNAMICS IN MULTIPHASE TURBULENT CHANNEL FLOWS

L.F. MORTIMER AND M. FAIRWEATHER

University of Leeds
School of Chemical and Process Engineering, University of Leeds, Leeds, LS2 9JT, UK
l.f.mortimer@leeds.ac.uk

Key words: Direct numerical simulation, Lagrangian particle tracking, Particle-laden flow, Fluid dynamics, Agglomeration, Four-way coupling, Channel flow

Abstract. The present work uses a fully coupled direct numerical simulation-Lagrangian particle tracking solver in conjunction with an interaction energy-based deterministic agglomeration algorithm to determine the effect of particle diameter on the aggregation properties of a wall-bounded, particle-laden channel flow at shear Reynolds number, $Re_\tau = 180$. Three primary particle diameters are considered of relevance to the nuclear industry resembling 200μm - 400μm calcite particles dispersed in water, with a Hamaker constant of 3.8×10^{-20} J. The simulations are initialized with randomly dispersed particles of numbers calculated to ensure a constant volume fraction $\Phi_P = 10^{-3}$. Analysis is focused on elucidating the collision and agglomeration behaviour throughout the channel flow over time. A statistically steady state for collision and agglomeration rate is observed 10 non-dimensional time units after the particles have been injected which persists until at least $t^* = 50$. Results indicate a decrease in particle agglomeration efficiency as diameter is increased, which provides for a reduction in agglomeration rate at large time scales as the particles begin to aggregate and the mean agglomerate diameter increases. Further to this, the normalized number of collisions is similar in all simulations, with the smallest particles showing a slightly increased collision rate. Arguments associated with energy dispersed in collisions are presented to substantiate these findings. Collision rates across the channel are approximately constant with an increase close to the walls which, when normalized by the total number of primary particles, are actually favoured by smaller particles. Finally, agglomeration outcomes after a collision are shown to be more likely towards the channel centreline, since the particle dynamics in this region favour collisions with low relative velocity.

1 INTRODUCTION

Particle-laden flows with high mass loading are ubiquitous in nature and industry, such as atmospheric transport [1], blood drop forensics [2] and mineral processing [3]. Of relevance to this study is the nuclear industry, which depends on a comprehensive understanding of the particle-scale and system-scale processes associated with such flows in order to predict the long-term behaviour of waste suspension slurries [4]. At present, a key challenge exists in the ability to transport legacy nuclear waste material from historic ponds and silos at Sellafield, UK to interim locations where they can be safely stored. In order to do so, knowledge must be generated surrounding the aggregation and interaction dynamics of densely dispersed two-

phase fluid-solid flow systems. Of importance is the long term morphology of the particles (size, shape and interaction profile information) in order to predict potential hazards over long time-frames. Fundamental knowledge of this kind could also be used to improve current waste transport designs.

At high particle-fluid volume fractions, the dynamics of both phases are governed by interparticle collisions, which in most cases can lead to particle-particle adhesion or agglomeration due to electrokinetic interactions between the dispersed phase elements [5]. These mechanisms cause long-term particle morphology changes which increase the risk of blockages, local concentration peaks and poor heat-transfer conditions. Furthermore, modifications to the particle concentration field can then impact on the turbulence properties of the carrier fluid, affecting the transport efficiency. The present study focuses on developing computational tools to predict and quantify these phenomena, before exploiting them to elucidate the physics surrounding long-term particle-particle agglomeration in wall-bounded flows.

Motivated by the inherent impracticality of experimental studies to capture individual particle-particle interactions on a sufficient analytical scale, along with the recent advances in computational performance, fluid dynamics modelling has become a powerful tool to study such phenomenon for multi-phase fluid flows. Typically, the carrier phase is simulated using direct numerical simulation (DNS) or large eddy simulation (LES), however the latter has been shown to provide less accurate results for dense flows, since the unresolved scales fail to provide the correct two-way coupled forcing field back to the continuous phase [6], despite its computational cost advantages. Over the last few decades, DNS has been used along with Lagrangian particle tracking (LPT) to study a wide variety of turbulent systems containing particles, droplets and bubbles. The majority of these studies simulate particles in isotropic or wall-bounded turbulence and focus on behaviours such as dispersion, wall deposition, entrainment, resuspension, turbulence modulation and particle-particle collisions.

The focus of the present work relies on modelling post-collision effects (i.e. adhesion or bouncing). Work in this field is sparse, despite most real multiphase systems possessing electrokinetic dynamics at close interparticle distances [7]. Typical attempts to consider agglomeration are divided into either stochastic [8], wherein the particles stick based on the outcome of a random process, or deterministic [9] approaches. In the deterministic approach an adhesion requirement is usually based on collision momentum [10, 11], kinetic/potential energy considerations [12] or local flow properties.

The present work utilizes a model based on energy budget arguments during the collision which has previously been successfully applied to the LES of multiphase turbulent channel flows [13]. We here aim to expand on this work by switching to a DNS continuous phase solver, which will allow us to further elucidate the fundamental dynamics which determine particle-particle adhesion throughout the various regions of the turbulent channel flow. In order to relate the present work to the systems present in the nuclear waste processing industry, we consider mechanical and chemical properties matching those of spherical calcite particles in water [14], which is a frequently used simulant for radioactive waste material.

2 METHODOLOGY

2.1 Fluid flow simulation

The spectral element method-based code Nek5000 is used to obtain a carrier-fluid field representing a fully developed turbulent channel flow. This was chosen due to its impressive and reliable testing and validation history, along with its scalability in terms of parallelisation. The element discretization ensures that all the smallest length and time scales are resolved, down to the structures and processes associated with the Kolmogorov length scale. The code solves the incompressible Navier-Stokes (NS) equations to 7th order accuracy on a Cartesian structured grid which consists of $27 \times 18 \times 23$ elements (i.e. 5.7M nodes). The elements are distributed more densely in the near-wall region in order to capture the smaller scales of turbulence in this location. The non-dimensional NS equations are presented in Eqs. (1) and (2), with distances, velocities and densities normalized by the channel half-height, δ, the bulk velocity, U_B, and the fluid phase density, ρ_F, respectively. From here on, any quantity with an asterisk (*) denotes a variable non-dimensionalised in this manner.

$$\boldsymbol{\nabla} \cdot \boldsymbol{u}^* = 0 \tag{1}$$

$$\frac{\partial \boldsymbol{u}^*}{\partial t^*} + \boldsymbol{u}^* \cdot \boldsymbol{\nabla} \boldsymbol{u}^* = -\boldsymbol{\nabla} p^* + \frac{1}{Re_B} \boldsymbol{\nabla} \cdot \boldsymbol{\tau}^* + \boldsymbol{f}^*_{2W,i} + \boldsymbol{f}^*_{PG} \tag{2}$$

Here, $\boldsymbol{u}^*$ is the fluid velocity, p^* is the fluid pressure, Re_B is the bulk Reynolds number defined as $Re_B = U_B \delta / \nu_F$, ν_F is the fluid kinematic viscosity and $\boldsymbol{\tau}^*$ is the viscous stress tensor. The additional term $\boldsymbol{f}^*_{2W,i}$ is cell-dependent and accounts for the two-way momentum exchange between particles in that cell and the surrounding fluid. Finally, the term $\boldsymbol{f}^*_{PG}$ is constant and accounts for a pressure gradient across the channel in the streamwise direction.

The NS equations are solved across the computational position domain (x, y, z), which corresponds to a $12\delta \times 2\delta \times 6\delta$ channel as illustrated in Fig. 1. We define x to be the streamwise direction, y to be the wall-normal direction, and z to be the spanwise direction. Periodic boundary conditions are enforced in the streamwise and spanwise directions, whereas the wall-normal axis uses no-slip conditions at $y^* = \pm \delta$. The flow rate is maintained by a constant pressure gradient. Using non-dimensional parameters this is:

$$\boldsymbol{f}^*_{PG} = \frac{\partial p^*}{\partial x^*} \widehat{\boldsymbol{x}} = \left(\frac{Re_\tau}{Re_B} \right)^2 \widehat{\boldsymbol{x}} \tag{3}$$

where Re_τ is the shear Reynolds number for the flow. The present simulations were carried out at $Re_B = 2800$ which corresponds to $Re_\tau = 180$. A constant fluid timestep of $\Delta t^*_F = 0.01$ was used throughout.
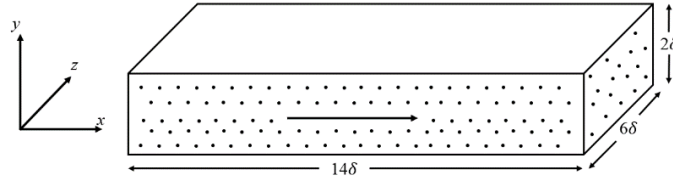
Figure 1: Schematic of the multi-phase turbulent channel flow at $Re_\tau = 180$.

2.2 Particle advection

To simulate the advection of large quantities of solid spherical particles throughout the fluid flow field, an LPT has been developed which runs concurrently after each fluid solution step. The non-dimensional Newtonian equations of motion for each particle are integrated to obtain trajectories at each timestep. The equation is based on the Maxey-Riley (MR) force-balance [15] and in the present work, contributions from drag forces, along with shear lift, virtual mass and pressure gradient forces are considered, since the study entails particles with low density ratio. The only term we neglect from the MR equation is the Basset history force term which would involve very long computation times for minimal increase in accuracy [16].

The Newtonian equations of motion for velocity and acceleration are, respectively:

$$\frac{\partial x_P^*}{\partial t^*} = u_P^* \tag{4}$$

$$\frac{\partial u_P^*}{\partial t^*} = \underbrace{\frac{3 C_D |u_S^*|}{4 d_p^* \rho_P^*} u_S^*}_{Drag} + \underbrace{\frac{3}{4} \frac{C_L}{\rho_P^*} (u_S^* \times \omega_F^*)}_{Lift} + \underbrace{\frac{1}{2\rho_P^*} \frac{D' u_F^*}{Dt^*}}_{Virtual\ Mass} + \underbrace{\frac{1}{\rho_P^*} \frac{D u_F^*}{Dt^*}}_{Pressure\ Gradient} \tag{5}$$

In Eqs. (4) and (5), x_P^* represents the coordinates of the particle position, u_P^* is the particle velocity, $u_S^* = u_F^* - u_P^*$ is the particle-fluid slip velocity, d_P^* is the diameter of the particle non-dimensionalised by the channel half-height, ρ_P^* is the particle-fluid density ratio and ω_F^* is the fluid vorticity at the particle position given by $\omega_F^* = \nabla \times u_F^*$. The drag coefficient, C_D, is taken from standard empirical observations [17] and the lift term uses the Saffman-Mei [18, 19] coefficient. A fourth-order accuracy Runge-Kutta method was used to integrate Eqs. (4) and (5) to obtain each particle's new position and velocity at each fluid step. The timestep used in the integration scheme was equal to that of the fluid, $\Delta t_P^* = 0.01$.

2.3 Two-way coupling

To account for each particle's inertial feedback effect on the fluid phase, an additional source term in the Navier-Stokes equations was included:

$$f_{2W,i}^* = \frac{1}{V_i^*} \sum_{j=1}^{N_P} \frac{\partial u_{P,j}^*}{\partial t^*}, \tag{6}$$

where V_i^* is the volume of computational cell i, and N_P is the total number of particles in that cell. This is applied at each fluid flow timestep and uses the particle acceleration calculation from the previous timestep.

659

2.4 Four-way coupling

The LPT also considers hard-sphere inelastic collisions between binary particles in order to predict more accurately systems at increased volume fraction. It is assumed here that the time it takes for a full collision to occur (touch, contraction, expansion and recoil) is lower than the particle integration timestep. We also assume that any other interactions between the particles are negligible, other than in the case of van der Waals attraction (which is modelled separately). A deterministic binary search algorithm is also implemented as described in Breuer and Almohammed [20] in order to reduce the computational cost associated with collision identification from $O(N_P^2)$ to $O(N_P)$.

Once identified, resultant velocities and positions are determined using kinetic-energy and momentum conservation equations, with particles also deflected a short distance, accounting for the time they spent travelling 'inside' their collision partner.

2.5 Deterministic energy-based agglomeration model

Upon collision, particles satisfying a certain energetic condition will agglomerate with their partner, producing a larger particle with volume equivalent to that of the two initial particles. The model, which is based upon the work of Njobuenwu and Fairweather [13], assumes that a collision will produce an agglomeration event if the resulting collision energy (after dissipation due to inelastic collision) is insufficient to overcome the attractive van der Waals potential between the two colliders, accounting for plastic deformation at the contact surface. The requirement is:

$$\boldsymbol{u}^{*2}_{P,r} - \frac{(1-e_n^*)(\boldsymbol{u}^*_{P,r} \cdot \widehat{\boldsymbol{n}})^2}{|(\boldsymbol{u}^*_{P,r} \cdot \widehat{\boldsymbol{n}})|} \leq \frac{H^*}{6\delta_0^{*2}} \left[\frac{6(1-e_n^*)}{\pi^2 \rho_P^* \bar{\sigma}^*} \left(\frac{d_{P,1}^{*3} + d_{P,2}^{*3}}{d_{P,1}^{*2} d_{P,2}^{*2} (d_{P,1}^{*2} + d_{P,2}^{*2})} \right) \right]^{\frac{1}{2}}, \quad (7)$$

where $\boldsymbol{u}^*_{P,r}$ is the relative particle collision velocity, e_n^* is the coefficient of normal restitution, $\widehat{\boldsymbol{n}}$ is a unit vector pointing from particle 2 to particle 1, H^* is the non-dimensional Hamaker constant of the fluid-particle phase, δ_0^* is the minimum contact distance, $\bar{\sigma}^*$ is the maximum contact pressure and $d_{P,i}^*$ is the diameter of particle i. If the requirement in Eq. (7) is met, then the particles agglomerate forming a new volume-equivalent spherical particle. The new diameter is therefore:

$$d_{agg}^* = \sqrt[3]{d_{P,1}^{*3} + d_{P,2}^{*3}}. \quad (8)$$

Positions and velocities of the agglomerate are also adjusted accordingly. Specifically:

$$\boldsymbol{u}_{agg}^* = \frac{1}{d_{agg}^{*3}} (d_{P,1}^{*3} \boldsymbol{u}_{P,1}^* + d_{P,2}^{*3} \boldsymbol{u}_{P,2}^*), \quad (9)$$

$$\boldsymbol{x}_{agg}^* = \frac{1}{2} (\boldsymbol{x}_1^* + \boldsymbol{x}_2^*), \quad (10)$$

where $\boldsymbol{u}_{agg}^*$ is the new velocity of the agglomerate and $\boldsymbol{r}_{agg}^*$ is the new position of the agglomerate.

3 RESULTS AND DISCUSSION

3.1 Unladen fluid flow statistics

The simulations were first performed unladen, allowed to develop from an arbitrary initial flow field to a state of statistically stationary turbulence. When the first and second moments of the velocity distribution across the channel were unchanging, the statistics were zeroed and new distributions were obtained between $0 \leq t^* \leq 300$, with t^* representing the time after the statistics were reset.
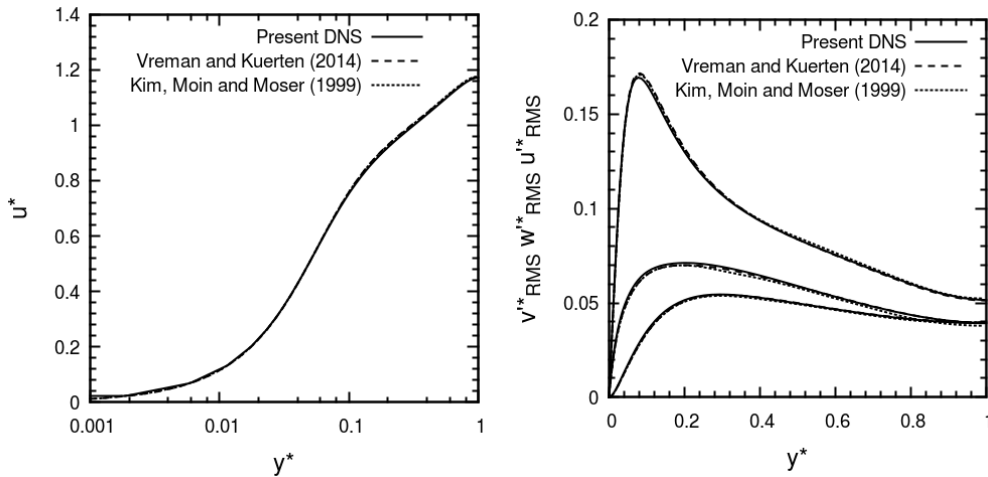

Figure 2: Statistical moments of unladen $Re_\tau = 180$ turbulent channel flow velocity field. Left: Mean streamwise velocity; Right: root mean square of streamwise, spanwise and wall-normal (top to bottom) velocity fluctuations. Present work (solid line) is compared with Vreman and Kuerten [21] (dashed) and Kim, Moin and Moser [22] (dotted).

The continuous phase predictions for mean streamwise velocity and turbulence intensities are presented in Fig. 2, which are compared to the work of [21] and [22] with excellent agreement obtained in all statistical moments considered.

3.2 Particle-laden flow statistics

Particles with diameters ranging between 202.5μm and 405.0μm were injected into the turbulent channel flow randomly throughout the domain. Initial velocities were set to be equivalent to that of the local fluid, obtained via spectral interpolation. The mechanical and chemical properties of each particle set are presented in Table 1.

Table 1: Particle-phase mechanical and chemical properties with dimensional equivalents based on calcite particles in a $\delta=0.02$m water channel at $Re_\tau = 180$.

Parameter	$St^+=0.5$	$St^+=1$	$St^+=2$	Unit
St^+	0.5	1	2	-
St^*	0.043	0.086	0.173	-
τ_P	6.17	12.35	2.47	ms
ρ_P	2710	2710	2710	kg m^{-3}
ρ_P^*	2.71	2.71	2.71	-
d_P	202.5	286.4	405.0	μm
d_P^*	0.0101	0.0143	0.0202	-
d_P^+	1.82	2.58	3.64	-
Θ_P	10^{-3}	10^{-3}	10^{-3}	-
N_P	309,185	109,313	38468	-
Δt^*	0.01	0.01	0.01	-
Δt^+	0.12	0.12	0.12	-
A	3.8×10^{-20}	3.8×10^{-20}	3.8×10^{-20}	J
A^*	2.42×10^{-16}	2.42×10^{-16}	2.42×10^{-16}	-
δ_0	2.0×10^{-10}	2.0×10^{-10}	2.0×10^{-10}	m
δ_0^*	1.0×10^{-8}	1.0×10^{-8}	1.0×10^{-8}	-
$\bar{\sigma}$	3.0×10^8	3.0×10^8	3.0×10^8	Pa
$\bar{\sigma}^*$	0.15×10^8	0.15×10^8	0.15×10^8	-
e_N	0.4	0.4	0.4	-

All simulations presented here were performed four-way coupled with the post-collision agglomeration mechanism switched on. Figure 3 demonstrates the time evolution of the number of particle collisions and agglomerations over the course of the time period $0 \leq t^* \leq 50$, where t^* now refers to the time after particle injection. Note that all quantities here have been normalized by the initial number of particles, N_P, which differs in each simulation to preserve a constant volume fraction between the studies.

The left plot indicates a very similar collision rate for all three particle diameters, with the larger particles exhibiting fewer collisions. This is explicable by the constant volume fraction for all three sizes. Furthermore, the particle's possess similar Stokes numbers which are all in the tracer regime, and so particle-fluid interaction dynamics such as low-speed streak clustering will be minimal. The righthand plot indicates varied behaviour in terms of the number of agglomeration events over time. The rate is approximately constant for all three particle diameters, and is much greater for the smaller particles than for the larger ones. Particle size plays an important role in the energetics associated with Eq. (7), and so provided the particles collide, those with lower diameter are more likely to agglomerate. Clearly, as the particles in the system begin to agglomerate, the mean particle diameter will increase, meaning the agglomeration rate will start to decrease over time, since adhesion of large particles is unfavourable.
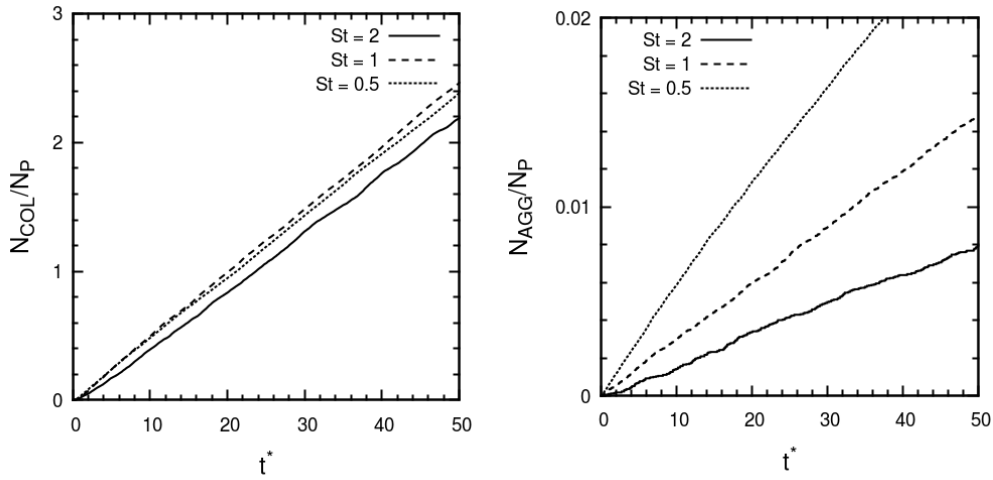
Figure 3: Effect of Stokes number on the temporal evolution of total number of particle-particle collision (left) and agglomeration (right) events normalized by the initial number of injected primary particles.

The left plot in Fig. 4 illustrates the rate of agglomeration, given a collision has occurred. After a short initial transient period, the rate reaches a steady state, with larger particles once again exhibiting lower frequency of agglomeration. Since this quantity is normalized by the number of collisions, it is expected that this rate will settle to a constant value as the simulation evolves. The right plot in Fig. 4 shows the evolution of the mean number of agglomerated primary particles over time. Again, we observe that the smaller particles exhibit more agglomeration events and as such, more primary particles form constituents of agglomerates as the simulation evolves.
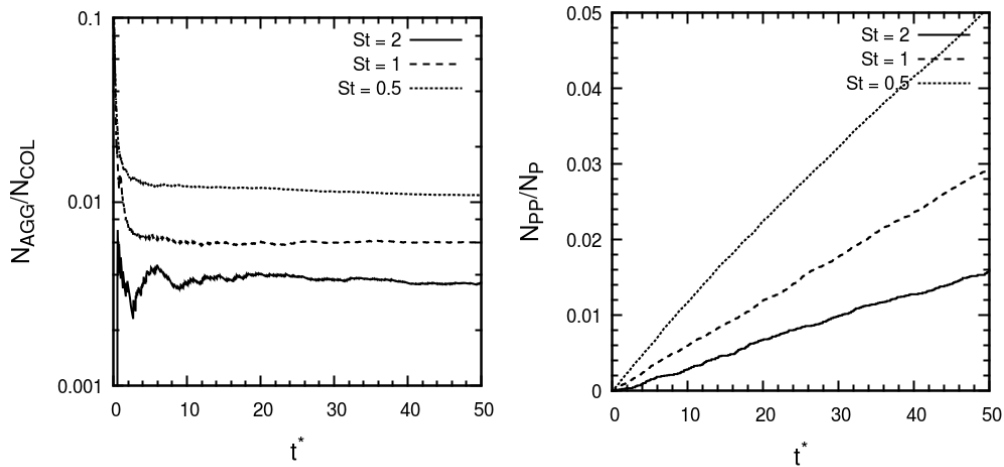

Figure 4: Effect of Stokes number on the temporal evolution of the agglomeration rate, N_{AGG}/N_{COL} (left) and on the mean number of agglomerated primary particles (right) normalized by the initial number of injected primary particles.

Figure 5 shows the time evolution of the percentage of agglomerates of size *N*, for each Stokes number particle type. As Stokes number increases, the rate at which *N*=2 and *N*=3 size agglomerates form is reduced. Over the timeframe studied, the number of *N*>2 size agglomerates formed is very low, accounting for below 0.1% of the total number of particles by the end of the simulation.
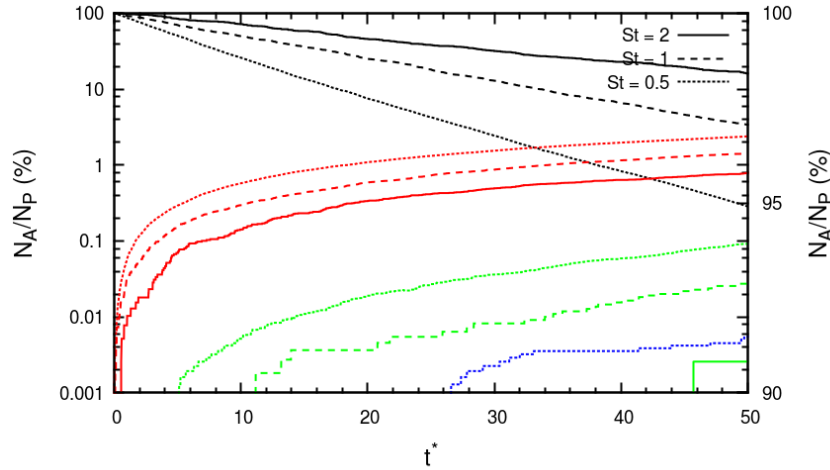

Figure 5: Effect of Stokes number on the temporal evolution of the number of agglomerates of size *N*. Black: *N*=1; red: *N*=2; green: *N*=3, blue: *N*=4.

To determine the variation in collision and agglomeration dynamics in the wall-normal direction of the channel flow, the collision and agglomeration rates have been sampled over the entire simulation time. These are plotted in Fig. 6, note that the scatter in the distributions is due to a limitation in the number of collision events which take place in the time sampled, but despite this the general trends are still evident. The left plot shows the number of collision events across the channel. The largest diameter particles show little variation in collision rate, whereas as the diameter is reduced, the particles at $St^+ = 1$ show more of a preference for collisions taking place in the wall region ($y^* < 0.2$). Although not plotted here, the same trend is observed for the wall-region local particle concentration around this Stokes number. This due to the strong preferential concentration exhibited by these particles, wherein the particle timescale and the fluid vortical timescales are similar. The right plot indicates the variation in agglomeration rate (given a collision has taken place) across the channel. Here, it is evident that the smallest particles actually show an increased agglomeration rate in the centre of the channel, despite the fewest collisions taking place within that region.

This last observation implies that the kinetics associated with agglomeration are more favourable closer to the channel centreline, which is to say that the collisions disperse more energy. Consulting Eq. (7), for a favourable agglomeration, either the term $\boldsymbol{u}^*_{P,r}$ must be small or the term $(1 - e^*_n)\left(\boldsymbol{u}^*_{P,r} \cdot \hat{\boldsymbol{n}}\right)^2 / \left|\left(\boldsymbol{u}^*_{P,r} \cdot \hat{\boldsymbol{n}}\right)\right|$ must be large within this region (or a combination of the two). Previous work [23] indicates an increase in collision angle close to the wall, hence the relative velocity will be large and the kinetic energy dispersed will be low leading to unfavourable conditions for agglomeration, despite the increase in particle concentration.
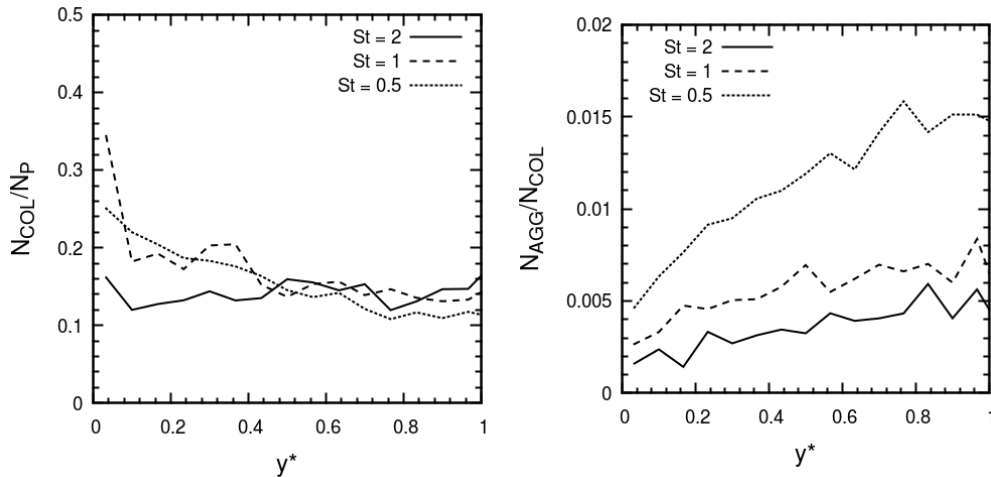
Figure 6: Effect of Stokes number on mean particle collision rate normalized by the initial number of injected primary particles (left) and mean particle agglomeration rate (right) across wall-normal direction of the channel. Sample time is $0 \leq t^* \leq 50$.

4 CONCLUSIONS

A deterministic energy-based agglomeration model has been applied to a DNS-LPT solver in order to determine the effect of particle diameter on collision and aggregation dynamics in multiphase turbulent channel flows. The continuous phase statistics have been validated against two very well regarded DNS databases at the same shear Reynolds number, with excellent agreement obtained.

Time evolution of various statistical quantities indicates that the system posseses a statistically steady state in terms of collision and agglomeration rate at $t^* > 10$, where t^* is the non-dimensional time after the particles have been injected. This persist throughout the entire simulation time considered here ($t^* \leq 50$). All three particle sizes considered exhibit similar collision rates when non-dimensionalized by the total number of injected primary particles, but agglomeration events are much enhanced for smaller particles. This is partially due to the inverse dependance of the required change in van der Waals attraction energy on particle diameter. Agglomeration rates (given a collision has occurred) are also observed to scale inversely with particle size, along with the mean number of primary particles which form a typical agglomerate in the system. Finally, collision and agglomeration rates across the wall-normal direction of the channel indicate that collisions favour the near-wall region. However, agglomeration events are actually more likely towards the channel centreline. We conclude that the bulk flow region posseses particles with favourable dynamic properties for agglomeration, whereas the wall region does not. It is likely that agglomerates forming in the centre of the channel at long timeframes may drift towards the walls through turbophoresis as their Stokes number increases, but these simulations should be extended to confirm such predictions.

5 ACKNOWLEDGEMENTS

REFERENCES

[1]   Folini, D., Ubl, S. and Kaufmann, P., Lagrangian particle dispersion modeling for the high Alpine site Jungfraujoch. *Journal of Geophysical Research: Atmospheres* (2008) **113**(18).

[2]   Chen, R., Zhang, L., Zang, D. and Shen, W., Blood drop patterns: Formation and applications. *Advances in Colloid and Interface Science* (2016) **231**: 1-14.

[3]   Guha, D., Ramachandran, P. and Dudukovic, M., Flow field of suspended solids in a stirred tank reactor by Lagrangian tracking. *Chemical Engineering Science* (2007) **62**(22): 6143-6154.

[4]   Chun, J., Oh, T., Luna, M. and Schweiger, M., Effect of particle size distribution on slurry rheology: Nuclear waste simulant slurries. *Colloids and Surfaces A: Physicochemical and Engineering Aspects* (2011) **384**(1-3): 304-310.

[5]   Krozel, J.W., Electrokinetic interactions between two spheres: The role of surface charge transport in coagulation. *Journal of Colloid and Interface Science* (1994) **163**(2): 437-453.

[6]   Kuerten, J. and Vreman, A., Can turbophoresis be predicted by large-eddy simulation? *Physics of Fluids* (2005) **17**(1): 011701-011704.

[7]   Wang, J., Shi, Q., Huang, Z., Gu, Y., Musango, L. and Yang, Y., Experimental investigation of particle size effect on agglomeration behaviors in gas–solid fluidized beds. *Industrial & Engineering Chemistry Research* (2015) **54**(48): 12177-12186.

[8]   Henry, C., Mineri, J.P., Pozorski, J. and Lefèvre, G., A new stochastic approach for the simulation of agglomeration between colloidal particles. *Langmuir* (2013) **29**(45): 13694-13707.

[9]   Schutte, K.C.J., Portela, L.M. and Twerda, A., Hydrodynamic perspective on asphaltene agglomeration and deposition. *Energy & Fuels* (2015) **29**(5): 2754-2767.

[10]   Balakin, B., Hoffmann, A.C. and Kosinski, P., The collision efficiency in a shear flow. *Chemical Engineering Science* (2012) **68**(1): 305-312.

[11]   Kosinski, P. and Hoffmann, A.C., Extended hard-sphere model and collisions of cohesive particles. *Physical Review E* (2011) **84**(3): 031303.

[12]   Alletto, M., Numerical investigation of the influence of particle-particle and particle-wall collisions in turbulent wall-bounded flows at high mass loadings. (2014). PhD Thesis, Univ. der Bundeswehr, Hamburg (Germany).

[13]   Njobuenwu, D.O. and Fairweather, M., Simulation of deterministic energy-balance particle agglomeration in turbulent liquid-solid flows. *Physics of Fluids* (2017) **29**(8): 083301.

[14]   Vdović, N. and Bišćan, J., Electrokinetics of natural and synthetic calcite suspensions. *Colloids and Surfaces A: Physicochemical and Engineering Aspects* (1998) **137**(1-3): 7-14.

[15]   Maxey, M.R. and Riley, J.J., Equation of motion for a small rigid sphere in a nonuniform flow. *Physics of Fluids* (1983) **26**(4): 883-889.

[16]   Daitche, A., On the role of the history force for inertial particles in turbulence. *Journal of Fluid Mechanics* (2015) **782**: 567-593.

[17]   Schiller, L. and Naumann, A., Fundamental calculations in gravitational processing. *Zeitschrift Des Vereines Deutscher Ingenieure* (1933) **77**: 318-320.

[18]   Saffman, P., The lift on a small sphere in a slow shear flow. *Journal of Fluid Mechanics* (1965) **22**(2): 385-400.

[19]   Mei, R., An approximate expression for the shear lift force on a spherical particle at finite Reynolds number. *International Journal of Multiphase Flow* (1992) **18**(1): 145-147.

[20]   Breuer, M. and Almohammed, N., Modeling and simulation of particle agglomeration in turbulent flows using a hard-sphere model with deterministic collision detection and enhanced structure models. *International Journal of Multiphase Flow* (2015) **73**: 171-206.

[21]   Vreman, A.W. and Kuerten, J.G.M., Comparison of direct numerical simulation databases of turbulent channel flow at $Re_\tau = 180$. *Physics of Fluids* (2014) **26**(1).

[22]   Kim, J., Moin, P., and Moser, R., Turbulence statistics in fully developed channel flow at low Reynolds number. *Journal of Fluid Mechanics* (1987) **177**: 133-166.

[23]   Rai, K., Mortimer, L.F. and Fairweather, M., Effect of Reynolds number on critical Stokes number in turbulent channel flow. in *ICMF2019* (2019) Rio de Janeiro, Brazil.

FLID-SOLID MULTIPHASE FLOW SIMULATOR USING A SPH-DEM COUPLED METHOD IN CONSIDERATION OF LIQUID BRIDGE FORCE RELATED TO WATER CONTENT

KUMPEI TSUJI [1] AND MITSUTERU ASAI [2]

[1] Department of Civil Engineering, Graduate School of Engineering, Kyushu University
Motoka744, Nishi-ku, Fukuoka 819-0395, JAPAN
e-mail: tsuji@doc.kyushu-u.ac.jp,
web page: https://kyushu-u.wixsite.com/structural-analysis

[2] Ph.D., Associate Prof., Department of Civil Engineering, Graduate School of Engineering, Kyushu University
Motoka744, Nishi-ku, Fukuoka 819-0395, JAPAN
e-mail: asai@doc.kyushu-u.ac.jp,
web page: https://kyushu-u.wixsite.com/structural-analysis

Key words: Fluid-Solid multiphase flow, SPH, DEM, Liquid bridge force, Ground collapse.

Abstract. Most of the recent natural disasters such as landslide and tsunamis are complex phenomena in which fluid, ground, structures, etc. affect each other. Therefore, it is necessary to study from various mechanical viewpoints. Among them, in this research, we focus on "soil-water mixed phase flow" where fluid and soil affect each other, such as slope failure and ground collapse. In this study, ISPH method is applied for fluid simulation while DEM is applied for modelling of soil behavior. Then, a general-purpose fluid-solid multiphase flow simulator is developed using the ISPH-DEM coupling method. In addition, in DEM analysis, there are problems in consideration of apparent cohesion related to water content. In our analysis method, in order to adapt to unsaturated ground, the liquid bridge force model proposed in the powder technology field.

1 INTRODUCTION

In Japan, there are huge inundation damage such as the tsunami disaster caused by the Great East Japan Earthquake and torrential rain disasters that occur frequently in various parts of Japan. In order to prevent such inundation damage, structures such as breakwaters and levees that are generally made of soil should prevent inundation. In the case of disasters occurred in recent years, damage could not be completely prevented and minimized. Now that the frequency of heavy rains is high due to the effects of global warming, and there are concerns about huge earthquakes and tsunamis, numerical analysis techniques are needed to know the limit state of structures such as breakwaters and levees. With these background, our research group has developed multi-scale and multi-physics disaster simulator based on particle method in order to estimate the level of damage caused by unexpected natural disasters. Among them, we are developing a fluid-soil multiphase flow simulator for seepage failure, scour failure and ground collapse phenomenon. In this simulator, SPH (Smoothed Particle Hydrodynamics) is applied for fluid simulation, and DEM (Discrete Element Method) is applied for soil behavior

analysis. And coupled analysis is performed through the empirical interaction force of both. In the previous study [1], the seepage and scouring analysis of the breakwater mound is analyzed, and its validity has been confirmed from the comparison with the experiment. In this research, the effect of apparent cohesion with moisture is newly introduced to expand the target area to unsaturated ground. Using the above analysis method, it is reproduced the ground collapse phenomenon that is with few examples. The ground collapse phenomenon is a large deformation and discrete phenomenon accompanied by the segregation of soil masses, and this method based on the particle method is one of the suitable examples.

2 SPH-DEM COUPLED ANALYSIS MODEL

A coupled model of SPH and DEM is important in the multiphase flow analysis. There are two models to couple those methods, one is the "Direct pressure model" we call. In general, a solid in fluid is moved by receiving a dynamic pressure from fluid. In this direct pressure model, a solid also moves in same way. However, if this model is adopted, the diameter of fluid particles need to be much smaller than the solid to calculate a force acting on its surface accurately. It is not desirable to adopt such a computationally expensive method to carry out the real-scale analysis that we aiming for. The other method is "Interaction force model". In this methods, a fluid particle can overlap with solid particles, and a fluid pressure don't act on its surface. Instead of a pressure, an interaction force acts on each particle, a resistance force on fluid and a drag force on solid. In addition, the diameter of fluid particle can be almost the same size with a solid particle. Then, the latter coupled model is adopted because it is possible to reduce the computational cost by using "Interaction force model".

3 ANALYSIS METHOD OF EACH PHASE

3.1 The unified governing equation

In fluid-solid(soil) multiphase flow analysis, fluid flow is regarded as free surface flow in the fluid region and seepage flow in the ground. According to Akbari, H. [2], a unified governing equation modeled to solve free surface flow and seepage flow continuously can be written as:

$$\frac{C_r(\varepsilon)}{\varepsilon}\frac{D\overline{\boldsymbol{v}}_f}{Dt} = -\frac{1}{\rho_f}\nabla P + \boldsymbol{g} + \nu_E(\varepsilon)\nabla^2\overline{\boldsymbol{v}}_f - a(\varepsilon)\overline{\boldsymbol{v}}_f - b(\varepsilon)\overline{\boldsymbol{v}}_f\left|\overline{\boldsymbol{v}}_f\right| \tag{1}$$

$$\frac{D\bar{\rho}_f}{Dt} + \bar{\rho}_f\nabla\cdot\left(\frac{\overline{\boldsymbol{v}}_f}{\varepsilon}\right) = 0 \tag{2}$$

where ρ_f, $\boldsymbol{g}$, P and ε represent the original fluid density, the gravitational acceleration, the fluid pressure and the porosity. $\overline{\boldsymbol{v}}_f$ is the Darcy velocity which is understood as a spatially averaged velocity given by $\overline{\boldsymbol{v}}_f = \varepsilon\boldsymbol{v}_f$, $\boldsymbol{v}_f$ is the intrinsic fluid velocity. Here, $\bar{\rho}_f$ denotes the apparent density, which is given by $\bar{\rho}_f = \varepsilon\rho_f$. This relation regarding the apparent density is necessary to be employed in order to satisfy the volume conservation of fluid inside the porous medium. Some of the coefficient are defined as:

$$C_r(\varepsilon) = 1 + 0.34\frac{1-\varepsilon}{\varepsilon} \tag{3}$$

$$v_E(\varepsilon) = \frac{v_w + v_T}{\varepsilon} \tag{4}$$

$$a(\varepsilon) = \alpha_c \frac{v_w(1-\varepsilon)^2}{\varepsilon^3 d_s^2} \tag{5}$$

$$b(\varepsilon) = \beta_c \frac{(1-\varepsilon)}{\varepsilon^3 d_s} \tag{6}$$

where $C_r(\varepsilon)$ is the inertial coefficient to evaluate the additional resistance force caused by the virtual mass, while $v_E(\varepsilon)$ is the effective viscosity including the kinematic viscosity of the fluid v_w and the turbulent viscosity v_T. The Smagorinsky model is adopted to define the eddy viscosity. $a(\varepsilon)$ and $b(\varepsilon)$ are the linear and non-linear coefficients, α_c and β_c in these equation are defined as the constant in our analysis. Moreover, d_s is the diameter of a solid particle. Here, the fourth and fifth terms in right side of Eq. (1) means the resistance force from the porous medium. This unified governing equation is proposed by Akbari to represent the seepage flow in a fixed porous medium with a low porosity. However, in the floating soil or on the soil mass surface, the soil as a porosity medium also moves and the porosity comes to be high. Therefore, the resistance force terms in Eq. (1) are modified referring to Wen and Yu [3], and the unified governing equation is rewritten as:

$$\frac{C_r(\varepsilon)}{\varepsilon}\frac{D\overline{v}_f}{Dt} = -\frac{1}{\rho_f}\nabla P + g + v_E(\varepsilon)\nabla^2\overline{v}_f \begin{cases} -a(\varepsilon)\varepsilon v_r - b(\varepsilon)\varepsilon^2 v_r|v_r| & (\varepsilon < 0.8) \\ \\ -c(\varepsilon)v_r|v_r| & (\varepsilon \geq 0.8) \end{cases} \tag{7}$$

Here, in considering the movement of the porous medium, the velocity in resistance force terms is changed to relative velocity v_r between fluid and solid which is given by $v_r = v_f - v_s$. In taking a relative velocity, the fluid velocity must not be a spatially averaged velocity $\overline{v}_f$ but an original velocity v_f. Thus, the porosity ε is multiplied by the linear and non-linear coefficients. In addition, the resistance force proposed by Wen and Yu for the high porosity domain ($\varepsilon \geq 0.8$) is considered. C_d is drag coefficient and defined with Reynolds number R_e as follows:

$$C_d = \frac{24\{1 + 0.15 * R_e^{0.687}\}}{R_e} \quad (R_e \leq 1000) \tag{8}$$

$$C_d = 0.43 \qquad\qquad (R_e > 1000) \tag{9}$$

$$R_e = \frac{\varepsilon \rho_f d_s |v_f - v_s|}{\mu_f} \tag{10}$$

According to Eq.(7), the fluid flow outside the porous medium can be given by the Navier-Stokes equation with the porosity $\varepsilon = 1$. On the other hand, the fluid flow inside the porous medium can be described by including the resistance force. Eq. (2) represents the unified continuity equation for a compressible fluid.

The resistance force in Eq. (7) acts on fluid as a resistance force, and it needs to act on the porous medium as a drag force in the opposite sign as well to satisfy the action-reaction law. Thus, this resistance force can be considered as the interaction force between fluid and solid.

3.2 SPH Formulation

In this paper, the Smoothed Particle Hydrodynamics (SPH) method is adopted to solve the unified governing equation for free surface and seepage flow. The basic concept in SPH method is that for any function ϕ attached to particle "i" located at $\boldsymbol{x}_i$ is represented by the following volume summation of contributions from neighbor particles:

$$\phi(\boldsymbol{x}_i) \approx \langle \phi_i \rangle := \sum_j \frac{m_j}{\rho_j} \phi_j W(r_{ij}, h) \tag{11}$$
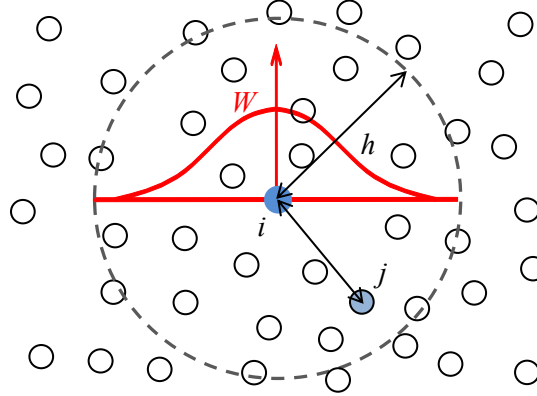

Figure 1: Particle placement and influence radius in the SPH

where m and W are the representative volume of particle and a weight function known as the smoothing kernel function. In this paper, the "Cubic B-Spline function" is adopted as the kernel function. j is a particle in the smoothing length h and r_{ij} is the length of the relative coordinate vector $\boldsymbol{r}_{ij}(= \boldsymbol{x}_j - \boldsymbol{x}_i)$. In this study, the smoothing length set to 2.4 times the initial diameter of the particle. Note that, the triangle bracket $\langle \phi_i \rangle$ means SPH approximation of a function ϕ. The divergence $\nabla \cdot \phi$, the gradient $\nabla \phi$ and the Laplacian $\nabla^2 \phi$ can be assumed by using the above defined SPH approximation as follows:

$$\langle \nabla \cdot \phi_i \rangle = \rho_i \sum_j m_j \left(\frac{\phi_j}{\rho_j{}^2} + \frac{\phi_i}{\rho_i{}^2} \right) \cdot \nabla W(r_{ij}, h) \tag{12}$$

$$\langle \nabla \phi_i \rangle = \rho_i \sum_j m_j \left(\frac{\phi_j}{\rho_j{}^2} + \frac{\phi_i}{\rho_i{}^2} \right) \nabla W(r_{ij}, h) \tag{13}$$

$$\langle \nabla^2 \phi_i \rangle = \sum_j m_j \left(\frac{\rho_i + \rho_j}{\rho_i \rho_j} \frac{\boldsymbol{r}_{ij} \cdot \nabla W(r_{ij}, h)}{\boldsymbol{r}_{ij}{}^2 + \eta^2} \right) (\phi_i - \phi_j) \tag{14}$$

η is the parameter to avoid division by zero and defined by the following expression $\eta^2 = 0.0001(h/2)^2$.

3.3 Formulation of the unified governing equation in the stabilized ISPH method

In this paper, fluid analysis is performed using the stabilized Incompressible SPH method proposed by Asai et al. [4]. In the ISPH method, the governing equations of incompressible fluid are time discretized by a separate method called a projection method based on the predictor modifier method, and the separated equations are spatially discretized based on the basic

formula of SPH method. In this method, the pressure is calculated implicitly and the velocity fields are updated explicitly. In this study, the same idea of ISPH for the Navier-Stoke equation is applied to solve the unified governing equation, Eq. (2) and Eq. (7). To begin with the discretization, $\overline{\boldsymbol{v}}_f$ at $n + 1$ step is written as:

$$\overline{\boldsymbol{v}}_f^{n+1} = \overline{\boldsymbol{v}}_f^* + \Delta\overline{\boldsymbol{v}}_f^* \tag{15}$$

where $\overline{\boldsymbol{v}}_f^*$ and $\Delta\overline{\boldsymbol{v}}_f^*$ are the predictor term and the corrector term. Based on the projection method. Eq. (7) can be separated as:

$$\overline{\boldsymbol{v}}_f^* = \overline{\boldsymbol{v}}_f^n + \frac{\varepsilon\Delta t}{C_r(\varepsilon)}\left(\boldsymbol{g} + \nu_E(\varepsilon)\nabla^2\overline{\boldsymbol{v}}_f^n - \boldsymbol{\gamma}^n\right) \tag{16}$$

$$\Delta\overline{\boldsymbol{v}}_f^* = \frac{\varepsilon\Delta t}{C_r(\varepsilon)}\left(-\frac{1}{\rho_f}\nabla P^{n+1}\right) \tag{17}$$

where $\boldsymbol{\gamma}$ summatizes the resistance terms in Eq. (7) at n step. The pressure P^{n+1} in Eq. (19) is determined by the Pressure Poisson Equation as follows:

$$\nabla^2 P^{n+1} = \frac{C_r(\varepsilon)\rho_f}{\varepsilon\Delta t}\nabla \cdot \overline{\boldsymbol{v}}_f^* \tag{18}$$

During numerical simulation, the 'particle' density may change slightly from the initial value because the particle density is strongly dependent on particle locations in the SPH method. If the particle distribution can keep almost uniformity, the difference between 'physical' and 'particle' density may be vanishingly small. In other words, accurate SPH results in incompressible flow need to keep the uniform particle distribution. For this purpose, the different source term in the pressure Poisson equation can be derived using the 'particle' density. In stabilized ISPH method, the pressure Poisson equation (18) reformulated as:

$$\langle\nabla^2 P^{n+1}\rangle \approx \frac{C_r(\varepsilon)}{\varepsilon}\left(\frac{\rho_f}{\Delta t}\langle\nabla \cdot \overline{\boldsymbol{v}}_f^*\rangle + \alpha\frac{\bar{\rho}_f^n - \langle\bar{\rho}_f^n\rangle}{\Delta t^2}\right) \tag{19}$$

where α is called as the relaxation coefficient and is generally set to be much less than 1.0. In this study, α is set to 0.01. The analysis with the stabilized ISPH method can get good conservation of volume.

3.4 The equation of motion of soil

In this study, the behavior of the soil particles constituting the ground is analyzed by Discrete Element Method (DEM). Here, the soil particles were modeled as spherical DEM particles, its diameter is d_s. In general, the contact detection is done every time step and a DEM particle moves by receiving the contact forces in DEM. In addition to that, the fluid force also acts on the DEM particles in the fluid domain. There some kinds of the fluid forces, however the all of them don't influence the particle motion. In this study, the buoyancy force and drag force are adopted to the fluid forces, the equation of motion of soil in fluid is written as follows with the contact force:

$$m_s\frac{d\boldsymbol{v}_s}{dt} = m_s\boldsymbol{g} - \nabla P V_s + \boldsymbol{F}_d + \sum\boldsymbol{F}_c + \sum\boldsymbol{F}_{coh} \tag{20}$$

$$F_d = \begin{cases} (a(\varepsilon)\varepsilon^2 \boldsymbol{v}_r + b(\varepsilon)\varepsilon^3 \boldsymbol{v}_r |\boldsymbol{v}_r|)\dfrac{V_s}{1-\varepsilon} & (\varepsilon < 0.8) \\ (-c(\varepsilon)\boldsymbol{v}_r |\boldsymbol{v}_r|)\dfrac{V_s}{1-\varepsilon} & (\varepsilon \geq 0.8) \end{cases} \tag{21}$$

where m_s, $\boldsymbol{v}_s$ and V_s are the mass, the velocity and the volume of a soil particle respectively. The second and third terms in right side are the fluid forces, the second is the buoyancy force and the third $\boldsymbol{F}_d$ is the drag force. $\boldsymbol{F}_c$ means the contact force between DEM particles. $\boldsymbol{F}_{coh}$ means the apparent cohesive force related to water content, which is explained in a 3.6 section. The drag force $\boldsymbol{F}_d$ has the same meaning as the interaction force. Therefore, the resistance force for fluid is adopted to the drag force for soil. The drag force acting on one particle is given by Eq. (21).

The equation of angular motion for the spherical DEM is written as:

$$I\frac{d\boldsymbol{\omega}}{dt} = \sum \boldsymbol{T} \tag{22}$$

The contact force between the particles or particle-wall is calculated by the intrusion of a particle with a spring-dashpot model in DEM. The contact force $\boldsymbol{F}_c$ is divided into two components, a repulsive force in the normal direction $\boldsymbol{F}_c^n$ and a friction force in the tangential direction $\boldsymbol{F}_c^t$, and described as:

$$\boldsymbol{F}_c = \boldsymbol{F}_c^n + \boldsymbol{F}_c^t \tag{23}$$

$$\boldsymbol{F}_c^n = (-k\delta^n - \eta|\boldsymbol{v}_r^n|)\boldsymbol{n} \tag{24}$$

$$\boldsymbol{F}_c^t = \begin{cases} (-k\delta^n - \eta|\boldsymbol{v}_r^t|)\boldsymbol{t} & |\boldsymbol{F}_c^t| < \mu|\boldsymbol{F}_c^n| \\ -\mu|\boldsymbol{F}_c^n|\boldsymbol{t} & |\boldsymbol{F}_c^t| \geq \mu|\boldsymbol{F}_c^n| \end{cases} \tag{25}$$

$$\eta = -2ln(e)\sqrt{\frac{k}{ln^2(e) + \pi^2}\frac{2m_i m_j}{m_i + m_j}} \tag{26}$$

where $k, \delta, \eta, \boldsymbol{n}, \boldsymbol{t}$ and e are the stiffness, the displacement, the damping coefficient, normal, tangential unit vector and the coefficient of restitution.

The equation of angular motion for the spherical DEM is written as follows. The torque is calculated from the tangential contact force.

$$I\frac{d\boldsymbol{\omega}}{dt} = \sum \boldsymbol{T} = \sum \boldsymbol{l} \times \boldsymbol{F}_c^t \tag{27}$$

where $\boldsymbol{l}$ indicates the vector from the center of a particle to a contact point.

3.5 Rolling friction

In order to reduce the calculation cost, DEM analysis is carried out using spherical particles whose contact judgment is relatively easy. However, real soil particles have unique concave and convex shapes, and it is impossible to express steep deposition shape. Therefore, in this research, rolling friction is introduced, which is an additional force artificially suppressing particle rotation. There are many rolling friction models proposed from the past research. Among them, in this study, rolling friction proposed by Fukumoto et al.[5] is used, and described as follows:

$$\boldsymbol{M}_r = |\boldsymbol{F}_n|a\widehat{\boldsymbol{\omega}} = |\boldsymbol{F}_n|\lambda r'\widehat{\boldsymbol{\omega}} = \lambda\sqrt{L(2r-L)}|\boldsymbol{F}_n|\widehat{\boldsymbol{\omega}} \tag{28}$$

where r, $\boldsymbol{F}_n$, $\widehat{\boldsymbol{\omega}}$ and L are the radius of particle, the acting force in the normal direction, unit angular velocity vector and displacement. b is the rolling friction coefficient representing the shape characteristic. And also, using a soil sample to be analyzed, examination was conducted by simple preliminary analysis as shown in the next chapter.
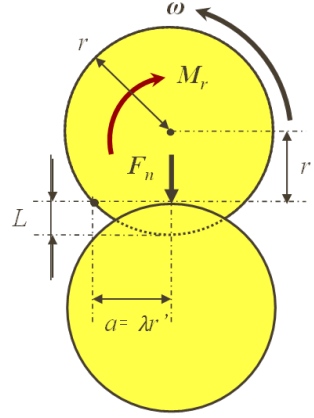

Figure 2: Rolling friction model

3.6 Apparent cohesive force

The method up to the previous section did not take into consideration of the cohesion effect related to the water content of the soil in the unsaturated ground. Depending on its moisture content, the soil forms aggregate shapes by sticking particles together, and the soil clumps become self-supporting. Therefore, by incorporating the effect of the apparent cohesive force into the method, a DEM analysis adapted to dry, saturated and unsaturated state is developed. In this study, the liquid bridge force model proposed by X. Sun et al. [6] is adopted as the apparent cohesive force related to the water content of the soil particles. This force model is presented based on a toroidal approximation of the liquid bridge profile. Its advantage resides in generality, which is applicable to a wide range of liquid volumes, contact angles and radius ratios. In addition, Laplace pressure, which is a suction in soil mechanics, can be taken into consideration. However, since spherical DEM particles are used in this study, the presence of fine particles filling the gaps is ignored. Then, the apparent cohesion, in particular Laplace pressure, is underestimated. In addition, suction is a field that has been studied in soil mechanics, so there is no mechanical model that can be used for DEM. In order to take account of this effect, a conversion parameter κ is introduced to the model proposed by X.Sun et al. , and this value is adjusted by comparison with a simple experiment.

$$\boldsymbol{F}_{coh} = \kappa(\Delta p \pi \rho_{in}{}^2 + 2\pi\gamma\rho_{in})\boldsymbol{n} \tag{29}$$

where Δp, ρ_{in}, γ and $\boldsymbol{n}$ are the Laplace pressure, the internal radius of the liquid bridge, surface tension and unit normal vector.
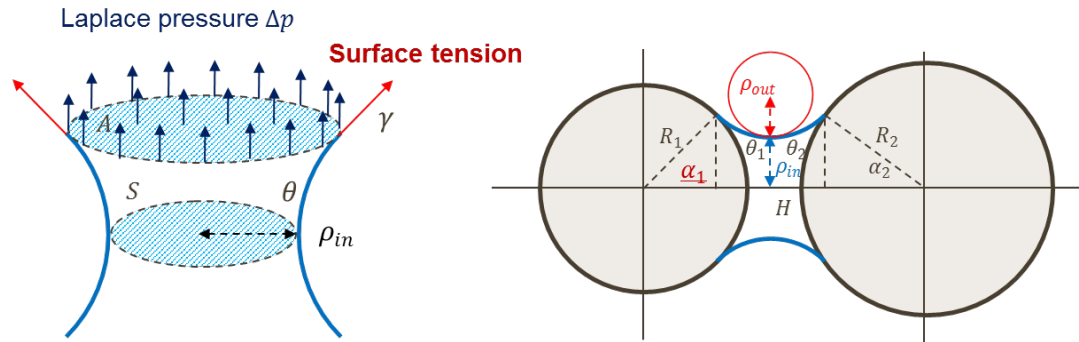
Figure 3: Liquid force model [6]

4   DETERMINATION OF VARIOUS PARAMETERS

It is necessary to identify various parameters corresponding to material property values in advance. Firstly, a pulling test of a cylindrical specimen filled with soil sample is carried out, and various parameters are identified. A simple experiment with dry soil are carried out to identify the rolling friction coefficient λ. Next, a series of experimental test with different water contents is carried out to identify the apparent parameter κ for estimating the magnitude in the apparent cohesion force.

4.1 Rolling friction parameter λ

Using the soil sample used in the road caving collapse experiment, a cylindrical specimen pulling test with a diameter of 5 cm and a height of 10 cm was repeated ten times, and an angle of repose of 26.5 degrees was obtained. As a result of the reproduction DEM analysis, when $\lambda = 0.9$, the angle closest to the repose angle of the experiment, and the same diameter as the sand cone after the experiment was obtained. Therefore, $\lambda = 0.9$ is adopted in this research.
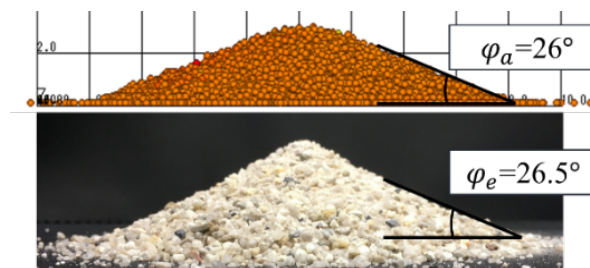

Figure 4: Comparison of angle of repose in experiment and DEM analysis

4.2 Conversion parameter κ in apparent cohesive force

Next, in order to reproduce the collapse behavior of unsaturated soil, the same experiment as previous one using wet sand. In the tests where water content was different, we focused on

the results of rapid lateral deformation after temporary stabilization. This time, the magnitude of the conversion parameter ($\kappa = 15$) required to reproduce this result was determined by DEM analysis.
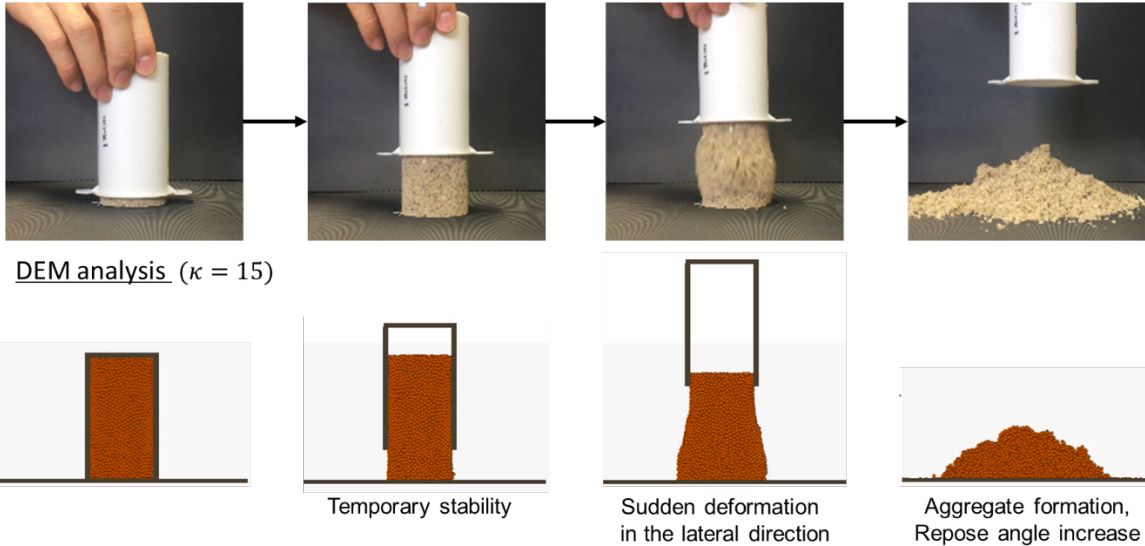
Experiment

DEM analysis ($\kappa = 15$)

Figure 5: Comparison of angle of repose in experiment and DEM analysis

5 ANALYSIS OF GROUND COLLAPSE PHENOMENON

In this research, we focused on the qualitative reproduction of the ground collapse process in the reproduction experiment of the ground collapse phenomenon under the condition corresponding to the experiment conducted by Konishi et al.[7]. A small ground model with a width of 300 mm, a height of 200 mm and a depth of 50 mm is prepared as an analysis model shown as follows.

Table 1: Analysis condition

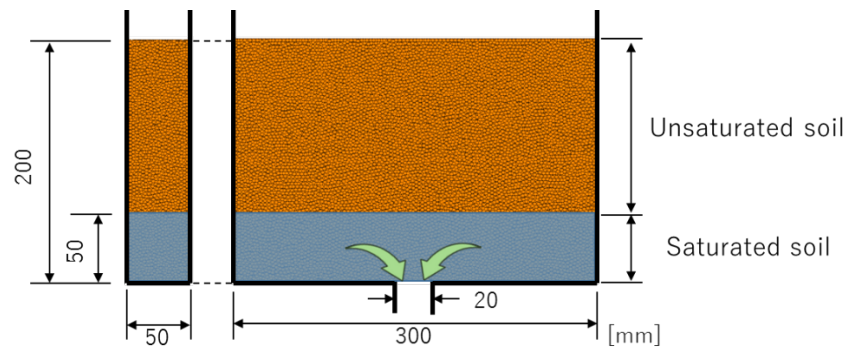| Water (SPH)		
Numbers of particles	Particle size [cm]	Density [g/cm^3]
12,626	0.3	1
Soil (DEM)		
Numbers of particles	Particle size [cm]	Density [g/cm^3]
132,124	0.3	2.6
Restitution coefficient	Spring constant[N/m]	Friction coefficient
0.5	1000	0.57
Rolling friction coefficient λ		Conversion parameter α
0.9		15

Figure 6: The small model of ground collapse phenomenon

5.1 Analysis without water level (only DEM analysis)

At first, the movement of soil particles of wet and dry sand is compared by the presence of apparent cohesion without considering groundwater level. In the case of dry sand analysis, cohesion is not considered, and in the case of wet sand analysis, it is considered.

As a result of the analysis of dry sand, the velocity distribution spreads to the left and right with time, and it has been confirmed that it flows out without stopping like an hourglass. On the other hand, in the case of wet sand, the outflow velocity of soil particles decreased significantly. Furthermore, since the velocity distribution is concentrated around the outflow hole, it can be said that the localization of the behavior can also be reproduced. In the analysis where the cohesion is increased, it is confirmed that the self-supporting of soil mass and the outflow of soil particles stopped. From the above results, it is considered that the behavior of wet sand can be reproduced and verified qualitatively by introducing the effect of adhesion. However, when there is no water, it is not possible to reproduce the hollows and occurring the ground collapse phenomenon.
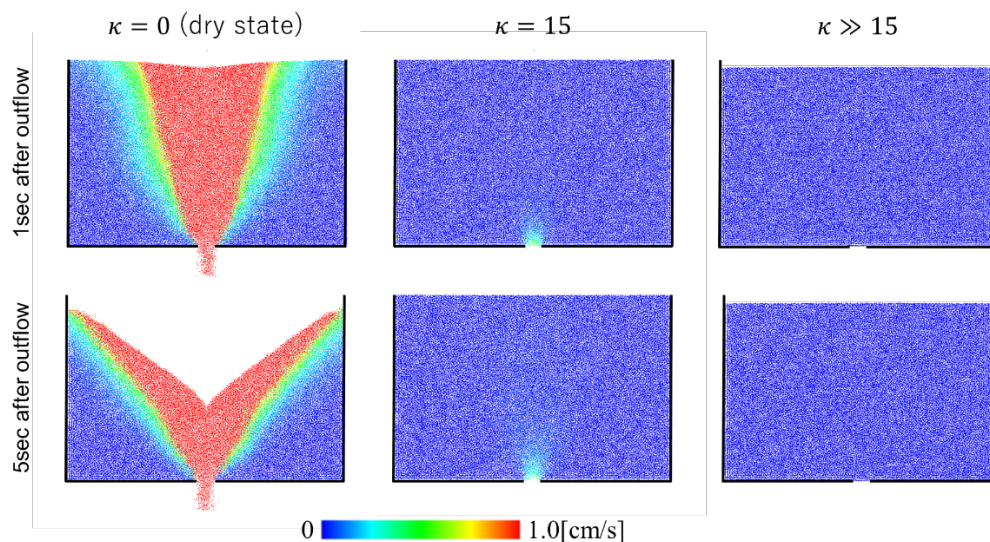

Figure 7: Analysis result without groundwater level (downward velocity ditribution)

677

5.2 Analysis with water level (SPH-DEM coupled analysis)

Next, a water level of 5 cm in height was set as groundwater, and coupled analysis of water (SPH) and soil (DEM) is carried out. In this case, both unsaturated and saturated ground give apparent cohesive force in DEM calculation. The saturated ground below the groundwater level was set to be smaller than the cohesive force of the unsaturated ground.

As a result, due to a large difference in apparent cohesive force near the free surface and the outflow of water, a hollow grows in the horizontal direction, and the ceiling is destabilized, collapsing, collapsing soil drainage, and repeating arched stability of the ceiling…The situation was confirmed.
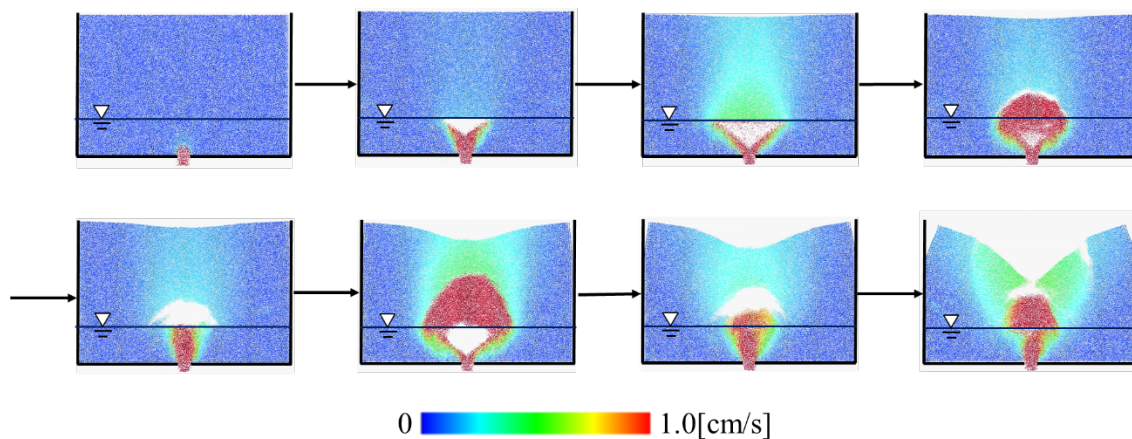

0 ▮▮▮ $1.0[cm/s]$

Figure 8: Analysis result with groundwater level (downward velocity ditribution)
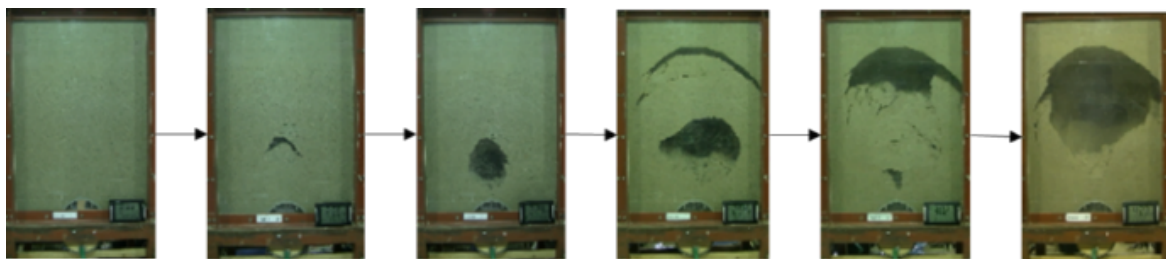

Figure 9: Experiment result conducted by Konishi et al.[7]

The same tendency of collapse has been confirmed in the experiment of Konishi et al. From this study, by carrying out coupled analysis of SPH and DEM, it was possible to show the collapse behavior of the ground sink which has not been reproduced so far.

678

6   CONCLUSIONS

In this study, we tried to analyze the behavior of unsaturated soil considering the apparent cohesion with moisture in the coupled analysis method of the previous research. As a result, in the reproduction analysis of the ground sinking phenomenon, the collapse tendency confirmed in the experiment could be qualitatively reproduced.

Through this research, it was confirmed that the ground collapse phenomenon cannot be reproduced only by increasing the cohesive force. In the future, in addition to the quantitative evaluation of cohesion, we will introduce a cluster DEM model that is composed of can explicitly give the effect of the shape of soil particles without rolling friction. By doing so, sedimentation of the upper ground can be suppressed, and more brittle collapse should be able to be reproduced.

REFERENCES

[1] K. Harasaki and M. Asai, Validation of a fluid-solid multiphase flow simulation by a SPH-DEM coupled method and soil foundation scour simulation with a coarse graining particle model, Transactions of JSCES, No.20182001, Japan, 2018.

[2] Akbari, H., Modified moving particle method for modeling wave interaction with multi layered porous structures, Coast. Eng., Vol.89, pp.1-19, 2014.

[3] C. Wen. and Y. Yu., Mechanics of fluidization, *Chemical Engineering Progress Symposium Series 62*, 100, 1966.

[4] M. Asai, Aly, AM., Y. Sonoda and Y. Sakai, A stabilized incompressible SPH method by relaxing the density invariance condition, Int. J. for Applied Mathematics, Vol. 2012, Article ID 139583, 2012.

[5] Y. Fukumoto, H.Sakaguchi and A. Murakami, Failure Criteria for Geomaterials in Simple Discrete Element Modeling, Int. J. for Applied Mathematics, Vol.67, No.1, Japan, 2011.

[6] X. Sun, M. Sakai, A liquid bridge model for spherical particles applicable to asymmetric configurations, Chemical Engineering Science, 182: 28-43, 2018.

[7] Y. Konishi, K. Fukunaga, S. Oomine, W. Hukutani and D. Takeuchi, Experimental Study on Risks for Underground Hollows Occurrence and Ground Surface Collapse Due to Underground Sewers, Journal of Japan Sewage Works Association, Vol.5, No.2, Japan (1988).

SOLID PARTICLE INTERACTION DYNAMICS AT CRITICAL STOKES NUMBER IN ISOTROPIC TURBULENCE

K. RAI[*], M. FAIRWEATHER AND L.F. MORTIMER

School of Chemical and Process Engineering, University of Leeds, Leeds LS2 9JT, UK
[*]pmkr@leeds.ac.uk

Key words: Direct numerical simulation, Immersed boundary method, Isotropic turbulence, DLVO interaction, Agglomeration.

Abstract. Binary solid spherical particle-particle interactions are studied in forced isotropic turbulence at $Re_\lambda = 29$ and 197 using direct numerical simulation and an immersed boundary method. Isotropic turbulence in a periodic box is forced using a linear forcing method to maintain statistically stationary turbulence, with inter-particle interaction modelled using DLVO interaction forces which include attraction and repulsion due to van der Waals and electric double layer potential forces, respectively. Particle collisions are modelled using the inelastic hard sphere model with a coefficient of restitution of 0.4. The DLVO parameters are chosen to be representative of calcite particles, a simulant of nuclear waste material found in storage ponds in the UK. The Reynolds numbers chosen for the boxes are equivalent to typical values of Re_λ that are found in the bulk flow and viscous sub-layer regions of a turbulent channel flow at $Re_\tau = 180$. The techniques described are used to study the dynamics of critical Stokes number particles in turbulence by analysing probability density functions (PDFs) of collision statistics such as particle displacement and the particles' relative velocities to determine the likelihood of agglomeration. The results indicate that agglomeration can occur in both the Re_λ turbulent boxes considered. However, the occurrence is much more likely at lower Re_λ values due to the higher dispersion of kinetic energy after impact.

1 INTRODUCTION

Particle-laden turbulent flows occur commonly in both natural and industrial environments. Understanding of the dynamics of such flows is of interest to many industries. One application of relevance to the present work is in the nuclear industry. In the UK, most spent nuclear fuel and nuclear waste is stored in ponds or silos, often occurring as a solid-liquid slurry. Over many years the structural integrity of the ponds has been deteriorating and there is an increased need to transport the waste to other safe storage facilities. A key problem remains in knowing how best to transport the solid-liquid slurry in the most efficient, effective and safe way. The present work addresses this issue with the help of particle-laden flow and particle-particle interactions simulations.

One method of simulating particle-laden flows is to consider particles to be point-like, meaning that the particle diameter must be less than the smallest scales found in a turbulent flow, namely the Kolmogorov length scale. By using Lagrangian particle tracking (LPT) in

multi-phase fluids, i.e. through solving the equation of motion for each particle in the flow [1], a relatively good understanding of particle dynamics in fluid flows can be obtained. However, this method is inherently problematic since particles in nature are not point-like. For example, LPT does not accurately resolve all the forces acting on a particle. To overcome this limitation in LPT simulations a more fundamental approach is to use, for example, the immersed boundary method (IBM). IBM emerged from Peskin's work [2] in 1972 on the mathematical modelling of the heart. This method allows a particle to have a finite size and shape, which in turn allows the realistic capturing of all the forces acting on particles in all directions from the fluid. Over the years, authors such as Mark and van Wachem [3], and Tseng and Ferziger [4], have worked on the development of this method, with various degrees of accuracy. However, to date there has been no previous work implementing IBM with resolved DLVO forces, which are the forces that describe the interaction between electrically charged particles.

The novelty of the present work therefore lies in the implementation of IBM using DLVO forces to study the dynamics of interacting particles. Particles not only interact with the fluid turbulence but also with each other through DLVO forces. The study focuses on using IBM to elucidate particle dynamics and the likelihood of particle agglomeration in isotropic turbulent boxes at two Reynolds numbers, based on the Taylor microscale, of $Re_\lambda = 29$ and $Re_\lambda = 197$. Conclusions are drawn by analysing PDFs of the relative velocity and displacement of interacting binary particles for critical Stokes number, $St_k = 1$, particles obtained through ensembles of interactions. Such particles are considered since one question of interest in particle-laden flows is at what Stokes number (for a given concentration) do particles start to affect the flow and turbulence dynamics. Elghobashi [5, 6] has demonstrated that at solid volume fractions between 10^{-6} and 10^{-3} there exists a critical Stokes number. Below this value, particles are considered small and their response time is much smaller than the Kolmogorov time scale, with such low inertia particles prone to becoming trapped in vortical structures of the flow, increasing the fluid turbulence kinetic energy and its dissipation rate. Above the critical Stokes number, particles are considered large and are less likely to respond to local fluctuations in the fluid velocity field and, unlike small particles, are ejected from vortical structures. The net result is that these large particles attenuate the turbulence kinetic energy and its dissipation rate within the fluid flow.

2 METHODOLOGY

2.1 Fluid flow simulation

The spectral-element method code, Nek5000 [7], was used to perform direct numerical simulations of single-phase homogeneous, isotropic turbulent boxes at $Re_\lambda = 29$ and $Re_\lambda = 197$. The domain of the isotropic box was $2\pi \times 2\pi \times 2\pi$ which was resolved using $48 \times 48 \times 48$ elements of 7th order, such that there were $336 \times 336 \times 336$ (or a total of ~38M) nodes in each box. These elements were distributed uniformly inside each box. The Re_λ of the isotropic boxes was chosen to match the Reynolds number that is typical of the bulk flow ($Re_\lambda = 29$) and viscous sub-layer ($Re_\lambda = 197$) regions of a turbulent channel flow at shear Reynolds number, $Re_\tau = 180$.

The code solves the following governing fluid flows equations, i.e. the mass conservation

and Navier-Stokes equation:

$$\frac{\partial \boldsymbol{u}}{\partial t} + \boldsymbol{u} \cdot \nabla \boldsymbol{u} = -\nabla p + \frac{1}{Re} \nabla \cdot \boldsymbol{\tau} + \boldsymbol{f} \tag{1}$$

$$\nabla \cdot \boldsymbol{u} = 0 \tag{2}$$

where $\boldsymbol{u}$ is the fluid velocity field, p is pressure, Re is Reynolds number, τ is the viscous deviatoric stress tensor and $\boldsymbol{f}$ is an arbitrary forcing or source term.

Isotropic turbulence in each box was obtained by implementation of the linear forcing method proposed by Lundgren [8], and Rosales and Meneveau [9], who demonstrated that linear forcing proportional to the velocity in physical space gives the same result as forcing in spectral space, and that linearly forced boxes converge to a statistically stationary state that depends only on domain size and Reynolds number.

It was demonstrated by Rosales and Meneveau [9] that $\boldsymbol{f} = A\boldsymbol{u}'$, where $A = \epsilon/3u_{rms}^2$, ϵ is the dissipation rate and u_{rms} is the root-mean-square (rms) of velocity fluctuations in any direction since isotropy is ensured. This term is a force (in physical space) with an appropriate parameter A necessary to obtain statistically stationary isotropic turbulence. Energy is injected at a variable rate of A until steady state has been achieved. After that, energy is injected at a constant rate of A since both ϵ and u_{rms} will have reached their stationary values. The initial conditions used to initiate the simulations were:

$$\begin{aligned} u &= \cos(y) + \sin(z) \\ v &= \sin(y) + \cos(z) \\ w &= \cos(x) + \sin(y) \end{aligned} \tag{3}$$

The parameters used to obtain the isotropic boxes are presented below in Table 1.

Table 1: Values of the parameter A in $\boldsymbol{f} = A\boldsymbol{u}'$ used to obtain stationary isotropic turbulence.

Re_λ	29	197
A	0.0667	0.1667

2.2 Immersed boundary method

The immersed boundary method represented each particle using an icosphere with 320 triangular faces, as illustrated in Fig. 1. The centroid of each triangular face on the icosphere has associated with it a position and a velocity. The Dirichlet boundary condition at the surface of the icosphere was enforced such that $\boldsymbol{u}_F = \boldsymbol{u}_p + \boldsymbol{\omega}_p \times \boldsymbol{r}_f$ on each particle face, where $\boldsymbol{u}_p$ is the particle linear velocity, $\boldsymbol{\omega}_p$ is the particle angular velocity and $\boldsymbol{r}_f$ is the position vector from the centre of the particle to the centroid of a face.

To ensure the immersed boundary condition was met, a second-order accurate ghost-cell method was employed [4]. Every time-step, each cell in the domain was identified as external fluid, an internal ghost-cell or internal fictitious fluid. The ghost cell was defined such that the immersed boundary intersected the cell and contained the cell midpoint. Internal and external fluid cells are those either inside or outside of the immersed boundary, respectively. The

velocities at the ghost-cells were maintained each time-step such that, through trilinear interpolation across the three closest neighbouring cells, the fluid velocity on the boundary was exactly the local face velocity [10].
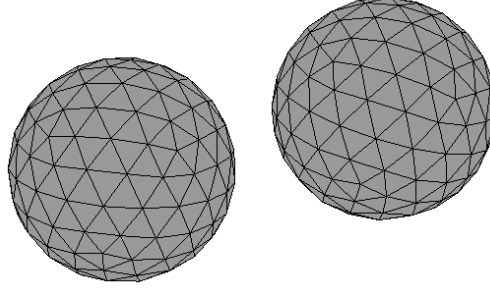

Figure 1: Icosphere mesh with 320 triangular faces.

The advection and rotation of each particle was derived from the hydrodynamic forces acting on an icosphere, as defined in Eq. (4) [10]:

$$F_j = \sum_{f=1}^{N_f} \left(-P^f \delta_{ij} + \tau_{ij}^f\right) n_j^f dS^f,$$ (4)

where the F_j is the total force acting on a particle, j is the current face, N_f is the total number of faces in a particle, P^f is the pressure interpolated at the centroid of the face, τ_{ij} is the viscous stress tensor, n_j^f is the unit normal vector to the face f and dS^f is the surface area of face f.

The orientation of a particle was tracked using quaternions. A unit quaternion describes the rotation of $\boldsymbol{v}$ by angle θ about the axis in the direction of $\boldsymbol{u}$ by $\boldsymbol{v}' = qvq^{-1}$, where $q(v_0, \boldsymbol{q}) = cos(\theta/2) + sin(\theta/2)\boldsymbol{u}$, and $\boldsymbol{u} = u_1 i + u_2 j + u_3 k$ is a unit vector, θ is the angle of rotation and $\boldsymbol{v}' = qvq^{-1} = \boldsymbol{v} + 2q_0(\boldsymbol{v} \times \boldsymbol{q}) + 2(\boldsymbol{v} \times (\boldsymbol{v} \times \boldsymbol{q}))$. The time evolution of the quaternion $\boldsymbol{Q}$ is described by the differential equation:

$$\frac{d\boldsymbol{Q}}{dt} = \begin{pmatrix} \dfrac{dq_0}{dt} \\ \dfrac{dq_1}{dt} \\ \dfrac{dq_2}{dt} \\ \dfrac{dq_3}{dt} \end{pmatrix} = \begin{pmatrix} q_0 & -q_1 & -q_2 & -q_3 \\ q_1 & q_0 & -q_3 & q_2 \\ q_2 & q_3 & q_0 & q_1 \\ q_3 & -q_2 & q_1 & q_0 \end{pmatrix} \begin{pmatrix} 0 \\ \omega_{x'} \\ \omega_{y'} \\ \omega_{z'} \end{pmatrix},$$ (5)

where $\boldsymbol{\omega} = (\omega_{x'}, \omega_{y'}, \omega_{z'})$ is the angular velocity vector in the particle co-moving frame. The unit quaternions were normalised to one after each time step to minimise the error due to

floating-point precision issues. The corresponding governing equation for angular acceleration can be expressed as:

$$I\,\frac{d\boldsymbol{\omega}}{dt} = \boldsymbol{T} = \sum_i \boldsymbol{r_i} \times \boldsymbol{F_i} \tag{6}$$

where $\boldsymbol{\omega}$ is the angular velocity of the sphere, $\boldsymbol{T}$ is the torque, $\boldsymbol{r_i}$ is the distance vector to the centroid of the face from the centre of a particle, $\boldsymbol{F_i}$ is the hydrodynamic force and $\boldsymbol{I}$ is the moment of inertia tensor of a solid sphere, given as:

$$\boldsymbol{I} = \begin{pmatrix} 2/5mr^2 & 0 & 0 \\ 0 & 2/5mr^2 & 0 \\ 0 & 0 & 2/5mr^2 \end{pmatrix}, \tag{7}$$

where m is the mass of the sphere and r is its radius.

Once the particle was advected, all pairs of particles were checked for potential collisions. The condition required for collision is the inter-surfacial distance is less than zero. The particles collided inelastically using a hard-sphere approach with the coefficient of restitution of 0.4 during the time of collision.

Particle-particle interaction was modelled using DLVO theory developed by Derjaguin and Landau [11], and Verwey and Overbeek [12]. It was proposed that the interaction between two electrically charged spheres can be expressed as:

$$\boldsymbol{f} = -\frac{edl}{\kappa}\,e^{-\kappa d_p} + \frac{A\,r_p}{6\,d_p^2} \tag{8}$$

where the first term on the right hand side is due to the electric double layer, and the second is due to van der Waals potential, with $edl \equiv 64\,\pi r_p n\,k_B T_F \gamma^2$ for the electric double layer. A is the Hamaker constant, n is the number density of electrolyte ions, $\gamma = \tanh\left(\frac{z\,e\,\psi}{4\,k_B T_F}\right)$, ψ is the reduced surface potential, κ is the inverse Debye length, T_F is the fluid temperature, d_p is the inter-surface distance and k_B is the Boltzmann constant.

The parameters associated with calcite particles in water are presented in Table 2.

Table 2: Parameters for calcite particles.

Parameter	r_p	e	ρ_p/ρ_F	A	n	θ	κ	T_F
Value	$50\mu m$	0.4	2.71	$22.3\,zJ$	$10^{-3}M$	$20mV$	$0.1/nm$	$300K$

3 RESULTS AND DISCUSSION

Validation of the IBM used in the simulations was performed in [10], reported here for completeness. It was based on comparing the simulated drag force on an icosphere with 20, 80 and 320 faces against empirical values [13]. The results of those simulations are presented

in Fig. 2. The results show that as the number of faces on the icosphere is increased, the simulated drag force increases in accuracy until at 320 faces the predicted and empirical values are in close accord. In the present work, 320 faces represented a good compromise between accuracy and computational cost.
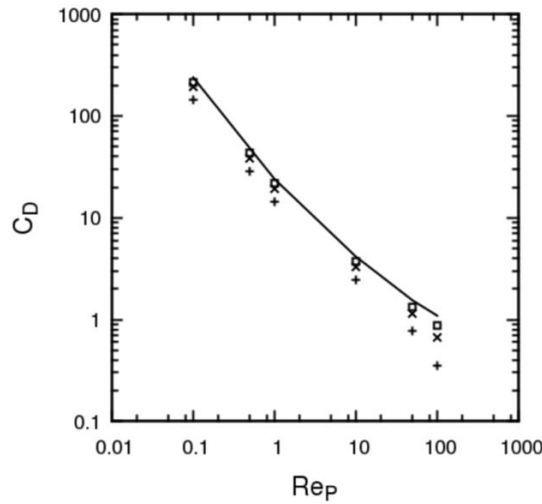

Figure 2: Simulated drag coefficient for icosphere face subdivisions, N_f, of 20 (+), 80 (×) and 320 (□) compared against empirical values (—).

The results presented in Fig. 3 for the isotropic boxes at $Re_\lambda = 29$ and $Re_\lambda = 197$ were validated against the predictions of Rosales and Meneveau [9]. The figure shows the time evolution of the total rms of the fluid velocity fluctuation field. The predictions show that the rms values ultimately reach statistically stationary values of 0.244 and 0.581 for boxes representative of the bulk flow and viscous sub-layer regions, respectively, with these values being in good agreement with those of Rosales and Meneveau [9].
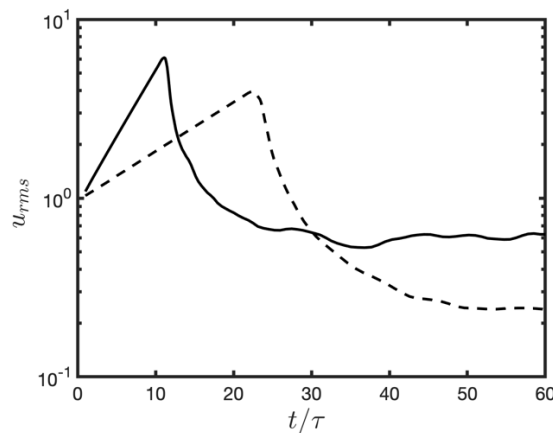
Figure 3: Time evolution of rms of fluid velocity fluctuations in the isotropic boxes (— $Re_\lambda = 197$ and --- $Re_\lambda = 29$).

Figure 4 shows the variation of Re_λ across a steady $Re_\tau = 180$ turbulent channel flow in

the wall normal direction. As we move from the bulk flow region ($y^+ = 36$ to 180) to the viscous sub-layer region ($y^+ = 0$ to $y^+ = 5$) Re_λ increases exponentially as the viscous region is approached, and then drops to zero at the wall. If Re_λ is used as a measure of turbulence, then the various regions in a turbulent channel flow can be simulated as an isotropic turbulent box by generating the required level of Re_λ in the box. By studying the particle dynamics using IBM in such isotropic boxes, the characteristic features of particle interactions, collisions and agglomeration in particular regions of the turbulent channel flow can be examined in detail.
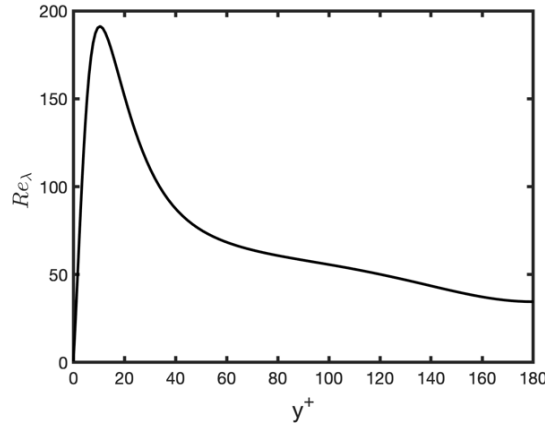
Figure 4: Variation of Re_λ in the wall normal direction of a $Re_\tau = 180$ turbulent channel flow.

Figures 5 and 6 show PDFs of the particle collision velocity and collision angles obtained from LPT simulations of a $Re_\tau = 180$ turbulent channel flow at $St_k = 1$ for the bulk flow and viscous sub-layer regions [14]. The most probable velocities and angles from these results were used as initial conditions for the isotropic box simulations to investigate the interaction of particles in those regions. In the two regions, the most probable collision velocity is dominated by the streamwise direction, with the corresponding collision angles indicating that collisions in the bulk flow region are generally at very low angles, almost head-on, whilst those in the viscous sub-layer show a wider distribution of angles.
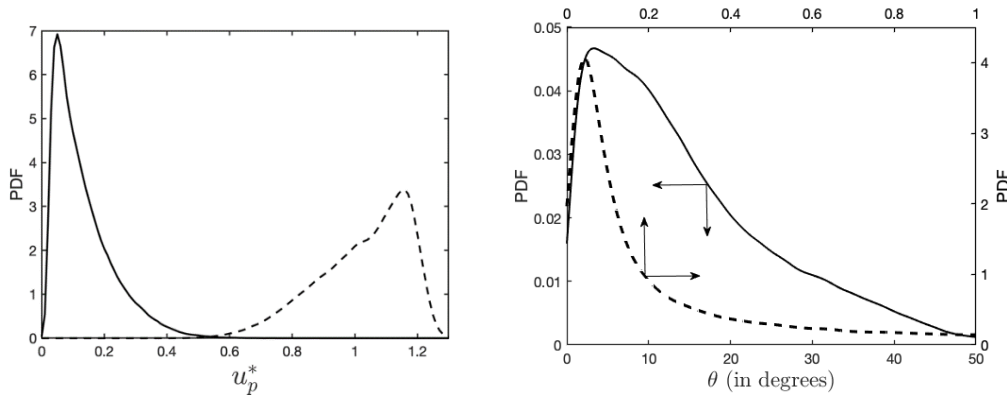

Figure 5: PDFs of streamwise particle collision velocity (left) and collision angle (right), both in viscous sub-layer and bulk flow regions of $Re_\tau = 180$ turbulent channel flow (—— $Re_\lambda = 197$ and --- $Re_\lambda = 29$).
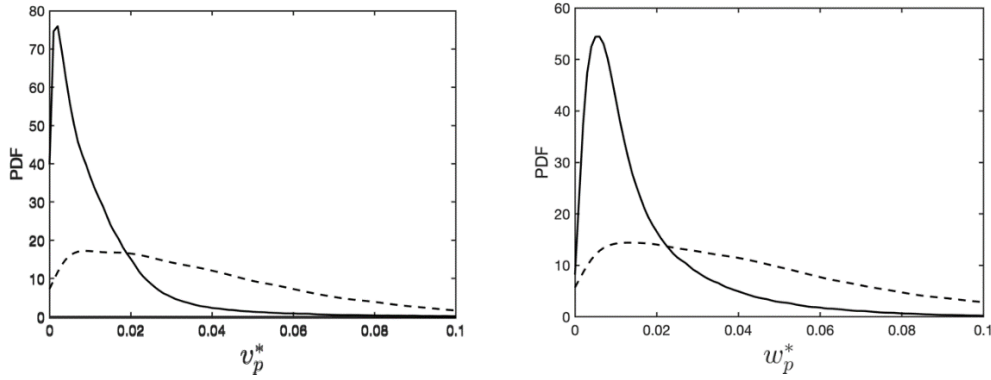
.

Figure 6: PDFs of wall-normal (left) and spanwise (right) particle collision velocities, both in viscous sub-layer and bulk flow regions of $Re_\tau = 180$ turbulent channel flow (—— $Re_\lambda = 197$ and --- $Re_\lambda = 29$).
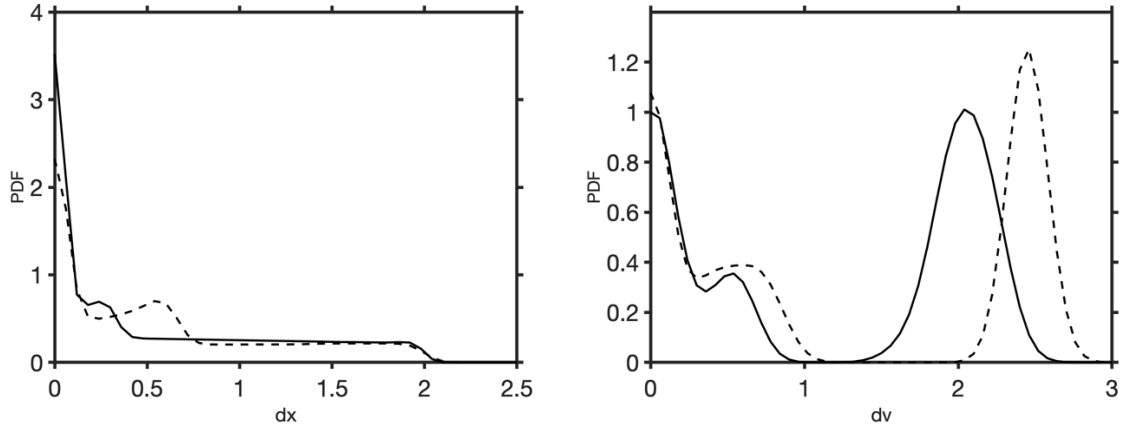

Figure 7: PDFs of particle displacement (left) and particle relative velocity (right) in the two isotropic turbulence boxes (—— $Re_\lambda = 197$ and --- $Re_\lambda = 29$).

Figure 7 shows PDFs of the magnitude of particle displacement and particle relative velocity in each isotropic box, at $Re_\lambda = 197$ (representative of the viscous sub-layer) and $Re_\lambda = 29$ (representative of the bulk flow). The PDFs were obtained by recording the displacement and the relative velocity after each time-step of the simulations, until the 2000th time-step had been reached. After this time, the whole process was restarted by randomly distributing the particles in the box whilst keeping their initial inter-surfacial displacement fixed at $2d_p$.

To analyse the distributions given in Fig. 7, first we consider the displacement of the particles. In the figure, $dx = 2$ represents the initial displacement and $dx = 0$ represents contact of the particles and their possible agglomeration. The two PDFs are similar in terms of their profile in that a peak at $dx = 0$ is observed, indicating interactions which resulted in agglomeration. The larger peak for the viscous sub-layer region suggests that interactions at $Re_\lambda = 197$ resulted in the particles spending more time in an agglomerated state. In both

cases, the PDF drops exponentially as the inter-surfacial distance is increased from $dx = 0$. At $dx \sim 0.25$ (viscous sub-layer) and $dx \sim 0.5$ (bulk flow) each PDF exhibits a minor secondary peak, which is the result of bounces to these separation distances. It is clear that the particles in the bulk flow region bounce almost twice as far as those in the viscous sub-layer. Over the range $0.8 \leq dx \leq 2.0$ the results are almost identical in both case since this is the range over which the particles initially travel as they approach one another. This indicates that during this time turbulence does not significantly affect the relative distance between the particles, which in turn means that all the effects due to turbulence over this period are on the translational and angular motion of the particles. Overall, the results given in this figure demonstrate that the particles in the viscous sub-layer box lose more kinetic energy due to collisions than those in the bulk flow box, which can be attributed to the hydrodynamic forces acting on the particles caused by the turbulence. This indicates that particles in the viscous region at this Stokes number are more likely to agglomerate than particles in the bulk flow region as they lose more energy after any collision which increases the impact of local hydrodynamic forces.

Considering the relative velocity PDFs, in Fig. 7 $dv = 2.5$ represents the initial relative velocity of the particles and $dv = 0$ indicates that the particles have agglomerated (such that they travel with the same velocity). Despite initiating the particles with the same initial relative velocity of 2.5 in both the viscous sub-layer and bulk flow boxes, the particles in the former case lose a significant amount of their velocity, $\sim$20%, equivalent to a loss $\sim$36% of their kinetic energy, in the first few time-steps due to turbulence interactions. As when considering particle displacement, over the range $0.0 \leq dv \leq 1.1$ collisions, bouncing and agglomeration of the two particles occur. The difference due to their initial approach velocity can be seen in the range $0.2 \leq dv \leq 1.1$. In that range, as the particles bounce off one another, the particles in the bulk flow box tend to move faster than those in the viscous sub-layer box, thereby reducing the chance of agglomeration due to their retained speed.

From the analysis of the distribution of both the relative displacement and velocity of the interacting particles, it is therefore clear that agglomeration of particles can occur in both the viscous sub-layer ($Re_\lambda = 197$) and bulk flow ($Re_\lambda = 29$) boxes. However, agglomeration is much more likely in the viscous sub-layer due to significant reductions in the particles' kinetic energy post-collision, in this case a reduction of $\sim$36%.

4 CONCLUSIONS

Direct numerical simulations of boxes of isotropic turbulence were performed using the Nek5000 code based on a 7th-order spectral element method, from which good agreement with the results from Rosales and Meneveau [9] was established. An immersed boundary method using icospheres and inelastic hard sphere collisions was used to describe inter-particle interactions, with inter-particle forces modelled using DLVO theory. Validation of the IBM was performed by comparing the calculated drag force on icosphere particles with 20, 80 and 320 triangular faces with empirical values, with good agreement found for the more resolved icosphere case.

Two regions of a turbulent channel flow were represented using these isotropic boxes at differing values of Re_λ, representative of those occurring in the viscous sub-layer and bulk flow regions of the channel. PDFs of inter-particle interactions, in this case the particle

relative displacement and velocity, were analysed. In both the bulk flow and viscous sub-layer cases, agglomeration was found to occur, but the chances of agglomeration were increased in the viscous sub-layer box. The results indicate that particles in the viscous box lose significantly more kinetic energy after particle impact than in the bulk flow case. Furthermore, in the first few time-steps of a simulation, particles in viscous sub-layer box lost ~20% of their initial velocity, which translates into a loss of ~36% of their kinetic energy which in turn encourages agglomeration of the particles.

Ultimately, this work aims to use simulations of the type described to assess the use of adjustable system parameters to encourage or discourage particle agglomeration in turbulent flows. Through such behavioural modification, it may be possible to accelerate nuclear waste removal and treatment processes in addition to reducing their cost. Future work will also extend these simulations and analysis to cover more realistic non-spherical particles such as prolate and oblate ellipsoids, representative of the needle- and disc-like particles encountered in practice.

5 ACKNOWLEDGEMENTS

REFERENCES

[1] Maxey, M.R. and Riley, J.J. Equation of motion for a small rigid sphere in a nonuniform flow. *Phys. Fluids* (1983) **26**: 883-889.

[2] Peskin, C.S. Flow patterns around heart valves: A numerical method. *J. Comput. Phys.* (1972) **10**:252-271.

[3] Mark, A. and van Wachem, B.G.M. Derivation and validation of a novel implicit second-order accurate immersed boundary method. *J. Comput. Phys.* (2008) **227**:6660-6680.

[4] Tseng, Y.H. and Ferziger, J.H. A ghost-cell immersed boundary method for flow in complex geometry. *J. Comput. Phys.* (2003) **192**:593-623.

[5] Elghobashi, S. On predicting particle-laden turbulent flows. *Appl. Sci. Res.* (1994) **52**:309-329.

[6] Elghobashi, S. An updated classification map of particle-laden turbulent flows. *Proc. IUTAM Symp. Computational Approaches to Multiphase Flow* (2004) 3-10.

[7] Fischer, P.F., Lottes, J.W. and Kerkemeier, S.G. Nek5000 Web page, http://nek5000.mcs.anl.gov (2008).

[8] Lundgren, T.S. Linearly forced isotropic turbulence. *Annual Research Briefs*, Center for Turbulence Research (2003) 461-473.

[9] Rosales, C. and Meneveau, C. Linear forcing in numerical simulations of isotropic turbulence: Physical space implementations and convergence properties. *Phys. Fluids* (2005) **17**:095106.

[10] Mortimer, L.M., Fairweather, M., and Njobuenwu, D.O. Simulation of fully resolved particle-particle interaction in turbulence with behavioural modification. *10th International Conference on Multiphase Flow* (2019) Paper OC.389.

[11] Derjaguin, B. and Landau, L. Theory of the stability of strongly charged lyophobic sols and of the adhesion of strongly charged particles in solutions of electrolytes. *Acta Physicochim.* (1941) **14**:633-662.

[12] Verwey, E.J.W. and Overbeek, J.T.G. Theory of the stability of lyophobic colloids. *J. Colloid Sci.* (1955) **10**:224-225.

[13] Rouson, D.W. and Eaton, J.K. On the preferential concentration of solid particles in turbulent channel flow. *J. Fluid Mech.* (2001) **428**:49-169.

[14] Rai, K., Mortimer, L.F. and Fairweather, M., Effect of Reynolds number on critical Stokes number in turbulent channel flow. *10th International Conference on Multiphase Flow* (2019) Paper OC.056.

TURBULENT HEAT TRANSFER IN NANOPARTICULATE MULTIPHASE CHANNEL FLOWS WITH A HIGH PRANDTL NUMBER MOLTEN SALT FLUID

B.H. MAHMOUD[1*], L.F. MORTIMER[1], M. COLOMBO[1], M. FAIRWEATHER[1], J. PEAKALL[2], H.P. RICE[1], D. HARBOTTLE[1]

[1]School of Chemical and Process Engineering, and [2]School of Earth and Environment,
University of Leeds, Leeds LS2 9JT, UK
[*]bgy9bm@leeds.ac.uk

Key words: Direct numerical simulation, Lagrangian particle tracking, Nanofluid heat transfer, Turbophoresis, Thermophoresis.

Abstract. The growing interest in energy efficient and sustainable technologies has created significant demand for novel heat transfer and thermal energy storage materials, such as nanofluids. The importance of nanoparticle science cannot be underestimated, since the motivation for the manipulation, through nanoparticle addition, of the properties of existing thermofluids (e.g. molten salt) arises from their poor thermal properties which represent a major limitation to the development of more energy-efficient processes. In this work, consideration is given to investigating the role of heat transfer in nanofluids in three-dimensional flows using an advanced computational modelling approach to simulate such flows. In the present work, we use direct numerical simulation coupled with a Lagrangian particle tracking technique. The heat transfer behaviour of a nanofluid within a turbulent wall-bounded flow is investigated, with the fluid phase properties chosen to represent a solar molten salt ($NaNO_3$-KNO_3, 60:40 weight ratio) thermofluid typical of those present in solar thermal power plants. The configuration is a fully developed channel flow with uniform heating/cooling from both walls. The continuous phase is modelled using the open source spectral element-based solver, Nek5000. Predictions of a statistically steady turbulent channel flow at shear Reynolds number $Re_\tau = 180$ and high turbulent Prandtl number $Pr_t = 5.0$ are first obtained and validated. A particle tracking routine is implemented to simulate the dispersed phase which can accommodate one-, two- and four-way coupling between the fluid and discrete phases. To investigate the effect of particles on the turbulent heat flux and temperature field, the nanoparticle concentration response to temperature variations and turbulence is obtained across the channel, with the associated first and second-order flow and temperature field statistics presented. The advantage of the model developed is its ability to study in detail phenomena such as interparticle collisions, agglomeration, turbophoresis and thermophoresis, with the approach also being of value in investigations of the heat transfer performance and long-term thermal stability of nanoparticle dispersions which as yet have not been considered in detail. The outcome of this study allows conclusions to be reached regarding the implications of nanoparticle-seeded molten salts for solar thermal energy storage systems.

1 INTRODUCTION

Particle-laden flows, containing micro-/nano-sized particulate (e.g. particles, colloids and surfactants) have gained increased attention recently because of their wide range of industrial applications. Of particular interest are nanofluids, which are dilute fluid suspensions of nanoparticles (1-100 nm) at modest concentrations (< 5.0% weight fraction) [1]. They are prepared by dispersing nanoparticles in fluids such as water, oil, molten salt or ethylene glycol. Unlike conventional fluids, the significant enhancement of the thermal properties of molten salt containing nanoparticles allows new pathways for its high temperature application, particularly in the energy sector. In this sector, the efficiency of heat removal and thermal management systems is presently the greatest technological challenge. The use of molten salt nanofluids as a heat transfer fluid and energy storage medium for power generation and storage is very promising and could result in increased efficiency and large energy savings [2]. The flow and heat transfer of such nanofluids is therefore gaining a lot of interest by researchers in the academic community due to their inherent improved thermal transport properties.

Understanding of the hydrodynamics, heat transfer and thermal enhancement of molten salt nanofluids is quite challenging if it is to be gained only experimentally. Apart from the restrictions of size and harsh environmental (i.e. high temperature differences), many other complications arise from the responsible hydrodynamic and interaction forces which are likely to take place at varied magnitudes and multiple time scales. The use of a numerical approach is therefore proposed to investigate these phenomena. More specifically, it is intended here to develop a multiscale computational model based on Lagrangian particle tracking (LPT) [3] coupled with direct numerical simulation (DNS) to investigate the dispersion stability, thermal properties and turbulent heat flux in nanofluids in a channel flow. The other benefit of this computational fluid dynamic (CFD) model is its ability to investigate more intrinsic phenomena such as turbophoresis (the tendency for particles to migrate in the direction of decreasing turbulence kinetic energy) and thermophoresis (particle motion induced by thermal gradients), and hence the long-term thermal stability of nanofluids that has not yet been well studied.

It is thought that agglomeration of nanoparticles to form larger particle clusters could lead to surface impact, deposition and erosion, although evidence of this in the literature is conflicting [4], with few quantitative studies reported. To capture these effects using CFD, a comprehensive description of both the fluid phase and solid nanoparticle phase evolution is necessary. Since these particles are very small, with Stokes numbers St ~ 0, they are expected to behave like tracers within the carrier phase. Hence, the focus here is on the fluid phase that dictates the spatial distribution of solid particles relative to the turbulent flow. The evolution of the particles' distribution is therefore highly dependent on the turbulent flow and temperature fields, and physical interactions between the particles and between the particle and the cold or hot wall heat flux boundaries. Moreover, whereas most transport models are not explicit and do not account for feedback between the turbulence and aggregation mechanisms, the model proposed does so.

2 METHODOLOGY

The focus of the present DNS-based work relies on modelling the heat transfer in nanoparticulate multiphase channel flows with a high Prandtl number fluid (i.e. molten salt). The method proposed uses a channel flow configuration in three-dimensions that is used to

simulate turbulent flows representative of those encountered in practice by providing a full range of length and time scales, down to the Kolmogorov scale [5]. This technique enables any quantity of interest to be analysed with great spatial and temporal precision, albeit at a large computational cost and for somewhat idealised conditions. DNS can generally be regarded as a complement to laboratory experiments. Particle-particle interactions are represented using detailed surface interactions based on DLVO interaction forces [6]. DLVO theory (after Derjaguin and Landau [7], and Verwey and Overbeek [8]) defines inter-particle forces as the sum of van der Waals and electric double-layer contributions, and these are fully resolved in the computations.

Turbulent heat transfer in a channel is characterized not only by the Reynolds number (Re) but also by the Prandtl number (Pr) of the fluids. Kawamura et al. [9] undertook DNS simulations of turbulent heat transfer for various Prandtl numbers ranging from $Pr = 0.025$ to 5 with a $Re_\tau = 180$ flow using a finite-difference method-based solver. They assumed a constant volumetric heating with a uniform wall temperature. Profiles of the mean temperature, temperature variance and turbulent heat flux were obtained, with detailed budgets within the transport equations for these quantities reported. The present work utilizes a similar turbulent heat transfer model to that of Kawamura et al. [9]. However, we here aim to expand on this work by seeding the continuous phase with nanoparticles to determine turbulence quantities such as the turbulent heat flux and temperature variance of the multiphase system considered with $Pr = 5$ and $Re_\tau = 180$.

In order to relate the present work to the systems present in solar thermal power plants, we consider mechanical and chemical properties matching those of Al_2O_3 nanoparticles in molten salt ($NaNO_3$-KNO_3, 60-40 weight ratio), which is a simulant for proposed heat transfer fluid and thermal energy storage media. In addition, a novel method is used here to describe the oscillating layered structure of molten salt fluids (represented by the matrix of liquid molecules around the nanoparticles), and the influence of the interfacial layer thickness on the system conductivity. Further details can be found elsewhere [10]. This innovative approach allows for the simulation of different flows, and modifications to them to gain a better understanding of the nanoparticle dynamics and heat transfer characteristics of the system. The final outcome is expected to provide the optimum characteristics of the nanofluid flows that can be used in solar power plants.

2.1 Fluid flow simulation

In the present study the simulations were performed using a numerical multiscale model with the continuous phase predicted using the open source spectral element-based DNS code, Nek5000 [11]. This code was chosen based on its extensive testing, efficient parallelization capabilities and validation history [12]. Within the code, the incompressible Navier-Stokes equations (mass and momentum conservation) are solved to high accuracy, with the code applied to a Cartesian grid consisting of $27\times18\times23$ 8th order elements (i.e. 5.7 M nodes) used to represent a turbulent channel flow at shear Reynolds number $Re_\tau = 180$ (equivalent to a bulk Reynolds number $Re_B = 2800$). A constant fluid timestep of $\Delta t_F^* = 0.01$ was used throughout. The elements were scaled such that those closest to the wall were distributed more densely. The geometry of the channel was $14\delta\times2\delta\times6\delta$, with $\delta = 0.1$ mm, as illustrated in Fig. 1. For the purpose of this study, the computational coordinates (x, y, z) were used to represent the three-

dimensional geometry of the channel, with x being the streamwise direction, y the wall-normal direction, and z the spanwise direction. Periodic boundary conditions were enforced in the streamwise and spanwise directions, while the wall-normal axis used solid impenetrable no-slip conditions at $y^* = \pm\delta$, with the walls maintained at a constant temperature. The flow was driven and maintained by a constant pressure gradient. The non-dimensional Navier-Stokes equations are presented in Eqs. (1) and (2), with distances, velocities and densities normalized by the channel half-height, δ, the bulk velocity, U_B, and the fluid phase density, ρ_F, respectively. From here on, any quantity with an asterisk (*) denotes a variable non-dimensionalised in this manner.

$$\nabla \cdot \boldsymbol{u}^* = 0 \tag{1}$$

$$\frac{\partial \boldsymbol{u}^*}{\partial t^*} + \boldsymbol{u}^* \cdot \nabla \boldsymbol{u}^* = -\nabla p^* + \frac{1}{Re_B} \nabla \cdot \boldsymbol{\tau}^* + \boldsymbol{f}c \tag{2}$$

Here, $\boldsymbol{u}^*$ is the fluid velocity, p^* is the fluid pressure, Re_B is the bulk Reynolds number defined as $Re_B = U_B \delta / \nu_F$, ν_F is the fluid kinematic viscosity and $\boldsymbol{\tau}^*$ is the viscous stress tensor. The additional term $\boldsymbol{f}c$ is cell-dependent and accounts for two-way momentum exchange between particles in a cell and the surrounding fluid. The flow is driven and maintained by a constant pressure gradient using the following parameters:

$$\frac{\partial p}{\partial x} = \left(\frac{Re_\tau}{Re_B}\right)^2 \tag{3}$$

where Re_τ and Re_B are the shear and bulk Reynolds numbers, respectively.
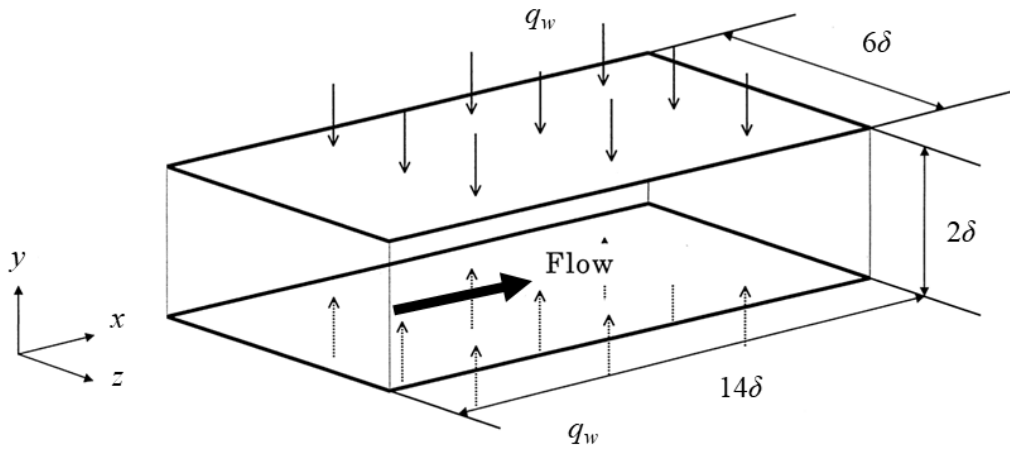

Figure 1: Configuration of DNS for turbulent heat transfer channel flow for hot wall case. Direction of q_W is reversed for cold wall case.

In addition to the fluid flow, Nek5000 also solves the following non-dimensional conservation equation for energy transport:

$$\frac{\partial T^*}{\partial t^*} + \mathbf{u}^* \cdot \nabla T^* = \frac{1}{Pe} \nabla \cdot \nabla T^* + q_{vol} \tag{4}$$

where T^* is the temperature, q_{vol} is the volumetric heat source term and $Pe = LU/\alpha$ with $\alpha = k/\rho_F C_p$, in which Pe is the Péclet number, L is a characteristic length, U the local flow velocity, k the thermal conductivity, ρ_F the fluid density, and C_p the heat capacity.

Two simulations were performed using Eq. (4) with different heat flux boundary conditions. The first had a fixed cold wall boundary with an associated temperature of 250 °C, whereas the second was set to have a fixed hot wall boundary with an associated temperature of 500 °C. The fluid used in these simulations was set to have a high Prandtl number (Pr = 5), representative of molten salt at 400 °C.

2.2 Dispersed phase simulation

The dispersed phase was represented by 500k, 100 nm diameter Al_2O_3 particles which were tracked through the fluid flow field. These were simulated using a Lagrangian particle tracking routine, which was developed for this work and implemented to interface concurrently with Nek5000. The motion of each nanoparticle is described using the Langevin equation, where the translational velocity of the i-th particle is obtained from the principle of conservation of linear momentum using:

$$m_p \frac{\partial \boldsymbol{v}_i}{\partial t} = \boldsymbol{F}_i \tag{4}$$

where

$$\boldsymbol{F}_i = \boldsymbol{F}_i^C + \boldsymbol{F}_i^e + \boldsymbol{F}_i^V + \boldsymbol{F}_i^f + \boldsymbol{F}_i^B \tag{5}$$

Here, m_p and $\boldsymbol{v}_i$ are the mass and the transitional velocity vector of the i-th nanoparticle, respectively. $\boldsymbol{F}_i^C$ is the particle contact force, $\boldsymbol{F}_i^e$ is the electric double layer repulsive force, $\boldsymbol{F}_i^v$ is the van der Waals attractive force, $\boldsymbol{F}_i^f$ is the fluid force and $\boldsymbol{F}_i^B$ is the random Brownian motion force. Other body forces such as gravity and buoyancy were found to be negligible for all length and time scales, since their magnitudes are much smaller than the aforementioned hydrodynamic and interaction forces . At each timestep, the motion of each particle was calculated accounting for the various forces noted. The temperature dependence of these force terms was obtained by interpolating the temperature field at the position of the particle, i.e. it was assumed that each nanoparticle had a temperature equal to that of the local fluid. Further details can be found elsewhere [3].

The model described was used to simulate the dynamics and mechanisms responsible for nanoparticle dispersion and aggregation, and was fully coupled (i.e. four-way coupled). Consideration of solely fluid forces acting upon the particulate phase is known as one-way coupling. Two-way coupling was achieved by implementing the point-source-in-cell method whereby particle forces were fed back to the local fluid cells. Particle collisions (four-way coupling) were resolved using the soft sphere approach, as described by Hertzian normal contact theory [13]. Finally, four-way coupled predictions were extended to include DLVO interparticle van der Waals attractive and electric double layer repulsive forces to allow the

prediction of particle-particle agglomeration events [3]. Chemical and mechanical properties were chosen to match Al_2O_3 in molten salt, with the parameters used in the simulations provided in Table 1.

Table 1: Parameters used in the simulations.

Parameter	Carrier phase (NaNO$_3$-KNO$_3$)	Particle phase (Al$_2$O$_3$)
Shear Reynolds number, Re_τ	180	-
Bulk Reynolds number, Re_B	2800	-
Particle diameter, d_p / nm	-	100
Number of particles, N_p	-	500,000
Volume, V / m^3	1.58×10^{-10}	4.07×10^{-13}
Volume fraction, Φ / vol %	-	0.26
Temperature, T / °C	420	420
Bulk velocity, U_B / m s^{-1}	25.67	25.68
Density, ρ / kg m^{-3}	1996.5	3850
Kinematic viscosity, v_F / m^2 s^{-1}	0.974×10^{-6}	-

The simulations were first performed as an unladen single-phase molten salt flow using an arbitrary initial turbulence profile with added chaotic terms in the wall-normal and spanwise directions. Once turbulence was established, fluid statistics were monitored every 1500 timesteps until the mean and fluctuating velocity and temperature fields reached a statistically steady state. Particles were then injected uniformly throughout the channel and given an initial velocity equal to that of the local fluid. Particle statistics in the wall-normal direction were obtained by splitting the domain into 120 equal volume cuboidal regions, and by averaging over all particles within each region. From this steady state condition, four-way coupled runs were started, reducing the fluid and particle time step initially to avoid divergences in the flow field due to the impact of particle forces. The statistics obtained in these runs are presented and discussed in the following section.
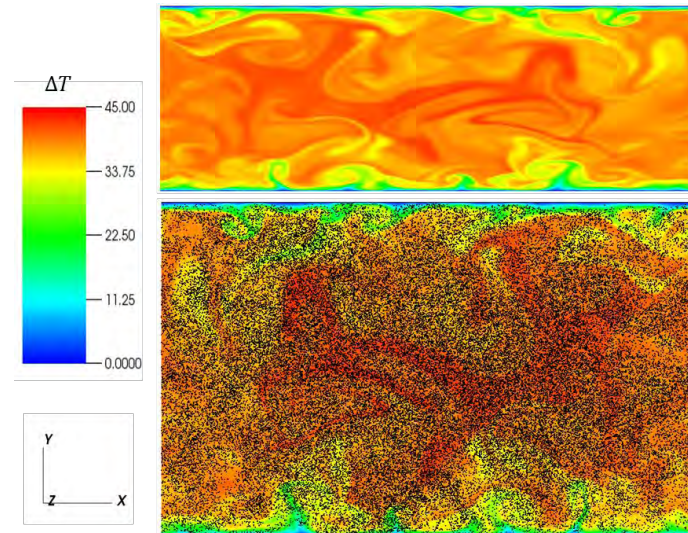

Figure 2: Instantaneous temperature distribution in unladen flow (top), and a zoomed in portion with nanoparticles for the hot wall case (bottom).

3 RESULTS AND DISCUSSION

3.1 Single-phase flow statistics

The results of each simulation were analysed to explain the flow and heat flux behaviour of the fluid and the nanoparticles within the channel. Figure 2 shows the instantaneous fluid temperature at the top of the figure, as well as illustrating the location of the nanoparticles in a zoomed in portion of the channel with hot walls in the lower part of the figure. Considering the results of Fig. 2, a trend in preferential concentration of particles within the coldest regions is noticeable. It is also evident that the particles exhibit increased concentrations in the centre of the channel. The reasons for this will be discussed later.
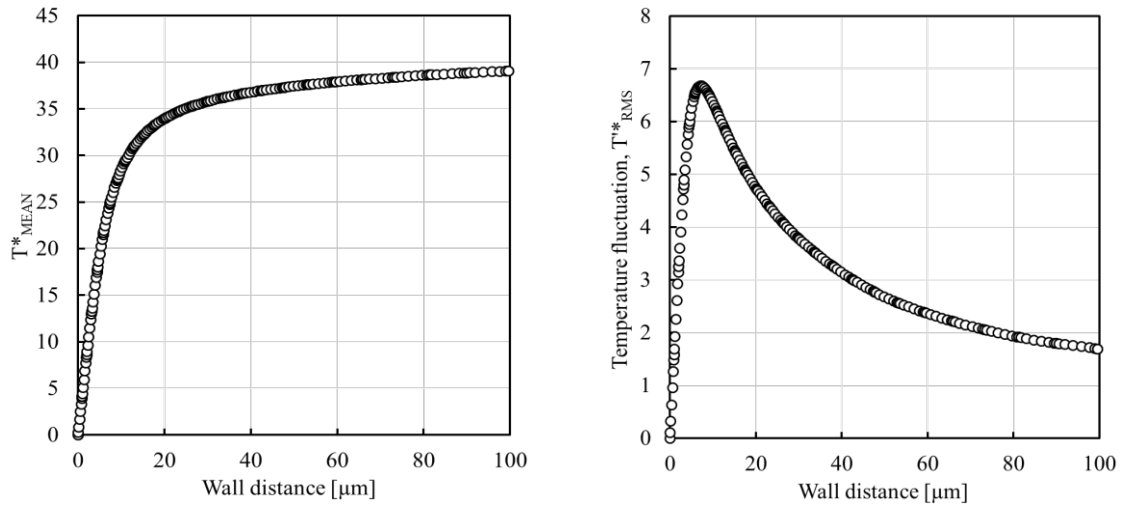
Figure 3: Mean temperature profile (left), and root-mean-square of temperature fluctuations (right).
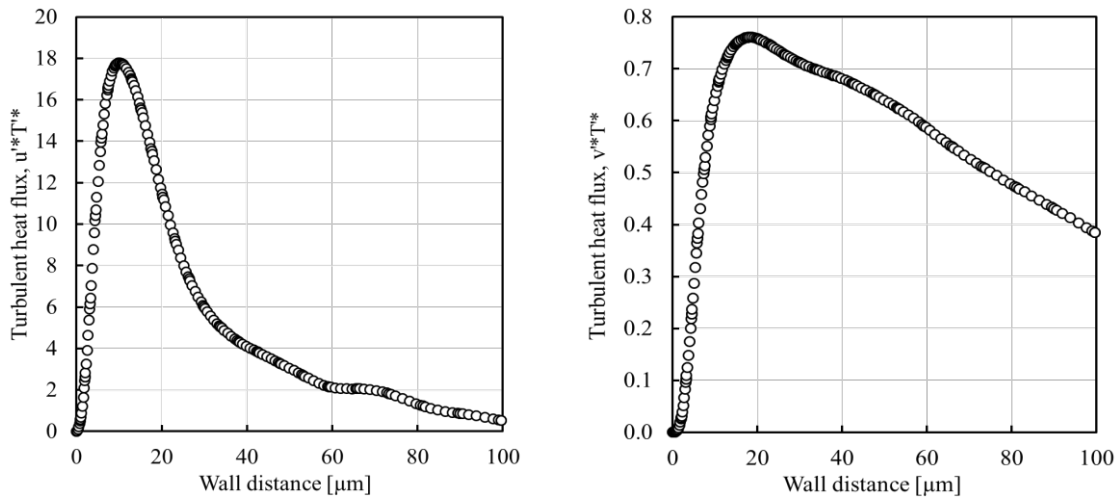
Figure 4: Turbulent heat flux components: streamwise (left) and spanwise (right).

Profiles of the mean temperature and root-mean-square (rms) of temperature fluctuations are presented in Fig. 3 for the single-phase flow. The statistics of Kawamura et al.'s [8] DNS of

697

turbulent heat transfer in a channel flow at $Re_\tau = 180$ and Prandtl number $Pr = 5$ were used for comparison and found to be in qualitatively good agreement. Small discrepancies were apparent between the two set of results, but these may be attributed to be a consequence of computational issues due to differences in the number of nodes and elements used in each simulation, with the present work using an order of magnitude higher number of nodes.

The turbulent heat fluxes in the streamwise and spanwise directions are also presented in Fig. 4. These determine the rate and direction of heat energy transfer via turbulence either towards (cold wall) or away from (hot wall) the wall.

3.2 Particle-laden flow statistics

Profiles of the streamwise mean particle velocity and the rms of particle streamwise velocity fluctuations are shown in Fig. 5.
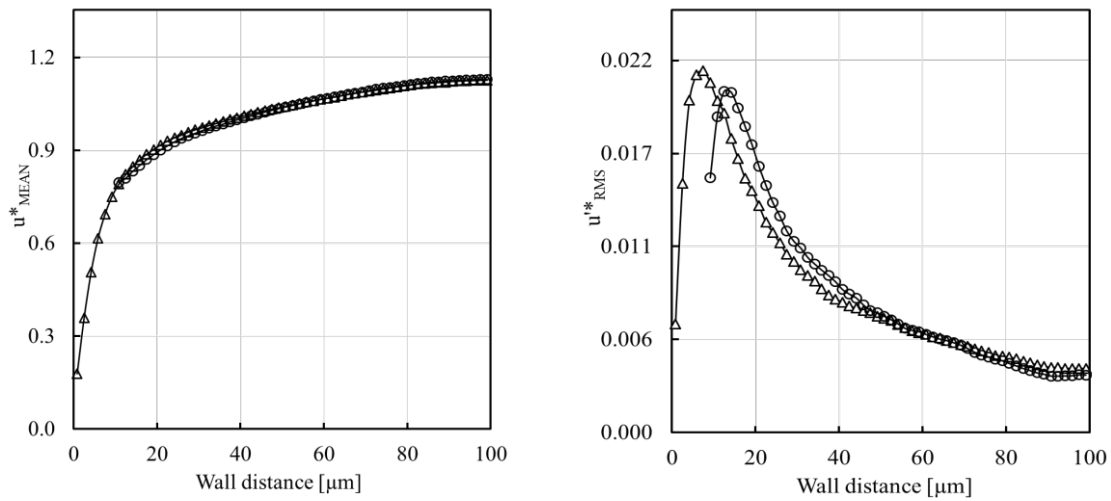
Figure 5: Streamwise mean particle velocity profiles (left), and root-mean-square of streamwise particle velocity fluctuations (right) – ○: hot wall; △: cold wall.

It is clear that the streamwise mean particle velocity distributions are similar for both the cold and hot wall configurations. This is likely due to the low particle Stokes number and the lack of dependence of mean streamwise flow behaviour on the temperature field. In the case of the hot wall, the statistics near the wall are not plotted due to insufficient particles in these regions to obtain meaningful averages. However, the rms of velocity fluctuation profiles show variation between the two configurations. In the case of the cold wall, the peak is closer to the wall, indicating that the particles behave in a more turbulent fashion within the near-wall region. This is likely to be due to thermophoresis causing a drift in the wall-normal direction towards the wall. For the hot wall case, the peak particle rms value is reduced and shifted towards the channel centre slightly, since particles which approach the wall are encouraged to move away from it due to increased local temperatures, although the spread of streamwise rms velocities further from the wall is maintained. The rms of velocity fluctuations in the wall-normal and spanwise directions is illustrated in Fig. 6. It can be seen that the wall-normal particle fluctuations exhibit similar behaviour near the wall, but the fluctuations are slightly increased for the cold wall

configuration in the outer layer. This is likely to be due to turbophoresis and thermophoresis working together to give the particles greater distributions in wall-normal velocity. The spanwise distributions exhibit similar behaviour, as expected since this direction is homogeneous in both fluid temperature and velocity distributions.
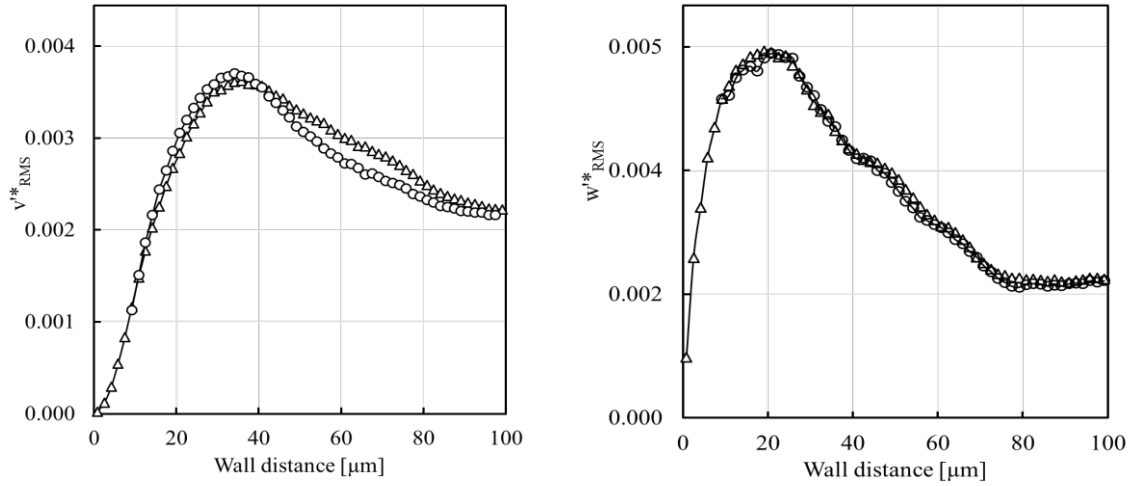

Figure 6: Root-mean-square of particle velocity fluctuations, wall-normal (left) and spanwise (right) – ○: hot wall; △: cold wall.
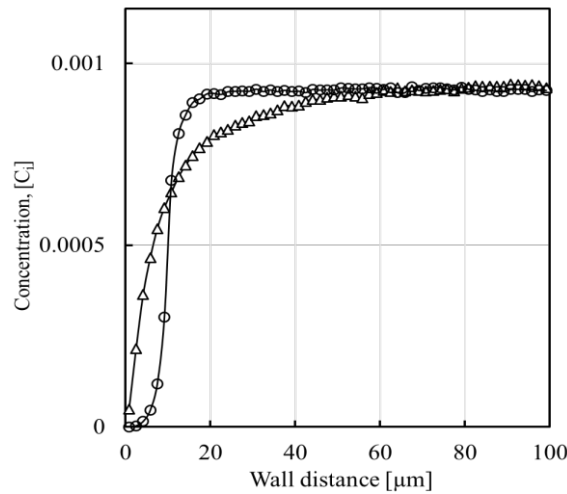

Figure 7: Comparison of mean particle concentrations across the channel – ○: hot wall; △: cold wall.

The predictions also demonstrate how particle concentrations differ in the near-wall regions due to thermophoresis, as illustrated in Fig. 7. Over the course of the cold wall simulation it is clear that both turbophoresis and thermophoresis take place, encouraging the particles to migrate to regions of low turbulence kinetic energy and temperature (i.e. near the walls). Over time this leads to a build-up of nano-particulate concentrations close to the wall. This has implications for particle collision and agglomeration rates since the local concentration in these regions is greater than the initial concentration once the system has reached a steady state. This also implies that, with time, particle deposition rates on the walls will likely increase due to

migration towards the walls. Conversely, the results for the hot wall boundary condition show particles are migrating away from the walls towards the channel centre. The preferential concentration of particles within the hottest zones of the channel in this case was also noted previously through the observations in regards to the results of Fig 2.

4 CONCLUSIONS

Direct numerical simulations of turbulent nanofluid flow and heat transfer were performed for two different thermal wall configurations (cold and hot walls) using a high Prandtl number fluid, and the effect on nanoparticle motion statistical quantities was investigated. Concentration plots indicate a notable difference in particle distributions between the cold and hot wall boundary conditions. Specifically, it was observed that an increase in particle concentration in the near-wall regions occurred over the run times considered for the cold wall configuration. The particles were found to behave in a more turbulent fashion in the near-wall regions, due to thermophoresis causing a drift in the wall-normal direction towards the wall. Combined turbophoresis and thermophoresis effects were also found to give the particles larger distributions in the wall-normal velocity. For the hot wall case, particle migration was observed to be in the opposite direction, away from both of the walls towards the channel centre, as particles that approach the wall are encouraged away due to the increased wall temperature. The results obtained highlight differences in particle migration due to the wall temperature boundary condition, which over time will lead to a build-up of a non-homogeneous particulate concentrations within the channel. Future work will further consider the influence of turbophoresis and thermophoresis in more detail, and will allow conclusions to be reached regarding the implications for thermal energy storage systems using nanofluids.

5 ACKNOWLEDGEMENTS

REFERENCES

[1] Choi, S.U.S. and Eastman, J.A. *Enhancing thermal conductivity of fluids with nanoparticles*. Developments and Applications of Non-Newtonian Flows, ASME, New York, FED-Vol 231/MD-Vol 66, 99-105 (1995).

[2] Lenert, A. and Wang, E.N. Optimization of nanofluid volumetric receivers for solar thermal energy conversion. *Sol. Energy* (2012) **86**:253-265.

[3] Mahmoud, B.H., Fairweather, M., Mortimer, L.F., Peakall, J., Rice, H.P. and Harbottle, D. Prediction of stability and thermal conductivity of nanofluids for thermal energy storage applications. *28th European Symposium on Computer Aided Process Engineering* (2018) **43**:61-66.

[4] Nguyen, C., Galanis, N., Polidori, G., Fohanno, S., Popa, C. and Bechec, A. An experimental study of a confined and submerged impinging jet heat transfer using Al_2O_3-water nanofluid. *Int. J. Therm. Sci.* (2009) **48**:401-411.

[5] Mortimer, L.F., Njobuenwu, D.O. and Fairweather, M. Near-wall dynamics of inertial particles in dilute turbulent channel flows. *Phys. Fluids* (2019) **31**:063302.

[6]   Henry, C., Minier, J.P., Pozorski, J. and Lefèvre, G. A new stochastic approach for the simulation of agglomeration between colloidal particles. *Langmuir* (2013) **29**:13694-13707.

[7]   Derjaguin, B. and Landau, L. Theory of the stability of strongly charged lyophobic sols and of the adhesion of strongly charged particles in solutions of electrolytes. *Acta Physicochim.* (1941) **14**:633-662.

[8]   Verwey, E.J.W. and Overbeek, J.T.G. Theory of the stability of lyophobic colloids. *J. Colloid Sci.* (1955) **10**:224-225.

[9]   Kawamura, H., Ohsaka, K., Abe, H. and Yamamoto, K. DNS of turbulent heat transfer in channel flow with low to medium-high Prandtl number fluid. *Int. J. Heat and Fluid Flow* (1998) **19**:482-491.

[10] Mahmoud B.H., Mortimer L.F., Fairweather, M., Rice, H.P., Peakall, J. and Harbottle D. Thermal conductivity prediction of molten salt-based nanofluids for energy storage applications. *29ᵗʰ European Symposium on Computer Aided Process Engineering* (2019) **46**:601-606.

[11] Fischer, P.F., Lottes, J.W. and Kerkemeier, S.G. Nek5000, http://nek5000.mcs. anl.gov, (2008).

[12] Mahmoud B.H., Mortimer, L.F., Fairweather, M., Rice, H.P., Peakall, J. and Harbottle, D. Nanoparticle behaviour in multiphase turbulent channel flow. *29ᵗʰ European Symposium on Computer Aided Process Engineering* (2019) **46**:607-612.

[13] Timoshenko, S. P. and Goodier, J.N. *Theory of Elasticity.* McGraw-Hill, New York, 3ʳᵈ Ed., (1970).

WCSPH FOR MODELLING MULTIPHASE FLOWS AND NATURAL HAZARDS

S. MANENTI

Dipartimento di Ingegneria Civile e Architettura (DICAr), University of Pavia
Via Ferrata, 3 – 27100 Pavia (Italy)
sauro.manenti@unipv.it - http://civrisk.unipv.it/teaching-staff/sauro-manenti/

Key words: Multiphase, WCSPH, high density ratio, limiting viscosity, non-Newtonian fluid, natural hazards.

Abstract. Among the numerous types of meshless particle methods, SPH is successfully applied to simulate complex multiphase flows with impact involving fluids with high-density ratio as well as non-Newtonian fluids. These problems are concern in the applied engineering dealing with water related natural hazards, such as landslide induced tsunami in artificial reservoir, intense rainfall induced shallow landslides. This contribution aims at providing an overview on the recent applications of the standard weakly compressible WCSPH for modelling these kinds of multiphase flows. The relevant aspects related with the interface treatment and numerical stability in high density multiphase flow will be discussed. Advanced modelling aspects connected with the SPH simulation of non-Newtonian fast dense granular flows and the interaction with pore water. The aspect of tuning model parameters is discussed.

1 INTRODUCTION

Multiphase flows are involved in several problems of practical interests and in many fields of the hydraulic engineering (Guandalini et al. 2015, Todeschini et al. 2019). Among these, the analysis of natural hazardous events related to water represents an important category (Manenti et al. 2018; Manenti et al. subm.). These problems are frequently characterized by fast dynamics, large deformation, flow impact and possibly large density ratio. These peculiar features of the multiphase flow may be difficult to handle from numerical point of view. This is especially the case of multiphase flows where high-density ratio between the phases can cause numerical instability (Monaghan & Ashkan 2013; Grenier et al. 2009; Hu & Adams 2007; Colagrossi & Landrini 2003). Other relevant issues in the numerical modelling of complex multiphase problems of practical interests are: (*i*) stochastic nature of modelling parameters influencing the model response (Manenti et al. 2016), and (*ii*) the large amount of computational time and resources required by complex problems and time step limitation when considering viscous non-Newtonian fluids (Manenti et al. 2018; Guandalini et al. 2012). Therefore fast-running reliable numerical models are strongly desirable, especially for application to multi-disciplinary decision support systems for natural hazard risk reduction and management where several scenarios should be explored to account for inherent uncertainty affecting influential model parameters (Newman et al. 2017).

In this paper will be discussed some modelling approaches for handling the above-mentioned issues in the WCSPH simulation of multiphase flows involved in natural hazards.

2 MODEL DESCRIPTION

In this section will be illustrated two different WCSPH models for the analysis of multiphase flows.

In section 2.1 are shown the analytical details of a relatively simple and novel approach based on standard weakly compressible SPH for simulating free-surface multiphase flows with high-density ratio involving violent impact (Manenti 2018). The proposed approach, which is relatively simple to implement, allows keeping sharp interfaces between the two phases and permits to overcome instability problems affecting standard SPH formulation in these kind of applications.

In section 2.2 is illustrated the FOSS code SPHERA v.9.0.0 (RSE SpA) (Amicarelli et al. subm.) that is based on the standard WCSPH formulation featuring a mixture model for the analysis of dense granular flows consistent with the Kinetic Theory of Granular Flow (KTGF) (Amicarelli et al. 2017). A numerical parameter, so-called limiting viscosity, has been subsequently introduced in the reference model of Amicarelli et al. (2017) as an appropriate means to reduce computational time in those kind of multiphase flows involving a viscous non-Newtonian fluid, as the case of landslide post-failure dynamics (Manenti et al. 2018).

2.1 Novel WCSPH for high-density ratio two-phase flow

In the following are described the governing equations of an alternative SPH model that derives from the discretized balance equations of fluid motion described in Monaghan (1994) which were defined as "standard" formulation in Colagrossi & Landrini (2003). Even if multiphase flows can be simulated following standard SPH (Manenti et al. 2012), serious numerical instability at the interface arises when the density ratio between involved phases increases at some order of magnitude. The principal causes of this instability was investigated in Manenti (2018) and were due mainly to the discontinuity of density across the interface. Adopting the formalism introduced in that work, the mass and momentum balance equations in the standard SPH formulation can be conveniently formulated, as explained in the following, substituting the density ρ_i of a given fluid particle at the point $\mathbf{x}_i$, which becomes discontinuous across the interface, with the inverse of the its particle volume V_i:

$$\rho_i = m_i \frac{1}{V_i} = m_i \varpi_i \tag{1}$$

The symbol ϖ_i in Eq. (1) is used to denote the inverse of the particle volume (or number density) which is referred to as the specific volume, according to the nomenclature adopted in Hu and Adams (2007). Note that, as the specific volume is continuous across the interface, the particle's mass is discontinuous. The particle mass m_i is assumed as constant.

Thus the differential balance equations for the mass and momentum ($\mathbf{v}$ velocity vector, $\mathbf{g}$ gravitational acceleration, p pressure) of a slightly compressible inviscid fluid can be written:

$$\frac{D\varpi_i}{Dt} = -\varpi_i \, \nabla \cdot \mathbf{v}_i \tag{2}$$

$$\frac{D\mathbf{v}_i}{Dt} = -\frac{1}{m_i \varpi_i} \nabla p_i + \mathbf{g}$$

The discretized form of the mass and momentum balance Eqs. (2) can be obtained by applying the standard SPH approximation principles after the following simple mathematical manipulations:

$$\frac{D\varpi_i}{Dt} = -\left[\nabla(\varpi \, \mathbf{v})_i - \mathbf{v}_i \cdot \nabla \varpi_i\right] \tag{3}$$

$$\frac{D\mathbf{v}_i}{Dt} = -\frac{1}{m_i}\left[\frac{p_i}{\varpi_i^2}\nabla \varpi_i + \nabla\left(\frac{p_i}{\varpi_i}\right)\right] + \mathbf{g} \tag{4}$$

If the support of the kernel is not truncated (as occurs when intersecting the fluid free surface), a useful relation can be derived for the derivative of a function f (Liu & Liu, 2003). Considers the following integral kernel approximation of the quantity ∇f evaluated at the i-th point of the continuum domain Ω:

$$\nabla f_i = \int_\Omega \nabla_j f_j \, W_{ij} \, d\Omega \tag{5}$$

In the Eq. (5), the gradient on the left side member is calculated at particle i (subscript i is omitted for nabla operator), while it is evaluated at particle j on the right-hand member (i.e. ∇_j). Taking into account the following identity:

$$\nabla_j f_j \, W_{ij} = \nabla_j\left[f_j W_{ij}\right] - f_j \, \nabla_j W_{ij} \tag{6}$$

the Eq. (5) can be rewritten in the following manner if the Gauss divergence theorem is applied at the first integral on the right side member:

$$\nabla f_i = \int_{\partial\Omega} f_j \, W_{ij} \cdot \mathbf{n} \, ds - \int_\Omega f_j \, \nabla_j W_{ij} \, d\Omega \tag{7}$$

Because the kernel W_{ij} is a central function of the relative distance between particles i and j, it can be easily demonstrated that the kernel gradient ∇W_{ij} evaluated at particle i has opposite sign with respect to the kernel gradient $\nabla_j W_{ij}$ at particle j. In addition, if the kernel compact support (which is function of the smoothing length h) is entirely contained in the domain Ω then the first integral on the right-hand side of Eq. (7) vanishes since it is evaluated on the frontiers $\partial\Omega$ of Ω and the kernel function is zero outside its support by definition. For the above-mentioned reasons Eq. (7) becomes:

$$\nabla f_i = \int_\Omega f_j \, \nabla W_{ij} \, d\Omega \tag{8}$$

As the discrete element volume is ϖ_j^{-1}, the particle approximation of Eq. (8) is given by:

$$\nabla f_i = \sum_{j=1}^{Ni} \frac{1}{\varpi_j} f_j \cdot \nabla W_{ij} \tag{9}$$

Taking into account Eq. (9) with f equal to ($\varpi_i \, \mathbf{v}_i$) and ϖ_i respectively, the mass balance in

Eq. (3) can be discretized as follows:

$$\frac{D\varpi_i}{Dt} = -\sum_{j=1}^{Ni} \nabla\left(\mathbf{v}_j - \mathbf{v}_i\right)\cdot\nabla W_{ij} \tag{10}$$

In a similar fashion, by replacing f into Eq. (9) with ϖ_i and (p_i / ϖ_i) respectively, from Eq. (4) can be obtained the discretized momentum balance equation:

$$\frac{D\mathbf{v}_i}{Dt} = -\frac{1}{m_i}\sum_{j=1}^{Ni}\left(\frac{p_i}{\varpi_i^2} + \frac{p_j}{\varpi_j^2}\right)\nabla W_{ij} + \mathbf{g} \tag{11}$$

In Eq. (11) the artificial viscosity term Π_{ij} is introduced to assure numerical stability and to keep interface sharply defined. This term derives from the artificial viscosity of Monaghan (1994) following proper adaptation to be consistent with the model formulation that adopts specific volume as independent variable instead of the density (Manenti 2018).

The discretized governing Eqs. (10) and (11) provide the following advantages when dealing with multiphase flows with large density ratio: (*i*) each phase is not treated as a boundary condition for the other and all neighboring particles in the interaction domain of an interface particle are included into its neighbor's list, regardless of the phase they belong to; (*ii*) kernel truncation is avoided, requiring no need for numerical correctives to improve the accuracy at the interface; (*iii*) no kind of cohesion force is required for eliminating particle penetration between heterogeneous phases at the interface; (*iv*) the algorithm is relatively simple to implement and reduce computational effort.

This model has recently been tested on air-water rapidly varied flow with impact showing reliable accuracy, especially if compared with its relative simplicity (Manenti 2018). Section 3.1 shows the results for another application to the rise of an air bubble in still water.

2.2 WCSPH with limiting viscosity

The numerical investigation of complex 3D problems of practical interest frequently requires the discretization of large domains with a high resolution. This lead to an exponential growth of required computational time and involved resources, especially in the case of SPH method, which could be much more expensive than traditional grid-based methods. A help comes from the recent increase of the parallel computational power of the hardware, especially in the branch of Graphics Processing Units (GPUs). Anyway, GPUs based computations require that the models are implemented using High Performance Computing (HPC) techniques to take advantage of the power of current hardware (Domínguez et al. 2013).

As explained in the following, a simple strategy may be applied in those cases involving viscous non-Newtonian fluid to carry out code optimization for reducing significantly the computational time while preserving suitable degree of accuracy.

The FOSS code SPHERA v.9.0.0 (Amicarelli et al. subm.) implements a WCSPH formulation of mixture model for the analysis of dense granular flows consistent with the KTGF (Amicarelli et al. 2017). This model has been successfully applied to the analysis of rapid multiphase flow involving the interaction of fast landslide with stored water (Manenti et

al. 2018). Post-failure landslide dynamics is simulated by assuming a non-Newtonian rheological model for the slide mass that mimics pseudo-plastic behavior. Time step reduction occurs when shear rate approaches zero and the apparent viscosity approaches higher values. In order to reduce computational time a numerical parameter is introduced which is referred to as limiting viscosity μ_0. Following the experimental behavior exhibited by high polymer solutions, the transition from frictional regime (i.e. solid particle in motion) to the elastic-plastic regime (i.e. solid particle at rest) occurs with an almost constant value of the apparent viscosity which is set equal to μ_0. This allows keep control of the growth of viscosity at very low shear rate, thus reducing computational time when the stability condition for the explicit integration scheme is dominated by viscous criterion.

This approach has been successfully tested on a laboratory experiment simulating, along a representative transversal section, the 2D run-out of the Vajont landslide and its interaction with the water stored in the artificial basin. The results showed that, with proper choice of the value assigned to μ_0, the model allowed obtaining the desired degree of accuracy in predicting maximum wave run-up along with a significant reduction of the computational time.

An ongoing research is devoted to the application of SPHERA v.9.0.0 to the simulation of the post-failure dynamics of rainfall-induced shallow landslides that represents one of the most common natural hazards in some areas of the world (Bordoni et al. 20015). These kind of landslides are triggered by intense rainfall events inducing water infiltration at slopes that increases the volumetric water content and pore water pressure that worsen the slope stability. Therefore, reliable assessment of landslide susceptibility requires proper definition of the rainfall characteristics considering recent climate trends affecting rainfall and intense storm events (Barbero et al. 2014).

SPHERA v.9.0.0 is particularly suitable for the analysis of the above-mentioned kind of shallow landslides that are classified as complex landslides because their run-out starts as shallow rotational-translational failure then it changes into earth flows owing to the large water content and behaves like dense granular flow (Zizioli et al. 2013).

The early results of these simulation are shown and discussed in section 3.2.

3   RESULTS ANALYSIS

This section illustrates some applications of the two WCSPH models described in sections 2.1 and 2.2.

Section 3.1 shows the application of the standard SPH model for the analysis of multiphase flow involving two fluids with high-density ratio, as the case of a circular bubble rising in water at rest.

Section 3.2 is devoted to the application of the FOSS code SPHERA v.9.0.0 (Amicarelli et al. subm.) to the analysis of multiphase flow involving a viscous non-Newtonian fluid, as the case of post-failure dynamics of a rainfall induced shallow landslide.

3.1 Bubble rise in still water

The WCSPH model described in section 2.1 has been applied to the analysis of the problem investigated in Colagrossi & Landrini (2003). The free rise of a circular air bubble with radius r inside a still water column with depth H is simulated.

As said in the section 1, no additional term is included in the momentum balance equations

to account for surface tension effects. However, Colagrossi & Landrini (2003) and Hoover (1998) noticed that the discretized form of pressure gradient in the standard SPH momentum balance equation implies fictitious surface-tension effects. The adopted formulation of the momentum balance Eq. (11) maintains the same structure of standard SPH momentum balance equation because it is obtained through the same discretization procedure.

Table 1: model parameters for test case of rising bubble in water at rest. Superscripts refer to *w*=water *a*=air.

parameter	value
δ	0.025 m
h	1.3 δ
water	45,488 part.ls
air	2,512 part.ls
H	10 m
r	1 m
γ^w	7.0
γ^a	7.0
ρ^w	1000 kg/m^3
ρ^a	1.2 kg/m^3
c^w	50 m/s
c^a	55 m/s
ϑ	0.4
α_M	0.075

Table 1 summarizes the model parameters adopted in the computation. After early trial simulations, the optimal inter-particle distance δ = 0.025 m is adopted, resulting in 48,000 total particles. This resolution represents a suitable compromise between required computational effort and results quality. The air sound speed c^a has been properly reduced to a value close to the water sound speed c^w in order to enhance bubble deformation. In Table 1 ϑ is the constant for periodic density smoothing, α_M is the constant of Monaghan artificial viscosity.

Figure 1(a) displays the initial state of the half system that has been simulated to reduce the computational effort. The left-hand panel shows the velocity modulus, which is expressed in non-dimensional form with respect to the reference velocity $(g\,r)^{0.5}$. The mid panel displays the hydrostatic pressure distribution in the water column and the atmospheric (relative) pressure inside the bubble, both of which are expressed in non-dimensional form with respect to the pressure at the bottom of the tank $(\rho^w g\,H)$. The right panel shows the density field. Note that the air particles are surrounded by a black circle in the left-hand and in the middle panels in order to distinguish them from the water particles. For this reason, air particles appear darker in the plots showing velocity magnitude and pressure distribution.

As the computation starts, the air bubble is suddenly compressed because of the strong pressure difference with respect to the surrounding water. Figure 1(b) shows the system at the instant at t = 0.70 s. The bubble assumes a lenticular shape because it is pushed upward by the water jet that rises from the bottom in the direction of the bubble vertical axis because of the pressure difference with respect to the air. The left panel shows the above-mentioned water jet
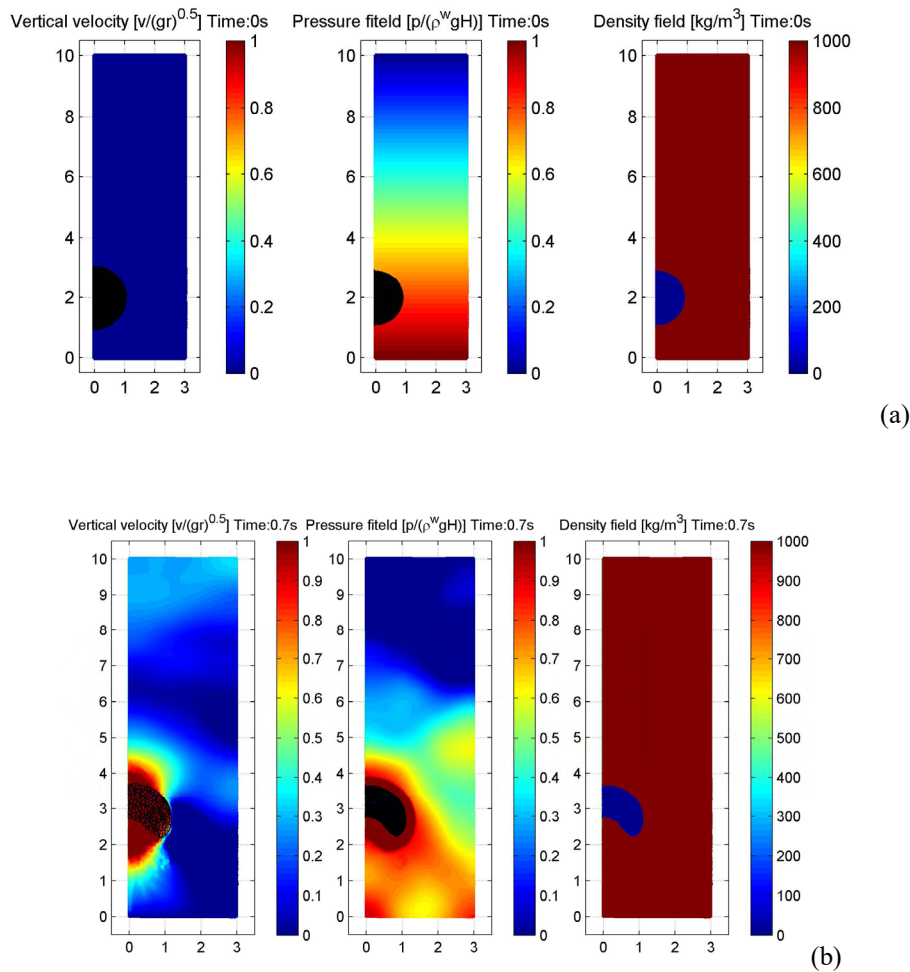
with a vertical velocity of about 4 m/s.

Figure 1: bubble rise at (a) $t = 0.0$s and (b) $t = 0.70$s. From the left-hand side: velocity, pressure and density fields. Cartesian axes in meters.

As seen in the middle panel, the water pressure is higher around the air bubble, causing it to become deformed during the upward motion. Both the velocity and pressure fields are quite smooth and vary in accordance with physical expectations.

The right-hand panel shows that the bubble contour remains quite regular, without penetration of water particles, thus highlighting fictitious surface tension effects even if the momentum balance equations does not include any term simulating physical surface tension. Owing to the hydrodynamic thrust of the upward water jet, the bubble vertical position increases, the bubble mean thickness decreases while the transversal length grows with respect to the early situation in Figure 1(b).

The bubble contour at time $t = 1.40$ s is shown in Figure 2 (red dots), and it is compared with the numerical result in the paper by Colagrossi & Landrini (2003), denoted by blue diamonds. It can be seen that the simulated bubble is characterized by a reduced vertical velocity and that its shape is rather different because the lower volute that subsequently

detaches from the upper main body does not form.
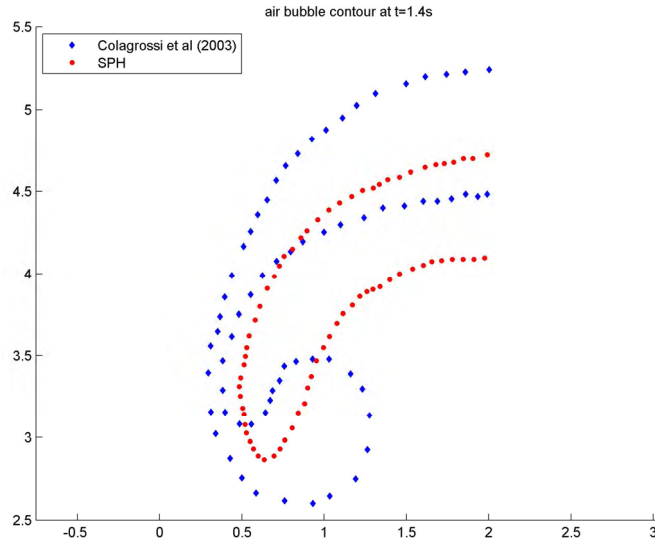
Figure 2: bubble position at t = 1.40 s. Comparison between present SPH model (red dots) and the model by Colagrossi & Landrini (2003).

Concerning the reduced rising speed of the air bubble, this may be related partly to the high dissipation effects induced by the artificial viscosity when both phases are compressed one to each other, as discussed in Manenti (2018).

Regarding the differences of the shape with respect to the reference results in Colagrossi & Landrini (2003), may be these are related to the fact that the present model does not implement any term for simulating physical surface tension effects in the momentum balance equation. Anyway, the adopted discretized form of the pressure gradient term implies fictitious surface-tension effects (Hoover, 1998) and this is partly confirmed by the inter-phase surface sharpness without heterogeneous particles penetration.

A similar problem was investigated in Sussman et al. (1994) considering a rising air bubble in a liquid with density ratio 1000/1, medium range Reynolds number and non-negligible surface tension effects (i.e. low Bond number). Qualitative comparison of the bubble shape shows that the results obtained with the present model are consistent with those of Sussman et al. (1994) showing that no fragmentation of the air bubble occurs even at subsequent instants. Anyway, a rigorous comparison is rather difficult owing to the following reasons. The governing equations for slightly compressible fluids are assumed in this model, while incompressible Navier-Stokes equations have been adopted in Sussman et al. (1994). The physical viscosity is neglected in the present model, and therefore it seems difficult to evaluate the Reynolds number based on the artificial viscosity contribution. The fictitious surface tension can not be easily quantified to estimate an equivalent physical surface tension for evaluating Bond number.

3.2 Rainfall induced shallow landslide

The FOSS code SPHERA v.9.0.0 (Amicarelli et al. subm.) illustrated in section 2.2 has

been tested for the post-failure analysis of a rainfall induced shallow landslide. This landslide occurred during an intense rainfall event on April 2009 in a hilly area of the Oltrepò Pavese named Recoaro valley – Northern Italy. Even if SPHERA has 3D formulation, a 2D approach has been conveniently adopted in this case because of the landslide peculiarity to be relatively narrow so as the flow may be assumed two-dimensional.
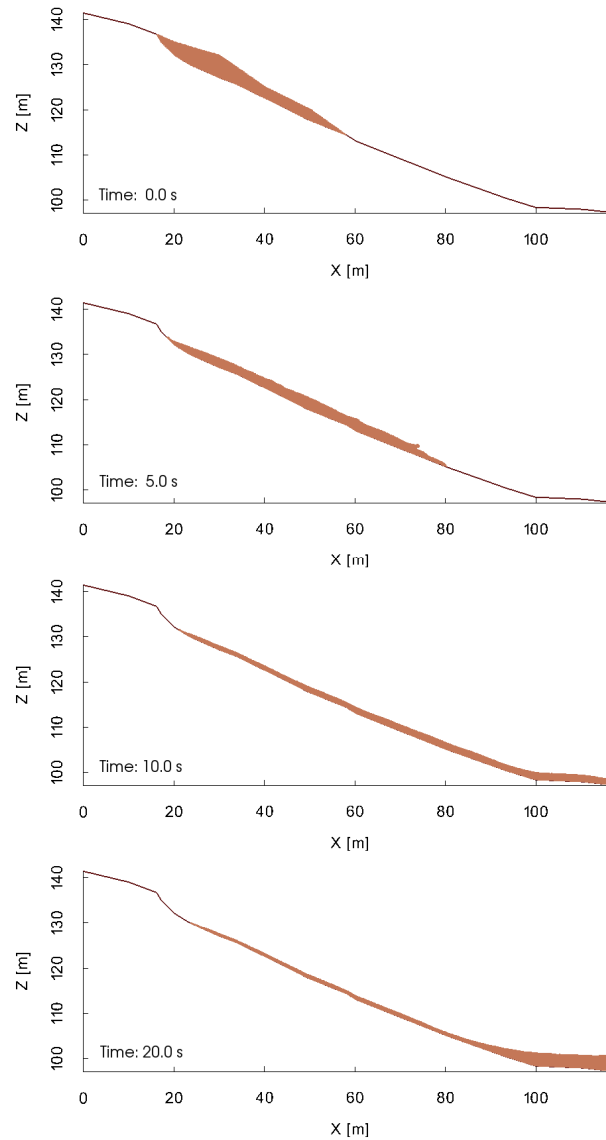

Figure 3: 2D SPH simulation of a rainfall induced shallow landslide. SPHERA v.9.0.0 (RSE SpA).

One of the first contribution to SPH modelling for predicting flow-like landslides including hydro-mechanical coupling was given by Pastor et al. (2009). They proposed a 2D depth-integrated, coupled, SPH model by assuming that the vertical flow structure would be the same as a uniform steady-state flow according to the so-called model of the infinite landslide having constant depth and moving at constant velocity on a constant slope. This assumption is

suitable for landslides whose average depths are small in comparison to their length and width.

In the present case, where initial landslide mean depth is of the same order of its length and width, significant variations of the vertical thickness and of the vertical velocity profile may occur along the landslide body in the flow direction. The proposed modelling approaches removes the hypothesis made by Pastor et al. (2009), thus allowing a numerical implementation of the problem that is closer to the actual behavior. The simulated falling time seems quite reasonable for the considered event. Comparison of the final landslide profile with in situ measurements shows suitable accuracy and will be illustrated in a future paper.

4   CONCLUSIONS

- A novel WCSPH based on standard formulation has been illustrated for the analysis of multiphase flows with large density ratio. By replacing the density (which is discontinuous at the interface) with specific volume, the numerical instability at the interface is prevented. Furthermore, no fictitious force should be added in the pressure gradient term inside the momentum balance equation to prevent interphase particle penetration and maintain the interface sharply defined. Kernel truncation is avoided at interface, thus reducing deterioration of computational accuracy.
- The FOSS code SPHERA v.9.0.0 (RSE SpA) was tested on the simulation of a rainfall induced shallow landslide occurred in Italy in 2009. The model, having full 3D formulation, allows removing the need for a depth integrated formulation. Fast computation is assured by introducing a numerical parameter, the limiting viscosity, for run optimization.

REFERENCES

[1] Amicarelli A., S. Manenti, R. Albano, G. Agate, M. Paggi, L. Longoni, D. Mirauda, L. Ziane, G. Viccione, S. Todeschini, A. Sole, L.M. Baldini, D. Brambilla, M. Papini, M.C. Khellaf, B. Tagliafierro, L. Sarno, G. Pirovano. Submitted to Computer Physics Communications; "SPHERA v.9.0.0: a Computational Fluid Dynamics research code, based on the Smoothed Particle Hydrodynamics mesh-less method".

[2] Amicarelli A., Kocak B., Sibilla S., Grabe, J. "A 3D smoothed particle hydrodynamics model for erosional dam-break floods" *Int. J. Comput. Fluid Dyn*. 31(10), 413–434, 2017. https://doi.org/10.1080/10618562.2017.1422731.

[3] Barbero G., Moisello U., Todeschini S. "Evaluation of the areal reduction factor in an urban area through rainfall records of limited length: a case study". *J. of Hydrologic*

Eng. (ASCE), (2014) 19(11): 05014016-1-10.

[4] Bordoni M., Meisina C., Valentino R., Bittelli M., Chersich S. "Site-specific to local-scale shallow landslides triggering zones assessment using TRIGRS". *Nat. Hazards Earth Syst. Sci.*, (2015) 15: 1025–1050 doi:10.5194/nhess-15-1025-2015.

[5] Ciaponi C., Murari E., Todeschini S. "Modularity-Based Procedure for Partitioning Water Distribution Systems into Independent Districts". *Water Resources Management*, (2016) 30(6): 2021-2036, doi:10.1007/s11269-016-1266-1.

[6] Colagrossi A., Landrini M. "Numerical simulation of interfacial flows by smoothed particle hydrodynamics". *J. Comp. Phy*. (2003) 191, pp: 448–475.

[7] Domínguez J. M., Crespo A. J. C., Gómez-Gesteira M. "Optimization strategies for CPU and GPU implementations of a smoothed particle hydrodynamics method," Comput. Phys. Commun. (2013) 184(3): 617-627.

[8] Grenier N., Antuono M., Colagrossi A., Le Touzé D., Alessandrini B. "An Hamiltonian interface SPH formulation for multi-fluid and free-surface flows(2009). *J. Comp. Phy*. (2009) 228, pp: 380-393.

[9] Guandalini R., Agate G., Manenti S., Sibilla S., Gallati M. "SPH Based Approach toward the Simulation of Non-cohesive Sediment Removal by an Innovative Technique Using a Controlled Sequence of Underwater Micro-explosions". *Procedia IUTAM*, (2015) 18, 28–39.

[10] Guandalini R., Agate G., Manenti S., Sibilla S., Gallati M. "Innovative numerical modeling to investigate local scouring problems induced by fluvial structures". *Proc. 6th Int. Conf. on Bridge Maintenance, Safety and Management* (IABMAS 2012), Stresa, Lake Maggiore, Italy, 8–12 July 2012; pp. 3110–3116, 2012.

[11] Hoover W.G. "Isomorphism linking smooth particles and embedded atoms". *Physica* A 260 (1998) 244–254.

[12] Hu X.Y., Adams N.A. "An incompressible multi-phase SPH method". *J. Comp. Phy*. (2007) 227, pp:264–278.

[13] Liu G.R. & Liu M.B. *Smoothed Particle Hydrodynamics – a meshfree particle method*. (2003) World Scientific.

[14] Manenti S., Wang D., Domínguez J.M, Li S., Amicarelli A., Albano R. Submitted to *Water*: "SPH modelling of water-related natural hazards".

[15] Manenti, S. "Standard WCSPH for free-surface multi-phase flows with a large density ratio". *Int. J. of Ocean and Coastal Eng.* - Vol. 1, No. 2 (2018) 1840001 (39 pages) World Scientific Publishing Company. DOI: 10.1142/S2529807018400018.

[16] Manenti, S., Amicarelli, A., Todeschini, S. "WCSPH with Limiting Viscosity for Modeling Landslide Hazard at the Slopes of Artificial Reservoir". *Water*, (2018) 10(4), 515; doi:10.3390/w10040515

[17] Manenti S., Pierobon E., Gallati M., Sibilla S., D'Alpaos L., Macchi E., Todeschini S. "Vajont Disaster: Smoothed Particle Hydrodynamics Modeling of the Postevent 2D Experiments". *J. Hydraul. Eng.*, (2016) 142, 05015007.

[18] Manenti S., Sibilla S., Gallati M., Agate G., Guandalini R. "SPH Simulation of Sediment Flushing Induced by a Rapid Water Flow". *J. of Hydr. Eng.* 2012, Vol. 138, No. 3, pp. 272-284, March 1 (2012) ISSN 0733-9429/2012/3-0–0 DOI:10.1061/(ASCE)HY.1943-7900.0000516.

[19] Monaghan J.J., Ashkan R. "A simple SPH algorithm for multi-fluid flow with high

density ratios". *Int. J. Numer. Meth. Fluids* (2013) 71:537–561.

[20] Monaghan, J. J. "Simulating free surface flows with SPH". *J. Comp. Physics*, (1994) 110(2), pp. 399–406.

[21] Newman J.P., Maier H.R., Riddell G.A. et al. "Review of literature on decision support systems for natural hazard risk reduction: Current status and future research directions". *Environmental Modelling & Software* (2017) 96, 378-409.

[22] Pastor M., Haddad B., Sorbino G., Cuomo S., Drempetic V. "A depth-integrated, coupled SPH model for flow-like landslides and related phenomena". *Int. J. Numer. Anal. Methods Geomech*. 2009, 33, 143–172. https://doi.org/10.1002/nag.705 .

[23] SPHERA v.9.0.0 (RSE SpA). https://github.com/AndreaAmicarelliRSE/SPHERA

[24] Sussman M., Smereka P., Osher S. "A level set approach for computing solutions to

[25] Todeschini S., Manenti S., Creaco E. "Testing an innovative first flush identification methodology against field data from an Italian catchment". *J. of Environmental Management*, (2019) 246: 418-425, doi:10.1016/j.jenvman.2019.06.007.

[26] Zizioli D., Meisina C., Valentino R., Montrasio L. "Comparison between different approaches to modeling shallow landslide susceptibility: a case history in Oltrepo Pavese, Northern Italy". *Nat. Hazards Earth Syst. Sci.*, 13, 559–573, 2013. doi:10.5194/nhess-13-559-2013.

Comparison of interface models

to account for

surface tension in SPH method

S. Geara* [a,c,d], S. Adami[b], S. Martin[a], O. Bonnefoy[a], J. Allenou[c], B. Stepnik[c], W. Petry[d]

[a]Mines Saint-Etienne, Univ Lyon, CNRS, UMR 5307 LGF
Centre SPIN, F - 42023 Saint-Etienne, France

[b]Chair of Aerodynamics and Fluid Mechanics,
Technical University of Munich, Garching, Germany

[c]Framatome - CERCA™
10 Rue Juliette Récamier, 69456 Lyon Cedex 06, France

[d]Research Neutron Source Heinz Maier-Leibnitz (FRM II),
Technical University of Munich, 85748 Garching, Germany

ABSTRACT

The Smoothed Particle Hydrodynamics method (SPH) is a meshfree Lagrangian simulation method widely applied for fluid simulations due to the advantages presented by this method for solving problems with free and deformable surfaces.

In many scientific and engineering applications, surface tension forces play an important or even dominating role in the dynamics of the system. For instance, the breakage (instability) of a liquid jet or film is strongly affected by the strength of the surface tension at the liquid-air interface. Simulating deforming phase interfaces with strong topological changes is still today a challenging task. As a promising numerical method, here we use SPH to predict the interface instability at a water-air interface.

With SPH, the main challenge in modelling surface tension at a free-surface is the accurate description of the interface (normal direction and curvature). When only the liquid phase is modelled (to decrease the computational cost), the standard SPH approximations to calculate the normal direction and curvature of the interface suffer from a lacking "full support", i.e. the omitted and therefore missing gas particles. Various models for such free surface surface tension corrections were presented, see e.g. among others Sirotkin et al., Ordoubadi et al. or Ehigiamusoe et al. Many of these models follow the classical Continuum Surface Force (CSF) approach (Morris, Adami et al.) and incorporate different corrections/treatments at the surface.

The objective of our ongoing study is to investigate the influence of different interface descriptions. We compare different free surface particle detection schemes, normal vector calculations and curvature estimations for the quality of the resulting surface-tension effect. In this work, we focus on two-dimensional problems and consider a static drop and oscillating drops as test cases.

KEYWORDS

Smoothed Particle Hydrodynamics, Free surface flow, Surface tension, Interface description

I. Introduction

Surface tension plays an important role in many engineering and industrial applications such as liquid atomization. Usually, these phenomena occur on small length scales, therefore the development of a proper surface tension model can help greatly in physically developing these applications. However, simulating deforming phase interfaces with strong topological changes is still today a challenging task.

Among existing methods for fluid simulations, the Smoothed Particle Hydrodynamics (SPH) presents the advantage of simulating free surfaces with high deformations. SPH is a meshfree Lagrangian numerical method that was first introduced independently in 1977 by Lucy [1] and Gingold and Monaghan [2] to solve astrophysical problems. The general idea behind SPH lies in representing the fluid by a series of discretization points/particles each representing a mass of fluid. The continuity of the fluid and its properties is recovered by the spatial convolution of the physical properties of each particle by a kernel or smoothing function.

Three general approaches for modeling surface tension with SPH can be found in the literature. The first one is the Inter Particle Force (IPF) where an attractive/repulsive force is applied to all the SPH particles [3], [4]. The implementation of the IPF is simple. However, the main drawback of this method is that the surface tension force needs to be calibrated with experimental results. The second one is the Continuum Surface Stress (CSS), where the surface tension force is formulated as a gradient of the stress tensor which is calculated from the surface normal with no need to calculate the curvature [5]. The third one is the Continuum Surface Force (CSF), initially proposed by Brackbill [6], where the surface tension force is converted to a force per unit volume and is applied only on particles close to the interface. The main challenge of this method is to accurately calculate the normal vectors and the curvature at the interface. In this work we are focusing on the CSF method because it is a general approach that uses the physical properties of the fluid and does not need to be tuned for each simulation case. Many of the CSF models found in the literature are only valid for fluid-fluid systems [7], [8]. However, for free surfaces, the standard SPH approximations to calculate the normal vector and curvature of the interface suffer from the lack of "full support"., i.e. the omitted and therefore missing gas particles. To overcome this problem many corrections were proposed in the literature, see e.g. amongst others [9]–[12].

In their model, Sirotkin *et al.* [9] used the correction matrix proposed by Bonet *et al.* [13] to adjust the kernel gradient for the calculation of the density, pressure force, normal vectos and curvature. This kernel gradient modification allows to obtain accurate normal vectors and curvature estimations, however a 1.5 times bigger smoothing length is required for more reliable results. Ordoubadi *et al.* [10] added imaginary particles near the free surface with a mirroring technique in order to accurately simulate the surface tension force. This technique seems complex to implement and not straightforward, but according to the examples shown it significantly improves the normal vectors and gives more accurate curvatures. However, in all their examples a high fluid viscosity was used (100 times the viscosity of water). Ehigiamusoe *et al.* [11] used a correction factor for only the curvature calculation without any additional correction for the normal vectors. This method may give stable and accurate results for simple examples, but in the cases with sharp corners and high surface deformation, another correction technique needs to be used for the normal vector calculation and curvature estimation. Russel *et al.* [12] adapted the model proposed by Morris [7] for free surface simulations by proposing a correction factor for the normal vectors and curvatures. However, once again this correction factor is valid only for simple cases but not for complex geometries with sharp edges or sudden changes in the curvature. It is worth mentioning that in most of the presented models the numerical validation examples were conducted at relatively high fluid viscosities.

The objective of our ongoing study is to investigate the influence of the interface properties estimation in the presented models on the surface tension force. We compare different free surface particle detection schemes, normal vector calculations and curvature estimations for the quality of the resulting surface-tension effect. In this work, we focus on two-dimensional problems and consider a static drop with Laplace law and oscillating drops as representative test cases.

II. Basics of SPH method

In the Lagrangian description, the Navier-Stokes set of equations for viscous flow can be expressed as

$$\frac{d\rho}{dt} = -\rho \nabla . v \tag{1}$$

$$\frac{dv}{dt} = g + \frac{1}{\rho}[-\nabla P + F^{(v)} + F^{(s)}] \tag{2}$$

where ρ, v, g, P, $F^{(v)}$, $F^{(s)}$ are density, velocity, body force, pressure, viscous force and surface tension force, respectively.

The idea of SPH is the discretization of the domain with a set of particles and the use of weighted integrals to approximate the field functions. The value of any function f (e.g. density or velocity) at a position r can be estimated according to the following summation form

$$f(\vec{r}) \approx \sum_j^N \frac{m_j}{\rho_j} f(\vec{r}_j) W(|\vec{r}_i - \vec{r}_j|, h), \tag{3}$$

where m_j and r_j are the mass and position of particle j, respectively. W represents the weighting kernel function with h being the smoothing length that determines the interpolation domain. A suitable kernel function should be normalized, positive and radially symmetric. It should converge to the Dirac delta function when h tends to 0 and it should have a compact support domain [14]. Here we use the Spike 3 kernel function (with a compact support of 3h) because it minimizes the instability due to compression [9].

Using Eq. (3), various SPH formulations can be obtained depending on the assumptions and purpose of the simulation [15]. In our study, we used the formulation proposed by Adami [8].

According to the CSF approach, the surface tension force is applied in the normal direction only on particles near the free surface to minimize the surface energy. It can be expressed as follows [7]

$$f^{(s)} = \delta_s \sigma k \hat{n} \tag{4}$$

where δ_s is the surface delta function used to smooth the surface tension force over a transition band, σ is the surface tension coefficient, k the curvature and $\hat{n}$ the normalized normal vector.

The accurate representation of the surface tension force at the interface depends on the normal vector calculation and curvature estimation.

III. Surface topology characterization

III.1. Surface particle detection

For multi-phase simulations a color function assigned to each particle is used to track the interface. The smoothing of the color function is defined as

$$c_i = \sum_j c_j^0 V_j W_{ij} \quad , \tag{5}$$

where c_j^0 is the color function. For single-phase simulations the color function of all fluid particles is equal to 1.

For Eq. (5) the value of c_i is theoretically equal to 1 for particles in the bulk with a full kernel support, while close to the free surface the number decreases. A threshold value of 0.9 can be defined for detecting surface particles. This method (Kernel summation) is very simple to implement and does not have a large computational cost. It presents the advantage of detecting a surface band instead of only surface particles by adjusting the threshold value. However, in some simulations, low density regions may appear inside the fluid. In these regions, spurious free surface particles can be detected due to the lack of neighboring particles, inducing non physical surface tension forces.

To avoid this problem, more accurate surface tracking algorithms were developed. Barecasco *et al.* [16] presented a simple method for detecting free-surface particles based on the idea of cover vectors. For each particle i, the cover vector b_i is defined as

$$b_i = \sum_j \frac{\vec{r}_i - \vec{r}_j}{|\vec{r}_i - \vec{r}_j|} \tag{6}$$

For detecting surface particles, a cone of angle θ_i (threshold angle) is considered around each b_i. If one of the neighboring particles j is inside the cone, then particle i is not considered as a surface particle, otherwise particle i belongs to the free surface. The value of θ_i plays an important role in boundary particle detection, it is usually chosen equal to $\pi/3$.

Another accurate surface particle detection algorithm [17] is to consider a disk, having twice the length of the supporting domain for good accuracy, around each particle i. This circular area is then split into sectors (in our case 8 sectors are considered), and each sector is checked for neighboring fluid particles. If at least one sector does not have any particle, than particle i is considered as surface particle.

Figure 1 shows a comparison between the three described methods for a classical dam break simulation. Surface particles can be detected by these methods even when the surface undergoes major deformations. As explained earlier, with the first method, cavities inside the fluid can be wrongly detected as free-surface, see Figure 1 a) (right side).
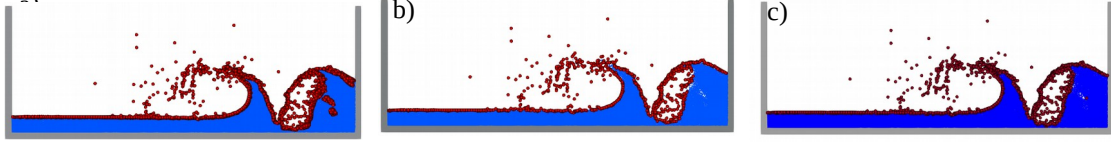
Figure 1: Surface particle detection (red particles represent surface particles): a) Kernel summation, b) Cover vector and c) Disk sectors

Because the two last methods are more time-consuming compared to the simple summation (Figure 2), it is interesting to combine these two techniques [10]. The first step consists of detecting the surface particles by the Kernel summation technique and then "Cover vector" (b) or "Disk sectors" (c) can be performed only on these surface particles.
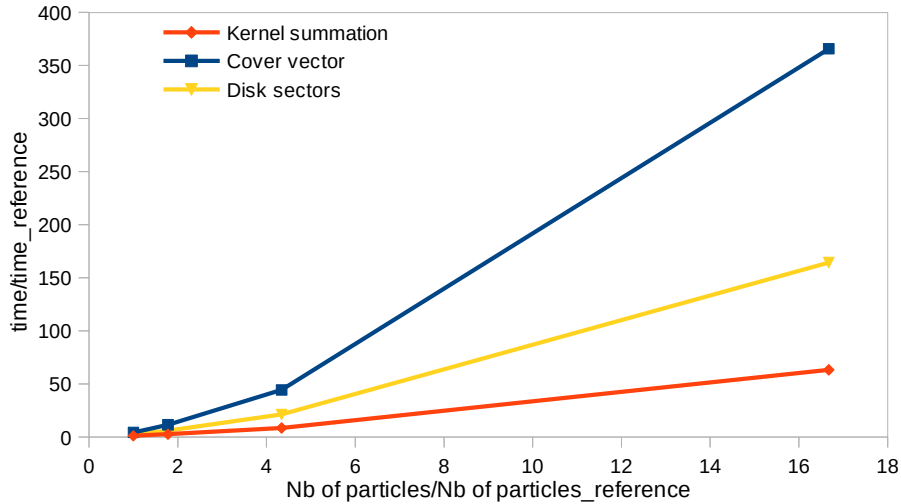

Figure 2: Computational time as a function of the number of particles

III.2. Normal vectors

Many of the CSF surface tension models are based on the model presented by Morris [7]. The normal vectors can be estimated as the gradient of the color function

$$\vec{n}_i = \vec{\nabla} c_i \tag{7}$$

with $\quad \vec{\nabla} c_i = \sum_j V_j (c_j - c_i) \vec{\nabla} W ij \qquad$ "NV-Color gradient" $\tag{8}$

where c_i is calculated according to Eq. (3).

When modeling only one phase, the number of interpolation points decreases near the free surface. One of the techniques that can be used to overcome this problem is the correction matrix proposed by Bonet *et al.* [13] to adjust the kernel gradient. Sirotkin *et al.* [9] used this correction matrix for the density, pressure force, normal vector and curvature calculation. For each particle i the matrix L_i is defined as

$$L_i = \sum_j V_j (\vec{\nabla} W_{ij}) \otimes \vec{r}_{ij} \qquad\qquad\qquad\qquad\qquad\qquad\qquad (9)$$

$$\vec{\nabla} \widetilde{W_{ij}} = L_i^{-1} \vec{\nabla} W_{ij} \qquad\qquad\qquad\qquad\qquad\qquad\qquad (10)$$

With this new correction for the kernel gradient, the normal vector for each particle i becomes

$$\vec{\nabla} c_i = \sum_j V_j (c_j - c_i) \vec{\nabla} \widetilde{W_{ij}} \qquad \text{"NV-Color gradient corrected"} \qquad (11)$$

Based on Eq. (7), Russel *et al.* [12] proposed the following normal vector calculation

$$\vec{n}_i = \sum_j V_j \left(\frac{1}{c_i} + \frac{1}{c_j} \right) \vec{\nabla} W_{ij} \qquad \text{"NV-Russel *et al.*".} \qquad (12)$$

Ordoubadi *et al.* [10] proposed another method that consists of adding imaginary particles by mirroring the particles in the transition band. These particles have the same mass as particle i with a color function equal to zero. If particle i is a surface particle, then for each particle j located in the support domain of i (but not a surface particle), a particle j' is created by mirroring particle j according to i. Otherwise, if particle i is not a surface particle, then for each particle j in the support domain of i and located on the free surface, a particle j' is created by mirroring i according to j.

Another method to calculate the normal vector is to use the cover vectors [16]. In fact, the direction of the cover vector can be used as an estimation of the direction of the normal vector of the surface.

In SPH, every field variable is evaluated by a smoothing function, thus it seems preferable to apply the surface tension force over a few smoothing lengths (transition band) and not only on one layer of surface particles. Regardless of the interface tracking techniques presented in the previous section, this transition band can be defined by the normal vectors. In fact, the direction and magnitude of the normal vector are only accurate near the interface. In the bulk, the normal vectors have small magnitude with erroneous directions. This may cause a problem when calculating the curvature because in this case, the normalized normal vectors are used. To address this issue, only well defined normal vectors are used in the surface tension calculation by applying the following filtering

$$\vec{n}_i = \begin{matrix} \vec{n}_i & , & \text{if } |n_i| > \varepsilon \\ 0 & , & \text{if } |n_i| \leq \varepsilon \end{matrix} \qquad\qquad\qquad\qquad (13)$$

where the value of ε is typically 0.01/dx and dx is the initial particle spacing.

With this condition, a transition band consisting of more than one layer of particles is automatically detected near the interface. Thus, the surface tension force is only applied on these particles. However, as explained earlier, with this technique voids and cavities inside the fluid will generate particles inside the transition band which lead to a nonphysical surface tension force. In this case, it seems important to detect surface particles using an appropriate technique. The transition band will consist of the particles that are in the support domain of the surface particles and have a well defined normal vector.
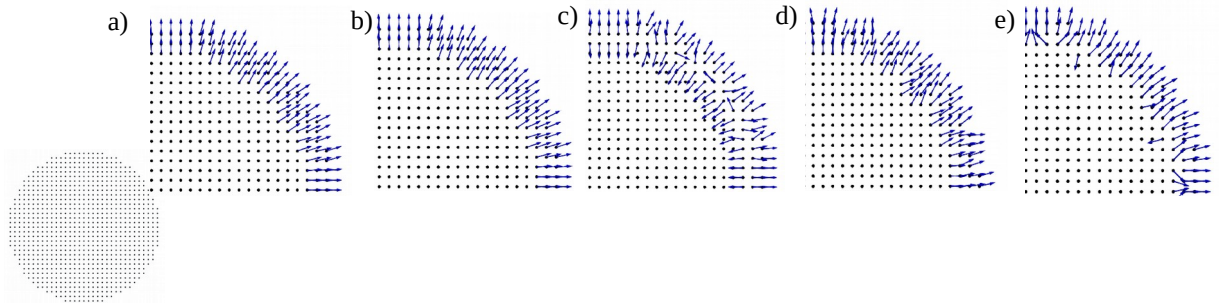

Figure 3: Normal vectors: a) NV- Color gradient, b) NV- Color gradient corrected,
c) NV- Russel et al., d) NV- Ordoubadi et al. and e) NV- Cover vector

Figure 3 presents a comparison between the different methods presented above. For this comparison, a disk of radius equal to 5 mm is considered. The particle spacing is equal to 0.3 mm and a total

number of 865 particles is considered. The normal vector calculated from the method presented by Russel (c) or from the cover vector (e) are only valid for the first layer of particles.

III.3. Curvature

The curvature at each particle i is calculated as follows

$$k_i = \nabla . \hat{n}_i \tag{14}$$

with $\quad \hat{n}_i = \dfrac{\vec{n}_i}{|n_i|}$ (15)

Only the reliable normal vectors should be taken into consideration for the calculation of the curvature. This means that the wrong direction for the normal vectors create a problem also in calculating the curvature. Moreover, the calculation of the curvature is sensitive because it is based on two consecutive derivations of the kernel function.

Here, we are going to compare different methods found in the literature to calculate the curvature (Figure 4). For this comparison, the same disk of radius equal to 5 mm was considered with 865 particles For the first test, and in order to eliminate the effect of the normal vector directions, prescribed normal vectors are used. We impose the normal vector of particle i to be exactly

$$\vec{n}_i = \vec{r}_i - (\vec{r})_{center} \tag{16}$$

Morris [7] added a normalization factor for the curvature calculation, thus the curvature is obtained by

$$k_i = \frac{\sum\limits_{j} V_j (\hat{n}_j - \hat{n}_i) . \nabla W_{ij}}{\sum\limits_{j} V_j W_{ij}} \tag{17}$$

According to Sirotkin et al. [8], with the correction matrix used for calculating the gradient of the kernel function the normalization factor is not required anymore, and the curvature is then calculated as follows

$$k_i = \sum\limits_{j} V_j (\hat{n}_j - \hat{n}_i) . \nabla \widetilde{W_{ij}} \tag{18}$$

Adami et al. [8] proposed another divergence approximation for calculating the curvature with lacking full support by

$$k_i = d \frac{\sum\limits_{j} V_j (\hat{n}_j - \hat{n}_i) . \nabla W_{ij}}{\sum\limits_{i} V_j |r_{ij}| \dfrac{dW_{ij}}{dr}} \tag{19}$$
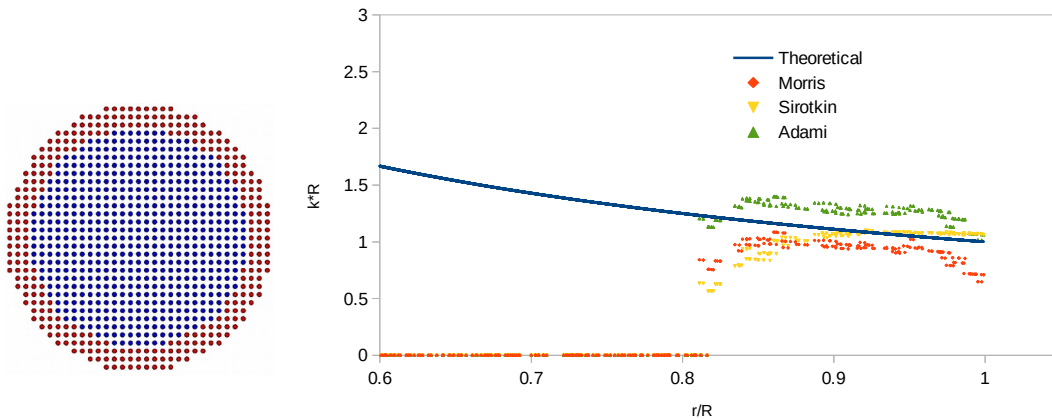

Figure 4: Different methods for curvature estimation

According to the results presented in Figure 4, it seems that the three methods give acceptable results for the curvature estimation. We are more interested in the region close to the free surface (r/R>0.95) where the surface delta function is maximum. In Adami and Morris models, the curvature tends to decrease slightly near the free surface because of the lack of the full support. On the other hand, the correction matrix used by Sirotkin compensates the missing particles near the free surface and hence it gives more accurate results. Note that Ordoubadi *et al.* [10] used the imaginary particles to calculate the curvature based on Eq. (17).

IV. Application of surface tension force

When calculating the surface tension force, we should only consider the surface particles and smooth this force by using an appropriate surface delta function or a kernel function. For example, Ehigiamusoe *et al.* [11] set the surface delta function equal to 1/dx at the interface. For the other methods, the smoothing of the force can be done using the norm of the normal vector, subsequently the delta function can be approximated as

$$\delta_s = \lambda |n| \tag{20}$$

where λ is a constant calibration parameter.

The surface tension force should be maximum at the surface or at the tip of sharp corners and it must decrease in magnitude gradually while moving away from the free surface to the interior. The comparison between different surface delta functions is presented in Figure 5. In order to compare them, the normal vectors are normalized to the maximum value depending on each method. The smoothing over the transition band with and without correction are completely different, knowing that the direction of the normal vectors are almost the same.
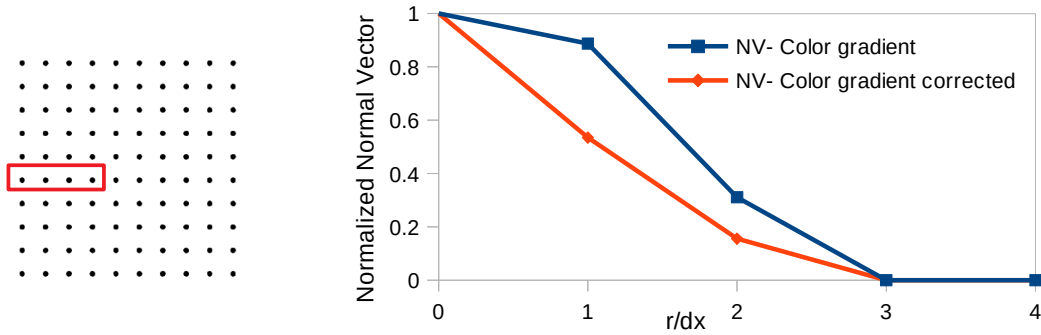

Figure 5: Comparison between the different surface delta functions

In order to obtain a proper surface tension force, many combinations of the different methods presented above for surface characterization were tested. For the surface particle detection, the kernel summation gives good results and it can be combined with the cover vector method for complex geometries. For the normal vector, all the presented methods give acceptable directions, at least for the first layer of surface particle. The crucial differences lay in the definition of the transition band for the curvature calculation and the choice of the smoothing surface delta function. For the curvature calculation, the three methods give good results. If the correction matrix is already calculated, Eq. (18) will be used to calculate the curvature because it is the most accurate. Otherwise, Eq. (17) could be used to minimize the computational cost.

The calculation of the surface properties and the accurate representation of the surface tension plays an important role in the stability of the simulation. However, other parameters should be considered, notably the density evaluation method and the momentum equation discretization. Many combinations can be tested, but we decided to work with the formulation proposed by Adami *et al.* [8] for the momentum equation and the density integration technique for the density evaluation.

To sum up, Table 1 presents the most promising methods/combinations that we decided to explore further in our ongoing study.

ID	Normal vector		Surface delta function + Smoothing		
	Sirotkin *et al.*	Cover vector	Sirotkin *et al.*	Morris	Kernel
A	X		X		
B	X		*no smoothing*		
C		X	*no smoothing*		

Table 1: Methods/Combinations for surface tension force in SPH

In the next section we present both static and dynamic numerical test cases to validate the models.

V. Numerical examples
V.1. Square droplet

One common test case is the transformation of a square droplet into a circular droplet under the effect of surface tension . For this example, an initial square of L=l=5 mm is placed in the center of a square domain (10*L). The particle spacing is equal to 0.1 mm and a total number of 2500 particles is considered. The physical properties of water were considered except that a higher viscosity (10 times the viscosity of water) was needed for a stable simulation. For all the test cases a smoothing length of h=3dx is used. Figure 6 presents the initial and final stable shape after t=0.2 s of the droplet. By comparing the final results, we can deduce that method C does not give a stable circular droplet even after t>0.2s.
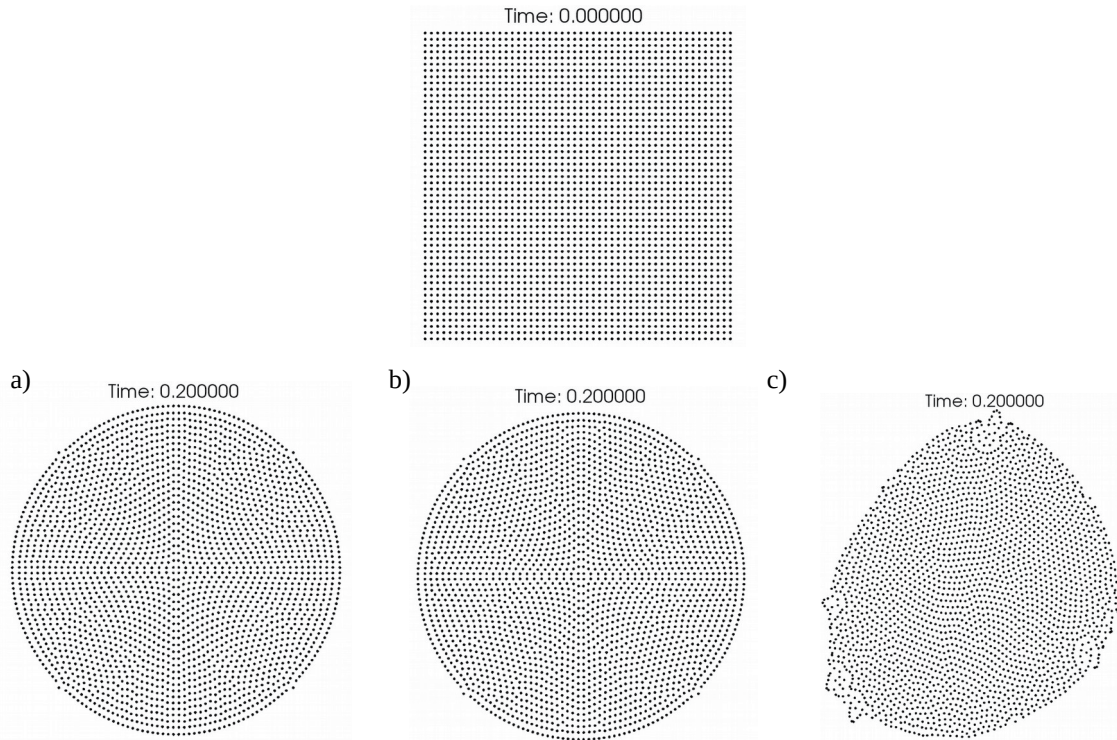

Figure 6: Particle positions at t=0 and t=0.2 s : a) Method A, b) Method B, and c) Method C

The pressure profile inside the droplet at t=0.2 s is compared to the Laplace pressure drop given by Eq. (21) (Figure 7). The pressure profile is almost constant inside the droplet and is equal to the theoretical pressure with some fluctuations near the free surface. The calibration coefficient λ is found equal to 3 for method A. An overall coefficient of around 6.5 is used for method B to compensate in part the drop in the curvature estimated values due to the use of only surface particles.

In methods A and B, this coefficient is independent on the physical size or the initial spacing of the particles.

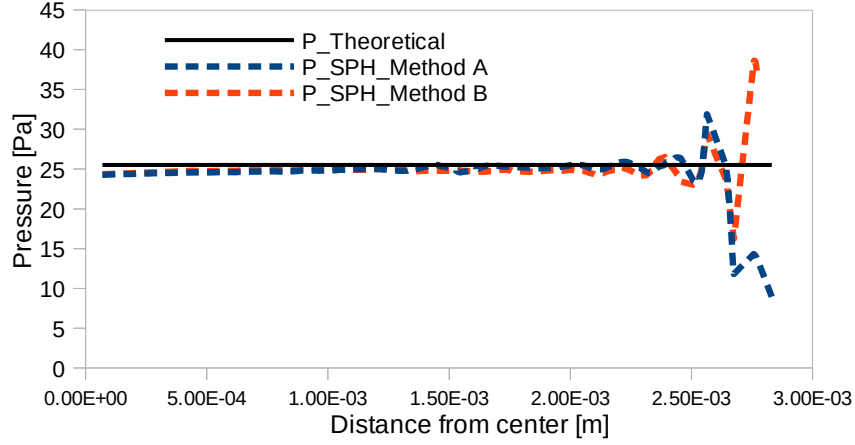$$P = \frac{\sigma}{R} = \frac{\sigma \sqrt{\pi}}{L} \tag{21}$$

Figure 7: Pressure profile of the droplet at t=0.2 s

V.2. Droplet oscillation

An other dynamic test case is the droplet oscillation under the effect of surface tension. Instead of starting from an elliptic droplet, an initial velocity field was prescribed as follows:

$$u_x = u_0 \frac{x}{r_O} (1 - \frac{y^2}{r_0 r}) * \exp(\frac{-r}{r_0}) \tag{22}$$

$$u_y = -u_0 \frac{y}{r_O} (1 - \frac{x^2}{r_0 r}) * \exp(\frac{-r}{r_0}) \tag{23}$$

The circular droplet of radius equal to 1.7 mm is placed at the center of the computational square domain. The total number of particles is equal to 912 with a particle spacing equal to 0.1 mm. Physical properties of water were considered. However, a dynamic viscosity of 0.003 Kg.m^{-1}.s^{-1} is considered. In this example u_0 and r_0 were taken equal to 2 m/s and 0.05 m, respectively. Figure 8 shows the position of the particles at different times for the three methods listed in Table 1. It can be deduced that the three methods give relatively stable results. However, by comparing the particles distribution, we can conclude that the first two methods based on the correction matrix are more accurate.

The distance between the top particle along the y axis and the center of the droplet is plotted over time in Figure 9. According to method A, the SPH period of oscillation is $T_{SPH}=21.6$ ms. We found good agreement by comparing the SPH period with the theoretical period of oscillations given by:

$$T_{theo} = 2\pi \sqrt{\frac{R^3 \rho}{s(s^2-1)\sigma}} = 21.2\, ms \quad, \tag{24}$$

where R is the droplet radius and s=2 if the shape of the drop remains close to an ellipse.
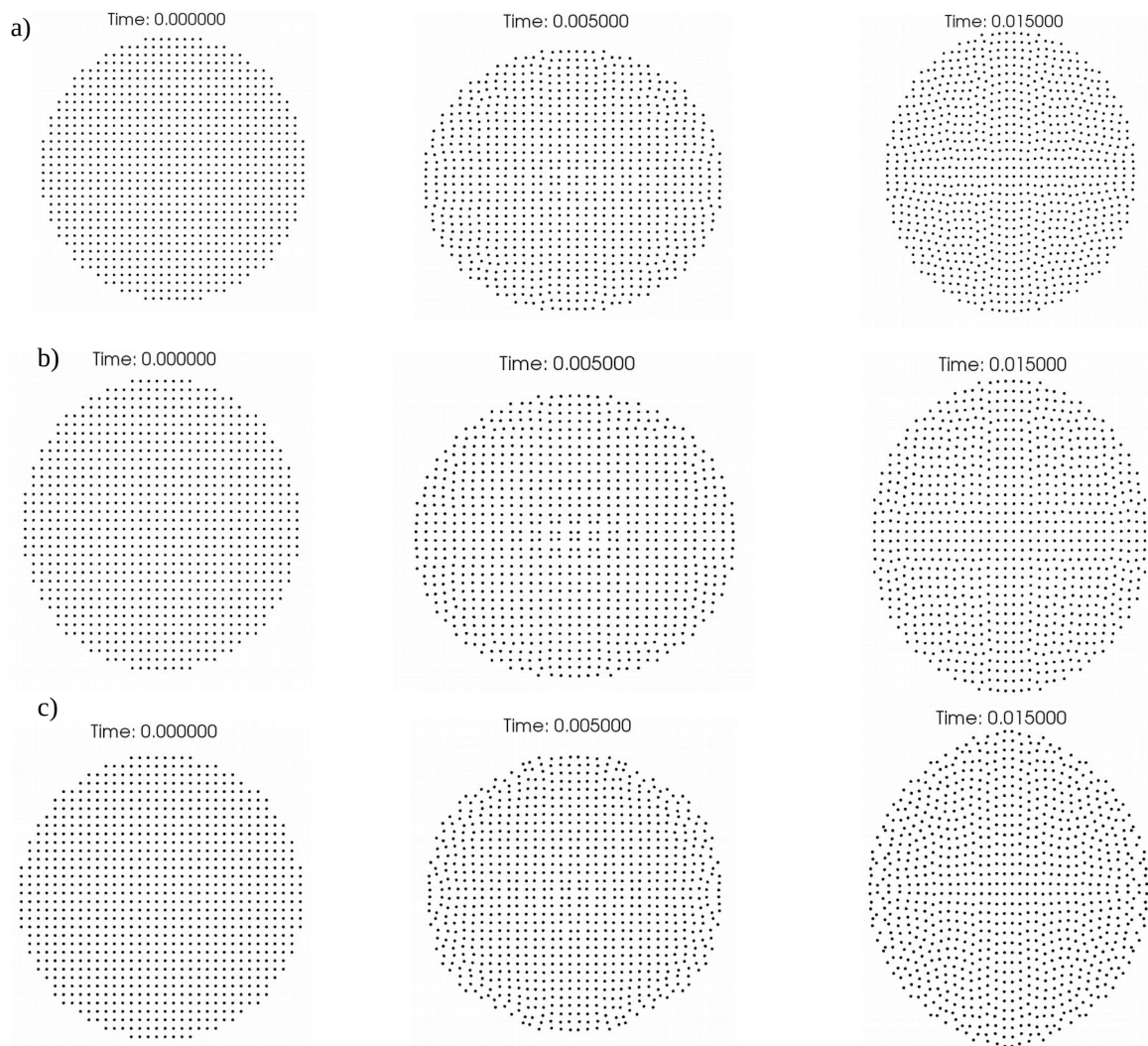
722

Figure 8: Evolution of the particles position at different time intervals: a) Method A, b) Method B and c) Method C
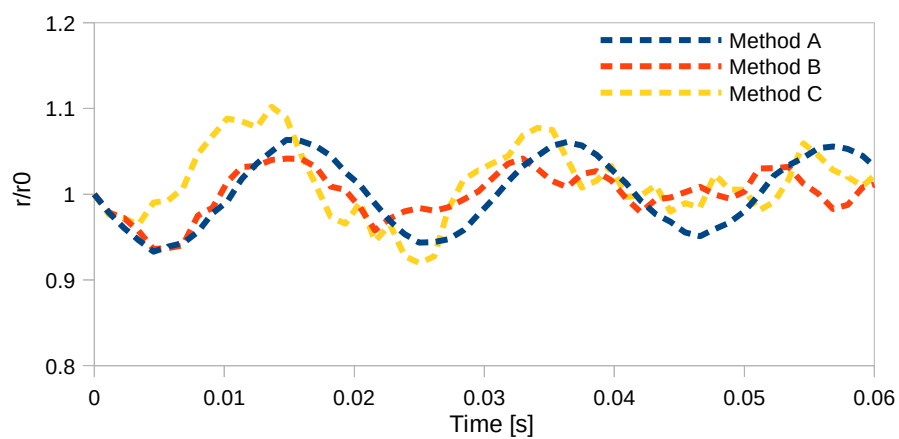

Figure 9: Evolution of the droplet size along the y axis

VI. Conclusions

In this work, we compare methods found in the literature for detecting surface particles, calculating normal vectors and curvature in order to estimate the proper surface tension force for free surface simulations. Other interesting methods can be explored in the future, like for example the reconstruction of the interface to calculate the normal vector and curvature [18].

Basically, once the normal vectors and curvature are correctly obtained the surface tension forces should be easily calculated. However, the choice of the transition band and the surface delta function plays an important role in defining the surface tension force. By comparing the three tested methods, we can conclude that the classical method presented by Sirotkin *et al.* [9] is the most stable one. The use of a transition band in method A is necessary for complex geometries. It ensures that a new surface particle will consider a surface tension force even though the particle is not detected as a surface particle but has at least one surface particle in its neighborhood. Another advantage of this method is the accuracy in calculating the curvature of the free surface.

Moreover, the stability of the simulation depends on many other factors like the pressure force, the viscosity force and the density calculation. These elements have a huge impact on the stability of the simulation. More importantly, the calculation of the density for free surface simulation needs to be adjusted near the free surface.

The objective of our future work is to improve the existing models to simulate low viscosity fluids such as water.

References

[1] L. B. Lucy, "A numerical approach to the testing of the fission hypothesis," *Astron. J.,* vol. 82, p. 1013, Dec. 1977.

[2] R. A. Gingold and J. J. Monaghan, "Smoothed particle hydrodynamics: theory and application to non-spherical stars," *Mon. Not. R. Astron. Soc.,* vol. 181, no. 3, pp. 375–389, Dec. 1977.

[3] A. Tartakovsky and P. Meakin, "Modeling of surface tension and contact angles with smoothed particle hydrodynamics," *Phys. Rev. E*, vol. 72, no. 2, Aug. 2005.

[4] N. Akinci, G. Akinci, and M. Teschner, "Versatile surface tension and adhesion for SPH fluids," *ACM Trans. Graph.,* vol. 32, no. 6, pp. 1–8, Nov. 2013.

[5] X. Y. Hu and N. A. Adams, "A multi-phase SPH method for macroscopic and mesoscopic flows," *J. Comput. Phys.,* vol. 213, no. 2, pp. 844–861, Apr. 2006.

[6] J. . Brackbill, D. . Kothe, and C. Zemach, "A continuum method for modeling surface tension," *J. Comput. Phys.,* vol. 100, no. 2, pp. 335–354, Jun. 1992.

[7] J. P. Morris, "Simulating surface tension with smoothed particle hydrodynamics," *Int. J. Numer. Methods Fluids*, vol. 33, no. 3, pp. 333–353, Jun. 2000.

[8] S. Adami, X. Y. Hu, and N. A. Adams, "A new surface-tension formulation for multi-phase SPH using a reproducing divergence approximation," *J. Comput. Phys.,* vol. 229, no. 13, pp. 5011–5021, Jul. 2010.

[9] F. V. Sirotkin and J. J. Yoh, "A new particle method for simulating breakup of liquid jets," *J. Comput. Phys.,* vol. 231, no. 4, pp. 1650–1674, Feb. 2012.

[10] M. Ordoubadi, M. Yaghoubi, and F. Yeganehdoust, "Surface tension simulation of free surface flows using smoothed particle hydrodynamics," *Sci. Iran.,* vol. 24, no. 4, pp. 2019–2033, Aug. 2017.

[11] N. N. Ehigiamusoe, S. Maxutov, and Y. C. Lee, "Modeling surface tension of a two-dimensional droplet using smoothed particle hydrodynamics: Modeling surface tension of a two-dimensional droplet using SPH," *Int. J. Numer. Methods Fluids*, vol. 88, no. 7, pp. 334–346, Nov. 2018.

[12] M. A. Russell, A. Souto-Iglesias, and T. I. Zohdi, "Numerical simulation of Laser Fusion Additive Manufacturing processes using the SPH method," *Comput. Methods Appl. Mech. Eng.,* vol. 341, pp. 163–187, Nov. 2018.

[13] J. Bonet and T.-S. L. Lok, "Variational and momentum preservation aspects of Smooth Particle Hydrodynamic formulations," *Comput. Methods Appl. Mech. Eng.,* vol. 180, no. 1–2, pp. 97–115, Nov. 1999.

[14] J. J. Monaghan, "Smoothed Particle Hydrodynamics," *Annu. Rev. Astron. Astrophys.,* vol. 30, no. 1, pp. 543–574, Sep. 1992.

[15] J. J. Monaghan, "Smoothed particle hydrodynamics," *Rep. Prog. Phys.*, vol. 68, no. 8, pp. 1703–1759, Aug. 2005.

[16] A. Barecasco, H. Terissa, and C. F. Naa, "Simple free-surface detection in two and three-dimensional SPH solver," *ArXiv13094290 Phys.*, Sep. 2013.

[17] G. A. Dilts, "Moving least-squares particle hydrodynamics II: conservation and boundaries," *Int. J. Numer. Methods Eng.*, vol. 48, no. 10, pp. 1503–1524, Aug. 2000.

[18] M. Zhang, "Simulation of surface tension in 2D and 3D with smoothed particle hydrodynamics method," *J. Comput. Phys.*, vol. 229, no. 19, pp. 7238–7259, Sep. 2010.

DAMAGE RESPONSE OF HULL STRUCTURE SUBJECTED TO CONTACT UNDERWATER EXPLOSION
VI INTERNATIONAL CONFERENCE ON PARTICLE-BASED METHODS - PARTICLES 2019

ZHANG ZHIFAN[1], WANG LONGKAN[2] AND HU HAOLIANG[1]

[1] State Key Laboratory of Explosion Science and Technology
Beijing Institute of Technology, Beijing 100081, China
E-mail address: heuzhangzhifan@hotmail.com

[2] China Ship Research and Development Academy
Beijing 100101, China
E-mail address: wanglongkan@hotmail.com

Key words: SPH, contact underwater explosion, shock wave, free surface, dynamic response.

Abstract. A high-pressure shock wave was produced during a process near-field underwater explosion, which led to serious damage into structures. A Smooth Particle Hydrodynamic (SPH) method is suitable for solving problems with large deformations. Hence, it is used to investigate pressure characteristics and dynamic response of hull structures subjected to near-field underwater explosion. Effect of free surface was taken into consideration. Propagation of shock wave in multi medium and its dynamic response to hull structures were analyzed.

1   INTRODUCTION

The probability of ship hull structure subjected to near-field underwater explosion increased with the wide application of precision guided weapons [1]. Therefore, in order to enhance ship's survivability, it is of great significance to study the damage mechanism of hull structures under near-field explosion. Many researchers both at home and abroad have studied underwater explosion and its damage into structures theoretically, experimentally and numerically [1-16]. With the rapid development of numerical technology, numerical simulation has become one of the main means to investigate underwater explosion. The traditional mesh methods have disadvantages of mesh distortion in the simulation of underwater explosion. However, SPH method with Lagrangian and particle properties is suitable for solving such problems as material motion tracking and strong discontinuous capture. Swegle *et al.* [10] discussed the related problems of stability in solving underwater explosion by SPH method. Liu *et al.* [11-13] demonstrated the feasibility of SPH method in solving underwater explosion problems through a large number of numerical tests. However, rare researches have reported the application of SPH method to near-field underwater explosion and its damage to hull structures, especially considering coupling effects of free-surface and damaged structures.

In this paper, a SPH model of hull structure subjected to near-field underwater explosion is first established. Then shock-wave propagation near hull structures and free surface and its damage into structures were studied. On this basis, effect of charge material on damage to

structures was discussed. The obtained results provide reference to dynamic response of ship structures subjected to underwater explosion and design of protective structures.

2 THEORETICAL AND NUMERICAL MODEL

2.1 Underwater explosion

Underwater explosion load [17] is composed by shock wave and bubble respectively generated in the early and later stages of explosion and bubble in the later stage, which is an important basis for prediction of structural dynamic response and anti-explosion design. The shock wave with high pressure and the bubble with long cycle can cause local and overall damage into structures, respectively. The shock wave which is the main impact load instantaneously results in the local damage for near-field underwater explosion while the bubble pulsation should be considered for mid-and far-field explosion [18]. This paper investigated the dynamic response of hull structures subjected to near-field explosion; hence, the shock-wave load is mainly analysed and studied.

2.2 Governing equation for underwater explosion

Large deformation is caused by near-field underwater explosion in a very short time, which may result in mesh distortion for the tradition mesh method. Thanks to Lagrangian and particle properties SPH method has natural advantages of dealing with problems of underwater explosion. The distortion of physical quantities is caused when the standard SPH method is used to solve problems with a large density ratio. Therefore, a modified SPH is used in this paper, given by [11]

$$
\begin{cases}
\dfrac{d\rho_i}{dt} = \rho_i \sum_{j=1}^{N} \dfrac{m_j}{\rho_j}(\boldsymbol{v}_i^b - \boldsymbol{v}_j^b)\dfrac{\partial W_{ij}}{\partial \mathrm{x}_i^b} \\[2mm]
\dfrac{d\boldsymbol{v}_i^b}{dt} = \sum_{j=1}^{N} \dfrac{m_j}{\rho_i \rho_j}(\sigma_i^{ab} + \sigma_j^{ab} + \Pi_{ij})\dfrac{\partial W_{ij}}{\partial \mathrm{x}_i^b} \\[2mm]
\dfrac{de_i}{dt} = \dfrac{1}{2}\sum_{j=1}^{N} \dfrac{m_j}{\rho_i \rho_j}(\sigma_i^{ab} + \sigma_j^{ab} + \Pi_{ij})(\boldsymbol{v}_i^b - \boldsymbol{v}_j^b)\dfrac{\partial W_{ij}}{\partial \mathrm{x}_i^b}
\end{cases}
\tag{3}
$$

where ρ is density; v is velocity; a and b are directions along axes; p is pressure; e is energy; t is time; x is coordinates; W_{ij} is smoothed function of a pair of particles j and i; Π_{ij} is artificial viscosity [11]; σ is stress composed of isotropic pressure and viscous shear stress.

(1) Stress of explosive products

The viscosity of explosive products and water is too small to be ignored. The stress can be obtained by the solution of pressure. Jones-Wilkins-Lee and Mie-Gruneisen equation of states (EoS) are used for these two media, expressed as [19]

$$
p = A\left(1 - \dfrac{\omega\eta}{R_1}\right)e^{-\frac{R_1}{\eta}} + B\left(1 - \dfrac{\omega\eta}{R_2}\right)e^{-\frac{R_2}{\eta}} + \omega\eta\rho_0 e ,
\tag{4}
$$

where p is pressure; η is the ratio of densities between explosive products and initial

explosive; ρ_0 is initial density of initial explosive; e_0 is initial energy; A, B, R_1 and R_2 are constants.

(2) Stress of water

When the water is in expansion state, the EoS is given by [20]

$$P = \frac{\rho_0 C^2 \mu [1 + \left(1 - \frac{\gamma_0}{2}\right)\mu - \frac{a}{2}\mu^2]}{[1 - (S_1 - 1)\mu - S_2 \frac{\mu^2}{\mu+1} - S_3 \frac{\mu^3}{(\mu+1)^2}]^2} + (\gamma_0 + a\mu)e,\tag{5}$$

while when it is in compressive state, the EoS is expressed as [20]

$$P = \rho_0 C_0^{\ 2}\mu + (\gamma_0 + a\mu)e,\tag{6}$$

where C is sound velocity; ρ_0 is the initial density of water; $\mu = \eta - 1$, η is the ratio of density before and after the explosion; γ_0 is Gruneisen coefficient ; S_1, S_2 and S_3 are the fitting coefficients.

(3) Stress of steel

Mie-Gruneisen EoS is used [21]

$$p(\rho, e) = (1 - \frac{1}{2}\Gamma(\zeta - 1))p_{\mathrm{H}}(\rho) + \Gamma\rho e,\tag{7}$$

where，Γ is Gruneisen coefficient，p_{H} is the pressure in the Hugoniot curve [11].

A shearing force in a metal liner with high shear strength is considered and Johnson-cook damage model is used [22].

3   NUMERICAL SIMULATION

A SPH model of hull structures near free surface subjected to near-field underwater explosion is established. Propagation of shock wave and its damage into structures are analysed.

3.1 NUMERICAL MODEL

Numerical model of ship structures attacked by a charge was simplified in Fig. 1. TNT and steel were used as materials of the charge and the structure, respectively. The surrounding water has a length of l_1 and a width of l_2. The thickness of the steel is d_1 and the length of the charge is d_2. The detailed geometrical parameters are shown in Tab. 1.
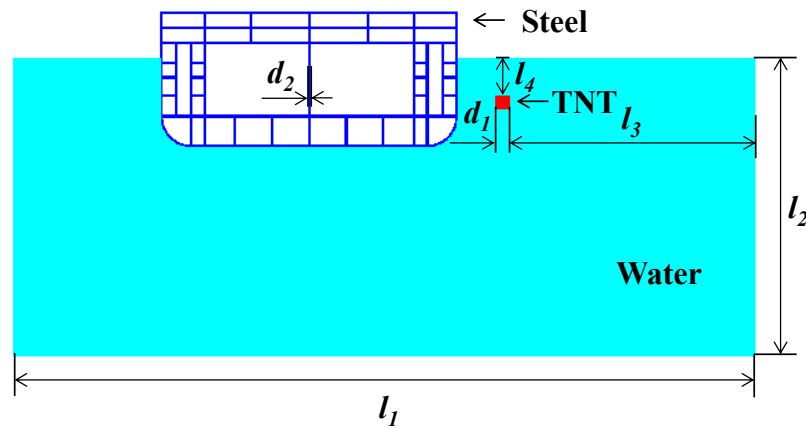
Figure 1: Numerical model

Table 1 Dimensions of the model

l_1	l_2	l_3	l_4	d_1	d_2
5.0	2.0	1.65	0.25	0.01	0.10

3.2 Results and discussion

Damage process of the hull structure was illustrated in Fig. 2. A spherical shock wave (SW1) propagated in the water and peaked at about 2 GPa at $t \approx 40\,\mu s$ in Fig. 2(a). When SW1 arrived at the steel a reflected shock wave (RSW1) was generated due to higher impedance of steel than that of water. Besides, a shock wave was also produced in the steel at about $85\,\mu s$. The shape of the explosive products has transformed from cubic to spherical in Fig. 2(b). At about $110\,\mu s$ SW1 reached the free surface in Fig. 2(c), resulting in a reflected rarefaction wave (RRW1). Fig. 2(d) shows that the shape of RSW1 developed to a non-spherical one. With the propagation of RRW1, the pressure around the free surface was low. It was found that the propagation velocity of the shock wave in the steel was much higher than that in the water in Fig. 2(e). The explosive products expanded in the water in Fig. 2(f). The free surface moves with the effect of the shock wave, with "spike" produced in the free surface. At about $205\,\mu s$ the pressure diminished to about 855 MPa, with a plastic deformation of the steel.

The spike increased with the effect of impact load. A hole was generated at the outer steel at about $305\,\mu s$. With the further effect of the high-pressure shock wave, the diameter of the hole increased. The surrounding water poured into and impacted the inner structure in Fig. 2(g). Due to the energy consumption of the reinforced and the spike the damage in the upper structure was declined.
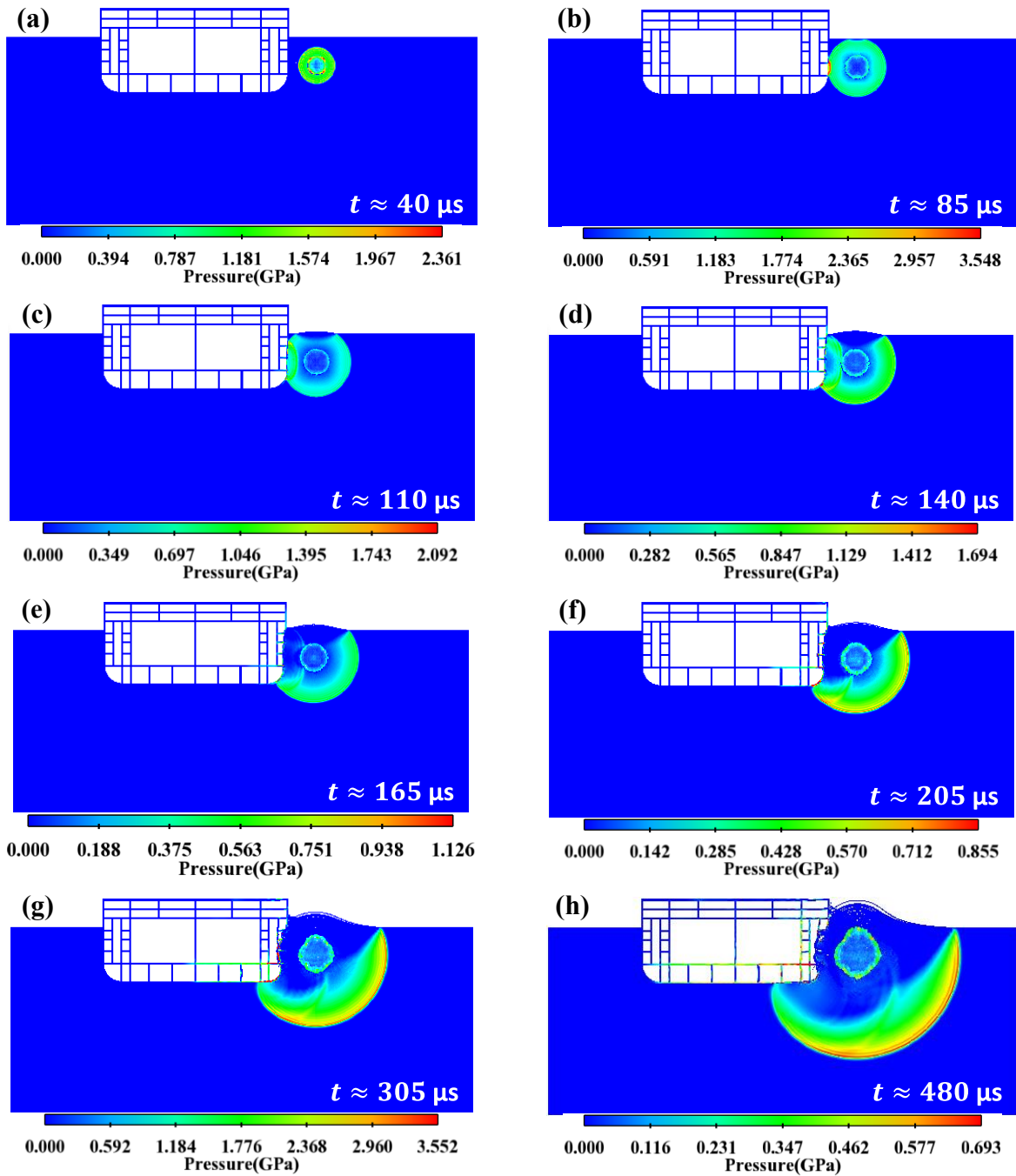
Figure 2: Pressure distribution in the process of underwater explosion; (a)-(f) correspond to moments at 40 µs, 85 µs, 110 µs, 140 µs, 165 µs, 205 µs, 305 µs and 480 µs.

5 CONCLUSIONS

The SPH method is used for the simulation of hull structures subjected to contact underwater explosion. Propagation of shock wave and its damage into structures were analysed. Conclusions were summarized as follows. Complex waves were produced in the process of structures subjected to underwater explosion. The superposition of these waves led

to complex pressure distribution. The phenomenon of "spike" was found and the truncation effect on the shock wave was caused by the free surface. It indicates that the shock wave has obvious irregular reflection effect near the free surface. Under the combined effect of transverse wall and "spike" which dispersed shock wave energy, the damage into the upper part of the side structure was weakened. The hole of the hull structure increased with the propagation of shock wave. After the water entered the hull, the inner structure was damaged.

REFERENCES

[1] Zhang A M, Zeng L Y, Cheng X D, et al. The Evaluation Method of Total Damage to Ship in Underwater Explosion. Applied Ocean Research, 2011, 33 (4): 240–251.

[2] Wierzbicki T, Hoo Fatt M S. Deformation and perforation of a circular membrane due to rigid projectile impact. Dynamic Response of structures to High-Energy Excitation, Geers T L and Shin Y S, ASME Book. 1991.

[3] Rajendran R, Narasimhan K. Damage prediction of clamped circular plates subjected to contact underwater explosion. International Journal of Impact Engineering, 2001, 25:373-386.

[4] Young-Woong L,Tomasz W. Fracture prediction of thin plates under localized impulsive loading. Part I: dishing. International Journal of Impact Engineering, 2005,31:1253-1276.

[5] Young-Woong L,Tomasz W. Fracture prediction of thin plates under localized impulsive loading. Part II: discing and petalling. International Journal of Impact Engineering, 2005, 31:1277-1208.

[6] Zhu Xi, Bai Xuefei, Huang Ruobo, et al. Crevasse experiment research of plate membrane in vessels subjected to underwater contact explosion. Shipbuilding China, 2003, 44(1):46-52. (in Chinese)

[7] Nurick G N, Shave G C. The Deformation and Tearing of Thin Square Plates Subjected to Impulsive Loads - an Experimental Study. International Journal of Impact Engineering, 1996, 18(l):99-116.

[8] Rajendran R, Narasimhan K. Damage prediction of clamped circular plates subjected to contact underwater explosion. International Journal of Impact Engineering, 2001, 25:373-386.

[9] Ramajeyathilagam K, Vendhan C P. Deformation and rupture of thin rectangular plates subjected to underwater shock. International Journal of Impact Engineering, 2004, 30:699-719.

[10] Swegle J W, Attaway S W. On the feasibility of using smoothed particle hydrodynamics for underwater explosion calculations. Computational Mechanics, 1995; 17:151-68.

[11] Liu G R and Liu M B. Smoothed Particle Hydrodynamics-A Meshfree Particle Method. World Sci., Singapore, 2003.

[12] Liu G R, Lam K Y, Zong Z. Smoothed particle hydrodynamics for numerical simulation of underwater explosion. Computational Mechanics, 2003(a), 30 (2):106-118.

[13] Liu G R, Zong Z, Lam K Y. Computer simulation of high explosive explosion using smoothed particle hydrodynamics methodology. Computers and Fluids, 2003(b), 32(3): 85-98.

[14] Liu M B, Liu G R, Lam K Y. A one dimensional meshfree particle formulation for simulating shock waves. Shock Waves, 2003, 13: 201-211.

[15] Zhang A M, Zhou W X, Wang S P, et al. Dynamic Response of the Non-Contact Underwater Explosion on Naval Equipment. Marine Structure, 2011, 24 (4), 396–411.

[16] Zhang A M, Yang W S, Chao H, et al. Numerical simulation of column charge underwater explosion based on SPH and BEM combination. Computers and Fluids, 2013; 71: 169-178.

[17] Cole R H. Underwater Explosion. New Jersey: Princeton University Press, 1948.

[18] Yao X L. Ship Vibration. Harbin: Harbin Engineering University Publishing Company, 2004: 51–66.

[19] Dobratz B M. LLNL Explosive Handbook. UCRL-52997, Lawrence Livermore National Laboratory, Livermore, CA. 1981.

[20] Steinberg D J. Spherical explosions and the equation of state of water. Report UCID-20974, Lawrence Livermore National Laboratory, Livermore, CA. 1987.

[21] Libersky L D, Petscheck A G, Carney T C, et al. High strain Lagrangian hydrodynamics: a three-dimensional SPH code for dynamic material response. Journal of Computational Physics, 1993, 109: 67-75.

[22] Johnson G R, Cook W H. A constitutive model and data for metals subjected to large strains, high strain rates and high temperatures. In Proc. 7th International Symposium on Ballistics, USA; 1983.

EVALUATION OF PUDDLE SPLASH IN AUTOMOTIVE APPLICATIONS USING SMOOTHED PARTICLE HYDRODYNAMICS

MURALEEKRISHNAN MENON[1], G. V. DURGA PRASAD[1], KEVIN VERMA[1], and CHONG PENG[1]

[1] ESS Engineering Software Steyr GmbH
Berggasse 35, 4400 Steyr, Austria
muraleekrishnan.menon@essteyr.com; www.essteyr.com

Key words: Fluid dynamics, Divergence Free SPH, Graphics Processing Unit

Abstract. The impact of splashing water as a car moves through water-soil puddle or flooded areas is significant to the automotive industry. Due to the multifold advantages of simulating this problem, several numerical approaches exists to understand the fluid dynamics and the fluid-structure interaction in such scenarios. The current research focuses on obtaining fluid dynamics of the splashing phenomena as a first step towards simulating such problems through a Computational Fluid Dynamic (CFD) approach by adopting the Smoothed Particle Hydrodynamics (SPH). As a mesh-free Lagrangian-based method, the SPH framework tracks particle behavior in the computational domain at each instant of dynamic simulations. In contrast to traditional grid-based methods, SPH is well suited for simulating fluid dynamic problems involving free-surfaces, multi-phase flows, and involving objects with high degree of deformations.

The current study presents results and discusses the observations from simulating a car Body-In-White (BIW) geometry with four tires that moves through a water puddle as a normal car would. The SENSE solver developed at ESS Engineering Software Steyr adopts the SPH framework and presents several formulations. The solvers are implemented on Graphics Processing Units (GPU) to enable its usage for industrial applications. The framework is developed to be easily parallelizable allowing multiple GPU simulations, that are useful for industrial problems involving huge number of particles. In addition to the ease of scaling, it also permits computations at higher particle resolutions when needed to handle specific physical constraints of a problem. The simulations discussed in the current study were performed using the Divergence-Free (DF-SPH) formulation in SPH, and implemented on multiple-GPU devices, with a particle discretization that allows to see the properties to the order of 5 mm.

1   INTRODUCTION

On a rainy day, it is inevitable in most parts of the world, that one needs to drive through stagnant water on roads, negotiate through ditches filled with rain water. Rain water, splashes and hits the lower side of the chassis and spreads onto the engine bottom, and other areas under engine hood. This can damage a vehicle's engine, cause the brake rotors to warp from rapid cooling when immersed in water, cause loss of power steering, and short circuiting of electrical components in a vehicle. Further the presence of water puddles at specified locations for long periods leads to the potential risk of rusting of metal objects. The acidic nature of polluted water (rain water mixed with mud particles) will damage the paint and eventually reduce the life of chassis. Automotive companies are continuously trying to reduce the cost of production and improve the design aspects to ensure longevity of products as well as customer satisfaction. The impact of splashing water on a car body as it moves through a water-soil puddle region or flooded areas is significant due to several reasons. These aspects have been of interest to the automotive manufacturers and component suppliers for several years. They have primarily relied on experimental investigations to improve design aspects of chassis, engine casing, and other relevant components. Recent years have seen increased usage of numerical methods and simulations to understand these phenomena. A preliminary investigation of fluid dynamics and the fluid-structure interaction in such scenarios can be helpful in estimating the impact at a reduced cost to the manufacturer. The current research focuses on establishing fluid dynamics of the splashing phenomena as a first step towards simulating such complex problems for automotive industry.

In the automotive industry, the adverse effects of puddle splashing are wide ranging and it is important to estimate the impact at an early stage of the design process [1, 2]. While negotiating a puddle with depth larger than the ground clearance of automobile, water is sucked into the engine through air intake passages which are present in the lower part of most modern cars (especially due to low ground clearance), which causes the engine to seize. This is known as 'hydrostatic lock' – water enters an engine cylinder and during the compression stroke will lock the engine piston in place. This in turn overloads the connection rod, causing it to deform and cause significant engine damage. An example of such a situation is shown in figure 1. In extreme case, this could even cause permanent and irreversible damage to engine or engine parts. Manufacturers provide protective and safety mechanisms to deal with such scenarios: the air intake passage is provided with water trap, which drains the sucked water back out; electrical wiring connectors in the engine bay are water-tight sealed with silicone gaskets, and so on. However, a detailed assessment of these protective mechanisms help the designers to preempt potentia dangers and device more advanced mechanisms to mitigate such adverse scenarios. A prior investigation of water splash scenario using advanced numerical simulation tools help to identify probable areas of a car body that are vulnerable for damage, if and where water enters, and to estimate potential risks of object deformation from suspended solid particles splashing with the water. There are several advantages of computational analysis of such scenarios, as opposed to setting up realistic simulations in an experimental lab.

734

Figure 1: Example of a flood situation that could cause static engine hydrolock [1].

With advancements in the field of Computational Fluid Dynamics (CFD), there are numerous approaches to simulating the splash phenomena for automotive application. The most traditional and established methods are Finite Volume based methods which rely on a spatial numerical grid to descritize the fluid and solid domains.However, such Eulerian-based methods are dependent on the quality of volumetric meshing, and are disadvantageous from the perspective of computational resources as well as time efficiency of simulation. Adding to this is the complexity of modeling scenarios such as splashing, which involves moving boundaries and rotating objects that force very low time steps. An alternative and promising approach is adopted in this study, which involves particle-based meshless method known as Smoothed Particle Hydrodynamics (SPH). Lack of a numerical grid makes SPH method more suited to handle complex geometries and moving objects. Nowadays, the SPH approach is more and more commonly used for hydro-engineering applications involving free-surface flows where the natural treatment of evolving interfaces makes it an attractive method.

Some relevant outcomes of simulating this problem is understanding the impact on underbody of the car, estimating water penetration in the engine compartment area, and visualizing the water splash distribution.

2 COMPUTATIONAL APPROACH: SENSE

The SPH solver used in this study was developed at ESS Engineering Software Steyr GmbH and will be referred to as SENSE solver. The pre-processor and post-processor parts of the SENSE were also developed in-house to be compatible with the SPH solver, and were used to set-up the problem as well as to analyze the results. The SPH is primarily a particle-based method that solves equations of motion for each particle in the domain based on their interaction with neighbouring particles. The SENSE approach for solver design is to simulate fluids and solids for specific physics-based problems such that simulation of industrial problems may be perfoemd with minimal to zero expertise in CFD. The computations are performed on Graphics Processing Units (GPU), which are much faster than Central Processing Units (CPU). Additionally, the algorithm for SPH is highly parallelizable on GPU devices, providing high speed-up possibilities for scaled

industrial solutions [3].

The main idea behind SPH is the use of integral interpolants to evaluate field properties of discretized particles at each time step (see [4, 5], [6] , and [7]). Based on the treatment of incompressibility, there are several options/approaches available in SPH technique. The solver used for this study adopts a Divergence Free formaulation to treat the incompressibility and hence is known as the DF-SPH solver **Peng2019**. The SPH approach primarily involves two stages - an integral interpolation of physical properties based on a suitable kernel function $W(r, h)$, and a field discretization of fluids (or solids) into particles that carry physical properties as a function of position $f(r)$. The integral interpolant for a field property $f(r)$ is written as,

$$\widehat{f}(\mathbf{r}) = \int_\Omega f(\mathbf{r}')W(\mathbf{r} - \mathbf{r}', h)d\mathbf{r}', \tag{1}$$

where r' is the neighbouring particles in a compact domain defined by the smoothing length h, W is the kernel function, and the integration is performed on the entire domain Ω. As the domain is discretized as particles, the integral interpolant maybe written in a summation form as,

$$\langle f \rangle (\mathbf{r}) = \sum_b f(\mathbf{r}_b)W(\mathbf{r} - \mathbf{r}_b, h)\Omega_b, \tag{2}$$

where r_b and Ω_b denote the position and volume of all particles b in the compact domain. An additional advantage of SPH method is the possibility to represent the gradient of the field property using the gradient of the kernel function due to the imposed symmetry condition and mathematical identities. The gradient of a preprty $f(r)$ can hence be written as,

$$\langle \nabla f \rangle (\mathbf{r}) = \sum_b f(\mathbf{r}_b)\nabla W(\mathbf{r} - \mathbf{r}_b, h)\Omega_b, \tag{3}$$

where ∇W is the gradient of the kernel, and hence the gradient of the field variable $f(r)$ dependents only on the field value and not on its gradient. This makes the implementation and computations much easier.

For fluid dynamic application such as the one covered in this study, SPH technique solves the Navier-Stoke's equations for incompressible fluid flow written in the Lagrangian form. The primary equations of interest are that of continuity and momentum conservation,

$$\frac{d\rho}{dt} = -\rho\nabla \cdot \mathbf{u}. \tag{4}$$

$$\frac{d\mathbf{u}}{dt} = -\frac{1}{\rho}\nabla p + \frac{1}{\rho}(\nabla \cdot \mu\nabla)\mathbf{u} + \mathbf{f}, \tag{5}$$

where $\rho = const$ is the density, $\mathbf{u}$ the velocity, t the time, p the pressure, ν the kinematic viscosity and $\mathbf{f}$ are accelerations due to external forces. These equations are then

written in SPH discretized format following equations 2 and 3 methodology and using certain mathematical identities. The SPH discretized mass and momentum equations are solved using explicit time integration scheme to march forward in time. In this work the second-order Symplectic integrator is employed. With the solution of the two conservation equations, we can obtain the motion of the particles and the evolution of the carried variables. More details of the fluid dynamic formulations maybe obtained by review of [8]. Conventiomally, the imcompressibility in SPH is treated by assuming a Weakly Compressible formulation, which involves the use of an additional equation of state. For stability purposes, this imposes a very small time steps making the simulation slower especially when it involves huge number of particles. To allow fast and efficient computations of industrial cases, a Divergence-Free formulation is used for incompressibility treatment, more information on which may be obtained from Chitneedi et. al. [9].

Despite all the benefits of particle-based modeling, one of the main disadvantages of SPH is the huge numerical complexity. In order to model real life phenomena in appropriate resolution, typically up to several hundred millions of particles need to be considered, which frequently results in large execution times. However, the discrete particle formulation renders the SPH method suitable for parallelization, which allows for a massive speedup – e.g. using the *General Purpose Computations on Graphics Processing Units* (GPGPU) technology. SPH solutions utilizing the computational power of GPUs have initially been introduced by [10] as well as [11], where the *Open Graphics Library* (OpenGL) was employed. Later, SPH implementations based on the *Compute Unified Device Architecture* (CUDA) have been developed by [12].

However, in order to simulate huge domains involving millions of particles, a single GPU device is usually not sufficient anymore. In these cases, the particle domain needs to be distributed over several devices – yielding a *multi-GPU architecture* as presented in [13]. These SPH multi-GPU solutions employ a spatial subdivision of the domain to partition the whole domain into individual subdomains. These subdomains are distributed to the corresponding GPUs and executed in parallel. Receiving optimal performance for SPH on multi-GPUs is a highly non-trivial task due to the massive amount of synchronization needed between the distinct subdomains. In order to overcome these shortcomings a range of optimization techniques are introduced as discussed in [14, 15]. Employing these techniques eventually allows for efficiently applying SPH to engineering applications that involve millions of particles.

3 COMPUTATIONAL CASE STUDY

In automotive industry, the comprehension of fluid dynamics in splashing scenario is relevant to improve component designs. The SENSE solver provides a convenient platform to perform fluid dynamic simulations without significant expertise. Preliminary simulations were conducted for a typical puddle splashing scenario, where a car body is moving through stagnant puddle of water at a nominal speed. The SENSE pre-processor capabilities were used to setup the initial and boundary conditions enabling SPH-based computations on multiple GPU devices, and the results were analyzed for visualizing the fluid dynamics and identifying impact regions. The current section covers the approach
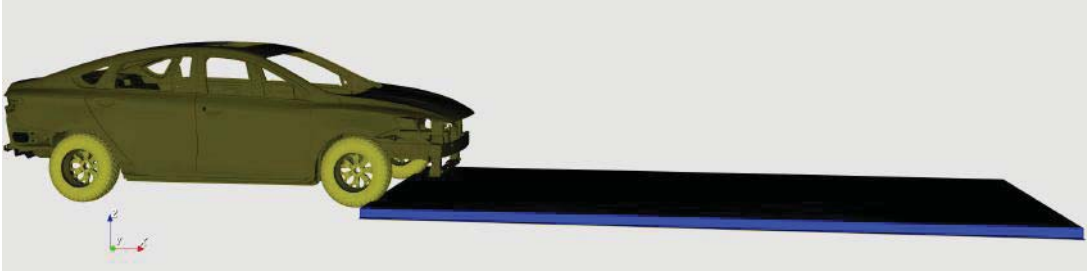
Figure 2: Sample of problem setup showing car geometry at the edge of water puddle.

adopted to setup the problem and presents some preliminary results and observations.

The puddle splashing case is setup with a Body-in-White (BIW) geometry, which is fitted with four tyres such as to emulate real car movement through puddle. The car geometry is approximately 4 m long, 2 m wide, and 1.2 m high, which is defined to moved along a straight line in the X-direction at a speed of 30 km/h. For the current scenario, the puddle consist of only water with density $\rho = 1000 \ kg/m^3$ and kinematic viscosity, $\nu = 8.94x10^{-4} \ m^2/s$. At the beginning of time, the car is placed outside of the puddle such that the front tyres are slightly in contact with the edge of the puddle. The puddle is a rectangular region 6 m long and 80 mm deep. To ensure that the splashing water stays within the computational domain, the puddle is designed to be wider than the total width of the car geometry. The computational domain is further extended in the axial and lateral directions to avoid bouncing of splashing fluid particles. Figure 2 shows a sample of the problem setup at the beginning of time. It is also relevant to note that the Lagrangian-based solver performs a single-phase SPH simulation that considers only water without the effects of air. Additionally, surface tension effects and fluid drag are not currently modelled.

The computational domain is discretized into fluid and solid particles whose physical properties are tracked by the SPH fluid dynamic equations. For the SPH solver, a smoothing length of $h = 0.0055 \ m$ is chosen along with an $\frac{h}{dr}$ value of 1.1, which ensures that results are captured to the resolution of 5 mm particle size. The initial setup consist of 13.6 million particles including both fluid and solid domains. Dynamic simulations are run for a time period such that the car geometry traverses till the end of the axial domain. Following sub-section presents some results from one such simulation, and discusses the observations. The numerical computations were deployed on multiple GPU devices, each having the configuration of an NVIDIA GeForce GTX 1080Ti with 11 GB memory.

3.1 Simulation Results

The results presented in this sub-section are from simulation of the BIW geometry moving at 30 km/h through a water puddle 80 mm deep and longer than the length of the car body itself. Simulation were deployed on 8 GPU devices with the configuration mentioned above. It takes approximately 0.72 s for the car geometry to move from the left part of the puddle till the other end. The total time required to simulate this physical sit-
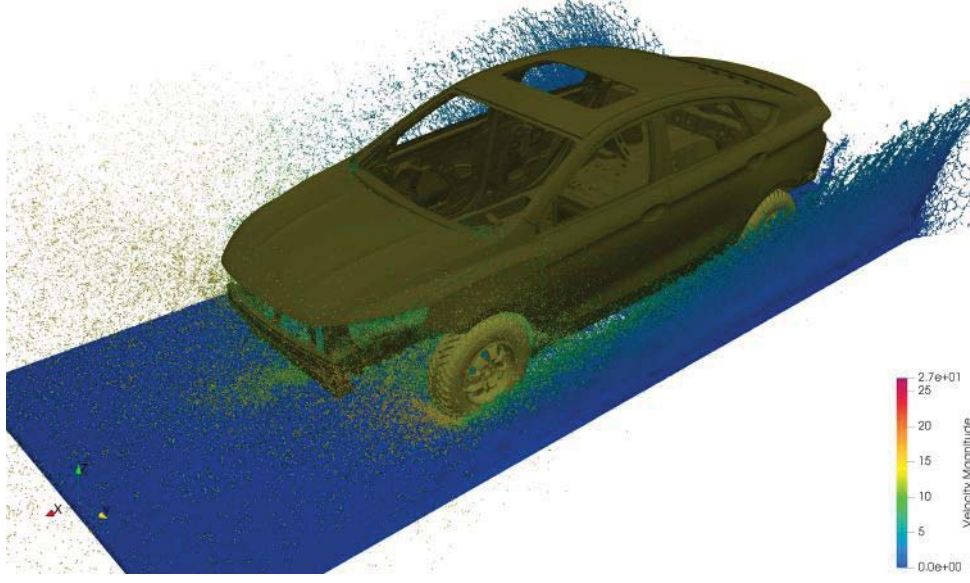
Figure 3: Puddle water distribution presented at $t = 0.5$ s, coloured by velocity magnitude of water.
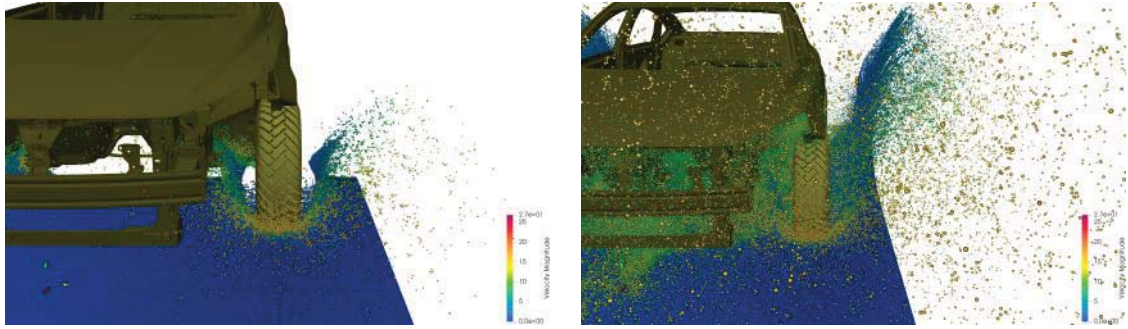

Figure 4: Velocity contour represetnation of water particles splashing near the front-right tyre shown at two stages. Left: $t = 0.1$ s and right: $t = 0.5$ s.

uation was 2.5 *hours*. As an example of fluid dynamics during car movement through the puddle, some velocity contours of water movement and some other observations relevant to impact analysis are shown below.

Understanding the dynamic motion of puddle water and potentially suspended solid particles is significant to the impact caused by car moving through flooded areas. As this study covers only the fluid dynamics, we discuss velocity profile of the water puddle at different stages of simulation. At time $t = 0.5$ s, the splash phenomena looks as shown in figure 3, where the car has moved completely into the puddle region. Initially, as the front tyres start moving into the puddle, water is pushed outside. Figure 4 shows this fluid distrbution at two time stages - $t = 0.1$ s and $t = 0.5$ s.

A different perspective of the fluid distribution can be seen in figure 5 showing the top view of the domain at the same stages of simulation. Additionally, figure 6 shows only
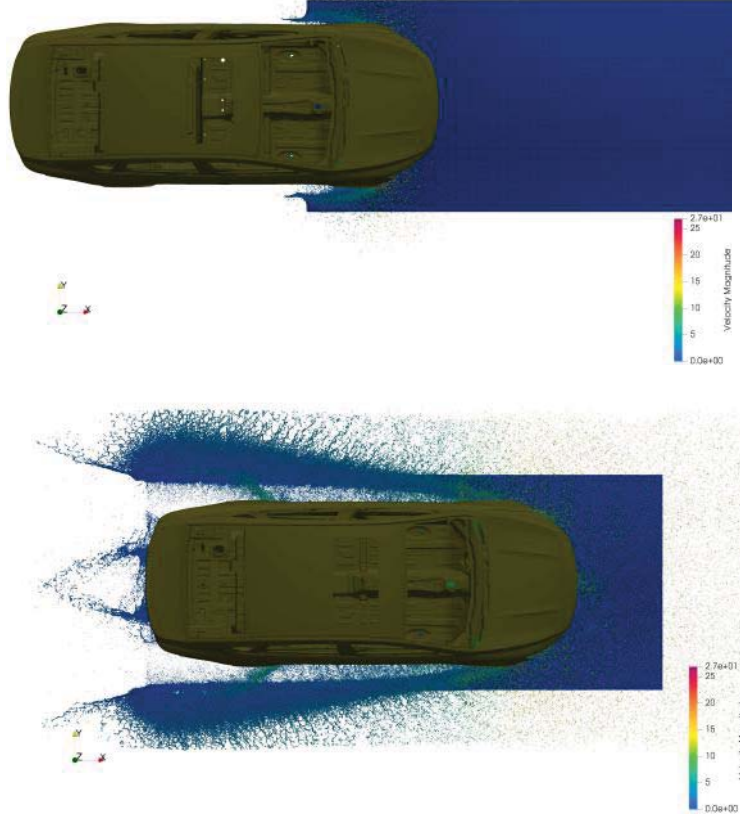
Figure 5: View of splash phenomena in the domain seen from above, fluid particles coloured by velocity magnitude. Top: $t = 0.1\ s$ and bottom: $t = 0.5\ s$.

the fluid domain at $t = 0.5\ s$. It may also be noted that the tread marks left by the tyres are noticeable here. This representation of free-surface fluids can be improved by increasing particle resolution, i.e. updating solver parameters to discretize the domain as smaller particles.

Another aspect of these simulations are the ability to understand impact on the car body due to splashing, which is of high importance to manufacturers and suppliers. From preliminary analysis, we are able to show the contact time of fluid particles hitting the solid car body. An example is shown in figure 7 that shows a contour plot if time (in s) that the car body comes in contact with splashing water, seen from underneath. This gives an initial estimation of car body regions impacted by splashing. Additionally, figure 8 also shows the contact impact on the front-underneath part at different time stages. The comparison of contact-time legend in figure 8 shows how regions with higher impact can be isolated.

The SENSE approach makes it easier to study several scenarios in a short time span. For example, the effect of different puddle depths or flooding situation can be simulated by merely changing a few parameters in the problem setup. Studying the effects on another
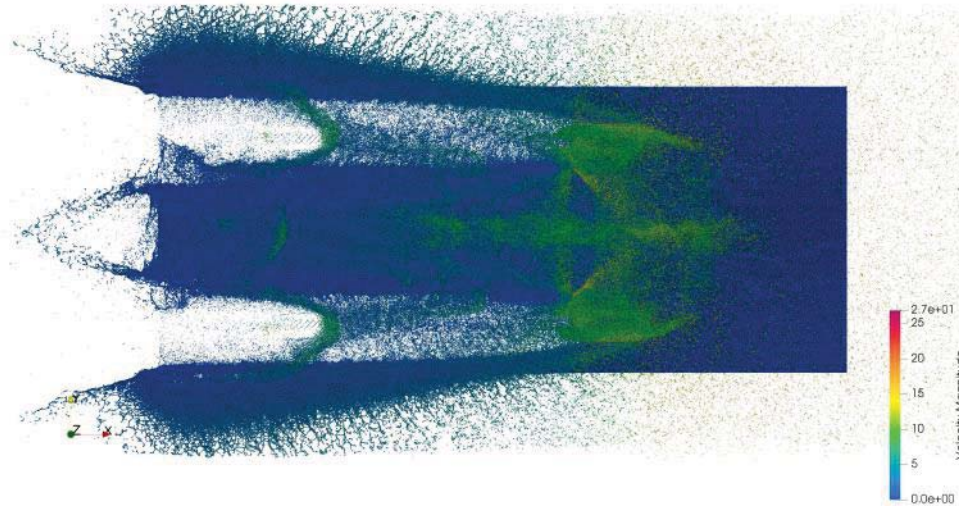
Figure 6: Representaion of fluid distribution viewed from top at $t = 0.5\ s$, fluid particles coloured by velocity magnitude.
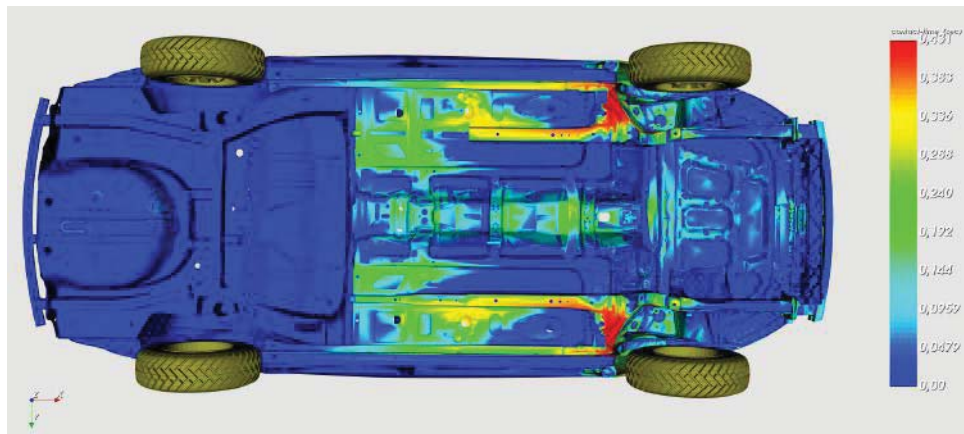

Figure 7: Depiction of splash impact underneath the car surface, shown as the fluid-solid contact time on the car body at $t = 0.5\ s$.
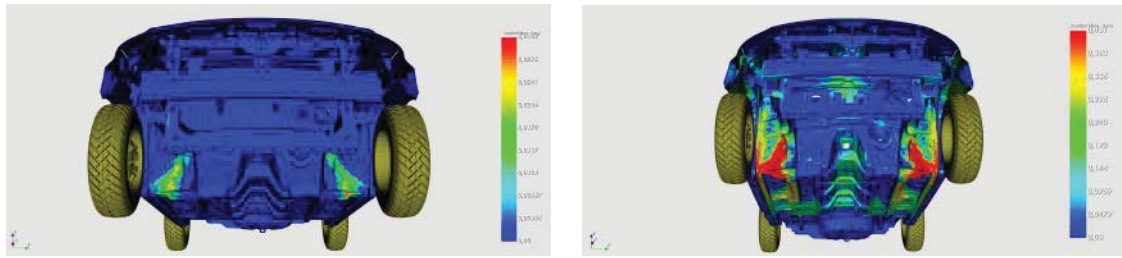
Figure 8: Comparison of impact at front-bottom of car body. Left: $t = 0.1\ s$ and right: $t = 0.5\ s$.

car geometry is also fairly easy by replacing the geometry in the pre-processor. It was also observed in the analysis that the particle-based study of such splashing scenarios makes it possible to evaluate where water seeps into the car body.

4   CONCLUSIONS

The current research presents a Lagrangian particle-based approach to study water splashing phenomena applicable to the automotive industry. Results are presented for an example fluid dynamic study that covered a Body-in-White with tyres moving through a water puddle region. Simulating splash phenomena using an advanced Lagrangian-based solver like this, allows to fairly understand the dynamic free-surface flow as well as to get an estimation of fluid impact on the car body. Implementing on GPUs, with an easy-to-scale framework for parallalezation on multiple devices, industrial cases can be evaluated in a relatively short period of time. This expands the scope of scenarios that can be studied in a given time frame, providing a good balance of expenditure and amount of data available for design updates.

REFERENCES

[1] Tutu, A. Engine hydrolock - how water can damage or destroy your engine. (Accessed Jun 2019).

[2] DrivingFast.net. Driving in deep water. (Accessed Jun 2019).

[3] Szewc, K., Mangold, J., Bauinger, C., Schifko, M., and Peng, C., 2018. "Gpu-accelerated meshless cfd methods for solving engineering problems in the automotive industry". In SAE Technical Paper, no. 2018-01-0492, SAE International.

[4] Monaghan, J., 1992. "Smoothed particle hydrodynamics". *Annual Review of Astronomy and Astrophysics,* **30**, pp. 543–574.

[5] Monaghan, J., 2012. "Smoothed particle hydrodynamics and its diverse applications". *Annual Review of Fluid Mechanics,* **44**, pp. 323–346.

[6] Liu, M., and Liu, G., 2003. *Smoothed Particle Hydrodynamics: A Meshfree Particle Method.* World Scientific, Singapore.

[7] Violeau, D., 2012. *Fluid Mechanics and the SPH method: theory and applications.* Oxford University Press.

[8] Liu, M. B., and Liu, G. R., 2010. "Smoothed particle hydrodynamics (sph): an overview and recent developments". *Archives of computational methods in engineering,* **17**(1), pp. 25–76.

[9] Chitneedi, B. K., Peng, C., and Verma, K., 2019. "Modeling flood waxing for automotive cavity protection using divergence-free smoothed particle hydrodynamics". In Proceedings of the14th SPHERIC Workshop.

[10] Kolb, A., and Cuntz, N., 2005. "Dynamic particle coupling for gpu-based fluid simulation". In Int. Proc. of the 18th Symposium on Simulation Technique, pp. 722–727.

[11] Harada, T., Koshizuka, S., and Kawaguchi, Y., 2007. "Smoothed Particle Hydrodynamics on GPUs". In Proceedings of 5th International Conference Computer Graphics, pp. 63–70.

[12] Herault, A., Bilotta, G., and Dalrymple, R., 2010. "SPH on GPU with CUDA". *Journal of Hydraulic Research,* **48**, pp. 74–79.

[13] Domínguez, J. M., Crespo, A. J. C., Valdez-Balderas, D., Rogers, B. D., and Gómez-Gesteira, M., 2013. "New multi-gpu implementation for smoothed particle hydrodynamics on heterogeneous clusters". *Computer Physics Communications,* **184**(8), pp. 1848–1860.

[14] Verma, K., Szewc, K., and Wille, R., 2017. "Advanced load balancing for SPH simulations on multi-GPU architectures". In IEEE High Performance Extreme Computing Conference (HPEC), pp. 1–7.

[15] Verma, K., Peng, C., Szewc, K., and Wille, R., 2018. "A multi-gpu pcisph implementation with efficient memory transfers". In IEEE High Performance extreme Computing Conference (HPEC), pp. 1–7.

MODELLING A PARTIALLY LIQUID-FILLED PARTICLE DAMPER USING COUPLED LAGRANGIAN METHODS

Chandramouli Gnanasambandham and Peter Eberhard

Institute of Engineering and Computational Mechanics,
Pfaffenwaldring 9, 70569 Stuttgart, Germany
chandramouli.gnanasambandham, peter.eberhard@itm.uni-stuttgart.de
www.itm.uni-stuttgart.de

Key words: Partially Liquid-Filled Particle Damper, Complex Particle Shapes, 3D Printed Particles, Coupled SPH-DEM Method

Abstract. Energy dissipation in particle dampers (PDs) is complex and occurs mainly due to the relative motion between particles and to their surroundings. The degree of relative motion is particularly sensitive to changes in the external vibration amplitudes. Low vibration amplitudes lower the relative motion between solid particles, and thus lead to significantly lower energy dissipation rates. In order to influence the degree of relative motion between solid particles, a method is investigated in which the PD is filled with a combination of solid and liquid fillings. Moreover, with the PD partially filled with a liquid, the solid particle shape plays a more profound role in enhancing the damping performance. In order to investigate the effects of complex particle shapes and an added liquid, a simulation model based on Lagrangian methods is presented in this work. In order to validate the simulation models, experiments were also carried out. The experimental setup consists of a PD mounted on a vertical leaf spring. The PD is a cylindrical container filled with complex shaped particles in combination with a liquid. The complex shapes, here chosen to be tetrapods, were manufactured using a Stereolithography 3D printer. A good agreement between simulations and experiments is observed. In order to gain a deeper insight, a numerical study is presented which investigates the effects of solid-liquid ratio on the dissipated kinetic energy.

1 INTRODUCTION

Particle dampers (PDs) are becoming a popular alternative to conventional dampers due to their relatively simple design and their flexible ability to dissipate energy over wide excitation frequencies [1]. A detailed review on PDs can be found in [2]. One of the main drawbacks of a conventional PD is, that it is highly sensitive to a change in vibration amplitudes. Especially, their damping performance reduces by a substantial amount under low forcing conditions [3]. One particularly promising idea to overcome such shortcomings is to partially fill the conventional PD with a liquid [4, 5]. The added liquid sloshes along with the solid particles which act as dynamic barriers, in turn dissipating

significant amounts of kinetic energy. This dissipative effect due to liquid sloshing through barriers can be further enhanced by replacing the conventional spherical shapes, which were used in [4], with complex shapes, in this work tetrapod shapes. The tetrapod shape has been popularly used in coastal engineering applications as wave breaker to dissipate energy carried by powerful waves and thereby reducing coastal erosion [6].

In order to gain deeper insights into the influence of various parameters on the dissipated energy, a model of the partially liquid-filled PD based on Lagrangian methods is investigated. The solid particle interactions involving non-convex particle shapes are modelled using the Discrete Element Method (DEM). The fluid motion is modelled using the Smoothed Particle Hydrodynamics (SPH) method. A coupled SPH-DEM approach according to [7] is used to model fluid-solid interactions. The focus of this paper lies in showing that fully resolved coupled SPH-DEM simulations can be used to reliably predict solid particle shape effects on the dissipated energy in partially liquid-filled PDs.

This paper is structured as follows. In Section 2 a short description of the experimental setup is given. In Section 3 details about the simulation model are outlined. Then, in Section 4 simulation results are compared against experiments. Section 5 showcases a numerical study to investigate the effect of solid-liquid fill ratio on the PD performance. Finally, in Section 6 some concluding remarks are provided.

2 EXPERIMENTAL SETUP

In order to better understand the simulation results and to build confidence in the simulation model, hardware experiments were conducted. The experimental apparatus, which is identical to the one used in [4, 5] except for the filling, consists of a vertically mounted steel leaf-spring (480 mm × 30 mm × 3 mm) on top of which a particle damper is rigidly mounted. The PD is a transparent acrylic cylindrical container of a fixed inner diameter of 44 mm and an adjustable length of L. Using an electromagnet, the vertical leaf-spring with the PD mounted on it's top is given an initial displacement, released from rest and allowed to oscillate freely in its fundamental mode. A PSV500 Polytec Laser Doppler Vibrometer is used to measure the displacement and velocity of the PD container. Depending on various PD parameters such as solid-liquid fill ratio, solid particle shape, amount of liquid among others, different damping performance is achieved.

The solid particles used in the experiments were manufactured on a Formlabs Form 2.0 Stereolithography (SLA) 3D printer, using a resolution of 100 μm and a Photopolymer resin ("Black Resin", Formlabs Inc.). In order to prevent wrapping of the solid particles, extra support structures are automatically added during the printing process. After the printing, the printed parts go through a 3-step finishing process. First, the parts are removed from the 3D-printer platform. The removed parts are then washed in Isopropyl alcohol in order to dissolve any leftover liquid resin. Finally, the support structures are removed to obtain the solid particles. An overview illustrating the 3D-printing procedure is shown in Figure 1.
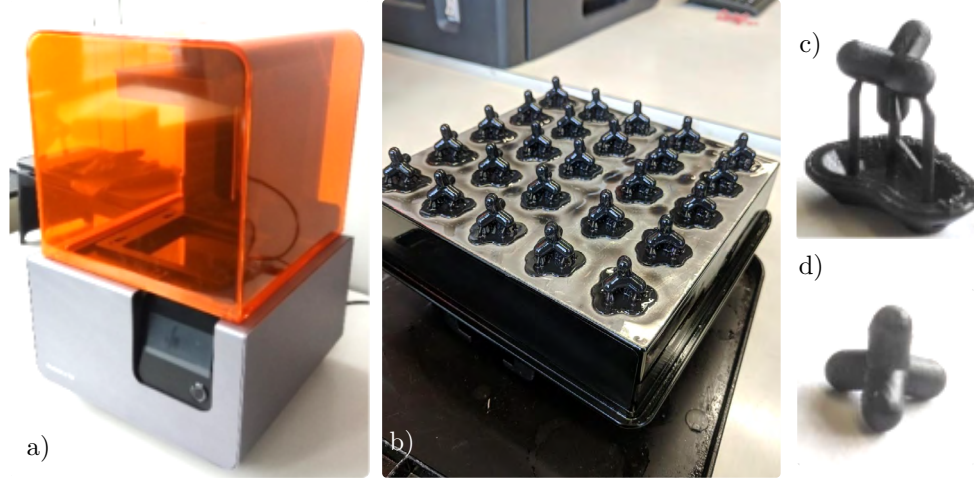
Figure 1: Non-convex polyhedron shapes manufactured using a 3D-printer. a) Formlabs Form 2.0 SLA 3D-printer. b) Multiple particles after 3D printing. A single tetrapod shaped particle c) before and d) after removing the support structure.

3 SIMULATION MODEL

3.1 Smoothed Particle Hydrodynamics

The Reynolds-averaged Navier-Stokes equations (RANS) are used to describe the fluid motion. The conservation of mass of the fluid with the Reynolds averaged velocity $\bar{\mathbf{v}}$ is given by

$$\frac{\mathrm{d}\rho}{\mathrm{d}t} = -\rho \nabla \cdot \bar{\mathbf{v}} \tag{1}$$

and the conservation of linear momentum is given by

$$\rho\left(\frac{\mathrm{d}\bar{\mathbf{v}}}{\mathrm{d}t}\right) = -\nabla \bar{p} + \mu \nabla^2 \bar{\mathbf{v}} - \nabla \mathbf{R} + \mathbf{f} \tag{2}$$

with density ρ, viscosity μ, Reynolds turbulence stresses $\mathbf{R}$ and external body forces $\mathbf{f}$. Here $\bar{p}$ is the Reynolds-averaged pressure. In this work, the weakly compressible Smoothed Particle Hydrodynamics (SPH) method is used to discretize the RANS equations according to [8]. In essence, the first two terms in Eq. 2, namely the pressure term $\nabla \bar{p}$ and the viscosity term $\mu \nabla^2 \bar{\mathbf{v}}$, are computed as proposed in [9]. An artificial stress term according to [10] and an artificial viscosity term as proposed in [11] are introduced in Eq. 2 to reduce the tensile instability and to smooth spurious numerical oscillations, respectively. In addition to this, a diffusive term is introduced in Eq. 1 to obtain smoother density fields according to [12]. Since the PD is only partially filled with a liquid, violent sloshing and large free surface deformations are expected. Therefore, an adequate modelling of turbulence is essential. In this work, the popular k-ε turbulence model according to [8] is used. Concerning the interaction between liquid and PD container, a penalty approach similar to the one described in [13] is used.

3.2 Discrete Element Method

The contacts between solid particles and PD container is modelled using the Discrete Element Method (DEM). The equations of motion of a single solid particle i is given by the Newton-Euler equations [14]

$$M_i \frac{d\mathbf{V}_i}{dt} = \mathbf{F}_i, \tag{3}$$

$$\mathbf{I}_i \frac{d\mathbf{\Omega}_i}{dt} + \mathbf{\Omega}_i \times \mathbf{I}_i \mathbf{\Omega}_i = \mathbf{L}_i. \tag{4}$$

In these equations, $\mathbf{I}_i$ is the inertia tensor, M_i is the mass, and $\mathbf{F}_i$ and $\mathbf{L}_i$ are the external forces and torques acting on the particle i. The external force $\mathbf{F}_i$ acting on a solid particle contains forces due to gravity and due to contact between other solid particles and the PD container. Traditionally, the DEM approach was conceptualized for simple spherical particles [15]. Since the solid particles used in this work have complicated geometry, as seen in Figure 1, the traditional approach should be extended to accommodate contacts between arbitrary shapes. There are different approaches to compute the forces $\mathbf{F}_i$ and torques $\mathbf{L}_i$ for complicated shapes. One approach, as suggested in [16], is to represent a rigid particle of arbitrary shape by a set of spherical particles whose relative positions remain unchanged. In a more sophisticated approach, the particles of arbitrary shapes can be represented using triangular meshes and the contact forces could be computed proportional to the overlap volume between two such meshes. Moreover, by using fast collision detection algorithms such as the Bounding Volume Hierarchy approach [17], the simulation time can be reduced drastically. In this work, this sort of an approach is used to model contacts between non-convex shapes, which is readily available in the particle simulation software package Pasimodo [18].

3.3 SPH-DEM Coupling

In this paper, these hydraulic forces, which are exchanged between SPH and DEM particles, are described using an approach as in [7]. In this approach a set of virtual SPH particles are placed uniformly around the boundary of the DEM particle. These virtual SPH particles are basically meant to mimic the interface atoms between SPH and DEM particle in a macroscopic scale. This approach has been applied to fluid-structure interaction problems recently in [19, 20, 21]. Moreover, this approach was also used in the partially liquid-filled PD context involving spherical shaped solids in [4].

For time integration the explicit second-order Leapfrog scheme with time step control is used for all the simulations. Moreover, all the simulations are set up and performed using the particle simulation software package Pasimodo [18], which has been developed at the ITM for over a decade.

4 MODEL VALIDATION

In this section the coupled SPH-DEM model is validated against experimental data, which is generated using the ring-down experimental setup introduced in Section 2. The

vertical leaf spring, which is used in the experiments, is modelled as a simple single degree of freedom spring-mass-damper system with the system parameters as identified in [4].

All the experiments and simulations presented in this section are conducted for an acrylic PD container of length $L = 100$ mm and inner diameter of 44 mm. In both cases, the PD container is loaded with 60 tetrapod shaped particles and 30 ml of distilled water. For the experiments each tetrapod particle is manufactured using a 3D printer, as seen in Figure 1. Moreover, each tetrapod has a bounding box dimension of $d = 8$ mm and a density of $\rho_\mathrm{p} = 1200$ kgm^{-3}. On the simulation side the same geometry STL file, which was given as input to the 3D printer, is loaded in Pasimodo to represent the non-convex shape during all the simulations. The most relevant model parameters identified are listed in Table 1.

Table 1: Relevant parameters for the simulations

parameter	value
no. of solid particles n_p	60
solid density ρ_p (kgm^{-3})	1200
liquid density ρ_liq (kgm^{-3})	1000
liquid viscosity ν (Pa.s)	8.9×10^{-4}
CFL number	0.7
SPH smoothing length h (m)	7.5×10^{-4}

In Figure 2 (left), the velocity of the partially liquid-filled PD with tetrapod shapes, measured during experiments and predicted by coupled SPH-DEM simulation is compared. Figure 3 visualizes the motion of the damper contents as predicted by coupled SPH-DEM simulations. In order to better understand the effect of solid particles, the velocity damper filled purely with a liquid measured during experiments is also plotted in Figure 2 (left). Macroscopically seen, there is a good agreement between simulations and experiments, showing that coupled SPH-DEM simulations can adequately model the dynamics involved in a partially liquid-filled particle damper. It can be clearly seen, that the velocity decay is faster for the case with both liquid and solid filling, than for the purely liquid filled case. There are two possible reasons for this. First, the solid particles due to the hydraulic forces applied by the liquid, remain agile even under lower vibration amplitude, thereby leading to more effective collisions and in turn more energy dissipation. Secondly, the liquid is squeezed between two approaching solid particles leading to shearing of liquid layers. This ultimately results in more energy dissipation. In this case, the non-convex tetrapod particles behave effectively as obstacles to waves created by liquid motion. So in essence, the energy dissipation in case of a liquid-filled PD is due to the combined effect of increased solid particle agility and the sloshing motion of the liquid.
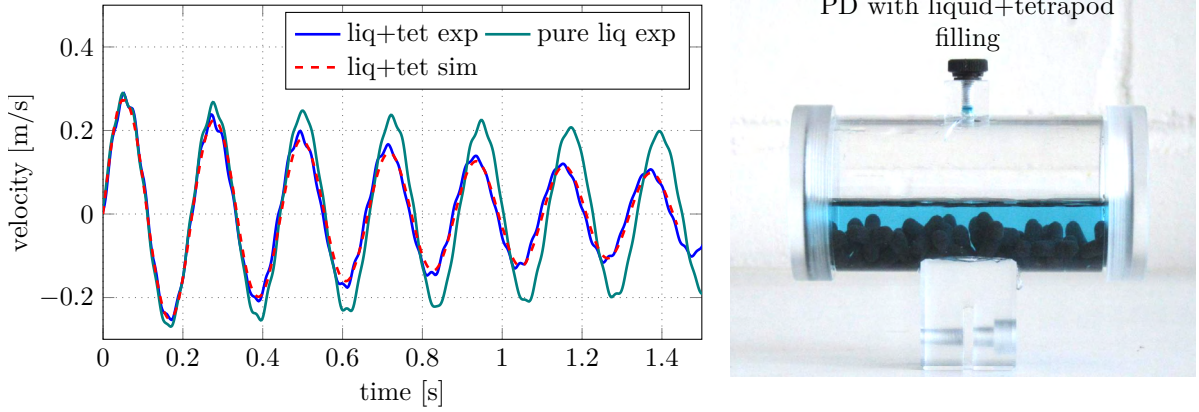
Figure 2: (left) The velocity of the damper container is compared for all the damper configurations. The red dashed line represents the container velocity predicted by coupled SPH-DEM simulations. The simulation and experiment are in good agreement. (right) The PD with liquid and tetrapod filling used in the experiments.
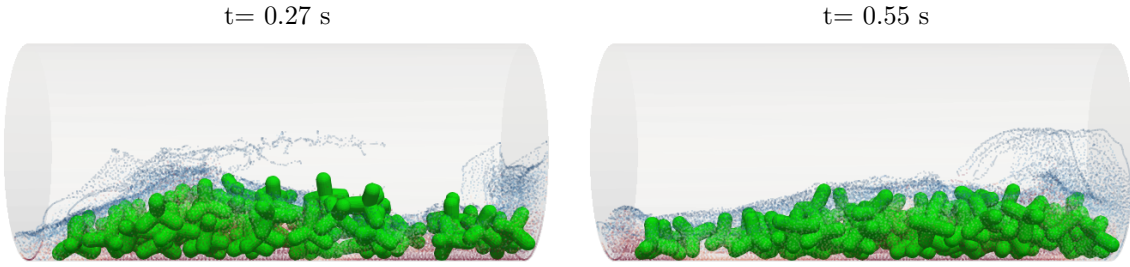

Figure 3: The motion of the damper contents, predicted by coupled SPH-DEM simulation, is visualized at two different time instances. The waves created by liquid motion are broken by the presence of agile solid particles. The fluid is visualized as colored balls, where the color gradient visualizes pressure from low (red) to high (blue).

5 INFLUENCE OF SOLID-LIQUID FILL RATIO

In the previous section it was seen that a combination of complex shaped solids and a liquid can substantially increase the dissipation performance. This newly gained insight rises a new question regarding the dynamics involved in partially liquid-filled PDs. What should the solid-liquid fill ratio be in order to maximize the dissipation rate? In order to gain further insights regarding this question a numerical investigation is performed.

In this numerical study the number of tetrapod solids are varied in three stages (0, 40, 60 solids) while the amount of liquid is kept at a constant 30 ml. By this way, the solid-liquid ratio is implicitly varied. For this study, the density of each solid tetrapod particle is chosen to be 7850 kgm^{-3}. While setting up the simulations, compensation masses were added to the system mass so that all the configurations have the same static mass. All the other parameters are carried over from Section 4 including the initial deflection of the spring which is 10 mm.

In Figure 4 (left) the simulated velocity decay for different solid-liquid fill ratios is compared and the corresponding average logarithmic decay rate is visualized in Figure 4 (right). It can be seen, that the decay rate for a damper filled purely with a liquid is lower than the PD with both solids and liquid. Moreover, increasing the number of solids particles seem to substantially increase the decay rate. This effect can be better understood using Figure 5 where the motion of the PD contents is visualized as predicted by coupled SPH-DEM simulations. Increasing the number of solid particles in the presence of a liquid effectively increases the number of solid particle collisions. Additionally, the liquid flow is observed to be more fierce with increase in the number of solid particles, leading to even more kinetic energy dissipation. With this investigation it can be said, that coupled SPH-DEM simulations can indeed be utilized to reliably predict complex dynamical effects present in partially liquid-filled PDs.
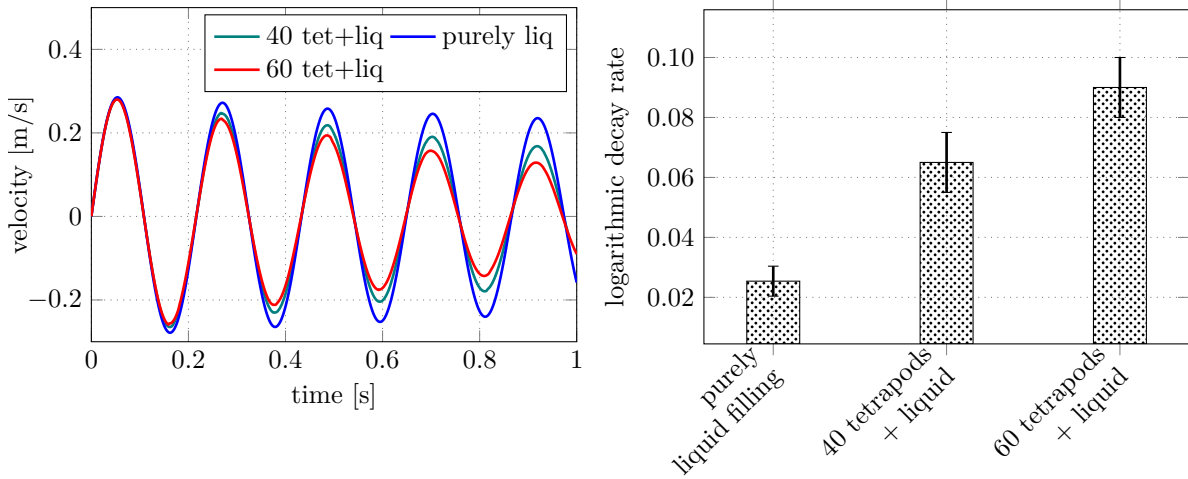
Figure 4: (left) The velocity of the damper container for various solid-liquid fill ratios is compared. (right) The average logarithmic decay rate, computed at the end of every cycle, is visualized with respect to different solid-liquid fill ratios.

6 CONCLUSIONS

In this work, it is shown that coupled SPH-DEM simulations can adequately predict the effect of complex particle shapes in enhancing dissipation performance of partially liquid-filled particle dampers. The tetrapod shape, inspired from coastal engineering, is the chosen particle shape for this investigation. In order to gain deeper insight into the various dissipation mechanisms and to increase confidence in the numerical models, experiments were performed. The experimental test bench is identical to the one used in [4] except that the solid particles were manufactured using a Stereolithography (SLA) 3D printer and have a different particle shape. A good agreement between experiments and simulations is observed on a macroscopic level. Both in simulations and experiments the partially liquid-filled PDs with non-convex particle shapes has superior damping performance than a purely liquid filled damper. The reasoning for this effect is twofold. Firstly,
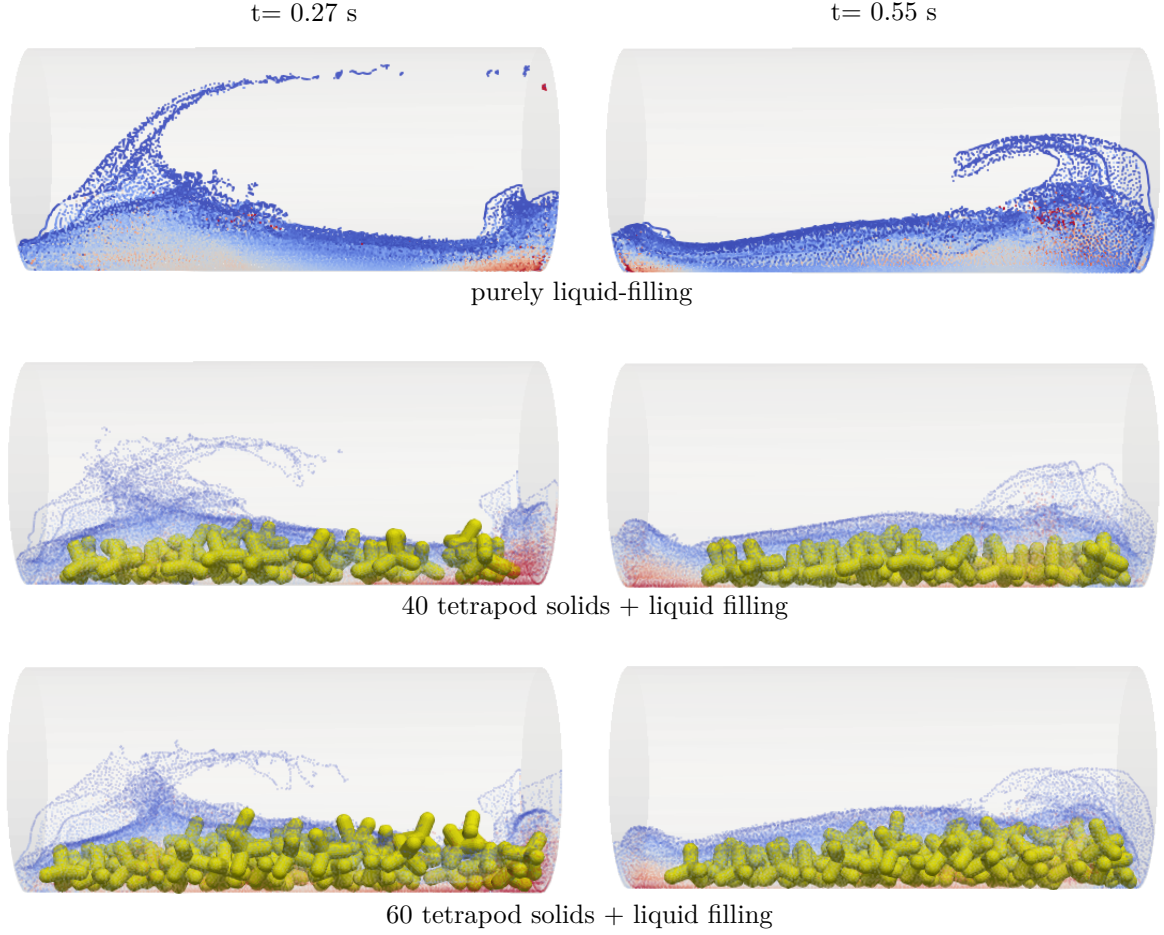
t= 0.27 s   t= 0.55 s

purely liquid-filling

40 tetrapod solids + liquid filling

60 tetrapod solids + liquid filling

Figure 5: The motion of damper contents visualized for (top row) purely liquid filled damper, (middle row) 40 tetrapod solids + liquid and (bottom row) 60 tetrapod solids + liquid, at two different time instances. In all cases, the fluid is visualized as colored balls, where the color gradient visualizes pressure from low (red) to high (blue).

due to the presence of a liquid the complex shaped solid particles remain agile even under low vibration amplitude, leading to more effective collisions and in turn higher energy dissipation. Secondly, the liquid sloshing in the presence of complex shaped particles leads to more shearing between liquid layers causing more energy dissipation. In order to test these insights, a numerical study to understand the effect of fluid-solid fill ratio was set up. In this study, the solid-liquid fill ratio was varied by keeping the amount of liquid constant and varying the number of solid tetrapod particles. Adding more solids particles seemed to increase the dissipation rate. Since the solid particles carry more momentum than a liquid, the collisions between adjacent solids is much more effective leading to higher kinetic energy dissipation.

7 ACKNOWLEDGEMENT

REFERENCES

[1]   Panossian, H.: Structural Damping Enhancement via Non-Obstructive Particle Damping Technique. Journal of Vibration and Acoustics, Vol. 114, pp. 101–105, 1992.

[2]   Lu, Z.; Wang, Z.; Masri, S.F.; Lu, X.: Particle Impact Dampers: Past, Present, and Future. Structural Control and Health Monitoring, Vol. 25, pp. 1–25, 2017.

[3]   Kollmer, J.E.; Sack, A.; Heckel, M.; Pöschel, T.: Relaxation of a Spring with an Attached Granular Damper. New Journal of Physics, Vol. 15, p. 093023, 2013.

[4]   Gnanasambandham, C.; Schönle, A.; Eberhard, P.: Investigating the dissipative effects of liquid-filled particle dampers using coupled DEM–SPH methods. Computational Particle Mechanics, Vol. 6, pp. 257–269, 2019.

[5]   Gnanasambandham, C.; Merten, S.; Hoffmann, N.; Eberhard, P.: Multi-Scale Dynamics of Particle Dampers using Wavelets: Extracting Particle Activity Metrics from Ring Down Experiments. Journal of Sound and Vibration, Vol. 454, pp. 1–13, 2019.

[6]   Goda, Y.; Kishara, Y.; Kamiyama, Y.: Laboratory Investigation on the Overtopping Rate of Seawalls by Irregular Waves. Report of the Port and Harbour Research Institute, Vol. 14, No. 4, 1975.

[7]   Canelas, R.B.; Domínguez, J.M.; Crespo, A.J.; Gómez-Gesteira, M.; Ferreira, R.M.: A Smooth Particle Hydrodynamics Discretization for the Modelling of Free Surface Flows and Rigid Body Dynamics. International Journal for Numerical Methods in Fluids, Vol. 78, No. 9, pp. 581–593, 2015.

[8]   Violeau, D.; Issa, R.: Numerical Modelling of Complex Turbulent Free-Surface Flows with the SPH Method: an Overview. International Journal for Numerical Methods in Fluids, Vol. 53, pp. 277–304, 2007.

[9]   Morris, J.P.; Fox, P.J.; Zhu, Y.: Modeling Low Reynolds Number Incompressible Flows Using SPH. Journal of Computational Physics, Vol. 136, No. 1, pp. 214–226, 1997.

[10] Monaghan, J.J.: SPH without a Tensile Instability. Journal of Computational Physics, Vol. 159, No. 2, pp. 290–311, 2000.

[11]   Monaghan, J.J.: Smoothed Particle Hydrodynamics. Reports on Progress in Physics, Vol. 68, No. 8, pp. 1703–1759, 2005.

[12]   Molteni, D.; Colagrossi, A.: A Simple Procedure to Improve the Pressure Evaluation in Hydrodynamic Context Using the SPH. Computer Physics Communications, Vol. 180, No. 6, pp. 861–872, 2009.

[13]   Mueller, M.; Schirm, S.; Teschner, M.; Heidelberger, B.; Gross, M.: Interaction of Fluids with Deformable Solids. Computer Animation and Virtual Worlds, Vol. 15, No. 3–4, pp. 159–171, 2004.

[14]   Schiehlen, W.; Eberhard, P.: Applied Dynamics. Heidelberg: Springer, 2014.

[15]   Cundall, P.A.: Formulation of a Three-dimensional Distinct Element Model – Part I. A Scheme to Detect and Represent Contacts in a System Composed of Many Polyhedral Blocks. International Journal of Rock Mechanics and Mining Sciences & Geomechanics Abstracts, Vol. 25, No. 3, pp. 107–116, 1988.

[16]   Cabiscol, R.; Finke, J.H.; Kwade, A.: Calibration and Interpretation of DEM Parameters for Simulations of Cylindrical Tablets with Multi-Sphere Approach. Powder Technology, Vol. 327, pp. 232–245, 2018.

[17]   Ericson, C.: Real-time collision detection. New York: CRC Press, 2004.

[18]   Pasimodo - Particle Simulations Software. www.itm.uni-stuttgart.de/software/pasimodo/index.html (last accessed on July 8, 2019).

[19]   Canelas, R.B.; Domínguez, J.; Crespo, A.; Gómez-Gesteira, M.; Ferreira, R.: Resolved Simulation of a Granular-Fluid Flow with a Coupled SPH-DCDEM Model. Journal of Hydraulic Engineering, Vol. 143, pp. 1 – 6, 2017.

[20]   Schnabel, D.; Özkaya, E.; Biermann, D.; Eberhard, P.: Transient Simulation of Cooling-Lubricant Flow for Deep-Hole Drilling-Processes. Procedia CIRP, Vol. 77, pp. 78–81, 2018.

[21]   Altomare, C.; Crespo, A.J.; Rogers, B.; Dominguez, J.; Gironella, X.; Gómez-Gesteira, M.: Numerical Modelling of Armour Block Sea Breakwater with Smoothed Particle Hydrodynamics. Computers & Structures, Vol. 130, pp. 34–45, 2014.

MONODISPERSE GAS-SOLID MIXTURES WITH INTENSE INTERPHASE INTERACTION IN TWO-FLUID SMOOTHED PARTICLE HYDRODYNAMICS

OLGA P. STOYANOVSKAYA[1,2], TATIANA A. GLUSHKO[2], VALERY N. SNYTNIKOV[2,3] AND NICOLAY V. SNYTNIKOV[4]

[1] Lavrentiev Institute of Hydrodynamics SB RAS
630090, Novosibirsk, Russia
Web page: http://www.ict.nsc.ru/en

[2] Novosibirks State University
630090, Novosibirsk, Russia
Web page: https://english.nsu.ru

[3] Boreskov Institute of Catalysis SB RAS
630090, Novosibirsk, Russia
3
Web page: http://en.catalysis.ru/

[4] Institute of Computational Mathematics and Mathematical Geophysics
630090, Novosibirsk, Russia
e-mail: nik@ssd.sscc.ru - Web page: https://icmmg.nsc.ru/en

Key words: Gas dust mixture, gas-solid mixture, aerosol particle, intense interphase interaction, stiff relaxation term, asymptotic preserving method, Smoothed Particle Hydrodynamics, SPH, Two Fluid Smoothed Particle Hydrodynamics, TFSPH

Abstract. Simulations of gas-solid mixtures are used in many scientific and industrial applications. Two-Fluid Smoothed Particle Hydrodynamics (TFSPH) is an approach when gas and solids are simulated with different sets of particles interacting via drag force. Several methods are developed for computing drag force between gas and solid grains for TFSPH.

Computationally challenging are simulations of gas-dust mixtures with intense intephase interaction, when velocity relaxation time t_{stop} is much smaller than dynamical time of the problem. In explicit schemes the time step τ must be less than t_{stop}, that leads to high computational costs. Moreover, it is known that for stiff problems both grid-based and particle methods may require unaffordably detailed resolution to capture the asymptotical bahaiviour of the solution. To address this problem we developed fast and robust method for computing stiff and mild drag force in gas solid-mixtures based on the ideas of Particle-in-Cell approach. In the paper we compare the results of new and previously developed methods on test problems.

1 INTRODUCTION

In the paper two-fluid model of gas-solid mixture is discussed. In this model gas is considered as a carrier phase and dust grains are considered as dispersed phase. It is assumed that the solid phase has one typical size in each volume (so this phase is monodisperse). Therefore, the continuity and motion equations for gas and dispersed phase have the following form:

$$\frac{\partial \rho_g}{\partial t} + \nabla(\rho_g v) = S_g, \quad \rho_g \left[\frac{\partial v}{\partial t} + (v \cdot \nabla)v \right] = -\nabla p + \rho_g g - f_{\text{drag}} + f_g, \tag{1}$$

$$\frac{\partial \rho_d}{\partial t} + \nabla(\rho_d u) = S_d, \quad \rho_d \left[\frac{\partial u}{\partial t} + (u \cdot \nabla)u \right] = \rho_d g + f_{\text{drag}} + f_d, \tag{2}$$

where ρ_g and ρ_d are volume density of gas and dust, v and u are velocities of gas and dust, p is pressure, g is gravity acceleration, S_g, S_d are sourses and sinks for gas and dust, f_g, f_d are forces affecting gas and dust except for pressure, gravitaion and drag, f_{drag} is drag force per unit volume:

$$f_{\text{drag}} = \rho_d \frac{v - u}{t_{\text{stop}}}, \tag{3}$$

where $t_{\text{stop}} = t_{\text{stop}}(a, \rho_g, c_s, v - u)$ is a velocity relaxation time. Here a is particle size, c_s is the sound speed in gas. In this work we consider particular case when t_{stop} does not depend on $v - u$ that corresponds to Epstein and Stokes regimes (see details, e.g. in [1]).

Computing of pure gas dymanics (solution of (1) with $f_{\text{drag}} = 0$) using explicit schemes requires time step τ that satisfies Courant condition:

$$\tau < \text{CFL} \frac{h}{\max(v, c_s)}, \tag{4}$$

where CFL < 1 is the Courant limeter. Additional necessary condition arises during computing of dusty gas dynamisc using explicit schemes

$$\tau < t_{\text{stop}}. \tag{5}$$

Violation of this condition leads to numerical instability. Condition (5) is extremally prohibitive for intense interphase interaction (for small t_{stop}). Intense interphase interaction arises in many applications of gas-particle mixtures (e.g. in modelling reactors with finely-dispersed catalyst, in planet formation from gas-dust circumstellar disks etc.) and is characterized by the fact that time of momentum transfer is much less than process time.

In the case of intense interphase interaction, f_{drag} is called stiff relaxation term [2]. Effective schemes for problems with stiff relaxation terms are designed in way that they could preserve asymptotical solution even with $\tau \gg t_{\text{stop}}$. Main ideas of such design are described in [3, 4] and assosiated with using of implicit approximation of stiff relaxation term along with explisit approximation of other terms. This approaches are developed for euler methods for solving fluid dynamics equations and are used in different applications

e.g. [5, 6]. Transfering this ideas to lagrangian methods (for example, to TFSPH in which gas and dust are modelled by different sets of particles) encounter new difficulties caused by the fact that carrier and disperse phases quantities are known in different points of space. For TFSPH authors of [7, 8, 9] shown that the way of interpolation this parametres for computing f_{drag} influences the method's property to preserve asymptotic. In particular, [7] demonstrated that classical method for computing drag force in TFSPH [10] captures the asymptotic of the solution for small t_{stop} only with

$$h < c_s t_{\text{stop}}. \tag{6}$$

Getting over this restriction is crucial for modelling mixtures with intense interphase interaction. For this reason authors of [8], [9] proposed other methods to computing drag forces. In this paper we present quantitative comparison of the classical [10] and new [8], [9] approaches focusing on their ability to preserve asymptotic properties of the solution. The methods are described in detail in section 2, the test problem results are given in section 3 and the summary is provided in section 4.

2 METHODS FOR COMPUTING DRAG TERMS IN TWO-FLUID SMOOTHED PARTICLE HYDRODYNAMICS

Let us rewrite the motion equations in (1)-(2) assuming $K = \dfrac{\rho_{\text{d}}}{t_{\text{stop}}}$:

$$\begin{cases} \dfrac{\mathrm{d}v}{\mathrm{d}t} = -\dfrac{\nabla p}{\rho_{\text{g}}} + g - \dfrac{K}{\rho_{\text{g}}}(v - u), \\ \dfrac{\mathrm{d}u}{\mathrm{d}t} = g + \dfrac{K}{\rho_{\text{d}}}(v - u). \end{cases} \tag{7}$$

Further we will give the schemes for solving the equations of gas and dust motion (7) in the standard SPH notation. We will consider only the schemes in which gas and dust are simulated by different sets of particles, i.e. by the two-fluid approach for smoothed particle hydrodynamics (TFSPH). Let n be the number of the time step. Following the notation introduced in [10], we will use a, b as the indices for gas particles, and j, k as the indices for dust particles.

2.1 The MK Monaghan–Kocharyan explicit scheme.

A method for computing the drag force, which was proposed in [10] (hereinafter referred to as MK (Monaghan-Kocharyan Drag)), is classical for smoothed particle hydrodynamics. This method is based on the computing of the relative velocity between each pair of gas-dust particles and is employed in astrophysical and engineering applications of two-phase medium mechanics [11, 12, 13, 14] and others.

We implemented this scheme so that the summand accounting for drag uses the velocities from the previous time step:

$$\frac{\mathrm{d}v_a^n}{\mathrm{d}t} = -m_{\text{g}} \sum_b \left(\frac{p_b}{(\rho_{b,\text{g}}^n)^2} + \frac{p_a}{(\rho_{a,\text{g}}^n)^2} \right) \nabla_a W_{ab}^n - \sigma m_{\text{d}} \sum_j \frac{K_{aj}}{\rho_{a,\text{g}}^n \rho_{j,\text{d}}^n} \frac{(v_a^n - u_j^n, r_{ja})}{r_{ja}^2 + \eta^2} r_{ja} W_{ja}^n + g_a, \tag{8}$$

$$\frac{du_j^n}{dt} = \sigma m_g \sum_a \frac{K_{aj}}{\rho_{a,g}^n \rho_{j,d}^n} \frac{(v_a^n - u_j^n, r_{ja})}{r_{ja}^2 + \eta^2} r_{ja} W_{ja}^n + g_j, \tag{9}$$

$$K_{aj} = \frac{\rho_{j,d}^n \rho_{a,g}^n c_{a,s}^n}{s_j^n \rho_{j,s}^n}, \tag{10}$$

where m_g and m_d are the masses of gas and dust particles, respectively, $r_{ja} = r_j - r_a$, η is a clipping constant, $\eta^2 = 0.001 h^2$, s_j is the radius of a spherical dust particle with index j, σ is the constant determined by dimensionality of the problem (for one-dimensional problems, $\sigma = 1$), and $W_{ab}^n = W(h, r_{ab})$ is the smoothing kernel.

The MK scheme (8)-(9) of the first order approximation with respect to time satisfies the momentum conservation law in the entire computational domain, which means that the momentum lost by gas due to drag on dust completely coincides with the momentum acquired by dust due to drag on gas.

2.2 The semi-implicit ISPH scheme with interpolation of the first order approximation with respect to time.

The second method for computing the drag consists in the calculation of gas characteristics at the points where dust particles are located (and vice versa) using the SPH interpolation formulas:

$$v_j^n = m_g \sum_a \frac{v_a^n}{\rho_{a,g}^n} W_{aj}^n, \quad u_a^n = m_d \sum_j \frac{u_j^n}{\rho_{j,d}^n} W_{ja}^n, \tag{11}$$

where u_a is the dust velocity at a spatial point where the gas particle with a index is located, and v_j is the gas velocity at a spatial point where the dust particle with j index is located.

As a result, all features of the gas-dust medium become known for each model particle. This method and its modifications are applied in refs. [8, 15, 16]. We apply this idea to construct a semi-implicit scheme that would not require the fulfillment of condition (5) for obtaining stable solutions. In particular, parsimonious is the following ISPH scheme with the first order approximation with respect to time (the quantities calculated using interpolation formulas are marked in blue, while the quantities derived from those calculated by interpolation formulas are marked in red):

$$\frac{v_a^{n+1} - v_a^n}{\tau} = -\sum_b m_b \left(\frac{p_b}{(\rho_{b,g}^n)^2} + \frac{p_a}{(\rho_{a,g}^n)^2} \right) \bigtriangledown_a W_{ab}^n - \frac{K_a^n}{\rho_{a,g}^n}(v_a^{n+1} - u_a^{n+1}) + g_a, \tag{12}$$

$$\frac{u_a^{n+1} - u_a^n}{\tau} = \frac{K_a^n}{\rho_{a,d}^n}(v_a^{n+1} - u_a^{n+1}) + g_a. \tag{13}$$

$$\frac{v_j^{n+1} - v_j^n}{\tau} = -\sum_i m_i \left(\frac{p_i}{(\rho_{i,g}^n)^2} + \frac{p_j}{(\rho_{j,g}^n)^2} \right) \bigtriangledown_j W_{ij}^n - \frac{K_j^n}{\rho_{j,g}^n}(v_j^{n+1} - u_j^{n+1}) + g_j, \tag{14}$$

$$\frac{u_j^{n+1} - u_j^n}{\tau} = \frac{K_j^n}{\rho_{a,\mathrm{d}}^n}(v_j^{n+1} - u_j^{n+1}) + g_j. \tag{15}$$

$$K_a^n = \frac{\rho_{a,\mathrm{g}}^n c_{a,\mathrm{s}}^n}{s_a^n \rho_{a,\mathrm{s}}^n}, \quad K_j^n = \frac{\rho_{j,\mathrm{g}}^n c_{j,\mathrm{s}}^n}{s_j^n \rho_{j,\mathrm{s}}^n}. \tag{16}$$

2.3   A new SPH-IDIC scheme – the implicit 'drag in cell".

In addition, computing of the drag force can be based on the idea of the particle-in-cell method for simulation of gas-dust flows [17]. The parsimonious semi-implicit SPH-IDIC approach based on this idea was suggested and tested in our earlier paper [9]. A detailed description of this approach is presented below.

At each time instant, we will decompose the entire calculation region into disjoint volumes so that the merging of these volumes will coincide with the entire region. Suppose a separate volume contains N gas particles of a similar mass m_g and L dust particles of a similar mass m_d, with $N > 0$, $L > 0$. Introduce the volume-averaged values of t_{stop}^* and ρ_d^* (anywise) and assume that

$$\varepsilon^* = \frac{m_\mathrm{d} L}{m_\mathrm{g} N}, \tag{17}$$

thus determining

$$K^* = \frac{\rho_\mathrm{d}^*}{t_{\mathrm{stop}}^*}, \quad \rho_\mathrm{g}^* = \frac{\rho_\mathrm{d}^*}{\varepsilon^*}. \tag{18}$$

Let us assume that in computing the drag force that acts from gas on dust, the gas velocity is constant over the entire volume and equal to v_*, whereas dust particles have different velocities (and vice versa). In addition, we will calculate the drag factor and density using values of the quantities from the preceding time layer, and relative velocity – from the subsequent layer. The resulting scheme will have the form

$$\frac{\mathrm{d}v_a^n}{\mathrm{dt}} = -\sum_b m_b \left(\frac{p_b}{(\rho_{b,\mathrm{g}}^n)^2} + \frac{p_a}{(\rho_{a,\mathrm{g}}^n)^2} \right) \nabla_a W_{ab}^n - \frac{K^*}{\rho_\mathrm{g}^{n,*}}(v_a^{n+1} - u_*^{n+1}) + g_a, \tag{19}$$

$$\frac{\mathrm{d}u_j^n}{\mathrm{dt}} = \frac{K^*}{\rho_\mathrm{d}^{n,*}}(v_*^{n+1} - u_j^{n+1}) + g_j, \tag{20}$$

$$v_* = \frac{\sum_{a=1}^N v_a}{N}, \quad u_* = \frac{\sum_{j=1}^L u_j}{L}. \tag{21}$$

If the time derivative in (19)-(20) is approximated to the first order, there exists a parsimonious method to calculate u^{n+1} v^{n+1}. In [9], it was shown that the semi-implicit scheme (19)-(21) with the first order approximation with respect to time satisfies the momentum conservation law for each cell, i.e. the momentum lost by gas due to drag on dust completely coincides with the momentum acquired by dust due to drag on gas.

3   RESULTS

To measure the ability of the schemes to preserve asymptotical properties of the solution in case of intense interphase interaction two well-known test problems with available reference solution are used. The first is a problem of sound-wave propagation in isothermal gas-dust mixture. This problem has a smooth solution and suits perfectly to study the way of drag computing in SPH. We will refer to this problem as Dustywave. The second is a problem of shock wave propagation in coupled gas-dust mixture with initial conditions known as Sod shock tube. Due to discontinuity of the solution and complexity of wave structure this problem is common and challenging test for computational gas dynamics. For this problem Dustyshock name is reserved. Both Dustywave and Dustyshock problems are described in detail [9]. Moreover, for all numerical experiments in the paper we take the same physical and numerical parameters as in [9]. In particular, for both problems we take high drag coefficient and high concentration of dust in gas

$$K = 500, \qquad \frac{\rho_{\mathrm{d}}}{\rho_{\mathrm{g}}} = 1, \tag{22}$$

which is guarantee intense interphase interaction and challenge for simulation.

Fig. 1 shows the solution of Dustywave problem at the time moment $t = 0.5$ with MK, ISPH, IDIC methods. In this case (22) leads to $t_{\mathrm{stop}} = 0.002$. The figure displays the dust and gas velocity obtained with different smoothing lengths h. The left panels show the results of computing for explicit schemes MK. At $h = 0.025, h = 0.01$, the time step $\tau = 0.001 < t_{\mathrm{stop}}$ and the number of particles $N_{total} = 2 \times 600$ are used; while at $h = 0.001$, the step $\tau = 0.0001$ and $N_{total} = 2 \times 6000$. The middle and right panels present the results of computing for semi-implicit schemes ISPH and IDIC with CFL $= 0.1$; in this case, the number of particles was the same as for the left panels.

Fig. 2 shows gas and dust velocity as the solution of Dustyshock problem at the time moment $t = 0.2$. The same methods MK, ISPH, IDIC as in Fig. 1 are used. For $h = 0.01$ we take $N_{total} = 2 \times 990$, CFL $= 0.1$, for $h = 0.001$ — $N_{total} = 2 \times 9900$, CFL $= 0.1$

One can see that the numerical solutions obtained by MK and ISPH methods with the smoothing length increased from $h = 0.001$ (the condition (6) is satisfied) to $h = 0.025$ ((6) is violated) acquire a pronounced dissipation. The observed tendency to solution dissipation was described in [8, 7]. We can see from Figs. 1, 2 and Tables 1, 2 that the maximum level of dissipation is obtained in the case of explicit schemes MK. As follows from the central panel in Fig. 1, the semi-implicit ISPH scheme gives a smaller dissipation at the same smoothing length as compared to MK. Moreover, thanks to semi-implicit approximation of the drag force, the ISPH scheme has no restrictions on the time step (5).

MK and ISPH are the fully Lagrangian methods, which means that all forces are calculated without the introduction of a spatial grid. The IDIC method is a combination of Lagrangian and Euler approaches because the drag force is computed using the decomposition of particles into Euler volumes. One can see on the right upper panel of Fig.1 that these numerical solutions obtained by IDIC are free of dissipation, and at $h = 0.025$ the wave amplitude is reproduced without visible error, in distinction to MK and ISPH.

Table 1: Error for dust velocity computed with 3 different methods in L_2 norm for DUSTYWAVE problem. $N_{total} = 2 \times 600$ SPH particles.

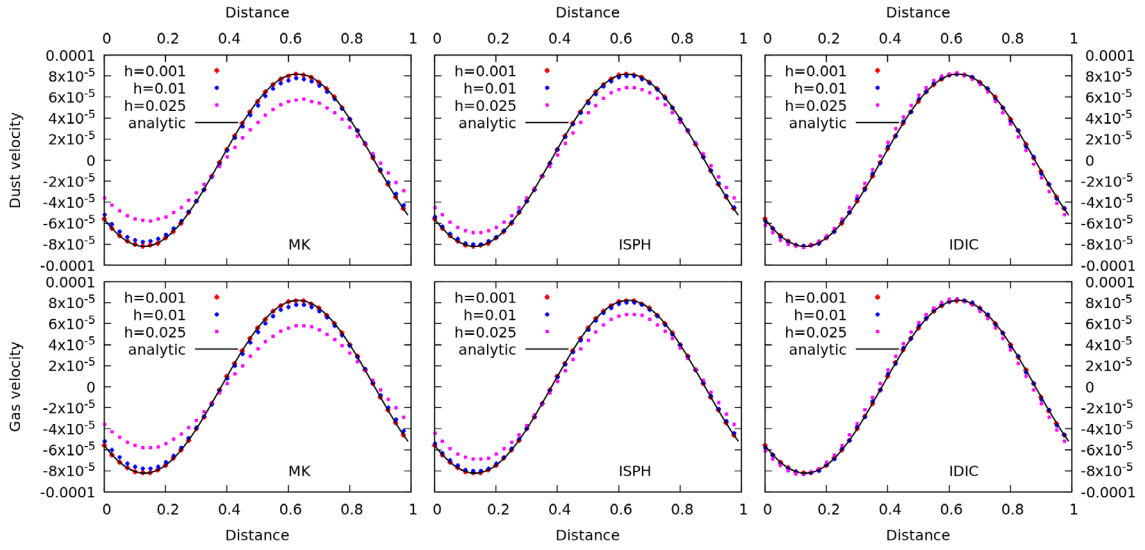|		MK	ISPH	IDIC
$h = 0.01$	$\tau = 0.00025$	0.0417	0.0332	0.0003
$h = 0.02$	$\tau = 0.001$	0.1486	0.079	0.0012

Figure 1: Solution of the DustyWave problem at the time instant $t = 0.5$ found with MK (left panels), ISPH (central panels) and IDIC (right panels) methods. Relaxation time of the dust velocity with respect to gas is $t_{\text{stop}} = 0.002$, i.e. $t_{\text{stop}} c_{\text{s}}/l \ll 1$, where l is the length of the computational domain. Solid black line corresponds to the analytical solution, and individual dots are the numerical solutions. At $h = 0.025$ and $h = 0.01$, the time step $\tau = 0.001 < t_{\text{stop}}$ and the number of particles $N_{total} = 2 \times 600$ are used; at $h = 0.001$, the step is $\tau = 0.0001$ and $N_{total} = 2 \times 6000$.

Table 2: Error for dust velocity computed with 3 different methods in L_2 norm for DUSTYSHOCK problem. $N_{total} = 2 \times 990$ SPH particles.

		MK	ISPH	IDIC
$h = 0.01$	$\tau = 0.000025$	0.1177	0.2101	0.0457
$h = 0.02$	$\tau = 0.0001$	0.1786	0.29	0.0605
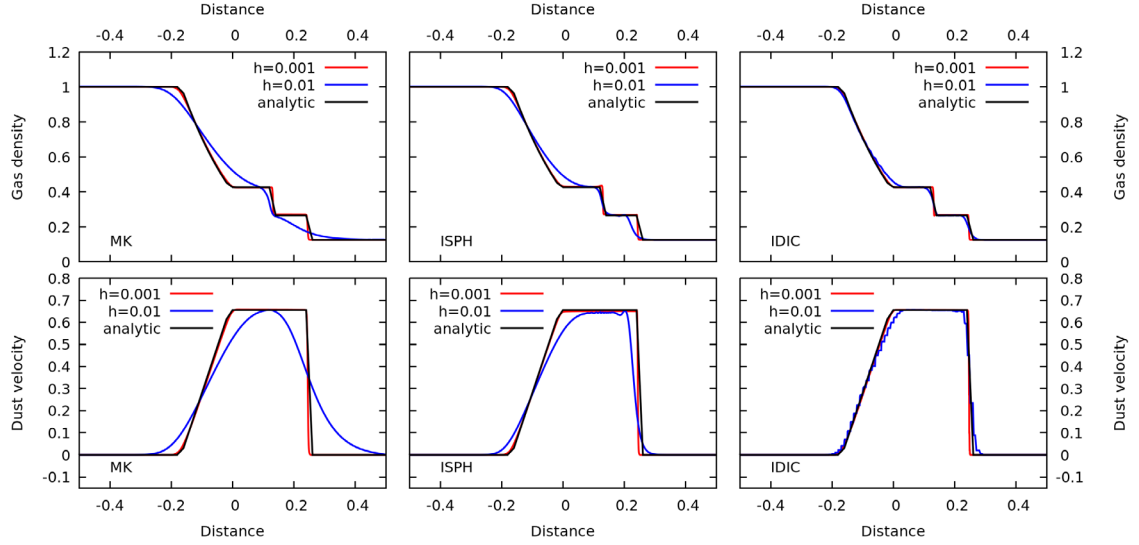
Figure 2: Solution of the DustyShock problem at the time instant $t = 0.2$ found with MK (left panels), ISPH (central panels) and IDIC (right panels) methods. Relaxation time of the dust velocity with respect to gas $t_{\text{stop}} = 0.00025$, i.e. $t_{\text{stop}}c_{\text{s}}/l \ll 1$, where l is the length of the computational domain. Solid black line corresponds to the analytical solution, color lines are the numerical solutions. At $h = 0.01$, the time step $\tau = 0.001$ and the number of particles $N_{total} = 2 \times 990$ are used; at $h = 0.001$, the step is $\tau = 0.0001$ and $N_{total} = 2 \times 9900$. For MK method time step is $\tau = 0.0001$ for all spatial resolution.

4   SUMMARY

Simulation of the dynamics of gas-aerosol particle mixtures is computationally challenging, especially in particle methods as Smoothed particle hydrodynamics. In the paper we compared ability of fully lagrangian methods MK [10] and ISPH [8] and euler-lagrangian method IDIC [9] to reproduce asymptotical properties of the solution for dynamics of gas-dust mixtures with intense interphase interaction. We found that IDIC method where drag is computed using euler cells is asymptotic preserving and allows to use timestep and smoothing length independent on drag intensity. MK and ISPH methods require fine spatial resolution for intense interphase interaction.

REFERENCES

[1] T. Saito, M. Marumoto, K. Takayama. Numerical investigations of shock waves in gas-particle mixtures. Evaluation of numerical methods for dusty-gas shock wave phenomena. Shock Waves 13: 299–322 (2003)

[2] S. Jin, C.D. Livermore. Numerical Schemes for Hyperbolic Conservation Laws with Stiff Relaxation Terms. Journal of Computational Physics 126, 449–467 (1996)

[3] S. Jin. Asymptotic preserving schemes for multiscale kinetic and hyperbolic equations: a review. Riv. Mat. Univ. Parma, 3, 177–216 (2012)

[4] G. Albi, G. Dimarco, L. Pareschi. Implicit-Explicit multistep methods for hyperbolic systems with multiscale relaxation. arXiv e-prints: 1904.03865

[5] O. P. Stoyanovskaya, V. N. Snytnikov, E. I. Vorobyov. Analysis of methods for computing the trajectories of dust particles in a gas-dust circumstellar disk. Astron.Rep., Vol. 61, No. 12:1044–1060 (2017)

[6] P. Degond, F. Deluzet. Asymptotic-Preserving methods and multiscale models for plasma physics. Journal of Computational Physics. 336, 429–457 (2017)

[7] G. Laibe, D. J. Price. DUSTYBOX and DUSTYWAVE: two test problems for numerical simulations of two-fluid astrophysical dust-gas mixtures. MNRAS, 418:1491–1497 (2011)

[8] P. Lorén-Aguilar, M. R. Bate. Two-fluid dust and gas mixtures in smoothed particle hydrodynamics: a semi-implicit approach. MNRAS, 443:927–945 (2014)

[9] O. P. Stoyanovskaya, T. A. Glushko, N. V. Snytnikov, V. N. Snytnikov, Two-Fluid Dusty Gas in Smoothed Particle Hydrodynamics: Fast and Implicit Algorithm for Stiff Linear Drag. Astronomy and Computing, 25:25–37 (2018)

[10] J. J. Monaghan, A. Kocharyan. SPH simulation of multi-phase flow. Computer Physics Communications, 87:225–235 (1995)

[11] S. T. Madisson, R. J. Humble, J. R. Murray. Building Planets with Dusty Gas. Bioastronomy 2002: Life Among the Stars, 213:231 (2004)

[12] L. Barriere-Fouchet, J. F. Gonzalez, J. R. Murray, R. J. Humble, S. T. Maddison. Dust distribution in protoplanetary disks. Vertical settling and radial migration. AAp, 443:185–194 (2005)

[13] J. F. Gonzalez, G. Laibe, S. T. Maddison. Self-induced dust traps: overcoming planet formation barriers. MNRAS, 467:1984–1996 (2017)

[14] Xiong, Qingang and Deng, Lijuan and Wang, Wei and Ge, Wei. SPH method for two-fluid modeling of particle–fluid fluidization. Chemical Engineering Science - CHEM ENG SCI, 66:1859–1865 (2011)

[15] R. A. Booth, D. Sijacki, C. J. Clarke. Smoothed particle hydrodynamics simulations of gas and dust mixtures. MNRAS, 452:3932–3947 (2015)

[16] W. K. M. Rice, G. Lodato, J. E. Pringle, P. J. Armitage, I. A. Bonnell. Accelerated planetesimal growth in self-gravitating protoplanetary discs. MNRAS, 355:543–552 (2004)

[17] M. J. Andrews, P. J. O'Rourke. The multiphase Particle-in-Cell (MP-PIC) method for dense particulate flows. Int. J. of Multiphase Flow, 22:379–402 (1996)

Numerical simulation of 2D hydraulic jumps using SPH method

Jinbo Lin*, Sheng Jin[†], Congfang Ai[†] and Weiye Ding[†]

* State Key Laboratory of Coastal and Offshore Engineering
Dalian University of Technology
Dalian 116024, China
e-mail: kingpo@mail.dlut.edu.cn

[†] State Key Laboratory of Coastal and Offshore Engineering
Dalian University of Technology
Dalian 116024, China
e-mail: tings@mail.dlut.edu.cn

ABSTRACT

A hydraulic jump that generally occurs in river or spillway is a rapid transition from supercritical to subcritical flow characterized by the development of large-scale turbulence, surface waves, energy dissipation and considerable air entrainment. The hydraulic jump is widely used as energy dissipaters in hydraulic engineering due to the high energy dissipation rate. In this study, a weakly compressible smoothed particle hydrodynamics model (WCSPH) is established to simulate the 2D hydraulic jump in open channel. To test the model, two hydraulic jump cases with different inflow Froude number are simulated. The comparison between numerical conjugate depths in the subcritical section with theoretical results show generally good agreement with theory. In addition, an aeration at the jump toe can be clearly observed in numerical results with only Single-phase flow. It is proved that SPH method has unique advantages dealing with the hydraulic jumps.

Keywords: Hydraulic jumps; SPH; Aeration.

1. INTRODUCTION

The hydraulic jumps are a common way to dissipate energy in hydraulic engineering. A hydraulic jump will occur when the supercritical flow discharged from sluice or overflow dam is lifted by the subcritical flow in downstream channel. The turbulence in a jump zone is intense and the energy loss is great. The energy dissipation rate can generally reach 60%-70%. In addition, the stilling basins installed downstream of discharge structures are often adopted to form hydraulic jumps behind gates in the design and construction of hydraulic projects. The stilling basins have the advantages of simple structure, convenient design and construction, and large energy dissipation rate. Therefore, the hydraulic jumps are widely used in large, medium and small hydraulic projects.

The hydraulic jumps have been widely investigated by researchers. López et al. [1] used a similar tank to obtain several jump shapes with different upstream Froude numbers. Then, the experimental data was adopted to check the SPH outcomes. The SPH model provided good average pressures values at the boundaries, but large dispersion was observed for instantaneous water depth. Federico et al. [2] developed a 2D SPH model with a new scheme to enforce different inlet and outlet flow conditions. The proposed treatment could correctly represent the boundary conditions without the generation of spurious pressure shock waves caused by a direct creation or deletion of fluid particles. The model has been successfully validated through several test cases of free-surface channel flows and hydraulic jumps. Babaali et al. [3] studied the hydraulic jump in a convergence stilling basin by a commercially software Flow-3D. The Navier-Stokes equations with standard k-ε and RNG model were solved by finite volume model. The comparison of the pressure, velocity, flow rate, kinetics energy, kinetics energy dissipation, and Froude number between numerical results and experimental data shown that this finite volume model could predict the hydraulic jump in a convergence stilling basin, accurately. Jonsson et al. [4] focused on the general behavior of the hydraulic jumps using the SPH methods. Four hydraulic jump cases with different particles resolution were set up and investigated by comparing the conjugate depth with the theoretical results. All of the numerical results shown good agreement with the analytical solution. Their work has shown the possibility to reproduce the internal velocity field

and its impact on the free surface in the hydraulic jumps by a relative simple and coarse SPH model. Azimi et al. [5] used a finite volume model with the volume of fluid scheme to study a hydraulic jump in U-shaped channel. A comparison between the numerical and experimental results shown that the numerical model simulated the flow field characteristics with good accuracy.

The present study uses the discretized governing equations proposed by Federico et al. [2] to simulate two test cases of undular and full hydraulic jumps. The integration of the discretized SPH equations in time is achieved by a two-stage Symplectic method [6]. The time step is a variable value updated in each step. The accuracy of the model is validated by comparing conjugate water depth with the analytical solution. Meanwhile, the evolution of the flow field for the two types of the hydraulic jumps is analyzed and compared.

2. NUMERICAL METHOD

2.1 Governing equations

The governing equations are viscous, weakly compressible Navier-Stokes equations. It is discretized by the SPH method, following Lagrangian form Navier–Stokes equations are obtained [2]

$$
\begin{cases}
\rho_a \dfrac{D\mathbf{u}_a}{Dt} = -\sum_b (p_a + p_b)\nabla_a W_b(\mathbf{r}_a)V_b + \rho_a \mathbf{g}_a + \mu \sum_b \dfrac{8\mathbf{u}_{ba}\cdot\mathbf{r}_{ba}}{\|\mathbf{r}_{ab}\|^2}\nabla_a W_b(\mathbf{r}_a)V_b \\[2mm]
\dfrac{D\rho_a}{Dt} = -\rho_a \sum_b \mathbf{u}_{ba}\cdot\nabla_a W_b(\mathbf{r}_a)V_b \\[2mm]
p_a = c_0^2(\rho_a - \rho_0) \\[2mm]
\dfrac{D\mathbf{r}_a}{Dt} = \mathbf{u}_a
\end{cases}
\tag{1}
$$

where ρ represents the density; $\mathbf{u}$ is the velocity vector; p represents the pressure; $\mathbf{r}$ represents the position of a generic material point; $\mathbf{g} = (0, 0, -9.81)$ m/s^2; ρ_0 is the reference density (1000 kg/m^3 for water); c_0 represents the reference speed of sound which usually adopts ten times of the maximum wave speed. $\mathbf{\Gamma}$ is the viscous stress tensor; and t is the time.

The sub-index is the a-th and b-th particles. More specifically, $\mathbf{u}_{ba} = \mathbf{u}_b - \mathbf{u}_a$; μ is the dynamic viscosity (1.0×10^{-3} N$\cdot$s/m^2 for water. For ideal fluid, there is no viscosity in fluid. An artificial viscosity is adopted to maintain computational stability. Here a formula $\mu = \rho_0 \alpha h c_0 / 8$ is adopted. Following Federico et al. [2], $\alpha = 0.02$ is taken.); V is the particle volume, $V = m / \rho$, where m represents the particle mass; $W_b(\mathbf{r}_a)$ refers to the kernel function at b-th particle induced by a-th particle. In this paper, a renormalized Gaussian kernel [7] is adopted with the smoothing length $h = 4\Delta x / 3$. A two-stage Symplectic method [6] is selected to integrate the discretized SPH equations in time. Meanwhile, the time step is a variable value updated in each step. The symplectic integration scheme is time reversible when there is no friction or viscous effects. The governing equations of N-S and motion can be rewritten as:

$$
\frac{d\mathbf{v}_a}{dt} = \mathbf{F}_a; \quad \frac{d\rho_a}{dt}; \quad \frac{d\mathbf{r}_a}{dt} = \mathbf{v}_a
\tag{2}
$$

At the predictor stage, the acceleration and density are updated:

$$
\mathbf{r}_a^{n+1/2} = \mathbf{r}_a^n + \mathbf{v}_a^n \frac{\Delta t}{2}; \quad \rho_a^{n+1/2} = \rho_a^n + D_a^n \frac{\Delta t}{2}
\tag{3}
$$

where the superscript n represents the time step.

At the corrector stage, half-time step values are used to calculate the next time step values of velocity and position.

$$
\mathbf{v}_a^{n+1} = \mathbf{v}_a^{n+1/2} + \mathbf{F}_a^{n+1/2} \frac{\Delta t}{2}; \quad \mathbf{r}_a^{n+1} = \mathbf{r}_a^{n+1/2} + \mathbf{v}_a^{n+1} \frac{\Delta t}{2}
\tag{4}
$$

2.2 Boundary conditions

For SPH model, the free surface can be captured naturally without additional special treatment. As for the wall boundaries, a fixed ghost particle technique is adopted to construct the wall boundary with four-layer fixed wall particles. The wall particles are fixed at its position while the density, velocity, and pressure of wall particles are determined by the mirror particles in the fluid domain. In this work, a slip boundary condition is selected to reproduce the inviscid condition. The inflow and outflow condition are treated by two buffer zone. Four-layer inflow and outflow particles are initially contained in the inflow and outflow buffer zone. Particles in buffer zone carry specific values of density, velocity, and pressure. The detail of boundary conditions can be found in [2].

3. NUMERICAL TEST CASES

An undular and full hydraulic jump test cases [2] are simulated to validate this model by comparing the numerical conjugate water depth with the analytical solution.
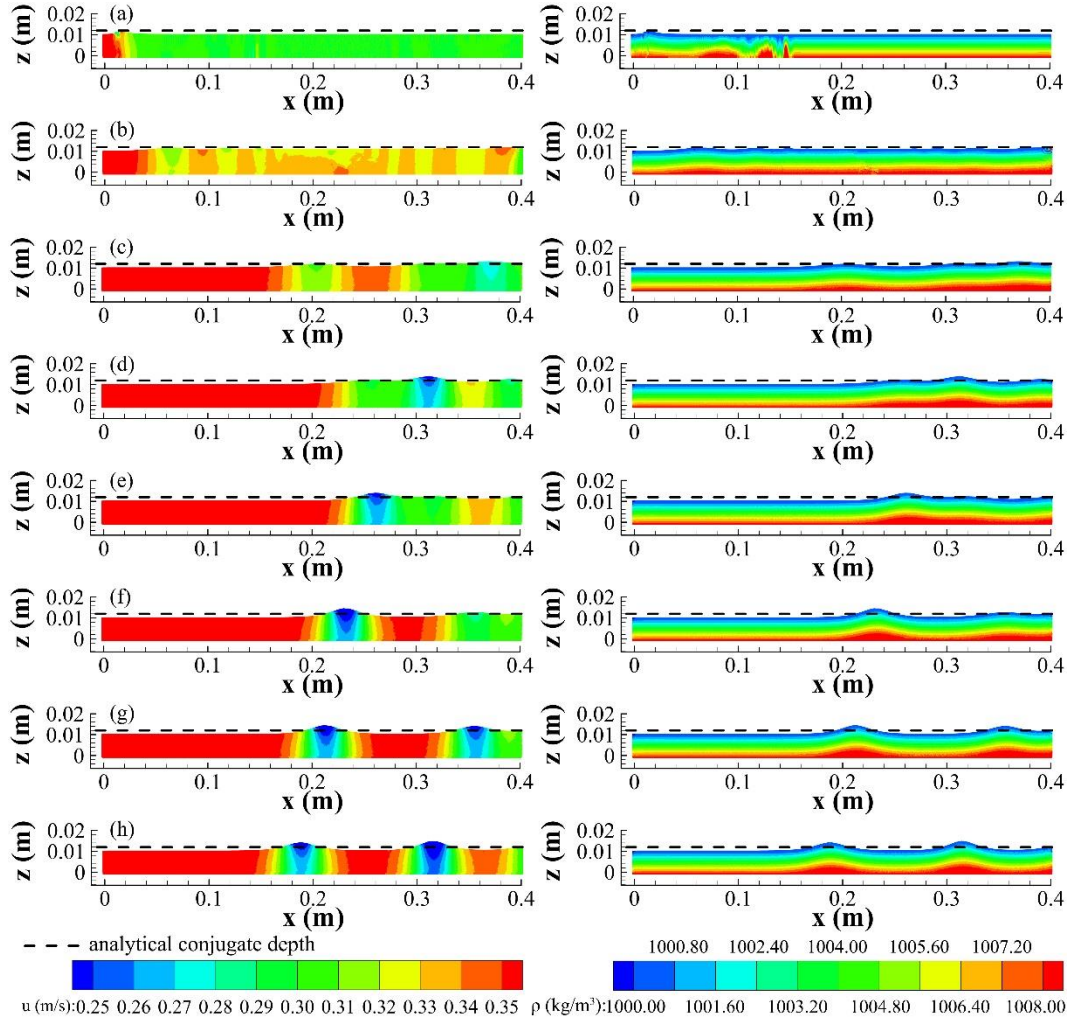
Fig. 1. Velocity (left) and density (right) magnitude field of case 1: (a) $t = 0.04$ s; (b) $t = 0.66$ s; (c) $t = 6.14$ s; (d) $t = 8.52$ s; (e) $t = 9.60$ s; (f) $t = 11.80$ s; (g) $t = 13.42$ s; (h) $t = 15.96$ s.

For ideal fluid, the conjugate water depth can be calculated as follow:

$$h_2 = \frac{h_1}{2}(\sqrt{1 + 8Fr_1^2} - 1) \tag{5}$$

where h_1 is the upstream water depth; h_2 is the downstream water depth; Fr_1 is the upstream Froude number $Fr_1 = U_1/\sqrt{gh_1}$, U_1 is the upstream velocity. The Fr_1 of case 1 and case 2 are 1.15 and 1.88, respectively. The upstream boundary condition sets to $h_1 = 0.01$ m and $U_1 = 0.36$ m/s for case 1. The corresponding downstream boundary condition is $U_2 = 0.3$ m/s. For case 2, $h_1 = 0.01$ m and

$U_1 = 0.589$ m/s are the upstream boundary condition. $U_2 = 0.268$ m/s is the downstream boundary condition. The length of numerical flume is $L = 40h_1$. The initial density and pressure are set according to the distribution of hydrostatic pressure. The space between particles is $h_1 / \Delta l = 50$.
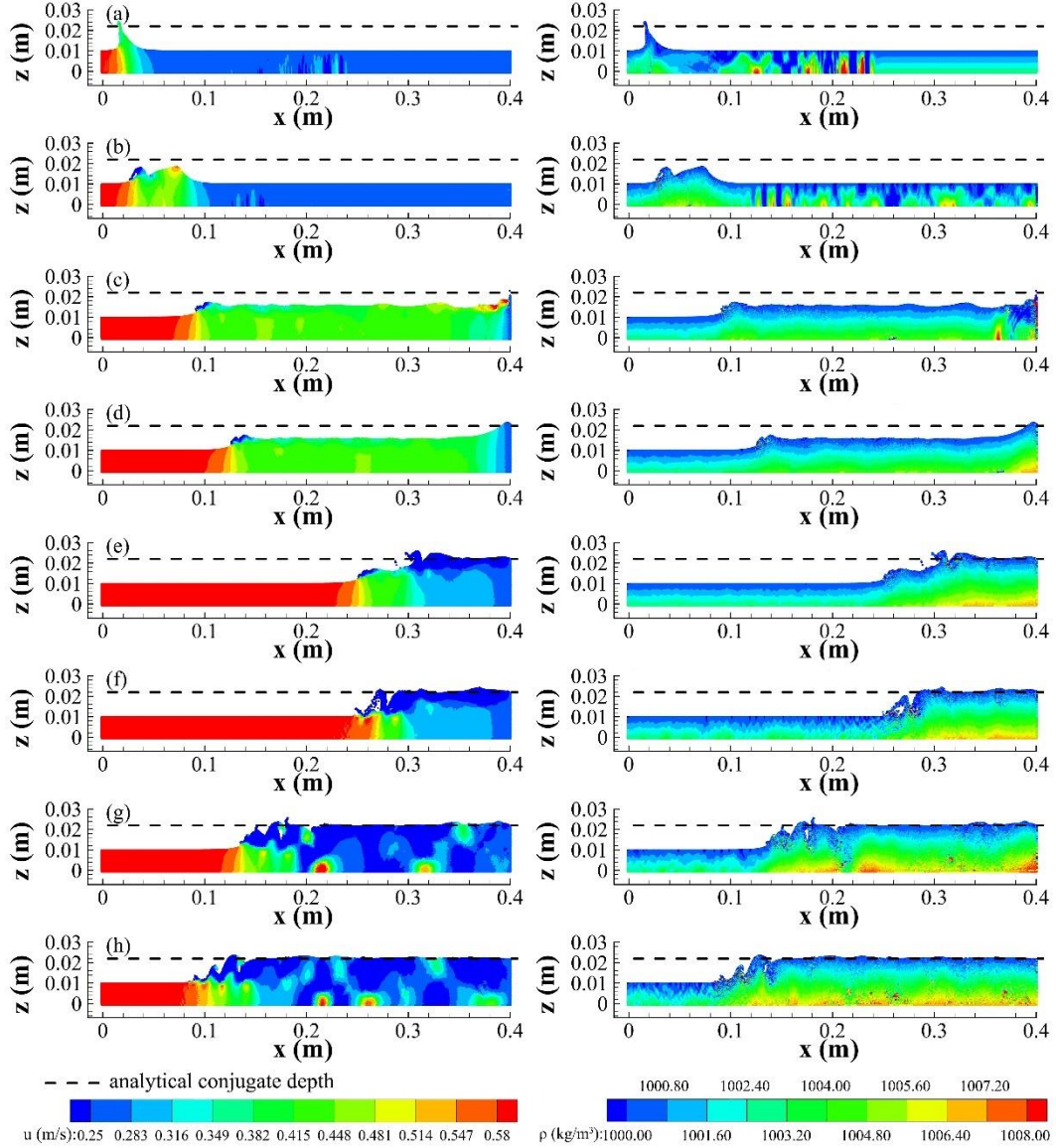
Fig. 2. Velocity (left) and density (right) magnitude field of case 1: (a) $t = 0.04$ s; (b) $t = 0.12$ s; (c) $t = 0.56$ s; (d) $t = 0.80$ s; (e) $t = 1.68$ s; (f) $t = 1.96$ s; (g) $t = 11.90$ s; (h) $t = 15.96$ s.

The velocity and density magnitude field of case 1 are shown in **Fig. 1**. Inflow particles interact with in-domain fluid particles and form a undular jump propagating to downstream at $t = 0.04$ s. Until $t = 0.66$ s, the jump reaches outflow boundary. Meanwhile, a series of weak wave are generated. Then, these waves move downstream until propagate upstream, firstly, at $t = 8.52$ s. Now, there is only one crest in the computational domain. The crest continually propagates upstream at $t = 9.60$ s and $t = 11.80$ s At $t = 13.42$ s, a new crest downstream of the first crest appears. Finally, the two crests move upstream for a little distance and basically reach quasi-constant state at $t = 15.96$ s. It can be seen that both of the velocity and density field are quite smooth in **Fig. 1**. In addition, the downstream water depth shows a good agreement with the analytical conjugate while the two crests are relatively higher than the analytical data. The maximum errors of the two crests are 0.002 and 0.0025, respectively.

Fig. 2 shows the velocity and density magnitude field of case 2. The evolution of the flow field can be described as follows. At $t = 0.04$ s, the inflow particles with large velocity interact with the slowly in-domain particles and generate a high jump. Two shock waves appear and move downstream at $t = 0.12$ s. Until $t = 0.56$ s, the shock wave arrives the outflow boundary. At $t = 0.80$ s, the shock wave reflects to upstream upstream until the upward shock wave merges with the slower shock wave

at t = 1.96 s. An aeration at the jump toe can be clearly observed at this time. Then, the merged jump continually moves upstream and basically reaches quasi-constant state at t = 15.96 s. Similar to **Fig. 1**, the velocity field in **Fig. 2** is very smooth. However, the density magnitude field is a little noisy in **Fig. 2**. The numerical conjugate water depth agrees very well with the analytical conjugate water depth.

4. CONCLUSIONS

Two types of 2D hydraulic jump, undular hydraulic jump and full hydraulic jump, are simulated by a WCSPH model. In this model, an artificial viscosity is adopted to stabilize the calculation due to the ideal fluid condition. Comparing the numerical conjugate depth with the analytical solution, the model can accurately reproduce the undular and full hydraulic jump. In addition, the numerical flow field shows that the aeration in the hydraulic jumps can be captured with this Single-phase model. In one word, the WCSPH model is a very power tool to investigate the hydraulic jumps.

5. FUTURE WORK

Though this model calculates the conjugate water depth with a good accuracy, the density field with large inflow Froude number is a little noisy. To eliminate the noise in density field will be our next step work. Besides, the time consumption of SPH model is very large. Therefore, a parallel version of the model is necessary to reduce the time consumption.

REFERENCE

[1] D. López, R. Marivela, L. Garrote, Smoothed particle hydrodynamics model applied to hydraulic structures: A hydraulic jump test case, J. Hydraul. Res. 48, 142–158 (2010).
[2] I. Federico, S. Marrone, A. Colagrossi, F. Aristodemo, M. Antuono, Simulating 2D open-channel flows through an SPH model, Eur. J. Mech. B/Fluids. 34, 35–46 (2012).
[3] H. Babaali, A. Shamsai, H. Vosoughifar, Computational Modeling of the Hydraulic Jump in the Stilling Basin with Convergence Walls Using CFD Codes, Arab. J. Sci. Eng. 40, 381–395 (2015).
[4] P. Jonsson, P. Jonsén, P. Andreasson, T.S. Lundström, J.G.I. Hellström, Smoothed Particle Hydrodynamic Modelling of Hydraulic Jumps: Bulk Parameters and Free Surface Fluctuations, Engineering. 08, 386–402 (2016).
[5] H. Azimi, S. Shabanlou, S. Kardar, Characteristics of Hydraulic Jump in U-Shaped Channels, Arab. J. Sci. Eng. 42, 3751–3760 (2017).
[6] C. Altomare, A.J.C. Crespo, J.M. Domínguez, M. Gómez-Gesteira, T. Suzuki, T. Verwaest, Applicability of Smoothed Particle Hydrodynamics for estimation of sea wave impact on coastal structures, Coast. Eng. 96, 1–12 (2015).
[7] D. Molteni, A. Colagrossi, A simple procedure to improve the pressure evaluation in hydrodynamic context using the SPH, Comput. Phys. Commun. 180, 861–872 (2009).

PHYSICAL REFLECTIVE BOUNDARY CONDITIONS APPLIED TO SMOOTHED PARTICLE HYDRODYNAMICS (SPH) METHOD FOR SOLVING FLUID DYNAMICS PROBLEMS IN 3-D DOMAINS

C.A.D. FRAGA FILHO[1,2*], C. PENG[1], M.R.I. ISLAM[1], C. McCABE[1], S. BAIG[1], G.V. DURGA PRASAD[1]

[1] ESS Engineering Software GmbH - Berggasse 35 - 4400 - Steyr, Austria

[2] Development, Implementation and Application of Computational Tools for Problem Solving in Engineering Research Group - Federal Institute of Education, Science and Technology of Espírito Santo - Av. Vitória, 1729, 29040-780, Jucutuquara, Vitória–ES, Brazil

*Correspondent author's email: cadff1@gmail.com

Key words: Smoothed Particle Hydrodynamics, reflective boundary conditions, fluid dynamics, continuum mechanics.

Abstract. This paper aims to present the physical reflective boundary conditions (RBC) in 3-D domains and applications in fluid dynamics problems. Currently, RBC have been used in meshfree particle methods as an attempt to respect the continuum physical laws at the macroscopic domain, without the application of fictitious/ ghost particles - that improperly mix molecular and continuum mechanics concepts [1]. RBC methodology, validation in 2-D domains and applications in hydrostatics and hydrodynamics cases were presented in [2]. Hydrostatics and hydrodynamics cases with the RBC implementation in 3-D domains are presented in this work. A Newtonian, incompressible, uniform and isothermal fluid inside an immobile reservoir open to the atmosphere and dam break flow have been studied. In the first case, a modified SPH formulation using a modified pressure concept [3] has been used. Dam breaking simulations used the standard SPH formulation. In both cases, the numerical results showed good agreement with the analytical results or literature data.

Notation

C_o initial position of the centre of mass of the particle (initial instant of the numerical iteration)

$(C_o)_k$ coordinates of the initial position of the centre of mass

C_1 position of the centre of mass, in a motion without obstacles, at the end of the numerical iteration

$(C_o)_k$ coordinates of the centre of mass position, in a motion without obstacles, at the end of the numerical iteration

$(C_1)_N$ coordinates of the centre of mass normal to the collision plane, in a motion without obstacles, at the end of the numerical iteration

C_f position of the centre of mass obtained after the collision response

$(C_f)_k$ coordinates of the centre of mass position, after the collision response

$(C_f)_N$ coordinates of the centre of mass position, normal to the collision plane, after the collision response

CR coefficient of restitution of kinetic energy

CF coefficient of friction

g gravity

g gravity magnitude

h support radius

H vertical coordinate of the free surface in the reservoir

k Cartesian direction

m_b mass of the neighbouring particle

P_a absolute pressure acting on the fixed particle

P_b absolute pressure acting on the neighbouring particle

P_{mod} modified pressure

$P_{mod(a)}$ modified pressure of the fixed particle

$P_{mod(b)}$ modified pressure of the neighbouring particle

P_0 pressure of reference

t time

v fluid velocity

$\mathbf{v}_a$ velocity of the reference particle

$\mathbf{v}_b$ velocity of the neighbouring particle

$\mathbf{v}_{ab}$ relative velocity between a fixed and a neighbouring particle

V_{ok} component of the initial velocity of the particle (initial instant of the numerical iteration)

V_{fk} component of the final velocity of the particle (final instant of the numerical iteration)

W kernel or interpolation function

X_a position of the reference particle

X_b position of the neighbouring particle

z   vertical coordinate of the fluid inside the reservoir

α_π coefficient used in the calculation of the artificial viscosity

β_π coefficient used in the calculation of the artificial viscosity

Δp parameter used in the calculation of the artificial pressure

ϵ parameter used in the calculation of the artificial pressure

υ kinematic viscosity of the fluid

υ_a kinematic viscosity of the reference particle

ρ density of the fluid

ρ_a density of the reference particle

ρ_b density of the neighbouring particle

∇ mathematical vector operator nabla

1. INTRODUCTION

Recent publications ([1],[2],[4-6]) have been realised proposing new boundary conditions techniques in meshfree particle methods, excluding the use of fictitious particles on or adjacent to the contours. Literature [2] presented the first implementation of the RBC, based on Newton's restitution law and foundations of analytic geometry, in 2-D domains. This paper extends the implementation of the RBC to a higher (3-D) dimension with validation tests and simulation results in both hydrostatics and hydrodynamics cases.

A collision detection and response algorithm has been implemented. Two coefficients were used in the collisions treatment: the kinetic energy restitution coefficient (CR), related to the energy loss in the direction normal to the collision plane, and the friction coefficient (CF), that measures the slow down in the particle's motion parallel to the collision plane. A complete description of the algorithm implementation (considering only the effects of the elastic restitution of energy) is in [2]. [1] presents the improvement of the algorithm considering the friction effects.

The remainder of this paper is organised in sections as follows. In Section 2, the algorithm validation is presented. Section 3 brings the cases studies, their numerical results and discussions. Finally, conclusions are in Section 4.

2. ALGORITHM VALIDATION

Analytical results have been employed to verify the positions and velocities that particles reached after the collisions treatment, at the end of each timestep. The velocity of the particle was considered constant in each step of time and its centre of mass moved linearly along the direction of the velocity from C_o to C_1 (considering a motion without obstacles).

Tests have been carried out, in which the particle radius was 0.01 m. The 3-D box had sides of 0.50 m. The time step was 0.25s. The coefficients of restitution of kinetic energy (CR) and friction (CF) received different values. Some tests results achieved are presented in Tables 1 - 6 and Figs. 1 - 4.

Test 1: Initial position of the centre of mass: C_o = (0.25, 0.25, 0.25) m; Initial velocity: V_o = (1.00, 0.00, 0.00) m/s; CR = 1.00; CF = 0.00 (see simulation results in Table 1 and Fig. 1).

Table 1: Results of the 1st validation test (SI units).

t^*	Input data									Output data					
	V_{ox}	V_{oy}	V_{oz}	C_{ox}	C_{oy}	C_{oz}	C_{1x}	C_{1y}	C_{1z}	C_{fx}	C_{fy}	C_{fz}	V_{fx}	V_{fy}	V_{fz}
0.25	1.00	0.00	0.00	0.25	0.25	0.25	0.50	0.25	0.25	0.48	0.25	0.25	-1.00	0.00	0.00
0.50	-1.00	0.00	0.00	0.48	0.25	0.25	0.23	0.25	0.25	0.23	0.25	0.25	-1.00	0.00	0.00
0.75	-1.00	0.00	0.00	0.23	0.25	0.25	-0.02	0.25	0.25	0.04	0.25	0.25	1.00	0.00	0.00
1.00	1.00	0.00	0.00	0.04	0.25	0.25	0.29	0.25	0.25	0.29	0.25	0.25	1.00	0.00	0.00
1.25	1.00	0.00	0.00	0.29	0.25	0.25	0.54	0.25	0.25	0.44	0.25	0.25	-1.00	0.00	0.00

*Number of collisions in every timestep: 1st - 01; 2nd - 0; 3rd - 01; 4th - 0; 5th - 01

Test 2: Initial position of the centre of mass: C_o = (0.25, 0.25, 0.25) m; Initial velocity: V_o = (0.00, 1.00, 0.00) m/s; CR = 1.00; CF = 0.00 (see simulation results in Table 2 and Fig. 2).

Table 2: Results of the 2nd validation test (SI units).

t^*	Input data									Output data					
	V_{ox}	V_{oy}	V_{oz}	C_{ox}	C_{oy}	C_{oz}	C_{1x}	C_{1y}	C_{1z}	C_{fx}	C_{fy}	C_{fz}	V_{fx}	V_{fy}	V_{fz}
0.25	0.00	1.00	0.00	0.25	0.25	0.25	0.25	0.50	0.25	0.25	0.48	0.25	0.00	-1.00	0.00
0.50	0.00	-1.00	0.00	0.25	0.48	0.25	0.25	0.23	0.25	0.25	0.23	0.25	0.00	-1.00	0.00
0.75	0.00	-1.00	0.00	0.25	0.23	0.25	0.25	-0.02	0.25	0.25	0.04	0.25	0.00	1.00	0.00
1.00	0.00	1.00	0.00	0.25	0.04	0.25	0.25	0.29	0.25	0.25	0.29	0.25	0.00	1.00	0.00
1.25	0.00	1.00	0.00	0.25	0.29	0.25	0.25	0.54	0.25	0.25	0.44	0.25	0.00	-1.00	0.00

*Number of collisions in every timestep: 1st - 01; 2nd - 0; 3rd - 01; 4th - 0; 5th - 01

Test 3: Initial position of the centre of mass: C_o = (0.01, 0.01, 0.01) m; Initial velocity: V_o = (1.00, 1.00, 1.00) m/s; CR = 1.00; CF = 0.00 (see simulation results in Table 3 and Fig. 3).

Table 3: Results of the 3th validation test (SI units).

t^*	Input data									Output data					
	V_{ox}	V_{oy}	V_{oz}	C_{ox}	C_{oy}	C_{oz}	C_{1x}	C_{1y}	C_{1z}	C_{fx}	C_{fy}	C_{fz}	V_{fx}	V_{fy}	V_{fz}
0	1.00	1.00	1.00	0.01	0.01	0.01	0.26	0.26	0.26	0.26	0.26	0.26	1.00	1.00	1.00
0.50	1.00	1.00	1.00	0.26	0.26	0.26	0.51	0.51	0.51	0.47	0.47	0.47	-1.00	-1.00	-1.00
0.75	-1.00	-1.00	-1.00	0.47	0.47	0.47	0.22	0.22	0.22	0.22	0.22	0.22	-1.00	-1.00	-1.00
1.00	-1.00	-1.00	-1.00	0.22	0.22	0.22	-0.03	-0.03	-0.03	0.05	0.05	0.05	1.00	1.00	1.00
1.25	1.00	1.00	1.00	0.05	0.05	0.05	0.30	0.30	0.30	0.30	0.30	0.30	1.00	1.00	1.00

*Number of collisions in every timestep: 1st - 0; 2nd - 01; 3rd - 0; 4th - 01; 5th - 0

Test 4: Initial position of the centre of mass: $C_o = (0.01, 0.01, 0.01)$ m; Initial velocity: $V_o = (1.00, 1.00, 0.00)$ m/s; CR = 1.00; CF = 0.00 (see simulation results in Table 4 and Fig. 4).

Table 4: Results of the 4th validation test (SI units).

t^*	Input data									Output data					
	V_{ox}	V_{oy}	V_{oz}	C_{ox}	C_{oy}	C_{oz}	C_{1x}	C_{1y}	C_{1z}	C_{fx}	C_{fy}	C_{fz}	V_{fx}	V_{fy}	V_{fz}
0.25	1.00	1.00	0.00	0.01	0.01	0.01	0.26	0.26	0.01	0.26	0.26	0.01	1.00	1.00	0.00
0.50	1.00	1.00	0.00	0.26	0.26	0.01	0.51	0.51	0.01	0.47	0.47	0.01	-1.00	-1.00	0.00
0.75	-1.00	-1.00	0.00	0.47	0.47	0.01	0.22	0.22	0.01	0.22	0.22	0.01	-1.00	-1.00	0.00
1.00	-1.00	-1.00	0.00	0.22	0.22	0.01	-0.03	-0.03	0.01	0.05	0.05	0.01	1.00	1.00	0.00
1.25	1.00	1.00	0.00	0.05	0.05	0.01	0.30	0.30	0.01	0.30	0.30	0.01	1.00	1.00	0.00

*Number of collisions in every timestep: 1st - 0; 2nd - 01; 3rd - 0; 4th - 01; 5th - 0

Test 5: Initial position of the centre of mass: $C_o = (0.49, 0.49, 0.49)$ m; Initial velocity: $V_o = (-1.00, -1.00, -1.00)$ m/s; CR = 1.00; CF = 0.00 (see simulation results in Table 5).

Table 5: Results of the 5th validation test (SI units).

t^*	Input data									Output data					
	V_{ox}	V_{oy}	V_{oz}	C_{ox}	C_{oy}	C_{oz}	C_{1x}	C_{1y}	C_{1z}	C_{fx}	C_{fy}	C_{fz}	V_{fx}	V_{fy}	V_{fz}
0.25	-1.00	-1.00	-1.00	0.49	0.49	0.49	0.24	0.24	0.24	0.24	0.24	0.24	-1.00	-1.00	-1.00
0.50	-1.00	-1.00	-1.00	0.24	0.24	0.24	-0.01	-0.01	-0.01	0.03	0.03	0.03	1.00	1.00	1.00
0.75	1.00	1.00	1.00	0.03	0.03	0.03	0.28	0.28	0.28	0.28	0.28	0.28	1.00	1.00	1.00
1.00	1.00	1.00	1.00	0.28	0.28	0.28	0.53	0.53	0.53	0.45	0.45	0.45	-1.00	-1.00	-1.00
1.25	-1.00	-1.00	-1.00	0.45	0.45	0.45	0.20	0.20	0.20	0.20	0.20	0.20	-1.00	-1.00	-1.00

*Number of collisions in every timestep: 1st - 0; 2nd - 01; 3rd - 0; 4th - 01; 5th

Test 6: Initial position of the centre of mass: $C_o = (0.01, 0.01, 0.01)$ m; Initial velocity: $V_o = (1.50, 1.00, 1.00)$ m/s; CR = 1.00; CF = 0.10 (see simulation results in Table 6).

Table 6: Results of the 6th validation test (SI units).

t^*	Input data									Output data					
	V_{ox}	V_{oy}	V_{oz}	C_{ox}	C_{oy}	C_{oz}	C_{1x}	C_{1y}	C_{1z}	C_{fx}	C_{fy}	C_{fz}	V_{fx}	V_{fy}	V_{fz}
0.25	1.50	1.00	1.00	0.01	0.01	0.01	0.39	0.26	0.26	0.39	0.26	0.26	1.50	1.00	1.00
0.50	1.50	1.00	1.00	0.39	0.26	0.26	0.76	0.51	0.51	0.22	0.47	0.47	-1.22	-0.81	-0.81
0.75	-1.22	-0.81	-0.81	0.22	0.47	0.47	-0.08	0.27	0.27	0.10	0.27	0.27	1.22	-0.73	-0.73
1.00	1.22	-0.73	-0.73	0.10	0.27	0.27	0.41	0.09	0.09	0.41	0.09	0.09	1.22	-0.73	-0.73
1.25	1.22	-0.73	-0.73	0.41	0.09	0.09	0.71	-0.10	-0.10	0.27	0.12	0.12	-0.98	0.59	0.59

*Number of collisions in every timestep: 1st - 0; 2nd - 02; 3rd - 01; 4th - 0; 5th - 02
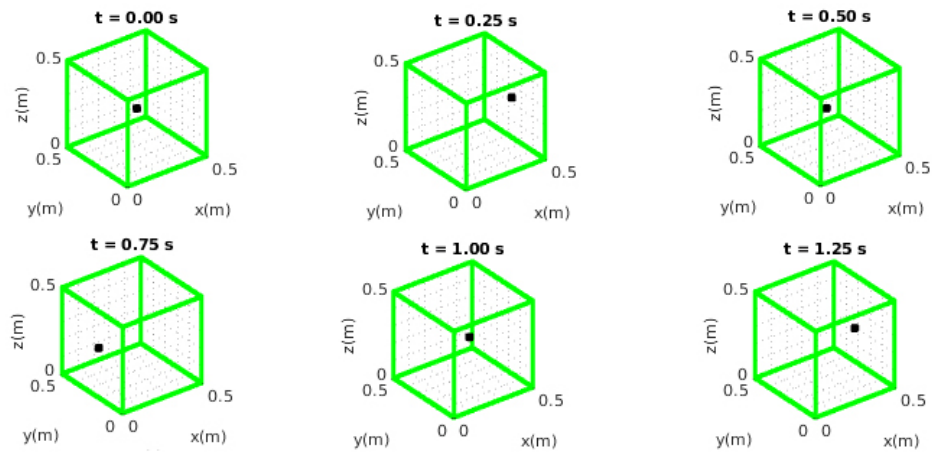
Figure 1. Positions of the centre of mass of the particle at the 1st validation test.
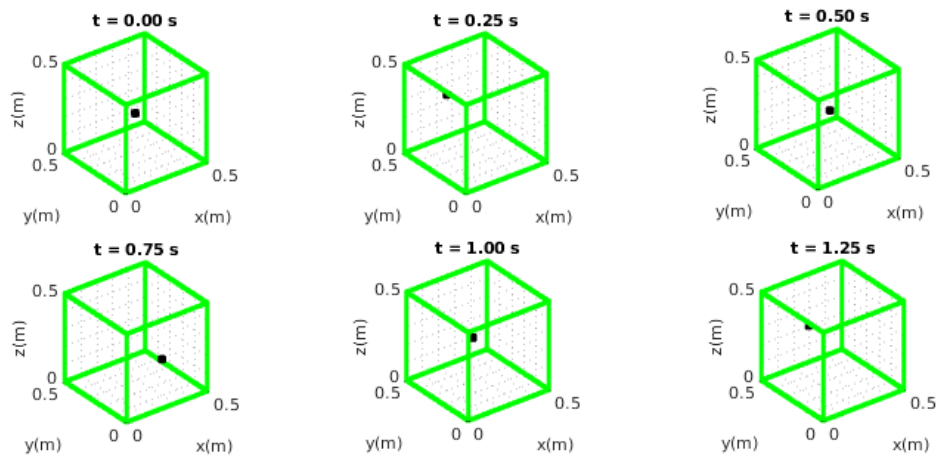
Figure 2. Positions of the centre of mass of the particle at the 2nd validation test.
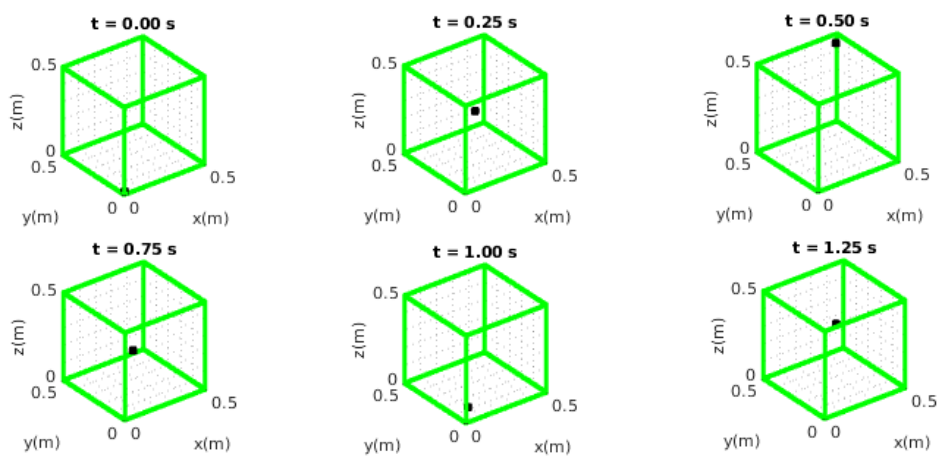
Figure 3. Positions of the centre of mass of the particle at the 3rd validation test.
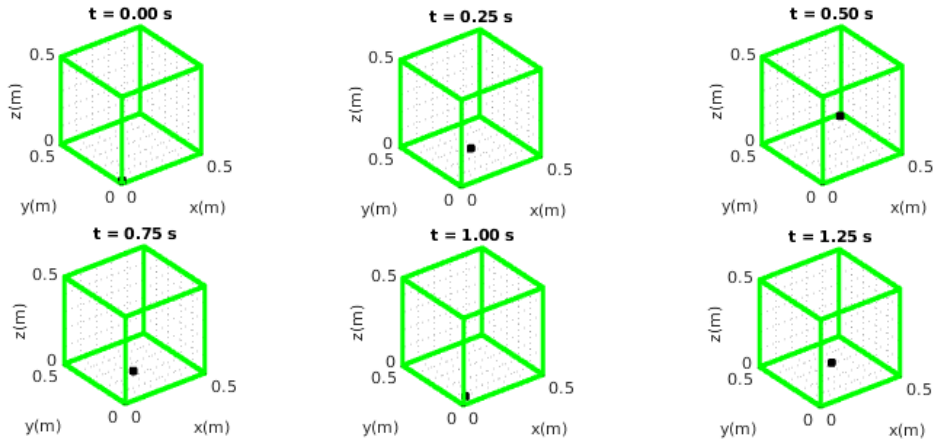
Figure 4. Positions of the centre of mass of the particle at the 4th validation test.

3. CASES STUDIES

3.1 Still Fluid Inside a Reservoir Open to the Atmosphere

This hydrostatics problem consists of a reservoir open to the atmosphere, filled with a Newtonian, incompressible, uniform and isothermal liquid. The dimensions of the tank are 1.0 m × 1.0 m × 1.0 m. The water particles inside the reservoir are at 20°C and at sea level ($\rho = 1.00 \times 10^3$ kg/m^3, $\nu = 1.00 \times 10^{-6}$ m^2/s). 25 particles per side of the tank (15,625 in total) were used in the discretisation of the fluid.

The modified pressure concept [3] has been used (Eq.(1)) and the physical reflective boundary conditions ensuring the non-motion of the particles and the obedience to the continuum laws.

$$P_{\text{mod}} = (P - P_0) - \rho g (H - z) \tag{1}$$

Taking into account that $(P - P_0)$ is the pressure exerted by the fluid column on the particle with vertical coordinate z, the modified pressure is zero to each particle in the domain. The SPH approximations to the physical laws of conservation of mass and momentum have been employed in the problem solving - Eqs. (2)-(3).

$$\frac{d\rho_a}{dt} = \sum_{b=1}^{n} m_b \left(\mathbf{v}_a - \mathbf{v}_b \right) . \nabla W (\mathbf{X}_a - \mathbf{X}_b, h) \tag{2}$$

$$\frac{d\mathbf{v}_a}{dt} = \frac{1}{\rho_a} \sum_{b=1}^{n} m_b \left(P_{\text{mod(b)}} - P_{\text{mod(a)}} \right) \nabla W \left(X_a - X_b, h \right) +$$
$$+ 2\upsilon_a \sum_{b=1}^{n} \frac{m_b}{\rho_b} \mathbf{v}_{ab} \frac{(X_a - X_b)}{|X_a - X_b|^2} . \nabla W \left(X_a - X_b, h \right) \tag{3}$$

where $\mathbf{v}_{ab} = \mathbf{v}_a - \mathbf{v}_b$.

Equation (3) is the SPH modified formulation for the momentum conservation equation obtained through application of the concept presented in Eq. (1).

The coefficients of restitution of kinetic energy (CR) and friction (CF) were 1.0 and 0.0, respectively. The time step employed was 1.00×10^{-4} s.

Figure 5 shows the hydrostatic and the modified pressure fields acting on the particles (represented by their centres of mass) inside the reservoir.
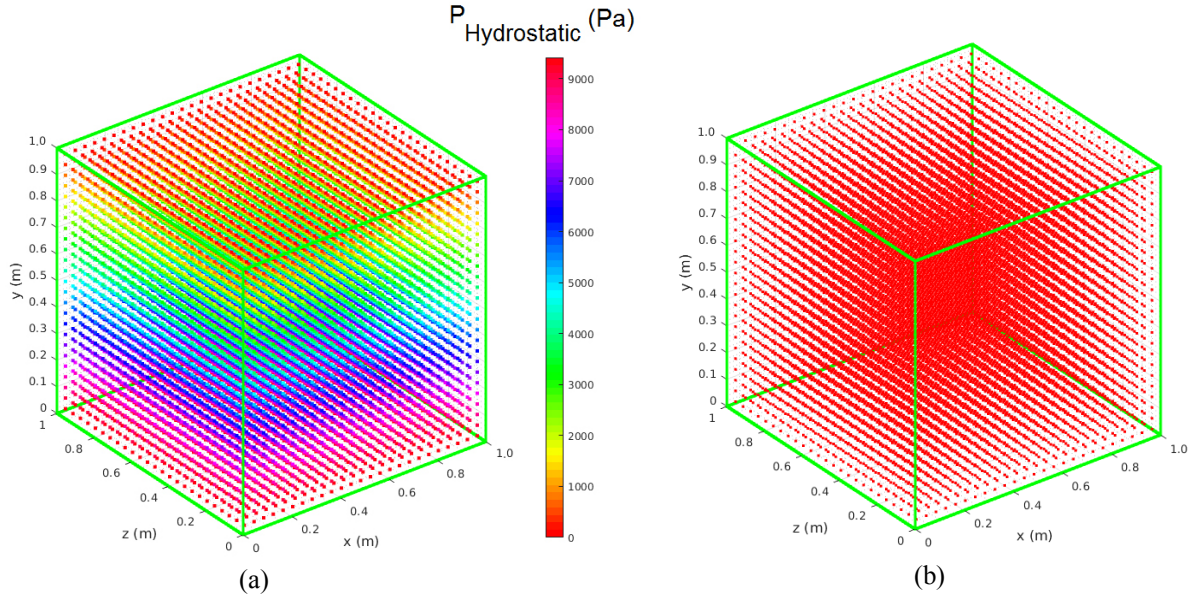
Figure 5. Pressure acting on the particles inside the reservoir. (a) The hydrostatic pressure field. (b) The modified pressure field (equal to zero). The particles are represented by their centres of mass.

The initial velocities of the particle were null. After the solution of the mass and momentum conservation equations and updating of the positions of the centres of mass and velocities of the particles, the positions of the particles remained unchanged (regardless of the interpolation function used in the particle method) and the hydrostatic equilibrium was maintained.

3.2 3-D Dam Break Flow over Dry Bed

The reservoir has length of 0.420 m, height of 0.440 m and depth of 0.228 m. The damned water has a volume with length of 0.114 m, height of 0.228 m, and depth of 0.228 m. 32,000 particles were used in the discretisation of the water (at 20°C with $\rho = 1.00 \times 10^3$ kg/m^3 and $\nu = 1.00 \times 10^{-6}$ m^2/s). The water damned was considered incompressible, uniform and isothermal. The standard SPH formulation to the equations of conservation of mass and momentum - Eqs. (2) and (4) - were employed combined with RBC in the boundary treatment (aiming to respect the continuum laws).

The absolute pressure acting on every fluid particle was composed by the sum of two parcels: the hydrostatic and the hydrodynamics (predicted by the Tait equation). The free surface particles were found at the initial time instant, marked and their absolute pressures set to zero (Newman boundary conditions). Those pressures were kept null throughout the

simulation. The timestep was 1.00×10^{-4} s. The temporal integration method employed was the Euler's method.

$$\frac{d\mathbf{v}_a}{dt} = -\sum_{b=1}^{n} m_b \left[\frac{P_a}{\rho_a^2} + \frac{P_b}{\rho_b^2} \right] \nabla W(\mathbf{X}_a - \mathbf{X}_b, h) +$$
$$+ \sum_{b=1}^{n} m_b \left[\frac{2\upsilon_a}{\rho_b} \frac{(\mathbf{X}_a - \mathbf{X}_b)}{|\mathbf{X}_a - \mathbf{X}_b|^2} . \nabla W(\mathbf{X}_a - \mathbf{X}_b, h) \right] (\mathbf{v}_a - \mathbf{v}_b) + \mathbf{g} \tag{4}$$

Density renormalisation was performed at every 30 timesteps and the correction of the kernel gradient near the boundaries has been done at each numerical iteration. A support radius varying with time, have been used [7, 8]. In the RBC implementation, CR and CF received the values 1.00 and 0.00, respectively. The artificial viscosity [7,8] (with the coefficients α_π = 0.04 and β_π = 0.00) and artificial pressure [9] (with the parameters ϵ equal to 0.10 and Δp equal to the initial lateral distance between two consecutives centres of mass) were used in simulations. The validation of the results has been done from experimental data and Eulerian finite element method (FEM) results provided by literature [10]. Figure 6 shows the SPH results achieved in this work for the dam breaking flow in some time instants of the simulation.
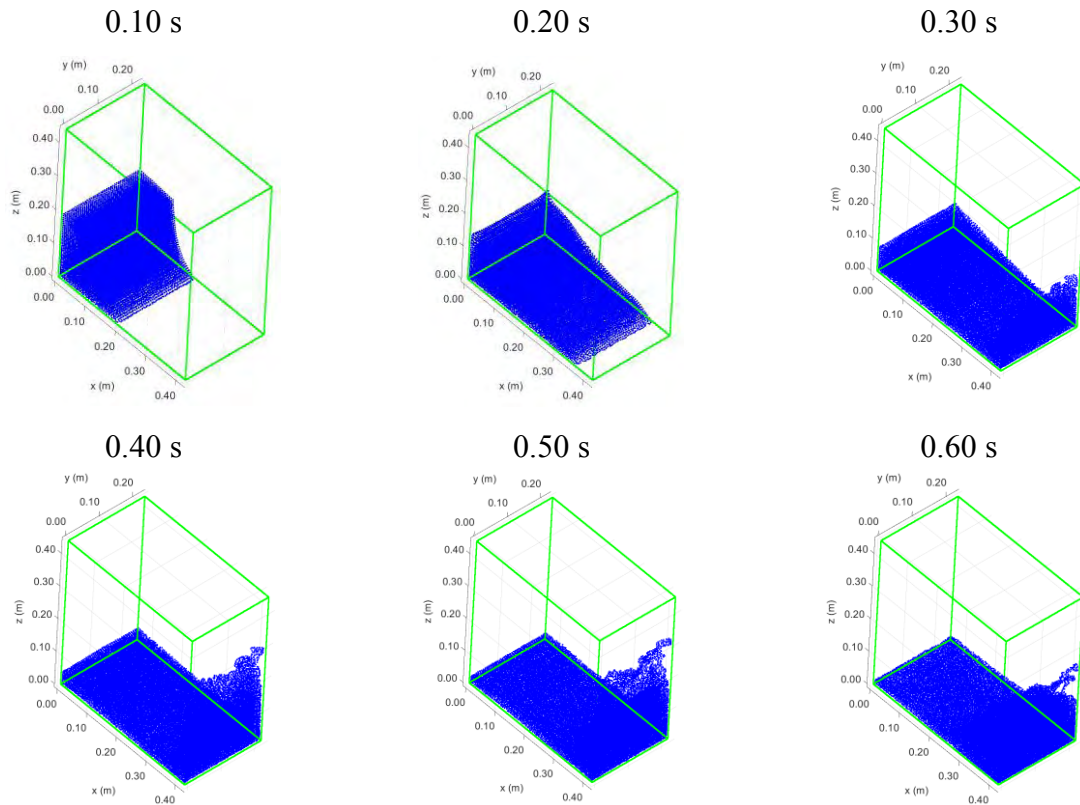
Figure 6. 3-D dam breaking flow evolution (SPH simulation results) until 0.60s.

The evolution of the dam breaking flow (lateral xz cross-section), in some instants of time, is shown in Figs. 7 and 8. In Figure 7 which there is a comparison between the experimental data [10] and the SPH results. The comparison between FEM results, provided by [10], and the SPH results (achieved in this work) is in Fig. 8.
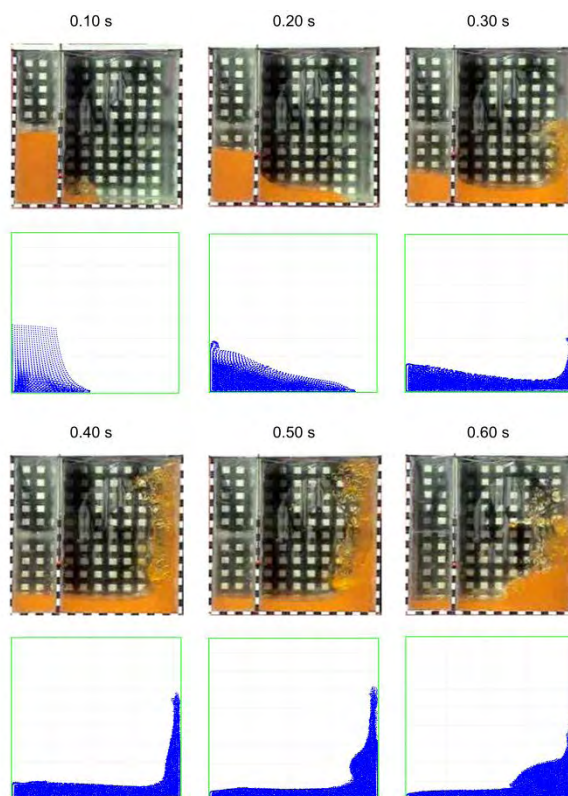
Figure 7. Experimental data [10] and SPH simulation results (in blue) for different time instants until 0.60 s.

From the analysis of Figs. 13 and 14, a good agreement, with the experimental data and particularly with the FEM results both provided by [10], has been seen.

4. CONCLUSIONS

In this work, the implementation of the RBC in the 3-D domain has been presented. Validation tests have been performed to verify the results provided by the 3-D collision detection and response algorithm. Simulations of two fluid dynamic cases (hydrostatics and hydrodynamics) have been performed.

In hydrostatics, a Newtonian, incompressible, uniform, and isothermal fluid at rest inside a reservoir has been simulated. The SPH results showed complete agreement with the analytical solution, regardless of the interpolation function employed in the SPH meshfree particle method.

In the hydrodynamics (dam break flow simulation), a good agreement between with the SPH results and the experimental data and Eulerian FEM results, both provided by [10], has been seen.
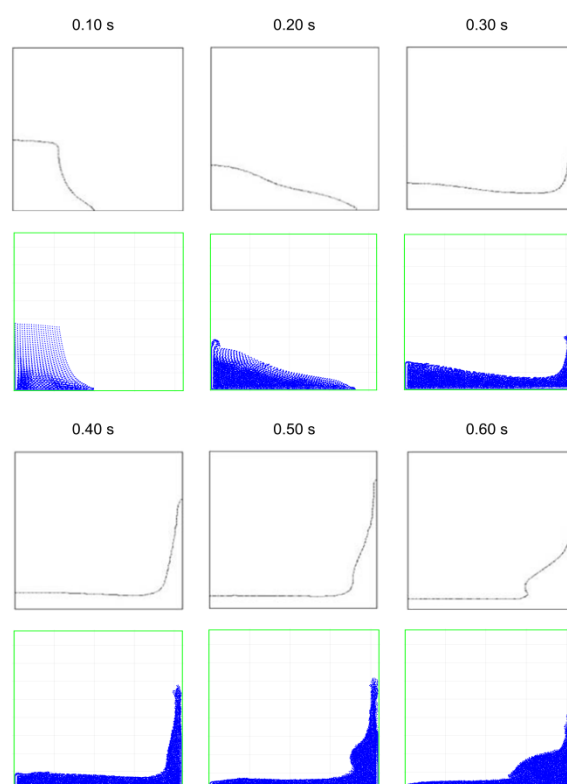
Figure 8. Finite element method (FEM) results [10] (free surface lines) and SPH results for different time instants until 0.60 s.

REFERENCES

[1] C.A.D. Fraga Filho, On the boundary conditions in Lagrangian Particle Methods and the physical foundation of continuum mechanics, *Continuum Mech. Thermodyn.* (2019), **31**(2):475–489. https://doi.org/10.1007/s00161-018-0702-2

[2] C.A.D. Fraga Filho, An algorithmic implementation of physical reflective boundary conditions, *Physics of Fluids* (2017) **29**, 113602. https://doi.org/10.1063/1.4997054

[3] C.A.D. Fraga Filho and J.T.A., Chacaltana, *Study of Fluid Flows using Smoothed Particle Hydrodynamics: the Modified Pressure Concept Applied to Quiescent Fluid and Dam Breaking.* In: Proceedings of the XXXVI Ibero-Latin American Congress of Computational Methods in Engineering – CILAMCE2015, Rio de Janeiro (2015). Available at

https://ssl4799.websiteseguro.com/swge5/PROCEEDINGS/PDF/CILAMCE2015-0071.pdf, accessed on May 12, 2019.

[4] M. Ferrand M., D. R. Laurence, B.D. Rogers, D. Violeau and C. Kassiotis, *Unified semi-analytical wall boundary conditions for inviscid, laminar or turbulent flows in the meshless SPH method.* Int. J. Numer. Methods Fluids (2013) **71**(4): 446–472, 2013. https://doi.org/10.1002/fld.3666

[5] A. Leroy, D. Violeau, M. Ferran and C. Kassiotis, *Unified semi-analytical wall boundary conditions applied to 2-D incompressible SPH*. J. Comput. Phys. (2014) **261**:106–129. https://doi.org/10.1016/j.jcp.2013.12.035

[6] A. Mayrhofer, M. Ferrand, C. Kassiotis, D. Violeau and F. Morel. *Unified semi- analytical wall boundary conditions in SPH: analytical extension to 3-D*. Numer. Algorithms (2015) **68**(1):15–34, 2015. https://doi.org/10.1007/s11075-014-9835-y

[7] C.A.D. Fraga Filho, *Smoothed Particle Hydrodynamics: Fundamentals and Basic Applications in Continuum Mechanics*. Springer Nature, Switzerland (2019).

[8] G.R. Liu and M.B. Liu, *Smoothed Particle Hydrodynamics: a Meshfree Particle Method*. World Scientific, Singapore (2003).

[9] J.J. Monaghan, *SPH without tensile instability*, J. Comput. Phys. (2000)**159**:290–311. https://doi.org/10.1006/jcph.2000.6439

[10] M.A. Cruchaga, D.J. Celentano and T.E. Tezduyar, *Collapse of a liquid column: numerical simulation and experimental validation*, Comput. Mech. (2007) **39**(4): 453–476. https://doi.org/10.1007/s00466-006-0043-z

Semi-Decoupled Second-Order Consistency Correction for Smoothed Particle Hydrodynamics

Cristian V. Achim · Roberto E. Rozas · Pedro G. Toledo

Abstract We present an approximate second-order consistent smoothed particle hydrodynamics method which uses the 1D solutions to approximate the 2D second order derivatives. The numerical tests of the analytic functions show that the method is exact for regular arrangements of interpolation points, while in the disordered areas the accuracy is lower than the exact solution of the second-order consistent modified smoothed particle hydrodynamics, but still better that the standard version or the so-called decoupled finite particle method. We applied the new model to the flow of a fluid around a circular solid obstacle and found that the use of a corrected semi-decoupled second-order consistent SPH gives better accuracy for lower resolutions allowing for a more efficient numerical model and also easier to extend to 3D.

Keywords MSPH · consistency · driven flow of solid-gas systems

1 Introduction

The modified smoothed particle hydrodynamics (MSPH) [1] and finite particle method (FPM) [2,3] are meshfree particle methods based on smoothed particle hydrodynamics (SPH) [4,5] with kernel corrections that improve the accuracy of the derivatives by imposing high order consistency. An n-order consistency C^n imposes that polynomials and their derivatives up to the nth order are exactly described for any distribution of the interpolation points. In these methods, the field variables and their derivatives are simultaneously obtained via inversion of corrective matrices which are computed at every time step for each SPH point. The FPM imposes C^1 and uses third order matrices in 2D and fourth order matrices in 3D, while the MSPH has C^2 with sixth order matrices in 2D and tenth order in 3D. While the standard SPH has been tuned and calibrated to work for modeling of incompressible fluids [6], some specific applications, such as driven flows of gas-solid mixtures, require higher order consistency [7].

C. V. Achim

Water Research Center for Agriculture and Mining (CRHIAM), Universidad de Concepción, Concepción, Chile
E-mail: cristian.v.achim@gmail.com

R. E. Rozas
Department of Physics, Universidad del Bío-Bío, Concepción, Chile
E-mail: rrozas@ubiobio.cl

P. G. Toledo
Department of Chemical Engineering, Universidad de Concepción, Concepción, Chile
E-mail: petoledo@udec.cl

However imposing a higher order consistency is in general accompanied by an increase in the accuracy [8], matrix inversions can be ill conditioned and the numerical error can be very large. This can happen in regions of space with extremely disordered configurations or for free-surfaces when the number of neighbors is too small. In order to avoid the matrix inversion problems Zhang et al [9] suggested a decoupled FPM which approximated the corrective matrix by neglecting its off-diagonal elements. This solution worked for the free-surface application, however for the driven flow of gas around solid obstacles Achim et al [10] showed that it was not enough and they presented a new way to construct decoupled corrections with C^1 using the 1D (FPM) solutions with results very close to the FPM [10] at a small computational cost. The approximations in our previous work [10] involves semi-decoupled FPM (SDFPM) and corrected semi-decoupled FPM (CSDFPM).

We expand the work done in Ref. [10] to impose second order consistency. The decoupling of the derivatives is computed using the normalized version of the kernel and its derivatives in which some of the non-diagonal elements in the correction matrices are exactly zero, while some non-diagonal cross terms are neglected. An extra advantage of our method is that in one dimension (1D) it is exact. Similar to Ref. [9], the effective quasi-diagonal matrices have no condition problems. We present two versions of SDMSPH and find that the corrected SDMPSH (CSDMSPH) gives very good results in practical applications and it can successfully replace the lower order methods, such as standard SPH and FPM for the modeling of pure fluid flows and solid-fluids flows. We present numerical tests of the second order derivatives for various selected analytic functions and finally, more important, we solve numerically the flow of a weakly compressible fluid around a solid obstacle using corrected gradients based on the new semi-decoupled MSPH (SDMSPH). The computational cost of the SDMSPH is the same as the FPM, but with higher accuracy.

2 Smoothed Particle Hydrodynamics and its Corrected Variants

In the SPH the relevant fields are interpolated from a set of points that move with the fluid [11]. In the continuum limit, for any field $f(\mathbf{r})$ the smoothed value is defined as [12,13]:

$$f(\mathbf{r}) \approx \int f(\mathbf{r}')W(|\mathbf{r} - \mathbf{r}'|, h)d\mathbf{r}', \tag{1}$$

where W is a kernel, a probability distribution function, and h is the smoothing length. The range of the kernel function can be infinite as in the case of a Gaussian function or it's limited to a few κ multiples of h, i.e. κh. All given values of the fields are approximated by the above formula in discrete form. The accuracy of the SPH is $O(h^2)$ [5,4,8].

2.1 Standard SPH

In the standard SPH [12,13], the integral in Eq. (1) can be expressed in a discrete form as follows

$$(f)_i^{SPH} \approx \sum_j f_j W(|\mathbf{r}_i - \mathbf{r}_j|, h)V_j, \tag{2}$$

where the index j goes over all particles in the range of the point where the evaluation is taking place, $\mathbf{r}_j$ denotes the position of the jth point, V_j is the associated volume, and f_j the value of the field at the respective point. Another advantage of the method is that in Eq. (2) the differential operators are applied to the kernel function, but not to f_j. The first order derivatives at $\mathbf{r}_i$ are

$$(\partial_x f)_i^{SPH} = \sum_j f_j \partial_{x,i} W_{ij} V_j \tag{3}$$

$$(\partial_y f)_i^{SPH} = \sum_j f_j \partial_{y,i} W_{ij} V_j,$$

where $f_j = f(\mathbf{r}_j)$, $V_j = m_j/\rho_j$ and W_{ij} the kernel function at $r_{ij} = |\mathbf{r}_i - \mathbf{r}_j|$.

Because $\sum_j \partial_{\alpha\beta,i} W_{ij} V_j$ (where α and β can be either component x or y) is zero only for the limit $h \to 0$ (when the kernel function W becomes the Dirac δ-function) [8], we use the following form for estimating the second order derivatives:

$$(\partial_{xx} f)_i^{SPH} = \sum_j (f_j - f_i) \partial_{xx,i} W_{ij} \tag{4}$$

$$(\partial_{xy} f)_i^{SPH} = \sum_j (f_j - f_i) \partial_{xy,i} W_{ij}$$

$$(\partial_{yy} f)_i^{SPH} = \sum_j (f_j - f_i) \partial_{yy,i} W_{ij},$$

2.2 The Corrected Variants, FPM and MSPH

FPM and MSPH are derived similarly, the only difference between them is their order. It is sufficient to present the derivation of MSPH, because the FPM can be obtained from the same equations neglecting the higher order terms. The MSPH [1,3,2] is derived from the Taylor expansion of the field f up to the second order

$$f_j = (f)_i + (\partial_x f)_i x_{ji} + (\partial_y f)_i y_{ji} + \frac{1}{2}(\partial_{xx} f)_i x_{ji}^2 + (\partial_{xy} f)_i x_{ji} y_{ji} + \frac{1}{2}(\partial_{yy} f)_i y_{ji}^2 + \ldots \tag{5}$$

Next a linear system with six unknowns is obtained by multiplying the right and left terms by $W_{ij} V_j$, $\partial_{x,i} W_{ij} V_j, \partial_{y,i} W_{ij} V_j$, , $\partial_{xx,i} W_{ij} V_j, \partial_{xy,i} W_{ij} V_j$, or $\partial_{yy,i} W_{ij} V_j$n and performing the summation over j. Formally, the solution is:

$$\begin{bmatrix} (f)_i^{MSPH} \\ (\partial_x f)_i^{MSPH} \\ (\partial_{xx} f)_i^{MSPH} \\ (\partial_{xy} f)_i^{MSPH} \\ (\partial_{yy} f)_i^{MSPH} \end{bmatrix} = M^{-1} \sum_j \begin{bmatrix} f_j W_{ij} V_j \\ f_j \partial_{x,i} W_{ij} V_j \\ f_j \partial_{y,i} W_{ij} V_j \\ f_j \partial_{xx,i} W_{ij} V_j \\ f_j \partial_{xy,i} W_{ij} V_j \\ f_j \partial_{yy,i} W_{ij} V_j \end{bmatrix} \tag{6}$$

In practice, this is equivalent to replacing the kernel function and its derivatives with the effective corrected kernel

$$\begin{bmatrix} (W_{ij})^{MSPH} \\ (\partial_{x,i} W_{ij})^{MSPH} \\ (\partial_{y,i} W_{ij})^{MSPH} \\ (\partial_{xx,i} W_{ij})^{MSPH} \\ (\partial_{xy,i} W_{ij})^{MSPH} \\ (\partial_{yy,i} W_{ij})^{MSPH} \end{bmatrix} = M^{-1} \begin{bmatrix} W_{ij} \\ \partial_{x,i} W_{ij} \\ \partial_{y,i} W_{ij} \\ \partial_{xx,i} W_{ij} \\ \partial_{xy,i} W_{ij} \\ \partial_{yy,i} W_{ij} \end{bmatrix} \tag{7}$$

With the correction matrix

$$M = \sum_j \begin{bmatrix} 1 & x_{ji} & y_{ji} & \frac{1}{2}x_{ji}^2 & x_{ji}y_{ji} & \frac{1}{2}y_{ji}^2 \\ \partial_{x,i} & x_{ji}\partial_{x,i} & y_{ji}\partial_{x,i} & \frac{1}{2}x_{ji}^2\partial_{x,i} & x_{ji}y_{ji}\partial_{x,i} & \frac{1}{2}y_{ji}^2\partial_{x,i} \\ \partial_{y,i} & x_{ji}\partial_{y,i} & y_{ji}\partial_{y,i} & \frac{1}{2}x_{ji}^2\partial_{y,i} & x_{ji}y_{ji}\partial_{y,i} & \frac{1}{2}y_{ji}^2\partial_{y,i} \\ \partial_{xx,i} & x_{ji}\partial_{xx,i} & y_{ji}\partial_{x,i} & \frac{1}{2}x_{ji}^2\partial_{xx,i} & x_{ji}y_{ji}\partial_{xx,i} & \frac{1}{2}y_{ji}^2\partial_{xx,i} \\ \partial_{xy,i} & x_{ji}\partial_{xy,i} & y_{ji}\partial_{xy,i} & \frac{1}{2}x_{ji}^2\partial_{xy,i} & x_{ji}y_{ji}\partial_{xy,i} & \frac{1}{2}y_{ji}^2\partial_{xy,i} \\ \partial_{yy,i} & x_{ji}\partial_{yy,i} & y_{ji}\partial_{yy,i} & \frac{1}{2}x_{ji}^2\partial_{yy,i} & x_{ji}y_{ji}\partial_{yy,i} & \frac{1}{2}y_{ji}^2\partial_{yy,i} \end{bmatrix} W_{ij} V_j \tag{8}$$

The FPM is derived in the same way as the MSPH, but the second order terms in the Taylor expansion (5) and the second order derivatives are not included.

2.3 Decoupled MSPH

An ill conditioned matrix (which happens when there are not enough neighbors or the configuration of the interpolation is extremely disordered) can yield very poor results. In addition to this, Zhang & Liu noted in Ref. [9] that in most cases, the non-diagonal terms of the matrix M are small and a simplified correction can be used to achieve an accuracy similar to that of the FPM. In the new correction we make the approximations

$$M_{i,j} \simeq 0, i \neq j. \tag{9}$$

The corrected values are

$$(f)_i^{DMSPH} = \frac{\sum_j f_j W_{ij} V_j}{\sum_j W_{ij} V_j} \tag{10}$$

$$(\partial_x f)_i^{DMSPH} = \frac{\sum_j f_j \partial_{x,i} W_{ij} V_j}{\sum_j x_{ji} \partial_{x,i} W_{ij} V_j}$$

$$(\partial_y f)_i^{DMSPH} = \frac{\sum_j f_j \partial_{y,i} W_{ij} V_j}{\sum_j y_{ji} \partial_{y,i} W_{ij} V_j}$$

Same in the standard SPH, the following form for estimating the second order derivatives is used

$$(\partial_{xx} f)_i^{DMSPH} = \frac{\sum_j (f_j - f_i) \partial_{xx,i} W_{ij} V_j}{\frac{1}{2} \sum_j x_{ji}^2 \partial_{xx,i} W_{ij} V_j} \tag{11}$$

$$(\partial_{xy} f)_i^{DMSPH} = \frac{\sum_j (f_j - f_i) \partial_{xy,i} W_{ij} V_j}{\sum_j x_{ji} y_{ji} \partial_{xy,i} W_{ij} V_j}$$

$$(\partial_{yy} f)_i^{DMSPH} = \frac{\sum_j (f_j - f_i) \partial_{yy,i} W_{ij} V_j}{\frac{1}{2} \sum_j y_{ji}^2 \partial_{yy,i} W_{ij} V_j}$$

This method is very easy to implement in both 2D and 3D.

2.4 The Semi-Decoupled MSPH

The formulas presented in the previous section have the advantage of being simple, however the DFPM does not really have C^0, C^1 nor C^2 and effectively it becomes standard SPH with a normalization. As shown in Ref. [7] more than C^0 consistency is needed for the driven solid-gas systems. We start the derivation from the Taylor expansion (5), but multiplying each equation with one of the functions $\tilde{W}_{ij} V_j$, $\partial_{x,i} \tilde{W}_{ij} V_j$, $\partial_{y,i} \tilde{W}_{ij} V_j$, $\partial_{x,i} \left[\frac{\partial_{x,i} \tilde{W}_{ij}}{\sum_j x_{ji} \partial_{x,i} \tilde{W}_{ij} V_j} \right] V_j$, $\partial_{y,i} \left[\frac{\partial_{x,i} \tilde{W}_{ij}}{\sum_j x_{ji} \partial_{x,i} \tilde{W}_{ij} V_j} \right] V_j +$ $\partial_{x,i} \left[\frac{\partial_{y,i} \tilde{W}_{ij}}{\sum_j y_{ji} \partial_{y,i} \tilde{W}_{ij} V_j} \right] V_j$, or $\partial_{y,i} \left[\frac{\partial_{y,i} \tilde{W}_{ij}}{\sum_j y_{ji} \partial_{y,i} \tilde{W}_{ij} V_j} \right] V_j$, with $\tilde{W}_{ij} = W_{ij}/S_i$ and $S_i = \sum_j W_{ij} V_j$. In the semi-decoupled MSPH (SDMSPH) the second order derivatives are

$$(\partial_{xx} f)_i^{SDMSPH} = \sum_j f_j \tilde{\tilde{\partial}}_{xx,i} \tilde{W}_{ij} V_j V_j \tag{12}$$

$$(\partial_{xy} f)_i^{SDMSPH} = \sum_j f_j \tilde{\tilde{\partial}}_{xy,i} \tilde{W}_{ij} V_j V_j$$

$$(\partial_{yy} f)_i^{SDMSPH} = \sum_j f_j \tilde{\tilde{\partial}}_{yy,i} \tilde{W}_{ij} V_j V_j.$$

These are practically the 1D MSPH solutions. The new derivative operators are defined as

$$
\tilde{\tilde{\partial}}_{xx,i} = \frac{\partial_{x,i}\left[\frac{\partial_{x,i}}{\sum_j x_{ji}\partial_{x,i}\tilde{W}_{ij}V_j}\right]}{\frac{1}{2}\sum_j x_{ji}^2\partial_{x,i}\left[\frac{\partial_{x,i}\tilde{W}_{ij}}{\sum_j x_{ji}\partial_{x,i}\tilde{W}_{ij}V_j}\right]V_j}
\tag{13}
$$

$$
\tilde{\tilde{\partial}}_{xy,i} = \frac{\partial_{y,i}\left[\frac{\partial_{x,i}}{\sum_j x_{ji}\partial_{x,i}\tilde{W}_{ij}V_j}\right] + \partial_{x,i}\left[\frac{\partial_{y,i}}{\sum_j y_{ji}\partial_{y,i}\tilde{W}_{ij}}\right]}{\sum_j x_{ji}y_{ji}\left\{\partial_{y,i}\left[\frac{\partial_{x,i}\tilde{W}_{ij}}{\sum_j x_{ji}\partial_{x,i}\tilde{W}_{ij}V_j}\right] + \partial_{x,i}\left[\frac{\partial_{y,i}\tilde{W}_{ij}}{\sum_j y_{ji}\partial_{y,i}\tilde{W}_{ij}V_j}\right]\right\}V_j}
$$

$$
\tilde{\tilde{\partial}}_{yy,i} = \frac{\partial_{y,i}\left[\frac{\partial_{y,i}}{\sum_j y_{ji}\partial_{y,i}\tilde{W}_{ij}V_j}\right]}{\frac{1}{2}\sum_j y_{ji}^2\partial_{y,i}\left[\frac{\partial_{y,i}\tilde{W}_{ij}}{\sum_j y_{ji}\partial_{y,i}\tilde{W}_{ij}V_j}\right]V_j}.
$$

Now the SDMSPH first order derivatives are

$$
(\partial_x f)_i^{SDMSPH} = \sum_j f_j\tilde{\partial}_{x,i}V_j - (\partial_{xx}f)_i^{SDMSPH}\frac{1}{2}\sum_j x_{ji}^2\tilde{\partial}_{x,i}V_j
\tag{14}
$$

$$
(\partial_y f)_i^{SDMSPH} = \sum_j f_j\tilde{\partial}_{y,i}V_j - (\partial_{xx}f)_i^{SDMSPH}\frac{1}{2}\sum_j y_{ji}^2\tilde{\partial}_{y,i}V_j.
$$

The fist order derivative operators defined as:

$$
\tilde{\partial}_{x,i} = \frac{\partial_{x,i}\tilde{W}_{ij}}{\sum_j x_{ji}\partial_{x,i}\tilde{W}_{ij}V_j}
\tag{15}
$$

$$
\tilde{\partial}_{y,i} = \frac{\partial_{y,i}\tilde{W}_{ij}}{\sum_j y_{ji}\partial_{y,i}\tilde{W}_{ij}V_j}
$$

Finally the corrected values of the field are obtained using

$$
(f)_i^{SDMSPH} = \sum_j f_j\tilde{W}_{ij}V_j - (\partial_x f)_i^{SDMSPH}\sum_j x_{ji}\tilde{W}_{ij}V_j - (\partial_y f)_i^{SDMSPH}\sum_j y_{ji}\tilde{W}_{ij}V_j
\tag{16}
$$

$$
- \frac{1}{2}(\partial_{xx}f)_i^{SDMSPH}\sum_j x_{ji}^2\tilde{W}_{ij}V_j - (\partial_{xy}f)_i^{SDMSPH}\sum_j x_{ji}y_{ji}\tilde{W}_{ij}V_j
$$

$$
- \frac{1}{2}(\partial_{yy}f)_i^{SDMSPH}\sum_j y_{ji}^2\tilde{W}_{ij}V_j.
$$

One of the advantage of the SDMPSH is that unlike the DFPM and DMSPH, the second derivative of a constant field is identically zero. In addition the corrected values of a field and its first order derivatives are coupled to the higher order derivatives. Finally the second order derivatives are almost exact when the non-diagonal terms, which we ignored in order to obtain Eq. (12), are small enough.

As shown in Ref. [10] the semi-decoupled forms can be further improved with few additional operations, but with significant improvement in results, by taking into account the non-diagonal terms

$$(\partial_{xx}f)_i^{CSDMSPH} = (\partial_{xx}f)_i^{SDMSPH} - (\partial_y f)_i^{SDMSPH} \sum_j y_{ji}\tilde{\bar{\partial}}_{xx,i}\tilde{W}_{ij}V_j \tag{17}$$

$$- (\partial_{xy}f)_i^{SDMSPH} \sum_j x_{ji}y_{ji}\tilde{\bar{\partial}}_{xx,i}\tilde{W}_{ij}V_j$$

$$- \frac{1}{2}(\partial_{yy}f)_i^{SDMSPH} \sum_j y_{ji}^2\tilde{\bar{\partial}}_{xx,i}\tilde{W}_{ij}V_j$$

$$(\partial_{xy}f)_i^{CSDMSPH} = (\partial_{xy}f)_i^{SDMSPH} - (\partial_x f)_i^{SDMSPH} \sum_j x_{ji}\tilde{\bar{\partial}}_{xy,i}\tilde{W}_{ij}V_j$$

$$- (\partial_y f)_i^{SDMSPH} \sum_j y_{ji}\tilde{\bar{\partial}}_{xy,i}\tilde{W}_{ij}V_j - \frac{1}{2}(\partial_{xx}f)_i^{SDMSPH} \sum_j x_{ji}^2\tilde{\bar{\partial}}_{xy,i}\tilde{W}_{ij}V_j$$

$$- \frac{1}{2}(\partial_{yy}f)_i^{SDMSPH} \sum_j y_{ji}^2\tilde{\bar{\partial}}_{xy,i}\tilde{W}_{ij}V_j$$

$$(\partial_{yy}f)_i^{CSDMSPH} = (\partial_{yy}f)_i^{SDMSPH} - (\partial_x f)_i^{SDMSPH} \sum_j x_{ji}\tilde{\bar{\partial}}_{yy,i}\tilde{W}_{ij}V_j$$

$$- \frac{1}{2}(\partial_{xx}f)_i^{SDMSPH} \sum_j x_{ji}^2\tilde{\bar{\partial}}_{yy,i}\tilde{W}_{ij}V_j$$

$$- (\partial_{xy}f)_i^{SDMSPH} \sum_j x_{ji}y_{ji}\tilde{\bar{\partial}}_{xx,i}\tilde{W}_{ij}V_j.$$

Similarly, for the first order derivatives we get

$$(\partial_x f)_i^{CSDMSPH} = (\partial_x f)_i^{SDMSPH} - (\partial_y f)_i^{SDMSPH} \sum_j y_{ji}\tilde{\partial}_{x,i}\tilde{W}_{ij}V_j \tag{18}$$

$$- (\partial_{xy}f)_i^{SDMSPH} \sum_j x_{ji}y_{ji}\tilde{\partial}_{x,i}\tilde{W}_{ij}V_j$$

$$- \frac{1}{2}(\partial_{yy}f)_i^{SDMSPH} \sum_j y_{ji}^2\tilde{\partial}_{x,i}\tilde{W}_{ij}V_j$$

$$(\partial_y f)_i^{CSDMSPH} = (\partial_y f)_i^{SDMSPH} - (\partial_x f)_i^{SDMSPH} \sum_j x_{ji}\tilde{\partial}_{y,i}\tilde{W}_{ij}V_j$$

$$- \frac{1}{2}(\partial_{xx}f)_i^{SDMSPH} \sum_j x_{ji}^2\tilde{\partial}_{y,i}\tilde{W}_{ij}V_j$$

$$- (\partial_{xy}f)_i^{SDMSPH} \sum_j x_{ji}y_{ji}\tilde{\partial}_{y,i}\tilde{W}_{ij}V_j.$$

The corrected values of the field are obtained using Eq. (16), but with the CSDMSPH values for the first and second-order derivatives.

3 Error estimates for the gradients for the different methods

In general we are interested in a method that allows the accurate estimation of second order derivatives that appears for example as the temperature laplacian in the heat equation, and in the divergence of velocity and pressure in the Navier-Stokes equation [12,13]. The accuracy of our approximations is evaluated by computing the derivatives of several analytic functions. We also test the performance of the various methods for the flow around a cylinder. [7].

3.1 Errors estimates of analytic functions close to solid boundaries

We are mainly interested in the errors of the methods close to a circular boundary because in a driven flow the wall particles remain fixed, while the fluid particles move with a average velocity close to the inlet velocity. This can result in less ordered configurations which require kernel correction for the calculations of the gradients. For the evaluation of the analytic functions, we arranged the SPH particles in a triangular lattice (Fig. 1) with distance $\Delta x = (3/4)h$ between them. In this configuration a circular solid obstacle with diameter $D = 30h$ was placed in the middle of the simulation box, as in the previous work [7]. Inside the solid a layer of virtual particles of thickness $3h$ was created, which complete the kernel support for the SPH particles close to the boundary. The volumes are assigned so that a zero gradient condition is imposed normal to the surface and various degrees of disorder are created near the solid boundary. In Fig. 1 some of the SPH fluid have less neighbors or more than in the ordered areas. We are particularly interested in what appears in the early stages of the simulations of a flow around a fixed or moving obstacle. While, in general, additional reordering techniques can provide a better configuration of the SPH particles, we believe that testing the various kernel corrections on this configuration is sufficient for our applications. For the kernel function we use the quintic B-spline function [14]. A detailed analysis of the different kernels done in Ref. [15] indicated that this kernel has the best accuracy. The kernel $W(r;h)$ is defined by

$$W(r,h) = \alpha_D \begin{cases} \left(3 - \frac{r}{h}\right)^5 - 6\left(2 - \frac{r}{h}\right)^5 + 15\left(1 - \frac{r}{h}\right)^5 & r \le h \\ \left(3 - \frac{r}{h}\right)^5 - 6\left(2 - \frac{r}{h}\right)^5 & h \le r < 2h \\ \left(3 - \frac{r}{h}\right)^5 & 2h \le r < 3h \end{cases} \tag{19}$$

with α_D a normalization constant.
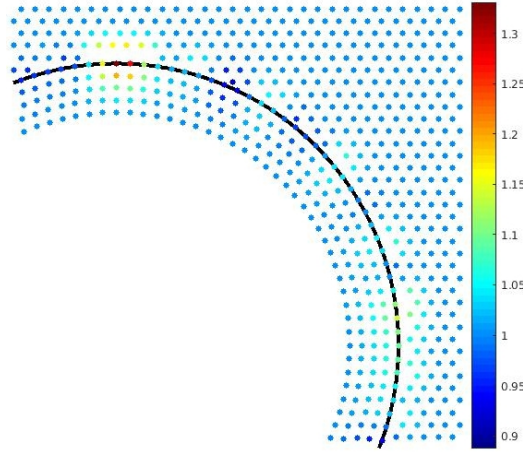
Fig. 1 The SPH interpolation points used to evaluate the gradients of the different functions. The color indicates the values of the volumes $V_j = m_j/\rho_j$. The black line gives the position of the solid boundary.

We analyzed three analytic functions, $1 - (x/2 - 1/4) \cdot (y/2 - 1/4)$, $1 - (x/2 - 1/4)^2 \cdot (y/2 - 1/4)^2$, and $\exp[-(x/2 - 1/4)^2 \cdot (y/2 - 1/4)^2]$.

The results are shown in Figures 2-7. Depending on the function, the SDMPSH and CSDMPSH can give up to one order of magnitude smaller errors. In addition we note that the SPH and
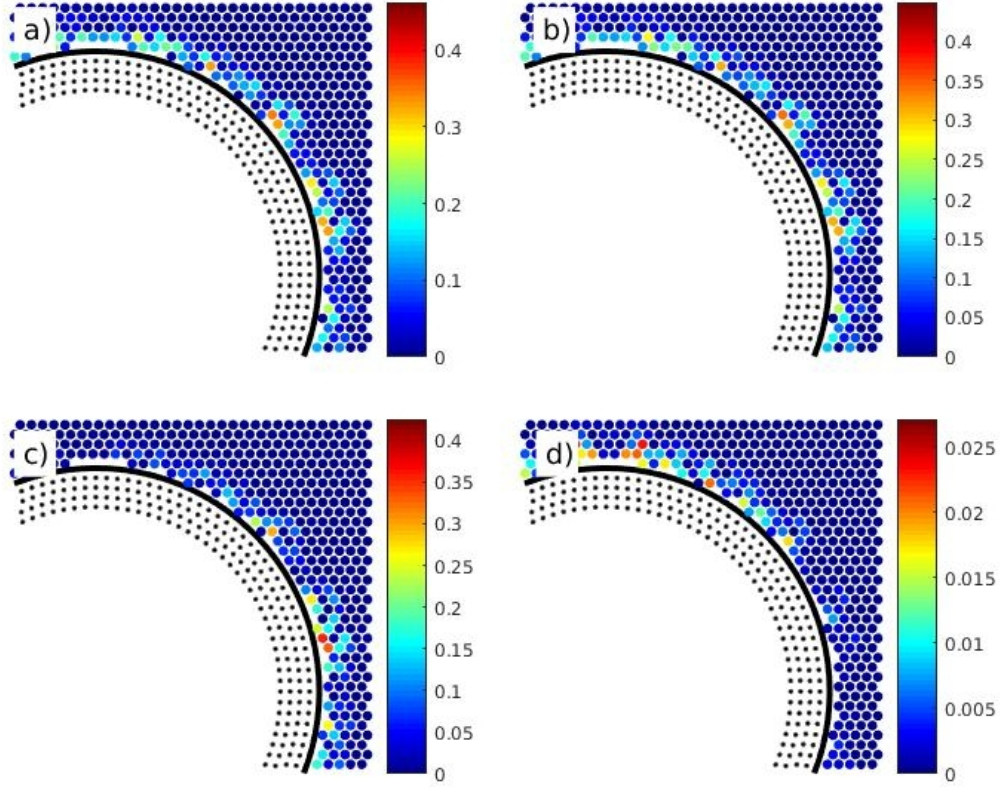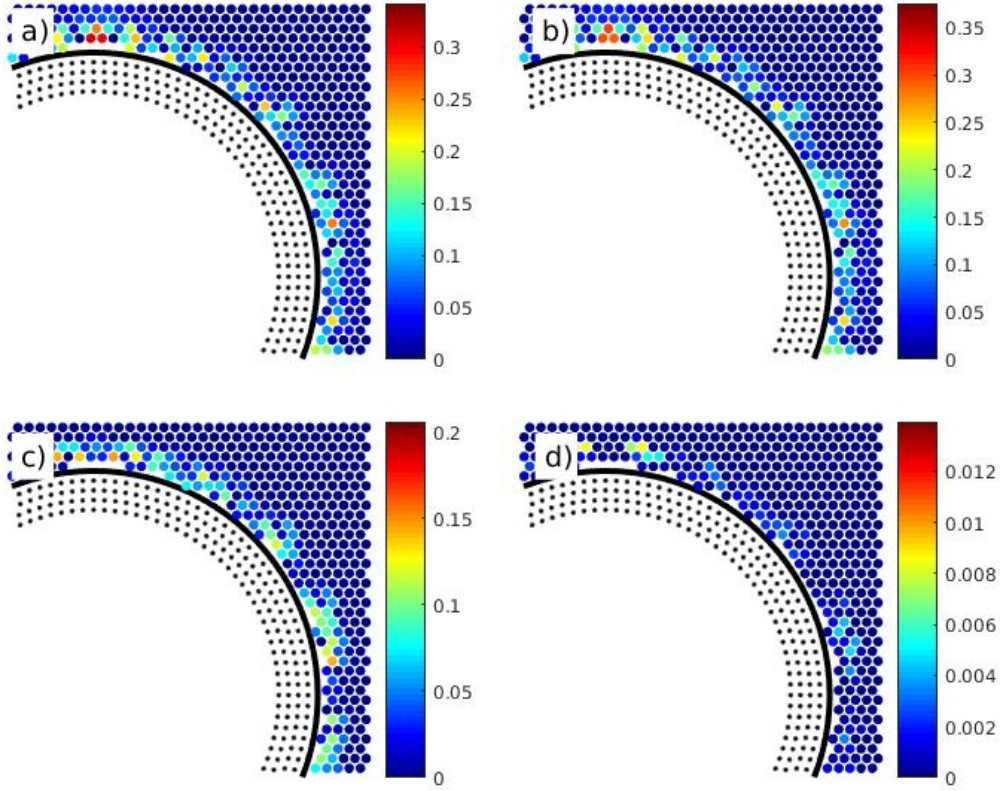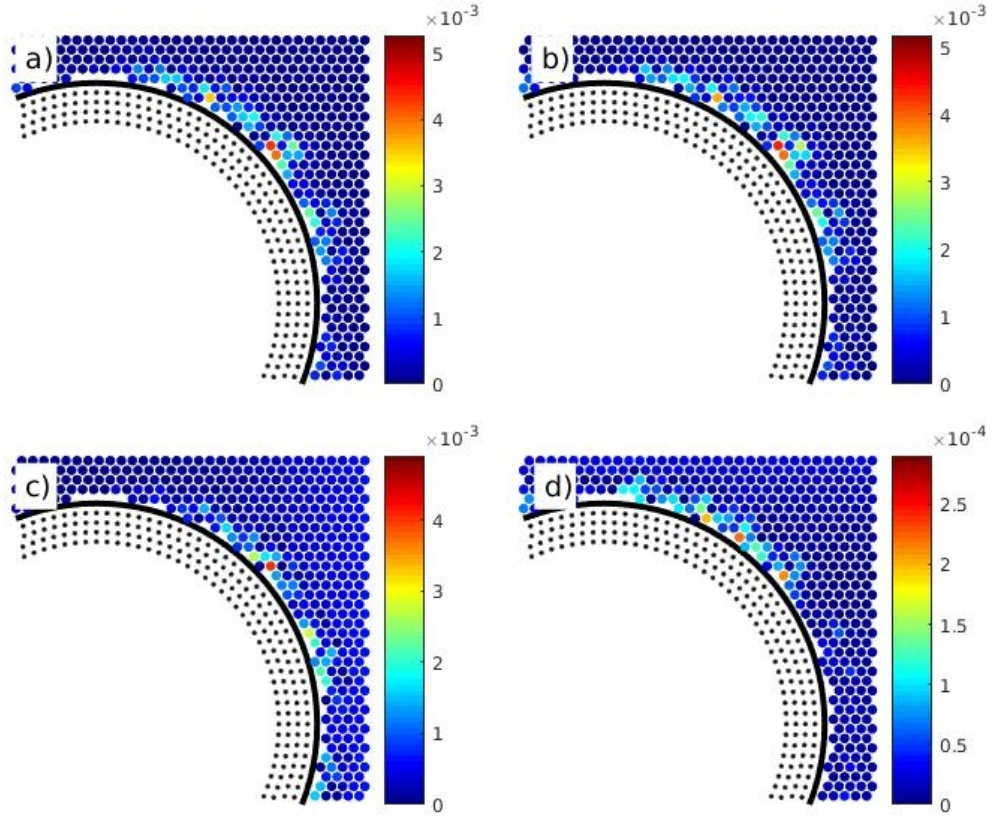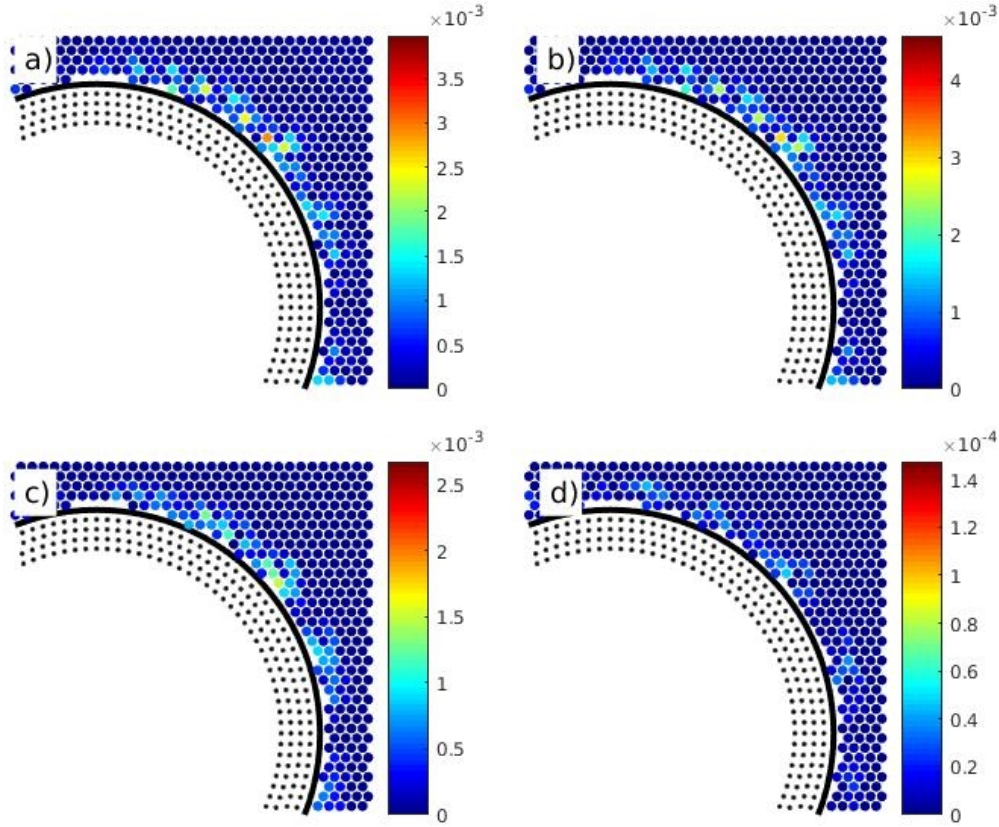
Fig. 2 Error evaluation when computing the second order x-derivative of the function $1 - (x/2 - 1/4) \cdot (y/2 - 1/4)$ as given by: a) standard SPH, b) decoupled MSPH, c) semi-decoupled MSPH, and d) corrected semi-decoupled MSPH.

DMPSH are more sensitive to the particle configurations. The evaluated derivatives begin to present deviations as soon as the particle is closer than $3h$ to the solid surface.

3.2 Comparison of different methods for flow around a cylinder

Lastly, we tested the different approximations for a driven flow around a fixed circular obstacle using the same method as [7]. For each method, everything was kept the same as in FPM except for the gradients used in the equations of motion. While the SPH model of the Navier-Stokes equations can be written in a form that contains only first order derivatives, we expect that a higher order consistency will give a better accuracy to the lower derivatives as well. We present below the drag coefficients C_d for two regimes, $Re = 40$ and $Re = 100$. We present also the results for the FPM as shown in [7]. These cases are very useful to test the accuracy of computing the gradients. The results are summarized in Tables 1-4

When comparing the different methods we see that the CSDMSPH achieves convergence faster than the other methods. Plotting the drag coefficients as a function of the ratio $D/\Delta x$ with $\Delta x = 4h/3$ (Figures 8 and 9), we note that the CSDMSPH achieves convergence for $D/\Delta x = 25$. While the difference is small, the other methods require $D/\Delta x > 30$ to converge, for both the two Re numbers investigated.
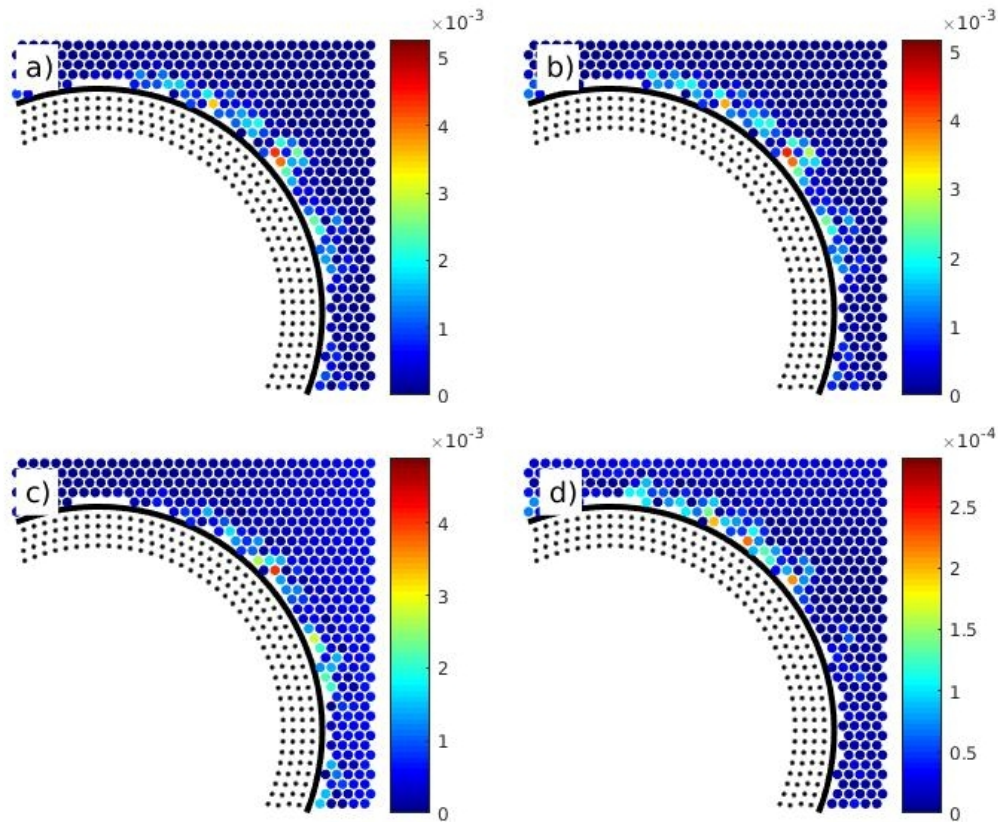
Fig. 3 Error evaluation when computing the second order xy-derivative of the function $1-(x/2-1/4)\cdot(y/2-1/4)$ as given by: a) standard SPH, b) decoupled MSPH, c) semi-decoupled MSPH, and d) corrected semi-decoupled MSPH.

Table 1 The drag coefficients for $Re = 40$ for the different methods as a function of the resolution keeping $h/\Delta x = 1.33$.

$D/\Delta x$	SDMSPH	CSDMSPH $h/\Delta x = 1$	CSDMSPH	FPM
10	1.6163 ± 0.0149	1.6161 ± 0.0220	1.6400 ± 0.0095	1.6024 ± 0.0075
15	1.6572 ± 0.0058	1.6583 ± 0.0153	1.6640 ± 0.0056	1.6440 ± 0.0054
20	1.6543 ± 0.0028	1.6638 ± 0.0114	1.6600 ± 0.0024	1.6531 ± 0.0029
25	1.6633 ± 0.0035	1.6650 ± 0.0088	1.6643 ± 0.0031	1.6588 ± 0.0035
30	1.6632 ± 0.0030	1.6600 ± 0.0083	1.6643 ± 0.0028	1.6584 ± 0.0031

Table 2 The drag coefficients for $Re = 100$ for the different methods as a function of the resolution keeping $h/\Delta x = 1.33$.

$D/\Delta x$	SDMSPH	CSDMSPH $h/\Delta x = 1$	CSDMSPH	FPM
10	1.1586 ± 0.0540	1.2080 ± 0.0350	1.1604 ± 0.0232	1.1151 ± 0.0160
15	1.3282 ± 0.0200	1.3685 ± 0.0210	1.3442 ± 0.0092	1.3252 ± 0.0093
20	1.3864 ± 0.0122	1.4031 ± 0.0134	1.3960 ± 0.0075	1.4013 ± 0.0080
25	1.4104 ± 0.0091	1.4141 ± 0.0121	1.4140 ± 0.0077	1.4158 ± 0.0076
30	1.4130 ± 0.0090	1.4166 ± 0.0115	1.4126 ± 0.0077	1.4129 ± 0.0080

4 Conclusions

Here we presented higher order corrections to impose C^2. The direct calculations of second order derivatives by CSDMSPH give smaller errors than other methods in the disordered regions. The

Fig. 4 Error evaluation when computing the second order x-derivative of the function $1-(x/2-1/4)^2 \cdot (y/2-1/4)^2$ as given by: a) standard SPH, b) decoupled MSPH, c) semi-decoupled MSPH, and d) corrected semi-decoupled MSPH.

Table 3 The lift coefficients for $Re = 100$ for the different methods as a function of the resolution keeping $h/\Delta x = 1.33$.

$D/\Delta x$	SDMSPH	CSDMSPH $h/\Delta x = 1$	CSDMSPH	FPM
10	± 0.4380	± 0.3547	± 0.2452	± 0.2072
15	± 0.3636	± 0.3877	± 0.3357	± 0.2962
20	± 0.4075	± 0.4219	± 0.3617	± 0.3738
25	± 0.3747	± 0.3830	± 0.3694	± 0.3700
30	± 0.3807	± 0.3982	± 0.3644	± 0.3655

Table 4 The Strouhal number for $Re = 100$ for the different methods as a function of the resolution keeping $h/\Delta x = 1.33$.

$D/\Delta x$	SDMSPH	CSDMSPH $h/\Delta x = 1$	CSDMSPH	FPM
10	0.1805	0.1751	0.1770	0.1744
15	0.1742	0.1742	0.1751	0.1758
20	0.1733	0.1751	0.1736	0.1738
25	0.1740	0.1752	0.1736	0.1735
30	0.1731	0.1747	0.1728	0.1736

corrections are useful in applications where the laplacian or bilaplacians are present in coupled equations. A surprising effect is the higher order accuracy results for the flow around a solid cylinder
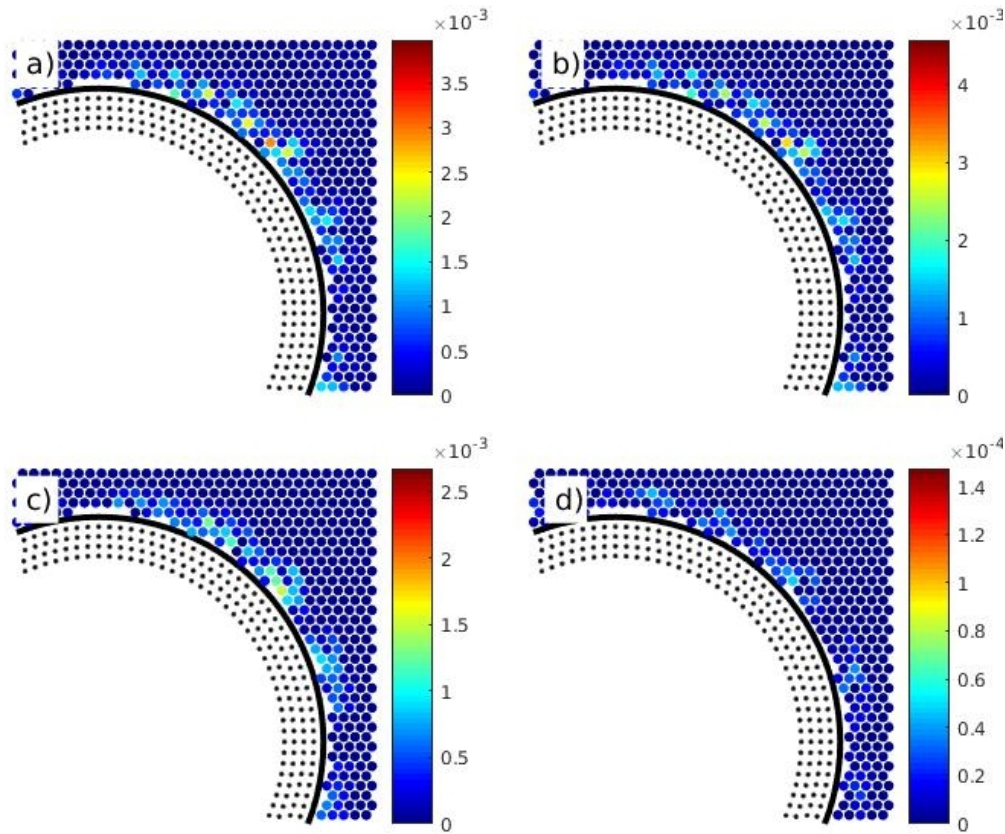
Fig. 5 Error evaluation when computing the second order xy-derivative of the function $1 - (x/2 - 1/4)^2 \cdot (y/2 - 1/4)^2$ as given by: a) standard SPH, b) decoupled MSPH, c) semi-decoupled MSPH, and d) corrected semi-decoupled MSPH.

where the CSDMSPH proved to give higher accuracy than the FPM and it obtains convergence of the drag coefficients at lower values of $D/\Delta x$ for both cases studied, $Re = 40$ and $Re = 100$. In addition we tested the effect of changing the ratio $h/\Delta x$ while keeping $D/\Delta x$. Aside to having numerical stability, the drag coefficients had fairly good values. This is explain by the fact that the SPH configurations are fairly regularly due to the particle shifting technique [16,17] which imposes the fluid particles to maintain distances close to the initial distance Δx. Unlike the case of standard δ-SPH [15] changing the ratio $h/\Delta x$ resulted in stable simulations with results very close to the FPM, but with higher standard errors in measuring the drag coefficients. This is important because decreasing the ratio $h/\Delta x$ results in decreasing the numbers of neighbors which can significantly accelerate the speed of simulation depending on the computer platform used.

Conflict of interest

The authors declare that they have no conflict of interest.

Fig. 6 Error evaluation when computing the second order x-derivative of the function $\exp[-(x/2 - 1/4)^2 \cdot (y/2 - 1/4)^2]$ as given by: a) standard SPH, b) decoupled MSPH, c) semi-decoupled MSPH, and d) corrected semi-decoupled MSPH.

References

1. G.M. Zhang, R.C. Batra, Computational Mechanics **34**(2), 137 (2004). DOI 10.1007/s00466-004-0561-5. URL https://doi.org/10.1007/s00466-004-0561-5
2. M. Liu, G. Liu, Applied Numerical Mathematics **56**(1), 19 (2006). DOI https://doi.org/10.1016/j.apnum.2005.02.012. URL http://www.sciencedirect.com/science/article/pii/S0168927405000565
3. M. Liu, W. Xie, G. Liu, Applied Mathematical Modelling **29**(12), 1252 (2005). DOI https://doi.org/10.1016/j.apm.2005.05.003. URL http://www.sciencedirect.com/science/article/pii/S0307904X0500096X
4. R.A. Gingold, J.J. Monaghan, Monthly Notices of the Royal Astronomical Society **181**, 375 (1977). DOI 10.1093/mnras/181.3.375
5. L.B. Lucy, The Astronomical Journal **82**(12), 1013 (1977). DOI 10.1086/112164. URL https://doi.org/10.1086/112164
6. S. Marrone, M. Antuono, A. Colagrossi, G. Colicchio, D.L. Touzé, G. Graziani, Computer Methods in Applied Mechanics and Engineering **200**(13), 1526 (2011). DOI https://doi.org/10.1016/j.cma.2010.12.016. URL http://www.sciencedirect.com/science/article/pii/S0045782510003725
7. C.V. Achim, R.E. Rozas, F. Concha, P.G. Toledo, Comparison between standard, zeroth and first order consistent smoothed particle hydrodynamics for flow around a cylinder. (2019). Submitted to International Journal of Computational Particle Mechanics
8. M.B. Liu, G.R. Liu, Archives of Computational Methods in Engineering **17**(1), 25 (2010). DOI 10.1007/s11831-010-9040-7. URL https://doi.org/10.1007/s11831-010-9040-7
9. Z.L. Zhang, M.B. Liu, Applied Mathematical Modelling **60**, 606 (2018). DOI https://doi.org/10.1016/j.apm.2018.03.043. URL http://www.sciencedirect.com/science/article/pii/S0307904X18301677
10. C.V. Achim, R.E. Rozas, P.G. Toledo, Semi-decoupled first-order correction for smoothed particle hydrodynamics (2019). Submitted to Applied Mathematical Modelling

Fig. 7 Error evaluation when computing the second order xy-derivative of the function $\exp[-(x/2 - 1/4)^2 \cdot (y/2 - 1/4)^2]$ as given by: a) standard SPH, b) decoupled MSPH, c) semi-decoupled MSPH, and d) corrected semi-decoupled MSPH.

11. M. Kelager. Lagrangian fluid dynamics using smoothed particle hydrodynamics. Online project report, Department of Computer Science, University of Copenhagen Universitetsparken, 1 DK-2100 Copenhagen, Denmark (2006). Micky@kelager.dk

12. J.J. Monaghan, Annual Review of Astronomy and Astrophysics **30**(1), 543 (1992). DOI 10.1146/annurev.aa. 30.090192.002551. URL https://doi.org/10.1146/annurev.aa.30.090192.002551

13. J.J. Monaghan, Reports on Progress in Physics **68**(8), 1703 (2005). DOI 10.1088/0034-4885/68/8/r01. URL https://doi.org/10.1088%2F0034-4885%2F68%2F8%2Fr01

14. J.P. Morris, P.J. Fox, Y. Zhu, Journal of Computational Physics **136**(1), 214 (1997). DOI https://doi.org/10.1006/jcph.1997.5776. URL http://www.sciencedirect.com/science/article/pii/S0021999197957764

15. M.G. Korzani, S.A. Galindo-Torres, A. Scheuermann, D.J. Williams, Water Science and Engineering **10**(2), 143 (2017). DOI https://doi.org/10.1016/j.wse.2017.06.001. URL http://www.sciencedirect.com/science/article/pii/S167423701730056X

16. R. Xu, P. Stansby, D. Laurence, Journal of Computational Physics **228**(18), 6703 (2009). DOI https://doi.org/10.1016/j.jcp.2009.05.032. URL http://www.sciencedirect.com/science/article/pii/S0021999109002885

17. C. Huang, D.H. Zhang, Y.X. Shi, Y.L. Si, B. Huang, International Journal for Numerical Methods in Engineering **113**(2), 179 (2018). DOI 10.1002/nme.5608. URL https://onlinelibrary.wiley.com/doi/abs/10.1002/nme.5608
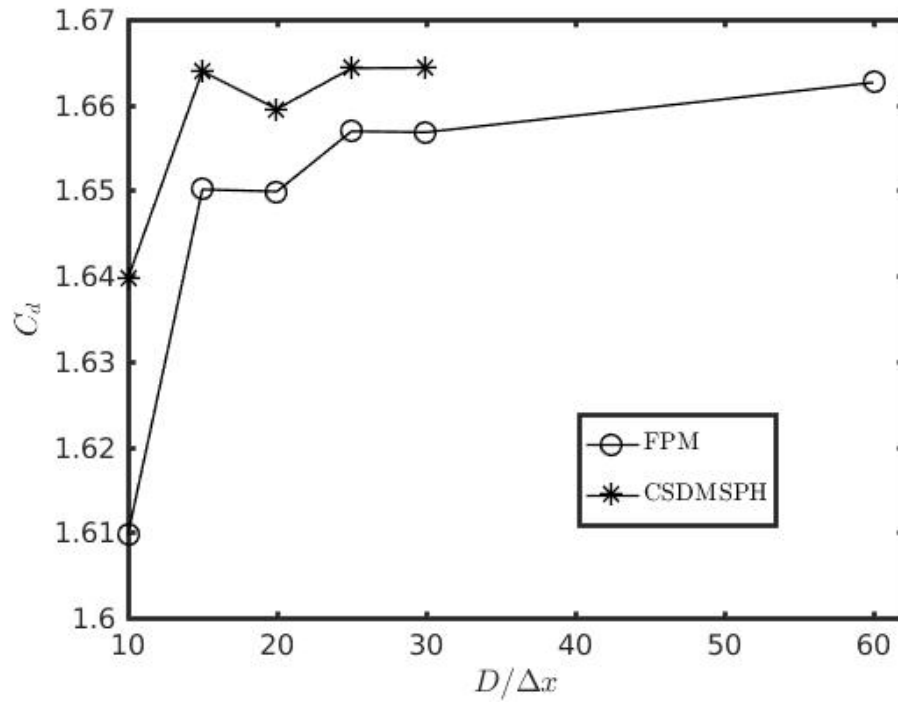
Fig. 8 The drag coefficient C_d as a function of the ratio between the particle diameter D and initial particle distance Δx for FPM ($-\circ$) and CSDMSPH ($-*$), $Re = 40$. The CSDMSPH reaches the saturated value of 1.6640 for $D/\Delta x = 15$. The ratio is significantly lower than in the case of FPM.
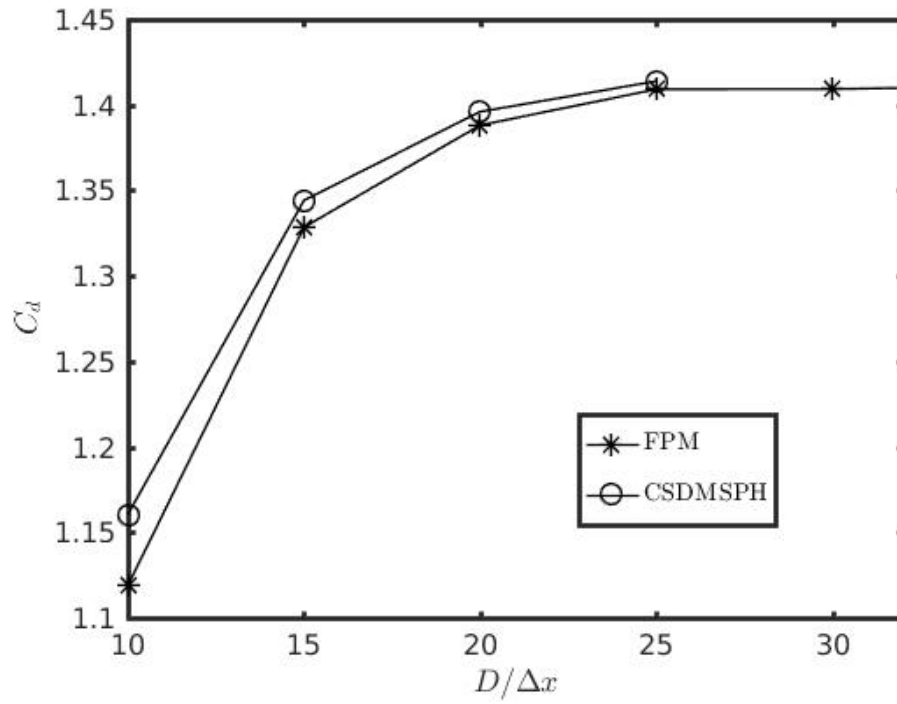
Fig. 9 The drag coefficient C_d as a function of the ratio between the particle diameter D and initial particle distance Δx for FPM ($-\circ$) and CSDMSPH ($-*$), $Re = 100$. The CSDMSPH reaches the saturated value of 1.414 for $D/\Delta x = 25$, very similar to the FPM, however for the lower resolution the values of the drag coefficient are closer to the saturated value than values obtained with FPM.

Simulation of Fluid Structure Interactions by using High Order FEM and SPH

Sebastian Koch[*], **Sascha Duczek**[†], **Fabian Duvigneau**[*] **and Elmar Woschke**[*]

[*] Institute of Mechanics
Otto von Guericke University Magdeburg
Universitätsplatz 2, 39106 Magdeburg, Germany
e-mail: sebastian.koch@ovgu.de, web page: www.ifme.ovgu.de/

[†] School of Civil and Environmental Engineering
University of New South Wales, Sydney

ABSTRACT

The investigation of fluid structure interactions is crucial in many areas of science and technology. This study presents a robust methodology for studying fluid structure interactions, which is characterized by high convergence behavior and is insensitive to distortion and stiffening effects. Therefore, the Smoothed Particle Hyodynamicy is coupled with the high order FEM. After various coupling methods for linear and quadratic elements from the literature have been described, a variant with higher-value approach functions is implemented. The two methods can be meshed independend without loss of accuracy. After successful validation, it is shown that only a few finite elements are necessary to obtain a convergent solution. The presented method is promising especially for thin-walled structures where significantly fewer degrees of freedom are required than for linear elements.

1 Introduction

In many fields of science and engineering, we know that the interaction of fluids with structures has an important effect on the behavior of the overall system. For this reason, effective and robust methods for describing these interactions have been the subject of intensive research activities throughout the last decades. Figure 1 shows three typical applications in which an accurate description of the Fluid Structure Interaction (FSI) is essential for capturing the dynamics of the system. A section of an automatic fluid ball balancing unit of a centrifuge is depicted in Figure 1a. Among other things, the ball position depends on the flow conditions and thus influences the vibration behavior of the system [1]. In Figure 1b components of a turbocharger system such as shaft, turbine and compressor are shown. Additionally, the pressure distribution in the floating ring bearings resulting from the operating condition are indicated. It should be clear that dynamical response of a turbocharger can only be described in a meaningful way by taking the hydrodynamics in the bearings into account [2]. As a third example, in which the consideration of FSI is essential, Figure 1c illustrates the sound radiation caused by the structural vibrations of an engine block. Here, the surrounding fluid (air) has to be considered for the simulation [3].

For the numerical investigation of FSI, various numerical procedures are available and their effectiveness depends on the specific characteristics of the problems that is investigated. An accurate description of the effect induced by the interaction provides an opportunity to estimate the performance of new products already in an early stage of the product development cycle. Thus, the design can be enhanced in order to reach project specific goals. In addition, expensive prototypes are only required for the final testing as well as for validation purposes. Due to the importance of considering FSI in several applications, the overarching goal of this contribution is to develop a robust numerical method which features high rates of convergence.

In this contribution the solid (deformable) structure is described using the finite element method (FEM) which is the dominant method for solving problems in structural dynamics. In order to improve this approach a special focus is placed on using high-order FE shape functions, making this numerical method

insensitive to locking effects and element distortion [5]. An additional advantage are high possibly exponential rates of convergence [6].

The liquid phase is described using the smoothed-particle hydrodynamics (SPH) method, which is a particle-based, meshless Lagrangian method [17]. Possible areas of application are multiphase flows, moving interfaces and problems with large changes in the fluid area. A coupling between SPH and FEM has been successfully realized with linear [7–9] or quadratic [10] FEs and is well-suited for the description of fluid structural interactions. The novelty of our approach lies in the coupling of SPH to high order FEs which results in advantages with respect to locking effects and element distortion being of interest when thin-walled structures are investigated.

The performance of the proposed methodology will be evaluated based on a simple academic benchmark test. As mentioned before due to the coupling of high order FEM and SPH the influence of a fluid phase on the vibrational behavior of a thin walled structure such as an oil pan can be straightforwardly investigated. By using the high order FEM, the thin-walled structures can be described effectively, since these elements are robust against distortion (large aspect ratios). Here, it is observed that the fluid has a significant effect on the dynamic behavior of the structure [3]. This has also a notable effect on the noise emission and is, therefore, of utmost importance for the acoustic properties of the structure.

2 High order finite element method

The basic idea of the FEM is the division of the considered domain in smaller sub-domains, so-called finite elements. The exact solution of the mathematical problem is often approximated by simple polynomial ansatz functions, which are defined only within a finite element. In order to obtain a convergent solution, a distinction is frequently made between the h-, p- and hp- versions of the FEM [11, 12]. In the h- version of the FEM, which is implemented in all commercial FE programs, convergence is achieved through the refinement of the mesh. A mesh refinement can be conducted both globally and locally, i.e. the element dimension h is reduced until a convergent solution is reached ($h \rightarrow 0$). In the case of the p version of the FEM, the element dimensions are kept constant and the polynomial degree p is successively increased. Commercial FE programs usually have maximally quadratic elements ($p \leq 2$). A combination of the two presented methods leads to the hp-FEM which ensures exponential convergence even for singular problems.

In general, it can be stated that higher-order ansatz functions are to be favored, since higher convergence rates (possibly even exponential ones) can be achieved. An additional advantage is their robust behavior with respect to locking phenomena and element distortions. As a result, highly accurate results can be achieved even with highly distorted elements [6]. Figure 2 illustrates the benefits of higher order ansatz functions in terms of improved convergence rates. The error is plotted in the energy norm over the number of degrees of freedom of the system in a log-log diagram. For problems that exhibit a smooth solution, the convergence curve for the p-FEM follows an exponential curve, while the h-FEM shows

(a) Ball balancing unit [1]	(b) Turbocharger [4]	(c) Sound radiation [3]
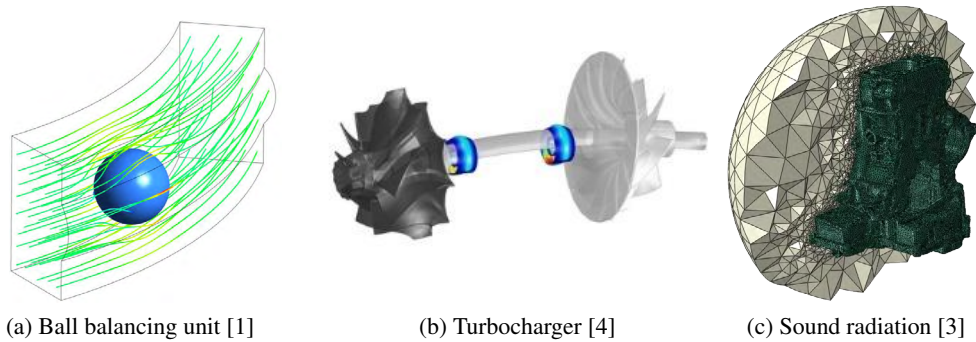
Figure 1: Typical problems with FSI.
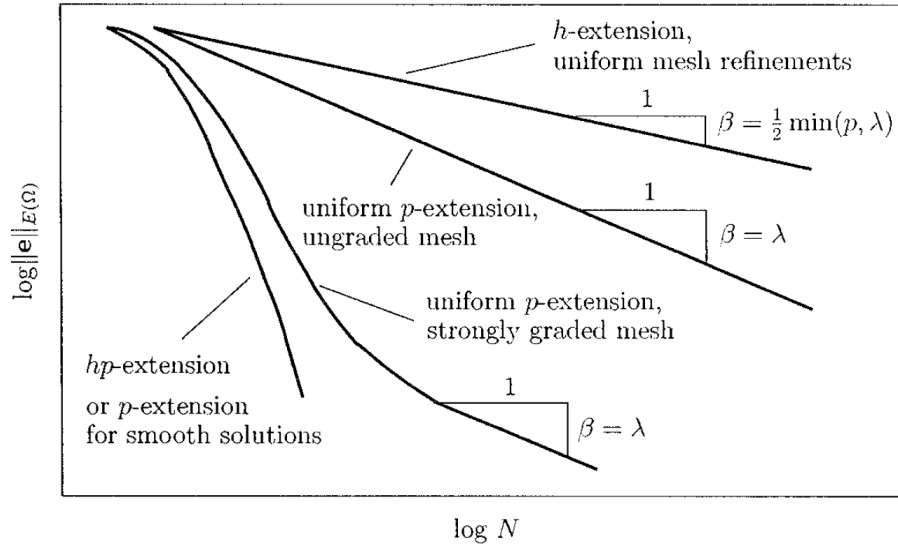
Figure 2: Convergence rates of the *h*-, *p*- and *hp*-Version FEM for a two dimensional linear problem with singularities [6].

only algebraic convergence. Even for problems involving singularities, the convergence rate of the *p*-version of the FEM is at least twice than of the *h*-FEM. If the *h*-refinement is suitably combined with the *p*-adaptation, an exponential convergence can be achieved even in the case of problems with singular locations. Therefore, the application of higher-order shape functions ($p \geq 3$) is recommended in many cases.

3 Smoothed-particle hydrodynamics

SPH is a numerical method in which the bodies and fluids in the solution area are approximated by a set of particles. In addition to position and velocity, these particles are associated with additional information such as mass, pressure and temperature of the approximated amount of material. SPH is a Lagrangian method and thus the particles move together with the approximated material. The method was presented by Lucy [13] and Gingold & Monaghan [14] for astrophysical investigations and is nowadays widely used for fluid dynamics [15, 16]. The fundamental idea is based on the integral approximation of a quantity *A* of the fluid particle *i* under consideration of the neighboring particles *j*

$$A_i(r) = \int A(r) \, W(r - r_j, h) \, dr_j, \tag{1}$$

where *W* is the kernel function, *h* the kernel length, *r* the location and dr_j a differential volume element. This approximation is exact if the delta function is chosen for the kernel. Hence, the integral given in Eq. (1) can be approximated by a summation over all particles *n* within the influence area

$$A_i(r) = \sum_{j=1}^{n} m_j \frac{A_j}{\rho_j} \, W(r - r_j, h_j). \tag{2}$$

A typical set-up of SPH simulations is sketched in Figure 3, where a particle *i* (red), its neighbor particles (blue), the influence area, which is a multiple of the kernel length *h* (depending on the kernel function) and the kernel function are depicted. The function value indicates the influence of a neighboring particle exerts on the central particle.

An advantage of SPH is that the path of a particle can be traced exactly. In this way, mixing and boundary layers can be effectively described. The treatment of different materials is very simple by introducing different particle properties and the interactions can be implemented in a straightforward fashion. Another advantage is that only domains that are filled with the material (fluid) need to be discretized and
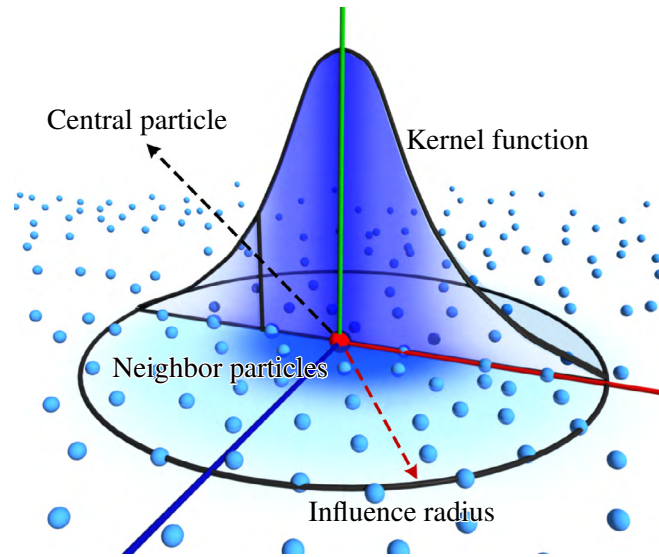
Figure 3: Central particle with neighbor particles, influence area and kernel function [18].

therefore, no numerical costs are incurred in areas that are not immersed. In Eulerian methods, the entire simulation area has to be meshed and calculations are executed for the whole domain in each time step. A detailed description of the method including its derivation for fluid dynamics can be found in [17].

In this contribution, dynamic boundaries are used [19]. That is to say, particles with the same properties as the fluid particles are placed at the boundaries of the structure. However, these particles have no translational degrees of freedom (fixed at the current position or move along a given path). In this way, a penetration of the boundary is prevented.

4 Fluid Structure Interaction – SPH-FEM coupling

In the following, FSI investigations based on coupling SPH and h-FEM are presented. It has been shown that it is adequate for some studies to consider the solid as a rigid body. A primary example for this case are offshore platforms, interactions of ships and tsunami, where the influence of the rigid body on the wave breaking is investigated [20, 21]. The influence of including elastic bodies was considered and was investigated by different authors. The first publication, which is known to the authors of this paper, is from Attaway [7]. This study showed an SPH-FEM interaction of two identical solid bodies which were pressed against each other. The coupling was realized with a master slave concept. Therefore, the penetration of the slave (SPH) body by the master (FEM) body was prevented using a penalty approach (coupling forces). This coupling was realized for solid-solid interaction, the possibility for FSI was not realized but already mentioned in the article. Another realization of FSI using FEM-SPH coupling was proposed by De Vuyust [22]. In this application, dynamic boundary conditions were used, i.e. in the area of contact SPH particles that coincide with the nodes of a FEM discretization were deployed. The displacement of the FE-Nodes directly translates to a displacement of the corresponding SPH boundary particles. By treating the FE nodes as SPH particles they act as boundary particles and cause a repulsive force as fluid particles approaches. The generated force acts equally on both fluid and solids. In this way, a penetration of the boundary is prevented and additionally the force is transferred from the fluid particles to the elastic body (FE model). The sum of the acting forces is equal to zero according to Newton's third law. Forces exerted by fluid particles on boundary particles are distributed among the nodes using the element ansatz functions. In Ref. [22] three application examples were discussed, whereby a coupling of fluid and elastic body was not presented. A different type of coupling conditions was introduced by Fourey [9] who uses the fluid pressure for FSI (referred to as pressure coupling). The pressure value at a FE node is calculated from the average of the pressures of the fluid particles that are in the influence area of the FE node. With this method, the mesh size of both variants is independent of each other. The

penetration of the solid by the fluid was prevented using so-called ghost particles. That is to say, the fluid particles are mirrored at the boundary and the new particles are treated like fluid particles, while their movements depend on their parent particles. Another concept, similar to Attaways [7] master-slave coupling, is used by Yang [8]. By using repulsive boundaries, fluid particles get a repulsive force as a function of their wall distance normal to the boundary. This force acts on the FE system in the same size and in the opposite direction. The element ansatz function distributes the force to the nodes of the element involved (penalty coupling).

The possibility to describe both fluid and solid with a SPH approach is also briefly mentioned. Rafiee [23] verified a pure SPH-based methodology and obtained a good agreement compared to previously published results. This approach will not be discussed in this study, since both the imaging quality of solids in comparison to the FEM is worsened and the numerical complexity increases significantly [24]. FEM is by far the most widely used method for solving partial differential equations and is therefore considered to be a useful supplement to SPH in order to efficiently describe the elastic bodies.

The presented couplings of SPH and FEM from literature uses linear FE elements, but even quadratic elements have already been implemented [10]. Higher ansatz functions have not been considered to the knowledge of the authors. Consequently, the paper at hand is an extension of the current state of the art.

5   High order FE-SPH-Coupling

FEM and SPH interact via pressure (nodal forces) respectively force that is exerted by the fluid particles on the FE mesh. This results in displacements of the FE nodes which are transferred to the particles; i.e. SPH provides the loads for the FEM, and the FEM transfers the resulting structural displacements and velocities to the SPH particles. The coupling implemented here is based on the work of Fourey [9]. The pressure at a FE node is determined by the mean value of the particle pressures in its influence domain. In Figure 4 this concept is visualized for a two-dimensional setting. Three fluid particles (blue) are detected in the influence area of the left FE-node (orange). The pressure values associated with these fluid particles are averaged and converted into an equivalent nodal load which is achieved by integrating the pressure distribution over the face of an immersed FE. In determining the nodal forces, it is important to accurately approximate the discrete pressure function (given only at the fluid particles). One idea is to interpolate the pressure function using a simple polynomial distribution along the boundary of immersed FEs. Figure 5 shows an example of the distribution of nodal forces for a constant pressure along an element boundary for linear, quadratic and higher-order finite elements. Here, already the non-constant distribution of the force values on the nodes is observed. This results from the computation of energetically equivalent nodal loads under consideration of the element ansatz functions. The equivalent nodal force F_e is calculated based on the pressure values $p(\xi)$ and the ansatz function $\mathbf{N}(\xi)$ along the surface Γ

$$F_e = \int_\Gamma \mathbf{N}^T(\xi)\, p(\xi) \mathrm{d}\Gamma. \tag{3}$$

De Vuyust [22] used a node-particle dualism creating points that are both SPH boundary particles and FE nodes. That is one suitable option but not necessary, especially when considering the coupling with high order FEM, because the nodal distribution is not equidistant for most variants [25] and therefore, it is recommended to discretize the two systems separately. In order to interpolate the particle movement of a SPH fluid particle, the element ansatz functions are used (note that fluid particles are located at arbitrary positions on the element boundary which do not generally coincide with a FE node). Therefore, the local coordinates ξ_j of the SPH particle within a FE are determined, at the beginning of the simulation by solving the following non-linear system of equations (inverse mapping)

$$x_{\mathrm{SPH},j} = \sum_{i=1}^{n} N_i(\xi_j)\, x_{i,j} \tag{4}$$
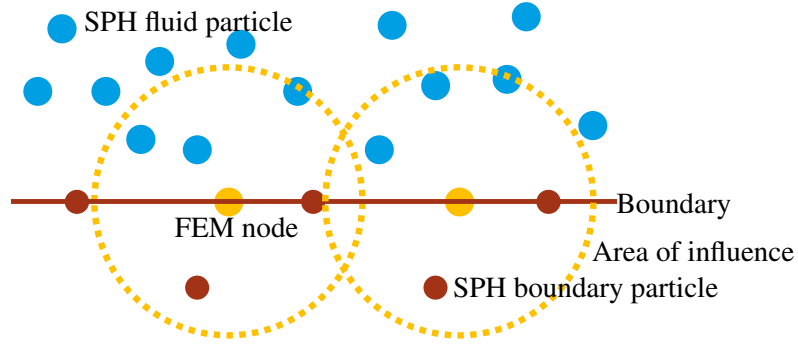
Figure 4: Two rows of boundary particles (brown) that prevent the fluid particles (blue) from penetrating the boundary and FE nodes (orange) with the area of influence, from which the fluid pressures are averaged.
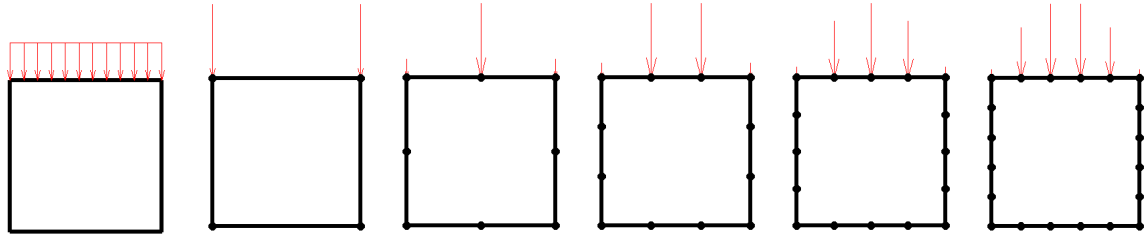

Figure 5: Determination of equivalent node load at a constant pressure distribution at different higher orders p of the ansatz function. From left to right: Element with constant pressure, Linear element, Quadratic element, Cubic element, Quadratic element, Quintic element

with respect to ξ_j. Where i is the number of FE nodes in an element, N_i is the ansatz function corresponding to node i, and $x_{i,j}$ is the global coordinate of the node i in the j-dimensional space. Now, the displacement of the SPH particle u_{SPH} can be determined using the displacement result u of the FE simulation

$$u_{\mathrm{SPH},j} = \sum_{i=1}^{n} N_i(\xi_j)\, u_{i,j}. \tag{5}$$

These determination does not cause loss of accuracy. By using the ansatz functions, the particular displacements are exact in terms of the discretization. In this way, the FEM and SPH systems can be independently discretized. That is to say, different to the approach taken by De Vuyust, it is not necessary that SPH particles and FEM nodes are at the same position. This is particularly advantageous because many high order FEM variants do not have an equidistant nodal distribution, which is, however, a prerequisite in the set-up of the initial SPH discretization.

6 Dam break with a rigid obstacle

For the FEM, an in-house developed FE code is used, which also allows different high order approaches [5]. In this contribution, conventional serendipity elements are deployed with an order of $p \leq 4$. For the description of the fluid, the open source software SPHysics is used. This code has been utilized in different scientific contexts [26–28] and has there been thoroughly verified and validated.

The well-known example of a dam break and a rigid obstacle is used to demonstrate the FSI with a solid structure. The dimensions can be taken by Figure 6. In Figure 7 the water profile obtained in the experiment (photo and red line), a SPH simulation from literature [23] (green line) and our own implementation in SPHysics are compared. A good agreement between our simulation results and the
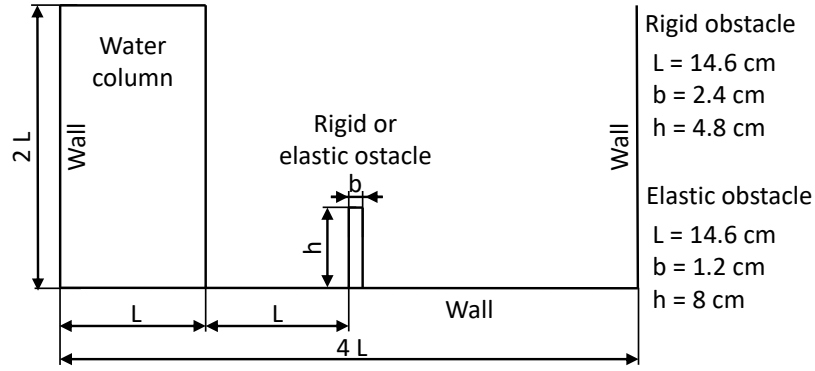
Figure 6: Initial geometry of the water column with a rigid respectively an elastic obstacle [23].
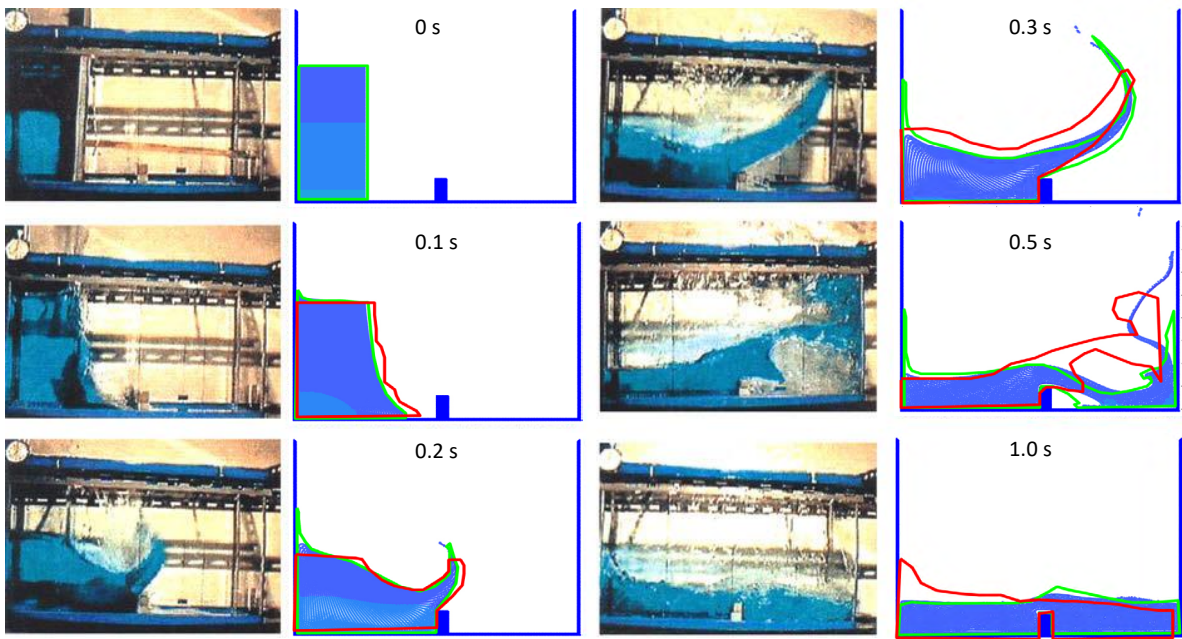
Figure 7: Comparison of water profile of experimental results (left and red line) with SPH simulations (Rafiee, green line) [23] and SPHysics implementation (blue particles) for a collapsing water column with rigid obstacle.

ones published by Rafiee [23] can be observed. The results at the left and right boundaries of the domain do not seem to be physical as a part of the fluid stays attached to the walls until 0.5 s after the dam break (green line). This effect does not occur in our simulations and is also not observed in the experimental measurements. In [23] the difference was attributed to the neglected air in the simulation. The input values used for this verification example (See Appendix 1) are used for all further investigations.

7 Dam brake with an elastic obstacle

The second example is a typical benchmark test that is often employed to verify FSI applications in the context of SPH. We use a similar geometry as in the previous example but for this simulation it is

assumed that the obstacle is not rigid any more and the dimensions of the obstacle are adjusted. The geometry is depicted in Figure 6. This example was already used by various authors [10, 23, 29, 30], but unfortunately experimental results are not available, at least to the authors's knowledge. Figure 8 shows the displacement of the upper left point of the obstacle over time, with 240 or 60 quadratic FE elements and 10000 SPH fluid particles, and a comparison with results taken from literature [10, 23]. In [10], Hu also used 60 or 240 FE elements but 5000, 80000 and 180000 fluid particles. He introduced an efficient search algorithm (which is currently not implemented in SPHysics) and therefore was able to deploy this large number of particles. At the beginning the results are comparable with the literature [10, 23, 29, 30], later on there are clear differences. This differences can be attributed to the large deformations that occur in the verification example. To account for the effects of geometrical non-linearity the second
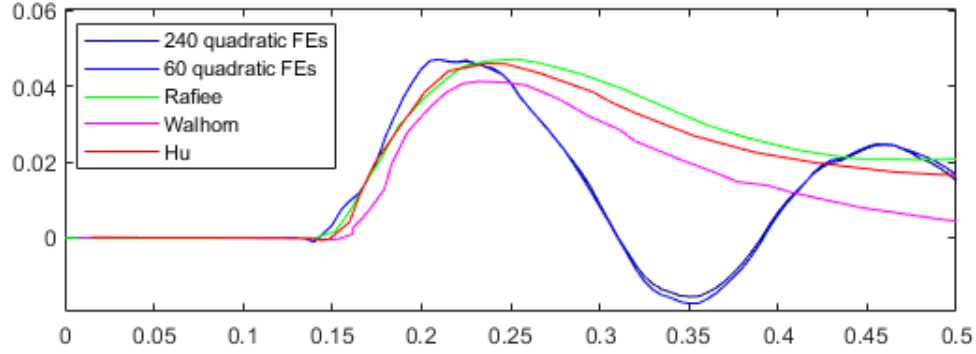
Figure 8: Comparison between numerical results for time history of the displacement of the upper left corner, using 10000 Fluid particles and 60 respectively 240 FEs.
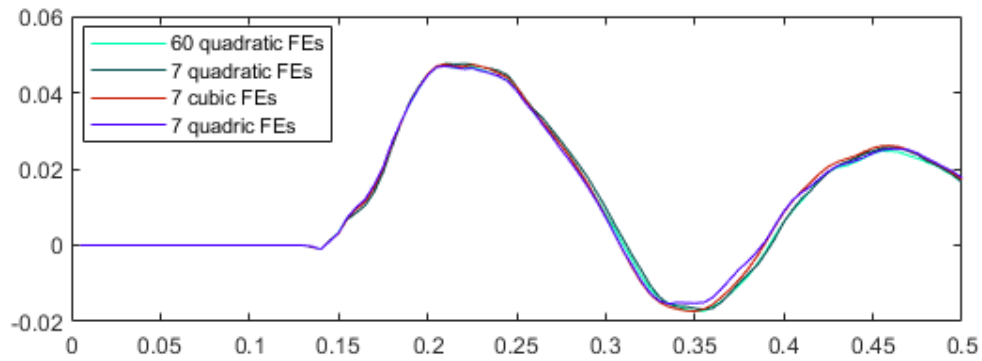
Figure 9: Comparison between numerical results for time history of the displacement of the upper left corner, using 10000 Fluid particles and seven FEs.
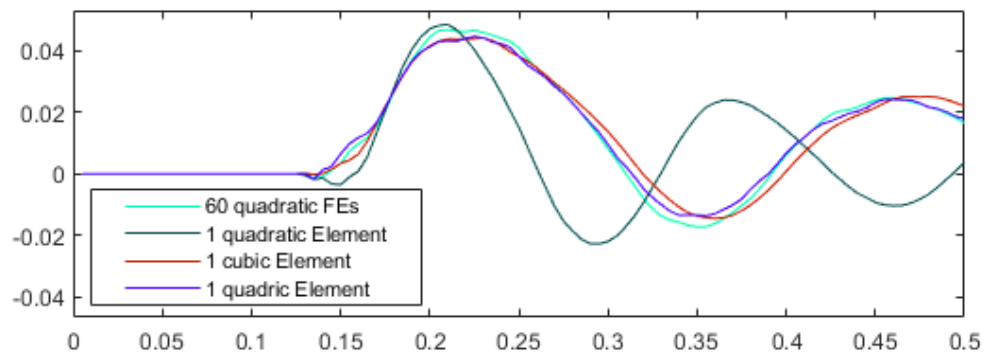
Figure 10: Comparison between numerical results for time history of the displacement of the upper left corner, using 10000 Fluid particles and one FE.

Piola-Kirchhoff stress tensor was used in [30]. The FEM program used in this work is based on the linear theory of elasticity which is sufficient to account for the influence of a fluid on the vibration behavior being investigated in forthcoming publications by the authors. This does not constitute a limitation of the proposed approach as geometrically and physically nonlinear behavior can be straightforwardly added to high order FE codes [31]. The deformations at 60 and 240 quadratic elements are similar, so the solution is converged. Subsequently, this solution is to be realized with significantly fewer elements and ansatz functions of different order. Figure 9 shows the displacement of the upper left corner using seven FE elements and different ansatz functions compared to 60 quadratic Elements. It is good to see that the higher elements are able to describe the vibration behavior of the obstacle. Already seven quadratic elements are sufficient. Despite the large deformations that occur, the results are still in relatively good agreement. In order to clarify the potential of high order FEM, Figure 10 shows the displacement using one FE of different order. It is good to see that a polynomial order of three or higher is sufficient for the vibration analysis. In future studies, validation examples with small deformations are considered to demonstrate the performance of high order FE-SPH coupling.

8   Conclusion

A coupling of SPH and high order FEM was shown and verified, which allows to describe the solid body efficiently using only a few FEs. The insensitivity of high order methods with respect to locking effects and element distortion makes it ideal for the discretization of thin-walled structures. The proposed pressure coupling can be easily implemented in existing codes. Other possible coupling schemes from literature were briefly mentioned but not implemented and validated in the context of high order FEM. Such an implementation is analogous to the one presented in this contribution and is easily possible. In addition to serendipity elements used here, other higher order approaches are conceivable. In further work, different coupling strategies as well as FE ansatz functions will be investigated and evaluated. Furthermore, a three-dimensional variant is to be implemented and experiments to validate the results are performed.

[1]   L. Spannan, C. Daniel, and E. Woschke. "Experimental study on the velocity dependent drag coefficient and friction in an automatic ball balancer". In: *Technische Mechanik - Scientific Journal for Fundamentals and Applications of Engineering Mechanics* 37.1 (2017), pp. 180–189.

[2]   Christian Daniel, Stefan Göbel, Steffen Nitzschke, Elmar Woschke, and Jens Strackeljan. "Numerical simulation of the dynamic behaviour of turbochargers under consideration of full-floating-ring bearings and ball bearings". In: *11th international conference on vibration problems*. Vol. 400. 2013, p. 23.

[3]   F. Duvigneau, S. Nitzschke, E. Woschke, and U. Gabbert. "A holistic approach for the vibration and acoustic analysis of combustion engines including hydrodynamic interactions". In: *Archive of applied mechanics : (Ingenieur-Archiv)* (2016).

[4]   S. Nitzschke, E. Woschke, C. Daniel, and J. Strackeljan. "Simulation von Schwimmbuchsenlagerungen in Abgasturboladern". In: *Journal of Mechanical Engineering of the National Technical University of Ukraine KPI* 61.2 (2011), pp. 7–12.

[5]   S. Duczek. *Higher Order Finite Elements and the Fictitious Domain Concept for Wave Propagation Analysis*. VDI Fortschritt-Berichte Reihe 20 Nr. 458, 2014.

[6]   A. Düster. *High Order Finite Elements for Three-Dimensional, Thin Walled Nonlinear Continua*. Shaker, 2002.

[17]   Joe J Monaghan. "Smoothed particle hydrodynamics". In: *Reports on progress in physics* 68.8 (2005), p. 1703.

[7]   SW Attaway, MW Heinstein, and JW Swegle. "Coupling of smooth particle hydrodynamics with the finite element method". In: *Nuclear engineering and design* 150.2-3 (1994), pp. 199–205.

[8]   Qing Yang, Van Jones, and Leigh McCue. "Free-surface flow interactions with deformable structures using an SPH–FEM model". In: *Ocean engineering* 55 (2012), pp. 136–147.

[9]   G Fourey, G Oger, D Le Touzé, and B Alessandrini. "Violent fluid-structure interaction simulations using a coupled SPH/FEM method". In: *IOP conference series: materials science and engineering*. Vol. 10. 1. IOP Publishing. 2010, p. 012041.

[10]   Dean Hu, Ting Long, Yihua Xiao, Xu Han, and Yuantong Gu. "Fluid–structure interaction analysis by coupled FE–SPH model based on a novel searching algorithm". In: *Computer Methods in Applied Mechanics and Engineering* 276 (2014), pp. 266–286.

[11]   B. Szabó, B. A. Szabo, and I. Babuška. *Finite element analysis*. John Wiley & Sons, 1991.

[12]   B. Szabó and I. Babuška. *Introduction to finite element analysis: formulation, verification and validation*. Vol. 35. John Wiley & Sons, 2011.

[13]   Leon B Lucy. "A numerical approach to the testing of the fission hypothesis". In: *The astronomical journal* 82 (1977), pp. 1013–1024.

[14]   R. A. Gingold and J. J. Monaghan. "Smoothed particle hydrodynamics: theory and application to non-spherical stars". In: *Monthly Notices of the Royal Astronomical Society* 181.3 (1977), pp. 375–389.

[15]   MS Shadloo, G Oger, and D Le Touzé. "Smoothed particle hydrodynamics method for fluid flows, towards industrial applications: Motivations, current state, and challenges". In: *Computers & Fluids* 136 (2016), pp. 11–34.

[16]   Hitoshi Gotoh and Abbas Khayyer. "Current achievements and future perspectives for projection-based particle methods with applications in ocean engineering". In: *Journal of Ocean Engineering and Marine Energy* 2.3 (2016), pp. 251–278.

[18]   R. Sampath, N. Montanari, N. Akinci, S. Prescott, and C. Smith. "Large-scale solitary wave simulation with implicit incompressible SPH". In: *Journal of Ocean Engineering and Marine Energy* 2.3 (2016), pp. 313–329.

[19]   AJC Crespo, M Gómez-Gesteira, and Robert A Dalrymple. "Boundary conditions generated by dynamic particles in SPH methods". In: *CMC-TECH SCIENCE PRESS-* 5.3 (2007), p. 173.

[20]   B. Ataie-Ashtiani and G. Shobeyri. "Numerical simulation of landslide impulsive waves by incompressible smoothed particle hydrodynamics". In: *International Journal for numerical methods in fluids* 56.2 (2008), pp. 209–232.

[21]   Tim Verbrugghe, José Manuel Domínguez, Alejandro JC Crespo, Corrado Altomare, Vicky Stratigaki, Peter Troch, and Andreas Kortenhaus. "Coupling methodology for smoothed particle hydrodynamics modelling of non-linear wave-structure interactions". In: *Coastal Engineering* 138 (2018), pp. 184–198.

[22]   Tom De Vuyst, Rade Vignjevic, and JC Campbell. "Coupling between meshless and finite element methods". In: *International Journal of Impact Engineering* 31.8 (2005), pp. 1054–1064.

[23]   Ashkan Rafiee and Krish P Thiagarajan. "An SPH projection method for simulating fluid-hypoelastic structure interaction". In: *Computer Methods in Applied Mechanics and Engineering* 198.33 (2009), pp. 2785–2795.

[24]   Zhifan Zhang, Longkan Wang, Vadim V Silberschmidt, and Shiping Wang. "SPH-FEM simulation of shaped-charge jet penetration into double hull: A comparison study for steel and SPS". In: *Composite Structures* 155 (2016), pp. 135–144.

[25]   C. Pozrikidis. *Introduction to Finite and Spectral Element Methods using MATLAB*. 2nd ed. Chapman and Hall/CRC, 2014, p. 830.

[26] Alejandro Jacobo Cabrera Crespo. "Application of the smoothed particle hydrodynamics model SPHysics to free-surface hydrodynamics". In: *Universidade de Vigo* (2008).

[27] Shan Zou. "Coastal sediment transport simulation by smoothed particle hydrodynamics". PhD thesis. The Johns Hopkins University, 2007.

[28] Moncho Gómez-Gesteira, Alejandro JC Crespo, Benedict D Rogers, Robert A Dalrymple, José M Dominguez, and Anxo Barreiro. "SPHysics–development of a free-surface fluid solver–Part 2: Efficiency and test cases". In: *Computers & Geosciences* 48 (2012), pp. 300–307.

[29] Elmar Walhorn, Andreas Kölke, Björn Hübner, and Dienter Dinkler. "Fluid–structure coupling within a monolithic model involving free surface flows". In: *Computers & structures* 83.25-26 (2005), pp. 2100–2111.

[30] Sergio R Idelsohn, Julio Marti, A Limache, and Eugenio Oñate. "Unified Lagrangian formulation for elastic solids and incompressible fluids: application to fluid–structure interaction problems via the PFEM". In: *Computer Methods in Applied Mechanics and Engineering* 197.19 (2008), pp. 1762–1776.

[31] U. Heisserer. "High-Order Finite Elements for Material and Geometric Nonlinear Finite Strain Problems". PhD thesis. Technical University Munich, 2008.

9   Appendix 1

Kernel	Cubic spline
Algorithm	Predictor corrector
Density Filter	Moving Least Squares every eight time steps
Viscosity	Laminar
Equation of state	Tait equation
dt	5e-5
Riemann solver	none
Kernel correction	none
Hughes and Graham correction	every eight time steps
CFL number	0.2

SMOOTHED PARTICLES HYDRODYNAMICS SIMULATION OF A U-TANK IN FORCED MOTION

ALDO PAPETTI[1], GIULIANO VERNENGO[1], STEFANO GAGGERO[1], DIEGO VILLA[1] AND LUCA BONFIGLIO[2]

[1] Dept. of Electric, Electronic and Telecommunication Engineering and Naval Architecture
(DITEN)
University of Genova, 16145, Italy
giuliano.vernengo@unige.it diego.villa@unige.it stefano.gaggero@unige.it

[2] MIT-Sea Grant College Program
Massachusetts Institute of Technology, Cambridge, 02138, MA, USA
bonfi@mit.edu

Key words: U-Tank, Roll motion, Smoothed Particles Hydrodynamics (SPH), Sloshing, Hydrodynamics

Abstract. The hydrodynamic forces generated by the water moving inside a U-shaped tank are predicted by using the open-source Smoothed Particle Hydrodynamic (SPH) solver *DualSPHysics*. In particular the study focuses on the roll moment prediction of the U-tank undergoing forced roll motion at different frequencies. The sensitivity of the hydrodynamic prediction with respect to variations of particle resolution density is investigated by a systematic set of numerical simulations. Results of the SPH simulations are validated by comparison against available experimental data on a particular U-tank shape and discussed both in terms of roll moment amplitude and phase lag with respect to the imposed motion.

1 Introduction

Anti-Roll Tanks (ARTs) represent a reliable device to reduce ship rolling motion in waves. Even tough they have some known problems in specific operating conditions, e.g. at low frequencies, there is a renewed interest in the form of Liquid Tuned Damper (LTD) devices for applications other than ships such in Wave Energy Converters (WECs) [1] and both onshore and offshore wind turbines [2, 3]. In the recent years CFD have started to be used in Simulation Based Design (SBD) frameworks to reach reliable predictions of the hydrodynamic behaviors of such a devices [4, 5, 6]. Considering ARTs from a hydrodynamic perspective there are some relevant non-linear phenomena that can fall in the categories of the *sloshing* and, eventually, of *slamming* which should be properly addressed by using high fidelity CFD solutions. There are many studies dealing with CFD analyses of partially filled rectangular tanks carried out by using different techniques. Smoothed Particle Hydrodynamics (SPH) technique has been applied to this class of problems [7, 8, 9],

reaching good agreement compared to experimental data, both in terms of dynamics and global loads.

In the present research an open-source SPH solver called *DualSPHysics* [10] has been used to analyze the forces and the moments exerted by a U-tank undergoing forced oscillation at a fixed motion amplitude. Results of the CFD simulations are validated by comparison against available experimental data on a particular U-tank design [11]. Results are discussed in the light of the assumptions of the selected CFD method, both as roll moment amplitude and phase lag with respect to the weave.

This SPH solver has been widely used in many coastal engineering studies (see for instance [12, 13, 14, 15, 16]) and, in a less extent, for naval architecture related problems (see e.g. [17, 18, 19, 20]). Such a SPH method, relying on a Lagrangian representation of the fluid flow, is particularly suitable for free surface flows with fragmented sprays such as the one experienced in sloshing in partially filled tanks.

2   Backgrounds of Anti-Roll Tank Physics and Design

The shape of a passive ART mainly depends on the hull type on which it will be installed. Despite possible local changes, two most used geometries show a rectangular or a U-shaped cross section. The latter shape has been considered in the present study. Compared to a rectangular tank the free surface of a U-shaped tank is generally divided in two parts, except for very shallow water depths. Particularly at relatively high water depths this will reduce the possible water impacts on the tank sides due to roll-induced sloshing. This in turn will reduce the dynamics effects involved in the physics of this ART type with respect to classic rectangular ones. Due to ship motions (in particular due to the roll motion) the water inside the ART will start sloshing back and forth exerting a roll moment on the tank and then on the ship itself. Hence the ART design is driven by the need to use such a roll moment as damping correction to ship roll motion. Ideally 90° phase lag with respect to roll motion should be the best situation, meaning that the water motion inside the tank is in phase with roll velocity. Stigter [21] proposed a mathematical formulation to design U-tank and LLoyd [22] provided some further suggestions based on Stigter's method e.g. on the maximum tank angle, on the loss of metacentric height and on the maximum stabilizing moment. Recent studies are instead based on numerical simulations both by RANSE [23, 24, 25] and, in a less extent, by SPH [26] methods.

3   Computational Fluid Dynamics by Smoothed Particle Hydrodynamics

The core of the open-source SPH solver [10] follows the original formulation proposed by Monaghan [27]. This solver has been developed to exploit GP-GPU computation, hence allowing the use of a relatively large number of particles. According to the SPH formulation the flow is solved in a mesh-free Lagrangian framework based on particles description. Field variables (e.g. V, ρ or p) and their derivatives are represented in a continuous integral form by a suitable kernel function (*kernel approximation*) and then discretized over the computational domain (*particle approximation*). Field variables on a specific particle are then computed by approximation using the nearest neighbor particles.

Giving a function $f(x)$ its integral form is expressed according to Eq. (1):

$$f(x) = \int_\Omega f(x')\delta(x - x')dx' \tag{1}$$

Using a kernel function $W(x - x', h)$ depending on a smoothing length h, Eq. (1) can be written in terms of Kernel approximation as in Eq. (2). Such a kernel is substituted by proper analytic functions that vanish for separations greater than kh (being k a given constant). The cubic spline kernel function has been chosen.

$$\langle f(x)\rangle = \int_\Omega f(x')W(x - x', h)dx' \tag{2}$$

Pressure are computed by the state equation of Eq. (3) assuming water as a weakly compressible fluid. c_0 is the sound speed ranging from 50 m/s up to 250 m/s to ensure $Mach < 0.1$ and γ is a constant generally taken equal to 7.

$$p = \frac{c_0^2 \rho_0}{\gamma}\left[\left(\frac{\rho}{\rho_0}\right)^\gamma - 1\right] \tag{3}$$

Both the mass and the momentum conservation laws, Eq. (4) and Eq. (5), respectively, are written in terms of particles approximation as follows:

$$\frac{d\rho_i}{dt} = \sum_{ij} m_j\left(u_i - u_j\right)\nabla_i W_{ij} \tag{4}$$

$$\frac{d\mathbf{u}_i}{dt} = -\sum_{ij} m_j\left(\frac{P_i}{\rho_i^2} - \frac{P_j}{\rho_j^2} + \Pi_{ij}\right)\nabla_i W_{ij} + g \tag{5}$$

The summation over the two indexes i and j accounts for particles interactions; m, u and P are the particle mass, velocity and the pressure at a particle respectively. Π_{ij} is a force contribution used to avoid tensile instabilities. being the artificial viscosity coefficient α the main parameter that controls this additional force term. A further diffusive term is introduced in the continuity equation by the *delta-SPH* formulation (see for instance [28]) in order to reduce density fluctuations generated by the combination of the stiff density field described by the state equation and the natural disordering of the particles, resulting in high-frequency low amplitude oscillations in the density scalar field.

4 Selected test case and numerical simulation settings

The proposed fluid dynamic study has been performed on one of the U-tanks tested by Field and Martin [11]. They carried out a systematic experimental campaign by varying both the dimensional ratios of the tank and the water depth inside of it. Fig. 1 displays a scheme of the U-tank where the reference system used for the computations has been highlighted. Table 1 instead reports the main dimensions of the configurations used for the numerical simulation.
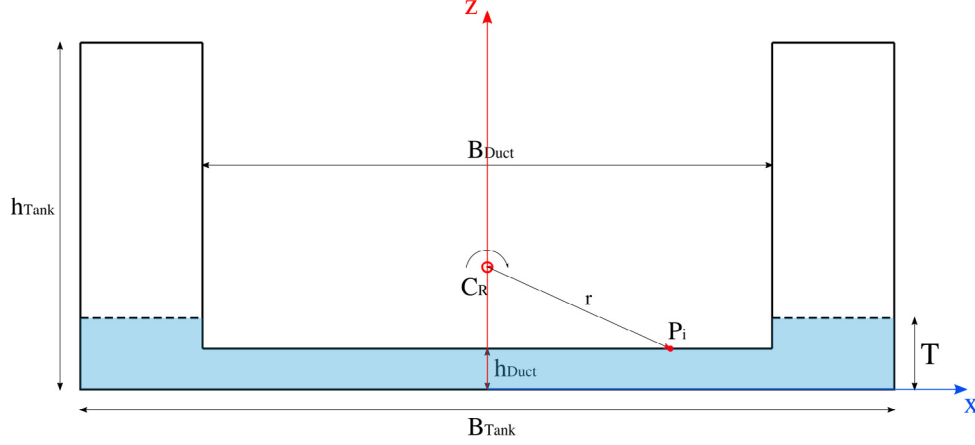
Figure 1: Sketch of the U-Tank. Main dimensions $[h_{Tank},\ B_{Tank},\ h_{Duct},\ B_{Duct}]$, draft T, center of rotation C_R and the position r of the ith pressure probe P_i are indicated.

Table 1: Main dimensions of the U-Tank (full scale).

h_{Tank}	10.0	[ft]	B_{Duct}	24.0	[ft]
B_{Tank}	42.0	[ft]	T	3.0	[ft]
h_{Duct}	1.0	[ft]	Z_{C_R}	4.5	[ft]

The CFD analysis has been performed by scaling the dimensions of the tested U-tank by a factor $\lambda = 8.0$. Froude similarity has been used since it is considered of general validity for sloshing-type problems [29] and for scaling gravity forces. Each of the six SPH simulations has been carried out for 8 roll periods T_{Roll}, hence changing the physical simulated time T_{Max} according to the specific frequency of oscillation ω. According to the experimental tests, the maximum roll angle has been taken equal to $\theta_{44} = 2°$.

Time-varying lateral and vertical forces, $F_X(t)$ and $F_Z(t)$, respectively, have been computed from pressures. The latter have been directly measured by pressure probes uniformly distributed along each side of the tank, placed at a distance along the normal to each boundary equal to $\delta_{Probe} = 1.5h$, being h the smoothing length of the simulation. The time-varying roll moment $M_{44}(t)$ with respect to the center of rotation of the tank C_R has then been computed from the forces. Fourier Transform has been used to obtain the amplitude $M_{44}(\omega)$ and phase $\phi_{44}(\omega)$ of the roll moment. An example of time histories of the lateral and vertical forces on the tank and of the roll moment exerted by the fluid is shown in Fig. 2.

5   Particle density sensitivity analysis

A preliminary analysis of the effect of the particle density with respect to the predicted roll moment has been carried out by using the extrapolation method proposed by Celick [30]. Table 2 reports the results of such a convergence analysis. The extrapolated value of the roll moment obtained by using the two finer densities $Phi_{21-EXTR}$ is very close to the value computed by using the medium size particle density ($\approx 200k$ particles). This
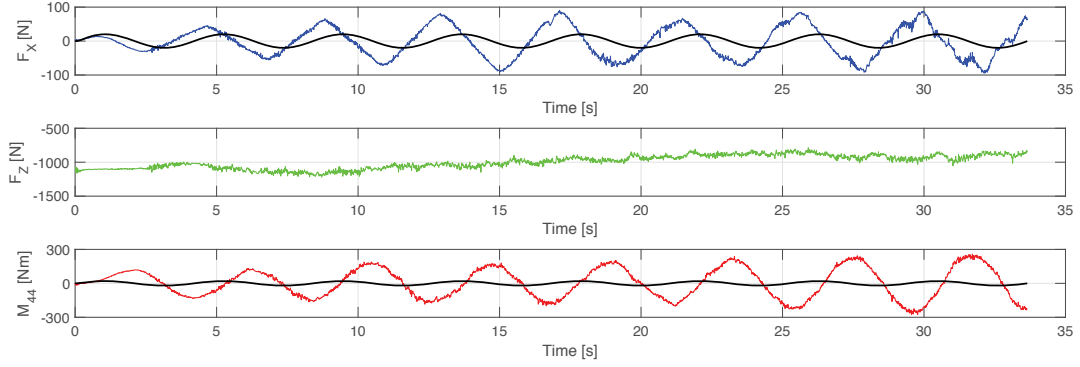
Figure 2: Time histories of the transverse force F_X (top figure), vertical force F_Z (middle figure) and roll motion (bottom figure). Tank sinusoidal motion is shown by a black solid curve.

Table 2: Particle density convergence analysis.

Case	n_P	M_{44}	$\Phi_{21,EXTR}$	$\Phi_{32,EXTR}$	$\Delta\epsilon_{\Phi_{21,EXTR}-M2}$
M1	400k	54.56			
M2	200k	55.40	54.439	56.361	1.76%
M3	100k	48.72			

ensures that the intermediate particle resolution used to compute M_{44} is accurate enough.

6   Validation by comparison against experimental measurements

The SPH simulations have been carried out on a two-dimensional case scaled according to Froude similarity with $\lambda = 8.0$. Hence the numerical results have been scaled considering the width of the tank in order to allow the comparison against the experimental measurements, shown in Fig. 3. A satisfactory agreement between the two results is found, being the trends of both the amplitude and the phase correctly predicted. The maximum deviation on the roll moment amplitude of the numerical prediction with respect to experimental measurements is about $\Delta M_{44} \simeq 12\%$ at $\omega = 0.62$. The prediction is even better close to the peaks where the error is significantly decreased, $\Delta M_{44} \leq 4.5\%$. A greater maximum deviation is found on the phase lag of the roll moment with respect to the imposed (sinusoidal) motion Φ_{44} in the extent of about $\Delta\Phi_{44} \simeq 20\%$. Again at the peak frequencies the quality of the prediction is higher on the phase lag too, being $\Delta\Phi_{44} \leq 5\%$.

Fig. 4 displays the fluid velocity magnitude at four characteristics phases over a roll period, $\psi = [0°, 45°, 90°, 135°, 180°]$, respectively, for two frequencies of oscillation, $\omega = 0.44 \ [rad/sec]$ and $\omega = 0.62 \ [rad/sec]$. The first correspond to the peak frequency while the latter is the one showing the larger error on the roll moment amplitude. Both set of snapshots have been taken at the 8th roll period of the corresponding simulation. At the lower frequency (the peak one) the fluid reaches higher velocities. This is mainly due to gravitational effects during the water transfer from one side to the other. In fact, the slower dynamics of the tank allow the flow to be more affected by the gravity forces. As a
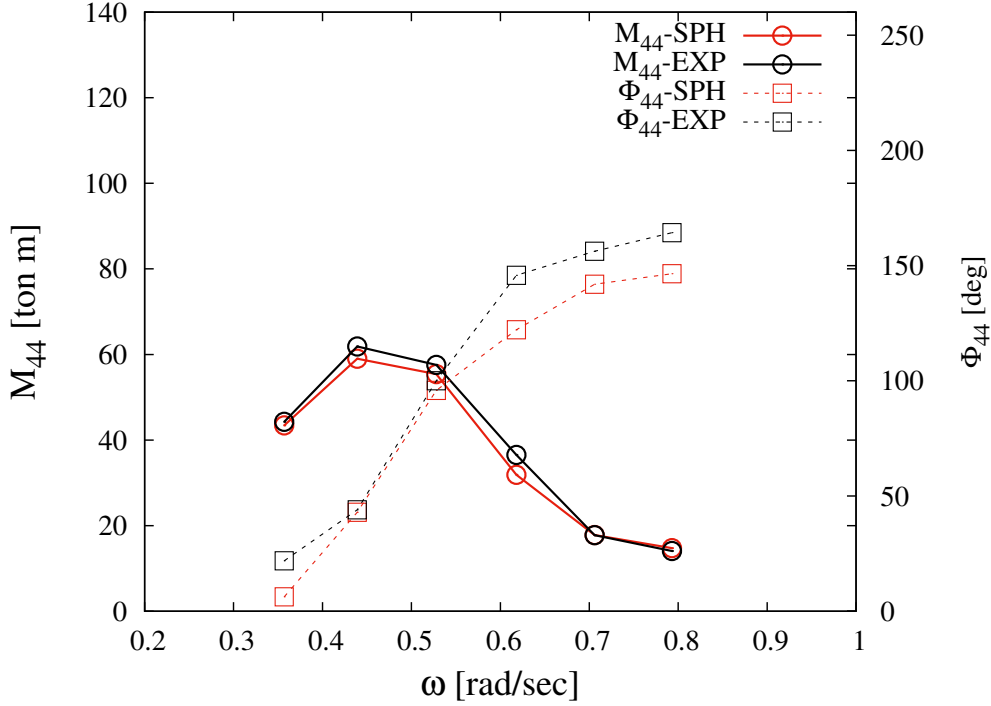
Figure 3: Comparison of the experimental measurements (black) against SPH results (red) in terms of amplitude (circles) and phase lag (squares) of the roll moment.

result the fluid is accelerated for a longer time lapse. For the same reasons, there is also a greater difference between the water levels on the two sides of the tank. Furthermore there are stronger vortexes at the inner corners of the tank that rise due to water re-circulation while the side is filling with water.

7   Conclusions

A CFD study on a U-Tank under forced oscillating motion has been carried out by using a Smoothed Particle Hydrodynamics (SPH) open source solver. Backgrounds of both the U-Tank analysis and the numerical solver have been briefly presented. The roll moment has been computed by the forces that in turn have been derived directly from pressures over the tank boundaries.

A preliminary analysis of the effect of the particle density on the solution has been carried out. Results have been extrapolated by using the Richardson's method providing information on the convergence properties of the solution. The proposed SPH solution has finally been validated by comparison against available experimental measurements on a U-tank. The tank has been scaled by considering Froude similarity. Both predictions of the amplitude and the phase lag of the roll moment provide satisfactory results. The maximum relative difference with respect to the experiments close to the peak frequencies is lower than 4.5% for the amplitude and 5.0% for the phase lag. It rises up to 12% and 20% at a higher frequency for the amplitude and the phase lag, respectively. Some insights of the fluid flow have also been provided by comparison of the snapshots over

(a) $\omega = 0.44 \ rad/sec \ \psi = 0°$

(b) $\omega = 0.62 \ rad/sec \ \psi = 0°$

(c) $\omega = 0.44 \ rad/sec \ \psi = 45°$

(d) $\omega = 0.62 \ rad/sec \ \psi = 45°$

(e) $\omega = 0.44 \ rad/sec \ \psi = 90°$

(f) $\omega = 0.62 \ rad/sec \ \psi = 90°$

(g) $\omega = 0.44 \ rad/sec \ \psi = 135°$

(h) $\omega = 0.62 \ rad/sec \ \psi = 135°$

(i) $\omega = 0.44 \ rad/sec \ \psi = 180°$
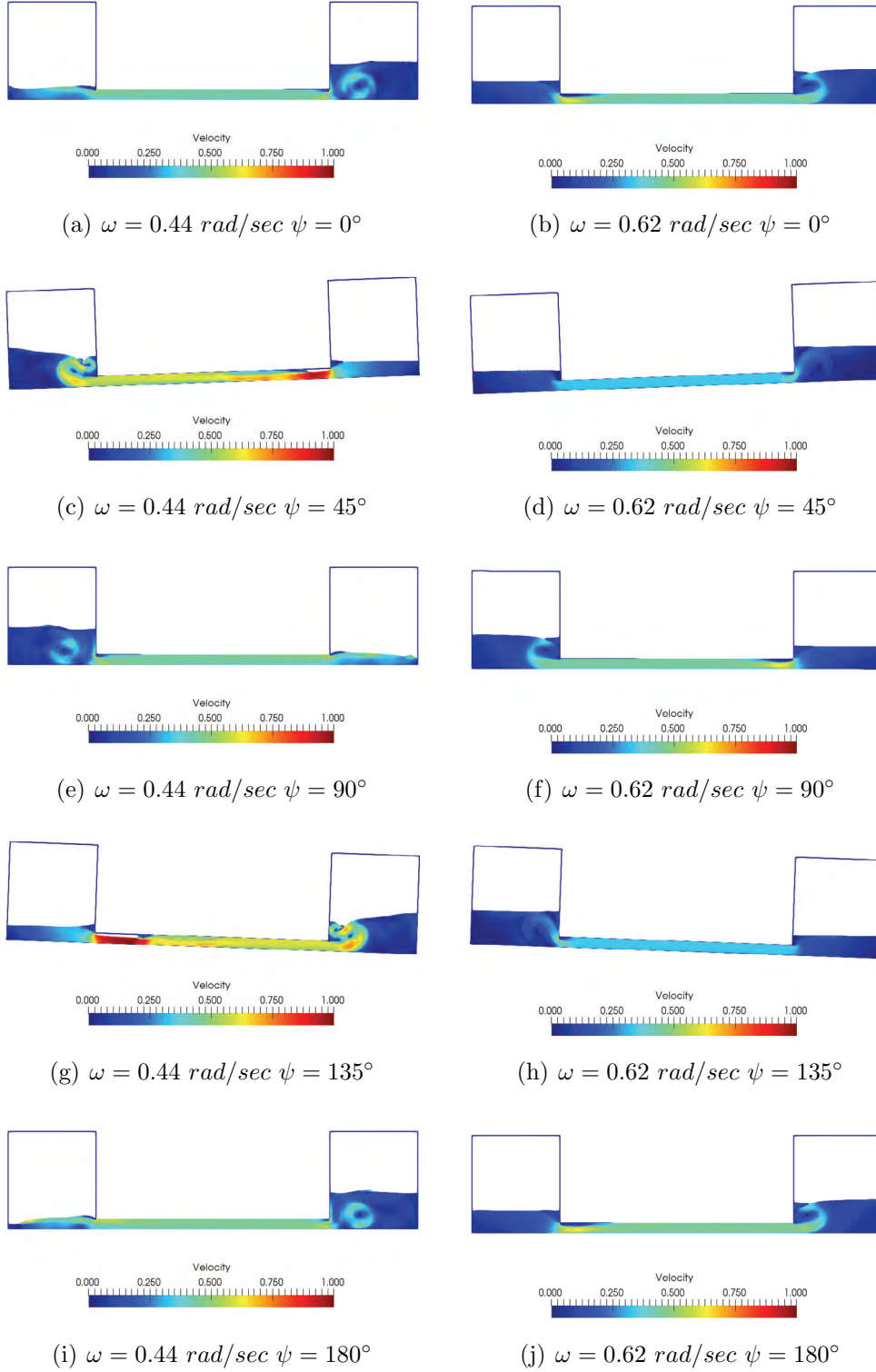
(j) $\omega = 0.62 \ rad/sec \ \psi = 180°$

Figure 4: Snapshots of the flow inside the tank at two oscillation frequencies, $\omega = 0.44 \ [rad/sec]$ (left column) and $\omega = 0.62 \ [rad/sec]$ (right column), respectively. The same phases ψ over the roll period has been compared on each row. Velocity magnitude is show by the colormap.

a roll period of the fluid flow at two frequencies. As expected, it has been shown that gravitational forces have a greater effect on the fluid properties as a slower dynamics is developed, hence at lower frequencies of oscillation.

References

[1] Sergej Antonello Sirigu, Mauro Bonfanti, Panagiotis Dafnakis, Giovanni Bracco, Giuliana Mattiazzo, and Stefano Brizzolara. Pitch resonance tuning tanks: A novel technology for more efficient wave energy harvesting. In *OCEANS 2018 MTS/IEEE Charleston*, pages 1–8. IEEE, 2018.

[2] Zili Zhang, Biswajit Basu, and Søren RK Nielsen. Real-time hybrid aeroelastic simulation of wind turbines with various types of full-scale tuned liquid dampers. *Wind Energy*, 22(2):239–256, 2019.

[3] Arash Hemmati, Erkan Oterkus, and Mahdi Khorasanchi. Vibration suppression of offshore wind turbine foundations using tuned liquid column dampers and tuned mass dampers. *Ocean Engineering*, 172:286–295, 2019.

[4] AH Day, Aurélien Babarit, A Fontaine, Y-P He, M Kraskowski, M Murai, Irene Penesis, F Salvatore, and H-K Shin. Hydrodynamic modelling of marine renewable energy devices: A state of the art review. *Ocean Engineering*, 108:46–69, 2015.

[5] Tim Verbrugghe, Vasiliki Stratigaki, Corrado Altomare, JM Domínguez, Peter Troch, and Andreas Kortenhaus. Implementation of open boundaries within a two-way coupled sph model to simulate nonlinear wave–structure interactions. *Energies*, 12(4):697, 2019.

[6] Nicolas Tomey-Bozo, Aurélien Babarit, Jimmy Murphy, Vicky Stratigaki, Peter Troch, Tony Lewis, and Gareth Thomas. Wake effect assessment of a flap type wave energy converter farm under realistic environmental conditions by using a numerical coupling methodology. *Coastal Engineering*, 143:96–112, 2019.

[7] A Souto-Iglesias, L Delorme, L Pérez-Rojas, and S Abril-Pérez. Liquid moment amplitude assessment in sloshing type problems with smooth particle hydrodynamics. *Ocean Engineering*, 33(11-12):1462–1484, 2006.

[8] Gabriele Bulian, Antonio Souto Iglesias, Luis Delorme, and Elkin Botia Vera. Smoothed particle hydrodynamics (sph) simulation of a tuned liquid damper (tld) with angular motion. *Journal of Hydraulic Research*, 48(Spécia):28–39, 2010.

[9] Luis Pérez Rojas and Jose L Cercos Pita. *3D GPU SPH Analysis of Coupled Sloshing and Roll Motion*, pages 257–272. 2019.

[10] Alejandro JC Crespo, Jose M Dominguez, Benedict D Rogers, Moncho Gomez-Gesteira, S Longshaw, R Canelas, Renato Vacondio, A Barreiro, and O Garcia-Feal.

Dualsphysics: Open-source parallel cfd solver based on smoothed particle hydrodynamics (sph). *Computer Physics Communications*, 187:204–216, 2015.

[11] SB Field and JP Martin. Comparative effects of u-tube and free surface type passive roll stabilisation systems. *Naval Architect*, (2), 1976.

[12] Dieter FA Vanneste, Corrado Altomare, Tomohiro Suzuki, Peter Troch, and Toon Verwaest. Comparison of numerical models for wave overtopping and impact on a sea wall. *Coastal Engineering Proceedings*, 1(34):5, 2014.

[13] Feng Zhang, Alejandro Crespo, Corrado Altomare, José Domínguez, Andrea Marzeddu, Shao-ping Shang, and Moncho Gómez-Gesteira. Dualsphysics: A numerical tool to simulate real breakwaters. *Journal of Hydrodynamics*, 30(1):95–105, 2018.

[14] Riccardo Angelini Rota Roselli, Giuliano Vernengo, Corrado Altomare, Stefano Brizzolara, Luca Bonfiglio, and Roberto Guercio. Ensuring numerical stability of wave propagation by tuning model parameters using genetic algorithms and response surface methods. *Environmental Modelling & Software*, 103:62–73, 2018.

[15] Tim Verbrugghe, José Manuel Domínguez, Alejandro JC Crespo, Corrado Altomare, Vicky Stratigaki, Peter Troch, and Andreas Kortenhaus. Coupling methodology for smoothed particle hydrodynamics modelling of non-linear wave-structure interactions. *Coastal Engineering*, 138:184–198, 2018.

[16] Riccardo Angelini Rota Roselli, Giuliano Vernengo, Stefano Brizzolara, and Roberto Guercio. Sph simulation of periodic wave breaking in the surf zone-a detailed fluid dynamic validation. *Ocean Engineering*, 176:20–30, 2019.

[17] Angelantonio Tafuni, Iskender Sahin, and Mark Hyman. Numerical investigation of wave elevation and bottom pressure generated by a planing hull in finite-depth water. *Applied Ocean Research*, 58:281–291, 2016.

[18] L. Bonfiglio, S. Gaggero, A. Papetti, G. Vernengo, and D. Villa. Systematic analysis of mesh and meshless cfd methods for water impact problems. In *7th International Conference on Computational Methods in Marine Engineering, MARINE 2017*, pages 568–582, Nantes, France, 15–17 May, 2017.

[19] Stefano Gaggero, Tomaso Gaggero, Marco Gaiotti, Stefano Ghelardi, Giuliano Vernengo, and Digeo Villa. Sensitivity analysis of impact loads by cfd solvers for structural fem computation on ship structures. In *The 28th International Ocean and Polar Engineering Conference (ISOPE-2018)*. International Society of Offshore and Polar Engineers, Sapporo, Japan, June 10–15, 2018.

[20] Giuliano Vernengo, Riccardo Angelini Rota Roselli, Stefano Brizzolara, and Roberto Guercio. Unsteady hydrodynamics of a vertical surface piercing strut by sph simulations. In *The 29th International Ocean and Polar Engineering Conference (ISOPE-2019)*. International Society of Offshore and Polar Engineers, Honolulu, Hawaii, USA, 16–21 June, 2019.

[21] C Stigter. The performance of u-tanks as a passive anti-rolling device. *International shipbuilding progress*, 13(144):249–275, 1966.

[22] ARJM Lloyd. *Seakeeping: ship behaviour in rough weather*. E. Horwood, 1989.

[23] EFG Van Daalen, KMT Kleefsman, J Gerrits, HR Luth, and AEP Veldman. Anti roll tank simulations with a volume of fluid (vof) based navier-stokes solver. In *23rd Symposium on Naval Hydrodynamics*, 2000.

[24] Worakanok Thanyamanta and David Molyneux. Prediction of stabilizing moments and effects of u-tube anti-roll tank geometry using cfd. In *ASME 2012 31st International Conference on Ocean, Offshore and Arctic Engineering*, pages 503–512. American Society of Mechanical Engineers, 2012.

[25] Bhushan Uday Taskar, Debabrata DasGupta, Vishwanath Nagarajan, Suman Chakraborty, Anindya Chatterjee, and Om Prakash Sha. Cfd aided modelling of anti-rolling tanks towards more accurate ship dynamics. *Ocean Engineering*, 92:296–303, 2014.

[26] A Souto Iglesias, L Pérez Rojas, and R Zamora Rodríguez. Simulation of anti-roll tanks and sloshing type problems with smoothed particle hydrodynamics. *Ocean Engineering*, 31(8-9):1169–1192, 2004.

[27] Joe J Monaghan. Smoothed particle hydrodynamics. *Annual review of astronomy and astrophysics*, 30(1):543–574, 1992.

[28] Diego Molteni and Andrea Colagrossi. A simple procedure to improve the pressure evaluation in hydrodynamic context using the sph. *Computer Physics Communications*, 180(6):861–872, 2009.

[29] BV. Design sloshing loads for lng membrane tanks. *Bureau Veritas, NI 554 DT R00 E, Guidance Note*, 2011.

[30] Ishmail B Celik, Urmila Ghia, Patrick J Roache, et al. Procedure for estimation and reporting of uncertainty due to discretization in {CFD} applications. *Journal of fluids {Engineering-Transactions} of the {ASME}*, 130(7), 2008.

PARTICLE DAMPING FOR VIBRATION SUPPRESSION OF A CLAMPED PLATE

MASATO SAEKI[1], YUJI KAZAMA[2] AND YU MIZOBUCHI[1]

[1] Dept. of Mechanical Engineering, Fuculty of Engineering,
Shibaura Institute of Technology
3-7-5 Toyosu, Koto-ku, Tokyo 135-8548, Japan
E-mail: saeki@sic. shibaura-it.ac.jp
URL: http://www.sic.shibaura-it.ac.jp/~saeki/index_E.html

[2] Graduate school Engineering and Science, Shibaura Institute of Technology,
3-7-5 Toyosu, Koto-ku, Tokyo 135-8548, Japan
E-mail: md14004@shibaura-it.ac.jp

Key words: Granular materials, DEM, Vibration suppression, Contact problems.

Abstract. In this paper, analytical and experimental studies of the vibration suppression of a square plate with a particle damper are discussed. The primary objective of this paper is to construct an analytical model to simulate the transient impact response of a plate with a particle damper. In the experimental approach, an acrylic resin plate with all sides clamped was used. The transient vibration of the plate caused by the impact of a steel ball was measured with a laser displacement sensor. The effects of the mass ratio, particle material and cavity shape on the damping efficiency were investigated. To capture the behavior of the entire system in detail, an analytical model based on coupling between the finite element method and the discrete element method was constructed. Rayleigh damping was used to approximate the damping behavior of the plate without granular materials. Comparison between the experimental and analytical results showed that accurate estimates of the response of a plate can be obtained.

1 INTRODUCTION

Particle damping is a typical cost-effective technique for vibration suppression. It involves the use of small metallic or plastic particles contained in a cavity of a primary mass. The damping effect results from the exchange of momentum during the impact of granular materials against the wall of the cavity. Owing to the simplicity of their construction, particle dampers have been widely used for structural damping applications in boring bars [1], printed circuit boards [2] and double-layered ceilings [3].

Many experimental and analytical studies have demonstrated the effectiveness of particle dampers. In the experimental studies, the effects of the mass ratio, particle size, cavity dimensions and excitation level on the efficiency of the damping system were investigated [4]. In the analytical studies, the discrete element method (DEM) [5, 6] and the direct simulation Monte Carlo approach [7] were used to predict particle damping. Most previous theoretical analyses have focused on single-degree-of-freedom systems with particle dampers. Recently, some researchers have been studying the vibration characteristics of continuous structures with

particle dampers [8, 9]. However, these studies were limited to predicting the dynamic responses of a cantilever beam with particle dampers.

In this paper, analytical and experimental studies of the vibration suppression of a square plate with a particle damper are discussed. The primary objective of this work is to construct an analytical model to simulate the transient impact response of a plate with a particle damper. In the experimental approach, an acrylic resin plate with all sides clamped was used. The transient vibration of the plate caused by the impact of a steel ball was measured with a laser displacement sensor. In the theoretical analysis, the simulation was performed by combining the finite element method (FEM) with the DEM. The damping characteristics of the plate without granular materials were approximated by Rayleigh damping.
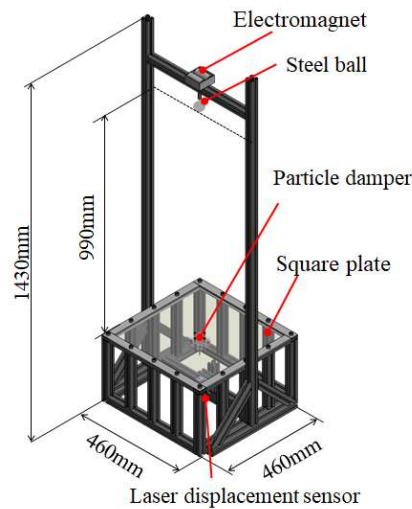
Figure 1: Experimental apparatus

2 EXPERIMENT

2.1 Experimental apparatus

Figure 1 shows the experimental apparatus used in this study. A square plate made of acrylic resin was clamped on all sides. The plate was 400mm wide and 5mm thick. A container enclosing granular materials was attached to the center of the plate as a particle damper. An electromagnet was located above the plate. A steel ball was attached to the electromagnet as an impactor. Upon cutting off the current to the electromagnet, the ball collides with the center of the plate and the plate is allowed to oscillate freely. The motion of the plate was measured with a laser displacement sensor. A ball with a diameter of 12.7mm was dropped from a height of 990mm.

Figures 2(a) and 2(b) show the shapes of the containers of the particle damper. To investigate the effect of the shape on the damping performance, cubic and cylindrical containers were used. Also, the effects of the mass ratio λ and particle material on the damping performance were investigated.
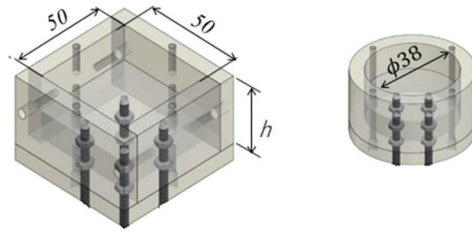
(a) Cubic container   (b) Cylindrical container

Figure 2: Shapes of containers of the particle damper
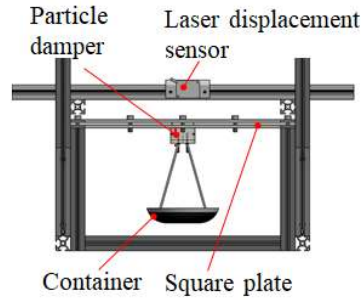
Figure 3: Measurement of the spring constant
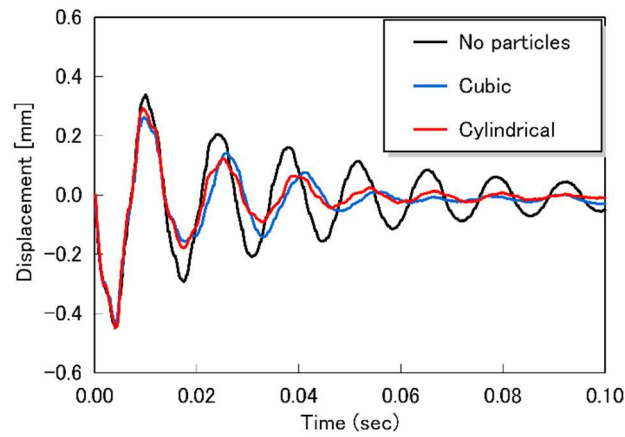
Figure 4: Effect of the shape of the container
(h=8.0mm, λ =14.6%, ϕ 6.35mm, copper particles)

Here, the mass ratio λ is the total mass of the granular materials divided by the equivalent mass of the first mode of the plate. The equivalent mass was obtained as follows. A container was hung from the plate and a predetermined mass was placed on the container. The displacement of the center part of the plate was measured with the laser displacement sensor, which was installed as shown in Figure 3. Because the weight is proportional to the displacement, the spring constant k_1 was determined from the proportionality constant. Then, the equivalent mass

is given by

$$m_1 = k_1/(2\pi f_{n1})^2, \tag{1}$$

where f_{n1} is the fundamental frequency of the plate.
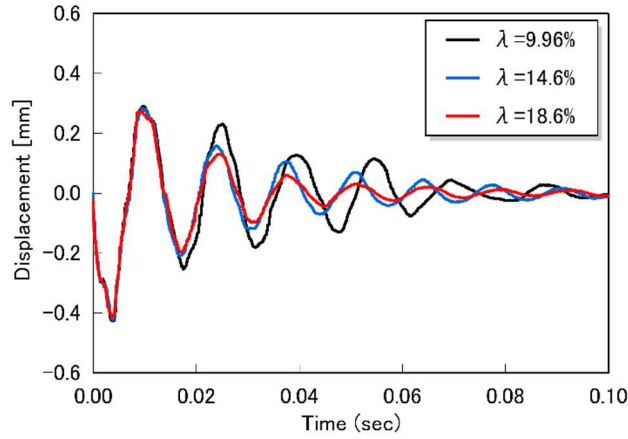
Figure 5: Effect of the mass ratio
(cubic container, h=8.0mm, ϕ 4.0mm, steel particles)
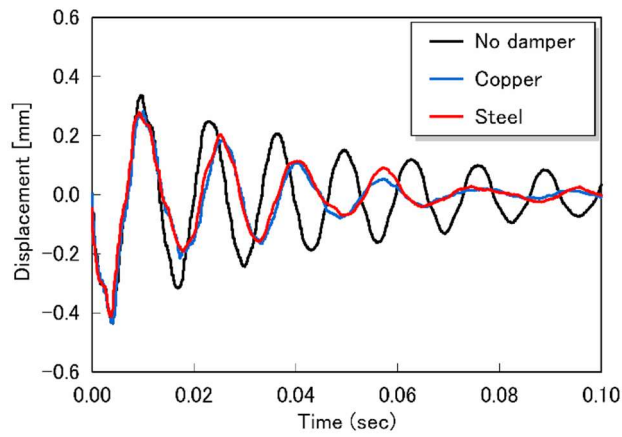
Figure 6: Effect of the particle material
(cubic container, h=8.0mm, λ =14.6%, ϕ 6.35mm)

2.2 Experimental results

Figure 4 shows the effect of the shape of the container on the damping performance. This figure also shows a plot of the displacement of the center of the plate versus time. It is clear that damping is efficient in the presence of granular materials. There is little difference in the time history between the cubic and cylindrical containers. Therefore, it is shown that the shape of the container does not affect the damping performance.

Figure 5 shows the effect of the mass ratio λ on the damping performance. It is shown that the damping performance increases with the mass ratio. This appears to be because more

momentum transfer occurs as the mass ratio increases.

Figure 6 shows the effect of the particle material on the damping performance under the same mass ratio. Although the same mass ratios were used for the steel and copper particles, the number of steel particles was different from the number of copper particles owing to the density difference. It is clear that the damping performance is independent of the particle material.

3 NUMERICAL METHOD

To capture the behavior of the entire system in detail, the equations of motion for the plate and each particle should be solved. In this paper, physical interpretations of the damping behavior of the plate with the particle damper are given with the help of coupled FEM-DEM simulations. In this study, the simulation code was developed using C++ language.
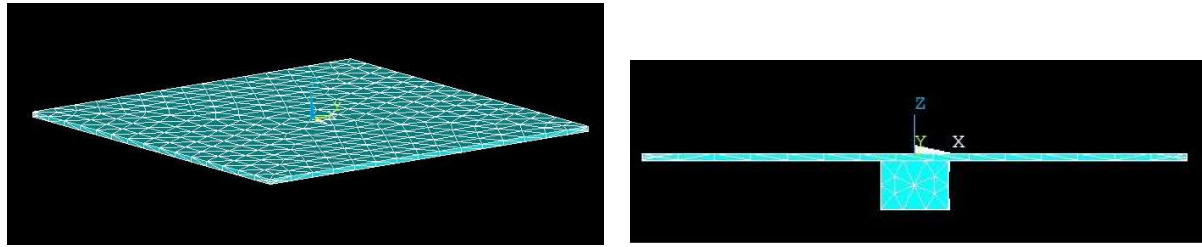
(a) Single view drawing   (b) Side view

Figure 7: FEM mesh representing the plate

3.1 Model of the vibration system

Figure 7 shows the FEM mesh representing the plate with the particle damper used in this numerical analysis. The plate was modeled with tetrahedral elements. The equation of motion for the plate is given by

$$[M]\{\ddot{u}\} + [C]\{\dot{u}\} + [K]\{u\} = \{f\}, \tag{2}$$

where $\{u\}$ is the displacement of each node and $[M]$, $[C]$ and $[K]$ are the mass, damping and stiffness matrices, respectively. The dots denote time derivatives and $\{f\}$ is the external force vector. Rayleigh damping was used to approximate the damping behavior of the plate without granular materials.

The equation of motion for particle i is given by

$$\begin{aligned} m\ddot{\boldsymbol{p}}_i &= \boldsymbol{F}_i - m\boldsymbol{g} \\ I\ddot{\theta}_i &= \boldsymbol{T}_i \end{aligned}, \tag{3}$$

where m is the particle mass, I is the moment of inertia of the particle, $\boldsymbol{p}$ is the position vector of the center of gravity of the particle, θ is the angular displacement vector, $\boldsymbol{F}_i$ is the sum of the contact forces acting on the particles and $\boldsymbol{T}_i$ is the sum of the torque generated by the contact forces.

The normal component of the contact force acting on a particle is given by [10]

$$f_N = k_N \delta_N{}^{3/2} + \eta_N \dot{\delta}_N, \tag{4}$$

$$\eta_N = \alpha \sqrt{m k_N} \delta_N^{1/4}, \tag{5}$$

where δ_N and $\dot{\delta}_N$ are the normal displacement and velocity of particle i relative to particle j, respectively. The value of α is determined by the coefficient of restitution.

The tangential component f_T of the contact force is given as follows if there is no slipping [10]:

$$f_T = k_T \delta_T{}^{1/2} \delta_T + c_T \dot{\delta}_T, \tag{6}$$
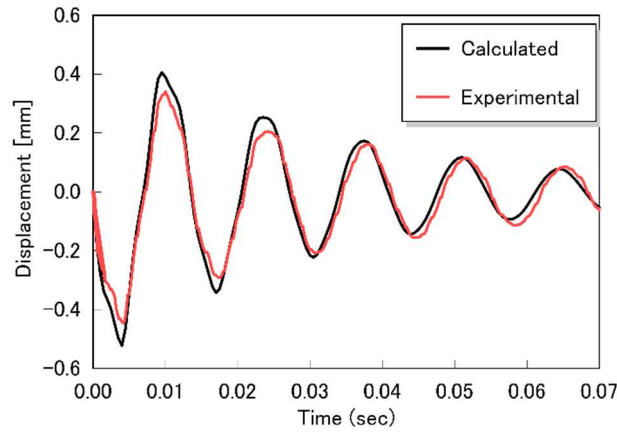
(a) Cubic container without granular materials
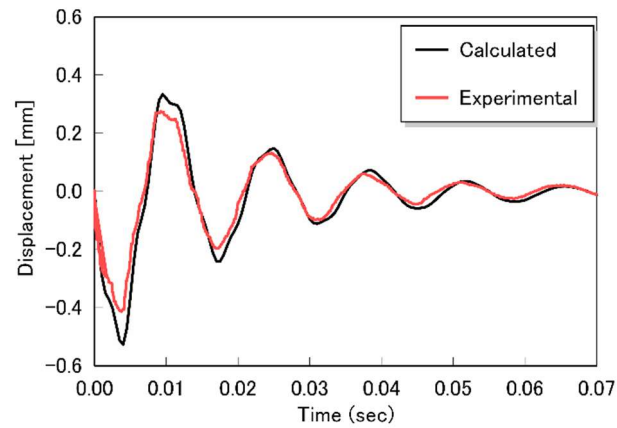
(b) Cubic container with granular materials
(h=8.5mm, λ =18.8%, ϕ 4.0mm, steel particles)
Figure 8: Experimental and analytical results

where δ_T and $\dot{\delta}_T$ are the tangential displacement and velocity, respectively.

In the case of slipping, the following equation is satisfied:

$$f_T > \mu_s |f_N|, \tag{7}$$

where μ_s is the coefficient of static friction.

When Eq. (7) is satisfied, the tangential component f_T of the contact force is expressed as

$$f_T = -\mu_k f_N \dot{\delta}_{T/} |\dot{\delta}_T|, \tag{8}$$

where μ_k is the coefficient of kinetic friction. The contact force acting on the impactor was also calculated using Eqs. (3)–(8).

The procedure for the calculation is as follows. First, collision detection is performed and the contact force is calculated. This force is used to analyze the vibration of the plate by the FEM. Then the particle motion is analyzed using Eq. (3). The same procedure is repeated for all the particles.

3.2 Analytical results

Figures 8(a) and 8(b) show experimental and analytical results in the same plane as in Figure 4. For the cases in Figures 8(a) and 8(b), the cubic containers without and with granular materials, respectively, were used. As shown in Figures 8(a) and 8(b), it was found that the calculated results agree with the experimental results. Therefore, the analytical approach in this study is very effective for estimating the damping effect in the dynamics of a plate with granular materials.

4 CONCLUSIONS

The dynamics of a square plate with a particle damper was investigated both experimentally and analytically. The combination of the finite element method with the discrete element method yielded an analytical solution for estimating the transient impact response of a plate with a particle damper. From the experimental results, it was shown that the shape of the container does not affect the damping performance. It was also shown that the mass ratio affects the damping performance whereas the particle material does not affect the damping performance. An analytical approach using the coupled FEM-DEM is very effective for estimating the transient vibration of a plate with a particle damper.

REFERENCES

[1] Kumar, M. S., Mohanasundaram, K. M. and Sathishkumar, B. A case study on vibration control in a boring barusing particle damping, *International Journal of Engineering Science and Technology* (2011) **3**(8): 177-184.

[2] Veeramuthuvel, P., Sairajan, K. K. and Shankar, K. Vibration suppression of printed circuit boards using an external particle damper, *Journal of Sound and Vibration* (2016) **366**: 98-116.

[3] Tomitaka, R., Nojima, R. and Masuda, K. Study on reduction of floor impact sound by heavy impact source using double-layered ceiling with damping by granular materials, *Journal of Environmental Engineering* (2016)**81**(719): 29-39.

[4] Marhadi, K. S. and Kinra, V. K. Particle impact damping: effect of mass ratio, material, and shape, *Journal of Sound and Vibration* (2005) **283**: 433-448.

[5] Saeki, M., Mizoguchi, T. and Bitoh, M. Particle damping: Noise characteristics and large-scale simulation, *Journal of Vibration and Control* (2018) 24(17): 3920–3930.

[6] Cundall, P. A. and Struck, O. D. A discrete numerical model for granular assemblies, *Geotechnique* (1979)**29**: 47-65.

[7] Fang, X. and Tang, J. A direct simulation Monte Carlo approach for the analysis of granular damping, ASME *J. Computational and Nonlinear dynamics* (2007) **2**: 180–189.

[8] Wang, D. and Wu, C. Vibration response prediction of plate with particle dampers using cosimulation method, *Shock and Vibration* (2015)**7**: 1-7.

[9] Xia, Z., Liu, X. and Shan, Y. Coupling simulation algolithm of dynamic feature of a plate with particle dampers under centrifugal loads, ASME *J. Vibration and Acoustics* (2011) **133**: 041002- 1–6.

[10] Tsuji, Y., Tanaka, T. and Ishida, T. Lagrangian numerical simulation of plug flow of cohesionless particles in a horizontal pipe, *Powder Technology* (1992)**71**: 239-250.

AUTHORS INDEX